

LATEST TRENDS on SYSTEMS - VOLUME I

**Proceedings of the 18th International Conference on Systems
(part of CSCC '14)**

**Santorini Island, Greece
July 17-21, 2014**

LATEST TRENDS on SYSTEMS - VOLUME I

**Proceedings of the 18th International Conference on Systems
(part of CSCC '14)**

**Santorini Island, Greece
July 17-21, 2014**

Copyright © 2014, by the editors

All the copyright of the present book belongs to the editors. All rights reserved. No part of this publication may be reproduced, stored in a retrieval system, or transmitted in any form or by any means, electronic, mechanical, photocopying, recording, or otherwise, without the prior written permission of the editors.

All papers of the present volume were peer reviewed by no less than two independent reviewers. Acceptance was granted when both reviewers' recommendations were positive.

Series: Recent Advances in Electrical Engineering Series | 37

ISSN: 1790-5117

ISBN: 978-1-61804-243-9

LATEST TRENDS on SYSTEMS - VOLUME I

**Proceedings of the 18th International Conference on Systems
(part of CSCC '14)**

**Santorini Island, Greece
July 17-21, 2014**

Organizing Committee

Editors:

Prof. Nikos Mastorakis, Technical University of Sofia, Bulgaria and HNA, Greece
Prof. Kleanthis Psarris, The City University of New York, USA
Prof. George Vachtsevanos, Georgia Institute of Technology, Atlanta, Georgia, USA
Prof. Philippe Dondon, École Nationale Supérieure d'Électronique, Talence, Cedex, France
Prof. Valeri Mladenov, Technical University of Sofia, Bulgaria
Prof. Aida Bulucea, University of Craiova, Craiova, Romania
Prof. Imre Rudas, Obuda University, Budapest, Hungary
Prof. Olga Martin, Politehnica University of Bucharest, Romania

Associate Editors:

Vladimír Vašek
Libor Pekař
Eduardo Mario Dias
Nikolaos Bardis

Steering Committee:

Prof. Theodore B. Trafalis, University of Oklahoma, USA
Prof. Charles A. Long, Professor Emeritus, University of Wisconsin, Stevens Point, Wisconsin, USA
Prof. Maria Isabel García-Planas, Universitat Politècnica de Catalunya, Spain
Prof. Reinhard Neck, Klagenfurt University, Klagenfurt, Austria
Prof. Myriam Lazard, Institut Supérieur d'Ingenierie de la Conception, Saint Die, France
Prof. Zoran Bojkovic, University of Belgrade, Serbia
Prof. Claudio Talarico, Gonzaga University, Spokane, USA

International Scientific Committee:

Prof. Lotfi Zadeh (IEEE Fellow, University of Berkeley, USA)
Prof. Leon Chua (IEEE Fellow, University of Berkeley, USA)
Prof. Michio Sugeno (RIKEN Brain Science Institute (RIKEN BSI), Japan)
Prof. Dimitri Bertsekas (IEEE Fellow, MIT, USA)
Prof. Demetri Terzopoulos (IEEE Fellow, ACM Fellow, UCLA, USA)
Prof. Georgios B. Giannakis (IEEE Fellow, University of Minnesota, USA)
Prof. George Vachtsevanos (Georgia Institute of Technology, USA)
Prof. Brian Barsky (IEEE Fellow, University of Berkeley, USA)
Prof. Aggelos Katsaggelos (IEEE Fellow, Northwestern University, USA)
Prof. Josef Sifakis (Turing Award 2007, CNRS/Verimag, France)
Prof. Hisashi Kobayashi (Princeton University, USA)
Prof. Kinshuk (Fellow IEEE, Massey Univ. New Zeland),
Prof. Leonid Kazovsky (Stanford University, USA)
Prof. Narsingh Deo (IEEE Fellow, ACM Fellow, University of Central Florida, USA)
Prof. Kamisetty Rao (Fellow IEEE, Univ. of Texas at Arlington, USA)
Prof. Anastassios Venetsanopoulos (Fellow IEEE, University of Toronto, Canada)
Prof. Steven Collicott (Purdue University, West Lafayette, IN, USA)
Prof. Nikolaos Paragios (Ecole Centrale Paris, France)
Prof. Nikolaos G. Bourbakis (IEEE Fellow, Wright State University, USA)
Prof. Stamatios Kartalopoulos (IEEE Fellow, University of Oklahoma, USA)
Prof. Irwin Sandberg (IEEE Fellow, University of Texas at Austin, USA),
Prof. Michael Sebek (IEEE Fellow, Czech Technical University in Prague, Czech Republic)
Prof. Hashem Akbari (University of California, Berkeley, USA)
Prof. Yuriy S. Shmaliy, (IEEE Fellow, The University of Guanajuato, Mexico)
Prof. Lei Xu (IEEE Fellow, Chinese University of Hong Kong, Hong Kong)
Prof. Paul E. Dimotakis (California Institute of Technology Pasadena, USA)

Prof. Martin Pelikan (UMSL, USA)
Prof. Patrick Wang (MIT, USA)
Prof. Wasfy B Mikhael (IEEE Fellow, University of Central Florida Orlando, USA)
Prof. Sunil Das (IEEE Fellow, University of Ottawa, Canada)
Prof. Panos Pardalos (University of Florida, USA)
Prof. Nikolaos D. Katopodes (University of Michigan, USA)
Prof. Bimal K. Bose (Life Fellow of IEEE, University of Tennessee, Knoxville, USA)
Prof. Janusz Kacprzyk (IEEE Fellow, Polish Academy of Sciences, Poland)
Prof. Sidney Burrus (IEEE Fellow, Rice University, USA)
Prof. Biswa N. Datta (IEEE Fellow, Northern Illinois University, USA)
Prof. Mihai Putinar (University of California at Santa Barbara, USA)
Prof. Wlodzislaw Duch (Nicolaus Copernicus University, Poland)
Prof. Tadeusz Kaczorek (IEEE Fellow, Warsaw University of Technology, Poland)
Prof. Michael N. Katehakis (Rutgers, The State University of New Jersey, USA)
Prof. Pan Agathoklis (Univ. of Victoria, Canada)
Dr. Subhas C. Misra (Harvard University, USA)
Prof. Martin van den Toorn (Delft University of Technology, The Netherlands)
Prof. Malcolm J. Crocker (Distinguished University Prof., Auburn University, USA)
Prof. Urszula Ledzewicz, Southern Illinois University, USA.
Prof. Dimitri Kazakos, Dean, (Texas Southern University, USA)
Prof. Ronald Yager (Iona College, USA)
Prof. Athanassios Manikas (Imperial College, London, UK)
Prof. Keith L. Clark (Imperial College, London, UK)
Prof. Argyris Varonides (Univ. of Scranton, USA)
Prof. S. Furfari (Direction Generale Energie et Transports, Brussels, EU)
Prof. Constantin Udriste, University Politehnica of Bucharest, ROMANIA
Dr. Michelle Luke (Univ. Berkeley, USA)
Prof. Patrice Brault (Univ. Paris-sud, France)
Prof. Jim Cunningham (Imperial College London, UK)
Prof. Philippe Ben-Abdallah (Ecole Polytechnique de l'Universite de Nantes, France)
Prof. Photios Anninos (Medical School of Thrace, Greece)
Prof. Ichiro Hagiwara, (Tokyo Institute of Technology, Japan)
Prof. Andris Buikis (Latvian Academy of Science, Latvia)
Prof. Akshai Aggarwal (University of Windsor, Canada)
Prof. George Vachtsevanos (Georgia Institute of Technology, USA)
Prof. Ulrich Albrecht (Auburn University, USA)
Prof. Imre J. Rudas (Obuda University, Hungary)
Prof. Alexey L Sadovskii (IEEE Fellow, Texas A&M University, USA)
Prof. Amedeo Andreotti (University of Naples, Italy)
Prof. Ryszard S. Choras (University of Technology and Life Sciences Bydgoszcz, Poland)
Prof. Remi Leandre (Universite de Bourgogne, Dijon, France)
Prof. Moustapha Diaby (University of Connecticut, USA)
Prof. Brian McCartin (New York University, USA)
Prof. Elias C. Aifantis (Aristotle Univ. of Thessaloniki, Greece)
Prof. Anastasios Lyrintzis (Purdue University, USA)
Prof. Charles Long (Prof. Emeritus University of Wisconsin, USA)
Prof. Marvin Goldstein (NASA Glenn Research Center, USA)
Prof. Costin Cepisca (University POLITEHNICA of Bucharest, Romania)
Prof. Kleanthis Psarris (University of Texas at San Antonio, USA)
Prof. Ron Goldman (Rice University, USA)
Prof. Ioannis A. Kakadiaris (University of Houston, USA)
Prof. Richard Tapia (Rice University, USA)
Prof. F.-K. Benra (University of Duisburg-Essen, Germany)
Prof. Milivoje M. Kostic (Northern Illinois University, USA)

Prof. Helmut Jaberg (University of Technology Graz, Austria)
Prof. Ardeshir Anjomani (The University of Texas at Arlington, USA)
Prof. Heinz Ulbrich (Technical University Munich, Germany)
Prof. Reinhard Leithner (Technical University Braunschweig, Germany)
Prof. Elbrous M. Jafarov (Istanbul Technical University, Turkey)
Prof. M. Ehsani (Texas A&M University, USA)
Prof. Sesh Commuri (University of Oklahoma, USA)
Prof. Nicolas Galanis (Universite de Sherbrooke, Canada)
Prof. S. H. Sohrab (Northwestern University, USA)
Prof. Rui J. P. de Figueiredo (University of California, USA)
Prof. Valeri Mladenov (Technical University of Sofia, Bulgaria)
Prof. Hiroshi Sakaki (Meisei University, Tokyo, Japan)
Prof. Zoran S. Bojkovic (Technical University of Belgrade, Serbia)
Prof. K. D. Klaes, (Head of the EPS Support Science Team in the MET Division at EUMETSAT, France)
Prof. Emira Maljevic (Technical University of Belgrade, Serbia)
Prof. Kazuhiko Tsuda (University of Tsukuba, Tokyo, Japan)
Prof. Milan Stork (University of West Bohemia , Czech Republic)
Prof. C. G. Helmis (University of Athens, Greece)
Prof. Lajos Barna (Budapest University of Technology and Economics, Hungary)
Prof. Nobuoki Mano (Meisei University, Tokyo, Japan)
Prof. Nobuo Nakajima (The University of Electro-Communications, Tokyo, Japan)
Prof. Victor-Emil Neagoe (Polytechnic University of Bucharest, Romania)
Prof. P. Vanderstraeten (Brussels Institute for Environmental Management, Belgium)
Prof. Annaliese Bischoff (University of Massachusetts, Amherst, USA)
Prof. Virgil Tiponut (Politehnica University of Timisoara, Romania)
Prof. Andrei Kolyshkin (Riga Technical University, Latvia)
Prof. Fumiaki Imado (Shinshu University, Japan)
Prof. Sotirios G. Ziavras (New Jersey Institute of Technology, USA)
Prof. Constantin Volosencu (Politehnica University of Timisoara, Romania)
Prof. Marc A. Rosen (University of Ontario Institute of Technology, Canada)
Prof. Thomas M. Gatton (National University, San Diego, USA)
Prof. Leonardo Pagnotta (University of Calabria, Italy)
Prof. Yan Wu (Georgia Southern University, USA)
Prof. Daniel N. Riahi (University of Texas-Pan American, USA)
Prof. Alexander Grebennikov (Autonomous University of Puebla, Mexico)
Prof. Bennie F. L. Ward (Baylor University, TX, USA)
Prof. Guennadi A. Kouzaev (Norwegian University of Science and Technology, Norway)
Prof. Eugene Kindler (University of Ostrava, Czech Republic)
Prof. Geoff Skinner (The University of Newcastle, Australia)
Prof. Hamido Fujita (Iwate Prefectural University(IPU), Japan)
Prof. Francesco Muzi (University of L'Aquila, Italy)
Prof. Claudio Rossi (University of Siena, Italy)
Prof. Sergey B. Leonov (Joint Institute for High Temperature Russian Academy of Science, Russia)
Prof. Arpad A. Fay (University of Miskolc, Hungary)
Prof. Lili He (San Jose State University, USA)
Prof. M. Nasseh Tabrizi (East Carolina University, USA)
Prof. Alaa Eldin Fahmy (University Of Calgary, Canada)
Prof. Paul Dan Cristea (University "Politehnica" of Bucharest, Romania)
Prof. Gh. Pascovici (University of Koeln, Germany)
Prof. Pier Paolo Delsanto (Politecnico of Torino, Italy)
Prof. Radu Munteanu (Rector of the Technical University of Cluj-Napoca, Romania)
Prof. Ioan Dumitrache (Politehnica University of Bucharest, Romania)
Prof. Miquel Salgot (University of Barcelona, Spain)
Prof. Amaury A. Caballero (Florida International University, USA)

Prof. Maria I. Garcia-Planas (Universitat Politecnica de Catalunya, Spain)
Prof. Petar Popivanov (Bulgarian Academy of Sciences, Bulgaria)
Prof. Alexander Gegov (University of Portsmouth, UK)
Prof. Lin Feng (Nanyang Technological University, Singapore)
Prof. Colin Fyfe (University of the West of Scotland, UK)
Prof. Zhaohui Luo (Univ of London, UK)
Prof. Wolfgang Wenzel (Institute for Nanotechnology, Germany)
Prof. Weilian Su (Naval Postgraduate School, USA)
Prof. Phillip G. Bradford (The University of Alabama, USA)
Prof. Ray Hefferlin (Southern Adventist University, TN, USA)
Prof. Gabriella Bognar (University of Miskolc, Hungary)
Prof. Hamid Abachi (Monash University, Australia)
Prof. Karlheinz Spindler (Fachhochschule Wiesbaden, Germany)
Prof. Josef Boercsoek (Universitat Kassel, Germany)
Prof. Eyad H. Abed (University of Maryland, Maryland, USA)
Prof. F. Castanie (TeSA, Toulouse, France)
Prof. Robert K. L. Gay (Nanyang Technological University, Singapore)
Prof. Andrzej Ordys (Kingston University, UK)
Prof. Harris Catrakis (Univ of California Irvine, USA)
Prof. T Bott (The University of Birmingham, UK)
Prof. T.-W. Lee (Arizona State University, AZ, USA)
Prof. Le Yi Wang (Wayne State University, Detroit, USA)
Prof. Oleksander Markovskyy (National Technical University of Ukraine, Ukraine)
Prof. Suresh P. Sethi (University of Texas at Dallas, USA)
Prof. Hartmut Hillmer (University of Kassel, Germany)
Prof. Bram Van Putten (Wageningen University, The Netherlands)
Prof. Alexander Iomin (Technion - Israel Institute of Technology, Israel)
Prof. Roberto San Jose (Technical University of Madrid, Spain)
Prof. Minvydas Ragulskis (Kaunas University of Technology, Lithuania)
Prof. Arun Kulkarni (The University of Texas at Tyler, USA)
Prof. Joydeep Mitra (New Mexico State University, USA)
Prof. Vincenzo Niola (University of Naples Federico II, Italy)
Prof. Ion Chrysosoverghi (National Technical University of Athens, Greece)
Prof. Dr. Aydin Akan (Istanbul University, Turkey)
Prof. Sarka Necasova (Academy of Sciences, Prague, Czech Republic)
Prof. C. D. Memos (National Technical University of Athens, Greece)
Prof. S. Y. Chen, (Zhejiang University of Technology, China and University of Hamburg, Germany)
Prof. Duc Nguyen (Old Dominion University, Norfolk, USA)
Prof. Tuan Pham (James Cook University, Townsville, Australia)
Prof. Rossella Cancelliere (University of Torino, Italy)
Prof. Dr-Eng. Christian Bouquegneau (Faculty Polytechnique de Mons, Belgium)
Prof. Wladyslaw Mielczarski (Technical University of Lodz, Poland)
Prof. Ibrahim Hassan (Concordia University, Montreal, Quebec, Canada)
Prof. Stavros J. Baloyannis (Medical School, Aristotle University of Thessaloniki, Greece)
Prof. Vilem Srovnal, (Technical University of Ostrava, Czech Republic)
Prof. J. M. Giron-Sierra (Universidad Complutense de Madrid, Spain)
Prof. Walter Dosch (University of Luebeck, Germany)
Prof. Rudolf Freund (Vienna University of Technology, Austria)
Prof. Erich Schmidt (Vienna University of Technology, Austria)
Prof. Alessandro Genco (University of Palermo, Italy)
Prof. Martin Lopez Morales (Technical University of Monterey, Mexico)
Prof. Ralph W. Oberste-Vorth (Marshall University, USA)
Prof. Vladimir Damgov (Bulgarian Academy of Sciences, Bulgaria)
Prof. P. Borne (Ecole Central de Lille, France)

Additional Reviewers

Santoso Wibowo	CQ University, Australia
Lesley Farmer	California State University Long Beach, CA, USA
Xiang Bai	Huazhong University of Science and Technology, China
Jon Burley	Michigan State University, MI, USA
Genqi Xu	Tianjin University, China
Zhong-Jie Han	Tianjin University, China
Kazuhiko Natori	Toho University, Japan
João Bastos	Instituto Superior de Engenharia do Porto, Portugal
José Carlos Metrôlho	Instituto Politecnico de Castelo Branco, Portugal
Hessam Ghasemnejad	Kingston University London, UK
Matthias Buyle	Artesis Hogeschool Antwerpen, Belgium
Minhui Yan	Shanghai Maritime University, China
Takuya Yamano	Kanagawa University, Japan
Yamagishi Hiromitsu	Ehime University, Japan
Francesco Zirilli	Sapienza Università di Roma, Italy
Sorinel Oprisan	College of Charleston, CA, USA
Ole Christian Boe	Norwegian Military Academy, Norway
Deolinda Rasteiro	Coimbra Institute of Engineering, Portugal
James Vance	The University of Virginia's College at Wise, VA, USA
Valeri Mladenov	Technical University of Sofia, Bulgaria
Angel F. Tenorio	Universidad Pablo de Olavide, Spain
Bazil Taha Ahmed	Universidad Autonoma de Madrid, Spain
Francesco Rotondo	Polytechnic of Bari University, Italy
Jose Flores	The University of South Dakota, SD, USA
Masaji Tanaka	Okayama University of Science, Japan
M. Javed Khan	Tuskegee University, AL, USA
Frederic Kuznik	National Institute of Applied Sciences, Lyon, France
Shinji Osada	Gifu University School of Medicine, Japan
Dmitrijs Serdjuks	Riga Technical University, Latvia
Philippe Dondon	Institut polytechnique de Bordeaux, France
Abelha Antonio	Universidade do Minho, Portugal
Konstantin Volkov	Kingston University London, UK
Manoj K. Jha	Morgan State University in Baltimore, USA
Eleazar Jimenez Serrano	Kyushu University, Japan
Imre Rudas	Obuda University, Budapest, Hungary
Andrey Dmitriev	Russian Academy of Sciences, Russia
Tetsuya Yoshida	Hokkaido University, Japan
Alejandro Fuentes-Penna	Universidad Autónoma del Estado de Hidalgo, Mexico
Stavros Ponis	National Technical University of Athens, Greece
Moran Wang	Tsinghua University, China
Kei Eguchi	Fukuoka Institute of Technology, Japan
Miguel Carriegos	Universidad de Leon, Spain
George Barreto	Pontificia Universidad Javeriana, Colombia
Tetsuya Shimamura	Saitama University, Japan

Table of Contents

Plenary Lecture 1: Floating Offshore Wind Turbines: The Technologies and the Economics <i>Paul D. Sclavounos</i>	22
Plenary Lecture 2: Detecting Critical Elements in Large Networks <i>Panos M. Pardalos</i>	24
Plenary Lecture 3: Overview of the Main Metaheuristics used for the Optimization of Complex Systems <i>Pierre Borne</i>	26
Plenary Lecture 4: Minimum Energy Control of Fractional Positive Electrical Circuits <i>Tadeusz Kaczorek</i>	28
Plenary Lecture 5: Unmanned Systems for Civilian Operations <i>George Vachtsevanos</i>	30
Plenary Lecture 6: Iterative Extended UFIR Filtering in Applications to Mobile Robot Indoor Localization <i>Yuriy S. Shmaliy</i>	32
PART I	33
Short Distance Earth Current Measurements Related to Atmospheric Electric Fields <i>Ernst D. Schmitter</i>	35
Implementation of Direction Cosine Matrix on a PSoC-5 Microcontroller for Robot Localization on Inclined Terrains <i>Garth Herman, Aleksander Milshteyn, Airs Lin, Manuel Garcia, Charles Liu, Khosrow Rad, Darrel Guillaume, Helen Boussalis</i>	39
Indirect Adaptive Control for Underwater Vehicles on Base of Nonlinear Estimator of Disturbances <i>V. Kh. Pshikhopov, M. Yu. Medvedev, B. V. Gurenko, A. M. Maevsky</i>	46
The Representativeness Reliability Importance Measure <i>Josep Freixas, Montserrat Pons</i>	52
CDM Controller Order and Disturbance Rejection Ability <i>Joao Paulo Coelho, Wojciech Giernacki, Jose Boaventura-Cunha</i>	57
The Influence of Variable Friction Coefficient on Spatial Stability of Slightly Curved Shallow Mixing Layers <i>Andrei Kolyshkin, Valentina Koliskina, Inta Volodko</i>	62

Equations of Motion and Physical Model of Quad-copter in Plain <i>Zdeněk Úředníček, Milan Opluštil</i>	66
OWA – Type Possibilistic Aggregations in a Decision Making Regarding Selection of Investments <i>Gia Sirbiladze, Gvantsa Tsulaia</i>	71
Identification of Dynamical Systems using Recurrent Complex-Valued Neural Networks <i>Víctor M. Arellano-Quintana, Ieroham S. Baruch</i>	74
Unitary Theory of Direct Electromechanical Transformers <i>Zdeněk Úředníček</i>	80
Anti-Synchronization of WINDMI Systems via Adaptive Backstepping Control Method and its FPGA Implementation <i>Sundarapandian Vaidyanathan, Christos K. Volos, Ionnis M. Kyprianidis, Ioannis N. Stouboulos, Karthikeyan Rajagopal, Prasina Alexander</i>	86
Analytical Modeling of Pneumatic Muscle Actuator Torque Characteristics <i>Mária Tóthová, Ján Pitel'</i>	92
Combined Effect of Small Curvature and Variable Friction on Temporal Instability of Shallow Mixing Layers <i>Ilmars Iltins, Marija Iltina, Andrei Kolyshkin</i>	96
Application of Self-Tuning Polynomial Controller <i>Stanislav Plšek, Vladimír Vašek</i>	100
Resistive Parameter Identification of a Li-ion Battery Using Sliding Mode Observer <i>Daehyun Kim, Taedong Goh, Seung Hun Kim, Sang Woo Kim</i>	104
Statistical Wound-Rotor IM Diagnosis Method Based on Standard Deviation using NVSA <i>Khalid Dahi, Soumia Elhani, Said Guedira</i>	109
A Seven-Term Novel 3-D Chaotic System with Three Quadratic Nonlinearities and its LABVIEW Implementation <i>Sundarapandian Vaidyanathan, Christos K. Volos, Ionnis M. Kyprianidis, Ioannis N. Stouboulos, Karthikeyan Rajagopal, Prasina Alexander</i>	117
The Surface Properties of Linear Low-Density Polyethylene After Radiation Cross-Linking <i>Martin Bednarik, David Manas, Miroslav Manas, Michal Stanek, Jan Navratil, Ales Mizera</i>	123
Pipe Measurement System Using a Laser Range Finder with KINECT <i>K. Yoshida, N. Hidaka, K. Kawasue</i>	127
Edible Oil Comparison by Terahertz Time Domain Spectroscopy System Tera OSCAT <i>Marie Tobolova, Vojtech Kresalek</i>	134

Application of the Static and Dynamic Models in Predicting the Future Strength of Pozzolanic Cements	138
<i>Dimitris C. Tsamatsoulis</i>	
Mobile Meteorological Radar Uses in Crisis Management	147
<i>David Šaur, Stanislav Plšek</i>	
Motion Detection in Thermal Images Sequence Using Wigner Distributions	153
<i>Sn. Pleshkova, Al.Bekyarski</i>	
Fuzzy Control of the Position Servo Motor Drives with Elasticity and Friction	157
<i>Dmitry V. Lukichev, Galina L. Demidova</i>	
Using Fuzzy Logic to Control an Innovative Active Vehicle Suspension System	161
<i>K. Hyniova, L. Smitkova-Janku</i>	
Using Neural Networks to Design Predictive Model of Creation of Aluminium Oxide Layer	168
<i>P. Michal, A. Vagaská, M. Gombár, J. Kmec, E. Spišák, D. Kučerka</i>	
Microwave Pulse Generator	174
<i>R. Krizan, L. Drazan</i>	
Synchronization Error Detection of Data Transmission Errors in Asynchronous Channels	179
<i>Olga Fedorechko, Oleksandr P. Markovskiy, Nikos Doukas, Nikos Bardis</i>	
Statistical Analysis of Surface Roughness in Grinding of Titanium	184
<i>Bílek Ondřej, Javořík Jakub, Sámek David</i>	
New Approach to Building Hierarchy for Patients Attendance in Intensive Care Unit with Use of Fuzzy Information and Dynamic Modeling	189
<i>Maria Milanova, Mikhail Matveev</i>	
3D Data Acquisition and CAD/CAM Systems for CNC Manufacturing of Artificial Limbs	193
<i>Bílek Ondřej, Javořík Jakub, Sámek David</i>	
Unidirectional Coupling Scheme of Nonlinear Circuits via a Memristor	198
<i>Christos K. Volos, Sundarapandian Vaidyanathan, Ioannis M. Kyprianidis, Nikos G. Bardis, Ioannis N. Stouboulos</i>	
Investigation of Thermal Degradation of Vegetable Oils During Frying using Terahertz Time-Domain Spectroscopy	202
<i>Marie Tobolova, Vojtech Kresalek</i>	
Architecture and Design of a Dynamic Real-Time Alarm System for Power Plants	206
<i>Ilse Leal Aulenbacher, Jose Maria Suarez Jurado, Efren R. Coronel Flores</i>	

Measuring and Identification of Oils	211
<i>Hana Vaskova, Martina Buckova</i>	
Tensional Psychological Mechanism and the Topological Invariants of the Tensional Configurations	216
<i>Alin Gilbert Sumedrea</i>	
A Thermoelectric Generator as an Electric Energy Source for the Building Sensors	226
<i>Michal Oplustil, Martin Zalesak, Stanislav Sehnalek, Pavel Chrobak</i>	
Diagnostics and Evaluation of Limit Strain States from Digital Image	230
<i>J. Kmec, E. Fechová, S. Hrehová</i>	
Device for Heat Transport Parameters Monitoring of Solids	234
<i>P. Košťial, I. Ružiak, R. Igaz, Z. Jančíková, V. Rusnák, R. Garzinová, P. Hlaváček</i>	
Oilmarks Detection Algorithm in Steel Plates	239
<i>Doo-Chul Choi, Yong-Ju Jeon, Sang Jun Lee, Jong Pil Yun, Sang Woo Kim</i>	
Temperature Stability of Construction Polymers After Radiation Cross-Linking	243
<i>Ales Mizera, Miroslav Manas, Zdenek Holik, David Manas, Michal Stanek, Jan Navratil, Martin Bednarik</i>	
Unsupervised Robot System using Computational Geometry and Neural Network	247
<i>Marios Poulos</i>	
Testing Thermal Images Characteristics for Thermal Images Quality Estimation	251
<i>Sn. Pleshkova, Al. Bekyarski, K.Peeva</i>	
Nano-Hardness of PA12 After Radiation	257
<i>Martin Ovsik, David Manas, Miroslav Manas, Michal Stanek, Petr Kratky, Vojtech Senkerik</i>	
Developing a Query Interface for Biomedical Questions Answering	262
<i>Ioana Branescu-Raspop, Victor Lorin Purcarea, Radu Dobrescu</i>	
Physical Properties' Determination of PA6/HDPEx Blends	268
<i>Jan Navratil, Miroslav Manas, Michal Stanek, David Manas, Martin Bednarik, Ales Mizera</i>	
Enhancing Images using the Forward-Backward UFIR Algorithm	273
<i>L. J. Morales-Mendoza, M. González-Lee, E. Morales-Mendoza, R. F Vázquez-Bautista, J. Huerta-Chua, S. Pérez-Cáceres, G. Triano-Carballo, O. G. Ibarra-Manzano, Y. S. Shmaliy</i>	
Impact of Irradiation Dose on Mechanical Properties of PA 11	279
<i>Petr Kratky, David Manas, Miroslav Manas, Michal Stanek, Martin Ovsik, Adam Skrobak, Martin Reznicek</i>	

Elearning Platform Assessment for Military Distance Education with Multicriteria Analysis	285
<i>George Rigopoulos, Nikolaos V. Karadimas</i>	
Impact of Irradiation Dose on Mechanical Properties of PMMA	290
<i>Petr Kratky, David Manas, Miroslav Manas, Michal Stanek, Martin Ovsik, Vojtech Senkerik, Jan Navratil</i>	
Visual Information Processing Routines for Intelligent Vehicles	296
<i>Jarnea Alexandru Daniel, Florea Gheorghe, Dobrescu Radu</i>	
The Behaviour of Recycled Material with Particles of Various Sizes at Increased Temperature and their Tensile Properties	302
<i>Vojtech Senkerik, Michal Stanek, Miroslav Manas, David Manas, Adam Skrobak, Jan Navratil</i>	
New Approach to Thresholding and Contour Detection for Object Surface Inspection in Machine Vision	306
<i>K. Židek, A. Hošovský, J. Dubják</i>	
Microcomputer I/O Converter and Control Unit for Heating Systems	310
<i>Libor Pekař, Petr Dostálek, Zdeněk Oborný</i>	
Defect Detection for Vertical Cracks in Hot-slabs using Dual Light Switching Lighting Method	315
<i>Yong-Ju Jeon, Doo-chul Choi, Sang Jun Lee, Jong Pil Yun, Sang Woo Kim</i>	
Two Suboptimal Controller Parameters Tuning Approaches for Systems with Delays: Selected Highlights of Preliminary Studies	321
<i>Libor Pekař, Roman Prokop</i>	
Belonging Probability Inverse Image Technique to Early Detection of Volcanic Eruption	326
<i>B. Yagoubi, S. Benkraouda, A. Bouziane</i>	
Optimization of a Batch Reactor Dimensions	330
<i>David Novosad, Lubomír Macků, Milan Navrátil</i>	
MAP and MMSE Estimation of HEV State of Charge	334
<i>Nazha Abed, Hatem Boujemaa, Sami Touati, Ramdane Hedjar</i>	
Scanning Probe Microscopy Method for Diagnostics of Ultra-Thin Tungsten Films on Silicon Substrate	338
<i>Milan Navrátil, Vojtěch Křesálek, František Hruška, Tomáš Martínek, Josef Kudělka, Jaroslav Sobota</i>	
Feature Level Compensation for Robust Speaker Identification in Mismatched Conditions	344
<i>Sharada V. Chougule, Mahesh S. Chavan</i>	

On Experimental Verification of Vehicle Active Suspension Robust Control	353
<i>K. Hyniova</i>	
A Study of Pressure Distribution Droplets Motion in Convergence-Divergence Shape Microchannel	359
<i>Maryam Ghelichkhani</i>	
Modeling and Optimization of Hydrolysate Yields in Leather Waste Processing	363
<i>Hana Vaskova, Karel Kolomaznik</i>	
Discrete-Time State Estimation Using Unbiased FIR Filters with Minimized Variance	367
<i>Shunyi Zhao, Fei Liu, Yuriy S. Shmaliy</i>	
Applying “ABCD Rule of Dermatoscopy” using Cognitive Systems	374
<i>Ionut Taranu, Iunia Iacovici</i>	
Obstacle Avoidance by Unmanned Aerial Vehicles using Image Recognition Techniques	378
<i>Priya Bajju Parappat, Anand Kumar, R. K. Mittal, Suhel Ahmad Khan</i>	
Pyramid Method for Reversible Discrete Wavelet Transformation of 3D Image	382
<i>Eustache Muteba Ayumba</i>	
Procedural Aspects of Data Seizure	385
<i>Jan Kolouch, Andrea Kropáčová</i>	
PART II	389
Robust Feature Matching for Aerial Visual Odometry	391
<i>Tarek Mouats, Nabil Aouf</i>	
The Cost Function for Extraction of Bound Component from Material	395
<i>D. Janáčková, V. Vašek, K. Kolomazník</i>	
Multiple Pattern-Dependent Controller Design for Markovian Jump Linear Systems	399
<i>Taesoo Kim, Sung Hyun Kim</i>	
Adaptive Continuous-Time Decoupling Control	402
<i>Marek Kubalčík, Vladimír Bobál</i>	
Comparing Accuracy and Solution Times in Coverage Models	408
<i>George P. Alexandris, Nikolaos G. Bardis</i>	
Determination of Thermal Steady State in the Wall with Semi Dirichlet Boundary Conditions	414
<i>Martin Zalesak</i>	

Performance Evaluation of Two Radial Basis Function Neural Network Models	419
<i>Nikolinka G. Christova, Gancho L. Vachkov</i>	
Graphical Analysis of Robust Stability for Fractional Order Time-Delay Systems Integer Order PID Controllers	424
<i>Radek Matušů, Roman Prokop</i>	
Building a Model of Family House Heating System using 1-Wire Sensor Network Protocol	430
<i>Dominik Kujawa</i>	
Multivariable Control of Unstable Systems – A Matrix Equation Approach	438
<i>Roman Prokop, Jiří Korbel</i>	
Comparison of Acoustic Barriers Noise Reductions Evaluated by Different Calculation Methods	443
<i>Claudio Guarnaccia, Joseph Quartieri, Nikos E. Mastorakis</i>	
Relay Feedback Identification of Dynamical SISO Systems – Analysis Settings	450
<i>Roman Prokop, Jiří Korbel, Radek Matušů</i>	
Control of Direct-Driven PMSG for Wind Energy System	455
<i>F. Khater, A. Shaltout, A. Omar</i>	
Signal Condition of Embedded Unit Inputs	462
<i>F. Hruska, M. Navratil, J. Otahal</i>	
An Operational Model of Bus Terminal Management based on Daily Passengers Demands	467
<i>José A. M. de Gouveia, Maurício L. Ferreira, Maria L. R. P. Dias, Melissa S. Porkorny, Eduardo M. Dias</i>	
Holonic Concept in the Heat Production Distribution Control Systems	474
<i>Lubomir Vasek, Viliam Dolinay, Tomas Sysala</i>	
Automatic Complexity Estimation based on Requirements	478
<i>Radek Silhavy, Petr Silhavy, Zdenka Prokopova</i>	
Dynamic Patients Scheduling in the Pediatric Emergency Department	482
<i>Sara Ben Othman, Nesrine Zoghalmi, Slim Hammadi, Alain Quillot, Alain Martinot, Jean-Marie Renard</i>	
Program Modules for Control Applications of Microcontrollers	488
<i>Jan Dolinay, Petr Dostálek, Vladimír Vašek</i>	
Evaluation of SolidWorks Flow Simulation by Ground-Coupled Heat Transfer Test Cases	492
<i>S. Sehnalek, M. Zalesak, J. Vincenec, M. Oplustil, P. Chrobak</i>	

Time Series Predictive Model Application to Air Pollution Assessment	499
<i>Claudio Guarnaccia, Julia Griselda Cerón Bretón, Joseph Quartieri, Carmine Tepedino, Rosa Maria Cerón Bretón</i>	
Educational Microprocessor Development Kit – Low-Cost Access System Application	506
<i>Tomas Sysala, Petr Neumann, Filip Zanka, Lubomir Vasek</i>	
Fuzzy Logic Controller in Servo Drive Control System with Speed Limitation	511
<i>Nikita Smirnov, Dmitry Lukichev</i>	
Chaos Enhanced Differential Evolution with the Dissipative Map for the PID Tuning Problem	516
<i>Roman Senkerik, Michal Pluhacek, Zuzana Kominkova Oplatkova</i>	
A VSC Approach for Wave Energy Converters	521
<i>Aitor J. Garrido, Izaskun Garrido, Mikel Alberdi, Modesto Amundarain, Edorta Carrascal</i>	
Control System for Chemical Thermal Processes	523
<i>Petr Chalupa, Martin Beneš, Jakub Novák, Michaela Bařinová</i>	
Galvanically Isolated Interface for an Oscilloscope	529
<i>Martin Pospisilik, Petr Neumann, Roman Honig, Peter Scheibenreiter</i>	
Identification Control of Oscillatory Dynamical Systems using Recurrent Complex-Valued Neural Networks	534
<i>Ieroham S. Baruch, Víctor M. Arellano-Quintana</i>	
Implementation of Fuzzy MPC on Embedded System	540
<i>Jakub Novak, Petr Chalupa</i>	
Analysis Web Structures Optimization	546
<i>Zdenka Prokopova, Radek Silhavy, Petr Silhavy</i>	
Artificial Intelligence Systems for Knowledge Management in e-Health: The Study of Intelligent Software Agents	551
<i>M. Furmankiewicz, A. Sořtysik-Piorunkiewicz, P. Ziuziański</i>	
Simulation of Time-Continuous Chaotic Systems for the Generating of Random Numbers	557
<i>Roman Senkerik, Michal Pluhacek, Zuzana Kominkova Oplatkova</i>	
Development of Control System for Rehabilitation Device Actuated by Pneumatic Artificial Muscles	562
<i>O. Lířka, M. More</i>	
Analysis of Behavior of Car Stabilizer Bushing	566
<i>Jakub Javorik, David Samek, Ondrej Bilek</i>	

Traffic Management Solutions in Large Cities – the Integrated Centre of Urban Mobility (CIMU) in São Paulo	570
<i>Dariusz Swiatek, Melissa S. Pokorny, Jilmar A. Tatto, José E. Gonçalo, Vidal A. Z. C. Melo, Eduardo M. Dias</i>	
Treatment of Chromium Wastewater using Membrane Separation Processes	577
<i>Pavel Kocurek, Karel Kolomazník, Michaela Bařinová</i>	
Return on Investment in Photovoltaic Panels Verification their Effectiveness	581
<i>P. Chrobak, M. Zalesak, M. Oplustil, S. Sehnalek, J. Vincenec</i>	
Big Data Processing for E-Health Applications using a Decentralized Cloud M2M System	588
<i>George Suciu, Victor Suciu, Octavian Fratu</i>	
Modeling of Protein Sorption on Chromium Sludge as a Tool for Optimization of its Deproteination	594
<i>Michaela Bařinová, Jiří Pecha, Karel Kolomazník</i>	
Real Time Monitoring of Public Transit Passenger Flows through Radio Frequency Identification - RFID Technology Embedded in Fare Smart Cards	599
<i>Maurício L. Ferreira, José A. M. de Gouveia, Eduardo Facchini, Melissa S. Pokorny, Eduardo M. Dias</i>	
Families of Spherical Polynomials: Description and Robust Stability Analysis	606
<i>Radek Matušů</i>	
Mathematical Description of Magnesium Oxide Extraction from Chrome-Tanned Leather Waste	611
<i>Michaela Bařinová, Karel Kolomazník</i>	
The ITS Components in the Optimization Control of People Vehicles Circulation at the Brazilian Ports	616
<i>Vander S. de Abreu, Luiz N. Rossi, Eduardo M. Dias</i>	
Computer Application for Determination of Optimal Economic Costs of Biomaterial Waste Treatment by Enzymatic Hydrolysis	621
<i>H. Charvátová, D. Janáčová, V. Vašek, K. Kolomazník</i>	
Automatic Recognition and Synthesis System of Arabic Digit	625
<i>H. Tebbi, M. Hamadouche, H. Azzoune</i>	
On the Usage of Differential Evolution for Effort Estimation	632
<i>T. Urbanek, Z. Prokopova, R. Silhavy</i>	
Measurement and Simulation of Electromagnetic Interference in Low Frequencies Range	636
<i>Jiří Otáhal, František Hruška, Stanislav Sehnálek</i>	

Power Spectral Density in the RFID Systems its Impacts in Celular Systems	640
<i>Leandro R. Sergio, Maria L. R. P. Dias, Sergio L. Pereira, Eduardo M. Dias</i>	
Parameterization of Module for Testing of Thermal Stability in the Room	647
<i>H. Charvátová, M. Zálešák, S. Sehnálek</i>	
Modelling and Analysis of Neural Network and Perturb and Observe MPPT Algorithm for PV Array Using Boost Converter	651
<i>Naoufel Khaldi, Hassan Mahmoudi, Malika Zazi, Youssef Barradi</i>	
Computer Simulation of the Heating Sensor PIR Detector by Radiation	656
<i>R. Drga, D. Janáčková, H. Charvátová</i>	
Electromagnetic Field Distribution within a Semi Anechoic Chamber	662
<i>Martin Pospíšilik, Josef Soldan</i>	
The Role of Traceability in the Pharmaceutical Safety Supply Chain	668
<i>Jair Calixto, Maria L. R. P. Dias, Melissa S. Pokorny, Eduardo M. Dias</i>	
Testing the Properties of Materials used for the Measurement of the PIR Detector in the Infrared Range	674
<i>R. Drga, D. Janáčková, H. Charvátová</i>	
Vehicle Inspection & Maintenance Program in São Paulo - Results and Environmental Benefits	679
<i>Marcelo C. Branco, Fábio C. Branco, Gabriel M. Branco, Eduardo M. Dias, Alfred Szwarc</i>	
Communication Requirements of Laboratory Management System	686
<i>M. Krbeček, F. Schauer, K. Vlček</i>	
ITS to Monitor Small Vessels Movements within Port Area - A Study at Santos Estuary	692
<i>Aureo E. P. Figueiredo, Sérgio L. Hoeflich, Maria L. R. P. Dias, Sergio L. Pereira, Luiz N. Rossi, Eduardo M. Dias</i>	
Numerical Model of Behavior of Pneumatic Actuator	696
<i>Jakub Javorik</i>	
Plasticity of the Error Monitoring and Processing System	700
<i>Menizibeya O. Welcome, Nikos E. Mastorakis, Vladimir A. Pereverzev</i>	
Conversion of the METCM into the METEO-11	708
<i>Karel Šilinger, Ladislav Potužák, Jiří Šotnar</i>	
Criteria for Efficiency Determination of Inspection Maintenance Programs	714
<i>Gabriel M. Branco, Fábio C. Branco, Marcelo C. Branco, Eduardo M. Dias, José M. Napoleone, Alfred Szwarc</i>	

Electronic Switch for Accumulator Connection in a Backup Power Source	720
<i>Martin Pospisilik, Tomas Dulik</i>	
ITS Components in Risk Management in the Port of Santos	726
<i>Alexsandro S. de Lima, Melissa S. Pokorny, Eduardo M. Dias</i>	
Authors Index	731

Plenary Lecture 1

Floating Offshore Wind Turbines: The Technologies and the Economics



Prof. Paul D. Sclavounos

Professor of Mechanical Engineering and Naval Architecture
Massachusetts Institute of Technology (MIT)

77 Massachusetts Avenue
Cambridge MA 02139-4307
USA

E-mail: pauls@mit.edu

Abstract: Wind is a vast, renewable and clean energy source that stands to be a key contributor to the world energy mix in the coming decades. The horizontal axis three-bladed wind turbine is a mature technology and onshore wind farms are cost competitive with coal fired power plants equipped with carbon sequestration technologies and in many parts of the world with natural gas fired power plants.

Offshore wind energy is the next frontier. Vast sea areas with higher and steadier wind speeds are available for the development of offshore wind farms that offer several advantages. Visual, noise and flicker impacts are mitigated when the wind turbines are sited at a distance from the coastline. A new generation of 6-10MW wind turbines with diameters exceeding 160m have been developed for the offshore environment. They can be fully assembled at a coastal facility and installed by a low cost float-out operation. Floater technologies are being developed for the support of multi-megawatt turbines in waters of moderate to large depth, drawing upon developments by the offshore oil & gas industry.

The state of development of the offshore wind energy sector will be discussed. The floating offshore wind turbine technology will be reviewed drawing upon research carried out at MIT since the turn of the 21st century. Floating wind turbine installations worldwide and planned future developments will be presented. The economics of floating offshore wind farms will be addressed along with the investment metrics that must be met for the development of large scale floating offshore wind power plants.

Brief Biography of the Speaker: Paul D. Sclavounos is Professor of Mechanical Engineering and Naval Architecture at the Massachusetts Institute of Technology. His research interests focus upon the marine hydrodynamics of ships, offshore platforms and floating wind turbines. The state-of-the-art computer programs SWAN and SML developed from his research have been widely adopted by the maritime, offshore oil & gas, and wind energy industries. His research

activities also include studies of the economics, valuation and risk management of assets in the crude oil, natural gas, shipping and wind energy sectors. He was the Georg Weinblum Memorial Lecturer in 2010-2011 and the Keynote Lecturer at the Offshore Mechanics and Arctic Engineering Conference in 2013. He is a member of the Board of the North American Committee of Det Norske Veritas since 1997, a member of the Advisory Committee of the US Navy Tempest program since 2006 and a member of the Advisory Board of the Norwegian Center for Offshore Wind Energy Technology since 2009. He has consulted widely for the US Government, shipping, offshore, yachting and energy industries.

<http://meche.mit.edu/people/?id=76>

Keynote Lecture 2

Detecting Critical Elements in Large Networks



Professor Panos M. Pardalos

Center for Applied Optimization (CAO)
Department of Industrial and Systems Engineering,
University of Florida, Gainesville, FL, USA.

and

Laboratory of Algorithms and Technologies for Networks Analysis (LATNA)
National Research University, Higher School of Economics
Moscow, Russia

E-mail: p.m.pardalos@gmail.com

Abstract: In network analysis, the problem of detecting subsets of elements important to the connectivity of a network (i.e., critical elements) has become a fundamental task over the last few years. Identifying the nodes, arcs, paths, clusters, cliques, etc., that are responsible for network cohesion can be crucial for studying many fundamental properties of a network. Depending on the context, finding these elements can help to analyze structural characteristics such as, attack tolerance, robustness, and vulnerability. Furthermore we can classify critical elements based on their centrality, prestige, reputation and can determine dominant clusters and partitions.

From the point of view of robustness and vulnerability analysis, evaluating how well a network will perform under certain disruptive events plays a vital role in the design and operation of such a network. To detect vulnerability issues, it is of particular importance to analyze how well connected a network will remain after a disruptive event takes place, destroying or impairing a set of its elements. The main goal is to identify the set of critical elements that must be protected or reinforced in order to mitigate the negative impact that the absence of such elements may produce in the network. Applications are typically found in homeland security, energy grid, evacuation planning, immunization strategies, financial networks, biological networks, and transportation.

From the member-classification perspective, identifying members with a high reputation and influential power within a social network could be of great importance when designing a marketing strategy. Positioning a product, spreading a rumor, or developing a campaign against drugs and alcohol abuse may have a great impact over society if the strategy is properly targeted among the most influential and recognized members of a community. The recent emergence of social networks such as Facebook, Twitter, LinkedIn, etc. provide countless applications for problems of critical-element detection.

In addition, determining dominant cliques or clusters over different industries and markets via critical clique detection may be crucial in the analysis of market share concentrations and debt

concentrations, spotting possible collusive actions or even helping to prevent future economic crises.

This presentation surveys some of the recent advances for solving these kinds of problems including heuristics, mathematical programming, dynamic programming, approximation algorithms, and simulation approaches. We also summarize some applications that can be found in the literature and present further motivation for the use of these methodologies for network analysis in a broader context.

Brief Biography of the Speaker: Panos M. Pardalos serves as Distinguished Professor of Industrial and Systems Engineering at the University of Florida. He is also an affiliated faculty member of the Computer and Information Science Department, the Hellenic Studies Center, and the Biomedical Engineering Program. He is also the Director of the Center for Applied Optimization. Dr. Pardalos is a world leading expert in global and combinatorial optimization. His recent research interests include network design problems, optimization in telecommunications, e-commerce, data mining, biomedical applications, and massive computing.

Full CV: http://www.ise.ufl.edu/pardalos/files/2011/08/CV_Dec13.pdf

Recent Achievements: <http://www.eng.ufl.edu/news/first-engineering-chair-appointed-under-ufs-preeminence-initiative-goes-to-big-data-expert/>

Profile in Scholar Google: scholar.google.com/scholar?q=P+Pardalos&btnG=&hl=en&as_sdt=0,5

Plenary Lecture 3

Overview of the Main Metaheuristics used for the Optimization of Complex Systems



Professor Pierre Borne

Co-author: Mohamd Benrejeb

Ecole Centrale de Lille

France

E-mail: pierre.borne@ec-lille.fr

Abstract: For complex systems such as in planning and scheduling optimization, the complexity which corresponds usually to hard combinational optimization prevents the implementation of exact solving methodologies which could not give the optimal solution in finite time. It is the reason why engineers prefer to use metaheuristics which are able to produce good solutions in a reasonable computation time. Two types of metaheuristics are presented here:

* The local searches, such as: Tabu Search, Simulated Annealing, GRASP method, Hill Climbing, Tunnelling...

* The global methods which look for a family of solutions such as: Genetic or Evolutionary Algorithms, Ant Colony Optimization, Particle Swarm Optimization, Bees algorithm, Firefly algorithm, Bat algorithm, Harmony search....

Brief Biography of the Speaker: Pierre BORNE received the Master degree of Physics in 1967 and the Master of Electrical Engineering, the Master of Mechanics and the Master of Applied Mathematics in 1968. The same year he obtained the Diploma of "Ingénieur IDN" (French "Grande Ecole"). He obtained the PhD in Automatic Control of the University of Lille in 1970 and the DSc in physics of the same University in 1976. Dr BORNE is author or co-author of about 200 Publications and book chapters and of about 300 communications in international conferences. He is author of 18 books in Automatic Control, co-author of an english-french, french-english « Systems and Control » dictionary and co-editor of the "Concise Encyclopedia of Modelling and Simulation" published with Pergamon Press. He is Editor of two book series in French and co-editor of a book series in English. He has been invited speaker for 40 plenary lectures or tutorials in International Conferences. He has been supervisor of 76 PhD Thesis and member of the committee for about 300 doctoral thesis . He has participated to the editorial board of 20 International Journals including the IEEE, SMC Transactions, and of the Concise Subject Encyclopedia . Dr BORNE has organized 15 international conferences and symposia, among them the 12th and the 17 th IMACS World Congresses in 1988 and 2005, the IEEE/SMC Conferences of 1993 (Le Touquet – France) and of 2002 (Hammamet - Tunisia) , the CESA IMACS/IEEE-SMC multiconferences of 1996 (Lille – France) , of 1998 (Hammamet – Tunisia) , of 2003 (Lille-France) and of 2006 (Beijing, China) and the 12th IFAC LSS symposium (Lille France, 2010) He was chairman or co-chairman of the IPCs of 34 international conferences (IEEE, IMACS, IFAC) and member of the IPCs of more than 200 international conferences. He was the

editor of many volumes and CDROMs of proceedings of conferences. Dr BORNE has participated to the creation and development of two groups of research and two doctoral formations (in Casablanca, Morocco and in Tunis, Tunisia). twenty of his previous PhD students are now full Professors (in France, Morocco, Tunisia, and Poland). In the IEEE/SMC Society Dr BORNE has been AdCom member (1991-1993 ; 1996-1998), Vice President for membership (1992-1993) and Vice President for conferences and meetings (1994-1995, 1998-1999). He has been associate editor of the IEEE Transactions on Systems Man and Cybernetics (1992-2001). Founder of the SMC Technical committee « Mathematical Modelling » he has been president of this committee from 1993 to 1997 and has been president of the « System area » SMC committee from 1997 to 2000. He has been President of the SMC Society in 2000 and 2001, President of the SMC-nomination committee in 2002 and 2003 and President of the SMC-Awards and Fellows committee in 2004 and 2005. He is member of the Advisory Board of the "IEEE Systems Journal" . Dr. Borne received in 1994, 1998 and 2002 Outstanding Awards from the IEEE/SMC Society and has been nominated IEEE Fellow the first of January 1996. He received the Norbert Wiener Award from IEEE/SMC in 1998, the Third Millennium Medal of IEEE in 2000 and the IEEE/SMC Joseph G. Wohl Outstanding Career Award in 2003. He has been vice president of the "IEEE France Section" (2002-2010) and is president of this section since 2011. He has been appointed in 2007 representative of the Division 10 of IEEE for the Region 8 Chapter Coordination sub-committee (2007-2008) He has been member of the IEEE Fellows Committee (2008- 2010) Dr BORNE has been IMACS Vice President (1988-1994). He has been co-chairman of the IMACS Technical Committee on "Robotics and Control Systems" from 1988 to 2005 and in August 1997 he has been nominated Honorary Member of the IMACS Board of Directors. He is since 2008 vice-president of the IFAC technical committee on Large Scale Systems. Dr BORNE is Professor "de Classe Exceptionnelle" at the "Ecole Centrale de Lille" where he has been Head of Research from 1982 to 2005 and Head of the Automatic Control Department from 1982 to 2009. His activities concern automatic control and robust control including implementation of soft computing techniques and applications to large scale and manufacturing systems. He was the principal investigator of many contracts of research with industry and army (for more than three millions €) Dr BORNE is "Commandeur dans l'Ordre des Palmes Académiques" since 2007. He obtained in 1994 the french " Kulman Prize". Since 1996, he is Fellow of the Russian Academy of Non-Linear Sciences and Permanent Guest Professor of the Tianjin University (China). In July 1997, he has been nominated at the "Tunisian National Order of Merit in Education" by the Republic of Tunisia. In June 1999 he has been nominated « Professor Honoris Causa » of the National Institute of Electronics and Mathematics of Moscow (Russia) and Doctor Honoris Causa of the same Institute in October 1999. In 2006 he has been nominated Doctor Honoris Causa of the University of Waterloo (Canada) and in 2007 Doctor Honoris Causa of the Polytechnic University of Bucharest (Romania). He is "Honorary Member of the Senate" of the AGORA University of Romania since May 2008 He has been Vice President of the SEE (French Society of Electrical and Electronics Engineers) from 2000 to 2006 in charge of the technical committees. He his the director of publication of the SEE electronic Journal e-STA and chair the publication committee of the REE Dr BORNE has been Member of the CNU (French National Council of Universities, in charge of nominations and promotions of French Professors and Associate Professors) 1976-1979, 1992-1999, 2004-2007 He has been Director of the French Group of Research (GDR) of the CNRS in Automatic Control from 2002 to 2005 and of a "plan pluriformations" from 2006 to 2009. Dr BORNE has been member of the Multidisciplinary Assessment Committee of the "Canada Foundation for Innovation" in 2004 and 2009. He has been referee for the nominations of 24 professors in USA and Singapore. He is listed in the « Who is Who in the World » since 1999.

Plenary Lecture 4

Minimum Energy Control of Fractional Positive Electrical Circuits



Professor Tadeusz Kaczorek (Fellow IEEE)

Warsaw University of Technology
Poland

Abstract: The talk will consist of two parts. In the first part the minimum energy control of standard positive electrical circuits will be discussed and in the second part the similar problem for fractional positive electrical circuits. Necessary and sufficient conditions for the positivity and reachability of electrical circuits composed of resistors, coils and capacitors will be established. The minimum energy control problem for the standard and fractional positive electrical circuits will be formulated and solved. Procedures for computation of the optimal inputs and minimal values of the performance indices will be given and illustrated by examples of electrical circuits.

Brief Biography of the Speaker: Prof. Tadeusz Kaczorek graduated from the Faculty of Electrical Engineering Warsaw University of Technology in 1956, where in 1962 he defended his doctoral thesis. In 1964, he received a postdoctoral degree. In the years 1965-1970 he was head of the Department of Electronics and Automation, 1969-1970, and Dean of the Faculty of Electrical Engineering University of Warsaw. In the years 1970-1973 Vice-Rector of the Technical University of Warsaw in the years 1970-1981 the director of the Institute of Control and Industrial Electronics Warsaw University of Technology. He was also head of the Department of Control of the above Institute. In 1971 he received the title of Professor and Associate Professor of Warsaw University of Technology. In 1974 he received the title of professor of Warsaw University of Technology. In 1987-1988 he was chairman of the Committee for Automation and Robotics. Since 1986, corresponding member, and since 1998 member of the Polish Academy of Sciences. In 1988-1991 he was Head of the Scientific Academy in Rome. For many years a member of the Foundation for Polish Science. From June 1999 ordinary member of the Academy of Engineering. He is currently a professor at the Faculty of Electrical Engineering of Bialystok and Warsaw University of Technology. Since 1991 he is a member, and now chairman of the Central Commission for Academic Degrees and Titles (Vice-President in 2003-2006). In 2012 he was chairman of the Presidium of the Scientific Committee of the conference devoted to research crash of the Polish Tu-154 in Smolensk methods of science.

Scientific achievements

His research interests relate to automation, control theory and electrical engineering, including analysis and synthesis of circuits and systems with parameters determined and random polynomial methods for the synthesis of control systems and singular systems. Author of 20 books and monographs and over 700 articles and papers in major international journals such as

IEEE Transactions on Automatic Control, Multidimensional Systems and Signal Processing, International Journal of Control, Systems Science and Electrical Engineering Canadian Journal.

He organized and presided over 60 scientific sessions at international conferences, and was a member of about 30 scientific committees. He has lectured at over 20 universities in the United States, Japan, Canada and Europe as a visiting professor. He supervised more than 60 doctoral dissertations completed and reviewed many doctoral theses and dissertations. His dozens of alumni received the title of professor in Poland or abroad.

He is a member of editorial boards of journals such as International Journal of Multidimensional Systems and Signal Processing, Foundations of Computing and Decision Sciences, Archives of Control Sciences. From 1 April 1997, is the editor of the Bulletin of the Academy of Technical Sciences.

Honours, awards and honorary doctorates.

Honours

Tadeusz Kaczorek has been honored with the following awards:

- * Officer's Cross of the Order of Polonia Restituta Polish
- * Meritorious Polish
- * Medal of the National Education Commission

Honorary doctorates

He received honorary degrees from the following universities:

- Silesian University of Technology (2014)
- Rzeszow University of Technology (2012)
- Poznan University of Technology (2011)
- Opole University of Technology (2009)
- Technical University of Lodz (3 December 2008)
- Bialystok University of Technology (August 20, 2008)
- Warsaw University of Technology (22 December 2004)
- Szczecin University of Technology (November 8, 2004)
- Lublin University of Technology (13 May 2004)
- University of Zielona Gora (27 November 2002)

Honorary Member of the Hungarian Academy of Sciences and the Polish Society of Theoretical and Applied Electrical (1999). He received 12 awards of the Minister of National Education of all levels (including 2 team).

Plenary Lecture 5

Unmanned Systems for Civilian Operations



Professor George Vachtsevanos

Professor Emeritus

Georgia Institute of Technology

USA

E-mail: george.vachtsevanos@ece.gatech.edu

Abstract: In this plenary talk we will introduce fundamental concepts of unmanned systems (Unmanned Aerial Vehicles and Unmanned Ground Vehicles) and their emerging utility in civilian operations. We will discuss a framework for multiple UAVs tasked to perform forest fire detection and prevention operations. A ground station with appropriate equipment and personnel functions as the support and coordination center providing critical information to fire fighter as derived from the UAVs. The intent is to locate a swarm of vehicles over a designated area and report at the earliest the presence of such fire precursors as smoke, etc. the UAVs are equipped with appropriate sensors, computing and communications in order to execute these surveillance tasks accurately and robustly. Meteorological sensors monitor wind velocity, temperature and other relevant parameters. The UAV observations are augmented, when appropriate, with satellite data, observation towers and human information sources. Other application domains of both aerial and ground unmanned systems refer to rescue operations, damage surveillance and support for areas subjected to earthquakes and other natural disasters, border patrol, agricultural applications, traffic control, among others.

Brief Biography of the Speaker: Dr. George Vachtsevanos is currently serving as Professor Emeritus at the Georgia Institute of Technology. He served as Professor of Electrical and Computer Engineering at the Georgia Institute of Technology from 1984 until September, 2007. Dr Vachtsevanos directs at Georgia Tech the Intelligent Control Systems laboratory where faculty and students began research in diagnostics in 1985 with a series of projects in collaboration with Boeing Aerospace Company funded by NASA and aimed at the development of fuzzy logic based algorithms for fault diagnosis and control of major space station subsystems. His work in Unmanned Aerial Vehicles dates back to 1994 with major projects funded by the U.S. Army and DARPA. He has served as the Co-PI for DARPA's Software Enabled Control program over the past six years and directed the development and flight testing of novel fault-tolerant control algorithms for Unmanned Aerial Vehicles. He has represented Georgia Tech at DARPA's HURT program where multiple UAVs performed surveillance, reconnaissance and tracking missions in an urban environment. Under AFOSR sponsorship, the Impact/Georgia Team is developing a biologically-inspired micro aerial vehicle. His research work has been supported over the years by ONR, NSWC, the MURI Integrated Diagnostic program at Georgia Tech, the U.S. Army's Advanced Diagnostic program, General Dynamics,

General Motors Corporation, the Academic Consortium for Aging Aircraft program, the U.S. Air Force Space Command, Bell Helicopter, Fairchild Controls, among others. He has published over 300 technical papers and is the recipient of the 2002-2003 Georgia Tech School of ECE Distinguished Professor Award and the 2003-2004 Georgia Institute of Technology Outstanding Interdisciplinary Activities Award. He is the lead author of a book on Intelligent Fault Diagnosis and Prognosis for Engineering Systems published by Wiley in 2006.

Plenary Lecture 6

Iterative Extended UFIR Filtering in Applications to Mobile Robot Indoor Localization



Professor Yuriy S. Shmaliy
Department of Electronics
DICIS, Guanajuato University
Salamanca, 36855, Mexico
E-mail: shmaliy@ugto.mx

Abstract: A novel iterative extended unbiased FIR (EFIR) filtering algorithm is discussed to solve suboptimally the nonlinear estimation problem. Unlike the Kalman filter, the EFIR filtering algorithm completely ignores the noise statistics, but requires an optimal horizon of N points in order for the estimate to be suboptimal. The optimal horizon can be specialized via measurements with much smaller efforts and cost than for the noise statistics required by EKF. Overall, EFIR filtering is more successful in accuracy and more robust than EKF under the uncertain conditions. Extensive investigations of the approach are conducted in applications to localization of mobile robot via triangulation and in radio frequency identification tag grids. Better performance of the EFIR filter is demonstrated in a comparison with the EKF. It is also shown that divergence in EKF is not only due to large nonlinearities and large noise as stated by the Kalman filter theory, but also due to errors in the noise covariances ignored by EFIR filter.

Brief Biography of the Speaker: Dr. Yuriy S. Shmaliy is a full professor in Electrical Engineering of the Universidad de Guanajuato, Mexico, since 1999. He received the B.S., M.S., and Ph.D. degrees in 1974, 1976 and 1982, respectively, from the Kharkiv Aviation Institute, Ukraine. In 1992 he received the Dr.Sc. (technical) degree from the Soviet Union Government. In March 1985, he joined the Kharkiv Military University. He serves as full professor beginning in 1986 and has a Certificate of Professor from the Ukrainian Government in 1993. In 1993, he founded and, by 2001, had been a director of the Scientific Center “Sichron” (Kharkiv, Ukraine) working in the field of precise time and frequency. His books *Continuous-Time Signals* (2006) and *Continuous-Time Systems* (2007) were published by Springer, New York. His book *GPS-based Optimal FIR Filtering of Clock Models* (2009) was published by Nova Science Publ., New York. He also edited a book *Probability: Interpretation, Theory and Applications* (Nova Science Publ., New York, 2012) and contributed to several books with invited chapters. Dr. Shmaliy has authored more than 300 Journal and Conference papers and 80 patents. He is IEEE Fellow; was rewarded a title, Honorary Radio Engineer of the USSR, in 1991; and was listed in *Outstanding People of the 20th Century*, Cambridge, England in 1999. He is currently an Associate Editor for *Recent Patents on Space Technology*. He serves on the Editorial Boards of several International Journals and is a member of the Organizing and Program Committees of various Int. Symposia. His current interests include statistical signal processing, optimal estimation, and stochastic system theory.

PART I

Short Distance Earth Current Measurements Related to Atmospheric Electric Fields

Ernst D. Schmitter

University of Applied Sciences Osnabrueck
 Faculty of Engineering and Computer Sciences
 49076 Osnabrueck, Germany
 Email: e.d.schmitter@hs-osnabrueck.de

Abstract—We present a novel system for the measurement of shallow running earth currents on short distances (tens of meters) that proves as a reliable and inexpensive sensor for the earth electric field. It is well suited to study electrified clouds, aerosol concentrations as well as averaged diurnal and seasonal surface electric field variations. It is less fragile than mechanical field mills, less prone to noise and more robust with regard to static discharges compared to electrometer (charge amplifier) devices. It is therefore well suited for continuous unattended operation.

Keywords—Earth currents, Earth electric field, signal processing

I. INTRODUCTION

We present a system sensing the surface earth electric field using earth ground as a conductor. The surface atmospheric electric field is an important parameter indicating aerosol concentration as well as cloud electrification [1], [2] on a diurnal time base. Seasonal variations of the averaged surface electric field are discussed to be related to climate change and solar activity, [3], [4]. A common instrument to measure the surface electric field is the field mill. It works by exposing an electrode plate to the electrostatic field and measuring it using a mechanical shutter rotating in front of the plate. Field mills can do very precise measurements, however they are quite expensive if a rugged outdoor device is needed. Other methods use different electrode geometries that are exposed to the electric field and are coupled to an electrometer (charge amplifier) to read the accumulated charge, [5]. Such devices however are very sensitive to static discharges and all electrodes directly exposed to the surface electric field suffer from local disturbances, especially wind drafts carrying along dust clouds.

We base our measurement approach on the observation that there is a closed current circuit between the lower ionosphere and earth ground, fig. 1. The vertical current density j , assumed as constant during fair weather conditions (about $2 \cdot 10^{-12} Am^{-2}$, [4]), is related to conductivity σ and vertical electric field E at height h through (cp. [6])

$$j = \sigma(h)E(h) \quad (1)$$

Atmospheric conductivity increases with height because of the growing ionization effect of cosmic rays, which means that the electric field decreases accordingly, having its maximum near the ground (about 130 V/m with fair weather). Conductivity within the surface layer can be subject to strong local

variations caused by cloud electrification but also air pollution (aerosols reducing the number of current contributing ions by attachment to particles). The atmospheric current has to enter the earth ground to close the circuit. Our earth electrode system is set up to record the horizontal circuit balancing currents. Another source for earth currents are geomagnetic storms, [7]. Solar activity causes variations of the geomagnetic field inducing electric fields in the earth ground which in turn generate earth currents. Such geomagnetically induced currents (GICs) according to Maxwell's equations are proportional to the time derivative of the geomagnetic field. During the observation campaign reported in this paper we did not record any geomagnetic signatures, the atmospheric electric field effects dominates our results. With regard to the mid latitude (52N) and the short measurement distance ($L = 36m$) this is comprehensible because geomagnetic effects strongly increase polewards. In the next chapter we explain the mode of operation of the measurement system. Afterwards we discuss single event records as well as diurnal and seasonal signal behavior.

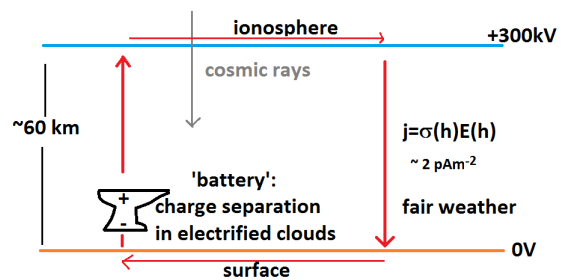


Fig. 1. The global electric circuit. Cosmic rays and very near to the surface also ground radioactivity generate positive and (consecutively by electron attachment) negative ions that render the atmosphere weakly conductive. Conductivity increases exponentially with height. The vertical electric field decreases accordingly. Charge separation in thunderclouds and electrified shower clouds are the batteries keeping up a voltage difference of about 300 kV between the lower ionosphere and the earth ground. A fair weather current density of about $2pAm^{-2}$ is continually discharging the global electric system.

II. THE MEASUREMENT SYSTEM

Fig. 2 shows the layout for our earth current measurement system. Two identical orthogonally oriented measurement systems each with two electrodes at a distance of $L = 36m$ are in operation: one in west-east direction and another one north-south oriented. Zinc-plated steel tent pegs of 0.5 m length driven into the ground serve as electrodes. The symmetric high pass input of the system not only rejects common mode noise but also suppresses the DC offset generated by the electrode-ground electro-chemical interfaces. The time constant is $T = RC = 1000s$. Analyzing the circuit (fig. 2) yields $V_{ext} = 2V_C + V_{mon}$, where V_C is the voltage drop at capacitor C. With $C\dot{V}_C = I$, where I is the current through C and $2RI = V_{mon}$ (assuming ideal circuit symmetry and infinitely high input impedance for the instrumentation amplifier) we get

$$\dot{V}_{ext} = \dot{V}_{mon} + \frac{1}{T}V_{mon} \quad (2)$$

and

$$V_{ext} = V_{mon} + \frac{1}{T} \int V_{mon} dt \quad (3)$$

For a conductor with a total resistance R_E , length L and cross section A consisting of a material of conductivity σ we get:

$$R_E = \frac{1}{\sigma} \frac{L}{A} \quad (4)$$

Typical values for ground conductivity are: $\sigma = 0.05..3 \cdot 10^{-2} S/m$ for earth ground depending on its dryness, $\sigma \cong 5 \cdot 10^{-2} S/m$ for sweet water and $\sigma \cong 5 S/m$ for sea water. (1 Siemens = $1\Omega^{-1}$). Measurement of R_E is done by applying an AC signal (to avoid electro-chemical DC offset problems) of known voltage (5V RMS, 90Hz, injected at the points marked as red in fig. 2) and measuring the current flowing. Several weeks after installing the electrodes the resistance in both directions settled to $R_E = 960..1040\Omega$. With an estimated value of $\sigma \cong 10^{-2} S/m$ for rather wet ground and $L = 36m$ we get from equ. 4 $A \cong 3.6m^2 \cong 1.9m \times 1.9m$ as a rough estimate for the earth cross section contributing to the conduction between the two electrodes. As expected we record near surface currents. The wires running from the electrodes to the recording device are isolated and shallowly buried in the ground, so that they are not exposed to the earth electric field.

III. RESULTS

All recordings discussed in this paper have been carried out at a mid latitude site (52.1N, 8.5E) between July 2013 and March 2014 in a rural environment. The measurement legs are situated at the edges of a group of trees, fig. 3. In this way they are shielded from the direct effect of rain or snow precipitation. Results are discussed in terms of V_{ext}/L (volt per meter), cp. equ. 3, with $L = 36m$. The earth current is related to V_{ext} by Ohm's law: $I_E = V_{ext}/R_E$ (neglecting the resistance

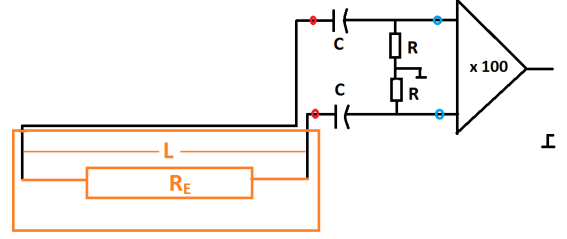


Fig. 2. Earth current monitoring schematic. Between the red dots: V_{ext} ; between the blue dots: V_{mon} . Both voltages are related by equations 2 and 3. $C = 100\mu F$, $R = 10M\Omega$, $T = RC = 1000s$; $L = 36m$; $R_E \cong 1000\Omega$; Data acquisition period: 1s. An instrumentation amplifier increases the voltage level by a factor of 100 for convenient recording. All results in this paper are discussed in terms of V_{ext}/L .



Fig. 3. Site at 52.1N8.5E with the Earth current monitoring lines in W-E and N-S directions along the edges of a group of trees. The recording device with two identical circuits according to fig. 2 is located near the electrode which is common to both lines (lower left).

of the wires to the electrodes). Regular measurements of the resistance R_E confirmed that its value did not change significantly during dry or wet weather conditions. Signal amplitudes on the W-E path typically proved to be about 3 times larger than with the N-S path despite $R_E \cong 1k\Omega$ is nearly equal in both directions. We now present some results of our campaign with regard to single events and afterwards with regard to the averaged diurnal and seasonal characteristics.

A. Single Events

On the late afternoon of the 29th of July 2013 a thunderstorm passed over the acquisition area from west to east, fig. 4. Its signature is clearly more developed with the N-S path orthogonal to the storm moving direction (note however the different scales of W-E and N-S channels). Times of sunrise and sunset are marked with red (rise) and black (set) vertical lines. The inlay shows the zoomed data between 12 and 17 UT. The first drop is correlated with an advancing thunderstorm cloud without near lightning, so acting by its electrification on the surface electric field. The events around 15 UT are related to near lightning strokes. The drop around 2 UT in

the night from the 30th to the 31st of July is caused by an west-east moving electrified cloud system with showers, also more prominent with the N-S recording path.

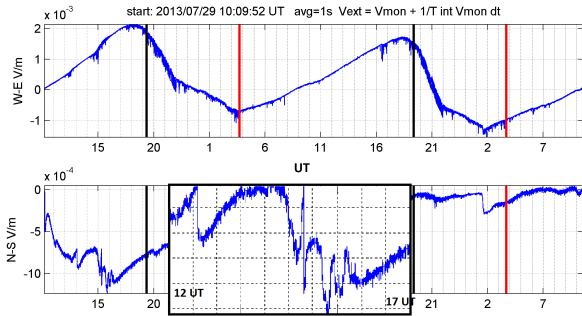


Fig. 4. Thunderstorm passing overhead the data acquisition area around 15 UT 29th July 2013. The disturbance is clearly more pronounced with the N-S channel than with the W-E channel. The inlay shows the zoomed data between 12 and 17 UT. The thunderstorm moved from W to E. Black lines: sunset, red lines: sunrise.

On the 5th of Dec. continuing to the 6th of Dec. 2013 the very strong storm front Xaver passed the acquisition area from west to east, fig. 5. Air pressure (4th panel from top in the figure) decreases the whole day (5th Dec.) and reaches a minimum around 16 UT. The main storm front passed the data acquisition area between 14 and 17 UT indicated by the sharp signal drops (where the minima coincide with sunset) on both channels (note the different scales). Only for about 20 minutes around 17 UT there was a rain shower. Thunderstorm cells have been observed within the storm front but did not pass directly overhead (at least 20 km distance to the nearest lightnings). So the main synchronous drops on both channels are not related to showers but to electric field changes caused by cloud electrification and surface near aerosols driven by the strong winds.

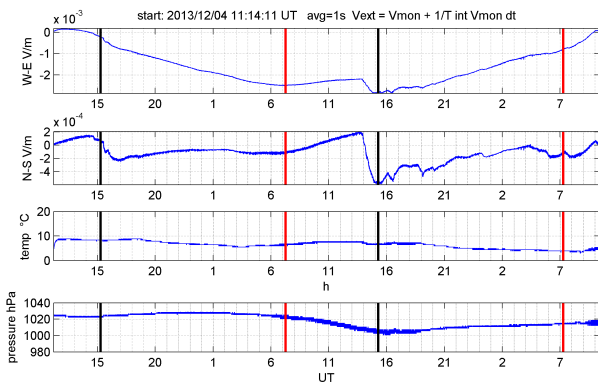


Fig. 5. Storm front Xaver, 5th/6th Dec. 2013. Air pressure (4th panel from top) decreases the whole day (5th Dec.), reaching its minimum around 16 UT. The main storm front passed the data acquisition area between 14 and 17 UT indicated by the sharp signal drops on both channels (note the different scales). Only for about 20 minutes around 17 UT there was a rain shower. Thunderstorm cells have been observed within the storm front but did not pass directly overhead (at least 20 km distance to nearest lightnings).

B. Diurnal and Seasonal Averages

More than a century ago Wilson, [8] identified thunderstorms and electrified shower clouds as the batteries driving the global electric circuit, fig. 1. He based his hypothesis on the similarity between the diurnal variation of thunderstorm days in universal time and the Carnegie curve of the electric field, named after the geophysical survey vessel of the Carnegie Institution of Washington on which the original measurements demonstrating the universal time variation of the surface electric field have been done, [9], [10], [11].

Fig. 6 shows diurnal signal averages in both channels for August, September, October 2013 (ASO) and fig. 7 for November, December 2013, January 2014 (NDJ). In all cases a 5-term Fourier-series (including a constant term, equ. 5) is fitted to the data yielding a near perfect fit, especially with the W-E channel. This implies that the superposition of 4 periods (24, 12, 8 and 6 hours) together with a constant offset explains the diurnal course of the averaged V_{ext}/L signals nearly completely.

$$E_{avg}(t) = \sum_{i=0}^{i=4} a_i \sin(i \frac{2\pi t}{24} + b_i) \quad (5)$$

Also displayed in the panels are the Carnegie-E-field-curves for the 3 months periods in question. These curves represent harmonic fits to the original Carnegie data. The parameters are tabulated in [9]. In our plots they are vertically scaled for a best fit to our data. We see quite good concordance during ASO (northern late summer-autumn) with the W-E channel and during NDJ (northern winter) with both channels. The N-S channel during ASO shows larger deviations. This might be due to the fact that the N-S channel is very sensitive to the frequent autumn time front systems moving from west to east leaving only few undisturbed days in that period. With regard to the seasonal behavior the ASO amplitudes with both channels are larger by a factor of 2 compared to the NDJ period.

A closer inspection of our data during NDJ shows a simple periodic structure with an early minimum near 8 UT and a late maximum near 16 UT in both channels. During ASO the situation is more complicated: the W-E channel has a minimum near 4 UT and a maximum near 19 UT. Both extrema are shifted by about 1.5 hours with the N-S channel. Also between the early minimum and late maximum additional structure appears. For comparison the Carnegie curves in both 3-month periods exhibit a minimum near 3 UT. With ASO the Carnegie maximum is near 20.5 UT and recedes to 18.5 UT in the NDJ period. Further recordings are in progress to allow calculating averages for other seasons and reveal more details. Especially the following question asks for an answer: which part of the characteristics observed is locked to local time (sunrise and sunset) and which part is globally caused (global distribution of electrified clouds) and locked to universal time.

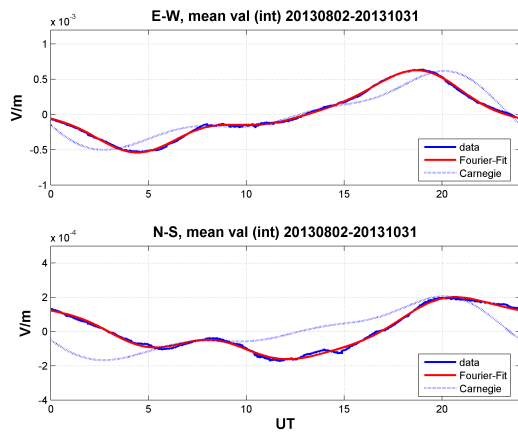


Fig. 6. August-September-October (ASO) seasonal averages with Fourier-fits and ASO Carnegie curves, see text.

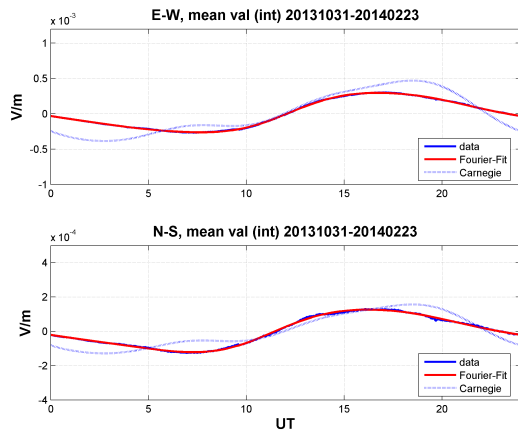


Fig. 7. November-December-January (NDJ) seasonal averages with Fourier-fits and NDJ Carnegie curves, see text.

IV. CONCLUSION

We have presented a novel measurement system that can be used as a reliable sensor for the earth surface electric field. Its effectiveness has been shown with regard to the detection of electrified clouds but also by displaying diurnal and seasonal characteristics. It avoids some disadvantages of common systems resulting from their direct exposition to the electric field, especially local noise and failure from static discharges with electrometer systems. Having no mechanical components and no openly accessible electrodes a continuous and unattended operation is easily possible. Our monitoring is continued to gain further insight into qualitative and quantitative aspects of single events (especially with regard to discriminate cloud electrification and aerosol caused signatures) and to get a better understanding of the diurnal and seasonal characteristics with regard to local and global drivers.

REFERENCES

[1] Bennett, A.J., Harrison, R.G., Variability in surface atmospheric electric field measurements, Journal of Physics, Conference Series 142, 012046,

2008, doi:10.1088/1742-6596/142/1/012046
 [2] Williams E.R., Heckman, S.J., The local diurnal variation of cloud electrification and the global diurnal variation of negative charge on the Earth, Journal of Geophysical Research , 98, D3, 5221-5234, 1993
 [3] Harrison, R.G., The global atmospheric electrical circuit and climate, Surv. Geophys., vol. 25, 441-484, 2004
 [4] Rycroft, M.J., Israelsson, S., Price, C., The global atmospheric electric circuit, solar activity and climate change. Journal of Atmospheric and Solar-Terrestrial Physics, 62, 1563-1576, 2000
 [5] Bennett, A.J., Harrison, R.G., Surface measurement system for the atmospheric electrical vertical conduction current density, with displacement current density correction, Journal of Atmospheric and Solar-Terrestrial Physics 70, 1373-1381, 2008
 [6] Rycroft, M.J., Harrison, R.G. Nicoll, K.A., Mareev, E.A., An overview of Earths global electric circuit and atmospheric conductivity, Space Sci. Rev., vol. 137, 83-105, 2008
 [7] Lehtinen, M., Pirjola, R., Currents produced in earthed conductor networks by geomagnetically-induced electric fields, Annales Geophysicae, 3, 4, 479-484, 1985
 [8] Wilson, C. T. R., Atmospheric electricity, Nature, 68, 101104, 1903
 [9] Harrison, R.G., The Carnegie Curve, Surv. Geophys., 34:209232, 2013, doi 10.1007/s10712-012-9210-2
 [10] Liu, C., Williams, E.R., Zipser, E.J., Burns, G., Diurnal Variations of Global Thunderstorms and Electrified Shower Clouds and Their Contribution to the Global Electrical Circuit, Journal of the Atmospheric Sciences 67.2, 309-323, 2010
 [11] Williams, E. R., The global electrical circuit: a review, Atmos. Res., vol. 91, 140-152, 2009

Implementation of Direction Cosine Matrix on a PSoC-5 Microcontroller for Robot Localization on Inclined Terrains

Garth Herman, Aleksander Milshteyn, Airs Lin, Manuel Garcia,
Charles Liu, Khosrow Rad, Darrel Guillaume, Helen Boussalis

Structures, Pointing, and Control Engineering (SPACE) University Research Center
College of Engineering
California State University, Los Angeles
5151 State University Drive
Los Angeles, CA 90032 USA
gherman@calstatela.edu

Abstract— Robots facilitate exploration of hazardous environments during response to catastrophe. Autonomous robots involved in search and rescue operations require accurate orientation information to navigate uneven or inclined terrains. A Hybrid Routing Algorithm Model has been proposed by the Structures, Pointing, And Control Engineering (SPACE) University Research Center (URC) at California State University of Los Angeles. This model envisions three-layered terrain mapping with obstacle representations from various information sources such as satellites, UAVs, and onboard range sensors. The orientation information of a robot is obtained from a 9 degrees-of-freedom inertial measurement unit. In the absence of external magnetic fields, a magnetometer sensor is capable of outputting accurate heading information if it is firmly mounted on the robot chassis and its reference frame is parallel to the ground. This paper demonstrates an implementation of a direction cosine matrix (DCM) algorithm on a Cypress Programmable System on a Chip-5 (PSoC-5) platform to obtain correct orientation information for the semi-autonomous robot. This semi-autonomous robot is capable of navigating and mapping the surrounding environment. A PSoC-5 is utilized as a microcontroller to control the platform and acquire data from multiple onboard sensors. The DCM algorithm is demonstrated to obtain and maintain global reference system information for a mobile robot under varied terrain inclinations.

This work was supported in part by the NASA University Research Center Program under Grant NNX08A44A and National Science Foundation (NSF) Grant 230953.

G. Herman is with the Structures Pointing and Controls Engineering (SPACE) University Research Center at California State University of Los Angeles, Los Angeles, CA 90032 USA (phone: 323-343-5445; e-mail: gherman@calstatela.edu).

A. Milshteyn is with the Structures Pointing and Controls Engineering (SPACE) University Research Center at California State University of Los Angeles, Los Angeles, CA 90032 USA (e-mail: amilsh@calstatela.edu).

A. Lin is with the Structures Pointing and Controls Engineering (SPACE) University Research Center at California State University of Los Angeles, Los Angeles, CA 90032 USA (e-mail: airslin@hotmail.com).

Keywords— *system-on-chip, mobile robot, Direction Cosine Matrix, IMU, inclined surfaces, semi-autonomous, data acquisition, environment-mapping.*

I. INTRODUCTION

ADVANCES in robotics technology increase the utility of diversely applied platforms. Robots mitigate risk to emergency responders, and facilitate exploration of dangerous environments. These applications require information about the position and orientation (localization) of a robot. Localization information is crucial if a robot is used to locate victims and hazards of a catastrophe, or explore inhospitable or extraterrestrial environments. Accurate localization information is required to optimally navigate a robot through an environment [1].

Robots have been successfully deployed for emergency response and extraterrestrial exploration. A robotic platform was used to investigate radiation levels after a tsunami decimated a Japanese nuclear reactor on May 11, 2011. The robot was tested and retrofitted to ascertain its efficacy withstanding the anticipated conditions within the reactor before it was deployed. The localization of the robot was tracked using a gyroscope and accelerometer to ensure stability [2]. Mars Exploration Rovers utilize multiple localization methods, including the deployment of an accelerometer, gyroscope, magnetometer and motor encoders, to navigate an extraterrestrial environment [3]. To build a robust mobile robot upon which multiple missions could be based, a mechanism of acquiring precise localization information must be explored.

In the system architecture, a Host Computing Station (HCS) assigns global tasks to the mobile robot, and is operated either manually or autonomously. The robot can be operated in three modes: 1) navigated by a human operator, 2) navigated by an operator for only critical operation, and 3) autonomously navigated once given a destination. The mobile platform initially informs the HCS of its facing direction and receives destination coordinates information from the HCS. An embedded computer determines an optimal path and commands the platform to move between intermediate nodes that lie along the calculated path towards the intended destination. It uses the data acquired from the mobile platform's sensors to inform the HCS of the current platform location within a margin of error relative to the sensors. The sensor suite includes an accelerometer, a gyroscope, and a magnetometer. Unfortunately, inaccuracies in the output collected from each individual sensor introduce unreliable data to the system.

The sensors provide unique information about the current position of a robot. An accelerometer indicates the direction of gravity when at rest. A gyroscope indicates radial velocity. A magnetometer measures the strength of surrounding magnetic fields. The combination of these sensors constitutes an inertial measurement unit (IMU). Each of these sensors introduces noise to the system, and the gyroscope error accumulates, introducing drift. A magnetometer indicates direction, but results do not provide high precision measurements.

The paper focuses on implementation of direction cosine matrix (DCM) on a Cypress Programmable System on a Chip-5 (PSoC-5) platform to combine IMU sensor data and obtain accurate orientation information for a semi-autonomous robot under various terrain inclinations. This semi-autonomous robot is capable of navigating and mapping the surrounding environment. The DCM algorithm is demonstrated to obtain and maintain orientation accuracy under varied inclinations of pitch and roll.

The outline of the paper is organized as follows: Chapter 1 presents the background information and motivation for this project. Chapter 2 describes multiple processing units that comprise the system architecture of the proposed mobile robot. Chapter 3 discusses robot's hardware interface and the IMU drivers. Chapter 4 describes the direction cosine matrix algorithm implementation on PSoC-5. Chapter 5 compares the results for the orientation information between raw magnetometer sensor data and the DCM output data for various levels of surface inclinations. Chapter 6 concludes the paper and presents future work.

II. SYSTEM ARCHITECTURE

The robotic system architecture consists of two primary components, the HCS, and the onboard Embedded Hardware. The HCS provides visual environment maps to the robot operator. The HCS creates Level 1 and Level 2 maps from incoming aerial map data. Environment mapping is divided into three maps, defined at resolutions of 1km by 1km (Level

1), 100m by 100m (Level 2), and 10m by 10m (Level 3). Fig. 1 depicts the three-level map.

An operator specifies a starting point and ending destination on the Level 1 map. The HCS is responsible for calculating static optimal paths for Level 1 and Level 2 scaled maps and communicates the path information to the mobile platform. The embedded computer performs a dynamic path finding algorithm to traverse Level 3 maps [4].

The HCS also processes robotic sensor data, maps

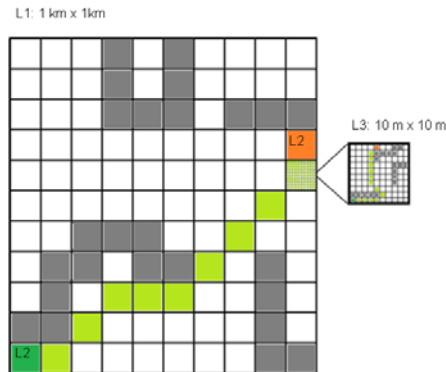


Fig. 1 Hybrid Routing Algorithm Model

visualization data in an Open Graphics Library environment on three scaled levels, and tags multimedia data to the appropriate coordinate location. Finally, the HCS provides remote control capabilities in missions requiring human intervention. The system components are illustrated in Fig. 2.

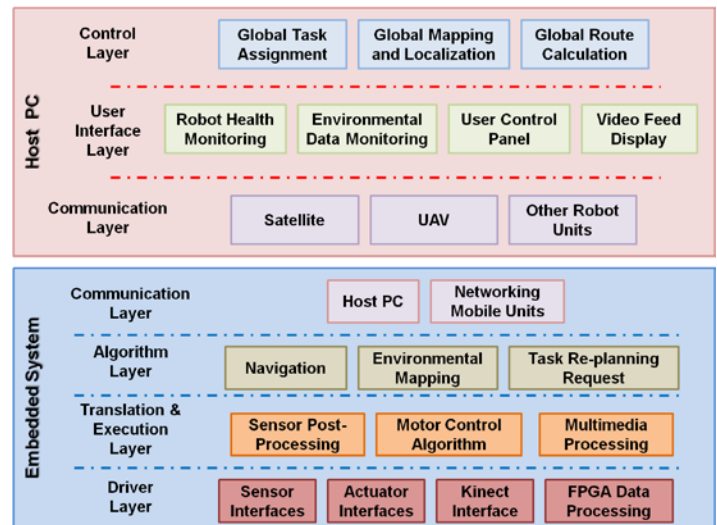


Fig. 2 System Architecture

The embedded hardware consists of three primary layers: the Algorithm Layer, Platform Layer, and Driver Layer. The Algorithm Layer is responsible for computing dynamic pathfinding algorithms, obstacle detection, and obstacle avoidance on Level 3 maps. The Platform Layer is responsible for the steering, sensor fusion, image processing, and kinematics of the mobile platform.

The Driver Layer contains the sensor and motor controller interfaces used for Robotic unit. The PSoC-5 serves as the microcontroller to support sensors, motor controllers, and communications for the mobile platform. The PSoC-5 provides the current localization of the mobile platform to the embedded computer through a serial port. The PSoC-5 performs data acquisition, applies control algorithms, and standardizes output, while the embedded computer handles all path-finding logic. An Analog-to-Digital Converter (ADC) samples data from range sensors. An Inter-Integrated Circuit (I2C) Master acquires data from the IMU. Pulse-Width Modulation (PWM) drives the motor controllers. One

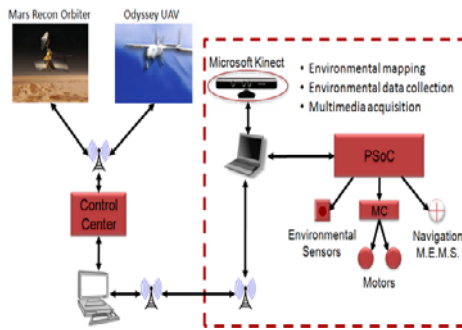


Fig. 4 System Layer Model

programmable array logic and programmable logic device functionality. A wide variety of peripherals are supported. In addition to the UDB array's flexibility, PSoC-5 provides configurable dedicated digital blocks that target specific functions. The Analog Subsystem of PSoC-5 includes multiplexors, comparators, voltage references, op-amps, mixers, and Trans Impedance Amplifiers (TIA). They can be routed out from any GPIO pin [5].

UDB units utilized by the mobile platform include up to 32-bit PWM, counter, and timer UDB units. A Dedicated I2C communication blocks is also used. Multiple clocks can be configured to drive the digital components. A lack of parallel processing, small RAM capacity, and a maximum clock rate of 48MHz limit the PSoC-5. A controlling embedded computer is responsible for pathfinding computations.

The manufacturer of the PSoC-5 microcontroller publishes a free software suite called PSoC Creator to facilitate design implementation. This software allows drag-and-drop component placement. Basic components include wires and sheet connectors, while more complex components include I2C Master controllers and PWM blocks [6].

III. IMU DRIVERS

Several hardware components are supported by software to facilitate the DCM algorithm. IMU data acquisition across I2C transactions requires software to facilitate control over an I2C master, as well as communicate with the IMU. The I2C master addresses the sensors in the IMU independently, and output from the sensors is delivered in specific units. Multiple registers in the IMU contain sensor configuration data and measurement values.

A transaction to read the IMU is initiated by a start signal followed by a concatenated register address and a write signal sent from the I2C master. The master writes the address of the register that to be read to a pointer register in the IMU. The IMU sends an acknowledgement, and the master responds with a second start signal followed by the device address concatenated with a read signal. An acknowledgement of to begin reading is sent to the master. The IMU begins transmitting data from the register indicated by the pointer one byte at a time. A negative acknowledgement is sent when the transaction is concluded. This allows three-dimensional accelerometer, gyroscope, and magnetometer data to be six

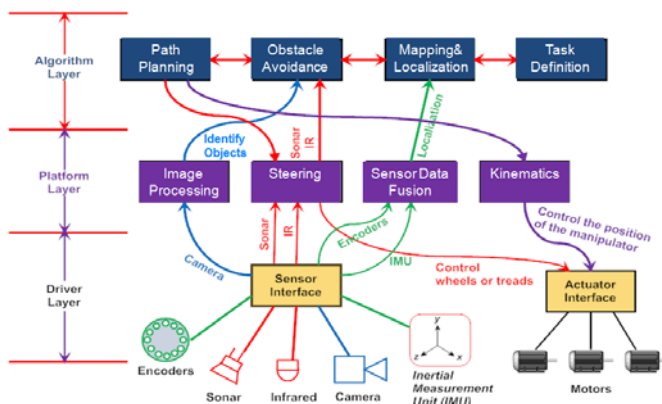


Fig. 3 System Layer Model

Universal Asynchronous Receiver/Transmitter (UART) connects the embedded computer or debugging terminal, and another connects the GPS. The system layer model is depicted in Fig. 3.

The PSoC-5 acquires kinematic sensor information. Navigation data is determined in the Algorithm Layer, passed through the Motor Control Algorithm block of the Platform Layer on the PSoC-5, and used to determine motor controller output. The kinematic sensors provide data for proper mapping and unit localization. IR and US sensors, along with Microsoft Kinect image acquisition, provide real time obstacle monitoring to allow the mobile platform to sustain autonomous and semi-autonomous missions. Fig. 4 illustrates the direction of information flow the embedded system layers, excluding communications.

Unique advantages of the Cypress PSoC-5 microcontroller include programmable voltage, instrumentation, and amplifiers. PSoC-5 allows the vendor to configure timers, counters, and PWM units, and each component is accessible through a proprietary application-programming interface (API). The PSoC-5 Digital Subsystem features configurable Universal Digital Block (UDB) units. Each UDB contains

bytes long, two bytes for each dimension.

A series of vector functions are used store the output of the IMU. Vectors are stored in a structure containing three floating-point numbers. Cross product, dot product, vector addition, and normalization functions are required to determine the direction of gravity, acceleration, radial velocity, and magnetic heading.

Vectors store the x, y, and z elements of accelerometer, gyroscope and magnetometer sensor data. The raw output of the sensors is defined in units of least significant bits (LSB) [7]. Acceleration in g-forces is given as the product of the accelerometer value and the scaling factor $1g/16,384$ LSB. For example, a sixteen bit value of 0010 0000 0000 0000 is equivalent to 8,192 LSB. The measured acceleration is given by:

$$8,192LSB \times 1g / (16,384LSB) = 1g \quad (1)$$

Gyroscope and magnetometer values are computed similarly. Gyroscope values are interpreted in units of degrees or radians per second per LSB, and magnetometer values are interpreted in units of gauss per LSB.

Functions to read the IMU are triggered by a timed interrupt, triggered when a timer expires. A control register is used to hold a reset signal on the timer high until the DCM has been updated.

Integration of the gyroscope utilizes another timer, which is restarted whenever the gyroscope has been read. This provides intervals accurate to $1 \mu s$.

IV. THE DIRECTION COSINE MATRIX

A DCM algorithm has been used to provide estimates of the robot localization to the PSoc-5 using accelerometer, gyroscope, and magnetometer data. The estimates are based on recursive DCM updates over small periods of time. The algorithm utilizes gyroscope values to track rotation of the inertial reference frame of the robot. A PI controller is used with the algorithm to reject external noise from the accelerometer and magnetometer, and correct gyroscope drift [8]. The PI controller also enhances compass heading results. The accelerometer, magnetometer, and gyroscope values provide input to the DCM algorithm.

It is necessary to maintain orientation information about the robot (body frame) with respect to the Earth (global frame). A global frame of reference (\mathbf{V}_G) is found by the product of the rotation vector (\mathbf{R}) and the body frame of reference (\mathbf{V}_B), given an angle of rotation about each axis belonging to the body frame:

$$\overrightarrow{V}_G = \overrightarrow{R} \times \overrightarrow{V}_B \quad (2)$$

The rotations about principal axes (x, y, z) are defined in terms of radians as follows:

$$\overrightarrow{R}_x = \begin{bmatrix} 1 & 0 & 0 \\ 0 & \cos \varphi & \sin \varphi \\ 0 & -\sin \varphi & \cos \varphi \end{bmatrix}$$

$$\overrightarrow{R}_y = \begin{bmatrix} \cos \theta & 0 & \sin \theta \\ 0 & 1 & 0 \\ -\sin \theta & 0 & \cos \theta \end{bmatrix} \quad (3)$$

$$\overrightarrow{R}_z = \begin{bmatrix} \cos \psi & \sin \psi & 0 \\ -\sin \psi & \cos \psi & 0 \\ 0 & 0 & 1 \end{bmatrix}$$

A complete rotation matrix is a product of three vectors:

$$\overrightarrow{R} = \overrightarrow{R}_z(\psi) \times \overrightarrow{R}_y(\theta) \times \overrightarrow{R}_x(\varphi) \quad (4)$$

The relation between the DCM and Euler angles are formed from the first column and last row of the resulting matrix [9]:

$$Pitch = -\arcsin(-\sin \phi)$$

$$Roll = -\arctan\left(\frac{\sin \phi}{\cos \phi}\right) \quad (5)$$

$$Yaw = -\arctan\left(\frac{\cos \psi}{\sin \psi}\right)$$

The DCM depends upon the rotation matrix, which transforms the orientation of the platform's Euler Angles (roll, pitch, and yaw) to a reference coordinate system. The gyroscope measures angular displacement of the robot. The accelerometer and magnetometer are used to correct gyroscope drift. The error between the angular displacements indicated by the gyro must be checked against the direction of gravity, and the magnetic heading to correct drift.

The velocity of a rotating vector is defined as:

$$\frac{d\overrightarrow{r}(t)}{dt} = \overrightarrow{\omega}(t) \times \overrightarrow{r}(t) \quad (6)$$

where $\omega(t)$ is a rotation rate vector and $r(t)$ is a tangential vector. If the initial conditions and the period between iterations are known, an approximation of the linear displacement of the vector is the cross product result of angular displacement $d\theta(\tau)$ and rotational vector $r(\tau)$ over some time interval t .

The location of the vector at any time t is therefore given by:

$$\overrightarrow{r}(t) = \overrightarrow{r}(0) + \int_0^t d\overrightarrow{\theta}(\tau) \bullet \overrightarrow{r}(\tau) \quad (7)$$

The resulting equation updates the rotation matrix using incoming gyroscope information in terms of robot angular rotations is as follows:

$$d\theta_x = \omega_x \times dt$$

$$d\theta_y = \omega_y \times dt \quad (8)$$

$$d\theta_z = \omega_z \times dt$$

Equation 5.3.8 will eventually accumulate numerical errors attributed to rounding and gyro drift [10]. As error accumulates, the axes are reported as non-orthogonal and no longer represent a rigid body. Renormalization enforces the

orthogonal relationship between the axes.

$$\vec{X} = \begin{bmatrix} r_{xx} & r_{yx} \\ r_{xy} & r_{yy} \\ r_{xz} & r_{yz} \end{bmatrix}, \vec{Y} = \begin{bmatrix} r_{yx} \\ r_{yy} \\ r_{yz} \end{bmatrix} \quad (9)$$

$$\varepsilon = \vec{X} \cdot \vec{Y} = \vec{X}^T \vec{Y} = \begin{bmatrix} r_{xx} & r_{xy} & r_{xz} \end{bmatrix} \times \begin{bmatrix} r_{yx} \\ r_{yy} \\ r_{yz} \end{bmatrix} \quad (10)$$

where ε is the error between the two vectors.

Apportioning half of the error for X and Y rows and rotating them in opposite direction by cross coupling leads to:

$$\vec{X}_{orthogonal} = \vec{X} - \varepsilon / 2 \times \vec{Y} \quad (11)$$

$$\vec{Y}_{orthogonal} = \vec{Y} - \varepsilon / 2 \times \vec{X}$$

Next the Z row of the matrix is adjusted to be orthogonal to the X and Y vectors. Cross product of corrected X and Y leads to:

$$\vec{Z}_{orthogonal} = \vec{X}_{orthogonal} \times \vec{Y}_{orthogonal} \quad (12)$$

Using Taylor's expansion to get magnitude adjustment equations for the row vectors yields:

$$\vec{X}_{normalized} = \frac{1}{2} (3 - \vec{X}_{orthogonal} \cdot \vec{X}_{orthogonal}) \cdot \vec{X}_{orthogonal} \quad (13)$$

$$\vec{Y}_{normalized} = \frac{1}{2} (3 - \vec{Y}_{orthogonal} \cdot \vec{Y}_{orthogonal}) \cdot \vec{Y}_{orthogonal} \quad (14)$$

$$\vec{Z}_{normalized} = \frac{1}{2} (3 - \vec{Z}_{orthogonal} \cdot \vec{Z}_{orthogonal}) \cdot \vec{Z}_{orthogonal} \quad (15)$$

An accelerometer is used for roll-pitch drift correction is used in conjunction with a magnetometer. The roll-pitch rotational correction vector is computed by cross-multiplying 3rd row of DCM matrix with normalized gravity reference vector [11]:

$$\varepsilon' = \begin{bmatrix} r_{zx} \\ r_{zy} \\ r_{zz} \end{bmatrix} \times \vec{g}_{reference} \quad (16)$$

Where ε' is a correction vector. Both of the correctional vectors are multiplied by their respective weights and fed to a Proportional Integral (PI) feedback controller. Then, the total correction is applied to the PI controller:

$$\omega p_{correction} = Kp \cdot \varepsilon' \quad (17)$$

$$\omega i_{correction} = Ki \cdot \varepsilon'$$

The total correction vector is summed with the gyroscope information.

$$\vec{\omega}(t) = \vec{\omega}(t)_{correction} + \vec{\omega}(t)_{gyroscope} \quad (18)$$

Finally, the DCM is updated utilizing the product of a time step and the corrected gyroscope vector:

$$\vec{R}(t) = dt \cdot \vec{\omega}(t). \quad (19)$$

The output of Euler Angles allows the mobile robot to report accurate rotation angles regardless of the inclination angle of a traversed plane. This maintains heading information when the robot encounters sloped or rough terrain. Figure 5 represents the DCM algorithm, as implemented on the PSoc.

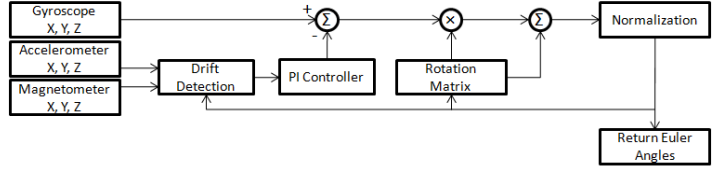


Fig. 5 System Layer Model

V. SOFTWARE IMPLEMENTATION OF THE DCM

The DCM implementation adapts existing Arduino software, and the uses custom IMU sensor and math functions [12]. The source software was written in C++, which the PSoc-5 does not support. The source software also implemented a different sensor suite than the one utilized by the robot.

The original software implemented matrices as objects that were defined as two-dimensional arrays of any size. A constructor would be called to define the number of rows and columns of a matrix. The equality, addition, subtraction, and multiplication operators were overloaded to perform unique matrix operations, each returning a newly created matrix object. In C, neither can objects be declared, nor operators overloaded. Each matrix is defined as a three-by-three array of floating-point numbers. Functions were created to support matrix operations, which take three matrices, passed by value, as input. The first two matrices are the operands, and the third stores the result of the operation.

The DCM is stored into a three-by-three floating-point array, representing. The roll, pitch, and yaw are respectively stored along the diagonal. The DCM is initialized to zero, and the accelerometer and magnetometer are read to provide the error estimates to the PI controller. The DCM does uses the accelerometer compare the roll and pitch measured by the accelerometer against those obtained by the DCM. This is implemented in a function to correct drift in the gyro.

$$\begin{aligned} MAG_X &= m.x \cdot \cos(pitch) \\ &+ m.y \cdot \sin(roll) \sin(pitch) \\ &+ m.z \cdot \cos(roll) \sin(pitch) \end{aligned} \quad (20)$$

$$MAG_Y = m.y \cdot \cos(roll) - m.z \cdot \sin(roll) \quad (21)$$

where m is the magnetometer reading, and MAG_X and MAG_Y are the tilt compensated components of the heading. The previous heading recorded in the DCM is stored in the first row of the matrix. The difference between these values and the tilt compensated magnetometer values provides an estimate of the error present in the DCM. The PI controller uses the error to offset the measured yaw. The error of the pitch and roll is determined by the cross product between that recorded in the DCM, and that measured by the accelerometer, as given in Eq. 5.4.15. This result is relative to the magnitude of the error between the two vectors. The PI controller scales the error, and adds to the pitch and roll recorded in the DCM.

The gyroscope is integrated over time. The result of the arc

measured by the gyroscope and the PI controller are added, and used to update the DCM. The matrix is then normalized, and Euler angles are computed.

VI. EXPERIMENTAL RESULTS AND DISCUSSIONS

An apparatus built to allow three axis rotations was used to test the navigation capability of the robot and to verify localization algorithms utilizing the IMU. This testing apparatus allows independent motion along each of three axes: roll, pitch, and yaw. Three methods of angular measurement were observed: 1) The heading provided by raw magnetometer data, 2) Raw, integrated, gyroscope data, and 3) Direction Cosine Matrix data utilizing a PI controller and the IMU. Each test case examines yaw information under fixed pitch positions. The IMU is affixed to a plate of wood on top of the apparatus. Wood was chosen because it does not influence magnetometer in the IMU.

To test the varied angular data acquisition methods, the servo that controls yaw is calibrated. The duty cycle to a PWM driving the pitch servo is experimentally investigated until the values that bring the servo nearest to 90 degrees from an initial position are found. Then the values that bring the pitch servo nearest 20 degrees pitch are determined. The compass heading determined by the DCM algorithm is observed once the servo is determined to be optimally configured. Values provided by the unfiltered gyroscope, and magnetometer, are also observed during the experiment.

The initial angle is reported by the gyroscope. For raw gyroscope values, this is zero degrees. The angular rate determined after servo is rotated to 90 degrees is reported when the servo stops moving. A short delay between executing servo motion allows the two filters to stabilize before initializing the next rotation. This delay is retained when measuring the raw gyroscope values to maintain identical test conditions between each experiment. Results are analyzed in terms of mean angle traversed in the clock-wise and counter-clockwise direction, and the mean heading in each direction. The mean angles and standard deviations are given for each experiment.

The servo calibration found the angle of rotation nearest 90 degrees to be 90 ± 2 degrees. The pitch angles of the platform were determined to be zero, pitched down 20 degrees, and pitched up 20 degrees. The initial heading is approximately 45 degrees east of geographic north. At each inclination, the yaw servo was rotated clockwise 100 times, and counter-clockwise 100 times. The resulting measure at the end of each rotation was tabulated. When using the DCM and the magnetometer, the measure reported is the compass heading. When using gyroscope values, the measure reported is relative to the initial yaw of the sensor. The result data is tabulated and includes the counter-clockwise measurement, clockwise measurement, and the difference between each measurement. Table 1 demonstrates the results.

Table 1. DCM, Gyroscope, and Magnetometer Results

Pitch:	Mag	°CW	°CCW	d□
--------	-----	-----	------	----

0°	μ	-49.86	51.45	101.33
	σ	2.84	3.44	4.26
10°	μ	-51.53	52.04	103.57
	σ	2.12	3.16	3.63
20°	μ	-50.46	47.08	97.54
	σ	2.67	3.45	4.37
30°	μ	-45.69	42.63	88.32
	σ	2.55	2.85	3.71
40°	μ	-45.25	35.51	80.76
	σ	2.39	2.28	3.5
<hr/>				
	Gyro	°CW	°CCW	d□
0°	μ	0.26	89.2	88.95
	σ	0.54	0.45	0.56
10°	μ	0.7	89.92	89.22
	σ	1.13	1.03	1.69
20°	μ	0.28	86.84	86.57
	σ	0.82	0.73	1.03
30°	μ	0.4	79.17	78.77
	σ	0.62	0.36	0.68
40°	μ	-0.19	70.82	71.01
	σ	0.84	0.74	1.17
<hr/>				
	DCM	°CW	°CCW	d□
0°	μ	-42.8	47.71	90.51
	σ	0.92	0.92	0.45
10°	μ	-44.66	47.77	92.43
	σ	1.4	1.27	0.86
20°	μ	-42.16	48.59	90.74
	σ	5.61	6.15	4.93
30°	μ	-42.8	47.42	90.23
	σ	3.2	1.52	3.23
40°	μ	-39.71	49.86	89.57
	σ	4.28	2.26	5.82

Pitch: Angle of Inclination of the IMU
 μ: Mean
 σ: Standard Deviation
 °CW: Heading Measured at Furthest Clockwise Position
 °CCW: Heading Measured at Furthest Counter Clockwise Position
 d□: Total Arc Traversed

The DCM meets or exceeds the accuracy of the magnetometer at all inclinations of pitch, especially when used to measure the traversed arc. The standard deviation of the DCM demonstrates improved heading information at low angles of inclination. At steeper pitches, the standard deviation of the DCM is near that of the magnetometer, though the mean

accuracy of the angles and arc measured is improved by the DCM. The gyroscope provides a lower standard deviation at all inclinations, though the accuracy is greatly impacted at all inclinations beyond 10° pitch. Figure 6 depicts the testing apparatus.

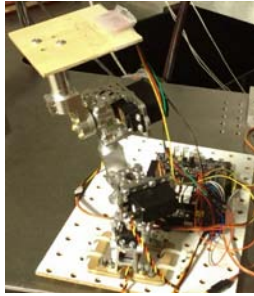


Fig. 6 Testing Apparatus

VII. CONCLUSION

A semi-autonomous robot requires control algorithms to accurately provide localization data. The PSoC-5 provides sufficient computational power to process algorithms to localize a mobile robot. A direction cosine matrix provides unique advantages when applied to localization.

Experimental results demonstrate the implemented DCM provides accurate measurements and improves the reliability of the magnetometer at various angles of inclination.

Future work includes replacing the PI controller in the DCM with a Kalman Filter and implementing GPS in the Kalman Filter to augment heading information of the robot as it changes position. These improvements would enhance the DCM control algorithm, and localization of a mobile robot.

REFERENCES

- [1] Kriechbaum, K.L. 2006. "Tools and Algorithms for Mobile Robot Navigation with Uncertain Localization." PhD diss., California Institute of Technology. <<http://thesis.library.caltech.edu/2363/1/kriechbaum-thesis.pdf>>.
- [2] Nagatani, K., Kiribayashi, S., Okada, Y., Otake, K., Yoshida, K., Tadokoro, S., Nishimura, T., Yoshida, T., Koyanagi, E., Fukushima, M. and Kawatsuma, S. 2013. "Emergency response to the nuclear accident at the Fukushima Daiichi Nuclear Power Plants using mobile rescue robots." *Journal of Field Robotics*, 30: 44–63. DOI: 10.1002/rob.21439
- [3] Powell, M.W., Crockett, T., Fox, J.M., Joswig, J.C., Norris, J.S., Rabe, K.J., McCurdy, M., and Pyrzak, G. 2006. "Targeting and Localization for Mars Rover Operations." Paper presented at the IEEE International Conference on Information Reuse and Integration, Waikoloa Village, Hawaii, September 16-18. DOI: 10.1109/IRI.2006.252382.
- [4] Stentz, A. 1996. "Map-Based Strategies for Robot Navigation in Unknown Environments." Paper presented at the AAAI Spring Symposium on Planning with Incomplete Information for Robot Problems, March. http://www.ri.cmu.edu/pub_files/pub2/stentz_anthony_tony_1996_1/stentz_anthony_tony_1996_1.pdf
- [5] PSoC[®] 5: CY8C55 Family Datasheet URL: <http://ecologylab.net/courses/sensoryInterfaces/resources/CY8C55DataSheet.pdf>
- [6] PSoC[®] Creator[™] Quick Start Guide URL: <http://www.cypress.com/index.cfm?docID=45972>
- [7] InvenSense, Inc. 2012. "MPU-9150 Register Map and Description Revision 4.2." Sunnyvale.

- <http://www.invensense.com/mems/gyro/documents/RM-MPU-9150A-00v4_2.pdf>.
- [8] D. Choukroun, H. Weiss, Bar-Itzhack, I.Y., Oshman, Y. 2010. "Direction cosine matrix Estimation from Vector Observations using a Matrix Kalman Filter." *IEEE Transactions on Aerospace and Electronic Systems* 46, 1: 128-136. DOI: 10.1109/TAES.2010.5417148
- [9] Premerlani, W. 2010. "Computing Euler Angles from Direction Cosines." URL: <<https://gentlenav.googlecode.com/files/EulerAngles.pdf>>.
- [10] Premerlani, W. and Bizard, P. 2009. "Direction Cosine Matrix IMU: Theory." URL: <<http://gentlenav.googlecode.com/files/DCMDraft2.pdf>>.
- [11] Macias, E., Torres, D., Ravindran, S. 2012. "Nine-Axis Sensor Fusion Using the Direction cosine matrix Algorithm on the MSP430F5xx Family." Texas Instruments Application Report, Dallas. <<http://www.ti.com/lit/an/slaa518a/slaa518a.pdf>>.
- [12] Pololu Corporation, "MiniIMU-9-Arduino-AHRS," URL: <<https://github.com/pololu/minimu-9-ahrs-arduino>>

Indirect adaptive control for underwater vehicles on base of nonlinear estimator of disturbances

V.Kh. Pshikhopov, M.Yu. Medvedev, B.V. Gurenko, and A.M. Maevsky

Abstract – The paper presents estimation algorithms of additive disturbances for autonomous underwater vehicles control systems. Peculiarity of the algorithms is nonlinear dependence of the estimator gains from estimation error. New algorithm of non-measurable error estimation is suggested. Developed method allows decrease integral error of disturbance estimation. In this paper computer experiment results are presented.

Keywords – control, estimation of disturbances, robust estimator, underwater vehicle.

I. INTRODUCTION

New applications of underwater vehicles require developments of new control systems [1], [2]. Position-path synthesis method can be applied to design indirect adaptive control for underwater vehicle [3] – [5]. Performance of indirect adaptive control system depends essentially from estimation algorithms [6], [7]. In this paper new method of robust estimation for underwater vehicles disturbances is developed.

Block diagram of position-path system of indirect adaptive control for underwater vehicles is presented on fig. 1.

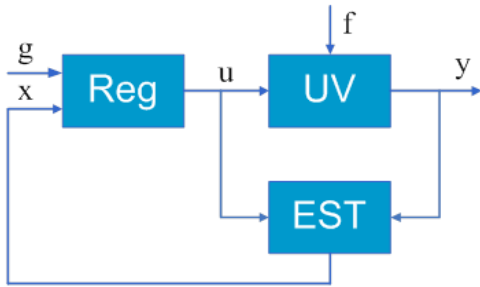


Fig. 1 Block diagram of underwater vehicle control system

This work was supported by the Ministry of Science and Education of the Russian Federation, government task of higher education and research organizations in the field of scientific work (№ 114041540005), Russian Federation President Council (Grant SSc-3437.2014.10, Grant YSc-1098.2013.10), and Russian Foundation of Basic Research (Grant 13-08-00315).

V.Kh. Pshikhopov is with Southern Federal University, Rostov-on-Don, Russian Federation (e-mail: pshichop@ranbler.ru).

M.Yu. Medvedev is with Southern Federal University, Rostov-on-Don, Russian Federation (phone: +78634371694; fax: +78634681894; e-mail: medvmihal@gmail.com).

B.V. Gurenko is with Southern Federal University, Rostov-on-Don, Russian Federation (boris.gurenko@gmail.com).

A.M. Maevsky is with Southern Federal University, Rostov-on-Don, Russian Federation (boris.gurenko@gmail.com).

The next notations are used on fig.1: Reg – regulator; UV – underwater vehicle; EST – estimator; g – reference input; u – control vector; y – output variables vector; x – estimated vector; f – vector of disturbances.

Advantage of the presented by fig. 1 adaptive system is independence of estimator from controller. But the diagram is based on superposition principle proper for linear systems. For nonlinear systems stability area depends from performance of estimation.

II. DESIGN OF DISTURBANCES ESTIMATOR

Let us introduce general form of underwater vehicle dynamic equation:

$$\dot{x} = M^{-1}(F_u + F_d + F_{est}) \quad (1)$$

$$\dot{F}_{est} = g(F_{est})$$

where x – speed vector of underwater vehicle in body coordinate system; F_u – control vector; F_d – dynamical forces and torques; F_{est} – disturbances vector; $g(F_{est})$ – function of disturbances model.

Consider vector of estimation errors:

$$e_n = F_{est} - \hat{F}_{est} \quad (2)$$

where \hat{F}_{est} – disturbances estimation.

The next substitution is applied

$$\hat{F}_{est} = \hat{z} + s(x) \quad (3)$$

where \hat{z} – vector of estimator state; $s(x)$ – function to be designed.

From (2) and (3) follows

$$e_n = F_{est} - \hat{z} - s(x) \quad (4)$$

Standard equation for disturbances estimator is

$$\dot{e}_n + L(x)e_n = 0 \quad (5)$$

where $L(x)$ – matrix of estimator gains.

By differentiating the equation (4), and taking into account the model equations (1), we have from equation (5)

$$g(F_{est}) - \dot{\hat{z}} - \frac{\partial s(x)}{\partial x} M^{-1}(F_u + F_d + F_{est}) + L(x)(F_{est} - \hat{z} - s(x)) = 0 \quad (6)$$

The independency of the equation (6) on non-measurable variables vector can be written as:

$$g(F_{est}) - \frac{\partial s(x)}{\partial x} M^{-1} F_{est} + L(x) F_{est} = 0 \quad (7)$$

Suppose that the function $g(F_{est})$ is

$$g(F_{est}) = G_{est} F_{est} \quad (8)$$

where G_{est} – matrix of constant gains.

Taking into account (8) from equation (7) we obtain

$$G_{est} F_{est} - \frac{\partial s(x)}{\partial x} M^{-1} F_{est} + L(x) F_{est} = 0 \quad (9)$$

From (9) we obtain

$$\frac{\partial s(x)}{\partial x} = (L(x) + G_{est}) M \quad (10)$$

In general case solution of the equation (10) is

$$s(x) = G_{est} Mx + \int L(x) M dx + f_0 \quad (11)$$

where f_0 – constant.

Then equations (3), (6) of the estimator of disturbances are:

$$\dot{\hat{z}} = -L(x)\hat{z} - (L(x) + G_{est})(F_u + F_d) - L(x)(G_{est} Mx + \int L(x) M dx + f_0) \quad (12)$$

$$\hat{F}_{est} = \hat{z} + G_{est} Mx + \int L(x) M dx + f_0 \quad (13)$$

Suppose that the matrix $L(x) = L$ is constant. If disturbances are constant then the matrix $G_{est} = 0$ is zero matrix. In this case equations (12), (13) are

$$\dot{\hat{z}} = -L\hat{z} - L(F_u + F_d) - L(LMx + f_0) \quad (14)$$

$$\hat{F}_{est} = \hat{z} + LMx + f_0 \quad (15)$$

By differentiating the equation (15), taking into account equations (1), (14), we obtain:

$$\dot{\hat{F}}_{est} = -L\hat{z} - L(LMx + f_0) + F_{est} \quad (16)$$

Substituting in (16) variable \hat{z} from (15) we have

$$\dot{\hat{F}}_{est} = -L(\hat{F}_{est} - F_{est}) \quad (17)$$

Equation (17) proves exponential stability of the estimator (16), (17). In attrition from (19) it is clear that the disturbances estimation \hat{F}_{est} does not depend from constant f_0 . If

$f_0 = 0$, then estimator equations (14), (15) are

$$\dot{\hat{z}} = -L\hat{z} - L(F_u + F_d) - L^2 Mx \quad (18)$$

$$\hat{F}_{est} = \hat{z} + LMx \quad (19)$$

III. NONLINEAR ESTIMATOR DESIGN

Performance of indirect control systems can be increased by increasing gains of estimator (18), (19). However increase in the matrix L leads to increase in the sensitivity of the estimator to noise. This problem can be solved on base of nonlinear estimator

$$\dot{\hat{z}} = -L(e_n)\hat{z} - L(e_n)(F_u + F_d) - L(e_n)L(e_n)Mx \quad (20)$$

$$\hat{F}_{est} = \hat{z} + L(e_n)Mx \quad (21)$$

In this case estimation error is not measured. Therefore in this paper method of indirect measurement is applied to estimate the error.

Let us introduce the next model of underwater vehicle:

$$\dot{x}_m = M^{-1}(F_u + F_d + \hat{F}_{est}) \quad (22)$$

From the first equation of model (1) and model (22) we have:

$$M(\dot{x} - \dot{x}_m) = F_{est} - \hat{F}_{est} = e_n \quad (23)$$

Thus estimation error can be calculated on base of underwater vehicle accelerations. In general case underwater vehicle accelerations are measured by navigation system. If the accelerations are not measured then asymptotical estimations are applied. Matrix form of accelerations estimators are:

$$\begin{aligned} \dot{\omega}_1^x &= \omega_2^x + k_1^x(x - \omega_1^x) \\ \omega_2^x &= k_2^x(x - \omega_1^x) \end{aligned} \quad (24)$$

$$\begin{aligned} \dot{x} &= \omega_2^x \\ \dot{\omega}_1^{xm} &= \omega_2^{xm} + k_1^{xm}(x_m - \omega_1^{xm}) \\ \omega_2^{xm} &= k_2^{xm}(x_m - \omega_1^{xm}) \end{aligned} \quad (25)$$

where $\omega_1^x, \omega_2^x, \omega_1^{xm}, \omega_2^{xm}$ – vectors of the accelerations estimator state space variables; $k_1^x, k_2^x, k_1^{xm}, k_2^{xm}$ – matrices of the accelerations estimator gains.

Matrix of the disturbances estimator gains is:

$$L(e_n) = L_0 + K_L \left\| M \left(\dot{x} - \dot{x}_m \right) \right\| \quad (26)$$

where L_0 – matrix of constant gains in the steady state mode;

K_L – matrix of constant; $\|*\|$ – norm calculation.

IV. MODELING RESULTS

Consider example of disturbance estimation in the control system of underwater vehicle described by equation (1). The parameters of the estimator are:

$$L_0 = \text{diag}([2; 2; 2; 2; 2; 2])$$

$$K_L = \text{diag}([2; 2; 2; 2; 2; 2])$$

where $diag(x)$ – diagonal matrix from vector x .

Matrices of the underwater vehicle accelerations estimator (24), (25) are:

$$k_1^x = diag([20; 20; 20; 20; 20; 20])$$

$$k_2^x = diag([100; 100; 100; 100; 100; 100])$$

$$k_1^{xm} = diag([20; 20; 20; 20; 20; 20])$$

$$k_2^{xm} = diag([100; 100; 100; 100; 100; 100])$$

Simulation results of the estimator (20), (21) for constant and variable gain matrix L are presented on fig. 2, 3.

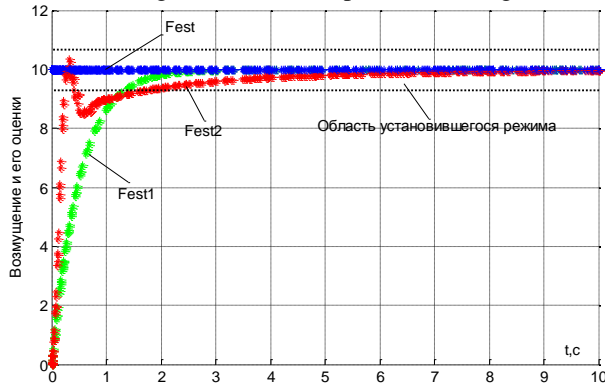


Fig. 2 Disturbances estimation

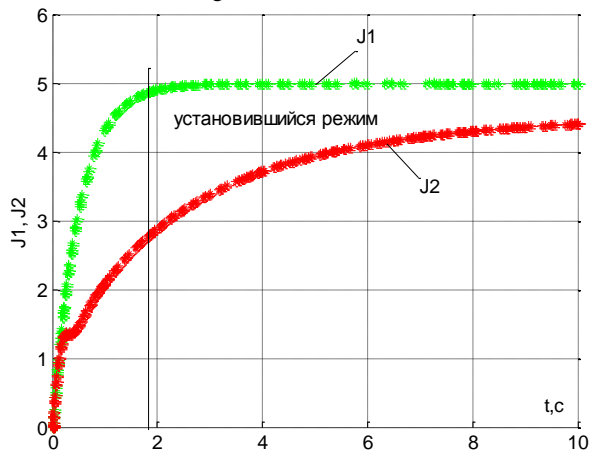


Fig. 3 Integral error of estimation

On fig. 2 disturbance F_{est}, estimation of disturbance F_{est1} with constant matrix L, and estimation of disturbance F_{est2} with variable matrix L are presented. On fig. 3 integral quality criterion J₁ of the linear estimator and criterion J₂ of the nonlinear estimator are presented. The area of steady state mode is presented on fig. 2 and fig. 3. From fig. 2 and fig. 3 it is clear that integral quality criterion of the nonlinear estimator is 15 % less than integral quality criterion of the linear estimator. In transient mode error of the nonlinear estimator is 40 % less than error of the linear estimator. Integral quality criterion is

$$J_1 = J_2 = \int (F_{est} - \hat{F}_{est})^2 dt \quad (27)$$

In steady state mode gain of the linear estimator is equal to gain of the nonlinear estimator. Therefore output noise of the linear estimator is equal to output noise of the nonlinear

estimator.

On fig. 4 we can see simulation results for estimator of time derivative (24), (25). There are estimated variable \dot{x} and estimation $\hat{\dot{x}}$ on fig. 4.

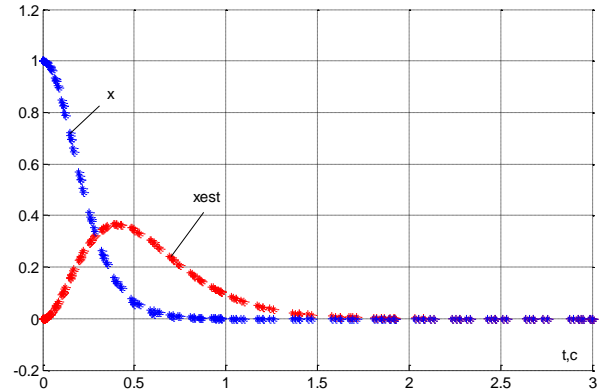


Fig. 4 Time derivative estimation

For the approximation of disturbances Taylor is used. Taylor series is a universal. Therefore the estimator (18), (19) can be applied for estimation of variable disturbances. For example, on fig. 5 and 6 simulation results of the estimator (18), (19) with variable disturbance are presented.

On fig. 5 the estimated variable disturbance F_{est}, the estimation F_{est1} by linear observer, and the estimation F_{est2} by nonlinear observer are presented.

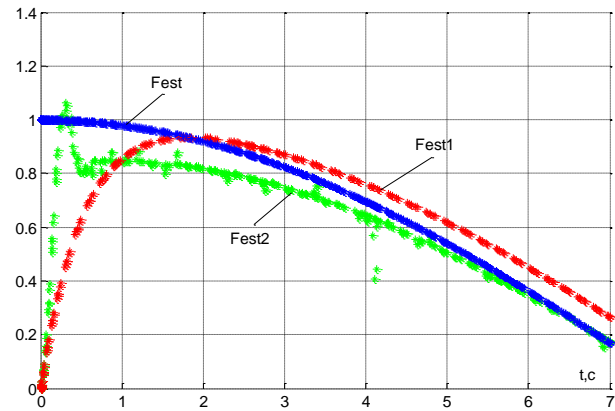


Fig. 5 Estimations of the variable disturbance

On fig. 6 integral errors of estimation for the linear observer J₁, and for the nonlinear observer J₂ are presented. From fig. 6 it is clear that the nonlinear estimator ensures zero error of steady state mode. In the transient mode error of the nonlinear estimator is 30 % less than error of the linear estimator.

For simulation demonstrated on fig. 5 and fig. 6 matrix $K_L = diag([20; 20; 20; 20; 20; 20])$.

closed loop system with nonlinear estimator (20), (21) are presented. Disturbance of the underwater vehicle operates in a time interval of 50 to 60 seconds. The controller is designed on base of position-path method [3], [8].

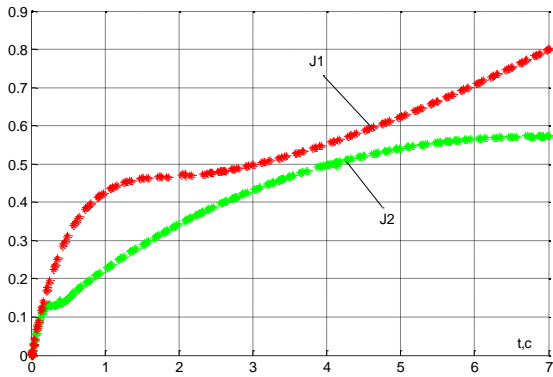


Fig. 6 Integral errors for the linear and nonlinear estimators
On fig. 7 – fig. 10 simulation of the underwater vehicle

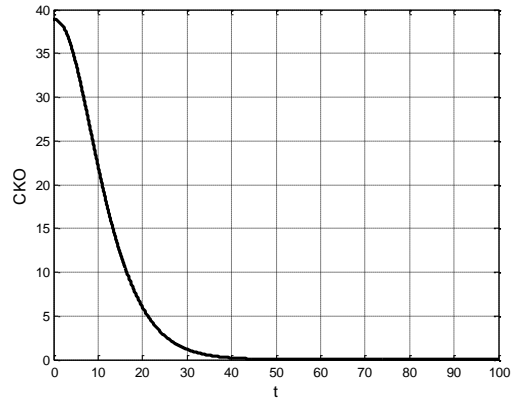


Fig. 10 Underwater vehicle speed with estimator

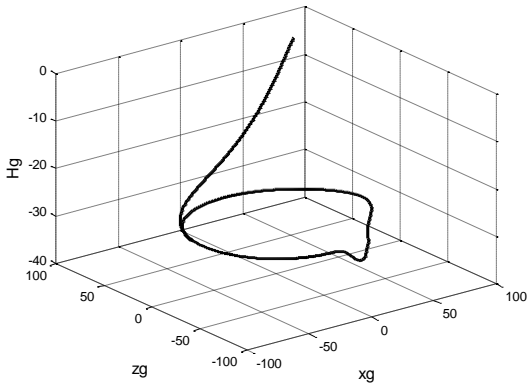


Fig. 7 Underwater vehicle path without estimator

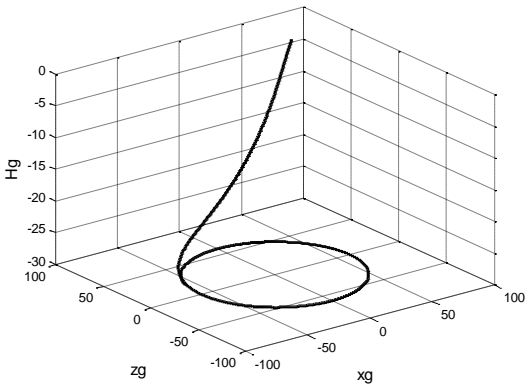


Fig. 8 Underwater vehicle path with estimator

Simulation results of the closed loop systems demonstrate the effectiveness of the estimator.

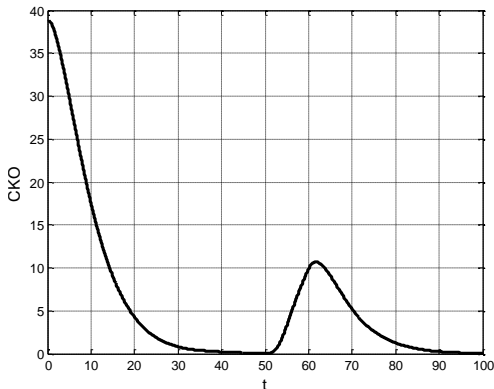


Fig. 9 Underwater vehicle speed without estimator

V. HARDWARE IMPLEMENTATION

Experimental verification of the proposed algorithms is performed with surface mini-vehicle. Block diagram of the layout is shown in Figure 11.

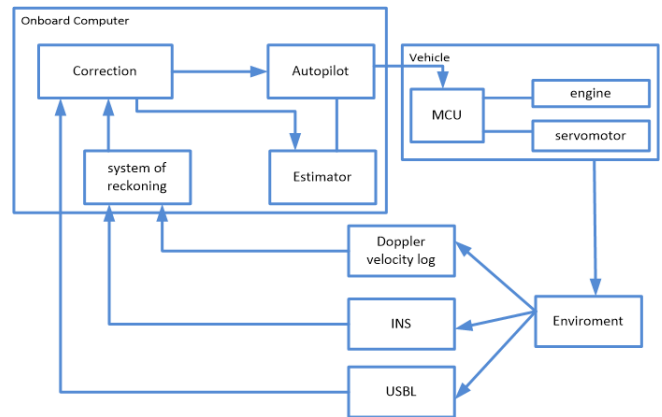


Fig. 11. Block diagram

MCU- microcontroller control unit, INS – inertial navigation system, USBL – ultra short base-line navigation system.

Equipment used in the model are shown in Table 1.

Equipment	Model
OnBoard computer	Intel Atom N270 (1.6 GHz, 512 kB L2 cache, FSB 533 MHz)
MCU	AVR-CRUMB2560, ATmega2560
Doppler velocity log	RD instruments ExplorerDVL
INS	Companav 2
USBL	Evo Logic S2C R 48/78 USBL Acoustic Modem

Model based on the mini-vehicle is shown in Fig. 8 and 9.



Fig.12. mini-vehicle

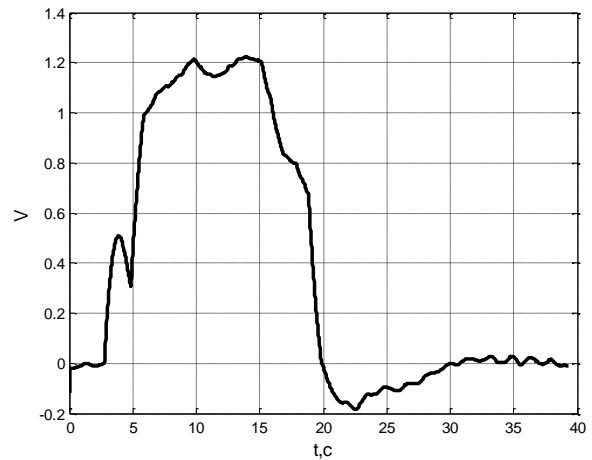


Fig.13. Velocity of mini-vehicle

Software on-board computer is written on the QNX operating system. The experimental results are shown in Fig. 10, 11, 12.

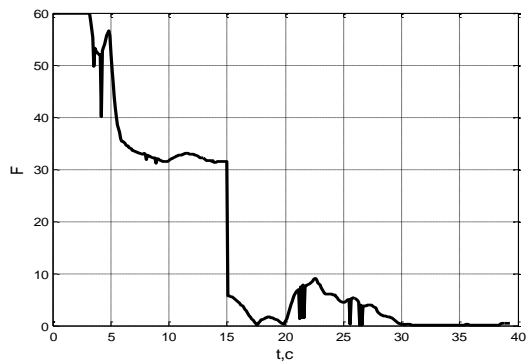


Fig.10. Control force

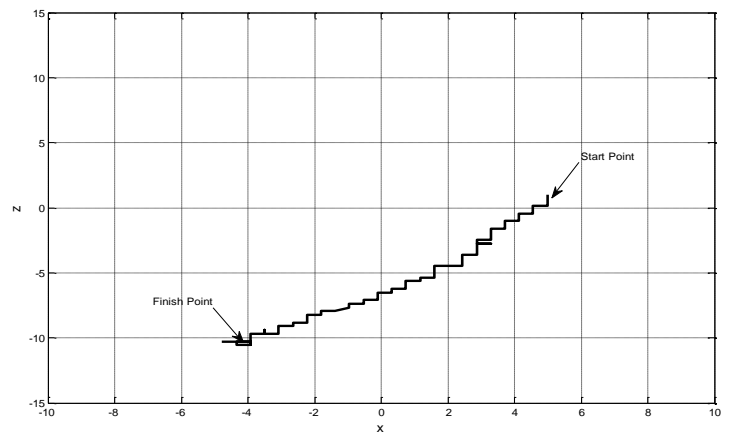


Fig.14. Trajectory of mini-vehicle

Mini-vehicle move from start point (0; 5) to finish point (-10; -4).

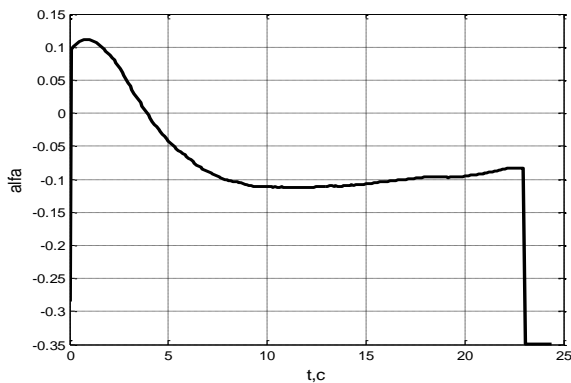


Fig.11. Control force Angle

VI. CONCLUSION

Suggested estimation method can be used for airships, helicopters, and other aircrafts. On base of the method estimation of speeds and accelerations of vehicles can be calculated. The main advantage of the method is high performance in steady state mode.

REFERENCES

- [1] Healey, Anthony J., Lienard, David. "Multivariable sliding mode control for autonomous diving and steering of unmanned underwater vehicles," *IEEE Journal of Oceanic Engineering*, vol 18 (3). 1993. Pp. 327-339.
- [2] D.J. Stilwell, B.E. Bishop, "Platoons of underwater vehicles," *IEEE Control Systems Magazine*, vol. 20 (6). 2000. Pp. 45-52.
- [3] V. Kh. Pshikhopov, M. Y. Medvedev, and B. V. Gurenko, "Homing and Docking Autopilot Design for Autonomous Underwater Vehicle" *Applied Mechanics and Materials* Vols. 490-491 (2014). Pp. 700-707. Trans Tech Publications, Switzerland. doi:10.4028/www.scientific.net/AMM.490-491.700.

- [4] V.Kh. Pshikhopov, M.Yu. Medvedev, "Block Design of Robust Control Systems by Direct Lyapunov Method," *IFAC PapersOnline*, vol. 18, 2012.
- [5] M.Y. Medvedev, V.Kh. Pshikhopov, "Robust control of nonlinear dynamic systems," *Proc. of 2010 IEEE Latin-American Conference on Communications*. September 14 – 17, 2010, Bogota, Colombia. ISBN: 978-1-4244-7172-0.
- [6] V. Pshikhopov, M. Medvedev, V. Kostjukov, R. Fedorenko, B. Gurenko, V. Krukhmalev, "Airship autopilot design," *SAE Technical Paper 2011*.
- [7] V.Kh. Pshikhopov, N.E. Sergeev, M.Y. Medvedev, A.E. Kulchenko, "Helicopter autopilot design," *SAE Technical Paper 2012*.
- [8] V.Kh. Pshikhopov, M. Y. Medvedev, M.Y. Sirotenko, V.A. Kostjukov, "Control System Design for Robotic Airship." *Preprints of the 9-th IFAC Symposium on Robot Control*. Gifu, Japan. September 9 – 12, 2009. Pp. 123 – 128.
- [9] P. Jantapremjit and P. A. Wilson, Autonomous homing and docking tasks for an underwater vehicle. In: 2nd International Conference on Underwater Systems, Bali, Indonesia, 04 - 05 Nov 2008. Bali, Indonesia, Underwater Society of Indonesia 6pp. (2008)
- [10] [Cowen et al., 1997] S. Cowen, S. Briest, and J. Dombrowski. Underwater docking of autonomous undersea vehicles using optical terminal guidance. In *Proceedings of MTS/IEEE OCEANS97*, volume 2, pages 1143–1147, 1997.
- [11] [Feezor et al., 2001] M.D. Feezor, F. Yates Sorrell, P.R. Blankinship, and J.G. Bellingham. Autonomous underwater vehicle homing/docking via electromagnetic guidance. *IEEE Journal of Oceanic Engineering*, 26(4):515–521, 2001.
- [12] [Lee et al., 2003] Pan-Mook Lee, Bong-Hwan Jeon, and Sea-Moon Kim. Visual servoing for underwater docking of an autonomous underwater vehicle with one camera. In *Proceedings of OCEANS 2003*, volume 2, pages 677–682, 2003.
- [13] Evans, J., Redmond, P., Plakas, C., Hamilton, K., and Lane, D. (22-26 Sept. 2003). Autonomous docking for intervention-AUVs using sonar a video-based real-time 3D pose estimation. In *Proc. OCEANS 2003*, volume 4, pages 220 Vol.4, San Diego, CA, USA.
- [14] Singh, H., Lerner, S., von der Heyt, K., and Moran, B. (1998). An intelligent dock for an autonomous ocean sampling network. In *Proc. of OCEANS'98*, volume 3, pages 1459–1462, France.
- [15] Stoney, R., Purcell, M., Forrester, N., Austin, T., Goldsborough, R., Allen, B., and von Alt, C. (6-9 Oct 1997). A docking system for REMUS, an autonomous underwater vehicle. In *Proc. OCEANS '97. MTS/IEEE*, volume 2, pages 1132–1136 vol.2, Halifax, Canada.
- [16] Wang, H., Rock, S., and Lees, M. (9-12 Oct 1995). Experiments in automatic retrieval of underwater objects with an AUV. In *Proc. OCEANS '95. MTS/IEEE*, volume 1, pages 366–373 vol.1.
- [17] Wettergreen, D., Gaskett, C., and Zelinsky, A. (1998). Development of a visually-guided autonomous underwater vehicle. In *Proc. of OCEAN'98 Conference*, volume 2, page 1200–1204, Nice, France.

The Representativeness reliability importance measure

Josep Freixas and Montserrat Pons

Abstract—A new reliability importance measure for components in a system, that we call Representativeness measure, is introduced. It evaluates to which extent the performance of a component is representative of the performance of the whole system. Its relationship with Birnbaum’s measure is analyzed, and the ranking of components given by both measures are compared. These rankings happen to be equal when all components have the same reliability but different in general. In contrast with Birnbaum’s, the Representativeness reliability importance measure of a component does depend on its reliability.

Keywords—Reliability importance measures, structural importance measures, node criticality relation, coherent structures, Birnbaum RIM, Birnbaum SIM.

ACRONYMS

RIM	reliability importance measure.
SIM	structural importance measure.
B–i.i.d.	Birnbaum RIM when all components are i.i.d.

NOTATIONS

N	set of components, which are assumed to be numbered consecutively from 1 to n .
x_i	binary random variable associated to component i : $x_i = 1$ if i is functioning, $x_i = 0$ otherwise.
$\phi(\mathbf{x})$	binary structure function of the system: $\phi(\mathbf{x}) = 1$ if system is functioning, $\phi(\mathbf{x}) = 0$ otherwise.
p_i	reliability of the i th component, $Pr\{x_i = 1\}$.
\mathbf{p}	reliability vector, $\mathbf{p} = (p_1, p_2, \dots, p_n)$.
(a_i, \mathbf{p})	vector \mathbf{p} with the i th component of \mathbf{p} changed to a .
π	collection of path sets of the system.
(N, π)	system defined by the collection π of path sets.
$h(\mathbf{p})$	system reliability, $Pr\{\phi(\mathbf{x}) = 1\}$.
$I_i^B(\mathbf{p})$	Birnbaum RIM of component i .
$I_i^{Bs}(\mathbf{p})$	Birnbaum SIM of component i .
$I_i^R(\mathbf{p})$	Representativeness RIM of component i .
$I_i^{Rs}(\mathbf{p})$	Representativeness SIM of component i .

Research partially supported by Grant MTM2012–34426/FEDER from “Ministerio de Economía y Competitividad” of the Spanish Government. The authors are with the Universitat Politècnica de Catalunya (UPC), in the Department of Applied Mathematics III (e-mails: [josep.freixas; montserrat.pons]@upc.edu). Postal address: EPSEM, Avda. Bases de Manresa, 61-73, E-08242 Manresa, Spain.

ASSUMPTIONS

- 1) the random variables x_i are mutually statistically independent.
- 2) the systems we consider are coherent:
 - the structure function ϕ is nondecreasing,
 - all components are relevant.
- 3) $0 < p_i < 1$ for any component i .

I. INTRODUCTION

If component reliability data is available then reliability importance measures allow the identification of those components that are more important from a reliability/safety or design point of view. This is specially relevant when the goal is to improve the system reliability through the improvement of the reliability of a component, although different goals can lead to different perspectives about which properties make one component more important than another. To define a reliability importance measure, we need to know the structure of the system and the reliability of its components.

Many reliability importance measures (RIM) have been defined till now (see [1] for a complete and detailed survey on importance measures¹). The most well-known, proposed by Birnbaum [2], evaluates the contribution of a component to the system reliability by the rate at which the system reliability improves as the reliability of the component improves. Other useful reliability importance measures are the Improvement potential RIM [3], the Criticality RIM [4], the Fussell–Vesely ([5]– [7]), the Reliability achievement worth [8] or the Reliability reduction worth [9].

Performing an structural analysis is the usual instrument for evaluating the security of a system when component reliabilities are not known. An structural analysis is usually performed when components with different reliabilities can be arbitrarily assigned to various nodes in the system, so that in this analysis the position of each node in the system determines its importance. Some structural importance measures (SIM) are defined from reliability importance measures by taking into account only some component reliabilities. In this way, B–i.i.d. importance is defined from Birnbaum RIM by assuming that all components independently have the same reliability p (see [10]–[12]), and Birnbaum SIM is defined from B–i.i.d. importance by setting $p = 1/2$. Other structural importance measures have been defined from reliability importance measures, like Fussell–Vesely SIM or Barlow–Proschan SIM [13]. In most cases what is more relevant about structural measures

¹Most of the names given to importance measures in the present article are taken from this book.

is the ranking that they establish among the components in the system, and some of them are defined only as preorderings (partial or total) between components. Examples of this importance rankings are the permutation importance [10], the domination importance (see [12] and [14]), the cut importance (see [15] and [16]) or the cut–path importance (see [17] and [18]).

In our work we propose a new index for measuring the reliability importance of a component. This index evaluates the degree of “coupling” between one component and the whole system, i.e., the likelihood that the system and the component are in the same state. We call it Representativeness Measure because by selecting and analyzing the performance of components with a high value of this measure we can have an acceptable estimation of the performance of the system. In this sense we think that this measure can be useful for maintenance purposes. This measure gives rise to an associated structural importance measure when all components have the same reliability equal to one half.

In section 2 the context of the work is established and some basic definitions are given. The Representativeness RIM and SIM are defined in section 3 and their main properties are proved. In section 4 we compare these new measures with Birnbaum measures, and section 5 concludes the article. All proofs of the different statements are collected in the Appendix.

II. FRAMEWORK

We consider binary systems, i.e., systems in which there is a random variable associated to each component which takes the value 1 if it is functioning and 0 otherwise. These random variables are assumed to be mutually statistically independent. The structure function of the system is a binary function of these random variables that takes the value 1 if the system is functioning and 0 otherwise. We assume that this structure function is nondecreasing.

The structure function of a system can be expressed in terms of its path sets. This is why we usually denote a system by (N, π) , where $N = \{1, 2, \dots, n\}$ is the set of components and π is the collection of path sets. Recall that a path set is a set of components which by functioning ensure that the system is functioning. A path set is minimal if it does not have proper path subsets. A component i is relevant if it belongs to at least one minimal path set.

The systems we consider have a nondecreasing structure function and all the components are relevant. They are referred to as *coherent systems*.

The reliability $h(\mathbf{p})$ of the system, i.e., the probability of it being functioning, depends on its structure function and on the reliability of each component. If p_i is the reliability of component i (the probability of it being functioning), and \mathbf{p} is the reliability vector (p_1, p_2, \dots, p_n) , then the system reliability can be expressed by means of path sets:

$$h(\mathbf{p}) = \sum_{S \in \pi} \prod_{i \in S} p_i \prod_{i \in N \setminus S} (1 - p_i). \quad (1)$$

Recall also that, by a conditional probability argument, for any component i we get:

$$h(\mathbf{p}) = p_i h(1_i, \mathbf{p}) + (1 - p_i) h(0_i, \mathbf{p}) \quad (2)$$

and from this expression we obtain:

$$\frac{\partial h}{\partial p_i}(\mathbf{p}) = h(1_i, \mathbf{p}) - h(0_i, \mathbf{p}). \quad (3)$$

Along the paper we will refer to the reliability importance measure *Birnbaum RIM* and to its associated structural importance measure *Birnbaum SIM*. The Birnbaum RIM of a component, introduced by Birnbaum in [2], measures the sensitivity of the system reliability with respect to small changes in the reliability of this component. The formal definitions of these measures are given next. For references on these and other importance measures see [1].

From now on we assume that (N, π) is a fixed coherent system, and all definitions and properties are to be thought in this system even though we do not specify their dependency on it. Also, \mathbf{p} denote an arbitrary reliability vector with $\mathbf{p} \in (0, 1)^n$, and i an arbitrary component in N .

Definition II.1 Birnbaum Importance Measures

a) *Birnbaum RIM:*

$$I_i^B(\mathbf{p}) = \frac{\partial h}{\partial p_i}(\mathbf{p})$$

b) *Birnbaum SIM:*

$$I_i^{Bs} = I_i^B(\mathbf{1}/2) \quad \text{where } \mathbf{1}/2 = (1/2, \dots, 1/2)$$

III. THE REPRESENTATIVENESS IMPORTANCE MEASURES

In this section we start by defining the Representativeness reliability importance measure (RIM). The aim of introducing it is to have a measure of the degree of “agreement” between the performance of a given component and the performance of the whole system. We define it as a sum of two probabilities: the probability that the system and the component are both functioning plus the probability that the system and the component are both in a failing state. In this way, the Representativeness RIM is nothing more than the probability that the system is in the same state as the component. If all component reliabilities are set to 1/2 then we obtain the Representativeness structural importance measure (SIM)

Definition III.1 Representativeness Importance Measures

a) *Representativeness RIM:*

$$I_i^R(\mathbf{p}) = p_i h(1_i, \mathbf{p}) + (1 - p_i)(1 - h(0_i, \mathbf{p}))$$

b) *Representativeness SIM:*

$$I_i^{Rs} = I_i^R(\mathbf{1}/2) \quad \text{where } \mathbf{1}/2 = (1/2, \dots, 1/2)$$

Let us see the value of these measures in the most basic systems: series or parallel.

Example III.2 *Series system*

In a series system it is $h(\mathbf{p}) = \prod_{k=1}^n p_k$. Then

$$I_i^R(\mathbf{p}) = 1 - p_i + h(\mathbf{p}),$$

$$I^{Rs} = 1/2 + 1/2^n.$$

Thus, in a series system, the value of the Representativeness RIM of any component is at least $h(\mathbf{p})$ (the system reliability). Also, notice that the more reliable the component the smaller its Representativeness RIM. The Representativeness SIM has the same value for all components.

Example III.3 *Parallel system*

In a parallel system it is $h(\mathbf{p}) = 1 - \prod_{k=1}^n (1 - p_k)$. Then

$$I_i^R(\mathbf{p}) = p_i + 1 - h(\mathbf{p}),$$

$$I^{Rs} = 1/2 + 1/2^n.$$

Thus, in a parallel system, the value of the Representativeness RIM of any component is at least $1 - h(\mathbf{p})$ (the system unreliability). Also, notice that the more reliable the component the larger its Representativeness RIM. Either in a series or in a parallel system the Representativeness SIM has the same expression.

The first basic properties of the Representativeness RIM are established in the following proposition:

Proposition III.4

- i) $0 \leq \min\{p_i, 1 - p_i\} \leq I_i^R(\mathbf{p}) \leq 1$.
- ii) $I_i^R(\mathbf{p}) \geq I_i^B(\mathbf{p})$.
- iii) $I_i^R(\mathbf{p}) = (1 - p_i)[1 - 2h(0_i, \mathbf{p})] + h(\mathbf{p})$.
 $I_i^R(\mathbf{p}) = p_i[2h(1_i, \mathbf{p}) - 1] + 1 - h(\mathbf{p})$.
- iv) $I_i^R(\mathbf{p})$ is a linear function of p_i .
- v) $I_i^R(\mathbf{p})$ is non-decreasing in p_i if and only if $h((1/2)_i, \mathbf{p}) \geq 1/2$.

The following property relates the Representativeness RIM of a component in a system with the Representativeness RIM of the same component in its dual system. Recall that the reliability function of the dual system, which we denote by h^D , verifies that $h^D(\mathbf{p}) = 1 - h(\mathbf{q})$, where $\mathbf{q} = (1 - p_1, \dots, 1 - p_n)$ and h is the reliability function of the original system.

Proposition III.5

- Let $I_i^R(\pi, \mathbf{p})$ and $I_i^R(\pi^D, \mathbf{p})$ denote the Representativeness RIM of component i for a vector \mathbf{p} in the system π and in its dual π^D respectively. Then,

$$I_i^R(\pi^D, \mathbf{p}) = I_i^R(\pi, \mathbf{q})$$

where $\mathbf{q} = \mathbf{1} - \mathbf{p}$.

- Let $I_i^R(\pi)$ and $I_i^R(\pi^D)$ denote the Representativeness SIM of component i in the system π and in its dual π^D respectively. Then,

$$I_i^{Rs}(\pi^D) = I_i^{Rs}(\pi)$$

Let now focus our attention in the Representativeness SIM. Notice that, as was seen in Examples III.2 and III.3, the expression of this measure for any component in these systems is $I^{Rs} = 1/2 + 1/2^n$. Since the expression for the Birnbaum SIM is $I^{Bs} = 1/2^{n-1}$, we see that $I_i^{Rs} = 1/2 + 1/2 I_i^{Bs}$. In the next proposition we prove that this expression is valid in any system and for any component.

Proposition III.6 *For any component $i \in N$ it is*

$$I_i^{Rs} = 1/2 + 1/2 I_i^{Bs}$$

A clear consequence of Proposition III.6 is that these two structural measures rank the components of the system in the same order. But the linear relationship between the Birnbaum SIM and the Representativeness SIM established in Proposition III.6 can not be extended in a general way between the Birnbaum RIM and the Representativeness RIM. In fact we can have $I_i^R(\mathbf{p}) > 1/2 + 1/2 I_i^B(\mathbf{p})$ and $I_i^R(\mathbf{p}) < 1/2 + 1/2 I_i^B(\mathbf{p})$ in a system, for the same components i, j , depending only on the reliability vector \mathbf{p} , as we show in the following example.

Example III.7 *Consider a 3-out-of-4 system.*

If we consider all components having the same reliability p then the Birnbaum RIM and the Representativeness RIM of all components are the same (thus we omit here the arbitrary subscript i) and their respective values are:

$$I^B(p) = 3p^2(1 - p) \quad \text{and} \quad I^R(p) = p^3(2 - p) + 1 - p.$$

Now, if $p = 0.6$ it is $I^B(0.6) = 0.432$ and $I^R(0.6) = 0.7024$ so that $I^R(0.6) < 1/2 + 1/2 I^B(0.6)$, but for $p = 0.4$ it is $I^B(0.4) = 0.288$ and $I^R(0.4) = 0.7024$ so that $I^R(0.4) > 1/2 + 1/2 I^B(0.4)$.

In the next theorem we prove that $\mathbf{p} = \mathbf{1}/2$ is the only reliability vector for which the linear relationship stated in Proposition III.6 is valid between Birnbaum RIM and Representativeness RIM:

Theorem III.8

$$I_i^R(\mathbf{p}) = 1/2 + 1/2 I_i^B(\mathbf{p})$$

for any system π , and for any component i

$$\Updownarrow$$

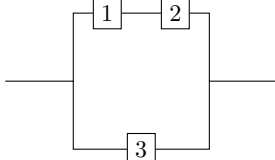
$$\mathbf{p} = \mathbf{1}/2$$

Theorem III.8 proves that the Representativeness RIM and the Birnbaum RIM are not only conceptually different but also analytically independent, as there is no way to derive one concept from the other, and only for the particular case $\mathbf{p} = (1/2, \dots, 1/2)$ there is an affine relationship between the two measures.

IV. COMPARING THE IMPORTANCE OF TWO COMPONENTS

In the former section we proved that the Representativeness SIM and the Birnbaum SIM rank the components of any system in the same way. It is also clear (see Examples III.2 and III.3) that the Representativeness RIM and the Birnbaum RIM rank components of a series (parallel) system in the same way. But this is not true in general, as is shown in the following example.

Example IV.1 Consider the 3-component system given in the following diagram:



The reliability function is $h(\mathbf{p}) = p_3 + p_1p_2 - p_1p_2p_3$.

If we take, for instance, $\mathbf{p} = (0.6, 0.9, 0.7)$, then components 1 and 2 verify:

$$\begin{aligned} I_1^R(\mathbf{p}) &= 0.702 &< & 0.822 = I_2^R(\mathbf{p}) \\ I_1^B(\mathbf{p}) &= 0.27 &> & 0.18 = I_2^B(\mathbf{p}) \end{aligned}$$

and, thus, the two measures rank them in an opposite order.

This section is devoted to comparing the Birnbaum RIM and the Representativeness RIM of two components, and in characterizing the cases in which the Birnbaum RIM and the Representativeness RIM rank the components of a system in the same order.

It is well-known the behavior of the Birnbaum RIM on a series system (the most reliable component has the smallest Birnbaum RIM) and on a parallel system (the most reliable component has the largest Birnbaum RIM), which happens to be the same of the Representativeness RIM in both kinds of systems (see Examples III.2 and III.3). Similar properties can be stated for systems which have a component in series (parallel) with the rest of the system, and we prove that they are verified also for the Representativeness RIM. These properties are proved in the next proposition:

Proposition IV.2

a) If a component i is in series with the rest of the system then, for any $j \neq i$:

$$p_i \leq p_j \Rightarrow I_i^B(\mathbf{p}) \geq I_j^B(\mathbf{p}) \quad \text{and} \quad I_i^R(\mathbf{p}) \geq I_j^R(\mathbf{p})$$

b) If a component i is in parallel with the rest of the system then, for any $j \neq i$:

$$p_i \geq p_j \Rightarrow I_i^B(\mathbf{p}) \geq I_j^B(\mathbf{p}) \quad \text{and} \quad I_i^R(\mathbf{p}) \geq I_j^R(\mathbf{p})$$

Another common property of Birnbaum RIM and Representativeness RIM is their relation with the node criticality pre-order, introduced by Boland et al. (see [10]), defined on the set of components. Let us recall the definition of this pre-order:

Definition IV.3 Node criticality relation

- $i \succeq j \Leftrightarrow h(1_i, 0_j, \mathbf{p}) - h(0_i, 1_j, \mathbf{p}) \geq 0$ for any \mathbf{p} .
- $i \succ j \Leftrightarrow i \succeq j$ and $h(1_i, 0_j, \mathbf{p}) - h(0_i, 1_j, \mathbf{p}) > 0$ for some \mathbf{p} .

Proposition IV.4

- If $i \succeq j$ and $p_i = p_j$ then $I_i^R(\mathbf{p}) \geq I_j^R(\mathbf{p})$.
- If $i \succ j$ and $p_i = p_j$ then $I_i^R(\mathbf{p}) > I_j^R(\mathbf{p})$.

In the next theorem we state that, if the system has more than two components, the Representativeness and the Birnbaum RIM rank them in the same order if all components have identical reliability p , but for different component reliabilities these rankings can be different.

Theorem IV.5 Let i, j be different components in N .

- i) If $p_i = p_j$ then $[I_i^R(\mathbf{p}) > I_j^R(\mathbf{p}) \Leftrightarrow I_i^B(\mathbf{p}) > I_j^B(\mathbf{p})]$ for any system π .
- ii) If $N = \{i, j\}$ then $[I_i^R(\mathbf{p}) > I_j^R(\mathbf{p}) \Leftrightarrow I_i^B(\mathbf{p}) > I_j^B(\mathbf{p})]$ for any system π .
- iii) If $p_i \neq p_j$ and there is a component $k \neq i, j$ with $p_k \neq 1/2$, then we can find a system π such that $[I_i^R(\mathbf{p}) - I_j^R(\mathbf{p})][I_i^B(\mathbf{p}) - I_j^B(\mathbf{p})] < 0$.
- iv) If $p_i \neq p_j$ and for any component $k \neq i, j$ it is $p_k = 1/2$, then we can find a system π such that $I_i^B(\mathbf{p}) \neq I_j^B(\mathbf{p})$ and $I_i^R(\mathbf{p}) = I_j^R(\mathbf{p})$.

Corollary IV.6 Let $n \geq 3$. Then,

$$\begin{aligned} [I_i^B(\mathbf{p}) > I_j^B(\mathbf{p}) \Leftrightarrow I_i^R(\mathbf{p}) > I_j^R(\mathbf{p})] \\ \text{for any system } \pi \quad \text{and for any } i, j \in N \\ \Downarrow \\ \text{all components of } \mathbf{p} \text{ coincide.} \end{aligned}$$

The Corollary IV.6 states that, if all components of N have the same reliability then, the Representativeness RIM and Birnbaum RIM rank them in the same way, independently of the system taken, but this is the only case in which this property occurs. Thus, under equal reliability of components both measures are qualitatively similar but in any other case the rankings they produce are different. As the two measures order components in different ways for arbitrary component reliabilities we should take into account both measures when analyzing a system. The Representativeness RIM reflects the degree of concordance between the component and the system, or its likelihood of replicating the system performance. In some way it measures how sensitive is a component in the system, and therefore how small changes in this component can cause the loss of this sensitivity. We do think that designers should pay attention to this measure and that it should be taken into account in the near future.

V. CONCLUSIONS

In this paper the Representativeness RIM for components in a system is defined. It evaluates the degree of agreement between

the performance of the component and the performance of the system, so that a component with a high Representativeness measure somehow reflects the performance of the system. This is why we give it this name.

There are similarities and differences with the well-known Birnbaum reliability importance measure. While the Birnbaum measure is the probability that the failure and functioning of the component coincide with system failure and functioning, being decisive for this to happen, the Representativeness measure is the probability that the failure and functioning of the component coincide with system failure and functioning taking into account all possible situations.

A clear difference between the two measures is that, in contrast with Birnbaum's, the Representativeness RIM of a component does depend on its reliability.

In any system, both measures rank components in the same way if they have the same reliability, and we have also described some particular cases in which the ranking given by both measures is the same, but in general these rankings do not coincide.

We think that the Representativeness RIM, which, as far as we know had not been defined before in system reliability analysis, has a good potential and it would be worth to analyze it more soundly. For instance, it would be interesting to study this measure in the basic k -out-of- n systems and in the different types of consecutive k -out-of- n systems, to compare the Representativeness RIM with Birnbaum's in these contexts and to analyze the possible rankings that can be obtained.

REFERENCES

- [1] W. Kuo and X. Zhu, *Importance measures in reliability, risk, and optimization*. UK: Wiley, 2012.
- [2] Z. Birnbaum, "On the importance of different components in a multicomponent system," in *Multivariate Analysis*. New York, USA: Academic Press, 1969, vol. 2.
- [3] T. Aven and U. Jensen, *Stochastic models in reliability*. New York: Springer, 1999.
- [4] W. Kuo and M. Zuo, *Optimal reliability modeling: principles and applications*. New York: Wiley, 2003.
- [5] J. Fussell, "How to hand-calculate system reliability and safety characteristics," *IEEE Transactions on Reliability*, vol. 24, pp. 169–174, 1975.
- [6] W. Vesely, "A time dependent methodology for fault tree evaluation," *Nuclear Engineering and Design*, vol. 13, pp. 337–360, 1970.
- [7] F. Meng, "Comparing the importance of system components by some structural characteristics," *IEEE Transactions on Reliability*, vol. 45, no. 1, pp. 59–65, 1996.
- [8] D. Vasseur and M. Llory, "International survey on PSA figures of merit," *Reliability Engineering and System Safety*, vol. 66, pp. 261–274, 1999.
- [9] L. P. G. Levitin and E. Zio, "Generalised importance measures for multi-state elements based on performance level restrictions," *Reliability Engineering and System Safety*, vol. 82, pp. 287–298, 2003.
- [10] P. Boland, F. Proschan, and Y. Tong, "Optimal arrangements of components via pairwise rearrangements," *Naval Research Logistics*, vol. 36, pp. 807–815, 1989.
- [11] F. Lin and W. Kuo, "Reliability importance and invariant optimal allocation," *Journal of Heuristics*, vol. 8, pp. 155–171, 2002.
- [12] J. Freixas and M. Pons, "Identifying optimal components in a reliability system," *IEEE Transactions on Reliability*, vol. 57, pp. 163–170, 2008.
- [13] R. Barlow and F. Proschan, "Importance of system components and fault tree event," *Stochastic processes and their applications*, vol. 3, pp. 153–172, 1975.
- [14] J. Freixas and M. Pons, "The influence of the node criticality relation on some measures of component importance," *Operations Research Letters*, vol. 36, pp. 557–560, 2008.
- [15] D. Butler, "A complete importance ranking for components of binary coherent systems with extensions to multi-state systems," *Naval Research Logistics Quarterly*, vol. 4, pp. 565–578, 1979.
- [16] F. Meng, "Some further results on ranking the importance of system components," *Reliability Engineering and System Safety*, vol. 47, no. 2, pp. 97–101, 1995.
- [17] F. Hwang, "A new index of component importance," *Operations Research Letters*, vol. 2, pp. 75–79, 2001.
- [18] —, "A hierarchy of importance indices," *IEEE Transactions on Reliability*, vol. 54, no. 1, pp. 169–172, 2005.

CDM Controller Order and Disturbance Rejection Ability

João Paulo Coelho, Wojciech Giernacki and José Boaventura-Cunha

Abstract—The coefficient diagram method is primarily an algebraic control design method whose objective is to easily obtain a good controller with minimum user effort. As a matter of fact, if a system model, in the form of linear differential equations, is known, the user only need to define a time-constant and the controller order. The later can be established regarding the expected disturbance type via a lookup table first published by Koksal and Hamamci in 2004. However an inaccuracy in this table was detected and pointed-out in the present work. Moreover the above mentioned table was expanded in order to enclose any k order type disturbance.

Keywords—Coefficient diagram method, control system design, disturbance rejection.

I. INTRODUCTION

THE coefficient diagram method (CDM), as a control design and analysis method, was presented by Shunji Manabe in the late nineties of the twentieth century [11], [12]. Since then many articles have been published in both CDM theoretical extensions [13], [1] and practical applications [2], [4], [16].

From the user point-of-view, the main feature of CDM is its simplicity. In fact the design process only requires the designer to define a single parameter: the equivalent time-constant. Then the controller transfer function is automatically obtained via an algebraic method similar to pole placement. However, unlike the latter, the characteristic polynomial in CDM is easily defined. An improved version of Kessler's standard form [7], commonly called Manabe's standard form, is selected as the target polynomial. This choice will lead to a zero overshoot closed-loop step response and a settling time within 2.5 to 3 time-constants.

Besides the CDM algebraic nature, this method also includes a diagram that can be used to understand the system behaviour. In fact the precise name of this method derives from this diagram. The plotted curves in this diagram can be used to analyse the system dynamic behaviour, its robustness regarding modelling errors and stability. The latter is added by taking into consideration the Lypatov-Sokolov sufficient stability conditions [10]. In this article only the algebraic steps

J.P. Coelho is with CITAB, centre for the research and technology of agro-environmental and biological sciences, and with ESTiG, Polytechnic Institute of Bragança, Campus de Santa Apolónia, Apartado 1134, 5301-857 Bragança, Portugal. e-mail: jpc Coelho@ipb.pt

W. Giernacki is with the Division of Control and Robotics, Institute of Control and Information Engineering, Poznan University of Technology, Poland. e-mail: wojciech.giernacki@put.poznan.pl

J. Boaventura Cunha is with INESC TEC - INESC Technology and Science (formerly INESC Porto) and Universidade de Trás-os-Montes e Alto Douro, UTAD, Escola de Ciências e Tecnologia, Vila Real, Portugal. e-mail: jboavent@utad.pt

Manuscript received May 1, 2014; revised May 1, 2014.

of the method are considered. Hence the reader is referred to [14] for extended treatment on the diagram nature of this method.

In the same document Shunji Manabe emphasize that CDM is a control design procedure tailored for people without a strong (or even any) theoretical background in control theory. This statement is further reinforced after the publication of [8] where a guideline for controller order selection is presented. However there are some issues regarding the published table that the present article tries to point out. In particular the controller order selection when the system is subject to sinusoidal type disturbances.

The reasons that lead us to make this affirmation will be presented in section III. However, before that, an overview on the algebraic nature of CDM will be presented in section II. This paper ends with section IV where this work conclusions are exposed.

II. THE CDM CONTROLLER DESIGN METHOD

The CDM design procedure can be summarized as follows. First a plant mathematical model, in polynomial format, is required. Then the characteristic equation is established regarding the desired dynamic performance.

The next step concerns the definition of the controller order and his description also in polynomial format. Then the controller coefficients are obtained by solving a design equation similar to the Diophantine equation.

The last step is to analyse the coefficient diagram and make inference about the desired and obtained system characteristics. Computer simulation of the overall system, taking into consideration disturbances and measurement noise or sensor faults, should be made.

This section presents the first four steps of the above design algorithm and will be divided into four subsections. The first will address the controller structure where a closed-loop block diagram is presented and the μ operator is defined. The controller mathematical description is presented in subsection II-B and the characteristic polynomial in II-C. The last subsection concerns the design equation and the shape of the Sylvester matrix.

A. CDM Controller Structure

This section begins with the block diagram presented in Fig. 1 where the overall CDM closed-loop system structure can be perceived.

The first fact to be highlighted regards the use of variable μ within the block diagram architecture. Generally, in the

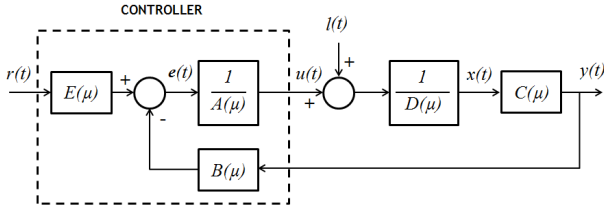


Fig. 1. Coefficient diagram method closed-loop system structure.

literature, a similar block diagram is presented but with the character s replacing μ . Even if this fact can be seen as irrelevant, the use of s can bias the reader to think that the above block diagram is expressed in the Laplace domain. However CDM handle the system in the time domain. Hence, in order to stress out this issue, the μ greek letter is used instead. Note that the relationship between the Laplace operator s and μ is equivalent to the relation between the Z -transform variable z and the backward shift operator q . The use of z character implies that the system representation is in the frequency domain while the use of q define it in the discrete-time domain. For example $Y(z) = (z^{-1} + 1)X(z)$ and $y(n) = (q^{-1} + 1)x(n)$ may resemble similar but, in fact, they are in different domains.

Within the CDM framework, the μ operator is define by the equality represented in equation (1).

$$\frac{d^i}{dt^i} = \mu^i \quad (1)$$

A general linear differential equation with constant coefficients a_i and b_j , for $i = 0, \dots, n$ and $j = 0, \dots, m$, with the following generic structure:

$$a_0 y(t) + \sum_{i=1}^n a_i \frac{d^i y(t)}{dt^i} = b_0 u(t) + \sum_{j=1}^m b_j \frac{d^j u(t)}{dt^j} \quad (2)$$

can assume an alternative formulation using the μ operator as shown in equation number (3).

$$y(t) \left(a_0 + \sum_{i=1}^n a_i \cdot \mu^i \right) = u(t) \left(b_0 + \sum_{j=1}^m b_j \cdot \mu^j \right) \quad (3)$$

This representation resembles a polynomial in μ with a_i and b_j as coefficient and n and m as their orders. Now if one define $A(\mu) = a_n \cdot \mu^n + \dots + a_0$ and $B(\mu) = b_m \cdot \mu^m + \dots + b_0$ then the system differential equation can be written, in a more compact way, as:

$$A(\mu) \cdot y(t) = B(\mu) \cdot u(t) \quad (4)$$

where the dot operation represent the product between each polynomial term and the related signal.

Remark that, even if equation (3) resembles a polynomial, in fact it does not represent a *true* polynomial since it does not possess the same properties. For example it is not allowed to express the signal $y(t)$ in equation (4) as,

$$y(t) = \frac{B(\mu)}{A(\mu)} \cdot u(t) \quad (5)$$

Another form of system representation requires the introduction of a state variable denoted by $x(t)$ and define as:

$$A(\mu) \cdot x(t) = u(t) \quad (6)$$

leading to a relationship between $y(t)$ and $x(t)$ expressed in (7).

$$y(t) = B(\mu) \cdot x(t) \quad (7)$$

Manabe in [11], [12] call the formulation expressed in equation (4) as *left polynomial form* and the one define by the pair of equations (6) and (7) by *right polynomial form*. This concept is fundamental to properly understand the block diagram system formulation.

In Fig. 1, it is possible to observe that some polynomials are represented in a fraction denominator. However this liberty must be properly understood as representing equation (6) or (7). For this reason, the quantity $\frac{1}{A(\mu)}$ must not be taken literally as there is no polynomial inverse in the μ domain. That is, this polynomial representation is algebraically define as a ring.

In the end, handling a polynomial in μ domain is different from the one expressed in s domain. However, in practice, the difference resumes to the fact that the numerator and denominator must be handled separately. They cannot co-exist in the same block since the polynomial inverse in μ is not defined

B. Controller Description

Consider again the block diagram of Fig. 1 where five different polynomials in the μ domain can be distinguished. All the signals involved in this schematic can be written using the following four relations:

$$y(t) = C(\mu) \cdot x(t) \quad (8)$$

$$D(\mu) \cdot x(t) = u(t) \quad (9)$$

$$A(\mu) \cdot u(t) = e(t) \quad (10)$$

$$e(t) = E(\mu) \cdot r(t) - B(\mu) \cdot y(t) \quad (11)$$

Both $C(\mu)$ and $D(\mu)$ concern the plant dynamics and the remaining three define the controller behaviour. Please note that if $B(\mu)$ was expressed in the Laplace domain it would be noncausal. Moreover, in CDM controller design, the pre-filte $E(\mu)$ is a zero order polynomial and his only coefficient is computed in order to achieve closed-loop zero steady state error.

Additionally, and for the sake of simplicity, let the order of both polynomials $A(\mu)$ and $B(\mu)$ be equal to n (even if some higher order coefficient of $B(\mu)$ must be set to zero). Moreover lets make the same assumption about the orders of polynomials $C(\mu)$ and $D(\mu)$. Let m be now its order value.

Also in equation (11) there must be a order match between the polynomials $E(\mu) \cdot r(t)$ and $B(\mu) \cdot y(t)$. In practice this mean that maybe higher order coefficient of one of the two polynomials are equal to zero.

After some simple algebraic manipulation, and by definin the $m + n$ order characteristic polynomial $P(\mu)$ as:

$$P(\mu) = A(\mu) \cdot D(\mu) + C(\mu) \cdot B(\mu) \quad (12)$$

the closed-loop system behaviour is represented by:

$$P(\mu) \cdot y(t) = C(\mu) \cdot E(\mu) \cdot r(t) \quad (13)$$

C. The Characteristic Polynomial

Obtaining a proper characteristic polynomial is a complex task usually requiring a deep knowledge on control theory in order to find the closed loop poles location. This task can be made easier by imposing a given structure to it. In [15] a comparison between several characteristic polynomial structures, regarding both time and frequency performance indexes, is presented. From the published results one can conclude that Manabe's and binomial polynomials present the best results.

We begin this section by rewriting the $n + m$ order characteristic polynomial $P(\mu)$ as:

$$P(\mu) = \sum_{i=0}^{n+m} p_i \cdot \mu^i \quad (14)$$

Let's define two additional figures the stability index, denoted by γ_i for $i = 1, \dots, (n + m) - 1$ and the predominant time constant τ . Both are described in further detail in [12] and presented hereafter in (15) and (16):

$$\gamma_i = \frac{p_i^2}{p_{i-1} \cdot p_{i+1}} \quad (15)$$

$$\tau = \frac{p_1}{p_0} \quad (16)$$

Each of the characteristic polynomial coefficient p_i in equation (14) can be written as a function of both stability indexes and predominant time constant. Hence the (normalized) characteristic polynomial can be expressed alternatively as:

$$\frac{P(\mu)}{p_0} = \sum_{i=2}^{n+m} \left\{ (\tau\mu)^i \left(\prod_{j=1}^{i-1} \frac{1}{\gamma_j} \right) \right\} + \tau\mu + 1 \quad (17)$$

For Manabe's polynomial, the coefficient are chosen in order to have the following stability index values [12]:

$$\gamma_i = \begin{cases} 2.5 & \text{if } i = 1 \\ 2 & \text{if } i = 2, \dots, n + m \end{cases} \quad (18)$$

D. Solving for the Controller

One of the hardest part in a pole placement method is to obtain the characteristic polynomial. The CDM method presents a simple way to obtain it by just defining the desired equivalent time constant. Having the desired characteristic polynomial, the next step is just algebraic and requires solving an system of equations with the formulation described by (12).

Due to the fact that the plant dynamics are fixed, the above mentioned equation has an appearance that resembles the Diophantine equation from the numbers theory field. In this case we don't look for integers but for polynomials in μ domain.

Giving p_0 , τ and γ_i beforehand, the problem resumes to the pole-placement problem [8]. However in the CDM method

the structure of the Sylvester matrix differs from the pole placement one. This is due to the knowledge of some $A(\mu)$ coefficient due to a priori assumptions about the type of system disturbances.

Assuming the Sylvester matrix Σ has the structure represented in (20) and that the unknown polynomial coefficients considering zero the lower k coefficient of $A(\mu)$, are arranged in a vector \mathbf{x} as expressed in (21) then the CDM controller solution is obtained by solving equation,

$$\mathbf{x} = \Sigma^{-1} \cdot \mathbf{p} \quad (19)$$

were

$$\Sigma = \begin{bmatrix} d_m & c_m & \cdots & 0 & 0 \\ \vdots & \vdots & & \vdots & \vdots \\ d_{m-n+k} & c_{m-n+k} & & 0 & 0 \\ \vdots & \vdots & & \vdots & \vdots \\ d_0 & c_0 & \ddots & 0 & 0 \\ 0 & 0 & & d_m & c_m \\ \vdots & \vdots & & \vdots & \vdots \\ 0 & 0 & \cdots & d_0 & c_0 \end{bmatrix} \quad (20)$$

and

$$\mathbf{x} = [a_n \quad b_n \quad \cdots \quad a_k \quad b_k \quad b_{k-1} \quad \cdots \quad b_0]^T \quad (21)$$

$$\mathbf{p} = [p_{n+m} \quad \cdots \quad p_1 \quad p_0]^T \quad (22)$$

III. CONTROLLER ORDER AND DISTURBANCE REJECTION

Consider again the block diagram shown in Fig. 1 and let's analyse the output effect of a disturbance in the controlled variable $u(t)$. In order to do this the reference signals is set to zero. This leads to a relationship between $l(t)$ and $y(t)$ given by the differential equation presented in (23).

$$C(\mu) \cdot A(\mu) \cdot l(t) = \left(A(\mu) \cdot D(\mu) + C(\mu) \cdot B(\mu) \right) \cdot y(t) \quad (23)$$

Assuming $C(\mu)$ and $A(\mu)$ are polynomials with order m and n respectively and with the following form:

$$A(\mu) = a_n \cdot \mu^n + \cdots + a_0 \quad (24)$$

$$C(\mu) = c_m \cdot \mu^m + \cdots + c_0 \quad (25)$$

Moreover let's impose $c_0 \neq 0$. The product $A(\mu) \cdot C(\mu)$, present in equation (23), is a $m + n$ order polynomial. This polynomial will be denoted by $G(\mu)$ and expanded as:

$$G(\mu) = \sum_{i=0}^{m+n} g_i \cdot \mu^i \quad (26)$$

At this point, the effect of particular disturbance types on the output $y(t)$, will be discussed. For the system to be able to absorb the disturbance effect, $y(t)$ must tend to the reference signal as quickly as possible. Assuming $r(t) = 0$ this steady state system behaviour will be easily handled in the Laplace

domain. By applying the final value theorem the following equality should hold:

$$\lim_{t \rightarrow \infty} y(t) = \lim_{s \rightarrow 0} s \cdot Y(s) \quad (27)$$

where $Y(s)$ is the Laplace transform of $y(t)$. That is $Y(s) = \mathcal{L}\{y(t)\}$. However, for this equality to hold, all the $Y(s)$ poles must have negative real parts and no more than one pole can be at the origin [3].

Assuming causality and zero initial conditions, the application of Laplace transform to the differential equation (23) leads to,

$$Y(s) = \frac{G(s)}{A(s) \cdot D(s) + C(s) \cdot B(s)} L(s) \quad (28)$$

where $Y(s) = \mathcal{L}\{y(t)\}$ and $L(s) = \mathcal{L}\{l(t)\}$.

Applying the final value theorem to the above expression and remembering that the equality (27) must hold, then,

$$\lim_{s \rightarrow 0} s \cdot G(s) \cdot L(s) = 0 \quad (29)$$

where $G(s) \cdot L(s) = \mathcal{L}\{G(\mu) \cdot l(t)\}$.

Now let's analyse this last expression for different type of disturbance signals. If $l(t)$ is the impulse signal $\delta(t)$ than its Laplace transform is equal to the unity. In addition, taking into consideration that $\lim_{s \rightarrow 0} G(s) = g_0$, expression (29) resumes to:

$$\lim_{s \rightarrow 0} s \cdot G(s) = g_0 \cdot \lim_{s \rightarrow 0} s = 0 \quad (30)$$

This expression allows us to conclude that the closed loop system will always be able to absorb disturbance impulses regardless the controller type.

Let's proceed by increasing the disturbance order now for a step type input $h(t)$. Since $\mathcal{L}\{h(t)\} = \frac{1}{s}$, expression (29) take the following format:

$$\lim_{s \rightarrow 0} s \cdot G(s) \cdot \frac{1}{s} = g_0 \quad (31)$$

Since g_0 is equal to the product of a_0 and c_0 and since $c_0 \neq 0$ is assumed than, in order for equation (31) result to be zero, the controller coefficient a_0 must be equal to zero. For this reason, to completely suppress step disturbances, the controller type must be one. In other words it must have a pole at the origin.

Now for a ramp type input disturbance, and performing the same steps as above, expression (32) is obtained.

$$\lim_{s \rightarrow 0} s \cdot G(s) \cdot \frac{1}{s^2} = \lim_{s \rightarrow 0} \frac{G(s)}{s} \quad (32)$$

The former limit can be expanded as:

$$\lim_{s \rightarrow 0} \frac{g_{n+m} \cdot s^{n+m} + \dots + g_2 \cdot s^2 + g_1 \cdot s + g_0}{s} \quad (33)$$

Hence, for a complete ramp disturbance rejection, it is straightforward to see that, at least, both g_1 and g_0 must be zero. If all the $C(\mu)$ coefficient are assumed non-zero than this disturbance rejection only can be achieved if, at least, a_0 and a_1 are equal to zero. In this case the controller type will increase to 2.

This last case, together with the previous two, allows us to foresee a pattern for the controller type as a function of disturbance order. In fact, if the disturbance can be mathematically expressed as a n order impulse integral, than at least a n type controller is needed to fully suppress the disturbance effect.

This conclusion cannot be extrapolated for other signal types. For example, let's assume a ω frequency sinusoidal signal $l(t) = \sin(\omega t)$, represented in Laplace domain by $L(s) = \frac{\omega}{s^2 + \omega^2}$. If one attempts to apply the final value theorem then:

$$\omega \cdot \lim_{s \rightarrow 0} \frac{s \cdot G(s)}{s^2 + \omega^2} = \omega \cdot \lim_{s \rightarrow 0} \frac{g_{m+n} \cdot s^{n+m+1} + \dots + g_1 \cdot s^2 + g_0 \cdot s}{s^2 + \omega^2} \quad (34)$$

It's easy to see that the above expression is always equal to zero. So one may think that even a zero type controller can be able to suppress the disturbance effect from the output. However this is not the case. It's not possible to bypass sinusoidal type disturbances with the same controller structure as for the impulse type despite the result obtained from equation (34). Sinusoidal disturbance cancelation is a hard problem and the reader is addressed to [9], [6] and [5] for more details. The reason we cannot treat impulse and sinusoidal disturbances in the same way is that one has applied the final value theorem to an expression that has imaginary conjugate poles. When this situation happens, the final value theorem cannot be applied. For this reason the fourth column of table I in [8] is not accurate since it gives the same polynomial controller condition for both impulse and sinusoidal disturbances.

The above referred table is replicated in this document, with some modifications and labelled Tab. I. In this case without the sinusoidal disturbance type and including an extra table line for a generic k order disturbance. This table, just like the one published in [8], only gives a suggestion regarding the controller order to be used.

TABLE I
CONTROLLER ORDER SELECTION AS A FUNCTION OF SIGNAL
DISTURBANCE TYPE.

Disturbance type	$A(\mu)$ degree	$B(\mu)$ degree	$P(\mu)$ degree	Condition
None	$n - 1$	$n - 1$	$2n - 1$	-
Impulse	$n - 1$	$n - 1$	$2n - 1$	-
Step	n	n	$2n$	$a_0 = 0$
Ramp	$n + 1$	$n + 1$	$2n + 1$	$a_0 = 0,$ $a_1 = 0$
k order	$n+k-1$	$n+k-1$	$2n+k-1$	$a_0 = 0$... $a_{k-1} = 0$

This value must also take into consideration that, in order to have an invertible Sylvester matrix, for a n order system the controller must have order equal to $n - 1$ leading to a characteristic polynomial of order $2n - 1$.

However, some of the $A(\mu)$ controller polynomial coefficient may be already known after assuming complete elimination of some disturbance type. For example, assuming a step input disturbance, $a_0 = 0$. In this context a lower number

of equations are required to make square the Sylvester matrix. Taking into consideration this step type disturbance input, and for a m order controller, one have $m - 1$ unknowns about polynomial $A(\mu)$. Assuming that the order of polynomial $B(\mu)$ is also equal to m and that the system order is n than, by observing (21), and since a_0 is known, the vector of unknowns \vec{x} has now $2n + 1$ entries. Hence the Sylvester matrix has $(n + m + 1)$ lines and $2m + 1$ columns. In order for it to be square m must be equal to n . For this reason, the characteristic polynomial has order $2n$. The third line in the $P(\mu)$ degree column of Tab. I condensates this conclusion.

The same idea can be applied to the case one wants to completely suppress a ramp type disturbance effects. In this case the lower order controller that can accomplish this task has $a_0 = a_1 = 0$. The vector \vec{x} includes $2m$ elements. This lead to the constraint $m + n + 1 = 2m$ for $\vec{\Sigma}$ to be invertible. That is $m = n + 1$ and $P(\mu)$ is now a $2n + 1$ order polynomial. Once again this result can be observed in the fourth line of Tab. I.

Finally, for a m order controller to be able to suppress a k order disturbance, the lower k coefficient of $A(\mu)$ must be equal to zero. This fact leads to a k type controller. That is, one in which $a_0 = \dots = a_{k-1} = 0$. For this reason the vector of unknowns \vec{x} has now $2m - k + 2$ elements. For $\vec{\Sigma}$ invertibility, $2m - k + 2$ must be equal to $n + m + 1$. That is $m = n + k - 1$ leading to a $2n + k - 1$ order characteristic polynomial.

Before ending this section we want to emphasize that Tab. I is only a guideline. In fact there is no absolute need for a square Sylvester matrix if only an approximated solution is enough. Usually this least squares solution can be sufficient to ensure closed-loop system specification while leading to lower order controllers. Additionally the controller numerator order do not need to be equal to the denominator order. However giving too much freedom will violate the basilar principle of CDM: to be an easy application technique.

IV. CONCLUSION

The CDM method cornerstone relies on the design simplicity from the user point-of-view. Indeed, if the system model is known, the control designer only needs to define two things: the value of τ and the controller order. The later can be established taking into account the expected system disturbance shape. The relationship between the CDM controller order and the disturbance type was first published by [8]. However an error was detected and pointed-out in the present work. Moreover, the above mentioned table, was expanded in order to enclose any k order type disturbance.

REFERENCES

- [1] T. Benjanarasuth J. Ngamwiwit A. Cahyadi, D. Isarakorn and N. Komine. Application of coefficient diagram method for rotational inverted pendulum control. In *Control, Automation, Robotics and Vision Conference*, volume 3, pages 1769–1773, 2004.
- [2] A. Willsky A. Oppenheim and S. Nawab. *Signals and Systems*. Prentice Hall, 1997.
- [3] A. Budiyono and T. Sudiyanto. An algebraic approach for the mimo control of small scale helicopter. In *Proceedings of ICIUS07*, pages 64–72, 2007.
- [4] Z. Ding. Adaptive estimation and rejection of unknown sinusoidal disturbances in a class of non-minimum-phase nonlinear systems. *IEEE Proceedings Control Theory Applications*, 153(4):379–386, September 2006.
- [5] M. Hou. Amplitude and frequency estimator of a sinusoid. *IEEE Transactions on Autom*, 50(6):855–858, June 2005.
- [6] C. Kessler. Ein Beitrag zur theorie mehrschleifige regulungen. *Regelungst*, 8:261–266, 1960.
- [7] M. Koksai and S. E. Hamamci. A program for the design of linear time invariant control systems: Cdmcad. *Computer Applications in Engineering Education*, 12-3:165–174, 2004.
- [8] R. Ortega L. Hsu and G. Damm. A globally convergent frequency estimator. *IEEE Transactions on Automatic Control*, 44(4):698–713, April 1999.
- [9] A. V. Lipatov and N. Sokolov. Some sufficient conditions for stability and instability of continuous linear stationary systems. *Automat Remote Contr*, 39:1285–1291, 1979.
- [10] S. Manabe. Coefficient diagram method as applied to the attitude control of controlled-bias-momentum satellite. In *13th IFAC Symposium on Automatic Control in Aerospace*, pages 322–327, September 1994.
- [11] S. Manabe. The coefficient diagram method. In *14th IFAC Symposium on Automatic Control in Aerospace*, pages 199–210, August 1998.
- [12] S. Manabe. Coefficient diagram method in mimo application: An aerospace case study. In *Proceedings of the 16th IFAC World Congress*, pages 1961–1966, 2005.
- [13] S. Manabe and Y. Kim. Coefficient diagram method for control system design.
- [14] M. S. Tavazoei and M. Haeri. Comparison of the existing methods in determination of the characteristic polynomial. *World Academy of Science, Engineering and Technology*, 6:720–723, 2007.
- [15] P. Roengruen T. Suksri V. Kongratana, A. Numsomran and S. Thuengsrirpan. Smith predictor design by cdm for temperature control system. In *Proceedings ICCAS07*, pages 1472–1477, 2007.
- [16] A. Birbal and B. Tibken. Digital design of coefficient diagram method. In *2009 American control conference*, pages 2849–2854, 2009.

The influence of variable friction coefficient on spatial stability of slightly curved shallow mixing layers

Andrei Kolyshkin, Valentina Koliskina, and Inta Volodko

Abstract—Spatial stability analysis is used in the present paper in order to investigate the effect of variable friction on spatial growth rates of an unsteady perturbation. The flow is assumed to be slightly curved in the longitudinal direction. Numerical scheme is developed for the solution of the spatial stability problem. Numerical results show that growth rate of a perturbation decreases in the presence of regions of non-uniform friction. In addition, small curvature stabilizes the flow.

Keywords—Spatial stability, rigid-lid assumption, shallow mixing layers, variable friction.

I. INTRODUCTION

STABILITY of shallow mixing layers is investigated in several papers [1]-[4]. Rigid-lid assumption is used in [1] to analyze linear stability of mixing layers and wakes in shallow water. The role of Froude number on the stability boundary is studied in [2] where it is shown that rigid-lid assumption works well (taking into account linear stability characteristics of the flow) for small Froude numbers. Gravitational and shear instabilities in compound and composite channels are analyzed in [3]. Linear stability analysis is one of the widely used methods for the analysis of shallow flows. Other methods include experimental investigation and numerical simulations [4].

Shallow mixing layers are also analyzed experimentally in [5]-[7]. It is shown in [5]-[7] that limited water depth in shallow flows has a stabilizing influence on the flow. Mixing layer width also decreases downstream in contrast to the case of unbounded mixing layers.

Recently an important practical problem is investigated experimentally in a series of papers [7]-[11] published by MIT group. The authors analyzed shallow mixing layers in the presence of a porous layer which can be formed, for example, by aquatic vegetation. Such flows can occur during floods. In

this case friction coefficient of the flow is not constant (as it is assumed, for example, in [1]-[4]), but varies in the transverse direction of the flow. Linear stability analysis of shallow mixing layer under the assumption that the friction coefficient is represented by a step function is performed in [7]. Later (see, for example, [12]) linear stability of shallow mixing layers is investigated for the case where the friction coefficient varies continuously with respect to the transverse coordinate from zero to some fixed constant.

In the present paper we analyze spatial stability of shallow mixing layers in compound channels for the case where two additional factors are considered: (a) the flow is assumed to be slightly curved in the longitudinal direction and (b) the friction coefficient of the flow varies continuously with respect to the transverse direction. The hyperbolic tangent function is used to model bottom friction. In addition, the friction coefficient approaches non-zero constant values (smaller value in the main channel and larger value in the floodplain). Numerical results are presented for different values of the parameters of the problem.

II. MATHEMATICAL FORMULATION OF THE PROBLEM

We consider the system of shallow water equations under the rigid-lid assumptions of the form

$$\frac{\partial u}{\partial x} + \frac{\partial v}{\partial y} = 0, \quad (1)$$

$$\frac{\partial u}{\partial t} + u \frac{\partial u}{\partial x} + v \frac{\partial u}{\partial y} + \frac{\partial p}{\partial x} + \frac{c_f(y)}{2h} u \sqrt{u^2 + v^2} = 0, \quad (2)$$

$$\frac{\partial v}{\partial t} + u \frac{\partial v}{\partial x} + v \frac{\partial v}{\partial y} - \frac{1}{R} u^2 + \frac{\partial p}{\partial y} + \frac{c_f(y)}{2h} v \sqrt{u^2 + v^2} = 0, \quad (3)$$

where u and v are the velocity components, $c_f(y)$ is the friction coefficient, p is the pressure, h is water depth and R is the dimensionless radius of curvature ($R \gg 1$).

Introducing the stream function $\psi(x, y, t)$ by the relations

$$u = \frac{\partial \psi}{\partial y}, \quad v = -\frac{\partial \psi}{\partial x} \quad (4)$$

and eliminating the pressure from (2) and (3) we obtain

A. Kolyshkin is with the Department of Engineering Mathematics, Riga Technical University, Riga, LV 1007, Latvia (e-mail: andrejs.koliskins@rtu.lv).

V. Koliskina is with the Department of Engineering Mathematics, Riga Technical University, Riga, LV 1007, Latvia (e-mail: v.koliskina@gmail.com).

I. Volodko is with the Department of Engineering Mathematics, Riga Technical University, Riga, LV 1007, Latvia (e-mail: inta.volodko@rtu.lv).

$$\begin{aligned}
 & (\Delta\psi)_t + \psi_y(\Delta\psi)_x - \psi_x(\Delta\psi)_y + \frac{2}{R}\psi_y\psi_{xy} + \\
 & + \frac{c_f(y)}{2h}\Delta\psi\sqrt{\psi_x^2 + \psi_y^2} + \frac{c_f(y)}{2h\sqrt{\psi_x^2 + \psi_y^2}}(\psi_y^2\psi_{yy} + \\
 & + 2\psi_x\psi_y\psi_{xy} + \psi_x^2\psi_{xx}) + \frac{c_{fy}(y)}{2h}\psi_y\sqrt{\psi_x^2 + \psi_y^2} = 0,
 \end{aligned} \quad (5)$$

where $c_{fy}(y) = c_{f_0}\gamma'(y)$ is the derivative of the function $c_f(y)$ with respect to y . It is assumed here that the dependence of the friction coefficient on the transverse coordinate y is given by the formula

$$c_f(y) = c_{f_0}\gamma(y), \quad (6)$$

where $\gamma(y)$ is sufficiently smooth “shape” function.

Using the method of small perturbations we represent the solution $\psi(x, y, t)$ in the form

$$\psi(x, y, t) = \psi_0(y) + \varepsilon\psi_1(x, y, t) + \dots \quad (7)$$

where $\psi_0(y)$ is the stream function of the base flow $U(y)$ such that $U(y) = \psi_{0,y}(y)$. The function $U(y)$ is usually assumed to be of the form a hyperbolic tangent function. In this study, we assume that

$$U(y) = \frac{1}{2}(1 + \tanh y). \quad (8)$$

Substituting (6) into (5) and linearizing the resulting equation in the neighborhood of the base flow (7) we obtain

$$\begin{aligned}
 & \psi_{1xxt} + \psi_{1yyt} + \psi_{0y}(\psi_{1xxx} + \psi_{1yyx}) - \psi_{0yyy}\psi_{1x} + \\
 & + \frac{c_f(y)}{2h}(\psi_{0y}\psi_{1xx} + 2\psi_{0yy}\psi_{1y} + 2\psi_{0y}\psi_{1yy}) \\
 & + \frac{c_{fy}(y)}{h}\psi_{0y}\psi_{1x} + \frac{2}{R}\psi_{0y}\psi_{1xy} = 0.
 \end{aligned} \quad (9)$$

In accordance with the method of normal modes a small unsteady perturbation of the stream function is assumed to be of the form

$$\psi_1(x, y, t) = \varphi(y)e^{i(\alpha x - \beta t)}, \quad (10)$$

where α and β , in general, are complex. Substituting (10) into (9) we obtain

$$\begin{aligned}
 & \varphi_{yy}(\alpha U - \beta - iS U \gamma) - iS(\gamma U_y + \gamma_y U)\varphi_y \\
 & + \varphi(\alpha^2 \beta - \alpha^3 U - \alpha U_{yy} + i\alpha^2 U S \gamma / 2) = 0,
 \end{aligned} \quad (11)$$

where $S = \frac{c_{f_0} b}{h}$ is the bed friction number (see [1]) and b is

a characteristic length scale of the problem (for example, mixing layer half-width).

The boundary conditions are

$$\varphi(\pm\infty) = 0. \quad (12)$$

There are two basic approaches to the solution of (11), (12).

The first (known as temporal stability analysis) is used under the assumption that α is real and $\beta = \beta_r + i\beta_i$ is complex.

Thus, from a temporal stability point of view the base flow is unstable with respect to the perturbation with wave number α if $\beta_i > 0$. The set of all values of the parameter S for which

$\beta_i = 0$ in the (α, S) –plane gives the neutral stability curve.

The second approach (known as spatial stability analysis) is based on the assumption that $\alpha = \alpha_r + i\alpha_i$ is complex and β is real. Flow (8) is said to be spatially unstable if at least one $\alpha_i < 0$.

From a computational point of view temporal stability analysis is simpler since one has to solve a linear generalized eigenvalue problem while in order to analyze spatial stability a polynomial generalized eigenvalue problem has to be solved. However, many experimental observations for shallow mixing layers deal with spatial variation of the characteristics of the flow. Hence, spatial stability analysis is used in practice more often.

In the present paper eigenvalue problem (11), (12) is solved as a spatial stability problem.

III. NUMERICAL METHOD

Problem (11), (12) is solved by means of a collocation method. First, the interval $-\infty < y < +\infty$ is mapped onto the interval $-1 \leq \xi \leq 1$ by means of the transformation

$$\xi = \frac{2}{\pi} \arctan y. \quad \text{The solution to (11) is sought in the form}$$

$$\varphi(\xi) = \sum_{k=0}^{N-1} a_k (1 - \xi^2) T_k(\xi), \quad (13)$$

where $T_k(\xi) = \cos k \arccos \xi$ is the Chebyshev polynomial of the first kind of order k and a_k are unknown coefficients.

The factor $(1 - \xi^2)$ is added in (13) in order to satisfy the zero boundary conditions

$$\varphi(\pm 1) = 0. \quad (14)$$

The collocation points are

$$\xi_m = \cos \frac{\pi m}{N}, \quad m = 1, 2, \dots, N-1. \quad (15)$$

Substituting (13) into (11) and using (15) we obtain the following generalized eigenvalue problem

$$(A + \alpha B)a = 0, \quad (16)$$

where A and B are complex-valued nonsingular matrices and $a = (a_0 a_1 \dots a_{N-1})^T$.

Problem (16) is solved numerically for different values of the parameters of the problem.

IV. NUMERICAL RESULTS

The variation of the friction coefficient in the transverse

direction is assumed to be of the form

$$c_f(y) = c_{f_2} \left(\frac{\gamma + 1}{2} + \frac{(\gamma - 1)}{2} \tanh \mu y \right), \quad (17)$$

where $\gamma = \frac{c_{f_1}}{c_{f_2}} \geq 1$ and $c_f(y) \rightarrow c_{f_1}$ as $y \rightarrow -\infty$,

$c_f(y) \rightarrow c_{f_2}$ as $y \rightarrow +\infty$. Here c_{f_1} and c_{f_2} are nonzero constants. Note that in [12] the friction coefficient varied in such a way that $c_f(y) \rightarrow 0$ as $y \rightarrow -\infty$ and $c_f(y) \rightarrow c_{f_2}$ as $y \rightarrow +\infty$. In other words, a frictionless flow is assumed in [12] as $y \rightarrow -\infty$. The parameter μ in (17) represents how sharp is the transition from the region of larger friction to the region of smaller friction.

Variability of the friction coefficient given by (17) is consistent with the velocity profile (8) since higher velocity is expected in the region where friction force is smaller.

Fig. 1 plots the spatial growth rates for the case $S = 0.15, \mu = 1$ and $R = \infty$ (no curvature). The case $\gamma = 1$ (top curve) corresponds to uniform friction. As can be seen from the graph, non-uniform friction of the form (17) has a stabilizing influence on the flow: the growth rate for the most unstable mode decreases as the parameter γ increases. Note that γ represents the degree of non-uniformity of the friction force in the transverse direction. Thus, flow with non-uniform friction is more stable than flow with uniform friction.

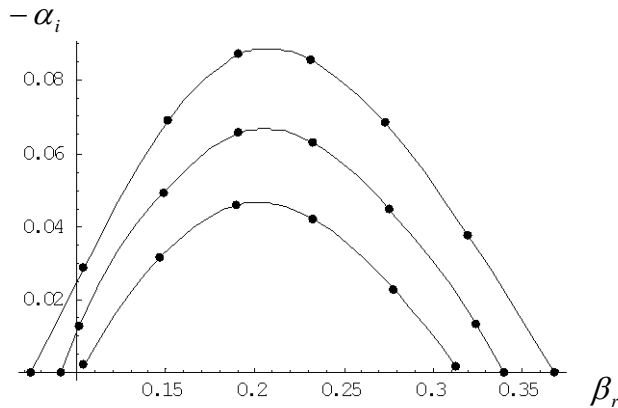


Fig. 1. Spatial growth rates $-\alpha_i$ versus β_r for three values of $\gamma : \gamma = 1, \gamma = 1.5$ and $\gamma = 2$ (from top to bottom).

The role of curvature on the stability characteristics of the flow is seen from Fig. 2 where the spatial growth rate for the case $S = 0.15$ and $\gamma = 1.5$ is shown for three values of the parameter $1/R$, namely, $1/R = 0$ (straight flow with no curvature), 0.01 and 0.02.

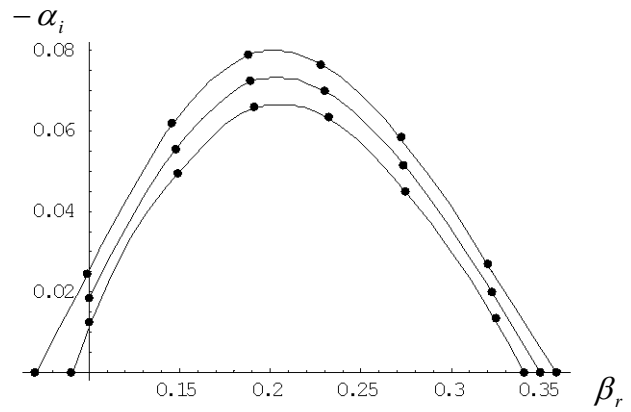


Fig. 2. Spatial growth rates $-\alpha_i$ versus β_r for three values of $1/R : 0, 0.01$ and 0.02 (from bottom to top).

The bottom curve in Fig. 2 corresponds to the case of no curvature and is the most stable among the three cases considered. Thus, increase in curvature has a destabilizing effect on the flow.

The effect of the parameter μ on the spatial growth rates is shown in Fig. 3 for the case $S = 0.15, \gamma = 2, 1/R = 0$.

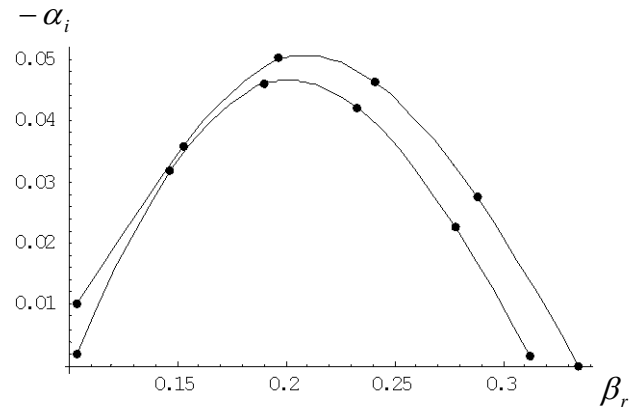


Fig. 3. Spatial growth rates $-\alpha_i$ versus β_r for two values of $\mu : 1$ and 10 (from bottom to top).

It is seen from Fig. 3 that steeper friction gradients result in less stable flow.

V. CONCLUSION AND DIRECTION OF FUTURE WORK

Spatial linear stability analysis of shallow mixing layers is performed in the present paper. The effect of several parameters of the stability characteristics of the flow is investigated. In particular, it is shown that non-uniform friction coefficient in the transverse direction of the flow has a stabilizing influence in comparison with the case of a uniform friction. In addition, numerical computations demonstrate that slightly curved mixing layers are more stable than layers without curvature. Finally, it is shown that steepness of the

change of the friction coefficient in the transverse direction has a destabilizing influence on the flow.

Linear stability analysis is performed in the present paper under the assumption of a parallel flow. In other words, the base flow profile (8) is assumed to be independent on the longitudinal coordinate. Experimental data (see, for example, [5] and [6]) show that the base flow is slightly changing along the longitudinal coordinate. Asymptotic schemes have been developing in the past in order to take into account slow longitudinal variation of the base flow. The authors are currently implementing the asymptotic scheme in order to derive the amplitude evolution equation for the most unstable mode.

ACKNOWLEDGMENT

This work was partially supported by the grant 623/2014 of the Latvian Council of Science.

REFERENCES

- [1] V.H. Chu, J.H. Wu, and R.E. Khayat, "Stability of transverse shear flows in shallow open channels", *J. Hydr. Engng.*, vol. 117, pp. 1370-1388, 1991.
- [2] M.S. Ghidaoui, and A.A. Kolyshkin, "Linear stability analysis of motions in compound open channels", *J. Hydr. Engng.*, vol. 125, pp. 871-880, 1999.
- [3] A.A. Kolyshkin, and M.S. Ghidaoui, "Gravitational and shear instabilities in compound and composite channels", *J. Hydr. Engng.*, vol. 128, pp. 1076-1086, 2002.
- [4] G.H. Jirka, "Large scale flow structures and mixing processes in shallow flows," *J. Hydr. Res.*, vol. 39, pp. 567-573, 2001.
- [5] W.S.J Uijttewaal, and J. Tukker, "Development of quasi two-dimensional structures in shallow free-surface mixing layer," *Exp. in Fluids*, vol. 24, pp. 192-200, 1998.
- [6] W.S.J Uijttewaal, and R. Booij, "Effect of shallowness on the development of free-surface mixing layers," *Phys. Fluids*, vol. 12, pp. 392-402, 2000.
- [7] H. Nepf, "Hydrodynamics of vegetated channels," *J. Hydr. Res.*, vol. 50, pp. 262-279, 2012.
- [8] H. Nepf, "Flow and transport in regions with aquatic vegetation," *Ann. Rev. of Fluid Mech.*, vol. 44, pp. 123-142, 2012.
- [9] X. Zhang, and H. Nepf, "Exchange flow between open water and floating vegetation," *Environ. Fluid Mech.*, vol. 11, pp. 531-546, 2011.
- [10] Jamali, M., X. Zhang, and H. Nepf, "Exchange flow between canopy and open water," *J. Fluid Mech.*, vol. 611, pp. 237-254, 2008.
- [11] B. White, and H. Nepf, "Shear instability and coherent structures in shallow flow adjacent to a porous layer," *J. Fluid Mech.*, vol. 593, pp. 1-32, 2007.
- [12] I. Eglite, and A. Kolyshkin, "Spatial stability analysis of curved shallow mixing layers", in *Mathematical models and methods in modern science*, WSEAS Press, Athens, pp. 104-108, 2013.

Equations of Motion and Physical Model of Quad-copter in Plain

Zdeněk Úředníček and Milan Opluštil

Abstract— Presented text documents the body quad-copter at plane with four propellers motion equations procedure creation, by force of Denavit -Hartenberg (DH) co - ordinate systems implementation and kinematic homogenous transformation matrices. Power interactions' physical model of this ordering was created and its behavior was compared with behavior of motional equations system.

Keywords— Quad-copter, Denavit-Hartenberg notation, motion equations, rigid mechanic bonded bodies, physical model, simulation experiments..

I. INTRODUCTION

Quad-copter can be seen as UAV (unmanned aerial vehicle) equipped by autonomous subsystems. it can be equipped e.g. by video subsystem, so its purpose could be the observation. But this subsystem can serve as well as the substantial part of object outside sensorial system, enabling sufficient orientation in 3D space (including distance measuring).

Because it has the capability to carry the small service load, is able to be used e.g. for small weight supply rescue deliverance to an inaccessible localities.

Nevertheless, maybe the biggest quad-copter importance is simply in skills creation at its intended complex structural project, including its movement control systems in 3D space and its independent orientation there.

Quad-copter selection motivations as top design project are different for various bands of designers.

For someone it's orientation on project and structural robot design, for others then on robot with sensors and autonomous capabilities, and eventually we meet the goal-directed orientation oriented from ground mobile robot to the flying object.

[Initially only the absorption in technical difficulties arisen, connected with flying object proposal and creation, notwithstanding flying object idea and its exploitation possibilities as well caused substantial interest, which was lastly accepted like challenge.

The main general aim of the works, one of which this text the first part, is methodology of motional equations derivation

First author is from Department of Automation and Control, Tomas Bata University in Zlin, Jižní Svahy, Nad Stráněmi 4511, 760 05, Zlin, Czech Republics. Email: urednicek@fai.utb.cz, web. fai.utb.cz.

Second author is student ending in this year the engineer study in field of technical resources in security technologies at Tomas Bata University.

of flying object with more propellers and achieved results, necessary for sensorial system proposal and the control, comparison with physical model created by compartment access to the mentioned system as to the stiff bodies system with finite points power interaction numbers.

This text constrains, in frame of methodology derivation, only to the rotational motion in plane (yaw) object under consideration, controlled by four propellers.

Next works will be dedicated to complete flying object movement and its motional equations.

II. QUAD-COPTER BODY ROTATION MOTIONAL EQUATIONS (SPIN) BY EFFECT OF FOUR PROPELLERS

A. Statement of a problem

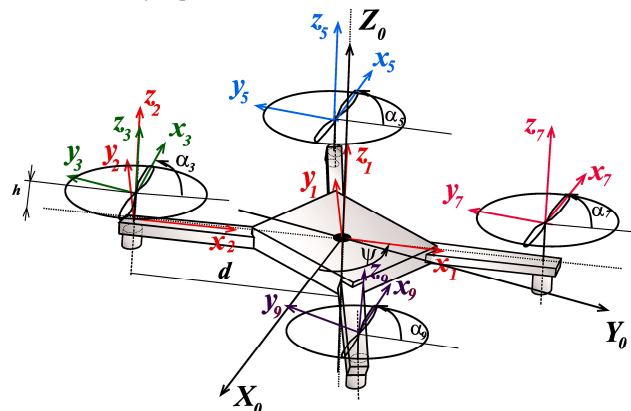


Fig. 1 Ideal quad-copter solid body in plane with four propellers and select coordinated systems

On Fig.1 quad-copter body is presented, situated in plane as a system with five freedom degrees. State quantities are quad-copter body angle of rotation ψ and its angular velocity and separate propeller fans rotation angles $\alpha_3, \alpha_5, \alpha_7$ and α_9 and their speeds.

Task is to derive the spin motional equations depending on revolving propellers' torques.

B. Quad-copter movement dynamics

By co-ordinate systems introduction, according to DH notation in compliance with introduced picture, it is possible to write homogenous transformation matrixes, by means of single co-ordinate systems parameters, e.g. for the first propeller $O_{x_3y_3z_3}$:

$${}^2T_3 = \begin{bmatrix} \cos \alpha_3 & -\sin \alpha_3 & 0 & 0 \\ \sin \alpha_3 & \cos \alpha_3 & 0 & 0 \\ 0 & 0 & 1 & h \\ 0 & 0 & 0 & 1 \end{bmatrix}; {}^1T_2 = \begin{bmatrix} 1 & 0 & 0 & -d \\ 0 & 1 & 0 & 0 \\ 0 & 0 & 1 & 0 \\ 0 & 0 & 0 & 1 \end{bmatrix};$$

$${}^0T_1 = \begin{bmatrix} \cos \psi & -\sin \psi & 0 & 0 \\ \sin \psi & \cos \psi & 0 & 0 \\ 0 & 0 & 1 & 0 \\ 0 & 0 & 0 & 1 \end{bmatrix}$$

$${}^0T_3 = \begin{bmatrix} \cos \psi \cos \alpha_3 - \sin \psi \sin \alpha_3 & -\cos \psi \sin \alpha_3 - \sin \psi \cos \alpha_3 & 0 & -d \cos \psi \\ \sin \psi \cos \alpha_3 + \cos \psi \sin \alpha_3 & -\sin \psi \sin \alpha_3 + \cos \psi \cos \alpha_3 & 0 & -d \sin \psi \\ 0 & 0 & 1 & h \\ 0 & 0 & 0 & 1 \end{bmatrix}$$

Because mass element of the first homogeneous propeller is

$$dm = \rho \cdot S \cdot dx = \frac{m_1}{S \cdot \ell} S \cdot dx = \frac{m_1}{\ell} \cdot dx$$

and this element has in $O_{x_3y_3z_3}$ absolute homogenous coordinates

$$\begin{bmatrix} x \cdot (\cos \alpha_3 \cos \psi - \sin \alpha_3 \sin \psi) - d \cdot \cos \psi \\ x \cdot (\cos \alpha_3 \sin \psi + \sin \alpha_3 \cos \psi) - d \cdot \sin \psi \\ h \\ 1 \end{bmatrix}$$

its absolute velocity vector size square is

$$|\vec{v}|^2 = (\dot{\psi}^2 + \dot{\alpha}_3^2 + 2 \cdot \dot{\alpha}_3 \dot{\psi}) \cdot x^2 - 2 \cdot d \cdot \cos \alpha_3 \cdot (\dot{\psi}^2 + \dot{\alpha}_3 \dot{\psi}) \cdot x + d^2 \cdot \dot{\psi}^2$$

and kinetic energy of the first propeller is

$$W_{kp1} = \frac{1}{2} \frac{m_1}{\ell} \cdot \int_{-\ell/2}^{\ell/2} [(\dot{\psi}^2 + \dot{\alpha}_3^2 + 2 \cdot \dot{\alpha}_3 \dot{\psi}) \cdot x^2 - 2 \cdot d \cdot \cos \alpha_3 \cdot (\dot{\psi}^2 + \dot{\alpha}_3 \dot{\psi}) \cdot x + d^2 \cdot \dot{\psi}^2] \cdot dx = \frac{1}{2} m_1 \cdot \left(d^2 + \frac{1}{12} \cdot \ell^2 \right) \cdot \dot{\psi}^2 + \frac{1}{24} m_1 \cdot \ell^2 \cdot \dot{\alpha}_3^2 + \frac{1}{12} m_1 \cdot \ell^2 \dot{\alpha}_3 \dot{\psi}$$

Similarly for other propellers reads:

$$W_{kp2} = \frac{1}{2} m_1 \cdot \left(d^2 + \frac{1}{12} \cdot \ell^2 \right) \cdot \dot{\psi}^2 + \frac{1}{24} m_1 \cdot \ell^2 \cdot \dot{\alpha}_5^2 + \frac{1}{12} m_1 \cdot \ell^2 \dot{\alpha}_5 \dot{\psi}$$

$$W_{kp3} = \frac{1}{2} m_1 \cdot \left(d^2 + \frac{1}{12} \cdot \ell^2 \right) \cdot \dot{\psi}^2 + \frac{1}{24} m_1 \cdot \ell^2 \cdot \dot{\alpha}_7^2 + \frac{1}{12} m_1 \cdot \ell^2 \dot{\alpha}_7 \dot{\psi}$$

$$W_{kp4} = \frac{1}{2} m_1 \cdot \left(d^2 + \frac{1}{12} \cdot \ell^2 \right) \cdot \dot{\psi}^2 + \frac{1}{24} m_1 \cdot \ell^2 \cdot \dot{\alpha}_9^2 + \frac{1}{12} m_1 \cdot \ell^2 \dot{\alpha}_9 \dot{\psi}$$

Quad-copter body kinetic energy is:

$$W_{kbase} = \frac{1}{2} J_{zz} \cdot \dot{\psi}^2$$

Quad-copter potential energy is invariable on the movement under consideration.

Resulting motional equations are:

$$\begin{aligned} \frac{d}{dt} \left(\frac{\partial L}{\partial \dot{\psi}} \right) - \frac{\partial L}{\partial \psi} &= \frac{d}{dt} \left(\frac{\partial W_k}{\partial \dot{\psi}} \right) - \frac{\partial W_k}{\partial \psi} = \\ &= \left[J_{zz} + 4m_1 \cdot \left(d^2 + \frac{1}{12} \cdot \ell^2 \right) \right] \cdot \ddot{\psi} + \frac{1}{12} m_1 \cdot \ell^2 \ddot{\alpha}_3 + \\ &+ \frac{1}{12} m_1 \cdot \ell^2 \ddot{\alpha}_5 + \frac{1}{12} m_1 \cdot \ell^2 \ddot{\alpha}_7 + \frac{1}{12} m_1 \cdot \ell^2 \ddot{\alpha}_9 = -b \cdot \dot{\psi} \\ \frac{d}{dt} \left(\frac{\partial L}{\partial \dot{\alpha}_3} \right) - \frac{\partial L}{\partial \alpha_3} &= \frac{1}{12} m_1 \cdot \ell^2 \cdot \ddot{\alpha}_3 + \\ &+ \frac{1}{12} m_1 \cdot \ell^2 \cdot \ddot{\psi} = M_3(t) - b_p \cdot \dot{\alpha}_3 \\ \frac{d}{dt} \left(\frac{\partial L}{\partial \dot{\alpha}_5} \right) - \frac{\partial L}{\partial \alpha_5} &= \frac{1}{12} m_1 \cdot \ell^2 \cdot \ddot{\alpha}_5 + \\ &+ \frac{1}{12} m_1 \cdot \ell^2 \cdot \ddot{\psi} = M_5(t) - b_p \cdot \dot{\alpha}_5 \\ \frac{d}{dt} \left(\frac{\partial L}{\partial \dot{\alpha}_7} \right) - \frac{\partial L}{\partial \alpha_7} &= \frac{1}{12} m_1 \cdot \ell^2 \cdot \ddot{\alpha}_7 + \\ &+ \frac{1}{12} m_1 \cdot \ell^2 \cdot \ddot{\psi} = M_7(t) - b_p \cdot \dot{\alpha}_7 \\ \frac{d}{dt} \left(\frac{\partial L}{\partial \dot{\alpha}_9} \right) - \frac{\partial L}{\partial \alpha_9} &= \frac{1}{12} m_1 \cdot \ell^2 \cdot \ddot{\alpha}_9 + \\ &+ \frac{1}{12} m_1 \cdot \ell^2 \cdot \ddot{\psi} = M_9(t) - b_p \cdot \dot{\alpha}_9 \end{aligned} \quad (1)$$

Matrix notation of motional equations brightly shows how it is possible to control angle ψ . With respect to select orientation coming-out:

$$\ddot{\psi} = - \frac{b \cdot \dot{\psi} + (M_3 + M_5 + M_7 + M_9)}{J_{zz} + 4 \cdot m_1 \cdot d^2} + \frac{b_p \cdot (\dot{\alpha}_3 + \dot{\alpha}_5 + \dot{\alpha}_7 + \dot{\alpha}_9)}{J_{zz} + 4 \cdot m_1 \cdot d^2} \quad (2)$$

and so, angle ψ is control by propellers' accelerating torques.

By mentioned equations' solution quad-copter dynamic behavior can be given, e.g. at sizes spin control process by force of propellers revolution control. Stated possibility is presented on Fig. 2, where's quad-copter body turning control to one or other side, made by all propellers turning control without dissipative forces.

Is evident, that it is impossible to quad-copter control in this manner, which has to, thanks to propellers, also to levitate, eventually it has to move laterally.

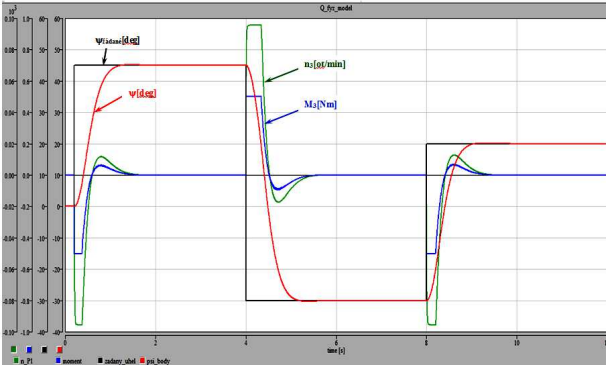


Fig. 2 Quad-copter dynamic behavior at yaw control

At total motion control will be necessary to combine various turning directions of all propellers and that way to achieve partly spin control, but also quad-copter levitation provision in a certain altitude (gravity compensation by propellers thrust) and e.g. its center of gravity lateral motion in space.

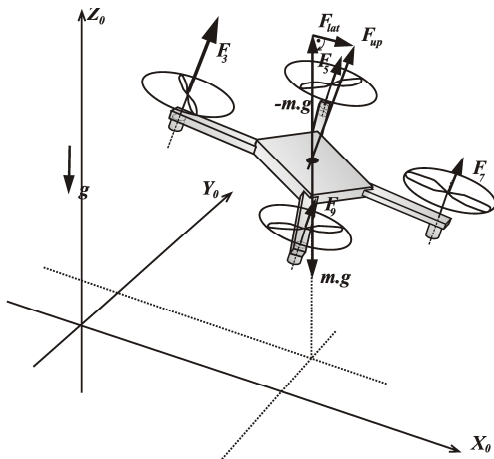


Fig. 3 Quad-copter lateral motion in axe X₀ direction.

C. Quad-copter motion physical model

Although resulting motional equations' form is simple, its derivation was labor-intensive. But it showed the universal procedure that can be used further for complete quad-copter motional equations' system in 3D space.

Next work goal is the stated arrangement physical model creation (energy interaction model) enabling simulation experiments with quad-copter rotating motion control in plane with synchronous levitation in required altitude..

1) Released body dynamics with rotary kinematic pairs

Primarily we will study the following general released body in plane with four rotational kinematic pairs according to Fig.4.

What is relation between point A local homogenous coordinates i. e. [x_A, y_A] and its global coordinates [X_A, Y_A]?

Rotation transformation matrix around global axis Z with angle ψ is.

$$Q_{Z,\psi} = \begin{bmatrix} \cos \psi & -\sin \psi & 0 \\ \sin \psi & \cos \psi & 0 \\ 0 & 0 & 1 \end{bmatrix}$$

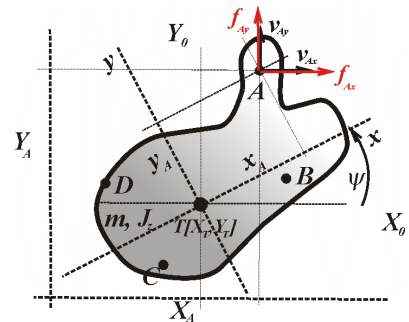


Fig. 4 General released body in plane with four rotational kinematic pairs.

So point A global homogenous coordinates are:

$$\begin{bmatrix} X_A(t) \\ Y_A(t) \\ 0 \\ 1 \end{bmatrix} = \begin{bmatrix} \cos \psi & -\sin \psi & 0 & X_T(t) \\ \sin \psi & \cos \psi & 0 & Y_T(t) \\ 0 & 0 & 1 & 0 \\ 0 & 0 & 0 & 1 \end{bmatrix} \cdot \begin{bmatrix} x_A(t) \\ y_A(t) \\ 0 \\ 1 \end{bmatrix} = \begin{bmatrix} X_T(t) + x_A \cos \psi(t) - y_A \sin \psi(t) \\ Y_T(t) + x_A \sin \psi(t) + y_A \cos \psi(t) \\ 0 \\ 1 \end{bmatrix}$$

For its absolute velocity components (velocity in global reference coordinate system) pays:

$$\begin{bmatrix} v_{A_x}(t) \\ v_{A_y}(t) \\ 0 \\ 1 \end{bmatrix} = \begin{bmatrix} \frac{dX_T(t)}{dt} - \omega(t) \cdot [x_A \sin \psi(t) + y_A \cos \psi(t)] \\ \frac{dY_T(t)}{dt} + \omega(t) \cdot [x_A \cos \psi(t) - y_A \sin \psi(t)] \\ 0 \\ 1 \end{bmatrix} \quad (3)$$

Point A absolute velocity is determined by two components of across variables (velocity) $\vec{v}_A = v_{A_x} \hat{I} + v_{A_y} \hat{J}$

(where \hat{I}, \hat{J} are global axes X₀ and Y₀ unitary vectors).

Similarly for other points B, C, D.

For across variables the flow variables (generalized forces) $\vec{F}_A = f_{A_x} \hat{I} + f_{A_y} \hat{J}$ appertain (see Fig.4).

We establish the following model of rigid body in plane

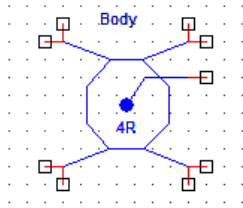


Fig. 5 Pictogram of rigid body in plane model with four rotational kinematic pairs.

Model „points of contact “ are points' appropriate traversable velocity components and body angular velocity. Similarly we specify rigid body with one kinematic rotational pair model TR:

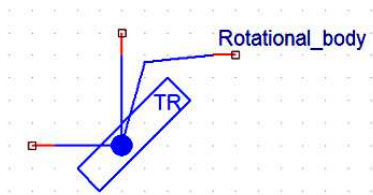


Fig. 6 Pictogram of rigid body in plane model with one rotational kinematic pair.

2) *Power interactions' dynamic model*

Resulting power interaction' model consists of:

1. **Quad-copter body dynamic behavior model**, body with four rotational kinematic pairs moving with one freedom degree-angle ψ .
2. **Four times propeller's dynamic behavior model** used as stiff body with one rotational kinematic pair.
3. **Four controlled torque sources**, actuating on four propellers with the aim of achieve
 - partly quad - copter body levitation,
 - as well as its turning around quad-copter body plane normal line.

The result is achieved by the torques applied on separate propellers with forms:

$$\begin{aligned} m_{prop_3}(t) &= m_{prop_7}(t) = M_{up} + m_{reg} \\ m_{prop_5}(t) &= m_{prop_9}(t) = -M_{up} + m_{reg} \end{aligned} \quad (4)$$

where M_{up} is constant levitation torque (the propellers side by side have inverse thrust) and m_{reg} it's controlled torque applied on individual propellers [see equation (2)].

Resulting layout under consideration with parameters describing its behavior is on Fig.7.

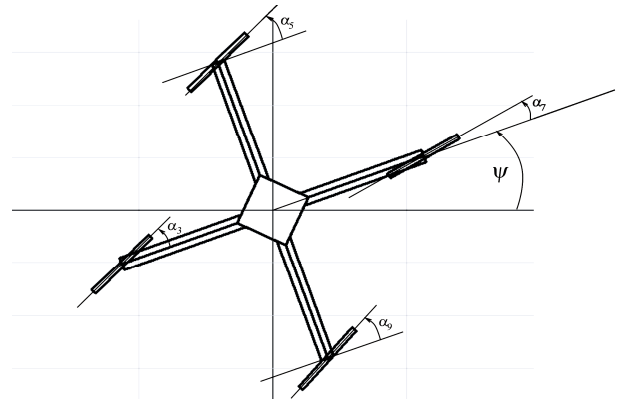


Fig. 7 The values indicative of instantaneous body and propellers position.

Physical model in system Dynast for mechatronics physical simulation is on Fig.8.

It can be seen, that by means of rotational kinematic pairs are mutually interconnected quad-copter body model and propellers' model namely by force of translational velocity components (turning propellers centers move in the same way like their interface points on quad-copter body) and torques revolving with propellers operate between appropriate propeller and quad-copter body.

Actuating variable torque is simply controlled by force of PID regulator of quad-copter body position with its output limitation on level of τ . This regulator output is transferred on torque by means of zero order system (multiplication by constant).

The result (time dependencies) of simple simulation experiment is on Fig.9. Requested quad - copter body angular position jumps are:

$$\begin{aligned} &45^\circ \left\{ \begin{array}{l} \text{pro}(t \geq 0.2s) \cap (t < 0.8s) \\ \text{pro}(t \geq 0.8s) \cap (t < 2s) \\ \text{pro}(t \geq 2s) \end{array} \right. \\ &- 30^\circ \left\{ \begin{array}{l} \text{pro}(t \geq 0.2s) \cap (t < 0.8s) \\ \text{pro}(t \geq 0.8s) \cap (t < 2s) \\ \text{pro}(t \geq 2s) \end{array} \right. \\ &20^\circ \left\{ \begin{array}{l} \text{pro}(t \geq 0.2s) \cap (t < 0.8s) \\ \text{pro}(t \geq 0.8s) \cap (t < 2s) \\ \text{pro}(t \geq 2s) \end{array} \right. \end{aligned} \quad (5)$$

Fig. 10 shows quad-copter body's position successive change at mentioned requested motion.

III. CONCLUSION

The paper is concerned with utilization of DH method coordinate systems introduction at kinematics and dynamism description of ideally rigid bodies system in space constrained by kinematic pairs and shows the universal physical models utilization possibility for dynamic behavior simulation of these systems.

Stated principle was used on quad-copter body motion model (yaw) levitating in existing altitude and its control in spin.

This contribution forms the first part of the works concerned with flying service robots (multi-copters) dynamics description.

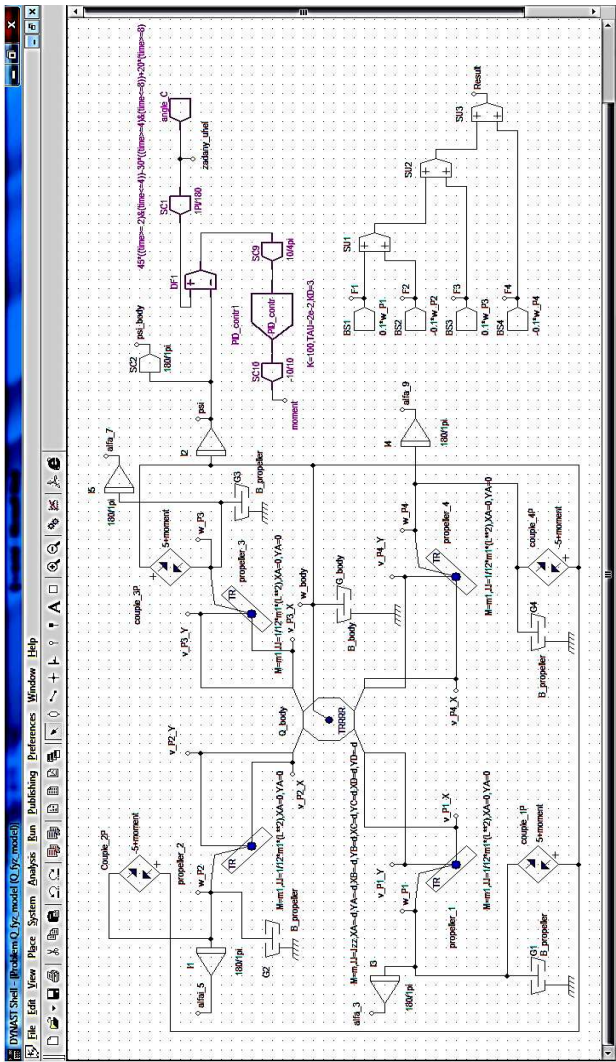


Fig. 8 Resulting physical model of quad-copter in plane.

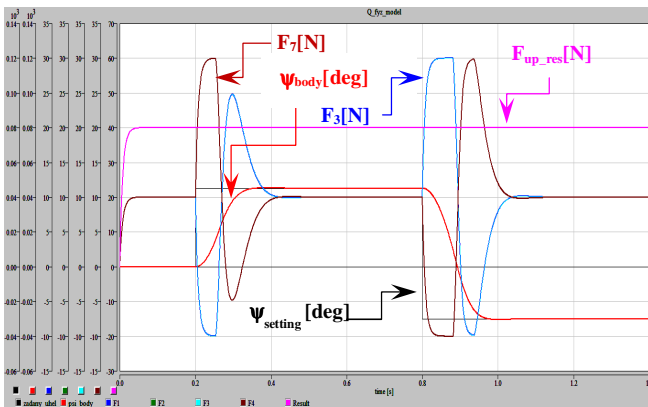


Fig. 9 Quad-copter levitation and its spin control in plane.

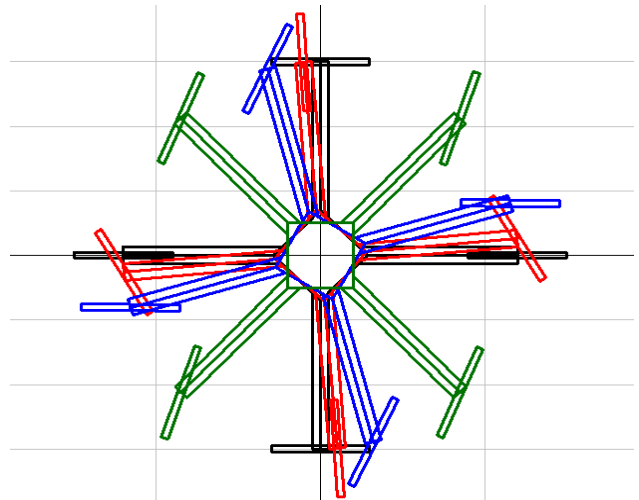


Fig. 10 Quad-copter model motion in plane

REFERENCES

- [1] S. Crandall, D. C. Karnopp, E.F. Kurz., *Dynamics of Mechanical and Electromechanical Systems*, McGraw-Hill, New York 1968.
- [2] D. C. Karnopp, R. C. Rosenberg. *System dynamics. A Unifies Approach*. Wiley & Sons, 1975.
- [3] P.Pillay., R.Krishnan, "Modeling, Simulation and analysis of permanent Magnet Motor Drives, Part II: The Brushless D.C. Motors Drives". IEEE Transaction on Industry Appl., vol. 25, 2/1989
- [4] R. C. Rosenberg,, "Multiport Models in Mechanics". Trans. ASME, sept 1972
- [5] H.M. Trent, "Isomorphism between oriented linear graphs and lumped physical systems". J.Acoust. Soc. Am., vol. 27 (1955).
- [6] Z. Uředniček, *Modelling and simulation. Simulation experiment utilization at mechatronics systems' proposal*, (In Czech) Inaugural dissertation. Transport and communications university ZILINA, 1997
- [7] J.U. Liceaga-Castro, I. I Siller-Alcalá, J. Jaimes-Ponce, R., Alcántara-Ramirez, and A. Ferreyra-Ramirez, "Information and Communication Technologies Applications in Control Theory Courses. Case of study: Speed Control". Proceedings of the 11th WSEAS International Conference on Circuits, Systems, Electronics, Control & Signal Processing (CSECS '12). Montreux, Switzerland. December 29-31, 2012
- [8] I.Astrov, M. Pikkov, R. Paluoja,, "Motion Control of Vectored Thrust Aerial Vehicle for Enhanced Situational Awareness". Proceedings of the WSEAS International Conference on Mathematical Applications in Science and Mechanics. Dubrovnik, Croatia, June 25-27, 2013
- [9] H.A. Darweesh, M. Roushdy, H.M. Ebied, and B.M. Elbagoury, "Design a Cost Effective Non-Holonomic Vehicle for Autonomous Driving Applications". Proceedings of the WSEAS International Conference Mathematical Applications in Science and Mechanics. Dubrovnik, Croatia, June 25-27, 2013
- [10] S. Hubalovsky, P.Kadlec, L. Mitrovic, and P. Hanzalova, "Computer simulation model of static mechanical properties of real technical device - elevator cab". Proceedings of the 3rd International Conference on Mathematical Models for Engineering Science (MMES '12). Paris, France, December 2-4, 2012
- [11] Z. Uředniček, *Robotics* (in Czech), T. Bata univerzity in Zlin, Zlin 2012,

OWA – type Possibilistic Aggregations in a Decision Making Regarding Selection of Investments

Gia Sirbiladze and Gvantsa Tsulaia

Department of Computer Sciences
 Iv. Javakhishvili Tbilisi State University
 13, University st., 0186, Tbilisi, Georgia

Abstract — In this work a new generalization of the OWA operator (introduced by R.R. Yager) is presented. Our focus is directed on the construction of the aggregation OWA operator – AsFPOWA in the possibilistic uncertainty environment. For the illustration of the applicability of the new aggregation operator - AsFPOWA an example of the fuzzy decision making problem regarding optimal selection of investment is considered. Several variants of the new aggregation operator are used for the comparing of decision making results.

Keywords — *Decision-making system, expert evaluations, OWA operator, possibility uncertainty, selection of investments.*

I. NEW POSSIBILISTIC AGGREGATIONS IN THE OWA OPERATOR

It is well recognized that intelligent decision making systems (IDMS) and technologies have been playing an important role in improving almost every aspect of human society. In this type of problem the decision making person (DMP) has a collection $D = \{d_1, d_2, \dots, d_n\}$ of possible uncertain alternatives from which he/her must select one or some rank decisions by some expert's preference relation values. Associated with this problem as a result is a variable of characteristics, activities, symptoms and so on, acts on the decision procedure. This variable normally called the state of nature, which affects the payoff, utilities, valuations and others to the DMP's preferences or subjective activities. This variable is assumed to take its values (states of nature) in the some set $S = \{s_1, s_2, \dots, s_m\}$. As a result the DMP knows that if he/her selects d_i and the state of nature assumes the value s_j then his/her payoff (valuation, utility and soon) is a_{ij} . The objective of the decision is to select the “best” alternative, get the biggest payoff. But in IDMS the selection procedure becomes more difficult. In this case each alternative can be seen as corresponding to a row vector of possible payoffs. To make a choice the DMP must compare these vectors, a

problem which generally doesn't lead to a compelling solution. Assume d_i and d_k are two alternatives such that for all $j, j = 1, 2, \dots, m$ $a_{ij} \geq a_{kj}$. In this case there is no reason to select d_i . In this situation we shall say d_i dominates d_k ($d_i \succeq d_k$). Furthermore if there exists one alternative (optimal decision) that dominates all the alternatives then it will be *optimal solution*. Faced with the general difficulty of comparing vector payoffs we must provide some means of comparing these vectors. Our focus in this work is on the construction of aggregation operator F that can take a collection of m values and convert it into a single value, $F : R^m \Rightarrow R^1$. In [5] R.R. Yager introduced a class of mean aggregation operators called Ordered Weighed Averaging (OWA) operator.

Definition 1: An OWA operator of dimension m is mapping $OWA : R^m \Rightarrow R^1$ that has an associated weighting vector W of dimension m with $w_j \in [0;1]$ and $\sum_{j=1}^m w_j = 1$, such that

$$OWA(a_1, \dots, a_m) = \sum_{j=1}^m w_j b_j, \quad (1)$$

where b_j is the j -th largest of the $\{a_i\}, i = 1, 2, \dots, m$.

The Triangular Fuzzy Numbers (TFNs, denoted by Ψ) has been studied by many authors ([1] and others). It can represent in a more complete way as an imprecision variable of an expert knowledge. In the role of uncertainty measure a possibility distribution is taken. So, we consider possibilistic aggregations based on the OWA operator. Therefore we introduce the definition of a possibility measure [1]:

Definition 2: A possibility measure - *Pos* on 2^S can be uniquely determined by its possibility distribution function $\pi : S \rightarrow [0,1]$ via the formula:

$$\forall A \in 2^S, Pos(A) = \max_{s \in A} \pi(s).$$

Let S_m be the set of all permutations of the set $\{1,2,\dots,m\}$, Let $\{P_\sigma\}_{\sigma \in S_m}$ be the associated probabilities class of a possibility measure - Pos [2-4]. Then, we have the following connections between $\{\pi_i\}$ and $\{P_\sigma\}_{\sigma \in S_m} : \forall \sigma \in S_m$,

$$P_\sigma(s_{\sigma(i)}) = \max_{\nu=1,i} \pi(s_{\sigma(\nu)}) - \max_{\nu=1,i-1} \pi(s_{\sigma(\nu)}),$$

for each $\sigma = (\sigma(1), \sigma(2), \dots, \sigma(m)) \in S_m$, which are called the associated probabilities.

Let $M : \Psi^k \Rightarrow \Psi$ ($k = m!$) be some deterministic mean aggregation function [5].

Definition 3: An associated fuzzy-probabilistic OWA operator $AsFPOWA$ of dimension m is mapping $AsFPOWA : \Psi^m \Rightarrow \Psi$, that has an associated objective weighted vector W of dimension m such that $w_j \in (0,1)$ and $\sum_{j=1}^m w_j = 1$ some possibility measure $Pos : 2^S \Rightarrow [0,1]$, according the following formula:

$$AsFPOWA(\tilde{a}_1, \tilde{a}_2, \dots, \tilde{a}_m) = \beta \cdot \sum_{j=1}^m w_j \tilde{b}_j + (1-\beta)M(E_{P_{\sigma_1}}(\tilde{a}), E_{P_{\sigma_2}}(\tilde{a}), \dots, E_{P_{\sigma_k}}(\tilde{a})), \quad (2)$$

where \tilde{b}_j is the j -th largest of the $\{\tilde{a}_i\}, i = 1, \dots, m$; $E_{P_{\sigma_i}}(\tilde{a})$ is a Mathematical Expectation of \tilde{a} with respect to associated probability P_{σ_i} .

We will consider concrete $AsFPOWA$ operators for concrete mean function $M : AsFPOWA_{min}$ if $M=Min$, $AsFPOWA_{max}$, if $M=Max$ and $AsFPOWA_{mean}$ if $M=Mean$.

II. THE PROBLEM OF THE SELECTION OF INVESTMENTS

We analyze an illustrative example of the using of the new $AsFPOWA$ operator in a fuzzy decision-making problem regarding selection of investments. The main reason for using our new aggregation operator is that we are able to assess the decision making problem considering possibility distribution and the attitudinal characters of the DMPs.

In the following, we study a Company that wants to invest some money in a new market. They consider five alternatives: d_1 : "Invest in the Asian market"; d_2 : "Invest in the South American market"; d_3 : "Invest in the African market"; d_4 : "Invest in all three markets"; d_5 : "Do not invest money in any market". In order to analyze these investments, the investor has brought together a group of experts. This group considers that the key factors are the economic situations of the world (external) and country (internal) economy for the next period. They consider 3 possible states of nature that in hole could occur in the future: s_1 : "Bad economic situation"; s_2 : "Regular economic situation"; s_3 : "Good economic situation". As a result the group of experts gives us union one opinions and results. The results depending on the state of nature s_i and alternative d_k that the company selects, are presented in the Table 1.

Table 1: Expert's valuations in TFNs

$D \backslash S$	S_1	S_2	S_3
d_1	(60,70,80)	(40,50,60)	(50,60,70)
d_2	(30,40,50)	(60,70,80)	(70,80,90)
d_3	(50,60,70)	(50,60,70)	(60,70,80)
d_4	(70,80,90)	(40,50,60)	(40,50,60)
d_5	(60,70,80)	(70,80,90)	(50,60,70)

Following the expert's knowledge on the world economy for the next period, experts decided the objective weights (as an external factor) of states of nature must be $W = (0,5; 0,3; 0,2)$, which the country (in which is founded or works this Company) economy for the next period takes only some possibilities to occur presented states of nature in the country (as an internal factor). So, there exists some possibilities (internal levels), as an uncertainty measure, to occur states of nature in the country.

So, we can define subjective possibilities $\pi_i = Pos(s_i)$ based on the experts' knowledge. Let on the basis of some fuzzy term of internal factor – country economy experts define the possibility levels of states of nature: $poss(s_1) \equiv \pi_1 = 0,7$; $poss(s_2) \equiv \pi_2 = 1$; $poss(s_3) \equiv \pi_3 = 0,5$.

$$Pos(A) = \max_{s_i \in A} \pi_i, \quad \forall A \subseteq S.$$

In this model weight $\beta \equiv 0,3$.

$$W = (0,5; 0,3; 0,2);$$

For $\tilde{a} = (\tilde{a}_1, \tilde{a}_2, \tilde{a}_3)$ we have:

$$AsFPOWA(\tilde{a}_1, \tilde{a}_2, \tilde{a}_3) = \beta \sum_{j=1}^3 \tilde{b}_j w_j + (1-\beta)M(E_{P_{\sigma_1}}(\tilde{a}), E_{P_{\sigma_2}}(\tilde{a}), \dots, E_{P_{\sigma_6}}(\tilde{a})).$$

It is clear that $k=m!=3!=6$ and for calculation of the $AsFPOWA$ operator we firstly define the associated probability class $\{P_\sigma^{Pos}\}_{\sigma \in S_3}$ for the $Pos : 2^S \Rightarrow [0,1]$.

For every

$$\sigma = \{\sigma(1), \sigma(2), \sigma(3)\} \in S_3$$

$$E_{P_\sigma}(d) = E_{P_\sigma^{Pos}}(\tilde{a}) = \sum_{i=1}^3 P_{\sigma(i)} \cdot \tilde{a}_{\sigma(i)}.$$

The results presented in the Table 2.

Table 2: Associated Probability Class - $\{P_\sigma\}_{\sigma \in S_3}$

$\sigma = (\sigma(1), \sigma(2), \sigma(3))$	$P_{\sigma(1)}$	$P_{\sigma(2)}$	$P_{\sigma(3)}$
$(1, 2, 3) = \sigma_1$	$P_1 = 0,7$	$P_2 = 0,3$	$P_3 = 0$
$(1, 3, 2) = \sigma_2$	$P_1 = 0,7$	$P_3 = 0$	$P_2 = 0,3$
$(2, 1, 3) = \sigma_3$	$P_2 = 1$	$P_1 = 0$	$P_3 = 0$
$(2, 3, 1) = \sigma_4$	$P_2 = 1$	$P_3 = 0$	$P_1 = 0$
$(3, 1, 2) = \sigma_5$	$P_3 = 0,5$	$P_1 = 0,2$	$P_2 = 0,3$
$(3, 2, 1) = \sigma_6$	$P_3 = 0,5$	$P_2 = 0,5$	$P_1 = 0$

Following the table 2 we calculate Mathematical Expectations - $\{E_{P_\sigma}(\cdot)\}_{\sigma \in S_3}$ (see Table 3).

Table 3: Mathematical Expectations - $\{E_{P_\sigma}(\cdot)\}_{\sigma \in S_3}$

$E_{P_\sigma}(\cdot) \sigma$	σ_1	σ_2	σ_3	σ_4	σ_5	σ_6
$E_{P_\sigma}(d_1)$	(54,64,74)	(54,64,74)	(40,50,60)	(40,50,60)	(49,59,69)	(45,55,65)
$E_{P_\sigma}(d_2)$	(39,49,59)	(39,49,59)	(60,70,80)	(60,70,80)	(59,69,79)	(65,75,85)
$E_{P_\sigma}(d_3)$	(50,60,70)	(50,60,70)	(50,60,70)	(50,60,70)	(55,65,75)	(55,65,75)
$E_{P_\sigma}(d_4)$	(61,71,81)	(61,71,81)	(40,50,60)	(40,50,60)	(46,56,66)	(40,50,60)
$E_{P_\sigma}(d_5)$	(63,73,83)	(63,73,83)	(70,80,90)	(70,80,90)	(58,68,78)	(60,70,80)

Now we may calculate the values of different variants of the AsFPOWA operator with respect to different averaging operators M (Table 4):

Table 4: Aggregation results

D/Agg. Op.	AsFPOWA _{min}	AsFPOWA _{max}	AsFPOWA _{mean}
d_1	(44,54,64)	(54,64,74)	(49,59,69)
d_2	(45,55,65)	(64,74,84)	(57,66,75)
d_3	(52,62,72)	(56,66,76)	(53,63,73)
d_4	(45,55,65)	(60,70,80)	(51,61,71)
d_5	(60,70,80)	(68,78,88)	(64,74,84)

Calculating numerical values of AsFPOWA_{min}, AsFPOWA_{max}, AsFPOWA_{mean} operators we can rank the alternatives from the most preferred to the less preferred. The results are shown in table 5.

Table 5: Ordering of the policies

N	Aggreg. Operator	Ordering
1	AsFPOWA _{min}	$d_5 \succ d_3 \succ d_2 = d_4 \succ d_1$
2	AsFPOWA _{max}	$d_5 \succ d_2 \succ d_4 \succ d_3 \succ d_1$
3	AsFPOWA _{mean}	$d_5 \succ d_2 \succ d_3 \succ d_4 \succ d_1$

It is clear that decision d_5 -“Do not invest money in any market” is an optimal solution (decision) in this problem.

III. CONCLUSION

In this work our focus is directed on the construction of a new generalization of the aggregation OWA operator – AsFPOWA in the possibilistic uncertainty environment. For the illustration of the applicability of the new aggregation operator - AsFPOWA an example of the fuzzy decision making problem regarding optimal selection of investments is considered, where we study a Company that is planning to invest some money in a new market.

REFERENCES

- [1] D. Dubois and H. Prade, Possibility Theory, New York: Plenum Press, 1988.
- [2] GiaSirbiladze, Extremal Fuzzy Dynamic Systems: Theory and Applications. IFSR International Series on Systems Science and Engineering, 28, 1st Edition, Springer, 2012.
- [3] GiaSirbiladze and Anna Sikharulidze, Generalized Weighted Fuzzy Expected Values in Uncertainty Environment, Proceeding of the 9-th WSEAS International Conference on Artificial Intelligence, Knowledge Engineering and Data Bases, 2010, pp. 54-64.
- [4] GiaSirbiladze, Anna Sikharulidze, Bezhan Ghvaberidze and Bidzina Matsaberidze, Fuzzy-probabilistic Aggregations in the Discrete Covering Problem, International Journal of General Systems, Vol.40, No. 2, 2011, pp. 169 - 196.
- [5] R.R. Yager, On Ordered Weighted Averaging aggregation operators in multi-criteria decision making, IEEE Trans. On Systems, Man and Cybernetics, Vol. 18, No.1., 1988, pp. 183-190.

Identification of dynamical systems using recurrent complex-valued neural networks

Víctor M. Arellano-Quintana and Ieroham S. Baruch

Abstract—The existing in the literature backpropagation algorithms for training Complex-Valued Neural Networks (CVNN) are very complicated, especially where we deal with a Recurrent CVNN (RCVNN). For that reason the paper proposed to use diagrammatic rules so to construct an adjoined RCVNN and propagate the complex output error through it so to perform the weight adjustment. Two different RCVNN topologies with different activation functions avoiding singularity are considered and their CV backpropagation learning algorithms are derived using the proposed learning methodology. Finally, some comparative simulation results of RCVNN identification of flexible-joint robot are given and discussed, and then a validation stage is presented in order to confirm the good quality of the proposed learning methodology.

Keywords—Diagrammatic rules, learning algorithms, recurrent complex-valued neural networks, systems identification

I. INTRODUCTION

UNTIL now there are few applications using Recurrent Complex-Valued Neural Networks (RCVNN). Most of them deal with oscillatory systems which by their physical nature it is convenient to be treated in the complex domain, such as electromagnetic waves, light waves, images processing, electric power systems etc. (see [1], [2], [3]). In [2] the authors apply a special type of a RCVNN for modeling of power transformer, obtaining good results. The drawback here is that nothing is mentioned about the presence of singularity points due to the activation function nature.

In the field of mechanical systems identification the RCVNN have had a minor presence. In spite of that, some papers like [3], [4] proposed to use RCVNN for mechanical plants identification and control, obtaining good results. In [3] the authors applied a CVNN for an industrial evaporator system identification using an evolutionary algorithm to design the network. They use also radial basis functions NN avoiding the gradient terms computation in the learning algorithm. Other papers like [4], [5] used CVNN for these kind of systems, obtaining satisfactory results.

In [6], a type of RCVNN is used for modeling of Lorenz system. In [7], Leung and Haykin derived a Complex Value Backpropagation (CVBP) algorithm used for pattern classifi-

cation. However, this learning algorithm presented some problems because of the activation function singularity. For that reason some authors (see [8]-[11]) proposed different activation functions that avoid activation function singularity.

So, to simplify the backpropagation learning of the RCVNN, the present paper proposed to use diagrammatic rules so to construct an adjoined RCVNN and propagate the complex output error through it so to obtain the weight adjustment. Two different RCVNN topologies with different activation functions avoiding singularity are considered and their CV backpropagation learning algorithms are derived using the diagrammatic rules and the constructed by them adjoined RCVNN. Finally, some comparative simulation results of RCVNN identification of flexible-joint robot are given and discussed, and then a validation stage is presented in order to confirm the good quality of the proposed learning methodology.

II. TOPOLOGY AND BACKPROPAGATION LEARNING OF REAL-VALUED RECURRENT NEURAL NETWORK

In Fig.1 it is shown the block-diagram of a Real Value Recurrent Neural Network (RVRNN) with Jordan Canonical topology, [12]. The canonical RNN topology possesses the controllability, observability, reachability and identifiability-properties, and minimum number of parameters, subject to learning. The RVRNN model is described by the following equations:

$$X(k+1) = JX(k) + BU(k) \quad (1)$$

$$J = \text{block-diag}(J_i); |J_i| < 1, i = 1, \dots, N$$

$$E(k) = Y_p(k) - Y(k) \quad (2)$$

$$Z(k) = \Gamma[X(k)] \quad (3)$$

$$Y(k) = \Phi[CZ(k)] \quad (4)$$

Where: $X(\cdot) \in \mathbb{R}^N$ - State vector; $U(\cdot) \in \mathbb{R}^M$ - Input vector; $Y(\cdot) \in \mathbb{R}^L$ - Output vector; $Z(\cdot) \in \mathbb{R}^L$ - Output vector of the hidden layer; $\Gamma(\cdot)$, $\Phi(\cdot)$ - Vector valued activation functions with compatible dimensions; J - Weight state diagonal matrix with elements J_i . The inequality in (1) is a stability preserving condition, imposed on the weights J_i ; B and C are weight input and output matrices with compatible dimensions. The RVRNN

V.M. Arellano-Quintana is MS student in the Department of Automatic Control, CINVESTAV-IPN, D.F., Mexico, e-mail: yarellano@ctrl.cinvestav.mx.

I.S. Baruch is with the Department of Automatic Control, CINVESTAV-IPN, D.F., Mexico, e-mail: baruch@ctrl.cinvestav.mx.

model is completely parallel, capable to issue weights J, B, C , and states X .

Applying the diagrammatic rules, [13], to the RVRNN topology, given on Fig.1 we could obtain the adjoined RVRNN model, given on Fig.2. The adjoined RVRNN is used for the backward pass of the backpropagation algorithm to pass the output error through it so to train RVRNN weights. The performance index to be minimized is given by:

$$\zeta(k) = \frac{1}{2} \sum_j [E_j(k)]^2, \quad j \in C, \quad \zeta = \frac{1}{N_e} \sum_j \zeta(k) \quad (5)$$

Where the instantaneous Means Squared Error (MSE) $\zeta(k)$ is minimized in real-time applications and the total MSE ζ is minimized for one epoch N_e in off-line applications. The general RVRNN real-time backpropagation learning algorithm with momentum term is given by the following vector-matrical equation:

$$W(k+1) = W(k) + \eta \Delta W(k) + \alpha \Delta W(k-1) \quad (6)$$

$$|W_{ij}| < W_o$$

Where: $W(\cdot)$ is a general weight matrix (in fact J, B, C); $\Delta W(\cdot)$ is the modification of $\Delta W(\cdot)$; η is a diagonal constant matrix of learning; α is a diagonal momentum term matrix; W_o is a restricted region for the weight W_{ij} . Using the specified in Fig.2 errors and the obtained in the forward pass (1)-(3) intermediate vectors, we could obtain the following weight update algorithm for the matrices J, B, C .

For the output layer:

$$\Delta C(k) = E_1(k) Z^T(k) \quad (7)$$

$$E_1(k) = \Phi'[Y(k)] E(k) \quad (8)$$

$$E(k) = Y_p(k) - Y(k) \quad (9)$$

For the hidden layer:

$$\Delta J(k) = E_3(k) X^T(k) \quad (10)$$

$$E_3(k) = \Gamma'[Z(k)] E_2(k) \quad (11)$$

$$E_2(k) = C^T(k) E_1(k) \quad (12)$$

$$\Delta v J(k) = E_3(k) \otimes X(k) \quad (13)$$

$$\Delta B(k) = E_3(k) U^T(k) \quad (14)$$

Where: $\Delta C, \Delta J, \Delta B$ are weight corrections of C, J, B ; the output error E is given by (9) and passed through the adjoined RVRNN so to obtain the intermediate error vectors E_1, E_2, E_3 ; Φ', Γ' are derivatives of the respective activation functions expressed with respect to its correspondent outputs. The equation (13) gives the learning solution for the diagonal matrix J as a dot product of two vectors. Equations (7)-(14) represented the complete backpropagation learning algorithm for RVRNN.

This solution could be applied for any NN topology and does not require computations of partial derivatives. Based on

the diagrammatic rules we could derive a similar learning solution for the complex value case.

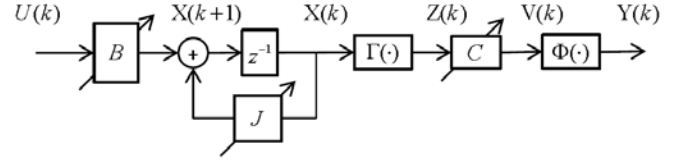


Fig. 1 Block-diagram of the RVRNN topology

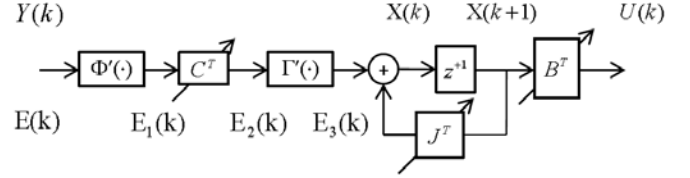


Fig. 2 Block-diagram of the adjoined RVRNN topology, obtained from the RVRNN topology using the diagrammatic rules

III. TOPOLOGY AND BACKPROPAGATION LEARNING OF RECURRENT COMPLEX-VALUED NEURAL NETWORK

The general Complex Valued Neural Network topology below consideration has complex valued input, output, and state vectors, and complex A, B, C weight matrices. In this part we consider two particular Recurrent CVNNs (RCVNNs) with different activation functions. In the same manner as in the real value case we could apply complex valued diagrammatic rules so to derive an adjoined RCVNN for each CVNN case.

The performance index to be minimized is given by:

$$\zeta(k) = \frac{1}{2} \sum_j [E_j(k)] [E_j^*(k)], \quad j \in C, \quad \zeta = \frac{1}{N_e} \sum_j \zeta(k) \quad (15)$$

This function $\zeta(k)$ is a mapping of the form $f: \mathbb{C} \rightarrow \mathbb{R}$, so it is not analytic in the sense that it does not have derivative and also it does not satisfy the Cauchy-Riemann equations. This complicates the use of the gradient descent algorithm, because we have to use the so-called Wirtinger's calculus. Using diagrammatic rules we avoid this complicated problem.

A. RCVNN Topology with First Type Activation Function

The first activation function that we consider is given by (16). This activation function has singularities in some parts of the complex domain and because of that, this function is evaluated in a region of the complex plane avoiding singularity points, [14]. The activation function is defined as:

$$f(z) = \tanh z, \quad z \in \mathbb{C} \setminus \left[-\frac{\pi}{2} - \epsilon; -\frac{\pi}{2} + \epsilon \right] \cup [-\epsilon; \epsilon] \quad (16)$$

The NN using this activation function is described in the given in Fig.3 block diagram. This type of representation allows us to apply diagrammatic rules so to derive the adjoined RCVNN and use it for NN learning. In the present

paper we propose a new approach of the CVBP for the given in Fig. 3 RCVNN extending the real-time real value NN algorithm of learning, [12], to the complex value case. The topology of this RCVNN is given on Fig.3.

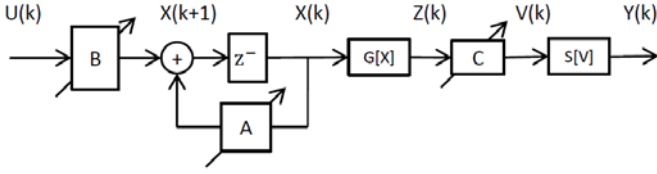


Fig. 3 Topology of the first type RCVNN

The mathematical description of that topology is the same as (1)-(4) for the real valued case but the variables are complex. The vectors and matrices of the RCVNN topology are given as follows:

- $A \in \mathbb{C}^{n \times n}$: Feedback Matrix;
- $B \in \mathbb{C}^{n \times n}$: Input matrix;
- $C \in \mathbb{C}^{n \times n}$: Output matrix;
- $X(k) \in \mathbb{C}^{n \times n}$: State vector;
- $U(k) \in \mathbb{C}^{n \times n}$: Network input;
- $Y(k) \in \mathbb{C}^{n \times n}$: Network output;
- $G[\cdot], S[\cdot]$: Complex-valued vector-*tanh* - activation functions, given by (16);
- m : Number of inputs;
- n : Number of neurons in the hidden layer;
- p : Number of neurons in the output layer.

The complex state feedback matrix A is defined as diagonal with the same weight restriction as the given in (1) for J .

As we could see the used *tanh* - activation function has singularity in some parts of the complex domain. To overcome that, the activation function is evaluated in regions outside these points, as it could be seen in(16).

Applying the complex valued diagrammatic rules we could obtain the adjointed RCVNN, given on Fig.4.

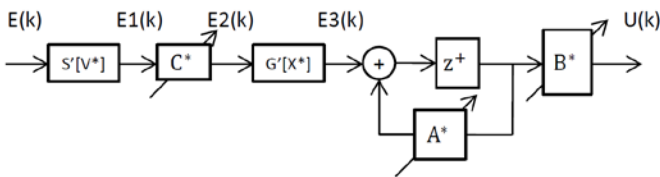


Fig. 4 Adjoined topology of the first type RCVNN

Now, the backpropagation learning rule (6) could be defined in a complex domain with the same significance of the participating variables. Using the adjointed RCVNN topology we could derive the following weight update algorithm:

For the output layer:

$$\Delta C(k) = E_1(k)Z^*(k) \quad (17)$$

$$E_1(k) = S'[Y[V^*(k)](k)]E(k) \quad (18)$$

$$E(k) = T(k) - Y(k) \quad (19)$$

For the hidden layer:

$$\Delta A(k) = E_3(k)X^*(k) \quad (20)$$

$$E_3(k) = G'[Z[X^*(k)](k)]E_2(k) \quad (21)$$

$$E_2(k) = C^*(k)E_1(k) \quad (22)$$

$$\Delta vA(k) = E_3(k) \otimes X^*(k) \quad (23)$$

$$\Delta B(k) = E_3(k)U^*(k) \quad (24)$$

Where:

- $G'[\cdot], S'[\cdot]$: Derivatives of the activation functions G, S ;
- a^* : Transpose and conjugate of the complex number a ;
- $T(k)$: Desired output vector.

As it could be seen, the application of the diagrammatic rules and the adjointed RCVNN topology simplified the learning with respect to the classical gradient descent learning in complex domain, [7].

B. RCVNN Topology with Second Type Activation Function

The second type activation function, [9], does not have singularity points. It is given by the next equation:

$$f(z) = \tanh \operatorname{Re}(z) + i \tanh \operatorname{Im}(z) \quad (25)$$

Unlike the RVNN, the topology of the CVNN will be defined by the second type activation function. In this case, the RCVNN is given by the following equations:

$$X(k+1) = AX(k) + BU(k) \quad (26)$$

$$Z(k) = G[X_{Re}(k)] + iG[X_{Im}(k)] \quad (27)$$

$$V(k) = Z_{Re}C_{Re} + iZ_{Im}C_{Im} \quad (28)$$

$$Y(k) = S[V_{Re}(k)] + iS[V_{Im}(k)] \quad (29)$$

The topology of the RCVNN in this case is given on Fig. 5.

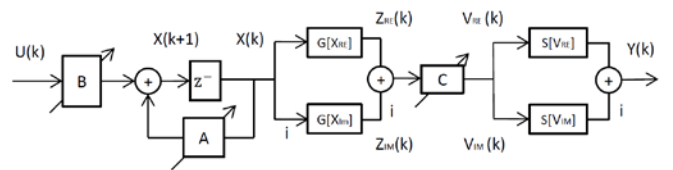


Fig. 5 Topology of the second type RCVNN

From Fig.5 and equation (25) it is clear that this topology separates the real and imaginary parts of the CV activation functions in order to simplify the CV learning algorithm.

The vectors and matrices of the RCVNN topology are defined as follows:

$G[\cdot], S[\cdot]$ are complex valued vector-*tanh*-activation functions given by (25).

$A \in \mathbb{C}^{n \times n}$: Feedback Matrix;
 $B \in \mathbb{C}^{n \times n}$: Input matrix;
 $C \in \mathbb{C}^{n \times n}$: Output matrix.
 $X(k) \in \mathbb{C}^{n \times n}$: State vector;
 $U(k) \in \mathbb{C}^{n \times n}$: Network input;
 $Y(k) \in \mathbb{C}^{n \times n}$: Network output;
 m : Number of inputs;
 n : Number of neurons in the hidden layer;
 p : Number of neurons in the output layer.

The complex state feedback matrix A is defined as diagonal with the same restriction as (1) for J .

Applying the complex valued diagrammatic rules we could obtain the adjoined RCVNN, given on Fig.6.

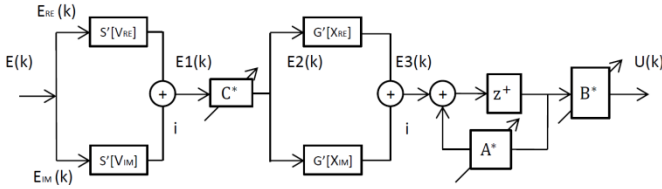


Fig. 6 Adjoined topology of the second type RCVNN

Now, the backpropagation learning rule (6) could be defined in a complex domain with the same significance of the participating variables. Using the adjoined RCVNN topology we could derive the following weight update algorithm:

For the output layer:

$$\Delta C(k) = E_1(k)Z^*(k) \quad (30)$$

$$E_1(k) = E_{Re}S'[Y[V_{Re}(k)]] + iE_{Im}S'[Y[V_{Im}(k)]] \quad (31)$$

$$E(k) = T(k) - Y(k) \quad (32)$$

For the hidden layer:

$$\Delta A(k) = E_3(k)X^*(k-1) \quad (33)$$

$$E_3(k) = E_{2Re}G'[Z[X_{Re}(k)]] + iE_{2Im}G'[Z[X_{Im}(k)]] \quad (34)$$

$$E_2(k) = C^*(k)E_1(k) \quad (35)$$

$$\Delta vA(k) = E_3(k) \otimes X^*(k) \quad (36)$$

$$\Delta B(k) = E_3(k)U^*(k) \quad (37)$$

Where:

$G[\cdot], S[\cdot]$: The derivatives of the activation functions G, S ;
 a^* : Transpose and conjugate of the complex number a ;
 $T(k)$: Desired output vector;
 E_{Re} : Real part of $E(k)$;
 E_{Im} : Imaginary part of $E(k)$.

As it could be seen, the application of the complex diagrammatic rules in the design of the adjoined RCVNN topology simplified the learning with respect to the classical gradient descent learning in complex domain.

IV. COMPLEX -VALUED NEURAL SOLUTION OF NONLINEAR IDENTIFICATION PROBLEM

This part of the paper illustrates the application of the RCVNN for nonlinear oscillatory plant identification. The nonlinear oscillatory plant under investigation is a flexible – joint robot arm. The model, the output and the input of the plant are given in continuous time. In order to use a recurrent neural network for its identification, the output/input signals of the plant are discretized with sampling period T_0 .

A. Description of the Nonlinear Plant Model

The identified system is an idealized nonlinear model of a flexible – joint robot arm, illustrated by Fig. 7. The flexibility of the robot joint is caused by a harmonic drive, which is a type of robot gear mechanism with high torque transmission, low backlash and compact size.

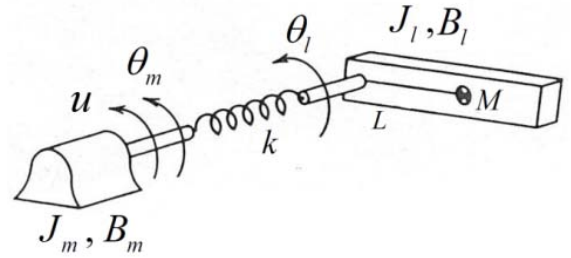


Fig. 7 Idealized model representing robot joint flexibility

The robot joint model consists of an actuator connected to a load through a torsional spring representing the joint flexibility. We take the motor torque as an input u . The equations of motion of the flexible - joint robot are given as follows.

$$\begin{aligned}
 J_l \ddot{\theta}_l + B_l \dot{\theta}_l + Mgl \sin \theta_l + k(\theta_l - \theta_m) &= 0 \\
 J_m \ddot{\theta}_m + B_m \dot{\theta}_m - k(\theta_l - \theta_m) &= u
 \end{aligned} \quad (378)$$

Where: J_l, J_m are load and motor inertias; B_l and B_m are load and motor damping constants; u is the input torque applied to the motor shaft; M and L are the mass of the link and the length between the shaft and the center of mass of the link; k represents the torsional stiffness constant of the harmonic drive gear.

As we can see, the plant is an oscillatory system, described by two second order differential equations, representing a system with two degrees of freedom but only one input which makes the system sub-actuated.

B. Plant Identification

The plant identification using the given up two RCVNN models is illustrated by Fig.8. Here the desired complex target vector is the output of plant. The identification objective is that the complex weight parameters of the RCVNN are adjusted in such manner that the RCVNN output follows the plant output with minimum MSE.

The RCVNN used has three neurons in the hidden layer, one input and one output neurons. The RCVNN dimensions are as follows: $m = 1$; $p = 1$; $n = 3$ and a sampling time $T_0 = 0.01$.

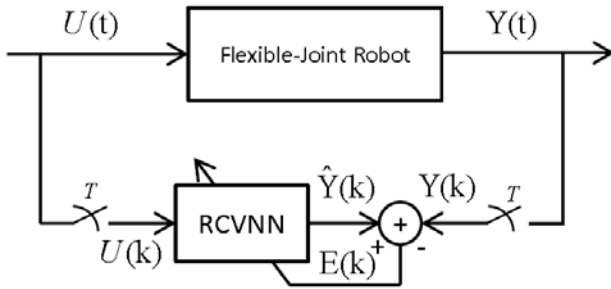


Fig. 8 Block diagram of RCVNN plant identification

C. Simulation Results

This section described the simulation results obtained using both type RCVNNs for nonlinear oscillatory plant identification. The simulation is done in two stages: stage of system identification and stage of NN generalization. During the first stage the RCVNN weights are learned until convergence and after that they are frozen and the input signal is changed so to validate (generalized) the result of identification. As a measure of comparison we use the final MSE% of identification and generalization. The input plant signals used for system identification $u(t)$ and generalization $u_v(t)$ are given by:

$$u(t) = \sin\left(\frac{t}{10}\right) + 0.5 \sin\left(\frac{2t}{50}\right) \quad (38)$$

$$u_v(t) = 0.5 \sin\left(\frac{t}{10}\right) + 0.8 \sin\left(\frac{t}{30}\right) \quad (40)$$

Simulation results obtained with the first type activation function RCVNN-1 topology. The graphical results of plant identification for the first case are given on Fig. 9 where the output of the plant is compared with the output of the RCVNN-1. The final MSE of RCVNN-1 convergence during system identification is given on Table 1 for 1000, 2000, and 3000 learning iterations. The results show a constant MSE decreasing, exhibiting a good BP NN convergence.

The graphical results of RCVNN-1 generalization are given on Fig. 10, where the NN weights are frozen and input signal is changed. The output of the plant is compared with the output of the RCVNN-1 exhibiting a good generalization. The final results of RCVNN-1 generalization are given on Table 1 for 3000 steps. The validation results show a constant MSE decreasing exhibiting a good RCVNN-1 generalization.

Simulation results obtained with the second type activation function RCVNN-2 topology. The graphical results of plant identification for the first case are given on Fig. 11 where the output of the plant is compared with the output of the RCVNN-2.

The final MSEs of RCVNN-2 convergence during system identification is given on Table 1 for 1000, 2000, and 3000

learning iterations. The results show a constant MSE decreasing exhibiting a good BP NN convergence.

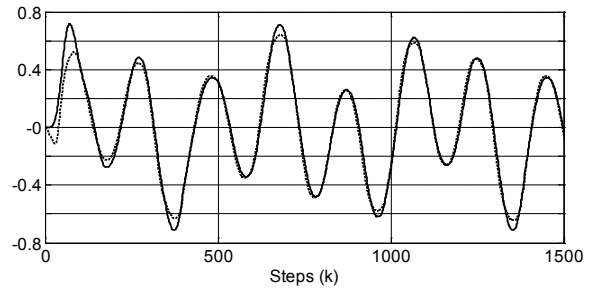


Fig. 9 Simulation results of RCVNN-1 BP learning; RCVNN-1 output (dotted line); plant output (continue line)

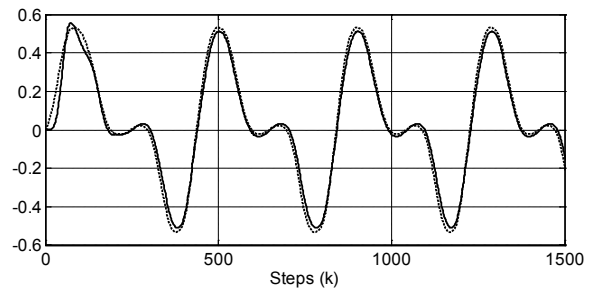


Fig.10 Simulation results of RCVNN-1 generalization; RCVNN-1 output (dotted line); plant output (continue line)

The graphical results of RCVNN-2 generalization are given on Fig. 12, where the NN weights are frozen and input signal is changed. The output of the plant is compared with the output of the RCVNN-2 exhibiting a good generalization. The final results of RCVNN-2 generalization are given on Table 1 for 3000 steps. The validation results show a constant MSE decreasing exhibiting a good RCVNN-2 generalization.

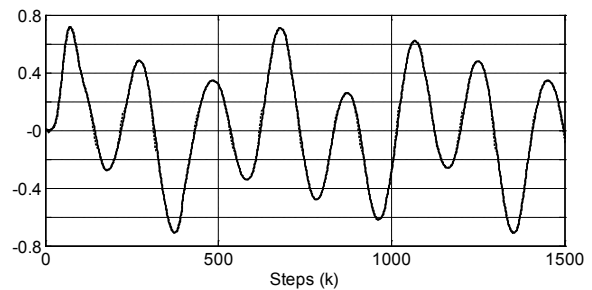


Fig. 11 Simulation results of RCVNN-2 BP learning; RCVNN-2 output (dotted line); plant output (continue line)

Comparative final MSE simulation results of nonlinear oscillatory plant identification and generalization using RCVNN-1 and RCVNN-2. The final MSE values obtained during identification and generalization experiments with both RCVNN-1,2 (see Table 1) show that the RCVNN-2 outperformed the RCVNN-1 because the RCVNN-1 activation func-

tion possess singular points that affects the BP learning and the RCVNN-2 activation function does not possess such singular points so its learning is perfect. In generalization stage the result are opposite but still good so the identification results are dominating.

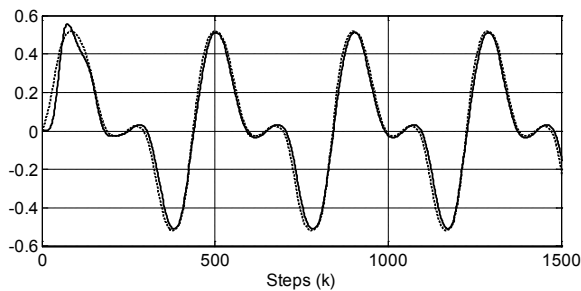


Fig.12. Simulation results of RCVNN-2 generalization; RCVNN-2 output (dotted line); plant output (continue line)

Table I. Final MSE of learning and generalization

Learning		
Number of steps	First type of activation function	Second type of activation function
1000	0.0264	0.0045
2000	0.0178	0.0029
3000	0.0097	0.0028
Generalization		
Number of steps	First type of activation function	Second type of activation function
3000	0.0014	0.0025

Finally we could make the conclusion that it is better to use RCVNN-2 which does not have singular points then to use RCVNN-1 which have singular points and try to overcome them.

V. CONCLUSIONS

In the present paper we use the diagrammatic rules, [13], for the complex case and applied them to obtain the backpropagation training algorithm. We studied two different RCVNNs topologies with two different activation functions. Using the diagrammatic rules we obtain the RCVNNs adjoined and derived the backpropagation algorithm for both cases in a simpler manner that coincides with the actual training algorithm using Wirtinger’s calculus. The obtained comparative simulation results for identification and generalization of a nonlinear oscillatory plant confirm the quality of the BP learning algorithm. The comparison of both RCVNN-1, and RCVNN-2 topologies for both activation functions give some priority to the second case in the sense that it is better to use activation functions without singular points then to use activation functions with singular points and try to avoid them.

REFERENCES

- [1] A. Hirose, *Complex-Valued Neural Networks*, 2nd ed., S. i. C. Intelligence, Springer-Verlag, 2012, vol. 400.
- [2] A. Minin, Y. Chistyakov, E. Kholodova, H. G. Zimmermann , and A. Knoll, "Complex Valued Open Recurrent Neural Network for Power Transformer Modeling ," *International Journal of Applied Mathematics and Informatics*, vol. 6, no. 1, pp. 41-48, 2012.
- [3] L. Ferariu, "Nonlinear System Identification Based on Evolutionary Dynamic Neural Network," in *Proc. of European Control Conference*, Cambridge, UK, paper no. 432, 2003.
- [4] K. Kawashima, and T. Ogawa, "Complex-Valued Neural Network for Group-Movement Control of Mobile Robots," in *Proc. SICE Annual Conference 2012*, Japan, 2012, pp. 1806 - 1809.
- [5] A. Hirose, "Motion Controls Using Complex-Valued Neural Networks with Feedback Loops," in *Proc. IEEE International Conference on Neural Networks*, vol. 1, San Francisco, CA, 1993, pp. 156-161.
- [6] H. G. H.G. Zimmermann, A. Minin, and V. Kuserbaeva, "Historical Consistent Complex Valued Recurrent Neural Network," in *ICANN 2011*, Espoo, Finland, 2011, pp. 185-192.
- [7] H. Leung, and S. Haykin, "The Complex Backpropagation Algorithm," *IEEE Transactions on Signal Processing*, vol. 39, no. 9, pp. 2101-2104, 1991.
- [8] T. Nitta, *Complex-Valued Neural Networks: Utilizing High-Dimensional Parameters*. IGI Global, 2009.
- [9] C. Woo, and D. S. Hong, "Adaptive equalization using the complex backpropagation algorithm," in *Proc. of IEEE International Conference on Neural Networks*, vol. 4, Washington, DC, 1996, pp. 2136-2141.
- [10] N. Miklos, and B. Salik, "Neural Networks with Complex Activations and Connection Weights," *Complex Systems*, vol. 8, pp. 115-126, 1994.
- [11] G. Georgiou, and C. Koutsougeras, "Complex Domain Backpropagation," *IEEE Transactions on Circuits and Systems-11: Analog and Digital Signal Processing*, vol. 39, no. 5, pp. 330-334, 1992.
- [12] I. S. Baruch, and C. R. Mariaca-Gaspar, "A Levenberg-Marquardt Learning Applied for Recurrent Neural Identification and Control of a Wastewater Treatment Bioprocess," *International Journal of Intelligent Systems*, no. 24, pp. 1094-1114, 2009.
- [13] E. Wan, and F. Beaufays, "Diagrammatic method for deriving and relating temporal neural networks algorithms," *Neural Computation*, pp. 182-201, 1996.
- [14] A. Minin, A. Knoll, and H. G. Zimmermann, "Complex Valued Recurrent Neural Network: From Architecture to Training," *Journal of Signal and Information Processing*, pp. 192-197, 2012.

Unitary theory of direct electromechanical transformers

Zdeněk Úředníček

Abstract— Text refers the basic information about unitary description of direct electromechanical power conversion dynamic behaviour – electric machines, enabling its uniform description, regardless to its type. Mentioned unified description is verified by means of single machines physical models and their control.

Keywords— Electromagnetic- mechanic interaction, standing magnetic field, rotating (moving) magnetic field, unitary description, electric machines dynamic behavior, actuators.

I. INTRODUCTION

Substantial parts of actuating devices in systems with motion control are converters of some controlled energy type to (controlled) mechanical energy.

Important and most widespread of these transformation components are systems with electromagnetic energy to mechanical energy direct conversion- electric machines.

For administration of correct system behavior with controlled mechanical torque source is, at motional states control laws proposal, inevitable simply, however enough accurately describe the mentioned transformation component dynamic behavior.

This work presents the basic simplified description procedure of electromagnetic and gravitational field interaction and applies it on three basic types familiarly used electric machines description.

Dynamic behavior description of three electrical machines' basic types is converted by the help of power invariable transformation to more or less identical formal form, which enables to use similar principles for their laws proposal of mechanical torque control.

Verification is performed by means of simulation experiments with physical (multi-ports) models.

II. EXCHANGE ENERGY BETWEEN ELECTRO-MAGNETIC AND GRAVITATIONAL FIELD

A. Rotating system with two windings, constant air gap and simple mechanical commutator

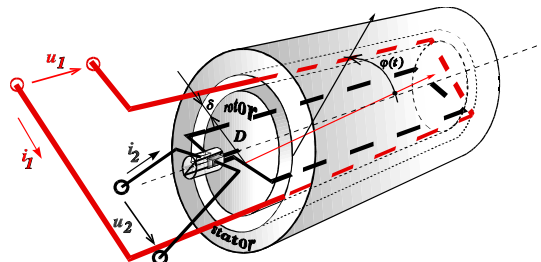


Fig. 1 Electrical and mechanical rotary energy exchange principle at rotary system with commutator.

On Fig.1 the rotating mechanical system with constant air gap, two windings and simple commutator is displayed. On the basis of total electromagnetic energy

$$W_{\text{magn}} = \frac{1}{2} \cdot \{L_{11} \cdot i_1^2(t) + 2 \cdot M[\varphi(t)] \cdot i_1(t) \cdot i_2(t) + L_{22} \cdot i_2^2(t)\}$$

is possible to write the dynamic equations detailing the context between electric and mechanical quantities:

$$\begin{aligned} u_1(t) &= \frac{d\psi_1}{dt} = \frac{d}{dt} \left(\frac{\partial W_{\text{magn}}}{\partial i_1} \right) = \frac{d}{dt} \{L_{11} \cdot i_1(t) + M[\varphi(t)] \cdot i_2(t)\} = \\ &= L_{11} \cdot \frac{di_1(t)}{dt} + M[\varphi(t)] \cdot \frac{di_2(t)}{dt} + \underbrace{\frac{dM[\varphi(t)]}{d\varphi}}_{\kappa_1[\varphi(t), i_2(t)]} \cdot i_2(t) \cdot \underbrace{\frac{d\varphi(t)}{dt}}_{\omega(t)} \end{aligned} \quad (1)$$

$$\begin{aligned} u_2(t) &= \frac{d\psi_2}{dt} = \frac{d}{dt} \left(\frac{\partial W_{\text{magn}}}{\partial i_2} \right) = \frac{d}{dt} \{L_{22} \cdot i_2(t) + M[\varphi(t)] \cdot i_1(t)\} = \\ &= L_{22} \cdot \frac{di_2(t)}{dt} + M[\varphi(t)] \cdot \frac{di_1(t)}{dt} + \underbrace{\frac{dM[\varphi(t)]}{d\varphi}}_{\kappa_2[\varphi(t), i_1(t)]} \cdot i_1(t) \cdot \underbrace{\frac{d\varphi(t)}{dt}}_{\omega(t)} \end{aligned} \quad (2)$$

$$m(t) = -\frac{\partial W_{\text{magn}}}{\partial \varphi} = -\frac{1}{2} \cdot \left\{ i_1(t) \cdot \underbrace{\frac{dM[\varphi(t)]}{d\varphi}}_{\kappa_1[x(t), i_2(t)]} \cdot i_2(t) + i_2(t) \cdot \underbrace{\frac{dM[\varphi(t)]}{d\varphi}}_{\kappa_2[x(t), i_1(t)]} \cdot i_1(t) \right\} \quad (3)$$

Multi-port equivalent diagram is next:

Author is from Department of Automation and Control, Tomas Bata University in Zlin, Jižní Svahy, Nad Stráněmi 4511, 760 05, Zlin, Czech Republics. Email: urednicek@fai.utb.cz, web: fai.utb.cz.

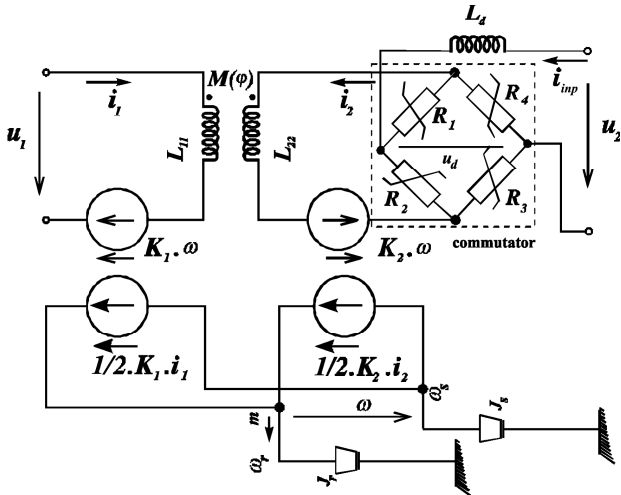


Fig. 2 Multi-port equivalent diagram of electric and rotational energy exchange for rotational system with commutator.

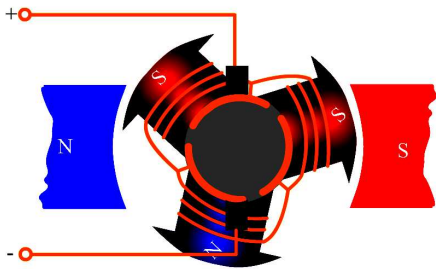


Fig. 3 Rotational system with commutator and three lamellas ordering.

Fig. 3 shows form of even system with three coils on rotor and three lamellas and Fig. 4 shows current and machine torque (including its floating mean value) time dependencies at these three coil and three lamellas.

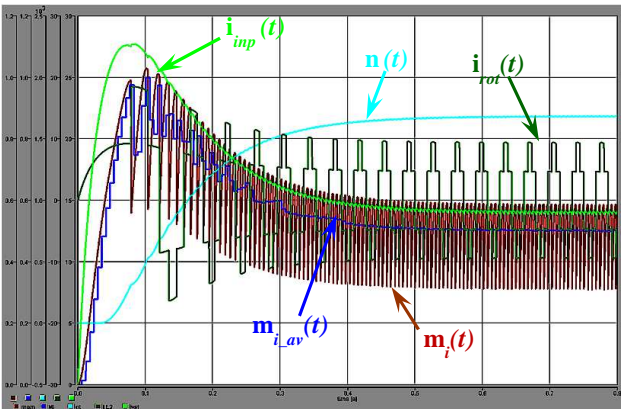


Fig. 4 Three lamellas machine current and machine torque time dependencies.

For the great (infinite) number of lamellas on so - called direct-current machine it is possible to achieve mutually perpendicular and stationary stator and rotor magnetic flows' position and equations pass to the form:

$$u_1(t) = R_1 \cdot i_1(t) + L_1 \cdot \frac{di_1(t)}{dt}$$

$$u_{inp}(t) = R_{rot} \cdot i_{inp}(t) + L_{rot} \cdot \frac{di_{inp}(t)}{dt} + K \cdot i_1(t) \cdot \omega(t) \quad (4)$$

$$m_i(t) = K \cdot i_1(t) \cdot i_{inp}(t)$$

where $i_1(t)$ is current of coil in stator,

$i_{inp}(t)$ is current to the commutator, input current to the rotor, ω is the mutual mechanical angular velocity rotor and stator of machine,

$$K = \frac{p_p \cdot N_v}{a \cdot \pi} \cdot L_{1rot}$$

R_{1rot} is substitute winding resistance of exciting or rotor circuit,

$L_{1,rot}$ is substitute self - inductance of exciting or rotor circuit,

L_{1rot} is substitute mutual inductance of exciting and rotor circuit,

a is the number of armature winding parallel branches,

p_p is number of pole pairs,

N_v is number of armature wires.

The resulting multi-port equivalent diagram is next:

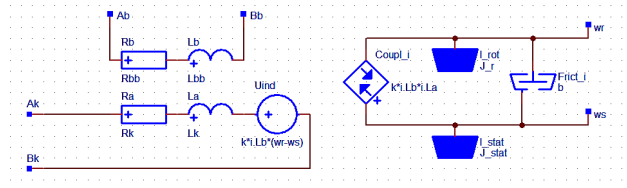


Fig. 5 Multi-port equivalent diagram of DC machine with infinite numbers of lamellas.

We can see, that DC machine inner torque is given by product of stator magnetic flow ($K \cdot i_1(t)$) and flow to the commutator.

Both currents have direct physical sense and there're directly measurable on real machine.

B. Rotating system with two windings and air gap variable and stator spinning magnetic field

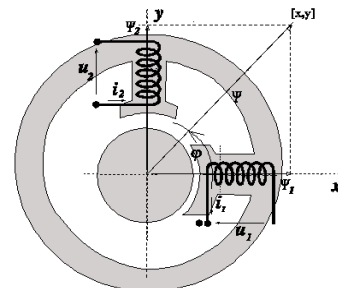


Fig. 6 Stator lay-out with spinning magnetic field.

Fig. 6 shows ordering, which enables to create rotating magnetic field also by standing stator windings.

If we distribute the windings on stator to the double-phase winding with phases' brought-out neutral points (so four

windings on stator) and as a rotor we use the permanent magnet (real ordering is on Fig. 7), it is possible to write for coupled magnetic flows of ordering:

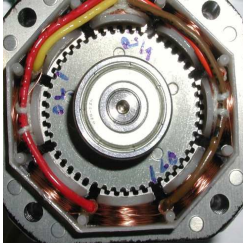


Fig. 7 Real stator and rotor ordering.

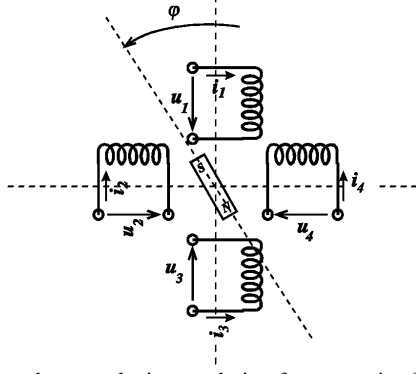


Fig. 8 Stator and rotor substitute ordering for magnetic flows determination.

$$\underline{\Psi}(t) = \underline{L}[\varphi(t)] \cdot \underline{i}(t) + \underline{c}[\varphi(t)]$$

φ is electrical rotor angle of rotation, for which pays

$$\varphi = z_r \cdot \Phi_m$$

z_r is number of rotor sprockets.

Inductions L_1, L_2 sense is clear from Fig. 9.

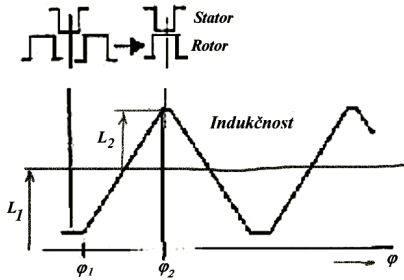


Fig. 9 Inductions L_1, L_2 sense.

By introduction

$$u_a(t) = u_1(t) - u_3(t)$$

$$u_b(t) = u_2(t) - u_4(t)$$

$$i_a(t) = i_1(t) - i_3(t)$$

$$i_b(t) = i_2(t) - i_4(t)$$

(we study the substitute two - phase windings with **a** and **b** phases) and by displaying of dynamic balance equations in **d, q** system coordinates, spinning at speed of rotor rotation, we obtain equations' system

$$u_d(t) = R \cdot i_d(t) + L_d \cdot \frac{di_d(t)}{dt} - z_r \cdot L_q \cdot i_q(t) \cdot \omega_m(t)$$

$$u_q(t) = R \cdot i_q(t) + L_q \cdot \frac{di_q(t)}{dt} + [z_r \cdot L_d \cdot i_d(t) + 2 \cdot k_n] \cdot \omega_m(t) \quad (5)$$

$$m_i(t) = [z_r \cdot (L_d - L_q) \cdot i_d(t) + 2 \cdot k_n] \cdot i_q(t) = 2 \cdot [k_n - 2z_r \cdot L_2 \cdot i_d(t)] \cdot i_q(t)$$

where between **x, y** quantities in original standing system and in **d, q** rotating po-wer invariant transformation system pays

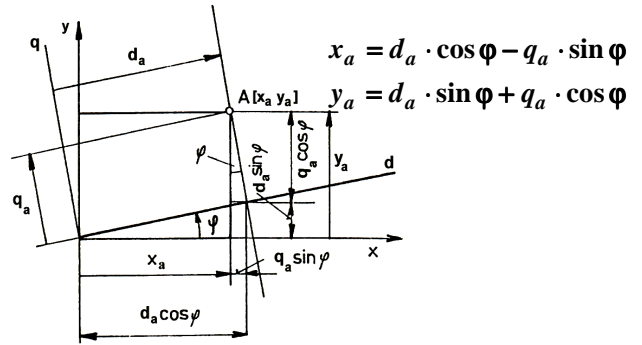


Fig. 10 Power invariant transformation to the rotating reference system.

and for L_d, L_q inductions pays

$$L_d = L_\sigma + 2L_1 - 2L_2$$

$$L_q = L_\sigma + 2L_1 + 2L_2$$

By (4) and (5) equations comparison we can see that for hybrid stepping motor (this is mentioned ordering) we have received after transformation "two dc machine rotor equations" and mainly, that inner torque hereof machine is expressed in the same way as at dc machine, it means as a product of magnetic flow given by permanent magnet and flow from current i_d and torque generating current i_q .

If we place three windings on stator and as power invariable transformation we use Park transformation (co - ordinate system **d, q** rotates again according with machine rotor), we'll obtain equations of synchronous machine with permanent magnet on rotor

$$R \cdot i_d(t) + L_d \cdot \frac{di_d(t)}{dt} - p_p \cdot \underbrace{L_q \cdot i_q(t)}_{\Psi_q(t)} \cdot \omega(t) = u_d(t)$$

$$R \cdot i_q(t) + L_q \cdot \frac{di_q(t)}{dt} + p_p \cdot \underbrace{[L_d \cdot i_d(t) + k_n]}_{\Psi_d(t)} \cdot \omega(t) = u_q(t)$$

$$m_i(t) = p_p \cdot \underbrace{[L_d \cdot i_d(t) + k_n]}_{\Psi_d(t)} \cdot i_q(t) - p_p \cdot \underbrace{L_q \cdot i_q(t)}_{\Psi_q(t)} \cdot i_d(t) = [p_p \cdot (L_d - L_q) \cdot i_d(t) + k_n] \cdot i_q(t) \quad (6)$$

p_p is pair of poles.

Certainly, there's not surprise, that (5) and (6) equations are identical. In both cases description is concerned about synchronic salient pole machine on stator and permanent magnet on rotor.

In contrast to the DC machine, the currents in equation for torque are now as the result of real currents transformation to the new rotating referential system and, which is important from these engines control standpoint, there are not directly measurable.

Invariable transformation utilization elegancy will excel moreover, if we match, by means of complex plane (complex number is as well as point co - ordinates in plane given by sequenced real numbers pair), except new referential system speed and turning rotor speed and stator field, also its d axis position with stator flow position. Resulting equations pass on form:

$$\begin{aligned}
 R \cdot i_d(t) + L_d \frac{di_d(t)}{dt} &= u_d(t) \\
 R \cdot i_q(t) + p_p [L_d \cdot i_d(t) + k_n] \cdot \omega(t) &= u_q(t) \\
 m_i(t) &= p_p \cdot i_q(t) \cdot [L_d \cdot i_d(t) + k_n]
 \end{aligned}
 \tag{7}$$

We can see that all parts of equations, which were related with coupled field, disappeared:

- Component of induced tension in **d** axis,
- in equation for **q**-tension component u_q , the component from time changes disappeared $\Psi_q(t)$,
- and torque equation already does not contain $\Psi_q(t)$ as well..

C. Rotating system with three windings, stator magnetic field spinning and short-circuit of rotor windings

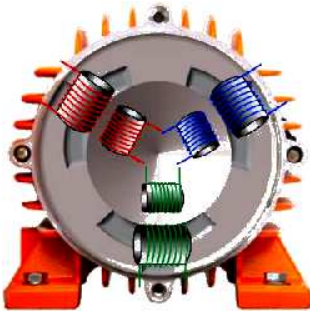


Fig. 11 Rotating system with three windings, stator magnetic field spinning and short-circuit of rotor windings.

Last controlled mechanical torque source representative with direct electromagnetic to mechanic energy conversion will be stated inductive (asynchronous) machine, although on the first look it can be considered that its simplified dynamic equations are more complicated and they will resist to the unitary access:

$$\begin{aligned}
 u_d(t) &= R_s i_d(t) + L_d \frac{di_d(t)}{dt} + L_m \frac{di_D(t)}{dt} - \omega_s \cdot L_d \cdot i_q(t) - \omega_s \cdot L_m \cdot i_Q(t) \\
 u_q(t) &= R_s i_q(t) + L_d \frac{di_q(t)}{dt} + L_m \frac{di_Q(t)}{dt} + \omega_s \cdot L_d \cdot i_d(t) + \omega_s \cdot L_m \cdot i_D(t) \\
 0 &= \frac{R_r}{s} i_D(t) + L_D \frac{di_D(t)}{dt} + L_m \frac{di_d(t)}{dt} - \omega_s \cdot L_D \cdot i_Q(t) - \omega_s \cdot L_m \cdot i_q(t) \\
 0 &= \frac{R_r}{s} i_Q(t) + L_D \frac{di_Q(t)}{dt} + L_m \frac{di_q(t)}{dt} + \omega_s \cdot L_D \cdot i_D(t) + \omega_s \cdot L_m \cdot i_d(t) \\
 m_i(t) &= p_p \cdot L_m \cdot [i_q(t) \cdot i_D(t) - i_d(t) \cdot i_Q(t)]
 \end{aligned}
 \tag{8}$$

where quantity with index **d, q** are stator quantities projection to the **d, q** axes and quantity with index **D, Q** are rotor quantities projection to the **d, q** rotating axes system.

$$s(t) = \frac{\omega_s - \omega}{\omega_s} \text{ is a slip of machine.}$$

If in addition we identify, by the help of complex plane, except new referential system speed and stator field turning speed, also its **d** axis position with rotor flow position, resulting equations at current feeding cross to the form:

$$i_d(t) = \tau_r \cdot \frac{di_{mr}(t)}{dt} + i_{mr}(t) \tag{9.1}$$

where

$$\begin{aligned}
 i_{mr}(t) &= \frac{\text{Re}\{\Psi_r(t)\}}{L_m}; \quad \tau_r = \frac{L_D}{R_r}; \\
 s \cdot \omega_s(t) &= \frac{I}{\tau_r} \cdot \frac{i_q(t)}{i_{mr}(t)}
 \end{aligned}
 \tag{9.2}$$

$$m_i(t) = p_p \cdot \frac{L^2}{L_D} \cdot i_{mr}(t) \cdot i_q(t) \tag{9.3}$$

We see, that statement for machine inner mechanical torque is, as well as at DC machine and synchronous machine, expressed as a product of magnetic flow given by current i_d , and torque creating current i_q .

Only because of inductive transmission, the current creating of magnetic flow isn't directly i_d , but is linked with him across first order system (9.1)

III. UNITARY ELECTRICAL MACHINES PHYSICAL MODELS AND THEIR APPLICATION

We present in the final part the stated unitary theory on three electrical machines example.

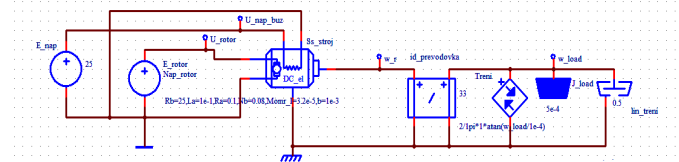


Fig. 12 DC machine physical model multi-port diagram with external excitation.

On Fig. 12 is multi-port diagram of DC machine with external excitation physical model supplied by tension and loaded by ideal gearbox and additional inertial mass with Coulomb friction.

Fig. 13 shows such model behaviour at four quadrant unipolar PWM rotor tension control.

Fig. 14 shows multi-port diagram of synchronous machine physical model with permanent magnet on rotor (PMSM) and Fig. 15 shows the example of its utilisation for torque control with rotor position sampling frequency of 1 kHz. The simulation of behaviour result is on Fig. 16.

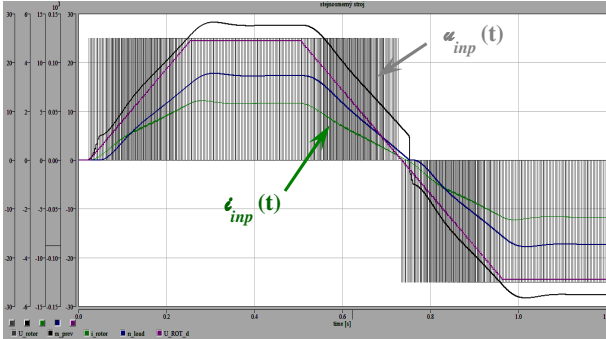


Fig.13 DC machine model behaviour at four quadrant unipolar PWM rotor tension control.

Fig. 17 shows asynchronous machine physical model multi-port diagram and Fig. 18 shows example of its application at torque control and rotor scanning position with sampling rate 5kHz.

On Fig. 19 is result its behaviour simulation.

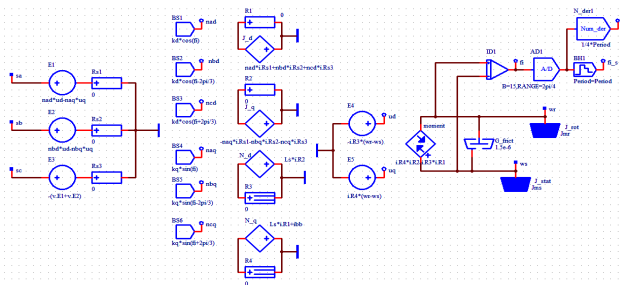


Fig. 14 PMSM machine physical model multi-port diagram.

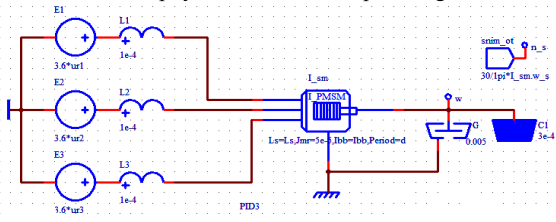


Fig. 15 Multi-port diagram of PMSM utilisation.

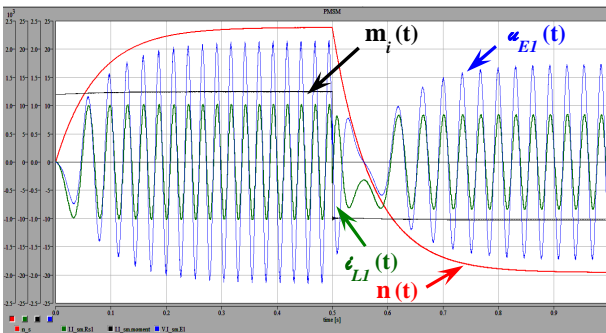


Fig.16 Currents supplied synchronous machine physical model with rotor position sampling in start and torque reversion processes.

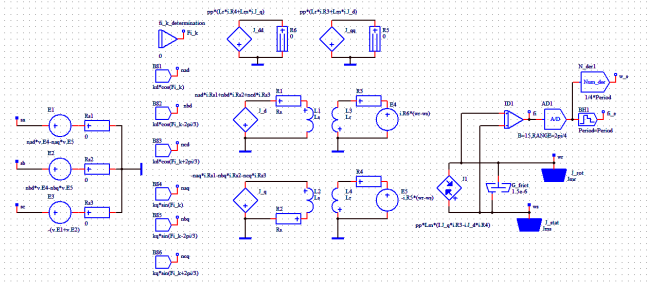


Fig.17 Asynchronous machine physical model multi-port diagram.

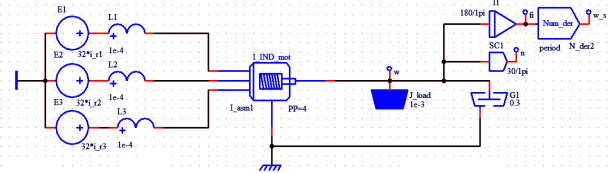


Fig. 18 Multi-port diagram of physical of asynchronous machine utilisation.

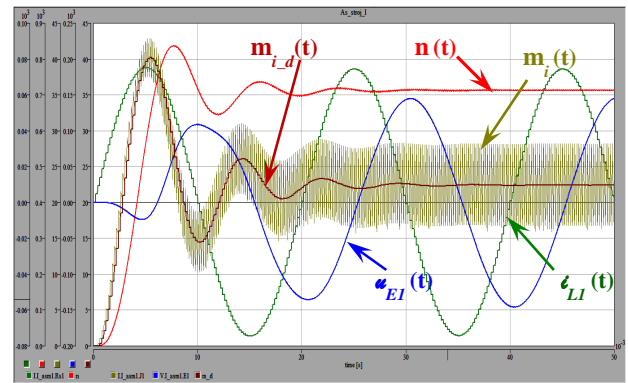


Fig. 19 Current fed inductive machine behaviour with rotor position sensor at start and with harmonic current power supply.

IV. CONCLUSION

Paper deals with uniform dynamic behaviour theory description possibility of actuating devices significant parts-electrical rotating machines.

On classic commutator DC machine equations, synchronous machine with permanent magnet (PMSM) and inductive (asynchronous) machine equations the fact that these direct converters of electromagnetic to the mechanical energy dynamic behaviour can be describe by uniform way is illustrated. It is important for purposes its utilization such as actuating device at motion control and it's also important from standpoint of their control.

Existing principle was used on these machines torque control demonstration by the help of simulation experiments by way of physical models.

REFERENCES

- [1] S. Crandall, D. C. Karnopp, E.F. Kurz, *Dynamics of mechanical and Electromechanical Systems*, McGraw-Hill, NewYork 1968.
- [2] D. C. Karnopp, R.C. Rosenberg, *System dynamics. A Unifies Approach*. Wiley & Sons, 1975.

- [3] R. C. Rosenberg, "Multiport Models in Mechanics". Trans. ASME, sept 1972
- [4] H. M. Trent, "Isomorfism between oriented linear graphs and lumped physical systems". J. Acoust. Soc. Am., vol. 27 (1955).
- [5] R.H. Park, „Two reaction Theory of Synchrononous Machines, Generalised Method of Analysis I“ TAIEE, 1929, str. 716-727
- [6] Z. Úředníček, *Modelling and simulation. Simulation experiment utilization at mechatronics systems' proposal*, (In Czech) Inaugural dissertation. Transport and communications university ZILINA, 1997
- [7] I. Astrov, M. Pikkov, R. Paluoja, "Motion Control of Vectored Thrust Aerial Vehicle for Enhanced Situational Awareness". Proceedings of the WSEAS International Conference on Mathematical APPLICATIONS in Science and Mechanics. Dubrovnik, Croatia, June 25-27, 2013
- [8] H.A. Darweesh, M. Roushdy, H.M. Ebied, B.M. Elbagoury, " Design a Cost Effective Non-Holonomic Vehicle for Autonomous Driving Applications". Proceedings of the WSEAS International Conference Mathematical Applications in Science and Mechanics. Dubrovnik, Croatia, June 25-27, 2013
- [9] S. Hubalovsky, P. Kadlec, L. Mitrovic, P. Hanzalova, "Computer simulation model of static mechanical properties of real technical device - elevator cab". Proceedings of the 3rd International Conference on Mathematical Models for Engineering Science (MMES '12). Paris, France, December 2-4, 2012
- [10] Z. Úředníček, Z.: *Electromechanical actuating devices*, (In Czech) Tomas Bata University in Zlin, Zlín 2012

Anti-Synchronization of WINDMI Systems via Adaptive Backstepping Control Method and its FPGA Implementation

Sundarapandian Vaidyanathan, Christos K. Volos, Ionnis M. Kyprianidis, Ioannis N. Stouboulos, Karthikeyan Rajagopal, and Prasina Alexander

Abstract—This paper derives new results for the anti-synchronization of identical WINDMI systems (Wind-Magnetosphere-Ionosphere models) via adaptive backstepping control method and also details the FPGA implementation of the proposed adaptive controller. In the anti-synchronization of chaotic systems, the sum of the outputs of master and slave systems is made to converge asymptotically to zero with time. The adaptive controller design for the anti-synchronization of identical WINDMI systems has been proved using Lyapunov stability theory. Numerical results using MATLAB have been presented for the illustration of the adaptive anti-synchronizing backstepping controller for identical WINDMI coupled systems. Finally, the proposed system have been implemented using FPGA and circuit simulation results have been detailed.

Keywords—Anti-synchronization, chaotic systems, WINDMI system, FPGA.

I. INTRODUCTION

CHAOTIC dynamical systems are nonlinear dynamical systems which are highly sensitive to small changes in the initial conditions of the states of the systems. Mathematically, chaotic dynamical systems can be defined as nonlinear dynamical systems having at least one positive Lyapunov exponent.

Since the pioneering works of Pecora and Carroll ([1], 1990) and Ott, Grebogi and Yorke ([2], 1990), chaos control and synchronization problems have received significant attention in the control literature. Chaos theory has important applications in a variety of fields like physical systems [3], chemical systems [4], optics [5], cardiology [6], biology [7], ecology [8-9], communications [10-11], cryptosystems [12-13], robotics [14-16], true random number generators

[17], neural networks [18-19], etc.

The phenomenon of anti-synchronization of chaotic systems can be stated as follows. If a particular chaotic system is called the *master* or *drive* system and another chaotic system is called the *slave* or *response* system, then the idea of anti-synchronization is to use the output of the master system to control the output of the slave system so that the states of the master and slave systems have the same amplitude but opposite signs asymptotically. Thus, in the anti-synchronization problems for chaotic systems, the sums of the states of the master and slave systems are expected to converge to zero asymptotically when anti-synchronization appears. This is an important research problem with many applications in engineering [20-21].

Various control schemes have been derived for the synchronization and anti-synchronization of chaotic systems such as PC method [1], OGY method [2], active control method [22-24], adaptive control method [25-28], time-delay feedback [29], sampled-data feedback [30-31], backstepping control method [32,33], sliding mode control method [34-36], etc.

In this paper, we deploy adaptive backstepping control for the anti-synchronization of identical WINDMI chaotic systems [37]. WINDMI systems are Wind-Magnetosphere-Ionosphere models which describe the energy flow through the solar wind-magnetosphere-ionosphere system. The main backstepping result derived in this paper is established using Lyapunov stability theory [38]. Numerical simulations using MATLAB are provided to illustrate the main results of this paper. Finally, we detail FPGA implementation of the adaptive backstepping controller proposed in this paper for the anti-synchronization of identical WINDMI chaotic systems.

This paper is organized as follows. In Section II, we describe the 3-D dynamics of the WINDMI chaotic system (2006). In Section III, we design an adaptive backstepping controller for the anti-synchronization of identical WINDMI chaotic systems, when the system parameters are unknown. In Section IV, we describe the FPGA implementation of the adaptive backstepping controller design for the anti-synchronization of the WINDMI systems. Section V contains the conclusions of this work.

Dr. Sundarapandian Vaidyanathan is with the R & D Centre, Vel Tech University, Avadi, Chennai-600 062, Tamil Nadu, India (phone: +91-04426841622; FAX: +91-04426840605; e-mail: sundarvtu@gmail.com).

Dr. Christos K. Volos is with the Physics Department, Aristotle University of Thessaloniki, Greece (e-mail: chvolos@gmail.com).

Dr. Ionnis M. Kyprianidis is with the Physics Department, Aristotle University of Thessaloniki, Greece (e-mail: imkypr@auth.gr).

Dr. Ioannis N. Stouboulos is with the Physics Department, Aristotle University of Thessaloniki, Greece (e-mail: stouboulos@physics.auth.gr).

Dr. Karthikeyan Rajagopal is with the Velammal Institute of Technology, Chennai-601 204, Tamil Nadu, India (e-mail: rkarthikeyan@gmail.com).

Dr. Prasina Alexander is with the Velammal Institute of Technology, Chennai-601 204, Tamil Nadu, India (e-mail: prasialex@rediffmail.com).

WINDMI Chaotic System

The 3-D dynamics of the WINDMI chaotic system (Wind-Magnetosphere-Ionosphere model) is described by the following normalized state equations.

$$\begin{cases} \dot{x}_1 = x_2 \\ \dot{x}_2 = x_3 \\ \dot{x}_3 = -ax_3 - x_2 + b - e^{x_1} \end{cases} \quad (1)$$

where x_1, x_2, x_3 are the states and a, b are positive parameters. The WINDMI system (1) exhibits a chaotic attractor, when the system parameter values are chosen as: $a = 0.7$ and $b = 2.5$.

Considering the initial conditions as:

$$x_1(0) = 1.8, \quad x_2(0) = 2.3, \quad x_3(0) = 0.7 \quad (3)$$

the 3-D portrait of the WINDMI chaotic attractor (1) for the parameter values (2) and the initial conditions (3) is depicted in Fig.1.

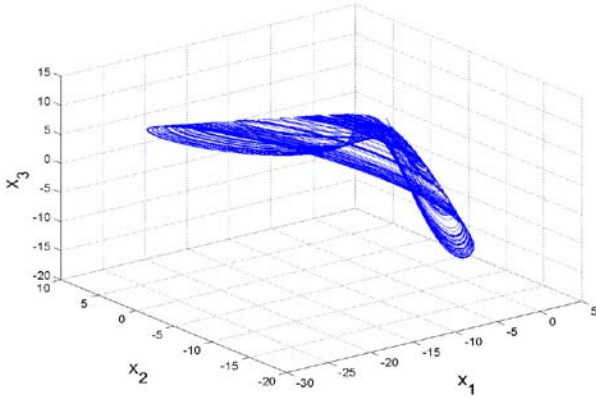


Fig. 1 Strange attractor of the WINDMI chaotic system

The spectrum of the Lyapunov exponents of the WINDMI chaotic attractor (1) for the parameter values (2) and the initial conditions (3) is depicted in Fig.2. The Lyapunov exponents of the WINDMI chaotic attractor are obtained as:

$$L_1 = 0.0945, \quad L_2 = 0, \quad L_3 = -0.7943 \quad (4)$$

The Lyapunov dimension of the WINDMI chaotic system is calculated as:

$$D_L = 2 + \frac{L_1 + L_2}{|L_3|} = 2.1190 \quad (5)$$

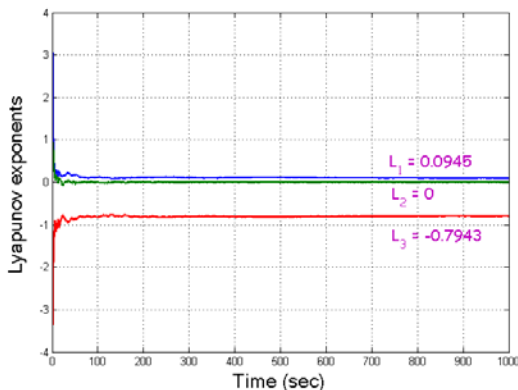


Fig. 2 Lyapunov exponents of the WINDMI chaotic system

II. ADAPTIVE BACKSTEPPING CONTROLLER DESIGN

In this section, we derive new results for the adaptive backstepping control design for the anti-synchronization of WINDMI systems, when the system parameters a and b are unknown.

As the master system, we consider the WINDMI dynamics:

$$\begin{cases} \dot{x}_1 = x_2 \\ \dot{x}_2 = x_3 \\ \dot{x}_3 = -ax_3 - x_2 + b - e^{x_1} \end{cases} \quad (6)$$

As the slave system, we consider the WINDMI dynamics:

$$\begin{cases} \dot{y}_1 = y_2 \\ \dot{y}_2 = y_3 \\ \dot{y}_3 = -ay_3 - y_2 + b - e^{y_1} + u \end{cases} \quad (7)$$

where u is the adaptive control to be designed.

The anti-synchronization error between the chaotic systems (6) and (7) is defined as:

$$\begin{cases} e_1 = y_1 + x_1 \\ e_2 = y_2 + x_2 \\ e_3 = y_3 + x_3 \end{cases} \quad (8)$$

The design problem is to find a control $u(t)$ using the states of (7) and (8), and to estimate the unknown parameters a and b so that the error converges to zero asymptotically with time, for all initial conditions.

The error dynamics is easily obtained as

$$\begin{cases} \dot{e}_1 = e_2 \\ \dot{e}_2 = e_3 \\ \dot{e}_3 = -ae_3 - e_2 + 2b - e^{y_1} - e^{x_1} + u \end{cases} \quad (9)$$

In the main result of this section, we shall consider an adaptive control law given by

$$u(t) = -2\hat{b} - 3e_1 - 4e_2 + (\hat{a} - 3)e_3 + e^{y_1} + e^{x_1} \quad (10)$$

where $\hat{a}(t)$ and $\hat{b}(t)$ are estimates of the unknown parameters a and b , respectively.

We define the parameter estimation errors as:

$$e_a(t) = a - \hat{a}(t) \quad \text{and} \quad e_b(t) = b - \hat{b}(t) \quad (11)$$

Then it is noted that

$$\dot{e}_a(t) = -\dot{\hat{a}}(t) \quad \text{and} \quad \dot{e}_b(t) = -\dot{\hat{b}}(t) \quad (12)$$

Next, we state and prove the main result of this paper.

Theorem 1. The identical WINDMI chaotic systems (6) and (7) with unknown parameters a and b are globally and exponentially anti-synchronized with the adaptive backstepping controller

$$u(t) = -2\hat{b} - 3e_1 - 4e_2 + (\hat{a} - 3)e_3 + e^{y_1} + e^{x_1} \quad (13)$$

where $\hat{a}(t)$ and $\hat{b}(t)$ are estimates of the unknown parameters a and b , respectively, and the update law for the parameter estimates is given by

$$\begin{aligned} \dot{\hat{a}} &= -e_3(2e_1 + 2e_2 + e_3) \\ \dot{\hat{b}} &= 2(2e_1 + 2e_2 + e_3) \end{aligned} \quad (14)$$

Proof. First, we take a Lyapunov function candidate

$$V_1 = \frac{1}{2}z_1^2 \quad (15)$$

where

$$z_1 = e_1. \quad (16)$$

The time derivative of V_1 is given by

$$\dot{V}_1 = z_1 \dot{z}_1 = e_1 e_2 = -z_1^2 + z_1(e_1 + e_2). \quad (17)$$

Next, we define

$$z_2 = e_1 + e_2. \quad (18)$$

Then we find that

$$\dot{V}_1 = -z_1^2 + z_1 z_2 \quad (19)$$

Secondly, we take a Lyapunov function candidate

$$V_2 = V_1 + \frac{1}{2}z_2^2 = \frac{1}{2}(z_1^2 + z_2^2) \quad (20)$$

The time derivative of V_2 is obtained as

$$\dot{V}_2 = -z_1^2 - z_2^2 + z_2(2e_1 + 2e_2 + e_3) \quad (21)$$

Next, we define

$$z_3 = 2e_1 + 2e_2 + e_3. \quad (22)$$

Then it follows that

$$\dot{V}_2 = -z_1^2 - z_2^2 + z_2 z_3 \quad (23)$$

Finally, we take a Lyapunov function candidate

$$V = V_2 + \frac{1}{2}z_3^2 + \frac{1}{2}(e_a^2 + e_b^2) \quad (24)$$

i.e.

$$V = \frac{1}{2}(z_1^2 + z_2^2 + z_3^2 + e_a^2 + e_b^2) \quad (24)$$

It is clear that V is a quadratic and positive definite function defined on R^5 .

The time-derivative of V is found as

$$\dot{V} = -z_1^2 - z_2^2 - z_3^2 + z_3 \left[\begin{matrix} 2b + 3e_1 + 4e_2 \\ -(a-3)e_3 - e^{y_1} - e^{x_1} + u \end{matrix} \right] - e_a \dot{a} - e_b \dot{b} \quad (25)$$

Substituting the backstepping controller u defined by (13) into (25), we obtain

$$\dot{V} = -z_1^2 - z_2^2 - z_3^2 + e_a(-e_3 z_3 - \dot{a}) + e_b(2z_3 - \dot{b}) \quad (26)$$

Since $z_3 = 2e_1 + 2e_2 + e_3$, the parameter update law equations (14) can be rewritten compactly as:

$$\dot{a} = -e_3 z_3 \quad (27)$$

$$\dot{b} = 2z_3 \quad (27)$$

Substituting (27) into (26), we obtain

$$\dot{V} = -z_1^2 - z_2^2 - z_3^2 \quad (28)$$

which is a negative semi-definite function on R^5 .

Thus, it can be concluded that the anti-synchronization error and the parameter estimation error are globally bounded.

Hence, using Eq.(28) and Barbalat's lemma [38], we can conclude that $e(t) \rightarrow 0$ exponentially as $t \rightarrow \infty$ for all initial conditions $e(0) \in R^3$.

This completes the proof. ■

For numerical simulations, the classical fourth-order Runge-Kutta method with initial step $h = 10^{-8}$ is deployed to solve the WINDMI chaotic systems (6) and (7) with the backstepping controller (13) and parameter update law (14).

The parameters of the WINDMI chaotic system are taken as:

$$a = 0.7, \quad b = 2.5 \quad (29)$$

The initial values of the parameter estimates are chosen as:

$$\hat{a}(0) = 6.3, \quad \hat{b}(0) = 12.8 \quad (30)$$

while the initial values of the master system (6) are chosen as:

$$x_1(0) = 1.5, \quad x_2(0) = 3.8, \quad x_3(0) = 0.4 \quad (31)$$

Also, the initial values of the slave system (7) are chosen as:

$$y_1(0) = 2.3, \quad y_2(0) = 4.7, \quad y_3(0) = 5.2 \quad (32)$$

Figures 3-5 depict the anti-synchronization of the WINDMI chaotic systems (6) and (7), while Fig.6 depicts the time-history of the anti-synchronization errors. For $t > 12s$ anti-synchronization occurs.

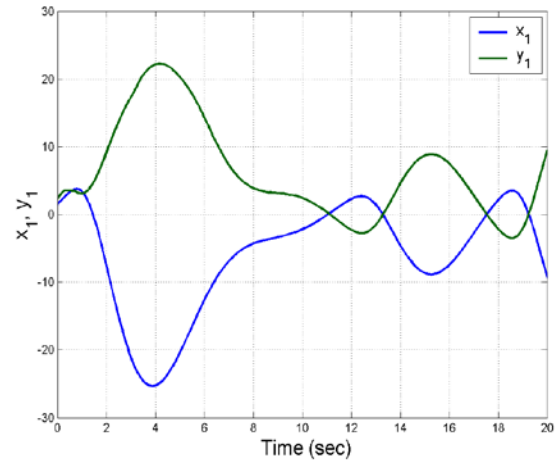


Fig. 3 Anti-synchronization of the states x_1 and y_1

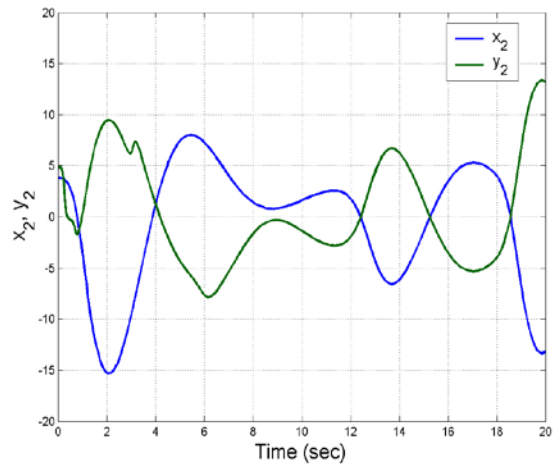


Fig. 4 Anti-synchronization of the states x_2 and y_2

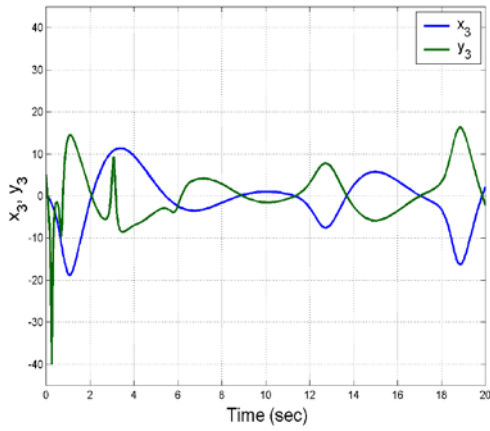


Fig. 5 Anti-synchronization of the states x_3 and y_3

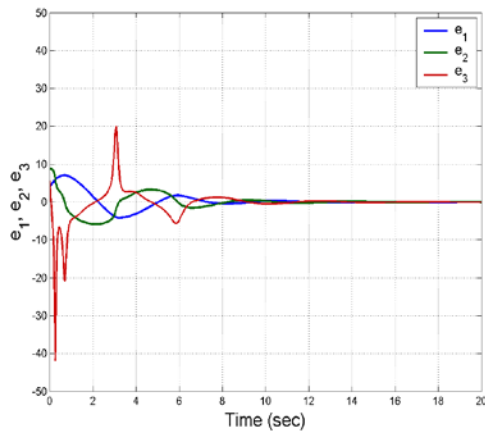


Fig. 6 Time-history of the anti-synchronization errors

III. FPGA IMPLEMENTATION OF THE ADAPTIVE BACKSTEPPING CONTROLLER

The proposed novel synchronization methodology was implemented in Xilinx for obtaining results in FPGA. The first step is to construct the synchronized chaotic systems using MATLAB Simulink blocks. Then MATLAB Simulink blocks are translated in to Xilinx system generator blocks using Xilinx blockset library. After missing blocks in Xilinx blockset library's are constructed, the design can be completed by arranging System Generator block in Xilinx blockset library. XST will be used to synthesize synchronized chaotic systems which were designed previously. Verilog Hardware Description Language (VHDL) is used to program FPGA. FPGA clock period can be arranged so that the desired outputs will be obtained. 100 ns is used as a clock period in all designs. The last thing which has to be arranged is Simulink system period section. It can be set as the same in Simulink fundamental sample time. After all requirements are done by pressing *Generate* button in System Generator block, ISE Project file will be obtained. From the ISE Project file, bitstream file is obtained. By loading *bitstream* file to FPGA, programming process of FPGA can be completed. We adopt the implementation with a fixed point and with a

representation of the real data on 32 bits, 12 for the entire and 20 for the fraction.

IV. IMPLEMENTATION OF MASTER CHAOTIC SYSTEM

The chaotic system (1) is implemented using Xilinx system generator blocks as in Fig. 1. The initial conditions are chosen as $x_1(0) = 0$, $x_2(0) = 10$ and $x_3(0) = 4$. The phase portraits of the system (1) are given in Fig.8.

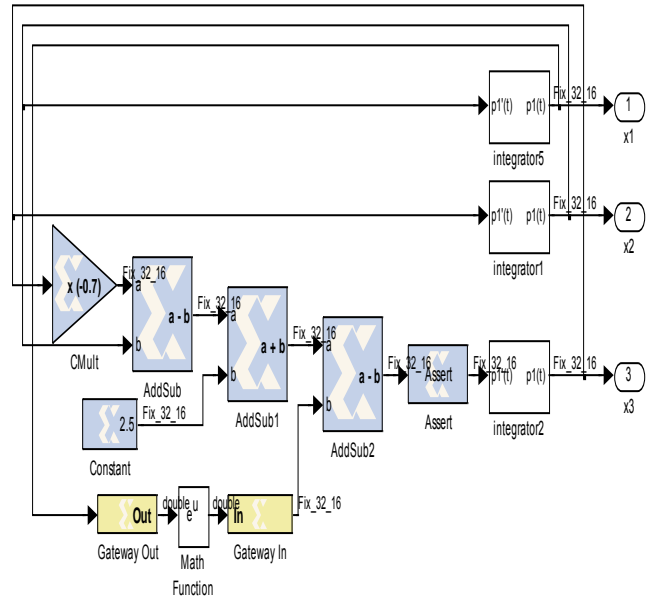


Fig. 7 SysGen Blocks of the Windmi System

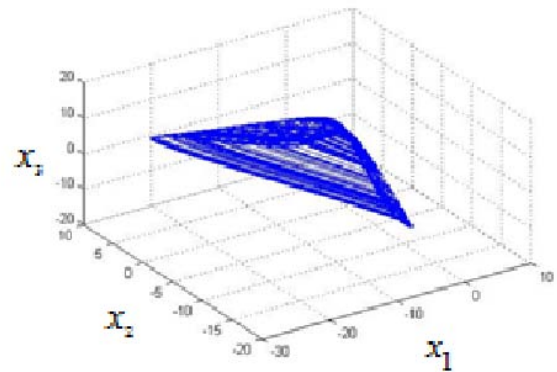


Fig. 8 Strange attractor of the WINDMI chaotic system using FPGA Blockset

V. IMPLEMENTATION OF BACKSTEPPING ADAPTIVE CONTROLLER

The System generator implementation of adaptive controller (13) which is used to synchronize two chaotic systems is shown in Fig.9. Also, in Fig.10 the FPGA Blockset of the Synchronised System is shown, while in Fig.11 the anti-synchronization phenomenon of the states x_3 and y_3 by using FPGA Blockset is depicted.

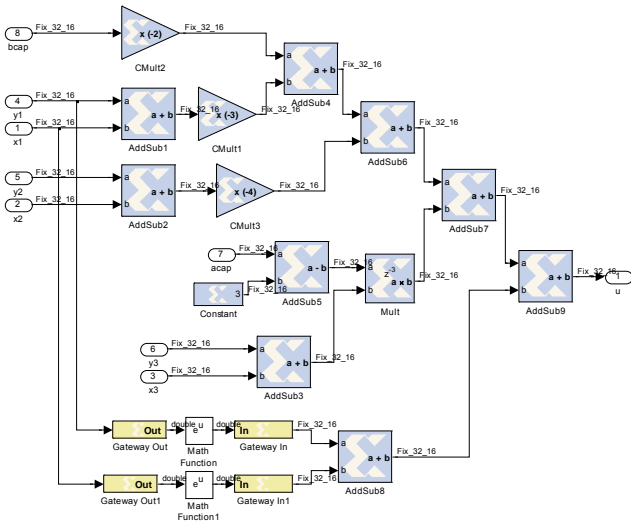


Fig. 9 FPGA Blockset of the Backstepping Adaptive controller U

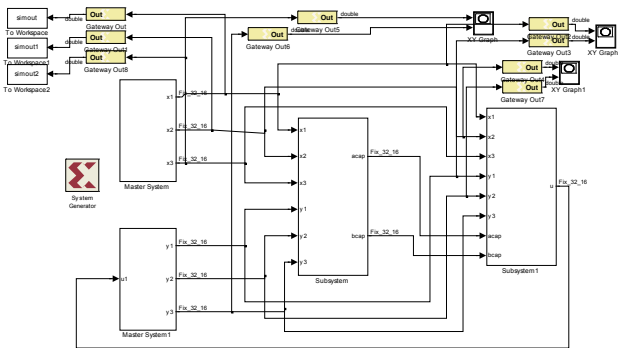


Fig. 10 FPGA Blockset of the Synchronised System



Fig. 11 Anti-synchronization of the states x_3 and y_3 using FPGA Blockset

After implementing synchronized Windmi system to FPGA, by using ISE program, how much source is consumed by synchronized system can be seen in Table 1.

VI. CONCLUSION

A nonlinear geometric controller and chaotic systems were implemented by FPGA for synchronization. This is, a nonlinear geometric controller which was designed to synchronize chaotic system individually. The controller's performances were such that the synchronization of identical WINDMI systems has been achieved. System Generators

provides an efficient way to design dynamic nonlinear control system using a FPGA board with hardware simulation. Therefore reconfigurable devices provide very powerful tool for the control of complex nonlinear systems. With respect to experimental results, WINDMI system consumes the source of FPGA most efficiently.

Table 1 Source Utilization of the Synchronised Windmi System

Number of Slice Registers	2,502	393,600	1%
Number of Slice LUTs	4,775	196,800	2%
Number of occupied Slices	1,466	49,200	2%
Number of LUT Flip Flop pairs used	5,401		
Number of bonded IOBs	193	600	32%
Number of RAMB36E1/FIFO36E1s	0	704	0%
Number of RAMB18E1/FIFO18E1s	0	1,408	0%
Number of BUFG/BUFGCTRLs	1	32	3%
Number of BSCANs	0	4	0%
Number of BUFHCEs	0	144	0%
Number of BUFOS	0	36	0%
Number of BUFIODQSS	0	72	0%
Number of BUFRRs	0	36	0%
Number of CAPTUREs	0	1	0%

REFERENCES

- [1] L. M. Pecora and T. L. Carroll, "Synchronization in chaotic systems," *Physical Review Letters*, vol. 64(8), pp. 821–824, 1990.
- [2] E. Ott, C. Grebogi, and J.A. Yorke, "Controlling chaos," *Physical Review Letters*, vol. 64(11), pp. 1196–1199, 1990.
- [3] M. Lakshmanan and K. Murali, *Nonlinear oscillators: Controlling and synchronization*. Singapore: World Scientific, 1996.
- [4] V. Petrov, V. Gaspar, J. Masera, and K. Showalter, "Controlling chaos in the Belousov-Zhabotinsky reaction," *Nature*, vol. 361, pp. 240–243, 1993.
- [5] G. Van Wiggern and R. Roy, "Communicating with chaotic lasers," *Science*, vol. 279, pp. 1198–1200, 1998.
- [6] A. Garfinkel, M. L. Spano, W. L. Ditto, and J. A. Weiss, "Controlling cardiac chaos," *Science*, vol. 257, pp. 1230–1235, 1992.
- [7] J. E. Skinner, "Low-dimensional chaos in biological systems," *Nature Biotechnology*, vol. 12, pp. 596–600, 1994.
- [8] B. Blasius, A. Huppert, and L. Stone, "Complex dynamics and phase synchronization in spatially extended ecological system," *Nature*, vol. 399, pp. 354–359, 1999.
- [9] B. Sahoo and S. Poria, "The chaos and control of a food chain model supplying additional food to top-predator," *Chaos, Solitons & Fractals*, vol. 58, pp. 52–64, 2014.
- [10] K. M. Cuomo and A. V. Oppenheim, "Circuit implementation of synchronized chaos with applications to communications," *Physical Review Letters*, vol. 71, pp. 65–68, 1993.
- [11] N. Li, W. Pan, L. Yan, B. Luo, and X. Zou, "Enhanced chaos synchronization and communication in cascade-coupled semiconductor ring lasers," *Communications in Nonlinear Science and Numerical Simulation*, vol. 19(6), pp. 1874–1883, 2014.

- [12] N. Smaoui and A. Kano, "Cryptography with chaos and shadowing," *Chaos, Solitons & Fractals*, vol. 42(4), pp. 2312–2321, 2009.
- [13] R. Rhouma and S. Belghith, "Cryptanalysis of a chaos-based cryptosystem on DSP," *Communications in Nonlinear Science and Numerical Simulation*, vol. 16(2), pp. 876–884, 2011.
- [14] Ch. K. Volos, I. M. Kyprianidis, and I. N. Stouboulos, "Experimental investigation on coverage performance of a chaotic autonomous mobile robot," *Robotics and Autonomous Systems*, vol. 61(12), pp. 1314–1322, 2013.
- [15] Ch. K. Volos, N. G. Bardis, I. M. Kyprianidis, and I. N. Stouboulos, "Motion control of a mobile robot based on double-scroll chaotic circuits," *WSEAS Trans. Systems*, vol. 11(9), pp. 479–488, 2012.
- [16] Ch. K. Volos, N. G. Bardis, I. M. Kyprianidis and I. N. Stouboulos, "Implementation of Mobile Robot by Using Double-Scroll Chaotic Attractors," In *Recent Researches in Applications of Electrical and Computer Engineering*, Proc. of 11th International Applications of Electrical Engineering, pp. 119–124, 2012, Vouliagmeni, Greece.
- [17] N. G. Bardis, A. P. Markovskiy, N. Doukas, and N. V. Karadimas, "True random number generation based on environmental noise measurements for military applications," *Mathematics And Computers In Science and Engineering archive*, Proc. of the 8th WSEAS International Conference on Signal Processing, Robotics and Automation, pp. 68–73, 2009, Cambridge, UK.
- [18] E. Kaslik and S. Sivasundaram, "Nonlinear dynamics and chaos in fractional-order neural networks," *Neural Networks*, vol. 32, pp. 245–256, 2012.
- [19] M. Sadeghpour, M. Khodabakhsh, and H. Salarieh, "Intelligent control of chaos using linear feedback controller and neural network identifier," *Communications in Nonlinear Science and Numerical Simulation*, vol. 17(12), pp. 4731–4739, 2012.
- [20] G. Zhang, Y. Shen, and L. Wang, "Global anti-synchronization of a class of chaotic memristive neural networks with time-varying delays," *Neural Networks*, vol. 46, pp. 1–8, 2013.
- [21] A. Wu and Z. Zeng, "Anti-synchronization of a class of memristive recurrent neural networks," *Communications in Nonlinear Science and Numerical Simulation*, vol. 18(2), pp. 373–385, 2013.
- [22] L. Lu, C. Zhang and Z. A. Guo, "Synchronization between two different chaotic systems with nonlinear feedback control," *Chinese Physics*, vol. 16, pp. 1603–1607, 2007.
- [23] U. E. Vincent, "Synchronization of identical and non-identical 4-D chaotic systems via active control," *Chaos, Solitons & Fractals*, vol. 37, pp. 1065–1075, 2008.
- [24] S. Vaidyanathan and K. Rajagopal, "Hybrid synchronization of hyperchaotic Wang-Chen and hyperchaotic Lorenz systems by active non-linear control," *International Journal of Systems Signal Control and Engineering Application*, vol. 4(3), pp. 55–61, 2011.
- [25] S. H. Chen and J. Lü, "Synchronization of an uncertain unified system via adaptive control," *Chaos, Solitons & Fractals*, vol. 14, pp. 643–647, 2002.
- [26] V. Sundarapandian and R. Karthikeyan, "Anti-synchronization of Lu and Pan chaotic systems by adaptive nonlinear control," *International Journal of Soft Computing*, vol. 6(4), pp. 111–118, 2011.
- [27] S. Vaidyanathan and K. Rajagopal, "Global chaos synchronization of hyperchaotic Pang and hyperchaotic Wang systems via adaptive control," *International Journal of Soft Computing*, vol. 7(1), pp. 28–37, 2012.
- [28] V. Sundarapandian and I. Pehlivan, "Analysis, control, synchronization and circuit design of a novel chaotic system," *Mathematical and Computer Modelling*, vol. 55(7-8), pp. 1904–1915, 2012.
- [29] J. H. Park and O. M. Kwon, "A novel criterion for delayed feedback control of time-delay chaotic systems," *Chaos, Solitons & Fractals*, vol. 23, pp. 495–501, 2005.
- [30] T. Yang and L. O. Chua, "Control of chaos using sampled-data feedback control," *International Journal of Bifurcation and Chaos*, vol. 9, pp. 215–219, 1999.
- [31] S. H. Lee, V. Kapila, M. Porfiri, and A. Panda, "Master-slave synchronization of continuously and intermittently coupled sampled-data chaotic oscillators," *Communications in Nonlinear Science and Numerical Simulation*, vol. 15, pp. 4100–4113, 2010.
- [32] V. Sundarapandian, "Adaptive backstepping controller and synchronizer design for Arneodo chaotic system with unknown parameters," *International Journal of Computer Science and Information Technology*, vol. 4(6), pp. 145–159, 2012.
- [33] V. Sundarapandian, "Anti-synchronizing backstepping control design for Arneodo chaotic system," *International Journal of Bioinformatics and Biosciences*, vol. 3(1), pp. 21–33, 2013.
- [34] V. Sundarapandian and S. Sivaperumal, "Sliding controller design of hybrid synchronization of four-wing chaotic systems," *International Journal of Soft Computing*, vol. 6(5), pp. 224–231, 2011.
- [35] S. Vaidyanathan and S. Sampath, "Anti-synchronization of four-wing chaotic systems," *International Journal of Automation and Computing*, vol. 9(3), pp. 274–279, 2012.
- [36] S. Vaidyanathan and S. Sampath, "Sliding mode controller design for the global chaos synchronization of Coulet systems," *International Journal of Information Sciences and Techniques*, vol. 2(2), pp. 65–76, 2012.
- [37] J. Wang, D. Lu, and L. Tian, "Global synchronization for time delay of WINDMI system," *Chaos, Solitons & Fractals*, vol. 30, pp. 629–635, 2006.
- [38] W. Hahn, *The Stability of Motion*, New York: Springer, 1967.

Analytical Modeling of Pneumatic Muscle Actuator Torque Characteristics

Mária Tóthová and Ján Pitel'

Abstract—Rotational motion of actuator with pneumatic artificial muscles in antagonistic connection is typically generated using a circular pulley. But torque and stiffness of such actuator decrease with increasing rotation of the actuator arm. This is due to the non-linear decrease of artificial muscles forces according to their contraction. By application of the eccentric pulley a smaller decrease in torque and thus the greater and symmetrical stiffness of the actuator can be obtained.

Keywords—artificial muscle, eccentric pulley, pneumatic actuator, torque characteristics

I. INTRODUCTION

ACTUATOR consisting of a pair of pneumatic artificial muscles (PAMs) in antagonistic connection is suitable as nonconventional actuator for industrial robotic applications [1] and also biomedical engineering applications [2]–[4]. It can be controlled by air pressure change only in one artificial muscle (active muscle) in a particular half of the arm trajectory through the corresponding solenoid valve (filling or discharge valve). The second antagonistic muscle acts as a passive non-linear pneumatic spring (passive muscle) and it does not require any control. In the second half of the arm trajectory the actuator function is the same but the muscle functions are mutually exchanged [5]–[8]. The presented solution simplifies the control of such system. But muscle contraction and size of muscle tensile force is changed non-linearly according to air pressure change in the muscle [9]–[12]. Each displacement of the shaft (due to a drop in the air volume of the related artificial muscle) is defined by equal torques between the PAMs. Then such actuator constitutes a non-linear system which dependence of arm position is non-linear centrally symmetric function of filling pressure in the muscles [13]–[15]. Due to the constant radius of pulley the torque characteristics of such pneumatic muscle actuator (PMA) are

This work was supported by the Project of the Structural Funds of the EU, Operational Programme Research and Development, Measure 2.2 Transfer of knowledge and technology from research and development into practice.

M. Tóthová is with Department of Mathematics, Informatics and Cybernetics, Faculty of Manufacturing Technologies, Technical University of Košice, Bayerova 1, 080 01 Prešov, Slovakia (e-mail: maria.tothova@tuke.sk).

J. Pitel' is with Department of Mathematics, Informatics and Cybernetics, Faculty of Manufacturing Technologies, Technical University of Košice, Bayerova 1, 080 01 Prešov, Slovakia (corresponding author to provide phone: +421 905 524605; fax: +421 421 51 7733453; e-mail: jan.pitel@tuke.sk).

also non-linear depending on the angle of the shaft rotation [16], [17]. Elimination or at least reduction of this phenomenon is possible when a pulley with constant radius rotating around a point not located in its geometric center (along the longitudinal axis of the actuator), i.e. circular eccentric pulley is applied instead of the pulley with the constant radius rotating around its geometric center. As a result, a smaller decrease of torque on the actuator shaft can be achieved when compared to the initial one and it has also higher stiffness of an actuator.

II. CHARACTERISTICS OF PAMS

The most common used type of PAM is the McKibben artificial muscle based on a flexible cylindrical isotropic rubber tube. When muscle is inflated, the tube extends causing a simultaneous extension and axial contraction of the length of netted nylon fibers on its surface. Thus the contraction of the whole muscle occurs and a tensile force of muscle thereby arises [7]. But muscle force depends on the muscle contraction in the range of extremely high value at zero contraction to zero value at the maximum contraction [18]. Characteristics showing the dependence between the muscle force F of PAM type FESTO MAS-20-250N and the muscle contraction κ under a constant muscle pressure P are shown in Fig. 1. These characteristics are specified by the manufacturer of PAM for seven values of the muscle pressure [19].

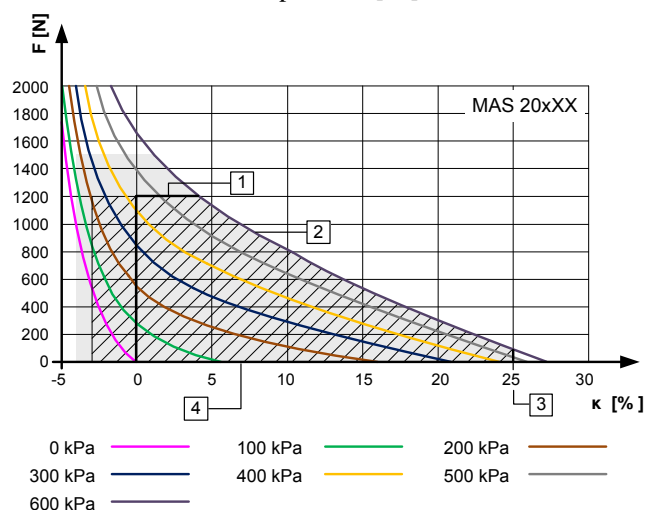


Fig. 1 Tensile force of the muscle FESTO MAS 20-200 depending on the muscle contraction [19]

Characteristics in Fig. 1 can be expressed as a function representing dependence between muscle tensile force, muscle contraction and pressure in the muscle. Numbers 1-4 indicate the borders applicability of PAMs which limit their work area with the given operating pressures. The maximal operating muscle force is 1200 N and maximal contraction is 25 % for this type of PAM.

III. TORQUE CHARACTERISTIC OF PMA

An antagonistic pneumatic muscle actuator consists of two PAMs connected through holders to a base plate. There are also two pillars mounted on a base plate with firmly attached bearing bushes. The actuator shaft supported by bearings is firmly connected with the circular pulley along which the flexible belt is passing through. Its ends are connected with PAMs. There is also hub of the arm firmly slid onto the actuator shaft connected to the actuator arm with external load. Such actuator constitutes a relatively long and slender unit with satisfactory weight and dimensional characteristics (Fig. 2).

A significant non-linear dependence there is in the PMA between change of the air pressure entering to the artificial muscles and the angle of rotating arm fixed to the shaft of the actuator. This is mainly due to non-linear decrease in muscle force depending on muscle contraction. It causes a decrease of the PMA torque with increasing value of the arm rotation angle. Then for circular pulley with constant radius r_{cp} the actuator torque M is determined by muscle force F . If parameters of the both PAMs are the same, then $M = F \cdot r_{cp}$.

Torque characteristic of the actuator with PAM in antagonistic connection is shown in Fig. 3. Both PAMs have the same filling pressure at point Z, which corresponds to the value of the muscle contraction 12.5%. At this point torque of actuator and its stiffness have maximum values. If pressure in the second muscle decreases contraction of the first muscle increases and torque of the actuator shaft decreases. Similarly, actuator torque decreases in the opposite direction of movement by deflation of the first muscle.

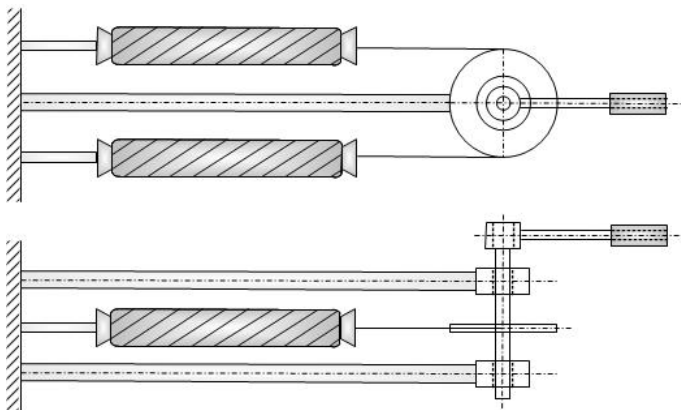


Fig. 2 PMA with circular pulley

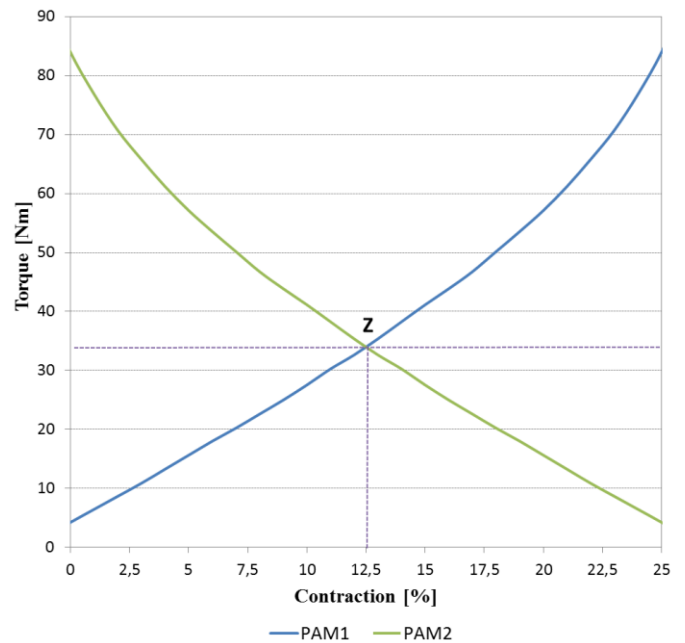


Fig. 3 Torque characteristic of the PMA with circular pulley

Due to the fact that torques from both PAMs decrease with increasing muscle contraction the actuator stiffness in both directions also decreases. PMA with such torque characteristic has therefore insufficient and asymmetric stiffness for larger angle rotations.

IV. PMA WITH ECCENTRIC PULLEY

Torque decrease of the pneumatic actuator with two PAMs in antagonistic connection can be reduced using an eccentric pulley, i.e. a pulley with also constant radius but rotating around a point not located in its geometric center (Fig. 4). Such actuator has a similar design as PMA with circular pulley in Fig. 2; the difference is only in using an eccentric pulley instead of classical circular pulley. The principle of the movement of PMA with eccentric pulley is shown in Fig. 5 [20].

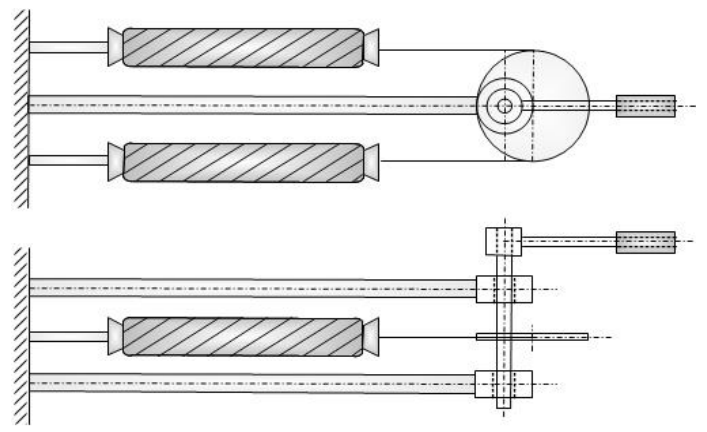


Fig. 4 PMA with eccentric pulley

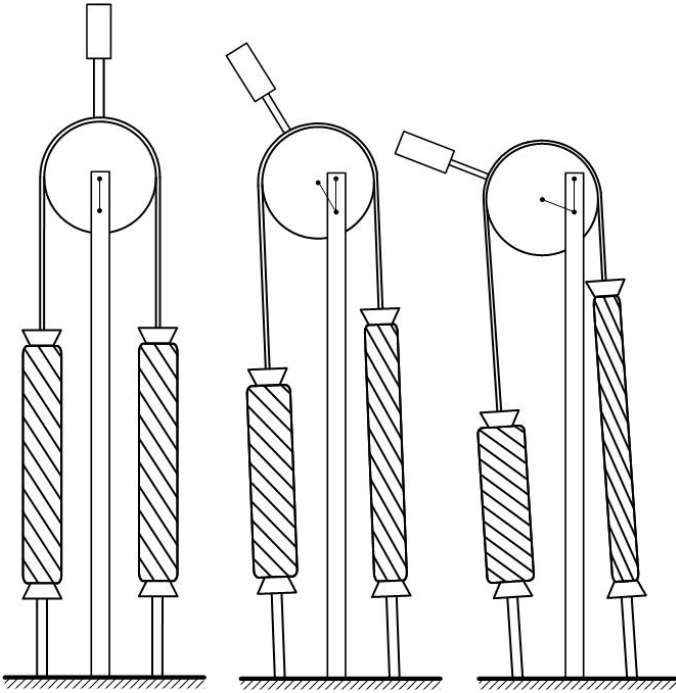


Fig. 5 The principle of movement of the PMA with eccentric pulley

V. TORQUE CHARACTERISTICS OF PMA WITH ECCENTRIC PULLEY

For torque M of PMA with axisymmetric eccentric pulley is valid:

$$M = F \cdot r = F \cdot d \cdot \cos \alpha, \quad (1)$$

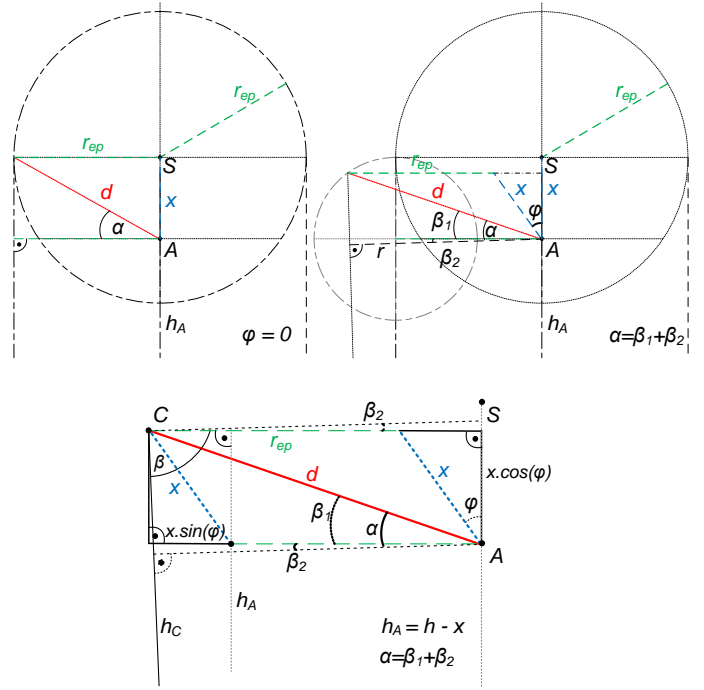
where F is muscle tensile force, r is perpendicular distance of muscle force vector from the axis of the eccentric pulley, d is length of the arm on which muscle force acts (i.e. the distance of the point of muscle force action from the axis of rotation of the eccentric pulley) and α is angle between vectors r and d . Basic parameters for geometric description of the PMA with eccentric pulley are radius r_{ep} of the pulley, the distance x of the axis of rotation of the eccentric pulley (i.e. the axis of rotation of the actuator arm) from the geometric center of the pulley and the height h_A of the PMA from a base plate to the axis of rotation of the eccentric pulley (Fig. 6).

The others important parameters in Fig. 6 can be expressed as a function dependent on the angle φ of the actuator arm rotation with constant parameters r_{ep} , x and h_A as follows:

$$d = \sqrt{x^2 + r_{ep}^2 + 2x \cdot r_{ep} \cdot \sin \varphi}, \quad (2)$$

$$\beta_1 = \arcsin \frac{x \cdot \cos \varphi}{\sqrt{x^2 + r_{ep}^2 + 2x \cdot r_{ep} \cdot \sin \varphi}}, \quad (3)$$

$$\beta_2 = \frac{\pi}{2} - \arcsin \frac{h_A + x \cdot \cos \varphi}{\sqrt{h_A^2 + x^2 + 2h_A \cdot x \cdot \cos \varphi}}. \quad (4)$$


 Fig. 6 Correlation between parameters of the eccentric pulley
Then for torque M using (2) can be written:

$$M = F \cdot \sqrt{x^2 + r_{ep}^2 + 2x \cdot r_{ep} \cdot \sin \varphi} \cdot \cos(\alpha), \quad (5)$$

where

$$\alpha = \beta_1 + \beta_2, \quad (6)$$

$$\alpha = \arcsin \frac{x \cdot \cos \varphi}{\sqrt{x^2 + r_{ep}^2 + 2x \cdot r_{ep} \cdot \sin \varphi}} + \frac{\pi}{2} - \arcsin \frac{h_A + x \cdot \cos \varphi}{\sqrt{h_A^2 + x^2 + 2h_A \cdot x \cdot \cos \varphi}}. \quad (7)$$

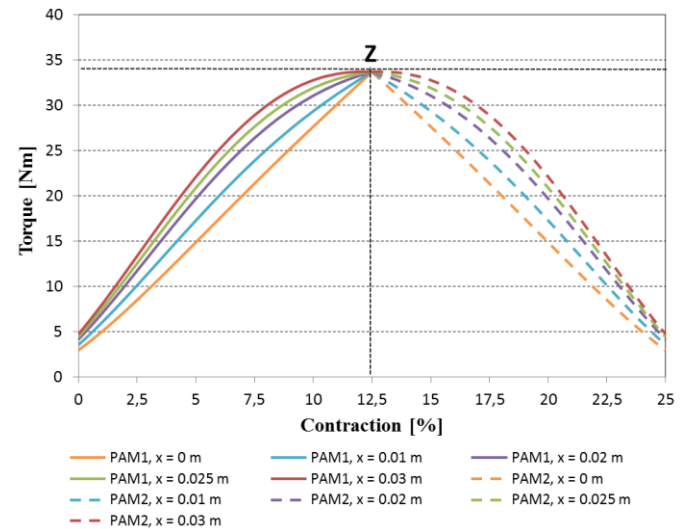


Fig. 7 Torque characteristics of the PMA with eccentric pulley

It follows from relations (5) and (7) that the torque of the PMA with eccentric pulley depends not only on the angle φ of the actuator arm rotation, but also on distance x of the axis of rotation of the eccentric pulley from the pulley center.

The torque characteristics of the actuator with PAMs in antagonistic connection for different distances x of the axis of rotation of the eccentric pulley from the geometric center of the pulley which radius is constant 0.05 m are shown in Fig. 7. These characteristics are mutually oppositely oriented for both muscles and at point Z both PAMs have the same maximum pressure.

VI. CONCLUSION

The torque characteristics in Fig. 2 and also in Fig. 6 show that the torque of the PMA with a circular pulley which the axis of rotation in the geometric middle of the pulley (displacement x of the axis of rotation of the actuator arm from the center of the pulley is zero) decreases depending only on the non-linearity of the muscle force. For the actuator with eccentric pulley (x different from zero) the torque decrease is smaller and it is given not only by non-linearity of artificial muscle, but also by the value of the distance x (Fig. 6). It is therefore possible to conclude that by using of the eccentric pulley it is possible to achieve even higher stiffness of the pneumatic actuator with artificial muscles in antagonistic connection. Determination of the optimal distance of the axis of rotation of the actuator arm from the center of the pulley will be the subject of further research and on the basis of its results an experimental PMA with eccentric pulley will be realized.

ACKNOWLEDGMENT

The research work is supported by the Project of the Structural Funds of the EU, title of the project: Research and development of intelligent nonconventional actuators based on artificial muscles, ITMS code: 26220220103.

REFERENCES

- [1] I. Vojtko, M. Kočíško, M. Janák and V. Fečová, "The new design of robot arm", *Proceedings of the IEEE 11th International Symposium on Applied Machine Intelligence and Informatics (SAMI 2013)*, January 31 - February 2, 2013, Herl'any, Košice: IEEE, pp. 53 - 56.
- [2] K. Židek, O. Líška and V. Maxim, "Rehabilitation device based on unconventional actuator", *Mechatronics: Recent Technological and Scientific Advances*, Heidelberg Springer-Verlag, 2011, pp. 697-702.
- [3] K. Židek and J. Šeminský "Automated rehabilitation device based on artificial muscles", *Annals of DAAAM for 2011*, Vienna: DAAAM International, 2011, pp. 1113-1114.

- [4] K. Židek, J. Piteľ, A. Galajdová and M. Fodor, "Rehabilitation device construction based on artificial muscle actuators", *Proceedings of the Ninth IASTED International Conference: Biomedical Engineering BioMed 2012*, February 15-17, 2012, Innsbruck: ACTA Press, pp. 855-861.
- [5] M. Balara, "The upgrade methods of the pneumatic actuator operation ability," *Applied Mechanics and Materials*, Vol. 308, pp 63-68, 2013.
- [6] A. Hošovský and K. Židek, "Experimental validation of nominal model characteristics for pneumatic muscle actuator," *Applied Mechanics and Materials*, Vol. 460, pp. 1-12, 2014.
- [7] M. Tóthová, J. Piteľ and J. Boržiková, "Operating modes of pneumatic artificial muscle actuator", *Applied Mechanics and Materials*, Vol. 308, pp 39-44, 2013.
- [8] M. Balara, "The linearised control system of the pneumatic actuator," *Annals of DAAAM for 2011*, pp. 1251-1252, Vienna: DAAAM International, 2011.
- [9] A. Macurová and S. Hrehová, "Some properties of the pneumatic artificial muscle expressed by the nonlinear differential equation," *Advanced Materials Research*, Vol. 658, pp. 376-379, 2012.
- [10] B. Tondu and P. Lopez, "Modeling and control of McKibben artificial muscle robot actuators," *Control Systems Magazine*, Vol. 20, No. 2, pp. 15-38, 2000.
- [11] J. Mižáková, J. Piteľ and M. Tóthová, "Pneumatic artificial muscle as actuator in mechatronic system," *Applied Mechanics and Materials*, Vol. 460, pp.81-90, 2014.
- [12] Ch-P. Chou and B. Hannaford, "Measurement and modeling of McKibben pneumatic artificial muscles," *Transaction on Robotics and Automation*, Vol. 12, No. 1 pp. 90-102, 1996.
- [13] A. Vagaská, "Mathematical description and static characteristics of the spring actuator with pneumatic artificial muscle," *Applied Mechanics and Materials*, Vol. 460, pp. 65-72, 2014.
- [14] J. Boržiková, "Non-linear approximation of the static characteristic $F=f(p,K)$ of antagonistic system," *Proceedings ARTEP 2008*, Stará Lesná, February 20-22, 2008, Košice: TU, pp. 4-1-5.
- [15] A. Hošovský, "Numerical approximation of static characteristic of PAM-based antagonistic actuator," *Journal of applied science in the thermodynamics and fluid mechanics*, Vol. 1, No. 1, pp. 1-4, 2007.
- [16] A. Vagaská and M. Balara, "Stiffness and torque of rotary actuator with artificial muscles," *Strojárstvo EXTRA*, Vol. XVII., No. 6/2013, pp. 92 - 94, 2013.
- [17] M. Balara and A. Vagaská, "Torque of rotary actuator with artificial muscles," *Proceedings ARTEP 2013*, Stará Lesná, February 20-22, 2013, Košice: TU, pp. 31-1-10.
- [18] L. Straka, "Operational reliability of mechatronic equipment based on pneumatic artificial muscle," *Applied Mechanics and Materials*, Vol. 460, pp. 41-48, 2014.
- [19] Fluid muscles DMSP / MAS [online] Actuators with special functions 2004/10 Available: <https://www.festo.com/cat/sk_sk/data/doc_sk/PDF/SK/MAS_SK.PDF>
- [20] J. Piteľ, M. Balara, M. Havran and M. Tóthová, "Actuator with artificial muscles - IV," Patent Publication No. 141-2011. Banská Bystrica: ÚPV SR, 2013.

Mária Tóthová is a PhD student in Faculty of Manufacturing Technologies of the Technical University of Košice with a seat in Prešov. Her research activities include research and development of nonconventional actuators.

Ján Piteľ is an Associate Professor and Vice-dean in Faculty of Manufacturing Technologies of the Technical University of Košice with a seat in Prešov. His research activities include modeling, simulation and automatic control of machines and processes.

Combined effect of small curvature and variable friction on temporal instability of shallow mixing layers

Ilmars Iltins, Marija Iltina, and Andrei Kolyshkin

Abstract— Temporal stability analysis of shallow mixing layers is performed in the present paper. It is assumed that flow is slightly curved along the longitudinal coordinate. In addition, friction force is assumed to be varied in the transverse direction. The corresponding linear stability problem is solved by a collocation method. Marginal stability curves are obtained for different values of the parameters of the problem. Combined influence of curvature and variable friction on the stability boundary is investigated. It is shown that both curvature and variable friction stabilize the flow.

Keywords—Linear stability analysis, shallow mixing layers, friction coefficient, curvature

I. INTRODUCTION

SHALLOW mixing layers are often observed in nature and engineering. The understanding of mass and momentum exchange between two layers moving with different velocities is quite important for design and maintenance of compound and composite channels. It is recognized nowadays that there are three basic methods of analysis of shallow mixing layers: experimental investigation, numerical modeling and stability analysis [1]. Linear stability of shallow mixing layers under the rigid-lid assumption is investigated in [2], [3] where it is shown that the bed-friction number (proportional to the friction coefficient) plays an important role in preventing the development of instability. Linear stability is also analyzed in [4] for the case where perturbations are also allowed to develop on a free surface. The validity of the rigid-lid assumption is also assessed in [4]. It is shown that errors in stability characteristics of shallow flows are small provided that the Froude number of the flow is much smaller than unity (this is quite reasonable assumption in many environmental flows). The effect of the Froude number of linear stability is analyzed in [5].

Experimental studies of shallow mixing layers are conducted in [6]-[9]. The major conclusions from [6]-[9] are

I. Iltins is with the Department of Engineering Mathematics, Riga Technical University, Riga, LV 1007, Latvia (e-mail: iltins@inbox.lv).

M. Iltina is with the Department of Engineering Mathematics, Riga Technical University, Riga, LV 1007, Latvia (e-mail: marijai@inbox.lv).

A. Kolyshkin is with the Department of Engineering Mathematics, Riga Technical University, Riga, LV 1007, Latvia (e-mail: andrejs.koliskins@rtu.lv).

as follows: (a) shallowness of mixing layer prevents the development of three-dimensional instabilities, (b) growth of the width of a shallow mixing layer downstream is reduced in comparison with free shear layer width, (c) growth rate of small perturbations is smaller for larger values of the bed-friction number.

The influence of small curvature on the growth rates of small perturbations developed in a free shear layer is investigated in [10]. It is shown in [10] that the effect of curvature is two-fold: (a) it stabilizes the flow if the mixing layer is stably curved and (b) it has a destabilizing influence for the case of unstably curved mixing layer.

In a typical linear stability problem for shallow mixing layers the friction coefficient is assumed to be constant in the region of the flow. However, the presence of vegetation can considerably increase the resistance in shallow mixing layers. Such a case can be observed in nature during floods. Several experimental papers [11]-[15] are devoted to the analysis of such flows. In addition, linear stability of a flow in partially vegetated areas is analyzed in [15] where the friction coefficient is modeled by a step function.

In the present paper temporal stability of shallow mixing layers is analyzed under the following assumptions: (a) rigid-lid assumption (perturbations do not develop on a free surface of the fluid); (b) the flow is slightly curved in the longitudinal direction; and (c) the friction coefficient varies continuously in the transverse direction of the flow. Marginal stability curves are presented for different values of the parameters of the problem. The combined effect of small curvature and variable friction on the stability characteristics of the flow is also investigated.

II. MATHEMATICAL FORMULATION OF THE PROBLEM

Consider the following form of shallow water equations under the rigid-lid assumption

$$\frac{\partial u}{\partial x} + \frac{\partial v}{\partial y} = 0, \quad (1)$$

$$\frac{\partial u}{\partial t} + u \frac{\partial u}{\partial x} + v \frac{\partial u}{\partial y} + \frac{\partial p}{\partial x} + \frac{c_f(y)}{2h} u \sqrt{u^2 + v^2} = 0, \quad (2)$$

$$\frac{\partial v}{\partial t} + u \frac{\partial v}{\partial x} + v \frac{\partial v}{\partial y} - \frac{1}{R} u^2 + \frac{\partial p}{\partial y} + \frac{c_f(y)}{2h} v \sqrt{u^2 + v^2} = 0, \quad (3)$$

where p is the pressure, h is water depth, u and v are the depth-averaged velocity components, $c_f(y)$ is the friction coefficient which is assumed to be dependent on the transverse coordinate y , and R is the dimensionless radius of curvature ($R \gg 1$).

Equation (1) is equivalent to the continuity equation in a two-dimensional hydrodynamics so that it is natural to introduce the stream function $\psi(x, y, t)$ by the relations

$$u = \frac{\partial \psi}{\partial y}, \quad v = -\frac{\partial \psi}{\partial x} \quad (4)$$

Using (1)-(4) we obtain

$$\begin{aligned} & (\Delta \psi)_t + \psi_y (\Delta \psi)_x - \psi_x (\Delta \psi)_y + \frac{2}{R} \psi_y \psi_{xy} + \\ & + \frac{c_f(y)}{2h} \Delta \psi \sqrt{\psi_x^2 + \psi_y^2} + \frac{c_f(y)}{2h \sqrt{\psi_x^2 + \psi_y^2}} (\psi_y^2 \psi_{yy} + \\ & + 2\psi_x \psi_y \psi_{xy} + \psi_x^2 \psi_{xx}) + \frac{c_{fy}(y)}{2h} \psi_y \sqrt{\psi_x^2 + \psi_y^2} = 0, \end{aligned} \quad (5)$$

where $c_{fy}(y)$ is the derivative of the function $c_f(y)$ with respect to y . The friction coefficient $c_f(y)$ is modeled by the formula

$$c_f(y) = c_{f_0} \gamma(y), \quad (6)$$

where $\gamma(y)$ is a differentiable shape function.

A perturbed solution $\psi(x, y, t)$ is assumed to be of the form

$$\psi(x, y, t) = \psi_0(y) + \varepsilon \psi_1(x, y, t) + \dots \quad (7)$$

where $\psi_0(y)$ is the stream function of the base flow $U(y)$, so that $U(y) = \psi_{0y}(y)$. In the present study the function $U(y)$ is given by

$$U(y) = \frac{1}{2} (1 + \tanh y). \quad (8)$$

Substituting (6) and (7) into (5) and linearizing the resulting equation in the neighborhood of the base flow we obtain

$$\begin{aligned} & \psi_{1xxt} + \psi_{1yyt} + \psi_{0y} (\psi_{1xxx} + \psi_{1yyx}) - \psi_{0yy} \psi_{1x} + \\ & + \frac{c_f(y)}{2h} (\psi_{0y} \psi_{1xx} + 2\psi_{0yy} \psi_{1y} + 2\psi_{0y} \psi_{1yy}) \\ & + \frac{c_{fy}(y)}{h} \psi_{0y} \psi_{1x} + \frac{2}{R} \psi_{0y} \psi_{1xy} = 0. \end{aligned} \quad (9)$$

The perturbed solution is represented in the form of a normal mode

$$\psi_1(x, y, t) = \varphi(y) e^{i\alpha(x-ct)}, \quad (10)$$

where α is the wave number and $c = c_r + ic_i$ is a complex eigenvalue. It follows from (9) and (10) that

$$\begin{aligned} & \varphi_{yy} [\alpha(U-c) - iS U \gamma] - iS (\gamma U_y + \gamma_y U) \varphi_y \\ & + \varphi [\alpha^3 (c-U) - \alpha U_{yy} + i\alpha^2 U S \gamma / 2] = 0, \end{aligned} \quad (11)$$

where $S = \frac{c_{f_0} b}{h}$ is the stability parameter and b is a length scale of the problem.

The boundary conditions have the form

$$\varphi(\pm\infty) = 0. \quad (12)$$

Problem (11), (12) is an eigenvalue problem. The sign of the imaginary part of the complex eigenvalue c is used to decide whether flow (8) is linearly stable or unstable: if all eigenvalues satisfy the inequality $c_i < 0$ then base flow (8) is said to be linearly stable. On the other hand, if at least one eigenvalue has a positive imaginary part ($c_i > 0$) then base flow (8) is said to be linearly unstable. Finally, if one eigenvalue satisfies the condition $c_i = 0$ while all other eigenvalues have negative imaginary parts, base flow is said to be marginally stable. The set of all values of the parameters α and S for which flow (8) is marginally stable determines the marginal stability curve.

III. NUMERICAL METHOD

Numerical solution of (11), (12) is obtained by a collocation method. It is convenient to map the interval $-\infty < y < +\infty$ onto the interval $-1 \leq \xi \leq 1$ using the new

variable $\xi = \frac{2}{\pi} \arctan y$. In terms of the transformed variable the solution to (11) is sought in the form

$$\varphi(\xi) = \sum_{k=0}^{N-1} a_k (1 - \xi^2) T_k(\xi), \quad (13)$$

where $T_k(\xi) = \cos k \arccos \xi$ is the Chebyshev polynomial of the first kind of order k and a_k are unknown coefficients.

The factor $(1 - \xi^2)$ in (13) guarantees that zero boundary conditions at $\xi = \pm 1$ will be satisfied automatically:

$$\varphi(\pm 1) = 0. \quad (14)$$

The collocation points are chosen in the form

$$\xi_m = \cos \frac{\pi m}{N}, \quad m = 1, 2, \dots, N-1. \quad (15)$$

Using (11), (13) and (15) we obtain the following generalized eigenvalue problem

$$(A + \alpha B) a = 0, \quad (16)$$

where A and B are complex-valued matrices and $a = (a_0 a_1 \dots a_{N-1})^T$. Note that both A and B are non-singular (this fact simplifies the solution of the generalized eigenvalue problem (16)).

IV. RESULTS OF COMPUTATIONS

Numerical results are presented in the paper for the case where variability of the friction coefficient in the transverse direction is described by (6), where

$$\gamma(y) = \frac{\beta + 1}{2} + \frac{(\beta - 1)}{2} \tanh y, \tag{17}$$

with $\beta = \frac{c_{f1}}{c_{f0}} \geq 1$. Here c_{f1} and c_{f0} are the friction coefficients in the vegetated area and main channel, respectively. Note that in [16] the friction coefficient varied in such a way that $c_{f0} = 0$ as $y \rightarrow -\infty$.

Marginal stability curves for the case $R = \infty$ and three values of the parameter β , namely, $\beta = 1, 1.5$ and 2 are shown in Fig. 1. Note that $\beta = 1$ corresponds to a constant friction coefficient in the whole region of the flow while values $\beta > 1$ represent the degree of non-uniformity of the friction force in the transverse direction. It is seen from Fig. 1 that the case with non-constant friction is more stable than the case of a uniform friction. In addition, the critical value of S decreases as the parameter β increases.

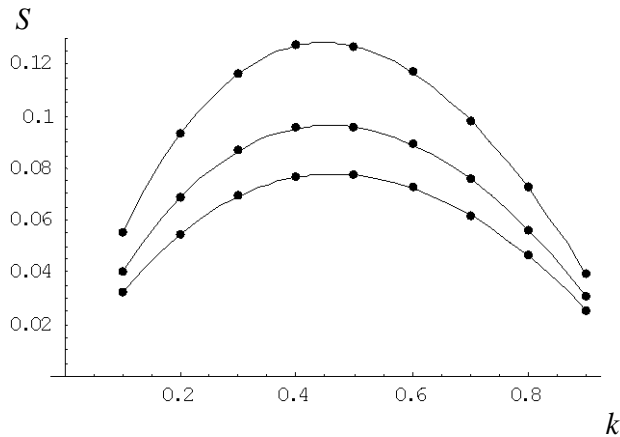


Fig. 1. Marginal stability curves for the case $R = \infty$ and three values of β : $\beta = 1, \beta = 1.5$ and $\beta = 2$ (from top to bottom).

Fig. 2 plots the marginal stability curves for the case $1/R = 0.03$ and three values of β : $1, 1.5$ and 2 . It is also seen from the graph that non-uniformity of the friction coefficient stabilizes the flow in the presence of a small curvature.

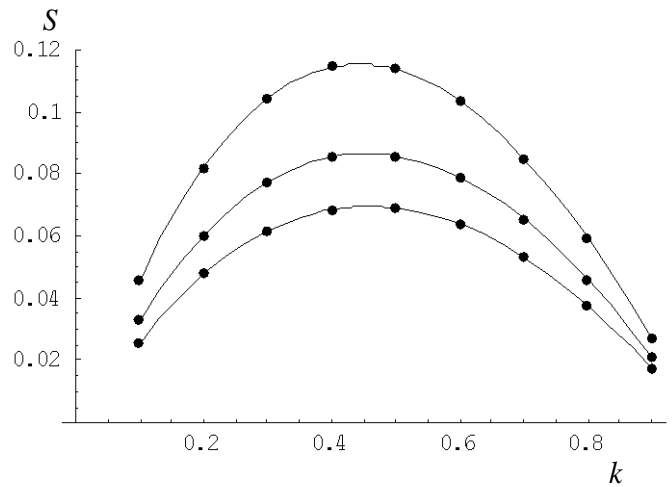


Fig. 2. Marginal stability curves for the case $1/R = 0.03$ and three values of β : $\beta = 1, \beta = 1.5$ and $\beta = 2$ (from top to bottom).

The effect of small curvature on the stability boundary is shown in Fig. 3 for the case of a non-constant friction. The marginal stability curves in Fig. 3 correspond to one value $\beta = 2$. It is seen from the graph that the increase in curvature leads to a more stable flow.

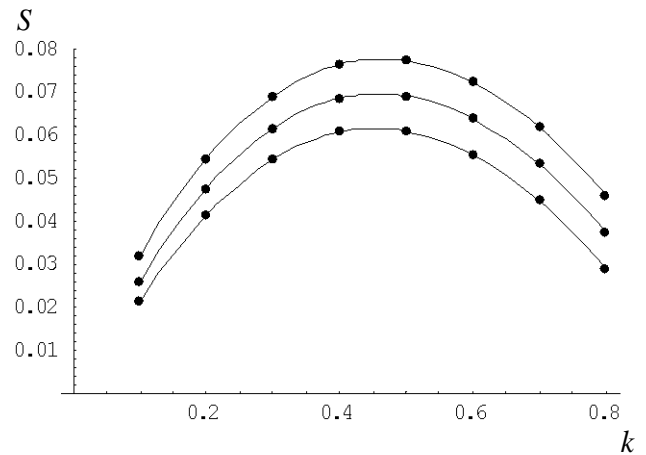


Fig. 3. Marginal stability curves for the case $\beta = 2$ and three values of $1/R$: $0, 0.03, 0.06$ (from top to bottom).

The combined effect of the variable friction and small curvature on the stability boundary is shown in Fig. 4 where the critical value of the parameter S (defined as $S_{cr} = \max_k S(k)$) is plotted versus β for three different values of $1/R$: $0, 0.03, 0.06$ (from top to bottom). Both parameters (small curvature $1/R$ and non-uniformity of the friction coefficient β) have a stabilizing influence on the flow.

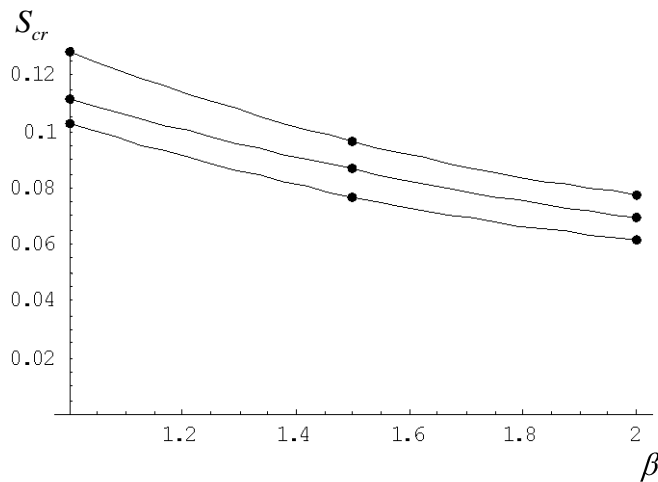


Fig. 4. Critical values S_{cr} versus β for three values of $1/R$: 1, 1.5 and 2 (from bottom to top).

V. CONCLUSION

The combined influence of two factors (non-uniformity of the friction coefficient in the transverse direction and small curvature) on temporal stability of shallow mixing layers is investigated in the present paper. The linear stability problem is solved by a pseudospectral collocation method based on Chebyshev polynomials. Marginal stability curves are presented for different values of the parameters of the problem. It is shown that both parameters stabilize the flow.

Linear stability analysis can be used only to determine the critical values of the parameters (in this particular case, the stability parameter S) for which the base flow becomes unstable. In order to study the evolution of the most unstable mode for the value of S which is slightly smaller than the critical value one can use weakly nonlinear theory. It can be shown that in this case the amplitude evolution equation for the most unstable mode in accordance with linear stability theory is the complex Ginzburg-Landau equation. The authors are currently working on the derivation of the Ginzburg-Landau equation and the analysis of the stability properties of the equation.

ACKNOWLEDGMENT

This work was partially supported by the grant 623/2014 of the Latvian Council of Science.

REFERENCES

- [1] G.H. Jirka, "Large scale flow structures and mixing processes in shallow flows," *J. Hydr. Res.*, vol. 39, pp. 567–573, 2001.
- [2] V.H. Chu, J.H. Wu, and R.E. Khayat, "Stability of transverse shear flows in shallow open channels," *J. Hydr. Engng.*, vol. 117, pp. 1370–1388, 1991.
- [3] D. Chen, and G.H. Jirka, "Linear stability analysis of turbulent mixing layers and jets in shallow water," *J. Hydr. Res.*, vol. 36, pp. 815–830, 1998.

- [4] M.S. Ghidaoui, and A.A. Kolyshkin, "Linear stability analysis of motions in compound open channels," *J. Hydr. Engng.*, vol. 125, pp. 871–880, 1999.
- [5] A.A. Kolyshkin, and M.S. Ghidaoui, "Gravitational and shear instabilities in compound and composite channels," *J. Hydr. Engng.*, vol. 128, pp. 1076–1086, 2002.
- [6] V.H. Chu, and S. Babarutsi, "Confinement and bed-friction effects in shallow turbulent mixing layers," *J. Hydr. Engng.*, vol. 114, pp. 1257–1274, 1988.
- [7] W.S.J. Uijttewaala, and J. Tukker, "Development of quasi two-dimensional structures in shallow free-surface mixing layer," *Exp. in Fluids*, vol. 24, pp. 192–200, 1998.
- [8] W.S.J. Uijttewaala, and R. Booij, "Effect of shallowness on the development of free-surface mixing layers," *Phys. Fluids*, vol. 12, pp. 392–402, 2000.
- [9] B.C. Prooijen, and W.S.J. Uijttewaala, "A linear approach for the evolution of coherent structures in shallow mixing layers," *Phys. Fluids*, vol. 14, pp. 4105–4114, 2002.
- [10] W. Liou, "Linear instability of free curved shear layers," *Phys. Fluids*, vol. 6, pp. 541–549, 1993.
- [11] H. Nepf, "Hydrodynamics of vegetated channels," *J. Hydr. Res.*, vol. 50, pp. 262–279, 2012.
- [12] H. Nepf, "Flow and transport in regions with aquatic vegetation," *Ann. Rev. of Fluid Mech.*, vol. 44, pp. 123–142, 2012.
- [13] X. Zhang, and H. Nepf, "Exchange flow between open water and floating vegetation," *Environ. Fluid Mech.*, vol. 11, pp. 531–546, 2011.
- [14] Jamali, M., X. Zhang, and H. Nepf, "Exchange flow between canopy and open water," *J. Fluid Mech.*, vol. 611, pp. 237–254, 2008.
- [15] B. White, and H. Nepf, "Shear instability and coherent structures in shallow flow adjacent to a porous layer," *J. Fluid Mech.*, vol. 593, pp. 1–32, 2007.
- [16] I. Eglite, and A. Kolyshkin, "Spatial stability analysis of curved shallow mixing layers," in *Mathematical models and methods in modern science*, WSEAS Press, Athens, pp. 104–108, 2013.

Application of self-tuning polynomial controller

Stanislav Plšek and Vladimír Vašek

Abstract—The article deals an implementation of digital adaptive polynomial controller for usage in 8-bit microcontroller from Freescale DZ family, which is intended for general and automotive purposes. The MC9S08DZ60 microcontroller is a main part of a dryer designed for a printed-circuit board production. The dryer system is identified by a recursive least square method. The control system is based on the polynomial controller that is calculated by a dead beat control method. The controller functionality is verified by a real device. The drying apparatus includes advanced control elements to ensure high comfort.

Keywords—Discrete controller, dryer, microcontroller, recursive identification.

I. INTRODUCTION

PRESENT days a fast production of printed circuits boards is needed – especially in processes of designing and developing electronic circuits. These devices are made in a wide range from simple circuits for specific purpose to universal circuits with configurable functions. Printed circuit boards (PCB) for those circuits can be produced with a different quality, an amount and types. The simplest type of boards is made as a one side board without any conformal protection layer (non-soldering mask, tin plating). Demands on board's quality rise together with development electronics, primarily number of layers (double-sided boards, four-layers boards) and surface treatment (non-soldering layers, HAL, golden plating).

Commonly available non-soldering mask resist to high temperatures during soldering (manual, reflow or wave soldering), chemical cleaning and mechanical damage. Due to these reasons, parameters of applying mask and specially drying temperature have to be kept during the PCB manufacturing. A tolerance is prescribed by producer of the mask; it usually achieves 10°C depending on drying method [9]. If the tolerance is exceeded, the mask lost an adhesion to the board or the mask holds on the board to strong on places where component pads are designed. It depreciates the board or the board is overall unusable. As can be seen on Fig. 1, the PCB is losing the mask, because the drying temperature was out of tolerances and didn't achieve the set temperature.

The project is supported by Internal Grant Agency of Tomas Bata University in Zlín, IGA/FAI/2014/012 and ERDF Project CEBIA Tech No. CZ.1.05/2.1.00/03.0089. This support is very gratefully acknowledged.

S. Plšek is with the Tomas Bata University in Zlín, nám. T. G. Masaryka 5555, 760 01 Zlín, Czech Republic (corresponding author to provide phone: +420 576 035 125; e-mail: splsek@fai.utb.cz).

V. Vašek is with the Tomas Bata University in Zlín, nám. T. G. Masaryka 5555, 760 01 Zlín, Czech Republic (corresponding author to provide phone: +420 576 035 254; e-mail: vasek@fai.utb.cz).

This work presents a design of polynomial adaptive controller for temperature control in the process of the PCB manufacturing. The controller is universally designed to using with large types of dryers independent on type, dimensions or power. Implementation is based on 8-bit Freescale microcontroller (HCS08 type). Controller calculation and hardware implementation are solved in next chapters. It is followed by verification of controller on real device.

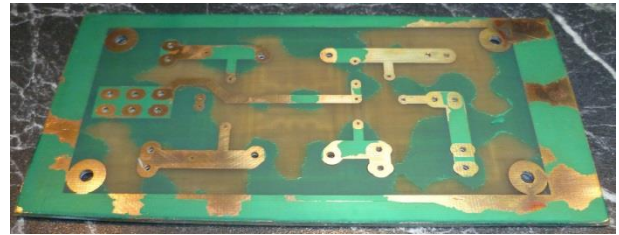


Fig.1 Non-soldering mask missing on the PCB

II. RECURSIVE IDENTIFICATION

The recursive identification – the least-square method [2], [4], [5] is used to ensure high stability of controlled temperature during the changing of surround conditions. This method need no huge space memory in microcontroller and complicated calculations, because two last steps of controller output value and temperature are sufficient to provide identification.

It can be deduced from dryer knowledge, that system can be described by second-order discrete function:

$$G(z) = \frac{b_1 z^{-1} + b_2 z^{-2}}{1 + a_1 z^{-1} + a_2 z^{-2}} \quad (1)$$

An implicit identification method is described next equation

$$\hat{\Theta} = (\mathbf{F}^T \mathbf{F})^{-1} \mathbf{F}^T \mathbf{y} \quad (2)$$

This equation can be rewritten for $k-1$ measurements into form

$$\hat{\Theta}(k-1) = (\mathbf{F}_{k-1}^T \mathbf{F}_{k-1})^{-1} \mathbf{F}_{k-1}^T \mathbf{y}(k-1) \quad (3)$$

where:

$$\mathbf{y}^T(k-1) = [y(1) \quad y(2) \quad \dots \quad y(k-1)] \quad (4)$$

is a vector of output variables in the interval $(1, k-1)$, and

$$\hat{\Theta}(k-1) = [\hat{\theta}_1(k-1) \quad \hat{\theta}_2(k-1) \quad \dots \quad \hat{\theta}_r(k-1)] \quad (5)$$

is vector of optimal estimates of parameter values of transfer function. A matrix

$$\mathbf{F}_{k-1} = \begin{bmatrix} f_1(1) & f_2(1) & \dots & f_r(1) \\ f_1(2) & f_2(2) & \dots & f_r(2) \\ \vdots & \vdots & \vdots & \vdots \\ f_1(k-1) & f_2(k-1) & \dots & f_r(k-1) \end{bmatrix} \quad (7)$$

is modified matrix \mathbf{F} for $(k-1)$ measurements. If k -measurement is done and

$$\mathbf{y}(k) = \begin{bmatrix} y(k-1) \\ y(k) \end{bmatrix} \quad (8)$$

is described, the matrix (9)

$$\mathbf{F}_k = \begin{bmatrix} \mathbf{F}_{k-1} \\ \mathbf{\Phi}^T(k) \end{bmatrix} \quad (10)$$

can be written, where

$$\mathbf{\Phi}^T(k) = [f_1(k) \quad f_2(k) \quad \dots \quad f_r(k)] \quad (11)$$

The vector (12) can be written for k -measured variable

$$\mathbf{y}(k) = \mathbf{\Theta}^T \mathbf{\Phi}(k) + e(k) \quad (12)$$

where $\mathbf{\Theta}^T$ is defined as:

$$\mathbf{\Theta}^T = [\theta_1 \quad \theta_2 \quad \dots \quad \theta_r] \quad (13)$$

A covariance matrix $\mathbf{C}(k)$ can be defined as

$$\mathbf{C}(k) = [\mathbf{F}_{k-1}^T \mathbf{F}_{k-1} + \mathbf{\Phi}(k) \mathbf{\Phi}^T(k)]^{-1} \quad (14)$$

And it can be written as

$$\mathbf{C}(k) = [\mathbf{C}^{-1}(k-1) + \mathbf{\Phi}(k) \mathbf{\Phi}^T(k)]^{-1} \quad (15)$$

A general recursive algorithm can be written as

$$\hat{\mathbf{\Theta}}(k) = \hat{\mathbf{\Theta}}(k-1) + \mathbf{K}(k) [y(k) - \hat{\mathbf{\Theta}}^T(k-1) \mathbf{\Phi}(k)] \quad (16)$$

where $\mathbf{K}(k)$ is time changing vector of gain and can be written as

$$\mathbf{K}(k) = \frac{\mathbf{C}(k-1) \mathbf{\Phi}(k)}{1 + \mathbf{\Phi}^T(k) \mathbf{C}(k-1) \mathbf{\Phi}(k)} \quad (17)$$

The recursive equation for covariance matrix is

$$\mathbf{C}(k) = \mathbf{C}(k-1) - \mathbf{C}(k-1) \frac{\mathbf{\Phi}(k) \mathbf{\Phi}^T(k) \mathbf{C}(k-1)}{1 + \mathbf{\Phi}^T(k) \mathbf{C}(k-1) \mathbf{\Phi}(k)} \quad (18)$$

The vector of parameters $\mathbf{\Theta}^T(k)$ and vector of measurement data $\mathbf{\Phi}^T(k)$ can be written for second order transfer function as:

$$\mathbf{\Theta}^T(k) = [a_1 \quad a_2 \quad b_1 \quad b_2] \quad (19)$$

$$\mathbf{\Phi}^T(k) = [-y(k-1) \quad -y(k-2) \quad u(k-1) \quad u(k-2)] \quad (20)$$

III. DISCRETE CONTROLLER

The dead beat controller was chosen for the dryer. This controller ensures the stability of regulated variable also among measurement periods [2-4]. The closed loop can be described by equations (21) and (22):

$$Y(z^{-1}) = \frac{B(z^{-1})}{A(z^{-1})} U(z^{-1}) \quad (21)$$

$$U(z^{-1}) = \frac{R(z^{-1})}{P(z^{-1})} W(z^{-1}) - \frac{Q(z^{-1})}{P(z^{-1})} Y(z^{-1}) \quad (22)$$

where $U(z^{-1})$, $Y(z^{-1})$ and $W(z^{-1})$ are polynomials of corresponding signals. It can be written after modification of (21) and (22):

$$Y(z^{-1}) = \frac{B(z^{-1})R(z^{-1})}{A(z^{-1})P(z^{-1}) + B(z^{-1})Q(z^{-1})} W(z^{-1}) \quad (23)$$

$$U(z^{-1}) = \frac{A(z^{-1})R(z^{-1})}{A(z^{-1})P(z^{-1}) + B(z^{-1})Q(z^{-1})} W(z^{-1}) \quad (24)$$

and control error $E(z^{-1})$

$$E(z^{-1}) = \left[1 - \frac{B(z^{-1})R(z^{-1})}{A(z^{-1})P(z^{-1}) + B(z^{-1})Q(z^{-1})} \right] W(z^{-1}) \quad (25)$$

If control error is required to be zero, the polynomial $E(z^{-1})$ has to be simple. This condition is satisfied if polynomial equation

$$A(z^{-1})P(z^{-1}) + B(z^{-1})Q(z^{-1}) = 1 \quad (26)$$

A solving of Diophantine equations leads to a system of matrixes

$$\begin{bmatrix} b_1 & 0 & 1 \\ b_2 & b_1 & a_1 \\ 0 & b_2 & a_2 \end{bmatrix} \begin{bmatrix} q_0 \\ q_1 \\ p_1 \end{bmatrix} = \begin{bmatrix} -a_1 \\ -a_2 \\ 0 \end{bmatrix} \quad (27)$$

The controller output can be described by (28):

$$u(k) = r_0 w(k) - q_0 y(k) - q_1 y(k-1) - p_1 u(k-1) \quad (28)$$

where r_0 is calculated by

$$r_0 = \frac{1}{b_1 + b_2} \quad (29)$$

IV. CONTROLLER HARDWARE

The adaptive polynomial controller was implemented on special hardware developed specially for limited space inside dryer. The hardware includes separate double-sided boards with main board, communication parts, power circuits providing heating control and HMI boards (displays, switches and theirs interfaces).

The main board includes general purpose 8-bit microcontroller MC9S08DZ60 on 40MHz core frequency, 4kb RAM and 60kb of flash memory for data program [6], power supplies (+5V, 3.3V, 3.6V for displays and 4.096V as reference voltage for temperature measurement), a backup battery for a RTC and a memory with last measured data (drying time, needed time to reach set temperature, time of a last power failure). An analog part measuring the temperature is also included on the main board.

The temperature is measured at two positions in the dryer chamber with purpose of avoid local overheating. These temperatures are compared and a higher value is used by the controller. The temperature measuring is provided by Pt1000 sensors and 16-bit AD converter [7]. This form provides a high resolution. A comparative method was chosen for

V. VERIFICATION OF THE CONTROLLER

The adaptive controller was verified on real device at changing ambient conditions (temperature differences at 20°C, different air flow). First, the step responses were measured and next the controller was verified

The verification was realized by connection through RS232 interface. The actually measured temperature, controller output and set value were sent each ones second. The period of PWM output signal was chosen $T_{PWM} = 5s$ (100 times of AC line period), because the output signal is generated by solid state relay with zero-cross detection circuit. The controller period was chosen $T_C = 10s$.



Fig. 2 Overview of the main controller board

measuring voltage on Pt1000 sensors, because it needs only one precious (0.01%) and temperature stable (5ppm/°C) resistor. If a resistor value is properly selected, the voltage can be easily determined and converted to the temperature. The price of the system is lower than the other method is used and it is not increased by high price of high amount of precious and temperature stable components (resistors, AD converters, voltage references).

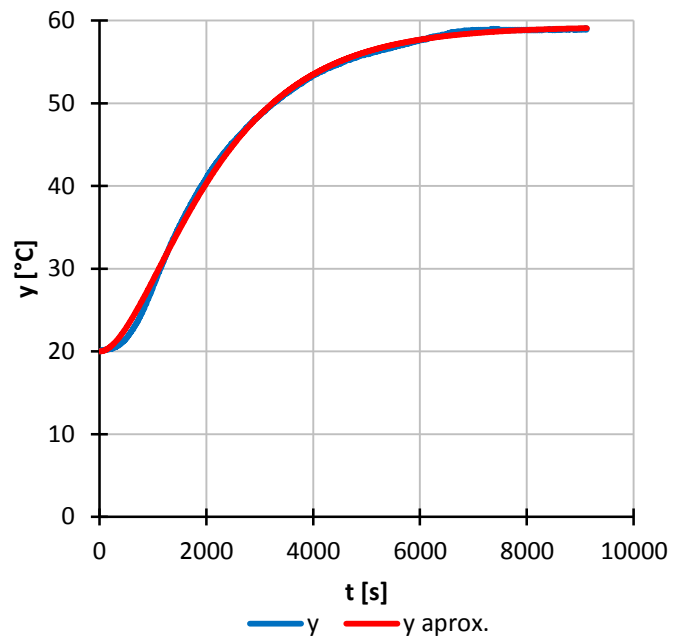


Fig. 3 System identification, u=3%

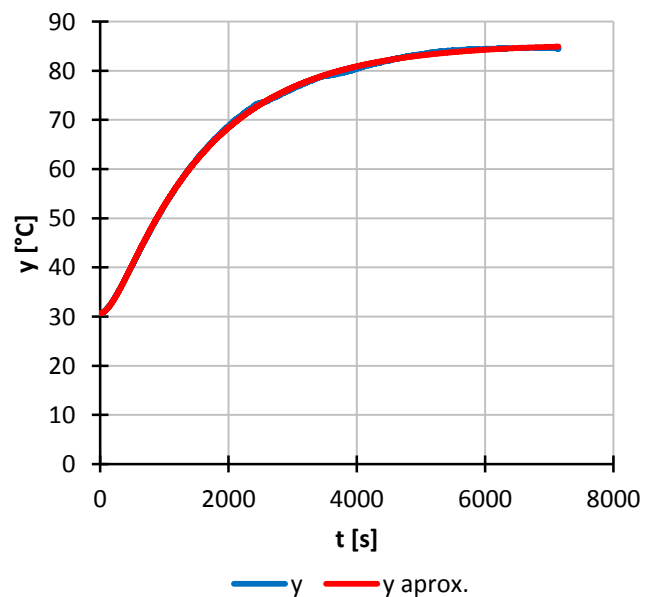


Fig. 4 System identification, u=5%

The first time identification of system was measured with $u_{OUT} = 3\%$ and $u_{OUT} = 5\%$ in order to the dryer not to be damaged by high temperature. Step responses of both measurements are shown on Fig. 3 and Fig. 4.

The continues step responses were calculated for these measurements and are written below (equation (27) corresponds to $u=3\%$; equation (28) corresponds to $u=5\%$). There can be seen some difference caused other measurement conditions.

$$G(s) = \frac{39,2}{(14849s + 1)(858,0s + 1)} \quad (27)$$

$$G(s) = \frac{54,8}{(15236s + 1)(209,7s + 1)} \quad (28)$$

The controll processes are shown in Fig. 5 and Fig. 6 for $w=50^\circ\text{C}$ and 80°C . As can be seen in graphs, instability at the process start occurs. It is influenced by parameters identifying of unknown system. This trait can be removed by using other controller (PID, two-state) at start of identification process and switching them if identified parameters are stabilized [3].

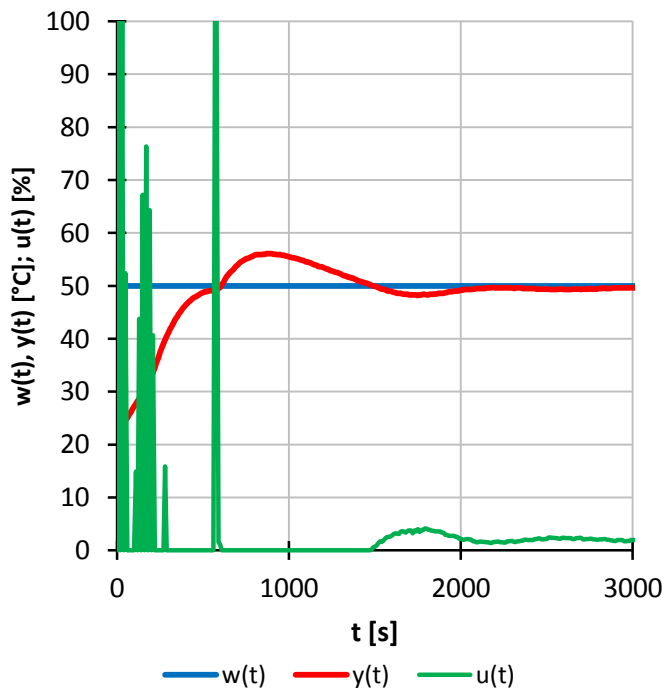


Fig. 5 Control process 1, $w=50^\circ\text{C}$

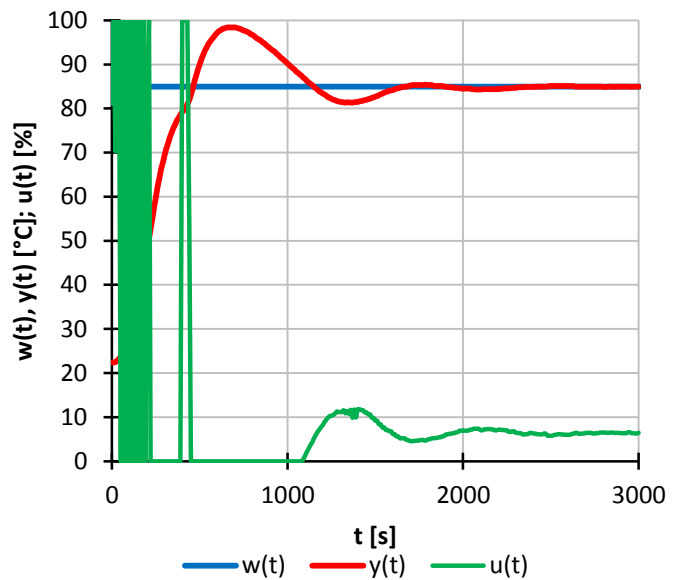


Fig. 5 Control process 2, $w=85^\circ\text{C}$

VI. CONCLUSION

The article deals with the application of adaptive polynomial controller to temperature regulation in the dryer chamber which is used for production of printed circuit boards, especially for drying non-soldering mask. The controller was implemented on base of 8-bit microcontroller, It proves sufficient performance of 8-bit microcontrollers, although controller needs high number of matrixes calculation and there can be used some 32-bit ARM microcontroller, which are massive used at present days. The design of device was universally conceptualized and the device can be used in other types of dryers. It is considered extension to oven for reflow soldering according to IPC/JEDEC standard [8].

REFERENCES

- [1] V. Bobál, *Adaptive and predictive control*. Zlín: Tomas Bata University in Zlín, 2008, 134 p. ISBN 978-80-7318-662-3.
- [2] V. Bobál, *Systems identification*. Zlín: Tomas Bata University in Zlín, 2009, 128 p. ISBN 978-80-7318-888-7.
- [3] P. Navrátil, *Time-continuous identification methods for design of self-tuning controllers*: dissertation thesis. Zlín, 2007. 119 p.
- [4] V. Bobál, *Practical aspects of self-tuning controllers: algorithms and implementations*. Brno: VUTIUM, 1999, 242 p. ISBN 80-214-129-92.
- [5] P. Dostálek, J. Dolinay, V. Vašek and L. Pekař, "Self-tuning digital PID controller implemented on 8-bit Freescale microcontroller", *International Journal of Mathematical Models and Methods in Applied Sciences*. 2010, vol. 4, iss. 4, p. 274-281. ISSN 1998-0140
- [6] Freescale Semiconductor. *MC9S08DZ60 datasheet* [online]. 2008. Freescale Semiconductor, Inc.: Freescale Semiconductor Literature Distribution Center, 2008 [cit. 2014-04-19]. Available on WWW: <http://www.freescale.com>
- [7] Microchip Technology. *MCP3426/7/8, 16-Bit, multi-channel $\Delta\Sigma$ analog-to-digital converter with I²C™ interface and on-board reference datasheet* [online]. 2009 Microchip Technology Inc. 2009, [cit. 2014-04-19]. Available on WWW: <http://www.microchip.com>
- [8] J-STD-020D.1. *Joint IPC/JEDEC standard for moisture/reflow sensitivity classification for non-hermetic solid state surface-mount devices*. Rev. D. 2008.
- [9] SunChemical. *XV501T-4 white screen datasheet*. 2008. SunChemical Circuits, Inc.

Resistive Parameter Identification of a Li-ion Battery Using Sliding Mode Observer

Daehyun Kim, Taedong Goh, Seung Hun Kim, and Sang Woo Kim

Abstract—The internal resistance varies depending on the conditions of battery operation, an accurate identification scheme is necessary for a reliable battery model. Therefore, this paper proposes a parameter identification method for internal resistance of a Li-ion battery using a sliding mode (SM) observer. In this method, the resistance update equation is deduced through a Lyapunov-based approach. The validation experiment is performed through step discharging tests at two different SOC levels. The experimental results show that the performance of proposed parameter identification scheme.

Keywords—Equivalent circuit-based model, Internal resistance, Li-ion battery, Parameter identification, Sliding mode observer.

I. INTRODUCTION

DUE to the demand for the zero emission vehicles, the interest in electric vehicles (EVs) and hybrid electric vehicles (HEVs) is increasing. Among the component parts of the EVs, the battery is the main component because the battery provides the power to drive an electric motor. Also, the battery management system (BMS) is important. It can decide the charging timing, expected driving distance, and whether the regenerative braking is possible or not. To implement the various functions of the BMS, the battery state and parameters, such as state of charge (SOC), state of health (SOH), and internal resistance have to be measured and estimated. There are many attentions estimating SOC and SOH [1]-[3]. Therefore, this paper will focus on the estimation of the internal resistance.

To determine the internal resistance of the battery, a variety of methods based on Ohm's Law, Joule's Law, impedance spectroscopy measurements, and battery modeling [4].

The method based on Ohm's Law is the most commonly used

This research was supported by the MSIP(Ministry of Science, ICT and Future Planning), Korea, under the "IT Consilience Creative Program" (NIPA-2014-H0201-14-1001) supervised by the NIPA(National IT Industry Promotion Agency).

D. Kim is with the Department of Electrical Engineering, Pohang University of Science and Technology, 77 Cheongam-Ro, Nam-gu, Pohang 790-784, Korea (corresponding author to provide phone: (+82) 54-279-5018; fax: (+82) 54-279-2903; e-mail: daehyunkim@postech.edu).

T. Goh and S. H. Kim are with the Department of Electrical Engineering, Pohang University of Science and Technology, 77 Cheongam-Ro, Nam-gu, Pohang 790-784, Korea(e-mail: ehd1116@postech.edu; pisics@postech.edu).

S. W. Kim is with the Department of Electrical Engineering and the Department of Creative IT Excellence Engineering and Future IT Innovation Laboratory, Pohang University of Science and Technology, 77 Cheongam-Ro, Nam-gu, Pohang 790-784, Korea (e-mail: swkim@postech.edu).

for resistance estimation because of its very simple to implement. However, the estimated result of resistance is strongly influenced several factors such as discharge time, magnitude of discharge current and SOC.

The Joule's law based method calculates the internal resistance through energy loss from the battery. In this method, the energy loss is measured using a calorimeter, so it is not suitable for actual battery usage condition.

The impedance spectroscopy method investigates the electro chemical impedance of the battery. The sensor for the impedance measurement is expensive and the dangerous situation can happen when the signal inject into the battery to measure the impedance while operating the battery. Thus, it is hard to on-line implementation.

The battery model-based identification method consists of a state equation and a state observer. The state equation of the battery can be derived from an equivalent circuit battery model. This method has received much attention because this approach enables to apply various existing observers.

In this paper, to estimate the resistive parameter and SOC at the same time, the sliding mode (SM) observer is used. The SM observer is widely used due to its simplicity and the robustness property to both parameter variations and external disturbances. As a result, the novel identification scheme for resistive parameter of a Li-ion battery is proposed using SM observer.

This paper is organized as follows. Section2 presents the equivalent circuit-based battery model and the parameter extraction method. Section3 proposes a parameter identification scheme. Section 4 and 5 present s our experimental results and conclusions.

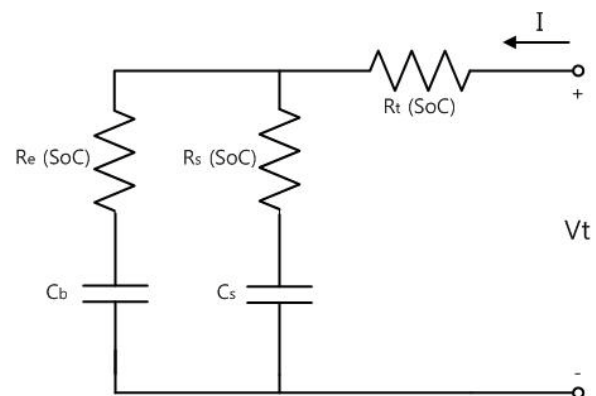


Fig. 1 Linear RC battery model

II. EQUIVALENT CIRCUIT BATTERY MODEL

A. Linear RC battery model

A linear RC battery model [5]-[6] consists of two capacitors and three resistances as shown in Fig. 1. In this RC battery model, a bulk capacitor C_b characterizes the capacity of the battery to store charge and a surface capacitor C_s represents the surface capacitance and diffusion effects of the battery. Also, terminal resistor R_t , end resistor R_e , and surface resistor R_s are used for resistance components of the RC battery model. V_{cb} and V_{cs} are the voltage across of the bulk and surface capacitor, respectively. V_t is the terminal voltage and I is the terminal current. The voltages and current characteristics of the electric circuit in Fig. 1 can be described by state equations as (1).

$$\dot{x} = Ax + Bu, \quad (1)$$

where

$$x = \begin{bmatrix} V_{C_b} \\ V_{C_c} \\ V_t \end{bmatrix}, \quad u = I,$$

$$A = \begin{bmatrix} -\frac{1}{C_b(R_e + R_s)} & \frac{1}{C_b(R_e + R_s)} & 0 \\ \frac{1}{C_s(R_e + R_s)} & -\frac{1}{C_s(R_e + R_s)} & 0 \\ A_{31} & 0 & A_{33} \end{bmatrix},$$

$$A_{31} = -\frac{R_s}{C_b(R_e + R_s)^2} + \frac{R_e}{C_s(R_e + R_s)^2} - \frac{R_s^2}{C_b R_e (R_e + R_s)^2} + \frac{R_s}{C_s(R_e + R_s)^2},$$

$$A_{33} = \frac{R_s}{C_b R_e (R_e + R_s)} - \frac{1}{C_s(R_e + R_s)},$$

$$B = \begin{bmatrix} \frac{R_s}{C_b(R_e + R_s)} \\ \frac{R_s}{C_s(R_e + R_s)} \\ \frac{R_e^2}{C_s(R_e + R_s)^2} - \frac{R_s R_t}{C_b R_e (R_e + R_s)} + \frac{R_t}{C_s(R_e + R_s)} + \frac{R_e R_s}{C_s(R_e + R_s)^2} \end{bmatrix}$$

B. Parameter Extraction

The initial parameters of the RC battery model are obtained from the battery characterization test data. The value of bulk capacitor C_b is calculated from the energy stored in the capacitor:

$$\begin{aligned} \text{Energy}_{C_b} &= \frac{1}{2} C_b V^2 = \frac{1}{2} C_b (V_{100\%SOC}^2 - V_{0\%SOC}^2) \\ &= \text{AmpSec} \times V_{100\%SOC} \\ \therefore C_{b_init} &= \frac{\text{AmpSec}_{\text{rated}} \times V_{100\%SOC}}{\frac{1}{2} (V_{100\%SOC}^2 - V_{0\%SOC}^2)} \end{aligned} \quad (2)$$

where $V_{100\%SOC}$ is the open circuit voltage (OCV) at 100% SOC and $\text{AmpSec}_{\text{rated}}$ is the rated battery capacity.

The value of surface capacitor C_s is derived from high-frequency excitation tests, which apply a discharge pulse

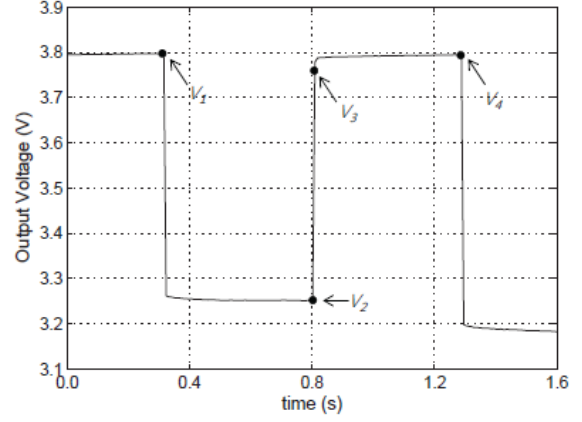


Fig. 2 Output voltage of high frequency excitation test in 0.5 s intervals. From the output voltage in Fig. 2, we calculate the time constant τ :

$$\begin{aligned} V_{no_load} &= V_1 = V_3 + (V_4 - V_3)(1 - e^{-\Delta t/\tau}) \\ \therefore \tau &= -\Delta t \ln \left(1 - \frac{V_4 - V_3}{V_1 - V_3} \right) \end{aligned} \quad (3)$$

The time constant associated with C_s can be represented by:

$$\begin{aligned} \tau &= C_s (R_b + R_s) \\ \therefore C_{s_init} &= \frac{\tau}{(R_b + R_s)} \end{aligned} \quad (4)$$

On the other hand, the internal resistance R_{int} is also obtained in Fig. 2:

$$R_{int} = \frac{V_3 - V_2}{I_{dis}} \quad (5)$$

where represents the pulse discharge current. Generally, it is assumed that R_b and R_s are a one-fourth of the value of R_{int} and R_t is taken to be 25% of R_{int} [7].

III. DESIGN OF SLIDING MODE OBSERVER

In this section, the SM observer for the estimation of the terminal voltage and the SOC is introduced. In addition, we propose an identification scheme for the resistive parameters in (1).

First of all, there is a general assumption in the PNGV Battery Test Manual that the end resistor R_e and surface resistor R_s have the same value and the terminal resistor R_t has a half value of the end resistor. Furthermore, for simplicity, it is assumed the capacitive parameters are constant, because its variation is negligibly small during the period of observation.

Under these assumptions, equation (1) is rewritten as follows:

$$\dot{x} = Ax + Bu, \quad (6)$$

where

$$A = \begin{bmatrix} \frac{1}{2C_b R_e} & \frac{1}{2C_b R_e} & 0 \\ \frac{1}{2C_c R_e} & -\frac{1}{2C_c R_e} & 0 \\ A_{31} & 0 & A_{33} \end{bmatrix}, \quad B = \begin{bmatrix} \frac{1}{2C_b} \\ \frac{1}{2C_c} \\ -\frac{1}{4C_b} + \frac{3}{4C_c} \end{bmatrix},$$

$$A_{31} = -A_{33} = -\frac{1}{2C_b R_e} + \frac{1}{2C_c R_e}.$$

A. Sliding Mode Observer without parameter variations

Assuming the resistive parameters are exactly known, the SM observer [6] was proposed to estimate the SOC and the terminal voltage.

The terminal voltage SM observer is designed by (7):

$$\hat{\hat{x}}_3 = A_{31}x_1 + A_{33}x_3 + B_3I + K_3 \operatorname{sgn}(e_3) \quad (7)$$

where K_3 is the observer gain for the terminal voltage estimation. From (6) and (7), the estimation error dynamics given by:

$$\dot{e}_3 = A_{31}e_1 + A_{33}e_3 - K_3 \operatorname{sgn}(e_3) \quad (8)$$

where $e_3 = V_t - \hat{V}_t$.

The convergence analysis is done based on the Lyapunov function, such as $V_3 = \frac{1}{2}e_3^2$. Consider now the following two cases: Case 1) Suppose that $e_3 > 0$. If the observer gain K_3 satisfies the inequalities:

$$K_3 > 0, \quad K_3 > \|A_{31}e_1\| \quad (9)$$

then $\dot{e}_3 < 0$ and also $e_3 \cdot \dot{e}_3 < 0$.

Case 2) Suppose that $e_3 < 0$. we can make $e_3 \rightarrow 0$ by choosing observer gain K_3 to satisfy the inequalities in (9).

After some finite time, according to the equivalent control method [8], the estimation error of terminal voltage is governed by (10)

$$e_1 = \left\{ \frac{K_3}{A_{31}} \operatorname{sgn}(e_3) \right\}_{eq} \quad (10)$$

Also like the observer for the terminal voltage, the observers for the voltage across of the bulk and surface capacitor are derived in (11) using the equivalent control concept.

$$\begin{aligned} \hat{\hat{x}}_1 &= A_{11}x_1 + A_{12}x_2 + B_1I + K_1 \operatorname{sgn}(e_1) \\ &= A_{11}\hat{\hat{x}}_1 + A_{12}x_2 + B_1I + K_1 \operatorname{sgn} \left(\left\{ \frac{K_3}{A_{31}} \operatorname{sgn}(e_3) \right\}_{eq} \right), \\ \hat{\hat{x}}_2 &= A_{21}x_1 + A_{22}x_2 + B_2I + K_2 \operatorname{sgn}(e_2) \\ &= A_{21}\hat{\hat{x}}_1 + A_{22}x_2 + B_2I + K_2 \operatorname{sgn} \left(\left\{ \frac{K_1}{A_{12}} \operatorname{sgn} \left(\left\{ \frac{K_3}{A_{31}} \operatorname{sgn}(e_3) \right\}_{eq} \right) \right\}_{eq} \right). \end{aligned} \quad (11)$$

Proof: A detail proof can be found in [6].

B. Sliding Mode Observer design with parameter variation

To account for parameter variation, we replace the end resistor R_e with $\hat{R}_e = R_e + \Delta R_e$ where ΔR_e denotes the resistive parameter variations. The observer of the terminal voltage is obtained as (12)

$$\begin{aligned} \hat{\hat{x}}_3 &= \hat{A}_{31}x_1 + A_{33}x_3 + B_3I + K_3 \operatorname{sgn}(e_3) \\ &= (A_{31} + \Delta A_{31})\hat{\hat{x}}_1 + (A_{33} + \Delta A_{33})x_3 + B_3I + K_3 \operatorname{sgn}(e_3), \end{aligned} \quad (12)$$

where

$$A_{31} = -\frac{1}{2C_b R_e} + \frac{1}{2C_c R_e}, \quad \hat{A}_{31} = -\frac{1}{2C_b \hat{R}_e} + \frac{1}{2C_c R_e},$$

$$\begin{aligned} \Delta A_{31} &= \left(-\frac{1}{2C_b} + \frac{1}{2C_c} \right) \left(\frac{1}{\hat{R}_e} - \frac{1}{R_e} \right) \\ &= -\Delta A_{33}. \end{aligned}$$

From (1) and (12), we obtain the estimation error dynamic equation:

$$\dot{e}_3 = A_{31}e_1 + A_{33}e_3 - \Delta A_{31}\hat{\hat{x}}_1 + \Delta A_{33}x_3 - K_3 \operatorname{sgn}(e_3). \quad (13)$$

Consider the following Lyapunov function candidate:

$$V_R = \frac{1}{2}e_3^2 + \frac{1}{2}\Delta\alpha^2, \quad (14)$$

where $\Delta\alpha = \frac{1}{\hat{R}_e} - \frac{1}{R_e}$.

Then, the derivative \dot{V}_R is given by

$$\begin{aligned} \dot{V}_R &= e_3\dot{e}_3 + \Delta\alpha\dot{\Delta\alpha} \\ &= \dot{V}_3 + e_3(-\Delta A_{31}\hat{\hat{x}}_1 - \Delta A_{33}x_3) + \Delta\alpha\dot{\Delta\alpha} \\ &= \dot{V}_3 + e_3(-\beta\Delta\alpha\hat{\hat{x}}_1 + \beta\Delta\alpha x_3) + \Delta\alpha\dot{\Delta\alpha} \end{aligned} \quad (15)$$

where V_3 is the Lyapunov function for terminal voltage estimation without parameter variations, and $\beta = \left(-\frac{1}{2C_b} + \frac{1}{2C_c} \right)$.

Since the \dot{V}_3 is negative definite as mentioned in the previous section, the $\dot{V}_R < 0$ is guaranteed when the following condition is satisfied.

$$e_3(-\beta\Delta\alpha\hat{\hat{x}}_1 + \beta\Delta\alpha x_3) + \Delta\alpha\dot{\Delta\alpha} = 0 \quad (16)$$

From (12), the parameter update equation can be derived as

$$\frac{d\Delta\alpha}{dt} = \beta e_3 (\hat{\hat{x}}_1 - x_3) \quad (17)$$

IV. EXPERIMENTAL RESULTS

The battery test bench consists of a power supply, an electrical load, and an NI data acquisition device. The power supply and the electrical load are used charge/discharge the battery, respectively. And the output voltage of the battery is measured by NI9229 voltage measurement module. In our experiment, a 18650-type Li-ion battery is used. It has a 3.0 Ah nominal capacity and a 3.7 V nominal voltage. Note that the Li-ion battery is charged at specific SOC level by the constant-voltage /constant-current (CV-CC) method. The initial parameters for RC battery model are given in Table I.

To verify the proposed parameter identification scheme, the step discharge current profile in Fig. 3 is used. The step discharge experiments are performed at two different SOC level. The gains for the SM observer are selected as

$$\begin{aligned} K^T &= [K_1 \quad K_2 \quad K_3]^T \\ &= [0.005 \quad 0.003 \quad 0.02]^T \end{aligned} \quad (18)$$

Table I Initial parameter of RC battery model at 100% and 70% SOC

SOC	C_b	C_s	R_b	R_s	R_t
100 %	14910 F	17.673 F	0.1251 Ω	0.1251 Ω	0.0625 Ω
70 %			0.1186 Ω	0.1186 Ω	0.0593 Ω

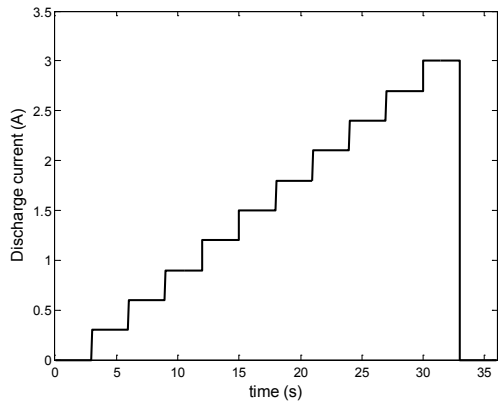
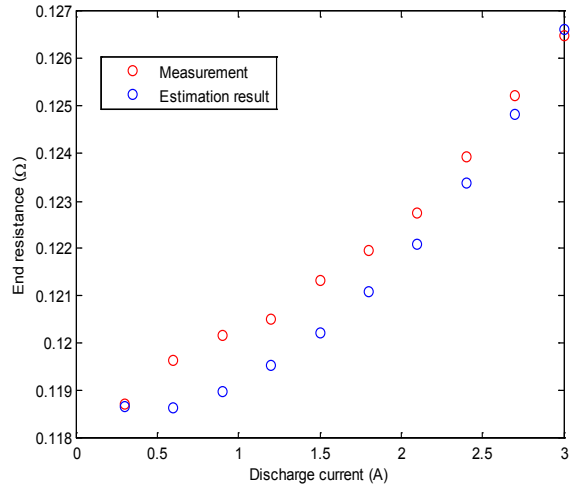
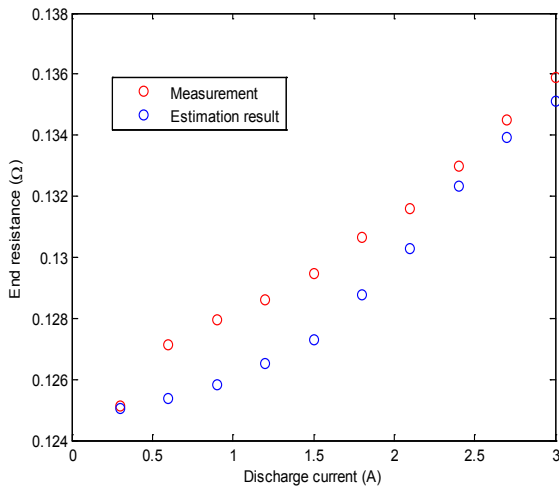


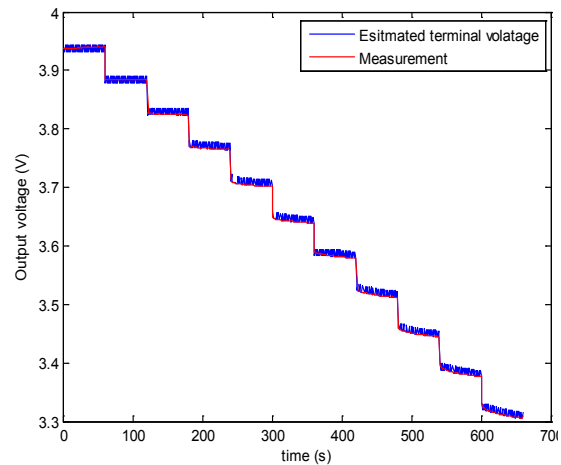
Fig. 3 Step discharge current profile



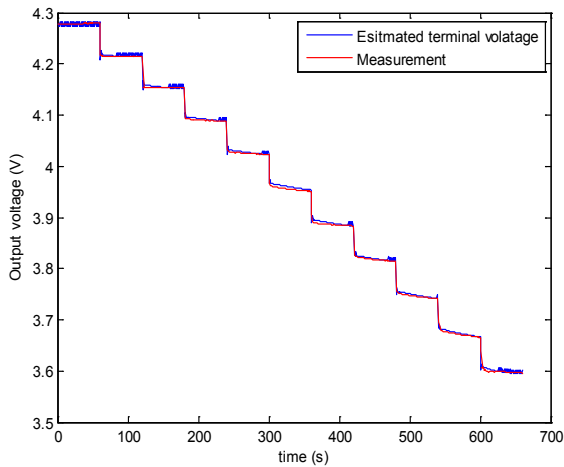
(a)



(a)



(b)



(b)

Fig. 4 Experimental results at 100% SOC (a) Estimated end resistance (b) Estimated output voltage

Fig. 5 Experimental results at 70% SOC (a) Estimated end resistance (b) Estimated output voltage

Note that the observer gain is chosen using a trial-and-error method. The adaptive gain based SM observer will be researched in a next study.

Fig. 4 shows the estimation results of the end resistor and output terminal voltage at 100% SOC. In Fig. 4 (a), the estimated end resistance shows a small estimation error with the maximum error of about 2 %. Also, it can be seen that the estimated output terminal voltage tracks well the measured terminal voltage. Fig. 5 shows the estimation results of the end resistor and output terminal voltage at 70% SOC. As expected, the results show that the SM observer can estimates the end resistance and terminal voltage with a high accuracy.

V. CONCLUSIONS

In this paper, the parameter identification scheme for internal resistance of a Li-ion battery is proposed. The parameter update

equation is derived using a sliding mode (SM) observer with the equivalent control approach. To verify the performance of scheme, the step discharge experiments are conducted on a Li-ion battery with 100% SOC and 70% SOC, respectively. The experimental results show that the tracking performance of the proposed parameter identification scheme.

ACKNOWLEDGMENT

This research was supported by the MSIP(Ministry of Science, ICT and Future Planning), Korea, under the "IT Consilience Creative Program" (NIPA-2014-H0201-14-1001) supervised by the NIPA(National IT Industry Promotion Agency).

REFERENCES

- [1] X. Hu, F. Sun, Y. Zou, "Estimation of State of Charge of a Lithium-ion Battery Pack for Electric Vehicles using an Adaptive Luenberger Observer," *Energies*, vol 3, pp.1586-1603, Sep. 2010.
- [2] M. Chen, G. A. Rincon-Mora, "Accurate Electrical Battery Model Capable of Predicting Runtime and IV performance," *IEEE Trans. Energy Convers.*, vol. 21, pp.504-511, June 2006.
- [3] S. Piller, M. Perrin, A. Jossen, "Methods for State-of-Charge Determination and their applications," *J. Power Source.*, vol. 96, pp.113-120, June 2001.
- [4] S. Hans-Georg, O. Ossama, K. Oliver, R. Andre, S. Michael, Z. Christian, G. Markus, K. Michael, and B. Peter, "Comparison of Several Methods for Determining the Internal Resistance of Lithium Ion Cells," *Sensors*, vol 10, pp.5604-5625, June 2010.
- [5] B. Bhangu, P. Bently, D. Ston, C. Bingham, "Nonlinear Observers for Predicting State-of-Charge and State-of-Health of lead-acid batteries for hybrid electric vehicles," *IEEE Trans. Veh Technol*, vol. 54, pp.783-794, May 2005.
- [6] I. S. Kim, "Nonlinear State of Charge estimator for hybrid electric vehicle battery," *IEEE Trans. Power Electron*, vol. 23, pp.2027-2034, July 2008.
- [7] NREL. Advanced Vehicle Simulator (ADVISOR), version 3.2. <http://www.NREL.org>
- [8] S. V. Drakunov, "Sliding-mode observers based on equivalent control method," in *Proc. 31th IEEE Conf. Decision and Control 1992*, pp. 2368-2369.

Statistical Wound-Rotor IM Diagnosis Method Based on Standard Deviation using NVSA

Khalid Dahi, Soumia Elhani and Said Guedira

Abstract— In this paper we address the problem of rotor faults in Wound Rotor Induction Machine by using two different signal processing methods to voltage between neutrals such as Standard deviation calculation and Hilbert Transform (HT). This last is employed as an effective technique for fault detection in induction machines. The mathematical simplicity of the proposed technique, compared with some commonly used algorithms from the literature, renders it competitive candidate for the on-line diagnosis of machines.

Experimental results are provided to verify the proposed method and to evaluate its performance as pre-processing for monitoring of Wound Rotor Induction Machine. An algorithm has been tested on neutral between voltages under different load conditions and rotor fault degrees that shows that the studied diagnosis method can be used as a valid methodology for this type of phenomena.

Keywords— Diagnosis; Rotor fault; WRIM; Neutral voltage; Standard deviation.

I. INTRODUCTION

WOUND Rotor Induction Machine WRIM has recently known a new life due to the worldwide development. The wound rotor induction machine offers a number of advantages over other types of asynchronous machines, including the ability to produce a high starting torque with low starting current, and also they are easy assembly compared to asynchronous squirrel cage machine, thanks to these benefits that the WRIM is frequently used in the industry for any application requiring large rotating machines. However, these wind generators suffer from some electric stresses that can affected the profitability of these machines.

In this type of application, monitoring of WRIM is crucial due to their working environment, and fault diagnostics requires measures sensitive to the change greatness of the WRIM and an appropriate method to obtain a diagnostic index and a threshold indicating the limit between the healthy state and the defective one. There are a number of research papers on technical monitoring of electrical machines which are most relevant are [1] - [6].

K.Dahi and S.Elhani are with the Department of electrical engineering, at the Ecole Normale Supérieure de l'Enseignement Technique, Mohammed V Souissi University, Rabat-Morocco
(e-mail: Khalid.dahi@um5s.net.ma; s.elhani@um5s.net.ma).

S. Guedira is with the "Ecole Nationale de l'Industrie Minérale" Rabat, Morocco, laboratoire de recherché commande protection et surveillance des installations industriels (e-mail: said.guedira@gmail.com).

Studies carried out by articles have shown that defects of the stator windings and rotor windings are assumed equal because they are inadequately protected. However, the vast majority of articles dealing mainly with rotor fault first and then with stator faults and finally bearing faults.

In this paper we focus on the rotor fault, this fault which physically resembles to the stator fault resulting either by short/open circuits or by increasing of the rotor resistance. In this case, the machine can also operate after the application of a fault, while in case of short/open circuits the machine operation is limited by a brief duration. In our case an additional resistance is added to one of the phases of the rotor to create the rotor fault.

Generally, MCSA "Motor Current Signal Analysis" [7] [8] [9][10]. (Widely known in the literature) is the most commonly used technique and well established. In fact, MCSA is simple and effective in appropriate operating conditions. However, this technique has significant limitations due to the increasing complexity of electrical machines and drives [1]:

- 1) It is influenced by the operating conditions (e.g. low load conditions, load oscillations);
- 2) The fault diagnosis is difficult or impossible if the system operates under time-varying conditions or the machine is supplied by a power converter;
- 3) The diagnosis is difficult or impossible in machines with special magnetic structure (e.g. machines with double cage in which there are a strong influence of interbar currents or only the outer cage has a fault).
- 4) The induction machines are now frequently installed with inverters which provide a number of advantages and therefore make the stator current inaccessible to diagnosis.

To reduce these limitations, the proposed work focuses on the use of voltage between neutrals NV "Neutral Voltage" [12] - [17] that we will name in this paper V_{NN} . The method has performance comparable to MCSA or better is based on the analysis of the potential difference between the neutral of star-connected stator and the neutral network in the case of a direct feed or artificial neutral in the case of a supply voltage by inverter in order to detect a rotor fault in induction machine.

In addition, by using this signal we follow the same steps as G.DIDIER [9] who has developed a method by MCSA for the detection of rotor faults without need to reference, this reference obtained in a healthy functioning. This approach is based on standard deviation calculations taken on two

frequency ranges, the first standard deviation will be calculated on the first frequency range, this range identifies where the phase jump whose frequency $(3-4s)fs$. The second standard deviation is a picture of measurement noise present between jumps being located at frequencies $(3-4s)fs$ and $(3-6s)fs$.

Thereafter, an analysis of phase spectra by the Hilbert transform is made, this transform is usually used in image processing, where the phase contains more relevant information than its module, its advantage is that the Hilbert transform calculated from the amplitude spectrum of the signal to analyze, which allows to conclude on the nature of fault.

This paper is organized as follows. Section II presents the theory background that we use in this study. The neutral voltage signal analysis NVSA is described in Section III. Proposed method is presented and explained in Section IV. In Section V, experimental results are validated and discussed.

II. THEORY BACKGROUND

The purpose of this section is to present some mathematical signal processing notions used to develop the studied method. To permit the reader to navigate the various strands, this section is subdivided into three main topics: Fourier and Hilbert transform, discrete Hilbert transform and standard deviation.

A. Phase Fourier transform

Recall the mathematical equation of the Fourier transform of a finite sequence $\{ps(0), \dots, P(N-1)\}$

$$\mathcal{F}(k) = \frac{1}{N} \sum_{n=0}^{N-1} p_s(n) e^{-j\frac{2\pi nk}{N}} \quad (1)$$

By applying this relationship, the result is a complex signal with a real part and an imaginary part such as:

$$\mathcal{F}(k) = \Re(\mathcal{F}(k)) + j\Im(\mathcal{F}(k)) \quad (2)$$

In our work we are interested in the form of the phase of NV, the phase of the Fourier transform is given by:

$$\phi_{FT}(k) = \arctan\left(\frac{\mathcal{F}_{\Im(k)}}{\mathcal{F}_{\Re(k)}}\right) \quad (3)$$

B. Hilbert Transform

To start we present first the theory of the Hilbert transform

Let's consider a real measurement signal: $x(t) \in \mathcal{L}^{(2)}$

Where $\mathcal{L}^{(2)}$ is the signal class with integral square

The Hilbert transform of the signal $x(t)$ is : [18][19]

$$\tilde{x}(t) = \mathcal{H}\{x(t)\} = \int_{-\infty}^{\infty} \frac{x(\tau)}{\pi(t-\tau)} d\tau \quad (4)$$

$\tilde{x}(t)$ is improper named the conjugate of $x(t)$, and we also have : $\tilde{\tilde{x}}(t) \in \mathcal{L}^{(2)}$

$x(t)$ is the inverse Hilbert transform of $\tilde{x}(t)$

$$x(t) = \mathcal{H}^{-1}\{\tilde{x}(t)\} = -\frac{1}{\pi} \int_{-\infty}^{\infty} \frac{\tilde{x}(\tau)}{t-\tau} d\tau \quad (5)$$

Let's observe that $\tilde{x}(t)$ is determined by the convolution of $x(t)$ with the signal $1/\pi t$:

$$\tilde{x}(t) = x(t) * \frac{1}{\pi t} \quad (6)$$

Like Fourier transforms, Hilbert transforms are linear operators.

The above relation allows the calculus of the spectral density of $\tilde{x}(t)$:

$$\tilde{X}(j\omega) = X(j\omega) \cdot \mathcal{F}\left\{\frac{1}{\pi t}\right\} \quad (7)$$

Since:
$$\mathcal{F}\left\{\frac{1}{\pi t}\right\} = -j \operatorname{sgn}(\omega)$$

It results:
$$\tilde{X}(j\omega) = X(j\omega)[-j \operatorname{sgn}(\omega)] \quad (8)$$

Or:

$$\tilde{X}(j\omega) = \begin{cases} -jX(j\omega), \omega > 0 \\ jX(j\omega), \omega < 0 \end{cases} \quad (9)$$

As a result, the spectral density function of the $x(t)$ signal's conjugate is obtained by changing the phase of the spectral density for $X(j\omega)$ by $\pm\pi/2$. And it results:

$$\tilde{x}(t) = \mathcal{H}\{x(t)\} = \mathcal{F}^{-1}\{\tilde{X}(j\omega)\} \quad (10)$$

Taking into account relation (8) it results:

$$x(t) = -\mathcal{H}\{\tilde{x}(t)\} = \begin{cases} -\mathcal{F}^{-1}\{j\tilde{X}(j\omega)\}, \omega > 0 \\ \mathcal{F}^{-1}\{-j\tilde{X}(j\omega)\}, \omega < 0 \end{cases} \quad (11)$$

The analytic signal

A useful point of view to understand and to compute the Hilbert Transform of $x(t)$ is using the analytic signal $z(t)$ associated with $x(t)$, defined, as explained before, as:

$$z(t) = x(t) + j\tilde{x}(t) \quad (12)$$

That can be rewritten also as:

$$z(t) = A(t) * e^{j\theta(t)} \quad (13)$$

Where $A(t)$ is called the envelope signal of $x(t)$ and $\theta(t)$ is called the instantaneous phase signal of $x(t)$. In terms of $x(t)$ and $\tilde{x}(t)$, it is clear that:

The use of Hilbert phase analysis is applied to the module of Fourier transformation frequency of the signal $x(t)$. Indeed, the analytic signal and the corresponding phase are given by:

$$A(t) = [x^2(t) + \tilde{x}^2(t)]^{1/2} \quad (14)$$

$$\phi(t) = \tan^{-1}\left[\frac{\tilde{x}(t)}{x(t)}\right] = 2\pi f_0 t \quad (15)$$

Or:

$$\phi(f) = \arctan\left[\frac{\mathcal{H}[|X(f)|]}{|X(f)|}\right] \quad (16)$$

And the "instantaneous frequency" is given by:

$$f_0 = \left(\frac{1}{2\pi}\right) \tan^{-1}\left[\frac{\tilde{x}(t)}{x(t)}\right] \quad (17)$$

C. Discrete Hilbert Transform

Having the signal $x(t)$ defined on the time interval $[0, t_N]$ using a sampling period T_e , we obtain the discrete signal $x[n]$:

$$x(n) = x(nT_e), n \in \overline{0, N-1} \quad (18)$$

Where: $T_e = t_N/N$

The sampling frequency f_e is chosen so that the frequency $f_e/2$ is greater or equal to the least significant frequency from the spectrum of $x(t)$. We consider the discrete frequency step:

$$f_0 = \frac{f_e}{N}, \quad \omega_0 = \frac{2\pi}{N} f_e \quad (19)$$

The discrete Fourier transform (DFT) is:

$$TFD\{x[n]\} = X[k] = \sum_{n=0}^{N-1} x[n] e^{-jnk \frac{2\pi}{N}}, k \in \overline{0, N-1} \quad (20)$$

The sample of the spectral density corresponding to frequency $k\omega_0$ is determined with the relation:

$$X(jk\omega_0) = T_e X[k] \quad (21)$$

Where $X(j\omega)$ is the Fourier transform in continuous time.

On the other hand:

$$X[k]^* = X[N-k] = X[-k] \quad (22)$$

Which show that the sample $X[N-k]=X[-k]$ has a correspondent sample of the spectral density, with the negative frequency $X(-k\omega_0)$.

Similarly to (10) the discrete Hilbert transform is defined as:

$$\mathcal{H}\{x[n]\} = \tilde{x}[n] = TFD^{-1}\{\tilde{X}[k]\} \quad (23)$$

Where for N-even:

$$\tilde{X}[k] = \begin{cases} -jX[k], k = 1, \frac{N}{2}-1, \text{Neven} \\ jX[k], k = \frac{N}{2}+1, N-1, \text{Neven} \end{cases} \quad (24)$$

D. Standard deviation formula:

The RMS can be computed in the frequency domain, using Parseval's theorem. For a sampled signal

$$\sum_n x^2(t) = \frac{\sum |X(f)|^2}{n} \quad (25)$$

Where $X(f)=FFT\{x(t)\}$ and n is number of $x(t)$ samples.

In this case, the RMS computed in the time domain is the same as in the frequency domain:

$$RMS = \sqrt{\frac{1}{n} \sum_n x^2(t)} = \sqrt{\frac{1}{n^2} \sum_n |X(f)|^2} \quad (26)$$

If is the arithmetic mean and is the standard deviation of a waveform then:

$$x_{rms}^2 = \tilde{x}^2 + \sigma_x^2 \quad (27)$$

The standard deviation (represented by the Greek letter sigma, σ) shows how much variation or dispersion from the average exists, and it's defined by:

$$\sigma_x = \sqrt{\frac{1}{N-1} \sum_{i=1}^N \left(x_i - \frac{1}{N} \sum_{i=1}^N x_i \right)^2} \quad (28)$$

III. NEUTRAL VOLTAGE SIGNAL ANALYSIS (NVSA)

A. NVSA frequency

1998, M.A.Cash [12] used the voltage between the neutral of the supply voltage and the neutral of induction machines (Fig. 1) to detect short circuits between spiral in stator coils. A similar analysis was carried out by [14] [15] in order to detect rotor fault in induction machines.

The voltage between the neutral and the neutral WRIM of the power source is given by the following mathematical relationship:

$$V_{NN} = R_a I_{sa} + L_a \frac{dI_{sa}}{dt} + \frac{dL_a}{d\theta} \Omega I_{sa} - V_{Supply} \quad (29)$$

Where:

- R_a represents the stator-phase resistance,
- L_a his inductance,
- I_{sa} the current passing through it,
- Ω Rotation speed, θ the angular position of the rotor and V_{supply} simple voltage generated by network supply.

The presence of a fault rotor reveals additional components in the spectrum of NV. Indeed, M.E.K. OUMAMMAR [17] demonstrated by a complex analysis, that the appearance of a rotor fault induces additional components in the frequency spectrum of the NV at frequencies given by the relation:

$$f_h = \lfloor 3h - (3h \pm 1)s \rfloor f_s \quad (30)$$

s : slip, f_s : supply frequency, $h = 1, 3, 5, \dots$

The speed ripple induced additional harmonic components around the previous frequency, and the frequencies of all components can be expressed as follows:

$$f_h = \lfloor 3h(1-s) \pm s(1+2k) \rfloor f_s \quad (31)$$

B. FFT Analysis

The information given by the spectrum of the voltage at the third harmonic [11], i.e., nears the spectral line having the frequency 150 Hz can be used for WRIM fault diagnosis. We present in Fig.3 the power spectral density of NV for a rotor fault near this harmonic. We note the presence of the main frequency component (2) and additional components around these main components.

It is important to note that the rotor fault is created by adding an extra resistance on one of the rotor phase in order to have a dissymmetry in the rotor. For that the value of the rotor resistance has been progressively varied during the experiment from $R_{add} = 0$ to $R_{add} = 1.25R_r$, from this variation we can see its effect on the spectrum of the NV according to (27), the value of $f_{fault} = 145$ Hz.

In fig.2 is shown that the magnitude of the characteristic harmonic frequency due to a rotor fault changes as function of the additional resistance.

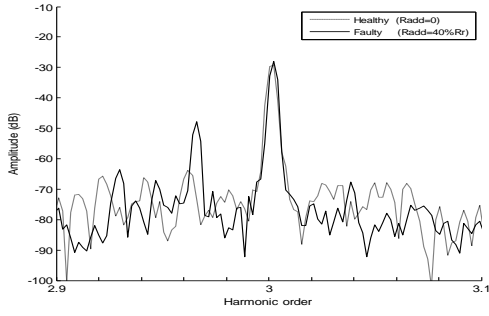


Fig. 1. Experimental results for the WRIM. Spectrum of neutral voltage in healthy (light black solid line) and faulty (solid line)

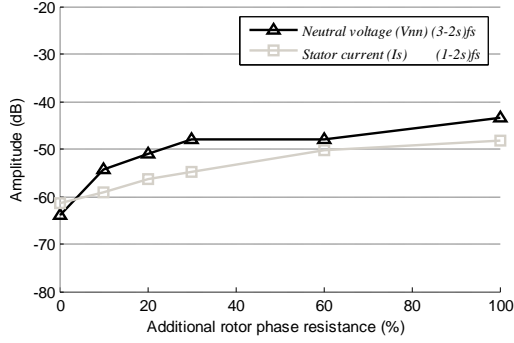


Fig. 2. Effect of a faulty operating conditions given by an increment of the rotor-phase resistance (neutral voltage and stator current)

IV. PROPOSED METHOD

In this work we perform a rotor fault diagnosis based on standard deviation calculation, for that we propose an algorithm to decision making by analyzing the exclusive NV signal.

Studies [15] [16] have shown that all asynchronous machines have a slight asymmetry of construction induced, in the spectrum of NV, a frequency component:

$$f_h = \lfloor 3h(1-s) \pm s(1+2k) \rfloor f_s \quad (32)$$

This method has been developed by G.DEDIER who used it on stator current analysis. We follow the same steps and we study first the phase $\varphi F(f)$, particularly the jump present at the frequency $(3-4s)f_s$. Normally, this phase jump is very small or even zero for a healthy induction machine whatever the level of load. For the studied machine, figure 4 shows this slight fluctuation.

We propose the detection of a rotor fault by studying exclusively the phase jump located at the frequency $(3-4s)f_s$. We compare the standard deviation of the phase $\varphi H(f)$ and the phase $\varphi F(f)$ based on two different frequency ranges. Indeed, the first standard deviation, noted σ_j will be calculated on the frequency range (R_1), this range identifies where is the phase jump whose frequency $(3-4s)f_s$. The second standard deviation, which we note σ_n will be calculated on the frequency range (R_2) This standard deviation is a picture of measurement noise

present between jumps being located at frequencies $(3-4s)f_s$ and $(3-6s)f_s$.

$$R_1 = \left[(3-4s)f_s - \frac{\delta}{2}, (3-4s)f_s + \frac{\delta}{2} \right] \quad (33)$$

$$R_2 = \left[(3-4s)f_s - \frac{\delta}{2}, (3-6s)f_s + \frac{\delta}{2} \right] \quad (34)$$

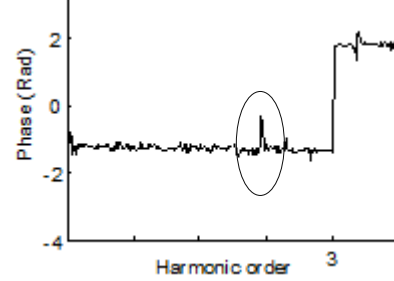


Fig. 3. Fluctuations at Spectrum phase in healthy case

The mathematical relationship to calculate the standard deviation σ_v , unbiased, of the Neutral Voltage is:

$$\sigma_v = \sqrt{\frac{1}{N-1} \sum_{i=1}^N \left(v_n - \frac{1}{N} \sum_{i=1}^N v_n \right)^2} \quad (35)$$

Fig. 5 shows a representation for an adequate understanding of the calculation of these deviations. The standard deviation σ_j is calculated on the gray frequency range while the standard deviation σ_n is calculated on the black frequency range.

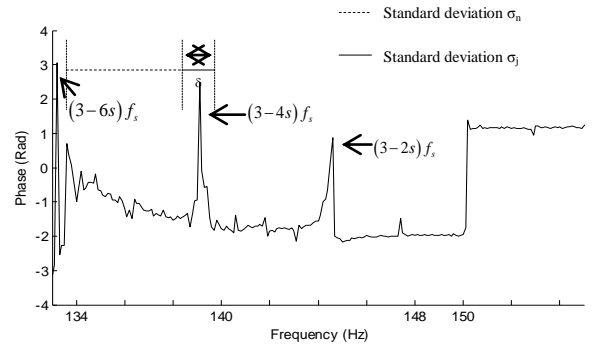


Fig. 4. Calculation of standard deviations σ_j and σ_n

For the further diagnosis it is necessary to calculate the slip s of the machine in both frequency ranges R_1 and R_2 .

In most machines, the jump located at the frequency $(3-4s)f_s$ is always present in the Fourier and Hilbert phase, it adds that is this jump is more pronounced among other jumps (same thing for stator current phase, where $(1-2s)f_s$ is the most pronounced in the spectrum). The calculation of this shift will inform us about the frequency $(3-4s)f_s$ desired. The detection of the jump located at the frequency $(3-2s)f_s$ is given since we know the fundamental frequency f_s .

The maximum slip of the machine allows obtaining the minimum frequency:

$$f_{def_{min}} = (3 - 2s_{max})f_s \quad (36)$$

The proposed methodology to diagnose rotor fault in WRIM is shown in Fig. 5 Based on these algorithm we present in the next section some experimental results to validate the proposed method.

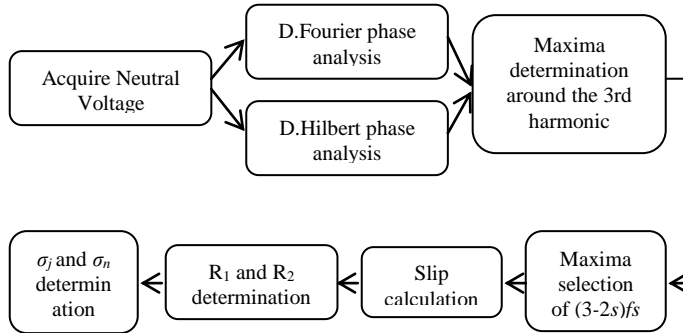


Fig. 5. Proposed methodology

V. RESULTS AND DISCUSSION:

The diagnostic procedure presented in this paper has been tested through an off-line approach in which different degrees of additional resistance to create the rotor asymmetry have been forced in the WRIM.

A. Experimental Setup

Experimental Tests were developed on a 3kW, 50Hz, 220V/380V, 4-poles Wound Rotor Induction Machine (Table.IV and V). The motor was directly coupled direct current machine acting as a load. Two voltage sensors are used to monitor the induction machine operation. The IM voltages are measured by means of the two sensors which are used as inputs of the signal conditioning and the data acquisition board integrated into a personal computer.

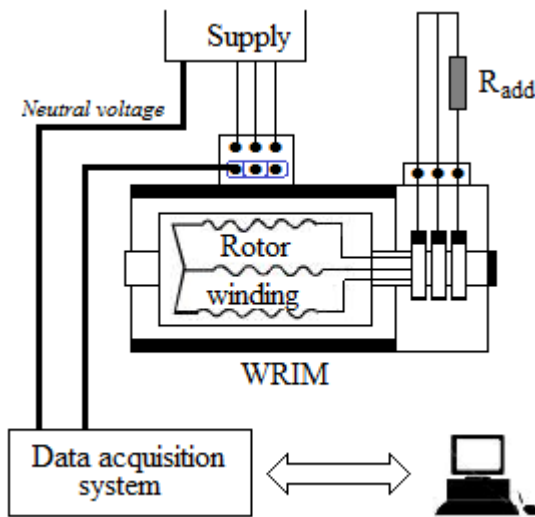


Fig. 6. Experimental set-up

For those two variables, the sampling frequency was 2 kHz and each data length was equal to 2^{14} values. Eight data sets of induction machines neutral voltage subject to different

numbers of rotor fault and load conditions were analyzed (Table I).

TABLE I ANALYZED DATA SETS

Set	Machine condition
s1	Healthy, unloaded
s2	Healthy, 75% Load
s3	Healthy, Full load
s4	Fault, unloaded
s5	Fault, 75 % load, $R_{add}=10\%R_r$
s6	Fault, 75 % load, $R_{add}=20\%R_r$
s7	Fault, 75 % load, $R_{add}=100\%R_r$
s8	Fault, 100 % load, $R_{add}=10\%R_r$

B. Method diagnosis based on Fourier transform phase analysis

In this section, we apply the detection method described above on NV when the machine is directly connected to the three-phase network.

The results are presented in Table II, the first column of this table corresponds to the rotor state, the second gives the value of the frequency $(3-2s)f_s$, third and fourth in succession values σ_j and σ_n calculated on the frequency ranges R_1 and R_2 , the fifth gives σ_j/σ_n report that allows the decision making by the last column. Thus, we represent in Fig.6 curve $\varphi F(f)$ phases for s2, s4,s5,s6,s7 and s8 tests.

According to the column giving σ_j/σ_n report we note that it is low for a machine operating with a healthy rotor, then we perceive that for some healthy functioning we do not detect jump phase $(3-2s)f_s$ in this case we consider the rotor in good condition.

The appearance of a partial rotor fault does not induce a significant increase of σ_j relative to σ_n , which does not allow to conclude on such a failure, it may be the low point method using $\varphi F(f)$. For an important rotor fault (s8) we note that this report is greater 10 times that in tests where the machine is healthy

From the results of the Table II, we can validate the proposed approach, even if σ_j/σ_n report in tests s6 and s5 is less pronounced as seen in Table II, but the results are satisfactory.

According to Fig. 7 and Table II, the first problem for this approach is the high level of noise in the frequency range studied. The second problem is the wrong detection of the phase jump at frequencies located at frequency characterizing the rotor fault for the NVSA. In fact, the presence of random phase jumps in the frequency range does not allow proper detection of the phase jump required to calculate the slip.

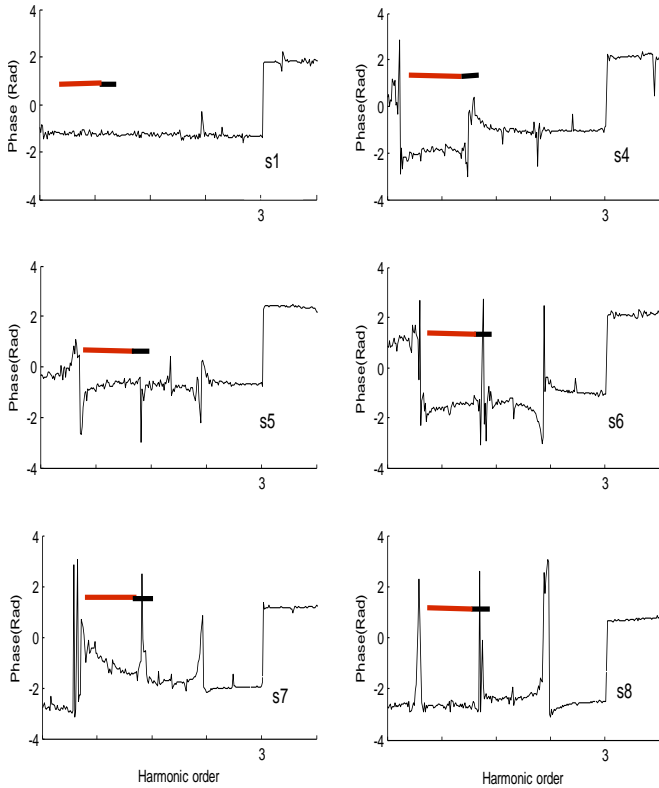


Fig. 7. Standard deviations σ_j and σ_n calculation by $\phi F(f)$

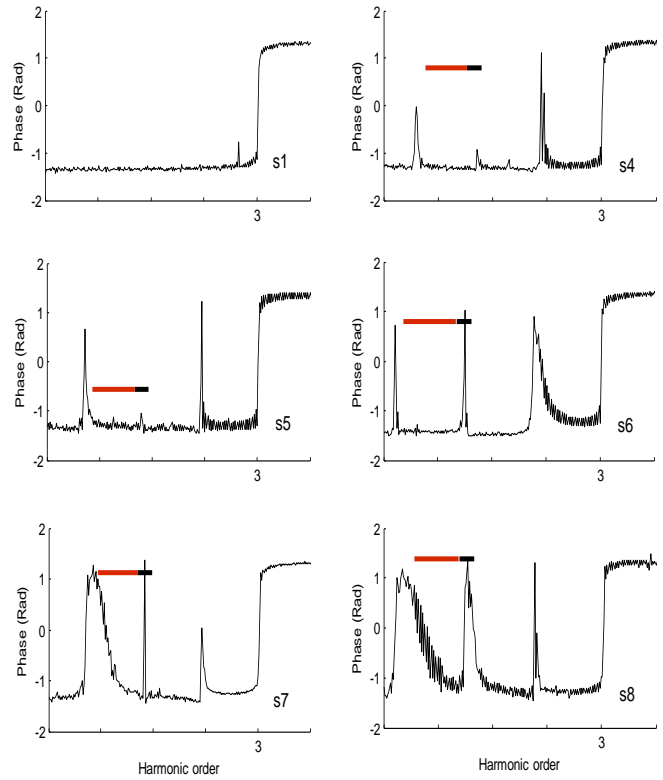


Fig. 8. Standard deviations σ_j and σ_n calculation by $\phi \mathcal{H}(f)$

TABLE II RESULTS OF DIAGNOSTIC METHOD APPLIED TO THE PHASE OF THE FOURIER TRANSFORM

Rotor state	(3-2s) f _s (Hz)	(3-4s) f _s (Hz)	σ_n	σ_j	$\frac{\sigma_j}{\sigma_n}$
s1	No max detection				
s2	No max detection				
s3	145.23	139.19	0.240	0.091	2.64
s5	144.40	138.81	0.065	0.063	1.03
s8	146.33	140	0.969	0.026	37.30
s4	144.40	138.81	0.240	0.091	2.64
s6	143.8	138	0.51	0.079	6.52
s7	142.95	137.31	0.42	0.051	8.34

C. Hilbert transform phase analysis

We have already seen that even the good results that phase spectrum analysis compared to the module spectrum analysis, this method has two drawbacks.

- 1) The noise level is high, which makes detection difficult.
- 2) The second is that the form of the phase is not fixed. Indeed, the real and imaginary parts can take random values.

To stabilize the form of phase, we must find a solution to control the values of the real and imaginary parts of the spectrum, the idea is to obtain a phase always equal to $[-\pi/2]$ to the left of f_s and equal to $[\pi/2]$ right f_s , the real part must be zero at frequencies $\pm f_{def}$ and f_s .

These problems can be circumvented with the use of the Hilbert transform, as we will see below.

In order to support the results obtained, we give in Fig. 8 the curves of phase $\phi \mathcal{H}(f)$ with different fault level. In these figures, we stand once again by a continuous gray line the frequency range where the standard deviation σ_j is calculated, for a continuous black line the frequency range where the standard deviation σ_n is calculated, and a red line the maximum of the phase jump at the frequency located at $(3-2s)f_s$.

By use of the Hilbert transform (Table III), the two sets s4 and s5 were detected which is not the case when using the Fourier transform. Except this particular case, the results are better than those given in Table II. This better detection is possible because the noise in the phase of the signal analysis is much less important when the machine is running at low load torque. In addition, it is important to note that the signals obtained by the Hilbert transform are much less noisy than those calculated from the Fourier transform.

We show in Fig. 9 a comparison between the Hilbert approach and Fourier one in both healthy and faulty cases. We note that the σ_j/σ_n report does not vary too much despite the variation in the load level. In the defective case we see a notable variation between fault conditions.

From Fig.9, we note that the σ_j/σ_n report does not exceed 3 for a healthy machine and it is greater than 3 for a defective machine. This conclusion led the authors in [9] to operate to make an induction machine diagnosis method without reference (this reference usually obtained from a healthy functioning). In other words if the report σ_j/σ_n is less than 3

then the machine is healthy, and defective if greater than 3.

From this result we can draw a law diagnostic decision support such as that given by G.DEDIER[9].

TABLE III RESULTS OF DIAGNOSTIC METHOD APPLIED TO THE PHASE OF THE HILBERT TRANSFORM

Rotor state	(3-2s)fs (Hz)	(3-4s)fs (Hz)	σ_n	σ_j	$\frac{\sigma_J}{\sigma_N}$
s1	No max detection				
s2	145.23	139.19	0.384	0.108	3.56
s3	145.23	139.19	0.105	0.073	1.45
s5	144.40	138.81	0.056	0.005	10.64
s8	146.33	140	0.29	0.003	79.30
s4	144.40	138.81	0.015	0.007	2.15
s6	143.8	138	0.302	0.006	48.01
s7	142.95	137.31	0.36	$\frac{0.006}{3}$	56.3

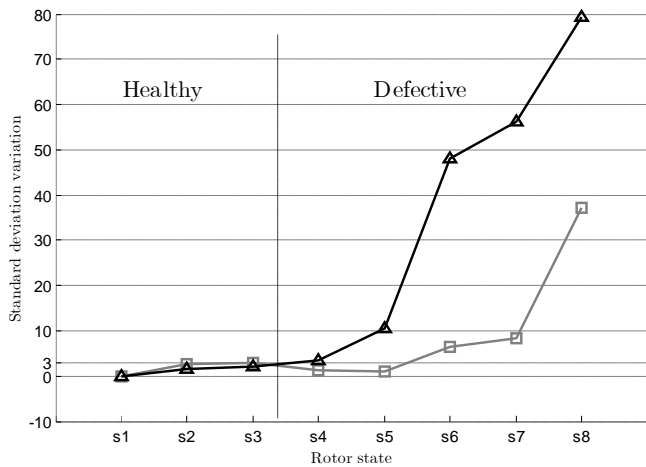


Fig. 9. Hilbert (Black line) and Fourier Transform (Gray line) method comparison

VI. CONCLUSION

Two approaches have been proposed to diagnose rotor fault. The first approach is based on the calculation of Fourier transform phase of Neutral Voltage. This phase contained relevant information on the status of the asynchronous machine. The results are relatively interesting.

To improve fault diagnosis, a second approach has been proposed. This method uses the same approach as described above, the only difference lies in the fact that this is not the phase of the Fourier transform of the Neutral Voltage which is analyzed by the program decision, but the phases of the analytic signal obtained by Hilbert transform of the amplitude spectrum of Neutral Voltage. This analysis helped to detect other defects that were not detected by the first approach.

In conclusion, the latest proposed method provides more meaningful results that the analysis of the phase spectrum of Neutral Voltage. Similarly, it would be interesting to validate this approach on asynchronous machines with different characteristics (higher power machines for example) to help

determine a law of behavior for α parameter used in the detection criterion.

APPENDIX

TABLE IV WRIM PARAMETERS

Parameter	Value
Rated power	kW 3
Rated stator voltage	V 220
Rated frequency	Hz 50
Rated speed	rpm 1400
Stator phase resistance	Ω 0.621
Rotor phase resistance	Ω 0.4
Rotor inductance	H 0.013
Pole pairs	2

TABLE V WRIM SENSORS

Parameter	Value
Current sensor type	LA100
Current sensor accuracy	% 0.45
Current sensor Bandwidth	kHz 200
Voltage sensor type	DV1200
Voltage sensor accuracy	% 0.3
Voltage sensor Bandwidth	kHz 6.5

REFERENCES

- [1] F.Filippetti, A.Bellini and G.A. Capolino " Condition Monitoring and Diagnosis of Rotor Faults in Induction Machines: State of Art and Future Perspectives" *Electrical Machines Design Control and Diagnosis (WEMDCD), IEEE Workshop on pp. 196 – 209, 2013*
- [2] A. Bellini, F. Filippetti, C. Tassoni, and G. Capolino, "Advances in diagnostic techniques for induction machines," *Industrial Electronics, IEEE Transactions on, vol. 55, no. 12, pp. 4109–4126, 2008.*
- [3] Mohamed El Hachemi Benbouzid, "A Review of Induction Motors Signature Analysis as a Medium for Faults Detection" *IEEE Transactions on industrial electronics, vol. 47, no. 5, pp. 984-993 , october 2000*
- [4] S. Nandi, H. Toliyat, and X. Li, "Condition monitoring and fault diagnosis of electrical motors review," *IEEE Transactions on Energy Conversion, vol. 20, no. 4, pp. 719–729, Dec. 2005.*
- [5] P. Zhang, Y. Du, T. G. Habetler, and B. Lu, "A survey of condition monitoring and protection methods for medium-voltage induction motors," *IEEE Transactions on Industry Applications, vol. 47, no. 1, pp. 34–46, 2011.*
- [6] Y. Gritli, L. Zarri, C. Rossi, F. Filippetti, G. Capolino, and D. Casadei, "Advanced diagnosis of electrical faults in wound rotor induction machines," *IEEE Transactions on Industrial Electronics, , p. 1, 2013.*
- [7] J. H. Jung, J. J. Lee, and B. H. Kwon, "Online diagnosis of induction motors using MCSA," *IEEE Transactions on Industrial Electronics, vol. 53, no. 6, pp. 1842–1852, Dec. 2006.*
- [8] A. Espinosa, J. Rosero, J. Cusido, L. Romeral, and J. Ortega, "Fault detection by means of hilbert-huang transform of the stator current in a pmsm with demagnetization," *Energy Conversion, IEEE Transactions on, vol. 25, no. 2, pp. 312 –318, june 2010.*
- [9] G. Didier, E. Ternisien, O. Caspary, H. Razik "A new approach to detect broken rotor bars in induction machines by current

spectrum analysis” *Mechanical Systems and Signal Processing* 21 pp. 1127–1142, 2007

- [10] M. E. K. Oumaamar, H. Razik, A. Rezzoug, A. Khezzar “Line Current Analysis for Bearing Fault Detection Induction Motors Using Hilbert Transform Phase” *acemp, Electromotion 2011*, pp. 289-294, 8-10 Sept 2011, Istanbul (Turkey).
- [11] Yuefeng Liao, Thomas A. Lipo, “Effect of saturation third harmonic on the performance of squirrel-cage induction machines” *Electric Machines & Power Systems*, vol. 22, no2, pp. 155-171, 1994
- [12] M. A. Cash, T. G. Habetler, G. B. Kliman, “Insulation Failure Prediction in AC Machines Using Line-Neutral Voltages”, in *IEEE Transactions on Industry Applications*, Vol. 34, No 6, pp. 1234–1239, November/December 1998.
- [13] H. Razik and G. Didier, “A novel method of induction motor diagnosis using the line-neutral voltage,” in *Proc. EPE-PEMC, Riga, Latvia, Sep. 2004*.
- [14] M.E.K. OUMAAMAR « Surveillance et diagnostic des défauts rotoriques et mécaniques de la machine asynchrone avec alimentation équilibrée ou déséquilibrée » *PhD thesis (Groupe de Recherche en Electrotechnique et Electronique de Nancy GREEN-UdL Faculté des Sciences et Technologies) March 2012*
- [15] Khezzar, A.; Oumaamar, M. E. K.; Hadjami, M.; Boucherma, M.; Razik, H.; “Induction Motor Diagnosis Using Line Neutral Voltage Signatures”, *Industrial Electronics, IEEE Transactions on*, Volume 56, Issue 11, Nov. 2009 Page(s):4581 – 4591.
- [16] M.E.K. Oumaamar, F. Babaa, A. Khezzar and M. Boucherma, “Diagnostics of Broken Rotor Bars in Induction Machines Using the Neutral Voltage”, *ICEM’2006 Conference. Chania. Greece, 2- 5 September 2006*.
- [17] M.E.K. Oumaamar, A. Khezzar, M. Boucherma, H. Razik, R. Andriamalala, L. Baghli, "Neutral Voltage Analysis for Broken Rotor Bars Detection in Induction Motors Using Hilbert Transform Phase" , *IAS 2007,43rd Annual meeting, New Orleans (USA),23-27 pp. 1940 - 1947 september.2007*
- [18] J. Antonino-Daviu, M. Riera-Guasp, M. Pineda-Sanchez, and R. Perez, “A critical comparison between dwt and hilbert Huang-based methods for the diagnosis of rotor bar failures in induction machines,” *Industry Applications, IEEE Transactions on*, vol. 45, no. 5, pp. 1794 –1803, sept.-oct. 2009.
- [19] Liru Han “ Gear fault detection and diagnosis based on Hilbert-Huang transform” *Image and Signal Processing (CISP), 3rd International Congress on* , Vol. 7 pp 3323 – 3326 , 2010



Dr. Said GUEDIRA, Professeur at ENIM (Ecole Nationale de l’Industrie Minérale - Rabat - Morocco) since 1983. Research Engineer and Director of the research laboratory CPS2I (Control, protection et surveillance des installations industrielles). Author of several publications in the field of Electrical Engineering, including diagnosis and control of mechatronic systems.



Khalid Dahi was born in Errachidia, Morocco, in 1988. He received the M.S. degree in electrical engineering in 2012 from the Mohammed V Souissi University, Rabat-Morocco- where he is currently working toward the Ph.D. degree in the department of electrical engineering. Since 2012, His research interests are related to electrical machines and drives, diagnostics of induction motors. His current activities include monitoring and diagnosis of

induction machines in wind motor.



Dr. Soumia El Hani, Professor at the ENSET (Ecole Normale Supérieure de l’Enseignement Technique-Rabat, Morocco) since October 1992. Research Engineer at the Mohammed V Souissi University Morocco. In charge of the research team electromechanical, control and diagnosis. Member of the eesearch eaboratory in electrical engineering at ENSET -Rabat. In charge of electrotechnic and power electronic competences group. Author of several publications in the field of electrical

engineering, including robust control systems, diagnosis and control systems of wind electric conversion.

A Seven-Term Novel 3-D Chaotic System with Three Quadratic Nonlinearities and its LABVIEW Implementation

Sundarapandian Vaidyanathan, Christos K. Volos, Ionnis M. Kyprianidis, Ioannis N. Stouboulos, Karthikeyan Rajagopal, and Prasina Alexander

Abstract—This paper introduces a seven-term novel 3-D chaotic system with three quadratic nonlinearities and discusses its qualitative properties. The new 3-D chaotic system has three unstable equilibrium points. The Lyapunov exponents of the new chaotic system are obtained as $L_1 = 2.71916$, $L_2 = 0$ and $L_3 = -13.72776$. Hence, the maximal Lyapunov exponent (MLE) of the system is obtained as $L_1 = 2.71916$. The Lyapunov dimension of the new chaotic system is obtained as $D_L = 2.19808$. The qualitative properties and the phase portraits of the novel chaotic system have been described in detail. The paper also discusses the LabVIEW implementation of the novel chaotic system.

Keywords—Chaos, stability theory, Lyapunov exponents, LABVIEW.

I. INTRODUCTION

CHAOS theory deals with theory and applications of chaotic systems, which can be defined as nonlinear dynamical systems, which are highly sensitive to small changes in the initial conditions of the states of the systems. Mathematically, chaotic dynamical systems are classified as nonlinear dynamical systems having at least one positive Lyapunov exponent.

In 1963, Lorenz discovered a 3-D chaotic system [1], while he was studying weather patterns. This was followed by the discovery of many 3-D polynomial chaotic systems such as Rössler system [2], Rabinovich system [3], ACT system [4], Chen system [5], Lü system [6], Liu system [7], Harb system [8], Chen-Lee system [9], Cai system [10], Tigan system [11], Pan system [12], Sundarapandian-Pehlivan system [13], Lu-Xiao system [14], Vaidyanathan systems [15-16], etc.

Dr. Sundarapandian Vaidyanathan is with the R & D Centre, Vel Tech University, Avadi, Chennai-600 062, Tamil Nadu, India (phone: +91-04426841622; FAX: +91-04426840605; e-mail: sundarvtu@gmail.com).

Dr. Christos K. Volos is with the Physics Department, Aristotle University of Thessaloniki, Greece (e-mail: chvolos@gmail.com).

Dr. Ionnis M. Kyprianidis is with the Physics Department, Aristotle University of Thessaloniki, Greece (e-mail: imkypr@auth.gr).

Dr. Ioannis N. Stouboulos is with the Physics Department, Aristotle University of Thessaloniki, Greece (e-mail: stouboulos@physics.auth.gr).

Dr. Karthikeyan Rajagopal is with the Velammal Institute of Technology, Chennai-601 204, Tamil Nadu, India (e-mail: rkarthikeyan@gmail.com).

Dr. Prasina Alexander is with the Velammal Institute of Technology, Chennai-601 204, Tamil Nadu, India (e-mail: prasialex@rediffmail.com).

Chaos theory has important applications in a variety of fields like lasers [17-18], oscillators [19-20], chemical systems [21-22], biology [23-24], ecology [25-26], communications [27-28], cryptosystems [29-30], robotics [31-34], true random number generators [35], neural networks [36-38], etc.

Since the pioneering works of Pecora and Carroll [39] and Ott, Grebogi and Yorke [40], chaos control and synchronization problems have received significant attention in the last two decades in the control literature [41-58].

In this paper, we introduce a seven-term novel 3-D chaotic system with three quadratic nonlinearities and discuss its qualitative properties. The new 3-D chaotic system has three unstable equilibrium points (one saddle-point and two saddle-foci).

The Lyapunov exponents of the new chaotic system are obtained as: $L_1 = 2.71916$, $L_2 = 0$ and $L_3 = -13.72776$.

Hence, the maximal Lyapunov exponent (MLE) of the system is obtained as $L_1 = 2.71916$. So, the Lyapunov dimension of the new chaotic system is $D_L = 2.19808$.

The qualitative properties and the phase portraits of the novel chaotic system have been described in detail. Numerical simulations using MATLAB are provided to illustrate phase portraits and the qualitative properties of the novel chaotic system.

Finally, we detail LABVIEW implementation of the seven-term novel chaotic system derived in this paper.

II. SEVEN-TERM NOVEL 3-D CHAOTIC SYSTEM

The 3-D dynamics of the seven-term novel 3-D chaotic system with three quadratic nonlinearities is described by

$$\begin{aligned}\dot{x}_1 &= a(x_2 - x_1) + dx_2x_3 \\ \dot{x}_2 &= bx_1 - x_1x_3 \\ \dot{x}_3 &= x_1x_2 - cx_3\end{aligned}\quad (1)$$

where x_1 , x_2 , x_3 are the states and a , b , c , d are positive parameters of the system.

The 3-D system (1) exhibits a chaotic attractor, when the system parameter values are chosen as:

$$a = 10, \quad b = 15, \quad c = 1, \quad d = 12 \quad (2)$$

We take the initial conditions as:

$$x_1(0) = 0.6, \quad x_2(0) = 1.8, \quad x_3(0) = 1.2 \quad (3)$$

The 3-D portrait of the strange chaotic attractor (1) for the

parameter values (2) and the initial conditions (3) is depicted in Fig.1, and the 2-D portraits are depicted in Figs.2-4.

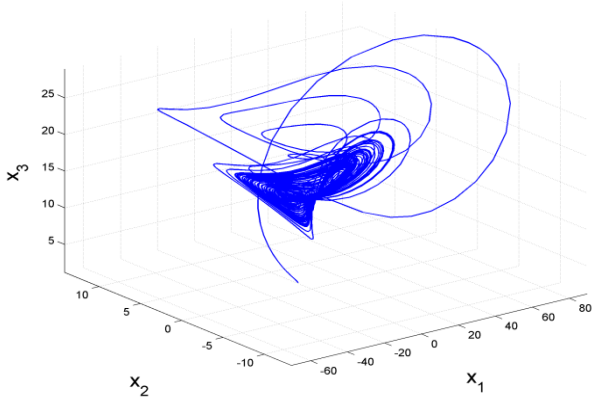


Fig. 1 Strange attractor of the novel chaotic system in R^3

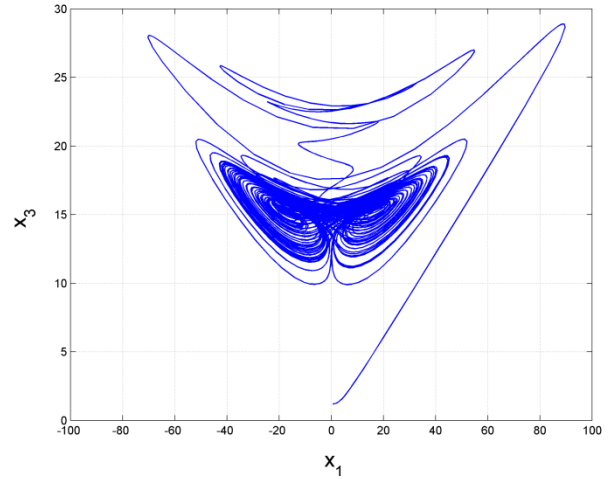


Fig. 4 2-D projection of the novel chaotic system in (x_1, x_3) – plane

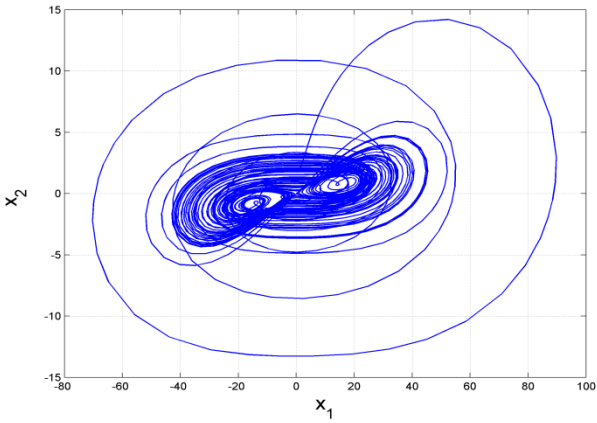


Fig. 2 2-D projection of the novel chaotic system in (x_1, x_2) – plane

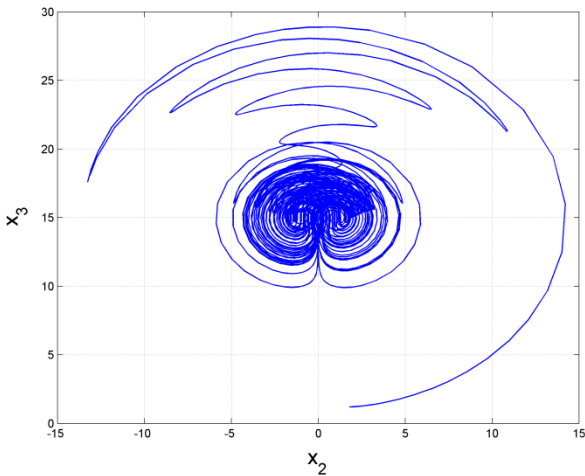


Fig. 3 2-D projection of the novel chaotic system in (x_2, x_3) – plane

III. ANALYSIS OF THE NOVEL 3-D CHAOTIC SYSTEM

A. Symmetry and Invariance

It is easy to see that the system (1) is invariant under the coordinates transformation

$$(x_1, x_2, x_3) \rightarrow (-x_1, -x_2, x_3) \quad (4)$$

which persists for all values of the system parameters. Thus, the system (1) has rotation symmetry about the x_3 -axis and any non-trivial trajectory of the system (1) must have a twin trajectory. It is also easy to see that the x_3 -axis is invariant under the flow of the system (1).

B. Dissipativity

The system (1) can be expressed in vector notation as:

$$\dot{x} = f(x) = \begin{bmatrix} f_1(x) \\ f_2(x) \\ f_3(x) \end{bmatrix} \quad (5)$$

where

$$\begin{cases} f_1(x) = a(x_2 - x_1) + dx_2x_3 \\ f_2(x) = bx_1 - x_1x_3 \\ f_3(x) = x_1x_2 - cx_3 \end{cases} \quad (6)$$

The divergence of the vector field f on R^3 is given by

$$\nabla \cdot f = \frac{\partial f_1(x)}{\partial x_1} + \frac{\partial f_2(x)}{\partial x_2} + \frac{\partial f_3(x)}{\partial x_3} \quad (7)$$

We note that $\nabla \cdot f$ measures the rate at which volumes change under the flow Φ_t of f .

Let D be a region in R^3 with a smooth boundary and let $D(t) = \Phi_t(D)$, the image of D under Φ_t , the time t map of the flow of f . Let $V(t)$ be the volume of $D(t)$.

By Liouville's theorem, we get

$$\frac{dV}{dt} = \int_{D(t)} (\nabla \cdot f) dx_1 dx_2 dx_3 \quad (8)$$

For the system (1), we find that

$$\nabla \cdot f = \frac{\partial f_1(x)}{\partial x_1} + \frac{\partial f_2(x)}{\partial x_2} + \frac{\partial f_3(x)}{\partial x_3} = -(a+c) < 0 \quad (9)$$

because a and c are positive constants.

Substituting (9) into (8) and simplifying, we get

$$\frac{dV}{dt} = -(a+c) \int_{D(t)} dx_1 dx_2 dx_3 = -(a+c)V(t) \quad (10)$$

Solving the first order linear differential equation (10), we obtain the unique solution as

$$V(t) = V(0)e^{-(a+c)t} \quad (11)$$

Eq. (11) shows that any volume $V(t)$ must shrink exponentially fast to zero with time.

Thus, the dynamical system described by (1) is a dissipative system.

As (1) is a dissipative system, all orbits of the system (1) are eventually confined to a specific subset of R^3 that has zero volume.

Hence, the asymptotic motion of (1) settles onto an attractor of the system (1).

C. System Equilibria

We take the parametric values for the system (1) as in the chaotic case, i.e.

$$a = 10, \quad b = 15, \quad c = 1, \quad d = 12 \quad (12)$$

To find the equilibria of the system (1), we solve the system of nonlinear equations

$$\begin{cases} f_1(x) = a(x_2 - x_1) + dx_2 x_3 = 0 \\ f_2(x) = bx_1 - x_1 x_3 = 0 \\ f_3(x) = x_1 x_2 - cx_3 = 0 \end{cases} \quad (13)$$

Solving the system (13), we obtain three equilibria

$$E_1 = \begin{bmatrix} 0 \\ 0 \\ 0 \end{bmatrix}, \quad E_2 = \begin{bmatrix} 16.88194 \\ 0.88852 \\ 15.00000 \end{bmatrix}, \quad E_3 = \begin{bmatrix} -16.88194 \\ -0.88852 \\ 15.00000 \end{bmatrix} \quad (14)$$

To investigate the stability type of the equilibria, we determine the Jacobian matrix of the system (1) at the equilibrium point x^* as

$$J(x^*) = \begin{bmatrix} -a & a + dx_3^* & dx_2^* \\ b - x_3^* & 0 & -x_1^* \\ x_2^* & x_1^* & -c \end{bmatrix} \quad (15)$$

Thus, the Jacobian matrix at E_1 is obtained as:

$$J_1 = J(E_1) = \begin{bmatrix} -10 & 10 & 0 \\ 15 & 0 & 0 \\ 0 & 0 & -1 \end{bmatrix} \quad (16)$$

The eigenvalues of J_1 are obtained as:

$$\lambda_1 = -18.2288, \quad \lambda_2 = -1, \quad \lambda_3 = 8.2288 \quad (17)$$

which shows that E_1 is a saddle point. Hence, E_1 is unstable.

Next, the Jacobian matrix at E_2 is obtained as:

$$J_2 = J(E_2) = \begin{bmatrix} -10 & 190 & 10.6622 \\ 0 & 0 & -16.8819 \\ 0.8885 & 16.8819 & -1 \end{bmatrix} \quad (18)$$

The eigenvalues of J_2 are obtained as:

$$\lambda_1 = -15.7860, \quad \lambda_{2,3} = 2.3930 \pm 18.8508i \quad (19)$$

which shows that E_2 is a saddle-focus. Hence, E_2 is unstable.

Finally, the Jacobian matrix at E_3 is obtained as:

$$J_3 = J(E_3) = \begin{bmatrix} -10 & 190 & -10.6622 \\ 0 & 0 & 16.8819 \\ -0.8885 & -16.8819 & -1 \end{bmatrix} \quad (20)$$

The eigenvalues of J_3 are obtained as:

$$\lambda_1 = -15.7860, \quad \lambda_{2,3} = 2.3930 \pm 18.8508i \quad (21)$$

which shows that E_3 is a saddle-focus. Hence, E_3 is unstable.

Hence, all the three equilibria of the system (1) are unstable.

D. Lyapunov Exponents and Lyapunov Dimension

We take the parametric values for the system (1) as in Eq.(12) and the initial conditions of the system (1) as:

$$x_1(0) = 0.6, \quad x_2(0) = 1.8, \quad x_3(0) = 1.2 \quad (22)$$

The Lyapunov exponents of the system (1) are obtained as:

$$L_1 = 2.71916, \quad L_2 = 0, \quad L_3 = -13.72776 \quad (23)$$

The maximal Lyapunov exponent (MLE) of the chaotic system is given by $L_1 = 2.71916$. The Lyapunov dimension of the novel chaotic system is calculated as:

$$D_L = 2 + \frac{L_1 + L_2}{|L_3|} = 2.19808 \quad (24)$$

The dynamics of the Lyapunov exponents of the novel chaotic system (1) is shown in Fig.5.

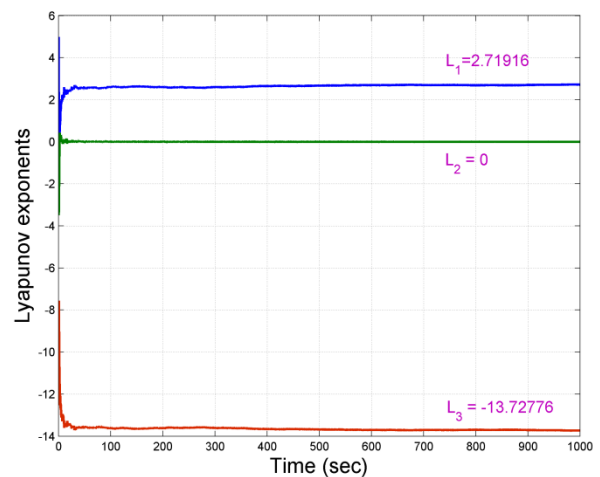


Fig. 5 Lyapunov exponents of the novel chaotic system

IV. LABVIEW IMPLEMENTATION AND SIMULATIONS OF THE NOVEL CHAOTIC SYSTEM

In this section, the proposed novel chaotic system is digitally implemented in LabVIEW. For implementing, the Control and Simulation loop of LabVIEW is used. Figure 6 shows the implemented system using LabVIEW. Figures 7, 8 & 9 shows the time versus the states plot obtained from the LabVIEW simulation.

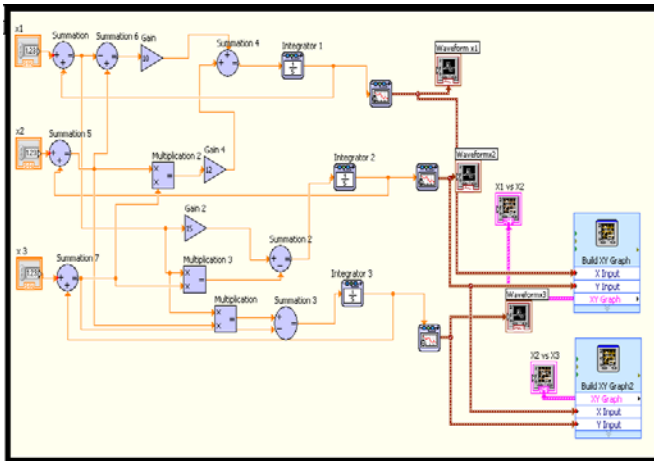


Fig. 6 LabVIEW implementation of the novel chaotic system

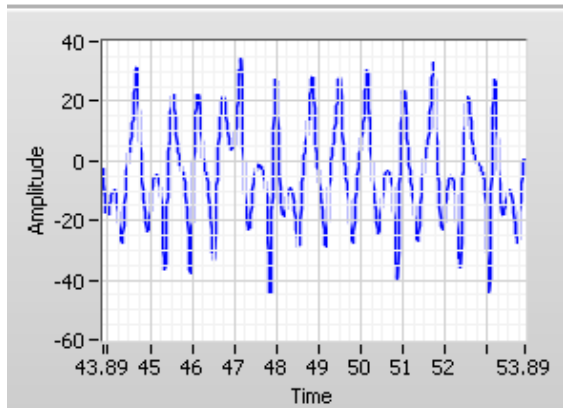


Fig. 7 Time versus x_1 of the novel chaotic system

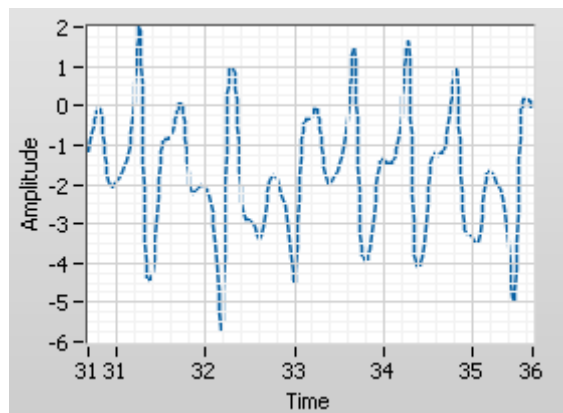


Fig. 8 Time versus x_2 of the novel chaotic system

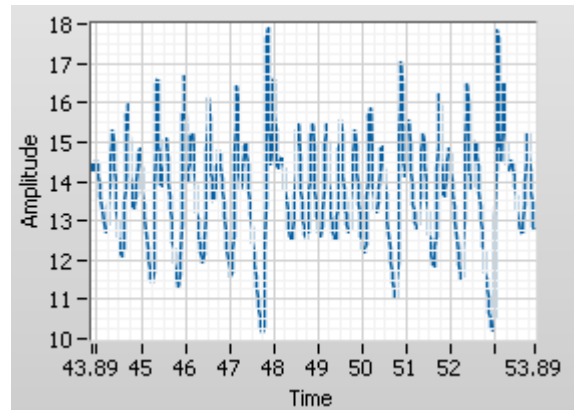


Fig. 9 Time versus x_3 of the novel chaotic system

Figures 10, 11 and 12 show the 2-D projection of the novel chaotic system in (x_1, x_2) -plane, (x_2, x_3) -plane and (x_1, x_3) -plane respectively.

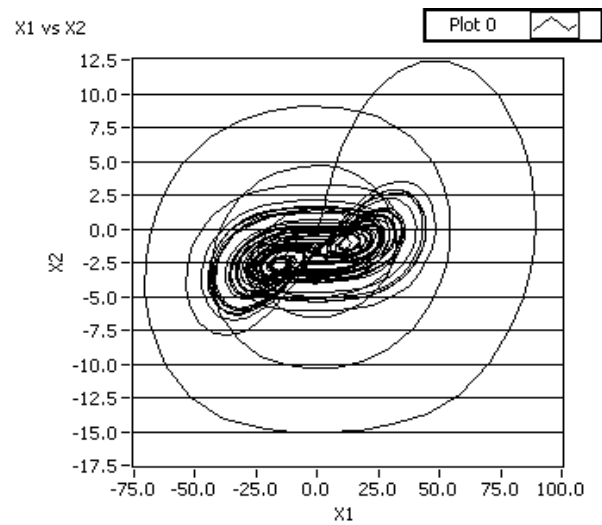


Fig. 10 2-D projection of the novel chaotic system in (x_1, x_2) -plane

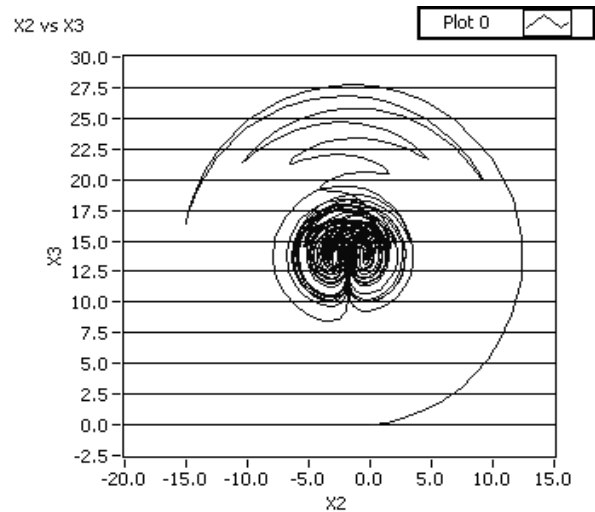


Fig. 11 2-D projection of the novel chaotic system in (x_2, x_3) -plane

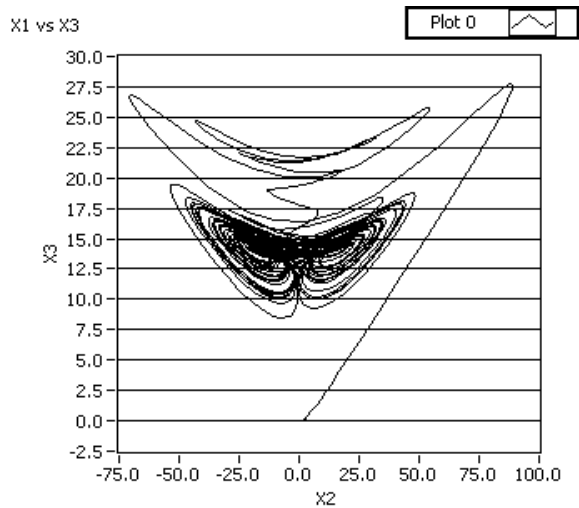


Fig. 12 2-D projection of the novel chaotic system in (x_1, x_3) -plane

V. CONCLUSION

In this paper we have proposed a Novel chaotic system with three quadratic non linearities. The proposed system is then proved for the properties of being a chaotic system. The Lyapunov exponents of the system are $L_1 = 2.71916$, $L_2 = 0$, $L_3 = -13.72776$. The proposed system is then digitally implemented in LabVIEW using control and simulation loop. The state portraits and time varying behavior of the proposed system are studied using LabVIEW.

REFERENCES

[1] E. N. Lorenz, "Deterministic nonperiodic flow," *J. Atmospheric Sciences*, vol. 20, pp. 130–141, 1963.

[2] O. E. Rössler, "An equation for continuous chaos," *Physics Letters*, vol. 57A(5), pp. 397–398, 1976.

[3] M. I. Rabinovich and A. L. Fabrikant, "Stochastic self-modulation of waves in nonequilibrium media," *Sov. Phys. JETP*, vol. 50(2), pp. 311–317, 1979.

[4] A. Arneodo, P. Coulet, and C. Tresser, "Possible new strange attractors with spiral structure," *Communications in Mathematical Physics*, vol. 79, pp. 573–579, 1981.

[5] G. Chen and T. Ueta, "Yet another chaotic attractor," *International Journal of Bifurcation and Chaos*, vol. 9, pp. 1465–1466, 1999.

[6] J. Lü and G. Chen, "A new chaotic attractor coined," *International Journal of Bifurcation and Chaos*, vol. 12, pp. 659–661, 2002.

[7] C. Liu, T. Liu, L. Liu, and K. Liu, "A new chaotic attractor," *Chaos, Solitons and Fractals*, vol. 22, pp. 1031–1038, 2004.

[8] A. M. Harb, "Nonlinear chaos control in permanent magnet reluctance machine," *Chaos, Solitons and Fractals*, vol. 19, pp. 1217–1224, 2004.

[9] H. K. Chen and C. I. Lee, "Anti-control of chaos in rigid body motion," *Chaos, Solitons and Fractals*, vol. 21, pp. 957–965, 2004.

[10] G. Cai and Z. Tan, "Chaos synchronization of a new chaotic system via nonlinear control," *Journal of Uncertain Systems*, vol. 1(3), pp. 235–240, 2007.

[11] G. Tigan and D. Opris, "Analysis of a 3D chaotic system," *Chaos, Solitons and Fractals*, vol. 36, pp. 1315–1319, 2008.

[12] L. Pan, D. Xu, and W. Zhou, "Controlling a novel chaotic attractor using linear feedback," *Journal of Information and Computing Science*, vol. 5(2), pp. 117–124, 2010.

[13] V. Sundarapandian and I. Pehlivan, "Analysis, control, synchronization and circuit design of a novel chaotic system," *Mathematical and Computer Modelling*, vol. 55(7-8), pp. 1904–1915, 2012.

[14] H. Lu and X. Xiao, "Analysis of a novel autonomous 3-D chaotic system," *International Journal of Advancements in Computing Technology*, vol. 4(1), pp. 248–255, 2012.

[15] S. Vaidyanathan, "A new six-term 3-D chaotic system with an exponential nonlinearity," *Far East Journal of Mathematical Sciences*, vol. 79(1), pp. 135–143, 2013.

[16] S. Vaidyanathan, "A new eight-term 3-D polynomial chaotic system with three quadratic nonlinearities," *Far East Journal of Mathematical Sciences*, vol. 84(2), pp. 219–226, 2014.

[17] J. Hu, K. Jia, and J. Ma, "Chaos synchronization and encoding in coupled semiconductor lasers of multiple modulated time delays," *Optik - International Journal for Light and Electron Optics*, vol. 122(23), pp. 2071–2074, 2011.

[18] G. Yuan, X. Zhang, and Z. Wang, "Generation and synchronization of feedback-induced chaos in semiconductor ring lasers by injection-locking," *Optik - International Journal for Light and Electron Optics*, vol. 125(8), pp. 1950–1953, 2014.

[19] J. Kengne, J. C. Chedjou, G. Kenne, and K. Kyamakya, "Dynamical properties and chaos synchronization of improved Colpitts oscillators," *Communications in Nonlinear Science and Numerical Simulation*, vol. 17(7), pp. 2914–2923, 2012.

[20] S. Sabarathinam, K. Thamilmaran, L. Borkowski, P. Perlikowski, P. Brzeski, A. Stefanski, and T. Kapitaniak, "Transient chaos in two coupled, dissipatively perturbed Hamiltonian Duffing oscillators," *Communications in Nonlinear Science and Numerical Simulation*, vol. 18(11), pp. 3098–3107, 2013.

[21] Y. Gong, Y. Xie, X. Lin, Y. Hao, and X. Ma, "Ordering chaos and synchronization transitions by chemical delay and coupling on scale-free neuronal networks," *Chaos, Solitons and Fractals*, vol. 43, pp. 96–103, 2010.

[22] M. Villegas, F. Augustin, A. Gilg, A. Hmadi, and U. Wever, "Application of the polynomial chaos expansion to the simulation of chemical reactors with uncertainties," *Mathematics and Computers in Simulation*, vol. 82(5), pp. 805–817, 2012.

[23] M. Kyriazis, "Applications of chaos theory to the molecular biology of aging," *Experimental Gerontology*, vol. 26(6), pp. 569–572, 1991.

[24] S. Das, D. Goswami, S. Chatterjee, and S. Mukherjee, "Stability and chaos analysis of a novel swarm dynamics with applications to multi-agent systems," *Engineering Applications of Artificial Intelligence*, vol. 30, pp. 189–198, 2014.

[25] J. C. Sprott, J. A. Vano, J. C. Wildenberg, M. B. Anderson, and J. K. Noel, "Coexistence and chaos in complex ecologies," *Physics Letters A*, vol. 335(2-3), pp. 207–212, 2005.

[26] B. Sahoo and S. Poria, "The chaos and control of a food chain model supplying additional food to top-predator," *Chaos, Solitons and Fractals*, vol. 58, pp. 52–64, 2014.

[27] O. I. Moskalenko, A. A. Koronovskii, and A. E. Hramov, "Generalized synchronization of chaos for secure communication: Remarkable stability to noise," *Physics Letters A*, vol. 374(29), pp. 2925–2931, 2010.

[28] N. Li, W. Pan, L. Yan, B. Luo, and X. Zou, "Enhanced chaos synchronization and communication in cascade-coupled semiconductor ring lasers," *Communications in Nonlinear Science and Numerical Simulation*, vol. 19(6), pp. 1874–1883, 2014.

[29] R. Rhouma and S. Belghith, "Cryptanalysis of a chaos-based cryptosystem on DSP," *Communications in Nonlinear Science and Numerical Simulation*, vol. 16(2), pp. 876–884, 2011.

[30] X. Wu, C. Bai, and H. Kan, "A new color image cryptosystem via hyperchaos synchronization," *Communications in Nonlinear Science and Numerical Simulation*, vol. 19(6), pp. 1884–1897, 2014.

[31] Ch. K. Volos, I. M. Kyprianidis, and I. N. Stouboulos, "A chaotic path planning generator for autonomous mobile robots," *Robotics and Autonomous Systems*, vol. 60(4), pp. 651–656, 2012.

[32] Ch. K. Volos, I. M. Kyprianidis, and I. N. Stouboulos, "Experimental investigation on coverage performance of a chaotic autonomous mobile robot," *Robotics and Autonomous Systems*, vol. 61(12), pp. 1314–1322, 2013.

[33] Ch. K. Volos, N. G. Bardis, I. M. Kyprianidis, and I. N. Stouboulos, "Motion control of a mobile robot based on double-scroll chaotic circuits," *WSEAS Trans. Systems*, vol. 11(9), pp. 479–488, 2012.

[34] Ch. K. Volos, N. G. Bardis, I. M. Kyprianidis and I. N. Stouboulos, "Implementation of Mobile Robot by Using Double-Scroll Chaotic Attractors," In *Recent Researches in Applications of Electrical and Computer Engineering*, Proc. of 11th International Applications of Electrical Engineering, pp. 119–124, 2012, Vouliagmeni, Greece.

- [35] N. G. Bardis, A. P. Markovskiy, N. Doukas, and N. V. Karadimas, "True random number generation based on environmental noise measurements for military applications," *Mathematics And Computers In Science and Engineering archive*, Proce. of the 8th WSEAS International Conference on Signal Processing, Robotics and Automation, pp. 68–73, 2009, Cambridge, UK.
- [36] G. He, Z. Cao, P. Zhu, and H. Ogura, "Controlling chaos in a chaotic neural network," *Neural Networks*, vol. 16(8), pp. 1195–1200, 2003.
- [37] G. He, M. D. Shrimali, and K. Aihara, "Threshold control of chaotic neural network," *Neural Networks*, vol. 21(2-3), pp. 114–121, 2008.
- [38] E. Kaslik and S. Sivasundaram, "Nonlinear dynamics and chaos in fractional-order neural networks," *Neural Networks*, vol. 32, pp. 245–256, 2012.
- [39] L. M. Pecora and T. L. Carroll, "Synchronization in chaotic systems," *Physical Review Letters*, vol. 64(8), pp. 821–824, 1990.
- [40] E. Ott, C. Grebogi, and J.A. Yorke, "Controlling chaos," *Physical Review Letters*, vol. 64(11), pp. 1196–1199, 1990.
- [41] M. Lakshmanan, and K. Murali, *Nonlinear Oscillators: Controlling and Synchronization*. Singapore: World Scientific, 1996.
- [42] L. Lu, C. Zhang and Z. A. Guo, "Synchronization between two different chaotic systems with nonlinear feedback control," *Chinese Physics*, vol. 16, pp. 1603–1607, 2007.
- [43] U. E. Vincent, "Synchronization of identical and non-identical 4-D chaotic systems via active control," *Chaos, Solitons & Fractals*, vol. 37, pp. 1065–1075, 2008.
- [44] S. Vaidyanathan and K. Rajagopal, "Hybrid synchronization of hyperchaotic Wang-Chen and hyperchaotic Lorenz systems by active non-linear control," *International Journal of Systems Signal Control and Engineering Application*, vol. 4(3), pp. 55–61, 2011.
- [45] S. H. Chen and J. Lü, "Synchronization of an uncertain unified system via adaptive control," *Chaos, Solitons & Fractals*, vol. 14, pp. 643–647, 2002.
- [46] V. Sundarapandian and R. Karthikeyan, "Anti-synchronization of Lu and Pan chaotic systems by adaptive nonlinear control," *International Journal of Soft Computing*, vol. 6(4), pp. 111–118, 2011.
- [47] S. Vaidyanathan and K. Rajagopal, "Global chaos synchronization of hyperchaotic Pang and hyperchaotic Wang systems via adaptive control," *International Journal of Soft Computing*, vol. 7(1), pp. 28–37, 2012.
- [48] V. Sundarapandian and I. Pehlivan, "Analysis, control, synchronization and circuit design of a novel chaotic system," *Mathematical and Computer Modelling*, vol. 55(7-8), pp. 1904–1915, 2012.
- [49] J. H. Park and O. M. Kwon, "A novel criterion for delayed feedback control of time-delay chaotic systems," *Chaos, Solitons & Fractals*, vol. 23, pp. 495–501, 2005.
- [50] T. Yang and L. O. Chua, "Control of chaos using sampled-data feedback control," *International Journal of Bifurcation and Chaos*, vol. 9, pp. 215–219, 1999.
- [51] S. H. Lee, V. Kapila, M. Porfiri, and A. Panda, "Master-slave synchronization of continuously and intermittently coupled sampled-data chaotic oscillators," *Communications in Nonlinear Science and Numerical Simulation*, vol. 15, pp. 4100–4113, 2010.
- [52] V. Sundarapandian, "Adaptive backstepping controller and synchronizer design for Arneodo chaotic system with unknown parameters," *International Journal of Computer Science and Information Technology*, vol. 4(6), pp 145–159, 2012.
- [53] V. Sundarapandian, "Anti-synchronizing backstepping control design for Arneodo chaotic system," *International Journal of Bioinformatics and Biosciences*, vol. 3(1), pp. 21–33, 2013.
- [54] V. Sundarapandian and S. Sivaperumal, "Sliding controller design of hybrid synchronization of four-wing chaotic systems," *International Journal of Soft Computing*, vol. 6(5), pp. 224–231, 2011.
- [55] S. Vaidyanathan and S. Sampath, "Anti-synchronization of four-wing chaotic systems," *International Journal of Automation and Computing*, vol. 9(3), pp. 274–279, 2012.
- [56] S. Vaidyanathan and S. Sampath, "Sliding mode controller design for the global chaos synchronization of Coulet systems," *International Journal of Information Sciences and Techniques*, vol. 2(2), pp. 65–76, 2012.
- [57] J. Wang, D. Lu, and L. Tian, "Global synchronization for time delay of WINDMI system," *Chaos, Solitons & Fractals*, vol. 30, pp. 629–635, 2006.
- [58] W. Hahn, *The Stability of Motion*, New York: Springer, 1967.

The surface properties of linear low-density polyethylene after radiation cross-linking

Martin Bednarik, David Manas, Miroslav Manas, Michal Stanek, Jan Navratil, and Ales Mizera

Abstract—In this study there was found that ionizing beta radiation increased the strength of bonded joints and improved the adhesion properties of linear low-density polyethylene (LLDPE). Generally, for the formation of quality bonded joint it is important to wet the adhesive bonding surface well. Wettability is characterized by the contact angle of wetting. The liquid has to have a lower surface tension than the solid in order to be able to wet the solid substance. The measurement results indicated that ionizing beta radiation was a very effective tool for the improvement of adhesive properties and increased the strength of bonded joints of linear low-density polyethylene. Bonded surfaces with ionizing beta radiation doses of 0, 33, 66, 99, 132, 165, and 198 kGy were irradiated. The best results were achieved by irradiation at dose of 132 kGy by which the highest surface energy and the highest strength of bonded joints of LLDPE were achieved. The strength of bonded joints after irradiation was increased up to 260 % compared to untreated material. A similar trend was observed even for contact angle of wetting and surface energy.

Keywords—Surface energy, linear low-density polyethylene, adhesion, bonded joints.

I. INTRODUCTION

BONDING has experienced tremendous expansion in the field of joining materials in the last years. Because of that expansion bonding is classed as new techniques even when it is in fact very old.

In comparison with conventional joining methods (riveting, welding and screwing) bonding provides a new combination of options and it allows obtaining special shapes and properties which cannot be created by conventional methods of coupling. Joining materials using adhesive joints offers several benefits, but also limiting factors if compared with

This paper is supported by the internal grant of TBU in Zlin No. IGA/FT/2014/016 funded from the resources of specific university research and by the European Regional Development Fund under the project CEBIA-Tech No. CZ.1.05/2.1.00/03.0089.

Martin Bednarik is with the Tomas Bata University in Zlin, nam. T. G. Masaryka 5555, 76001 Zlin, Czech Republic (phone: +420 57 603 5152, email: mbednarik@ft.utb.cz).

David Manas is with the Tomas Bata University in Zlin, nam. T. G. Masaryka 5555, 76001 Zlin, Czech Republic (email: dmanas@ft.utb.cz).

Miroslav Manas is with the Tomas Bata University in Zlin, nam. T. G. Masaryka 5555, 76001 Zlin, Czech Republic (email: manas@fai.utb.cz).

Michal Stanek is with the Tomas Bata University in Zlin, nam. T. G. Masaryka 5555, 76001 Zlin, Czech Republic (email: stanek@ft.utb.cz).

Jan Navratil is with the Tomas Bata University in Zlin, nam. T. G. Masaryka 5555, 76001 Zlin, Czech Republic (email: j.navratil@ft.utb.cz).

Ales Mizera is with the Tomas Bata University in Zlin, nam. T. G. Masaryka 5555, 76001 Zlin Czech Republic (email: mizera@ft.utb.cz).

using mechanical joints. To decide about the type of coupling it is necessary to consider the advantages and disadvantages of bonding in comparison with traditional joining technique. [2, 4, 5, 9]

The advantage of bonded joints is that we can connect the same and dissimilar materials and do not take into account the thickness. Application of adhesives does not undermine the coherence of the connect parts and watertight and gastight joints may be prepared. It does not disturb profile or aesthetic appearance of bonded file and does not increase its weight. Joints can be transparent or colored and it is possible to achieve their high strength.

Adhesive bonding has also several technological disadvantages, in comparison with mechanical joints. The disadvantages of bonded joints are the requirements for planeness and cleanness of surface to be bonded and sensitivity to peel stress. Special surface treatments are required for bonded materials with poor adhesion properties and maximum bond strength is reached after the certain time. [2, 12, 14]

II. EXPERIMENTAL

The aim of the experiment was to examine the effect of beta irradiation on the strength of bonded joints for selected type of material.

A. Material

For this experiment linear low-density polypropylene (LLDPE) were used. Linear low-density polyethylene is the youngest of all types of polyethylene. Its structure is similar to the structure of HDPE but has a low crystallinity given to a large number of short chains. Linear low-density has penetrated almost all traditional markets for polyethylene. It is used to produce plastic bags and sheets, plastic wrap, stretch wrap, pouches and toys. [15, 16, 19]

For bonding LLDPE it is necessary to modify surfaces which will be bonded. Surface modification improves its wettability in aqueous media and also improves adhesive properties. [10, 13]

The samples were made using the injection molding technology on the injection molding machine Arburg Allrounder 420C.

The samples had the shape and dimensions according to the CSN EN ISO 527 – 2. Before bonding surfaces of samples ionization beta radiation were irradiated with doses of 0, 33,

66, 99, 132, 165, and 198 kGy at Beta – Gamma Service GmbH & Co. KG, Germany. [3, 6, 17]

B. Surface treatment by beta radiation

Ionizing beta radiation gives inexpensive commodity plastics and technical plastics the mechanical, thermal, and chemical properties of high-performance plastics. This upgrading of the plastics enables them to be used in conditions which they would not be able to with stand otherwise. The energy-rich beta rays trigger chemical reactions in the plastics which results in networking of molecules (comparable to the vulcanization of rubbers which has been in industrial use for so long). [1, 3, 7]

The energy from the rays is absorbed by the material and cleavage of chemical bonds takes place. This releases free radicals which in next phase form desired molecular bonds. [3, 8, 20]

The irradiation cross-linking of thermoplastic materials via electron beam or cobalt 60 (gamma rays) is performed separately, after processing. Generally, ionizing radiation includes accelerated electrons, gamma rays and X-rays. Radiation processing with an electron beam offers several distinct advantages when compared with other radiation sources, particularly γ -rays and x-rays.

The process is very fast, clean and can be controlled with much precision. There is no permanent radioactivity since the machine can be switched off. In contrast to γ -rays and x-rays, the electron beam can be steered relatively easily, thus allowing irradiation of a variety of physical shapes.

The electron beam radiation process is practically free of waste products and therefore is no serious environmental hazard. These are not only capable of converting monomeric and oligomeric liquids, but also can produce, due to cross-linking, major changes in the properties of solid polymers. The cross-linking level can be adjusted by the irradiation dosage. The absorbed dosage means the value of energy of ionizing radiation absorbed by a unit of mass of the processed material. The unit of absorbed dose is 1 Gray (1 Gy = 1J/kg). [1, 3-8]

The main difference between beta and gamma rays is in their different abilities to penetrate the irradiated material. Gamma rays have a high penetration capacity.

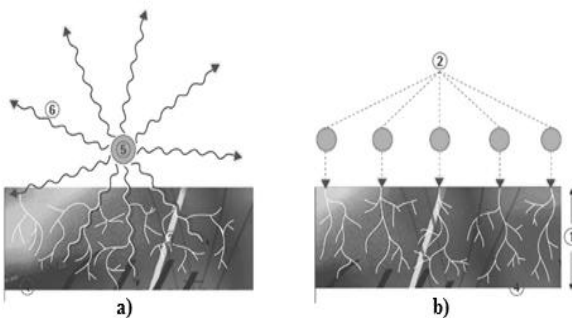


Fig. 1 Design of Gamma Rays (a) and Electron Rays (b) [3]

a) 3 – Secondary electrons, 4 – Irradiated material,

5 – Encapsulated Co – 60 Radiation source, 6 – Gamma rays
b) 1 – Penetration depth of an electron, 2 – Primary electron, 3 – Secondary electron, 4 – Irradiated material

The penetration capacity of electron rays depends on the energy of the accelerated electrons. Due to electron accelerator, the required dosage can be applied within seconds, whereas several hours are required in the gamma radiation plant (Fig. 1). [3-5]

Beta and gamma rays can be used for the irradiation of polyolefines, polyesters, halogen polymers and polyamides from the thermoplastics group, elastomers and thermoplastic elastomers. Some of them need the addition of a cross-linking agent. Polymers can be classified into two groups according to their response to ionizing radiation. One group exhibits predominant cross-linking, the other predominant chain scission. [1, 3, 11, 18]

Irradiation cross-linking of thermoplastic materials deals with creation of a cross-link among the macromolecular strings. Intermolecular forces are replaced by a covalent bond. As a result, we can optimise properties of standard and engineering polymers and impart them the properties of high performance polymers (Fig. 2). [3-8]

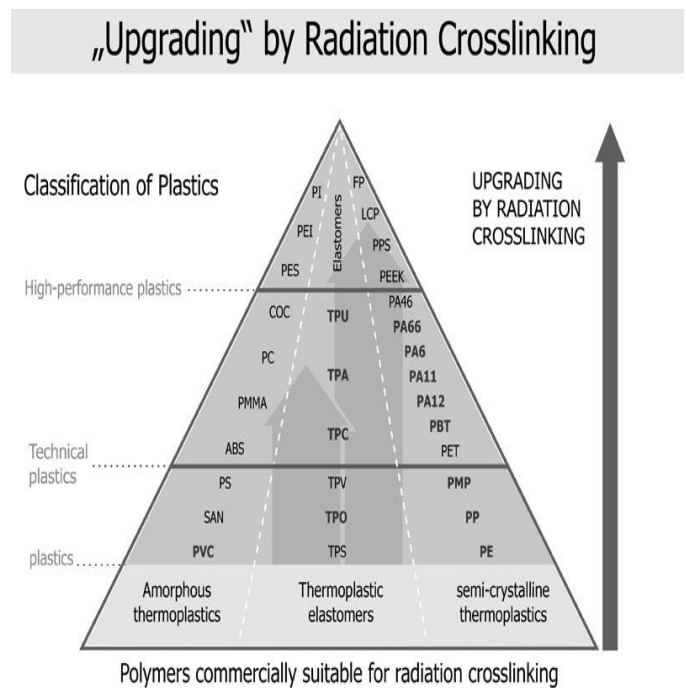


Fig. 2 Pyramid of Polymers [3]

Irradiation of polymers turned out to be interesting because of economic reasons, production costs and a life time of products. However, these benefits depend on the type of irradiated polymer and the radiation dosage. Behaviour of each material is different after irradiation.

We cannot expect the improvement in all areas (in mechanical, thermal and chemical). Most of polymers are not

suitable for irradiation because of degradation and deterioration of their properties. [3-8]

C. Wetting contact angle measurements

The angle of contact was measured by using the sessile drop (Fig. 3) and surface energy was determined by OWRK method (Owens – Wendt – Rabel – Kaoble method).

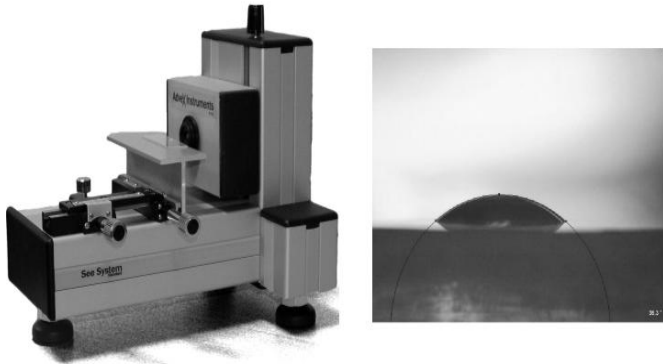


Fig. 3 Surface Energy Evaluation System (See System)

The liquids water, glycerol and ethylene glycol with known γ^p (polar component) and γ^d (dispersive component) were used for calculating the surface energy of LLDPE. [2, 11]

Table 1 Surface energy of liquids

Liquid	γ_1 (mJ/m ²)	γ_1^d (mJ/m ²)	γ_1^p (mJ/m ²)
Distilled water	72.8	21.8	51.0
Glycerol	64.0	34.0	30.0
Ethylene glycol	48.0	29.0	19.0

D. Testing the strength of bonded joints

After sample preparation (production and irradiation) contact angles were measured and surface energy was calculated. Then the samples were bonded and their strength was measured. For testing the strength of bonded joints there was used a tensile test on the test machine Zwick 1456. Test conditions were according to the CSN EN ISO 527-1 and CSN EN ISO 527-2. Speed was 10 mm/min and evaluation software was Test Expert Standard. [18, 20-24]

III. RESULTS AND DISCUSSION

A. Contact angle and surface energy

The variation in contact angle of LLDPE for different doses of radiation and for different test liquids is shown in Fig. 4.

It shows that the contact angle on the untreated surface is 84.9°, 76.6°, and 62.9° for distilled water, glycerol, and ethylene glycol, respectively. The contact angle values were

considerably reduced after irradiation by a dose of 132 kGy to lower values of 60.1°, 59.3°, and 49.0° for distilled water, glycerol, and ethylene glycol, respectively (referring to: Fig. 4).

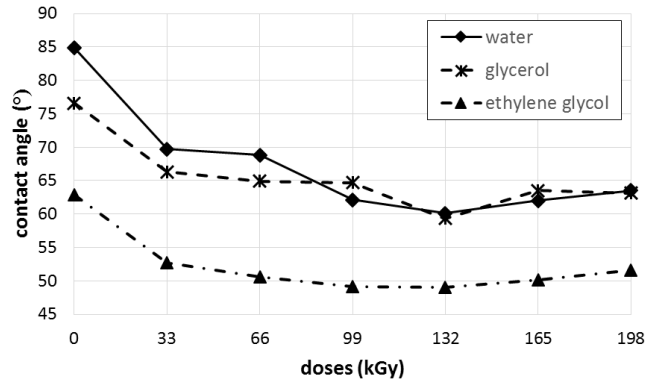


Fig. 4 Variation of contact angle with respect to radiation dose for material LLDPE

Fig. 5 shows a plot of surface energy γ_s from the measured contact angles on the surface of the LLDPE. It shows that surface energy of untreated surface is 27.1 mJ/m² and 26.7 mJ/m² for water + glycerol and water + ethylene glycol, respectively. Ionization beta radiation increases the surface energy. The surface energy values considerably increased after irradiation by a dose of 132 kGy to higher values of 42.1 mJ/m² for water + glycerol and 42.3 mJ/m² for water + ethylene glycol.

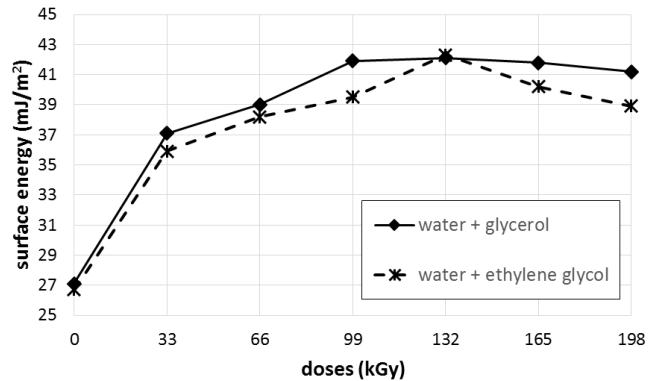


Fig. 5 Variation of surface energy with respect to radiation dose for material LLDPE

B. Strength of bonded joints

Strength of bonded joints is characterized by the maximum burdensome force which endured bonded sample. For bonding of LLDPE one type of two-component methacrylate adhesive (Cyberbond A806), one type of two-component epoxy adhesive (Cyberbond E705), and one type of cyanoacrylate adhesive (Cyberbond 2028) were used.

The highest strength of bonded joints samples of LLDPE (adhesives Cyberbond 2028) have those which were irradiated by a dose of 132 kGy. After the irradiation by a dose of 132 kGy strength is increased by 260 % (referring to: Fig. 6).

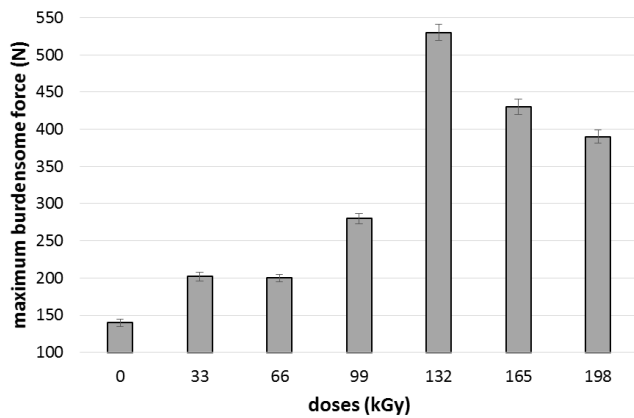


Fig. 6 Variation of strength of bonded joints with respect to radiation dose (Cyberbond 2028)

The highest strength of bonded joints samples of LLDPE (adhesives Cyberbond A806) have those which were irradiated by a dose of 132 kGy. After the irradiation by a dose of 132 kGy strength is increased by 200 % (referring to: Fig. 7).

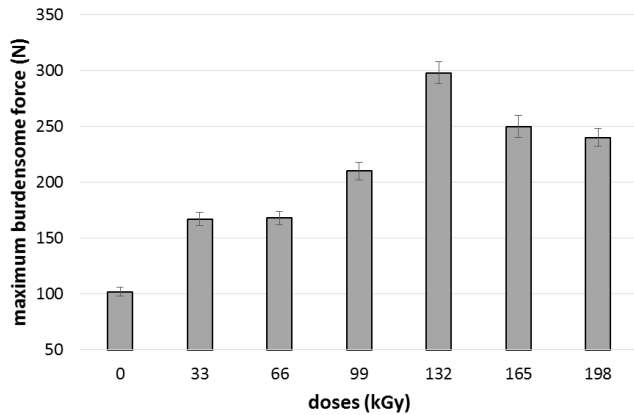


Fig. 7 Variation of strength of bonded joints with respect to radiation dose (Cyberbond A806)

The highest strength of bonded joints samples of LLDPE (adhesives Cyberbond E705) have those which were irradiated by a dose of 132 kGy. After the irradiation by a dose of 132 kGy strength is increased by 200 % (referring to: Fig. 8).

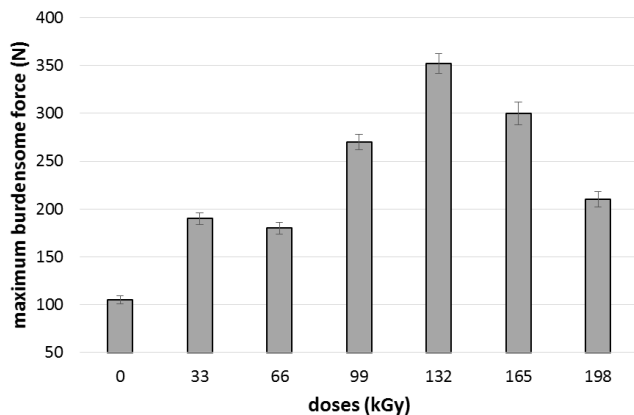


Fig. 8 Variation of strength of bonded joints with respect to radiation dose (Cyberbond E705)

IV. CONCLUSION

This article describes the effect of beta radiation on the contact angle of wetting, on the surface energy and on the final strength of bonded joints of LLDPE. Beta radiation increases the strength of bonded joints of LLDPE and improves their adhesion properties. The best results were achieved by irradiation at doses of 132 kGy by which the highest surface energy and the highest strength of bonded joints of LLDPE were achieved.

REFERENCES

- [1] J. G. Drobny, *Radiation Technology for Polymers*, Boca Raton: CRC Press, 2003, ISBN 1-58716-108-7.
- [2] B. Lapcikova et al., "Application of radio frequency glow discharge plasma for enhancing adhesion bonds in polymer/polymer joints", *Journal of Applied Polymer Science*, Vol. 102, 2006, pp. 1827-1833.
- [3] BGS – Beta Gama Service. [online]. www: <http://bgs.eu>
- [4] W. Brockmann, *Adhesive Bonding: Materials, Applications and Technology*, Wiley - VCH, Weinheim, 2009, ISBN 978-3-527-31898-8.
- [5] Z. Brocka, *Werkstoff-und Einsatzpotential Strahlenvernetzter Thermoplaste*, Lehrstuhl für Kunststofftechnik (LKT), Nürnberg, 2008.
- [6] R. J. Woods, *Applied Radiation Chemistry: Radiation Processing*, A Wiley-Interscience publication, New York, 1994, ISBN 0-471-54452-3.
- [7] M. Manas et al., "Temperature stability of irradiated polymers". *Chemicke Listy*, Vol. 105, 2011, pp. 254-256.
- [8] Z. Holik et al., "Effect of irradiation cross-linking on mechanical properties of selected types of polymer". *Chemicke Listy*, Vol. 105, 2011, pp. 269-271.
- [9] M. Stanek et al., "Optimization of injection molding process", *International Journal of Mathematics and Computers in Simulation*, Vol. 5, 2011, pp. 413-421.
- [10] M. Stanek et al., "Simulation of injection molding process by cadmould rubber", *International Journal of Mathematics and Computers in Simulation*, Vol. 5, 2011, pp. 422-429.
- [11] D. Manas et al., "Thermal effects on steels at different methods of separation", *Chemicke Listy*, Vol. 105, 2011, pp. 713-715.
- [12] M. Manas et al., "Improvement of mechanical properties of the TPE by irradiation", *Chemicke Listy*, Vol. 105, 2011, pp. 828-829.
- [13] V. Pata et al., "Visualization of the wear test of rubber materials", *Chemicke listy*, Vol. 105, 2011, pp. 290-292.
- [14] D. Manas et al., "Influence of mechanical properties on wear of heavily stressed rubber parts", *KGK – Kautschuk Gummi Kunststoffe*, Vol. 62, 2009, pp. 240-245.
- [15] M. Manas et al., "Modification of polyamides properties by irradiation", *Chemicke Listy*, Vol. 103, 2009, pp. 24-26.
- [16] D. Manas et al., "Wear of multipurpose tire treads", *Chemicke Listy*, Vol. 103, 2009, pp. 72-74.
- [17] S. Sanda et al., "Injection mold cooling system by DMLS", *Chemicke Listy*, Vol. 103, 2009, pp. 140-142.
- [18] S. Sanda et al., "Gate effect on quality of injected part", *Chemicke Listy*, Vol. 105, 2011, pp. 301-303.
- [19] M. Stanek et al., "How the filler influence the fluidity of polymer", *Chemicke Listy*, Vol. 105, 2011, pp. 303-305.
- [20] D. Manas et al., "Influence of radiation on polymer properties", *Chemicke Listy*, Vol. 101, 2007, pp. 27-28.
- [21] M. Ovsik et al., "Micro-hardness of glass fiber-filled PA6 influenced by beta irradiation", *International Journal of Mechanics*, Vol. 7, 2013, pp. 500-507.
- [22] M. Ovsik et al., "Effect of beta low irradiation doses on the nano-hardness of PBT", *International Journal of Mechanics*, Vol. 7, 2013, pp. 310-317.
- [23] J. Navratil et al., "Hardness and micro-indentation hardness comparison of recycled modified HDPE", *Key Eng. Mater. J.*, Vol. 606, 2014, pp. 217-220.
- [24] M. Bednarik et al., "Effect of beta irradiation on the strength of bonded joints", *Key Eng. Mater. J.*, Vol. 586, 2014, pp. 79-82.

Pipe Measurement System Using a Laser Range Finder with KINECT

K. Yoshida, N. Hidaka, and K. Kawasue

Abstract— We propose a handheld system that can measure the precise shape and arrangement of pipes in chemical plants without contacting the targets. This system consists of a laser range finder and KINECT. In measurements of pipes, the user directs the laser slit ray at the measurement target. KINECT then detects point cloud data while the Laser range finder simultaneously detects position data at the location on the pipe where the laser slit ray is directed. The user manually scans the system by directing the laser slit ray along the measurement pipe. The point cloud data obtained by KINECT are used to detect the movement information of the system by adjusting overlapping data in consecutive frames using the ICP (Iterative Closest Point) algorithm. This permits free scanning by the system. The pipe cross section is estimated from data obtained by the laser range finder. The shape and the arrangement of the pipe are reconstructed by reference to the detected cross-sections of the pipe and the movement information of the system.

Keywords— Computer vision, KINECT, Laser Range Finder, Pipe.

I. INTRODUCTION

IN a chemical plant, the shapes and the arrangement of existing pipes should be investigated before replacement or the construction of new pipes begins. Generally, measurement is conducted manually using a metal tape measure and is a cumbersome task. Recently, some kinds of laser scanner have been introduced for the measurement of pipes. In the typical laser scanner, an infrared laser is sent out and reflected back to the system. The distance is measured by the time of flight of the laser pulse between the device and targets, or the shift in the wavelength of the return beam [1][2]. Three-dimensional information of the pipe can be obtained from point cloud data obtained by the laser scanner. A point cloud is a set of vertices in a three-dimensional (3D) coordinate system, and the data are used as the basic data for a computer vision application. The laser scanner is very attractive, since it can obtain thousands of sets of point cloud data in a short time. However, the volume of the data obtained is very large, since the data include unnecessary information such as ground data, wall data, and data of other equipment. Extra work is required to extract the appropriate information from the huge volume of point cloud data for the design of new pipes. Therefore, development of an effective method is required for extracting the desired

information from the point cloud data. In addition, some pipes located at high positions that the laser cannot reach are not measured by the occlusion, since the laser scanner is fixed on stable ground.

In order to cope with these problems, we developed a handheld pipe measurement system composed of a laser range finder and a KINECT sensor [3]-[6]. 3D point cloud data can be obtained easily by use of KINECT. The KINECT sensor is low cost, as it is widely sold as a controller for Xbox360 dedicated game machines. KINECT is compact enough to be used as a handheld-scanner. There is no limitation on the measurement area size, since individual 3D point cloud data sets recorded from different positions can be combined by computer processing. The iterative closest point (ICP) algorithm [7]-[11] is often employed to combine data sets. This algorithm automatically determines the overlapping area between 3D point cloud data sets and constructs a single 3D image.

However, the measurement accuracy of the KINECT is unstable especially for long-distance targets. On the other hand, the laser range finder that we use with KINECT has a maximum measurement range of about 30 m. The laser range finder is a two-dimensional radial range finder that measures distance within an angular range of 270 degrees. Since the laser projected from the laser range finder is invisible, our system includes an extra, visible laser (wavelength 650 nm) projector oriented along the direction of the laser range finder. In measurements of pipes, the user directs the visible laser slit ray with our system at the measurement target. KINECT detects point cloud data while the laser range finder simultaneously detects the cross section of the target surface. The user manually scans the system by directing the laser slit ray along the measurement pipe. The point cloud data obtained by KINECT are used to detect the movement of the system by adjusting overlapping data in consecutive frames using the ICP algorithm. The measured data of the laser range finder are more accurate than the original point cloud data obtained by KINECT. The pipe cross section is estimated from data obtained by the Laser Lange Finder. The 3D shape of the pipe is constructed on a computer from cross sections obtained from different positions and angles. Experimental results show the feasibility of our system.

K. Yoshida, N. Hidaka and K. Kawasue are with the University of Miyazaki, Miyazaki 889-2192, JAPAN (phone: +81-985-58-7583; fax: +81-985-58-7583; e-mail: kawasue@cc.miyazaki-u.ac.jp).

II. MEASUREMENT SYSTEM

Fig.1 shows the measurement system. This system is composed of a laser range finder and KINECT. It is sufficiently compact that it can be hand held. The laser range finder (UTM-30LX:HOKUYO Automatic Co., LTD) adopts the time of flight distance measurement method, and the maximum measurable distance from the sensor is about 30 m. The laser is scanned radially in steps of 0.25 degree resolution, and the scan rate is 25 ms/scan. The radial range is from -135 degrees to +135 degrees, where the orientation 0 degree corresponds to the front of the sensor. Meanwhile, the KINECT sensor consists of an infrared laser projector, an infrared camera, and an RGB camera. The depth information can be obtained by triangulation processing. In order to obtain the depth information, a constant pattern of speckles created by the laser source is projected onto the target and recorded by the infrared camera. As the speckle is projected, the position of the speckle in the infrared image is shifted in the direction of the baseline between the laser projector and the perspective center of the infrared camera. All shifts of speckles are measured by the image correlation procedure, which yields a depth image from the sensor.

Since the projected laser from the laser range finder is invisible, the visible laser slit (wavelength 650 nm) is directed along the laser scanning plane from the laser range finder. This visible laser slit helps user to recognize the measurement portion on the targets.

Fig.2 shows the setup of the measurement. Multi laser spots (532 nm, 500 * 500 dots) are adopted for the markers to connect two point cloud data sets obtained from different angles. The multi laser spots are projected from a fixed position to the target, and help in finding the correspondence between point cloud data sets detected from different positions. The 3D positions of multi laser spots are easily extracted by finding the green colored data from the point cloud data obtained by KINECT.

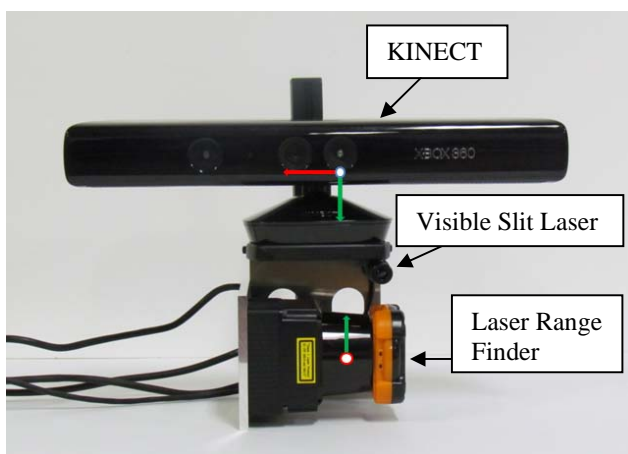


Fig. 1 System configuration

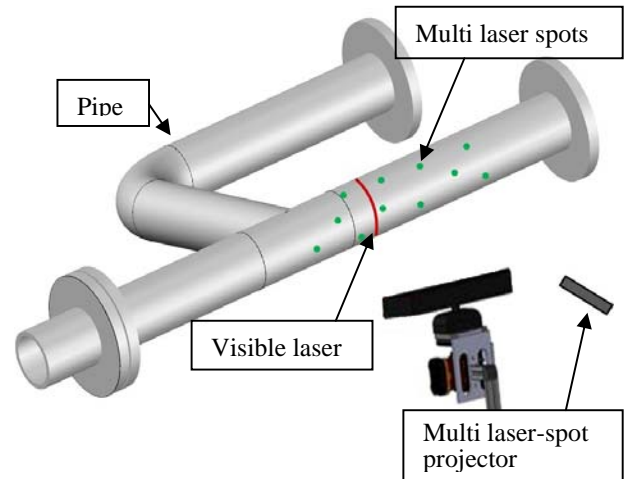


Fig. 2 Setup of measurement

III. MEASUREMENT FLOW

Fig.3 shows the flow of the measurement system. Firstly, the user directs the visible laser slit ray with the system to the target and starts measurement. The laser range finder and KINECT sensor detect the data simultaneously. The Laser Range finder detects the distance data along the visible laser slit. Since the measurement area is selected by the laser streak, the number of data points is limited and the desired data, such as pipe cross-section data, can be extracted easily. The laser streak on the pipe draws an ellipse, and our ellipse estimation algorithm detects the ellipse information, such as the center and widths of the ellipse. KINECT detects the point cloud data, whose coordinate system is fixed on the KINECT. The point cloud data include the laser dot markers projected from the fixed point. Secondly, the user moves the system manually along the pipe and directs the visible laser slit ray to different portions of the pipe. While selecting the measurement area, the user should take care to include the common laser dot markers. The movement information of the measurement system can be estimated by finding the correspondence of the markers between point cloud data sets, since the three-dimensional position of each marker is premeasured by the KINECT. Adoption of the marker lasers enables robust measurement. The cross section of the pipe is displayed as the estimated ellipse, and the estimated ellipses acquired on each shot are located in the world coordinate system considering the movement information of the measurement system. Finally, reconstruction of the pipe is established on the computer by interpolating the cross sections between these ellipses.

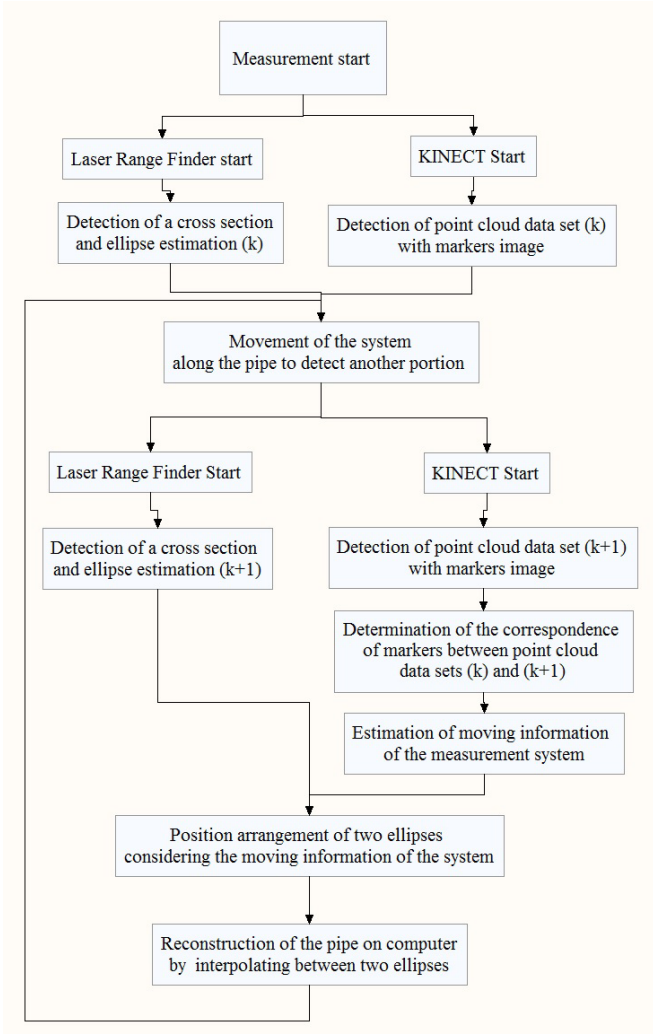


Fig. 3 Measurement flow

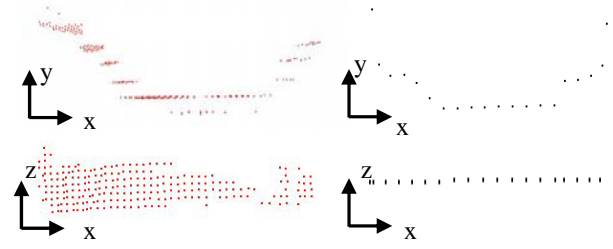
IV. UNIFICATION OF COORDINATE SYSTEMS

The laser range finder and KINECT have different coordinate systems fixed on their respective bodies. In order to convert the coordinate systems into the other world coordinate systems, the common area on the visible laser is used to be aligned. Since the measurement area is colored by the visible laser, the point cloud data on the visible laser can be extracted easily by selecting the colored data. The coordinate systems are unified by aligning the measured data of the laser range finder and the extracted point cloud data. Fig.4 shows the example of the data obtained by KINECT and laser range finder on the visible laser. These data are aligned and the coordinate systems are unified using the simplified ICP algorithm explained in the following chapter.

V. ESTIMATION OF MOVING INFORMATION OF THE MEASUREMENT SYSTEM

Fig. 5 shows an example of the system position on the measurement procedure. A laser-spot pattern (Green dots) is projected from the laser projector fixed on the ground. The user

directs the visible laser slit ray and takes an initial shot to obtain the cross section data from the laser range finder and point cloud data from KINECT. The point cloud data of KINECT include the laser dot markers projected from a fixed point. After moving the measurement system along the pipe, the user directs the visible laser to another position of the pipe and takes a second shot at the different angle. The movement information of the measurement system can be estimated by finding the correspondence of the common markers between point cloud data sets. It should be noted that these point cloud data should include the common laser markers between two shots.



a. KINECT data b. Data of laser range finder
Fig.4 Point cloud data of KINECT and the laser range finder.

The ICP algorithm is used to estimate the moving information of the measurement system. Fig. 6 shows the outline of the ICP algorithm. In this figure, the ICP algorithm tries to match data set A to data set B.

The procedure is as follows.

- 1) Closest point of each data point in data set A is searched from data set B.
- 2) The distances between these closest points are totaled. The total is used for the evaluation value of the matching.
- 3) Data set A is moved and rotated in the predetermined possible area.
- 4) The ICP algorithm repeats 2) and 3).
- 5) The position of data set A with the minimum evaluation value (total of distances) is determined for the matching position.

Equation (1) is used to evaluate the result of the ICP algorithm. The coordinate system (x_{2i}, y_{2i}, z_{2i}) of the Laser Markers in the second shot are rotated and displaced to the point $(x'_{2i}, y'_{2i}, z'_{2i})$. R_d is a rotation matrix and t_d is a displacement vector in (1). ϕ is the evaluation value between the markers on the first shot and the second shot in the matching process. The moving information of the system can be estimated by the process of the ICP algorithm, and this information is used for reconstruction of the pipe on the computer in the subsequent steps.

$$\begin{cases} \begin{bmatrix} x'_{2i} \\ y'_{2i} \\ z'_{2i} \\ 1 \end{bmatrix} = R_d \begin{bmatrix} x_{2i} \\ y_{2i} \\ z_{2i} \\ 1 \end{bmatrix} + t_d \\ \varphi = \sum_{i=1}^n ((x_{1i} - x'_{2i})^2 + (y_{1i} - y'_{2i})^2 + (z'_{1i} - z'_{2i})^2) \end{cases} \quad (1)$$

Fig. 7 shows an image of point cloud data obtained by KINECT by this procedure. The ICP algorithm tries to match the four markers between these two point cloud data sets. The result of the matching is shown in Fig. 8.

Upon executing the ICP algorithm, the initial location where the ICP algorithm starts is important for obtaining stable results. In our method, the center of gravity of each data set is estimated and the ICP algorithm starts from the position where these centers of gravity match.

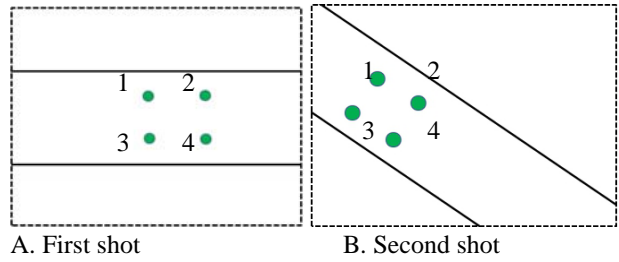


Fig. 7 Point cloud data include laser markers.

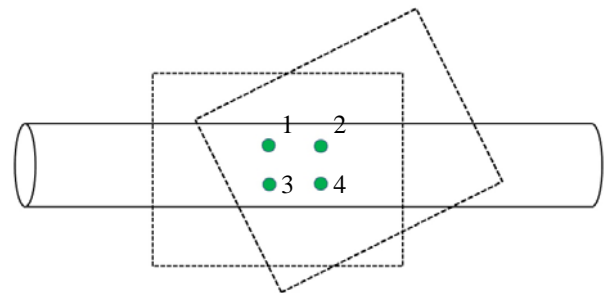


Fig. 8 Matching result of ICP algorithm.

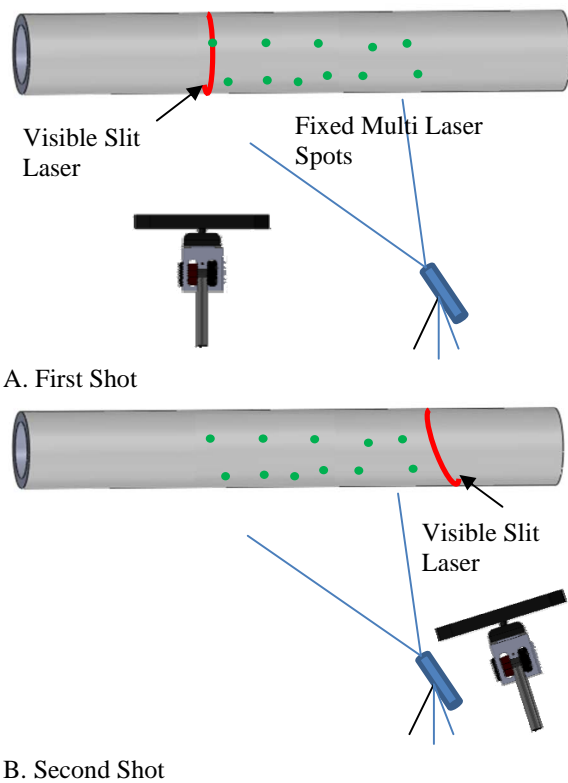


Fig. 5 System positions in the measurement procedure

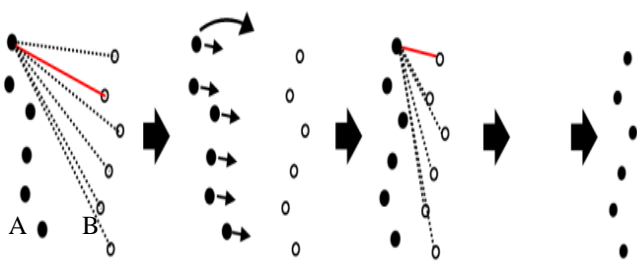


Fig. 6 ICP (Iterative Closest Point) algorithm

VI. RECONSTRUCTION OF THE PIPE ON COMPUTER

The cross section of the pipe is estimated using the distance data from the laser range finder. Fig. 9 shows the estimation process of the cross section from the distance data of the laser range finder. Since the direction of the laser slit ray is usually not perpendicular to a pipe axis, the cross section forms an ellipse. Firstly, ellipse formula is estimated by the least squares method as B. Positions of two estimated ellipses obtained in different shots are converted to the same world coordinate system while considering the movement information of the measurement system as shown in Fig. 10.

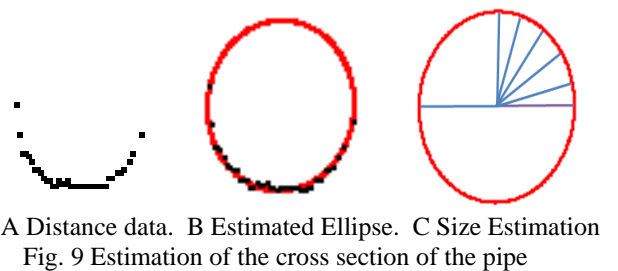


Fig. 9 Estimation of the cross section of the pipe

Fig. 11 shows the flow of the reconstruction of the pipe on the computer. Firstly, the center of the estimated ellipse is determined and the centers of the detected ellipses are connected by the line. This line is assumed to be the central axis of the measured pipe. Point cloud data obtained by the laser range finder are used to determine the size of the pipe.

The reconstruction of the pipe is established on the computer by interpolating the cross sections between these ellipses along the central axis of the pipe. Fig. 12 shows an example of the reconstruction of the pipe (Blue pipe) on the computer.

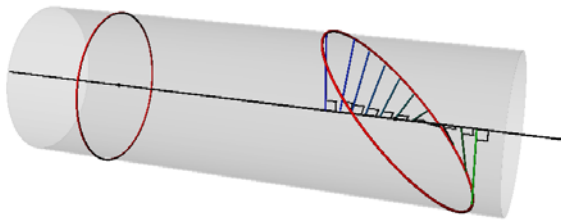


Fig.10 Estimation of the cross section of the measured pipe

VII. SYSTEM PERFORMANCE

In order to check the performance of our system, the measurement accuracy of detecting the movement information of the system was examined experimentally. Two kinds of experiments were conducted, for the displacement and rotation detections of the system. Fig. 13 shows the experimental setup for the displacement measurement test. The measurement system is set on the linear translation stage and is displaced in one direction along the stage. Fig. 14 shows the accuracy of the displacement detection. The accuracy was examined on 100mm and 200mm displacements. The error was less than about 2 mm for the 2,400 mm distance from the KINECT sensor. Fig. 15 shows the accuracy of the rotation (0, 5 ,10 degree) detection. The KINECT was rotated at its position, and the rotation detection was examined. The system performs best at distances of less than 1600 mm.

However, these results do not limit the range of the measurement, since the range of the laser range finder is about 30 m. When we have to measure a target located at long distance, some extra fixed object for markers at a near position enable determination of the movement information of the system.

VIII. RESULTS OF PIPE RECONSTRUCTION ON COMPUTER

The pipes in the laboratory were measured in one of the experiments. Fig. 16 shows a photograph of a measured pipe. Fig. 17 shows the reconstructed pipe on the point cloud data. The point cloud data include extra data such as wall data. The pipe is reconstructed from 4 shots from different positions and is shown in blue in Fig. 17. The reconstructed pipe information is stored in the computer.

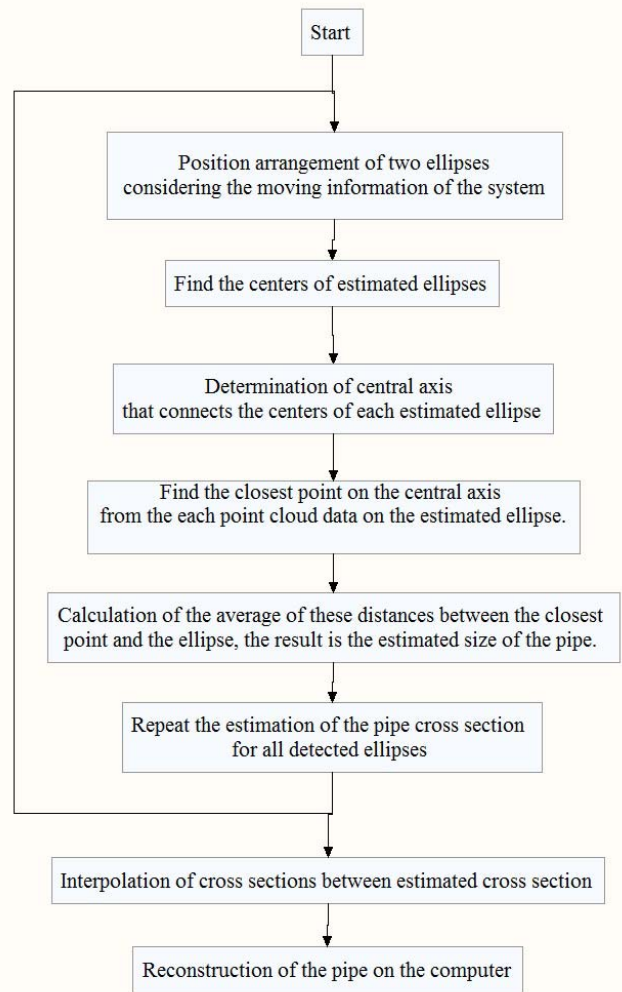


Fig. 11 Flow of the reconstruction of the pipe on computer

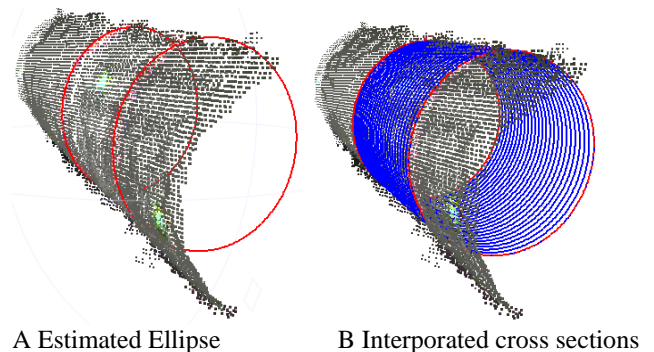


Fig. 12 Reconstructed pipe on computer

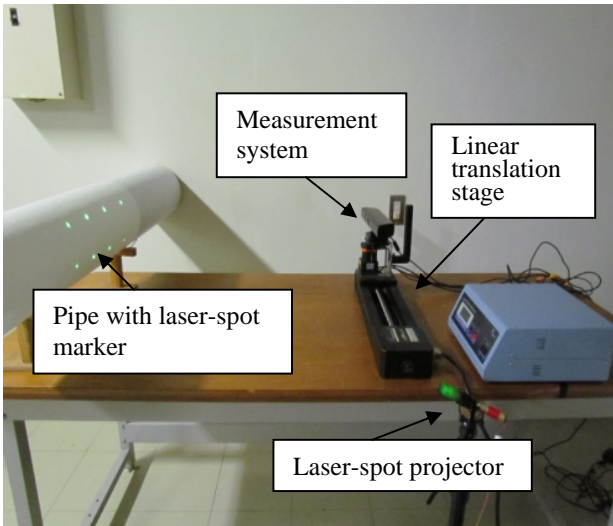


Fig. 13 Experimental setup for the displacement test

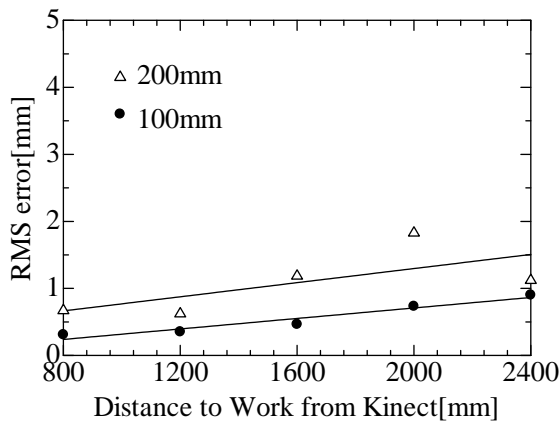


Fig. 14 Accuracy of the displacement detection.

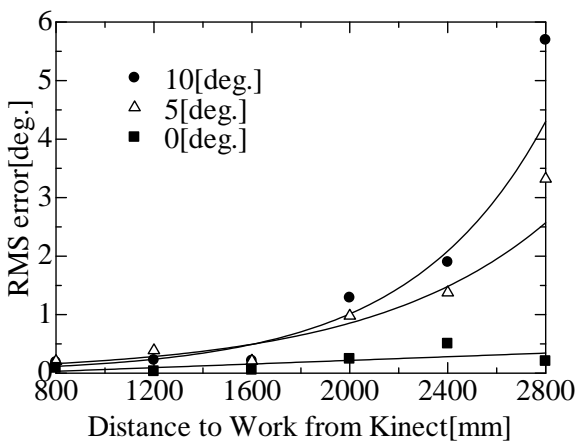


Fig. 15 Accuracy of the rotation detection.



Fig. 16 Photograph of the measured pipe

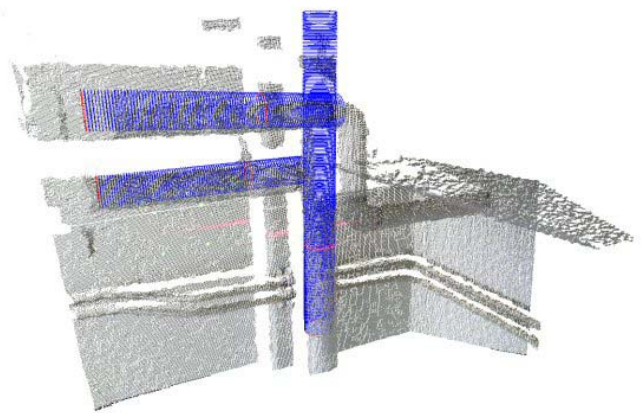


Fig. 17 Reconstructed pipe on point cloud data

IX. CONCLUSION

We describe a pipe measurement system using a laser range finder and KINECT. The system is sufficiently compact that it can be handheld. KINECT simultaneously detects point cloud data, enabling the user to freely scan the measurement system. The user manually scans the system and directs the laser slit ray along the measured pipe. Since the measurement area is selected by the laser streak, the number of data points is limited and the desired data, such as pipe cross-section data, can be extracted easily. The point cloud data obtained by Kinect are used to detect the movement of the measurement system. The cross section of a pipe is estimated from the data obtained by the laser range finder, and the 3D shape of the pipe is constructed on the computer. Experimental results demonstrate the effectiveness of our system.

REFERENCES

- [1] Jarvis, R. A perspective on range finding techniques for computer vision. PAMI(5), 1983,122-139
- [2] Pueschel, P. The influence of scanner parameters on the extraction of tree metrics from faro photon 120 terrestrial laser scans. PandRs(78) ,2013, pp.58-68
- [3] Mahoney, J. Testing the goods: Xbox kinect. ,PopSci,2010

- [4] Bigdelou, A., Benz, T., Schwarz, L., Navab, N. Simultaneous categorical and spatio-temporal 3d gestures using kinect. In: 3DUI12 ,2012, pp. 53-60.
- [5] Dal Mutto, C., Zanuttigh, P., Cortelazzo, G. Time-of-Flight Cameras and Microsoft Kinect. Springer, 2012
- [6] Zhang, Z. Microsoft kinect sensor and its effect. *MultMedMag*(19), 2012, pp.4-10.
- [7] Kapoutsis, C., Vavoulidis, C., Pitas, I. Morphological techniques in the iterative closest point algorithm., *ICIP98*, I: 808-812.,1998
- [8] Sharp, G., Lee, S., Wehe, D. Icp registration using invariant features. *PAMI*(24) , 2002, pp.90-102
- [9] Feldmar, J., Declerck, J., Malandain, G., Ayache, N. Extension of the icp algorithm to nonrigid intensity-based registration of 3d volumes. *CVIU*(66) , 1997, pp.193-206
- [10] Lee, B., Kim, C., Park, R. An orientation reliability matrix for the iterative closest point algorithm. *PAMI*(22), 2000, pp. 1205-1208
- [11] Gupta, S., Sengupta, K., Kassim, A. Compression of dynamic 3d geometry data using iterative closest point algorithm. *CVIU*(87) , 2002, pp.116-130

Edible oil comparison by terahertz time domain spectroscopy system Tera OSCAT

Marie Tobolova and Vojtech Kresalek

Abstract—In this paper, the optical characteristics of edible oils' samples have been investigated with THz-Time Domain Spectroscopy (THz-TDS). For the first time, the unique THz-TDS system Tera OSCAT is used for this experiment. Main difference from other THz-TDS systems lies in its original time delay construction. The refraction indices are calculated in the frequency range of 0.25 – 0.85 THz, statistically analyzed and evaluated. Based on the results, the samples of oils are compared to determine whether the THz-TDS system is able to distinguish the tested oils from each other.

Keywords—edible oil, OSCAT, refractive index, THz time domain spectroscopy.

I. INTRODUCTION

THERE is a growing interest in the healthy food and its preparation in recent years. The study of chemical composition of food becomes trendy, because this knowledge allows the assessment of the product quality. Following the diets and some radical directions of healthy food, oils and all fatty components are often understood as something wrong but the opposite is true. Fats are necessary part of our diet because some important vitamins and essential substances are contained in or fat-soluble. Therefore, it is evident that there is an increased interest in new methods for studying the properties of oils. Because of its non-polar character, oil is the good sample for the terahertz spectroscopic methods [1]. A lot of non-polar liquids are quite transparent to THz pulse, while polar liquids (typically water and alcohols) cause strong absorption and attenuation of THz radiation [2]. The properties of oils can be tested by variety of techniques; chemical analyses, chromatography, organoleptic assessment methods, etc. [3]. Usually, these are expensive and time consuming methods, therefore new approaches, that could save time and also reduce costs, are invited. Spectroscopic techniques seem to be as a good alternative; measurement is

fast and relatively inexpensive. Fluorescence spectroscopy [4], Fourier transform infrared spectroscopy, Raman [5] and nuclear magnetic resonance spectroscopy [6] have been used in this application, yet. Also some first experiments investigating oils using terahertz technique have appeared [7], [8]. The aim of this study is to analyze several kinds of edible oils using THz-TDS system Tera OSCAT.

II. MATERIALS AND METHODS

A. Instrumentation

Eight types of edible oil for both cold and hot meals' preparation were the objects of this study. There were included three refined oils (sunflower, rapeseed and rice bran oil), four virgin oils made from the pumpkin seeds, hemp, linseed and coconuts, and one extra virgin olive oil.

Tera OSCAT used in this experiment is a new THz-TDS device made by MenloSystems, Ltd. It works as a classical THz-TDS system based on the pump-probe principle, but the novelty of this spectrometer lies in the technique of electronic generation of time delay between the pump and probe pulses. The method named Optical Sampling by Cavity Tuning (OSCAT) is based on a direct control of the time delay between the pulses by varying the pulse repetition rate of laser source. The most important parts are a femtosecond laser with a tunable repetition rate and a passive delay line [9]. It allows time-resolved optical experiments without any external mechanical delay line or two synchronized femtosecond lasers as it is typical for other systems to achieve a defined temporal delay between pulses [10]. Due to these properties, it is very compact, robust and also cost-efficient experimental setup.

B. Experimental Design

The samples of oils were prepared for measurement in a liquid form at room temperature 25°C. A glass Petri dish was filled with the amount of 1 ml of just investigated oil. The average thickness of the dish bottom was about 1606.6 microns and the thickness of the oil layer moved in the range 900 – 1303 microns, therefore the thickness of the whole two-layer structure moved around 2.5 millimeters. The measurement was carried out immediately after the filling Petri dish to prevent oxidation processes of the oil.

The experimental adjustment has standard transmission geometry (see Fig. 1). The laser source is a mode-locked

This paper is supported by the European Regional Development Fund under the project CEBIA-Tech No. CZ.1.05/2.1.00/03.0089.

Marie Tobolova is with the Department of Electronics and Measurements, Tomas Bata University, Zlin, Czech Republic (corresponding author, phone: +420 576 035 228; e-mail: tobolova@fai.utb.cz). She is at the same time the Ph.D. student of the Department of Biomedical Engineering, Brno University of Technology, Brno, Czech Republic.

Vojtech Kresalek is with the Department of Electronics and Measurements, Tomas Bata University, Zlin, Czech Republic (e-mail: kresalek@fai.utb.cz).

femtosecond Er-doped fiber oscillator producing 90 fs pulses at 1560 nm with a repetition rate of 250 MHz [11]. The fs laser beam is divided into two pulses, one for exciting the emitter antenna to produce the THz pulse, and the second for activating the receiver antenna to measure the THz signal. THz pulse passes through the investigated sample (oil in Petri dish) and the signal reflecting the interaction with sample is detected. THz-TDS relies on comparing this THz response with the same THz pulse transmitted only through air (reference measurement). Reference (air), empty Petri dish and each sample (Petri dish with oil) were measured ten times.



Fig. 1 Design of experiment, transmission geometry

C. Data analysis

The refractive indices for all samples were calculated using the TeraMat software. These calculations require a priori information about the sample thickness. Other mathematical corrections were necessary because the measured values were not the parameters of the oil itself but the Petri dish included. All measured data were processed and evaluated using the statistical software Statistica 10 by Statsoft Company.

The investigated frequency range was limited to 0.25 – 0.85 THz because of the increased incidence of Fabry-Perot artifacts out of these bounds. Ten measured refractive indices for each sample of oil were averaged to get representative values for a total overview of the refractive index behavior in specified frequency interval, see Fig. 2. We can see the different ranges of refractive index for each type of oil; exact values of mean, median, minimum, maximum, standard deviation and standard error are summarized in the descriptive statistics (Table I).

For other detailed analysis, the original data from ten measurements of each type of oil were considered. There was chosen frequency of 0.65 THz for the analysis because the closest region around this frequency point was least affected by artifacts. The data are summarized in Table II. Based on the histograms and Box-Whisker plot (Fig. 3), the non-normal distribution of the data was evident.

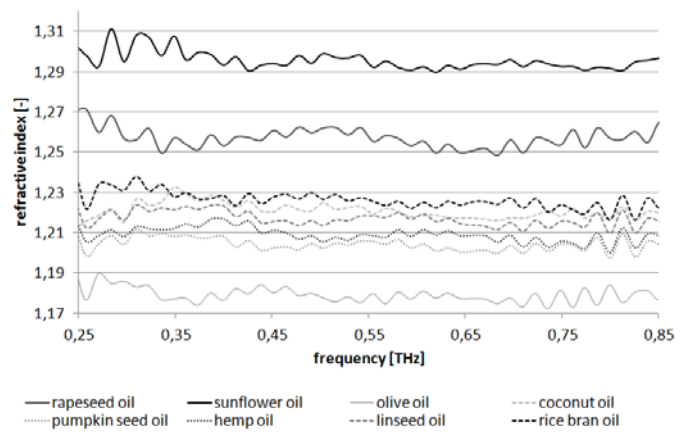


Fig. 2 Refractive indices of measured oils in the frequency range of 0.25 – 0.85 THz

Table I Descriptive Statistics of Refractive Indices for oils measured in frequency range 0.25 - 0.85 THz

	Mean	Median	Minimum	Maximum	Std. Dev.	Standard-Error
rapeseed oil	1,2572	1,2571	1,2486	1,2716	0,0001	0,0050
sunflower oil	1,2958	1,2943	1,2810	1,3115	0,0001	0,0048
olive oil	1,1793	1,1786	1,1725	1,1901	0,0001	0,0038
coconut oil	1,2213	1,2211	1,2155	1,2329	0,0001	0,0040
pumpkin seed oil	1,2041	1,2043	1,1972	1,2118	0,0001	0,0034
hemp oil	1,2092	1,2090	1,2003	1,2170	0,0001	0,0038
linseed oil	1,2172	1,2166	1,2099	1,2242	0,0001	0,0038
rice bran oil	1,2265	1,2261	1,2167	1,2384	0,0001	0,0044

Table II Descriptive Statistics of Refractive Indices of oils for the frequency of 0.65 THz

	Mean	Median	Minimum	Maximum	Std. Dev.	Standard-Error
rapeseed oil	1,2511	1,2529	1,2380	1,2618	0,0001	0,0084
sunflower oil	1,2937	1,2930	1,2930	1,2977	0,0001	0,0016
olive oil	1,1778	1,1787	1,1686	1,1865	0,0001	0,0069
coconut oil	1,2175	1,2208	1,2068	1,2255	0,0001	0,0072
pumpkin seed oil	1,2009	1,2008	1,1940	1,2076	0,0001	0,0058
hemp oil	1,2090	1,2115	1,2010	1,2173	0,0001	0,0056
linseed oil	1,2142	1,2146	1,2112	1,2158	0,0001	0,0019
rice bran oil	1,2257	1,2262	1,2240	1,2284	0,0001	0,0018

Because of a number of variables (oils), the multivariate statistics was chosen for the comparison of oils. Cluster Analysis is statistical method able to work with a large number of objects and distinguish between more and less similar objects. This is based on the distances between them. The resulting tree diagram is shown in Fig. 4.

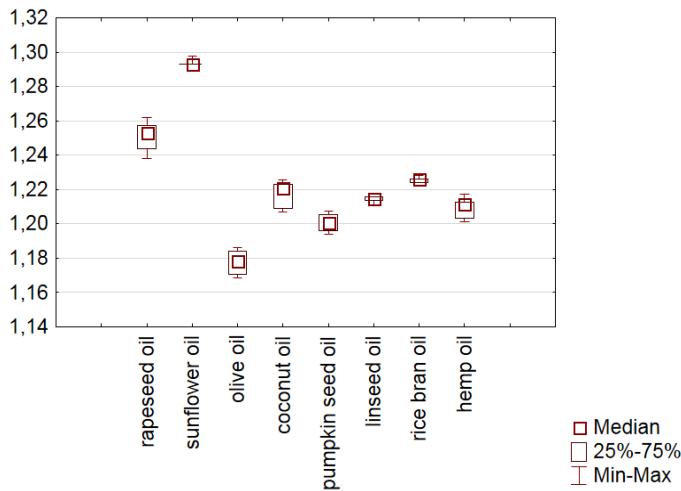


Fig. 3 Box-Whisker plot of refractive index distribution for measured oils

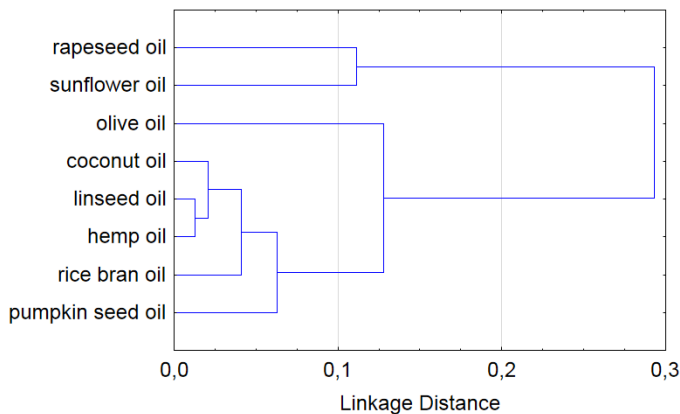


Fig. 4 Tree Diagram based on the complete linkage clustering of the Euclidean distances between all types of oils at the frequency 0.65 THz

III. RESULTS

The aim of the whole experiment was to investigate the samples of various oils by THz time-domain spectroscopy and compare them. First, the averaged refractive indices of all measured oil samples were plotted in specific frequency range 0.25 – 0.85 THz to get the basic information about properties of examined data (Fig. 2). Each type of oil has its typical range of refractive index values. The exact values of their mean, median and other descriptive parameters specified for each oil are shown in Table I. Based on the curves of refractive index in Fig. 2, we can make some assumptions.

At first sight, no curves overlap significantly, therefore we could consider a good separation of oils and each of them could be represented by its own refractive index at each frequency. The exception represents only the coconut oil which has refractive index similar to rice bran oil and linseed oil in some parts of the frequency range. Further, there is obvious separation of two refined oils (sunflower and rapeseed) from the virgin oils. Conversely, the refined rice bran oil is very close to the group of virgin oils (coconut,

linseed, hemp, and pumpkin seed) that have the smallest differences between them. The unique position has the extra virgin olive oil; its refractive index is the lowest and the separation from the other virgin oils is apparent. These hypotheses could denote relatively good recognition of refined, virgin and extra virgin oils but they require regular statistical analysis.

Ten values of refractive index measured for each sample at the frequency of 0.65 THz were considered for further analysis. Basic properties of all oils are summarized in descriptive statistics Table II, again. Normality of the data was analyzed using histograms and was not confirmed. This can be shown also in Box-Whisker plot, see Fig. 3. Median in most samples is shifted to some of the extreme values. Also in this plot, we can observe the similarity of virgin oils and separation of extra virgin oil and two refined oils.

Finally, the similarity among the oils was solved by the Cluster analysis. All eight objects (oils at given frequency) form the basis of the distance matrix which defines the degree of similarity of the objects. The tree diagram (Fig. 4) shows clear separation of refined sunflower and rapeseed oil from others. Second large cluster is formed by virgin oils with the extra virgin olive oil connected as the last one with the largest distance to other objects of this cluster. As we can see the distances between individual objects, the linseed, hemp and coconut oils are very similar, further the cluster was expanded by refined rice bran oil and pumpkin virgin oil.

IV. DISCUSSION

The similarity/dissimilarity of oils should be based on their physical and chemical properties that will depend on a number of factors such as the quality of used raw material, growing region and especially the processing procedures. Crude vegetable oils contain mainly triacylglycerols (95%), free acids, monoacylglycerols and diacylglycerols. Further, variable amounts of phospholipids, sterols, triterpene alcohols, tocopherols and tocotrienols, carotenes, chlorophylls, hydrocarbons, traces of metals, oxidation products and some other compounds may be part. Refining procedures convert crude oil into a bland product with a defined specification. Some of the minor components are retained in the refined oil and some of them removed for other utilization. Virgin oils should be from the cold pressed seeds but it may not be a rule and there can be applied heating before or during pressing[12]. Virgin oils exceed refined oils in their nutritional value because they contain more natural ingredients such as tocopherols, sterols, carotenoids, and phospholipids. All virgin oils used in this study were cold-pressed as declared by the manufacturer.

We can summarize some important properties of oils based on their chemical composition by [13] and [14]. Refined rapeseed oil contains oleic, linoleic, linolenic, palmitic and stearic acids with less saturated acids than any other oil. Sunflower oil contains linoleic and oleic acids, and practically

no linolenic acid. Olive oil is typical by a high level of oleic acid. It contains unsaponifiable constituents that cause high oxidative stability, next squalene is contained at a higher level than in other oils. Coconut oil is important lauric oil because of its high level of lauric acid. Linseed oil is one of the most unsaturated vegetable oils with high level of linolenic acid. Hemp oil contains linoleic, α -linolenic, oleic, palmitic, stearic, γ -linolenic and stearidonic acid. Rice bran oil contains oleic, linoleic, and palmitic acids, and other minor compounds. Refined rice bran oil has high oxidative stability resulting from its high level of tocopherols and the presence of oryzanols. It contains almost no cholesterol. Pumpkin seed oil is rich in linoleic acid, oleic, palmitic and stearic acids.

The rapeseed and sunflower oils have similar oil content (around 40%), close iodine and saponification values, but fundamentally differ in fatty acid content. They are two very often used refined oils for hot meals. It seems that just refining makes them very similar as it may be observed in our results. The third refined oil, rice bran oil, was assigned to virgin oils. This we could explain by its special composition. It has very little in common with rapeseed and sunflower oil except the refining process. It has the oil content only 10% and lower iodine value is responsible for better oxidative stability. Linseed and hemp oils have similar oil content (around 35%) and correspond approximately also in the fatty acid composition. There dominates linolenic, linoleic and oleic acids. Both oils have high iodine value (around 190) therefore the oxidative stability is lower. Coconut oil is the most specific oil of all because of its special composition. There dominates lauric and myristic acids and common acids in other oils are in very small amount. The coconut oil has the lowest iodine value (81.4) and the highest saponification value (250) of all. Pumpkin seed oil is high linoleic oil and has good oxidative stability (low iodine value). Extra virgin olive oil has the highest content of oleic acid (up to 83%) of all, approximately the same amount of palmitic and linoleic acids, and relatively uncommon palmitoleic acid. It has very good stability according to low iodine value (88.4).

Our results do not correspond with the values of classical optical refractive index presented in [15], but relatively good distinguishing of the types of oil into three groups (refined, virgin and extra virgin) is evident. Nevertheless, the chemical analysis of the investigated oils is needed for more precise comparison and description of the oils.

V. CONCLUSION

The experiment shows the capability of THz time-domain spectroscopy system to study the optical properties of oils in THz frequency region.

REFERENCES

- [1] J. E. Pederson and S. R. Keiding. "THz time domain spectroscopy of nonpolar liquids," *IEEE Journal of Quantum Electronics*, vol. 28, no. 10, October 1992, pp. 2518 – 2522.
- [2] M. van Exter, Ch. Fattinger and D. Grishkowsky. "Terahertz time-domain spectroscopy of water vapor," *Optics Letters*, vol. 14, issue 20, October 1989, pp. 1128 – 1130.
- [3] A. Dieffenbacher and W. D. Pocklington. "Standard Methods for the Analysis of Oils, Fats and Derivatives," Oxford: Blackwell Scientific Publications, 1992.
- [4] K. Nikolova et al. "Quick Fluorescence Method for the Distinguishing of Vegetable Oils," *Journal of Food Science and Engineering*, vol. 2, December 2012, pp. 674 – 684.
- [5] H. Vaskova and M. Buckova, "Measuring and Identification of Oils," in *Proc. 18th WSEAS (CSCC'14)*, Greece, to be published.
- [6] S. B. Engelsen. "Explorative Spectrometric Evaluations of Frying Oil Deterioration," *Journal of the American Oil Chemists' Society*, vol. 74, no. 12, December 1997, pp. 1495 – 1508.
- [7] L. Jiu-sheng and Y. Jian-quan. "Highly precise determination of optical constants olive oil in terahertz time-domain spectroscopy," *Proceedings of SPIE*, vol. 7277, no. 1, December 2008.
- [8] R. Bao et al. "Spectroscopy studies on the Tuha crude oil in the terahertz range," *Proceedings of SPIE: Terahertz Wave Technologies and Applications*, vol. 8195, August 2011.
- [9] R. Wilk et al. "OSCAT: Novel Technique for Time-Resolved Experiments Without Moveable Optical Delay Lines," *Journal of Infrared, Millimeter, and Terahertz Waves*, vol. 32, issue 5, May 2011, pp. 596 – 602.
- [10] T. Hochrein et al. "Optical sampling by laser cavity tuning," *Optics Express*, vol. 18, issue 2, January 2010, pp. 1613 – 1617.
- [11] *TERA OSCAT: User manual*. MenloSystems, GmbH, Martinsried, Germany, 2013.
- [12] M. Wroniak, K. Krygier and M. Kaczmarczyk. "Comparison of the quality of cold pressed and virgin rapeseed oils with industrially obtained oils," *Polish Journal of Food and Nutrition Sciences*, 2008, vol. 58, no. 1, pp. 85 – 89.
- [13] F. Shahidi and Y. Zhong. "Vegetable Oils," in *Bailey's Industrial Oil and Fat Products*, 6th ed. vol. 6, F. Shahidi, Ed. New Jersey: John Wiley & Sons, Inc., 2005, pp. 213–267.
- [14] N. Karak. "Vegetable oils and their derivatives," in *Vegetable Oil-Based Polymers: Properties, Processing and Applications*, 1st ed., N. Karak, Woodhead Publishing, 2012, pp. 54 – 95.
- [15] M. Bockisch. "Fats and Oils Handbook," Hamburg: AOCS Press, 1998, pp. 90 – 120.

Application of the static and dynamic models in predicting the future strength of pozzolanic cements

Dimitris C. Tsamatsoulis

Abstract— The objective of this study is to analyze static and dynamic models predicting the future typical compressive strength of Pozzolanic cements. Both classes of models are based on physical and chemical characteristics and on the early strength of this cement type. The models performance was investigated and the superiority of the dynamic models was proved based on different criteria. Based on the dynamic models, the industrial quality control can daily evaluate the reactivity of cement compounds and take preventive or corrective actions if needed in order to maintain a low variance of typical strength.

Keywords—Cement, model, prediction, strength

I. INTRODUCTION

BLENDED cements are largely produced and utilized in construction. With these types of cement high performance concrete can be obtained as regards strength and durability under expected environmental conditions. On the other hand, the composite cements due to their lower Clinker/Cement ratio contribute to the reduction of the emitted CO₂ per ton of produced cement having a very positive environmental impact. According to the European Norm EN 197-1:2011 [1] several components can be used as main cement constituents, except the clinker: Limestone, natural or artificial pozzolane, fly ash, granulated blast furnace slag and silica fume. The most of these compounds are characterized as pozzolanic or cementitious materials, contributing effectively on the strength development of cement and concrete. Consequently concerning strength development, a binary or ternary mixture of Portland clinker with these components shows a behavior completely different from that of pure Portland cement composed only from clinker and gypsum.

Cement quality is mainly characterized by its stability concerning the compressive strength in mortar and concrete. The stability of 28 days strength of mortar is thought as sufficient indicator of the product quality. In case the cement strength is far from the predefined target, the delay of 28 days of receiving results is enough long and likely the reasons causing strength divergence already have vanished. A second drawback related with this delay is that if the producer does

not start any action during this period, a product outside of specifications could be manufactured. Therefore the construction of models predicting the 28-day strength of blended cements is a challenging issue compared to the models predicting the Portland cement strength.

A relatively extended literature exists for models predicting the compressive strength of Portland cement [2] –[11]. No such large bibliography exists for blended cements especially if the constituents contribute drastically in the 28-day strength. Douglas et al. [12] performed an experimental design for mixtures of three components including Portland cement, granulated blast furnace slag and fly ash. Using seven design points, a statistical approach was used to find the equations describing strength development of the ternary systems at 1, 7, 28 and 91 days. For the same ternary mixture Wang et al. [13] applied a simplex-centroid design to study the compressive strengths of mortars at different ages and they found three cubic polynomial models. They also designed ternary diagrams allowing to predict the compressive strengths from the iso-strength contour lines. Kostoglou et al. [14] developed a multiple linear regression model for predicting the 28-day compressive strength of Portland cement with pozzolana. Except other variables, they utilized the cement insoluble residue and the pozzolanic activity factor to describe the pozzolane effect on the strength. Nehdi et al. [15] used factorial designs to optimize ternary cementitious mortar blends. The ternary mixtures included ordinary Portland cement (OPC) -silica fume (SF) - fly ash (FA) and OPC-SF-granulated blast furnace slag (GBFS). Response surfaces for several properties including compressive strength at 1, 7, 28 and 56 days were obtained for up to 20%, 40%, and 60% replacement levels of OPC by SF, FA and GBFS, respectively. Chen et al. [16] applied the method of the simplex-lattice design for predicting the strength of ternary cementitious systems composed from cement, silica fume and fly ash with constant water to binder ratio and a mass fraction of mineral admixtures not exceeding 30%. With the aid of the optimization theory they optimized the mixture proportioning, using compressive strength as a criterion. Khan [17] investigated the iso-responses for strength, permeability and porosity of high performance mortars composed from cement, fly ash and silica fume, with the aim at developing high performance-low environmental impact concrete. The same author [18] developed analytical models for the strength

D. C. Tsamatsoulis is with Halyps Building Materials S.A., Italcementi Group, 17th Klm Nat. Rd. Athens – Korinth, Aspropyrgos, GREECE (e-mail: d.tsamatsoulis@halyps.gr).

prediction of high performance concrete composed from various binary and ternary combinations of Portland cement, fly ash, slag and silica fume. He derived quadratic response surfaces correlating the compressive strength at 7, 28, 90, 180 days with the proportions of fly ash, slag, silica fume and with the ratio of water to cement. Abd-El Aziz et al. [19] studied the physico-chemical and mechanical characteristics of pozzolanic cement pastes and mortars hydrated at different curing temperatures. Their results indicated that, the pozzolanic cement mortars give higher strength than the Portland cement mortars, especially at curing temperatures above 35 °C. Heikal et al. [20] investigated the characteristics of blended cements containing nano-silica (NS). They considered as control sample a standard mix of Portland (OPC) cement and GBFS. The composite OPC–GBFS–NS cements containing 45 % of GBFS and 3–4 % of NS possess the highest improvement of mechanical properties, hydration kinetics and microstructure of hardened cement pastes and mortars.

The effect of the mentioned pozzolanic or cementitious materials on the compressive strength of concrete has been also investigated and modeled. Several researchers utilized multiple regression models to quantify the impact of the referred materials on the strength [21]-[27]. Another category of research includes modeling based on artificial neural networks (ANN) or fuzzy logic (FL) [28]-[32].

The most of these models are used for design purposes and are based on laboratory experimental data. The predictions are accurate inside their field of application. In case of important change of the value of a parameter not contained in the set of the independent variables, the predictive model could fail. Therefore the most of the models could be called “static”. Tsamatsoulis [33] performed a detailed comparison of static and dynamic models of Portland cements based on regression algorithms. The dynamic models incorporate the uncertainty due to the time variability of non involved factors during the modeling procedure. The main aim of this study is to extend the comparison between static and dynamic models to the class of pozzolanic cements, characterized as CEM IV in EN 197-1 norm. The major difficulty in predicting strength of this cement type is that except clinker at least one other component affecting strength participates. Usually the pozzolanic materials are characterized from elevated variability as concerns their composition, especially in case they are by-products from another industrial process. In the current study natural pozzolane and calcareous fly ash originating from electricity plants are the main constituents of the CEM IV cements. The applicability of such models on the daily quality control was examined in detail. This article is structured as follows: The experimental methods and the applied standards are referred to the first section. Afterwards, the suggested predicting models are developed. The implementation of the models is analyzed in the last section.

II. EXPERIMENTAL

Pozzolanic cements belonging to two strength classes according to EN 197-1:2011 were studied: CEM IV/B (P-W)

32.5 N and CEM IV/B (P-W) 42.5 N. Both cements contain natural pozzolane (P) and calcareous fly ash (W) as main components. The modeling is based on the results of the daily average samples of cement produced in two cement mills (CM) of Halyps plant. The analyses made on these samples were the following:

- (i) Residue at 40 μm sieve, R40, measured with air sieving.
- (ii) Specific surface, Sb, measured according to EN 196-6.
- (iii) Loss on ignition, LOI, and insoluble residue, Ins_Res, of the cement measured according to EN 196-2.
- (iv) Oxides analysis (SO₃, CaO, SiO₂, Al₂O₃, Fe₂O₃) measured with X-ray fluorescence.
- (v) Compressive strength at 1, 7 and 28 days. The preparation, curing and measurement of the specimens were made according to the standard EN 196-1.
- (vi) The cement composition was computed using the results of the steps (iii) – (iv) and the average analysis of the raw materials, by applying the method presented in [34]. In this way the clinker content was calculated.

III. MATHEMATICAL MODELS PREDICTING STRENGTH

Exclusively plant data of cement produced in the cement mills CM5 and CM6 during height years were utilized. The modeling predicting the 28-day strength was based on more than 1500 data sets of cement fineness, chemical analyses, composition, 1, 7 and 28 days strength. Two categories of models were elaborated: (a) the static ones, wherein for a given data set, the values of the parameters were calculated with multiple linear regression. Afterwards these values were utilized to predict the future strengths, each time the input data were available and (b) the dynamic models, where the parameters were estimated from a moving set of data belonging to past time interval of predefined size, e.g. 3 months, 6 months etc. For all the dynamic models, the latest date of the time interval has two characteristics: (i) the 28-day strength has been measured; (ii) its distance from the date of prediction is the minimum. The dependent and independent variables of static and dynamic models are shown in Tables 1 and 2 respectively.

Table 1. Variables of the static models

Model	Variable						
	Clink (%)	Pz (%)	Ash (%)	Sb/10 ⁴ (cm ² /gr)	R40 (%)	Str_1 (Mpa)	Str_7 (Mpa)
Str28_1	+	+	+	+	+	+	
Str28_7	+	+	+	+	+	+	+

Table 2. Variables of the dynamic models

Variable	Model CM5		Model CM6	
	Str28_1	Str28_7	Str28_1	Str28_7
LOI (%)	+			
Ins_Res (%)	+	+	+	+
CaO (%)			+	+
SiO ₂ (%)	+	+	+	+
Al ₂ O ₃ (%)			+	

	Str28_1	Str28_7	Str28_1	Str28_7
Sb/10 ⁴ (cm ² /gr)	+	+	+	+
R40 (%)	+	+	+	+
Str_1 (Mpa)	+	+	+	+
Str_7 (Mpa)		+		+

where Clink, Pz, Ash = clinker, pozzolane, fly ash contents (%) respectively, CaO, SiO₂, Al₂O₃ = the contents (%) of the corresponding oxides, LOI = loss on ignition (%), Ins_Res = insoluble residue (%), Sb = cement specific surface (cm²/gr), Str_1 and Str_7 = compressive strengths (Mpa) after one and seven days curing correspondingly, Str28_1, Str28_7 = 28-day strength (Mpa) estimated from the respective model.

A. Static Models

The models correlating the 28-day strength with 1-day strength (Str28_1) and both 1 and 7 days' strength (Str28_7) were investigated. The models are described by (1):

$$Y = A_0 + \sum_{i=1}^N A_i X_i + \sum_{i=1}^N A_{ii} X_i^2 + \sum_{i=1}^N \sum_{j=i+1}^N A_{ij} X_i X_j \quad (1)$$

where X_i, X_j = the independent variables, Y = the dependent variable. The coefficients A_i, A_{ii}, A_{ij} are determined by minimizing the residual error S_{Res} calculated by (2):

$$S_{Res}^2 = \sum_{i=1}^M \frac{(Y_{calci} - Y_{acti})^2}{M - k} \quad (2)$$

where Y_{act} = actual 28 days strength, Y_{calc} = the calculated one from the model, M = number of data sets, k = number of independent variables. The full set of data involves all results of the two mentioned cement types from 2006 to 2013 for CM5 and CM6. For each CM the model parameters were determined using the data of 2006-2008 by applying multiple linear regressions. With t-test and 95% probability, the non significant parameters were excluded. The statistically significant coefficients (A_i, A_{ii}, A_{ij}) for both models and mills are presented in Tables 3 and 4.

Based on the parameters of the models calculated with data of three full years, a further search was performed as regards the accuracy of future strength prediction. For each CM, the models were applied for the results of 2009 to 2013, using the parameters computed with the 2006-2008 data. The residual errors are presented in Table 5. The last row shows the S_{Res} for the full range of data from 2009 to 2013.

It is clearly observed from the Table 5 that the accuracy of the static models in predicting future strength is deteriorated as long as the time distance between the parameters estimation and the prediction of strength augments. The most probable causes are the changes of the clinker reactivity or other cement constituent contributing to strength and of cement particle size distribution. If these characteristics are not kept relatively stable, then the probability of failure in prediction becomes not negligible.

Variable	Str_28_1	Str_28_7
Constant	0	0
Clink	0.397	0.316
Ash		0.139
Sb/10 ⁴	10.2	1.929
R40	-0.105	
Str_1	3.59	-0.558
Str_7		0.900
Clink·Pz	5·10 ⁻³	3·10 ⁻³
Clink·Ash	8·10 ⁻³	
Pz·Ash		1·10 ⁻³
Pz·Sb/10 ⁴	-0.653	
Ash·Sb/10 ⁴	-0.324	-0.263
Clink·R40	-4·10 ⁻⁴	-0.012
Ash·R40	-3·10 ⁻⁴	
Clink·Str_1	-0.039	
Ash·Str_1	-0.022	-0.02
Clink·Str_7		-3·10 ⁻³
R40·Str_7		0.026
Num. of data	454	454
S _{Res}	1.811	1.362

Variable	Str_28_1	Str_28_7
Constant	0	0
Clink	0.248	0.247
Ash		-0.416
Sb/10 ⁴	42.6	-30.7
R40	1.404	
Str_1	6.238	0.034
Str_7		3.192
Clink·Pz	0.014	-2·10 ⁻⁴
Clink·Ash	5·10 ⁻³	
Pz·Ash		-3·10 ⁻³
Pz·Sb/10 ⁴	-2.864	
Ash·Sb/10 ⁴	-0.403	0.894
Clink·R40	-0.016	0.026
Ash·R40	-0.020	
Clink·Str_1	-0.078	
Ash·Str_1	-0.025	1·10 ⁻³
Clink·Str_7		-0.029
R40·Str_7		-0.056
Num. of data	169	169
S _{res}	1.572	1.224

	Str28_1		Str28_7	
	CM5	CM6	CM5	CM6
2006-08	1.811	1.572	1.362	1.224
2009	2.529	2.529	1.452	1.604
2010	2.195	2.026	1.429	1.426
2011	1.982	3.780	1.401	2.245
2012	3.994	5.087	2.247	2.669
2013	5.979	8.654	3.377	4.545
2009-13	3.452	4.353	1.966	2.415

B. Dynamic Models

To improve the predictability of the modeling a second approach was selected by including dynamical characteristics and maintaining the simplicity of implementation. The two models referred in Table 2 were implemented by excluding with t-test the non-significant variables, by omitting the coefficients A_{II} , A_{IJ} and considering movable time horizon as concerns the introduced data. Thus, for each date a new 28-day strength result appears, the models' coefficients are recalculated with the following algorithm:

(i) At date t a new 28-day strength result appears. The specimen was prepared 28 days ago. The production date is in distance t-29 days from the current date t.

(ii) A time interval of T_D days and the samples belonging to the period $[t-29-T_D, t-29]$ are presumed. The dynamic data set consists of this population of samples.

(iii) Using multiple regression the model parameters A_I ($I=0 \dots N$) and s_{res} are computed.

(iv) At date t, the chemical and physical results of the cement produced in the previous day, the 1 day strength of the cement produced 2 days ago and the 7 days strength of cement produced 8 days ago have been measured.

(v) With the set of parameters computed in step (iii) the 28 days strength of cement produced at t-2 and t-8 days are estimated, by applying the models Str28_1 and Str28_7 respectively.

(vi) The procedure is repeated for the date t+t_N, where t+t_N is the date a new 28 days result appears. Consequently t_N ≥ 1.

(vii) If t_N>1, the future strength of the cement produced in the time intervals $[t-1, t+t_N-2]$, $[t-7, t+t_N-8]$ is computed according to the equation of step (v). Otherwise using the equation computed in step (vi).

(viii) As the time span remains T_D , when a new result is added, the time interval is moved on. Thus the future 28 days strengths are calculated using models applied to data sets of movable time horizon.

(ix) Parameter T_D shall be optimized with one of the two criteria: (a) minimum s_{Res} during modeling and (b) minimum error during the future application of the models. A T_D interval from 90 to 720 days was investigated.

(x) For each date J a set ($A_I(J)$, $s_{Res}(J)$) is computed from the samples belonging to $[J-T_D, J]$ time interval. Depending on T_D value, the number of the consecutive sets ($A_I(J)$, $s_{Res}(J)$) is K_{TD} and the number of sets for a date J is $N_{TD}(J)$. The average residual errors, $s_{Res,Aver}$, during modeling is calculated by (3):

$$s_{Res,Aver} = \sqrt{\frac{\sum_{I=1}^{K_{TD}} s_{Res}(I)^2}{K_{TD}}} \quad (3)$$

The average number of data sets per T_D , $N_{TD,Aver}$ and $s_{Res,Aver}$ for the results of both cement mills are presented in Tables 6 and 7.

Table 6. s_{Res} during modeling for CM5

T_D	N_{TD}	$s_{Res,Aver}$	
		Str28_1	Str28_7
90	42	1.49	1.06
120	55	1.56	1.12
180	81	1.64	1.22
270	119	1.71	1.30
360	156	1.78	1.35
450	197	1.80	1.36
540	236	1.83	1.52
720	310	1.89	1.58

Table 7. s_{Res} during modeling for CM6

T_D	N_{TD}	$s_{Res,Aver}$	
		Str28_1	Str28_7
90	22	1.38	0.94
120	29	1.49	1.02
180	43	1.58	1.12
270	62	1.69	1.20
360	83	1.75	1.25
450	103	1.81	1.29
540	125	1.86	1.31
720	165	1.94	1.36

The following comparison of the two kinds of models is made based on the results of Tables 3, 4 and 6, 7. Increasing N_{TD} , s_{Res} of the dynamic models also increases. Despite the dynamic models are much simpler than the static ones, the residual errors are comparable for $N_{TD} = 450$ for CM5 and $N_{TD}=180$ for CM6.

IV. ANALYSIS OF RESULTS AND DISCUSSION

A. Prediction of Future Strength with the Dynamic Models

The worsening of prediction of future strength with the static models was presented in Table 5. The dynamic models have the flexibility to include the tuning parameter TD which needs optimization. The residual errors in predicting the future strength by applying the dynamic Str28_1, Str28_7 models are shown in Table 8 from where the following remarks can be made:

Table 8. s_{Res} during predicting future strength for CM5, CM6.

Year	T_D	Str28_1		Str28_7	
		CM5	CM6	CM5	CM6
2008-13	90	2.26	2.57	2.00	1.93
2008-13	120	2.26	2.21	1.92	1.64
2008-13	180	2.26	2.12	1.76	1.59
2008-13	270	2.23	2.10	1.69	1.50
2008-13	360	2.19	2.16	1.63	1.53
2008-13	450	2.19	2.21	1.61	1.53
2008-13	540	2.19	2.24	1.67	1.54
2008-13	720	2.27	2.42	1.76	1.60

- For CM5 both models show minimum s_{Res} for $T_D=360-450$ days while for CM6 the minimum is located at $T_D=270$ days.

- The optimum s_{Res} values for both dynamic models are lower than the s_{Res} of the static models for the data sets of 2009-2012 shown in the last row of Table 5. The ratios of $s_{Res,Dyn}/s_{Res,Stat}$ are depicted in Fig. 1 for both models and cement mills from where it is observed that the dynamic models provide a 15-50% lower error than the static ones as concerns the prediction of future strength. The improvement is greater in the case of Str28_1 model.

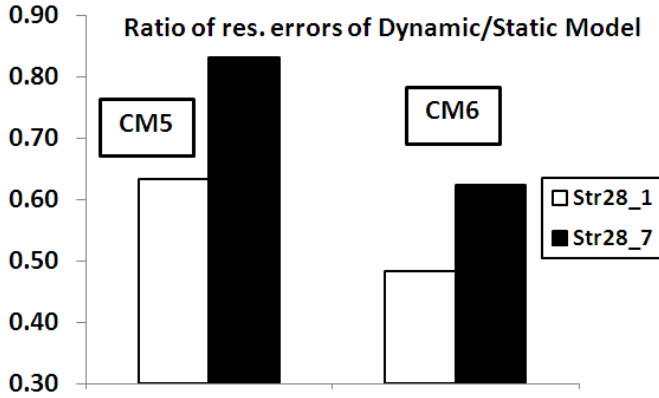


Fig. 1 Ratio of s_{Res} of Dynamic to Static model

- The optimum residual errors computed during modeling and during predicting the future strength were also compared for both models and CM. The ratio of average s_{Res} during prediction and modeling, $s_{Res,Pred}/s_{Res,Mod}$, for dynamic and static models are shown in Fig. 2, from where it is clear that this ratio is much lower in case of dynamic models than this of static models. This is an additional proof that the dynamic models predict the future strength much better than the static ones.

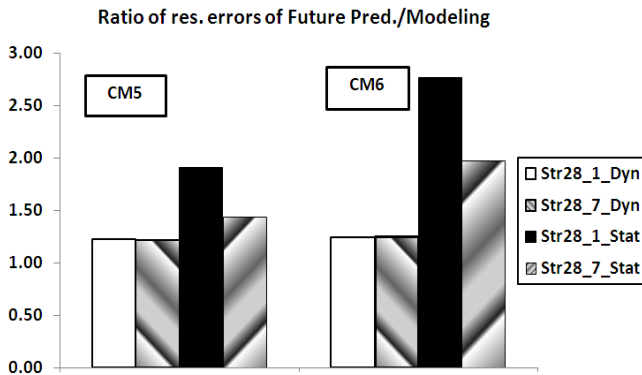


Fig. 2 Ratio of s_{Res} during prediction of future strength and modeling.

To investigate the structure of the distribution of s_{Res} computed during the future strength prediction the following algorithm was chosen.

- (i) For the T_D providing an optimum dynamic model, an average number of data sets N_{TD} corresponds.
- (ii) Data sets arrays of size N_{TD} were created, which are of movable type: When a next data set is added, the older one is subtracted. The number of consecutive arrays is around equal

to K_{TD} .

(iii) For each array I, the $s_{Res}(I)$ was calculated and the distribution was constructed.

(iv) The s_{Res} distributions for the dynamic model Str28_1 for the results of CM5, CM6 are depicted in Figs. 3 and 4 correspondingly. From these two figures it is observed that all the s_{Res} for both CM are lower than the average s_{Res} of static models during strength prediction. The above is a very strong indication of the superiority of the dynamic models in predicting the 28-day strength.

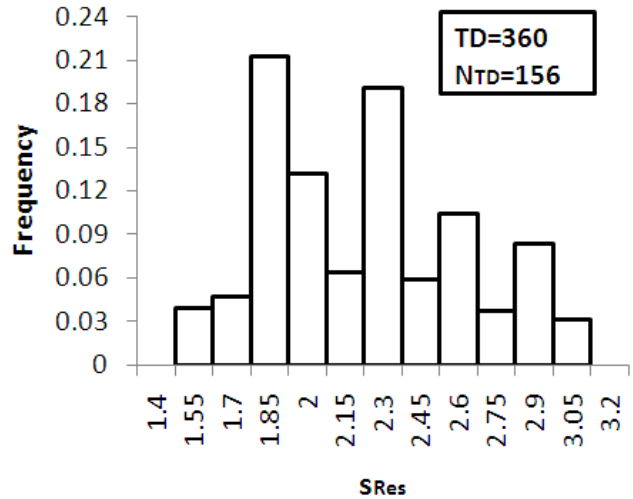


Fig. 3 Distribution of s_{Res} of dynamic Str28_1 model for CM5 results

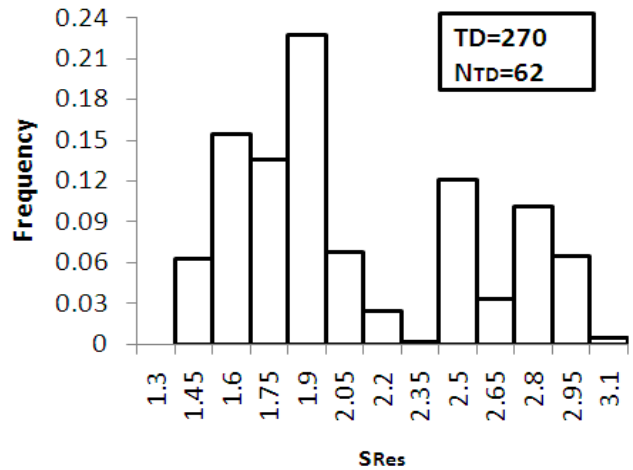


Fig. 4 Distribution of s_{Res} of dynamic Str28_1 model for CM6 results

B. Impact of the chemical, physical cement characteristics on the 28-day strength

The dynamic models predicting the 28-day cement strength are very useful because the impact of each variable can be investigated as function of time. Continuous information can be provided by implementing this model, about the reactivity of the raw materials and the impact of the fineness on the 28 days strength. The traditional Shewhart control charts [35] were proved very helpful in monitoring the cement

characteristics as it was analyzed in detail by Tsamatsoulis [9].

For the coefficients A_I of the two dynamical models the average value X_{Aver} , and the standard deviation, σ_X , were calculated. The control charts of the coefficients of variables LOI and SiO_2 for the results of CM5 obtained from the model Str28_1 with $T_D=360$ days are presented in Figs. 5 and 6. The average values, X_{Aver} and the upper and lower control limits, $X_{Aver} \pm 2\sigma_X$, are also shown.

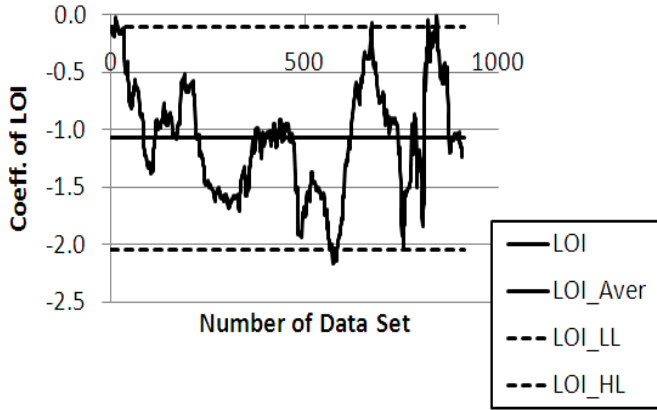


Fig. 5 Control chart of coefficient of LOI variable for dynamic Str28_1 model and CM5 results.

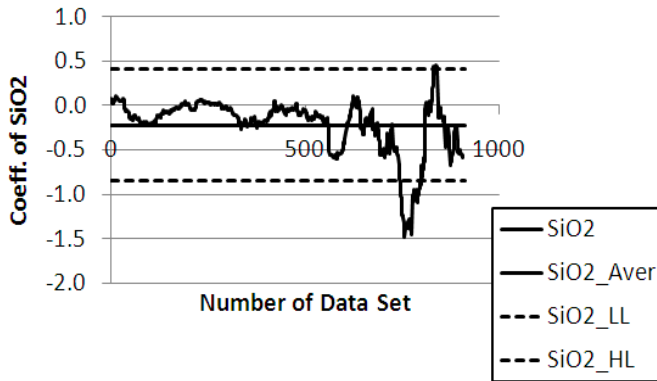


Fig. 6 Control chart of coefficient of SiO_2 variable for dynamic Str28_1 model and CM5 results.

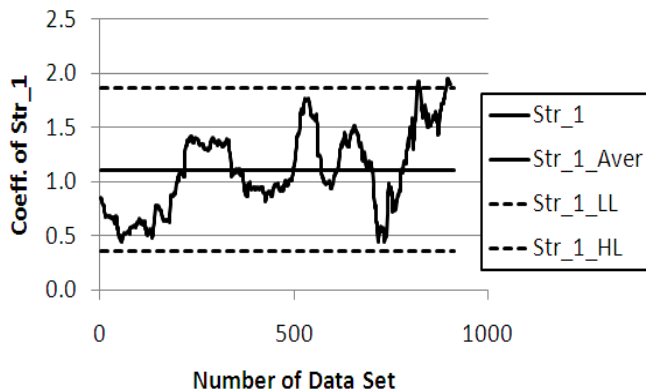


Fig. 7 Control chart of coefficient of Str_1 variable for dynamic Str28_1 model and CM5 results.

The control charts of the coefficients of Str_1 derived from the str28_1 model of CM5 and of the Str_7 derived from Str28_7 model of CM5 with $T_D=360$ are demonstrated in Figs. 7 and 8.

The average values and standard deviations of all the independent variables of the three dynamic models for CM5, CM6 are presented in Tables 9 and 10 correspondingly.

Table 9. Parameters of the dynamic models for CM5

T_D	Average Values	
	360	360
Coeff.	Str28_1	Str28_7
Constant	46.0	20.6
Sb/ 10^4	3.2	-6.2
R40	-0.26	-0.11
LOI	-1.07	
Ins_Res	-0.09	-0.03
CaO		-0.05
SiO_2	-0.22	-0.01
Str_1	1.11	-0.27
Str_7		1.11
Standard Deviations		
Constant	12.3	17.0
Sb/ 10^4	10.7	9.7
R40	0.14	0.09
LOI	0.48	
Ins_Res	0.17	0.14
CaO		0.21
SiO_2	0.31	0.27
Str_1	0.38	0.27
Str_7		0.23

Table 10. Parameters of the dynamic models for CM6

T_D	Average Values	
	270	270
Coeff.	Str28_1	Str28_7
Constant	47.5	20.2
Sb/ 10^4	-10.3	-10.7
R40	-0.28	-0.13
LOI	-0.01	0.12
Ins_Res		0.04
CaO	-0.43	-0.09
SiO_2	0.59	
Str_1	1.14	-0.23
Str_7		1.14
Standard Deviations		
Constant	17.7	34.0
Sb/ 10^4	14.7	11.0
R40	0.31	0.18
LOI	0.32	0.20
Ins_Res		0.41
CaO	0.54	0.51
SiO_2	1.36	
Str_1	0.30	0.49
Str_7		0.29

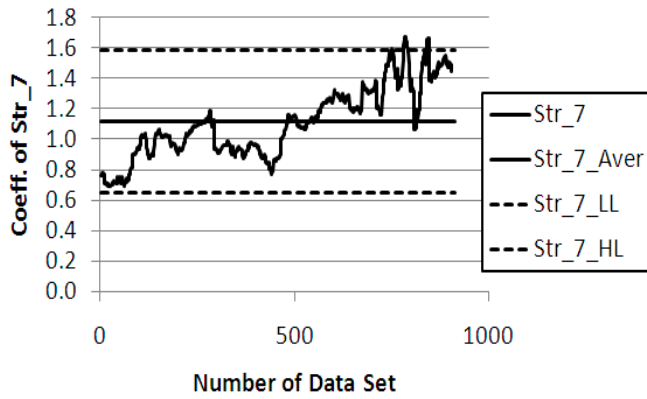


Fig. 8 Control chart of coefficient of Str_7 variable for dynamic Str28_7 model and CM5 results.

C. Uncertainty of the Dynamic Models Parameters

The standard deviations shown in Tables 9, 10 correspond to the optimum T_D in predicting the future strength. A detailed search was made as regards the function between parameters uncertainty and time horizon T_D . The functions between average coefficients, their standard deviation and T_D are shown in Figs. 9 to 12: In Figs. 9, 10 and 11 the statistics of the coefficients of SiO_2 , R40 and Str_1 computed from the Str28_1 model are demonstrated. In Fig. 12 the respecting statistics of Str_7 coefficients calculated from the Str28_7 model is also depicted.

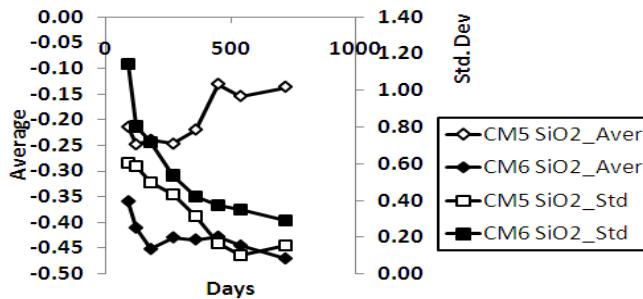


Fig. 9 Average and std. dev. of SiO_2 coefficient of Str28_1 model

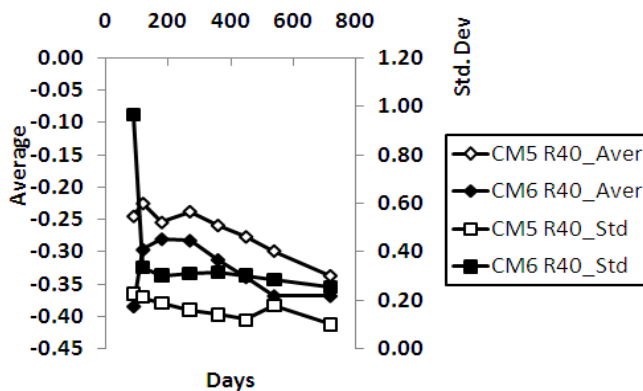


Fig. 10 Average and std. dev. of R40 coefficient of Str28_1 model

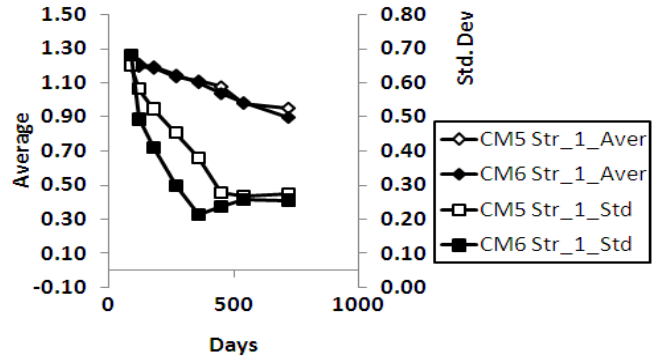


Fig. 11 Average and std. dev. of Str_1 coefficient of Str28_1 model

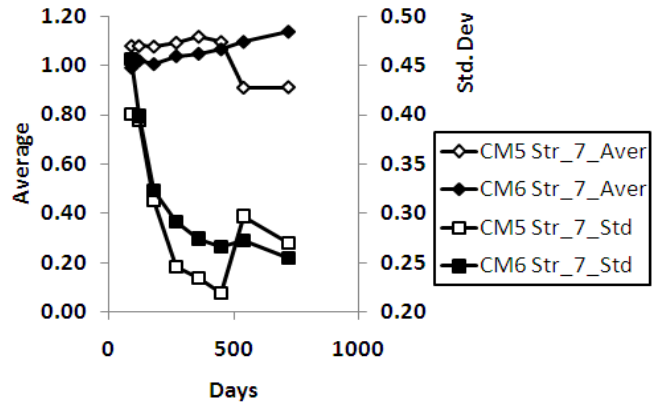


Fig. 12 Average and std. dev. of Str_7 coefficient of Str28_7 model

A big drop of the standard deviations occurs with T_D increasing. Therefore the models with a large T_D provide a more robust estimation of the average value of parameters in long-term.

D. Evaluation of the Reactivity of Cement

The dynamic models constitute a tool to evaluate the reactivity of the different cement compounds, including also the grinding aid. This assessment is shown by the following example. A cement CEM IV B (P-W) 32.5 was selected with $S_b = 3900 \text{ cm}^2/\text{gr}$, $R40 = 11.3\%$, $LOI = 3.9\%$, $Ins_Res = 24.8\%$, $SiO_2 = 35.7\%$, $Al_2O_3 = 9\%$, $CaO = 39.9\%$ and $Str_1 = 4.5 \text{ Mpa}$ produced in CM5 and CM6. The dynamic model Str28_1 for $T_D=360$ days for CM5 and $T_D=270$ days for CM6 was applied for all the parameters sets in CM5, CM6 and the average 28-day strength was calculated. The difference of each strength result from this average was computed. The results are demonstrated in Figs. 13, 14.

When the difference is negative, i.e. the strength is lower than the average; the current reactivity of cement compounds is lower than the long-term mean reactivity. The inverse happens in case of positive difference. This analysis is a simple example showing the ability of the dynamic models to contribute in the daily quality control of cement.

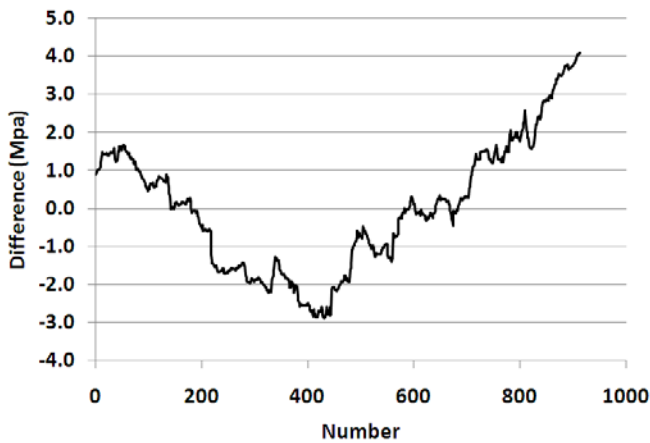


Fig. 13 Application of Str28_1 model for constant composition and fineness in CM5

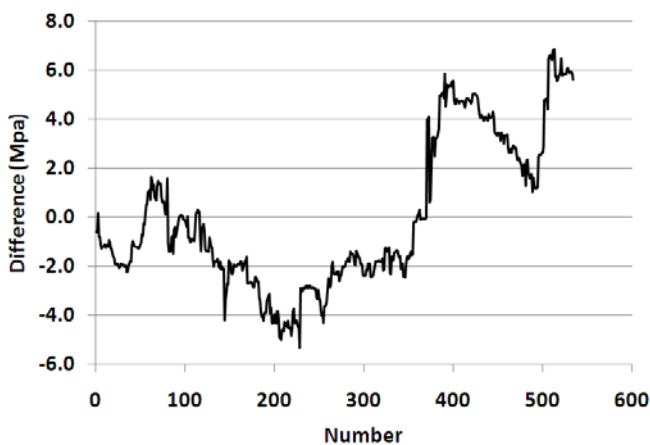


Fig. 14 Application of Str28_1 model for constant composition and fineness in CM6

V. CONCLUSIONS

The prediction of the 28-day strength of cements where more than one component contribute in strength development is a challenging issue due to its high importance in the product design, in the daily quality control and in the concrete mix design. The pozzolanic cements belong to this category, where the 28-day compressive strength becomes as a result of the interaction of clinker, pozzolane, fly ash and the cement fineness as well. Two classes of models were developed: (a) the static ones, where based on a predetermined data set, the parameters values were calculated and applied to predict the future strengths and (b) the dynamic models, where the parameters were estimated from a moving set of data belonging to a predefined past time interval, T_D in days. Exclusively industrial data of Halyps cement plant were used.

The future strength predictions obtained by the static models are sufficient only if negligible or small changes to the processes or to the materials reactivity occur. The dynamic models are able to detect such changes due to the continuous calculation of their parameters. The time period T_D was optimized using as criterion the minimum residual error of the

future strength prediction. The solutions found were between 270 and 360 days depending on the model applied and the mill.

Independently of the category of model, static or dynamic, two types of models were developed having as independent variables the cement chemical analysis, the fineness expressed as residue at 40 μm and specific surface, and the early strength measured at one and seven days. The static models contain linear terms, the squares and the linear combinations of the above variables whether they are statistically significant. The dynamic models were simplified including only the linear terms. Despite their simpler structure, the dynamic models predict much better the future strength than the static models.

Using the dynamic models the effect of the cement composition, fineness and early strength on the 28-day strength can be investigated as function of time. The continuous implementation of these models and the daily calculation of the coefficients provide this information. On the other hand the uncertainty of the models' coefficients is a monotonic function of T_D . The standard deviation of the coefficients of the models declines, as T_D increases. Consequently the application of the models with large T_D provides a more robust estimation of the average value of parameters in long-term.

The analysis of the two categories of models verified the ability and superiority of the dynamic models against the static ones in predicting the strength of pozzolanic cement. Moreover the implementation of these methods contributes noticeably in improving the cement quality by maintaining a low variance of typical strength. The further improvement of these techniques can follow the next directions.

- Investigation of non-linear dynamic models and possible coupling of the models that include as variables the early strengths at one and seven days, to enhance the predictability.
- Exploitation of the dynamic models to develop robust controllers based on Model Predictive Control (MPD) techniques or other advanced methods.

REFERENCES

- [1] EN 197-1:2011, *Cement. Part 1: Composition, specifications and conformity criteria for common cements*, CEN, 2011, pp. 10-15.
- [2] S. Tsvivilis, and G. Parissakis, "A Mathematical Model for the Prediction of Cement Strength", *Cem. Concr. Res.*, vol. 25, no 1, pp. 9-14, January 1995.
- [3] B. Osbaeck, and V. Johansen, "Particle Size Distribution and Rate of Strength Development of Portland Cement", *J. Am. Ceram. Soc.*, vol. 72, no 2, pp. 197-201, February 1989.
- [4] A. Tepecik, Z. Altin, and S. Erturan, "Modeling, Compressive Strength of Standard CEM I 42.5 Cement Produced in Turkey with Stepwise Regression Method", *Journal of Chemical Society of Pakistan*, vol. 31, no 2, pp. 213-220, April 2009.
- [5] P. E. Garcia-Casillas, C. A. Martinez, H. Montes, and A. Garcia-Luna, "Prediction of Portland Cement Strength Using Statistical Methods", *Mater. Manuf. Process.*, vol. 22, no 3, pp. 333-336, 2007.
- [6] J. M., Mechling, A., Lecomte, and C. Diliberto, "Relation between Cement Composition and Compressive Strength of Pure Pastes", *Cement Concrete Comp.*, vol. 31, no 4, pp. 255-262, April 2009.
- [7] D. Tsamatsoulis, "Kinetics of Cement Strength Development Using Different Types of Cement and Aggregates", *WSEAS Trans. Syst.*, vol. 8, no 10, pp. 1166 - 1176, October 2009.

- [8] G. F. Kheder, A. M. Gabban, and S. M. Abid, "Mathematical model for the prediction of cement compressive strength at the ages of 7 and 28 days within 24 hours", *Mater. Struct.*, vol. 36, no 10, pp. 693-701, December 2003.
- [9] D. Tsamatsoulis, "Control Charts and Models Predicting Cement Strength: A Strong Tool Improving Quality Control of Cement Production", in *Proc. 16th WSEAS International Conference on SYSTEMS*, Kos, Greece, 2012, pp. 136-145.
- [10] M. Relis, W. B. Ledbetter, and P. Harris, "Prediction of Mortar-Cube Strength from Cement Characteristics", *Cem. Concr. Res.*, vol. 18, no 5, pp.674-686, September 1988.
- [11] D. Tsamatsoulis, "Prediction of cement strength: analysis and implementation in process quality control", *Journal of Mechanical Behavior of Materials*, vol. 21, no 3-4, pp. 81-93, December 2012.
- [12] E. Douglas, and G. Pouskouleli, "Prediction of compressive strength of mortars made with Portland cement - blast-furnace slag - fly ash blends", *Cem. Concr. Res.*, vol. 21, no 4, pp. 523-534, July 1991.
- [13] D. Wang, and Z. Chen, "On predicting compressive strengths of mortars with ternary blends of cement, ggbfs and fly ash", *Cem. Concr. Res.*, vol. 27, no 4, pp. 487-493, April 1997.
- [14] G. Kostogloudis, J. Anagnostou, Ch. Ftikos, and J. Marinos, "Development of a multiple linear regression model for predicting the 28-day compressive strength of Portland pozzolane cement", *Mater. Struct.*, vol. 32, no 2, pp. 98-102, March 1999.
- [15] M. L. Nehdi, and J. Summer, "Optimization of ternary cementitious mortar blends using factorial experimental plans", *Mater. Struct.*, vol. 35, no 8, pp. 495-503, September – October 2002.
- [16] H. S. Chen, W. Sun, and P. Stroeven, "Prediction of compressive strength and optimization of mixture proportioning in ternary cementitious systems", *Mater. Struct.*, vol. 36, no 6, pp. 396-401, July 2003.
- [17] M. I. Khan, "Iso-responses for strength, permeability and porosity of high performance mortar", *Build. Environ.* vol. 38, no 8, pp. 1051-1056, August 2003.
- [18] M. I. Khan, "Analytical Model for the Strength Prediction of HPC Consisting of Cementitious Composites", *Architecture Civil Engineering Environment Journal*, vol. 2, no 1, pp. 89-96, 2009.
- [19] M. A. Abd-El-Aziz, S. Abd-El-Aleem, and M. Heikal, "Physico-chemical and mechanical characteristics of pozzolanic cement pastes and mortars hydrated at different curing temperatures", *Constr. Build. Mater.*, vol. 26, pp. 310-316, January 2012.
- [20] M. Heikal, S. Abd El Aleem, and W. M. Morsi, "Characteristics of blended cements containing nano-silica", *HBRC Journal*, vol. 9, pp. 243-255, December 2013.
- [21] K. Hwang, T. Noguchi, and F. Tomosawa, "Prediction model of compressive strength development of fly-ash concrete", *Cem. Concr. Res.*, vol. 34, no 12, pp. 2269-2276, December 2004.
- [22] N. P. Rajamane, J. Annie Peter, and P. S. Ambily, "Prediction of compressive strength of concrete with fly ash as sand replacement material", *Cement Concrete Comp.*, vol. 29, no 3, pp. 218-223, March 2007.
- [23] M. F. M. Zain, S. M. Abd, K. Sopian, M. Jamil, M. , and A. I. Che-Ani, "Mathematical regression model for the prediction of concrete strength", in *Proc. 10th WSEAS International Conference on Mathematical Methods, Computational Techniques and Intelligent Systems*, Corfu, Greece, 2008, pp. 396-402.
- [24] A. N. S. Alqadi, K. N.B. Mustapha, S. Naganathan, S., and Q. N. S. Al-Kadi, "Uses of Central Composite Design and Surface Response to Evaluate the Influence of Constituent Materials on Fresh and Hardened Properties of Self-Compacting Concrete", *KSCE Journal of Civil Engineering*, vol. 16, no 3, pp.407-416, March 2012.
- [25] M. Sayed-Ahmed, "Statistical Modeling and Prediction of Compressive Strength of Concrete", *Concrete Research Letters*, vol. 3, no 2, pp. 452-458, June 2012.
- [26] T. R. Neelakantan, S. Ramasundaram, R. Shanmugavel, and R. Vinoth, "Prediction of 28-day Compressive Strength of Concrete from Early Strength and Accelerated Curing Parameters", *International Journal of Engineering and Technology*, vol. 5, no 2, pp. 1197-1201, April – May 2013
- [27] H. S. Chore, and N. L. Shelke, "Prediction of compressive strength of concrete using multiple regression model", *Struct. Eng. Mech.*, vol. 45, No 6, pp. 837-851, March 2013.
- [28] I. C. Yeh, "Modeling Of Strength Of High-Performance Concrete Using Artificial Neural Networks", *Cem. Concr. Res.*, vol. 28, No 12, pp. 1797-1808, December 1998.
- [29] M. Pala, E. Özbay, A. Öztaş, A., and M. I.Yuce, "Appraisal of long-term effects of fly ash and silica fume on compressive strength of concrete by neural networks", *Constr. Build. Mater.*, vol. 21, no 2, pp. 384-394, February 2007.
- [30] F. Özcan, C. D. Atis, O. Karahan, E. Uncuoğlu, and H. Tanyildizi, "Comparison of artificial neural network and fuzzy logic models for prediction of long-term compressive strength of silica fume concrete", *Adv. Eng. Softw.*, vol. 40, no 9, pp. 856-863, September 2009.
- [31] Y. Aggarwal, and P. Aggarwal, P., "Prediction of Compressive Strength of SCC Containing Bottom Ash using Artificial Neural Networks", *World Academy of Science, Engineering and Technology*, vol. 53, pp. 662-667, 2011.
- [32] P. Aggarwal, and Y. Aggarwal, "Prediction of Compressive Strength of Self- Compacting Concrete with Fuzzy Logic", *World Academy of Science, Engineering and Technology*, Vol. 53, pp. 745-752, 2011.
- [33] D. Tsamatsoulis, "Application of the Static and Dynamic Models in Predicting the Future Strength of Portland Cement", submitted for publication in *18th International Conference on Circuits, Systems, Communications and Computers (CSCC '14)*.
- [34] D. Tsamatsoulis, "Calculation of Cement Composition and Uncertainty Analysis" in *Proc. 14th Greek Congress of Concrete*, Kos, Greece, vol. B, 2003, pp. 263-270.
- [35] ISO 8258: 1991, "Shewhart control charts" in *Statistical methods for quality control*, vol. 2, 1995, pp. 355-383.

Mobile meteorological radar uses in crisis management

David Šaur and Stanislav Plšek

Abstract— The article is focused on the practical use of the MMR50 mobile meteorological radar for Information, Notification and Warning System project of the Zlín Region (further only, IVVS ZK). This project creates an information support system for Crisis Management in the Zlín Region. The benefits of using mobile meteorological radar are based upon the ability to predict monitor hazardous weather phenomena (torrential rainfall) which can cause floods. The article describes the functions and location of the mobile meteorological radar, and presents the output data for Crisis Management purposes, including a description of output data conversion from the meteorological radar to map the IVVS ZK environment. The Conclusion will include a description of the comparison of the outputs of the mobile meteorological radar with meteorological radars using the national weather service for two typical meteorological situations and will provide the knowledge gained from the two meteorological situations that were measured.

Keywords— Crisis Management, radar meteorology, meteorological radars, floods

I. INTRODUCTION

WEATHER affects a whole range of processes and phenomena, not only in nature but also in human activities, and especially in transport, agriculture, and in many other industry and services sectors. Currently, one of the negative effects of the weather is dangerous atmospheric phenomena. Such phenomena include floods caused by heavy rainfall (i.e. flash floods), accompanied by hail and strong wind gusts which occur more often in the summer-time. Another phenomenon is the intensive and prolonged precipitation, which causes long-lasting floods in the winter and summer times. Two typical situations (e.g. radar measurement of convective and stratiform precipitation clouds) were selected for both these phenomena. The knowledge and observations gained from radar measurements are set out in the last chapter of the article.

In the Czech Republic (in the Zlín Region), there have been eight floods in recent years that have caused loss of life and

significant material and economic losses. The Zlín Region as the state-mandated crisis management authority, is responsible for managing emergency flood situations. During floods the Zlín Region receives information from Czech Hydrometeorological Institute, which however is not considered sufficient in terms of its accuracy and the quality of weather forecasts, based on experience from previous years. Therefore, the Zlín Region decided to implement the IVVS ZK project MMR50 Meteorological Radar in order to refine forecasts and obtain more detailed data on the actual situation in the region. Another important goal of MMR50 Meteorological Radar is to ensure coverage of the territory in the course of the possibility of failure of the CZRAD Radar Network.

In the Czech Republic, the radar measurement of precipitation is in the purview of the Radar Department of the Czech Hydrometeorological Institute. The role of this department is to manage the CZRAD Radar Network. The CZRAD Radar Network uses two meteorological radars (i.e. one located in Brdy in Central Bohemia and the other in Skalky u Protivanov).

The aim of this article is to describe and unify the relevant substantive information on the basis of radar measurements of two meteorological situations using the MMR50 meteorological radar and the radar based in Skalky in the CZRAD Radar Network. From these radar measurement results, conclusions and knowledge will be drawn. It will be used in the implementation of the MMR50 Meteorological Radar in terms of its location and for setting the parameters for ensuring the efficiency and accuracy of radar measurements of precipitation over the Zlín Region.

II. THE INFORMATION, NOTIFICATION AND WARNING SYSTEM OF THE ZLÍN REGION

The overall objective of the Information, Notification and Warning System of the Zlín Region (IVVS ZK) project is to build a robust and secure communications infrastructure for the purpose of the mutual interlinkage of Municipalities with Extended Competence in the Zlín Region. Further, the creation of the Regional Crisis Management Office of the Zlín Region intended for the processing of the data. The main benefit of this project is to improve the population warning system and for notifying the authorities in the event of emergencies and crisis situations. Early warning of the population ensures a faster response and reduces the extent of the damage on the lives, health and property in the course of

This work was supported by the Department of Security Engineering under internal grant of IGA/FAI/003 (sponsor and financial support acknowledgment goes here).

First author (Ing. David Saur) is with the Department of Security Engineering, Faculty of Applied Informatics, and Tomas Bata University in Zlín (corresponding author to provide, mail: saur@fai.utb.cz). Second author (Ing. Stanislav Plšek) is with Department of Automation and Control Engineering, Faculty of Applied Informatics, and Tomas Bata University in Zlín (corresponding author to provide mail: splšek@fai.utb.cz).

crisis situations. In the IVVS ZK project eleven municipalities with extended competence, thirteen municipalities and two Permanent Control workplaces in which the crisis management staff of the Zlín Region works full-time.

The Information, Notification and Warning System of the Zlín Region is composed of various elements which are the final output elements of the audiovisual warning systems (e.g. sirens, detectors, speakers), municipal CCTV surveillance systems, measuring sensors (i.e. level meters and rain gauges), the meteorological radar system itself, information boards, hazardous chemical substances detection elements, video-conferencing systems, alternative back-up sources of electric power and other systems.[1]

A. The Functions and Location of the IVVS ZK MMR50 Meteorological Radar

The MMR50 Meteorological Radar from MicroStep-MIS s.r.o is a compact device designed for monitoring the current state of the Earth's atmosphere and for obtaining information on hazardous weather phenomena detectable using the X-band (9.41 GHz) radar frequency within a radius of 150 kilometers from the installation site.

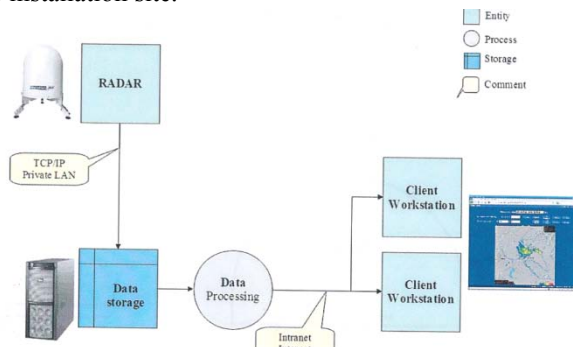


Fig. 1 Diagram of the IVVS ZK MMR50 Meteorological Radar project [4]

The MMR50 Meteorological Radar consists of an antenna, the elevation and azimuth drive, a radar unit, the controlling computer, heating and cooling systems, the power source, and the structure for mounting the actual radar itself. Part of the control computer is the control software for the fully-automatic, unattended operation of the device. The control software ensures the successful completion of the measurements, in the course of which the settings for the radar and motion control are performed. The MMR50 Meteorological Radar assures the following functions:

- Scanning the backscatter of meteorological objects from the volume of the radar horizon (i.e. current intensity and phase precipitation).
- The processing and assignment of data into a spatial matrix,
- Processing input data into data-bases for analysis and forecasting purpose and meteorological radar maps (storms, showers, rain, snow, hail) and the subsequent distribution of these supporting documents to other systems.

The MMR50 Meteorological Radar will be placed on the roof of the municipal authority in Kroměříž in consultation with

experts from MicroStep-MIS, and simulations by Visibility Product software. The advantage of this location is its relatively easy connection to the IVVS ZK information and communication infrastructure. [4]

B. Presentation of the Output Radar Data

The MMR50 Meteorological Radar provides many radar products in support of Crisis Management situations. Users can find detailed information on the composition of precipitation clouds from these products. A part of the software is the so-called “Nowcasting” system with very short-term weather forecasts (about one hour lead-time). The persons responsible (meteorologists) in the Crisis Management Authority are then able to provide precise, accurate and understandable information about the weather forecast on the basis of information from these radar products, which are:

- The PPI (Plan Position Indicator) is the field reflectance at each individual conical sections atmosphere. The PPI level is an elementary measurement product. The Generation Algorithm is based on the bilinear interpolation for each pixel separately.
- The CAPPI (Constant Altitude Plan Position Indicator) is the field of reflection in constant elevation level, interpolated from the bordering levels of the PPI.
- ColumnMax (Composite Reflectivity) - for each point of the image its reflectivity-height over a particular point on the ground is depicted.
- The Range Height Indicator RHI is a vertical cross-section through the atmosphere, where the main parameter is the azimuth.
- ECHO TOP represents the upper border of the cloud-tops, expressed as a height field in which reflectivity greater than a defined threshold occurs.
- VIL – Vertically Integrated Liquid water content, determined on the assumptions of the Marshall-Palmer Distribution; the VIL value is determined by the following equation:

$$VIL = 3,44 \times 10^{-6} \int_{h_z}^{h_t} Z^7 dh, \quad (1)$$

Where Z [$\text{mm}^6 \cdot \text{m}^{-3}$] is Radar Reflectivity, h_z [m] Height and h_t [m] is the height of cloud tops. In the course of the calculations, each surface element, summation is carried out the various individual levels of PPI is performed.

- TITAN – is the “Nowcasting” system implemented in a user interface. In the context of this system, characteristic hazardous atmospheric phenomena based on the selected limits. Precipitation field is marked in red, together with arrows indicating the direction of movement for approximately 60 minutes in advance. [2],[4]

C. Output Data Conversion

The MMR-50 Meteorological Radar will be connected through a communication infrastructure network with the

central control server located in the building of the Regional Authority of the Zlín Region. Two-way data communication, information processing for distribution and its display within the dispatching control centers will be assured by this network. Data conversion will be addressed in the coming months through the use of MicroStep-MIS which uses its own geographic information system. While the MMR-50 Meteorological Radar will fulfill the main data source function; radar images from the CZRAD Radar Network will be used to verify the accuracy of the measurements. Images from the MMR-50 Meteorological Radar will not be implemented into the merged CZRAD Radar Network due to different output data, beam patterns and frequency bands. [4]

III. RADAR MEASUREMENT

Two main types of precipitation clouds are commonly encountered in the Czech Republic; i.e. convective and stratiform precipitation clouds. This chapter presents the results of varying radar measurements of the Skalky Meteorological Radar in the CZRAD Radar Network and that of the MMR-50 Meteorological Radar. The outputs of measurements by the MMR-50 Meteorological Radar match the outputs from the Skalky Meteorological Radar measurements. For Tables I and III, the value of radar reflectivity Z in dBZ is shown at first, and in the next column, the recalculated value I of rainfall in mm / hr according to the following equation:

$$I = 10^{\frac{[Z-10\log(a)]}{10b}}, \quad (2)$$

Where the values of (a) and (b) are experimentally-determined constants ($a = 16, b = 200$). Precipitation is shown in fifteen-minute intervals and amount of precipitation is given in mm.

A. Measurement of Convective Precipitation

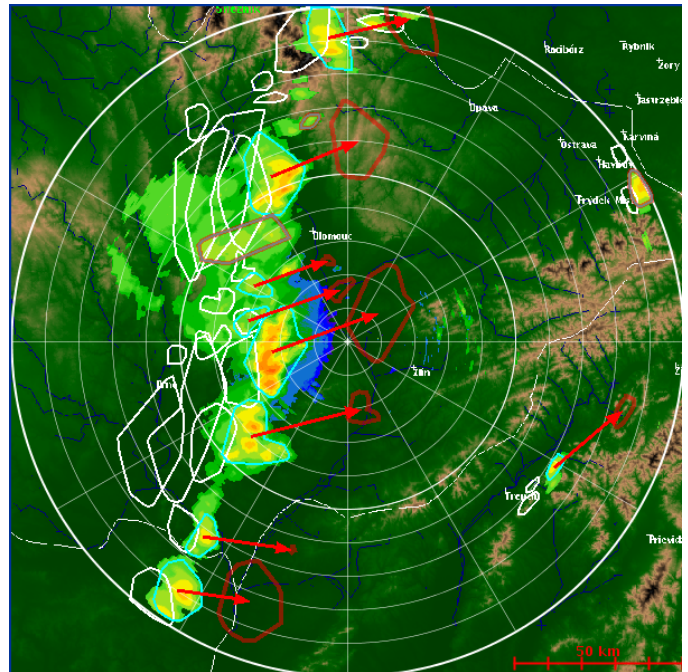


Fig. 2 Radar Image from the MMR50 Meteorological Radar of June 15, 2013



Fig. 3 Radar image from the Skalky Meteorological Radar from the CZRAD Radar Network of June 15, 2013 [8]

In the context of this chapter, precipitation measurements were taken for two types of precipitation clouds. In Figs. 2 and 3, we can contrast and compare the distribution of precipitation from the MMR50 Meteorological Radar measurements (Fig. 2) and those of the Skalky Meteorological Radar (Fig. 3). In the first case (Table I), these were of convective precipitation clouds on a cold front from the west - typical for the summer, dating from 15.6.2013. Tables I and III, show the relatively great difference between the measured intensity of precipitation and data from the meteorological stations in the Zlín Region. This, however, has to do with a humidity rate of 80% of water in the atmosphere, which does not fall on the earth's surface. The resultant amount of rainfall from meteorological stations makes up a very small percentage of the total volume of water (humidity) in the atmosphere. X-band meteorological radars are therefore eminently suitable for the detection of this type of cloud with

its characteristic high radar reflectivity (above 40 dBZ) even at great distances.

Date	Convective precipitation cloud	MMR50 Radar		Skalky Radar	
		Z[dBZ]	I[mm/h]	Z[dBZ]	I[mm/h]
15. 6. 2013	Measurement time				
	0:45	44	20,5	42	15,4
	1:00	41	13,3	38	8,6
	1:15	45	23,7	40	11,5
	1:30	42	15,4	42	15,4
	1:45	46	27,3	44	20,5
	2:00	44	20,5	42	15,4
	2:15	39	10,0	40	11,5
	2:30	36	6,5	38	8,6

Table I Comparison of the MMR-50 and Skalky Meteorological Radar Output Measurements of June 15, 2013

Date	Meteorological stations	1:00-1:30	1:30-2:00	2:00-2:30	Amount of precipitation
15. 6. 2013	Holešov	2,2	0,3	0	2,5
	Kroměříž	3,2	0,1	0	3,3
	Staré město	2,2	0	0	2,2
	Luhačovice	0,1	1,6	0,1	1,8
	Štítná nad Vláří	0	0,1	0,4	0,5
	Vizovice	0,2	0,9	0	1,1
	Vsetín	1,5	1,6	0,3	3,4
	Valašské Meziříčí	0,6	1,1	0,1	1,8

Table II Precipitation Totals in the Zlín Region June 15, 2013 [9]

Figs. 4 and 5 illustrate the dynamics in developments of convective precipitation over time. From Tables I and II, it is clear that the intensity of convective precipitation changes very rapidly over time. For this very reason, it is essential to respond quickly to these meteorological situations from the Crisis Management perspective when dealing with floods caused by heavy torrential rainfall.

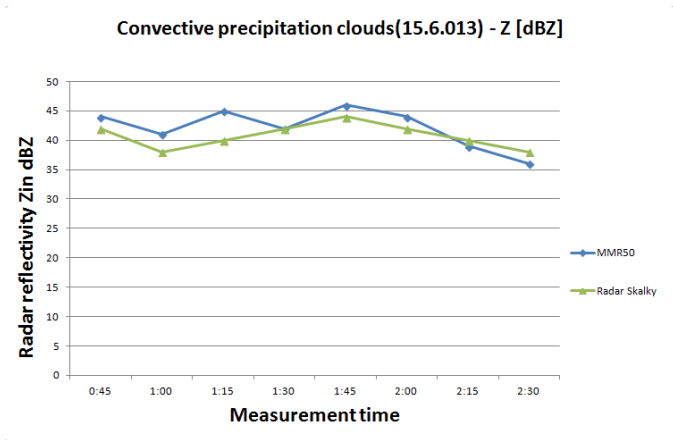


Fig. 4 A Comparison of the Radar Reflectivity Z [dBZ] Parameters of the MMR50 Meteorological Radar and Skalky Meteorological Radar for Convective Precipitation Clouds Formations of June 15, 2013

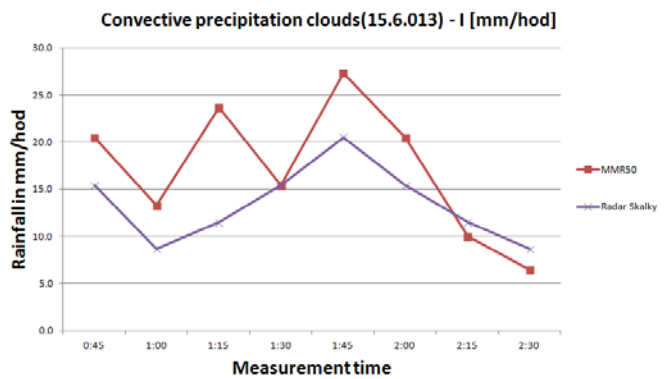


Fig. 5 A Comparison of the Rainfall Parameters I [mm / h] Parameters of the MMR50 Meteorological Radar and Skalky Meteorological Radar for Convective Precipitation Clouds Formations of June 15, 2013

B. Measurement of Convective Precipitation

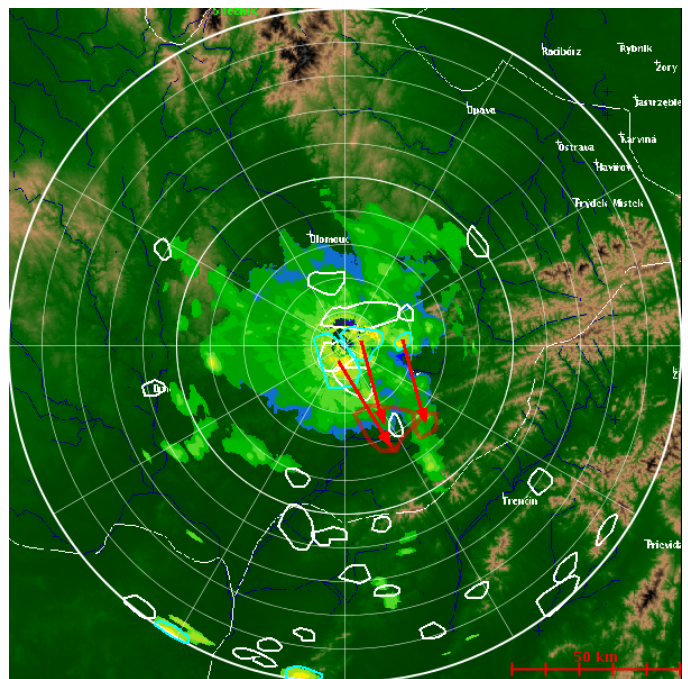


Fig. 6 Radar Image from the MMR50 Meteorological Radar of November 7, 2013



Fig. 7 Radar image from the Skalky Meteorological Radar from the CZRAD Radar Network of November 7, 2013 [8]

In the second case (Table III and IV), this involved stratified precipitation clouds on a warm front from the southwest, measured on 7.11. 2013. Stratified precipitation cloud formations are characteristic for the winter period in mild, temperate climates. Unlike convective precipitation clouds, there is not such a noticeable difference between radar reflectivity, rainfall intensity and the data from the ground-based meteorological stations. This type of precipitation in the course of the passage of a front mostly falls directly onto the earth's surface. The disadvantage for mobile meteorological radars is their low impulse power with which these radars cannot detect weak rainfall (usually less than 1 mm / hr) at a great distance. This deficiency can mean big problems - especially in wintertime, in predicting icy weather.

Date	Stratiform precipitation cloud	MMR-50 Radar		Skalky Radar	
		Z[dBZ]	I[mm/h]	Z[dBZ]	I[mm/h]
7.11.2013	Measurement time				
	0:15	26	1,5	28	2,1
	0:30	32	3,6	32	3,6
	0:45	28	2,1	29	2,4
	1:00	26	1,5	27	1,8
	1:15	24	1,2	23	1,0
	1:30	24	1,2	22	0,9
	1:45	22	0,9	22	0,9
	2:00	22	0,9	20	0,6

Table III Comparison of the MMR-50 and Skalky Meteorological Radar Output Measurements of November 7, 2013

Date	Meteorological stations	0:00-0:30	0:30-1:00	1:00-1:30	1:30-2:00	Amount of precipitation
7.11.2013	Holešov	0,3	0,5	0,5	0,3	1,6
	Kroměříž	0,4	0,3	0,4	0,4	1,5
	Staré město	0,3	0,5	0,4	0,3	1,5
	Luhačovice	0,4	0,6	0,4	0,5	1,8
	Štítná nad Vláří	0	0	0	0	0
	Vizovice	0,1	0,3	0,3	0,3	1,0
	Vsetín	0,7	0,6	0,6	0,5	2,4
	Valašské Meziříčí	0,4	0,3	0,3	0,2	1,2

Table IV Precipitation Totals in the Zlín Region 7 November 2013 [9]

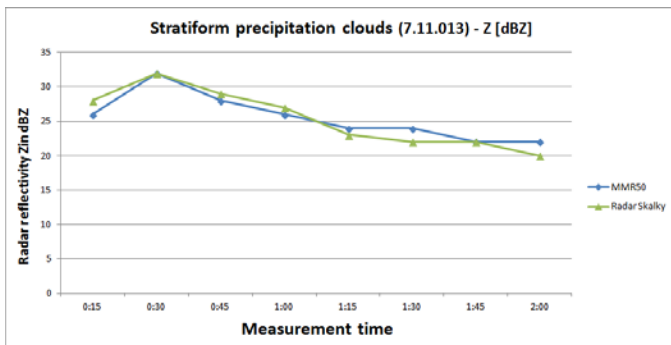


Fig. 8 A Comparison of the Radar Reflectivity Z [dBZ] Parameters of the MMR50 Meteorological Radar and Skalky Meteorological Radar for Convective Precipitation Clouds Formations of November 7, 2013

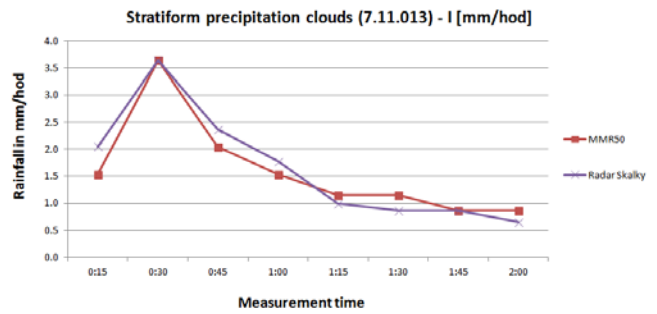


Fig. 9 A Comparison of the Rainfall Parameters I [mm / h] Parameters of the MMR50 Meteorological Radar and Skalky Meteorological Radar for Convective Precipitation Clouds Formations of 7.11.2013

For stratiform precipitation cloud formations, the reflectivity and intensity of precipitation does not change dramatically in terms of their dynamics. The intensity of the rainfall remains constant. When dealing with flood situations caused by prolonged rainfall, it is not a problem to detect these collisions in terms of their intensity, but the problem is to determine their duration. Not only weather prediction model, but even experienced meteorologists have problems with estimating duration. [2], [3], [4], [10]

IV. COMPARISON OF METEOROLOGICAL RADAR PARAMETRES (MMR50 AND SKALKY METEOROLOGICAL RADAR)

Location	Město Kroměříž	Skalky u Protivanova	Brdy-Praha
Region	Zlínský kraj	Jihomoravský kraj	Středočeský kraj
Latitude	49°17'45.477"N	49,501 N	49,658 N
Longitude	17°23'42.861"E	16,790 E	13,818 E
Altitude	200 m	730 m	860 m
In operation since	2014	1995	2000
Interval measurement	2 minutes	5 minutes	5 minutes
Producer	Microstep-MIS	Gematronik	EEC
Type of radar	MMR-50	Gematronik METEOR 360AC	EEC DWSR-2501 C
Range	X-pásmo	C-pásmo	C-pásmo
ANTENNA			
Diameter parabolic antenna	0,55 m	4,2 m	4,27 m
Antenna Elevation Angle Span	-1 do +90°	-2 do +92°	-2 do +92°
Number of Elevation Angle	13	16	16
Antenna Gain	32 dB	44 dB	45 dB
Polarization	Linear, horizontal	Linear, horizontal	Linear, horizontal
TRANSMITTER			
Frequency band	9,41 GHz	5,645 GHz	5,630 GHz
Wavelength	3,0 cm	5,3 cm	5,3 cm
Transmitter Power Peak	50 kW	250 kW	305 kW
Pulse Repetition Frequency	1500 Hz	584 Hz	584 Hz
RECEIVER			
Receiver Sensitivity	- 111 dBm	-109 dBm	-110 dBm
Dynamic Range	85 dB	100 dB	80 dB
Maximum Range	100 km	260 km	256 km

Table V Comparison of the MMR50 Meteorological Radar and CZRAD Radar Network Parameters [5],[6]

The MMR50 Meteorological Radar operates in the X-band with a wavelength of about 3 centimeters. It is suitable for the detection of precipitation clouds formation with a high radar reflectivity, even at greater distances (up to about 100 km). Another advantage is its more frequent measurements (every

two minutes) than for the Skalky and Brdy Meteorological Radars (CZRAD Radar Network).

Maximum radar range r_{\max} :

$$r_{\max} = \frac{cT_s}{2} = \frac{c}{2f_r} \quad (3)$$

The time between sending two consecutive pulses is called T_s or PRT (Pulse Repetition Time); and its inverse value f_r is called PRF (Pulse Repetition Frequency). The maximum radar range of the MMR50 Meteorological Radar at a Pulse Repetition Frequency where $f_r=1500$ Hz, is approximately 100 kilometers.

The CZRAD Radar Network is intended for radar measurement in the Czech Republic. Two meteorological radars, one located in the Czech Hydrometeorological Institute at Brdy near Prague and the other Skalky u Protivanov are used for the measurements. The Creation of merged radar information from the CZRAD Radar Network is carried out every five minutes by their server at the workplace located in Praha-Libuše. The transmission power of 250-300 kW ensures the possibility of broad coverage of the given territory with significantly less attenuation than meteorological radars working in the X-band. A web browser (based on JavaScript) was created to enable new universal imaging radar products. To view these on a user's computer one only needs a standard web browser (MSIE 5 +, Netscape 6 +, Mozilla Firefox, Opera, Google Chrome). [5], [6], [7]

V. CONCLUSION

The aim of this article was to summarize current knowledge and experience acquired from measurements from the Czech Hydrometeorological Institute's Meteorological Radars and the MMR50 Meteorological Radar within the context of the implementation of the Information, Notification and Warning System project of the Zlín Region. The acquired knowledge can be used to improve accuracy of measurements made by the MMR50 Meteorological Radar and find better ways of measuring these phenomena.

For both meteorological radars (i.e. MMR50 Meteorological Radar and Skalky Meteorological Radar), congruent results were achieved when monitoring precipitation with higher radar reflectivity (35 dBZ and higher). Mobile meteorological radars in the X-band can detect convective cloud precipitation at greater distances (for the MMR50 Meteorological Radar up to 100 km; while the CZRAD Radar Network's range is up to 250 km). The fundamental problem with these radars is that at low transmit power. There is great attenuation of cloud precipitation formations with high radar reflectivity. This can cause the problem that the radar cannot "see" a cloud precipitation formation following just behind the first cloud precipitation formation detected. Major attenuation also occurs in the detection of snowfall and rainfall occurring directly above the radar. This drawback can be minimized radar images by

merging MMR50 with images from the CZRAD Radar Network to reliably cover the whole area which is being monitored. The MMR50 Meteorological Radar has great difficulty in detecting very difficult a lower radar reflectivity (15 dBZ below) and only up to a distance of 40 km from the antenna.

All of the previous issues are related to the location of the MMR50 Meteorological Radar. In the course of detection of precipitation, this can lead to disruptive reflections in the town as well as the windward side of the nearby hills. Due to its low altitude (200 m) there is a reduction in the coverage area of the Beskids Mountains area in the northeast of the Zlín Region. If after a year of trial operations, the MMR50 Meteorological Radar does not prove successful in this location, it will be moved to a place with a higher altitude. This problem will be solved operatively through the merging of the MMR50 Meteorological radar images with those of the CZRAD Radar Network.

The MMR50 Meteorological Radar is particularly suitable for the detection of convective cloud precipitation, which it can detect up to the limits of its maximum range (about 100 km). Thereby, this device fulfills its purpose - the detection and prediction of heavy rainfall. Although the study found a number of shortcomings with the MMR50 Meteorological Radar, the device can still be used for Crisis Management purposes in the IVVS ZK project.

REFERENCES

- [1] "Information, notification a warning system of Zlín Region" – Integrated project, Zlín Region [online]. 2012 [2014-03-31]. Available: <http://www.kr-zlinsky.cz/-informacni-vyrozumivaci-a-varovaci-system-zlinskeho-kraje-integrovaný-projekt-cl-1392.html>
- [2] D. Řezáčová, et al. *Physics of clouds and precipitation*. Vol. 1. Prague: Academia, 2007. 574 pp. with. Fig.Gerstner; sv. 2. ISBN 978-80-200-1505-1.
- [3] J. Kráčmar, *Meteorological radars*. Czech Hydrometeorological Institute. [online]. 1997-2011 [cit. 2014-04-01]. Available: http://portal.chmi.cz/files/portal/docs/meteo/rad/info_radar/index.html
- [4] MicroStep-MIS. *Mini-Portable Meteorological Radar MMR50: User's Guide Version 1.3*. 2013.
- [5] Radar network ČHMÚ. Czech Hydrometeorological Institute [online]. 2010-2011 [cit. 2014-04-01]. Available: http://portal.chmi.cz/files/portal/docs/meteo/rad/info_czrad/index.html
- [6] L. Gregor, *The possibility of using small radars to detect meteorological situation*. Diploma thesis. Brno: University of Defence, Faculty of Military Technology, 2011.
- [7] P. Dvorak, *Aviation Meteorology*. 2004th Cheb: World of Wings. 221 pp.
- [8] Meteoradar | CZ. Meteopress s.r.o. [online]. [cit. 2014-04-02]. Available: <http://radar.meteopress.cz/>
- [9] ČHMÚ HPPS - Current information hydrological forecasting services. Czech Hydrometeorological Institute. [online]. [cit. 2014-04-03]. Available: http://hydro.chmi.cz/hpps/hpps_act_rain.php
- [10] M. Caletka, *Identification of convective and stratiform precipitation formations based on remote sensing data* [online]. 2013 [cit. 14.04.2014]. Diploma thesis. Masaryk University, Faculty of Science. Supervisor cup is RNDr. Milan Šálek. Available from: http://is.muni.cz/th/323980/prif_m/.

Motion Detection in Thermal Images Sequence Using Wigner Distributions

Sn. Pleshkova, Al.Bekyarski

Abstract—Motion detection is wide spread action in video systems to discover objects or people in images. A number of methods and algorithms have been proposed for estimating 2D motion detection in images. Some of these methods may be classified as matching methods, other as methods of differentials, spectral methods like Fourier methods, Wigner distribution etc. Matching and differential methods are simple to use, but not always work, because of noise presence usually in the images and because the variation in the gray-scale intensities from one image to the other. The Fourier methods are very popular and are based on phase spectrums subtraction of the images from two neighbor frames in images sequences. This leads to a set of two algebraic equations with two unknowns. The Fourier methods work well for motion estimation of single object, but for the case of multiple objects these methods cannot distinguish the motion of one object from that of the other. All of these methods are possible to modify and apply as methods and algorithms of motion detection in thermo visual systems. In this article is developed the method and algorithm for motion detection in thermal images carried out the analysis of two dimensional Wigner distributions. The proposed method is tested in simulations and in real working thermal image system to detect motion and tracking people in sequences of thermal images and the results of the experiments are shown in comparison with the similar methods.

Keywords—Motion Detection, Thermo Vision Systems, Thermal Image Sequence, Motion Detection, Wigner Distributions

I. INTRODUCTION

HERMO vision is a technique for capturing the temperature Tdistribution of the points of objects and people [1]. This distribution is presented as pseudo visual images using the relationship between temperature of each point and the color assigned to these values. The main advantages of using thermal images are the possibility to “seen” the objects and people in the darkness and in the night. The applications of thermo visual systems are quite wide in: military or police systems, security or surveillance systems, industrial inspection systems, medical systems, robots, etc. In the area of security and surveillance thermo visual systems motion detection is

very important operation using to detect people or objects movements in area of surveillance system observation and applying this operation is realized also the objects and people tracking [2]. The idea of motion detection is proposed for visible images [3] and a lot of methods and algorithms are proposed, most important of which are: matching methods, methods of differentials, spectral methods like Fourier methods, Wigner distribution etc. All of these methods can be applied also in thermo visual systems for motion detection with some modifications typical for thermal images. The choice of a concrete method of motion detection in a real working thermo visual system can be made analyzing the advantages and disadvantages of the well known motion detection methods for visible images. After preparing this precise analysis in this article is chosen to develop a method and algorithm for motion detection in thermal images carried out the analysis of two dimensional Wigner distributions.

II. THERMO VISION IMAGES MOTION DETECTION METHOD BASED ON WIGNER DISTRIBUTIONS

The application of Wigner distributions is wide spread in signal processing, image processing, etc.[4] One of the application of two dimensional Wigner distributions is motion detection in visible images[5]. Analyzing these methods is possible to decide whether or not is suitable to apply Wigner distributions also for motion detection in thermal images. A brief description of two dimensional Wigner distributions theory is presented first to explain the main principles of motion detection, processing thermal images with two dimensional Wigner distributions. The Wigner distribution [6] was introduced first as a representation of a signal in time and frequency variables. Subsequently, Ville [7] derived for the signals the same distribution that Wigner proposed several years ago. There exists also for images the 2D Pseudo Wigner Distribution (PWD) given by [8]:

$$PWD(n_1, n_2, \theta_1, \theta_2) = \sum_{k=-N_2+1}^{N_2-1} \sum_{l=-N_1+1}^{M_1-1} h_{N_2 N_1}(k, l) * \sum_{r=-M_2+1}^{M_2-1} \sum_{s=-M_1+1}^{M_1-1} g_{M_2 M_1}(r, s) z(n_1 + r + k, n_2 + s + l) *$$

Sn. Pleshkova is with the Faculty Telecommunication of Technical University - Sofia, Bulgaria, CO +359 Bulgaria (corresponding author to provide phone: 895 55 888 51; e-mail: snegpl@ tu-sofia.bg).

Al. Bekyarski, was with the Faculty Telecommunication of Technical University - Sofia, Bulgaria, CO +359 Bulgaria (corresponding author to provide phone: 895 55 888 51; e-mail: aabbv@ tu-sofia.bg).

$$z^*(n_1 + r - k, n_2 + s - l)e^{-j2(k\theta_1 + l\theta_2)} \quad (1) \quad \{(x, y, t, w_x, w_y, w_t) : v_x w_x + v_y w_y + w_t = 0\} \quad (6)$$

where

z and z^* is input thermal image and it complex conjugation;

M_1, M_2, N_1, N_2 - discrete spatial-averaging variables;

$h_{N_2 N_1}(k, l)$ - spatial-frequency averaging window;

$g_{M_2 M_1}(r, s)$ - spatial averaging window;

$n_1, n_2, \theta_1, \theta_2$ - discrete spatial variables:

$$\begin{aligned} \theta_1 &= 2\pi f / N_1 \\ \theta_2 &= 2\pi f / N_2 \end{aligned} \quad (2)$$

The 2D Pseudo Wigner Distribution (PWD) for described with equation (1) is applied for static thermal images. It can be modify, for dynamic thermal images or thermal image sequences containing usually moving objects, as a 6D function PWD_i , for the current i frame in thermal images sequence, defined by:

$$\begin{aligned} PWD_i(x, y, t, w_x, w_y, w_t) = \\ \sum_t \sum_x \sum_y R_i(x, y, t, \alpha, \beta, \tau) * \\ * \exp[-j(\alpha w_x + \beta w_y + \tau w_t)] \end{aligned} \quad (3)$$

where

$$\begin{aligned} R_i(x, y, t, \alpha, \beta, \tau) = z_i(x + \alpha, y + \beta, t + \tau) * \\ * z_i^*(x - \alpha, y - \beta, t - \tau) \end{aligned} \quad (4)$$

z and z^* represent current i input frame in thermal images sequence and it complex conjugation;

x, y, α, β - correspond to $n_1, n_2, \theta_1, \theta_2$ - discrete spatial variables in equation (1) for the static thermal images.

In the case, where in a thermal image sequences (a time-varying thermal image) in the current i frame $z_i(x, y, t)$, exist an uniformly translation at some constant velocity with horizontal and vertical v_x, v_y components, the PWD of this thermal image is:

$$\begin{aligned} PWD_i(x, y, t, w_x, w_y, w_t) = \delta(v_x w_x + v_y w_y + w_t) \\ PWD_i(x - v_x t, y - v_y t, w_x, w_y) \end{aligned} \quad (5)$$

It is possible to define from (5), that in case of a linearly translation with velocity v_x, v_y in thermal image sequence (usually when there are the objects or people in area of thermal camera observation), the values of PWD_i are everywhere zero except in the plane defined by

Therefore, it can be mentioned, that for a pixel with position (x, y) in current time t of the current i thermal image frame, each local spatially, temporary and frequency (STF) spectrum of the PWD_i is zero everywhere except on the plane defined by (6). From this can be concluded, that estimating the velocity from a given (STF) spectrum is equivalent of motion detection in thermal images sequence applying method of optical flow calculation.

The general approach for optical flow calculation in thermal images sequence is based on assumption that the intensity structures of local time-varying thermal image regions are approximately constant under motion for at least a short duration. This means, that changes in thermal images intensity are due only to translation of the local image intensity and not due to changes in lighting, reflectance, etc. According to this assumption, the total derivative with respect to time of the thermal image intensity function should be zero at each position in the image and at every time. For the intensity function of a current i thermal image frame $z_i(x, y, t)$ is possible to claim that intensity remain constant if it is satisfy the following condition:

$$z_i(x, y, t) = z_i(x + \delta x, y + \delta y, t + \delta t) \quad (7)$$

where

$\delta x, \delta y$ define the displacement of the local thermal image region at position (x, y) after a little time interval δt .

Equation (7) can be represented as an appropriate Taylor series:

$$v_x \frac{\partial z_i(x, y, t)}{\partial t} + v_y \frac{\partial z_i(x, y, t)}{\partial t} + \frac{\partial z_i(x, y, t)}{\partial t} = 0 \quad (8)$$

Therefore, it is proposed here in this article to use equation (6) of PWD transformation or (11) of FFT for motion detection in thermal images sequences with a procedure for estimating the slope of the motion plane found in the appropriate spectrums.

III. ALGORITHM FOR THERMO VISION IMAGES MOTION DETECTION BASED ON WIGNER DISTRIBUTIONS

The slope of motion can be determined using different methods. There are many possibilities to find this plane and their slope. In this article is proposed to develop an algorithm for slope of motion finding using Hough transform. The main advantages of Hough transform in this case is the ability to discard cross-terms that can be introduced by the PWD transform, using it for motion detection purpose. It is known that a line can be characterized in the Hough plane, as well as a line and also a plane. This is the used in this article as feature

for determine the velocity of motion detected objects or people in thermal images sequences applying Hough transform to the spatially, temporary and frequency (STF) spectrum. The main steps of the proposed algorithm for thermo vision images motion detection based on Wigner distributions are presented in Fig. 1.

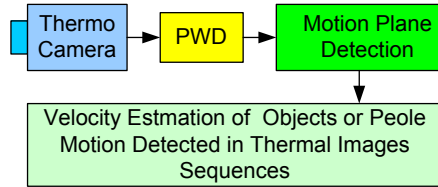


Fig.1. The main steps of the proposed algorithm for motion detection in thermo vision images sequences based on Wigner distributions

Thermal images are captured from **Thermo Camera**. The sequences of thermal images are treated to calculate 2D Pseudo Wigner Distribution – **PWD**. The information from **PWD** block is entered in the block preparing **Motion Plane Detection** applying Hough transform to the 2D Pseudo Wigner Distribution of the thermal images sequences. The results from Hough transform are used in the last block for **Velocity Estimation** of objects or people detected in thermal images sequences.

The importance of the block **Motion Plane Detection** for the processed thermal images sequences is the reason to present them more precise in Fig. 2. The Hough transform **HT** is prepared in parallel form to a number of **Frames 1 to n** of the 2D Pseudo Wigner Distribution of the thermal images sequences. Then a **Local maximum** of each of all HT of frames 1 to n is calculated, which is information of the position of local existence of motion line in each frame of thermal images sequences. In the next step is determined the **Sum of all local maximums**, assuming that every straight line found in one frame is parallel to the others. This means that every line of the HT spectrum has the same angle θ . The information provided by the angle θ of one of the peaks would be sufficient to estimate **Velocity Direction** and **Velocity Magnitude** of the moving objects in thermal images sequences. To improve the precision of moving detection in in thermal images sequences is proposed to use the redundant information of all 1 to n frames by applying the Hough transform HT to the summation of all local maximums, when calculating **Velocity Direction** and **Velocity Magnitude**. This allows discarding the existence of erroneous peaks from sum of all local maximums. This possibility is depicted in Fig. 2 as **(HT)** in parentheses in the blocks **Velocity Direction** and **Velocity Magnitude**.

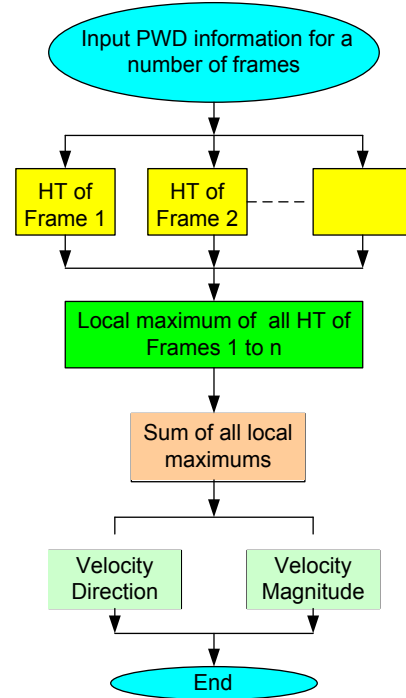
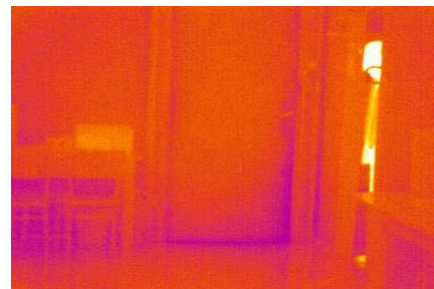


Fig.2. Motion Plane Detection and velocity determination for thermal images sequences

IV. RESULTS AND CONCLUSION

The proposed algorithm for thermo vision images motion detection based on Pseudo Wigner Distributions (PWD) is examined with a lot of test thermal images sequences. For brevity here in this article are presented only some parts of input (Fig. 3) and outputs (Fig. 4.) sequence of frames from a whole used in one of the experiments test thermal images sequence. It can be seen from Fig. 4, that the arrows are an indication of right calculate direction of moving person analyzing motion in two adjacent input frames of thermal images shown in Fig. 3. This indicates proper operation of the developed algorithm for thermo vision images motion detection based on Pseudo Wigner Distributions (PWD). All experiments are carried out with test thermal images sequences from a real working thermal image camera EasIR-9 [9].



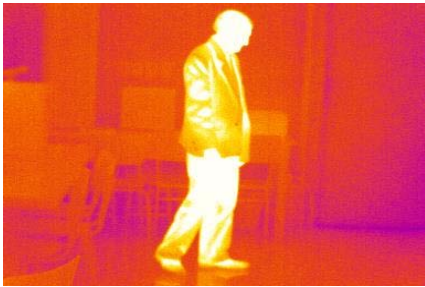


Fig.4. The same three adjacent frames of thermal images as outputs results from motion detection (shown with arrows) in a test thermal images sequence



Fig.3. Three adjacent input frames E9IRCAP 1, 2 and 3 from a test thermal images sequence



ACKNOWLEDGMENT

This work was supported by National Ministry of Science and Education of Bulgaria under Contract DDVU 02/4-7: “Thermo Vision Methods and Recourses in Information Systems for Customs Control and Combating Terrorism Aimed at Detecting and Tracking Objects and People”.

REFERENCES

- [1] L.J. Kozłowski, K. Vural, J. Luo, A. Tomasint, T. Liu, and W.E. Kleinhans, “Low-noise infrared and visible focal plane arrays,” *Opto-Electron. Rev* **4**, 259–269 (1999).
- [2] M. Andriluka, S. Roth, and B. Schiele. Monocular 3D Pose Estimation and Tracking by Detection. In CVPR, 2010.
- [3] A. Ess, B. Leibe, K. Schindler, and L. Van Gool. Robust Multi-Person Tracking from a Mobile Platform. PAMI, 2009.
- [4] Wigner, E. On the quantum correction for thermodynamic equilibrium. *Phys. Rev.* 1932, 40:749–759.
- [5] Zhu, Y., Goutte, R., and Amiel, M.. On the use of a two-dimensional Wigner-Ville distribution for texture segmentation. *Signal Proc.*, 1993,30:205–220.
- [6] T. A. C. M. Claasen and W. F. G. Mecklenbräuker, “The Wigner distribution—A tool for time-frequency signal analysis,” *Philips J. Res.*, Vol. 35, pt. I, pp. 217–250; pt. II, pp. 276–300; pt.III, pp. 372–389, 1980.
- [7] Suzuki, H. and Kobayashi, F. A method of two-dimensional spectral analysis using the Wigner Distribution. *Electronics and Communications in Japan*, 75(1), 1992,1006–1013.
- [8] Ville, J.. Theorie et applications de la notion de signal analytique. *Cables et Transmission*, 1948, 2A:61–74.
- [9] GUIDE® EasIR-9 Thermal Camera User Manual. Wuhan Guide Infrared Co., Ltd, 2010.

Fuzzy Control of the Position Servo Motor Drives with Elasticity and Friction

Dmitry V. Lukichev, Galina L. Demidova

Abstract— It is known that existing algorithms for control position of precision electric drive of systems with nonlinearities: elasticity and friction do not provide damping of autooscillations at infralow tracking speed. Therefore control algorithms, which ensure smooth motion of the load at acceptable transient response has high priority. Mathematical modeling has shown that the use of Fuzzy-controller in position loop instead of the traditional PI-controller can significantly reduce tracking errors and eliminate system oscillation. The proposed technique can improve the accuracy and robustness of precision servo drives of tracking and positioning.

Keywords— Fuzzy system, Fuzzy logic control system, control for electric machine, servo drive, object positioning, intelligent control, two-mass load.

I. INTRODUCTION

The most common principle of servo drive control is the subcontrol principle. However, influence on the accuracy of the system of elasticity between the engine and the load often makes it impossible to track a reference signal, varying with low speed. As a consequence the system has oscillations, which leads to increased wear and sometimes breakage of parts [1].

There are several ways to solve this problem. One of the ways is feeding of the second derivative from the reference angle signal directly to the input of the position control loop [2]. Another possible solution is addition of the adaptation loop with a reference model to the basic system loops [3].

However, the addition of such corrective devices complicates the system and does not give satisfactory results in cases where the description of the properties of the system is inaccurate and non-complete or in the process of work it is changes the parameters of the object (the real system). It is known that in such situations, due to its features, the most constructive is Fuzzy control technology.

Below a description of the use of Fuzzy-controller in the system of servo drive with nonlinearities moving at infralow

speed is given. Research was realized by mathematical modeling using interactive environment for scientific and engineering calculations *MATLAB/Simulink*.

II. MODEL DESCRIPTION

Structure diagram of four-loop system of control of object with Fuzzy-controller in position loop is shown in Fig. 1 [2].

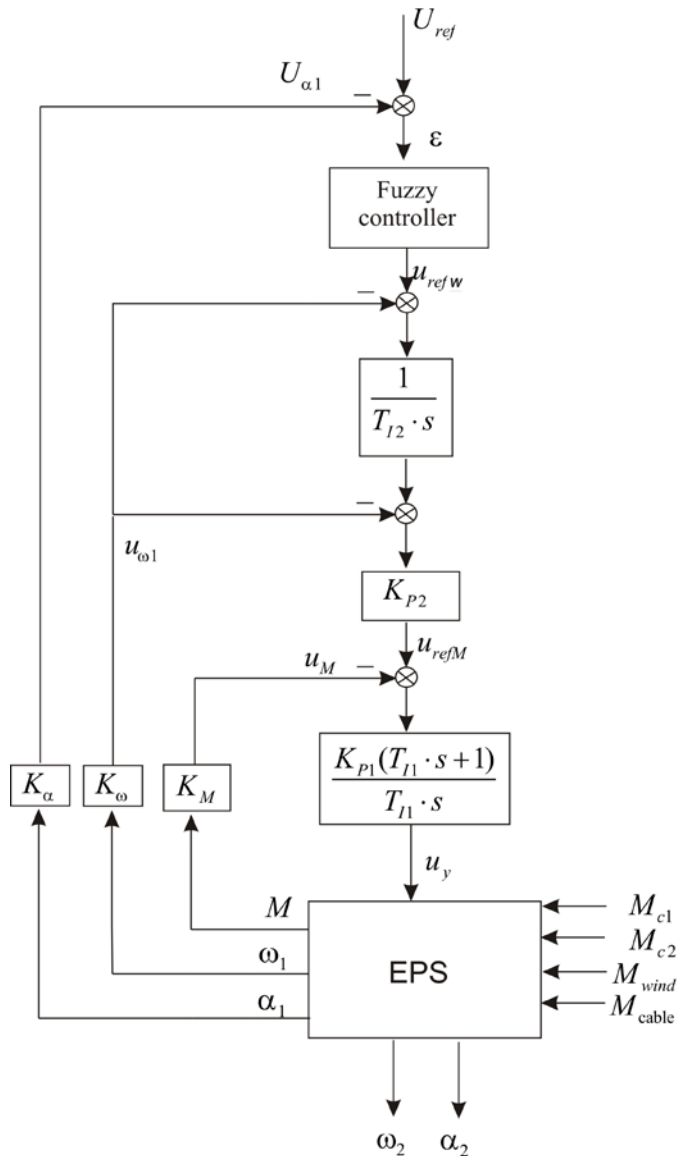


Fig. 1. Structure diagram of four-loop control system

This work was financially supported by Government of Russian Federation, Grant 074-U01

D.V.Lukichev is with the Electrical Engineering and Precision Electromechanical Systems Department, National Research University of Information Technologies, Mechanics and Optics, Saint Petersburg, Russia, IEE Member (phone: +78122325096; e-mail: lukichev@ets.ifmo.ru).

G.L.Demidova is with the Electrical Engineering and Precision Electromechanical Systems Department, National Research University of Information Technologies, Mechanics and Optics, Saint Petersburg, Russia (e-mail: demidova@ets.ifmo.ru).

EPS block describes the processes in the energy subsystem of the drive containing the three-phase synchronous electromechanical motor with active rotor and the number of pole pairs p , transistor inverter, forming a three-phase symmetrical voltage system on the motor windings using shaft position sensor, and dual-mass model of the load.

EPS block can be described by a generalized block diagram of EPS, shown in Fig. 2, where β - rigidity of linearized mechanical characteristic of an electric motor T_e - electrical time constant of motor phase winding; K_{sh} - static coefficient of inverter's transfer in the linear zone of its regulating characteristic [2].

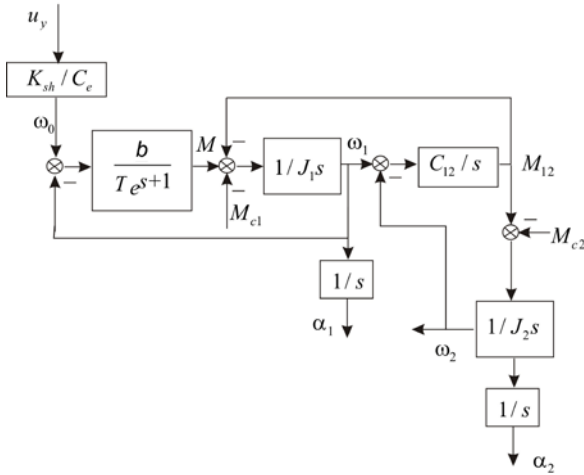


Fig. 2. Generalized structure diagram of EPS

Turning of inner loop of torque and speed are given in [2]. The digital Fuzzy-controller with given value of time discretization T_0 was used at simulation.

Fuzzy-controller, the structure diagram of which is shown in Fig. 3, built from static error compensation conditions.

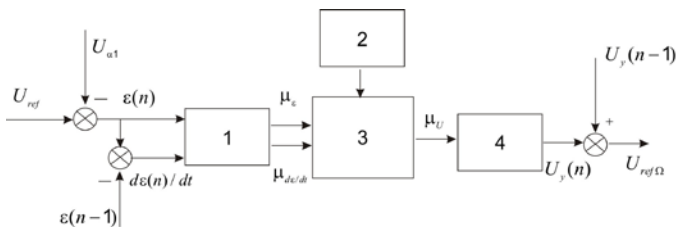


Fig. 3. Structural diagram of Fuzzy control system: 1 - fuzzification block 2 - rule base, 3 - logical solution generating unit, 4 - defuzzification block

Stabilize angle is achieved by introduction of two input variables - error and rate of error change calculated by formulas:

$$\begin{aligned} \varepsilon(n) &= U_{ref\alpha} - U_{\alpha 1}; \\ d\varepsilon(n)/dt &= \varepsilon(n) - \varepsilon(n-1). \end{aligned} \quad (1)$$

In fuzzification block 1 input linguistic variables - position error and rate of error change are characterized by term-sets, such as: BN - large negative; MN - mean negative; LN - small negative; Z - approximately zero; LP - small positive; MP - mean positive; BP - large positive, which are described by the universal set U by membership functions (MF) μ_ε and $\mu_{d\varepsilon/dt}$.

Base of rules is presented in Table 1, where $\mu_\varepsilon, \mu_{d\varepsilon/dt}, \mu_u$ are

values of normalized position error, rate of its change and control action in the n -th moment of time.

Table 1 - Rule base of Fuzzy-controller

$\mu_{d\varepsilon/dt} \backslash \mu_\varepsilon$	BN	MN	LN	Z	LP	MP	BP
BN	BN	BN	MN	MN	LN	LN	Z
MN	BN	MN	MN	LN	LN	Z	LP
LN	MN	MN	LN	LN	Z	LP	LP
Z	MN	LN	LN	Z	LP	LP	MP
LP	LN	LN	Z	LP	LP	MP	MP
MP	LN	Z	LP	LP	MP	MP	BP
BP	Z	LP	LP	MP	MP	BP	BP

Mamdani algorithm (min-max method) is used in this system.

Behaviour of the algorithm for the first two rules from knowledge base is presented below with the following Fuzzy rules [4]:

- if $\varepsilon = a_1^1$ and $d\varepsilon/dt = a_2^1$, then $u_y = a_y^1$;
- if $\varepsilon = a_1^2$ and $d\varepsilon/dt = a_2^2$, then $u_y = a_y^2$;

where a_i^j - linguistic estimates (term-sets) of input variables (for example, $a_i^j \in \{ \text{large negative value } (j = 1), \text{ middle negative value } (j = 2) \}$), a_y^j - linguistic estimates of actual output variable u_y in single universal set.

1. Fuzzification procedure:

$$\mu_1(\varepsilon), \mu_2(\varepsilon), \mu_1(d\varepsilon/dt), \mu_2(d\varepsilon/dt), \quad (2)$$

where $\mu_1(\varepsilon), \mu_2(\varepsilon)$ - membership functions for ε variable; $\mu_1(d\varepsilon/dt), \mu_2(d\varepsilon/dt)$ - membership functions for $d\varepsilon/dt$ variable.

2. Fuzzy output:

$$\begin{cases} A = \mu_1(\varepsilon) \wedge \mu_1(d\varepsilon/dt), \\ B = \mu_2(\varepsilon) \wedge \mu_2(d\varepsilon/dt), \end{cases} \quad (3)$$

where \wedge - logical minimum operation.

Then truncated membership functions for output variable u_y (activation procedure) are determined: [5,6]

$$\begin{cases} \mu_{1y}(u) = A \wedge \bar{\mu}_1(u), \\ \mu_{2y}(u) = B \wedge \bar{\mu}_2(u), \end{cases} \quad (4)$$

where $\mu_{1y}(u), \mu_{2y}(u)$ - membership functions for u_y variable.

3. Compositing (accumulation procedure). Determined truncated functions are combined. As a result, we obtain the total Fuzzy set for output variable with resulting membership function:

$$\mu_y(u) = \mu_{1y}(u) \vee \mu_{2y}(u), \quad (5)$$

where \vee - logical maximum operation.

4. Defuzzification procedure. It is implemented using centroid method:

$$u_y = \frac{\int_{u_1}^{u_2} u \mu_y(u) du}{\int_{u_1}^{u_2} \mu_y(u) du}. \quad (6)$$

When going to numerical integration using method of trapezoids (with sampling interval T_0), formula for determination of output variable u_y will be as follows [5,6]:

$$u_y = \frac{\frac{u_1\mu_0}{2} + \sum_{i=1}^{m-1} u_i\mu_i + \frac{u_2\mu_m}{2}}{\frac{\mu_0}{2} + \sum_{i=1}^{m-1} \mu_i + \frac{\mu_m}{2}}, \quad (7)$$

where $\frac{u_2 - u_1}{m} = T_0$ – sampling interval; m – number of samples on the interval $u_2 - u_1$; $i = 1, 2, 3 \dots m - 1$.

For piecewise linear resulting membership function indicated in fig. 4 and 5, the absciss is determined as:

$$u_y = \frac{\sum_{k=1}^N (a_{k+1} - a_k) [(2a_{k+1} + a_k)b_{k+1} + (2a_k + a_{k+1})b_k]}{3 \sum_{k=1}^N (a_{k+1} - a_k) (b_{k+1} + b_k)}, \quad (8)$$

where N – number of vertices; a_k, b_k – coordinates of vertices of resulting figure.

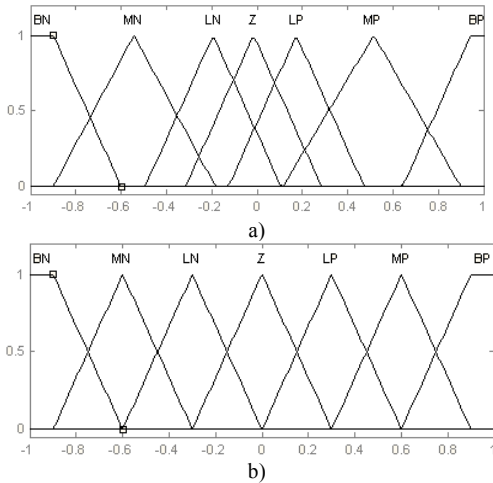


Fig. 4. Terms of input linguistic variables of Fuzzy-controller: a – μ_ϵ ; b – $\mu_{d\epsilon/dt}$

Then value of u_y is translated into value of controlling action on controlled object by means of inverse mapping of u_y value from single universal set onto variation range $[u_{\min}, u_{\max}]$ of linguistic variable.

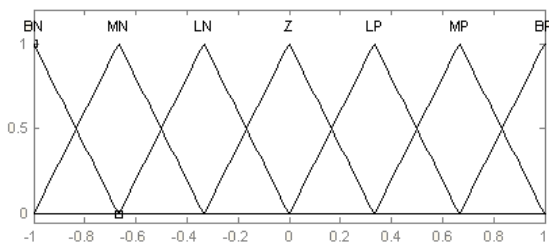


Fig. 5. Terms of output linguistic variables μ_u of the controller

“Triangle” membership functions with range $(-1 - +1)$ are used for analyzed algorithms [7]. This feature applies to input

values of the controller as well as output ones (fig. 4, 5). Fuzzy-controller model is represented in fig. 6.

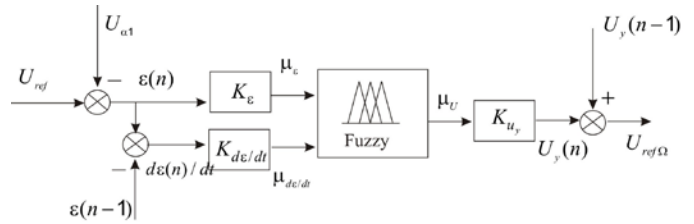


Fig. 6. Model of Fuzzy-controller

Motor RM36-401-50BS with dual-mass load, with moment of inertia of the first mass $J_1 - 340.6 \text{ kg}\cdot\text{m}^2$, the second mass - $J_2 - 1524.3 \text{ kg}\cdot\text{m}^2$, with rigidity $C_{12} - 3.9 \cdot 10^7 \text{ N}\cdot\text{m}/\text{rad}$ was chosen as the controlled motor. Load torque at the first mass $M_{C1} - 50 \text{ N}\cdot\text{m}$ and load torque at the second mass $M_{C2} - 80 \text{ N}\cdot\text{m}$, wind moment $M_{\text{wind}} - 220 \text{ N}\cdot\text{m}$, and also moment of cable junction $M_{\text{cable}} - 60 \text{ N}\cdot\text{m}$ have an effect on the motor. Model with Stribeck effect is chosen as friction model.

Adjustment of Fuzzy-controller is carried out to obtaining of minimum mismatch error. Dynamic optimization method for control system design, implemented in *Simulink* is used at adjusting the coefficients of units which normalize error signal and the rate of its change and also output control signal of position. As a result, normalizing constants of Fuzzy-controller (9) – (10) were obtained, which afterwards were associated with system parameters:

$$k_\epsilon = \frac{k_\omega}{20(8T_\mu + T_0)k_\alpha}, \quad (9)$$

where k_ω, k_α – coefficients of speed and position sensor respectively;

$$k_{d\epsilon/dt} = \frac{20k_\epsilon}{(8T_\mu + T_0)} \quad (10)$$

$$k_{u_y} = 0,05,$$

where $T_\mu = \frac{1}{2\omega_{op}}$ – small uncompensated variable [8-10],

$$\omega_{op} = \frac{2\pi f_p}{4\sqrt{\gamma^3}} - \text{angular resonance frequency};$$

$f_p = \frac{1}{2\pi} \sqrt{\frac{C_{12}(J_1 + J_2)}{J_1 \cdot J_2}}$ – resonance frequency; $\gamma = (J_1 + J_2)/J_1$ – mass ratio factor.

Modeling of system was carried out at tracking mode linearly changing position target with a tracking speed of 1 ang. second per second. At modelling T_0 was accepted as being equal to 0.001 s.

Angular oscillations with amplitude of 3 ang. seconds are clearly distinguished in the system of subcontrol regulation with PI controller, and also moment fluctuations with amplitude of 100 N·m are present (fig. 7).

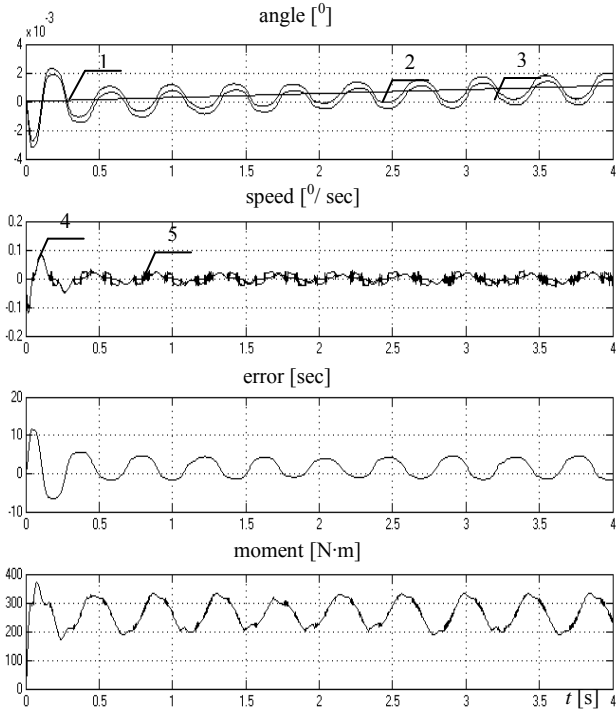


Fig. 7. Transient processes in the system of subordinated regulation with PI controller of angle: 1 – α_{ref} ; 2 – α_1 ; 3 – α_2 ; 4 – ω_1 ; 5 – ω_2

Maximum position error of the second mass in steady-state is equal to 1.489 ang. seconds in the system with Fuzzy-controller (fig. 8) at infralow tracking speed of 1 ang. second per second. Constant tracking error with respect to the first mass is absent; moment fluctuations are also absent.

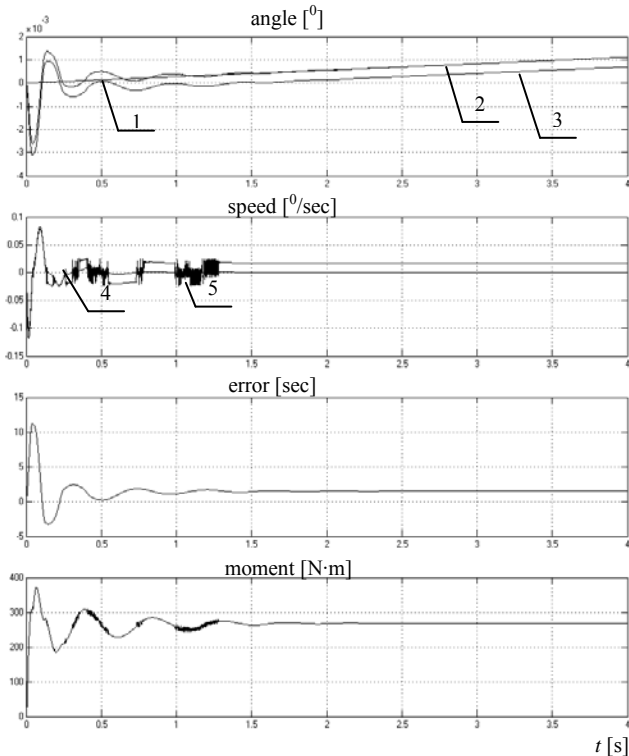


Fig. 8. Transient processes in the system with Fuzzy-controller of angle: 1 – α_2 ; 2 – α_1 ; 3 – α_2 ; 4 – ω_1 ; 5 – ω_2

III. CONCLUSION

We proposed a method of Fuzzy-controller adjustment for use in positional systems with nonlinearities: elasticity and friction. Use of Fuzzy-controller in loop of position instead of traditional PI, PID-controllers allows to considerably improve tracking accuracy and also to remove fluctuations at infralow speed.

REFERENCES

- [1] Yu.A. Bortsov, G.G. Sokolovskiy, Automatic Electric with elastic ties. Saint-Petersburg, Energoatomizdat, 1992.
- [2] V.A. Tolmachev, Synthesis of the electric servo axes of positioner. *Scientific and Technical Journal «Priborostroenie»*, vol. 51, no. 6, pp. 68-72, 2008.
- [3] G.L. Demidova, S.Yu Lovlin, M.Kh. Tsvetkova, Synthesis of Follow-up Electric Drive of telescope's azimuth axis with reference model in position contour. *Vestnik IGEU*, no. 2, pp. 77–81, 2011.
- [4] V.I. Gostev, Design of Fuzzy controllers for automatic control systems. Saint-Petersburg, BKhV-Peterburg – 416 p. , 2011
- [5] E.H. Mamdani, Advances in the linguistic synthesis of Fuzzy controllers, *International Journal of Man-Machine Studies*, vol. 8, pp. 669-678, 1976.
- [6] E.H. Mamdani, Application of Fuzzy logic to approximate reasoning using linguistic synthesis, *IEE Transaction on Computers*, vol. 26, no.12, pp. 1182-1191, 1977.
- [7] R.M. Rodriguez, L. Martinez, F. Herrera, Hesitant Fuzzy Linguistic Term Sets for Decision Making, *Fuzzy Systems, IEEE Transactions on*, Volume 20, Issue 1, pp. 109-119, 2012
- [8] V.A. Tolmachev, I.V. Antipova, S.G. Fomin, Mathematical model motor drive axis positioner, *Scientific and Technical Journal of Information Technologies, Mechanics and Optics*, No 44, pp. 142-146, 2007
- [9] V.A. Tolmachev, G.L. Demidova, Mathematical models and dynamic characteristics electromechanical converters with a limited angle rotation, *Scientific and Technical Journal «Priborostroenie»*, volume 51, No 6, pp. 18-23, 2008
- [10] A.G. Ilina, D.V. Lukichev, A.A. Usoltsev Optimal motion control for positioning and its simulation in environment Matlab Simulink, *Scientific and Technical Journal of Information Technologies, Mechanics and Optics*, No 6, 2008 pp. 63-67, 2008

Using Fuzzy Logic to Control an Innovative Active Vehicle Suspension System

K. Hyniova, L. Smitkova-Janku

Abstract— In the paper, fuzzy logic is used to simulate active suspension control of a one-half-car model. Velocity and acceleration of the front and rear wheels and undercarriage velocity above the wheels are taken as input data of the fuzzy logic controller. Active forces improving vehicle driving, ride comfort and handling properties are considered to be the controller outputs. The controller design is proposed to minimize chassis and wheels deflection when uneven road surfaces, pavement points, etc. are acting on tires of running cars. As a result, a comparison of an active suspension fuzzy control and a spring/damper passive suspension is shown using MATLAB simulations.

Keywords— active suspension, fuzzy logic control, one-half-car model, sprung mass, unsprung mass, vehicle

I. INTRODUCTION

At the Czech Technical University in Prague various alternative strategies and innovations to classical passive suspension systems improving ride comfort of the passengers, providing steering stability, maximizing safety and improving handling properties of vehicles has been researched. In order to improve handling and comfort performance instead of a conventional static spring and damper system, an unique active suspension systems has been developed. Certainly there are numerous variations and different configurations of vibration suspension. In known experimental active systems the force input is usually provided by hydraulic or pneumatic actuators. As an alternative approach to active suspension system design, electromechanical actuators have been studied by the research group. Such actuators provide a direct interface between electronic control and the suspension system. Connection of a passive spring-damper suspension to an active system has a potential of improving safety and

comfort under nominal conditions. Perhaps more important is that such a combination allows continuous adaptation to different road surface quality and driving situations.

A number of studies on structural vibration control have been done recently and practical applications have been realized [1]. It is used both, a passive solutions for vibration isolation, and active systems, usually based on PID controllers. In addition, semi-active vibration isolation methods are often proposed and used. Yoshida and Fujio (1999) applied such a method to a base in which the viscous damping coefficient is changed for vibration control. Fukushima *et al.* (1996) developed a semi-active composite-tuned mass damper to reduce the wind and the earthquake induced vibrations on tall structures. Different active control methods of various structures were offered by Nishimura *et al.* (1996). Yagiz (2001) applied sliding mode control for a multi degree of freedom analytical structural system. In the area of semi-active structural control, Zhou and Chang (2000) and Zhou *et al.* (2002) developed a fuzzy controller and an adaptation law for a structure MR damper system. Shurter and Roschke (2001) used a neuro-fuzzy technique to control building models [2]. Liu *et al.* (2001) designed a slightly more intricate fuzzy controller for a MR damper and were able to reduce vibrations of a SDOF bridge model subjected to random inputs.. Simulation of active Vibration Isolation of a one-quarter-car model with Fuzzy Logic Device has been designed by Nastac in [6].

II. PROBLEM FORMULATION

For the design of active suspension we know how to create a suspension model and how to define objectives of control in order to reach a compromise between contradictory requirements like ride comfort and road holding by changing the force between a wheel and chassis masses. In the past, it has been reported on this problem successively, about the base of optimization techniques, adaptive control and even, H-infinity robust methods [6]. In this paper, fuzzy logic is used to control the active suspension of a one-half-car model that uses linear electrical motor as an actuator. There are taken velocity and acceleration of the front and rear wheels and undercarriage velocity and vertical acceleration above these wheels as input data of the fuzzy logic controller,

Research supported by Project MSMT INGO II LG14.

Assoc. Prof. K. Hyniova is with the Department of Digital Design, Faculty of Information Technology, Czech Technical University in Prague, Thakurova 9, 160 00 Prague, Czech Republic, (phone: (+420) 722575989; e-mail: hyniova@fit.cvut.cz)

L. Smitkova-Janku is a PhD student at the Department of Digital Design, Faculty of Information Technology, Czech Technical University in Prague, Thakurova 9, 160 00 Prague, Czech Republic, (e-mail: jankul@fit.cvut.cz)

and active forces f_1 and f_2 as its output data. The objective of fuzzy control is to minimize chassis and deflections to reach passenger comfort and wheels (not to damage the road surface, respectively) when road disturbances are acting on the running car.

Passenger comfort can be interpreted as an attenuation of sprung mass acceleration or as peak minimization of sprung mass vertical displacement, while good handling can be characterized as an attenuation of unsprung mass acceleration. This effort devoted to passive suspension design is ineffective because improvements to ride comfort are achieved at the expense of handling and vice versa. Instead, the best net result can be achieved by active suspension, i.e. when an additional force (Fig. 1) can act on the system and simultaneously improve both of these conflicting requirements. Another important goal of the control design is to maintain robustness of the closed loop system.

III. ACTIVE SUSPENSION SYSTEM

All suspension systems are designed to meet various specific requirements. In suspension systems, mainly two most important points are supposed to be improved – vibrations absorbing (videlicet passenger comfort) and attenuation of the disturbance transfer to the road (videlicet car handling). The first requirement could be understood as an attenuation of the sprung mass acceleration or as a peak minimization of the sprung mass vertical displacement. The second one is characterized as an attenuation of the force acting on the road or – in simple car models – as an attenuation of the unsprung mass acceleration. The goal is to satisfy both these contradictory requirements.

Satisfactory results can be achieved when an active suspension system generating variable mechanical force acting between the sprung and unsprung masses is used.

Such an actuator can be a linear electric motor [1]. In comparison with traditional actuators that use revolving electromotors and a lead screw or toothed belt, the direct drive linear motor enables contactless transfer of electrical power according to the laws of magnetic induction. The gained electromagnetic force is applied directly without the intervention of mechanical transmission then. Linear electric motors are easily controllable and for features like low friction, high accuracy, high acceleration and velocity, high values of generated forces, high reliability and long lifetime, their usage as shock absorbers seems to be ideal.

Fig.1 shows the basic principle and structure of the linear electric motor used as an actuator in the designed unique active suspension system. The appreciable feature of linear motors is that they directly translate electrical energy into usable mechanical force and motion and back. They are linear shaped.

Linear motor translator movements reach high velocities (up to approximately 4 m/s), accelerations (up to g multiples) and forces (up to 10 kN). The

electromagnetic force can be applied directly to the payload without an intervention of mechanical transmission.

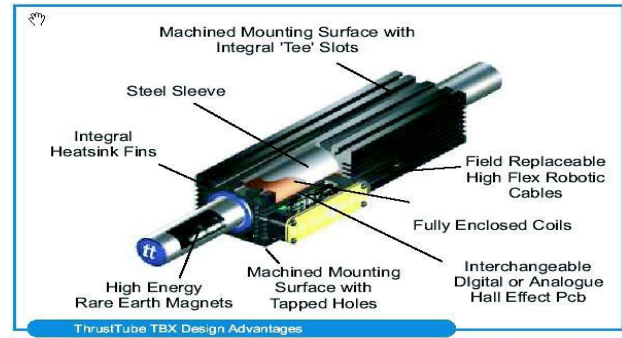


Fig.1 linear motor basic design (manufacturer spreadsheet)

IV. LINEAR MOTOR MODEL

In order to verify control algorithms we created a linear motor model including a power amplifier in Matlab/Simulink™. The model enables to demonstrate the conversion of electrical energy to mechanical energy.

In the model, it is assumed that the magnetic field of the secondary part with permanent magnets is sinusoidal, the phases of the primary part coils are star-connected, and a vector control method is used to control the phase current. Here, PWM voltage signal is substituted by its mean value to shorten (about 10 times) the simulation period (inaccuracies caused by such a substitution can be neglected).

The principal inner representation of the model is shown in Fig.2. The model input vector is given by the instantaneous position [m] necessary to compute the commutation current of the coils, instantaneous velocity [m/s] (the induced voltage of the coils depends on the position and velocity) and desired force [N].

The designed model function we verified comparing dynamics of the model and the real motor See Fig. 3 and Fig4). The simulation parameters correspond to catalogue parameters of TBX3810 linear motor fy Thrust-tube.

For example, time responses caused by changes of the desired force has been compared.

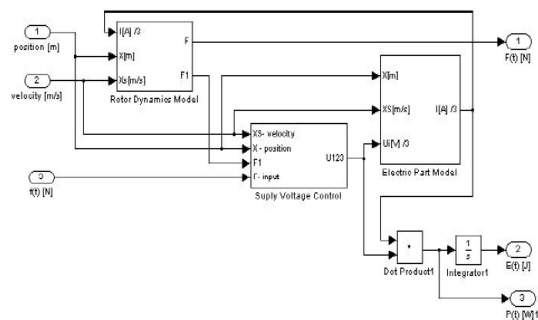


Fig.2 principal inner model representation

The linear motor input-output model is shown in Fig. 3.

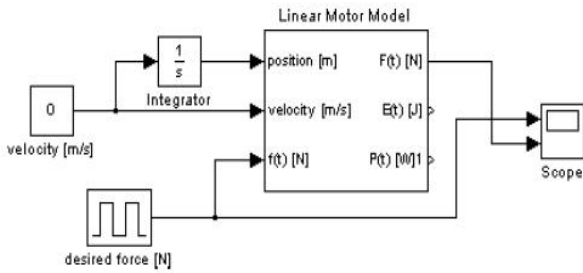


Fig. 3 linear motor input/output model for dynamics verification

Fig.4 and Fig.5 represent simulated and real time responses, respectively (rightangular force signal: 0→200 [N], power supply of 150 [V], velocity: 0 [m/s]).

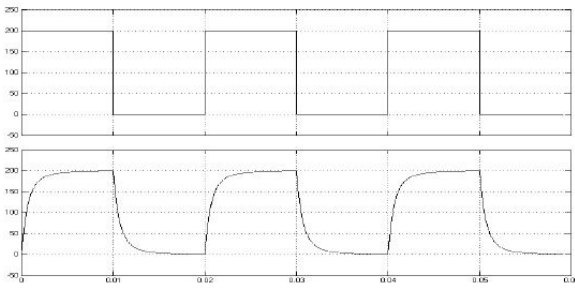


Fig.4 simulated time response

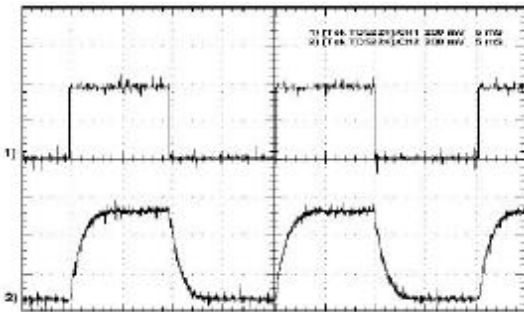


Fig.5 real time response

Comparing the time responses in Fig.4 and Fig.5 it can be seen a very good matching level of the model and real motor behavior.

On the base of the experiments that we completed on the model, we gained values of electric power necessary to be supplied or consumed when velocity and force of the motor are constant. In Fig. 6 an input/output model of the linear motor (with concrete simulation values) is represented.

It results from many experiments we made [6] with TBX3810 linear motor that the designed model describes the real linear motor equipped with necessary auxiliary circuits very authentically and enables to verify control algorithms developed to control the linear motor as an actuator of the active suspension system.

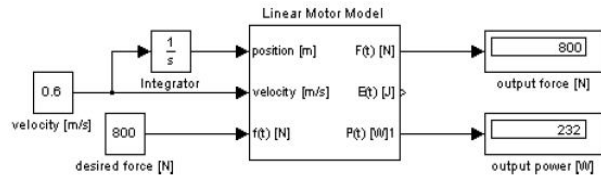


Fig.6 linear motor input-output model

V. ONE-HALF-CAR SUSPENSION MODEL

In this paper, we are considering a one-half-car model (Fig.7) which includes two one-quarter-car models connected to a homogenous undercarriage [10]. The undercarriage is determined by its mass m [kg] (taken as one half of the total body mass - 500 kg), length L [m] ($L = L_1 + L_2 = 1,5m + 2,5m = 4m$), center of gravity position T [m] (given by L_1 and L_2) and moment of inertia J_p [kgm^2] ($2700kgm^2$).

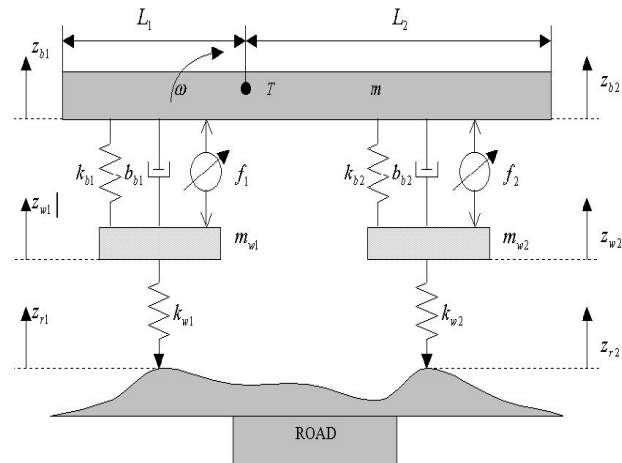


Fig.7 one-half-car model

The motion equations of the car body and the wheels are as follows:

$$m_{w1} Z_{w1}'' = -f_1 + k_{b1}(Z_{b1} - Z_{w1}) - k_{w1}(Z_{w1} - Z_{r1}) + b_{b1}(z_{b1} - z_{w1}) \quad (1)$$

$$m_{w2} Z_{w2}'' = -f_2 + k_{b2}(Z_{b2} - Z_{w2}) - k_{w2}(Z_{w2} - Z_{r2}) + b_{b2}(z_{b2} - z_{w2}) \quad (2)$$

$$m Z_{b1}'' = f_1 - k_{b1}(Z_{b1} - Z_{w1}) - b_{b1}(z_{b1} - z_{w1}) = F_1 \quad (3)$$

$$m Z_{b2}'' = f_2 - k_{b2}(Z_{b2} - Z_{w2}) - b_{b2}(z_{b2} - z_{w2}) = F_2 \quad (4)$$

where the position variables respect the static equilibrium position:

m_{w1}, m_{w2} ... wheel masses (35 kg each),

k_{b1}, k_{b2} ... passive suspension spring stiffness (16 kN/m each),

k_{w1}, k_{w2} ... tire stiffness (160 000 N/m each),

b_{b1}, b_{b2} ... passive suspension damping coefficients (980 Ns/m each),

f_1, f_2 ... active forces between the sprung and unsprung masses [N],

z_{r1}, z_{r2} road displacements [m],
 z_{b1}, z_{b2} body (chassis) displacements [m],
 z_{w1}, z_{w2} wheel displacements [m].

To model the road input we assume that the vehicle is moving at a constant forward speed. Then the vertical velocity is a white noise process which is approximately true for most of real roadways.

The pitching equation is given as :

$$F_1 L_1 - F_2 L_2 + J_p \dot{\omega} = 0 \tag{5}$$

and motion of the gravity center as:

$$F_1 + F_2 - m_p \dot{v}_r = 0 \tag{6}$$

Note, that:

$$v_{b1} = v_T + \omega L_1 \tag{7}$$

$$v_{b2} = v_T - \omega L_2 \tag{8}$$

where the meaning of constants and variables is follows:

- v_T [ms^{-1}] velocity of the center of gravity
- ω [$rads^{-1}$] angular velocity
- v_{b1} [ms^{-1}] undercarriage velocity above the front wheel
- v_{b2} [ms^{-1}] undercarriage velocity above the rear wheel

VI. STATE-SPACE MODEL

To transform the motion equations of the one-half-car model to a state space model, the following state variables vector, input vector, and the vector of disturbances, are considered:

$$x = [x_1, x_2, x_3, x_4, x_5, x_6, x_7, x_8]^T \tag{9}$$

$$u = [f_1, f_2]^T \tag{10}$$

$$v = [\dot{z}_{r1}, \dot{z}_{r2}]^T \tag{11}$$

Where:

$$\begin{aligned} x_1 &= z_{b1} - z_{w1} & x_5 &= z_{w2} - z_{r2} \\ x_2 &= z_{w1} - z_{r1} & x_6 &= \dot{z}_{w2} \end{aligned} \tag{12}$$

$$x_3 = \dot{z}_{w1} \quad x_7 = v_T$$

$$x_4 = z_{b2} - z_{w2} \quad x_8 = \omega$$

Then the motion equations of the one-half-car model for the active suspension can be written in the state space form as follows:

$$\dot{x} = Ax + Bu + Fv \tag{13}$$

where for the given data:

$$A = \begin{pmatrix} 0 & 0 & -1.0 & 0 & 0 & 0 & 1.0 & 1.5 \\ 0 & 0 & 1 & 0 & 0 & 0 & 0 & 0 \\ 457.1 & -4571.4 & -28.0 & 0 & 0 & 0 & 28.0 & 42.0 \\ 0 & 0 & 0 & 0 & 0 & -1.0 & 1.0 & -2.5 \\ 0 & 0 & 0 & 0 & 0 & 1.0 & 0 & 0 \\ 0 & 0 & 0 & 457.1 & -4571.4 & -28.0 & 28.0 & -70.0 \\ -32.0 & 0 & 2.0 & -32.0 & 0 & 2.0 & -3.9 & 2.0 \\ -8.9 & 0 & 0.5 & 14.8 & 0 & -0.9 & 0.4 & 3.1 \end{pmatrix}$$

$$B = \begin{pmatrix} 0 & 0 \\ 0 & 0 \\ -0.02860 & 0 \\ 0 & 0 \\ 0 & 0 \\ 0 & -0.02860 \\ 0.00200 & 0.00200 \\ 0.00055 & 0.00092 \end{pmatrix} \quad F = \begin{pmatrix} 0 & 0 \\ -1 & 0 \\ 0 & 0 \\ 0 & 0 \\ 0 & -1 \\ 0 & 0 \\ 0 & 0 \\ 0 & 0 \end{pmatrix} \tag{14}$$

Thanks to the negative real parts of all eigen values of matrix A, the model is stable.

VII. FUZZY LOGIC CONTROLLER

The fuzzy control system consists of three stages: fuzzification, fuzzy inference and defuzzification (Fig.8).

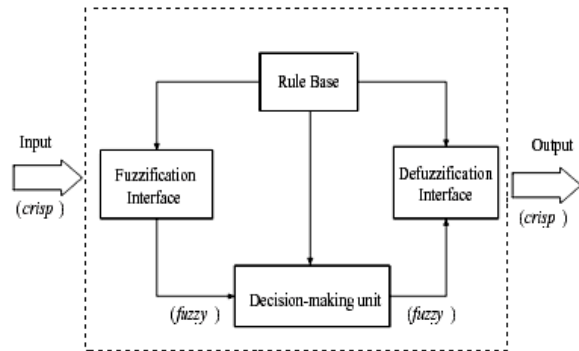


Fig.8 fuzzy controller structure

The fuzzification stage converts real-number (crisp) input values into fuzzy values whereas the fuzzy inference machine processes the input data and computes the controller outputs in cope with the rule base and data base. These outputs, which are fuzzy values, are converted into real-numbers by the defuzzification stage.

The fuzzy logic controller used for the active suspension has nine inputs:

$$[v_{b1}, \dot{v}_{b1}, v_{b2}, \dot{v}_{b2}, v_{w1}, v_{w2}, v_T, \dot{v}_T, \omega]^T \tag{15}$$

and two outputs: f_1 and f_2 . All membership functions are of triangular form. Variables ranges are stated experimentally [2] and are given in Table I bellow.

TABLE I variables ranges

z_i [cm]	$ f_1 _{max}$ [N]	$ f_2 _{max}$ [N]	$ v_T _{max}$ [m.s ⁻¹]	$ \dot{v}_T _{max}$ [m.s ⁻²]	ω [rads ⁻¹]
5	2876.4	2949.4	0.3	6.6	0.1
10	5752.8	6062.5	0.5	13.5	0.2

$ v_{b1} _{max}$ [m.s ⁻¹]	$ \dot{v}_{b1} _{max}$ [m.s ⁻²]	$ v_{w1} _{max}$ [m.s ⁻¹]
0.3	6.8	2.4
0.5	13.5	4.8

$ v_{b2} _{max}$ [m.s ⁻¹]	$ \dot{v}_{b2} _{max}$ [m.s ⁻²]	$ v_{w2} _{max}$ [m.s ⁻¹]
0.3	6.8	2.2
0.5	13.5	4.9

The rule base used in the active suspension system for one-half-car model is represented by 160 rules with fuzzy terms derived by modeling the designer’s knowledge and experience.

There are two types of rules for the one-half-car model in here. The rules for unsprung masses (several examples given in Table 2) are corresponding to the rules of the one-quarter-car model [3], [9], [11] and considering: $[v_{b1}, \dot{v}_{b1}, v_{b2}, \dot{v}_{b2}, v_{w1}, v_{w2}]$ as fuzzycontroller inputs, and f_1 and f_2 as controller outputs. The rules for sprung masses (several examples given in Table III) describe a mutual influence of the wheels and taking $[v_T, \dot{v}_T, \omega]$ as fuzzy controller inputs and f_1 and f_2 as controller outputs.

The abbreviation used in Table II and Table III correspond to:

- NV Negative Very Big
- NB..... Negative Big
- NM.....Negative Medium
- NS..... Negative Small
- ZR..... Zero
- PS..... Positive Small
- PM.....Positive Medium
- PB..... Positive Big
- PV.....Positive very Big

Big

The output of the fuzzy controller is a fuzzy set of control. As processes usually require non-fuzzy values of control, a method of defuzzification called “center of gravity method” is used here.

TABLE II rules for unsprung mass

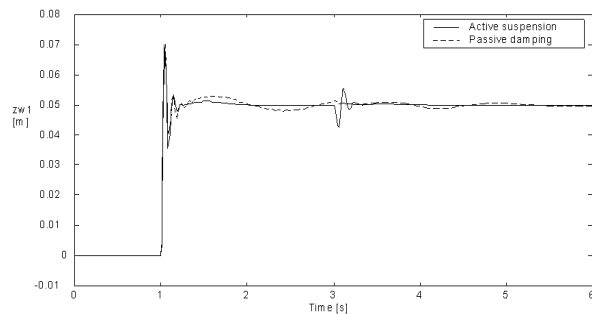
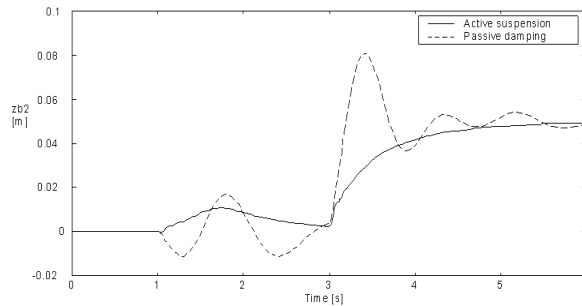
$If [v_{w1}=PM]AND[v_{b1}=NM]AND[\dot{v}_{b1}=P]THEN[f_1 =PV]$
$If [v_{w1}=PS]AND[v_{b1}=NS]AND[\dot{v}_{b1}=P]THEN[f_1 =PB]$
$If [v_{w1}=PM]AND[v_{b1}=NM]AND[\dot{v}_{b1}=ZE]THEN[f_1 =PM]$
$If [v_{w1}=PS]AND[v_{b1}=NS]AND[\dot{v}_{b1}=ZE]THEN[f_1 =PS]$
$If [v_{w1}=NM]AND[v_{b1}=PM]AND[\dot{v}_{b1}=P]THEN[f_1 =NV]$
$If [v_{w2}=PM]AND[v_{b2}=NM]AND[\dot{v}_{b2}=P]THEN[f_2 =PV]$
$If [v_{w2}=PS]AND[v_{b2}=NS]AND[\dot{v}_{b2}=P]THEN[f_2 =PB]$
$If [v_{w2}=PM]AND[v_{b2}=NM]AND[\dot{v}_{b2}=ZE]THEN[f_2 =PM]$
$If [v_{w2}=PS]AND[v_{b2}=NS]AND[\dot{v}_{b2}=ZE]THEN[f_2 =PS]$
$If [v_{w2}=NM]AND[v_{b2}=PM]AND[\dot{v}_{b2}=P]THEN[f_2 =NV]$

TABLE III rules for sprung mass

$If [v_T=PS]AND[\omega =PM]AND[\dot{v}_T=P]THEN[f_1 =NV]AND[f_2 =PM]$
$If [v_T=NS]AND[\omega =PM]AND[\dot{v}_T=P]THEN[f_1 =NM]AND[f_2 =PV]$
$If [v_T=NM]AND[\omega =PM]AND[\dot{v}_T=P]THEN[f_1 =ZE]AND[f_2 =PV]$
$If [v_T=PS]AND[\omega =PS]AND[\dot{v}_T=P]THEN[f_1 =NB]AND[f_2 =PS]$
$If [v_T=ZE]AND[\omega =PS]AND[\dot{v}_T=P]THEN[f_1 =NB]AND[f_2 =PB]$
$If [v_T=NS]AND[\omega =PS]AND[\dot{v}_T=P]THEN[f_1 =NS]AND[f_2 =PB]$
$If [v_T=PS]AND[\omega =NS]AND[\dot{v}_T=P]THEN[f_1 =NV]AND[f_2 =PV]$
$If [v_T=NS]AND[\omega =NS]AND[\dot{v}_T=P]THEN[f_1 =PS]AND[f_2 =NB]$
$If [v_T=PS]AND[\omega =NM]AND[\dot{v}_T=P]THEN[f_1 =PM]AND[f_2 =NV]$
$If [v_T=NS]AND[\omega =NM]AND[\dot{v}_T=P]THEN[f_1 =PV]AND[f_2 =NM]$

VIII. SIMULATION RESULTS

In this section, the controller was tested in order to compare the results of the designed fuzzy logic control with a traditional passive suspension system. As an example, step responses of the unsprung and front/rear sprung masses are shown in Fig. 9- Fig.7.



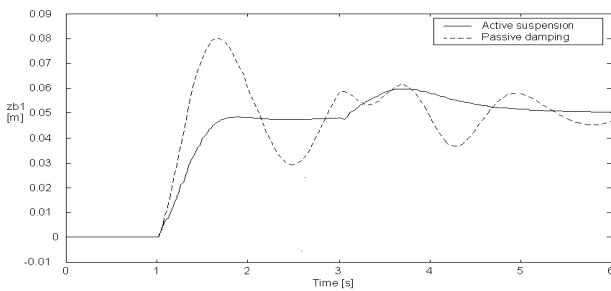


Fig.9 sprung mass deflection above the front wheel

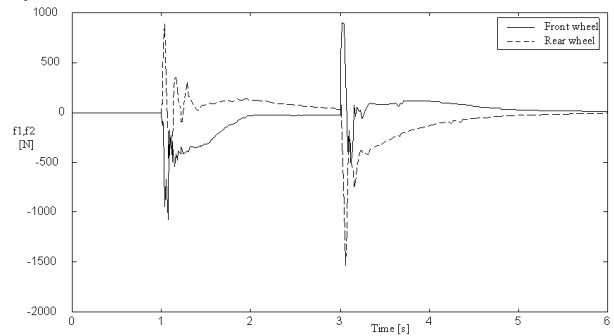


Fig.10 sprung mass deflection above the rear wheel

Fig.11 front unsprung mass (front wheel) deflection

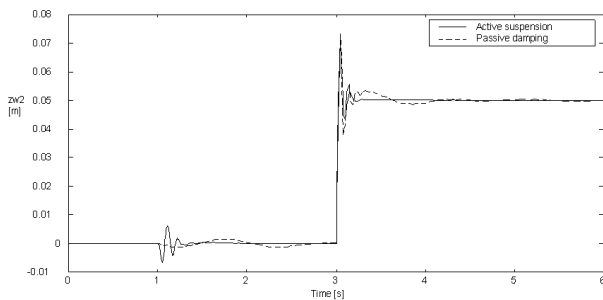


Fig.12 rear wheel deflection

Fig. 13 active forces acting on front /rear wheel

Analyzing the diagram in Fig.12, it is evident that the classical (passive) suspension device provides almost the same performance as the active suspension system based on the designed fuzzy machine. Assuming a large complexity of active isolation in comparison with the passive suspension, it seems to be inadequate to use a fuzzy machine for active suspension control.

From Fig.9 and Fig.10, it is evident that fuzzy controlled active suspension efficiently suppresses sprung mass oscillations that occur when only passive suspension was used.

Diagram in Fig. 13 represent active forces acting on front and rear wheels in order to optimize ride comfort and good handling of the vehicle.

IX. CONCLUSION

In the paper, we briefly described a basic way of fuzzy controlled active suspension system designed for a vehicle one-half-car model.

The entire analysis was developed in Matlab™ - Simulink, with Fuzzy Logic Toolbox. In this case, the fuzzification and defuzzification processes have been done by the special modules of Simulink™.

The fuzzy inference machine is also on custody of a special module of Simulink. Practically, the entire process of fuzzification - inference - defuzzification is automaton made by the Fuzzy Logic Controller of Simulink™. The

inference machine working is based on the set of rules which link the input variables by the outputs. The set of input variables, output variables and inference rules base derived by modeling the designers knowledge and experience on vibroisolation devices.

REFERENCES

[1] Bratu, P.: *Sisteme Elastice de Rezemare Pentru Masini si Utilaje*, Ed. Tehnica, Bucuresti, 1990

[2] Cuclu, R.: Fuzzy Logic Control of Vibration of Analytical Multi-Degree-of-Freedom Structural Systems, Turkish J. Eng. Env. Sci., p157-167, 2003

[3] Hyniova, K. - Stribrsky, A. - Honcu, J.: *Fuzzy Control of Mechanical Vibrating Systems*, International Carpatian Control Conference ICC 2001, pp. 393-398, Krytyca, Poland, 2001

[4] Minarik, D.: *Fuzzy Control System for Active Suspension of Vehicles*, Diploma thesis, FEE CTU , Prague, 2002

[5] Stribrsky, A. - Hyniova, K. - Honcu, J.: *Using Fuzzy Logic to Control Active Suspension of Vehicles*, Intelligent Systems in Practice, pp.41-49, Luhacovice, 2000

[6] Nastac, S.: Simulation of active Vibration Isolation with Fuzzy Logic Device, In: *Proceedings of the 10th international Conference on mathematical and computational methods in Science and Engineering (MACMESE '08)*, pp. 346-351 Brasov, 2008.

[7] Stribrsky, A. - Hyniova, K. - Honcu, J.: *Reduction of Vibrations in Mechanical Systems*, Proceedings of Workshop 2001, Part A, pp.174-175, CTU Prague, 2001

[8] G.C.D. Sousa and B.K. Bose, A fuzzy set theory based control of a phase-controlled converter DC machine drive, IEEE Trans. Industrial Applications 30 (1994) 34-44.

[9] M.H. Sunwoo, K.C. Cheok and H.J. Huang, Model reference adaptive control for vehicle active suspension systems, IEEE Log. No. 9144904.

[10] P.J.Th. Venhovens, The development and implementation of adaptive semi-active suspension control, Vehicle System Dyn. 23 (1994) 211-235.

[11] E.C. Yeh and Y.J. Tsao, A fuzzy preview control scheme of active suspension for rough road, Int. J. Vehicle Design 15 (1994) 166-180.



K. Hyniova (born in 1963)

Ing. in technical cybernetics at the Faculty of Electrical Engineering at the Czech Technical university (CTU) in Prague, Czech Republic, (1987), PhD in technical cybernetics at the Faculty of Electrical Engineering, CTU in Prague, Czech Republic, (1991), Assoc. Prof. in control engineering and measurement, at Faculty of Electrical Engineering, at the CTU in Prague, CZ, (2000).

She has worked at the Department of Control Engineering, Faculty of Electrical Engineering, CTU in Prague, CZ first as an assistant professor, later as an Associated Professor. Currently she is working as an Associated Professor at the Department of Digital Design, Faculty of Information technology, CTU in Prague, CZ. She published 5 books and over 70 papers (Hyniova, K.: Instrumentation of processes, Prague, Czech Republic, CTU Publishing, 1999; Hyniova, K.: Control Systems, Prague, Czech Republic, CTU Publishing, 2012; Hyniova, K.: An Innovative Active Suspension System for Autonomous Vehicles: A Safe and Comfortable Ride and Good Handling, In *ERCIM NEWS*, No. 94, published by ERCIM EEIG, France, pp.28-29, 2013)). She is interested in intelligent vehicles control systems, vehicle dynamics and in consistency in networks of relations.

She is a member of Technical Committee 4.2 on Mechatronic Systems, IFAC.

Using Neural Networks to Design Predictive Model of Creation of Aluminium Oxide Layer

P. Michal, A. Vagaská, M. Gombár, J. Kmec, E. Spišák, D. Kučerka

Abstract—This paper shows an influence of amount of sulphuric acid in the electrolyte and an impact of electrolyte temperature on the thickness of aluminium oxide layer created with varying anodizing time and applied voltage. Impact of these variables is shown by using design of experiments methodology (DoE) for six factors (amount of sulphuric acid, oxalic acid, amount of aluminium cations, electrolyte temperature, anodizing time, applied voltage). Oxide layer was created with current densities of $1 \text{ A}\cdot\text{dm}^{-2}$ and $3 \text{ A}\cdot\text{dm}^{-2}$ respectively.

Keywords—anodizing, corrosion protection, layer thickness, neural networks

I. INTRODUCTION

PURE aluminium and its alloys, such as weight-saving materials, play an increasingly important role of technical, technological and economic terms [1] in the aerospace and automotive industries[2], where lightweight and rigid structure are preferred[3]. Anodic aluminium oxide (AAO) coating has recently attracted the scientists' attention because of its self-organizing nature of vertical (cylindrical) pores in the form of hexagonal arrays, which provides a controlled and narrow distribution of pore diameters and inter-pore distances in addition to the possibility of forming the pores with extremely high aspect ratio [4]. Anodizing is one of the most important processes in corrosion protection and colour finishes for aluminium [5]. Anodizing of aluminium surfaces is carried out in a wide variety of plants for numerous uses in industries. It is an effective process applied to producing decorative and protective films on articles made from aluminium [6]. With the oxidation of aluminium, when forming the electrolyte, the most frequently used are sulphuric acid and oxalic acid,

alternatively a combination of them, because of their environmental friendliness [7],[8]. The mechanism of an oxide layer formation when using sulphuric acid solution has been examined by Tsangaraki-Kaplanogloua et al.[9], Patermarakis [10], and Aerts et al.[11], who managed to design a mathematical model of local turbulences in the electrolyte and examine their influence on the geometrical dimensions of the pores. Aerts et al. were also dealing with the temperature effect on the growth of the oxide layer [12] and the layer porosity [4] of 99.50 % aluminium using the electrolyte comprising sulphuric acid based on which it followed that the structure of the layer, the layer porosity, its thickness and hardness are not so much under the influence of the temperature of the electrolyte compared to that of the electrode.

II. EXPERIMENT REALIZATION

Alloy EN AW 1050-H24 with dimensions 101x70x1 mm was used for specimens. Each applied specimen was degreased in a 38.00% solution of NaOH at 55.00 to 60.00 ° C for 2 minutes and stained in a 40.00% solution of NaOH at the temperature 45.00 ° - 50.00 ° C for 0.50 min. Consequently, the specimen was immersed in a nitric acid bath (4.00% HNO₃) at the temperature from 18.00 to 24.00 ° C for 1.00 min. Between each operation, the sample was rinsed with distilled water.

Electrolyte for each anodizing sample was made from sulphuric acid, oxalic acid and aluminium cations (added like powdered aluminium oxide). Table 1 shows transfers of factors between nature scale and coded scale. Coded scale is used to prevent influence of the absolute value of the studied factors in evaluating the results of the experiment.

Table 1 table of transfers between natural scale and coded scale of examined factors

Factor		Factor level				
Coded scale	Nature scale	-2.37	-1	0	+1	+2.37
x_1	H_2SO_4 [g.l ⁻¹]	33.51	130.00	200.00	270.00	366.49
x_2	$C_2H_2O_4$ [g.l ⁻¹]	1.49	7.00	11.00	15.00	20.51
x_3	Al^{3+} [g.l ⁻¹]	0.18	5.00	8.50	12.00	16.82
x_4	T [°C]	-1.78	12.00	22.00	32.00	45.78
x_5	t [min]	6.22	20.00	30.00	40.00	53.78
x_6	U [V]	5.24	8.00	10.00	12.00	14.76

P. Michal, Technical University of Košice, Faculty of Manufacturing Technologies, Department of Mathematics, Informatics and Cybernetics, 08001 Prešov, Slovak Republic (e-mail: peter.michal@tuke.sk)

A. Vagaská, Technical University of Košice, Faculty of Manufacturing Technologies, Department of Mathematics, Informatics and Cybernetics, 08001 Prešov, Slovak Republic (e-mail: alena.vagaska@tuke.sk)

M. Gombár, University of Prešov in Prešov, Faculty of Management, Department of Management, 08001 Prešov, Slovak Republic (e-mail: gombarmirek@gmail.com)

J. Kmec, Institute of Technology and Businesses in České Budějovice, The Department of Mechanical Engineering, Okružní 10, 37001 České Budějovice, Czech Republic, (e-mail: doc.kmec@gmail.com)

E. Spišák, Technical University of Košice, Faculty of Mechanical Engineering, Department of Technologies and Materials, 042 00 Košice, Slovak Republic (e-mail: emil.spisak@tuke.sk)

D. Kučerka, Institute of Technology and Businesses in České Budějovice, The Department of Mechanical Engineering, Okružní 10, 37001 České Budějovice, Czech Republic, (e-mail: kucerka@mail.vstecb.cz)

III. PROBLEM SOLUTION

A higher-order neural unit (HONU), especially the 3rd order HONU based on the iterative Levenberg-Marquardt (LM) algorithm [13],[14],[15] was used to determine the influence of input factors on the thickness of the final AAO layer. This algorithm is often used for training technique of the neural unit [16]. It is a process of updating individual weights in a predetermined number of steps to achieve a minimum difference between the actual and calculated values of observed variable [17], [18], [19]. The equation describing the investigated model is the characteristic equation of given type of neural unit (1st order HONU, 2nd order HONU a 3rd order HONU) for observed factors $x_1, x_2, x_3, x_4, x_5, x_6$.

IV. RESULTS AND DISCUSSION

After the learning process of neuron unit is done, we get a prediction model that describes the thickness of AAO layer. The final thickness of oxide layer, α is preliminary thickness of oxide layer is expressed in $\text{mm} \cdot 10^{-3}$.

Table 2 shows significant statistical indicator for compiled prediction models of surface AAO layer thickness for surface current densities $1 \text{ A} \cdot \text{dm}^{-2}$ and $3 \text{ A} \cdot \text{dm}^{-2}$. Those indicators are sum of square errors "SSE", mean square error "RMSE", correlation coefficient "R", coefficient of determination "R", standard deviation of errors "se", variation of errors " s^2e " and biggest error of prediction "maxe".

Table 2 significant statistical indicators for compiled mathematical models

	$1 \text{ A} \cdot \text{dm}^{-2}$	$3 \text{ A} \cdot \text{dm}^{-2}$
SSE	87.51	60.30
RMSE	1.90	1.31
R^2	0.93	0.96
R	0.97	0.98
se	1.38	1.15
s^2e	1.90	1.32
maxe	6.6	5.64

Fig. 1, Fig. 2, Fig. 3, Fig. 4 and Fig. 5 show the influence of factor x_1 (concentration of sulphuric acid in the electrolyte) and x_4 (temperature of the electrolyte) on the thickness of aluminium oxide created on sample surface. These graphs also demonstrate influence of factor x_5 (anodizing time) on the oxide thickness. The level of factor x_5 is set to level "-2.38" (6.22 min) Fig. 1, "-1" (20 min) Fig. 2, "0" (30 min) Fig. 3 "1" (40 min) Fig. 4 and "2.38" (53.78 min) Fig. 5. Aluminium oxide layer was created on the surface areas at $1.00 \text{ A} \cdot \text{dm}^{-2}$ of current density. Factors x_2, x_3 and x_6 have zero factor level for all these graphs. Zero factor level for factor x_2 is $11 \text{ g} \cdot \text{l}^{-1}$, for factor x_3 it is $8.5 \text{ g} \cdot \text{l}^{-1}$ and for factor x_6 it is 10 V .

From these graphical characteristics it can be surmised that the thickness of AAO layer is proportional to concentration of sulphuric acid in the electrolyte (factor x_1). Thus we can state that with increasing amount of sulphuric acid in the electrolyte also rises an amount of dissociated ions. Increased ion amount in an electrolyte increase its conductivity. Oxygen, which is bound to a part of these ions, is used to create a layer of an aluminium oxide. Electrolyte temperature (factor x_4) influences

the speed of oxide layer creating and also the thickness of AAO layer. With increasing temperature also rises the speed of chemical reactions on metal-electrolyte interface. However, general claim that with increasing electrolyte temperature also proportionally increases the thickness of AAO layer is not true. This claim is true only in a specific case. It means that some others variables significantly influences the thickness of AAO layer, specifically, the time of oxidation (factor x_5). If the concentration of sulphuric acid in electrolyte influences the amount of ions in electrolyte and if electrolyte temperature influences the speed of chemical reactions on a metal-electrolyte interface, then not only does time of oxidation determinate time of chemical reactions between meal and electrolyte but also between electrolyte and already created oxide layer. Reactions between metal and electrolyte create new molecules of aluminium oxide on the surface of metal and thus contribute to the rise of oxide layer. However, reactions between oxide layer and electrolyte cause reduction in thickness of created oxide layer due to it dissolving in the solution. Thus with the increase in time of oxidation, the thickness of oxide layer decreases, due to increase in electrolyte temperature. After crossing a certain temperature threshold (factor level -1 for Fig. 2, factor level 0 for Fig. 3, Fig. 4, Fig. 5), the resulting oxide layer thickness increases. Speed of oxide layer creating is higher than speed at which it before it reaches the temperature of factor -1.

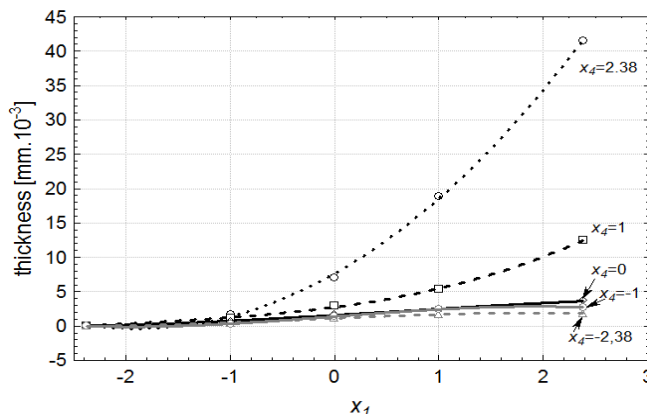


Fig. 1 Influence of factor x_1 and x_4 on AAO layer thickness at current density $1 \cdot \text{Adm}^{-2}$ and factor x_5 which is set to level -2.38

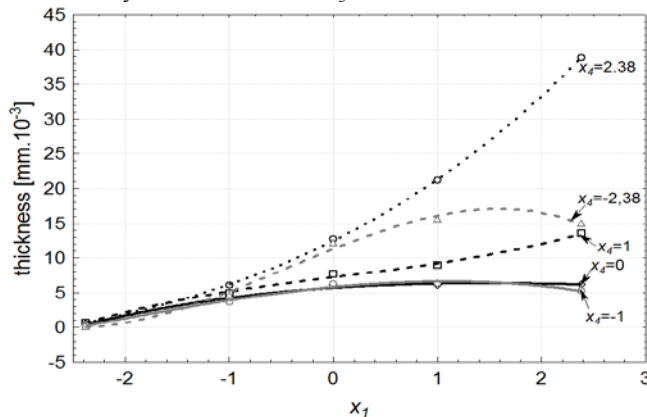


Fig. 2 Influence of factor x_1 and x_4 on AAO layer thickness at current density of $1 \cdot \text{Adm}^{-2}$ and factor x_5 which is set to level -1

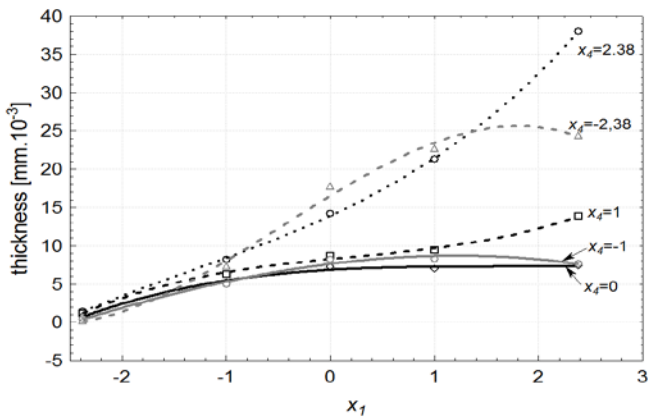


Fig. 3 Influence of factor x_1 and x_4 on AAO layer thickness at current density of $1 \cdot \text{Adm}^{-2}$ and factor x_5 which is set to level 0

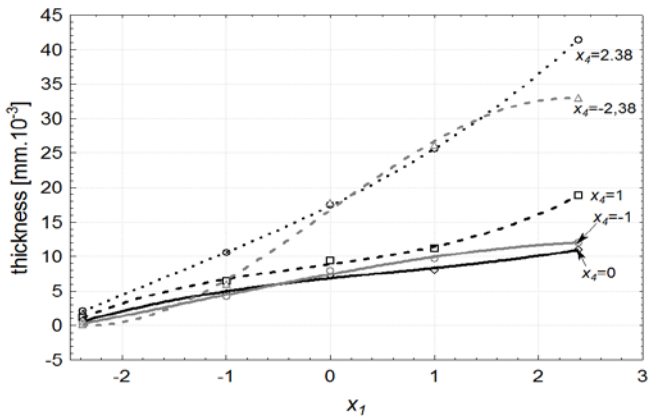


Fig. 4 Influence of factor x_1 and x_4 on AAO layer thickness at current density of $1 \cdot \text{Adm}^{-2}$ and factor x_5 which is set to level 1

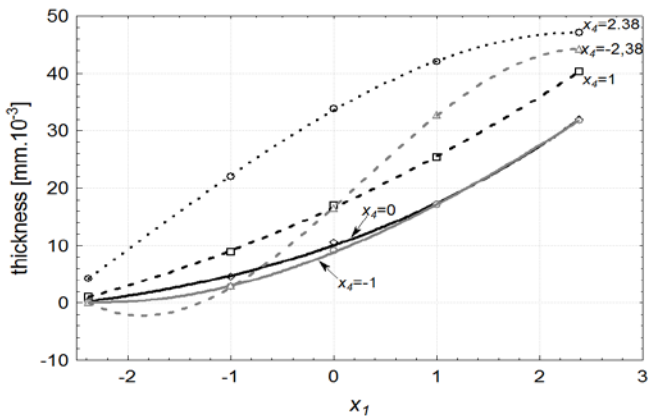


Fig. 5 Influence of factor x_1 and x_4 on AAO layer thickness at current density of $1 \cdot \text{Adm}^{-2}$ and factor x_5 which is set to level 2.38

Fig. 6, Fig. 7, Fig. 8, Fig. 9 and Fig. 10 shows influence of factors x_1 (concentration of sulphuric acid in the electrolyte) and x_4 (temperature of the electrolyte) on thickness of aluminium oxide created on sample surface. These graphs also demonstrate influence of the factor x_5 (anodizing time) on the oxide thickness. Level of factor x_5 is set to level "-2.38" (6.22 min) Fig. 6, "-1" (20 min) Fig. 7, "0" (30 min) Fig. 8 "1" (40 min) Fig. 9 and "2.38" (53.78 min) Fig. 10. Aluminium oxide layer was created on $3.00 \text{A} \cdot \text{dm}^{-2}$ current density surface areas. Factors x_2 , x_3 and x_6 have zero factor level for all these

pictures. Zero factor level for factor x_2 is $11 \text{ g} \cdot \text{l}^{-1}$, for factor x_3 it is $8.5 \text{ g} \cdot \text{l}^{-1}$ and for factor x_6 it is 10 V .

From comparison of thickness based on concentration of sulphuric acid in electrolyte, electrolyte temperature and time of oxidation for current densities of $1 \text{ A} \cdot \text{dm}^{-2}$ and $3 \text{ A} \cdot \text{dm}^{-2}$ (Fig. 1 - Fig. 10), it is evident that current density does not have a significant influence on the thickness of oxide layer if concentration of sulphuric acid is lower as at factor level 0. With its higher concentration, the thickness of oxide layer increases by approximately $5 \text{ mm} \cdot 10^{-6}$ at current density of $3 \text{ A} \cdot \text{dm}^{-2}$.

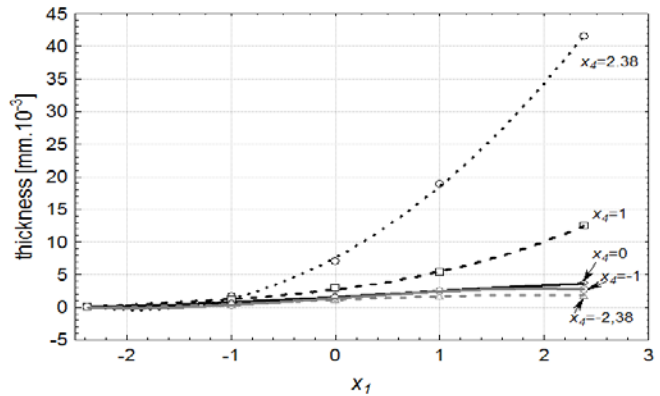


Fig. 6 Influence of factor x_1 and x_4 on AAO layer thickness for current density $3 \cdot \text{Adm}^{-2}$ and factor x_5 which is set to level -2.38

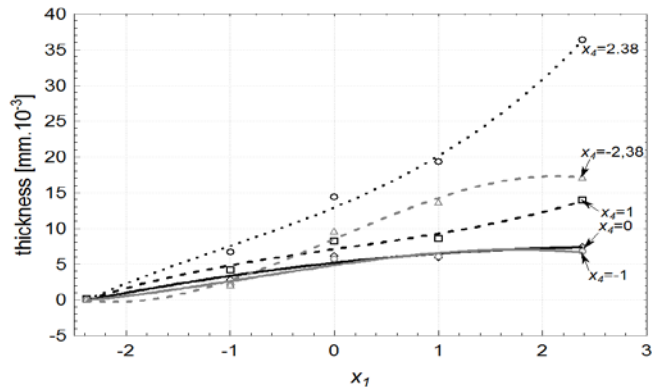


Fig. 7 Influence of factor x_1 and x_4 on AAO layer thickness at current density of $3 \cdot \text{Adm}^{-2}$ and factor x_5 which is set to level -1

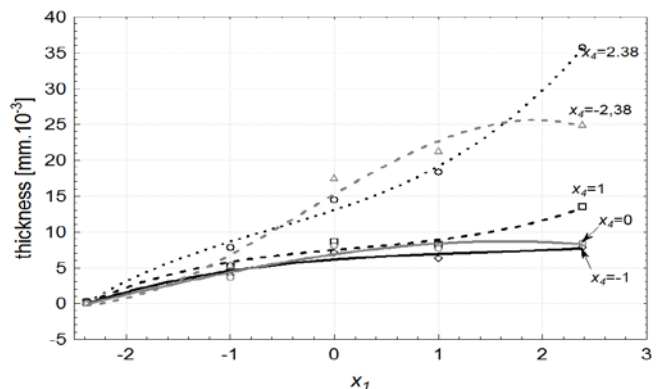


Fig. 8 Influence of factor x_1 and x_4 on AAO layer thickness at current density of $3 \cdot \text{Adm}^{-2}$ and factor x_5 which is set to level 0

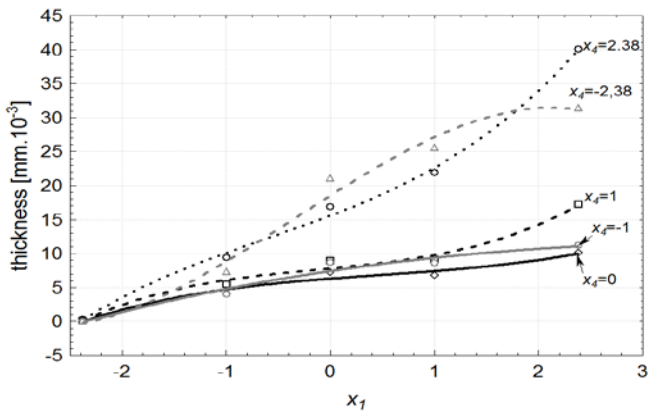


Fig. 9 Influence of factor x_1 and x_4 on AAO layer thickness at current density of $3 \cdot \text{Adm}^{-2}$ and factor x_5 which is set to level 1

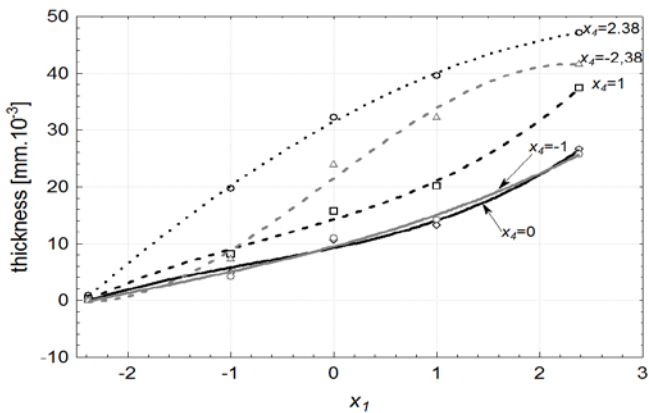


Fig. 10 Influence of factor x_1 and x_4 on AAO layer thickness at current density of $3 \cdot \text{Adm}^{-2}$ and factor x_5 which is set to level 2.38

Just as figures Fig. 1 through Fig. 10 examine the relationship between the amount of sulphuric acid in electrolyte, electrolyte temperature, oxidation time and thickness of oxide layer, figures Fig. 11 through Fig. 20 show the influence of amount of sulphuric acid in electrolyte, electrolyte temperature and voltage levels in relation to the thickness of the oxide layer. Results are shown for cases of current densities $1 \text{ A} \cdot \text{dm}^{-2}$ a $3 \text{ A} \cdot \text{dm}^{-2}$.

Fig. 11, Fig. 12, Fig. 13, Fig. 14 and Fig. 15 show the influence of factor x_1 (concentration of sulphuric acid in the electrolyte) and x_4 (temperature of the electrolyte) on the thickness of aluminium oxide created on sample surface. These graphs also demonstrate the influence of factor x_6 (the size of an applied voltage) on the oxide thickness. Level of factor x_6 is set to level "-2.38" (5.24 V) Fig. 11, "-1" (8 V) Fig. 12, "0" (10 V) Fig. 13 "1" (12 V) Fig. 14 and "2.38" (14.76 V) Fig. 15. Aluminium oxide layer was created at $1.00 \text{ A} \cdot \text{dm}^{-2}$ current density surface areas. Factors x_2 , x_3 and x_5 have zero factor level for all these graphs. Zero factor level for factor x_2 is $11 \text{ g} \cdot \text{l}^{-1}$, for factor x_3 is $8.5 \text{ g} \cdot \text{l}^{-1}$ and for factor x_5 is 30 min.

Connected voltage levels are proportional to the electric potential. Electric potential is proportional to electrodynamic forces. These electrodynamic forces determine the force with which are positively charged ions attracted to the negatively charged electrode (cathode) and the force with which are negatively charged ions attracted to the positively charged electrode (anode). If we increase voltage, electric potential on

anode will also increase. Higher electric potential on anode will attract higher number of oxygen anions. Thus, the surface of aluminium sample will contain higher amount of oxygen anions and more molecules of aluminium oxide will be created on the surface of the sample. Through this, the thickness of AAO layer increases. It is possible to see this process on figures Fig. 11 through Fig. 20— same for current densities of $1 \text{ A} \cdot \text{dm}^{-2}$ (Fig. 11 through Fig. 15) and $3 \text{ A} \cdot \text{dm}^{-2}$ (Fig. 16 through Fig. 20), where the thickness of oxide layer increases faster with the increase of voltage.

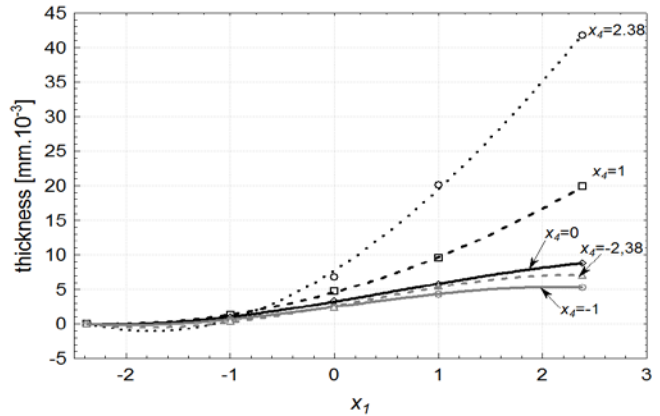


Fig. 11 Influence of factor x_1 and x_4 on AAO layer thickness at current density of $1 \cdot \text{Adm}^{-2}$ and factor x_6 which is set to level -2.38

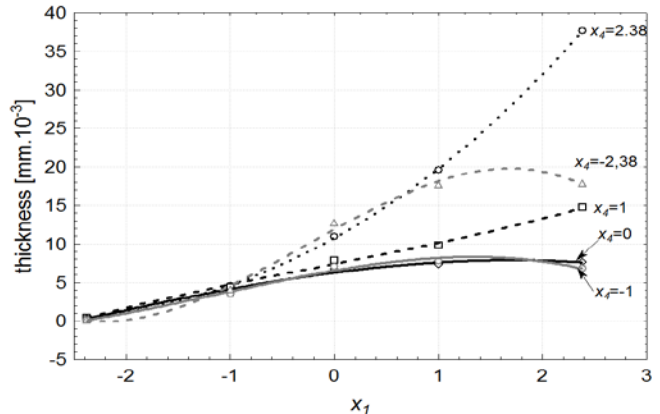


Fig. 12 Influence of factor x_1 and x_4 on AAO layer thickness at current density of $1 \cdot \text{Adm}^{-2}$ and factor x_6 which is set to level -1

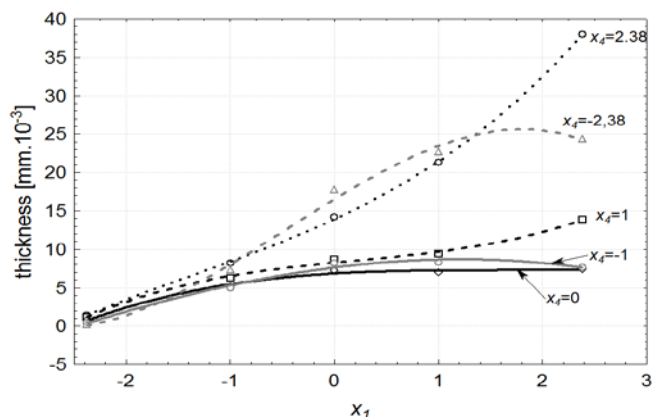


Fig. 13 Influence of factor x_1 and x_4 on AAO layer thickness at current density of $1 \cdot \text{Adm}^{-2}$ and factor x_6 which is set to level 0

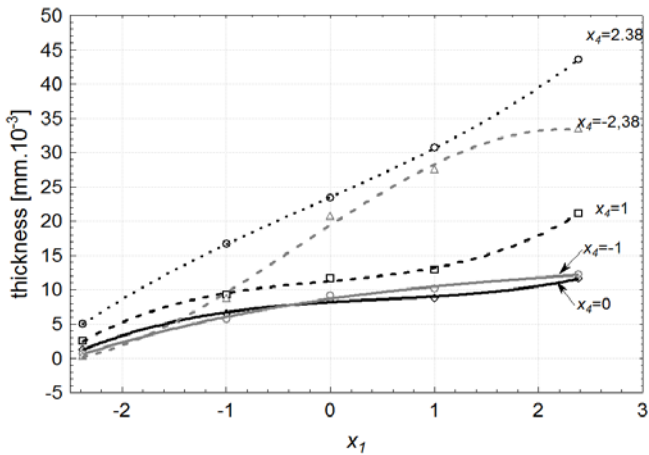


Fig. 14 Influence of factor x_1 and x_4 on AAO layer thickness at current density of $1 \cdot \text{Adm}^{-2}$ and factor x_6 which is set to level 1

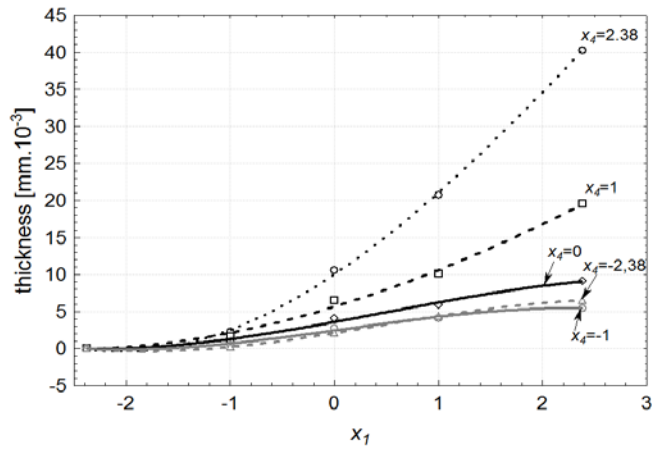


Fig. 16 Influence of factors x_1 and x_4 on AAO layer thickness at current density $3 \cdot \text{Adm}^{-2}$ and factor x_6 which is set on level -2.38

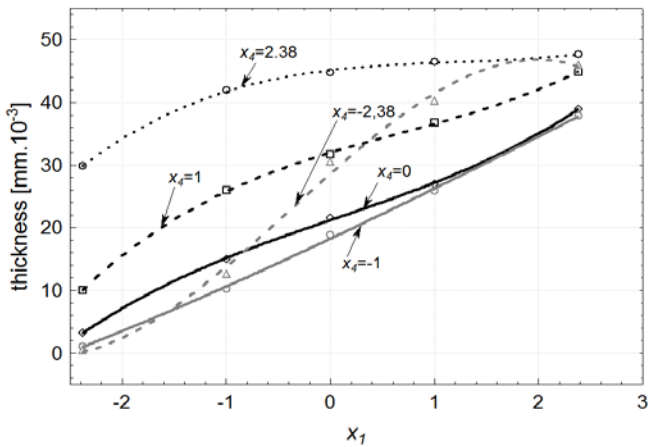


Fig. 15 Influence of factor x_1 and x_4 on AAO layer thickness at current density of $1 \cdot \text{Adm}^{-2}$ and factor x_6 which is set to level 2.38

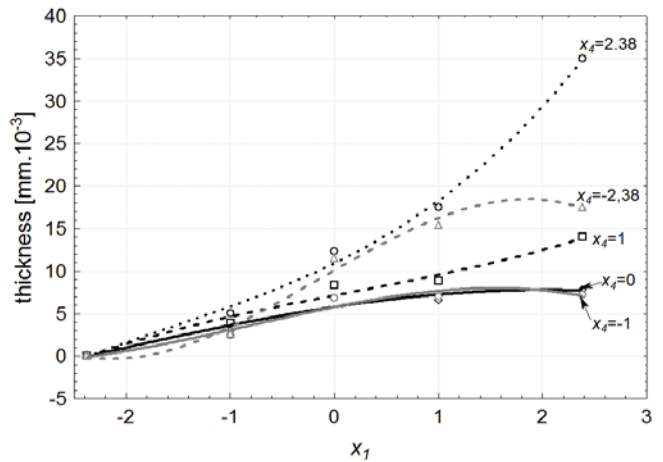


Fig. 17 Influence of factors x_1 and x_4 on AAO layer thickness at current density of $3 \cdot \text{Adm}^{-2}$ and factor x_6 which is set on level -1

Fig. 16, Fig. 17, Fig. 18, Fig. 19 and Fig. 20 show the influence of factors x_1 (concentration of sulphuric acid in the electrolyte) and x_4 (temperature of the electrolyte) on the thickness of aluminium oxide created on sample surface. These graphs also demonstrate the influence of the factor x_5 (anodizing time) on the oxide thickness. Level of factor x_5 is set to level "-2.38" (6.22 min) Fig. 16, "-1" (20 min) Fig. 17, "0" (30 min) Fig. 18 "1" (40 min) Fig. 19 and "2.38" (53.78 min) Fig. 20. Aluminium oxide layer was created at $1.00 \text{A} \cdot \text{dm}^{-2}$ current density surface areas. Factors x_2 , x_3 and x_6 have zero factor level for all these pictures. Zero factor level for factor x_2 is $11 \text{ g} \cdot \text{l}^{-1}$, for factor x_3 is $8.5 \text{ g} \cdot \text{l}^{-1}$ and for factor x_6 is 10 V . By comparing the effects of input factors x_1 (concentration of sulphuric acid in electrolyte), x_4 (electrolyte temperature) and x_6 (voltage level) at current density $1 \text{ A} \cdot \text{dm}^{-2}$ (Fig. 11 through Fig. 15) and at current density $3 \text{ A} \cdot \text{dm}^{-2}$ (Fig. 16 through Fig. 20) it is possible to surmise, that levels of surface current density have no influence on the resulting thickness of oxide layer. Differences in thickness of AAO layer are minimal – as is the case with input factors x_1 (concentration of sulphuric acid in electrolyte), x_4 (electrolyte temperature), x_5 (time of oxidation) for current density $1 \text{ A} \cdot \text{dm}^{-2}$ (Fig. 1 - Fig. 5) and at current density $3 \text{ A} \cdot \text{dm}^{-2}$ (Fig. 6 - Fig. 10).

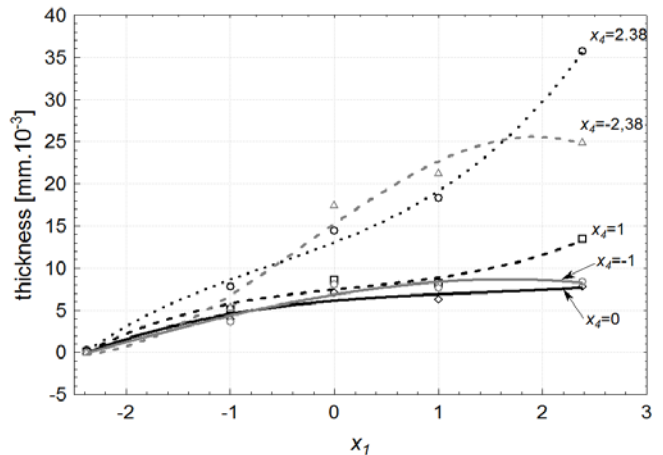


Fig. 18 Influence of factors x_1 and x_4 on AAO layer thickness at current density of $3 \cdot \text{Adm}^{-2}$ and factor x_6 which is set on level 0

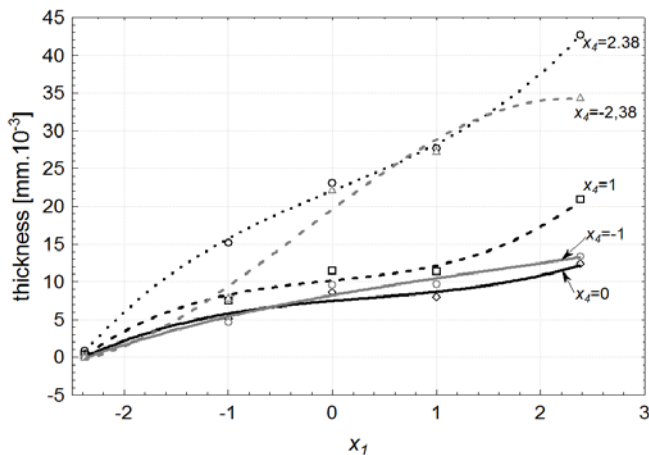


Fig. 19 Influence of factors x_1 and x_4 on AAO layer thickness at current density of $3 \cdot \text{Adm}^2$ and factor x_6 which is set on level 1

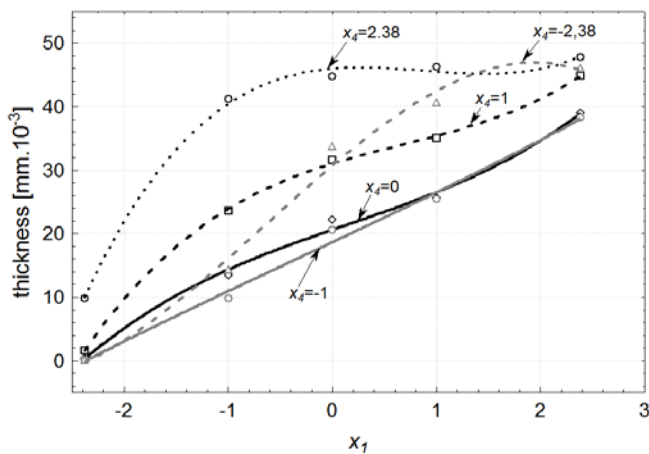


Fig. 20 Influence of factors x_1 and x_4 on AAO layer thickness at current density of $3 \cdot \text{Adm}^2$ and factor x_6 which is set on level 2.38

V. CONCLUSION

As shown by the evaluation process of experimental results presented above, the use of 3rd order neural unit based on the iterative Levenberg-Marquardt (LM) optimization algorithm provides a wide range of options to investigate influence of input factors on the final AAO layer thickness. By using of neural unit we can quickly and simply describe the behaviour of the monitored system. This neural unit allowed us to monitor the impact of input factors (concentration of sulphuric acid, electrolyte temperature, anodizing time and applied voltage) on the final thickness of the AAO layer at surface current density $1 \text{ A} \cdot \text{dm}^{-2}$ and $3 \text{ A} \cdot \text{dm}^{-2}$. Also by using the neural unit of 3rd order HONU it was possible to describe the influence of input factors on the thickness of final AAO layer with confidence interval of 93.45% at surface current density $1 \text{ A} \cdot \text{dm}^{-2}$, and with confidence interval of 95.60% of surface current density $3 \text{ A} \cdot \text{dm}^{-2}$.

ACKNOWLEDGMENT

The research work is supported by the Project of the Structural Funds of the EU, Operational Programme Research and Development, ITMS project code: 26220220103.

REFERENCES

- [1] J. Baumeister, J. Banhart, M. Weber, "Aluminium foams for transport industry", *Materials & Design*, Vol. 18, No. 4, 1997, pp. 217-220.
- [2] M. Gombár, J. Kmec, M. Badida, L. Sobotová, A. Vagaská, P. Michal, "The simulation of the temperature effects on the microhardness of anodic alumina oxide layers", *Metalurgija*, vol. 53, 2014, pp. 59-62.
- [3] M. Badida, M. Gombár, J. Kmec, L. Sobotová, A. Vagaská, P. Michal, P "Štúdium vplyvu chemického zloženia elektrolytu na mikrotrvdosť vrstvy vytvorenej anodickou oxidáciou hliníka", *Chemické Listy*, vol. 107, 2013, pp. 973-977.
- [4] P. Michal, M. Gombár, A. Vagaská, J. Piteľ, J. Kmec, "Experimental study and modeling of the zinc coating thickness", *Advanced Materials Research*, vol. 712-715, 2013, pp. 382-386.
- [5] I. Tsangaraki-Kaplanogloua, S. Theohari, Th. Dimogerontakis, N. Kallithrakas-Kontos, Yar-Ming Wang, Hong-Hsiang (Harry) Kuo, Sheila Kia, "Effect of alloy types on the electrolytic coloring process of aluminium", *Surface & Coatings Technology*, Vol. 200, No. 12-13, 2006, pp. 3969 – 3979.
- [6] Dj. Djozan, M. Amir-Zehni, "Anodizing of inner surface of long and small-bore aluminum tube", *Surface & Coatings Technology*, Vol. 173, No. 2-3, 2003, pp. 185-191.
- [7] M. Badida, M. Gombár, L. Sobotová, J. Kmec, A. Vagaská, P. Michal, "The influence of sodium chloride on the resulting AAO film thickness", *Advanced Materials Research*, Vol. 816-817, 2013, pp. 18-22.
- [8] M. Gombár, A. Vagaská, J. Kmec, P. Michal, "Microhardness of the coatings created by anodic oxidation of aluminium", *Applied Mechanics and Materials*, vol. 308, 2013, pp. 95-100.
- [9] I. Tsangaraki-Kaplanogloua, S. Theohari, Th. Dimogerontakis, N. Kallithrakas-Kontos, W. Yar-Ming, K. Hong-Hsiang, K. Sheila, "Effect of alloy types on the anodizing process of aluminium", *Surface & Coatings Technology*, Vol. 200, No. 8, 2006, pp. 2634 – 2641.
- [10] G. Patermarakis, "Development of a theory for the determination of the composition of the anodizing solution inside the pores during the growth of porous anodic Al_2O_3 films on aluminium by a transport phenomenon analysis", *Journal of Electroanalytical Chemistry*, Vol. 447, No. 1-2, 1998, pp. 25-41.
- [11] T. Aerts, I. DeGraeve, G. Nelissen, J. Deconinck, S. Kubacki, E. Dick, H. Terryn, "Experimental study and modelling of anodizing of aluminium in a wall-jetelectrode set-up in laminar and turbulent regime", *Corrosion Science*, Vol. 51, No. 7, 2009, pp. 1482-1489.
- [12] T. Aerts, I. DeGraeve, G. Nelissen, "Comparison between the influence of applied electrode and electrolyte temperatures on porous anodizing of aluminium", *Electrochimica Acta*, Vol. 55, No. 12, 2010, pp. 3957-3965.
- [13] E. Evin, J. Kmec, E. Fehová, "Optimizing of Electric Discharge Texturing Parameters of Rolls of the Rolling Mill of Steel Sheets", *Applied Mechanics and Materials*, vol. 420, 2013, pp. 78-84.
- [14] A. Vagaská, M. Gombár, J. Kmec P. Michal, "Statistical analysis of the factors effect on the zinc coating thickness", *Applied Mechanics and Materials*, vol.378, 2013, pp. 184-189.
- [15] R. Rodriguez, I. Bukovsky, N. Homma, "Potentials of quadratic neural unit for applications", *Journal of Software Science and Computational Intelligence (IJSSCI)*, Vol. 3, No.3, IGI Global, Publishing, Hershey PA, USA, 2011, pp. 1-12.
- [16] J. Piteľ, J. Mižák, "Computational intelligence and low cost sensors in biomass combustion process", *Proceedings of the 2013 IEEE Symposium Series on Computational Intelligence: 2013 IEEE Symposium on Computational Intelligence in Control and Automation (CICA)*. Singapore: IEEE, 2013, pp. 165-168.
- [17] I. Bukovsky, N. Homma, L. Smetana, R. Rodriguez, M. Mironovova, S. Vrana, "Quadratic neural unit is a good compromise between linear models and neural networks for industrial applications", *The 9th IEEE Inter. Conference on Cognitive Informatics ICCI 2010*, Beijing: Tsinghua University, 2010.
- [18] V. Vita, A. Vitas, G.E. Chatzarakis, "Design, implementation and evaluation of an optimal iterative learning control algorithm", *WSEAS Transactions on circuits and Systems*, Vol. 10, No. 2, 2011, pp. 39-48.
- [19] J. Mižáková, "The support of the applied mathematics by chosen programming languages", *7. Mathematical workshop*, Brno: VUT, 2008, pp. 1-4.

Microwave Pulse Generator

Krizan R., Drazan L.

Abstract—The article is aimed at analyzing and describing feasible effects of electromagnetic high-power weapons, their potentialities and ways of penetrating and affecting a part or the entire system. Furthermore, it deals with increasing efficiency of electromagnetic weapons and protection against their effects. The paper describes the device based on a dual microwave pulse generator that can be used for verifying and setting the standards suitable for measuring and mapping a high-frequency electromagnetic field at great power.

Keywords— microwave generator, EMP, high-power pulse, HIRF, controlled generator, pulse generator.

I. INTRODUCTION

ELECTROMAGNETIC pulse (EMP) is characterized as a very short pulse of approximately hundreds of nanoseconds with a high-level intensity of electromagnetic field. In other words, the principle lies in generating a high-energy pulse in a very short time interval. The need to accurately map and measure a high-frequency electromagnetic field at great power has arisen during the EMP research. For this reason a microwave pulse generator with variable parameters for verifying and setting parameters suitable for this type of measurement had to be assembled.

II. EFFECTS OF ELECTROMAGNETIC WEAPONS

Electromagnetic weapons have similar effects as electromagnetic fields in nonobservance of the principles of electromagnetic compatibility; thus they can be described by similar characteristics and procedures.

First, we are going to describe how an electromagnetic field can affect an arbitrary system, then how these systems can be distinguished in terms of their resistance, and how to design a system that would be resistible to this electromagnetic field.

Affecting a system by an electromagnetic weapon:

temporary faults— faults which the system can by itself evaluate, correct or replace;

reduced operation (efficiency) of the system – faults that have more disruptive effects on the system leading to its so-called “employment” in order to correct the failures about

which the operator is informed, but his intervention is not required;

putting a part of the system temporarily out of operation – requires the operator’s intervention (reset, restart);

permanent functional failure – the system cannot be reactivated after a simple intervention by the operator (reset, restart), more complex intervention from the operator is necessary (update);

permanent damage to the system – usually destructive; components, parts or blocks must be replaced.

Immunity Degrees.

Degrees of a system immunization (protection), or its parts, are often selected by a level of its financial demands, importance or safety:

unprotected – no protection is used, very low financial costs;

partly protected – a part of the system is protected, low financial costs;

protected – as a whole, the entire system is protected, very high financial costs.

Protection procedures:

protection applied on parts or the entire system;

designing hardware and software fault-tolerance;

monitoring electromagnetic energy;

system’s physical security;

overdesigning the system’s functions.

There are two ways how electromagnetic energy can penetrate into the system:

A. “*Front Door*“ – electromagnetic energy penetrates via the antenna system, the system’s input parts, etc. Based on the principle of functioning such receiving devices and sensors, it is obvious that power electromagnetic signals cannot be, in real conditions, prevented from penetrating into the device or system. It is only possible to limit their destructive effects.

“*Back Door*“ – is the case when interfering and destructive electromagnetic signals penetrate into the electronic device or system through cables, electric contacts, bus-bars, supply conductors, connectors, various openings, grids, gaps, etc. In contrast to the “front door” penetration, the interfering and destructive effects can be significantly reduced directly by their design in the stage of drafting the electronic device/system, or by additional modifications. The ways and methods of such reductions are now well-known and rest primarily in a perfect compact electric screening effect on both the electronic circuits and all contacts together with wires, and also in limiting the metallic inputs and outputs (replaced by

R.Krizan, University of Defence, Brno, Czech Republic (e-mail: rene.krizan@unob.cz)

L. Drazan, University of Defence, Brno, Czech Republic (e-mail: libor.drazan@unob.cz).

optical cables), placing the critical blocks in suitable locations inside buildings, etc.

A low-frequency weapon can develop a strong effect upon telephone lines, net cables and distribution of electric energy. In most cases, this cabling is long enough and differently twisted, so the relative orientation of electromagnetic field in the weapon is not an important factor, as the segment of the conductive system will nearly always find suitable orientation to the travelling electromagnetic wave. Manufacturers display different breakdown voltage values for some typical semiconductor devices, such as high-frequency bipolar transistors (amply used, for example, in communication equipment). Elements controlled by the GaAs pole are rated at approximately 10V. DRAM memories used in computers are rated at 7V, basic CMOS technology at 7-15V and, for instance, a processor supply voltage moves around 3.3V or 5V. Many modern circuits, in spite of being equipped with extra circuits for protecting each pin against electrostatic discharge, are often destroyed by constant or repeated high voltage effects.

Communication interfaces and supply lines must meet typical requirements for electrical safety; therefore, these components are usually protected by insulation transformers that are rated at approx. 2-3kV. Thus it is obvious that even such a low voltage as 50V has destructive effects on these components if the insulation transformer or screening fails. Many items of equipment (PC, consumer electronics, etc.) are known, even from our own experience, that were destroyed or necessitated a complicated technical intervention after being exposed to low-frequency high-voltage peak levels (e.g. near a place hit by lightning, etc.).

Electromagnetic weapons operating in the centimeter and millimeter-wave band have the capability of enlarging the “back door” structure by another possibility of penetrating into the equipment through vent holes, gaps between individual constructional parts, and unshielded places. In this band any gap behaves as a slot in a microwave cavity permitting the microwave electromagnetic energy to enter this equipment. Thanks to its properties, the penetrating microwave energy generates standing waves inside this space. Individual components found in the places of a high-value electromagnetic field will be destroyed by the effects of this field. From these facts we can obviously conclude that microwave weapons are more used because of their enlarged structures and potentiality of penetrating through barriers at low frequencies, in contrast to low frequency weapons.

As inferred from previous paragraphs, an unambiguous and accurate specification when and what will be destroyed is impossible, since geometric arrangements, cable systems and variety of components are always different and depend on even the smallest constructional details.

What can be generalized are only structures across the cable systems that are determined by known destructive levels, then their usage for finding the demanded intensity of electromagnetic field for the specific construction, and potentialities of the electromagnetic weapon.



Fig. 1. Impact of high-power electromagnetic pulse after penetrating through the “back door” – printed circuit side.

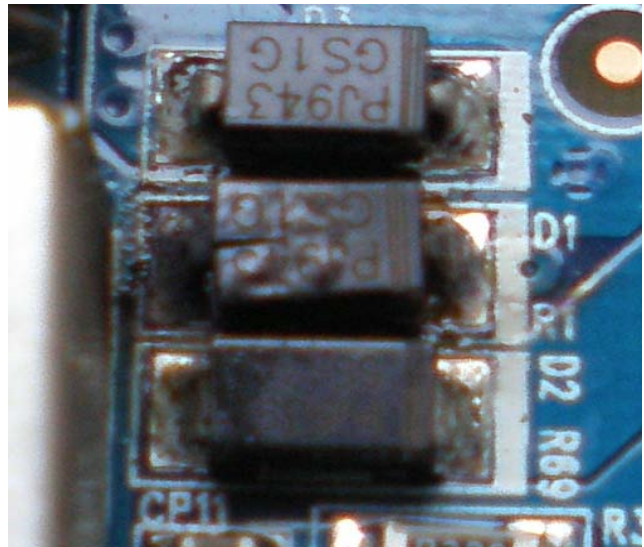


Fig. 2. Impact of high-power electromagnetic pulse after penetrating through the “back door” – side of components.

III. ENHANCING EFFICIENCY OF ELECTROMAGNETIC BOMBS

To enhance efficiency of electromagnetic bombs, the coupled power for penetrating into the system must be maximized.

First, it is necessary to maximize peak power of the electromagnetic weapon and duration of the pulse, and then maximally increase the efficiency of binding into the system, especially using every binding opportunity that is available in the weapon's frequency band.

In order to achieve a good binding energy into the surrounding, low-frequency weapons will use “a big” antenna. These weapons mostly use, for the purpose of adapting a low impedance of the output generator to much higher antenna impedance, a high-power coupling transformer. As these are broadband weapons and most of radiated power is found in the band up to 1 MHz, use of a compact antenna is impossible here.

Another option rests in transporting an electromagnetic bomb to a close vicinity of the target and relying on the nearby field generated by the output winding which, in comparison with an operating wavelength, takes the role of a very “small” loop antenna. In this case, binding efficiency of the electromagnetic weapon is very low; however, this drawback can be alleviated by guiding the weapon to a vicinity of the target with an accuracy of few meters.

Microwave weapons have larger binding capabilities and, in contrast to their size, generate signals of a “small” wavelength that can be easily aimed at systems using compact antennas. If an area is covered by a radiation characteristic, the weapon’s efficiency can be increased by activating a frequency sweep, alias generator warbling, which improves, comparing with a weapon working on one frequency, its binding efficiency. Bindings are enabled through various openings, and resonances via the weapon’s frequency band. This method is based on using a high quantity of bindings into the system. Furthermore, in order to improve bindings of the emitted electromagnetic field, polarization of the weapon can be taken into consideration. For example linear polarization to binding gaps, if properly selected, results in 50% binding efficiency, as compared to a circularly polarized wave that uses more binding gaps and develops resonance. For its complicated design, practical limitations of a circularly polarized antenna can cover the entire bandwidth in maintaining a high efficiency. A narrowing helical antenna may be an example of a suitable type.

Detonation distance is another aspect having an influence on efficiency of an electromagnetic bomb. It is based on the proper rate of the affected area and degree of electromagnetic field intensity in this area.

As concluded from the facts stated above, microwave weapons appear to be more suitable for enhancing efficiency of electromagnetic bombs for the reason of aiming energy of larger binding capabilities and more efficient transfer of energy between the generator and environment.

IV. PROTECTION AGAINST ELECTROMAGNETIC WEAPONS

The most effective protection against electromagnetic weapons rests in preventing electromagnetic energy from being emitted (e.g. destroying or disabling them). As this is not always possible, the systems call for an efficient protection against electromagnetic weapons, which is implemented in a similar manner as protection against electromagnetic incompatibility. The most effective method is the so-called Faraday cage, the principle of which lies in placing the system into an electrically conductive space which prevents electromagnetic field from penetrating into the protected space. A problem associated with these devices can be seen in the fact that they must communicate with the surroundings and be supplied from an external network. These factors may contribute to creating passage gaps in this area that an electromagnetic weapon may use as bindings, and thus damage the system. There are many protective measures to safeguard supplying and communication conductors. In choosing these devices, it is

necessary to select thoroughly their parameters, so as to suppress or prevent undesired signals from entering and, at the same time, be permeable enough for the signal that we need. Furthermore, it is important to see the process of consolidating at the system level, since any disruption of a single element by an electromagnetic weapon can result in malfunctions or even disability of the entire system. Similarly, this problem may appear in the process of modernizing equipment when a new device meets all the protection criteria, but the old parts do not, or are insufficient. Therefore, such an intervention, if carried out in the phase of implementing a system protection, necessitates higher financial costs, so consolidation in the stage of drafting is much simpler solution than interventions into the already existing system.

V. MICROWAVE GENERATOR

To assemble the generators, two channels (S and X) have been selected. Within these bands we can find the channel S generator which is amply used as a source of microwave energy in microwave ovens. The channel X generator represents the other range that is used, for example, as a source for ship radars. Such a configuration has been chosen on purpose, since its acquisition is easy and cheap, but on the other hand these easily accessible parts can fall into hands of terrorist groups. In both channels of the generator, the pulse width and pulse duty factor can be adjusted as shown in Table I and II.

TABLE I. CHANNEL S ELECTRICAL CHARACTERISTICS

Channel	S
Frequency	2.45 GHz
Pulse width	100 μs to CW
Pulse duty factor	0.01 to 1
Peak power of pulses	1 kW
Waveguide	R32

TABLE II. CHANNEL X ELECTRICAL CHARACTERISTICS

Channel	X
Frequency	9.4 GHz
Pulse width	0.5 μs to 2 μs
Pulse duty factor	0.001
Peak power of pulses	40 kW
Waveguide	R100

Each channel is ended with a horn antenna, which is also found on the side of checking reception, but here equipped with a directional coupler that enables connecting a power meter, see Fig 3.

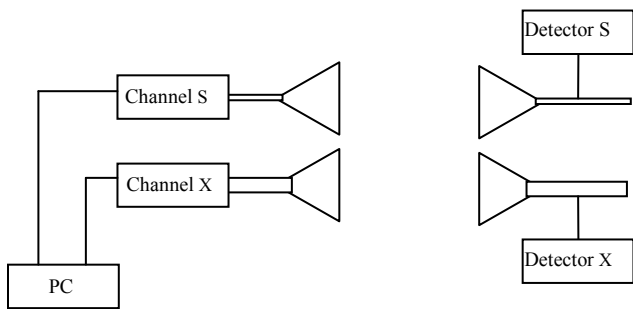


Fig. 3. Diagram of a high-power two-channel microwave pulse generator

The generator is controlled via standard USB interface by a computer that can be placed beyond the reach of electromagnetic field. The generator is supplied with AC 230V from the electric network.



Fig. 4. The generator of the band S

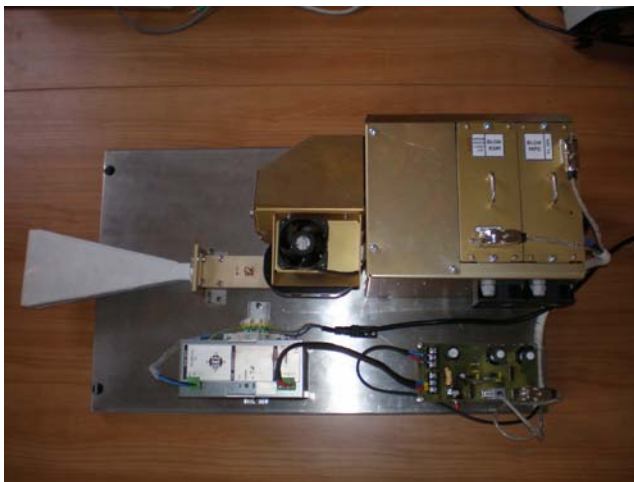


Fig. 5. The generator of the band X

VI. TESTS

After solving the design problems, the first experiments on the generator could be conducted. The tests focused on the functionality of the generator. One of the tests is shown in Fig. 6. The effect HF energy transmitted from the generator to the tube light is clearly visible. The tube light stayed on the stand without any physical connections. Fig. 6 also shows the focusing effect of the directivity horn antenna.



Fig. 6. Functionality test.

In another part of the tests was carried out measuring signal, as shown in next Fig.

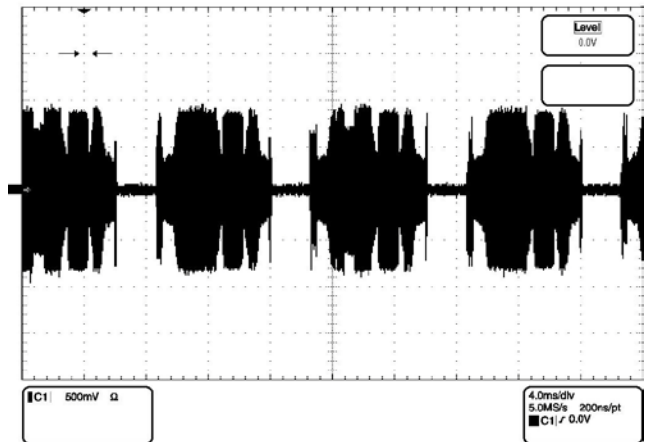


Fig. 7. Functionality test S band.

Fig. 7 shows that the generator does not operate continuously and to vary the signal amplitude and frequency. Frequency change is clearly seen in the following Fig. 8 which shows the frequency range.

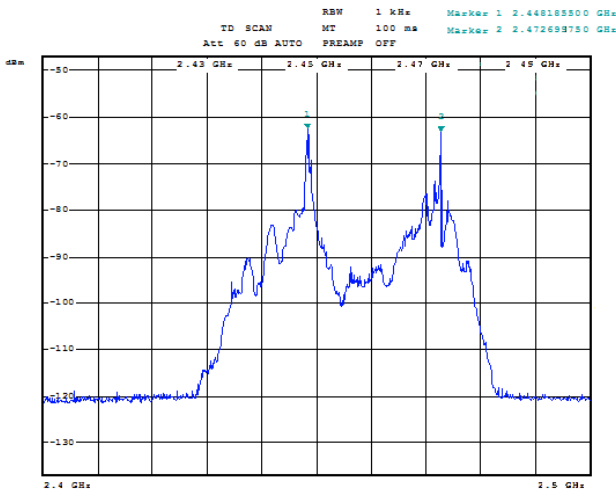


Fig. 8. Frequency domain S band.

The generator does not operate continuously and frequency is two peaks because the voltage rectifier is not sufficiently smooth. Fig. 9 shows the frequency envelope signal X channel generator.

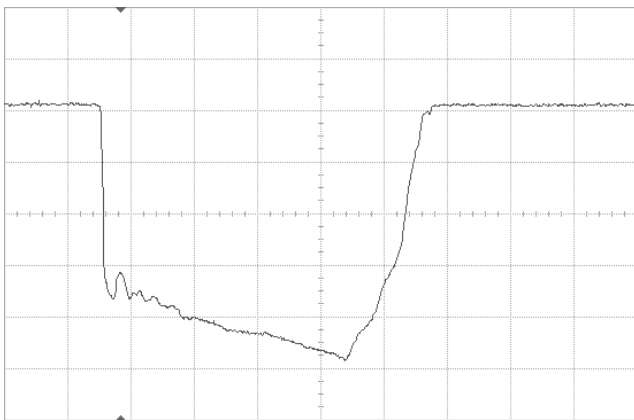


Fig. 9. The signal range X band

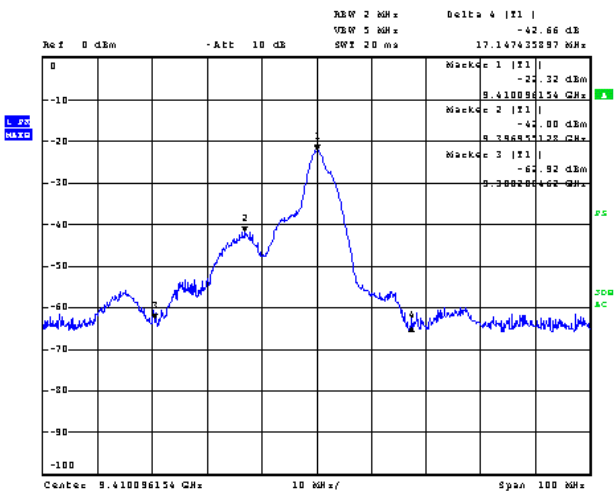


Fig. 10. Frequency domain X band

Fig. 10 shows the spectrum of the signal X band generator.

VII. DESIGNING PROBLEMS

In the process of its designing, it was necessary to solve not only controlling and regulating the generator with the PC that was placed outside the measuring point, but also protection of individual components while being retroactively affected by the generated high-frequency energy.

VIII. EXPECTED RESULTS

This generator will be used for developing, verifying and setting standards that are appropriate for measuring and mapping high-frequency electromagnetic field of great power, such as calorimeter. It can also be used as a source of high-frequency electromagnetic field of great power imitating interferences in the channels S and X. At the same time it may be applied for running EMP resistance and EMC (electromagnetic compatibility) tests.

REFERENCES

- [1] Palisek, L.: *Zbrane s rizenou energií*, VTÚPV Vyškov, 2002.
- [2] Drazan, L.: *Vybrane problemy konstrukce elektromagnetických zbrani pracujících v pasmu radiových vln a mikrovln*, VA Brno, 2007
- [3] Drazan, L., Vrana, R.: *Axial Vircator for Electronic Warfare Applications*, (RADIOENGINEERING, VOL. 18, NO. 4, DECEMBER 2009), VA Brno, 2009
- [4] Krogager, E., et al. Lecture Series SCI-249 : Phenomenology and Basic Theory of Electromagnetic Fields. In *Radio Frequency Directed Energy Weapons*, Liptovsky Mikulas, Academy of the Armed Forces, Slovakia, 2012
- [5] Roemer, B., et al. Lecture Series SCI-249 : Electromagnetic Field Generation (Sources). In *Radio Frequency Directed Energy Weapons*, Liptovsky Mikulas, Academy of the Armed Forces, Slovakia, 2012
- [6] Roemer, B., et al. Lecture Series SCI-249 : Attack Detection & Modeling and Simulation of EM Field Interaction with Targets. In *Radio Frequency Directed Energy Weapons*, Liptovsky Mikulas, Academy of the Armed Forces, Slovakia, 2012
- [7] Chevalier, B., et al. Lecture Series SCI-249 : Electromagnetic Pulses. In *Radio Frequency Directed Energy Weapons*, Liptovsky Mikulas, Academy of the Armed Forces, Slovakia, 2012
- [8] Chevalier, B., et al. Lecture Series SCI-249 : Methodology and Test Facilities. In *Radio Frequency Directed Energy Weapons*, Liptovsky Mikulas, Academy of the Armed Forces, Slovakia, 2012
- [9] Arnesen, O.H., et al. Lecture Series SCI-249 : Protection Against EM Threats. In *Radio Frequency Directed Energy Weapons*, Liptovsky Mikulas, Academy of the Armed Forces, Slovakia, 2012
- [10] Petekin, F., et al. Lecture Series SCI-249 : High Power Microwave Applications. In *Radio Frequency Directed Energy Weapons*, Liptovsky Mikulas, Academy of the Armed Forces, Slovakia, 2012
- [11] Petekin, F., et al. Lecture Series SCI-249 : RF DEW Scenarios and Threat Analysis. In *Radio Frequency Directed Energy Weapons*, Liptovsky Mikulas, Academy of the Armed Forces, Slovakia, 2012

Synchronization Error Detection of Data Transmission Errors in Asynchronous Channels

Olga Fedorechko, Oleksandr P. Markovskiy, Nikos Doukas, Nikos Bardis

Abstract—In this paper a method for detecting single and multiple synchronization errors that occur in asynchronous data channels is presented. The method is based on the weighted checksum controlling changes in the lengths of sequences of identical bits. In this paper the mathematical foundations of the method and a procedure for the error detection are presented. The paper additionally analyzes the theoretical and experimental evaluation of the effectiveness of the proposed method.

Keywords—Synchronization error detection, weighted checksum.

I. INTRODUCTION

THE evolution of transmission technologies at all levels of the computer data processing hardware plays an important role in the development of modern information technology. The largest proportion of such data transmission, currently takes place over sequential channels.

Most serial channels are characterized by the frequency utilized for asynchronous data transmission. This is due to the limited number of interface lines, as well as due to the tendency to minimize interface line changes. More specifically, for the asynchronous encoding and transmission of data, serial interfaces are used such as the Universal Serial Bus (USB) and FireWire. The USB protocol employs the Non Return to Zero Invert (NRZI) encoding scheme (bit stuffing).

The technological evolvement of the serial data transmission is interconnected with the constant increase of the transmission rates. For example, a typical SATA interface has during the last decade increased its capacity by five times, while a USB 3.0 connection has a transmission speed increased by ten times compared to the previous standard and reaching 5 Gb/s.

Increases in transmission rates inevitably lead to increases in error rate values, since data transmission is one of the least reliable subsystems of modern computer hardware. The reason for this is that a large number of complex physical processes are simultaneously happening in a means of data transfer and lead to distortions and damage of the transmitted information. In general, the larger the transmission rate is, the more are the

physical processes and phenomena that appear and may seriously affect the transmission process.

Apart from the above considerations, during the operation of any physical means of data transfer, noise interference that will be added to the transmitted data and distort it are inevitable. These noises are usually of different intensity, random and their structure resembles that of the information signals, thus making them difficult to detect [1]. Therefore, the physical processes imply that the satisfaction of the need for larger transmission rates needs to be balanced by the design of innovative methods for the detection and correction of errors that enable the safe and reliable information transmission at high transfer rates [4], [5].

The problem of guaranteeing information reliability in control computer systems is even more critical. In such systems, data transfer errors may have significant negative consequences. Hence the exercise of achieving increased efficiency in timing error detection and correction in the context of asynchronous digital communication lines, is currently significant for the field of development of information technology.

II. ANALYSIS OF EXISTING TECHNIQUES FOR THE DETECTION AND CORRECTION OF TIMING ERRORS

Information transmission is one of the fundamental processes during the operation of a computer system. This process traverses individual units of the computer system and reaches remote peripheral devices or even remote systems. For the transmission of data at the physical level, a series of encoding schemes have been developed such as Non Return to Zero (NRZ), Alternate Mark Inversion (AMI), Manchester encoding etc. A drawback of most methods is the lack of self-synchronization, i.e. a tendency for suffering from timing errors [1].

The appearance of these errors is due to the fact that the timing period τ_s , at the transmitter is different by a random value δ from the corresponding timing period τ_R , appearing at the receiver, so that:

$$\tau_R = \tau_s + \delta. \quad (1)$$

During the transmission of a series of q unit ("1") bits that is timed at the transmitter and the receiver, the timing difference is $q \cdot \delta$. If $q \cdot \delta$ is proportional to τ_s , there exists a probability that the transmitted sequence of q unit bits is perceived by the receiver as a series of $q+1$ or $q-1$ unit bits. It may be shown that the probability for this type of error that is caused from a

Olga Fedorechko and Oleksandr P. Markovskiy are with Department of Computer Engineering, National Technical University of Ukraine, (Polytechnic Inst. of Kiev), Peremohy pr., Kiev 252056, KPI 2003, Ukraine. (markovskyy@i.ua)

Nikos Doukas and Nikos Bardis are with the Informatics Lab, Department of Military Sciences, Faculty of Mathematics and Engineering Science, Hellenic Army Academy, Vari - 16673, Greece. (bardis@ieee.org, nikolaos@doukas.net.gr)

timing violation increases with the length of consecutive unit values in the transmitted packet [1].

In order to reduce the timing error probability in the USB protocol, a bit stuffing mechanism is used. This mechanism consists of a process of inserting a zero after each series of six consecutive ones. Utilization of this mechanism complicates the transmission process significantly and leads to the necessity of transmitting an important number of additional binary digits. It should be noted [1] that bit stuffing may increase the number of transmitted bits by as much as 17%.

From the above considerations it may be deduced that the case of the appearance of errors that are due to timing violations at the receiver during the transmission of a series of ones, is equivalent to the slipping of the sequence of bits. An interference of this sort for a sequence of bits is significantly different than the usual error appearance model that concern the distortion of individual bits or groups of bits, that do not affect the remaining bit sequence.

Consequently, this type of simple distortion during the transmission of information is oriented towards the use of traditional error detection principles such as the Cyclic Redundancy Check (CRC) and the Check Sum (CS). More specifically, it has been shown that the error control in USB transfer using CRC [2] enables the detection of one or two isolated distorted bits. Additionally, the CRC guarantees the detection of a burst of errors, whose number does not exceed the order of the polynomial that formulates the CRC. In the context of USB, for the control of the data transmission process, the use of the CRC polynomial $x^{16} + x^{15} + x^2 + 1$ has already been studied. For the marker point check in the case of USB, a smaller order CRC polynomial has been studied: $x^5 + x^2 + 1$.

In the case of the appearance of a unified timing error, there may in reality appear a change the values of $m-r$ bits of the packet, where r the number of inserted or deleted bits at the traces of the timing errors. From this it may be deduced that the use of the CRC does not guarantee the detection of even one of the errors that are due to the timing violation.

For example, assume a USB connection that transmits the hexadecimal code represented as 4003. The code contains two series of unit values, one of which contains one unit and the other one containing two units. At the transmitter, the result of division of the CRC polynomial $x^{16} + x^{15} + x^2 + 1$, of the code 40030000 is the code 7FF8. Consequently the code transmitted to the receiver is 40037FF8. Assuming that as a result of the timing errors, another unit has been added to the data, the code arriving at the receiver may be 80077FF8. The remainder of the division with the polynomial corresponding to the CRC is zero. This implies that the synchronization error caused upon the data has not been detected by the CRC.

It follows that the use of traditional error control and correction techniques is ineffective in the case of errors in the bit sequence that have been caused by timing violations. The purpose of this research is to increase the effectiveness of the detection and the correction of timing errors that arise during

the transmission of digital data in a serial asynchronous communication channel.

III. METHOD FOR DETECTING MULTIPLE TIMING ERRORS

In order to guarantee the detection of errors caused by the distortion of the timing between the transmitter and the receiver [4], [5], a method is proposed whose essence is the control of the unity bit sequence length whose transmission is not synchronized. Assume that the information consists of a packet of m bits, $B = \{b_1, b_2, \dots, b_m\}$, $b_l \in \{0, 1\}$, $\forall l = 1, \dots, m$. In the packet it is proposed that a sequence of values is contained, whose transmission is also asynchronous. Without loss of generality, it may be assumed that a series of ones is transmitted. This case corresponds to the USB mode of operation. The symbol E_e^k is defined as the sequence of e units that may correspond with an order k in the control packet.

This implies that until the E_e^k sequence the transmitted packet consists of an order $k-1$ sequence of units of the same length e . Similarly, $E_{>e}^k$ signifies the k^{th} sequence in the controlled packet of the following order, the length of which exceeds e . Assuming that the k^{th} sequence contains $L_{ke} > e$ units and that the total number of sequences of the subsequent order that contain more than e units is K_e , then taking into consideration the definition as it has already been stated, the total number of units in the transmitted packet may be presented in the form:

$$\sum_{i=1}^m b_i = \sum_{k=1}^{K_0} L_{k0} \cdot$$

In order to guarantee the detection of errors that are caused by the violation of the timing during the transmission of a series of ones, a method is proposed that focuses in changes in the lengths of the sequences, since a timing violation may cause the length of the sequences of one to be increased or reduced at the receiver, compared to the one that was transmitted. The method involves the control of the changes in the length of the sequences for which there exists an increased risk of synchronization violation. In reality, the sequences contained in this class are the sequences $E_{>u}$, whose lengths exceed a predefined threshold u . For example, in the case of USB it is advisable that sequence length changes of sequences that contain no more than four (4) ones.

The control code V is proposed in order to calculate a weighted checksum. For this purpose, each one of the k units of the $E_{>u}^k$ sequence that is controlled, is assigned a weight W_k , that uniquely corresponds to the symbol k in the sequence $E_{>u}^k$ in the packet that is transmitted.

During the transmission to the receiver of the packet, the parity bit is calculated for every k sequence of length L_k . The code V that represents the weighted checksum is calculated at the receiver and the transmitter as the XOR sum of the parity bits of the length of the sequence that is being controlled and as the subsequent XOR of the produced parity bit of the length of the sequence with the corresponding weighted sum:

$$V = \bigoplus_{k=1}^{K_u} (L_{ku} \text{ mod } 2) \parallel \bigoplus_{k=1}^{K_u} W_k \cdot (L_{ku} \text{ mod } 2). \quad (2)$$

If the values calculated at the sender and the receiver using expression (2) are symbolized as V_s and V_R , then the error control code is calculated as $\Delta = V_s \oplus V_R$. If $\Delta=0$, then it is considered that errors that alter the length of sequences of ones do not exist.

The selection of weighting coefficients W_k is performed based on the given multiplicity for guaranteed detection of errors due to timing violations. Due to the first factor in expression (2) the detection of all timing violation errors of odd multiplicity is guaranteed. For $W_k=k$, apart from errors of odd multiplicity, all double errors are also guaranteed to be detected. Indeed if the length of odd multiplicity changes, for example for the q^{th} and the d^{th} sequence, i.e. $E_{>u}^q$ and $E_{>u}^d$, from the sets of units of the control packet $q, d \in \{1, \dots, K_u\}$, then the difference between the codes of the sender and the receiver will be equal to $\Delta = W_q \oplus W_d$. As $W_q \neq W_d$ which is in turn due to the fact that $d \neq q$, then $\Delta \neq 0$ and this implies that all double errors are guaranteed to be detected.

In order to detect errors that are caused by timing violations and are of even multiplicity, weighting factors that represent partially orthogonal codes may be used [3]. With reference to the K factors of the set Ω of the partially orthogonal codes of class h , is the set $\Omega = \{W_1, W_2, \dots, W_K\}$, consisting of K codes such that for the XOR sum of any subset \mathcal{Q} , containing no more than h such codes that are non – zero, it is true:

$$\forall \mathcal{Q} = \{X_1, X_2, \dots, X_{q_s}\} \subset \Omega, q_s \leq h: \quad (3)$$

$$X_1 \oplus X_2 \oplus \dots \oplus X_{q_s} \neq 0.$$

In reality this means that any subset $\mathcal{Q} \subset \Omega$, $|\mathcal{Q}| \leq h$, is an orthogonal base in an h -dimensional space. In Table 1, the values of Ω are presented for $K=64, h=4$, whose usage enables the guaranteed detection of errors with even multiplicity that does not exceed 4. In Table 2, the values of Ω are presented for $K=64, h=6$, whose usage enables the guaranteed detection of errors with even multiplicity that does not exceed 6.

The analysis of the bits referred to in Tables 1 and 2 shows that the numbers with length q bits are partially orthogonal codes that are used for the guaranteed detection of errors of multiplicity h (h even) depends approximately logarithmically from the length m of the control packet [3], i.e. the dependence of the bits q_w of the weighting coefficient on the number K_u of the sequence of ones may be approximately expressed as:

$$q_w \approx a_h \cdot \log_2 K_u \quad (4)$$

k	W _k						
1	0001	17	00F7	33	0458	49	0CD4
2	0002	18	0100	34	0491	50	0D9B
3	0004	19	0117	35	0535	51	0DE5
4	0009	20	0129	36	0541	52	0EB3
5	000F	21	01C7	37	0654	53	1000
6	0010	22	0200	38	074A	54	101D
7	0020	23	0219	39	0800	55	1027
8	0033	24	022D	40	081C	56	104E
9	0040	25	0252	41	0825	57	1153
10	0055	26	0283	42	0889	58	116B
11	006A	27	0323	43	0944	59	1175
12	0080	28	035F	44	0998	60	1191
13	0096	29	03E6	45	0A3A	61	1290
14	00AB	30	0400	46	0AF0	62	1487
15	00BD	31	041B	47	0B39	63	1664
16	00ED	32	042E	48	0C37	64	16AC

Table 1: Weighting factors for guaranteed detection of errors with even multiplicity that does not exceed 4.

Table 2: Weighting factors for guaranteed detection of errors with even multiplicity that does not exceed 6

k	W _k						
1	00001	17	00800	33	0A247	49	44436
2	00002	18	009D6	34	0D198	50	4A1F4
3	00004	19	00AE3	35	10000	51	575C0
4	00008	20	00B3A	36	110DC	52	59839
5	00010	21	00CF8	37	120AD	53	708AB
6	00020	22	00D1D	38	15291	54	7B22D
7	00040	23	00E4E	39	1C2BF	55	80000
8	0007F	24	00FA4	40	1E169	56	8116C
9	00080	25	01000	41	20000	57	8A30C
10	00100	26	02000	42	210E6	58	9372D
11	00200	27	03097	43	261BF	59	A2191
12	003F8	28	04000	44	29303	60	A52BE
13	00400	29	050AD	45	2E75C	61	B197F
14	005B3	30	060CB	46	3D605	62	BFD5B
15	006D5	31	08000	47	40000	63	C2DEA
16	00769	32	090CB	48	410F0	64	CDB2C

The weighting factors in Tables 1 & 2 are presented in hexadecimal form. The theoretical and experimental studies that have been carried out show that the actual arithmetic values for coefficients α_4 and α_6 do not remain constant and tend to decrease as the number K_u of the sequence of units of the data control packet increases. However the length of the packet remains restricted in reality, therefore the

approximations that for $h=4$ the coefficient becomes $a_4 \approx 2.3$, for $h=6$ the coefficient becomes $a_6 \approx 3.65$ and for $h=8$ the coefficient is $a_8 \approx 7.1$, are sensible and safe.

A fundamental aspect of the evaluation of the effectiveness of the proposed error control method, for errors that dominate serial interfaces of information systems with asynchronous data encoding, is concerned with the calculation of the number of control bits.

It is apparent that the number s of the control bits is determined by the length of the weighting factors W which in turn depend on the number K_u of the sequences, whose transmission is not synchronized and are controlled by the proposed method. It is hence important to determine the dependence of the number K_u of the controlled sequences on the minimum length $u+1$ and on the length m of the packet being transmitted.

Assuming that the appearance of a one – symbol and a zero – symbol in the sequence being controlled is equiprobable and independent of the remaining bits, then the probability that a sequence consists of a single “one” is determined by the fact that the next symbol must be a zero and is 0.5. The probability P_2 that the sequence consists of two “ones” is determined by the fact that the second bit needs to be “one” and the third “zero” and is equal to 0.5^2 . Similarly, it may be shown that the probability of a sequence having a length of e “ones” is calculated as 0.5^e . The average length of a sequence of “ones” is defined as L_a and this may be calculated as the sum of the following series:

$$L_a = \sum_{i=1}^m \frac{i}{2^i} \approx \sum_{i=1}^{\infty} \frac{i}{2^i} = \frac{1}{(1-0.5)} = 2 \quad (5)$$

As in the assumptions for the above calculation of the average length of sequences of “ones” in the transmitted packet are balanced for “zeroes” as well, the probability distribution of the length of sequences of “zeroes” is similar to the above one for sequences of ones. Hence the mean number of sequences of “zeroes” is approximately equal to the mean of the sequences of “ones”. From expression (5) it follows that the mean length of the sequence is 2 and that respectively, the mean number of transmitted packets is $m/2$, half out of which (i.e. $m/4$) are sequences of “ones”. From the above analysis it may be deduced that half of the sequences of “ones” contain just one unit, $1/4$ contain two units etc. Hence the mean number v_e of sequences that contain e “ones” in the m bit packet are determined by the formula:

$$v_e = \frac{m}{2^{e+2}} \quad (6)$$

It follows immediately that:

$$\sum_{e=1}^m v_e \cdot e \approx \sum_{e=1}^{\infty} v_e \cdot e = \frac{m}{4} \cdot \sum_{e=1}^{\infty} \frac{e}{2^e} = \frac{m}{2} \quad (7)$$

The mean number of the sequences K_e that contain more than e “ones” are calculated as the sum:

$$K_e = \sum_{i=e+1}^m v_i \approx \sum_{i=e+1}^{\infty} v_i = \frac{m}{2^{e+2}} \cdot \sum_{l=1}^{\infty} \frac{1}{2^l} = \frac{m}{2^{e+2}} \quad (8)$$

The number s of control bits that are used depends on two factors: the length m of the control packet and the multiplicity of the errors that should be detected. Hence for the detection of all errors with odd multiplicity and with double multiplicity, the length of the weighting factor is equal to $\log_2 K_e$. More specifically, for serial USB interfaces the length of the packet has been determined at 1024 bytes ($m=8192$) [1]. With the use of bit stuffing, it is necessary that changes in sequence s with lengths 1 to 6 are controlled. The number K of such sequences is defined as the sum:

$$K = \sum_{i=1}^6 v_i = K_0 - K_7 = \frac{m}{4} - \frac{m}{512} \approx \frac{m}{4}$$

The length of the weighting factor for the guaranteed detection of double errors is calculated as $\log_2 m - 2 = \log_2 8192 - 2 = 11$ bits. Taking into account the parity bit of the total length of the transmitted packet control code as well, the total number of control bits becomes 12. The characteristics of the number of control bits and the capability for guaranteed detection of errors via the proposed method, to be used in current USB technology for CRC, are presented in Table 3.

Table 3. Comparative characteristics of efficient errors detection caused by the insertion of the sync USB.

Method of errors detection	Quantity of guaranteed error detection caused by the faulted of synchronize	Quantity control bits
Proposed error control method based on the length change of asynchronous serial bits	All odd errors multiplicity	1
	Odd errors multiplicity and double errors	12
	Odd errors multiplicity and even errors multiplicity less than 6	24
CRC	Guaranteed of not detected errors	16

The data analysis of the Table 3, shows that the developed method allows the comparison with known methods. The proposed method significantly improves the efficiency of error detection in the serial interfaces which faulted synchronization of data transmission.

IV. FUTURE RESEARCH

A further research on the proposed method and implementation to efficiently error correction [6], [7], in order to complete a novel method of errors detection and correction in high speed data transmission channels are suggested.

V. CONCLUSION

For guarantee detection of single and multiple errors, which caused by the faulted of synchronize, a control method based on the set changing of non-synchronization bits during the data transmission are proposed.

The method is based on the modification of the weighted checksum method with coefficients formed as the product of the control bits of the length of weighted coefficient. The proposed method is oriented for applications in high speed data transmission channels between the units of computer control systems.

REFERENCES

- [1] Klove T. Error Detecting Codes: General Theory and Their Application in Feedback Communication Systems / T. Klove, V. Korzhik.- Norwell, MA: Kluwer, 1995. – 433 p.
- [2] A. J. McAuley, Weighted sum codes for error detection and their comparison with existing codes, IEEE/ACM Trans. On Networking, vol. 2, no. 1, pp. 16–22, Feb. 1994.
- [3] Zumbragel J. Skachek V., Flanagan M. On the Pseudocodeword Redundancy of Binary Linear Codes / J. Zumbragel, V. // IEEE Trans. of Information Theory.-2012.-Vol.58.- № 7.-P.4848-4861.
- [4] Bardis N.G, Markovskyy A.P, "Utilization of Avalanche Transformation for Increasing of Echoplex and Checksum Data Transmission Control Reliability", ISITA 2004 - INTERNATIONAL SYMPOSIUM ON INFORMATION THEORY AND ITS APPLICATIONS, IEEE / SITA, Parma, Italy, October 10-13, ISBN: 4-902087-08-1, 2004
- [5] Nikolaos G. Bardis, Athanasios Drigas and Olexandr P. Markovskiy, Performance Increase of Error Control Operation on Data Transmission, 3rd International Conference on New Technologies, Mobility and Security, IEEE, IEEE COMMUNICATIONS SOCIETY, Egypt – Cairo, 20-23 December 2009.
- [6] Bardis N. G, Doukas, N., Markovskiy O.P, Transmission Error Correction Based on the Weighted Checksum, Proceedings of the APPLIED COMPUTING CONFERENCE 2009 (ACC '09), MATHEMATICAL METHODS AND APPLIED COMPUTING Volume II, Vouliagmeni-Athens, Greece, pp.758-763, September 28-30, 2009.
- [7] Nikolaos Bardis, Nikolaos Doukas, Olexander Markovskiy, "Efficient Burst Error Correction Method for Application in Low Frequency Channels and Data Storage Units", DSP/IEEE 2011 17th International Conference on Digital Signal Processing, 6-8 July 2011 Corfu, Greece.

Statistical analysis of surface roughness in grinding of titanium

Bílek Ondřej, Javořík Jakub, and Sámek David

Abstract— This paper gives the investigation on surface roughness of grinding of titanium material. The experiments were carried out under dry cutting conditions and results were compared to grinding with coolant. Surface roughness was characterized by a parameter R_a , moreover was evaluated the effect of process conditions. The surface of titanium was worse at high cutting conditions with increasing standard deviation. Application of coolant during the grinding improves the titanium surface. In addition, the results were statistically analyzed using ANOVA and correlated to other metallic materials. Comparing the ultimate tensile strength clearly showed that the titanium material to its behavior differs significantly from the other metallic materials, primarily for its poor machinability.

Keywords—ANOVA, Grinding, Metals, Surface Roughness, Titanium.

I. INTRODUCTION

Grinding is one of the crucial technology to achieve the desired surface quality of the components. It is categorized as the last technological operation that takes only a small amount of material, by a tool that has a stochastic structure [1], [2]. Although external feature characteristics of the tool are definable, the layout, size and geometry of the micro tools - abrasive grains - therefore cannot be determined clearly. Even though grinding is much used in industry remains perhaps the least understood machining method. Even if grinding is one of the oldest ways of machining today, does not lose its importance. Grinding technology may not only be used as a finishing operation, but in the case of in-depth, high-performance grinding becomes a high stock removal technique [3-5]. Most of the materials can be ground. Grinding is successfully used for machining of metals and non-metallic materials, such as plastics [6]. It is the only method that allows conventional way to machine brittle materials, superalloys and difficult-to-machine metals [7]. The tool is a grinding wheel composed of abrasive grains of superhard materials [8], [9], such as Cubic Boron Nitride (CBN) or diamond.

Surface roughness generated by the grinding process determines a range of component characteristics such as the

minimal tolerances, the ability of lubrication, reflectance, durability, [10] etc. The grinding is a complex material removal process, with a great number of influencing factors which are also nonlinear and difficult to quantify [11-13].

Surface quality of grinding is influenced by following parameters: [14]

- a) wheel characteristic: grain material, size, grade, structure, binder, dimensions, etc.
- b) workpiece material: mechanical properties and chemical composition.
- c) process parameters: cutting speed, feed rate, depth of cut, dressing, etc.
- d) machine parameters: static and dynamic behavior, table and clamping system [15], spindle system, etc.

Nevertheless, it is an effort to describe and predict the grinding process and quantify resulting surface roughness. If we consider all the input characteristics, a complete prediction of surface topography is a complex problem [16], [17]. The typical parameter which is used in the industry to evaluate the surface arithmetic mean roughness is value of R_a . It is a widespread parameter, although does not carry comprehensive information of surface roughness. Generally, the longitudinal surface roughness has a lower value than traversal value, and therefore is more frequently used in industry [18]. Roughness parameter R_a is generally defined as:

$$R_a = \frac{1}{lr} \int_0^{lr} |Z(x)| dx \quad (1)$$

describing the roughness profile on the sampling length lr from the profile height function $Z(x)$.

The surface of titanium and titanium alloy is easily disrupted during grinding due to their poor machinability [19]. Titanium and titanium alloys are widely used in the aerospace, chemical, petrochemical industry and for fabrication of medicinal prosthetics. Titanium is characteristic by their low density compared to other structural metals and alloys, excellent corrosion resistance, high level of proof strength. On the other hand, have poor wear resistance and suffer embrittlement at higher temperatures [20]. Titanium and titanium alloys are among the most difficult-to-machine materials [21], [22]. Low thermal conductivity and high chemical reactivity cause heat generation during machining and strong adhesion between the tool and the workpiece

O. Bílek (e-mail: bilek@ft.utb.cz; phone: +420-576-035-227; fax: +420-576-035-176), J. Javořík (e-mail: javorik@ft.utb.cz), D. Sámek (e-mail: samek@ft.utb.cz) are with the Department of Production Engineering, Faculty of Technology, Tomas Bata University in Zlin, nam. T.G. Masaryka 5555, 76001 Zlin, Czech Republic.

material. That is also the cause of poor surface quality [23], [24].

This paper presents a statistical analysis of the arithmetic mean roughness Ra , depending on the diameter of the wheel depth of cut and feed rate of titanium material. The method of analysis of variance (ANOVA) was used to evaluate the correlation with titanium to other metal materials. Dry grinding results are compared in addition to the grinding process using a coolant.

II. EXPERIMENT SETTINGS

To understand the effect of process conditions on the surface quality of the grinding was applied statistical analysis. The aim is to understand the impact of process conditions during grinding of titanium. The input parameters of the experiment are cutting depth, feed rate and the diameter of the grinding wheel. Details are presented in Table I.

Table I Process parameters and cutting conditions

Grinding machine	BRH 20.03F
Type of grinding wheel	99A90J9V
Grinding wheel diameter	195, 250 mm
Depth of cut	0.01, 0.02, 0.03, 0.04 mm
Feed rate	8, 12, 16, 24 m/min
Revolution of grinding wheel	2 500 min ⁻¹

The first group of experiments was carried out under dry machining environment. Another group of experiments assessed the effect of coolant on the surface roughness depending on the grinding wheel diameter and hence the cutting speed. All samples were the same size (50x50x20 mm) and their chemical composition is shown in Table II, while the mechanical properties are given in Table III.

Table II Nominal chemical composition of the titanium

Work material	Chemical composition (wt. %)		
	Fe	C	Addition of
Ti	0.08	0.01	Al, V, Mn, Si

The last group of experiments was focused on the surface roughness while grinding of titanium by comparison with other metallic materials. Their ultimate strength was the categorization parameter added on the graphical axis. Ultimate strength of aluminum alloy was 270 N/mm², 245 N/mm² for copper, 530 N/mm² for structural steel C45 (1.1191), 668 N/mm² for bearing steel 100Cr6 (1.3505), 825 N/mm² for stainless steel X46Cr13 (1.4034), and 2850 N/mm² for tool steel X210Cr12 (1.2080).

Table III Mechanical properties of work material

Work material	Ti
Ultimate tensile strength	350 N/mm ²
Modulus of elasticity	116 × 10 ⁶ N/mm ²
Hardness	970 HV

For industrial purposes was selected measurement and classification of surface as a two-dimensional (2D) analysis of surface roughness. The value of Ra was calculated from equation (1) from the measured 2D roughness profile. Roughness was measured after grinding onto clean and dry sample in the direction of the largest surface roughness, in a direction transverse to the feed rate vector. The surface roughness measurements were carried out with a stylus type testing instrument Mitutoy SJ-301 according to ISO 3274, ISO 4287 and ISO 4288 standard and specification.

III. RESULTS AND DISCUSSIONS

It appears that with increasing cutting depth in all experiments increase the surface roughness Fig. 1-4. However, with increasing feed rate is conversely surface roughness lower and thus the surface quality better Fig. 5. Similar but slightly lower values of surface roughness Ra is obtained by changing the diameter of the grinding wheel from the initial 250 mm to smaller diameter of 195 mm Fig. 6-10, while keeping constant all other process parameters.

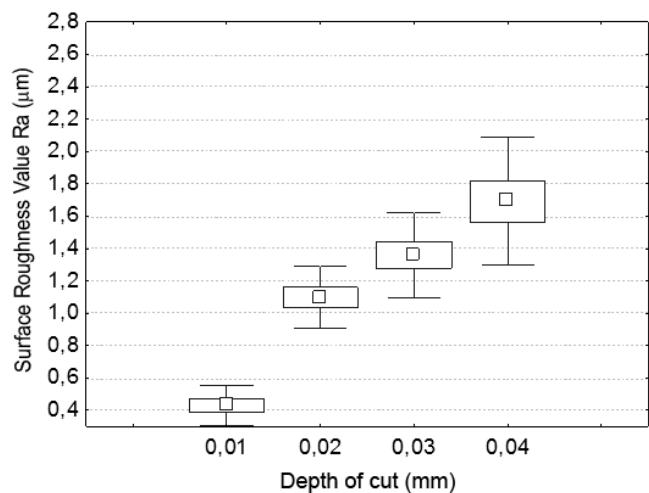


Fig. 1 The relationship between surface roughness Ra and depth of cut when grinding at feed rate of 8 m/min and grinding wheel diameter 250 mm

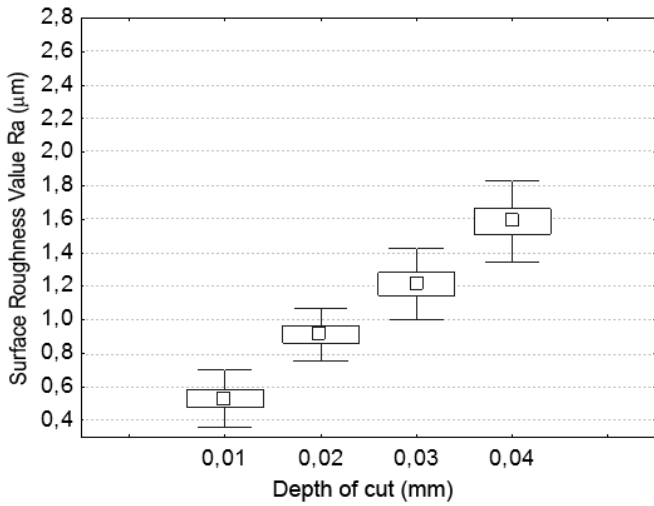


Fig. 2 The relationship between surface roughness Ra and depth of cut when grinding at feed rate of 12 m/min and grinding wheel diameter 250 mm

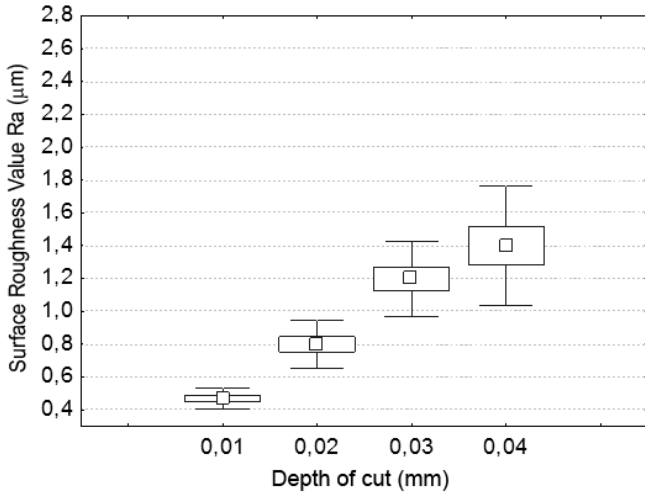


Fig. 3 The relationship between surface roughness Ra and depth of cut when grinding at feed rate of 16 m/min and grinding wheel diameter 250 mm

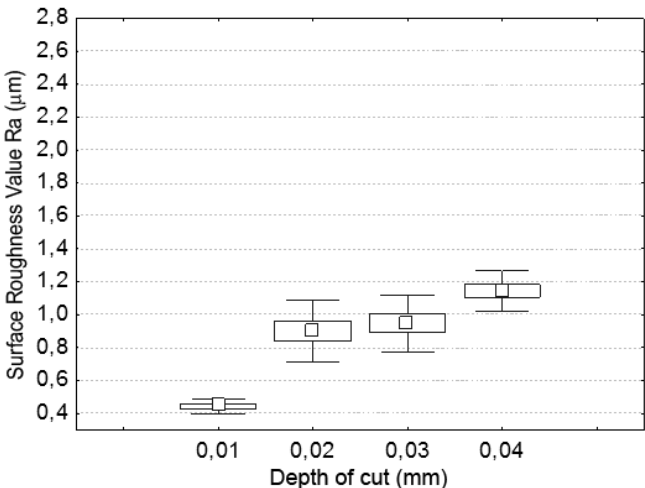


Fig. 4 The relationship between surface roughness Ra and depth of

cut when grinding at feed rate of 24 m/min and grinding wheel diameter 250 mm

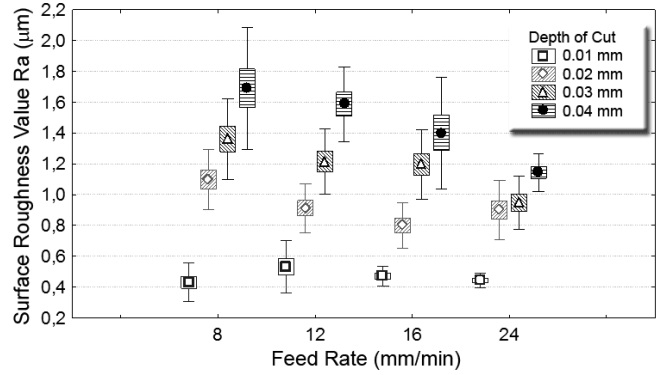


Fig. 5 Surface roughness value Ra vs feed rate and depth of cut for grinding wheel diameter 250 mm

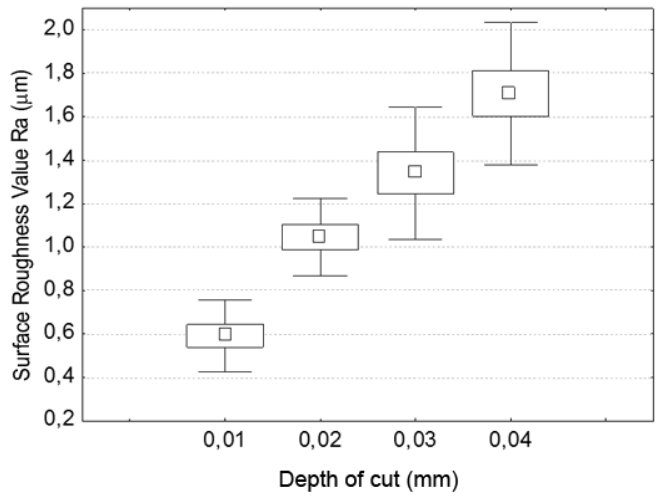


Fig. 6 The relationship between surface roughness Ra and depth of cut when grinding at feed rate of 8 m/min and grinding wheel diameter 195 mm

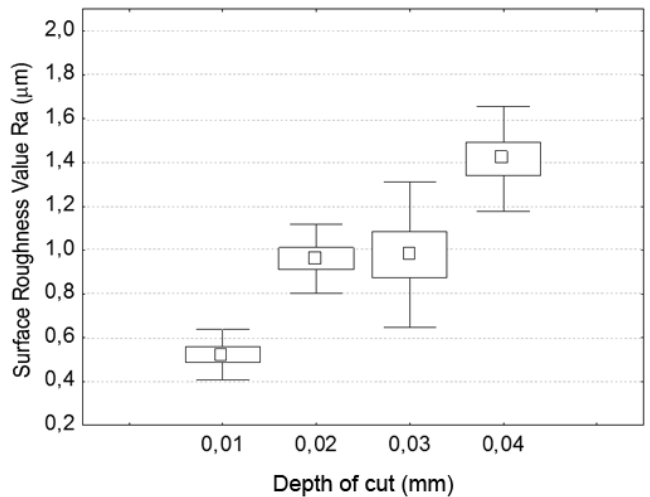


Fig. 7 The relationship between surface roughness Ra and depth of cut when grinding at feed rate of 12 m/min and grinding wheel diameter 195 mm

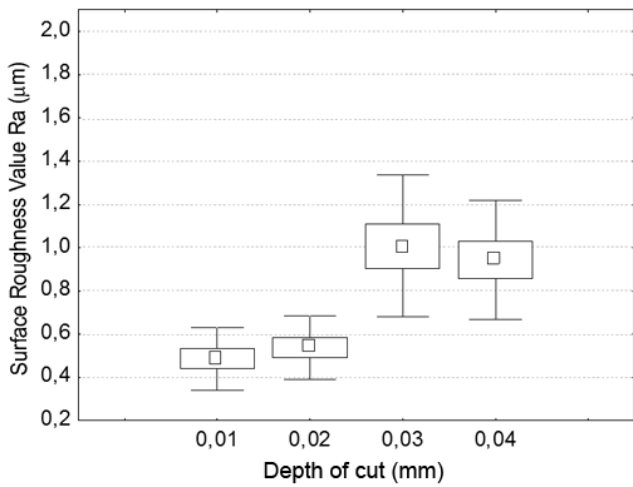


Fig. 8 The relationship between surface roughness Ra and depth of cut when grinding at feed rate of 16 m/min and grinding wheel diameter 195 mm

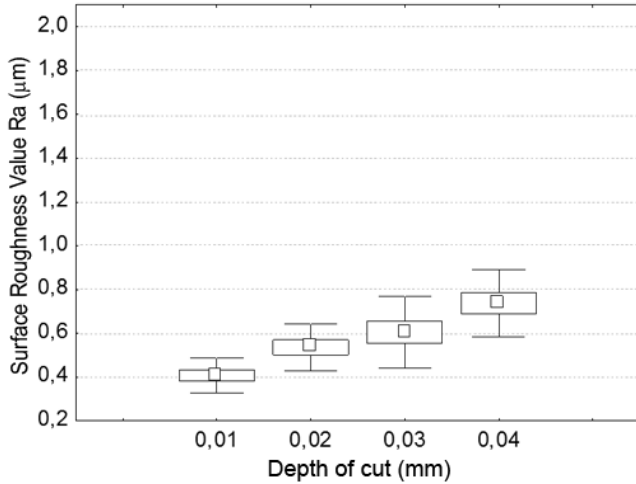


Fig. 9 The relationship between surface roughness Ra and depth of cut when grinding at feed rate of 24 m/min and grinding wheel diameter 195 mm

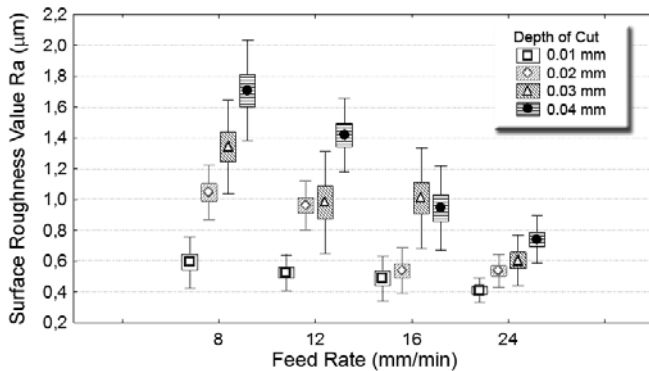


Fig.10 Surface roughness value Ra vs feed rate and depth of cut for grinding wheel diameter 195 mm

In addition, it was proven that cooling has the significant effect on surface roughness while grinding. Cooling not only considerably changes the roughness profile (Fig. 11 and Fig. 12) but it also affects the surface roughness value Ra. The best

value (Fig. 13) of surface roughness is achieved by grinding the titanium with coolant and a smaller diameter of grinding wheel.

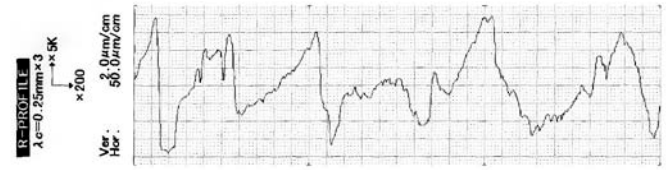


Fig. 11 Roughness profile of dry grinding

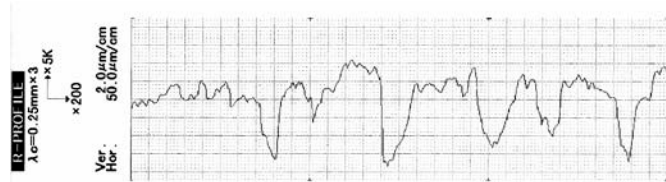


Fig. 12 Roughness profile of grinding with coolant

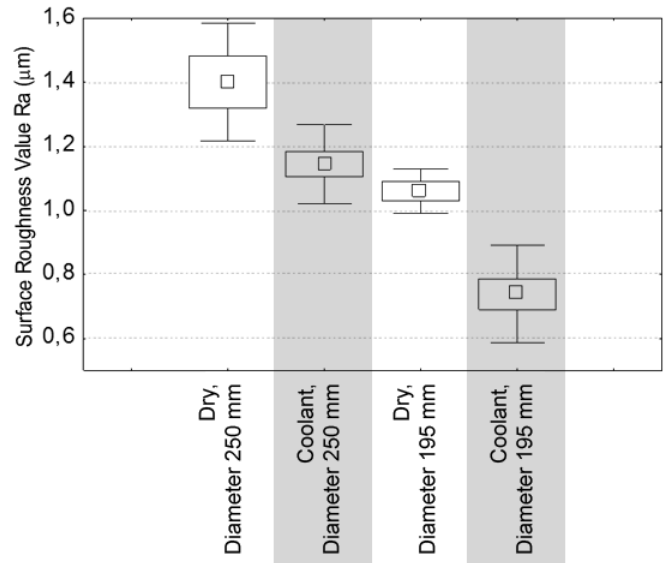


Fig.13 The effect of coolant and grinding wheel diameter on surface roughness Ra

Finally was performed ANOVA to take into consideration the influence of input factors (feed rate, depth of cut, ultimate strength). In one-dimensional tests of significance came out statistically significant effect of all studied factors including their mutual interaction ($p = 0.00001$). The Figure 14 presents a designed regression model of influencing factors on the surface roughness Ra after grinding. The expected model is disrupted at ultimate strength of 350 N/mm^2 , corresponding to titanium material. As one of the metals has a significantly different behavior depending on process parameters.

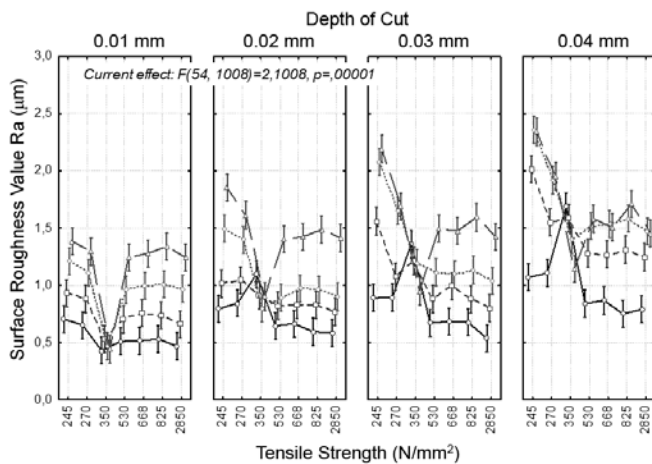


Fig. 14 Analysis of variance considering process condition and tensile strength of metallic materials

IV. CONCLUSIONS

In this investigation, the effect of process conditions on the surface quality was compared in grinding titanium. Based on the statistical analysis of the measured data and trend behavior may be predicted that with increasing depth of cut, the surface roughness deteriorates, whereas with increasing feed rate, the surface roughness becomes better. Change of the grinding wheel diameter, and thereby reducing peripheral speed, results in better surface roughness as well as application of coolant. To achieve high surface quality of titanium is strongly advised to use cooling during the grinding process. Furthermore, the ANOVA analysis determined that all observed input parameters are significant and an interaction among them.

REFERENCES

- [1] O. B. Abouelatta, "Prediction of machining operations and surface roughness using artificial neural network," *J. Eng. Sci.*, vol. 41, no. 3, pp. 1021–1044, 2013.
- [2] N. Alagumurthi, K. Palaniradja, and V. Soundararajan, "Optimization of Grinding Process Through Design of Experiment (DOE)—A Comparative Study," *Mater. Manuf. Process.*, vol. 21, no. 1, pp. 19–21, Jan. 2006.
- [3] J. Beňo, J. Stahovec, P. Ižol, and M. Tomáš, "Decomposition of form surfaces for planning of machining," *Manuf. Technol.*, vol. 12, no. 13, 2012.
- [4] S. Malkin and C. Guo, *Grinding Technology: Theory and Application of Machining with Abrasives*. Industrial Press Inc., 2008, p. 372.
- [5] E. Brinksmeier, J. C. Aurich, E. Govekar, C. Heinzl, H.-W. Hoffmeister, F. Klocke, J. Peters, R. Rentsch, D. J. Stephenson, E. Uhlmann, K. Weinert, and M. Wittmann, "Advances in Modeling and Simulation of Grinding Processes," *CIRP Ann. - Manuf. Technol.*, vol. 55, no. 2, pp. 667–696, Jan. 2006.
- [6] M. Novak, "Surfaces with high precision of roughness after grinding," *Manuf. Technol.*, vol. 12, pp. 66–70, 2012.
- [7] M. Čilliková, M. Mičuch, M. Neslušán, and A. Mičietová, "Nondestructive micromagnetic evaluation of surface damage after grinding," *Manuf. Technol.*, vol. 13, no. 2, pp. 152–157, 2013.
- [8] H. C. Yang and M. Q. Wu, "Machined Surface Quality Improvement Measures Affecting Factors and Research," *Appl. Mech. Mater.*, vol. 496–500, pp. 516–519, Jan. 2014.
- [9] X. Zhou and F. Xi, "Modeling and predicting surface roughness of the grinding process," *Int. J. Mach. Tools Manuf.*, vol. 42, no. 8, pp. 969–977, Jun. 2002.

- [10] M. Iliescu and M. Costoiu, "Surface roughness statistic models of metallized coatings in grinding manufacturing system," *WSEAS Trans. Syst.*, vol. 7, no. 9, pp. 824–833, 2008.
- [11] P. Govindan, "Investigations on the Influence of Processing Conditions on Grinding Process," *Int. J. Eng. Res. Technol.*, vol. 2, no. 9, pp. 648–654, 2013.
- [12] J. Jersák and L. Vrkoslavová, "The influence of process fluids on the properties of the surface layer of machined components," *Manuf. Technol.*, vol. 13, no. 4, pp. 466–473, 2013.
- [13] H. K. Tönshoff, J. Peters, I. Inasaki, and T. Paul, "Modelling and Simulation of Grinding Processes," *CIRP Ann. - Manuf. Technol.*, vol. 41, no. 2, pp. 677–688, Jan. 1992.
- [14] J.-S. Kwak, "Application of Taguchi and response surface methodologies for geometric error in surface grinding process," *Int. J. Mach. Tools Manuf.*, vol. 45, no. 3, pp. 327–334, Mar. 2005.
- [15] M. Iliescu, L. Vladareanu, and M. Soceanu, "Machining force regression models and real time control when turning MET 4 metallized coating," in *Recent Researches in System Science - Proceedings of the 15th WSEAS International Conference on Systems, Part of the 15th WSEAS CSCC Multiconference*, 2011, pp. 346–351.
- [16] K. Kandananond, "The determination of empirical model for surface roughness in turning process using design of experiment," *WSEAS Trans. Syst.*, vol. 8, no. 10, pp. 1135–1144, 2009.
- [17] M. Kasina and K. Vasilko, "Experimental verification of the relation between the surface roughness and the type of used tool coating," *Manuf. Technol.*, vol. 12, pp. 27–30, 2012.
- [18] R. L. Hecker and S. Y. Liang, "Predictive modeling of surface roughness in grinding," *Int. J. Mach. Tools Manuf.*, vol. 43, no. 8, pp. 755–761, Jun. 2003.
- [19] K. Kocman, "Application of magnetic correlation analysis on the choice and correction of cutting parameters for automated manufacturing systems," *Manuf. Technol.*, vol. 11, pp. 28–32, 2011.
- [20] A. Bloyce, P. H. Morton, and T. Bell, "Surface Engineering of Titanium and Titanium Alloys," *ASM Handbook*, vol. 5, pp. 1–17, 1994.
- [21] M. Novak, "Surface quality of hardened steels after grinding," *Manuf. Technol.*, vol. 11, pp. 55–59, 2011.
- [22] A. Czân, M. Sajgalik, J. Holubjak, and K. Kouril, "Studying of cutting zone when finishing titanium alloy by application of multifunction measuring system," *Manuf. Technol.*, vol. 13, no. 4, pp. 428–431, 2013.
- [23] C. H. Che-Haron and a. Jawaid, "The effect of machining on surface integrity of titanium alloy Ti–6% Al–4% V," *J. Mater. Process. Technol.*, vol. 166, no. 2, pp. 188–192, Aug. 2005.
- [24] X. Yang and C. Richard Liu, "Machining titanium and its alloys," *Mach. Sci. Technol.*, vol. 3, no. 1, pp. 107–139, Jan. 1999.

New approach to building hierarchy for patients attendance in intensive care unit with use of fuzzy information and dynamic modeling

Maria Milanova and Mikhail Matveev

Abstract— Every intensive care unit (ICU) admits critically ill patients with disturbed vitally important functions. Time is a critical factor with such patients and the optimum behaviour of the medical team is decisive. They require optimised distribution of the staff and material resources, hence an adequate model of the structure and activities in an ICU is needed. Such a model was built using generalized nets (GNs) in terms of fuzzy information.

The workflow presented as a GNs-model is based on principles and prerequisites typical of ICU. Structure of the information included in the model. The goal attained with GNs is: solution for the admission and servicing of patients at the ICU in a dynamically changing situation at any moment of the night and day.

The dynamic workflow model in ICU in the form of a GNs is an adequate approach for optimum distribution of the resources and optimum conduct in the care for patients with severe disorders of the vital functions.

Keywords—Intensive care unit, Generalized Nets, fuzzy information.

I. INTRODUCTION

Patient could enter in intensive care unit from several basic sections - surgical ward, other wards and hospitals or direct from outside. There are many different reasons and diagnoses. But in intensive care unit always enter patients in critical status, with supposed or existing disturbances of vital functions. The indications for entrance are: recovery after an operation and anaesthesia, preoperative intensive monitoring and treatment, postoperative intensive monitoring and treatment, other indications. The time is a critical parameter for this ward. The immediate action of the medical personnel is of exclusive importance, because of the critical status of the patients. A little delay could be fatal. The real process describes the steps - from patient entrance to the stabilization of his status and the preparation for operation or discharge.

When patient enter in intensive care unit many processes pass in parallel, most of which are of primary importance. But the apparatuses, personnel and material limitations impose many of the parallel actions to be made consecutively. That is why the classification of needed operations is very important.

M. Milanova is with the University Hospital of Emergency Medicine, Sofia, Bulgaria (corresponding author to provide phone: 303-555-5555; fax: 303-555-5555; e-mail: milanovamaria@abv.bg).

M. Matveev is with the Institute of Biophysics and Biomedical Engineering, Bulgarian Academy of Sciences, Sofia, Bulgaria (corresponding author: phone: +359 2 870 0326; fax: +359 2 872 3787; e-mail: mgm@clbme.bas.bg)

But that classification must not increase the risk for the patient. That's why the priorities of the operations are needed. These priorities are complex determined of: the rate of importance of the disturbed vital function compared to the other vital functions; the rate of disturbance of the function; the combination with other disturbed functions. So, when it's needed and the patient status allows it, the disturbed functions could be rehabilitated consecutively.

The following situations could be considered:

- In the ward there are specialists of all basic fields and the available apparatuses is sufficient. In this case when a patient with disturbed functions enters there is no problem for him to be assumed from the specialists and to have all needed manipulations and tests. This is represented by only one token in the Generalized Nets (GNs, see [1]).

- In the ward there are specialists of all basic fields and the available apparatuses is sufficient, but there enter a few patients with disturbed in different rates vital functions at the same time. This is represented by entrance of several tokens at the same time in the ON. The entered tokens are arrayed by their priorities. The priority is determined by the patient status - the more critical is it, the higher priority has the related token. So, the harder cases are first served. To be described this situation could be used fuzzy information.

- In the ward there are a few specialists and the available apparatuses are the needed minimum. If there is only one patient with disturbed vital functions, the doctors take a decision who of them to take care of the patient and if it's needed - which operations could be made consecutively.

- In the ward there are a few specialists and the available apparatuses are the needed minimum. There enter a few patients with disturbed vital function. In this case, the use of Intuitionistic Fuzzy Sets (IFSs; see [2]) is compulsory, because appear situations with indetermination.

In Intensive Care Unit the last described situation is most frequent - when there are several patients with disturbed vital functions at the same time. This is a critical moment for the ward, especially if everybody is in hard status. To decrease the risks this situation must be provided. If the available materials, apparatuses and personnel are sufficient, the ward will function normally. But in other case a consecutively attendance of the patients necessitates. The precise estimations of the statuses of the entered are needed for the decision to the sequence of attendance. For this purpose determined criterions

are used.

The GNs and IFSs are used to describe the processes in intensive care unit [3,4,5,6,7,8]. The GNs afford an opportunity for description of the time linked parameters, the logical conditions and the history of the modeling processes. Besides, they function as expert systems as like as information systems for collecting, processing and analysis of information.

GN model of ward of intensive care could be in great favour of students and beginning specialists. It will give opportunity to simulate real situations, which require right decision as quickly as possible. This estimates and supplements beginners' knowledge. It could be used, simultaneously, from specialists for self-control. It improves on quality of service in the ward and increases the speed of reaction.

IFSs afford an opportunity for estimation the dynamic of the patient status. They allow more accurate determination of the importance rate of a function. The IFSs could be used for the operations priorities construction.

The made GN model describes the steps - from the patient entrance in the ward to his discharge. From the intensive care unit the patient could be moved to: another ward, surgical ward, another hospital, or he could be discharged to go home. Exituses are possible too. Every one of these variants is considered as a discharge from the ward. The ward of intensive care is not isolated system. Contrariwise, it is in close relationship with other outer sections, which could be a reason for a fatal delay.

The aims of the stay in the ward are: restoration of the disturbed vital functions and assertion of the stable status of the patient. In the ward is needed DB with information for the patients and specialists, and the made manipulations and tests.

II. A GN MODEL

The model has 5 transitions. They describe: enter of a patient and estimation of his state (Z_1), disturbances of vital functions (Z_2), analysis and evaluation of other functions (Z_3), other tests and relations with outer sections (Z_4), assertion of the stable status (Z_5) - Fig. 1.

The operations of restoration and assertion of the status are made in parallel. But every one of them has a priority.

$$Z_5 = \langle \{I_1, I_5, I_7, I_9, I_{11}, I_{12}\}, \{I_2, I_3, I_4, I_5, e\}, t_1', t_1'', r_1, I_1 \rangle,$$

where:

$W_{1,2}$ = "vital functions of the patient are disturbed - breathing, circulation, consciousness, body temperature, presence of pain";

$W_{1,3}$ = "necessity of estimation of other functions";

$W_{1,4}$ = "necessity of relation with other sections";

$W_{5,e}$ = "work with the DB";

$W_{9,3} = W_{1,3} = W_{11,3} = W_{12,3}$;

$W_{9,4} = W_{1,4} = W_{11,4} = W_{12,4}$;

$W_{9,3} = W_{11,e} = W_{12,e}$ = "discharge from the unit".

r_1	I_2	I_3	I_4	I_5	e
I_1	$W_{1,2}$	$W_{1,3}$	$W_{1,4}$	true	false
I_5	false	false	false	true	$W_{5,e}$
I_7	false	false	false	true	true
I_9	false	$W_{9,3}$	$W_{9,4}$	true	$W_{9,e}$
I_{11}	false	$W_{11,3}$	$W_{11,4}$	true	$W_{11,e}$
I_{12}	false	$W_{12,3}$	$W_{12,4}$	true	$W_{12,e}$

$$Z_2 = \langle \{I_2\}, \{I_6, I_7\}, t_2', t_2'', r_2, I_2 \rangle,$$

where:

r_2	I_6	I_7
I_2	$W_{2,6}$	$W_{2,7}$

$W_{2,6}$ = "restoring vital functions and necessity of asserting treatment";

$W_{2,7}$ = "not restoring vital functions".

$$Z_3 = \langle \{I_3\}, \{I_8, I_9\}, t_3', t_3'', r_3, I_3 \rangle,$$

where:

r_3	I_8	I_9
I_3	$W_{3,8}$	$W_{3,9}$

$W_{3,8}$ = "estimation of other functions is needed for the asserting treatment";

$W_{3,9}$ = "necessity of other tests".

$$Z_4 = \langle \{I_4\}, \{I_{10}, I_{11}\}, t_4', t_4'', r_4, I_4 \rangle,$$

where:

r_4	I_{10}	I_{11}
I_4	$W_{4,10}$	$W_{4,11}$

$W_{4,10}$ = "the relation with other sections is important for the asserting treatment";

$W_{4,11}$ = "necessity of other tests".

$$Z_5 = \langle \{I_6, I_8, I_{10}, I_{13}\}, \{I_{12}, I_{13}\}, t_5', t_5'', r_5, I_6 \rangle,$$

where:

r_5	I_{12}	I_{13}
I_6	$W_{6,12}$	$W_{6,13}$
I_8	$W_{8,12}$	$W_{8,13}$
I_{10}	$W_{10,12}$	$W_{10,13}$
I_{13}	$W_{13,12}$	$W_{13,13}$

$W_{6,12}$ = "necessity of asserting treatment and other tests";
 $W_{8,12}$ = "other tests are necessity for the asserting treatment of the patient status";
 $W_{10,12} = W_{8,12} = W_{13,12}$;
 $W_{6,13}$ = "necessity of asserting treatment";
 $W_{8,13} = W_{6,13} = W_{10,13} = W_{13,13}$.

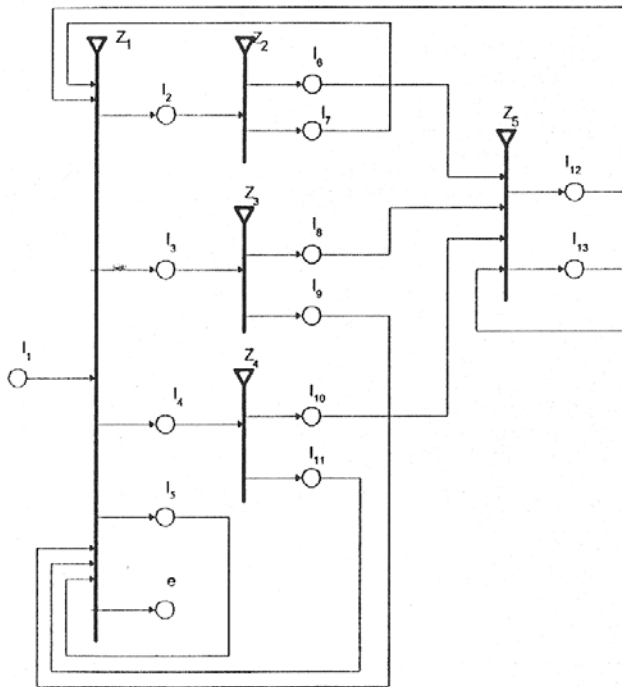


Fig. 1

In position I_1 the specialists estimate the status of the entered patient. The tokens in this position have a characteristic: disturbed breathing and/or blood circulation, and/or consciousness lost, and/or higher/lower body temperature, and/or presence of pain, and/or necessity of other functions estimation, and/or relation with other sections, μ_{ij} , υ_{ij} . The tokens enter in position I_2 in case of disturbed vital function.

In positions I_3 and I_4 the tokens obtain characteristic: necessity of other tests. After vital functions restoration, the token enters from position I_6 in position I_{13} , where obtain a characteristic - assertion of the stable status.

μ_{ij} , υ_{ij} are used for status estimation. They are determined from the criteria of making the priority of the patient and his

functions - rate of disturbance of the vital function, rate of importance of that function, rate of coincidence between specialist's qualification and patient's disturbances, μ_{ij} presents the rate of: importance of a vital function, disturbance of that function, coincidence between qualification and disturbance; υ_{ij} - the rate of unimportance of a relevant criteria; i is a criteria for estimation, and j - the relevant function. For instance, most important are disturbances in the blood circulation, and this function has the highest priority. For μ_{ij} and υ_{ij} is true:

$$\mu_{ij} + \upsilon_{ij} \leq 1 \text{ and } \mu_{ij} + \upsilon_{ij} + \pi_{ij} = 1$$

If relevant vital function is not disturbed $\upsilon_{ij} = 1$.

π_{ij} is the rate of indetermination.

μ , υ and π give an estimation of the patient status. With their use could be made the priorities of the operations. The priority could be made by estimation of the value of μ_{ij} . The priorities of the operations give the conditions for tokens movement from one position to another. The made GN model is generalized - in position (I_2) are collected restorations of all vital functions: breathing, circulation, consciousness, body temperature, presence of pain. If the model is more detailed the movement of the tokens in dependence of the priorities could be easily seen.

III. CONCLUSION

Even the described variants, there are a situations, in which we couldn't avoid the parallelism. There are situations when we couldn't estimate correctly the importance of the disturbed function, or the rate of disturbance. This complicates the decision taking. The status of the patient could be misjudged, which could be reason for a bad effect. The insufficiency of personnel and apparatuses is always possible. In these situations are taken hard decisions - who of the patients to be attended. But the aim is these moments to be predicted as it's possible and the risks to be minimized. The GN model above is liable to program realization, in which the predicates will be estimated with the real use of IFSs.

REFERENCES

- [1] K. Atanassov, *Generalized Nets*. Singapore, New Jersey, London: World Scientific, 1991.
- [2] K. Atanassov, *Intuitionistic Fuzzy Sets*. Heidelberg: Springer-Verlag, 1999.
- [3] A. Shannon, D. Peneva, E. El-Darzi, K. Atanassov, M. Matveev, P. Chountas, P. Vassilev, V. Tasseva. "The generalized net modeling of information healthcare system", in *Proceedings of the International Conference "Automatics and Informatics'06"*, 2006, Sofia, Bulgaria, pp. 119-122.
- [4] M. Matveev, K. Atanassov, E. Pazvanska, V. Tasseva. "Dynamic Model of Intensive Care Unit Workflow Based on Generalized Nets", *Int. J. Bioautomation*, 2, pp. 85-92, 2005.
- [5] K. Atanassov, M. Matveev, A. Shannon, V. Tasseva. "Information model of workflow and resources in general hospital", in: *Proc. of the International conference on advanced information and telemedicine technologies for health*, Minsk, Belarus, vol.2, pp. 42-46, 2005.
- [6] V. Tasseva, K. Atanassov, M. Matveev, E. El-Darzi, P. Chountas, F. Gorunescu. "Modelling the flow of patient through intensive care unit using generalized net", in: *F. Gorunescu, E. El-Darzi, M. Gorunescu*,

- editors, Health Care Modelling and Computation, Medical University Press, Craiova, Romania, pp. 290-299, 2005.*
- [7] V. Chakarov, K. Atanassov, V. Tasseva, M. Matveev, E. El-Darzi, P. Chountas, I. Petrounas. "Generalized net model for some basic clinical administrative decision making", in: *F. Gorunescu, E. El-Darzi, M. Gorunescu, editors, Health Care Modelling and Computation, Medical University Press, Craiova, Romania, pp. 72-78, 2005.*
- [8] M. Matveev, K. Atanassov, E. Pazvanska, V. Tasseva. "Optimization of workflow in ICU with generalized net". *Journal of Clinical Monitoring and Computing*, vol. 18 Nos 5-6, pp. 421-422, 2004.

3D data acquisition and CAD/CAM systems for CNC manufacturing of artificial limbs

Bílek Ondřej, Javořík Jakub, and Sámek David

Abstract— There is no doubt that Computer Aided (CA) systems enable automation of manufacturing processes, increase production flexibility and make possible manufacturing of complex parts. Integration of Computer Aided Design (CAD) and Computer Aided Manufacturing (CAM) systems in addition to the primary engineering applications, have increasingly prominent position in medicine. CAD/CAM systems are deployed on the production of prostheses. This paper deals with the integration of CAD/CAM systems into the production of artificial human limb as a master model for prosthesis creation. On the basis of 3D scanning of healthy limb, a virtual model was created. Subsequently was created a spatial model of the amputated limb by CAD/CAM and programmed tool paths for manufacturing. Manufacturing was performed on three axis Computer Numerical Control (CNC) machine tool.

Keywords—CAD/CAM, Prosthesis, 3D model, CNC Machining.

I. INTRODUCTION

There is no doubt that any disability significantly reduces the quality of human life. Disability from birth or accidents that lead to loss of organ, limb or other part of the human body, can be for handicapped the cause that prevents being self-reliant. In addition to associated health problems may disability be accompanied by inability to perform basic movements and thus its applicability in human society, moreover in the labor market becomes less likely. Amputation of limbs may be in addition to accidents also as a result of other health problems. Amputate is in many cases the only way of saving human life even at the expense of the organ loss. At present, orthopedics has sophisticated methodology to replace missing limbs [1]. Their purpose is to help the patient return to the greatest extent possible to wide-ranging independence. In addition to basic orthopedic compensation to control basic movements and grip ability, goes further development of prostheses to construction of the bionic prosthesis, the prosthesis for disabled athletes for above average physical activities and prostheses allowing a sense of touch [2-6].

Prostheses replace in part or in full the missing limb. The necessary requirement is to replace the defect, although the functionality of the prosthesis may not be completely perfect.

O. Bílek (e-mail: bilek@ft.utb.cz; phone: +420-576-035-227; fax: +420-576-035-176), J. Javořík (e-mail: javorik@ft.utb.cz), D. Sámek (e-mail: samek@ft.utb.cz) are with the Department of Production Engineering, Faculty of Technology, Tomas Bata University in Zlin, nam. T.G. Masaryka 5555, 76001 Zlin, Czech Republic.

A secondary requirement is the function of health and cosmetic compensation of anatomic loss [7]. Replacement of the function of the prosthesis is tied to the overall condition of the organism, the size of the residual stump and varies with age of the patient.

Prostheses are derived from the original missing body parts. Their shape is dependent on the type and extent of amputation. Prostheses are a complex element that is requested by a series of often conflicting requirements [8]. Prosthesis material must be resistant to wear, high-strength but lightweight, harmless, and their appearance should be realistic [9], [10]. Each prosthesis is customized to disabled person, which excludes many industrial production technologies. Production of prostheses is associated with a request for special medical supplies, short fabrication time and last but not least the price as the deciding factor. These requirements are demanding for the use of new technologies. In case of replacement of the paired organ for artificial replacement is successfully used technology of acquisition and conversion into 3D digitized model. Having these data can be independent of the presence of the patient further. The subsequent step is the processing using Computer Aided Design (CAD) systems that govern data for conventional production technologies. CAD systems work with 2D and 3D structural shapes often interconnected. The advent of CAD system was accompanied by a significant efficiency increase of the design, creation and modification of geometric entities. In today's modern manufacturing plant life cannot be imagined working without them. It replaces the original drawings to electronic agenda management with all data management capabilities [11], [12]. CAD systems are available free of charge (DesignSpark) for general use. On the other hand for professional use the licensed CAD systems are required and small and medium-sized enterprises deploy CAD software that allows designing and editing 2D and 3D engineering components (e.g., Solid Edge, Inventor, PTC Creo and others). Mass production deploys CAD systems with coherent production modules (such as in NX, Catia or SolidWorks software, etc.). One of the most common synergistic modules of CAD systems, that can be a stand-alone application, is Computer Aided Manufacturing (CAM) systems. Likewise CAD, the CAM systems are tied to the emergence and development of computer technology. CAM systems are used for comfortable tool path planning of Computer Numerical Control (CNC) machine tools [13]. The complexity of engineering elements and functional

requirements is necessary for the use of CAM systems. The output is a CNC program in the instructions for the machine tool, still the most commonly interpreted as a G-code according to standard ISO 6983 [14], [15]. The instructions for the machine are post processed from Cutter Location Data (CL data) as the output of CAM system. Firstly, CL data is used to verify the cutting tool movements of the machining operation and to detect collision among tool, workpiece and clamping devices of the machine. On the other hand, the CL data is input information to the postprocessor that translate instruction for a particular type of CNC machine with certain type of control system.

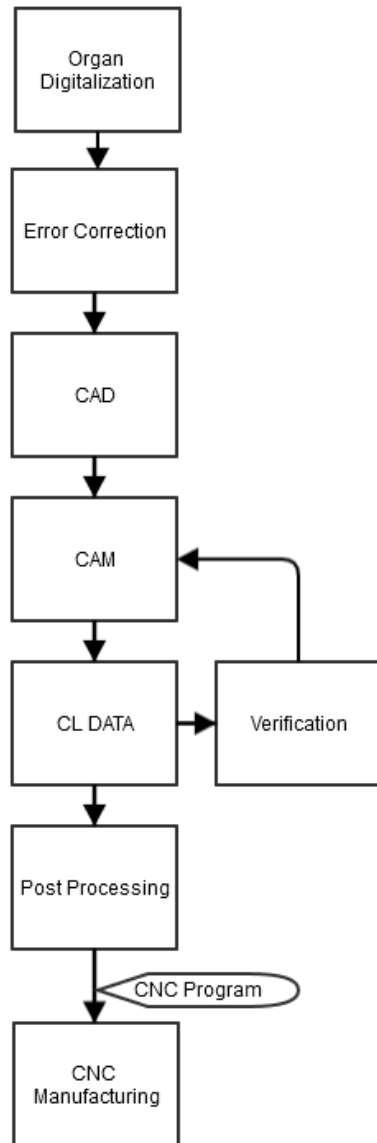


Fig. 1 Process of artificial limb production using CAD/CAM system

In recent years have been significant advances in artificial limbs and their production. New materials and technologies enable faster production of reliable prostheses [16]. This is achieved by using modern CAD/CAM systems that can semi-automatically create functional prosthesis with a realistic

appearance [17], [18]. This paper focuses on the use of CAD/CAM systems for modeling of transradial prosthetic limbs from the digitally scanned data of the existing healthy limb. The implementation was carried out in Tomas Bata University in Zlín. Figure 1 shows the flowchart of the integrated systems of 3D scanning, CAD/CAM and CNC machining as used in article.

II. 3D DATA ACQUISITION METHODOLOGY

The aim is to propose an appropriate procedure and fast method for fabrication a model of the human left upper limb amputated before the elbow. Procedure begins with examination of patient condition. The right upper limb is scanned since has no surgical intervention. When follows the implementation of the experiment is used 3D scanning device Atos II Triple Scan from GOM mbH. A characteristic of the device and setting parameters are shown in Table I. During the testing process was unsuitable direct scanning of the patient's arm. To obtain quality data was needed to make multiple scanning from different angles. The requirement is the absolute limb fixation in the same position throughout the entire scan. Although the scanning process is long and in this case in about minutes, any patient movement during scanning is the cause of the error rate of the spatial data. Has proven to be included an operation of casting arm preproduction. It is the fast process of obtaining limb imprint, into non-toxic alginate [19] casting die. This solution is advantageous in many ways: for scanning is obtained a solid limb model that can be fixed on a rotating table, thereby ensures a faster process of scanning and patient may not be present during the scanning. The material for making imprinted limb is a gypsum plaster, the material commonly used in medical application, in addition having excellent reflective properties for scanning by 3D scanner.

Table I Technical parameters of Atos II Triple Scan

Camera Pixels	2x 5 000 000
Measuring Area	2000 x 1500 mm ²
Point Spacing	0.02 – 0.79 mm
Measuring principle	Optical
Processing software	ATOS 7.5 Professional, GOM Inspect

The process of 3D data acquisition technology uses blue light spectrum in high resolution 2x5MPix with the lowest resolution 0.02 mm. The output is 3D point of cloud. While the control software to scan is the Atos Professional, for processing scan data was used GOM Inspect software SR1. Notwithstanding Atos 7.5 Professional allows working with the lowest resolution, during the scanning and processing of data was appropriate to work with a less level of detail. This results in faster processing without loss of details of the limb. Point of cloud carry information about the spatial coordinates in X, Y, Z. The data are difficult to process with engineering systems and therefore in GOM Inspect 7.5 is converted into a

polygon mesh. Such solution allows identifying defects in the scanned model and repairs them. After the reconstruction a polygon mesh is stored in the Standard Tessellation Language (STL), supported by many applications as for modeling, machining, as well as for rapid prototyping.

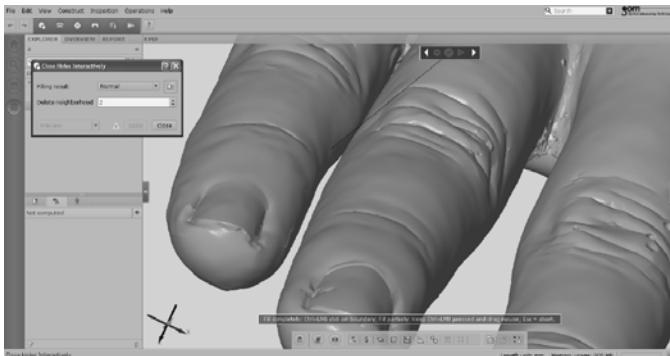


Fig. 2 Limb shape as a polygon mesh created by Atos system

III. CAD/CAM PROCESSING

The physical model of the limb is directly generated from collected spatial data. CAD/CAM systems work with a model in a graphical environment. To address adjustments is used CAD system Catia v5r18 from Dassault Systèmes. Catia allows retrieving data from STL and enables conversion into surface or volume objects. This phase is an important pre-machining step, because the model of the limb must comply with all medical requirements. Design modifications are made depending on the initial state of the patient's limb, to adjust the dimensions of the individual part, to subtract or union entities, or to improve appearance of the limb. Further, mirror transformation of the 3D model obtains the copy of the missing limb (Fig. 3).

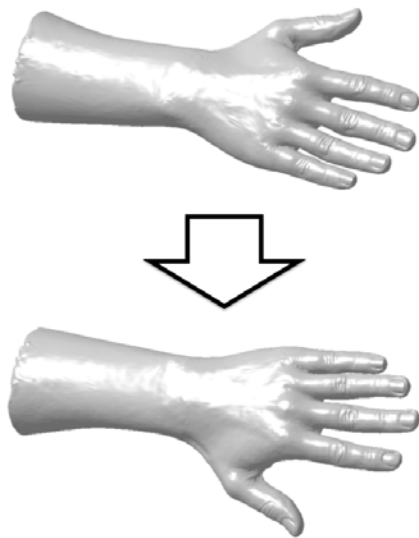


Fig. 3 Mirror transformation of the limb in CAD system

Socket is reconstructed on the resulting solid model of the limb according to amputation by subtraction of the scanned model. The most important aspect of the leg prosthesis is the

socket design - the socket is the interface between the human limb and a mechanical support system. Note that the average amputee requires three to five prostheses during five years, because of changes in the residual limb.

Preferably, the volumetric model of the limb is used for prosthesis reconstruction, but also for making cosmetic prostheses or molds for fabrication (Fig. 4). Computer CAD systems allow storing 3D models and promptly remodel to the current requirements and inexpensively create a new prosthesis custom made and particularly comfortable.

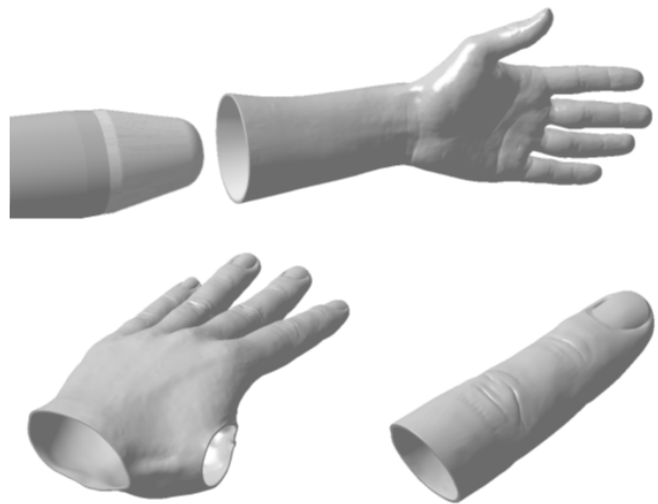


Fig. 4 Prosthesis and cosmetic covers

In order to ensure rapid production of prosthesis with the required quality offers the CAM systems necessary solution. The technology uses automated operations for creating tool paths for machining on a CNC machine tool. This study uses CAM system NX 8.5 by Siemens. NX is not limited to one machining technology: allows milling and turning in two or more axes, the automation of drilling machining, unconventional machining methods and other engineering technologies. In the case of mono block workpiece machining, first are arranged roughing operations that using large diameter tool withdraw as much material as possible in the shortest time. The surface after machining contains more or less residual material depending on the previous set of cutting conditions. It must be therefore followed by the finishing operations. Finishing operation in comparison to roughing, cuts minimum amount of material, for machining of common surfaces are used cutting tools with the radius and diameter gradually decreasing. In this case, three-axis milling technology has been used with double workpiece clamping. Cavity Mill was used as roughing algorithm, where machining takes place in the gap between the workpiece material and the model of the limb. Since the vector of the fingers of the limb is parallel to the Y axis, moreover model contains a minimum surface area of steep and therefore is applied Contour Area algorithm. Tool paths in the Contour Area are projected off the reference plane on the surface of the limb (Fig. 5), and

individual cuts take place incrementally in the parallel ZY planes.

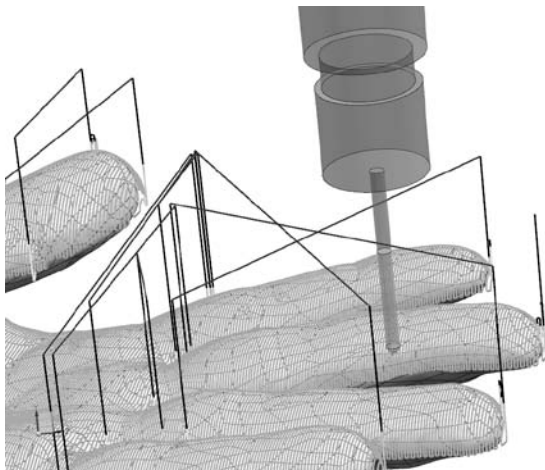


Fig. 5 Tool paths of finishing operation programmed by NX CAM system

CAM system ensures that the limb is machined to the required quality, without collisions and in the shortest possible time. To this end, the vast majority as well as NX includes a module for tool path verification and collision detection. In the event that the proposed machining strategy by CAM system is acceptable, follows a conversion of CL data into instructions for the CNC machine tool, transfer to the CNC machine and manufacturing. Below is a part of the CNC program for roughing the top of the limb model:

```
%
N0010 G40 G17 G90
;operation: Roughing1
N0020 T00 M06
N0030 G00 X129.698 Y169.794 S0 M03
N0040 G43 Z10. H00
N0050 Z-.846
N0060 G01 Z-3.846 F2500. M08
N0070 X124.698 Y169.594
N0080 G02 X120.01 Y169.5 I120. J287.
N0090 G01 X-40.
N0100 G02 X-44.698 Y169.594 I-40. J287.
N0110 G01 Y162.406
N0120 G02 X-40. Y162.5 I-40. J45.
N0130 G01 X120.
...
N5090 X.881
N5100 Y272.023
N5110 X5.881
N5120 Z-47.
N5130 G00 Z10.
N5140 M02;end of the program
```

IV. CNC MACHINING

Machining is the final step in the fabrication of the artificial limb. All data prepared in the previous steps must ensure to

build the prosthesis adapted to different medical requirements. Successful production is the result of synthesis of design data, processing conditions, but also an accurate machine tool, cutting tool and the workpiece material. In our case, for the model of the limb is selected plastic material based on polyurethane resin as shown in table II .

Table II Technical data and processing of polyurethane resin

Hardness (ISO 868)	62 Shore D
Coefficient of thermal expansion (ISO 75)	$52 \times 10^{-6} \text{ K}^{-1}$
Density	0.70 g/cm^3
Compressive strength (ISO 604)	26 N/mm^2
Flexural strength (ISO 178)	30 N/mm^2
Application	master and copy models, general modeling
Cutting tools	for wood and metal cutting

Polyurethane is physiologically harmless, has excellent processing properties, together with a fine structure and smooth and paintable surface. This material supports the use of high cutting conditions and high speed machining (HSM). It is a material that is used also in the automotive industry for the production of general models. Three-axis CNC milling HWT AZK-C442 was used, intended for plastics machining, graphite and light metals. In CAM systems were designed tool paths, optimal process conditions and tools. In the table III are listed the process parameters and associated tools from SECO company.

Table III Process parameters and cutting tools

	Roughing	Finishing
Cutting speed	314 m/min	169 m/min
Feed per tooth	0.125 mm	0.250 mm
Revolutions	$10\ 000 \text{ min}^{-1}$	$18\ 000 \text{ min}^{-1}$
Feed rate	2500 mm/min	2500 mm/min
Axial depth of cut	4 mm	-
Radial depth of cut	$75\% \times \text{Tool diameter}$	$8\% \times \text{Tool diameter}$
Tool type	End mill	Ball mill
Tool specification	SECO 93L100	SECO 971032
Tool diameter	10 mm	3 mm
Tool length	72 mm	41 mm
Flute length	52 mm	23 mm
Flutes	2	2

CAM system estimates the total cutting time based on process parameters. Roughing time was calculated to 56 minutes, while finishing operations, due to the small radial depth of cut and takes 1 hour and 32 minutes. It is necessary to consider during machining that the real processing time on CNC machines will be longer, depending on the machine type, degree of automation and tool changer and the dynamics of movements. The resulting machining time can be extended by

up to 60%. The result of processing is shown in figure 6.

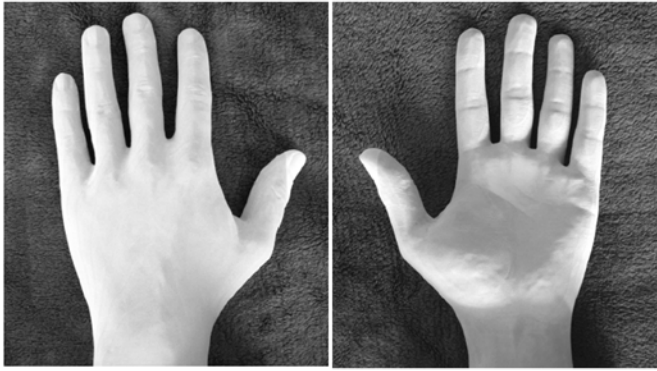


Fig. 6 Final part of the limb machined by three-axis CNC machine tool

V. CONCLUSION

The proposed process for the fabrication of artificial limb is rapid owing to the application of Computer Aided systems. Procedure includes making a plaster casting of the limb which is better for the patient, since this step requires a few minutes on average. The resulting artificial limb can be obtained by CNC machining within 4 hours. Further acceleration can be achieved by multi-axis CNC machining.

The advantage of this solution is in making solid model of the missing limbs, moreover the electronic data can be archived, as well as adjusted to custom requirements, and besides prostheses can also be created tools such as molds for casting or injection moldings.

REFERENCES

- [1] J. Farserotu, "Smart skin for tactile prosthetics," in *6th ISMIC*, 2012, pp. 1-8.
- [2] J. Sensinger, P. F. Pasquina, and T. Kuiken, "The future of artificial limbs," in *Care of the combat amputee*, Washington, 2009, pp. 721-730.
- [3] N. Antoanela and D. Gherghel, "The application of the finite element method in the biomechanics of the human upper limb and of some prosthetic components," *WSEAS Trans. Comput.*, vol. 8, no. 8, pp. 1296-1305, 2009.
- [4] N. Čuboňová, "Postprocessing of cl data in CAD/CAM system edgcam using the constructor of postprocessors," *Manuf. Technol.*, vol. 13, no. 2, pp. 158-164, 2013.
- [5] E. Franti, G. Stefan, and P. Schiopu, "Modular software for artificial arms design," *Recent Res. Autom. Cont.* pp. 387-391, 2011.
- [6] N. I. Galanis, A. P. Markopoulos, I. D. Giannakopoulos, and D. E. Manolakos, "Manufacturing of femoral heads from ti-6al-4v alloy with high speed machining: 3d finite element modelling and experimental validation," *Manuf. Technol.*, vol. 13, no. 4, pp. 437-444, 2013.
- [7] D. Koutny, D. Palousek, and T. Koutecky, "3D Digitalization of the Human Body for Use in Orthotics and Prosthetics," *World Acad. Sci. Eng. Tech.*, pp. 1487-1494, 2012.
- [8] A. E. Lam and J. O. Gomes "A methodology for human prosthesis modelling in the CAD / CAM system," in *Third Int. Conf. on Prod. R.*, 2006. pp. 1-13.
- [9] J. Lee, H. Chen, C. Luo, and K. Chang, "Rapid prototyping and multi-axis NC machining for the femoral component of knee prosthesis," *Life Sci. J.*, 2010.
- [10] T. V. Light, I. A. Gorchach, and G. J. Wiens, "Dynamic modelling of a special purpose CNC machine," in *Recent Researches in System Science - Proceedings of the 15th WSEAS International Conference on Systems, Part of the 15th WSEAS CSCC Multiconference*, 2011, pp. 207-213.

- [11] M. Mitsuishi, N. Sugita, and K. Fujiwara, "Development of a medical CAD/CAM system for orthopedic surgery," *CIRP Ann.*, vol. 56, no. 1, pp. 405-410, Jan. 2007.
- [12] A. Knaislová, M. Peterka, P. Novák, and D. Vojtěch, "Porous Ti-Si alloys for implants," *Manuf. Technol.*, vol. 13, no. 3, pp. 330-333, 2013.
- [13] A. Naaji, "Using computer-aided techniques in the dynamic modeling of the human upper limb," *WSEAS Trans. Comput.*, vol. 7, no. 7, pp. 1030-1039, 2008.
- [14] A. Naaji and D. Gherghel, "Aspects regarding the validation of mechanical solutions through the finite element method for the human upper limb," in *Proceedings of the 13th WSEAS International Conference on Computers - Held as part of the 13th WSEAS CSCC Multiconference*, 2009, pp. 71-76.
- [15] P. Salvetr, P. Novák, and D. Vojtěch, "Magnesium alloys for implants," *Manuf. Technol.*, vol. 13, no. 3, pp. 395-399, 2013.
- [16] S. Rama Murthy and M. Mani, "Design for sustainability: The role of CAD," *Renew. Sustain. Energy Rev.*, vol. 16, no. 6, pp. 4247-4256, Aug. 2012.
- [17] J. Novak-Marcincin, J. Torok, J. Barna, and L. Novakova-Marcincinova, "Technology of Perspective Scanning Methods for Realization of 3D Models of Manufacturing Devices," *Manuf. Technol.*, vol. 12, no. 13, 2012.
- [18] J. Novak-Marcincin, V. Fecova, J. Barna, M. Janak, and L. Novakova-Marcincinova, "Using of the virtual reality application with the scanning device kinect for manufacturing processes planning," *Manuf. Technol.*, vol. 13, no. 2, pp. 215-219, 2013.
- [19] K. Y. Lee and D. J. Mooney, "Alginate: properties and biomedical applications," *Prog. Polym. Sci.*, vol. 37, no. 1, pp. 106-126, Jan. 2012.

Unidirectional Coupling Scheme of Nonlinear Circuits via a Memristor

Christos K. Volos, Sundarapandian Vaidyanathan, Ioannis M. Kyprianidis, Nikos G. Bardis and Ioannis N. Stouboulos

Abstract—The fourth fundamental circuit element, the memristor, which realized in a physical model by HP’s scientists, revealed a number of applications in which memristor can be used. The most interesting of these, is in neuromorphic computing circuits, in which this new element could be used as an artificial synapse. So, in this work a first step to this approach by studying the effect of using the HP memristor in the coupling of two nonlinear circuits is made. As a circuit, the most well-known nonlinear circuit, the Chua oscillator, is chosen. The two identical circuits are coupled unidirectionally via the proposed memristor, by using a recently new proposed window function. The simulation results show an interesting dynamical behavior depending on memristor’s initial state and the parameters of the chosen window function.

Keywords—Artificial synapse, chaotic synchronization, memristor, unidirectional coupling.

I. INTRODUCTION

Until the beginning of 70ies, the electronic circuit theory has been spinning around the three known, fundamental two-terminal circuit elements, which are known as: resistor (R), capacitor (C) and inductor (L). These elements reflect the relations between pairs of the four basic electrical quantities of charge (q), current (i), voltage (v) and magnetic flux (ϕ) that mathematically can be written as:

$$\begin{aligned} dv &= R(i)di \\ dq &= C(v)dv \\ d\phi &= L(i)di \end{aligned} \quad (1)$$

However, as it can be derived from the previous equations, a relation between the charge (q) and the flux (ϕ) is missing.

Professor Leon Chua of the University of California at Berkley, in 1971, was the first to define this missing link, by introducing the fourth fundamental element based on symmetry arguments [1]. This fourth circuit element was named Memristor (M), an acronym for memory resistor, which its existence was conjectured due to the following missing

Christos K. Volos is with the Physics Department of the Aristotle University of Thessaloniki, GR-14451, Greece (+30 2310998284, e-mail: chvolos@gmail.com).

Sundarapandian Vaidyanathan is with the R & D Centre, Vel Tech University #42, Avadi-Vel Tech Road, Avadi Chennai-600062, Tamil Nadu, INDIA (e-mail: sundarvtu@gmail.com).

Nikos G. Bardis is with the Department of Military Science- Faculty of Mathematics and Engineering Sciences, Hellenic Army Academy, Greece (e-mail: bardis@ieee.org).

Ioannis M. Kyprianidis and Ioannis N. Stouboulos are with the Physics Department of the Aristotle University of Thessaloniki, GR-14451, Greece (e-mail: imkypr@auth.gr and stouboulos@physics.auth.gr).

relation between the charge (q) and the flux (ϕ).

$$d\phi = M(q)dq \quad (2)$$

The multiplicative term $M(\cdot)$ is called the memristance function.

Dividing both sides of (2) by dt one obtains

$$v = M(q)i \quad (3)$$

Memristor proved to have a very interesting behavior. As it can be shown from Eqs.(1) & (3), if M is constant, the previous equation presents nothing else, but the defining relation of a linear resistor (R). However, Chua has proved theoretically that a memristor is a nonlinear element because its v - i characteristic is similar to that of a Lissajous pattern. So, a memristor with a non-constant M describes a resistor with a memory, more precisely a resistor which resistance depends on the amount of charge that has passed through the device.

Another interesting feature of a memristor is its response to a sinusoidal input. The “pinched hysteresis loop current-voltage characteristic” is a fingerprint of this new element. So, if any element or device has a current-voltage hysteresis curve of this kind, then it is either a memristor or a memristive device. Also, the memristor has as a signature that the “pinched hysteresis loop” shrinks with the increase in the excitation frequency. The fundamentality of the memristor can also be deduced from this figure, as it is impossible to make a network of capacitors, inductors and resistors with a v - i behavior forming a pinched hysteresis curve [2].

Summarizing, the memristor has the following properties [1]:

- Non-linear relationship between current (i) and voltage (v).
- Does not store energy.
- Similar to classical circuit elements, a system of memristors can also be described as a single memristor.
- Behaves like a linear resistor for large frequencies as evident in the v - i characteristic curve.
- Memory capacity based on different resistances produced by the memristor.
- Non-volatile memory possible if the magnetic flux and charge through the memristor have a positive relationship ($M > 0$).

Furthermore, a more generalized class of systems, in regard to the original definition of a memristor, called memristive systems [2], is introduced. An n th-order current-controlled memristive one-port is represented by

(9)

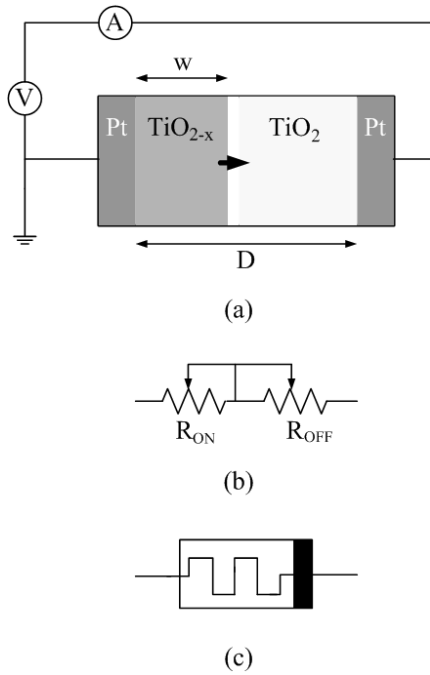


Fig. 1 (a) Structure of TiO_2 memristor, in which TiO_{2-x} and TiO_2 layers are sandwiched between two platinum electrodes, (b) equivalent circuit and (c) symbol of the memristor.

So, the dynamics of the memristor can therefore be modeled through the time dependence of the width (w) of the doped region. Integrating Eq.(9) with respect to time,

$$w = w_0 + \frac{\mu_v R_{ON}}{D} q(t) \quad (10)$$

where (w_0) is the initial width of the doped region at $t = 0$ and (q) is the amount of charges that have passed through the device. Substituting (6), (10) into equation (7) gives:

$$M(q) = R_0 - \frac{\mu_v R_{on} \Delta R}{D^2} q(t) \quad (11)$$

where

$$R_0 = R_{ON} \frac{w_0}{D} + R_{OFF} \left(1 - \frac{w_0}{D}\right) \quad (12)$$

and $\Delta R = R_{OFF} - R_{ON}$. The term (R_0) refers to the net resistance at $t = 0$ that serves as the device's memory. This term is associated with the memristive state, which is essentially established through a collective contribution, i.e. it depends directly on the amount of all charges that have flown through the device. That's why, we can say that the memristor has the feature to "remember" whether it is "ON" or "OFF" after its power is turned on and off respectively.

The model of memristor which has been presented by HP scientists, does not take into consideration the boundary

effects, as the speed of the boundary between doped and undoped regions get suppressed at either edge. For this reason, Biolek et al. proposed an alternative window function which considers the boundary speeds of the approaching and receding from the thin film edge [22]. This function (Fig.2) is given as:

$$F_p(x) = 1 - (x - \text{stp}(-i))^{2p} \quad (13)$$

where (p) is a positive integer, (i) is the memristor's current, which is considered to be positive if it increases the width of the doped layer, or $x \rightarrow 1$ and

$$\text{stp}(i) = \begin{cases} 1, & \text{if } i \geq 0 \\ 0, & \text{if } i < 0 \end{cases} \quad (14)$$

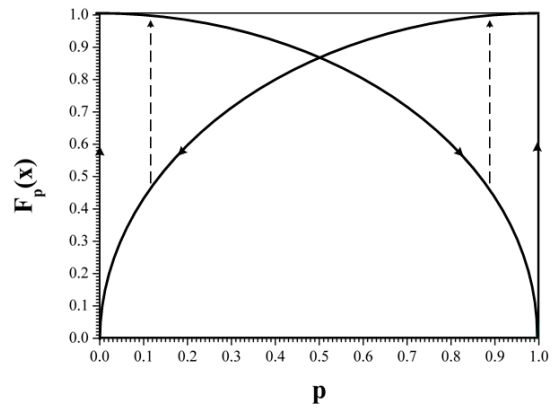


Fig. 2 The window function proposed by Biolek et al.

III. THE COUPLING SCHEME

For studying the effect of the HP's memristor as a coupling element between coupled chaotic circuits the unidirectional coupling, have been used. In this coupling scheme one system drives another one and the system described by the following set of differential equations [23]:

$$\begin{cases} \dot{x}_1 = F(x_1) \\ \dot{x}_2 = F(x_2) + C(x_1 - x_2) \end{cases} \quad (15)$$

In this work, as a nonlinear circuit, the Chua oscillator, which is structurally the simplest and dynamically the most complex member of the Chua's circuit family, is chosen [24]-[26]. Until now, a great number of nonlinear phenomena concerning chaos theory have been discovered by using the specific circuit. This is the reason for choosing the Chua oscillator as a nonlinear circuit in this work.

The dynamics of the unidirectionally coupled Chua oscillators via an HP memristor (Fig.3(a)) is described by the following set of differential equations:

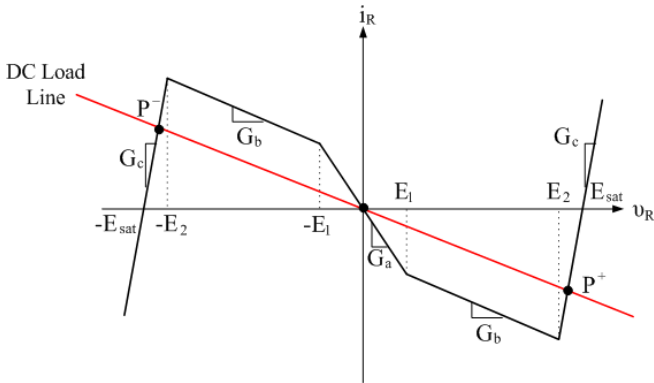


Fig. 4 The five-segment v - i characteristic of the nonlinear element N_R

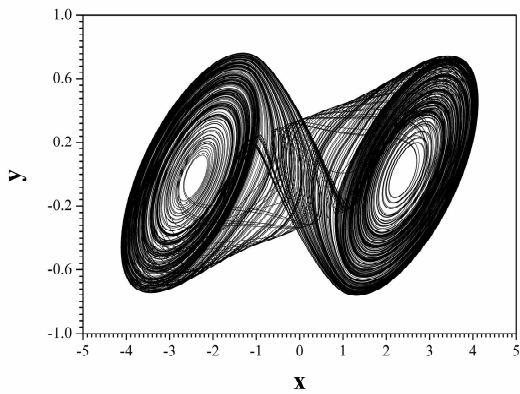


Fig. 5 The projection on the x - y plane of the double-scroll chaotic attractor of the Chua oscillator

$(x_1 - x_2)$ and so of the state of the second coupled circuit. As it is shown in Fig.6(b), the difference signal is changed due to the change of the oscillation of the second circuit around the two equilibrium points (Fig.6(c)). So, the state of the second circuit and the state of the memristor affect its other.

In Figs.6(d)-(e) the effect of the resistance (R_{OFF}) in system's behavior is shown. From these figures it is deduced that when (ω) varies the range around its initial value ($\omega_0 = 0.5$) is reduced by increasing the value of R_{OFF} .

Finally, by increasing the value of the parameter (p) of the window function the range of the state variable (ω) increases (see Figs.7(a)-(d)). This means that the space-charge region (x) of the memristor tends to cover all the range (D) of the titanium dioxide layer ($x = D$), as in the case of mutual coupling. Also, with this window function, the variable reaches the upper limit ($\omega = 1$) and the lower limit ($\omega = 1$) without remain therein, but oscillates chaotically around a value near to these ones. Also, with the increasing of the value of the parameter (p) the duration of the memristor's staying in these two states increases, as it is clearly shown in Figs.7(b)-(d). In Figs.7(e)-(h) the phase portraits of x_2 vs. x_1 and y_2 vs. x_2 , for $p = 10$, are shown.

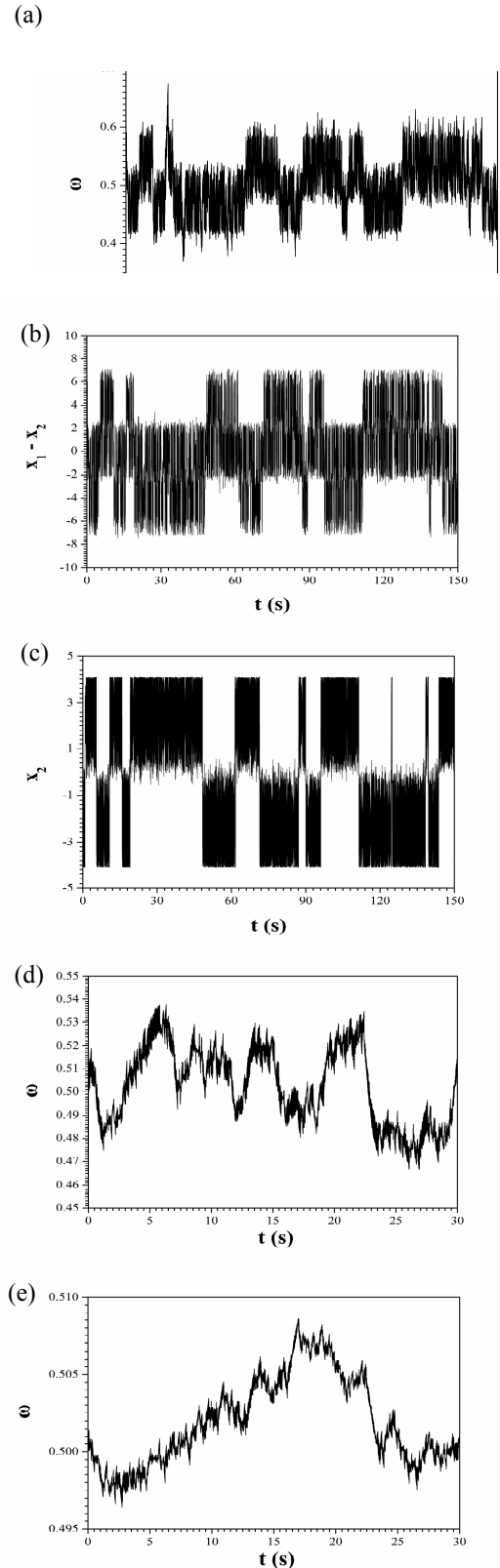


Fig. 6 Time-series of the normalized variable (ω) of the width of the doped region, the difference signal $(x_1 - x_2)$ and the signal (x_2) , in (a)-(c) for $R_{OFF} = 1 \text{ k}\Omega$ and $p = 1$ and time-series of the normalized variable (ω) of the width of the doped region for (d) $R_{OFF} = 10 \text{ k}\Omega$ and (e) $R_{OFF} = 100 \text{ k}\Omega$

- [3] D. Strukov, G. Snider, G. Stewart, and R. Williams, "The missing memristor found," *Nature*, vol. 453, pp. 80–83, 2008.
- [4] M. Sapoff and R. M. Oppenheim, "Theory and application of self-heated thermistors," in *proc. of the IEEE*, vol. 51, pp. 1292–1305, 1963.
- [5] Y. V. Pershin and M. Di Ventra, "Spin memristive systems: Spin memory effects in semiconductor spintronics," *Physics Review B*, vol. 78, pp. 113309/1–4, 2008.
- [6] Y. Chen, G. Y. Jung, D. A. A. Ohlberg, X. M. Li, D. R. Stewart, J. O. Jeppesen, K. A. Nielsen, J. F. Stoddart, and R. S. Williams, "Nanoscale molecular-switch crossbar circuits," *Nanotechnology*, vol. 14, pp. 462–468, 2008.
- [7] Y. V. Pershin and M. Di Ventra, "Experimental demonstration of associative memory with memristive neural networks," *Neural Networks*, vol. 23, pp. 881, 2010.
- [8] Y. V. Pershin, S. La Fontaine, and M. Di Ventra, "Memristive model of amoeba learning," *Physics Review E*, vol. 80, pp. 021926/1–6, 2009.
- [9] T. Chang, S.-H. Jo, K.-H. Kim, P. Sheridan, S. Gaba, and W. Lu, "Synaptic behaviors and modeling of a metal oxide memristive device," *Applied Physics A*, vol. 102, pp. 857–863, 2011.
- [10] M. Laiho and E. Lehtonen, "Cellular nanoscale network cell with memristors for local implication logic and synapses," in *proc. IEEE of International Symposium on Circuits and Systems (ISCAS 2010)*, pp. 2051–2054, 2010.
- [11] B. Linares-Barranco and T. Serrano-Gotarredona, "Memristance can explain spike-time-dependent-plasticity in neural synapses," in *proc. of Nature*, pp. 1–4, 2009.
- [12] M. Itoh and L. O. Chua, "Memristor oscillators," *International Journal of Bifurcation and Chaos*, vol. 18, pp. 3183–3206, 2008.
- [13] B. Muthuswamy and P. P. Kokate, "Memristor based chaotic circuits," *IETE Technical Review*, vol. 26, pp. 415–426, 2009.
- [14] B. Muthuswamy, "Implementing memristor based chaotic circuits," *International Journal of Bifurcation and Chaos*, vol. 20, pp. 1335–1350, 2010.
- [15] Ch. K. Volos, I. M. Kyprianidis, S. G. Stavrinos, I. N. Stouboulos, and A. N. Anagnostopoulos, "Memristors: A New approach in nonlinear circuits design," in *proc. 14th WSEAS International Conference on Communications*, pp. 25–30, 2010.
- [16] Ch. K. Volos, I. M. Kyprianidis, I. N. Stouboulos, and C. Cepisca, "Complex dynamics of a memristor based Chua's canonical circuit," in *Recent Researches in Communications and IT, Proc. 15th WSEAS International Conference on Communications*, pp. 111–116, 2011.
- [17] J. Hrusak, M. Stork, and D. Mayer, "On chaotic behavior of a class of linear systems with memristive feedback control," in *proc. of the 13th WSEAS International Conference on Systems*, pp. 28–29, 2009.
- [18] V. Biolkova, Z. Kolka, Z. Biolek, and D. Biolek, "Memristor modeling based on its constitutive relation," in *proc. of the European Conference of Circuits Technology and Devices, World Scientific and Engineering Academy and Society (WSEAS)*, pp. 261–264, 2010.
- [19] S. Banerjee, *Chaos synchronization and cryptography for secure communications: Applications for encryption*, U.S.A.: IGI Global, 2010.
- [20] S. Boccaletti, J. Kurths, G. Osipov, D.L. Valladares, and C.S. Zhou, "The synchronization of chaotic systems," *Physics Reports*, vol. 366, pp. 1–101, 2002.
- [21] A. Pikovsky, M. Rosenblum, and J. Kurths, *Synchronization: a universal concept in nonlinear sciences*, New York: Cambridge University Press, 2001.
- [22] Z. Biolek, D. Biolek, and V. Biolkova, "Spice model of memristor with nonlinear dopant drift," *Radioengineering*, vol. 18, pp. 210–224, 2009.
- [23] I. M. Kyprianidis, Ch. K. Volos, S. G. Stavrinos, I. N. Stouboulos, and A. N. Anagnostopoulos, "Master-slave double-scroll circuit incomplete synchronization," *J. Engineering Science & Technology Review*, vol. 3, pp. 41–45, 2010.
- [24] L. O. Chua, C. W. Wu, A. Huang, and G.-Q. Zhong, "A universal circuit for studying and generating chaos - Part I: Routes to chaos," *IEEE Trans. Circuits Syst.*, vol. CAS-40, pp. 732–744, 1993.
- [25] L. Fortuna, M. Frasca, and M. G. Xibilia, *Chua's circuit implementations: Yesterday, today and tomorrow*, Singapore: World Scientific, 2009.
- [26] C. W. Wu and L. Pivka, *From Chua's circuit to Chua's oscillator: A picture book of attractors*, Singapore: World Scientific, 1994.

Investigation of thermal degradation of vegetable oils during frying using terahertz time-domain spectroscopy

Marie Tobolova and Vojtech Kresalek

Abstract—This paper deals with Terahertz Time Domain Spectroscopy (THz-TDS) of the vegetable oils commercially available for the preparation of hot meals. There were investigated the samples of fresh oils and the same oils thermally prepared. The optical parameters in the frequency range of 0.4 – 0.8 THz are calculated, statistically analyzed and evaluated. Based on the results, the samples of oils (before heating and after it) are compared to determine whether the THz-TDS method could be used for detecting the thermal changes that occur during the oil heating.

Keywords—frying oils, thermal degradation, THz time domain spectroscopy, vegetable oil.

I. INTRODUCTION

LAST few decades years, a big boom came in the propagation of healthy eating habits and healthy food preparation, because series of common diseases come from the bad lifestyle, diet and stress. These “modern” problems form the basis of diseases of civilization that were not so common in previous generations. We could mention the heart diseases, obesity, diabetes mellitus, cancer illness and some chronic diseases. The greatest blame is often given to excessive consumption of fats and sugars that are usually not of the natural origin. These are often contained in calorie bombs that generally miss any really necessary components for our metabolism. On the other hand, we cannot forget the fats are also important because of some unique substances contained. Therefore, it depends both on the quantity and quality. Moreover, the oil is necessary component for the preparation of most meals whether it is cooking, baking, frying or flavoring. Especially frying is very popular but also the least healthy method. To a certain extent, we can manage the quality of the meal by using the appropriate oil, i. e. to distinguish the oils for cold and hot meals, and by following the recommended conditions for storage and also the

This paper is supported by the European Regional Development Fund under the project CEBIA-Tech No. CZ.1.05/2.1.00/03.0089.

Marie Tobolova is with the Department of Electronics and Measurements, Tomas Bata University, Zlin, Czech Republic (corresponding author, phone: +420 576 035 228; e-mail: tobolova@fai.utb.cz). She is at the same time the Ph.D. student of the Department of Biomedical Engineering, Brno University of Technology, Brno, Czech Republic.

Vojtech Kresalek is with the Department of Electronics and Measurements, Tomas Bata University, Zlin, Czech Republic (e-mail: kresalek@fai.utb.cz).

principles of their preparation, especially thermal processing. It is known that some changes occur during heating the oil. These changes are detectable by various chemical methods. The aim of this study is to find out if the THz-TDS system is suitable alternative method for investigation of the changes caused by thermal degradation during pan frying.

II. MATERIALS AND METHODS

A. Instrumentation

Two types of edible oil were the objects of this study. There were included refined oils made from sunflower seeds and rapeseed. These oils are widespread in hot meals preparation. Two samples of each oil were prepared: one taken directly from the bottle and one heat treated. Finally, four samples were available for measurement. The heat-treated samples were prepared by heating the oil to the temperature around 170°C in the pan and this temperature was maintained for 3 minutes. The optimal temperature of frying was indicated by small piece of bread. After this period, the oil was left to cool and the sample was taken out. These samples of oils were marked as a “heated”.

THz-TDS system Tera OSCAT by MenloSystems, Ltd. was used as a analyzing device in this experiment. It operates on the traditional pump and probe principle but unlike other similar systems it uses a new approach for time-resolved experiments without moveable optical delay lines. The delay line is controlled electronically and consequently, it allows the precise step scan as well as the rapid scan, therefore the measurements are very fast [1].

B. Experimental Design

The samples of oils were prepared in a liquid form at room temperature 24°C for measurement. A glass Petri dish was filled with the amount of 1 ml of just investigated oil. The average thickness of the dish bottom was about 1606.6 microns and the thickness of the oil layer moved in the range 900 – 1171 microns, therefore the thickness of the whole two-layer structure was around 2.6 millimeters. The measurement was carried out immediately after the filling Petri dish to prevent oxidation processes of the oil.

The experimental adjustment has standard transmission geometry. The laser source is a mode-locked femtosecond

Er-doped fiber oscillator producing 90 fs pulses at 1560 nm with a repetition rate of 250 MHz [2]. The fs laser beam is divided into two pulses, one for exciting the emitter antenna to produce the THz pulse, and the second for activating the receiver antenna to measure the THz signal. THz pulse passes through the investigated sample (oil in Petri dish) and the signal reflecting the interaction with sample is detected. THz-TDS relies on comparing this THz response with the same THz pulse transmitted only through the air (reference measurement). Reference (air), empty Petri dish and each sample (Petri dish with oil) were measured ten times.



Fig. 1 Design of experiment, transmission geometry

C. Data analysis

The refractive indices for all samples were calculated using the TeraMat software. These calculations require a priori information about the sample thickness. The results needed other mathematical corrections because the measured values were not the parameters of the oil itself but the Petri dish included. All measured data were processed in tables and statistically evaluated. The software Statistica 8 by Statsoft Company was used for statistical analysis of the measured data.

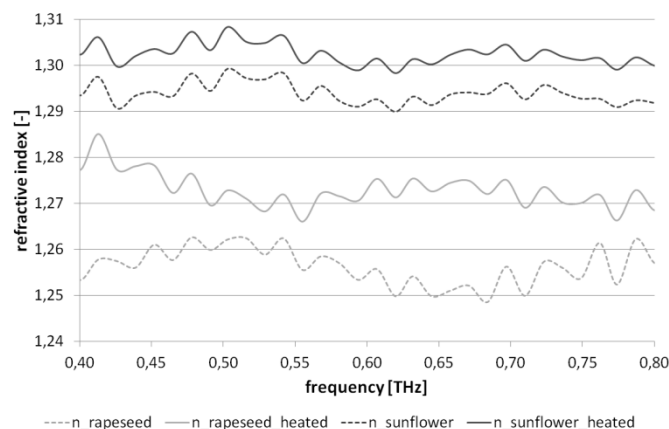


Fig. 2 Refractive indices of the normal/heated oils measured in the frequency range of 0.4 – 0.8 THz

Because of the Fabry-Perot artifacts' influence, the frequency range of 0.4 – 0.8 THz was taken into account. Ten measurements of refractive index in this frequency range for each sample were averaged. Fig. 2 shows the dependence of calculated refractive indices on frequency. At first sight, it is obvious that each type of oil has different range of refractive index; it can be seen also in the descriptive statistics (Table I).

Table I Descriptive Statistics of Refractive Indices for normal/heated oils measured in frequency range 0.4 - 0.8 THz

	Mean	Median	Minimum	Maximum	Std.Dev.	Standard - Error
n_rapeseed	1,257	1,257	1,249	1,263	0,005	0,001
n_rapeseed heated	1,273	1,273	1,266	1,285	0,004	0,001
n_sunflower	1,294	1,294	1,290	1,230	0,003	0,001
n_sunflower heated	1,303	1,303	1,299	1,309	0,003	0,001

For detailed analysis, the original data from ten measurements for each oil were considered. The frequencies 0.4 THz, 0.6 THz and 0.8 THz were chosen for the analysis. The descriptive statistics of the data is summarized in Table II. According to histograms for all variables (oil/oil_heated), the non-normal distribution of the data was evident. Therefore, the nonparametric statistics was used.

Table II Descriptive Statistics of Refractive Indices of oils for 0.4 THz, 0.6 THz and 0.8 THz

	Mean	Median	Minimum	Maximum	Std.Dev.	Standard - Error
rapeseed_0.4THz	1,254	1,255	1,240	1,264	0,001	0,003
rapeseed_heated_0.4THz	1,278	1,277	1,273	1,281	0,004	0,002
rapeseed_0.6THz	1,250	1,251	1,239	1,260	0,008	0,003
rapeseed_heated_0.6THz	1,272	1,272	1,268	1,276	0,004	0,002
rapeseed_0.8THz	1,258	1,259	1,243	1,269	0,010	0,004
rapeseed_heated_0.8THz	1,269	1,271	1,263	1,274	0,006	0,002
sunflower_0.4THz	1,294	1,294	1,292	1,296	0,002	0,001
sunflower_heated_0.4THz	1,303	1,303	1,301	1,305	0,002	0,001
sunflower_0.6THz	1,290	1,290	1,290	1,294	0,002	0,001
sunflower_heated_0.6THz	1,230	1,298	1,296	1,301	0,002	0,001
sunflower_0.8THz	1,292	1,293	1,288	1,295	0,003	0,001
sunflower_heated_0.8THz	1,300	1,300	1,297	1,306	0,003	0,001

For the comparison of normal and heated oils, the nonparametric paired design of the Wilcoxon test was used. The null hypothesis of no difference between the normal and heated type of each oil was tested at significance level 0.05. The results were summarized in Table III and Table IV.

Table III Wilcoxon Matched Pairs Test for Rapeseed Oil samples (tests are significant at $p < 0.05$)

	T	Z	p-level
rapeseed_0.4THz & rapeseed_heated_0.4THz	0,000	2,521	0,012
rapeseed_0.6THz & rapeseed_heated_0.6THz	0,000	2,521	0,012
rapeseed_0.8THz & rapeseed_heated_0.8THz	0,000	2,521	0,012

Table IV Wilcoxon Matched Pairs Test for Sunflower Oil samples (tests are significant at $p < 0.05$)

	T	Z	p-level
sunflower_0.4THz & sunflower_heated_0.4THz	0,000	2,803	0,005
sunflower_0.6THz & sunflower_heated_0.6THz	0,000	2,803	0,005
sunflower_0.8THz & sunflower_heated_0.8THz	0,000	2,803	0,005

Next step was the Cluster Analysis, the method of multivariate statistics. Cluster Analysis is able to distinguish between more and less similar objects considering the distance between them. The resulting tree diagram based on the complete-linkage clustering of the distance matrix shows the precise separation of the heated and normal oils at all frequencies, see Fig. 3.

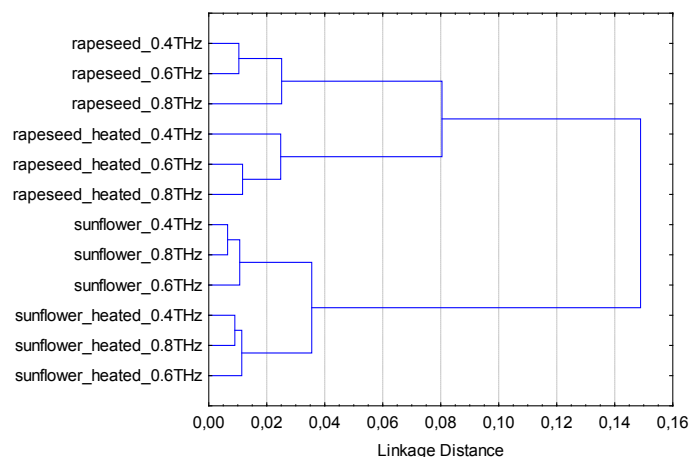


Fig. 3 Tree Diagram based on the complete linkage clustering of the Euclidean distances between normal/heated types of oils at frequencies 0.4 THz, 0.6 THz, and 0.8 THz

III. RESULTS

The aim of the whole experiment was to investigate if the thermal changes that occur during heating the oil are

detectable by THz time-domain spectroscopy. First, the averaged refractive indices of all measured oil samples were plotted in specific frequency range to get the basic information about properties of examined data (Fig. 2). Each type of oil has its typical range of refractive index values; 1.257 ± 0.005 for rapeseed oil and 1.294 ± 0.003 for sunflower oil. Finding differences between these oils and their heated form is much more important. As it could be seen in Fig. 2, a clear boundary between heated and normal sample is visible at both oils. The shift to higher values is evident at both heated samples ($n_{rapeseed_heated}$, $n_{sunflower_heated}$). Further, it could be observed greater deviation of heated rapeseed oil from its normal form compared with the sunflower oil. If the square deviations of two forms of oils are calculated in each frequency and summarized, the sum of squares (SS) can be evaluated. The SS values confirm the previous assumption; the $SS_{rapeseed}$ of 0.01 shows a greater difference between the normal/heated forms of rapeseed oil than sunflower with $SS_{sunflower}$ equal 0.003. Moreover, the curves differ also in shape. While the curves for sunflower oils to some extent correlate, the curves for rapeseed oils are not very similar. These remarks were supported also by descriptive statistics (Table I).

For other analysis, there were chosen three frequencies in measured THz range; 0.4 THz, 0.6 THz, and 0.8 THz. Basic properties of all groups (marked as: type_of_oil_frequency) are summarized in descriptive statistics Table II, again. Normality of the data was analyzed using normal probability plots and histograms and it was not confirmed. Therefore, the nonparametric statistics was chosen for other investigation. The results of Wilcoxon matched pairs test (see Table III and Table IV) showed that the refractive indices of normal oils are significantly different from heated samples of the same oils. The null hypothesis could be rejected for both the rapeseed and sunflower oil ($p < 0.05$).

The conclusion of Wilcoxon test was checked by the Cluster analysis. All twelve variables (normal/heated oils at given frequency) form the basis of the distance matrix which defines the degree of similarity of the objects (variables). The final tree diagram shows clear separation of heated and normal forms of both oils, and also the good differentiation of sunflower and rapeseed oils. First, the separate clusters of normal sunflower, heated sunflower, normal rapeseed and heated rapeseed oil formed, next the clusters determining the type of oil established, i. e. sunflower and rapeseed oil.

IV. DISCUSSION

For pan frying, a variety of oils may be used. Their physical and chemical properties influence the reactions that occur during frying, but there are other multiple factors playing the role; the mode of frying, applied frying temperature, length of frying, and type of food being fried [3]. At relatively high temperatures, the lipid oxidation occurs and produces compounds that affect the food flavor but also its quality. The oxidative changes are associated with a decrease in the unsaturation of the fat and with increases in the free fatty acid

content, content of polar compounds and polymeric material, foaming, color, and viscosity. Quality of fats can be evaluated by standard physical (molecular weight, smoke point, refractive index, chromatic parameter, viscosity, surface tension, dielectric constant) and chemical methods (iodine value, saponification value, free fatty acid content, peroxide value etc.). The degree of oxidation could be also tested by spectroscopic methods (infrared and nuclear magnetic resonance technique), and chromatography provides both qualitative and quantitative evaluation of oxidative changes. In order to prevent oxidation, the natural and synthetic antioxidants are added in fats and fat-containing food. Generally, antioxidants increase the oxidative stability of the oil and the antioxidant activity can be also measured. [4]

For this experiment, two most frequently used oils were chosen and purchased at the shop; refined sunflower oil, representing a high linoleic vegetable oil, and refined rapeseed oil as a high oleic vegetable oil. The sunflower oil contains up to 90% combination of oleic and linoleic acids (of which 60 – 75% of linoleic acid), and virtually no linolenic acid. Rapeseed oil typically contains 56% of oleic, 26% of linoleic, 10% of linolenic and traces of palmitic and stearic acids and less saturated acids than any other oil [5]. Obviously, there are considerable differences in the chemical composition but they have some common properties such as near smoke point (209°C for sunflower, 218°C for rapeseed) and iodine number (136 for sunflower, 120 for rapeseed) [6]. Further, the both oils contain antioxidants that can be natural or artificially added [7], [8]. Generally, the greater iodine number and lower smoke point as well as the lower content of antioxidants make the stability of the oil lower. Therefore, the rapeseed oil should have better stability and also high temperature resistance. This hypothesis is also supported by the study [9].

According to measured data, sunflower oil shows higher refractive index in THz frequencies than rapeseed. This corresponds with values of classical optical refractive index for both oils [6]. Sunflower oil seems to be more stable than rapeseed oil as the difference between the normal and heated form is lower. But this hypothesis disagrees with the previous statements; therefore the additional detailed chemical analysis

is necessary, because for instance the content of the antioxidants that could play the role in our samples is unknown. For this reason, we cannot exactly determine which oil is really more stable. Other statistical analyses show the good differentiation between oils without heating and oils passed elevated temperature during frying.

V. CONCLUSION

The experiment shows the capability of THz time-domain spectroscopy to study the oils and their changes. Based on the results, we present the possibility to use THz-TDS as a relatively low-cost screening method for detecting the thermal changes that occur in the oil during pan frying.

REFERENCES

- [1] R. Wilk et al. "OSCAT: Novel Technique for Time-Resolved Experiments Without Moveable Optical Delay Lines," *Journal of Infrared, Millimeter and Terahertz Waves*, vol. 32, May 2011, pp. 596 – 602.
- [2] *TERA OSCAT: User manual*. MenloSystems, GmbH, Martinsried, Germany, 2013.
- [3] Ch. Gertz. "Fundamentals of the frying process," *European Journal of Lipid Science and Technology*, vol. 116, April 2014, pp. 1 – 6.
- [4] F. Shahidi and Y. Zhong. "Lipid Oxidation: Measurement Methods," in *Bailey's Industrial Oil and Fat Products*, 6th ed. vol. 6, F. Shahidi, Ed. New Jersey: John Wiley & Sons, Inc., 2005, pp. 357–385.
- [5] F. Shahidi and Y. Zhong. "Vegetable Oils," in *Bailey's Industrial Oil and Fat Products*, 6th ed. vol. 6, F. Shahidi, Ed. New Jersey: John Wiley & Sons, Inc., 2005, pp. 213–267.
- [6] M. Bockisch. "*Fats and Oils Handbook*," Hamburg: AOCS Press, 1998, pp. 90 – 120.
- [7] M. Cvjetko. "Antioxidant properties of rapeseed," *Zbornik radova Tehnološkog fakulteta u Leskovcu*, vol. 19, September 2009, pp. 27 – 33.
- [8] E. O. Aluyor and M. Ori-Jesu. "The use of antioxidants in vegetable oils – A review," *African Journal of Biotechnology*, vol. 7, issue 25, December 2008, pp. 4836 – 4842.
- [9] Ch. Gertz, S. Klostermann, S. P. Kochhar. "Testing and comparing oxidative stability of vegetable oils and fats at frying temperature," *European Journal of Lipid Science and Technology*, vol. 102, issue 8 – 9, October 2000, pp. 543 – 551.

Architecture and Design of a Dynamic Real-Time Alarm System for Power Plants

Ilse Leal Aulenbacher, *Member, IEEE*, José María Suárez Jurado, and Efrén R. Coronel Flores

Abstract—In the context of power plants, alarm systems aid operator by bringing their attention to abnormal conditions that require attention. However, a common problem with this kind of systems is that alarms can become ineffective when too many alarms are presented. Another problem is that alarms may not be relevant in relation to a power plant current operation conditions. In this paper, we present a series of strategies we have incorporated into the architecture and design of a Real-Time Dynamic Alarm System. We believe that hierarchical organization of alarms and dynamic alarm processing with respect to power plant operation conditions can help solve these problems.

Index Terms—alarm processing, power plant, real-time.

I. INTRODUCTION

ALARMS are defined as “an audible and/or visible means of indicating to the operator an equipment malfunction, process deviation, or abnormal condition requiring a response [1]. Although alarm systems have been used for a long time, there are some problems that make managing alarms difficult and can even become a burden to operators.

One common problem is that too many alarms may be presented to an operator during mode changes or plant transients [2]. Operators need to analyze each alarm to determine what needs to be done. Therefore, operators may be able to properly handle only a limited number of alarms at a given time. If too many alarms are presented at the same time, the process of handling alarms may prove too time-consuming and may become a burden. In fact, research suggests one alarm in ten minutes (about 150 alarms per day) can be considered acceptable. Even up to two alarms in ten minutes can be manageable. However, anything higher than that, can hinder an operator’s capacity to properly manage alarms [3].

Another problem is that certain alarms may not be relevant with respect to a power plant operation mode. In many cases, alarm limits are configured assuming certain ideal operation conditions. However, it is important to recognize that operation conditions often change dynamically. For instance, if a power plant is undergoing maintenance, certain alarms might not be relevant anymore.

In this paper, we describe our approach in trying to solve these problems. In section II, we describe our systems main architectural drivers and design principles. In section III, we describe how we intend to tackle the problem of presenting too many alarms to operators by categorizing and processing alarms through a hierarchical arrangement that models power plant structure. We then describe, in section IV, how our system uses alarm hierarchy to handle alarms that have not been acknowledged for a considerable amount of time. Section V describes how we address the issue of alarms being irrelevant

with respect to power plant operation conditions by defining dynamic alarm plans. We then describe our system architecture in section VI. Finally, we present our conclusions and future work.

II. KEY DESIGN PRINCIPLES

To design our system architecture, we first identified the most important requirements for our system. One important aspect is that our alarm system will be integrated to a real-time data acquisition system (DAS) for a nuclear power plant. This system acquires, processes and stores data in real-time from multiple data sources [4] [5]. Therefore, our architecture must meet strict performance and reliability criteria.

Since one of our main objectives was to organize alarms so that they would be congruent with power plant organization and division of responsibilities, flexibility was another key consideration. Therefore, although our system will be integrated to a specific power plant, our design allows it to be highly configurable, so that it can be configured for other power plants.

In the next sections, we describe the main strategies we incorporated into our system design in order to make it capable of presenting relevant alarms to operators and adapting dynamically to power plant operation conditions.

III. ALARM SUBSYSTEMS

We base our alarm subsystems strategy on the premise that alarms are useful when presented to operators that actually find them relevant. Our approach is based on the idea of dividing alarms into *alarm subsystems*. An alarm subsystem is basically a category of alarms.

Power plants or any big system for that matter, can usually be subdivided into smaller parts or *subsystems*. For example, in a power plant we can have a turbine subsystem, a reactor subsystem, an electric subsystem, etc. Each subsystem is usually under the responsibility of an operator. Because subsystems are not isolated, their relationships can be represented through a hierarchical organization. This organization should be carefully modeled based on the actual power plant structure. Fig. 1 shows an hypothetical and very simplified example of how a hierarchical subsystem arrangement could look like in a nuclear power plant. In this example, on the lower level there are two subsystems: electric (*EL*) and turbine (*TR*). These subsystems, are overseen by an auxiliary operation (*AO*) subsystem. At the same time, the auxiliary operation subsystem is supervised by the main control room subsystem (*CR*), which also oversees the reactor (*RE*) subsystem. We

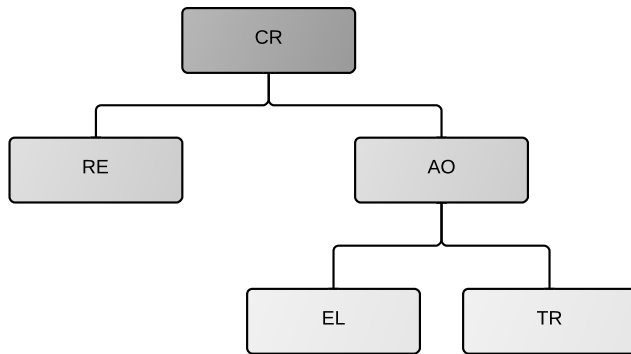


Fig. 1. An example alarm subsystem hierarchy

will use this example in the next sections to illustrate how our alarm subsystem works.

In our design, when alarms are configured, they are assigned to a specific alarm subsystem. Ideally, each alarm subsystem should be assigned to the operator responsible for it in the power plant.

When operators log into our system, they can manage alarms that are assigned to them. When we refer to managing alarms, we mean the action an operator takes to acknowledge or reset an alarm. For instance, if the user responsible for the auxiliary operation (AO) subsystem logs in, he can view and manage alarms that belong to the auxiliary operation subsystem itself. This is a good first step, but because alarm subsystems are arranged hierarchically, there are certain important considerations. If the system is too restrictive and limits users to their own subsystems, dividing alarms may become impractical. For that reason, we consider that hierarchy should play an important role on how alarms are managed and presented. Looking again at our example in Fig. 1, if an OA operator logs in, shouldn't he be able to supervise EL or TR alarms? At the same time, should an EL operator be able to see OA alarms? To solve this issue, we decided to take a flexible approach and thus, based our alarm management system on the following principles:

1) *Operators can view and manage alarms that belong to their own subsystem:* For example, an EL operator would be able to manage EL alarms.

2) *Operators can view alarms from a subsystem in a lower hierarchy level:* Operators should be able to supervise and take actions on alarms directly under them in the subsystem hierarchy. For instance, if an OA operator logs in, he can view and manage both EL and TR alarms.

3) *Operators can view alarms from a subsystem at a higher hierarchy level:* It is easy to see that operators should not be able to manage alarms from a higher hierarchy level, since such alarms are not under their responsibility. However, operators may occasionally need to see alarms in a higher hierarchy level. With this in mind, our system allows operators to view alarms from the subsystem directly above them in the hierarchy; yet, it does not allow them to manage such alarms.

With this approach, not all alarms are presented to all operators. Rather, alarms are categorized so that certain alarms

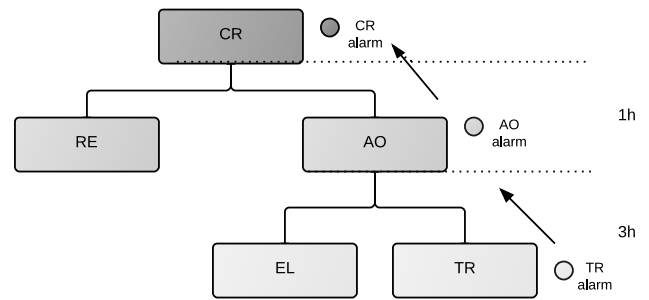


Fig. 2. Example alarm timeout

are presented to operators who will find them relevant. In section I, we mentioned that presenting too many alarms to operators can become unmanageable. By dividing alarms into subsystems, we can help to address this issue by presenting fewer alarms to operators.

IV. TIMEOUTS

In section III, we described how we designed our system to tackle the issue of presenting too many alarms to a single operator. However, another important key principle in our design was to promote good division of responsibility practices. One way to do so is by implementing mechanisms that ensure that alarms are actually managed. For instance, there may be a case where an operator notices an alarm and postpones handling it because he is busy monitoring other events or is not sure what to do about it at that time. After a while, the operator may end up forgetting such alarm. In these cases, it may be useful to bring such alarm to the attention of the subsystem directly above it in the hierarchy.

To achieve this, we designed a mechanism where each subsystem has a *timeout*. This means that if an alarm is not acknowledged within a certain period of time, it will be assigned to the subsystem above it in the hierarchy.

Returning to the example hierarchy shown in Fig. 1, let us suppose that an alarm is raised in the TR subsystem. Let us also suppose that this subsystem has a timeout of three hours. If an TR alarm is not acknowledged within those three hours, our system would move the alarm to the AO subsystem. Therefore, if for some reason an TR operator was unable to manage the alarm, an operator one level higher in the hierarchy (in this case, AO) would be able to see it and manage it. Similarly, let us suppose the AO subsystem has a timeout of one hour. If the alarm is not acknowledged within one hour, it would be moved to the CR subsystem. This example is illustrated in Fig. 2.

Timeouts are configurable and assigned in a per-subsystem basis. This provides greater flexibility, because the system can adapt to the needs and policies of each power plant.

V. ALARM PLANS

For an alarm system to be effective, alarm limits must be configured properly. Most data acquisition systems are designed to operate for extended periods of time. Hence, it is important to recognize that power plant operation conditions

are likely to change at certain times. Therefore, we consider that it is important for alarm systems to take this into consideration.

In order to address this issue, we propose the concept of *dynamic alarm plans*. An alarm plan is a configuration file that specifies a group of data points with their corresponding alarm limits, among other parameters. In our system design, several alarm plans can be defined, one for each set of operation conditions. For example, we can define an alarm plan for normal operation conditions and another one for “under maintenance” conditions.

Our system supports any number of different alarm plans. Some plants might find it easier to define one alarm plan at first. Other plants might require to define several alarm plans in order to have better alarm management when certain systems are under maintenance.

These alarm plans can enter or go out of processing dynamically, either manually or automatically.

- **Manually.** An operator can manually specify which alarm plan will be used at a given time. Usually, such operation is limited to the operator assigned to the subsystem highest in the alarm subsystem hierarchy.
- **Automatically.** Alarm plans can be associated with an arbitrary data point, which we call “operation-mode data point”. Such data point is assumed to have several discrete states, which should indicate the operation conditions of the plant. For instance, a data point value of zero could be associated to normal operation and a value of one to operation under maintenance. Our design assumes that the process of assigning the correct value to the operation-mode data point is a black box. This is to ensure that our system can be easily adapted to different data acquisition systems and power plants.

VI. SYSTEM ARCHITECTURE

A high-level view of our system architecture is shown in Fig. 3. The diagram shows how key modules, databases and shared memory areas interact. Before describing the architecture in detail, we give an overview of the main elements in our application: shared memory areas, databases and modules.

A. Shared memory areas and databases

As we mentioned in section II, our alarm system will be integrated to a real-time data acquisition system. Therefore, performance is one of our main architectural drivers. For that reason, we decided to load alarm system databases (such as alarm plans) into Shared Memory Areas (SMAs). Shared memory is the fastest form of inter-process communication (IPC) available [6]. This mechanism allows several processes to exchange data efficiently by sharing a memory area. Since information contained in our system databases need to be read by several processes without compromising performance, the use of shared memory areas is ideal. Our databases are stored as text files on disk and then copied to shared memory. Our main databases are:

- **Subsystems database.** Contains a list of alarm subsystems and their hierarchy. It also contains configuration parameters such as a timeout for each subsystem.
- **Operation mode database.** In this database is where power plant operation modes can be configured. As we mentioned earlier, the number of operation modes can vary depending on the power plant requirements. Each operation mode is associated with an alarm plan.
- **Alarm plans.** These databases contain a list of data points to be monitored in real-time to determine if an alarm must be triggered. As we mentioned above, the number of alarm plans that must be configured depends on how many operation modes were defined.

Our shared memory areas are organized as follows:

- **Alarm Plans SMA.** During the initialization phase of our alarm system, alarm plans are loaded to memory. A shared memory segment is created for each alarm plan database.
- **Alarm Configuration SMA.** This area of memory contains both the operation mode database and the subsystems database.
- **Active Alarms SMA.** During the execution of our system, both the Alarm Configuration SMA and Alarm Plan SMAs are mostly read-only. However, the Active Alarms memory area is updated each second to reflect current alarms and their status (acknowledged, reset, etc.).

B. Modules

Our system is divided into the following key modules:

- **Alarm Configuration.** This module validates and manages alarm plans.
- **Operation Mode.** Determines the power plant operational mode. If a data point is associated with the operational mode (*operation-mode data point*, which was described in section V), it constantly monitors its value. It also handles requests for manual operation mode changes. This module is very important because its functionality is what enables dynamic alarm processing. Depending on the current operation mode in the plant, this module switches to the correct alarm plan, which becomes the *active alarm plan*.
- **Alarm Detection.** This is the core module in our system, since it analyzes values and states of the data points, which appear in the active alarm plan. This module also analyzes each alarm to determine if its timeout has expired.
- **Historical Archive.** Generates a circular historical archive that records each alarm, as well as alarm-related events.
- **Alarm List.** Manages detected alarms, keeping them organized in chronological order.
- **Alarm Operations.** Manages operations that can change an alarm status, such as acknowledging an alarm.

C. Architecture diagram

Fig. 3 shows how our main system elements interact. The Alarm Configuration module reads the subsystem, operation

mode and alarm plan databases. Through the Alarm Plans module, alarm plans are validated and loaded into shared memory areas.

Similarly, operation mode and subsystem databases are loaded into the Alarm Configuration SMA. The Operation Mode module uses the information in this memory area to determine the Power Plant operation mode and switch alarm processing to the corresponding alarm plan.

Alarm Plans are used by the Alarm Detection Module to read important information such as alarm limits from the current active alarm plan. This module also interacts with the Active Alarms memory by updating the alarm list.

Both the Alarm Detection and Alarm Operations module interact with the Historical Archive module to record any changes in alarm status.

VII. CONCLUSIONS

In this paper, we described a real-time alarm system architecture that incorporates different strategies to present alarms in a more efficient way. Strategies such as dividing alarms in categories and establishing an alarm hierarchy can help avoid problems such as presenting operators with too many alarms. Our architecture was designed so that this system can be adapted to different power plant configurations. This system is in its final development phase and initial functional tests have been successful.

VIII. FUTURE WORK

We would like to evaluate how our alarm processing strategies impact how operators manage alarms by obtaining further feedback from operators.

REFERENCES

- [1] "ANSI/ISA-18.2-2009 Management of Alarm Systems for the Process Industries," 2009.
- [2] "Advanced control room alarm system: Requirements and implementation guidance," EPRI, Technical Report, 2005.
- [3] B. H. Wayne Crawford, "Better management of plant alarms," *Energy-Tech Magazine*, May 2010.
- [4] I. L. Aulenbacher, J. M. S. Jurado, and E. R. C. Flores, "A real-time data acquisition system for the Laguna Verde nuclear power plant," *W. Trans. on Comp.*, vol. 9, no. 7, pp. 778–787, July 2010. [Online]. Available: <http://dl.acm.org/citation.cfm?id=1852450.1852461>
- [5] I. L. Aulenbacher and J. M. S. Jurado, "A data acquisition system for the laguna verde nuclear power plant," in *Proceedings of the 8th WSEAS international conference on Data networks, communications, computers*, ser. DNCOCO'09. Stevens Point, Wisconsin, USA: World Scientific and Engineering Academy and Society (WSEAS), 2009, pp. 142–146. [Online]. Available: <http://dl.acm.org/citation.cfm?id=1670344.1670365>
- [6] W. Stevens, *UNIX Network Programming: Interprocess Communications*, 2nd ed. Prentice Hall, 1999, vol. 2.

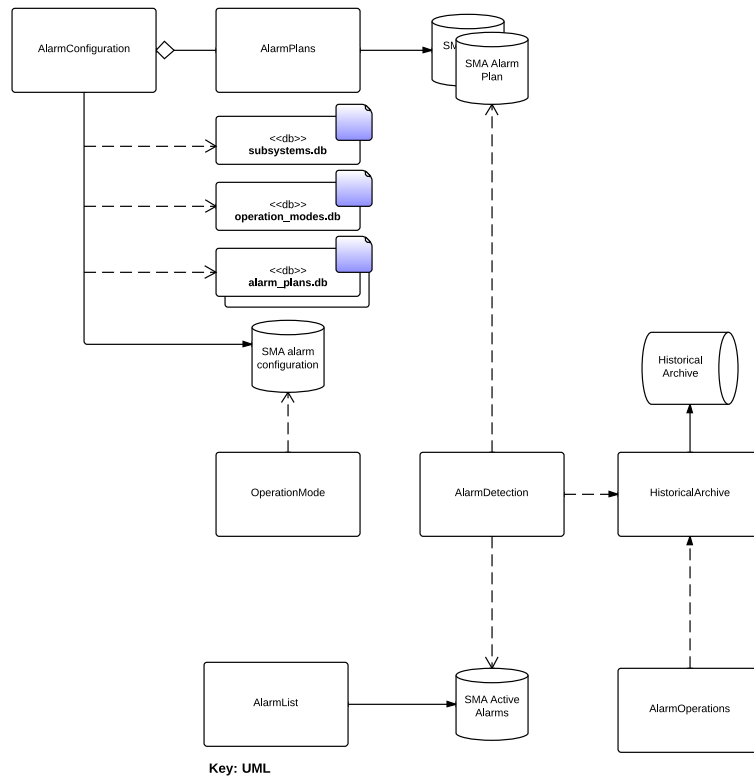


Fig. 3. An example alarm subsystem hierarchy

Measuring and Identification of Oils

Hana Vaskova and Martina Buckova

Abstract—For the process control of oils quality, both in terms of food technology and in terms of maintaining the nutritional value of edible oils, it is necessary to look for methods of measurement that are fast, independent of the number of chemicals, portable and whose measurement procedure can be automated, which conventional laboratory procedures cannot be. Raman spectroscopy is an effective tool for material identification that offers these benefits. This paper presents an innovative method of using Raman spectroscopy for various edible oils identification and the determination of their degradation products based on monitoring changes in the characteristic vibration peaks in the Raman spectra depending on the duration of their heating. The result is the ability to use this method to verify the appropriate maximum heat load at which there is no undesired decomposition of the oil.

Keywords—Edible oils, identification, measurement, Raman spectra, thermal degradation

I. INTRODUCTION

LIPIDS are an irreplaceable part of the human diet. They represent not only a major source of energy, but their functional properties also participate in a large extent in metabolism, they are a component of biomembranes and other biologically active substances carriers, especially lipid-soluble vitamins. From this point of view the intake of vegetable oils is very important. Except saturated fatty acids they also contain a substantial proportion of mono- and polyunsaturated fatty acids. These unsaturated fatty acids represent on one hand the health benefit of edible oils in their consumption by humans or livestock, but on the other hand also a source of instability of oils in the process of technological processing, storage or cooking.

Therefore it is very important to monitor changes in the quality of edible oils from the source of raw material (oil content in seeds, fruits, etc.) until their usage by the final user either as food or as highly popular dietary supplements. The most frequently observed adverse changes are just in oils with higher content of polyunsaturated fatty acids. Double bonds are sensitive to external factors causing the degradation of these double bonds to form degradation products based on peroxides, acids, aldehydes and ketones.

This work is supported by the Ministry of Education, Youth and Sports of the Czech Republic, by European Regional Development Fund under the project CEBIA-Tech No. CZ.1.05/2.1.00/03.0089.

Hana Vaskova is with the Faculty of Applied Informatics, Tomas Bata University in Zlin, nám. T. G. Masaryka 5555, 760 01 Zlín, Czech Republic (e-mail: vaskova@fai.utb.cz)

Martina Buckova is with the Faculty of Technology, Tomas Bata University in Zlin, nám. T. G. Masaryka 5555, 760 01 Zlín, Czech Republic (e-mail: buckova@ft.utb.cz)

The conventional methods for fatty acids determination are generally used for the quality of vegetable oils evaluation as well as for degradation products of unsaturated fatty acids monitoring. These methods are mostly based on volumetric methods or chromatography techniques, mainly gas chromatography coupled to FID or MS detector, what require the use of reagents and solvents that might be hazardous, also time consuming sample pre-treatment and necessary laboratory equipment. Example of the importance of all described features is published in [1]. Described demands represent main reasons why methods noted above are not proper for process control purposes. From this point of view Raman spectroscopy is a very promising technique that is rapid, does not require any sample preparation, no reagents are needed, measurements are relatively simple. Another advantage is the possibility to obtain Raman spectra via transparent covering layers from glass or plastic. Raman spectroscopic measurements seem to be practically applicable for automated measurements on the basis of the features of this innovative method.

II. THEORY

A. Edible oils

Vegetable oils are the important source of saturated and mostly unsaturated fatty acids, which are essential for humans as was mentioned above. Evaluation of the oils health benefits is based on fatty acids composition: mainly on high content of monounsaturated and polyunsaturated fatty acids. There is palmitic acid (C16:0) and stearic acid (C18:0) as the main saturated fatty acids in vegetable oils, their concentration is quite low compare to unsaturated fatty acids except coconut oil. Oleic acid is the major monounsaturated fatty acid (C18:1), linoleic acid (C18:2) and linolenic acid (C18:3) are the major polyunsaturated fatty acids. Each one of vegetable oils is characterized by its own specific fatty acids ratio content [2-4].

According to high level of double bonds presented in edible oils they are quite sensitive to oxidative conditions generated many degradation products, including aldehydes, ketones, epoxides, hydroxy compounds, oligomers and polymers. The content of these oxidation products can correspond to oil technological treatment, method and duration of storage and it has undesirable influence on nutritional quality, safety and sensory properties [5].

The oxidative degradation of oils can be increased by heating under 100°C. Using Raman spectroscopy chemical changes corresponding to C=C bond during oxidation as well as degradation products formation is expected to be reflected in spectral changes [6].

Edible oils analysis is actually developing field for application of Raman spectroscopy. Collecting the real spectra is fast and quite easy, the quantitative determination is more difficult. The complexity of Raman spectra requires the use of advanced spectra treatment approaches [7]. Raman spectroscopy combined with chemometrics has been successfully used for characterization of different kinds of edible oils [8], for quantitative detection of extra virgin olive oils adulterated with cheaper edible oils [9,10], for quantitative analysis of enriched virgin olive oil with other ingredients such as aromatic plant to improve its culinary, cosmetic and medicinal properties [7]. The quality control of olives for producing high-quality olives [11] and prediction of oil content of soybeans are published too [12]. Raman spectroscopy seems to be a suitable tool for recognizing oxidative deterioration of oil, for monitoring lipid oxidation process [6, 13].

B. Raman spectroscopy

In principle, Raman spectroscopy as a vibrational spectroscopic method has the potential to answer a number of questions related to chemical details of molecular structure what makes this technique definitely proper for material identification [14]. This method becomes a valuable part of laboratories around the world in recent years.

Raman spectroscopy provides very specific chemical „fingerprint“ of every single chemical substance in the form of the Raman spectrum. The method is based on so called Raman scattering. Raman scattering is an inelastic scattering resulting from an interaction of a photon and a molecule. In inelastic scattering photons have slightly changed wavelengths that are characteristic for specific bonds in surveyed material. Since most photons are on molecules scattered elastically (Rayleigh scattering i.e. without changing the wavelength), it is necessary to filter out of the spectrum of the strongly present wavelength of laser. Diagram of the measurement using Raman spectroscopy is shown in Fig.1.

Although the fundamental phenomenon is known since thirties of the 20th century, its effective use in Raman spectroscopy occurs in about last decade. The rebirth of this method goes hand in hand with advances in technology: powerful lasers as sources of monochromatic light, efficient Notch filters transmitting all the wavelengths except the excitation wavelength of the laser, sensitive detectors and last but not least computer technology.

Raman spectroscopy brings many advantages. The method is:

- Relatively rapid, Raman spectra can be acquired within seconds.
- Non-destructive what allows undergoing investigated samples further analyses or simply repetition of Raman analyses.
- Contactless what is convenient, samples are not contaminated, also it is advantageous when toxic, dangerous samples or those with strong aroma are measured. There also exists a possibility of measuring samples through transparent glass or polymeric covering layers or containers.

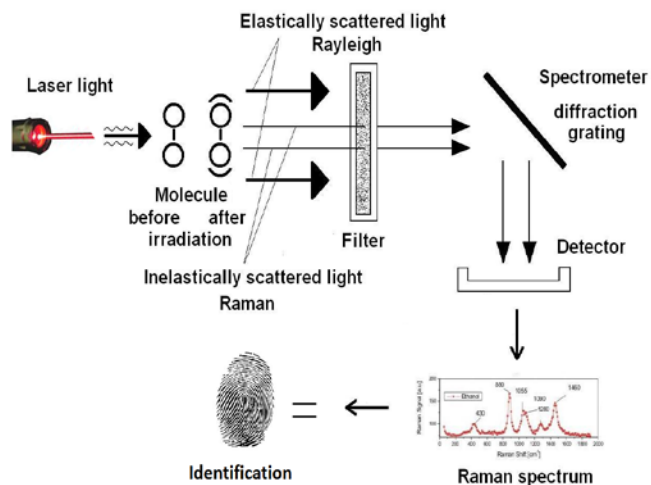


Fig. 1 Laser irradiate the sample, molecules vibrate, filter eliminates intense Rayleigh scattering, the grating disperses the light onto a detector to generate a spectrum, which gives the information about molecule bonding and provides a chemical fingerprint utilizable for identification.

Raman spectra of the covered sample and the cover can be then subtracted via software.

- Applicable to all states of matter and different its forms (crystals, powders, fibres, solutions, etc.).
- Without special requirements for sample preparation, what is convenient and prompt.
- Usable as in situ analysis.

The greatest drawback of the method is the fact that Raman scattering is a weak effect. Luminescence as much stronger quantum effect with bigger intensity can overlap Raman spectra and mask spectral information. Another disadvantage is eventual degradation of a sensitive sample when using intense laser beam [15].

Raman spectroscopy finds many applications in recent years in a number of scientific areas such as chemistry, biochemistry, material science, mineralogy, arts, medicine, also is used for pharmaceutical or forensic and security purposes.

III. EXPERIMENTAL PART

A. Samples

Fourteen samples of oils were used for spectroscopic analysis: pumpkin oil, grape seed oil, hemp oil, coconut oil, almond oil, olive oil, Milk thistle oil, groundnut oil, wheaten oil, rice oil, canola, sesame oil, sunflower oil and safflower oil. All of these oils were purchased from common supermarkets.

Sunflower oil was used to monitor the thermal degradation process. Sunflower oil was heated up to 160 ° C, the temperature was maintained, while continually stirred, and after every 30 minutes the samples were taken and consequently analyzed on a Raman microscope.

B. Instrumentation

Raman spectra of all samples were measured by Renishaw InVia Basis Raman microscope. The Raman instrument uses two lasers as light sources: argon ion laser with the excitation wavelength 514 nm and maximum output power of 20 mW and 785 nm NIR diode laser with maximum output power 300mW. Both were tested but more precise results were obtained using NIR laser.

A Leica DM 2500 confocal microscope with the resolution 2µm was coupled to the Raman spectrometer. All measurements were collected with 30 s exposure time and 10 accumulations. The samples were firstly scanned in range 100 to 3200 cm⁻¹ with 2 cm⁻¹ spectral resolution. After determining the principle peaks the spectral range was reduced approximately to the area 800 - 1800 cm⁻¹.

C. Results

Raman spectrum of sunflower oil is displayed in Fig.2. To evaluate and identify edible oils there are five essential bands in the range 1200 – 1800 cm⁻¹ in Raman spectra which can be correlated with the most important parts of the molecular structure. Bands and their assignments are presented in table 1.

Raman spectra of different oils are mostly alike in the distribution of characteristic peaks, shown in Fig.3. This is due to the content of similar components such as triacylglycerols,

saturated and unsaturated fatty acids with straight aliphatic chains and predominantly with 16 or 18 number of carbon atoms in chains. Each oil has, however various ratios of these components what affects the intensity of the peaks and can be used for their identification.

Fig. 4 shows these differences for Raman bands 1267cm⁻¹ and 1303 cm⁻¹ for different types of oil. Spectra were normalized. As an internal standard was taken 1747 cm⁻¹ band which does not exhibit any changes in the structure

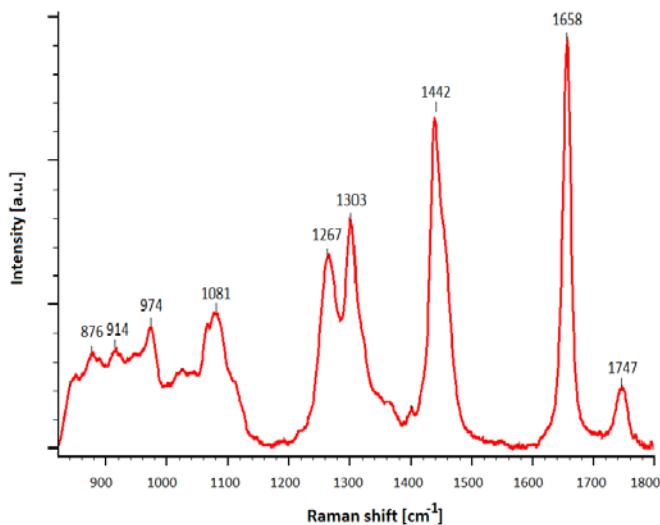


Fig. 2 Raman spectrum of sunflower oil

Table 1 Raman bands and their assignments

Wavelength	Assingment
1276	=C-H symmetric rocking
1303	CH2 in-phase twist
1442	CH2 scissoring
1658	C=C cis double bond stretching
1747	C=O ester-carbonyl stretching

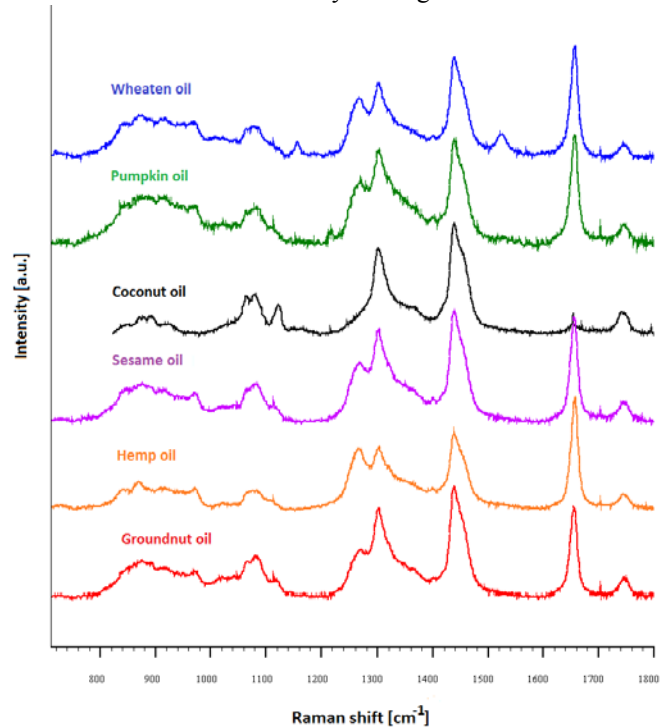


Fig. 3 Raman spectra of six different oils: wheaten, pumpkin, coconut, sesame, hemp and groundnut.

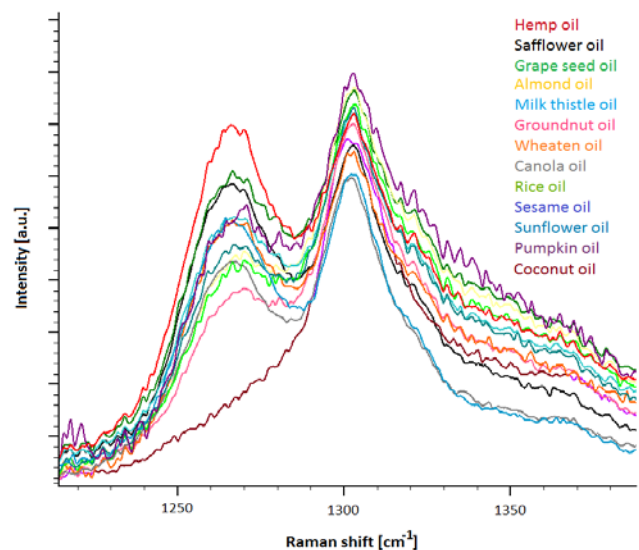


Fig. 4 Focus on characteristic bands 1267cm⁻¹ and 1303 cm⁻¹ for different oils

corresponding to C=O ester carbonyl band. It is obvious that oils such as sunflower, wheaten, safflower, pumpkin or grape seed have higher share of linoleic acid than for example groundnut, almond, rice or olive oil and also coconut which has the most dissimilar composition. These results can be confirmed by the known amounts of C18:2 [2-4].

Raman spectroscopy was also successfully used for monitoring thermal degradation of edible oils. In other words changes of characteristic peaks corresponding to the formation of degradation products were observed mainly at 1640 cm⁻¹ as is shown in Fig. 5. This band can be assigned to formation of *trans*, *trans*-2,4-decadienal as a major decomposition product of heated oxidized linoleate which corresponds to the C=C stretching vibration in conjugated system [6].

Thermal degradation can be described by a linear dependence of increasing Raman intensity at 1640 cm⁻¹ on time, shown in Fig. 6. Intensities were acquired using normalization via 1747 cm⁻¹ band and subtraction of the intensity at the room temperature.

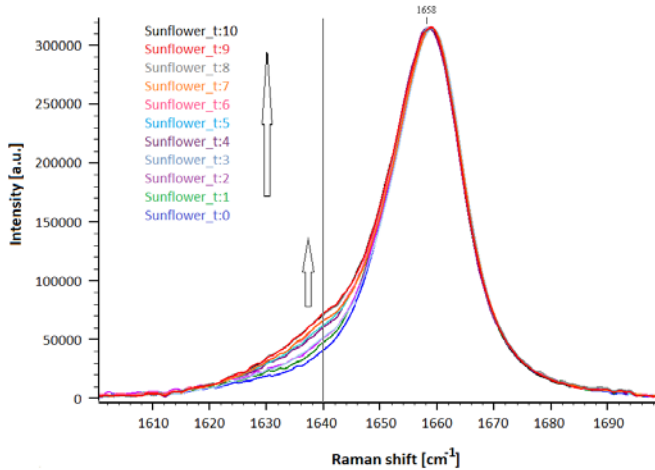


Fig. 5 Raman spectra of increasing 1640 cm⁻¹ band pertaining to the product of thermal degradation

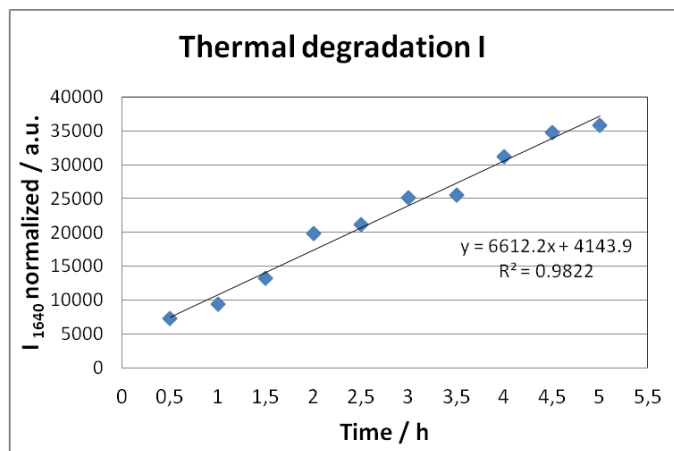


Fig. 6 Thermal degradation product formation: the dependence of normalized intensity of 1640 cm⁻¹ on time

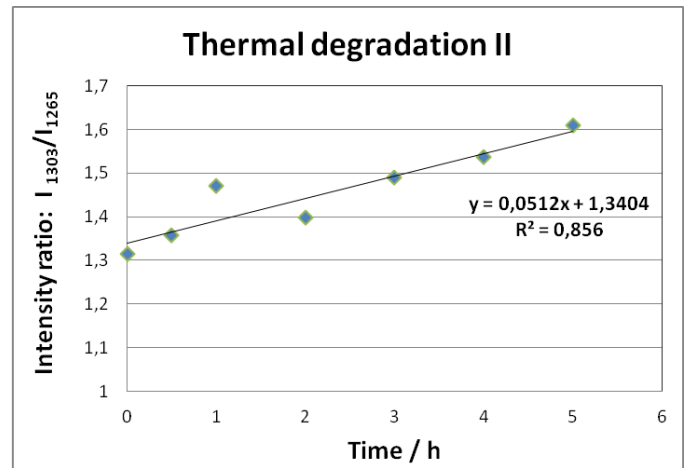


Fig. 7 Thermal degradation related to the increase of Raman intensity ratio I₁₃₀₃/I₁₂₆₇ on time corresponding to amount variety of saturated and unsaturated bonds.

As a result of oil heating C=C double bonds downgrade while the amount of CH₂ bonds increase. This behavior is represented by the changes of Raman intensity: decrease at 1276 cm⁻¹ and coincidental rise up at 1303 cm⁻¹. That means the ratio I₁₃₀₃ / I₁₂₆₇ grows in time as demonstrate Fig. 7. The thermal degradation can be then observed on several different spectral parameters.

IV. CONCLUSION

Raman spectroscopy was used as an innovative method for edible oils identification and monitoring their thermal degradation. Results acquired in this study show that on the basis of characteristic ratios of unsaturated fatty acids contained in oils it is possible to distinguish different species. Further the thermal stress of sunflower oil can be monitored and evaluated via the amount of arising degradation products. Raman spectroscopic evaluation of mentioned features brings advantages over traditional methods mainly in sense of rapidity, simplicity and no need of chemical reagents and sample preparation, what saves time and costs.

REFERENCES

- [1] Vávra Ambroyová, J., Mišurcová, L., Vicha, R., Machů, L., Samek, D., Baron, M., Mlček, J., Sochor, J., Juříková, T. Influence of Extractive Solvents on Lipid and Fatty Acids Content of Edible Freshwater Algal and Seaweed Products, the Green Microalga *Chlorella kessleri* and the Cyanobacterium *Spirulina platensis*. *Molecules*. 2014, 19, 2344-2360.
- [2] Rajah K.K.: Fats in food technology. Sheffield: Sheffield Academic Press. 2002, 379pp. ISBN 0-8493-9784-7
- [3] Zambiasi R.C., Przybylski R., Zambiasi M.W., Mendonca C.B.: Fatty acid composition of vegetable oils and fats. *B.CEPPA, Curitiba*, v. 25, n.1, p.111-120, 2007
- [4] Fathi-Achachlouei B., Azadmard-Damirchi S.: Milk thistle seed oil constituents from different varieties grown in Iran. *Journal of the American Oil Chemists Society* 86, 7, 643-649, 2009
- [5] Barriuso B., Astiasarán I., Ansorena D.: A review of analytical methods measuring lipid oxidation status in foods: a challenging task. *Eur Food Res Technol* 236:1-15, 2013
- [6] Muik B., Lendl B., Molina-Diaz A., Ayora-Canada M.J.: Direct monitoring of lipid oxidation in edible oils by Fourier transform Raman spectroscopy. *Chemistry and Physics of Lipids* 134, 173-182, 2005

- [7] Omar J., Sarmiento A., Olivares M., Alonso I., Etxebarria N.: Quantitative analysis of essential oils from rosemary in virgin olive oil using Raman spectroscopy and chemometrics. *J. Raman Spectrosc.* 43, 1151-1156, 2012
- [8] Dong W., Zhang Y., Zhang B., Wang X.: Quantitative analysis of adulteration of extra virgin olive oil using Raman spectroscopy improved by Bayesian framework least squares support vector machines. *Anal. Methods* 4, 2772, 2012
- [9] Zhang X., Zou M., Qi X., Liu F., Zhang C. Yin F.: Quantitative detection of adulterated olive oil by Raman spectroscopy and chemometrics. *J. Raman Spectrosc.* 42, 9, 1784-1788, 2011
- [10] Lopez-Diez E.C., Bianchi G., Goodacre R.: Rapid quantitative assessment of the adulteration of virgin olive oils with hazelnut oils using Raman spectroscopy and chemometrics. *J. Agric. Food Chem.* 51, 6145-6150, 2003
- [11] Guzman E., Baeten V., Pierna J.A.F., Garcia-Mesa J.A.: A portable Raman sensor for the rapid discrimination of olives according to fruit quality. *Talanta* 93, 94-98, 2012
- [12] Lee H., Cho B.K., Kim M.S., Lee W.H., Tewari J., Bae H., Sohn S.I., Chi H.Y.: Prediction of crude protein and oil content of soybean using Raman spectroscopy. *Sensors and Actuators B* 185, 694-700, 2013
- [13] Machado N.F.L., Batista de Carvalho L.A.E., Otero J.C., Marques M.P.M.: The autooxidation process in linoleic acid screened by Raman spectroscopy. *J. Raman Spectrosc.* 43, 9, 1991-2000, 2012
- [14] CHALMERS, John M, Howell G EDWARDS a Michael D HARGREAVES. *Infrared and Raman spectroscopy in forensic science*. 1st pub. Chichester, West Sussex, UK: Wiley, 2012, 618 p. ISBN 978-0-470-74906-7.
- [15] COLTHUP, Norman B, Lawrence H DALY a Stephen E WIBERLEY. *Introduction to infrared and Raman spectroscopy*. 3rd ed. San Diego: Academic Press, 1990, xii, 547 p. ISBN 0-12-182554-x.

Tensional Psychological Mechanism and the Topological Invariants of the Tensional Configurations

Alin Gilbert Sumedrea

Abstract—The paper presents an alternative theory of the functionality of the tensional psychological mechanism, starting from the hypothesis that psychological dynamics is aligned with physiological dynamics and is also aligned with scenic dynamics in which the person plays an apparently impossible role of actor and spectator at the same time. The psyche as a generator of internal tensions is specialized in the reading of certain tensional configurations which are capable of generating action. Four pairs of tensional configurations are evinced and two of these are read only once. Each pair of tensional configurations is characterized by a topological invariant. The manner and the order in which these configurations are read explain behaviour complexity and also the experiences of life which seem to be independent!

Keywords—Euler characteristic, psychological system, reader of tensional configurations, tensional configurations.

I. INTRODUCTION

THE idea of considering the person as an entity endowed with specific motivational and attitudinal resources responds to certain unanimously recognized expectations (the right to work, to teach, to be in complete charge of his/her own life). The overlapping of a scene over a coherent psychological dynamics is not enough to accredit the idea that the psychological entity disposes of an internal resource which is capable of creating, confirming or multiplying successful models. The irresistible temptation to produce attitudinal patterns which are conform to time and to perceptible realities is thwarted by the person's incapacity to modify realities in a manner capable of changing any impulse into a gratified desire.

Persons as psychological engines are reactive to present scenes. The existential details seem to be restricted to the person's freedom to interpret a scenic representation which is identical at the perceptual level but particularized at the introspective level. The attempt to assess the importance of the scene and the response of the actors to this scene hides an important clue. Both aspects are equally important, even though the level of reporting is different. If the playing out of the scene constitutes in itself a justification for the dynamics of creation, the response of the actors to the scene seems to represent a good answer to justify life and its quality.

Alin Gilbert Sumedrea is with the Department of Psychology, Lucian Blaga University of Sibiu, Romania (e-mail: alin.sumedrea@gmail.com).

Furthermore, both aspects are synchronous and this fact suggests a rigid alignment of them.

Psychological disorders as atypical behaviour could be the result of a deficient alignment between the dynamics of internal resources and external dynamics. Inadequate alignments, in the above sense, are the result of certain patterns capable of explaining them. What is the source of these patterns? Claiming that patterns are activated instantly gives rise to further questions of the type: do these patterns have a preconscious capable of anticipating correctly a scenic dynamics? Are there elements which subordinate the behaviour dynamics?

The uniqueness of the person as a psychological entity is justified by a particularized pattern which is only intelligible as interpreted for past facts. But this reality could be extended to the whole life of the person. The negation of any association between the existence of a person and a superior reason which governs it would lead to the idea that nature allows itself to waste resources on an undefined target, or even to the idea that played out realities do not carry consequences. However, species evolve towards the saturation of their capacity to reveal areas of reality which are accessible to them and thus implicitly necessary. The scenic overlapping over a specific pattern of action can prove the presence of masks of attitudinal and adaptive resources specific to them in the sense that the psyche as a hyper-complex structure reads certain configurations translatable into tensional states. The idea of the existence of certain configurations identical in all persons responds to the necessity of the administration of the evolutionary dynamics of species with minimal resources. The uniqueness of the person which explains the reason and the desideratum of affiliation to specific social environments manifests itself as a result of its psychological performance [5]. In this context, the psychological performance refers to the unconscious resort which is capable of subordinating the vulnerability of the conscious instance to experiential dynamics.

Hyper-complex systems dispose of remarkable resources which apparently make it impossible to explain the functionality of their structures. On the other hand, the efficient management of these suggests a minimal construction, maximally efficient. The explanation of their functionality and behaviour raises a fundamental problem; how can we conceive a mechanism which generates a very large

number of distinctly observable behaviour instances, using a much reduced number of behaviour generators? The psychological system, which has been the object of far ranging research, provides a plausible response to this question.

II. EQUIINVARIANCE OF THE TENSIONAL PSYCHOLOGICAL STATES

The construction of the operating mechanism of the psychological system is surprising, especially in terms of the reasons of the existence of its components. The functionality of the unconscious instance which is coupled directly to the conscious instance counterpoises the cold reasoning, which transcends the person, to the hedonic reasoning which is meant to conceal the sense of the evolution of human species. On the other hand, the relationship between invulnerable-vulnerable, which is present in the psychological construct through the two instances, must justify the very existence of the quasi-complexity of creation through the capacity of the unconscious instance to maintain the person in a conscious state and through the capacity of the conscious instance to create a psychological state that is personalized faced with the scenic play, whose actor and spectator the person is at the same time.

Surprisingly, human interactions are felt only at the conscious instance. This fact is likely to highlight, at the level of the person, two qualitatively distinct realities, one of which operates at the level of inter-psychological interaction. Nevertheless, inter-psychological interaction is determined by the intra-psychological one which configures the reason of the transactional environment.

Although the two psychological instances operate with psychological tensions, the dimension of the invincibility of the unconscious instance suggests at the level of this resort the presence of potential psychological tensions, while the dimension of vulnerability which operates at the level of the conscious instance suggests the presence of two types of psychological tensions; potential and effective ones.

The maximally efficient, coherent and parallel functioning of the two psychological instances involved in the provision of the psychological tensional continuum can be satisfied under conditions of equivalent tensional sequences which a specialized reader should be able to read. The representation of the effective tensional states through contractible spaces offers an alternative of the representation of the pair tensional sequences (for the conscious instance and the unconscious one) through equivalent homotopic spaces. The homologies of the two spaces should be identical and this fact imposes the same Euler characteristic for each pair of tensional sequences.

The tensional psychological coherence between two successive readings is assured by the subconscious instance which is endowed with a reader specialized in the reading of the current sequence as well as of the following one; it is also endowed with a mechanism which changes the current tensional configurations (specific to the unconscious instance and the conscious one) into the following tensional ones.

Such a representation presupposes the existence of a tensional mechanism composed of the following components (see fig. 1):

- a set of tensional configurations which are arranged in a sequential manner and are also specific to the unconscious instance (potential tensional psychological sequences);
- a set of tensional configurations which are arranged in a sequential manner and are also specific to the conscious instance (effective tensional psychological sequences);
- a reader of tensional configurations which reads simultaneously the tensional sequences of the conscious instance and of the unconscious one (the sequence *i* of the unconscious instance is paired with the sequence *i* of the conscious one);
- a reader of the subconscious instance having as its task the assurance of tensional psychological continuity.

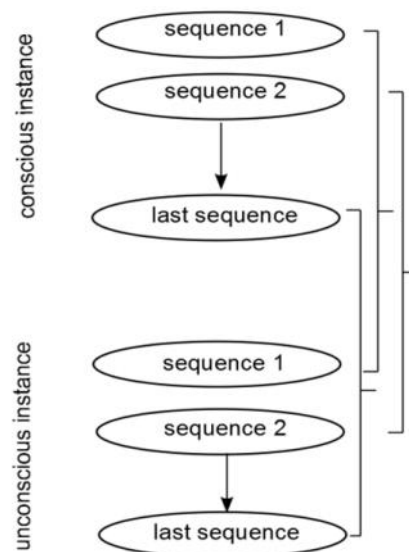


Fig.1 The reader of the tensional psychological configurations

The miracle of creation is revealed by its very products. The entities of any species are equivalent between them and this fact presupposes the existence of the same information which is readable by the specialized mechanisms (enzymatic, psychological etc.). Although the psychological and physiological constructions are identical, their manner of activation determines a great variety of particular behaviours. The theory of the germination of the tensional states [6] offers the possibility of the two-dimensional representation of tensional sequences as tensional generators. The equivalence of each tensional state of the conscious instance with each tensional state of the unconscious one suggests the possibility of reading them as pairs. At the psychological level the reader of the tensional psychological information is specialized in the decryption of four configurations which are presented in fig. 2-5. The effective psychological tensions are represented by shaded areas, whereas the potential psychological ones are represented by un-shaded areas.

The history of the psychological experiences of the person is composed of a very large number of tensional sequences,

each of these containing one of the above configurations. The manner in which these sequences are arranged presents certain particularities. There are two tensional configurations which describe two extreme experiential moments, respectively the initial and final moment of life. These configurations are read only once in life (see fig. 2 and fig. 5). Surprisingly, at the conscious instance and also at the initial moment, this construction induces the highest tensional psychological intensity. The other configurations are multiplied and placed in a specific order which also matches the scenic play. The order in which these are placed determines the personalized way of manifestation of observable behaviour.

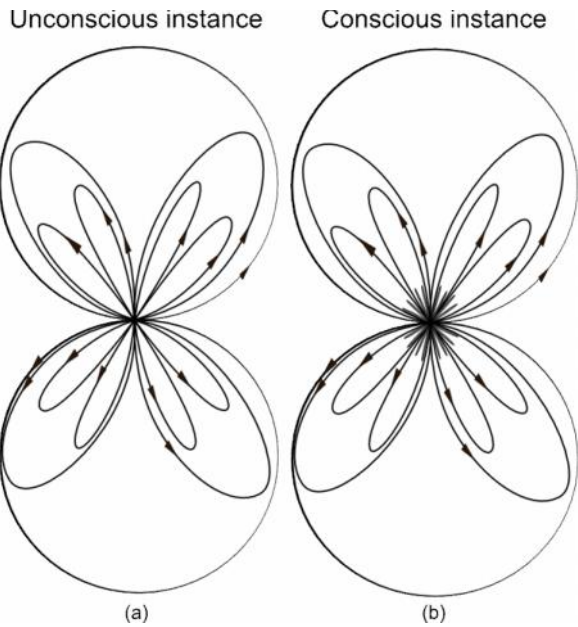


Fig. 2 The first pair of tensional psychological configurations

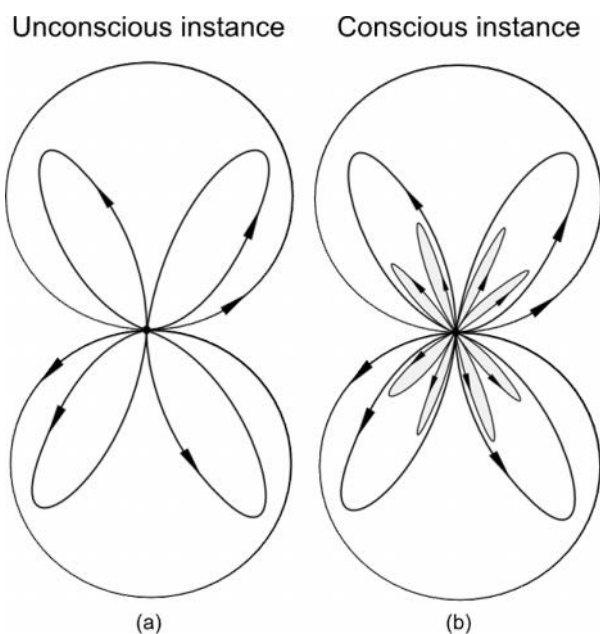


Fig. 3 The tensional strategy with maximal intensity

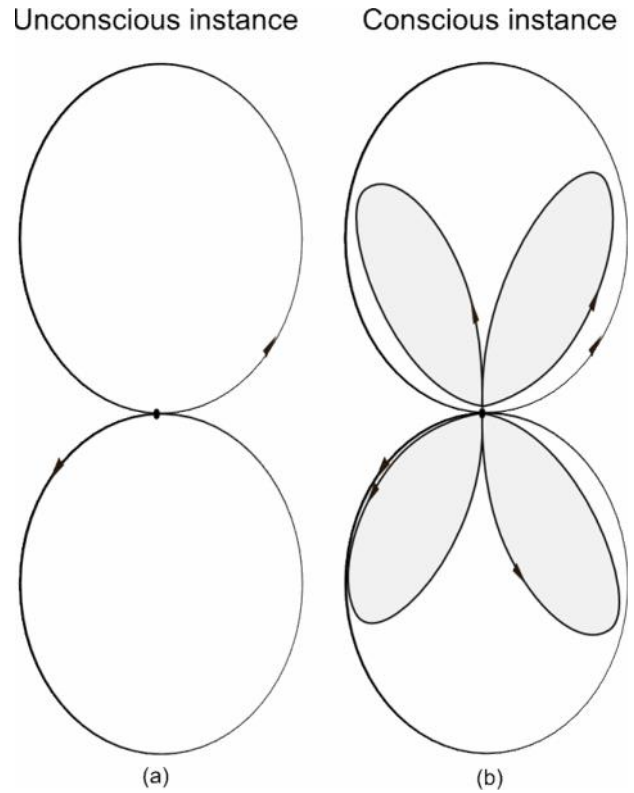


Fig. 4 The tensional strategy with minimal intensity

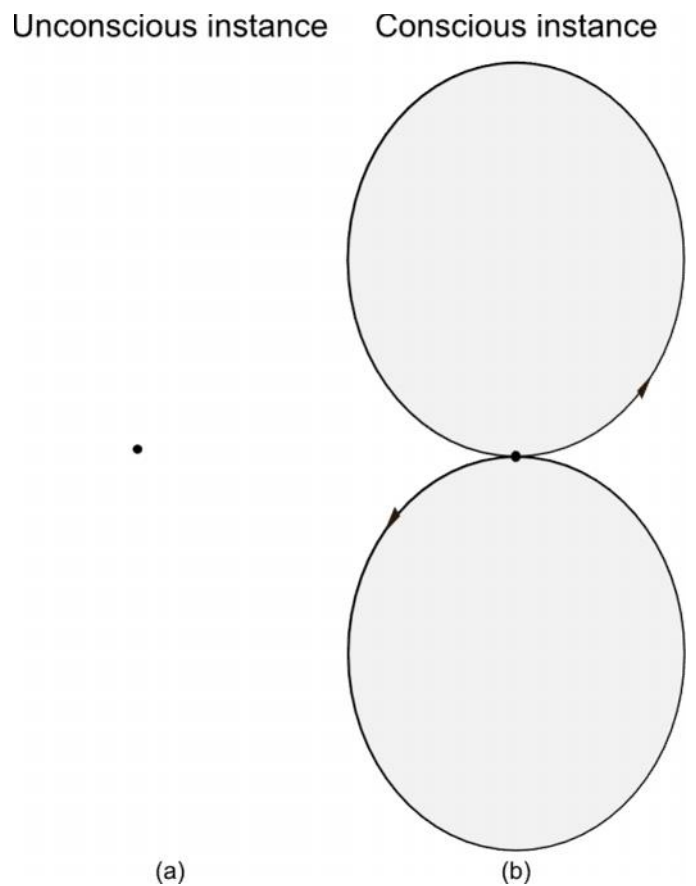


Fig. 5 The last pair of tensional psychological configurations

$$\begin{aligned} & \partial_1(a_1 30 + a_2 31 + a_3 32 + a_4 51 + a_5 52 + a_6 53 + \\ & + a_7 33 + a_8 34 + a_9 35 + a_{10} 36 + a_{11} 37 + a_{12} 38 + \\ & + a_{13} 54 + a_{14} 55 + a_{15} 56 + a_{16} 57 + a_{17} 58 + a_{18} 59) = \\ & = a_1(4-3) + a_2(5-4) + a_3(3-5) + a_4(3-1) + \\ & + a_5(2-3) + a_6(1-2) + a_7(10-3) + a_8(11-10) + \quad (5) \\ & + a_9(3-11) + a_{10}(12-3) + a_{11}(13-12) + \\ & + a_{12}(3-13) + a_{13}(9-8) + a_{14}(3-9) + a_{15}(8-3) + \\ & + a_{16}(7-6) + a_{17}(3-7) + a_{18}(6-3) = 0 \end{aligned}$$

where a_i are constant. These will be determined from the following system using (5):

$$a_1 - a_2 = 0 \quad (6)$$

$$a_2 - a_3 = 0 \quad (7)$$

$$a_6 - a_4 = 0 \quad (8)$$

$$a_5 - a_6 = 0 \quad (9)$$

$$a_{18} - a_{16} = 0 \quad (10)$$

$$a_{16} - a_{17} = 0 \quad (11)$$

$$a_{15} - a_{13} = 0 \quad (12)$$

$$a_{13} - a_{14} = 0 \quad (13)$$

$$a_7 - a_8 = 0 \quad (14)$$

$$a_8 - a_9 = 0 \quad (15)$$

$$a_{10} - a_{11} = 0 \quad (16)$$

$$a_{11} - a_{12} = 0 \quad (17)$$

$$a_3 - a_1 + a_4 - a_5 - a_7 + a_9 - a_{10} + \quad (18)$$

$$+ a_{12} + a_{14} - a_{15} + a_{17} - a_{18} = 0$$

The solution is:

$$a_1 = a_2 = a_3$$

$$a_4 = a_5 = a_6$$

$$a_{16} = a_{17} = a_{18}$$

$$a_{13} = a_{14} = a_{15}$$

$$a_7 = a_8 = a_9$$

$$a_{10} = a_{11} = a_{12}$$

Thus $\ker \partial_1$ becomes:

$$\ker \partial_1 = \left\langle \begin{matrix} 30 + 31 + 32, 51 + 52 + 53, \\ 57 + 58 + 59, 54 + 55 + 56, \\ 33 + 34 + 35, 36 + 37 + 38 \end{matrix} \right\rangle =$$

$$= Z \oplus \dots \oplus Z$$

6 times

Therefore

$$H_1(X) = \frac{\ker \partial_1}{\text{Im} \partial_2} = \frac{Z \oplus \dots \oplus Z}{0} = Z \oplus \dots \oplus Z \quad (26)$$

6 times

Case 2 The tensional strategy with minimal intensity

For fig. 4b the homology groups $H_i(X)$ and the Euler characteristic χ are:

$$H_0(X) = Z, H_1(X) = Z \oplus Z, \quad (27)$$

$$H_i(X) = 0, i \geq 2, \chi = -1$$

In the case of fig. 4a the homeomorphic representation and the necessary calculations are presented below:

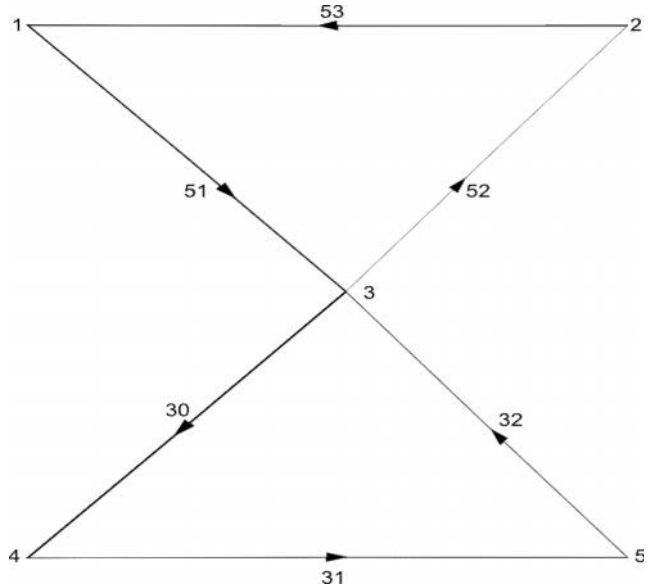


Fig. 7 The homeomorphic representation of fig. 4a

Vertices: 1,2,3,4,5.

Edges: 30,31,32,51,52,53.

The chain complex for this case is:

$$\dots \xrightarrow{\partial_2} C_1 \xrightarrow{\partial_1} C_0 \xrightarrow{\partial_0} 0 \quad (28)$$

The Euler characteristic is

$$\chi = \text{rank } H_0(X) - \text{rank } H_1(X) + \dots = -1 \quad (29)$$

Indeed

$$H_0(X) = \frac{\ker \partial_0}{\text{Im} \partial_1} = \quad (30)$$

$$= \frac{\langle 1, 2, 3, 4, 5 \rangle}{\langle 1-2, 3-1, 4-3, 5-4 \rangle} = Z \quad (24)$$

On the other hand

$$\begin{aligned} & \partial_1(a_1 30 + a_2 31 + a_3 32 + a_4 52 + a_5 53 + a_6 51) = \\ & = a_1(4-3) + a_2(5-4) + a_3(3-5) + a_4(2-3) + \quad (31) \\ & + a_5(1-2) + a_6(3-1) = 0 \end{aligned}$$

where a_i are constant. These will be determined from the following system using (31):

$$a_1 - a_2 = 0 \quad (32)$$

$$a_2 - a_3 = 0 \tag{33}$$

$$a_5 - a_6 = 0 \tag{34}$$

$$a_4 - a_5 = 0 \tag{35}$$

$$a_3 - a_1 - a_4 + a_6 = 0 \tag{36}$$

The solution is:

$$a_1 = a_2 = a_3 \tag{37}$$

$$a_4 = a_5 = a_6 \tag{38}$$

Thus $\ker \partial_1$ becomes:

$$\ker \partial_1 = \langle 30 + 31 + 32, 51 + 52 + 53 \rangle = \tag{39}$$

$$= Z \oplus Z$$

Therefore

$$H_1(X) = \frac{\ker \partial_1}{\text{Im } \partial_2} = \frac{Z \oplus Z}{0} = Z \oplus Z \tag{40}$$

Case 3 The first pair of tensional psychological configurations

For fig. 2a the homology groups $H_i(X)$ and the Euler characteristic χ are:

$$H_0(X) = Z, H_1(X) = \frac{\ker \partial_1}{\text{Im } \partial_2} = \frac{Z \oplus \dots \oplus Z}{0} = Z \oplus \dots \oplus Z, \tag{41}$$

$$H_i(X) = 0, i \geq 2, t = -13$$

In the case of fig. 2b the homeomorphic representation and the necessary calculations are presented below:

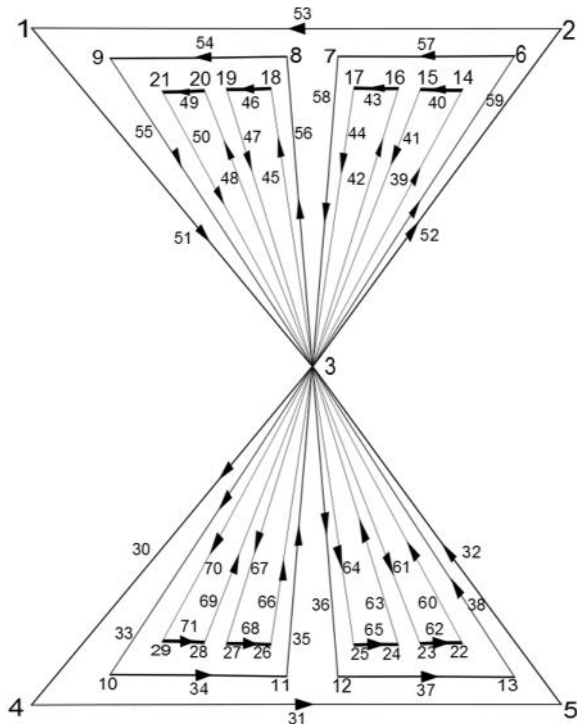


Fig. 8 The homeomorphic representation of fig. 2b

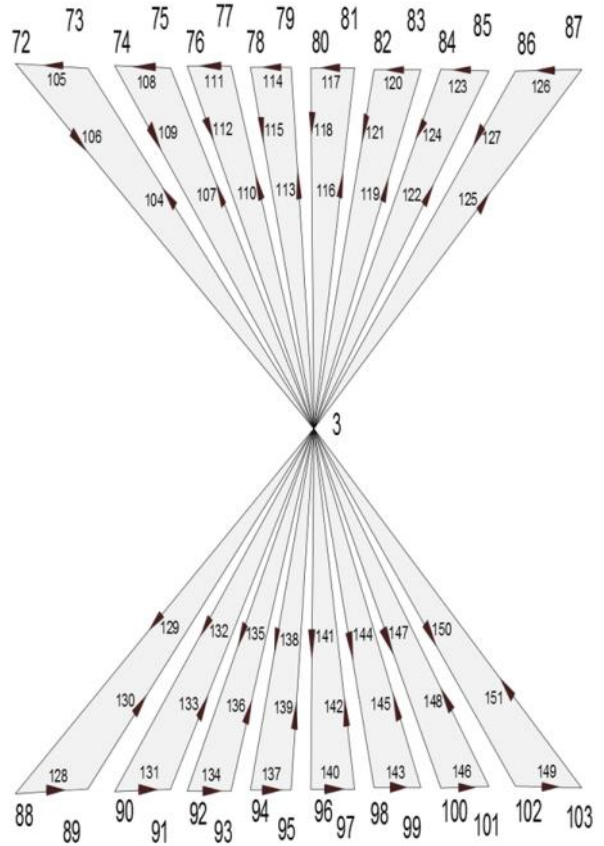


Fig. 9 The homeomorphic representation of fig. 2b

Vertices: 1,2,3,4,5,6,7,8,9,10,11,12,13,14,15,16,17,18,19,20, 21,22,23,24,25,26,27,28,29,72,73,74,75,76,77,78,79,80,81,82, 83,84,85,86,87,88,89,90,91,92,93,94,95,96,97,98,99,100,101, 102,103.

Edges: 30, 31, 32, 51, 52, 53, 54, 55, 56, 57, 58, 59, 45, 46, 47, 48, 49, 50, 42, 43, 44, 39, 40, 41, 33, 34, 35, 36, 37, 38, 66, 67, 68, 69, 70, 71, 63, 64, 65, 60, 61, 62, 104, 105, 106, 107, 108, 109, 110, 111, 112, 113, 114, 115, 116, 117, 118, 119, 120, 121, 122, 123, 124, 125, 126, 127, 128, 129, 130, 131, 132, 133, 134, 135, 136, 137, 138, 139, 140, 141, 142, 143, 144, 145, 146, 147, 148, 149, 150, 151.

Faces: 160, 161, 162, 163, 164, 165, 166, 167, 168, 169, 170, 171, 172, 173, 174, 175 (effective psychological tensions), having:

$$\begin{aligned} \partial_2 160 &= \langle 104 + 105 + 106 \rangle, & \partial_2 161 &= \langle 107 + 108 + 109 \rangle, \\ \partial_2 162 &= \langle 110 + 111 + 112 \rangle, & \partial_2 163 &= \langle 113 + 114 + 115 \rangle, \\ \partial_2 164 &= \langle 116 + 117 + 118 \rangle, & \partial_2 165 &= \langle 119 + 120 + 121 \rangle, \\ \partial_2 166 &= \langle 122 + 123 + 124 \rangle, & \partial_2 167 &= \langle 125 + 126 + 127 \rangle, \\ \partial_2 168 &= \langle 128 + 129 + 130 \rangle, & \partial_2 169 &= \langle 131 + 132 + 133 \rangle, \\ \partial_2 170 &= \langle 134 + 135 + 136 \rangle, & \partial_2 171 &= \langle 137 + 138 + 139 \rangle, \\ \partial_2 172 &= \langle 140 + 141 + 142 \rangle, & \partial_2 173 &= \langle 143 + 144 + 145 \rangle, \\ \partial_2 174 &= \langle 146 + 147 + 148 \rangle, & \partial_2 175 &= \langle 149 + 150 + 151 \rangle. \end{aligned}$$

Also,

$$\begin{aligned} 160, 161 &\subset \langle 48 + 49 + 50 \rangle, \\ 162, 163 &\subset \langle 45 + 46 + 47 \rangle, \\ 164, 165 &\subset \langle 42 + 43 + 44 \rangle, \\ 166, 167 &\subset \langle 39 + 40 + 41 \rangle, \\ 168, 169 &\subset \langle 69 + 70 + 71 \rangle, \\ 170, 171 &\subset \langle 66 + 67 + 68 \rangle, \\ 172, 173 &\subset \langle 63 + 64 + 65 \rangle, \\ 174, 175 &\subset \langle 60 + 61 + 62 \rangle. \end{aligned}$$

The chain complex for this case is:

$$\dots \xrightarrow{\partial_3} C_2 \xrightarrow{\partial_2} C_1 \xrightarrow{\partial_1} C_0 \xrightarrow{\partial_0} 0$$

The Euler characteristic is

$$\begin{aligned} \mathfrak{t} &= \text{rank } H_0(X) - \text{rank } H_1(X) + \\ &+ \text{rank } H_2(X) + \dots = -13 \end{aligned}$$

Indeed

$$H_0(X) = \frac{\ker \partial_0}{\text{Im } \partial_1} =$$

$$\begin{aligned} & \left\{ \begin{array}{l} 1, 2, 3, 4, 5, 6, 7, 8, 9, 10, 11, \\ 12, 13, 14, 15, 16, 17, 18, 19, \\ 20, 21, 22, 23, 24, 25, 26, 27, \\ 28, 29, 72, 73, 74, 75, 76, 77, \\ 78, 79, 80, 81, 82, 83, 84, 85, \\ 86, 87, 88, 89, 90, 91, 92, 93, \\ 94, 95, 96, 97, 98, 99, 100, \\ 101, 102, 103 \end{array} \right\} \end{aligned}$$

$$= \frac{\quad}{\quad} = Z$$

$$\begin{aligned} & \left\{ \begin{array}{l} 1-2, 3-1, 4-3, 5-4, 8-3, 9-8, \\ 6-3, 7-6, 10-3, 11-10, 12-3, \\ 13-12, 14-3, 15-14, 16-3, 17-16, \\ 18-3, 19-18, 20-3, 21-20, 29-3, \\ 28-29, 27-3, 26-27, 25-3, 24-25, \\ 23-3, 22-23, 73-3, 72-73, 75-3, \\ 74-75, 77-3, 76-77, 79-3, 78-79, \\ 81-3, 80-81, 83-3, 82-83, 85-3, \\ 84-85, 87-3, 86-87, 88-3, 89-88, \\ 90-3, 91-90, 92-3, 93-92, 94-3, \\ 95-94, 96-3, 97-96, 98-3, 99-98, \\ 100-3, 101-100, 102-3, 103-102 \end{array} \right\} \end{aligned}$$

On the other hand

$$\begin{aligned} & \partial_1(a_1 30 + a_2 31 + a_3 32 + a_4 51 + a_5 52 + a_6 53 + \\ & + a_7 33 + a_8 34 + a_9 35 + a_{10} 36 + a_{11} 37 + a_{12} 38 + \\ & + a_{13} 57 + a_{14} 58 + a_{15} 59 + a_{16} 54 + a_{17} 55 + a_{18} 56 + \\ & + a_{19} 69 + a_{20} 70 + \dots + a_{71} 132 + a_{72} 133 + a_{73} 134 + \\ & + a_{74} 135 + a_{75} 136 + a_{76} 137 + a_{77} 138 + a_{78} 139 + \\ & + a_{79} 140 + a_{80} 141 + a_{81} 142 + a_{82} 143 + a_{83} 144 + \\ & + a_{84} 145 + a_{85} 146 + a_{86} 147 + a_{87} 148 + a_{88} 149 + \\ & + a_{89} 150 + a_{90} 151) = a_1(4-3) + a_2(5-4) + \\ & + a_3(3-5) + a_4(3-1) + a_5(2-3) + a_6(1-2) + \\ & + a_7(10-3) + a_8(11-10) + a_9(3-11) + \\ & + a_{10}(12-3) + a_{11}(13-12) + a_{12}(3-13) + \\ & + a_{13}(7-6) + a_{14}(3-7) + a_{15}(6-3) + \\ & + a_{16}(9-8) + a_{17}(3-9) + a_{18}(8-3) + \\ & + a_{19}(3-28) + a_{20}(29-3) + \dots + a_{71}(90-3) + \\ & + a_{72}(3-91) + a_{73}(93-92) + a_{74}(92-3) + \\ & + a_{75}(3-93) + a_{76}(95-94) + a_{77}(94-3) + \\ & + a_{78}(3-95) + a_{79}(97-96) + a_{80}(96-3) + \\ & + a_{81}(3-97) + a_{82}(99-98) + a_{83}(98-3) + \\ & + a_{84}(3-99) + a_{85}(101-100) + a_{86}(100-3) + \\ & + a_{87}(3-101) + a_{88}(103-102) + a_{89}(102-3) \\ & + a_{90}(3-103) = 0 \end{aligned} \tag{42}$$

(42)

(43)

(45)

where a_i are constant. These will be determined from the following system using (45):

$$a_1 - a_2 = 0 \tag{46}$$

$$a_2 - a_3 = 0 \tag{47}$$

$$a_6 - a_4 = 0 \tag{48}$$

$$a_5 - a_6 = 0 \tag{49}$$

$$a_{15} - a_{13} = 0 \tag{50}$$

$$a_{13} - a_{14} = 0 \tag{51}$$

$$a_{18} - a_{16} = 0 \tag{52}$$

$$(44) \quad a_{16} - a_{17} = 0 \tag{53}$$

$$a_7 - a_8 = 0 \tag{54}$$

$$a_8 - a_9 = 0 \tag{55}$$

$$a_{10} - a_{11} = 0 \tag{56}$$

$$a_{11} - a_{12} = 0 \tag{57}$$

$$a_{31} - a_{32} = 0 \tag{58}$$

$$a_{32} - a_{33} = 0$$

$$a_{34} - a_{35} = 0$$

$$a_{35} - a_{36} = 0$$

$$a_{37} - a_{38} = 0$$

$$a_{38} - a_{39} = 0$$

$$a_{40} - a_{41} = 0$$

$$a_{41} - a_{42} = 0$$

$$a_{30} - a_{28} = 0$$

$$a_{29} - a_{30} = 0$$

$$a_{27} - a_{25} = 0$$

$$a_{26} - a_{27} = 0$$

$$a_{24} - a_{22} = 0$$

$$a_{23} - a_{24} = 0$$

$$a_{21} - a_{19} = 0$$

$$a_{20} - a_{21} = 0$$

$$a_{44} - a_{45} = 0$$

$$a_{43} - a_{44} = 0$$

$$a_{47} - a_{48} = 0$$

$$a_{46} - a_{47} = 0$$

$$a_{50} - a_{51} = 0$$

$$a_{49} - a_{50} = 0$$

$$a_{53} - a_{54} = 0$$

$$a_{52} - a_{53} = 0$$

$$a_{56} - a_{57} = 0$$

$$a_{55} - a_{56} = 0$$

$$a_{59} - a_{60} = 0$$

$$a_{58} - a_{59} = 0$$

$$a_{62} - a_{63} = 0$$

$$a_{61} - a_{62} = 0$$

$$a_{65} - a_{66} = 0$$

$$a_{64} - a_{65} = 0$$

$$a_{68} - a_{67} = 0$$

$$a_{67} - a_{69} = 0$$

$$a_{71} - a_{70} = 0$$

$$a_{70} - a_{72} = 0$$

$$a_{73} - a_{75} = 0$$

$$a_{74} - a_{73} = 0$$

$$(59) \quad a_{77} - a_{76} = 0$$

$$(60) \quad a_{76} - a_{78} = 0$$

$$(61) \quad a_{80} - a_{79} = 0$$

$$(62) \quad a_{79} - a_{81} = 0$$

$$(63) \quad a_{83} - a_{82} = 0$$

$$(64) \quad a_{82} - a_{84} = 0$$

$$(65) \quad a_{86} - a_{85} = 0$$

$$(66) \quad a_{85} - a_{87} = 0$$

$$(67) \quad a_{89} - a_{88} = 0$$

$$(68) \quad a_{88} - a_{90} = 0$$

$$(69) \quad a_3 - a_1 + a_4 - a_5 - a_7 + a_9 - a_{10} +$$

$$(70) \quad + a_{12} + a_{14} - a_{15} + a_{17} - a_{18} + a_{19} -$$

$$(71) \quad - a_{20} + a_{22} - a_{23} + a_{25} - a_{26} + a_{28} - a_{29} -$$

$$(72) \quad - a_{31} + a_{33} - a_{34} + a_{36} - a_{37} + a_{39} - a_{40} +$$

$$(73) \quad + a_{42} - a_{43} + a_{45} - a_{46} + a_{48} - a_{49} + a_{51} -$$

$$(74) \quad - a_{52} + a_{54} - a_{55} + a_{57} - a_{58} + a_{60} - a_{61} +$$

$$(75) \quad + a_{63} - a_{64} + a_{66} - a_{68} + a_{69} - a_{71} + a_{72} -$$

$$(76) \quad - a_{74} + a_{75} - a_{77} + a_{78} - a_{80} + a_{81} - a_{83} +$$

$$(76) \quad + a_{84} - a_{86} + a_{87} - a_{89} + a_{90} = 0$$

$$(77) \quad \text{The solution is:}$$

$$(78) \quad a_1 = a_2 = a_3$$

$$(79) \quad a_4 = a_5 = a_6$$

$$(80) \quad a_{16} = a_{17} = a_{18}$$

$$(81) \quad a_{13} = a_{14} = a_{15}$$

$$(82) \quad a_7 = a_8 = a_9$$

$$(83) \quad a_{10} = a_{11} = a_{12}$$

$$(84) \quad a_{31} = a_{32} = a_{33}$$

$$(85) \quad a_{34} = a_{35} = a_{36}$$

$$(86) \quad a_{37} = a_{38} = a_{39}$$

$$(87) \quad a_{40} = a_{41} = a_{42}$$

$$(88) \quad a_{28} = a_{29} = a_{30}$$

$$(89) \quad a_{25} = a_{26} = a_{27}$$

$$(90) \quad a_{22} = a_{23} = a_{24}$$

$$(91) \quad a_{19} = a_{20} = a_{21}$$

$$(92) \quad a_{43} = a_{44} = a_{45}$$

$$(93) \quad a_{46} = a_{47} = a_{48}$$

$$(94) \quad a_{49} = a_{50} = a_{51}$$

$$(95) \quad a_{52} = a_{53} = a_{54}$$

$$(96)$$

$$(97)$$

$$(98)$$

$$(99)$$

$$(100)$$

$$(101)$$

$$(102)$$

$$(103)$$

$$(104)$$

$$(105)$$

$$(106)$$

$$\begin{aligned}
 a_{55} &= a_{56} = a_{57} \\
 a_{58} &= a_{59} = a_{60} \\
 a_{61} &= a_{62} = a_{63} \\
 a_{64} &= a_{65} = a_{66} \\
 a_{67} &= a_{68} = a_{69} \\
 a_{70} &= a_{71} = a_{72} \\
 a_{73} &= a_{74} = a_{75} \\
 a_{76} &= a_{77} = a_{78} \\
 a_{79} &= a_{80} = a_{81} \\
 a_{82} &= a_{83} = a_{84} \\
 a_{85} &= a_{86} = a_{87} \\
 a_{88} &= a_{89} = a_{90}
 \end{aligned}$$

Thus $\ker \partial_1$ becomes:

$$\ker \partial_1 = \left\{ \begin{array}{l} 30+31+32, 51+52+53, \\ 57+58+59, 54+55+56, \\ 33+34+35, 36+37+38, \\ 39+40+41, 42+43+44, \\ 45+46+47, 48+49+50, \\ 60+61+62, 63+64+65, \\ 66+67+68, 69+70+71, \\ 104+105+106, 107+108+109, \\ 110+111+112, 113+114+115, \\ 116+117+118, 119+120+121, \\ 122+123+124, 125+126+127, \\ 128+129+130, 131+132+133, \\ 134+135+136, 137+138+139, \\ 140+141+142, 143+144+145, \\ 146+147+148, 149+150+151 \end{array} \right\} =$$

$$= Z \oplus \dots \oplus Z$$

30 times

$$\text{Im } \partial_2 = \left\{ \begin{array}{l} 104+105+106, 107+108+109, \\ 110+111+112, 113+114+115, \\ 116+117+118, 119+120+121, \\ 122+123+124, 125+126+127, \\ 128+129+130, 131+132+133, \\ 134+135+136, 137+138+139, \\ 140+141+142, 143+144+145, \\ 146+147+148, 149+150+151 \end{array} \right\}$$

Therefore

$$H_1(X) = \frac{\ker \partial_1}{\text{Im } \partial_2} = \frac{Z \oplus \dots \oplus Z}{Z \oplus \dots \oplus Z} = Z \oplus \dots \oplus Z \quad (139)$$

(127) Now let us calculate $H_2(X)$.

$$\begin{aligned}
 (128) \quad & \partial_2(a_1 160 + a_2 161 + a_3 162 + a_4 163 + \\
 (129) \quad & + a_5 164 + a_6 165 + a_7 166 + a_8 167 + \\
 (130) \quad & + a_9 168 + a_{10} 169 + a_{11} 170 + a_{12} 171 + \\
 (131) \quad & + a_{13} 172 + a_{14} 173 + a_{15} 174 + a_{16} 175) = \\
 (132) \quad & = a_1 (104 + 105 + 106) + a_2 (107 + 108 + 109) + \\
 (133) \quad & + a_3 (110 + 111 + 112) + a_4 (113 + 114 + 115) + \\
 (134) \quad & + a_5 (116 + 117 + 118) + a_6 (119 + 120 + 121) + \\
 (135) \quad & + a_7 (122 + 123 + 124) + a_8 (125 + 126 + 127) + \\
 (136) \quad & + a_9 (128 + 129 + 130) + a_{10} (131 + 132 + 133) + \\
 & + a_{11} (134 + 135 + 136) + a_{12} (137 + 138 + 139) + \\
 & + a_{13} (140 + 141 + 142) + a_{14} (143 + 144 + 145) + \\
 & + a_{15} (146 + 147 + 148) + a_{16} (149 + 150 + 151) = 0
 \end{aligned} \quad (140)$$

The solution for (140) is $a_i = 0$ for $i=1, \dots, 15$. Thus $\ker \partial_2 = 0$. Therefore

$$H_2(X) = \frac{\ker \partial_2}{\text{Im } \partial_3} = 0 \quad (141)$$

because

$$\text{Im } \partial_3 = 0 \quad (142)$$

Case 4 The last pair of tensional psychological configurations For fig. 5a and fig. 5b the homology groups $H_1(X)$ and the Euler characteristic χ are:

$$H_0(X) = Z, H_1(X) = 0, i \geq 1, \chi = 1 \quad (143)$$

IV. CONCLUSION

The psychological system administrates two specialized instances, the conscious instance and the unconscious one, which contain two types of tensional psychological configurations: potential and effective.

The tensional psychological dynamics is generated by a reader which reads at a very large speed the tensional configurations disposed in a specific order in the two instances mentioned. The gap of continuity between two consecutive readings is covered by the activity of the subconscious instance which turns the pair of tensional configurations that have been read into the next pair of tensional configurations. In terms of tension the activity of the subconscious instance has the exclusive role of covering the gap of time between two consecutive readings and thereby to give coherence to the tensional continuity.

The synchronous functionality of the two psychological instances is determined by the presence of a reader which is specialized in the reading of certain equivalent tensional configurations. The handling of two types of psychological

tensional configurations suggests the existence of a space X/A , where X is a total tensional space and A is an effective tensional subspace that can be contracted to a point, the homotopic equivalent of space (X,A) . In this construction space (X,A) is handled by the conscious instance and space X/A is handled by the unconscious one. For reasons that pertain to the logic of the psychological construct the two spaces must have the same homology and implicitly the same Euler characteristic.

The pairs of tensional sequence identical in terms of the chronology of the activation are: the tensional pair with the Euler characteristic equal to -13 (represented in fig. 2a, 2b) and the tensional pair with the Euler characteristic equal to 1 (represented in fig. 5a, 5b). The other two pairs of sequences can succeed in a random manner and these are characterized by the Euler characteristics -5 and -1 .

The existence of a hyper-complex psychological entity in a state of perfect equilibrium can justify the generation of different psychological intensities at the level of each person in each moment of his/her existence. This aspect might suggest the existence of some holes of psychological intensity which manifests itself in advance at the level of this hyper-complex entity.

REFERENCES

- [1] T. T. Diek, *Algebraic Topology*, E.M.S., 2002.
- [2] A. Hatcher, *Algebraic Topology*, Cambridge University Press, 2002.
- [3] V.V. Prosolov, *Elements of Homology Theory*, A.M.S., 2007.
- [4] A.G. Sumedrea, "A Topological Theory of the Tensional Psychological Determinism," *International Journal of Mathematical Models and Methods in Applied Sciences*, Issue 8, Volume 7, pp. 772-781, 2013.
- [5] A.G. Sumedrea, "A Relativistic Theory of the Tensional Psychological State," *International Journal of Mathematical Models and Methods in Applied Sciences*, Issue 5, Volume 5, pp. 982-990, 2011.
- [6] A.G. Sumedrea, L. Sangeorzan, "A Mathematical Theory of Psychological Dynamics," *WSEAS Transactions on Mathematics*, Issue 10, Volume 8, pp. 604-613, October 2009.

Alin Gilbert SUMEDREA was born in Timisoara, ROMANIA, on April 02, 1964. He received a Ph.D in statistics (1993) and a Ph.D in psychology (1998) at the University of Bucharest, ROMANIA. Since 2006 he has been a Professor at Lucian Blaga University of Sibiu, ROMANIA. The main articles published by the author are: A Topological Theory of the Tensional Psychological Determinism – *International Journal of Mathematical Models and Methods in Applied Sciences*, Issue 8, Volume 7, 2013, pp. 772-781; A Relativistic Theory of the Tensional Psychological State - *International Journal of Mathematical Models and Methods in Applied Sciences*, Issue 5, Volume 5, 2011, pp. 982-990; Towards a Mathematical Theory of Unconscious Adaptation and Emotions – *WSEAS Transactions on Mathematics*, Issue 5, Volume 9, May 2010, pp. 355-364; A Mathematical Theory of Psychological Dynamics - *WSEAS Transactions on Mathematics*, Issue 10, Volume 8, October 2009, pp. 604-613. His current research interests are: Algebraic Topology Applied in Psychology and Mathematical Modelling of Psychological Insight Processes.

A thermoelectric generator as an electric energy source for the building sensors

Michal Oplustil, Martin Zalesak, Stanislav Sehnalek, and Pavel Chrobak

Abstract—There are several ways for an alternative power source of the intelligent building sensors as for example: energy sources based on electromechanical, electromagnetic and thermoelectric principles. This paper deals with the using of the human body waste heat as an energy source for the intelligent building sensors. The thermoelectric cooler module is used as a heat converter. The temperature difference in this case of use of the thermoelectric cooler is very low. This difference is only of 10 °C to 12 °C Therefore the output voltage is only in the range of tens or one hundred mV. So we need to increase the amplitude of the output voltage to range of 3 V - 5 V for the sensor needs. This paper describes a design of the prototype of thermoelectric generator as an electric energy source for building sensors.

Keywords— heat transfer, Peltier cell, Seebeck effect, step-up DC/DC converter, thermal energy.

I. INTRODUCTION

THE physical principles on which are thermoelectric coolers based on are actually date back to the early 19th century. The first of the commercial thermoelectric modules were not available until 1960. The thermoelectric semiconductor materials used for the thermoelectric coolers are usually made of the Bismuth Telluride (Bi_2Te_3). There exists also other semiconductor materials e.g. Lead Telluride (PbTe), Silicon Germanium (SiGe) and Bismuth-Antimony (Bi-Sb) which may be used in the specific applications. For the application in temperature range of tens of centigrade are convenient thermoelectric material based on Bismuth Telluride.

The main research works in the field of generating of electric energy from human waste heat have been done in last 10 years. Some experts and companies have done a great deal with this problem. For increase performance it was designed a new type of micro-generator based on nanowire array micro-

This work was supported in frame of Internal Grant Agency of Tomas Bata University in Zlin, Faculty of Applied Informatics IGA/FAI2014/050, IGA/FAI2014/047, IGA/FAI2014/015 and under the project CEBIA-TECH NO. CZ.1.05/2.1.00/03.00089

M. Oplustil is with the Tomas Bata University in Zlin, Faculty of Applied Informatics, Department of Automation and Control Technologies, Zlin, 76005 Czech Republic (e-mail: oplustil@fai.utb.cz).

M. Zalesak is with the Tomas Bata University in Zlin, Faculty of Applied Informatics, Department of Automation and Control Technologies, Zlin, 76005 Czech Republic (e-mail: zalesak@fai.utb.cz).

S. Sehnalek is with the Tomas Bata University in Zlin, Faculty of Applied Informatics, Department of Automation and Control Technologies, Zlin, 76005 Czech Republic (e-mail: sehnalek@fai.utb.cz).

P.Chrobak is with the Tomas Bata University in Zlin, Faculty of Applied Informatics, Department of Automation and Control Technologies, Zlin, 760005 Czech Republic (e-mail: chrobak@fai.utb.cz).

zones with dimensions of 50 μm x 50 μm [1]. The problem of using of human waste heat as an energy source for wearable micro thermoelectric generator was presented [4].

This paper deals with the design of a prototype of low temperature thermoelectric generator. The main usage of the designed generator is in the field of power supply for building sensors. The input heat to the designed generator is acquired by a human palm.

The energy source for described electric energy generator is represented by the thermoelectric cooler (TEC). The primary usage of this device is for the application in cooling, but it can be used as the electric energy generator as well. Required value of generated energy by described device is not in the same level as the energy generated by the thermoelectric generator (TEG). But production cost of the device is lower and availability is higher than that of TEG cells.

In the relevant device the Peltier type of cells is applied. The amplitude of the output voltage of the used cell, which operates as the thermoelectric generator, depends on the temperature difference between cold side and hot side of the cell. But the application of this cell for voltage generation from human waste heat is limited by the maximum temperature of the human palm available, as it reaches only 31 °C. This temperature represents hot side of the cell and temperature of the cold side of the cell is depends on the application. In this particular case the cold side of the cell is created as a cooler (heat sink), which is exposed to the ambient air.

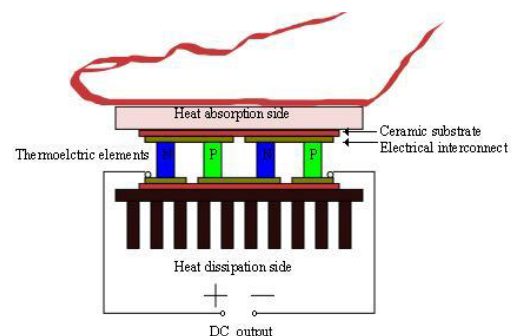


Fig. 1 the structure of the Peltier cell

The thermoelectric cooler consists of the two layers of ceramic substrate, between that are placed thermoelectric elements (thermocouples). The thermocouples used are made

of the N-type and P-type material in electrical and thermal connections. Fig. 1 illustrates the structure of the thermoelectric cooler.

A. *Thermoelectric power generation*

As long as the hot ends of the N-type and P-type materials are electrically connected the output voltage occurs due to the Seebeck effect [14]. The output voltage depends on the temperature difference and the parameters of the used thermocouples. The voltage at the load is reduced when the electrical circuit is closed by a voltage drop due to internal resistance. The efficiency of the generating power from the Peltier cell depends on the internal resistance of the cell.

B. *Peltier cell*

As a heat converter was used three types of commercial Peltier modules from different producers. The output voltage of Peltier cells is relatively small as a result of low temperature difference between the cells sides. In the measurement process were the cold sides of each cell thermally connected to the heatsink (air cooler) with a thermal resistance of 4.8 K/W. The cold side cells temperature at the start of the measurement equals to the ambient air temperature. The hot side of Peltier cell temperature was at the same level as a palm temperature. Measurement conditions and parameters of used heatsink are listed in Table I.

Table I measurement conditions

Measurement conditions	
Ambient temperature (°C)	20.3
Palm temperature (°C)	31.9
Dimension of heat sink (mm ³)	50x46x33(h)
Material of heat sink	aluminium
Number of fins (heat sink)	7
Base thickness of heat sink (mm)	4
Fin thickness of heat sink (mm)	2

II. DESIGN OF A PROTOTYPE

As shown in Fig. 2 designed device contains three blocks. The first block of the device is formed by the heat converter used as a thermoelectric cooler. The output voltage generated by the cooler is used as start-up voltage for the low input voltage DC/DC converter which creates the second block.

This converter is based on the integrated circuit LTC31081 and it is convenient as for the small dimensions which match to the required small dimensions of the whole device. Further advantages of the used integrated circuit are of the low start-up voltage, type of the power management and regulated voltage possibilities. The third blocks represents by a circuit load.



Fig. 2 the prototype block diagram

A. *Used TEC*

The three types of TEC were used during measurement as the electric generators from the waste heat produced by the human palm. Table II lists parameters of used TEC.

Table II TEC parameters

Model	TEC12708	MCHPE-127-10-08-E	RC 12-4
Dimensions (mm)	50x50x4.5	30x30x3.1	34x30x3.4
Voltage (V)	15.4	15.7	14.6
Current (A)	8.5	6.0	3.7
Maximal Power (W)	81.0	56.7	39.0
Number of Thermocouples	127	127	-
Device ZT	0.65	-	0.75
AC Resistance (ohms)	2.7	2.3	3.2

The output voltage at the temperature difference of 11.6 °C in TEC during measurement process, results in tens of mV only. This value of the voltage level obtained is not equivalent to the supply voltage required by the sensors. It is necessary then to transform the output voltage to the higher level by a converter (second block in Fig.2).

B. *Low input DC/DC converter*

The low input DC/DC converter consists of a boost transformer and a DC/DC boost converter.

The boost transformer is directly connected to the output of TEC and converts amplitude of the output voltage to the required level of the boost converter. The conversion ratio of the boost transformer depends on start-up voltage of the DC/DC converter and on the amplitude of the output voltage from TEC. The required conversion ratio in this case is 1:100.

The function of the DC/DC boost converter contains of power management facility and an energy accumulator (storage capacitor) with a high storage capacity.

III. DEVICE MEASUREMENT

In order to evaluate the suitable prototype there were set of measurement prepared. Based on the constant temperature conditions 11,6 °C (apart from C) three types of TEC modules as listed in the Table II were tested with different circuits loads. There were used as a load two types of resistors 47 kΩ, 1 kΩ, white LED and the AUREL-SAW RF Transmitter Module. The adjustable voltage output from the DC/DC converter was set to the value of 4.5V. The circuit load is connected with the output of the DC/DC converter after certain time (approximately 4 s) after startup of the charging the device. Further the results of the tests are described.

A. *TEC module TEC12708*

The Fig.3 presents the output of the generator in case of load by the AUREL-SAW RF Transmitter Module working on frequency 433 MHz. The amplitude of the output voltage drops to the value of 3.0 V during the first 40 ms of the transmission. The test signal was represented by a log. 1

connected to the input of the module. The area of heat transfer surface is 900 mm^2



Fig. 3 the output of the device with TEC module TEC12708

B. TEC module MCHPE-127-10-08-E

The Fig. 4 presents the output voltage of the generator in case of load by the AUREL-SAW RF Transmitter Module working on frequency 433 MHz. The amplitude of the output voltage drops to the value of 3.0 V during the first 40 ms of the transmission. The test signal was represented by a log. 1 connected to the input of the module. The area of heat transfer surface is 2500 mm^2 .



Fig. 4 the output of the device with TEC module MCHPE-127-10-08-E

C. TEC module RC12-4

The Fig. 5 shows the output voltage of the generator in case of load by the AUREL-SAW RF Transmitter Module. However the temperature difference was in this case $10.5 \text{ }^\circ\text{C}$.



Fig. 5 the output of the device with TEC module RC 12-4

D. Output of DC/DC converter with load $47 \text{ k}\Omega$

The Fig.6 shows the amplitude of the output voltage with the load $47 \text{ k}\Omega$. In this case it was used TEC module TEC12708.

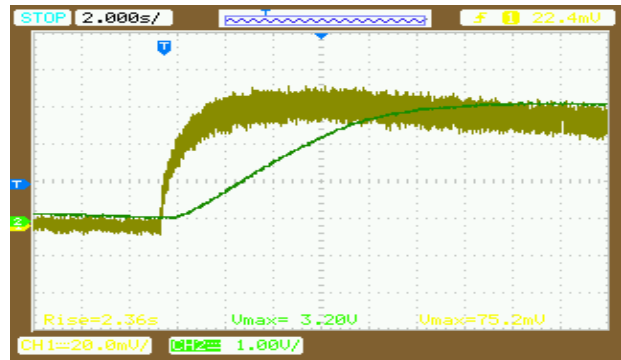


Fig. 6 the output sequencing with $47 \text{ k}\Omega$ load TEC12708

E. Output of DC/DC converter with load $47 \text{ k}\Omega$

As can be seen in the Fig.7 the output voltage in case of use TEC module MCHPE-127-10-08-E was higher than the previous case described in the Fig.6 (at the same temperature difference). The amplitude of the output voltage rises sharply because of the input voltage rises faster and stops at the value of 92 mV.

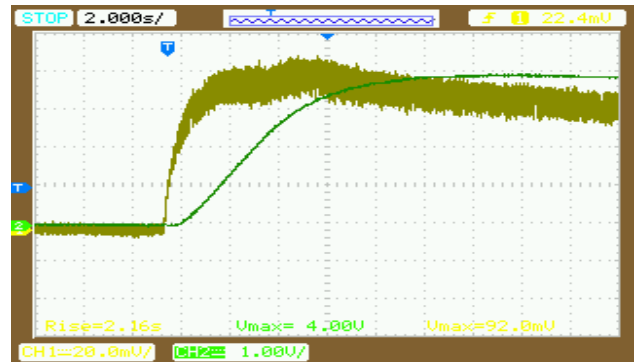


Fig. 7 the output with $47 \text{ k}\Omega$ load MCHPE-127-10-08-E

F. Output of DC/DC converter with load $1 \text{ k}\Omega$

In the case described in the Fig.8 the TEC module RC 12-4 was used. As shown the voltage level drops with the lower load resistance. The input voltage stops at the value of 88 mV and the output voltage does not exceed value of 120 mV.



Fig. 8 the output sequencing with $1 \text{ k}\Omega$ load RC12-4

G. Output of DC/DC converter with white LED as load

In the case described in the Fig. 9 the TEC module RC 12-4 was used with white LED connected as a circuit load. The output voltage stops at the value of the forward voltage of the LED used (2.52 V).



Fig. 9 the output sequencing with white LED load

H. Output converter in time with the white LED load

The time delay between the start of heat absorption in the TEC module and the output voltage required level is shown in the Fig.10. The time delay was approximately 4 seconds with set amplitude of the output voltage at the value of 4.5 V. When the output voltage is set at the higher level, the time response is longer.



Fig. 10 the output of converter in longer time

IV. DESIGNED DEVICE

The prototype of described device was designed on one side PCB with dimensions of 55 mm x 28 mm. Fig. 11 provides PCB of DC/DC converter as a part of designed thermoelectric generator. The used TEC module was connected to pin JP1. The main output of this device is represented by pin JP3.

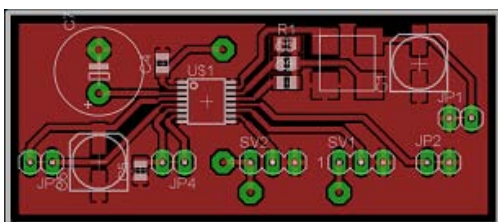


Fig. 11 DC/DC converter PCB

wireless sensors. The amplitude of the output voltage of TEC is not on the required level and that is a reason why the DC/DC converter was designed in order to increase the output voltage, to the adjustable higher values. Designed device was built in the prototype and its parameters were evaluated by experimentally by measurements. Three types of the Peltier cells as an energy source for prototype of DC/DC converter were compared in the experiment. The time delay between the amplitude of the input voltage and amplitude of the output voltage was studied. The time delay depends on the selected output voltage. Measurement was performed with the load represented by AUREL-SAW RF Transmitter module. The described prototype of the generator was able to provide current of 10 mA during the time of 15 ms. Better performance of described device can be achieved by a modification of the storage capacitor and by the better setup parameters of DC/DC converter according to the requirements of the used load. The future work will deal with optimization of the prototype for demands of the higher output power and longer availability of the output current.

REFERENCES

- [1] W. Wang, F. Jia, Q. Huang, J. Zhang, "A new type of low power thermoelectric micro-generator fabricated by nanowire array thermoelectric material, vol. 77, pp. 223-229, April 2005.
- [2] D.T. Crane, J.W. Lagrandeur, F. Harris, L.E. Bell, "Performance results of high-power-density thermoelectric generator: Beyond the couple, Journal of Electronic Materials, Vol.38, No.7, 2009, pp. 1376-1381.
- [3] G. F. Rinalde, L. E. Juanicó, E. Tagliavore, S. Gortari, M. G. Molina, "Development of thermoelectric generators for electrification of isolated rural homes," *International Journal of Hydrogen Energy*, vol. 35, pp. 5818- 5822, June 2010.
- [4] L. Francioso, C. De Pascali, I. Farella, C. Martucci, P. Creti, P. Siciliano, A. Perrone, "Flexible thermoelectric generator for ambient assisted living wearable biometric sensors," *Journal of Power Sources*, vol. 196, pp. 3239-3243, March 2011.
- [5] P. Phaga, A. V. Ud, T. Seetawan, "Invention of low cost thermoelectric generator," *Procedia Engineering*, vol. 32, pp. 1050-1053, 2012.
- [6] S. Karabetoglu, A. Sisman, Z. F. Ozturk, T. Sahin, "Characterization of a thermoelectric generator at low temperatures," *Energy Conversion and Management*, vol. 63, pp. 47-50, October 2012.
- [7] Ch. Ch. Wang, Ch. I. Hung, W. H. Chen, "Design of heatsink for improving the performance of thermoelectric generator using two-stage optimization," *Energy*, vol. 39, pp. 236-245, March 2012.
- [8] A.Z. Sahin, B.S. Yilbas, "Thermodynamic irreversibility and performance characteristic of thermoelectric power generator, Energy, Vol 55, 2013, pp 899-904.
- [9] N. Wojtas, L. Rütthemann, W. Glatz, C. Hierold, "Optimized thermal coupling of micro thermoelectric generators for improved output performance," *Renewable Energy*, vol. 60, pp. 746-753, December 2013.
- [10] Ch.Ch. Weng, M. J. Huang, "A simulation study of automotive waste heat recovery using a thermoelectric power generator," *International journal of thermal science*, vol. 71, pp. 302-309, September 2013.
- [11] S. Kim, "Analysis and modeling of effective temperature temperature differences and electrical parameters of thermoelectric generators," *Applied Energy*, vol. 102, pp. 1458-1463, February 2013.
- [12] N. Q. Nguyen, K. V. Pochiraju, "Behavior of thermoelectric generators exposed to transient heat sources," *Applied Thermal Engineering*, vol. 51, pp. 1-9, March 2013.
- [13] M. Oplustil, M. Zalesak, "The power options for transmitting systems using thermal energy generator, "Recent advances in Environment, Energy, Ecosystems and Development, pp. 212-215, September 2013.
- [14] M. Oplustil, M. Zalesak, "A human body waste heat as power option for wireless transmitter for building sensors," *International Journal of Energy and Environment*, vol. 8, pp 40-45, January 2014.

Diagnostics and Evaluation of Limit Strain States from Digital Image

J. Kmec, E. Fečhová, S. Hrehová

Abstract—By means of an appropriate choice of methodology of measurement and evaluation of the forming limit curves (equivalence point method, graphic method, interpolation method and so on) it is possible to eliminate inaccuracies at reading the measurements from deformation network at the place of sheet metal crack. Methodology for elimination of these inaccuracies at determining forming limit curves from digital image of deformation network by means of computing technique is proposed in the paper. Matlab and its Image Processing Toolbox software package is used for direct measurement and evaluation of forming limit curves. Dispositional solution of the tool, which mainly serves to determine the position of forming limit curves, is also described in the paper.

Keywords— Camera system, forming limit curves, forming limit diagrams Matlab.

I. INTRODUCTION

RAISING requirements for manufacture qualities of cars heighten requirements for development of new material types, lubricants, new technologies of preparation and realization of sheet metal pressed parts production. One of the possibilities how to increase technical and economical levels of products is an application of steel sheets and steel sections with special properties. Technological processing of those materials causes problems too, because in most cases the change of stampability parameters occurs in consequence of higher strength and special properties.

It is not possible to imagine to predict stampability of these materials for particular stamping conditions without computing simulation. Reliability and accuracy of numeric simulation results depends on accuracy of the used model and completeness of input data. It results from analyses that apart from the tool model and kinematics of stamping the following

The research work is supported by the Project of the Structural Funds of the EU „Research and Development of the Intelligent Non-conventional Actuators Based on Artificial Muscles”, ITMS code: 26220220103.

J. Kmec, Technical University of Kosice, Faculty of Manufacturing Technologies with a seat in Presov, Department of Mathematics, Informatics and Cybernetics, Bayerova 1, 080 01 Presov, Slovakia, (e-mail: jozef.kmec@tuke.sk).

E. Fečhová, Technical University of Kosice, Faculty of Manufacturing Technologies with a seat in Presov, Department of Mathematics, Informatics and Cybernetics, Bayerova 1, 080 01 Presov, Slovakia, (phone: +421 55 602 6421, e-mail: erika.fechova@tuke.sk).

S. Hrehová, Technical University of Kosice, Faculty of Manufacturing Technologies with a seat in Presov, Department of Mathematics, Informatics and Cybernetics, Bayerova 1, 080 01 Presov, Slovakia, (e-mail: stella.hrehova@tuke.sk).

material data are necessary to predict stampability of steel sheets by means of computing simulation: ν - Poisson number, E - modulus of elasticity, the curves of natural deformation resistances, r - normal anisotropy coefficient, FLC - forming limit curves, f - friction factor [1], [2], [9].

II. EXPERIMENTAL

A. Material and software used

The following steel sheets were used for an experimental research:

- DX 54D – a hot-dip zinc coated extra deep-drawing sheet, suitable for complex large sheet pressings of automobile bodies and other pressed parts (described further as an E material)
- DIN 1.4301 – chrome and nickel anti-corrosion steel suitable for cold forming (STN 17 241 – described further as a D material).

Matlab is an integrated environment for scientific and technical calculation, modelling, simulation, presentation and data analysis. It is a tool for both comfortable interactive work and development of wide spectrum of applications. Open architecture called into existence the libraries of functions that are called toolboxes, which spread the use of the program in particular scientific and technical areas.

Image Processing Toolbox is efficient, flexible and easily manageable tool for digital processing and image analysis.

B. Methodology of measurement and evaluation of forming limit curves

The network deposition technique is used to determine deformation distribution at the plane of steel sheet dependant on deformation history.

Objective definition of limiting state is difficult, because in the crack area it is necessary at evaluation of changes of deformation network measurements to eliminate uncertainty of reading measurements of deformation network at the place where the crack arose. Deficiencies of above mentioned way can be eliminated by the use of digital recording by means of the camera system (Fig. 1).



Fig. 1 Camera system

Recordings of camera systems enable to sort and choose any arbitrary moment of deformation history of a selected element (deformations right before a crack arose) [8] – Fig. 2 and Fig. 3.

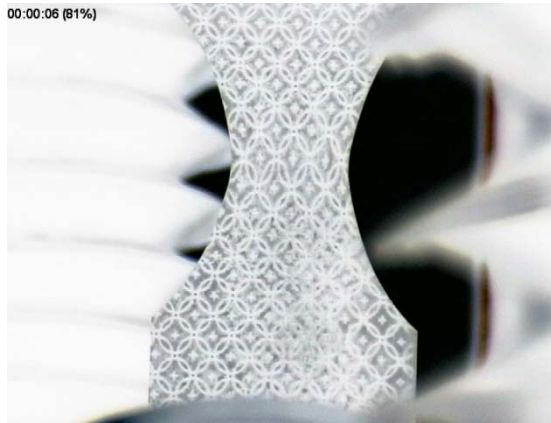


Fig.2 Sample before breakdown

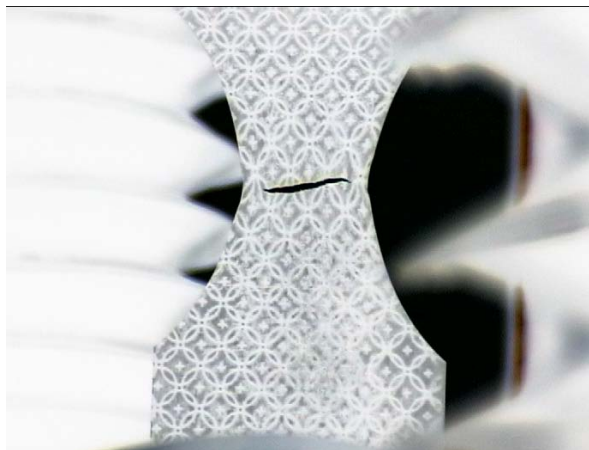


Fig.3 Sample after breakdown

Digital Video Camera NV-GS15EG was used to record deformation history at tensile test on the samples with a notch. Deformation networks with diameter of 5 mm were installed on the sample with notches of 5 mm, 10 mm, 17,5 mm and 25 mm. The samples underwent plastic deformation in the TIRATEST 2300 machine at punch velocities $v_1 = 5$ mm/min and $v_2 = 60$ mm/min. Deformation history of D material at reference velocities $v_{ref} = v_1$ can be found in Tab.1, Fig. 4.

Tab. 1 The values of minor and major strain for D material with the notch $r = 10$ mm and v_{ref}

Minor Strain φ_2	Major Strain φ_1
0.0000000e+000	0.0000000e+000
9.8866869e-003	3.1881308e-002
9.7403662e-003	3.7639459e-002
-2.7151101e-002	9.0789417e-002
-3.6842625e-002	7.7904806e-002
-9.6262896e-002	1.3289385e-001
-1.2026155e-001	1.6930185e-001
-8.7964383e-002	1.8076916e-001
-1.3063527e-001	1.8668616e-001
-1.3432791e-001	2.1874718e-001
-1.2965071e-001	2.3548079e-001
-1.9263607e-001	3.0876358e-001
-1.9696853e-001	3.6470233e-001
-2.0215792e-001	4.0835615e-001
-1.7149364e-001	4.8327883e-001
-1.4833130e-001	6.4200583e-001

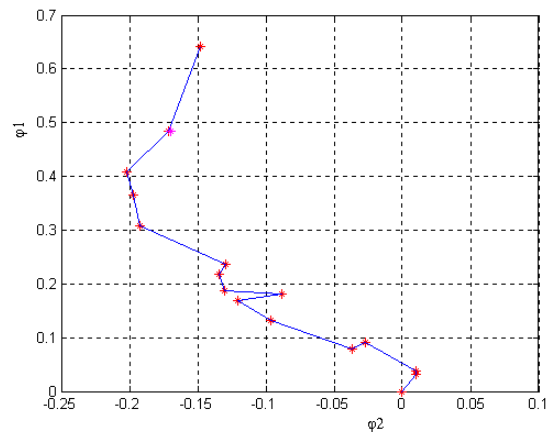


Fig.4 Deformation history of D material for Tab.1

1 ... n images are recorded at proper measurement of deformations during material test. Ten images at an interval from the beginning of deformation to the sample breakdown are selected to describe deformation history (Fig. 3).

The diameter of deformation network on the samples with a notch was measured by means of Abbe linear meter and Image Processing Toolbox. 41.6 pixels conforms to the diameter of

deformation network before deformation of 4.98 mm.

Corresponding measurement sizes of deformation network for selected images, which are specific to deformation history, are written interactively into the created matrix (e.g. Tab. 1).

The images from an industrial camera were put into the Matlab environment in BMP (bitmap) format. Circular deformation network, from which starting position (L_0 diameter before deformation) and final position (L_1 and L_2 lengths of main and secondary axes after deformation) are read by means of Matlab instruction `ginput`, is deposited on the sample. The distance between two points is determined several times and arithmetic average is calculated. φ_1 and φ_2 deformations are calculated by means of relations $\varphi_1 = \ln(L_1/L_0)$ and $\varphi_2 = \ln(L_2/L_0)$. After that the dependence of major strain on minor strain is recorded in the graph (Fig. 4). φ_{1K} and φ_{2K} deformations are evaluated from the images for defined limiting state. The second degree curve is formed by given points (bold numbers in Tab.1) and recorded in the graph (one point in the graph represents one notch and one velocity).

It is possible to determine the left side of the forming limit curve on the samples with a notch by means of the tensile test. The left and right sides of the forming limit curve can be determined by Nakazima and Marciniak methods. The designed tool (Fig. 5) is a part of the TIRATEST 2300 machine in order to study the influence of deformation velocity on the position of the forming limit curves.

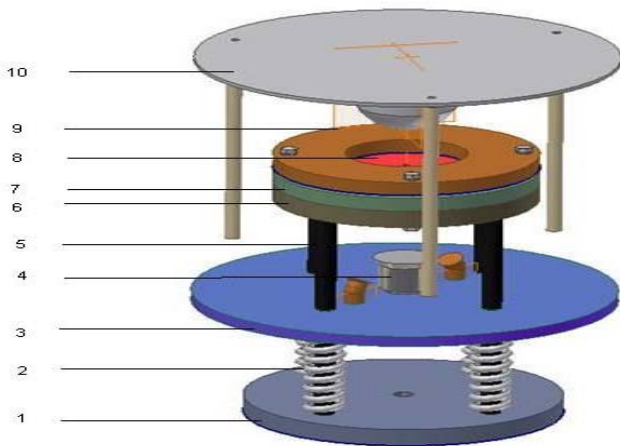


Fig.5 Dispositional solution of the tool (1 – base plate; 2 - springs; 3 – camera system board; 4 – camera system; 5 – carrier bar; 6 – steel sheet mounting plate; 7 - die; 8 - sample; 9 – blank holder; 10 – punch)

III. OBTAINED RESULTS

Stress on material by uniaxial and biaxial tension occurs at stretching and bending. Deformations at the plane of steel sheet for these deformation states can be described by forming limit diagrams - *FLD*. It results from the measured results of

deformation distribution on the samples with notches at the tensile test that deformation path is not linear (Fig. 6 and Fig. 7). Limiting values of deformations at the plane of steel sheet (deformations right before a crack arose) are more significant to define limiting conditions of stampability. It means that if a curve is transferred through critical values of deformations, the left side of *FLD* is obtained. It results from the comparison of the forming limit curves determined at the austenitic steel sheet (D material–Fig. 6) and ferritic steel sheet (E material–Fig. 7) that the higher material values of A_{80} ductility and n strain hardening exponent, the higher is the position of the forming limit curve. The values of those material characteristics are higher at austenitic steel sheets than at low carbon steel sheets – E material. The position of the curves is not significantly influenced by the normal anisotropy coefficient ($r=1$ at austenitic steel and $r=1.8$ at low carbon steel - E material). Obtained forming limit curves are in accordance with current knowledge [1], [3]. The statement that position of the forming limit curves depends mainly on ductility and strain hardening exponent is proved by the results obtained at deformation velocity $\dot{\varphi} = 0,0083s^{-1}$. There was a shift (decrease) of the forming limit curve at D material as well as low carbon steel E material at change of deformation velocities from $0,0007 s^{-1}$ to $0,0083 s^{-1}$.

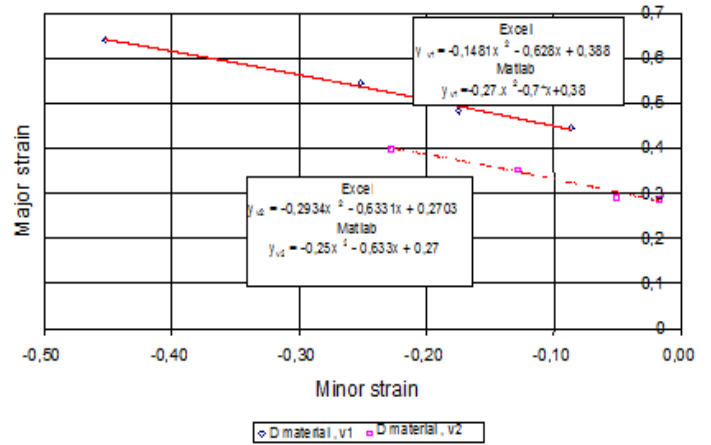


Fig. 6 Forming limit curves determined at D material

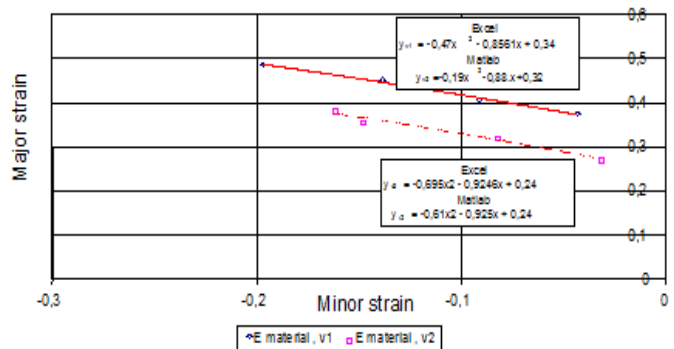


Fig. 7 Forming limit curves determined at E material

Relations to predict $FLD0$ $(\varphi_{1K})_{\varphi_2=0}$ by means of ductility and strain hardening exponent were derived in the paper [3], [7] based on extensive research of various material types:

$$FLD0 = (\varphi_{1K})_{\varphi_2=0} = (2,78 + 3,244.a_0 + 0,892.A_{80}) \quad (1)$$

$$FLD0 = \varphi_{1K} = (23,3 + 14,3.a_0) \cdot \frac{n}{0,21} \quad (2)$$

The values calculated according to the relation (1) (Bethlehem relation) are at about 3 % higher than in the relation (2) (Keller relation). The difference between measured values of $FLD0$ $(\varphi_{1K})_{\varphi_2=0}$ and values calculated by means of above mentioned relations was in the interval from +0,25% to -5%. As mentioned before, if deformation velocity increases, there is a slight decrease of ductility and strain hardening exponent [4], [5]. If changes of ductility dependant on deformation velocity are inducted into the relation (1), it is proved that there is a decrease of position of $FLD0$ at about $\Delta FL D0 = 0,09$ and at low carbon steel there is a decrease of $FLD0$ at about $\Delta FL D = 0,023$. Similarly, if the change of the strain hardening exponent dependant on deformation velocity is inducted into the relation (2), it is proved that at austenitic steel sheets there is a change of $FLD0$ at about $\Delta FL D0 = 0,12$ to $0,132$ and at E material there is a change at about $\Delta FL D0 = 0,003$ to $0,02$. The differences between measured and calculated values are lower at D material in comparison to E material.

IV. CONCLUSION

Obtained results can be summarized as follows:

- 1) The camera system for measurement and evaluation of the forming limit curves, which enables to record entire deformation history, was proposed and verified in the paper. The system was verified on the samples with notches of $r = 5mm$, $r = 10mm$, $r = 17,5mm$, $r = 25mm$ by means of the tensile test.
- 2) To evaluate the changes of measurements of deformation network, the program, which enables to evaluate deformation size, write them into the table and process them graphically, was prepared in Matlab. The advantage of this system in comparison to formerly used system is in the fact that it enables to record entire deformation history, define limiting deformation state and evaluate major and minor critical strain at the plane of the steel sheet (right before the crack arose).
- 3) With regard to the fact that influence of deformation velocity in the examined area became evident in ductility, position of the curve in FLD , strain hardening exponent at D material and did not become evident in the change of normal anisotropy coefficient, it is possible to assume that the higher values of ductility and strain hardening exponent, the higher is the position of the curve in FLD . The curve in FLD slightly decreases at increasing

deformation velocity [6]. For velocities of movement of the shredder traverse $v_1 = 5$ mm/min and $v_2 = 60$ mm/min equations for prediction of the left FLD were inducted from measured critical values of deformations at the plane of steel sheet

- D material

$$v_1 \text{ velocity: } \varphi_{1K,v1} = -0,27\varphi_2^2 - 0,7\varphi_2 + 0,388$$

$$v_2 \text{ velocity: } \varphi_{1K,v2} = -0,25\varphi_2^2 - 0,633\varphi_2 + 0,27$$

- E material

$$v_1 \text{ velocity: } \varphi_{1K,v1} = -0,19\varphi_2^2 - 0,88\varphi_2 + 0,32$$

$$v_2 \text{ velocity: } \varphi_{1K,v2} = -0,61\varphi_2^2 - 0,91\varphi_2 + 0,24$$

The influence of the normal anisotropy coefficient did not become evident in the position of the curve in FLD . The curve in FLD was positioned higher at austenitic steel with $r \cong 1$ than at E material with $r \cong 2$.

REFERENCES

- [1] K. Lange, *Umformtechnik. Blechbearbeitung*, Berlin, Springer-verlag, 1990.
- [2] E. Mielnik, *Metalworking science and engineering*, McGraw-Hill Inc., New York, 1991, pp. 282–286.
- [3] J. L. Geoffroy, Validity of the FLD's Calculations, *In: IDDRG Working Group 3*, 1998.
- [4] E. Evin, A. Hrivňák, J. Tkáčová, "Optimization of Selection of Drawn Parts Production by the Pattern Method", *Mechanics*, vol. 179, 2000, pp. 91-96.
- [5] A. Hrivňák, E. Evin, "Stampability of sheet metals", Košice, Elfa, 2004.
- [6] J. Kmec, P. Piňko, "The desing of structural tool for determining of forming limit diagrams", *In: VII. Vedecká konferencia doktorandov*, SjF TU Košice, 2004.
- [7] A. Labellarte, L. Rizzo, C. Sebastiani, "High Strain Rate Forming Limit Diagram for Steel and Titanium with an Optimised Methodology", *In: IDDRG Working Group 2 Materials*, Ann Arbor Michigan: IDDRG, 2000.
- [8] W. Szczepinski, "Introduction to the mechanics of plastic forming of metals", Sijthoff & Nordhoff Inst. pub., Netherlands, 1979, p. 24.
- [9] W. F. Hosford, R. M. Caddell, "Metal forming", Prentice-Hall, Inc., Englewood Cliffs New Jersey, 1983, pp. 266-269.

Device for heat transport parameters monitoring of solids

P. Košťial, I. Ružiak, R. Igaz, Z. Jančíková, V. Rusnák, R. Garzinová, P. Hlaváček

Abstract— The paper is devoted to the presentation of apparatus for measurement of thermal conductivity k ($\text{W}\cdot\text{m}^{-1}\cdot\text{K}^{-1}$), specific heat capacity c_p ($\text{J}\cdot\text{kg}^{-1}\cdot\text{K}^{-1}$) and thermal diffusivity α ($\text{m}^2\cdot\text{s}^{-1}$) applying the lumped capacitance model (LCM) as a special case of Newton's model of cooling. At the specific experimental conditions resulting from the theoretical analysis of the used model, we present relatively very precise method for experimental determination of all three above mentioned thermal parameters for materials with different thermal transport properties. The input experimental data provide a cooling curve of the tested material obtained in special experimental arrangement. The evaluation of experimental data is realized by special software the fundamental features of which are presented here. The statistical analysis of experimental data was performed. The precision of k , c_p and α determination is relatively high which is demonstrated by statistical confidence interval P_{99} as well as by comparison with table data or independent measurements.

Keywords— Heat capacity, thermal conductivity, diffusivity, solid state materials.

I. INTRODUCTION

Specific properties of materials demand a large spectrum of measuring methods suitable for thermal parameters

This work was created in the framework of the projects SP2013/49, SP2014/53 and SP2014/81 and also it was supported by the Academy of Sciences of the Czech Republic, project RVO 68145535 and project of Institute of clean technologies for mining and utilization of raw materials for energy use, reg.no. CZ.1.05/2.1.00/03.03.0082.

P. Košťial, Faculty of Metallurgy and Materials Engineering, VŠB-Technical University of Ostrava, Ostrava, Czech Republic (phone +420597324498; e-mail: pavel.kostial@vsb.cz).

I. Ružiak, Faculty of Wood Sciences and Technology, Technical University of Zvolen, Zvolen, Slovak Republic (e-mail: ruziak@tuzvo.sk).

R. Igaz, Faculty of Wood Sciences and Technology, Technical University of Zvolen, Zvolen, Slovak Republic (e-mail: igaz@tuzvo.sk).

Z. Jančíková, Faculty of Metallurgy and Materials Engineering, VŠB-Technical University of Ostrava, Ostrava, Czech Republic (e-mail: zora.jancikova@vsb.cz).

V. Rusnák, Faculty of Metallurgy and Materials Engineering, VŠB-Technical University of Ostrava, Ostrava, Czech Republic (e-mail: vladimir.rusnak@form-composite.com).

R. Garzinová, Faculty of Metallurgy and Materials Engineering, VŠB-Technical University of Ostrava, Ostrava, Czech Republic (e-mail: romana.garzinova@vsb.cz).

P. Hlaváček, Institute of Geonics of the ASCR, Institute of Clean Technologies for Mining and Utilization of Raw Materials for Energy Use, Ostrava, Czech Republic (e-mail: petr.hlavacek@ugn.cas.cz).

measurements. Some of them are based on a photoacoustic effect and they are described in [1].

Another group of experiments is based on the application of thermal impulse on the sample surface and its propagation through a sample. These impulse applications either have contact of the heat source with the sample or they are in a contactless (flash) mode. The fundamental theoretical work in this sense is [2]. The so-called flash method has a large spectrum of realizations [3]-[6].

Contact impulse methods with different position of the heat source were described in [7]-[9]. The heat sources in this case usually have a meander shape.

Heat generation in the measured sample can also be realized by mechanical stress. The sample is pulled in a tensile test machine and the generated heat is caused by deformation of its structure. The temperature decay of the pre-pulled sample is measured by a thermovision camera. This measuring system allows measuring specific heat capacity, thermal diffusivity and thermal conductivity as well as the mechanical parameters usually obtained from a tensile test [10]. The evaluation of c_p from cooling curves was studied also in [11].

The cooling of objects is often described by a law, attributed to Newton, which states that the temperature difference of a cooling body with respect to the surroundings decreases exponentially with time. Such behavior has been observed during many laboratory experiments, which led to a wide acceptance of this approach. However, the heat transfer from any object to its surrounding is not only due to conduction and convection but also due to radiation. The latter does not vary linearly with temperature difference, which leads to deviations from Newton's law. A discussion of this topic is provided in work [12]-[13].

In this paper, we present a method for measurement of k , c_p and α applying the lumped capacitance model as a special form of Newton's model of cooling [14]. Used method offer relatively reliable results and has a very good repeatability. Obtained results are statistically treated and they are also compared with known table values or results obtained on independent measurements.

II. THEORETICAL BACKGROUND

It is clear that the conditions of heat transport from a cooling body may not be in general determined solely by convective heat transfer from the surface of heat exchange area

S_c into the surroundings. There is also simultaneous demonstration of radiation heat transfer through the surface of the heat exchange area S_r .

If the body has internal sources of heat with a total output of W_g and, at the same time, a flow of heat with a density of q_s is supplied or discharged through some part of its surface S_s (e.g. by conduction due to contact with other bodies), the differential equation of energy balance of "thermally thin" body has the form of [15]

$$\rho V c_p \frac{dT(t)}{dt} = \pm q_s S_s - h_c S_c [T(t) - T_\infty] - \varepsilon \sigma S_r [T(t)^4 - T_\infty^4] \pm W_g, \quad (1)$$

where ε is the emissivity coefficient of area surface with radiation heat transfer, while σ is Stefan-Boltzmann constant.

If there is an evidence of radiation heat transfer and provided that

$$q_s = 0, \quad W_g = 0 \quad a \quad S_c = S_r = S, \quad (2)$$

(1) acquires the form of

$$\rho c_p L \frac{dT(t)}{dt} = - h_c [T(t) - T_\infty] - \varepsilon \sigma [T(t)^4 - T_\infty^4]. \quad (3)$$

If the radiation heat flow density is expressed using the coefficient of radiation heat transfer h_r in the form of

$$\varepsilon \sigma \{T(t)^4 - T_\infty^4\} = h_r [T(t) - T_\infty], \quad (4)$$

then

$$h_r = \varepsilon \sigma [T(t) + T_\infty] \{T(t)^2 + T_\infty^2\}, \quad (5)$$

and after adjustments, we acquire

$$\rho c_p L \frac{dT(t)}{dt} = - h_i [T(t) - T_\infty], \quad (6)$$

Where

$$h_i = h_c + h_r \quad (7)$$

represents the heat-dependent total, or the so called combined heat transfer coefficient through convection with the coefficient of h_c and radiation with the coefficient of h_r .

In cases when the heat difference between the cooling body and the surrounding space is very little, the combined heat transfer coefficient h_i must be accepted as a constant which does not depend on temperature or time. Integration of (6) with the initial condition of

$$T(t_0 = 0) = T_0 = const \neq T(\bar{r}),$$

provides a clear analytical solution in the form

$$T(t) = T_\infty + (T_0 - T_\infty) e^{-\frac{t}{\tau}}, \quad (8)$$

with relaxation time of

$$\tau = \frac{\rho c_p L}{h_i}. \quad (9)$$

In our case, when both sides of the sample are cooled the relation 9 has the form

$$\tau = \frac{\rho c_p L}{2h_i}. \quad (10)$$

Relation among k , c_p and α has the form

$$k = \alpha \cdot \rho \cdot c_p. \quad (11)$$

where ρ is the sample density.

A general model of concentrated heat capacitance will then be applicable only for Biot number

$$Bi = \frac{h_i L}{\lambda} \ll 1. \quad (12)$$

The analysis of simulation results has shown that the radiation heat transfer coefficient observed at the temperature range of 25-26 °C is practically a linear function of temperature with increasing trend. However, the value of h_r coefficient within the monitored temperature interval does not change by more than 0.5 %, which is why, taking into account the approximate 5 % model accuracy, it can be approximated by its arithmetic average or median, which is less sensitive to deviation and extreme values.

The comparison shows that even at room temperatures and relatively very little temperature differences between the cooling body and the surroundings, the value of radiation heat flow density is considerably high. Radiation heat flow in the given case has an average of more than 23.88 % share on the total heat discharge from the surface of the body. That is why the description of the cooling process must usually take into account both convective and radiation heat transfer mechanism, and it must take into account the combined nature of the thermal interactions of the body with the surroundings, which more accurately corresponds to the macroscopic description of the heat exchange processes than during the application of a simple exponential model of the first order which neglects radiation.

The value of the radiation heat transfer coefficient is calculated from the relation [15]

$$h_r = - \frac{\varepsilon \sigma \{T(t)^4 - T_\infty^4\}}{\{T(t) - T_\infty\}}. \quad (12)$$

With increasing temperature differences between the cooling body and its surroundings, the possibility of approximation of the radiation heat transfer coefficient using a constant value is definitively lost. At higher temperatures and temperature differences, the temperature dependence of the convective heat transfer coefficient begins to show [15].

Higher temperatures can also show thermal dependence of other physical parameters concentrated in the relaxation time, thus losing the character of a constant value.

III. EXPERIMENTAL APPARATUS AND SOFTWARE PROCEDURES

The measured samples must have an area of about (10 x 10 x 2) mm³ and must be finely ground. Matt black spray-paint is applied on all sides of the samples in order to ensure they have the same emissivity.

The equipment consists of a thermally insulated chamber [16]. The cover of the chamber has an opening for a pyro-electric sensor Raytek THERMALERT MID 02. The fundamental characteristic of the sensors is as follows. The temperature ranges from -40 to 600 °C, spectral response from 8 to 14 μm, response time 150 ms (95 % response), accuracy ± 1 % or ± 1°C (± 2 °F) whichever is higher.

The sample is heated above room temperature in a thermostat. After removal from the thermostat, the sample is quickly placed into the measuring chamber which will be closed.

The input data are represented by the cooling curves, which are obtained by contactless temperature measurement using an infrared sensor. The set of data is automatically *e-sampled*. This data can be used to select a suitable compact curve area with constant τ . This data selection also allows to minimize the radiation heat transfer coefficient h_r (see the text above). This procedure together with adiabatic chamber construction satisfies the validity of the (11). The data are provided in the form of a text file with the specified parameters.

We have measured every sample more than ten times to obtain a solid base (ten chosen values of τ) for statistical evaluation. It has been observed a small drift of the infrared sensor. For the best statistical parameters we usually removed 3-4 values of τ from the beginning of the data set and statistics has been done from ten remaining chosen data.

The time constant τ is the basis for determining other heat-transport parameters of the material. Equation (8) which represents the master equation of the problem is linearized by logarithmic function and we obtain relation $\ln(T - T_\infty) = \ln(T_0 - T_\infty) - t/\tau$ which is fitted by using the method of the smallest squares and the term $-1/\tau$ indicates the slope of line. The initial temperature T_0 is known from the measurement. When the relaxation time τ has been determined, this value is used to determine of c_p .

In the second step we start to find further unknown physical value c_p . Because the (9) expressing the relation of c_p versus h_r has infinite number of solutions, which means that only fitting procedures can be used to determine the required thermal and

physical quantities. The basic prerequisite is the knowledge or at least an estimate of the total heat transfer coefficient h_t from the material to the surrounding environment. This can be estimated if the dimensions of the individual groups of samples (metals, plastics, laminates, etc.) are nearly the same, which in our case means the sample surface of about 100 mm² and the thickness approximately of 2 mm. The size of the sample and its weight is also used to determine the density of the sample material. In this step, we can set h_t (15-25) according to above described conditions. For further unknown c_p we set qualified estimate according to the type of material – metals, plastics, laminates, etc (Table I).

The algorithm in the initial step is based on the intersection of the given and possible intervals of both quantities. Once the common intervals of meaningful values have been determined, the algorithm tries to find a single value using the interval division method by gradually decreasing the interval of both required values. After this procedure c_p is known and it is used for evaluation of thermal conductivity and thermal diffusivity.

Similar procedure is used for the further unknown pair of thermal parameters α and k , where the following equation is applied $\alpha \rho c_p = k$, $B c_p = k$, $B = \alpha \rho$ and where for both quantities will use qualified guesses according to the type of material at the beginning of fitting.

For easier orientation in the process of fitting, the sum of deviation quadrates of these trajectories with the original cooling curve of the material is calculated. The smallest *sum* R^2 indicates the best fit of both experimental and estimated curves. Finally, if we have determined all k , c_p and α it is necessary to verify validity of the condition given by relation (11), which is satisfying for model validity. (Biot number have to be smaller than 0.1).

Table I Qualified estimates (intervals) of k , c_p and α for the distinguished types of materials

Material	Heat capacity interval (J·kg ⁻¹ ·K ⁻¹)	Thermal diffusivity interval (m ² ·s ⁻¹)	Thermal conductivity interval (W·m ⁻¹ ·K ⁻¹)
Copper	315-470	(1-1.35) · 10 ⁻⁴	380-420
Epoxide + glass fibres	1000-1500	(1-10) · 10 ⁻⁷	0.1-2
PMMA	1300-1500	(0.9-1.1) · 10 ⁻⁷	0.18-0.20
Rubbers	1200-1600	(1-3) · 10 ⁻⁷	0.1-0.3

IV. RESULTS AND DISCUSSION

After this analysis, the experiment proceeds with the presentation of data obtained from selected materials with relatively high, respectively low value of k , c_p and α . Firstly,

we present the measurements of thermal parameters of rubber mixture. Since we did not have a table value available to compare, we used a different method to obtain the reference values described in work [9]. The results measured by means of the two methods are shown in Table II. The relatively good agreement of both methods is clearly seen.

Table II Comparison of thermo-physical parameters obtained by applying the method of exponential model of cooling body with the parameters obtained by EDPS method [9]

Compared thermo-physical parameters	Method	Results
c_p (J·kg ⁻¹ ·K ⁻¹)	Method EDPS	1218.92
	Exponential model	1288.44
α (m ² ·s ⁻¹)	Method EDPS	1.89 ·10 ⁻⁷
	Exponential model	1.98 ·10 ⁻⁷
k (W·m ⁻¹ ·K ⁻¹)	Method EDPS	0.29
	Exponential model	0.30

In Table III we present results obtained for lead which have higher thermal transport parameters.

Table III Thermal parameters of lead

Material Pb	Measured	P ₉₉	Table values
c_p (J·kg ⁻¹ ·K ⁻¹)	134.2±1.88	(128.09-140.31)	129
α (m ² ·s ⁻¹)	(2.48±0.03)·10 ⁻⁵	(2.38-2.58)·10 ⁻⁵	2.44 ·10 ⁻⁵
k (W·m ⁻¹ ·K ⁻¹)	36.1±0.38	(34.87-37.33)	35
Bi	0.016		

Next experiments with the highest thermal parameters have been realized on silver. Results are presented in Table IV.

Table IV Thermal parameters of silver

Material Ag	Measured	P ₉₉	Table values
c_p (J·kg ⁻¹ ·K ⁻¹)	236.21 ± 2.51	(228.04-244.36)	235

α (m ² ·s ⁻¹)	(1.86 ± 0.02)·10 ⁻⁴	(1.78-1.93)·10 ⁻⁴	1.7·10 ⁻⁴
k (W·m ⁻¹ ·K ⁻¹)	434.22 ± 5.06	(417.74-450.66)	420
Bi	0.016		

V. CONCLUSION

The presented method used to measure k , c_p and α is based on Newton's model of cooling body, respectively on its modification in the form of lumped capacitance model. The method uses a set of data of temperatures from the cooling body in predominantly convective- radiative cooling mode in a specially designed chamber to perform further software processing. Further software processing, based on qualified guesses of k , c_p and α and h_t , provides approximate solution of the characteristic equations, which allow relatively highly accurate determination of k , c_p and α . The advantage of the method is that it is contactless; it requires only small amounts of tested sample, whose surface treatment is not very demanding. The presented results show good conformity of the measured and tabular, respectively reference values of k , c_p and α .

ACKNOWLEDGMENT

This work was created in the framework of the projects SP2013/49, SP2014/53 and SP2014/81 and also it was supported by the Academy of Sciences of the Czech Republic, project RVO 68145535 and project of Institute of clean technologies for mining and utilization of raw materials for energy use, reg.no. CZ.1.05/2.1.00/ 03.03.0082.

REFERENCES

- [1] A. Mandelis, *Progress in Photothermal and Photoacoustic Science and Technology*, Elsevier, New York, 1991, pp. 207-284.
- [2] W. J. Parker, R. J. Jenkins, C. P. Butler., G. L. Abbott, "Flash method of determination thermal diffusivity, heat capacity and thermal conductivity," in *Journal of Applied Physics*, vol. 32, no. 9, 1961.
- [3] M. Akoshima, T. Baba, "Study on a thermal-diffusivity standard for laser flash method measurements," in *Int. J. Thermophysics*, vol. 27, no. 4, 1189-1203, 2006.
- [4] P. S. Gaal, M. A. Thermitus, D. E. Stroe, "Thermal conductivity measurements using the flash method," in *Journal of Thermal Analysis and Calorimetry*, vol. 78, no. 1, 185-189, 2004.
- [5] M. Akoshima, T. Baba, "Study on a thermal-diffusivity standard for laser flash method measurements," in *Int. J. Thermophysics*, vol. 26, no. 1, pp. 1189-1203, 2005.
- [6] Y. Ezzahri, S. Dilhaire, S. Grauby, J. M. Rampnoux, W. Claeys, Y. Zhang, G. Zeng, A. Shakouri, "Study of thermomechanical properties of Si/SiGe superlattices using femtosecond transient thermoreflectance technique," in *Applied Physics Letters*, vol. 87, no. 10, 2005.
- [7] Y. R. Jeng, J. T. Chen, C. Y. Cheng, "Thermal contact conductance of coated surfaces," in *Wear*, vol. 260, no. 1-2, pp. 159-167, 2006.
- [8] <http://www.transientms.com>
- [9] S. Malinarič, P. Dieška, P. Krupa, "Modified Dynamic Plane Source Method for Measuring Thermophysical Parameters of Solids," in *Int. J. Thermophysics*, vol. 33, no. 3, pp. 528-539, 2012.

- [10] P. Košťal, I. Ružiak, Z. Jonšta, I. Kopal, R. Hrehuš, J. Kršková, „Experimental Method for Complex Thermo-mechanical Material Analysis,” in *Int.J. of Thermophysics*, vol. 31, no. 3, 630 -636, 2010.
- [11] I. Kopal, K. Kováč, R. Puchký, in *Metalurgical Journal*, **LXV**, vol 7, no. 94/96, 2012.
- [12] U. Besson, “The History of the Cooling Law: When the Search for Simplicity can be an Obstacle,” in *Science and education*, vol. 8, 2012, pp. 1085-1110.
- [13] K. C. Cheng, “Some Observations on the Origins of Newton's Law of Cooling and Its Influences on Thermofluid Science”, in *Applied Mechanics Reviews*, vol. 62, no. 6, 2009.
- [14] J. H. Lienhard, A Heat Transfer Textbook, Phlogiston Press, Cambridge, 2004.
- [15] I. Kopal, P. Košťal, *Investigation of thermal parameters of materials I*, VŠB-TU Ostrava, Ostrava, 2010.
- [16] P. Košťal, I. Ružiak, Z.Jančíková, Patent NO 303269 CS, 2012

Pavol Košťal

Born 5. 7. 1949, Žilina, Slovakia,
1967 - 1972 Comenius University of Bratislava, Slovakia,
1972 – 1975 RNDr. Comenius University of Bratislava, Slovakia,
1975 – 1980 CSc. (Ph.D.) Comenius University of Bratislava, Slovakia,
1976 Associated Professor of Solid State Physics in Comenius University of Bratislava, Slovakia,
1993 - 1996 Vice rector of University of Žilina, Slovakia,
1997 – 2000 Dean of the Faculty of Industrial Technologies in Puchov, Slovakia,
1998 Professor of Solid State Physics, University of Žilina, Slovakia,
1999-2008 Dean of the Faculty of Industrial Technologies in Puchov, Slovakia,
2009 Professor at the VŠB Technical University of Ostrava, Czech Republic.

Oilmarks Detection Algorithm in Steel Plates

Doo-chul Choi, Yong-Ju Jeon, Sang Jun Lee, Jong Pil Yun, and Sang Woo Kim

Abstract—In steel manufacturing industry, vision based inspection system is an important topic to increase quality of products. The shape of an oilmark is circular form and the gray value is uniform. Based on these characteristics, we have developed an algorithm for detecting oilmarks in steel plates. To classify the oilmarks and pseudo-defects, we calculated the features of oilmarks, and applied Support Vector Machine (SVM) classifier. We have tested proposed algorithm on images obtained from a real production line. Experimental results show that the proposed algorithm is possible to detect oilmarks in steel plates.

Keywords—defect detection, steel inspection, image processing

I. INTRODUCTION

IN steel manufacturing industry, vision based inspection system is an important topic to increase quality of products. Product inspection for quality assurance is manually operated by human. Manual inspection is inefficient and time-consuming. On the otherhand, vision based automatic inspection system provides low-cost, high-speed, and 100% inspection. Therefore, development of an automatic inspection system is very important issue in steel industry.

Various defect detection algorithms have been developed for steel products. Defect detection in steel wire rods using orthogonal wavelet filters optimized by an univariate dynamic encoding algorithm for searches (uDEAS) has been proposed [1]. Pinhole detection algorithm in steel slabs has been developed [2]. An algorithm for detecting corner cracks in steel billets has been suggested based on a wavelet reconstruction method [3].

Defect detection algorithm for steel plates using dual light switching lighting method have been developed [4], but target of detection was lumpy defects. A steel plate is a finished product manufactured by continuous casting and hot rolling mill process. Because defects on the surface of a steel plate directly influence the quality of products, developing an automatic inspection system is necessary. In this paper, we focus on oilmarks in steel plates. Oilmark is generated when oil drops to the surface of the steel plate directly or a roller coated with oil pass the surface of the steel plate. To detect oilmarks efficiently, we have developed binarization method based on the histogram of image. To classify oilmarks and pseudo-defects, we have extracted features based on the characteristics of an oilmark.

Doo-chul Choi, Yong-Ju Jeon, and Sang Jun Lee are with the Department of Electrical Engineering, Pohang University of Science and Technology (POSTECH), Pohang, 790-784, South Korea e-mail: ({dooshe, jjeon83, lsj4u0208}@postech.ac.kr).

Jong Pil Yun is with Rolling Technology Research Group, Pohang Steel and Iron Company (POSCO), Pohang 790-300, South Korea e-mail: (re-birth@posco.com).

Sang Woo Kim is with Department of Electrical Engineering (EE) and Department of Creative IT Excellence Engineering (CITE), Pohang University of Science and Technology (POSTECH), Pohang 790-784, South Korea e-mail: (swkim@postech.ac.kr).

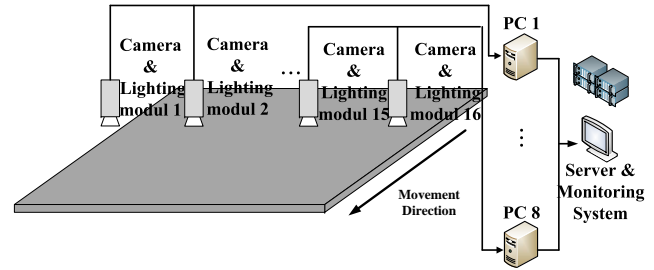


Fig. 1. Structure of automatic inspection system

In Section 2, we explain the configuration of the automatic inspection system and analysis of images. In Section 3, we present the detection algorithm for oilmarks. In Section 4, we show the experimental results. Finally, conclusion of this paper is reported in Section 5.

II. SYSTEM CONFIGURATION & IMAGE ANALYSIS

To obtain the high quality images of thick plates, automatic inspection system is installed as shown in Fig.1. The automatic inspection system consists of four components: cameras, lightings, frame grabbers, and PCs. Owing to the disadvantages of an area-scan camera such as blurring, inspection speed, lighting problem, and restriction of the inspection range [5], line scan cameras are used. These cameras scan one line for each 0.5 mm vertical movement of the thick plate. A frame consists of 1000 lines, and each line therefore consists of 1024 pixels. Sixteen images were acquired from the frame grabbers, and the PCs run the algorithm to detect oilmarks. The original images and results are stored at the server and monitoring system.

In this paper, the target of detection is an oilmark, which can be defect-causing factor. Oil that directly drops to the surface and a roller coated with oil generate an oilmark on the surface of the steel plate. If a foreign substance is attached to the oilmark, it could be defect in subsequent process. In order to detect a foreign substance which is defect-causing factor existing in an oilmark, an oilmark should be detected. The image of an oilmark is shown in Fig.2 (a). The normal surface of a steel plate is shown in Fig.2 (b). When the oil is dropped to the surface of a steel plate, the oilmark is commonly generated with the shape of circular form. Moreover, the gray value of oilmark is low, and uniform. The detection algorithm is developed by using these characteristics of the oilmark.

III. PROPOSED ALGORITHM

A. Segmentation

We obtained the images of a steel plate from the sixteen cameras. In images containing the boundary of a steel plate,

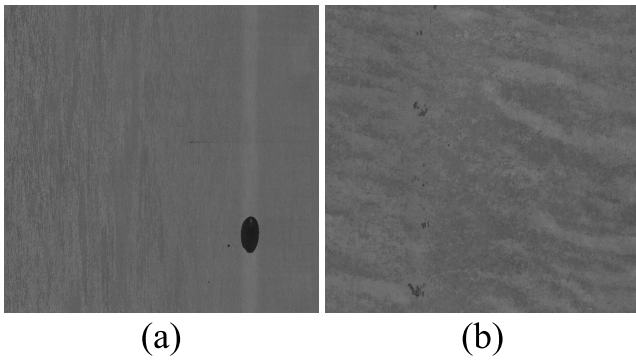


Fig. 2. One frame images of steel plate: (a) A image with an oilmark (b) A image of normal surface

background that does not include information. In order to remove unnecessary information of an image, segmentation process was performed to boundary images of a steel plate. Using the vertical and horizontal projection profiles, segmented images were obtained.

B. ROI Extraction

To detect oilmarks, binarization process should be performed. We selected proper threshold value based on the histogram of an image. Owing to the low gray values of an oilmark, the histogram has a gaussian distribution in the region of low gray values. On the otherhand, the histogram of a normal surface has a gaussian distribution in the relatively right region compared to the oilmark. If there exists an oilmark in an image, the histogram of an image has two gaussian distributions as shown in Fig.3 (a). The histogram of normal surface has a gaussian distribution as shown in Fig.3 (b). We plotted the histograms as logscale function to identify the distributions in detail. To binarize the region of an oilmark,

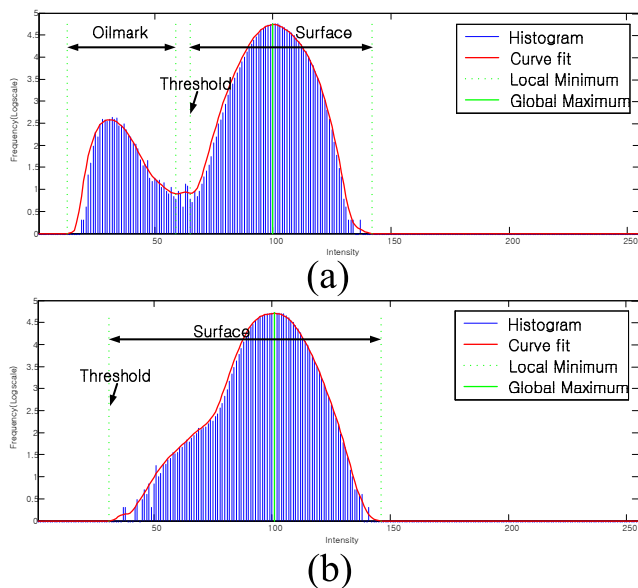


Fig. 3. Histogram plot with threshold value: (a) A histogram of an oilmark (b) A histogram of normal surface

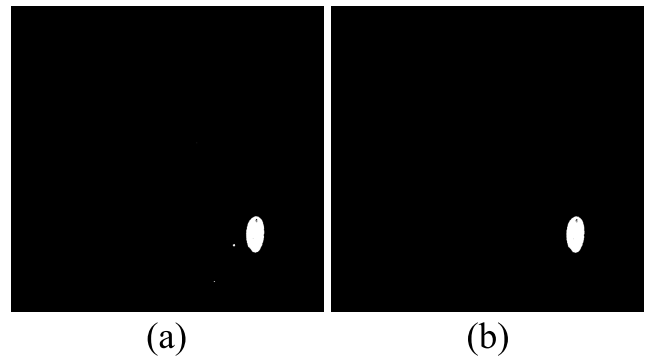


Fig. 4. (a) A binary image using threshold (b) A binary image after sizefiltering

threshold value should be the maximum gray value of the oilmark. If there exists an oilmark in an image, the histogram has mixture of two gaussian distributions: small one is for an oilmark, and large one is for normal surface as shown in Fig.3 (a). Therefore, proper threshold value is local minimum point between the distributions of an oilmark and a normal surface. Threshold value is determined as the maximum point among the local minimums of histogram which are less than the global maximum point of it as shown in Fig.3 (a).

Using the threshold value determined abovementioned method, binarization is performed. The binary image $B(x, y)$ (Fig.4 (a)) was represented as follows:

$$\text{If } T > R(x, y) \text{ then } B(x, y) = 1, \text{ else } B(x, y) = 0 \quad (1)$$

where T is a threshold value.

In order to remove small noise components, size filtering was applied to $B(x, y)$ as shown the Fig.4 (b). By labelling $B(x, y)$, we obtained the ROI images $R_{gray}(x, y)$ and $R_{bin}(x, y)$ of oilmark as shown in Fig.5 (a) and (b), respectively.

C. Feature Extraction

Gray-level image (Fig.5 (a)) and binary image (Fig.5 (b)) of oilmark are obtained by the ROI extraction process. However, noise components were also detected in the normal surface as shown in Fig.6. Therefore, we classified oilmarks and noise components based on the characteristics of oilmarks. Because of the circular shape of an oilmark, features based on the morphological shape were used. Moreover, features based on the histogram were also used.

A signature is a 1-D functional representation of boundaries of a binary blob in Fig.5 (a) [6]. It may be generated various way. We used the distance from the centroid and the boundary as a function of angle. Signature $S(\theta)$ of a binary blob is plotted in Fig.5 (b). From the $S(\theta)$, we note three features: mean, and standard deviation, and ratio of maximum value and minimum value of $S(\theta)$.

Because the shape of an oilmark is circular form, we extracted four features from the binary image: extent, eccentricity, solidity, and perimeter/diameter [7]. Extent is a scalar that specifies the ratio of the area in the total bounding

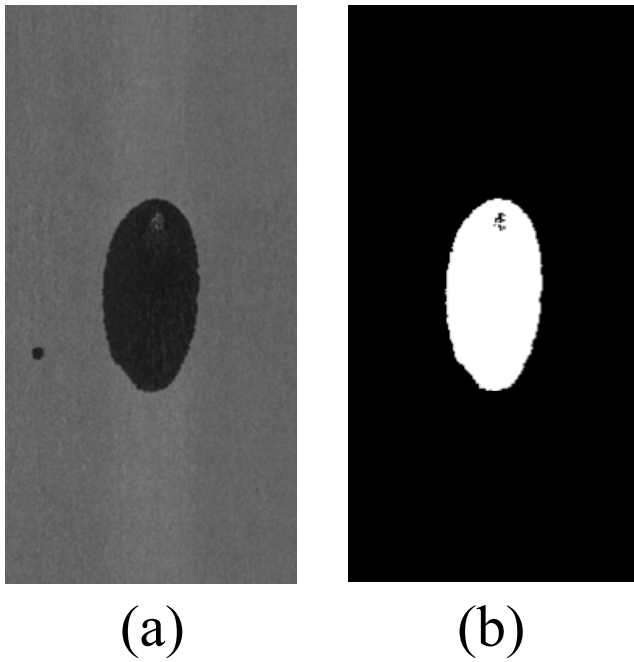


Fig. 5. ROI images: (a) A gray-valued ROI image of an oilmark (b) A binary ROI image of an oilmark

box. Eccentricity is the ratio of the distance between the foci and major axis length of ellipse that has the same second-moments as the binary blob. Solidity is the ratio specifying the proportion of a blob in its convex hull. Perimeter is the distance of the boundaries of a blob.

We calculated two histograms of $R_{gray}(x, y)$ and an oilmark in $R_{gray}(x, y)$ as shown in Fig. 6 (b) and (c), respectively. From the each histogram, we extracted six features: mean, standard deviation, smoothness, third momentum, uniformness, and entropy [6].

We have extracted six features based on the shape of the oilmark in $R_{bin}(x, y)$, and twelve features based on the histogram of the $R_{gray}(x, y)$.

IV. EXPERIMENTAL RESULTS

To enhance the performance of the proposed algorithm, we employed SVM to classify oilmarks and pseudo-defects.

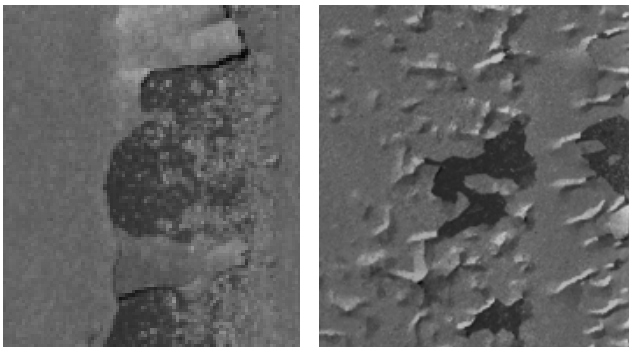


Fig. 6. ROI images: (a) A gray-valued ROI image of an oilmark (b) A binary ROI image of an oilmark

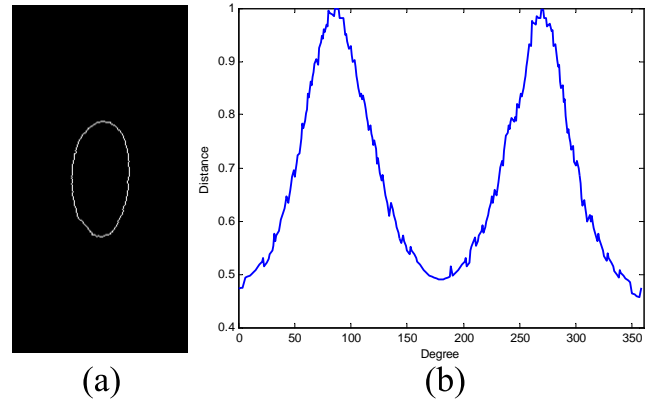


Fig. 7. (a) Boundaries of $R_{bin}(x, y)$ (b) Signature of (a)

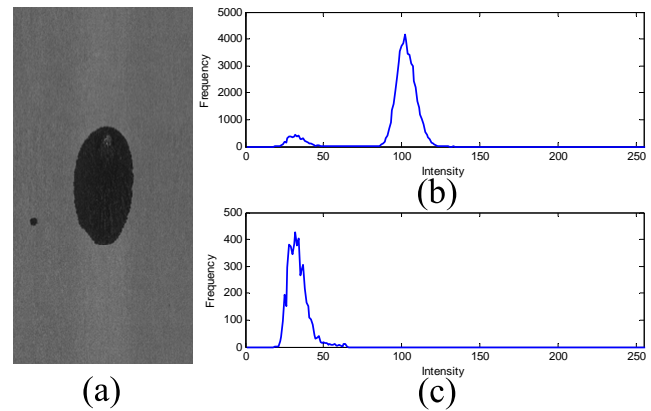


Fig. 8. (a) $R_{gray}(x, y)$ (b) Histogram of a ROI image (c) Histogram of an oilmark region

SVM is a supervised machine learning algorithm based on the statistical learning methods [8]. In this study, C-SVM with radial basis function kernel was used [9]. The training result of SVM is listed in Table. 1.

To evaluate the performance of the proposed algorithm, we tested 844 images containing 156 images of oilmarks directly acquired from a real production line. From the 844 images, 183 ROI images with oilmarks and 221 ROI images with pseudo-defects. SVM was applied to classify oilmarks and pseudo-defects. The dimension of feature vector is nineteen: seven for shape and twelve for histogram. The experimental results are summarized in Table. 2. Consequently, the proposed algorithm was suitable for detecting oilmarks in the steel plates.

TABLE I
THE TRAINING RESULT OF SVM

Training		Validation	
defect	pseudo-defect	defect	pseudo-defect
89/91 (97.80%)	108/110 (98.18%)	85/92 (92.37%)	108/111 (97.30%)

TABLE II
EXPERIMENTAL RESULTS

	defect	defect-free
ROI extraction	146/157 (92.99%)	149/687 (21.69%)
Feature extraction	144/157 (91.72%)	3/687 (0.43%)

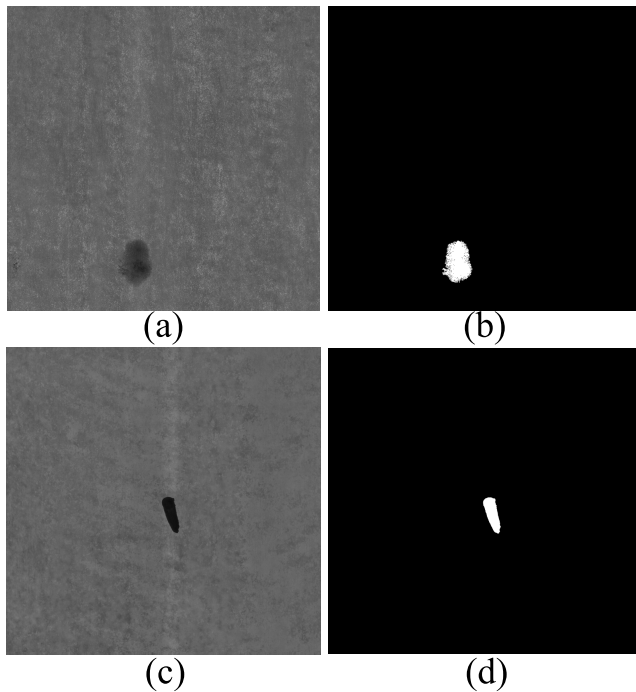


Fig. 9. (a) $R_{gray}(x, y)$ (b) Histogram of a ROI image (c) Histogram of an oilmark region

V. CONCLUSION

In this study, we have developed an oilmark detection algorithm using feature extraction method. Using the characteristics of oilmarks that are circular shape and uniform distribution of gray values, we have extracted features based on the morphological shape of binarized blob in a binary image, and histogram of a gray image. Moreover, SVM classifier increased the performance of detecting oilmarks. We have tested the proposed algorithm on actual images of steel plates. The experimental results show that the proposed algorithm is possible to detect oilmarks in steel plates.

ACKNOWLEDGMENT

“This research was supported by the MSIP(Ministry of Science, ICT and Future Planning), Korea, under the “IT Consilience Creative Program”(NIPA-2014-H0201-14-1001) supervised by the NIPA(National IT Industry Promotion Agency)”.

“This research was supported by the MSIP(Ministry of Science, ICT & Future Planning), Korea, under IT/SW Creative research program supervised by the NIPA(National IT Industry Promotion Agency)” (NIPA-2013-H0502-13-1109).

REFERENCES

- [1] J. P. Yun, Y. -J. Jeon, D. -c. Choi, and S. W. Kim, Real-time defect detection of steel wire rods using orthogonal wavelet filters optimized by univariate dynamic encoding algorithm for searches (uDEAS), J. Opt. Soc. Am. A, vol 29, pp. 797-807, 2012.
- [2] D.-c. Choi, Y.-J. Jeon, J.P. Yun, and S.W. Kim, Pinhole detection in steel slab images using Gabor filter and morphological features, Appl. Opt. vol 50, pp. 5122-5129, 2011.
- [3] Y. J. Jeon, D. C. Choi, S. J. Lee, J. P. Yun, and S. W. Kim, Defect detection for corner cracks in steel billets using a wavelet reconstruction method. JOSA A, vol 31(2), pp. 227-237, 2014.
- [4] Y. J. Jeon, D. C. Choi, J. P. Yun, C. H. Park, H. M. Bae, and S. W. Kim, Automated Inspection Algorithm for Thick Plate Using Dual Light Switching Lighting Method, in Proc. World Academy of Science, Engineering and Technology, vol 72, Dec. 2012.
- [5] C. S. Cho, B. M. Chung, and M. J. Park, Development of real-time vision-based fabric inspection system. Industrial Electronics, IEEE Transactions on, vol. 52(4), pp. 1073-1079, 2005.
- [6] R. C. Gonzalez, and R. E. Woods, Digital image processing, Prentice Hall, 2002.
- [7] R. C. Gonzalez, and R. E. Woods, and S. L. Eddins, Digital image processing using MATLAB, Pearson Education India, 2004.
- [8] C. Cortes, and V. Vapnik, Support-vector networks. Machine learning, vol 20(3), pp. 273-297, 1995.
- [9] C. W. Hsu, C. C. Chang, and C. J. Lin, A practical guide to support vector classification, <https://www.cs.sfu.ca/people/Faculty/teaching/726/spring11/svmguide.pdf>, 2003.

Temperature stability of construction polymers after radiation cross-linking

Ales Mizera, Miroslav Manas, Zdenek Holik, David Manas, Michal Stanek, Jan Navratil, and Martin Bednarik

Abstract—Radiation processing involves the use of natural or manmade sources of high energy radiation on an industrial scale. The principle of radiation processing is the ability of high energy radiation to produce reactive cations, anions and free radicals in materials. The industrial applications of the radiation processing of plastics and composites include polymerization, cross-linking, degradation and grafting. Radiation processing mainly involves the use of either electron beams from electron accelerators or gamma radiation from Cobalt-60 sources. The PBT polybutylene terephthalate and PA6 polyamide 6 tested showed significant changes of temperature stability and mechanical properties after irradiation. From this point-of-view, new applications could also be seen in areas with service temperatures higher than their former melting point. The comparison of the temperature stability and mechanical properties of irradiated and non-irradiated PBT and PA6 are presented in this paper.

Keywords—Polymers, irradiation, cross-linking, temperature stability.

I. INTRODUCTION

THE cross-linking of rubbers and thermoplastic polymers is a well-proven process for the improvement of thermal properties. The chemical cross-linking or rubber vulcanization is normally induced by the effect of heating after processing with the presence of a curing agent. The cross-linking process for thermosets is very similar. In thermosets, the polymer molecules are also chemically linked due to heat after processing. Cross-linked rubbers have a wide-meshed

molecular network that keeps them soft and their properties change only slightly on a wide temperature scale. On the other hand, thermosets are characterized by a very narrow-meshed network. Due to this fact, they hardly change their high level of stiffness on a wide temperature scale at all. The irradiation cross-linking of thermoplastic materials via electron beam or cobalt 60 (gamma rays) is performed separately, after processing. Generally, ionizing radiation includes accelerated electrons, gamma rays and X-rays. [1]

Radiation processing with an electron beam offers several distinct advantages when compared with other radiation sources, particularly γ -rays and x-rays. The process is very fast, clean and can be controlled with much precision. There is not permanent radioactivity since the machine can be switched off. In contrast to γ -rays and x-rays, the electron beam can be steered relatively easily, thus allowing irradiation of a variety of physical shapes. The electron beam radiation process is practically free of waste products and therefore is no serious environmental hazard. These are not only capable of converting monomeric and oligomeric liquids, but also can produce, due to cross-linking, major changes in the properties of solid polymers. The cross-linking level can be adjusted by the irradiation dosage. The absorbed dosage means the value of energy of ionizing radiation absorbed by a unit of mass of the processed material. The unit of absorbed dose is 1 Gray (1 Gy = 1J/kg). The main difference between beta and gamma rays is in their different abilities to penetrate the irradiated material. Gamma rays have a high penetration capacity. The penetration capacity of electron rays depends on the energy of the accelerated electrons. Due to electron accelerators, the required dosage can be applied within seconds, whereas several hours are required in the gamma radiation plant (Fig. 1). [1, 2]

Beta and gamma rays can be used for the irradiation of polyolefines, polyesters, halogen polymers and polyamides from the thermoplastics group, elastomers and thermoplastic elastomers. Some of them need the addition of a cross-linking agent. Polymers can be classified into two groups according to their response to ionizing radiation. One group exhibits predominant cross-linking, the other predominant chain scission. [1, 2]

Ales Mizera is with the Tomas Bata University in Zlin, nam. T. G. Masaryka 5555, 760 01 Zlin, Czech Republic (phone: +420 57 603 5226; fax: +420 57 603 5176; e-mail: mizera@ft.utb.cz).

Miroslav Manas is with the Tomas Bata University in Zlin, nam. T. G. Masaryka 5555, 760 01 Zlin, Czech Republic (e-mail: manas@ft.utb.cz).

Zdenek Holik is with the Tomas Bata University in Zlin, nam. T. G. Masaryka 5555, 760 01 Zlin, Czech Republic (e-mail: holik@ft.utb.cz).

David Manas is with the Tomas Bata University in Zlin, nam. T. G. Masaryka 5555, 760 01 Zlin, Czech Republic (e-mail: dmanas@ft.utb.cz).

Michal Stanek is with the Tomas Bata University in Zlin, nam. T. G. Masaryka 5555, 760 01 Zlin, Czech Republic (e-mail: stanek@ft.utb.cz).

Jan Navratil is with the Tomas Bata University in Zlin, nam. T. G. Masaryka 5555, 760 01 Zlin, Czech Republic (e-mail: j1navratil@ft.utb.cz).

Martin Bednarik is with the Tomas Bata University in Zlin, nam. T. G. Masaryka 5555, 760 01 Zlin, Czech Republic (e-mail: mbednarik@ft.utb.cz).

ACKNOWLEDGMENT: This paper is supported by the internal grant of TBU in Zlin No. IGA/FT/2014/016 funded from the resources of specific university research and by the European Regional Development founder under the project CEBIA-Tech No. CZ.1.05/2.1.00/03.0089.

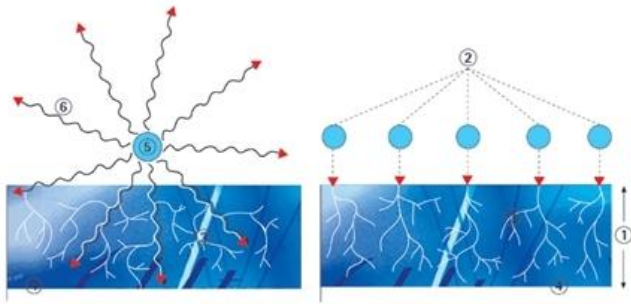


Fig. 1 Design of Gamma Rays (a) and Electron Rays (b),
 1 – Penetration depth of an electron, 2 – Primary electron,
 3 – Secondary electron, 4 – Irradiated material,
 5 – Encapsulated Co – 60 Radiation source, 6 – Gamma Rays [2]

Irradiation cross-linking of thermoplastic materials deals with creation of a cross-link among the macromolecular strings. Intermolecular forces are replaced by a covalent bond. As a result, we can optimise properties of standard and engineering polymers and impart them the properties of high performance polymers (Fig. 2). Irradiation of polymers turned out to be interesting because of economic reasons, production costs and a life time of products. However, these benefits depend on the type of irradiated polymer and the radiation dosage. Behaviour of each material is different after irradiation. We cannot expect the improvement in all areas (in mechanical, thermal and chemical). Most of polymers are not suitable for irradiation because of degradation and deterioration of their properties. [8]

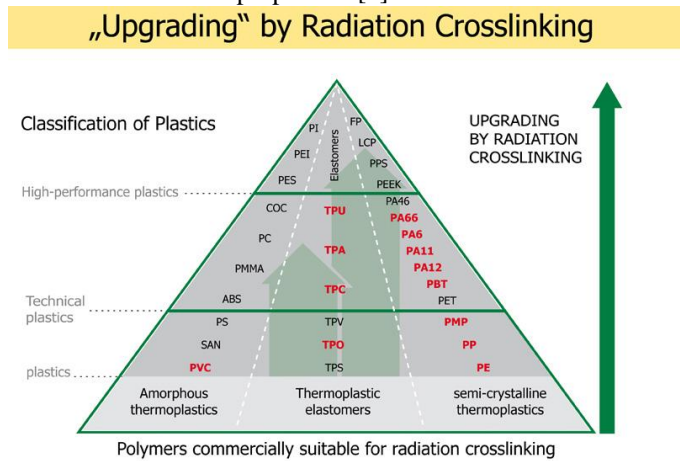


Fig. 2 Pyramid of Polymers [2]

Radiation cross-linking usually improves strength, reduces creep, contributes to chemical resistance improvement and in many cases improves tribological properties. Effect of radiation cross-linking significantly improves temperature stability. Because of that, materials which belong to group of standard polymers can be used in applications, which would be in term of temperature stability intended only to constructive thermoplastic polymers.

In comparison with other construction / engineering materials, mainly metals; polymers including TPE, PE and PAs have limited levels of both mechanical and thermal

properties. These limitations significantly reduce the applicability of polymers. Every improvement of these properties, of course, makes their applicability wider. Irradiation of thermoplastics is an important way to change their thermal properties. From the usage point-of-view, it is mainly the temperature stability which is a very important factor. Polymers can be irradiated in many forms, such as pellets and powder, films, extruded and molded parts or as wire and cable insulation [1]. Plastic parts suitable for radiation cross-linking are extruded products like tubes, pipes and profiles as well as injection-moulded parts.

II. MATERIAL AND METHODS

A. Material Preparation

As the basic polymer materials were used polybutylene terephthalate (V-PTS-CREATEC-B3HZC*M800/25 natur) made in PTS company and Polyamide 6 (PA6, FRISETTA, Frianyl B63 VN) made in NILIT Plastics company. An ARBURG Allrounder 420C Advance Injection molding machine was used for sample preparation, with the processing conditional to comply with the each polymers producer’s recommendations. Irradiation of tested polymers were performed with the kind help of BGS Germany, in the BGS Wiehl plant using accelerated electrons with a dosage range of 0 to 198kGy. The temperature stability of non-irradiated and irradiated selected polymers were tested after irradiation.

B. Used Methods for the Testing

The thermo-mechanical properties and the temperature stability were measured. Perkin – Elmer Thermal Analyser TMA7 was used for the thermo-mechanical analysis, heated from 50°C to 400°C at 20°C/min, hold for 1 min at 50°C. Temperature stability was determined the visual observation in the temperature chamber.

III. RESULTS AND DISCUSSION

The temperature behaviour of selected polymers (PBT and PA6), before and after irradiation, was studied. The temperature stability was evaluated by TMA measurement and by visual observation.

A. Thermomechanical analysis (TMA)

The graphical depiction of TMA results and description of a test record of the temperature stability inside a temperature chamber are described the dose of radiation from 0 to 198 kGy.

1) Polybutylene terephthalate (PBT)

Irradiation affects the thermo-mechanical properties of the studied PBT (Fig. 3).

Non-irradiated and irradiated PBT sample with the dose of irradiation 33 kGy are melted at the temperature 230°C. PBT with the increased dose above 132kGy is not lost the temperature stability up to 300°C. Irradiated PBT specimens above the dose of irradiation 132 kGy evince the significant improvement of temperature stability.

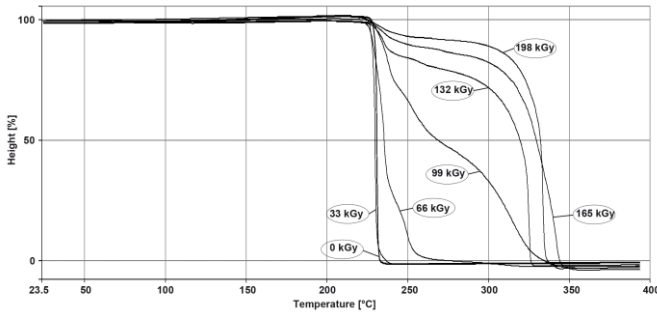


Fig. 3 Thermo-mechanical Analysis of PBT

1) Polyamide 6 (PA6)

Irradiation affects the thermo-mechanical properties of the studied PA6 (Fig. 4).

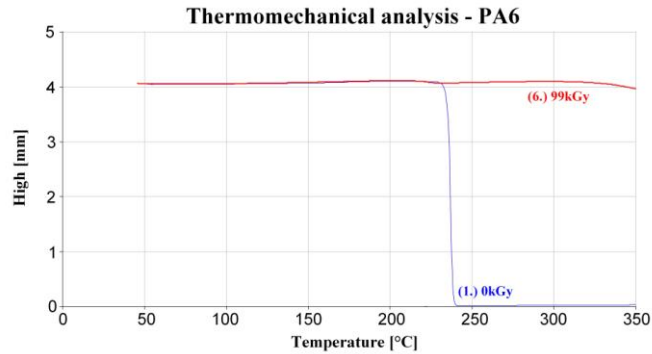


Fig. 4 Thermo-mechanical Analysis of PA6

Non-irradiated PA6 was melted at 240°C. However, irradiated PA6 with the dose 99kGy moves the temperature stability for short time up to 350°C.

2) Visual Observation of Selected Polymers in the Temperature Chamber

The visual observation of sample behaviour after one hour exposition at 250°C is given on Fig. 5. Specimens are fitted horizontally in the temperature chamber and loaded by the bending moment both from its own weight and the weight on the end of specimen. Specimen deformation is decreasing with increasing dose of radiation at elevated temperature. At 250°C the specimen from not irradiated PBT is totally melted while the polymer irradiated by the dose of 198kGy keeps its cross-section without changes, there is only deformation by its own weight. The surface quality worsens and the colour of polymer specimen change due to thermo-oxidation.

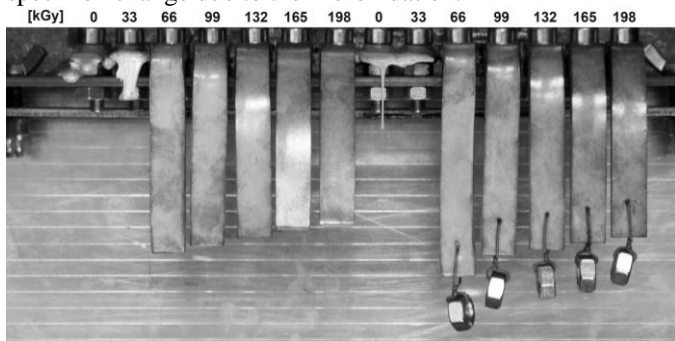


Fig. 5 PBT specimen deformation at 250°C

The temperature stability of polymers is very low in comparison with other construction materials. Experiments done in this project showed that irradiation cross-linking markedly affected the temperature stability of the studied selected polymers. The higher irradiation dosage, the better the temperature stability of these polymers is. The tested specimens remained without dimensional changes at the higher temperatures after irradiation. The same specimen, at higher temperatures, creates changes of colour due to thermal oxidation - but its dimension/cross-section remains without change. Their better temperature stability make possible to use the studied selected polymers even at service temperatures higher than their former melting point.

PA6 (C) [t = 90 min, T = 300°C]

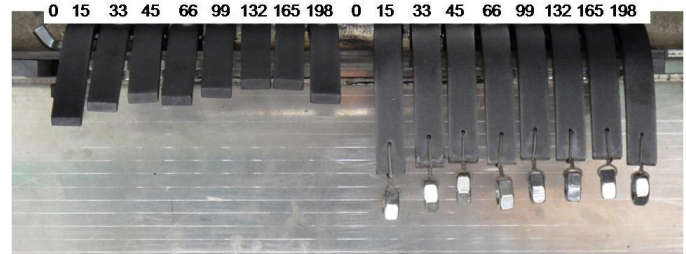


Fig. 6 PA6 specimen deformation at 300°C

PA6 (D) [t = 120 min, T = 350°C]

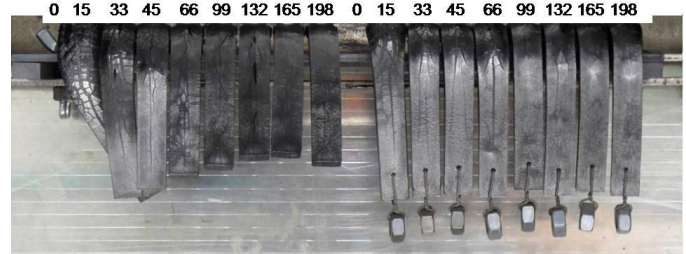


Fig. 7 PA6 specimen deformation at 350°C

IV. CONCLUSION

Plastics are by far the largest group of polymeric materials being processed by electron beam irradiation. Cross-linking of construction polymers are a common practice. Radiation cross-linking of PA requires considerably less overall energy and space, and is faster, more efficient and more environmentally acceptable. The disadvantage of electron beam cross-linking is a more or less nonuniform dose distribution. This can happen, particularly in thicker objects, due to intrinsic dose-depth profiles of electron beams. Another problem can be a nonuniformity of rotation of cylindrical objects as they traverse a scanned electron beam. However, the mechanical properties often depend on the mean cross-link density. [1]

The results of the measurements of PBT and PA6 after irradiation showed significant changes of its thermo-mechanical properties. A very important point is the improvement of the PBT and PA6's temperature stability, after irradiation. This significantly moves the application possibilities of the PBT and PA6's we tested to an area with service temperatures much higher than their former melting-point.

REFERENCES

- [1] J. G. Drobny, *Radiation technology for polymers*, Boca Raton: CRC press, 2003, ISBN 1-58716-108-7.
- [2] BGS – Beta Gama Service. [online]. www: <<http://bgs.eu>>
- [3] Z. Brocka, *Werkstoff- und Einsatzpotential strahlenvernetzter Thermoplaste*, Lehrstuhl für Kunststofftechnik (LKT), Nürnberg, 2008.
- [4] R. J. Woods, *Applied radiation chemistry: radiation processing*, A Wiley-Interscience publication, New York, 1994, ISBN 0-471-54452-3.
- [5] J. G. Drobny, *Handbook of thermoplastic elastomers*, William Andrew Publishing, Norwich, NY, 2007, ISBN: 978-0-8155-1549-4
- [6] M. Manas, M. Stanek, D. Manas, at all, “Temperature stability of irradiated polymers”. *Chemické listy*, 105(S), p254-256, ISSN 0009-2770.
- [7] Z. Holik, M. Danek, M. Manas, at all, “Effect of irradiation cross-linking on mechanical properties of selected types of polymer”. *Chemické listy*, 105(S), p269-271, ISSN 0009-2770.
- [8] Z. Holik, M. Danek, M. Manas, J. Cerny, “The influence of cross-linking agent on mechanical properties of polyamide modified by irradiation cross-linking”, in *Proc. 13th WSEAS International Conference on Automatic Control, Modelling & Simulation*, Lanzarote, Spain, 2011, pp.222-225.
- [9] Z. Holik, K. Kyas, M. Krupal, J. Cerny, M. Danek, “Improvement of polypropylene properties”, *21st International DAAAM Symposium*, 2010, Zadar, Croatia, p. 1191-1192.
- [10] H. Vaskova, V. Kresalek, „Raman spectroscopy of epoxy resin crosslinking“, in *Proc. 13th WSEAS International Conference on Automatic Control, Modelling & Simulation*, Lanzarote, Canary Islands 2011, p.357-360.
- [11] M. Manas et al., “Improvement of mechanical properties of the TPE by irradiation”, *Chemické listy*, Vol.105, 2011, pp. 828-829.
- [12] M. Manas et al., “Modification of polyamides properties by irradiation”, *Chemické listy*, Vol.103, 2009, pp. 24-26.
- [13] D. Manas, M. Manas, M. Stanek, T. Drga, “Influence of radiation on polymer properties”, *Chemické listy*, Vol. 101, 2007, pp. 27-28.
- [14] D. Manas et al., “Thermal effects on steels at different methods of separation”, *Chemické listy*, Vol.105, 2011, pp. 713-715.
- [15] D. Manas et al., “Influence of mechanical properties on wear of heavily stressed rubber parts”, *KGK – Kautschuk Gummi Kunststoffe*, Vol.62, 2009, pp. 240-245.
- [16] D. Manas et al., “Wear of multipurpose tire treads”, *Chemické listy*, Vol.103, 2009, pp. 72-74.
- [17] D. Manas, M. Stanek, M. Manas, “Workability and wear of rubber parts”, *chapter 54 in DAAAM International Scientific Book 2007, Published by DAAAM International, DAAAM International*, Vienna, Austria, p.611-626
- [18] M. Stanek et al., “Optimization of injection molding process”, *International Journal of Mathematics and Computers in Simulation*, Vol.5, 2011, pp. 413-421.
- [19] M. Stanek et al., “Simulation of injection molding process by cadmould rubber”, *International Journal of Mathematics and Computers in Simulation*, Vol.5, 2011, pp. 422-429.
- [20] M. Stanek et al., “Plastics parts design supported by reverse engineering and rapid prototyping”, *Chemické listy*, Vol.103, 2009, pp. 88-91.
- [21] M. Stanek et al., “How the filler influence the fluidity of polymer”, *Chemické listy*, Vol.105, 2011, pp. 303-305.
- [22] M. Stanek, D. Manas, M. Manas, J. Javorik, “Simulation of injection molding process,” in *Proc. 13th WSEAS International Conference on Automatic Control, Modelling & Simulation*, p.231-234.
- [23] M. Stanek, D. Manas, M. Manas, O. Suba, “Optimization of injection molding process by MPX,” in *Proc. 13th WSEAS International Conference on Automatic Control, Modelling & Simulation*, p.212-216.
- [24] M. Stanek, M. Manas, T. Drga, D. Manas, “Testing injection molds for polymer fluidity evaluation”, *17th DAAAM International Symposium: Intelligent Manufacturing & Automation: Focus on Mechatronics and Robotics*, Vienna, Austria, 2006, p.397-398.
- [25] S. Sanda et al., “Injection mold cooling system by DMLS”, *Chemické listy*, Vol.103, 2009, pp. 140-142.
- [26] S. Sanda et al., “Gate effect on quality of injected part”, *Chemické listy*, Vol.105, 2011, pp. 301-303.
- [27] V. Pata et al., “Visualization of the Wear test of rubber materials”, *Chemické listy*, Vol.105, 2011, pp. 290-292.
- [28] V. Pata et al., “Visualization of the wear test of rubber materials”, *Chemické listy*, Vol.105, 2011, pp. 290-292.
- [29] K. Kyas et al., “Simulation of rubber injection holding process”, 2011, *Chemické listy*, Volume 105, Issue 15, pp. S354-S356
- [30] J. Javorik et al., “The Shape optimization of the pneumatic valve diaphragms”, *International Journal of Mathematics and Computers in Simulation*, Vol.5, 2011, pp. 361-369.
- [31] M. Ovsik et al., “Microhardness of modified thermoplastics”, *Annals of DAAAM for 2011 & Proceedings of the 22nd International DAAAM Symposium*, 23-26th November 2011, Vienna, Austria, ISSN 1726-9679, ISBN 978-3-901509-83-4, p. 1187-1188, Published by DAAAM International Vienna, Vienna
- [32] J. Navratil et al., “Utilization of DMLS in injection mold design”, *Annals of DAAAM for 2011 & Proceedings of the 22nd International DAAAM Symposium*, 23-26th November 2011, Vienna, Austria, ISSN 1726-9679, ISBN 978-3-901509-83-4, p. 1507-1508, Published by DAAAM International Vienna, Vienna
- [33] J. Javorik, and D. Manas, “The specimen optimization for the equibiaxial test of elastomers,” in *Proc. 13th WSEAS International Conference on Automatic Control, Modelling & Simulation*, Lanzarote, Spain, 2011, pp. 121-124.
- [34] Z. Holik, M. Manas, M. Danek, J. and Macourek, “Improvement of mechanical and thermomechanical properties of polyethylene by irradiation crosslinking”. *Chemické listy*. Volume 103, 2009, s.60-63, ISSN 0009-2770 (IF: 0,593 MF: 1,256)
- [35] M. Ovsik et al., “Micro-hardness of glass fiber-filled PA6 influenced by beta irradiation”, *International Journal of Mechanics*, Volume 7, Issue 4, 2013, pp. 500-507, ISSN 1998-4448
- [36] M. Ovsik et al., “Effect of beta low irradiation doses on the nano-hardness of PBT”, *International Journal of Mechanics*, Volume 7, Issue 3, 2013, pp. 310-317, ISSN 1998-4448.
- [37] J. Navratil et al., “Cooling systems comparison”, *Plasty a kaučuk – Special 49*, 2012, pp. 24-26, ISSN 0322-7340.
- [38] J. Navratil et al., “Tensile toughness of irradiated HDPE,” *Intl J. of Mech.*, Vol. 7, No. 3, pp. 327-334, 2013.
- [39] J. Navratil et al., “Hardness and micro-indentation hardness comparison of recycled modified HDPE,” *Key Eng. Mater. J.*, Vol. 606, pp. 217-220, 2014.
- [40] M. Bednarik et al., “Effect of beta irradiation on the strength of bonded joints,” *Key Eng. Mater. J.*, Vol. 586, pp. 79-82, 2014.

Unsupervised Robot System using Computational Geometry and Neural Network

Marios Poulos

Abstract— This study introduces a new coherent theoretical system that coordinates border patrol coverage. To implement the system, a hybrid global-local optimization algorithm for Elman-Recurrent networks, and dependent autoregressive (Elman-AR) models parameter estimation, are adapted in the processing stage using the topologic feature of a convex polygon. The proposed methodology promises a low $O(\log(n))$ value of complexity and should be the first step towards solving the border patrol automatic system identification.

Keywords— Convex polygon, AR model, Elman neural network, border patrol security

I. INTRODUCTION

Interest in border patrol systems has recently grown in response to concerns regarding national security. Conventional border patrol systems suffer from intensive human involvement. However, newer unmanned border patrol systems employ high-tech devices: unmanned aerial vehicles, unattended ground sensors, and surveillance towers equipped with camera sensors [1, 2]. There has been increased emphasis on linking Wireless Sensor Networks (WSN) with military applications, particularly in the context of border safety [3, 4]. To achieve its full proposed functionality, researchers working on WSN used in border protection must resolve many interesting challenges, including energy efficiency [5,6], communication and hardware consistency and security issues [7,8].

Problems. Any single technique can encounter inextricable problems, such as high false alarm rates and line-of-sight-constraints. There is no single coherent system able to coordinate border patrol. Border security systems cannot distinguish between a cow and a terrorist (biometric problems) [9]. Also, the high costs of tower and sensor locations create an additional problem. Finally, there is the issue of high costs associated with the computational complexity of scanning points on the border $O(n^3)$ [1].

Aims and Scopes. A new coherent system is proposed that coordinates border patrol coverage. It entails minimum tower locations and sensors, uses a low-complexity procedure based on a computational geometry algorithm and finally, and includes a biometric control that uses a neural network. A schematic of the proposed system is depicted in Figure 1.

The paper is organized in three stages, as follows: stage 1 provides the theoretical basis for the first two steps of the algorithm (convex sensor installation, and inside or outside identification). In the second stage, the biometric features extraction method is explained in two steps (gradient signal generation and AR model). Finally, in the third stage the connection between the algorithms with a biometric learning machine is described (decision part).

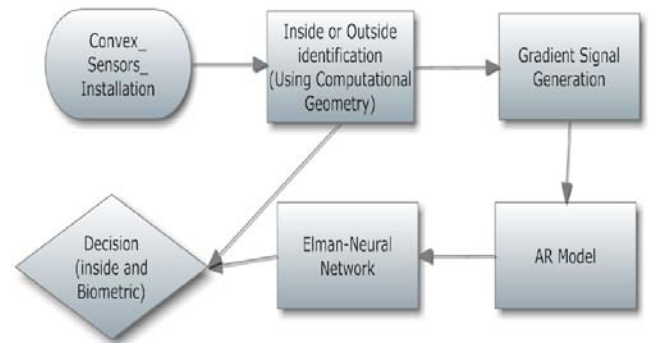


Figure 1: A schematic representation of the proposed method

The paper is organized in three stages, as follows: stage 1 provides the theoretical basis for the first two steps of the algorithm (convex sensor installation, and inside or outside identification). In the second stage, the biometric features extraction method is explained in two steps (gradient signal generation and AR model). Finally, in the third stage the connection between the algorithms with a biometric learning machine is described (decision part).

I. METHOD STAGE 1: THE BASIS OF THE ALGORITHM

A. Convex Sensor Installation

The basis of the proposed method is depicted by a unique convex polygon; a point is recognized as being either inside or outside the polygon [10]. A given set, P_i , is determined by convex polygon A of i vertexes (see Figure 2). Then, point C is inside the polygon if all Q_i have the same sign with $\vec{A} \times \vec{B}$ or in the counterclockwise case (see Figure 2a, 2b):

$$Q_i = \vec{A} \times \vec{B} < 0 _ C \in H(A) \tag{1}$$

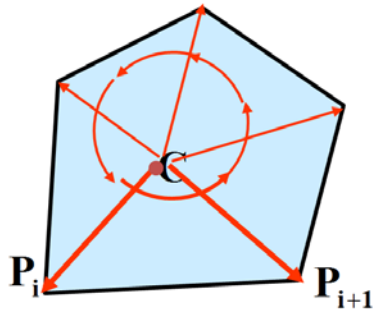


Figure 2a: The counterclockwise case cross-product in the interior point of convex polygon detection

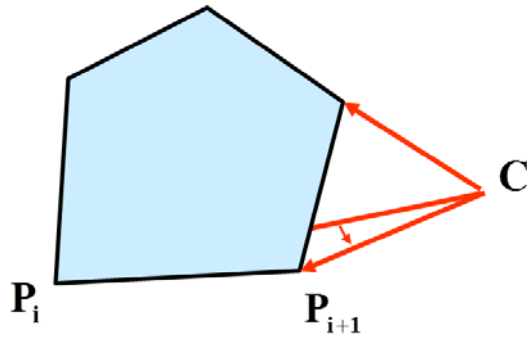


Figure 2b: The counterclockwise case cross-product in the exterior point of convex polygon detection

B. Identification Procedure

In a scenario that implements the above feature, a number of sensors (i) fit in the convex configuration polygon (Figure 3).

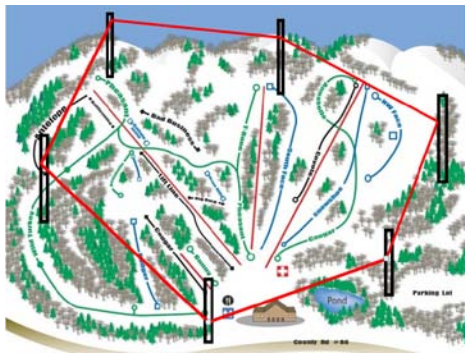


Figure 3: The architecture of the convex configuration polygon using sensors

This scenario is based on the position of the unknown object being found by at least three (3) sensors. Then the sensors detect and produce coordinates for two possible positions (inside and outside) (Figures 4a, 4b).



Figure 4a: The counterclockwise case cross-product in the interior and exterior point (person) of convex polygon detection

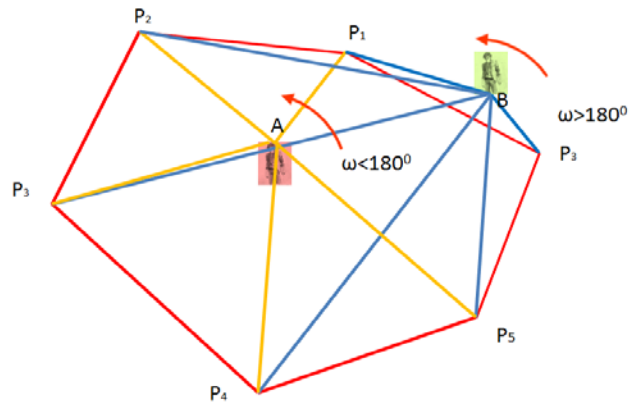


Figure 4b: The schematic counterclockwise case cross-product in the interior and exterior point (person) of convex polygon detection

II. METHOD STAGE 2: BIOMETRIC PROCEDURE

A. Gradient Signal Generation

It is known that it is possible to distinguish between the biometrical movements of humans, animals and cars. This paper introduces a new method using the previous algorithm may be considered in the same strategy.

Then if $u = \left| \vec{A} \times \vec{B} \right|$ which represents the cross-product of equation (1).

Visualize a vector field: at a point in space, the field has a vector value. Let $g = \nabla u$ [11] represent the gradient of u obtained when moving from a point x in space to a nearby point $(x + dx)$ in the convex area $d\vec{u} = g(d_x)$. Then, the signal received by the stable pair of sensors, I1 and I2, at time tn .

$$s_m(n) = \sum_{x=1}^n d\vec{u} \tag{2}$$

and is represented by a multichannel array

B. AR Model

According to equation (2), a set of linear systems is adopted using the AR model [12], which is

$$y_{i,n} = \sum_{i=1}^p a_i s(n) \tag{3}$$

$$y_{i,n} = \sum_{i=1}^p b_i s(n) \tag{4}$$

$$y_{i,n} = \sum_{i=1}^p c_i s(n) \tag{5}$$

$$z = \begin{bmatrix} a_1 & b_1 & c_1 \\ \vdots & \vdots & \vdots \\ a_p & b_p & c_p \end{bmatrix} \tag{6}$$

Thus, the AR multidimensional (3xp) vector (z) is adopted and is depicted in equation (6)

III. DECISION STAGE

A. Elman Neural Network

The present study investigates the training of these vectors in the detection of three different objects (human, animal and car) whose movements are captured by sensors [13]. The Elman network is based on a two-layer network with feedback in the first (hidden recurrent) layer and a second output layer, and is considered ideal in this case. The recurrent connection permits the Elman network to detect and generate time-varying patterns. The hidden recurrent layer consists of neurons with a hyperbolic tangent activation function (tansig) as described in the application, and is represented by the following equation:

$$\tan \sin(z) = \frac{1 - e^{-2z}}{1 + e^{-2z}} \tag{7}$$

Classes (A, B, C) are determined in the training procedure; after training a new array is produced where the error (in the case of an output unit) simply represents the discrepancy between the target output of the unit and the actual output, while $f'(net)$ represents the derivative of the receiver unit's activation.

A. Testing Procedure

The output prediction value is derived for the outer layer using the same procedure from the hidden layer. The log-sigmoid transfer function is used and the relationship inputs and outputs are as follows:

$$f(x) = \frac{1}{1 + e^{-x}} \tag{8}$$

This function leads to construct a rule for classification into the class A or B or C This transfer function in comes the input (which can have any value between plus and minus infinity) and squashes the output into the range -1 to 1. In this study the space these values is divided into 3 sub-regions and the decision of the classification is extracted by the following piecewise-linear function [16]:

$$f(x) = \begin{cases} +1 \rightarrow \text{if } +1.5 < x \leq +0.5 \\ 0 \rightarrow \text{if } +0.5 < x \leq -0.5 \\ -1 \rightarrow \text{if } -0.5 < x \leq -1.5 \end{cases} \tag{9}$$

Thus, the function f(1) corresponds to class A, while the functions f(0) and f(-1) correspond to classes B and C respectively.

IV. CONCLUSION

This study introduces a new coherent theoretical system that coordinates the coverage of border patrol. To implement this system, a hybrid global-local optimization algorithm for Elman-Recurrent networks and dependent autoregressive (Elman-AR) model parameter estimation is adapted in the processing stage, using the topologic feature of a convex polygon. The proposed methodology promises a low Olog(n)) value of complexity.

Future research should focus on testing the accuracy of this method using simulation data and video games, before being applied in a real environment. The next step for the proposed algorithm is to apply it using the real-time Neuro Evolution of Augmenting Topologies (rt-NEAT) method for developing increasingly complex artificial neural networks in real time, as a game is being played [14]. Finally, this method should be applied in RFID systems in order to direct the selection and testing of additional applications (e.g., airplane transponders, library security, etc.).

REFERENCES

- [1] Sun, Z., Wang, P., Vuran, M.C., Al-Rodhaan, M.A., Al-Dhelaan, A.M., and I. F. Akyildiz. "BorderSense: Border patrol through advanced wireless sensor networks", *Ad Hoc Networks*, vol. 9, no, pp. 468-477, 2011.
- [2] Girard, A. R., Howell, A.S. and J. K. Hedrick. "Border patrol and surveillance missions using multiple unmanned air vehicles", *Στο Decision and Control*, 2004. CDC. 43rd IEEE Conference on, vol. 620-625, 2004.
- [3] Felemban, E. "Advanced border intrusion detection and surveillance using wireless sensor network technology". *Int. J. Communications, Network and System Sciences*, vol. 6, pp. 251-259, 2013.
- [4] [Luo, H., Wu, K., Guo, Z. et al., "Ship Detection with Wireless Sensor Networks", *IEEE Transaction on Parallel and Distributed Systems*, 2011.
- [5] Essendorfer, B., Monari, E., and H. Wanning. "An Integrated System for Border Surveillance", *IEEE Fourth International Conference on Systems (ICONS 09)*, Gosier, vol. 1-6, March, 2009.
- [6] Thattil V. and N. Vasantha. "Energy Efficient Approach to Intruder Detection in Militarily Sensitive Border Using Wireless Sensor Networks", *IEEE Conference on Elec-tronics Computer Technology*, 2011.

- [7] Yuping, D., Chang, H., Zou, Z. and S. Tang, "Energy Aware Routing Algorithm for WSN Applications in Border Surveillance", 2010 IEEE International Conference on Technologies for Homeland Security, Waltham, 8-10 November 2010, pp. 530-535.
- [8] Arampatzis, T., Lygeros, J. and S. Manesis, "A survey of applications of wireless sensors and wireless sensor networks", in Intelligent Control, 2005. Proceedings of the 2005 IEEE International Mediterranean Conference on Control and Automation, 2005, pp. 719-724.
- [9] M. Endler. "Large scale body sensing for infectious disease control". In: Position paper submitted to the Sentient Future Competition, Rio de Janeiro, Brazil, 2005.
- [10] J. Pineda. "A parallel algorithm for polygon rasterization". In: Proceedings of SIGGRAPH '88 (August 1988), pp. 17-20.
- [11] De Bruyne, F., and P. Carrette. "Synthetic generation of the gradient for an iterative controller optimization method". In: Proceedings of the fourth European control conference. Bruxelles, Belgium, 1997.
- [12] H. Akaike. "A new look at the statistical identification model". IEEE Trans Auto Contro., pp. 716-723, 1974.
- [13] Kulkarni, R., Foster, A. and G. Venayagamoorthy. "Computational intelligence in wireless sensor networks: A survey", IEEE Communications Surveys & Tutorials, vol.13, no.1, pp. 68-96, 2011.
- [14] Stanley, K.O., Bryant, B.D. and R. Miikkulainen. "Evolving neural network agents in the NERO video game". In: Proceedings of the IEEE 2005 Symposium on Computational Intelligence and Games, 2005.
- [16] S. Papavlasopoulos, M. Poulos, N. Korfiatis, και G. Bokus, 'A non-linear index to evaluate a journal's scientific impact', Information Sciences, vol. 180,n. 11, pp 2156-2175, 2010.

Marios Poulos

Since 2003 he has been a member of staff in the Department of Archives, Library Science and Museology at the Ionian University and, in 2007, became Associated Professor of Semantic Processing of Information at the Ionian University.

He is a member of several technical committees and working groups on subjects relating to medical informatics, information science and pattern recognition systems. He is a member of the senate of the Ionian University in the academic year 2008-2009.

Research Interests

He is primarily interested in Medical Informatics with a particular interest in the digital processing of EEG. He is also interested in Semantic Web-metadata, Biometrics System, Pattern Recognition, Computational Geometry, Neural Networks, Image Processing, Text Categorization, Copyright Techniques and Social Networks.

Activities

He is a reviewer for the following prestigious journals: IEEE Transactions on Image Processing Journal, IEEE Transactions on Pattern Analysis and Machine Intelligence, Pattern Analysis & Applications Journal (Springer Verlag) and the BioMedical Engineering OnLine journal. He is also a member of the Expert Committee of MTSR Conference and the American Association for the Advancement of Science and is member of the editorial board of the "International Journal of Cognitive Biometrics"

Publications

Forty two (42) of his studies have been published in prestigious international journals, thirty nine (39) of his studies have been published in the proceedings of international conferences, and he has co-written two (2) scientific books.

Current Project Related Activities

He is currently developing appropriate data formats and structural descriptions in order to permit search and retrieval mechanisms to facilitate data interchange and collaboration concerning data representations of the Electroencephalogram (EEG).

Testing Thermal Images Characteristics for Thermal Images Quality Estimation

Sn. Pleshkova, Al. Bekyarski, K. Peeva

Abstract—The thermal images are produced from real working thermo vision cameras, which work as electro-optical imaging systems, sensitive to the mid and long wave infrared radiation, that generates images of the observed scenes, by using the thermal radiation emitted from the scenes. There are numerous applications of thermal imaging systems in defense, security, military, border guards, police, etc. and also a lot of civilian application like industrial non-contact temperature measurement, non-destructive thermal testing, tests of electrical power lines, building industry, medical applications, fire rescue etc. There exist many publications in the area of thermal cameras, thermal systems and their applications, but all the applications of these thermal cameras and systems are greatly depending from the quality of thermal images produced from thermal or infrared cameras. Also there is a need of rules how to choose the optimal thermal image characteristics. Of course, the first reason to think about thermal image quality is thermo visual camera models offered on the market. These models vary significantly, but generally there is a tendency to permanently increase their technical characteristics. Therefore, if it is assumed that thermal image cameras gives the thermal images with the preliminary defined characteristics, it is necessary to have the appropriate methods, algorithms or devices to test and after these test to be sure about the quality of thermal images. Another case, when the thermal image quality is important to be known, is the case of quality of thermal images after processing or transmitting through some communication system. Testing thermal images quality is difficult task because of the necessarily extended knowledge from different areas and practical experience with thermal cameras, thermal images processing etc. There are several standards and publications in the area of visible images subjective or objective characteristics and the correspondent quality estimation, but here in this article is proposed to use and modify these methods by applying them in the testing of thermal images characteristics. The results from this proposition are presented as experiments with thermal images with different estimated quality from real working thermal image surveillance system for detection motion and tracking people in sequences of thermal images and the obtained results from the experiments show the dependence of the algorithm for motion detection and people tracking from thermal images quality, which is estimated by the proposed testing algorithm for thermal images characteristics.

Sn. Pleshkova is with the Faculty Telecommunication of Technical University - Sofia, Bulgaria, CO +359 Bulgaria (corresponding author to provide phone: 895 55 888 51; e-mail: snegpl@tu-sofia.bg).

Al. Bekyarski, was with the Faculty Telecommunication of Technical University - Sofia, Bulgaria, CO +359 Bulgaria (corresponding author to provide phone: 895 55 888 52; e-mail: aabv@tu-sofia.bg).

K. Peeva is with the Faculty Telecommunication of Technical University - Sofia, Bulgaria, CO +359 Bulgaria (corresponding author to provide phone: 884 55 833 63; e-mail: kala_peeva@yahoo.com).

Keywords— Thermal Images Characteristics, Thermal Images Quality, Thermo Vision Systems, Motion Detection Precision Estimation

I. INTRODUCTION

THERMO vision systems work with static or dynamic thermal images in all numerous applications like night military or surveillance systems, medical systems or industrial systems [1]. In all these applications the characteristics of thermal images produced from thermal image sensors or cameras can affect the precision or the correct final results from thermal images observation, processing, treating or transmitting [2]. This necessity can be satisfied applying suitable methods and algorithms for thermal images characteristics testing and measuring. The combinations of all determined in testing thermal images characteristics can be analyzed and treated as a general objective quality estimation of thermal images. These statements outline the goal of this article – to propose, develop and examine a method and an algorithm for testing the main thermal images characteristics. For the realization of this goal, first it is included a brief description of the main important thermal image characteristics suitable in many of wide spread thermal image systems applications.

II. THERMAL IMAGES CHARACTERISTICS UNDER TEST FOR ESTIMATION OF THERMAL QUALITY

Here are outlined only thermal images characteristics which differ from these of the visible images. An essential different thermal images characteristic is the longer wavelengths [3]. This difference lead to surface reflections for many materials and tend to be more specula and less diffuse than in the visible images, since the same surface irregularities are relatively smaller compared with the long IR wavelengths than for the short visible ones. This effect can produce errors in detection systems as the objects may be detected twice in some extreme cases. All other characteristics can be related not only for thermal images, but they are typical also for the visible images. Nevertheless, it can find some specific differences for thermal images. Some of these characteristics are listed in Fig. 1.

It is seen from Fig. 1 that **Thermal Image Characteristics** can be defined or estimates from **Subjective** and **Objective** points of view. They can be treated also as subjective or objective thermal images **Quality**. Some of the presented in Fig. 1 thermal image characteristics like **Resolution**, **Noise**

and **Geometry** are possible to evaluate both as subjective or objective thermal images quality.

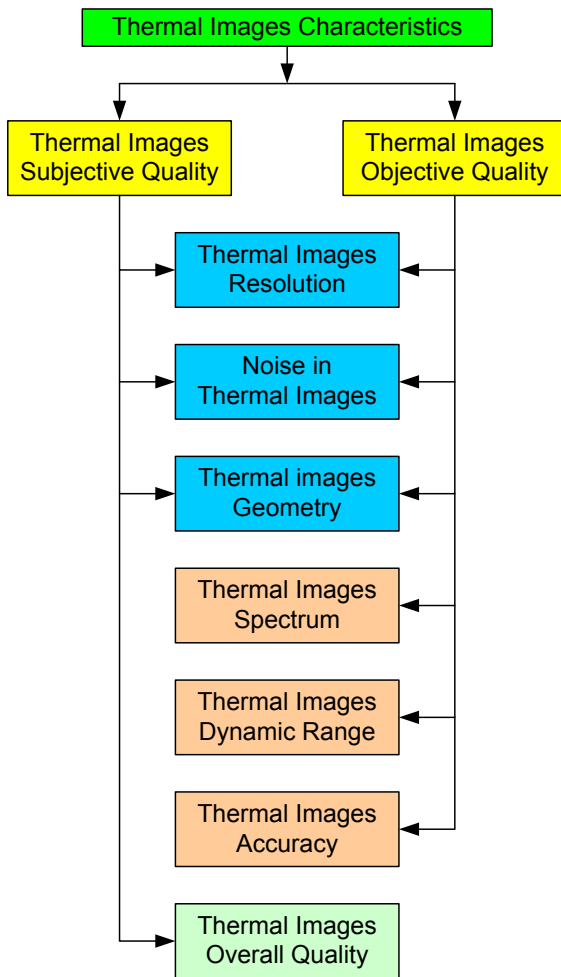


Fig. 1 The main thermal images characteristics

There are other thermal image characteristics: **Spectrum**, **Dynamic Range** and **Accuracy** typical only in the objective quality of thermal images. For human subjective thermal image quality estimation is used the method of **Overall Quality**. The subjective image quality parameters give information about the ability of human observer with thermal camera in a thermal image surveillance system to detect, recognize, and identify targets at different scenarios and also information about the response of the thermal camera to variable size or variable temperature targets in thermal images. The method of **Overall Quality** can be applied also for the objective thermal image quality estimation if all of the listed thermal images characteristics can be considered together, but in this case it is necessary to mention that all of objective exiting methods of overall thermal image quality estimation approach in one way or another to the accuracy of the subjective methods, which are based on human perception of thermal images quality [4]. For the purpose of this article it is convenient to apply only objective thermal images characteristics for thermal images quality estimations, since the purpose of the article is to apply the results from the

thermal images quality estimations into applications, which are related to thermo vision surveillance systems. The main goal of these systems is observation of objects or people in a secure area, tracking these objects or people and transmitting these thermal images as static or dynamic sequences using an appropriate communication system. It is evident that the subjective thermal images characteristics are not applicable in these cases of automatic working thermo vision systems.

The **Objective Quality** characteristics of thermal images, shown in Fig. 1, are very important for the above mentioned automatic working thermo vision systems, because of following impacts on the quality of thermal images processing algorithms:

- noise limits camera sensitivity detecting low contrast targets (objects or people);
- image resolution parameters or characteristics carry out information about the thermal camera ability to perceive small details in targets (objects or people) from high contrast thermal images;
- geometric parameters give information about the geometrical relations between the targets (objects or people) and its corresponding thermal image;
- accuracy parameters or characteristics give information about the precision of non-contact temperature measurements using thermal cameras and methods for thermal images processing.

The described objective quality characteristics of thermal images, shown in Fig. 1, are included in the proposed in this article algorithm for testing and measuring of thermal images characteristics for thermal images quality estimation.

III. ALGORITHM OF TESTING THERMAL IMAGES CHARACTERISTICS FOR ESTIMATION THERMAL IMAGES QUALITY

The proposed in this article algorithm of testing and measuring thermal images characteristics for thermal images quality estimation is presented on Fig. 2. After activation of the algorithm start the operation “**Choosing Thermal Image Source**”. There are three possibilities to choose Thermal images from Thermal Camera, from File and from Test synthesized thermal image. On these chosen thermal images are prepared different types of tests to measure a lot of thermal images important characteristics. The proposed algorithm is arranged in such a way that it is possible to choose from all, included in algorithm list of thermal images characteristics, only these, which are important for a concrete case of thermal images applications. For this reason and for facilitate the choice of thermal images characteristics, they are grouped in **M** groups (**Group 1**, **Group 2**,....., **Group M**) according to their similarity for the quality of thermal images testing scenarios. In each group are provided several thermal images characteristics: **Characteristics 1**, **Characteristics 2**,, **Characteristics N**. The values as results from measurements of each one of the chosen, in some concrete case, thermal images characteristics are entered in block of

Thermal Images Objective Quality Estimation. The operations of this block in algorithm depend from chosen list of thermal image characteristics in each case of testing thermal images quality and from concrete application of thermal images. However, in general, the output of this block gives an overall estimation of tested thermal images, which must be precise and closer in accuracy to such a subjective assessment of tested thermal images.

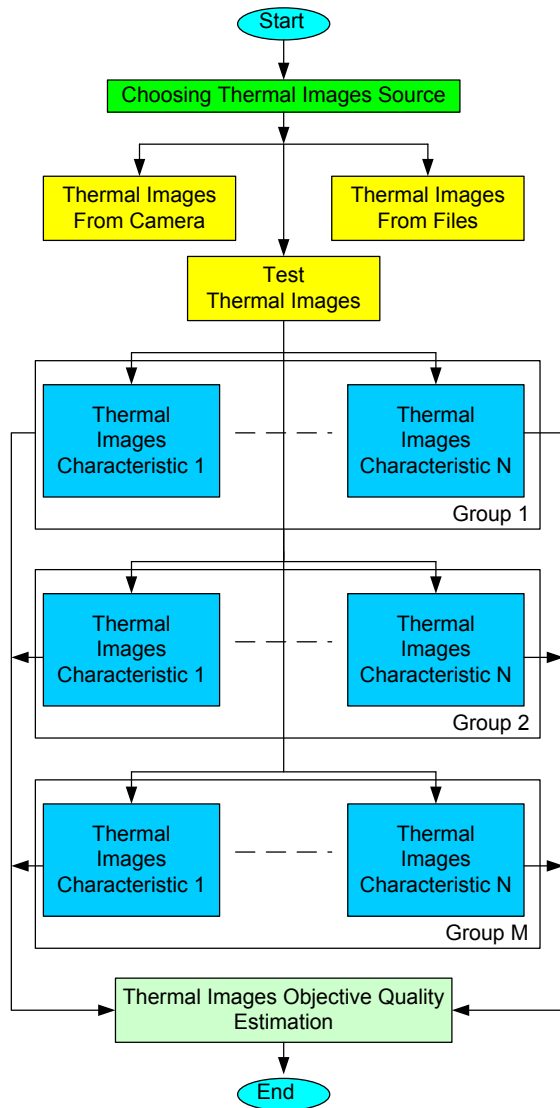


Fig.2. Algorithm of testing and measurements thermal images characteristics for thermal images quality estimation

There are many possibilities to choose thermal images characteristics for testing. Here in this article are used some thermal images characteristics, defined a suitable standard for this purpose [5].

One of these characteristics is concerning to the noise in thermal images. The noise in thermal images is tested to estimate thermal images cameras limits to sensitivity detecting low contrast (temperature contrast or differences) objects or people in thermal images [6]. The measurement algorithm is based on determination of minimum resolvable temperature difference (MRTD). This measurement can be done

automatically (Auto MRTD), i.e. without human observer, after calibration with human’s help as correction factors on resolving each target. As testing thermal images are used four bar targets or a trained observer. After calibration, Auto MRTD does not require four bar targets or a trained observer. The value of $MRTD(\nu)$ calculated when testing the ν number of thermal images is used as a base for determination of a relative coefficient $K(\nu)$ of thermal images quality related to the noise in these images:

$$K(\nu) = \frac{MRTD(\nu).MTF(\nu)}{NETD}, \quad (1)$$

where

$MRTD(\nu)$ is the modulation transfer function of the ν -th thermal image in a sequence of tested thermal images;

$NETD$ - is the Noise Equivalent Temperature Difference of tested thermal images.

Testing thermal images and measurement of $MRTD$ is an ability to detect and recognize targets (moving objects or people) on a non-uniform background. $MRTD$ is considered as the most important measure of thermal surveillance systems (usually military, police or civil).

After measurements of $MRTD(\nu)$ and calculating $K(\nu)$ from equation (1) is possible to use these results for determination of Auto $MRTD(\nu)$, which does not require four bar targets or a trained observer for measurements and calculations. Auto $MRTD(\nu)$ can be calculated using the following equation:

$$MRTD_{auto}(\nu) = \frac{K(\nu).NETD}{MTF(\nu)} \quad (2)$$

Another thermal images characteristic is minimum detectable temperature difference (MDTD), which is equivalent of human ability to detect targets on uniform background. The real targets of interest are usually located on non-uniform backgrounds, i.e. moving objects or people in the zone of thermal camera observation.

There are a lot of other important test parameters, which are proposed and are object of standardizations, but it is not possible here in this article to list and describe all of them. Many of these existing test thermal images characteristics are applied in the proposed and developed simulation model of algorithm presented in Fig. 2 for testing thermal images characteristics for estimation thermal images quality.

IV. SIMULATION OF PROPOSED ALGORITHM OF TESTING THERMAL IMAGES CHARACTERISTICS FOR ESTIMATION THERMAL IMAGES QUALITY

In Fig. 3 is presented the proposed simulation model of described algorithm testing thermal images characteristics for estimation thermal images quality.

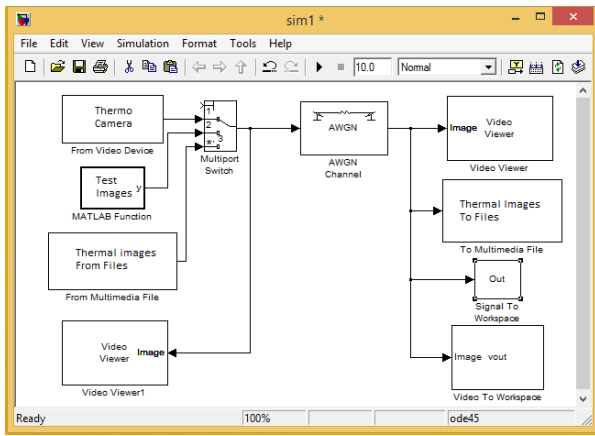


Fig.3. Simulation model of algorithm testing thermal images characteristics for estimation thermal images quality

The simulation model of algorithm testing thermal images characteristics for estimation thermal images quality is arranged with the capabilities to work with real thermal images from **Thermal Camera**. In the same time it is possible to use as source for static or dynamic thermal images, preliminary saved in files, the simulation block **From Multimedia File**. Also in some of the tests of thermal images characteristics it is necessary to have some synthesized artificial testing thermal images. This possibility is realized by applying into the simulation model on Fig. 3 a simulation block, named as **Test Images**. The preliminary existing thermal images or thermal images sequences saved in files can be entered by using the block **Thermal Images from File**. Thermal images from these three sources are viewed on **Video Viewer** after choosing one of these sources with the **Multiport Switch**. In simulation model on Fig. 3 is included the block **AWGN Channel** for simulating a transmission of thermal images using an appropriate model of communication channel. In the receiving part the input thermal images can be viewed on **Video Viewer**. Other possibilities for using the received thermal images, presented in Fig. 3, are the following: save received thermal images or thermal images sequences **To Multimedia File**; using blocks **Out** or **Video To Workspace** to transfer thermal images in work space.

The simulation block **Test Images** in simulation model on Fig. 3 is of great importance, because of possibility to synthesis of test thermal images proposed in some thermal images standards [7] and publications [8, 9] for thermal images quality estimation. The block **Test Images**, shown in Fig. 3, is realized as a program for generating a number of synthesized test thermal images some of which are proposed in the mentioned above thermal images standards.

Here are presented only a little part of generated with the appropriate program, used in block **Test Images**, number of synthesized test thermal images. One of these synthesized test thermal images, suitable for the described with equations (1) and (2) thermal images characteristic minimum resolvable temperature difference $MRTD(\nu)$ and their corresponding Auto $MRTD(\nu)$ is shown in Fig. 4 as a synthesized test

thermal image containing uniform (with chosen value of temperature) background and also a triangle (with chosen different from the temperature of background other value of temperature).

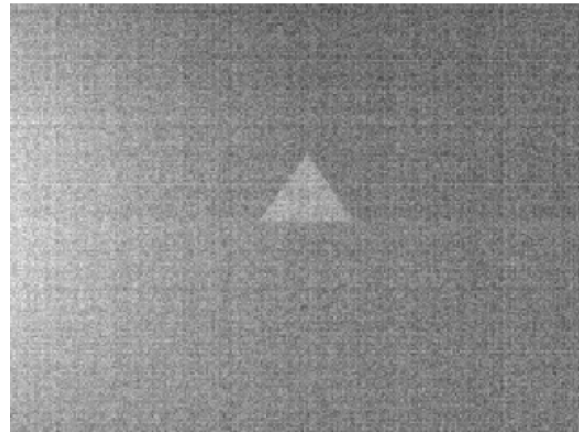


Fig.4. Synthesized test thermal image containing uniform background and triangle with different temperatures for measure of $MRTD(\nu)$

This test image of triangle object can be realized with a different temperature thermal images contrast. Therefore, it is very useful to testing temperature sensitivity or temperature contrast of thermal images, using the proposed in Fig. 3 simulation model of algorithm testing thermal images characteristics for estimation thermal images quality. When carried out the thermal images test with this test image (Fig. 4.), is proposed to use the defined Triangle Orientation Discrimination (TOD) threshold as an alternative to MRTD method to characterize performance of thermal imagers. The TOD method proposes to use a series of triangle objects for measurements of thermal images characteristics.

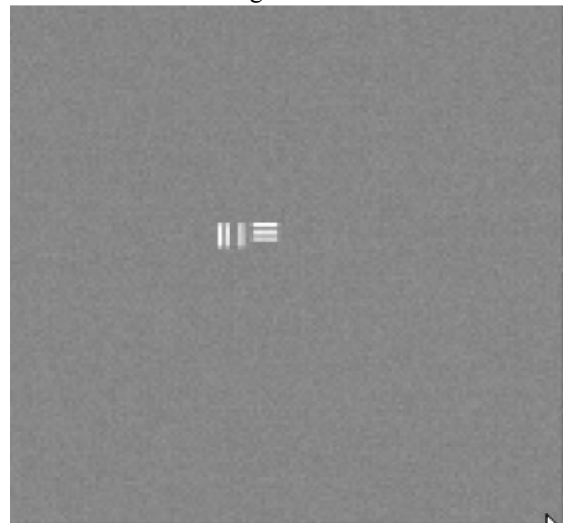


Fig.5. Synthesized test thermal image containing uniform background and four bar as object for testing thermal images characteristics

In Fig. 5 and Fig 6 are presented other types of synthesized test thermal images:

- first, containing uniform background and four bar as object for

testing thermal images characteristics;

- second, containing synthesized test thermal image with uniform background and objects as combination from different size, positions and orientation of four bar object (Fig. 5.) for testing thermal images characteristics.

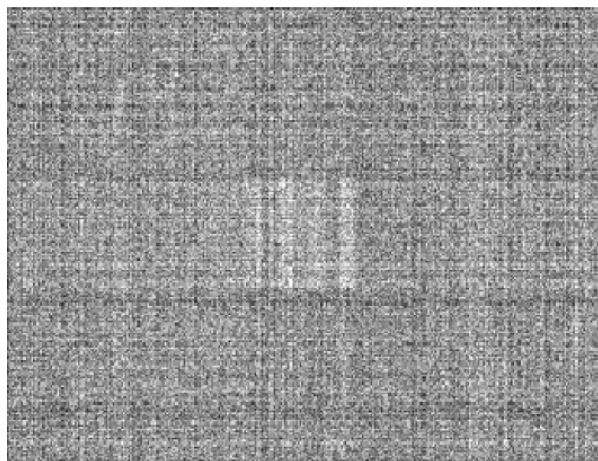
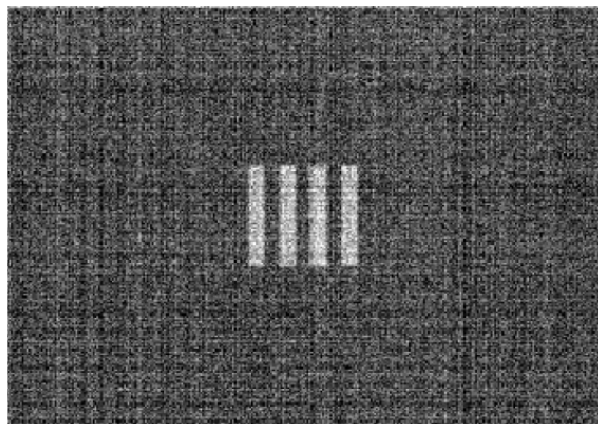
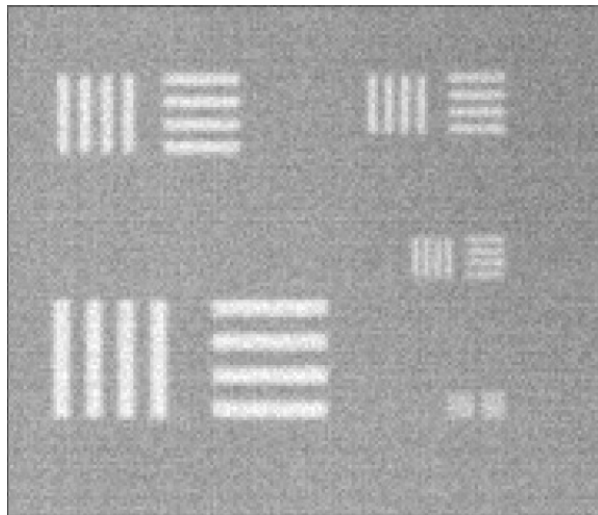


Fig.6. Synthesized test thermal image with uniform background and objects as combination from different size, positions and orientation of four bar object (Fig. 5.) for testing thermal images characteristics

All of these presented here in this article test thermal images are used in experiments to prove the proposed algorithm in Fig.2 and corresponding simulation model from Fig. 3.

Except of presented above synthesized test thermal images in the experiments are used also real thermal images from **Thermal Camera**, shown in Fig. 3 and in this concrete case the model of thermal camera is EasIR-9 [10].

V. RESULTS AND CONCLUSION

For the presentation of the results from the experimental carried out test of thermal images characteristics measurements using the developed simulation model (Fig. 3) and the synthesized numerous thermal images is prepared the following Table 1.

Table 1

Objects in synthesized thermal images	Relative Spatial Frequency (Respective Objects Size)	Minimum resolvable temperature difference (MRTD)
Triangle	0.3	0.11
	0.4	0.2
	0.5	0.36
	0.6	0.98
	0.7	1.26
Four bar as object	0.3	0.09
	0.4	0.22
	0.5	0.36
	0.6	0.88
	0.7	1.13
	0.7	1.13

In this table in a comparative form are collected only (for brevity) some more important results as values of measured thermal images characteristics (in this case values of measurements of minimum resolvable temperature difference MRTD) for two types (triangle and four bar) objects.

The relative values in Table 1 show that there exist the relations between the object type in test thermal image and the value of measured minimum resolvable temperature difference MRTD. Also the Relative Spatial Frequency, respective or Regardless of Objects Size) are important to achieve a good (greater values) of minimum resolvable temperature difference MRTD.

The comparison of the values for measured minimum resolvable temperature difference MRTD of two types (triangle and four bar) objects show that they are greater of simple triangle object.

The presented analysis of the brief described results in Table 1 give the possibility to conclude, that the proposed algorithm and corresponding simulation model can be used with success to perform test of thermal images characteristics and from these results to estimate the quality of thermal images, used in thermo vision systems.

ACKNOWLEDGMENT

This work was supported by National Ministry of Science and Education of Bulgaria under Contract DDVU 02/4-7: “Thermo Vision Methods and Recourses in Information Systems for Customs Control and Combating Terrorism Aimed at Detecting and Tracking Objects and People”.

REFERENCES

- [1] K. Beier, H. Gemperlein, Simulation of infrared detection range at fog conditions for Enhanced Vision Systems in civil aviation. *Aerospace Science and Technology* 8, 2004, 63 – 71
- [2] M. Vollmer, S. Henke, D. Kartadt, K. Mollmann, F. Pinno, Identification and Suppression of Thermal Reflections in InfraredImaging, *InfraMation*, 2004
- [3] Zhang, Z.M., Tsai, B.K. and Machin, G. Radiometric Temperature Measurements: II., 2010.
- [4] H. R. Sheikh, M. F. Sabir, A. C. Bovik, "A Statistical Evaluation of Recent Full Reference Quality Assessment Algorithms", *IEEE Transactions on Image Processing*, vol. 15, no. 11, pp. 3440-3451, Nov. 2006
- [5] ASTM standard E 1213-2002 “Standard Test Method for Minimum Resolvable Temperature Difference for Thermal Imaging Systems”
- [6] Holst G.C., *Infrared Imaging System Testing*, Vol.4, Chapt. 4 in *The Infrared & Electro-Optical Systems Handbook*, Michael C. Dudzik ed, SPIE 1993
- [7] ASTM standard E1311-99 “Standard Test Method for Minimum Resolvable Temperature Difference for Thermal Imaging Systems
- [8] D'Agostiono, Webb C., 3-D Analysis Framework and measurement methodology for infrared systems noise, *Infrared Imaging Systems: Design, Analysis, Modeling and Testing*, SPIE
- [9] Rumen Yordanov, Rosen Miletiev, Ivaylo Simeonov, Emil Iontchev - Spectrum analysis of the suspension dynamics measured by MEMS inertial system, *International Journal of New Computer Architectures and their Applications (IJNCAA)*, Vol.3, Issue 4, 2013, pp.94-99
- [10] GUIDE® EasIR-9 Thermal Camera User Manual. Wuhan Guide Infrared Co., Ltd, 2010.

Nano-hardness of PA12 after radiation cross-linking

Martin Ovsik, David Manas, Miroslav Manas, Michal Stanek, Petr Kratky, and Vojtech Senkerik

Abstract—This article describes the effect of radiation cross-linking on the nano-mechanical properties of polyamide 12. These nano-mechanical properties were measured by the DSI (Depth Sensing Indentation) method on samples which were non-irradiated and irradiated by different doses of the β - radiation. The best results were achieved by the irradiation with doses of 132 kGy. The nano-mechanical properties (nano-hardness, elastic modulus, deformation work, creep) after irradiation was increased up to 61 % compared to untreated material.

Keywords—Polyamide 12, modification, cross-linking, β - radiation, Depth sensing indentation, nano-indentation hardness.

I. INTRODUCTION

POLYAMIDES are one of the most commonly used polymers. Due to their very high strength and durability polyamides are commonly used in textiles, carpets and floor coverings or automotive. Probably more familiar name designation is nylon. Polyamide 12 (PA12) is a semi-crystalline thermoplastic material with very high toughness, good chemical stability and impact resistance. PA12 is also a good electrical insulator and as other polyamide insulating properties will not be affected due to moisture. It is also resistant to corrosion. PA12 has many features and enhancements in terms of plasticization of improved varieties. Polyamide 12 is thanks to its very good mechanical properties, which can be even improved as shown in the results, suitable for applications with great demand on the stiffness and resistance of surface layers for instance friction parts used in automotive industry. The chemical formula of PA12 is shown in Fig. 1. In comparison with PA6 and PA66 has PA12 lower

This paper is supported by the internal grant of TBU in Zlin No. IGA/FT/2014/016 funded from the resources of specific university research and by the European Regional Development Fund under the project CEBIA-Tech No. CZ.1.05/2.1.00/03.0089.

M. Ovsik is with the Tomas Bata University in Zlin, nam. T. G. Masaryka 5555, 76001 Zlin, Czech Republic (phone: +420576035100; e-mail: ovsik@ft.utb.cz).

D. Manas is with the Tomas Bata University in Zlin, nam. T. G. Masaryka 5555, 76001 Zlin, Czech Republic (e-mail: dmanas@ft.utb.cz).

M. Manas is with the Tomas Bata University in Zlin, nam. T. G. Masaryka 5555, 76001 Zlin, Czech Republic (e-mail: manas@ft.utb.cz).

M. Stanek is with the Tomas Bata University in Zlin, nam. T. G. Masaryka 5555, 76001 Zlin, Czech Republic (e-mail: stanek@ft.utb.cz).

P. Kratky is with the Tomas Bata University in Zlin, nam. T. G. Masaryka 5555, 76001 Zlin, Czech Republic (e-mail: kratky@ft.utb.cz).

V. Senkerik is with the Tomas Bata University in Zlin, nam. T. G. Masaryka 5555, 76001 Zlin, Czech Republic (e-mail: vsenkerik@ft.utb.cz).

melting point and density, with very high moisture regain [1], [2].

Polyamides are polymers whose repeating units are characterized by the amide group. Through radiation crosslinking, thermoplastic polyamides are turned into plastics which behave like elastomers over a wide temperature range. Crosslinking makes the originally thermoplastic product able to withstand considerably higher temperatures of up to 350 °C. The dimensional stability under thermal stress is also improved. Radiation crosslinked polyamide can often replace thermosetting plastics or high-performance plastics such as PPS, PEI, LCP, etc. [3].

Crosslinking is a process in which polymer chains are associated through chemical bonds. Crosslinking is carried out by chemical reactions or radiation and in most cases the process is irreversible. Ionizing radiation includes high-energy electrons (electron beam), γ -rays, and x-rays. These not only are capable of converting monomeric and oligomeric liquids into solids, but also can produce major changes in properties of solid polymers [1], [4].

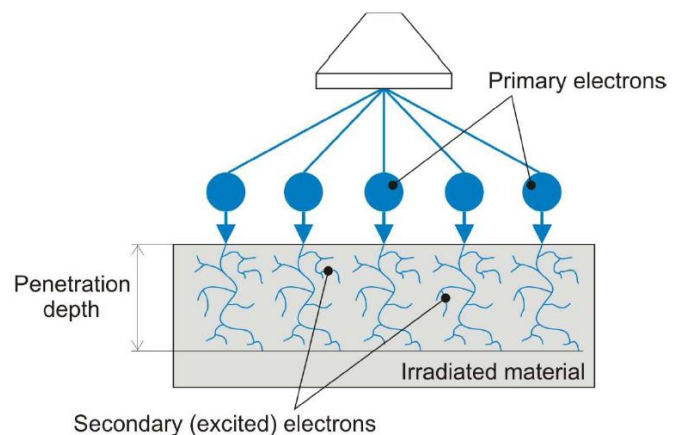


Fig. 1 Radiation crosslinking by electrons rays

Electron beams (β -rays) generated by accelerators are monoenergetic and the absorbed dose is greatest just below the surface of the irradiated material and falls rapidly at greater depths in the material (Fig. 1). The energy range of electron beams used in radiation processing is from 0.15 to 10 MeV. Compared with gamma irradiation, electron accelerators have advantages of higher power and directional beams. The time of irradiation by β -rays is in seconds. The limited

penetrating power of electron beams means that they are mainly used for irradiating relatively thin objects like wires and cable insulation [1], [3].

Gamma radiation has a high penetration capability at relatively low dose intensity as shown. The most used source of gamma rays (Fig. 2) is cobalt-60 (Co60). The energy of emitted gamma rays is about 1.3 MeV. Conversely the electron accelerators, source of gamma rays cannot be turned off. Therefore the rays are sheltered, in most cases by water tank. Time of irradiation depends on dose intensity and reaches up to several hours. The gamma radiation is mainly used for radiation sterilization [1], [2], [6].

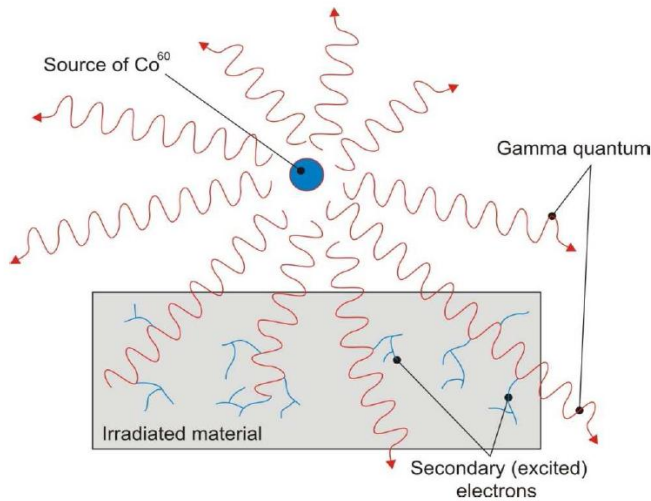


Fig. 2 Radiation crosslinking by gamma rays

Common PA12, when exposed to the effect of the radiation cross-linking, degrades and its mechanical properties deteriorate. Using cross-linking agent TAIC (triallyl isocyanurate) produces a cross-linking reaction inside the PA12 structure. The utility properties of PA12 improve when the noncrystalline part of PA12 is cross-linked.

The aim of this paper is to study the effect of ionizing radiation with different doses, on nano-mechanical properties of polyamide 12 and compare these results with those of non-irradiated samples. The study is carried out due to the ever-growing employment of this type of polymer.

II. EXPERIMENTAL

A. Material and irradiation

For this experiment polyamide 12 V-PTS-Creamid-12-AMN 0 TLD, that were supplied by PTS Plastics Technology Service, Germany (unfilled, PA12+TAIC) was used. The material already contained the special cross-linking agent TAIC - triallyl isocyanurate (6 volume %), which should enable subsequent cross-linking by ionizing β - radiation. The prepared specimens were irradiated with doses of 0, 66, 132 and 198 kGy at BGS Beta-Gamma Service GmbH & Co. KG, Germany.

B. Injection moulding

The samples (fig. 3) were made using the injection molding technology on the injection moulding machine Arburg Allrounder 420C. Processing temperature 220–250 °C, mold temperature 60 °C, injection pressure 80 MPa, injection rate 50 mm/s.

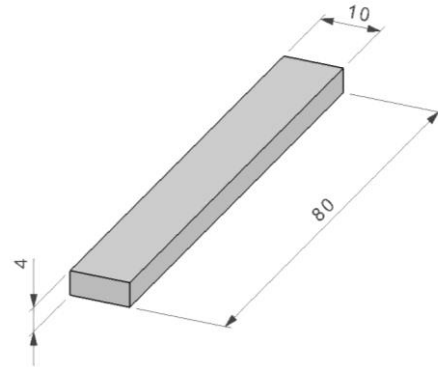


Fig. 3 Dimension of sample

C. Nano-indentation test

Nano-indentation (nano-hardness) tests were done using a Nano-indentation tester (NHT), CSM Instruments (Switzerland) according to the CSN EN ISO 14577. Load and unload speed was 20 mN/min. After a holding time of 90 s at maximum load 10 mN the specimens were unloaded (Fig. 4).

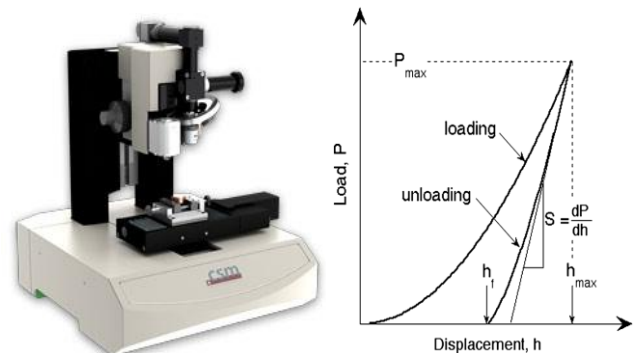


Fig. 4 Nano-hardness tests

The indentation hardness (H_{IT}) was calculated as maximum load (F_{max}) to the projected area of the hardness impression (A_p): [5], [7], [8]

$$H_{IT} = \frac{F_{max}}{A_p} \quad (1)$$

The indentation modulus (E_{IT}) is calculated from the Plane Strain modulus (E^*) using an estimated sample Poisson's ratio (ν) according to: [5], [9]

$$E_{IT} = E^* \cdot (1 - \nu_s^2) \quad (2)$$

Determination of indentation hardness C_{IT} : [10], [11]

$$C_{IT} = \frac{h_2 - h_1}{h_1} \cdot 100 \quad (3)$$

Where h_1 is the indentation depth at time t_1 of reaching the test force (which is kept constant), h_2 is the indentation depth at time t_2 of holding the constant test force [5], [12], [13].

III. RESULTS AND DISCUSSION

The values measured during the nano-hardness test showed that the lowest values of indentation hardness and Vickers hardness were found for the non-irradiated PA12. On the contrary, the highest values of indentation hardness and Vickers hardness were obtained for PA12 irradiated by a dose of 132 kGy (by 61% higher in comparison with the non-irradiated PA12), as can be seen at Fig. 5.

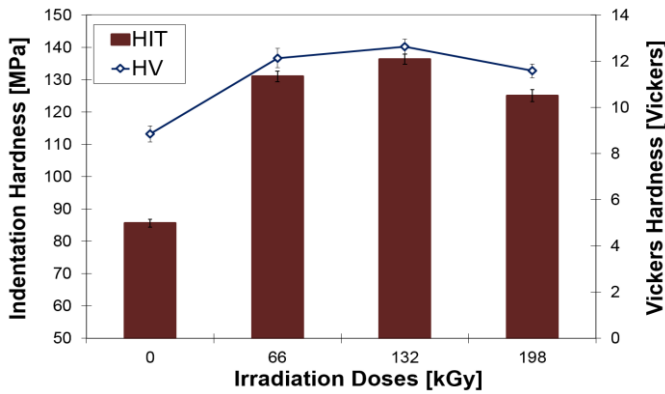


Fig. 5 Hardness H_{IT} of PA12 vs. irradiation doses

According to the results of measurements of nano-hardness, it was found that the highest values of indentation modulus of elasticity were achieved at the PA12 irradiated with dose of 132 kGy (by 21% higher than compared with non-irradiated PA12). On the contrary, the lowest values of the indentation modulus of elasticity were found for non-irradiated PA12, as is seen at Fig. 6.

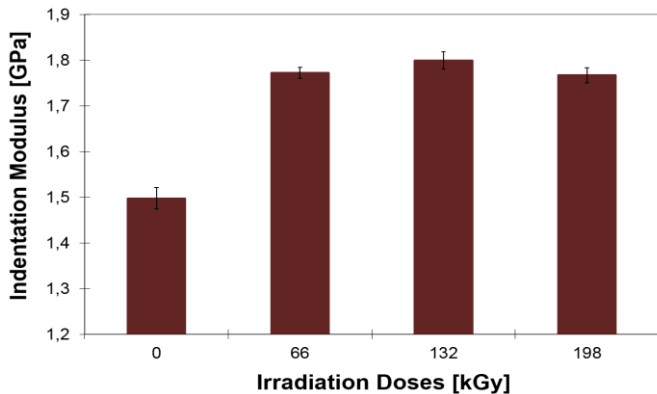


Fig. 6 Elastic modulus E_{IT} of PA12 vs. irradiation doses

Higher radiation dose does not influence significantly the nano-hardness value. An indentation hardness increase of the surface layer is caused by irradiation cross-linking of the tested specimen. A closer look at the nano-hardness results reveals that when the highest radiation doses are used, nano-hardness decreases which can be caused by radiation induced degradation of the material.

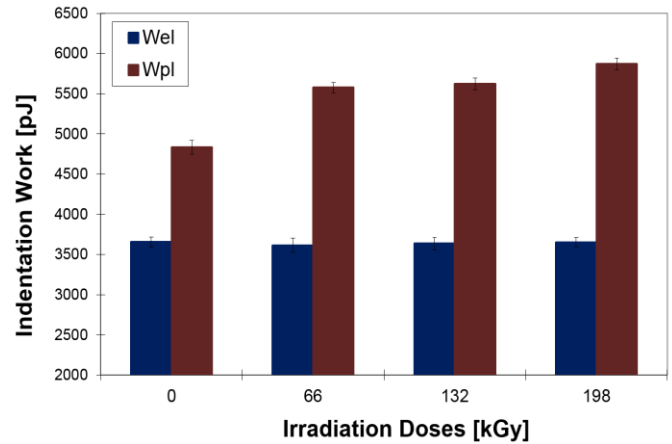


Fig. 7 Deformation work vs. irradiation dose

Other important material parameters obtained during the nano-hardness test were elastic (W_{el}) and plastic deformation work (W_{pl}). The lowest values of plastic and elastic deformation work were obtained for non-irradiated PA12. The greatest values of both elastic and plastic deformation work were obtained for PA12 irradiated with dose of 198 kGy. Radiation of specimens caused lower values of elastic as well as plastic deformation work which is apparent in Fig. 7.

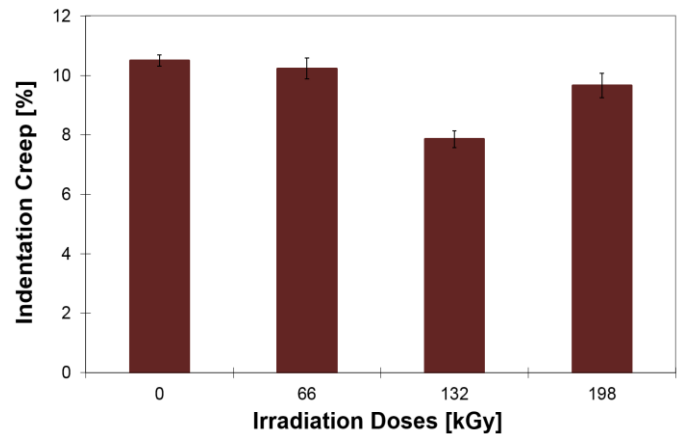


Fig. 8 Creep of PA12 vs. irradiation doses

According to the results of measurements of nano-hardness, it was found that the lowest values of indentation creep were achieved at the PA12 irradiated with dose of 132 kGy (by 34% lower than compared with non-irradiated PA12). On the contrary, the highest values of the indentation creep were found for non-irradiated PA12 as is seen on Fig. 8.

There is also a very important correlation between the force and the depth of the indentation (Fig. 9, Fig. 10). The correlations provide very valuable information on the behavior of tested material and the modified surface layer.

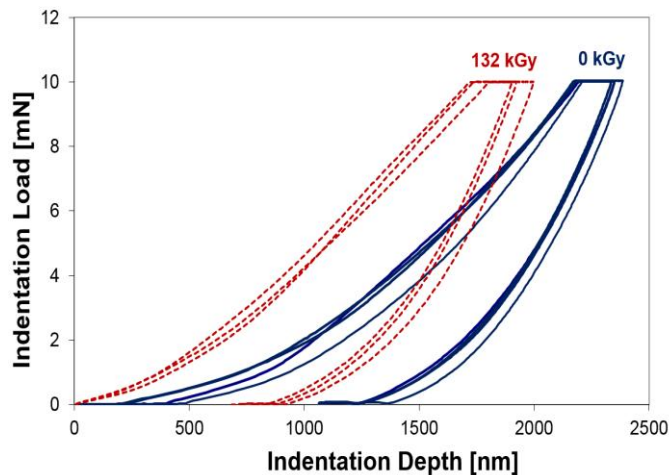


Fig. 9 Indentation depth vs. time

The correlation between the force and the depth of the indentation in PA12 also proved very interesting. It demonstrated the influence of radiation on the change of nano-mechanical properties in the surface layer of specimens. The non-irradiated material showed low hardness as well as increasing impression of the indenter in the surface layer. On the contrary, the irradiated PA12 showed considerably smaller depth of the impression of the indenter which can signify greater resistance of this layer to wear.

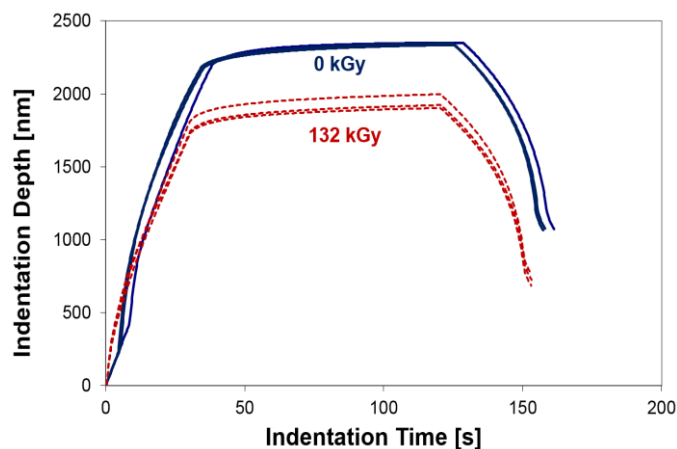


Fig. 10 Force vs. Indentation depth

IV. CONCLUSION

The article is the assessment of nano-mechanical properties (nano-hardness) of the surface layer of modified polyamide 12. The surface layer of the polymer material such as polyamide 12 is modified by β – radiation with doses of 66, 132 and 198 kGy.

Irradiation of Polyamide 12 with a β -radiation influences the nano-mechanical properties in the following way:

- Radiation of specimens caused improvement values of indentation hardness and indentation modulus.
- The highest values of indentation hardness and indentation modulus were achieved at the Polyamide 12 irradiated with dose of 132 kGy (nano-hardness values increased by about 61%, stiffness of surface layer increased significantly by 21%, creep values decreased by 34% as a result of radiation).
- Higher radiation dose does not influence the indentation hardness and indentation modulus significantly, on the contrary due to degradation processes the properties deteriorate.
- Values of indentation hardness and indentation modulus correspond to the deformation works.

The results of nano-mechanical properties of surface layer of modified Polyamide 12 show that it can be used in more difficult applications in some industrial fields, in particular where there are high requirements for strength, stiffness and hardness of surface layer which appears to be the most suitable area of application.

REFERENCES

- [1] M. Ovsik, D. Manas, M. Manas, M. Stanek, M. Hribova, K. Kocman, D. Samek, "Irradiated polypropylene studied by microhardness and WAXS", *Chemické listy*, vol. 106, 2012, pp. 507-510.
- [2] D. Manas, M. Hribova, M. Manas, M. Ovsik, M. Stanek, "The effect of beta irradiation on morphology and micro hardness of PP thin layers", *Thin Solid Films*, vol. 530, 2012, pp. 49-52.
- [3] G. Zamfirova, V. Gaydarov, T. Zaharescu, L. G. Silva, "Micro indentation study of electron beam irradiated polyamide samples", *Chemické Listy*, 104, 2010, pp. 283-286.
- [4] M. Ovsik, D. Manas, M. Manas, M. Stanek, M. Bednarik, P. Kratky, A. Mizera, "Micro-indentation hardness of glass fiber-filled PA6 influenced by beta irradiation" in *Proc. 17th WSEAS International Conference on Systems*, 2013, pp. 225-229.
- [5] G. M. Pharr, "Measurement of mechanical properties by ultra-low load indentation", *Materials Science and Engineering*, 1998, pp. 151 – 159.
- [6] D. Manas, M. Ovsik, M. Manas, M. Stanek, P. Kratky, A. Mizera, M. Bednarikl, "Effect of beta low irradiation doses on the microhardness of PC" in *Proc. 17th WSEAS International Conference on Systems*, 2013, pp. 196-200.
- [7] W. C. Oliver, G. M. Pharr, "Measurement of hardness and elastic modulus by instrumented indentation", *Journal of Materials Research*, 2004, vol. 19, no. 1.
- [8] A. Bolshakov and G. M. Pharr, "Influences of pile-up on the measurement of mechanical properties by load and depth sensing indentation techniques", *J. Mater. Res.* 13, 1998, pp. 1049-1058.
- [9] W. D. Nix and H. Gao, "Indentation size effects in crystalline materials: A law for strain gradient plasticity". *J. Mech. Phys. Solids*. 46, 1998, pp. 411-425.
- [10] M. Ovsik, D. Manas, M. Manas, M. Stanek, K. Kyas, M. Bednarik, A. Mizera, "Microhardness of HDPE influenced by beta irradiation", *International Journal of Mathematics and Computers in Simulation*, vol. 6, Issue 6, 2012, pp. 566-574.
- [11] M. Ovsik, D. Manas, M. Manas, M. Stanek, M. Bednarik, P. Kratky, "Effect of beta irradiation on microhardness of polyamide 6", *Key Engineering Materials*, vol. 586, 2014, pp 218-221.
- [12] M. Manas, D. Manas, M. Stanek, A. Mizera, M. Ovsik, "Modification of polymer properties by irradiation properties of thermoplastic elastomer after radiation cross-linking", *Asian Journal of Chemistry*, vol. 25, Issue 9, 2013, pp. 5124-5128.

- [13] Y. H. Lee, U. Baek, Y. I. Kim, S. H. Nahm, "On the measurement of pile-up corrected hardness based on the early Hertzian loading analysis", *Materials Letters*, vol. 61, 2007, pp. 4039-4042.

Developing a Query Interface for Biomedical Questions Answering

Ioana Branescu-Raspop, Victor Lorin Purcarea and Radu Dobrescu

Abstract— The paper presents a portable question-answering system named MQAS (Medical Question Answering System) which takes queries expressed in natural language and an ontology as input, and returns answers drawn from one or more knowledge bases. It exploits the availability of semantic statements to provide precise answers to complex queries, allowing the use of inference and object manipulation and includes a learning component, which ensures that the performance of the system improves over the time. The prototype is still under tests, but the experiments proved that using ontology as query support allowed to enrich the data analysis process and to extract the knowledge needed to answer medical questions.

Keywords— biomedical ontology, query interface, semantic web technologies, web services.

I. INTRODUCTION

It is challenging for biomedical researchers to stay current with the literature in their field. At the other hand, to ensure best practice and treatment for patients, clinicians must access medical information, acquire new knowledge, and achieve information mastery in their field. Information retrieval systems are widely used; however, they return documents that have to be read by the user to extract relevant information. Inspired by the work of Cimino and Ayres [1] which developed a self-service query interface for re-use in clinical and translational research of the data captured in the course of routine patient available in the Biomedical Translational Research Information System (BTRIS) at the US National Institutes of Health (NIH), we have developed an ontology-driven Question Answering system to interface the Semantic Web to provide answers for a wide array of questions that arise in clinical work and biomedical research..

While semantic information can be used in several different ways to improve question answering, an important consequence of the availability of semantic markup on the web

is that this can indeed be queried directly. In other words, we can exploit the availability of semantic statements to provide precise answers to complex queries, allowing the use of inference and object manipulation. Moreover, as semantic markup becomes ubiquitous, it will become important to be able to ask queries and obtain answers, using natural language (NL) expressions, rather than the keyword-based retrieval mechanisms used by the current search engines. More of that, our methodology for question answering was implemented in a prototype tool which returns answers (known facts) first, and only later the documents from which the facts are extracted.

The proposed prototype titled MQAS (Medical Question Answering System) is a natural language based front-end for the semantic web which takes queries expressed in natural language and an ontology as input, and returns answers drawn from one or more knowledge bases (KBs), which instantiate the input ontology with domain-specific information. Also, MQAS is coupled with a portable and contextualized learning mechanism to obtain domain-dependent knowledge by creating a lexicon. The learning component ensures that the performance of the system improves over time, in response to the particular community jargon of the end users.

II. SEMANTIC WEB TECHNOLOGIES

The goal of the Semantic Web is to solve the current limitations of the Web by augmenting Web information with a formal representation of its meaning. A direct benefit of this machine processable semantics would be the enhancement and automation of several information management tasks, such as search or data integration. The current focus of Semantic Web research is more and more directed towards supporting intelligent data exchange. In this case the information that is being annotated is not unstructured text but rather semi-structured information available from databases or exchanged between Web services.

Semantic Web service technology aims to automate performing such tasks based on the semantic description of Web services. Using these descriptions the right services can be selected and combined in a way that would solve the task at hand. There are two major approaches to Web service composition. First, given the specification of a start and final state, pre/post condition reasoning is performed to select and combine the right services. Second, using the parametric design paradigm, generic task workflows are formally specified and then populated with the right Web services depending on the task at hand.

This work was supported in part by doctoral program POSDRU/107/1.5/S/76813.

Eng Ioana Branescu-Raspop is PhD. student, Faculty of Automatic Control and Computers, University POLITEHNICA of Bucharest, Romania, e-mail: ioana.branescu@gmail.com

Prof. Victor Lorin Purcarea, Ph.D., is with Department of Healthcare Marketing, Technology and Medical Devices, Medical Informatics and Biostatistics, "Carol Davila" University of Medicine and Pharmacy, Bucharest, Romania, e-mail: victor.purcarea@gmail.com.

Prof. Radu Dobrescu, Ph.D, is with Faculty of Automatic Control and Computers, University POLITEHNICA of Bucharest, Romania, e-mail: rd_dobrescu@yahoo.com

In this paper is presented a methodology which allows to utilize the expressiveness of ontologies in an incremental manner within a distributed environment. This novel integration methodology is oriented towards the requirements and challenges of the application domain. It utilizes the expressiveness of ontologies to bridge semantic heterogeneity that originates from the distributed and autonomous manner in which data is collected throughout the domain. The basic idea is that an integrated access to co-existing datasets is already useful for researchers. A concept is presented which implements this methodology within a distributed environment based on Semantic Web technologies, i.e., the Resource Description Framework (RDF) data model and the WSMO (Web Service Modelling Ontology) which overlaps the OWL-S ontology. The resulting system is flexible and built upon loosely coupled components.

A. Resource Description Framework

Resource Description Framework (RDF) is the standard model for data interchange on the Web; prescribed framework for representing resources in a common format [2]. RDF is a graph-structured data model in which information is modelled as a set of triples. Each triple defines an atomic statement of the form (Subject, Predicate, Object) which states that the Subject has a property Predicate with value Object. RDF defines two different types of nodes. Subjects and predicates are always resources whereas objects are either resources or literals. Resources are identified by globally unique Uniform Resource Identifiers (URIs), which are a proper superset of URLs. In order to simplify the representation of structures which consist of several triples (such as lists) RDF allows for anonymous resources whose identifiers are only unique within the local context. Each object is either a resource or a literal. Literals are atomic values with optional type information (e.g., integer or string). RDF uses XML Schema data types, but users are also able to define their own.

An RDF graph is a directed labeled graph in which subject and object are labeled nodes and predicates are directed, labeled edges ranging from the subject to the object. The following definitions determine the meaning of terms used in the characterization of an RDF graph [3]:

Definition 1 (RDF Node)

The set of RDF Nodes T is defined as $I \cup B \cup L$ where I is an infinite set of URIs, B is an infinite set of Blank Node Identifiers, L is an infinite set of Literals and I , B and L are pairwise disjoint.

Definition 2 (RDF Triple)

A RDF Triple T is a tuple $(s, p, o) \in (I \cup B) \times I \times (I \cup B \cup L)$.

Definition 3 (RDF Graph)

An RDF Graph G is a set of RDF triples.

The RDF data model offers several properties that render it interesting for a deployment in the biomedical domain. First, it combines flexibility with expressiveness. As data is modeled as a network of objects, RDF is well-suited for the canonical representation of heterogeneous datasets and structures and therefore fosters interoperability. Second, RDF provides

explicit formal semantics which allow to decompose an RDF dataset into comprehensible atomic statements, even if there is no thorough understanding of the data, e.g., due to missing schema information. Third, RDF enforces the explicit definition of entities, identifiers and relationships. For this reason, under the assumption of a suitable naming convention, resources can be uniquely identified on a global scale and RDF data can be easily combined with information from other datasets. This supports the development of incremental ontology-based approaches to information integration. For example, metadata, annotations or lineage information can be easily added to existing data. Furthermore, new attributes or concepts can be introduced and added to other datasets. At the same time RDF is characterized by its consistency, as data, metadata and semantics can be represented within one model.

B. Generic Web Service Ontologies

The recent developments in Web Services for Ontologies are based on the Web Ontology Language (OWL) [4] and are defined as OWL-S. [5]. OWL is a semantic markup language for publishing and sharing ontologies on the world wide web, and together with RDFS is considered a more expressive way for describing things in the world and how they are related using classes and properties.

A common characteristic of all emerging frameworks for semantic Web service descriptions (OWL-S) is that they combine two kinds of ontologies to obtain a service description. First, a generic Web service ontology, such as OWL-S, specifies generic Web service concepts (e.g., Input, Output) and prescribes the backbone of the semantic Web service description. Second, a domain ontology specifies knowledge in the domain of the Web service, such as types of service parameters and functionalities that fills in this generic framework.

The OWL-S ontology is conceptually composed of three sub-ontologies for specifying what a service does (Profile), how the service works (Process) and how the service is implemented (Grounding). A fourth ontology contains the Service concept which links together a ServiceProfile, a ServiceModel and a ServiceGrounding concept [6].

1. The *Profile Ontology* specifies the functionality offered by the service, the semantic type of the inputs and outputs, the details of the service provider and several service parameters, such as quality rating or geographic radius. This description is used for discovering the service.

2. The *Process ontology*. Many complex services consist of smaller services executed in a certain order. OWL-S allows describing such internal process models. These are useful for several purposes. First, one can check that the business process of the offering service is appropriate (e.g., product selection should always happen before payment). Second, one can monitor the execution stage of a service. Third, these process models can be used to automatically compose Web services. A Profile contains several links to the Process. Figure 1 shows these links, where terms in bold-face belong to the Profile ontology and the rest to the Process ontology.

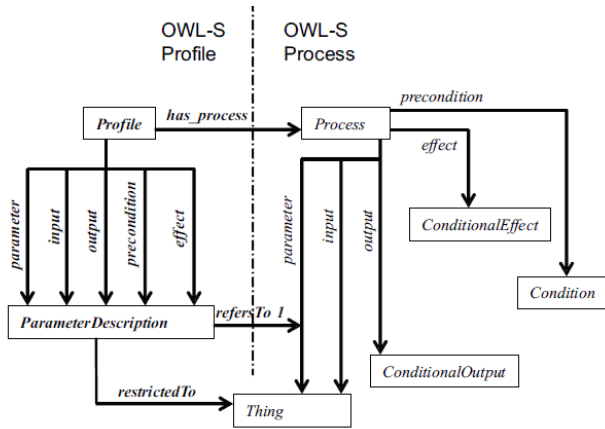


Fig. 1 Connection between OWL-S Profile and Process (after [7])

Firstly, a *Profile* states the *Process* it describes through the unique property *has_process*. Secondly, the *Input*, *Outputs*, *Preconditions* and *Effects* (IOPE) of the Profile correspond to the IOPEs of the Process. The IOPEs play different roles for the *Profile* and for the *Process*. In the *Profile* ontology they are treated equally as parameters of the *Profile*. In the *Process* ontology only *Inputs* and *Outputs* are regarded as sub-properties of the *process:parameter* property. The *Preconditions* and *Effects* are just simple properties of the *Process*. The link between the IOPEs in the *Profile* and *Process* part of the OWL-S descriptions is created by the *refersTo* property which has as domain *ParameterDescription* and ranges over the *process:parameter*.

3. The *Grounding ontology* provides the vocabulary to link the conceptual description of the service, specified by the Profile and Process, to actual implementation details, such as message exchange formats and network protocols. The Grounding ontology specializes the *ServiceGrounding* as a *WSDLGrounding* which contains a set of *WsdAtomicProcessGrounding* elements, each grounding one of the atomic processes specified in the *ProcessModel*. The grounding to a WSDL description is performed according to three rules:

- R1. Each *AtomicProcess* corresponds to one WSDL operation.
- R2. Each input of an *AtomicProcess* is mapped to a corresponding message-part in the input message of the WSDL operation. Similarly for outputs, each output of an *AtomicProcess* is mapped to a corresponding message-part in the output message of the WSDL operation.
- R3. The type of each WSDL message part can be specified in terms of a OWL-S parameter (i.e., an XML Schema data type or a OWL concept).

Let remind that OWL is particularly designed for use by applications that need to process the content of information, and to facilitate greater machine interpretability of Web content than what is supported by XML and RDF, by providing additional vocabulary along with a formal semantics. In fact, it allows constraints on properties,

equivalence and disjointness of classes; union, intersection and complement of classes, and finally to characterize properties [8].

III. MQAS ARCHITECTURE

MQAS provides an API, which allows future integration in other platforms and independent use of its components. Fig. 2 shows the different components of the architectural solution, which is modular, flexible and scalable. The Linguistic Component (LC) and the Relation Similarity Service (RSS) are the two central components of MQAS. A key feature of MQAS is the use of a plug-in mechanism, which allows MQAS to be configured for different Knowledge Representation (KR) languages. For now the plug-in mechanisms is set for the RDF and OWL servers.

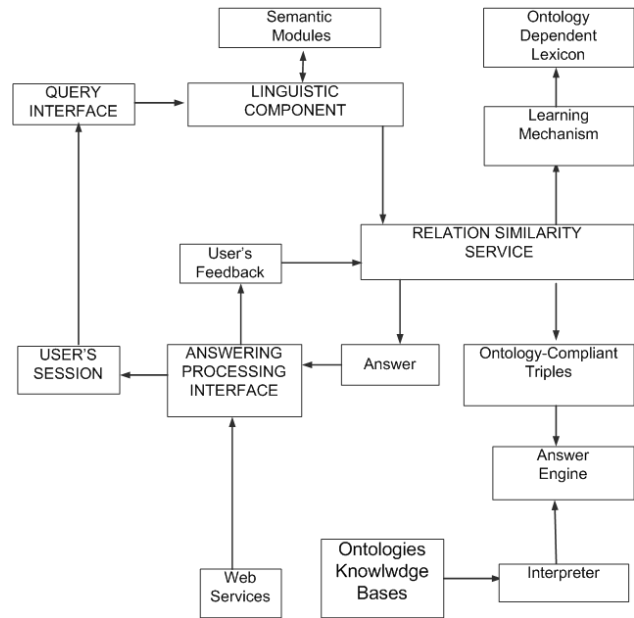


Fig. 2 The MQAS Global Architecture

To reduce the number of calls/requests to the target knowledge base and to guarantee real-time question answering, even when multiple users access the server simultaneously, the MQAS server accesses and caches basic indexing data from the target Knowledge Bases (KBs) at initialization time. The cached information in the server can be efficiently accessed by the remote clients. Therefore, a mechanism is provided to update the cached indexing data on the MQAS server. This mechanism is called by these agents when they update the KB.

As regards portability, the only entry points which require human intervention for adapting MQAS to a new domain are the configuration files. Through the configuration files it is possible to specify the parameters needed to initialize the MQAS server. The most important parameters are: the ontology name and server, login details if necessary, the name of the plug-in, and slots that correspond to alternative names that an instance may have. Optionally, the main concepts of interest in an ontology can be specified.

The core to the overall architecture is the triple-based data representation approach. A major challenge in the

development of the current version of MQAS is to efficiently deal with complex queries in which there could be more than one or two terms. These terms may take the form of modifiers that change the meaning of other syntactic constituents, and they can be mapped to instances, classes, values, or combinations of them, in compliance with the ontology to which they subscribe. Moreover, the wider expressiveness adds another layer of complexity mainly due to the ambiguous nature of human language. So, naturally the question arises of how far the engineering functionality of the triple-based model can be extended to map a triple obtained through a NL query into a triple that can be realized by a given ontology.

To accomplish this task, the triple in the current MQAS version has been slightly extended. Therefore an existing linguistic triple now consists of one, two or even three terms connected through a relationship. A query can be translated into one or more linguistic-triples, and then each linguistic triple can be translated into one or more Ontology-Compliant-Triples. Each triple also has additional lexical features in order to facilitate reasoning about the answer, such as the voice and tense of the relation. Another key feature for each triple is its *category*. These *categories* identify different basic structures of the NL query and their equivalent representation in the triple. Depending on the category, the triple tells us how to deal with its elements, what inference process is required and what kind of answer can be expected [9]. In what follows we provide an overview of the main components of the MQAS architecture.

A. Linguistic Component (LC)

When a query is asked, the LC’s task is to translate from NL to the triple format used to query the ontology (Query-Triples). This preprocessing step helps towards the accurate classification of the query and its components by using standard research tools and query classification. Classification identifies the type of question and hence the kind of answer required. The annotations returned after the sequential execution of these resources include information about sentences, tokens, nouns and verbs. These features, returned for each annotation, are important to create the triples, for instance, in the case of verb annotations, together with the voice and sense it also includes information that indicates if it is the main verb of the query (the one that separates the nominal group and the predicate). This information is used by the Linguistic Component to establish the proper attachment of prepositional phrases previous to the creation of the Query-Triples.

Some examples can be seen in Table 1), including 2 basic queries requiring an affirmation/negation or a description as an answer (the first 2 rows) and queries constituted by a wh-question, where the relation is implicit or unknown (the last 2 rows).

Categories not only tell us the kind of solution that needs to be achieved, but also they give an indication of the most likely common problems that the Linguistic Component and Relation Similarity Services will need to deal with to understand this particular NL query and in consequence it guides the process of creating the equivalent intermediate representation or Query-Triple. For the intermediate representation, we use the

triple-based data model rather than logic, mainly because at this stage we do not have to worry about getting the representation completely right. The role of the intermediate representation is simply to provide an easy and sufficient way to manipulate input for the RSS.

TABLE I. EXAMPLES OF NL QUERIES AND EQUIVALENT TRIPLES

wh-generic term	Linguistic Triple	Ontology Triple
Who are the researchers in the semantic web research area?	<person/organization, researchers, semantic web research area>	<researcher, has-research-interest, semantic-web-area>
description	Linguistic Triple	Ontology Triple
Who are the academics?	<who/what is, ?, academics>	<who/what is, ?, academic-staff-member>
wh-combination (and)	Linguistic Triple	Ontology Triple
Does anyone has interest in ontologies and is a member of research group?	<person / organization, has interest, ontologies> <person/organization, member, research group >	<person, has-research-interest, ontologies> <research-staff-member, has-project-member, research group >
wh-generic with wh-clause	Linguistic Triple	Ontology Triple
What researchers, who work in faculty, have interest in ontologies?	<researchers, work, faculty> <researchers,has-interest,ontologies>	<researcher, has-project-member, faculty > <researcher, has-research-interest, ontologies >

B. Relation Similarity Service (RSS)

The RSS is the backbone of the question-answering system. The RSS component is invoked after the NL query has been transformed into a term-relation form and classified into the appropriate category. The RSS is the main component responsible for generating an ontology-compliant logical query. Essentially, the RSS tries to make sense of the input query by looking at the structure of the ontology and the information stored in the target KBs, as well as using string similarity matching, generic lexical resources, and a domain-dependent lexicon obtained through the use of a Learning Mechanism.

An important aspect of the RSS is that it is interactive. In other words, when ambiguity arises between two or more possible terms or relations the user will be required to interpret the query. Relation and concept names are identified and mapped within the ontology through the RSS and the Class Similarity Service (CSS) – not represented in fig.2 considering it is part of RSS. The similarity services should use the ontology semantics to deal with ambiguous situations.

Where the ambiguity cannot be resolved by domain knowledge the only reasonable course of action is to get the user to choose between the alternative readings. Moreover, since every item on the Onto-Triple is an entry point in the knowledge base or ontology, they are also clickable, giving the user the possibility to get more information about them. Note also that the category to which each Onto-Triple belongs can be modified by the RSS during its life cycle, in order to satisfy

the appropriate mappings of the triple within the ontology.

The RSS procedure for basic queries has several steps. The query is classified by the Linguistic component as a basic generic-type, then the first step for the RSS is to identify that validity (consistence) of terms through the use of string distance metrics. Whenever a successful match is found, the problem becomes one of finding a relation which links these terms. By analyzing the taxonomy and relationships in the target KB, MQAS finds that the only correct relation between two terms. Having done this, the answer to the query is provided. Whenever multiple relations are possible candidates for interpreting the query, if the ontology does not provide ways to further discriminate between them, *string matching* is used to determine the most likely candidate, using the relation name, the learning mechanism, eventual aliases.

C. Answer Engine

The Answer Engine is a component of the RSS. It is invoked when the Onto-Triple is completed. It contains the methods which take as an input the Onto-Triple, and infer the required answer to the user’s queries. In order to provide a coherent answer, the category of each triple tells the answer engine not only about how the triple must be resolved (or what answer to expect) but also how triples can be linked with each other. For instance, MQAS provides three mechanisms (depending on the triple categories) for operationally integrating the triple’s information to generate an answer. These mechanisms are: 1) And/or linking; 2) Conditional link to a term; 3) Conditional link to a triple.

D. Learning Mechanism

Since the universe of discourse we are working within is determined by and limited to the particular ontology used, normally there will be a number of discrepancies between the natural language questions prompted by the user and the set of terms recognized in the ontology. In such a case, it becomes necessary to learn the new terms employed by the user and disambiguate them in order to produce an adequate mapping of the classes of the ontology. The learning mechanism (LM) in MQAS consists of two different methods, the *learning* and the *matching*. The latter is called whenever the RSS cannot relate a linguistic triple to the ontology or the knowledge base, while the former is always called after the user manually disambiguates an unrecognized term (and this substitution gives a positive result). When a new item is learned, it is recorded in a database together with the relation it refers to and a series of constraints that will determine its reuse within similar contexts

IV. TESTS AND EXPERIMENTAL RESULTS

MQAS is implemented in Java as a modular web application, using a client-server architecture and is supported by the platform INSER@SPACE, which was developed within the INSEED project. INSEED was a research project having the aim to create a modern framework for training and skills forming in higher education in science, design and services

management and to promote innovation in service industry based on a model of open, continuous education and cloud type distributed computing infrastructure with virtualized resources and accesible as services, interconnected at European structures.

INSER@SPACE, like collaborative environment for dissemination of the INSEED project results, is an approach developed in the UPB that provides support for a modern education of the future, both at research and curricula development level in many services sectors. This involves using cutting edge technology infrastructure of cloud in different ways, among them organizing and providing content area dedicated to Service Science - through a shared environment knowledge (SSKE - Service Science Knowledge Environment); The discussed application was integrated in connection with the E Health top-level ontology (see <http://sske.cloud.upb.ro/sskemw/index.php/E-Health>) included in SSKE. The prototype is still under tests, but in the same time it will be developed to include more data.

Test scenario

In order to demonstrate the functionality of a self-service query interface, we developed a first simplified version of a software tool based on a set of domain-specific query modules that can be selected by the users and related to each other only through “AND” and “OR” relationships. We assessed the theoretical capabilities for the query tool to address the previous user query requirements with respect to the various domains, attributes and relationships. Analysis considered the capabilities of the initial version of the tool as well as of a subsequent extended version. System requirements were enumerated and then divided into those to be included in the first version of the new tool and in the later version.

User queries were collected by the courtesy of a research team of the Clinical Institute of Fundeni, Bucharest, as part of their routine user interactions. Each query was developed manually after discussion between a database analyst and user. Requests were classified based on the data domains requested (demographics, laboratory results, etc.), the types of data attributes specified (date range, value range, cardinality, etc.), and the relationships between the data.

Multiple modules may be selected. Each module includes a collection of optional query prompts (e.g., date and value and patient age ranges). The modules are defined using XML data structures that specify the prompts to be included and the SQL queries generated by the tool based on user input to the prompts. The domains and features of the initial and in work a later version of the system are shown in Table 2.

TABLE II. FEATURES PLANNED FOR THE QUERY TOOL

Query Function	Version 1	Added features in later Version
Domains	Laboratory Results Clinical Documents Medications	Diagnoses ECG& Echo Procedures
Query Features	Age Range, Date Ranges, Value Range	Controlled Terminology Cardinality
Relationships	AND, OR	NOT, Before, After

Rather than wait until all modules and all prompts were completed, we chose to deploy an initial version of the system with what we consider to be a “critical mass” of the most popular data domain modules and the most important query parameter prompts.

Collection of User Queries

A total of 22 user queries were collected over the past year. Some examples of correlation between the domains of interest and the attributes of those domains are shown in Table 3, according to the following key to Domains: A=Admission, B=Blood Bank, C=Clinical Documents, D=Demographics, Dx=Diagnosis, L=Laboratory Tests, E=Echo, M=Medications, P=Pathology and the key to Attributes: a=age, c=controlled terms, d=date range, t=text search, v=discrete values. Italic items represent features planned for the future version. For example, Query #3 involved the domains Laboratory (implemented) and Pathology (planned); Query #5 involved the domains Clinical Documents and Laboratory (implemented), respectively Diagnosis and Pathology (planned).

TABLE III. CHARACTERISTICS OF USER QUERIES

Query #	Domains	Relationshi p	Attributes
1	<i>B, C, D, L, M</i>	AND	c, d, t, v
2	<i>A, D, E</i>	AND	a, t, v
3	<i>L, P</i>	AND	d, t, v
4	<i>D, L, M</i>	AND	a, d, t, v
5	<i>C, Dx, L, P</i>	AND, OR	t, v
6	<i>L, M, P</i>	AND, OR	a, v

Comments on results

Till now we do not collect enough queries to have a concluding analysis. From the mentioned 22 queries, only four can be handled totally by the initial version of the tool, but only 2 of them should not be handled by the later planned version of the tool. Based on our experience with the implementation of the tool thus far, we believe that the addition of new domains and attributes will be straightforward; their limitations are development time, not algorithmic complexity.

The user queries touched on all the domains implemented in the current version of the query tool, as well as most of the planned domains. As of this writing, a few domains (Alerts, Allergies, ECG, and Pulmonary Function) have yet to be requested. Four queries involved domains that we had not previously planned to provide: Research Study (three queries) and Discharge/Transfer events (one query).

V. CONCLUSION

Ontologies are now increasingly used in information systems to enrich the data analysis process, allowing the user to use ontology concepts for semantic queries. They can represent a domain knowledge that is not possible with a relational database information model. In the present study, we

proposed a framework to link a database to an external ontology using a semantic web tool.

We demonstrated the performance impact of ontology use in the querying process. Using the ontology as query support enriched the data analysis process and extracted the knowledge needed to answer medical questions. The ontologies include structured vocabulary and formalized knowledge to express queries, and act as a mediator between the user and the data.

The framework we propose is designed to promote progress in the healthcare services, with the goal, not of developing an underlying formal ontology for biomedical purpose, but rather of achieving appropriate mappings of existing available biomedical ontologies.

The results of our study are likely to lead to the development of additional requirements for the tool. We hope to continue with all the current planned extensions, even those that have not yet been required of user queries, because we believe it is only a matter of time before a user makes a request that will need them. The objectives for this future work aim including optimization of query performance, expanding the synonyms in our controlled terminology lookup tool, rendering query results into formats that meet user requirements, and adding post-processing data analysis and visualization tool.

We acknowledge that the proposed approach is not easy to apply because of several distinctions and constraints it requires. We believe, however, that the approach promises significant benefits, both practical (clinical) and theoretical (scientific), in the long run.

REFERENCES

- [1] J.J. Cimino and E. J. Ayres, “The clinical research data repository of the US National Institutes of Health”, *Studies in Health Technology and Informatics*, 2010, 160(Pt 2), pp. 1299-1303.
- [2] RDF vocabulary description language 1.0: RDF schema. Website. Available online at <http://www.w3.org/TR/rdf-schema>
- [3] F. Prasser, A. Kemper, and K. A. Kuhn, “Efficient distributed query processing for autonomous RDF databases”. In *Proceedings of the 15th International Conference on Extending Database Technology*, 2012, pp. 372-383
- [4] OWL web ontology language overview. Website. <http://www.w3.org/TR/owl-features/>
- [5] *The OWL-S Services Coalition*. ‘OWL-S: Semantic Markup for Web Services. White Paper.’, Available online at www.daml.org/services/owl-s/1.0/owl-s.pdf, 2003.
- [6] J. Zhang, “A Review of Ontology and Web Service Composition”, *Project Report*. CSIRO Publishing., Available online at <http://eprints.usq.edu.au/5640/>
- [7] M. Sabou, D. Oberle, and D Richards, “Enhancing Application Servers with Semantics”, Available online at <http://www.researchgate.net/publication/2872473>
- [8] L. Anticoli and E. Toppano, “Technological Mediation of Ontologies: the Need for Tools to Help Designers in Materializing Ethics”, *International Journal of Philosophy Study*, Vol. 1, Issue 3, 2013, pp.23-31
- [9] D. L. Castillo and N.S. Abraham, „Knowledge management: how to keep up with the literature”, *Clinical Gastroenterology Hepatol.*, 2008, 6(12), pp.1294-1300

Physical properties' determination of PA6/HDPE_x blends

Jan Navratil, Miroslav Manas, Michal Stanek, David Manas, Martin Bednarik, and Ales Mizera

Abstract—Irradiation of thermoplastics is a well-known modification improving their properties, yet little research has been done to investigate possible utilization of such modified materials after the end of their lifetime. This research paper gives possible solution of using this material as a filler into some other one. The emphasis is put on utilization of irradiated high-density polyethylene (HDPE_x) which has been blended with non-modified polyamide 6 (PA6). Mechanical properties of the resulting blend were investigated and compared.

Keywords—HDPE, PA6, radiation crosslinking, recycling, physical properties.

I. INTRODUCTION

KNOWLEDGE of polymer irradiation has led to an increasing usage of cheap commodity plastics in the areas where it was unthinkable before. Original purpose was sterilization but since positive effect on plastics was discovered it is used in plastic industry as well. Irradiation causes crosslinking or degradation in the structure of exposed polymer. Those polymers which tend to crosslinking (Fig. 1) have significantly improved mechanical, thermal and chemical properties. [1]-[18]

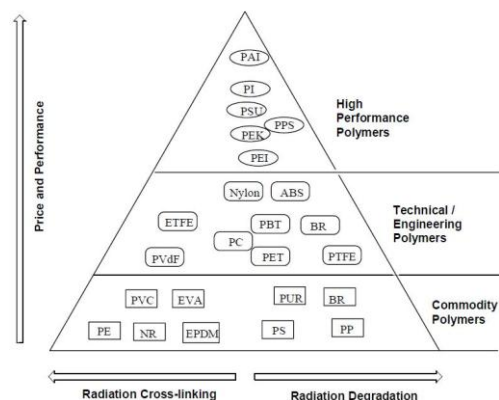


Fig. 1 Material classification [3]

Crosslinking, i.e. formation of a 3D network in a polymer structure occurs mainly in the amorphous region of the polymer. The degree of crosslinking depends on the radiation dose and radiation energy. From chemical point of view is crosslinking intermolecular bond formation of polymer chains. The mechanism of crosslinking involves the cleavage of the C-H bond on one polymer chain to form a hydrogen atom H followed by abstraction of a second hydrogen from another polymer chain to produce a hydrogen molecule H₂. Then the two adjacent polymer radicals combine and form a crosslink.

The source of radiation may be an electron beam accelerator emitting beta radiation or a radioactive source such as Cobalt-60 emitting gamma radiation. Electron beam accelerator is the most used radiation source which emits monoenergetic beam. The highest dose is just below the surface of the irradiated material and falls rapidly at higher penetration depths, therefore it is not suitable for irradiating thick materials. The energy range of electron beams used in irradiation of polymers varies between 0.15 and 10 MeV. Irradiation takes place at ambient conditions and on the final product hence processability is not influenced. [19]-[33]

Jan Navratil is with the Tomas Bata University in Zlín, nam. T. G. Masaryka 5555, 76001 Zlín, Czech Republic (phone: +420 57 603 5152, email: j1navratil@ft.utb.cz).

Miroslav Manas is with the Tomas Bata University in Zlín, nam. T. G. Masaryka 5555, 76001 Zlín, Czech Republic (email: manas@fai.utb.cz).

Michal Stanek is with the Tomas Bata University in Zlín, nam. T. G. Masaryka 5555, 76001 Zlín, Czech Republic (email: stanek@ft.utb.cz).

David Manas is with the Tomas Bata University in Zlín, nam. T. G. Masaryka 5555, 76001 Zlín, Czech Republic (email: dmanas@ft.utb.cz).

Martin Bednarik is with the Tomas Bata University in Zlín, nam. T. G. Masaryka 5555, 76001 Zlín, Czech Republic (email: mbednarik@ft.utb.cz).

Ales Mizera is with the Tomas Bata University in Zlín, nam. T. G. Masaryka 5555, 76001 Zlín Czech Republic (email: mizera@ft.utb.cz).

This paper is supported by the internal grant of TBU in Zlín No. IGA/FT/2014/016 funded from the resources of specific university research and by the European Regional Development Fund under the project CEBIA-Tech no. CZ.1.05/2.1.00/03.0089.

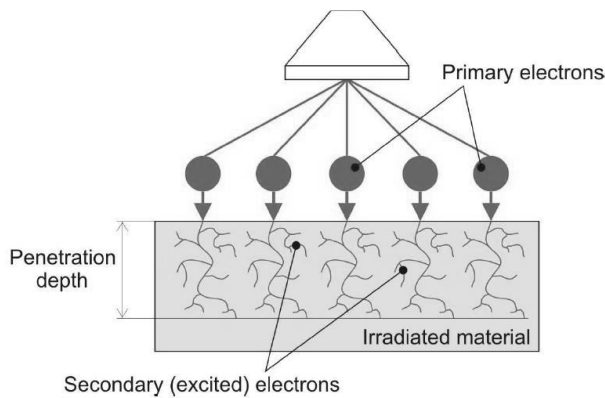


Fig. 2 Principal of electron beam accelerator [23]

II. EXPERIMENT

This experiment deals with preparation of PA6/HDPEx blends and thus with determination of possible utilization of irradiated HDPE waste. Resulting blends underwent series of tests to investigate their physical properties.

A. Materials

Two materials were tested – neat polyamide 6 (PA6) and waste of irradiated high-density polyethylene (HDPE). HPDEx waste was used as a filler into the PA6 in two concentrations (10 and 30 %).

PA6 has, as an engineering plastics, very good mechanical properties and therefore it was chosen as a polymer matrix. Producer of this material was Frisetta, type FRIANYL B63 V0. This material was provided in form of granules, its basic properties are shown in table I.

Table I PA6 material properties [19]

FRIANYL B63 V0	
Density	1.2 [g/cm ³]
Water Absorption (23 °C)	2-3 [%]
Tensile Modulus	3500 [MPa]
Tensile Strength	60 [MPa]
Tensile Elongation at Break	3 [%]
Charpy Impact (notched 23 °C)	5 [kJ/m ²]

HPDEx waste was provided in form of pipes, which were crushed into a grit of 3 to 5 mm particle size. Pipes were originally irradiated by beta radiation with the energy 10 MeV by the total dose of 165 kGy. Irradiation caused irreversible creation of 3D network in the HDPE structure and therefore this material could not be remelted repeatedly and had to be used as a filler. Properties of the original HDPE are shown in table II; however properties of the used HDPEx slightly differ due to the irradiation. Producer of the original material was Slovnaft, type TIPELIN 6300B.

Table II HDPE material properties [18]

TIPELIN 6300B	
---------------	--

Density	0.954 [g/cm ³]
Melt Flow Rate (190 °C / 2.16 kg)	0.3 [g/10 min]
Vicat Softening Temperature	126 [°C]
Tensile Strength	29 [MPa]
Shore D Hardness	65 [-]
IZOD Impact Strength (notched 23 °C)	9 [kJ/m ²]

B. Specimens' Preparation

Materials were mixed together in a laboratory pneumatic blender in concentrations 10 and 30 % of the filler. Resulting raw mixture was dried for five hours at 80 °C and then injection molded in injection molding machine arburg allrounder 470H. Specimens' shape for tensile behavior testing was according to the ISO 527 standard (Fig. 3).



Fig. 3 Test specimen [20]

III. RESULTS

Tensile properties were tested to describe mechanical properties in the most complex way. Properties were tested at ambient temperature conditions (23 °C) and at elevated temperature conditions (80 °C). Zwick tensile testing machine was used to test testing samples. Testing velocity was 50 mm/min.

A. Ambient temperature conditions

First observed parameter was elastic modulus E. This parameter represents toughness of the resulting material.

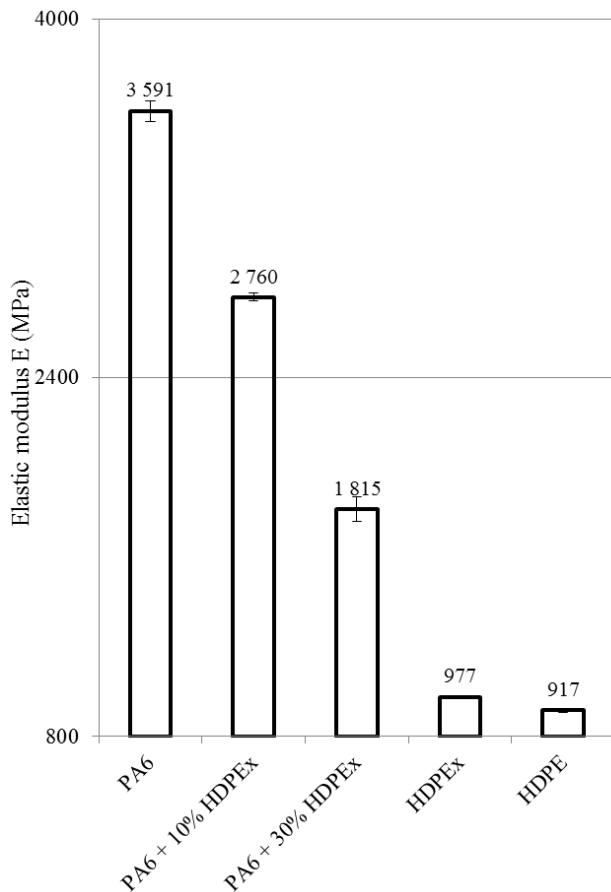


Fig. 4 Elastic modulus comparison

As can be seen from Fig. 4 elastic modulus decreased with increasing amount of the filling. Reference value of non-modified PA6 was not achieved. First concentration of filling (10 %) resulted in 23 % drop from reference value. Second concentration (30 %) resulted in almost 50 % drop. This suggests that there was not very good adhesion between filler particles and polymer matrix. However despite this significant drop from reference value both concentration have still higher elastic modulus than irradiated (977 MPa) and non-irradiated (917 MPa) HDPEs. By comparing these HDPEs can be seen that irradiation has little influence on elastic modulus.

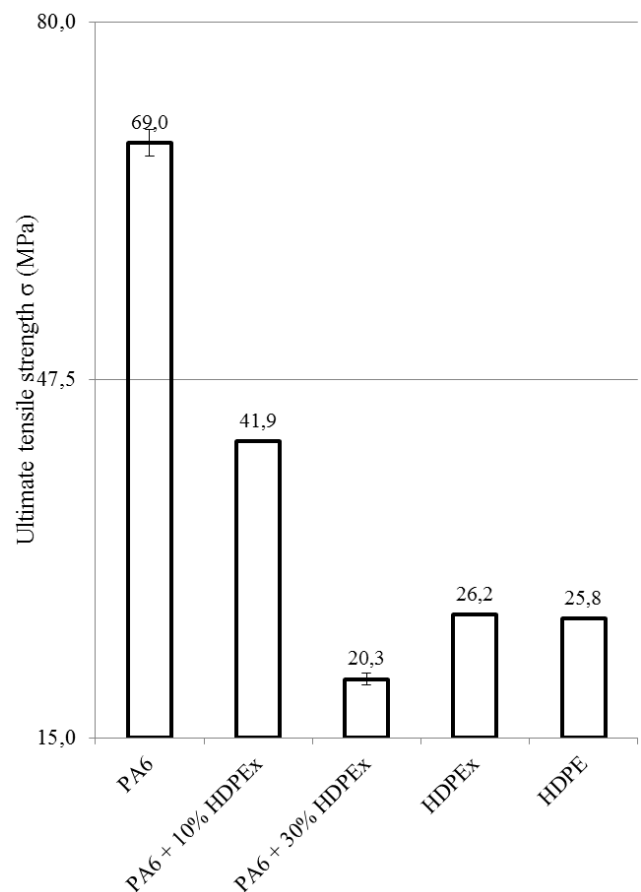


Fig. 5 Ultimate tensile strength comparison

Ultimate tensile strength results show similar trend as elastic modulus (Fig. 5); however the drop is even more significant. First concentration dropped from 69 MPa to 41.9 which represents 40 % decrease. Second concentration dropped to 20.3 MPa which represents 70 % decrease. This shows that our presumption of bad adhesion is confirmed and thus filling PA6 is not suitable for improving tensile behavior of the resulting material. Ultimate tensile strength of non-filled yet modified HDPE is 26.2 MPa which is fully comparable with non-filled and non-modified HDPE (25.8 MPa). This again confirms little influence of radiation crosslinking on resulting tensile behavior.

Results of tensile behavior measurements at ambient temperature conditions show that adding waste of irradiated HDPE into to the PA6 does not improve final mechanical behavior; nevertheless there is an improvement comparing blends with both, modified and non-modified HDPE.

B. Elevated temperature conditions

80 °C was chosen as an elevated temperature due to the original purpose of the irradiated HDPE pipes. Those were used for floor heating with water heated up to 80 °C.

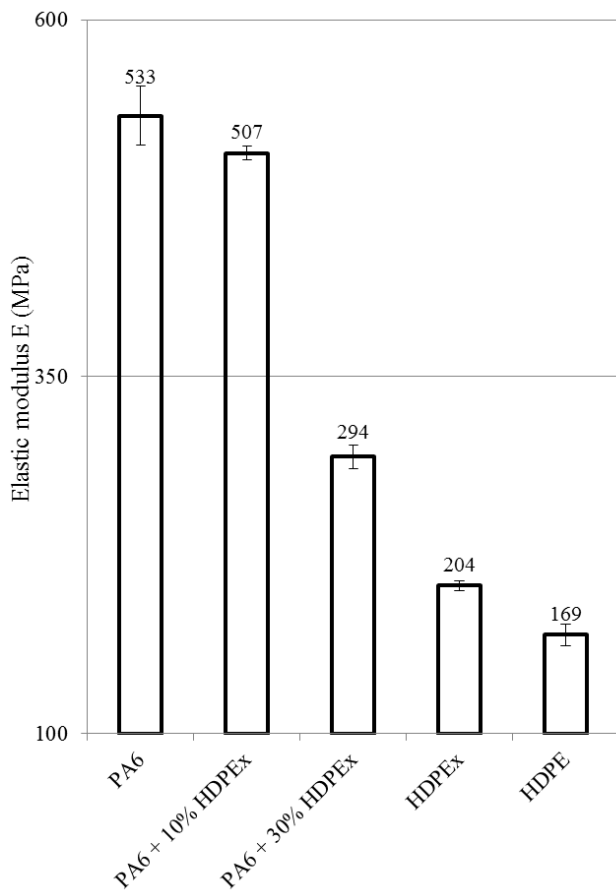


Fig. 6 Elastic modulus comparison

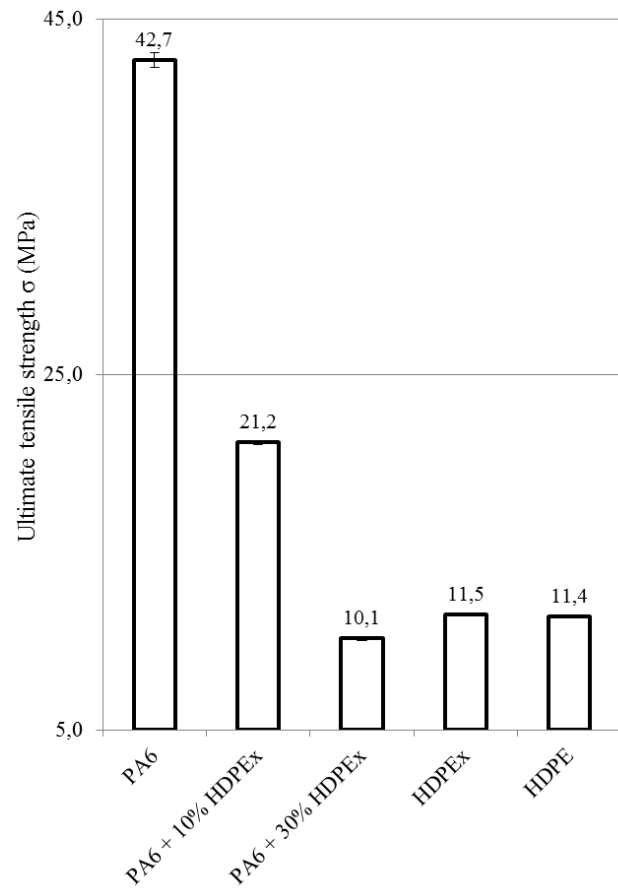


Fig. 7 Ultimate tensile strength comparison

Elastic modulus was reduced from 533 MPa to 507 MPa at the PA6+10 % HDPEX blend (Fig. 6). This reduction is significantly lower than at ambient temperature conditions, it represents only 6 % reduction which might mean that intermolecular forces between the matrix and filler are stronger at higher temperatures. Second blend with 30 % of the filler dropped to 294 MPa which is similar decrease to the ambient temperature results (45 % drop.). Comparably to the elastic modulus measured at ambient temperature conditions, measured data of all concentrations are higher than both HDPEs. Irradiated HDPE has elastic modulus 204 MPa and non-irradiated HDPE has elastic modulus 169 MPa. This also shows that influence of irradiation is higher at increased temperature.

Ultimate tensile strength results have again similar trend as elastic modulus (Fig. 7). There is a significant drop in this property even at the lowest concentration of filling where the difference between non-modified PA6 and PA6+10 % HDPEX is 51 %. Another addition of the filler resulted in another 50 % drop comparing it with the previous concentration. Results of both HDPEs are very similar and the difference between them is negligible. Influence of irradiation on measured material strength is thus very limited.

IV. CONCLUSION

The main aim of this research paper was to determine possible utilization of HDPE modified by radiation crosslinking after its service life. This paper dealt with using grit of recycled HDPEX as a filler into granules of non-modified PA6. Two concentrations of proposed blends were prepared and testing specimens were injection molded. Mechanical properties of the resulting blends were tested when tensile test was chosen to describe mechanical behavior the most. Testing was carried out at two temperature conditions (ambient and elevated) and two material characteristics were compared – elastic modulus and ultimate tensile strength. Results show that with increasing concentration of the filler decreases both those properties in case of comparing it with non-modified PA6. But when comparing it with non-modified or irradiated HDPE the values are higher. Therefore it may be concluded that it is possible to use such modified material as the filler; however it has to be carefully chosen what the final application will be and what material characteristics are important.

REFERENCES

- [1] J. Gehring, A. Zyball, "Radiation crosslinking of polymers - status, current issues, trends and challenges," *Radiat. Phys. and Chem. J.*, Vol.46, No.4-6, pp. 931-936, 1995.
- [2] S. Rouif, "Radiation cross-linked polymers: recent developments and new applications," *Nucl. Instrum. and Methods in Phys. Res. B J.*, Vol.236, No.1-4, pp. 68-72, 2005.

- [3] D.R. Kerluke, S. Cheng, "Radiation processing for modification of polymers," *ANTEC 2003 Conference Proceedings*, 2003, pp. 2694-2699.
- [4] D.R. Kerluke, S. Cheng, "Radiation processing of polymers: the current status and prospects for the future," *ANTEC 2004 Conference Proceedings*, 2004, pp. 3738-3739.
- [5] S. Bhatt, R. Hoffman, "Outgassing behavior of e-beam irradiated HDPE and ETFE," *ANTEC 2006 Conference Proceedings*, 2006, pp. 1540-1543.
- [6] J. Chen, M. Czayka, R.M. Uribe, "Effects of electron beam irradiations on the structure and mechanical properties of polycarbonate," *Radiat. Phys. and Chem. J.*, Vol.74, No.1, pp. 31-35, 2005.
- [7] R. Feulner et al., "The effects of e-beam irradiation induced cross linking on the friction and wear of polyamide 66 in sliding contact," *Wear J.*, Vol.268, No.7-8, pp. 905-910, 2010.
- [8] J. Gehring, "With radiation crosslinking of engineering plastics into the next millennium," *Radiat. Phys. and Chem. J.*, Vol.57, No.3-6, pp. 361-365, 2000.
- [9] S. Machi, "Radiation technology for sustainable development," *Radiat. Phys. and Chem. J.*, Vol.46, No.4-6, pp. 399-410, 1995.
- [10] A. Bhattacharya, "Radiation and industrial polymers," *Prog. in Polym. Sci. J.*, Vol.25, No.3, pp. 371-401, 2000.
- [11] M. Stanek, D. Manas, M. Manas, O. Suba, "Optimization of injection molding process," *Intl. J. of Math. and Computers in Simul.*, Vol.5, No.5, pp. 413-421, 2011.
- [12] J. Javorik, M. Stanek, "The shape optimization of the pneumatic valve diaphragms," *Intl. J. of Math. and Computers in Simul.*, Vol.5, No.4, pp. 361-369, 2011.
- [13] A. Mizera et al., "Properties of selected polymers after radiation cross-linking," *Intl. J. of Math. and Computers in Simul.*, Vol.6, No.6, pp. 592-599, 2012.
- [14] A. Mizera et al., "Properties of HDPE after radiation cross-linking," *Intl. J. of Math. and Computers in Simul.*, Vol.6, No.6, pp. 584-591, 2012.
- [15] M. Stanek, D. Manas, M. Manas, J. Javorik, "Simulation of injection molding process by cadmould rubber," *Intl. J. of Math. and Computers in Simul.*, Vol.5, No.5, pp. 422-429, 2011.
- [16] M. Stanek et al., "How the filler influence the fluidity of polymer," *Chem. Listy S J.*, Vol.105, No.s15, pp. 303-305, 2011.
- [17] K. Kyas et al., "Simulation of rubber injection molding process," *Chem. Listy S J.*, Vol.105, No.s15, pp. 354-356, 2011.
- [18] HDPE TIPELIN 6300B, *Material datasheet*, Slovnaft.
- [19] PA6 B63 V0, *Material datasheet*, Frisetta.
- [20] ČSN EN ISO 527-2, *Czech technical standard*.
- [21] K. Kyas et al., "Rubber product properties influenced by runners trajectory," *Intl. J. of Math. and Computers in Simul.*, Vol.7, No.1, pp. 1-8, 2013.
- [22] J. Navratil et al., "Recyclation of modified HDPE," *Intl. J. of Syst. Appl., Eng. & Dev.*, Vol. 8, pp. 33-40, 2014.
- [23] J. Navratil et al., "Mechanical properties of recycled irradiated HDPE," *Intl. J. of Syst. Appl., Eng. & Dev.*, Vol. 8, pp. 108-115, 2014.
- [24] M. Bednarik et al., "Effect of ionizing beta radiation on the strength of bonded joints and adhesive properties," *Intl. J. of Syst. Appl., Eng. & Dev.*, Vol. 8, pp. 84-91, 2014.
- [25] P. Kratky et al., "Nanohardness of electron beam irradiated PMMA," *Intl. J. of Math. Models and Methods in Appl. Sci.*, Vol. 7, No. 12, pp. 957-964, 2013.
- [26] A. Mizera et al., "Properties of irradiated PA11 by electron beams," *Intl. J. of Mech.*, Vol. 7, No. 3, pp. 164-171, 2013.
- [27] M. Stanek et al., "How amount of talc influence the polymer flow," *Intl. J. of Mech.*, Vol. 7, No. 3, pp. 277-284, 2013.
- [28] A. Mizera et al., "Properties of irradiated PA12 by electron beams," *Intl. J. of Mech.*, Vol. 7, No. 3, pp. 435-442, 2013.
- [29] J. Navratil et al., "Tensile toughness of irradiated HDPE," *Intl. J. of Mech.*, Vol. 7, No. 3, pp. 327-334, 2013.
- [30] A. Skrobak et al., "Comparison of mechanical properties of injection molded and compression molded rubber samples," *Intl. J. of Mech.*, Vol. 7, No. 4, pp. 409-416, 2013.
- [31] J. Navratil et al., "Hardness and micro-indentation hardness comparison of recycled modified HDPE," *Key Eng. Mater. J.*, Vol. 606, pp. 217-220, 2014.
- [32] J. Navratil et al., "Tensile toughness of irradiated HDPE," *Intl. J. of Mech.*, Vol. 7, No. 3, pp. 327-334, 2013.
- [33] M. Bednarik et al., "Surface and adhesive properties of low-density polyethylene after radiation cross-linking," *Key Eng. Mater. J.*, Vol. 606, pp. 265-268, 2014.

Enhancing Images using the Forward-Backward UFIR Algorithm

L. J. Morales-Mendoza, M. González-Lee, E. Morales-Mendoza, R. F Vázquez-Bautista, J. Huerta-Chua, S. Pérez-Cáceres, G. Triano-Carballo, O. G. Ibarra-Manzano and Y. S. Shmaliy

Abstract— In this paper, we present a novel implementation of the Unbiased FIR (UFIR) filter to enhance binary images for computer vision applications. The Forward-Backward (FB) algorithm is implemented to enhance piecewise-smooth images. Furthermore, we present several computer simulation examples where geometrical binary images are used to illustrate the outstanding usefulness of this method. Finally, the results are evaluated in terms of the root mean square errors (RMSEs) and the signal-to-noise ratio (SNR).

Keywords— Binary Images, Computer Vision, Forward-Backward Filtering, Unbiased FIR Filter.

I. INTRODUCTION

THE problem of saving a sharp edges with a simultaneously enhancing the image, is typical in image processing. An overall panorama of nonlinear filtering that follows the median strategy has been given by Pitas and Venetsanopoulos in [1], including the important modifications for a large class of nonlinear filters employing order statistics. This type of nonlinear filters is applied in a variety of areas such as biomedical images processing [2], and remote sensing [3]. Currently, computer vision is a powerful tool for feature extraction and image processing [4], [5] and is used in many systems for robots development. Human vision is a sophisticated system that senses and reacts on visual stimuli; computer vision is intended to mimic the same function. The purpose of both systems is to interpret spatial data, data that

This work was supported in collaboration between the Veracruzana University and Guanajuato University.

L. J. Morales-Mendoza is with Veracruzana University, Av. Venustiano Carranza s/n, Poza Rica Ver., México, 93390 (e-mail: javmorales@uv.mx).

M. Gonzalez-Lee is with Veracruzana University, Av. Venustiano Carranza s/n, Poza Rica Ver., México, 93390 (e-mail: mgonzalez01@uv.mx).

E. Morales-Mendoza is with Veracruzana University, Av. Venustiano Carranza s/n, Poza Rica Ver., México, 93390 (e-mail: efmorales@uv.mx).

R. F. Vazquez-Bautista is with Veracruzana University, Av. Venustiano Carranza s/n, Poza Rica Ver., México, 93390 (e-mail: favazquez@uv.mx).

J. Huerta-Chua is with Veracruzana University, Av. Venustiano Carranza s/n, Poza Rica Ver., México, 93390 (e-mail: jeshuerta@uv.mx).

S. Perez-Caceres is with Veracruzana University, Av. Venustiano Carranza s/n, Poza Rica Ver., México, 93390 (e-mail: sperezuv.mx).

G. Triano Carballo is with Veracruzana University, Av. Venustiano Carranza s/n, Poza Rica Ver., México, 93390.

O. G. Ibarra-Manzano is with Guanajuato University, Ctra. Salamanca-Valle km 3.5 + 1.8, Comunidad Palo Blanco, Salamanca Guanajuato, México, (e-mail: ibarrao@ugto.mx).

Y. S. Shmaliy is with Guanajuato University, Ctra. Salamanca-Valle km 3.5 + 1.8, Comunidad Palo Blanco, Salamanca Guanajuato, México, (e-mail: shmaliy@ugto.mx).

have more than one dimension. Even though computer and human vision are functionally similar, you cannot expect that a computer vision system would be able to replicate exactly the function of the human sight. It is well known that a computer image is a matrix of pixels; the value of each pixel is a sample of the brightness of the corresponding points in the scene. The matrix of pixels, that is to say the image, is usually square and an image may be describe as $N \times N$ m -bit pixels, where N is the number of points and m is related to the number of brightness values. Using m bits values, ranging from 0 to $2^m - 1$ are obtained. A binary image is a digital image that has only two possible values for each pixel ($m = 1$). Typically the two colors used for a binary image are black and white. Binary images often arise in digital image processing as masks or as the result of certain operations such as segmentation, threshold, and dithering [5], [6]. Typical applications of the binary images are for example in the analysis of documents, industrial applications for the recognition of objects, as a priori information in complex algorithms, among others.

Besides, in off-line processing, *forward-backward* (FB) filters and smoothers are often used. There are two typical rules of how apply and combined forward and backward estimates and thus implement and connect both the causal and non-causal filter structures. The first way implies conducting forward and backward processing simultaneously and the combine the results at the output [7], [9]. Another way is to process a signal forward and then repeat it backward. Denoising is commonly more efficient here, although the procedure requires extra time [8]. The approach can be implemented using the time-variant FIR smoothers, which are able to unite advantages of linear filtering with nonlinear filtering robustness. Moreover, the UFIR filter is a new family of orthogonal polynomials [10] and was originally derived by Shmaliy [11] to have unique coefficients of the polynomial FIR function for the same degree. The filter was then developed to be p -shift with filtering ($p=0$), $|p|$ -lag smoothing ($p < 0$) [11], [12], and p -step prediction ($p > 0$) [11] properties. Thus, in this paper we use the FB algorithm with UFIR filters to enhance binary images.

II. MAIN IDEA OF FB-ALGORITHM AND UFIR SMOOTHER

The main idea behind the solution proposed is illustrated in Fig 1. Suppose that a discrete-time piecewise smooth signal x_n (dashed) is measured in the presence of noise as y_n and the breakpoints k_q , $q = 0, 1, \dots$ are known. To filter noise out, the following algorithm can be used [13]:

1. Smooth measurement Forward by the UFIR smoother [9] from $k_0 + 1 = 0$ to $n = k_1$. If noise is White Gaussian with variance $\sigma^2_{Forward} = \sigma^2/(k_1 + 1)$. Next, smooth the result Backward, from k_1 to $k_0 + 1$. The Backward estimate variance $\sigma^2_{Backward}$ at $k_0 + 1$ can be expected to be a bit larger than $\sigma^2_{Forward}$, but much smaller than σ^2 .

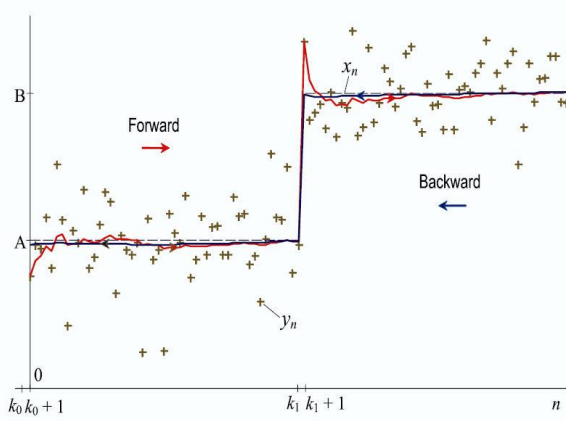


Fig. 1: FB FIR denoising of a piecewise-smooth signal with known breakpoints k_q

2. Next, smooth the result in the same manner Backward. The Backward estimate variance can be expected to be nearly the same, $\sigma^2_{Backward} \approx \sigma^2/(k + 1)$.
3. Pass across the edge, from k_1 to $k_1 + 1$, with the ramp UFIR filter on the window of $N = 2$ points.
4. Repeat this procedure for all segments of the piecewise signal from $k_q + 1$ to k_{q+1} .

A. Polynomial Smoother Impulse Response

Linear FB denoising algorithm can be implemented out based on the time-variant UFIR structures if we first modify the smoothing UFIR filter proposed in [12]. The relevant modification is discussed below. Suppose that a piecewise-smooth signal (or image) x_n is represented from $k_0 + 1$ to k_1 (Fig. 1) with the finite Taylor series of order $K - 1$ as follows [15], [14]:

$$x_n = b_0 + b_1 \tau n + b_2 \frac{(\tau n)^2}{2} + \dots + b_{K-1} \frac{(\tau n)^{K-1}}{(K-1)!}, \quad (1)$$

where, $\tau = t_n - t_{n-1}$ is sampling time and $b_r, r \in [0, K - 1]$, is some constant coefficient. By a time-shift (1) can be applied to any smooth part of x_n from $k_q + 1$ to k_{q+1} . Assume that x_n is measured in the presence of zero mean AWGN v_n as

$$y_n = x_n + v_n. \quad (2)$$

If we introduce $h_{li}(N, p)$ as the gain of l -degree polynomial p -step dependent filter, then the estimate of the electronic image \hat{x}_n can be obtained based on averaging concept by the convolution on horizon of N points

$$\hat{x}_n = \sum_{m=p}^{N-1+p} h_{li}(N, p) y_{n-m} \quad (3)$$

where the positive step, $p > 0$, is supposed for predictive FIR filtering, $p = 0$ for FIR filtering, and $p < 0$ for smoothing FIR filtering. Measurement y_n can be smoothed on an interval of $N \geq k_{q+1} - k_q - 1$ points, with the polynomial impulse response $|p|$ -lag, represented in the forms of

$$\tilde{h}_{li}(N, p) = \sum_{j=0}^l a_{ji}(N, p) (i + p)^j \quad (4)$$

and

$$\tilde{h}_{li}(N, p) = \sum_{j=0}^l \tilde{a}_{ji}(N, p) i^j, \quad (5)$$

where $l = K - 1$ and the coefficients $a_{ji}(N, p)$ is specified by

$$a_{ji}(n, p) = (-1)^j \frac{M(j+1)1(N, p)}{|D(N, p)|}, \quad (6)$$

via a short $(l + 1) \times (l + 1)$ Hankel matrix

$$\mathbf{D}(N, p) = \begin{bmatrix} d_0(N, p) & d_1(N, p) & \dots & d_n(N, p) \\ d_1(N, p) & d_2(N, p) & \dots & d_{n+1}(N, p) \\ \vdots & \vdots & \ddots & \vdots \\ d_n(N, p) & d_{n+1}(N, p) & \dots & d_{2n}(N, p) \end{bmatrix}, \quad (7)$$

each component in (6) can be found using the recursive relation of the Bernoulli polynomials $B_n(x)$ established in [11], [12]. Note that, so far, the following low-degree polynomials, $h_{li}(N, p)$, were found and investigated:

A model that is uniform over an averaging horizon of N points is the simplest one. The relevant signal is characterized with one state and the filter gain is represented, by (3), with the 0-degree polynomial as

$$h_{0i}(p) = \begin{cases} \frac{1}{N} & p \leq N - 1 + p \\ 0 & \text{otherwise} \end{cases} \quad (8)$$

For linear models, the p -lag gain, existing from p to $N - 1 + p$, becomes ramp

$$h_{1i}(p) = a_{01}(p) + a_{11}(p)i \quad (9)$$

having the coefficients

$$a_{01}(p) = \frac{2(2N-1)(N-1) + 12p(N-1+p)}{N(N^2-1)} \quad (10a)$$

$$a_{11}(p) = -\frac{6(N-1+2p)}{N(N^2-1)} \quad (10b)$$

For the quadratic and cubic models, the gain of the unbiased smoothing FIR filters are shown in [11] and [12].

B. FB-UFIR denoising Algorithms

Follow the [14]; the operation principle of the FB UFIR smoothing algorithm is development using the Forward (FW) and Backward (BW) structures. First, consider if a binary

image is considered as a signal in 2D, and this is composed of bar pieces, the FB UFIR smoothing algorithm can be developed as follow:

The FW smoother output can thus be computed starting with $k_0 + 1$ and finishing at k_1 using the follow algorithm

$$\hat{x}_{k_1+p|k_1}^{FW} = \sum_{m=0}^{k_1-k_0-1} \tilde{h}_{li}(k_1-k_0, p)y_{k_1-m} \quad (11)$$

if $k_0 + 1 \leq n < k_0 + 1 + l$, set $\hat{x}_{n|k_1}^{FW} = y_n$.

The output provided in such a way that is further inverted in time as the procedure (11) applied once again in order to smooth Backward (BW) as follow

$$\hat{x}_{k_1+p|k_1}^{BW} = \sum_{m=0}^{k_1-k_0-1} \tilde{h}_{li}(k_1-k_0, p)\hat{x}_{k_1-i|k_1}^{FW} \quad (12)$$

If $k_0 + 1 \leq n < k_0 + 1 + l$, set $\hat{x}_{n|k_1}^{BW} = \hat{x}_{n|k_1}^{FW}$. The FB estimate of the first smooth part is now formed the time-reversal of

$$\hat{x}_{n|k_1}^{FW} = \hat{x}_{k_0+k_1+1-n|k_1}^{BW} \quad k_0 + 1 \leq n \leq k_1. \quad (13)$$

The image edge following after k_1 is viewed as a linear function, from k_1 to $k_1 + 1$. Thus, the UFIR filter passes across the edge with the ramp impulse having $N = 2$ and $p = 0$. Denoising the subsequent smooth parts can be accomplished in the same manner. Just substitute in (12)-(13) k_0 with k_q and k_1 by k_{q+1} . The FB estimate of the piecewise image will thus be

$$\hat{x}_{n|k_{q+1}}^{FW} = \hat{x}_{k_q+k_{q+1}+1-n|k_{q+1}}^{BW} \quad k_q + 1 \leq n \leq k_{q+1}. \quad (14)$$

and the output taken from $k_q + 1$ to k_{q+1} .

III. SIMULATIONS

In this section, we present some computational evaluations to verify the improvement of FB UFIR algorithm. We employed two special cases, in the first case; we use a square pulse signal of 512 samples and for the second case, an artificial image of 512 by 512 pixels. All evaluation is carried out using a personal computer that used an Intel CORE 2 DUO processor with 2.4GHz of speed and 2GB of RAM.

In Fig. 2, we showed the original and noisy signals, respectively. The original signal is a square pulse. This signal is contaminated with a variance of 0.1 of white noise. The approximation order of p -UFIR filters is linear and quadratic with $N = 11$. The horizon is calculated as shown in [9] and [11]. The values of horizon in each case are, $p = -5$ and -8 to the linear and quadratic cases, respectively. In Fig. 3 and 4 we can see the enhanced square pulse using the FB p -UFIR algorithm. The quantitative evaluations are reported in the Table I. We can see that the linear impulse response performs best in the sense of Signal-to-Noise Ratio (SNR) and Root-Mean-Square-Error (RMSE), respectively.

TABLE I. QUANTITATIVE EVALUATION OF p -UFIR

	RMSE	SNR(dB)
$h_1(x, N, p)$	0.0415	22.9017
$h_2(x, N, p)$	0.0442	22.3561

Fig. 5 shows the original test image and the blurred image or measurement image is contaminated with Gaussian noise (AWGN) based on (2). The initial conditions for filtering the image are the same as used for the signals. Thus, consider two case studies; with variance of 0.1 and 0.2. Both images are shown in Fig. 6 and 7, respectively.

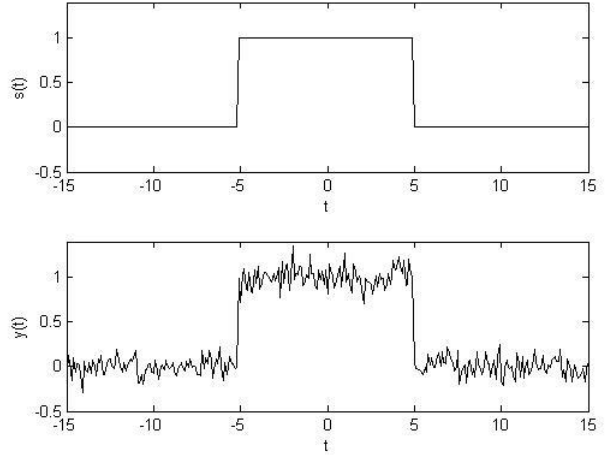


Fig. 2: Square pulse: (upper) original and (lower) noisy signals.

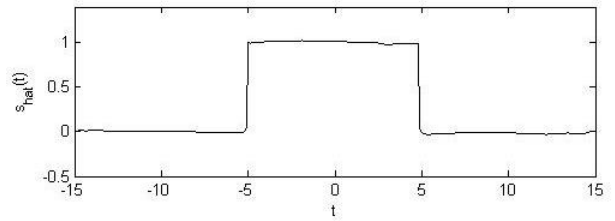


Fig. 3: Square pulse processed: enhanced signal with FB-UFIR with linear response.

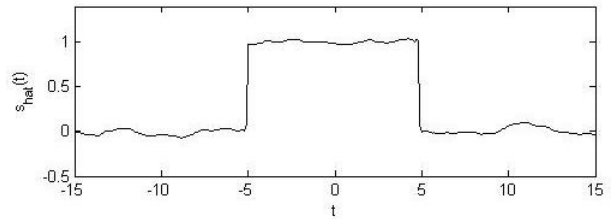


Fig. 4: Square pulse processed: enhanced signal with FB-UFIR with quadratic response.

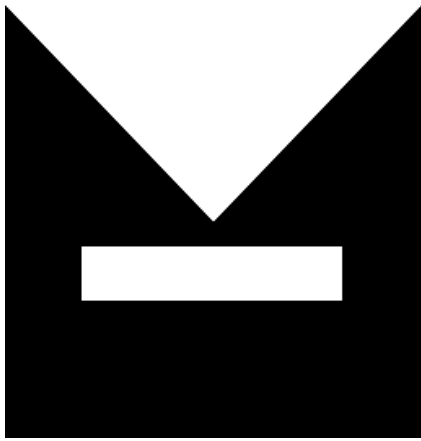


Fig. 5: Original binary image test

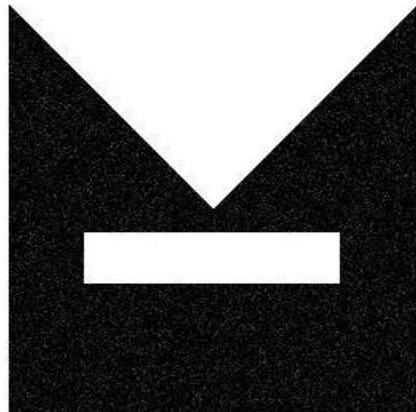


Fig. 6: Noisy image with $\sigma^2 = 0.1$

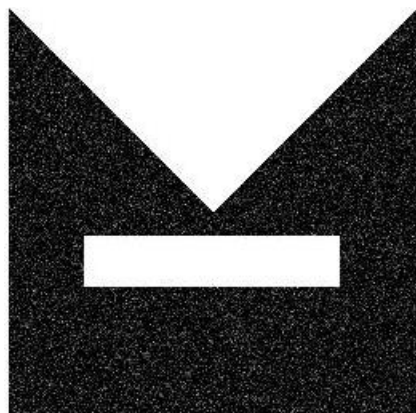


Fig. 7: Noisy image with $\sigma^2 = 0.2$

For the proper operation of the FB algorithm, it is important to establish spatially, the location of the edges throughout the image. To perform this process, we have used the Prewitt edge detector [6]. The use of this edge detector is based on that detection can be performed in vertical and horizontal edges. The edge detection is shown in Fig. 8 and 9, respectively. The threshold of edge detector was set at $th = 0.2$.

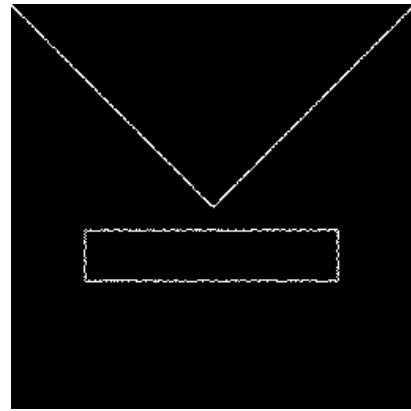


Fig. 8: Edge detection of Fig. 3 with $th = 0.2$



Fig. 9: Edge detection of Fig. 4 with $th = 0.2$

In Fig. 10 and Fig. 11 we had shown the enhanced binary images using the FB p -UFIR algorithm. The quantitative evaluation of image processing is present in the Table II and III, respectively. Finally, the quantitative evaluations are carrying out using the Signal-to-Noise Ratio (SNR) and the Root Mean Square Error (RMSE). Both metrics are employed in determining the performance of the FB algorithm.



Fig. 10: Enhanced binary image using the FB-algorithm with $h_{1i}(N, p)$ and $\sigma^2 = 0.1$



Fig. 11: Enhanced binary image using the FB-algorithm with $h_{1i}(N, p)$ and $\sigma^2 = 0.2$

TABLE II: QUANTITATIVE EVALUATION OF FB P-UFIR WITH $\sigma^2 = 0.1$

	$h_{0i}(N, p)$	$h_{1i}(N, p)$	$h_{2i}(N, p)$	$h_{3i}(N, p)$
RMSE	1.3780	0.9724	1.4032	1.3850
SNR (dB)	17.4668	19.4949	17.3095	16.4225

TABLE III: QUANTITATIVE EVALUATION OF FB P-UFIR WITH $\sigma^2 = 0.2$

	$h_{0i}(N, p)$	$h_{1i}(N, p)$	$h_{2i}(N, p)$	$h_{3i}(N, p)$
RMSE	1.1835	0.9481	1.1603	1.0696
SNR (dB)	17.7879	19.7148	17.9602	18.6675

IV. CONCLUSION

This article presented a suitable way to derive p -UFIR filters focused to the enhancing images. The FB algorithm have been employed for piecewise-smooth images with breakpoints detected using the Prewitt edge detector. Qualitative results are shown in Fig. 4 and 5 to signals and Fig. 10 and 11 to binary images, respectively. We can see that some lines in both enhanced images are due to errors during the detection of the edges in the image. Finally, in the Tables I, II and III show the performance obtained by the algorithm with the impulse response of the linear p -UFIR filter, $h_{1i}(N, p)$.

ACKNOWLEDGMENT

The authors thanks to the FIEC Veracruzana University and DICIS Guanajuato University for the whole research support.

REFERENCES

- [1] I. Pitas and A. Venetsanopoulos, *Nonlinear Digital Filters - Principles and Applications*, Boston: Kluwer Academic Publisher, 1990.
- [2] K. Najarian. and R. Splinter., *Biomedical Signal and Image Processing*, New York: Taylor & Francis, 2006.
- [3] Jensen JR., *Introductory Digital Image Processing - A Remote Sensing Perspective*. 2da Ed. New Jersey; Prentice Hall, 1996.
- [4] R. J. Schalkoff, *Digital Image Processing and Computer Vision*, Jhon Wiley & Sons, Inc, 1989.
- [5] M. Nixon and A. Aguado, *Feature Extraction & Image Processing*, Academic Press, New York, 2008.
- [6] R. F. Gonzalez and R. E. Woods, *Digital Image Processing*, Prentice-Hall, New Jersey, 2002.
- [7] S. H. Chung and R. A. Kennedy, "Forward-Backward non-linear filtering techniques for extracting small biological signal from noise", *Journal of Neuroscience Methods*, vol. 40, pp. 71 - 86, January, 1991.
- [8] F. Gustafsson, "Determining the initial state in forward-backward filtering", *IEEE Trans. Signal Processing*, vol. 44, pp. 988-992, April, 1996.
- [9] L. J. Morales-Mendoza, Y. Shmaliy and O. G. Ibarra-Manzano, "Enhancing ultrasound images using hybrid FIR structures", *Image Processing* (edited by Yung-Sheng Chen), Chapter 16, pp. 287-310, In-Tech press, December, 2009.
- [10] L. J. Morales-Mendoza, H. Gamboa-Rosales and Y. Shmaliy, "A new class of discrete orthogonal polynomials for blind fitting of finite data", *Signal Processing ELSEVIER*, vol. 93, no. 7, pp. 1785-1793, July 2013.
- [11] Y. Shmaliy, *GPS-based Optimal FIR Filtering of Clock Models*, NOVA Science Publishers, New York, 2009.
- [12] Y. Shmaliy, and L. J. Morales-Mendoza, "FIR smoothing of discrete-time polynomial signals in state space", *IEEE Trans. Signal Processing*, vol. 58, pp. 2544-2555, May, 2010.
- [13] O. Vite-Chavez, R. Olivera-Reyna, J. Muñoz-Minjares, Y. Shmaliy, O. G. Ibarra-Manzano and L. J. Morales-Mendoza, "Efficient denoising of piecewise-smooth signals with forward-backward FIR smoothers", *Proceeding of Applied Mathematics in Electrical and Computer Engineering*, WSEAS-12, 2012.
- [14] O. Vite-Chavez, R. Olivera-Reyna, O. G. Ibarra-Manzano, Y. Shmaliy and L. J. Morales-Mendoza, "Time-variant forward-backward FIR denoising of piecewise-smooth signals", *International Journal of Electronics and Communications*, ELSEVIER, pp. 406-413, vol. 67, 2013.
- [15] R. Olivera-Reyna, O. Vite-Chavez, L. J. Morales-Mendoza and Y. Shmaliy, "A forward-backward UFIR algorithm for denoising of piecewise-smooth signals", *proceeding of 10th International Conference on Electrical Engineering, Computing Science and Automatic Control*, CCE-13, Mexico DF., pp. 191-194, from September 30 to October 4, 2013.



Luis J. Morales-Mendoza received the B.S. degree in Electronics and Communications Engineering from Veracruzana University in 2001, M.S. in Electrical Engineering from the Guanajuato University, Mexico, 2002, and Ph.D. degree in Electrical Engineering from CINVESTAV, Guadalajara in 2006. From 2006 to 2009, he had been with the Electronics Department of the Guanajuato University of Mexico as an assistant Professor. He is currently a Professor of the FIEC of the Veracruz University of Mexico. His scientific interests are in the artificial Neural Networks applied to Optimization Problems, Image Restoration and Enhancing, and Ultrasound Image Processing. He has authored and co-authored more of the 60 Journal and Conference papers.



Mario González-Lee Received the B. S. degree in Electronics and Communications Engineering from Veracruzana University in 2000; the M. S. in Microelectronics Engineering and Ph.D. in Communications and Electronics, booth in IPN- México in 2002 and 2007, respectively. From 2007 to 2011, he was with the Electronics Department of the IPN of Mexico as an assistant Professor. He is currently a Professor of the FIEC of the Veracruz University of Mexico. His scientific interests are in the Signal & systems, digital watermarking and biometry. He has authored and co-authored more of the 30 Journal and Conference papers.



Efrén Morales-Mendoza received the B. S. degree in Electronics and Communications Engineering from Veracruzana University in 1993. M. S. in Computational Science from Engineering Institute of Veracruzana University in 2005. Currently, he is a Ph.D. Student in Education from Veracruz Institute of High Education. From 1995, he is professor of the FIEC of the Veracruz University of México. His research interests are the Application of the Education in the Engineering, Numerical methods for applications in Education.



René F. Vazquez-Bautista received the B.S. degree in Electronics and Communications Engineering from Veracruzana University; the M. Eng. in Electrical Engineering from Guanajuato University; and Ph.D. degree by CINVESTAV, Guadalajara in 2000, 2002 and 2006, respectively. From 2007 to 2009, he had been with the ITESM, Campus Guadalajara as an assistant Professor. Nowadays, He is full Professor with

Universidad Veracruzana in FIEC, Campus Poza Rica. His scientific interests are Digital Signal and Image Processing, Data and Sensor Fusion, Biomedical Applications and Embedded Systems.



Jesús Huerta-Chua received the B.E. degree by honors in Electronics and Communication Engineering from Veracruzana University, Veracruz, Mexico, in 1998, the M.S. and Ph.D. degree from INAOE (National Institute of Astrophysics, Optics and Electronics), Puebla, Mexico, in 2002 and 2008. From 2009 to 2013. He was metrologist in CENAM (The National Laboratory of Metrology from Mexico) during this period he developed a National Measurement Reference System for calibration of Artificial Mains Networks. He is currently a full time academic engineer in the Veracruzana University. His main research interests are in microelectronics devices, high frequency modeling and characterization of electronic devices, high frequency metrology.

Gresia Triano-Carballo She is student the B. S. degree in Electronics and Communications Engineering from Veracruz University.



Silverio Pérez-Caceres Received the B. S. degree in Electronics and Communications Engineering from Veracruzana University in 1993. M. S. in Computational Science from Engineering Institute of Veracruz University in 2005 and Ph.D. in Education from Veracruz Institute of High Education in 2012. From 1995, he is professor of the FIEC of the Veracruz University of México. His research interests are applied the Numerical

Methods in image processing and non-linear control



Oscar G. Ibarra-Manzano received the B.S. degree in Communications and Electronics Engineering and the M. Eng. in Electrical Engineering from Guanajuato University. Finally, Ph.D. degree from the INAOE (National Institute of Astrophysics, Optics and Electronics), Puebla, Mexico.



Yuriy Shmaliy received the B.S., M.S., and Ph.D. degrees, all in electrical engineering, from the Kharkiv Aviation Institute, Ukraine, in 1974, 1976, and 1982, respectively, and the Doctor of Technical Sc. degree from the Kharkiv Railroad Institute in 1992. In March 1985, he joined the Kharkiv Military University, where he has served as a Full Professor since 1986. Since 1999 to 2009, he has been with the Kharkiv National

University of Radio Electronics, and, since November 1999, he has been a Full Professor with the Guanajuato University of Mexico. He has published 249 journal and conference papers and holds 80 patents. He has three published books: *Continuous-Time Signals* (Springer, 2006), *Continuous-Time Systems* (Springer 2007), and *GPS-Based Optimal FIR Filtering of Clock Models* (Nova Science Publ., 2009).

Impact of irradiation dose on mechanical properties of PA 11

Petr Kratky, David Manas, Miroslav Manas, Michal Stanek, Martin Ovsik, Adam Skrobak, and Martin Reznicek

Abstract — The submitted work compares mechanical properties of the hard surface layer of modified polyamide 11. The mechanical properties were acquired by nanohardness test with using the DSI method (Depth Sensing Indentation). Hard surface layer was created by radiation cross-linking technology. This technology allows polymer materials modification followed by the change of their end-use properties. The surface layer of polymer material is modified by β - radiation. When the polymer material is exposed to the β - radiation, it is possible to observe changes of the surface layer at applied load.

Keywords — Crosslinking, irradiated, nano-hardness, PA 11.

I. INTRODUCTION

POLYAMIDE belongs to the group of synthetic thermoplastics polymers. This group consists of aliphatic polyamides and aromatic polyamides. Family of aliphatic polyamides is well known as Nylon. The Nylon is one of used the most polymers.

As Polymers belong to constructive materials which find use at the most industry branches. The advantage is a low weight together with the excellent mechanical properties, very good chemical resistance and other properties, which assign them for various applications. Disadvantage is mainly low temperature stability which significantly reduces usage of these polymers.

Every properties improvement especially temperature stability helps to increase application possibilities. In addition,

This paper is supported by the internal grant of TBU in Zlin No. IGA/FT/2014/016 funded from the resources of specific university research and by the European Regional Development Fund under the project CEBIA-Tech No. CZ.1.05/2.1.00/03.0089.

Petr Kratky is with the Tomas Bata University in Zlin, nam. T. G. Masaryka 5555, 76001 Zlin, Czech Republic (phone: +420576035237; e-mail: kratky@ft.utb.cz).

David Manas is with the Tomas Bata University in Zlin, nam. T. G. Masaryka 5555, 76001 Zlin, Czech Republic (e-mail: dmanas@ft.utb.cz).

Miroslav Manas is with the Tomas Bata University in Zlin, nam. T. G. Masaryka 5555, 76001 Zlin, Czech Republic (e-mail: manas@ft.utb.cz).

Michal Stanek is with the Tomas Bata University in Zlin, nam. T. G. Masaryka 5555, 76001 Zlin, Czech Republic (e-mail: stanek@ft.utb.cz).

Martin Ovsik is with the Tomas Bata University in Zlin, nam. T. G. Masaryka 5555, 76001 Zlin, Czech Republic (e-mail: ovsik@ft.utb.cz).

Adam Skrobak is with the Tomas Bata University in Zlin, nam. T. G. Masaryka 5555, 76001 Zlin, Czech Republic (e-mail: skrobak@ft.utb.cz).

Martin Reznicek is with the Tomas Bata University in Zlin, nam. T. G. Masaryka 5555, 76001 Zlin, Czech Republic (e-mail: mreznicek@ft.utb.cz).

properties modification of standard polymers, which are relatively cheap products, gives them advantage for another usage. One of the possibilities of polymers improvement is their radiation cross-linking.

The irradiation cross-linking of thermoplastic materials via electron beam or cobalt 60 (gamma rays) is performed separately, after processing. Generally, ionizing radiation includes accelerated electrons, gamma rays and X-rays.1

Radiation processing with an electron beam offers several distinct advantages when compared with other radiation sources, particularly γ -rays and x-rays. The process is very fast, clean and can be controlled with much precision. There is no permanent radioactivity since the machine can be switched off. In contrast to γ -rays and x-rays, the electron beam can be steered relatively easily, thus allowing irradiation of a variety of physical shapes. The electron beam radiation process is practically free of waste products and therefore is no serious environmental hazard. The main difference between beta and gamma rays is in their different abilities to penetrate the irradiated material. Gamma rays have a high penetration capacity. The penetration capacity of electron rays depends on the energy of the accelerated electrons. Due to electron accelerators, the required dosage can be applied within seconds, whereas several hours are required in the gamma radiation plant. (Fig. 1) [1]–[12],[31].

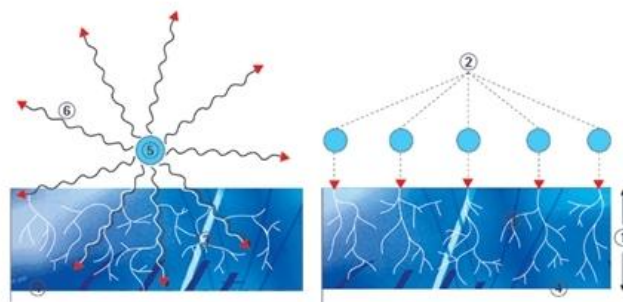


Fig. 1 Design of gamma rays (a) and electron rays (b), 1 - Penetration depth of an electron, 2 - Primary electron, 3 - Secondary electron, 4 - Irradiated material, 5 - Encapsulated Co - 60 Radiation source, 6 - Gamma rays [2]

Beta and gamma rays can be used for the irradiation of polyolefines, polyesters, halogen polymers and polyamides from the thermoplastics group, elastomers and thermoplastic elastomers. Some of them need the addition of a cross-linking

agent.

Radiation cross-linking usually improves strength, reduces creep, contributes to chemical resistance improvement and in many cases improves tribological properties. Effect of radiation cross-linking significantly improves temperature stability. Because of that, materials which belong to group of standard polymers can be used in applications, which would be in term of temperature stability intended only to constructive thermoplastic polymers [1]–[18], [27]–[31].

II. EXPERIMENTAL

For this experiment polyamide 11 (PA11) PTS – CREAMID - 11T * M600/13 transparent; PTS Plastics Technologie Service, Germany was used. The material already contained a special cross-linking agent TAIC - triallylisocyanurate (5 volume %), which should enable subsequent cross-linking by ionizing β – radiation. The prepared specimens were irradiated with doses of 132, 165 and 198 kGy at BGS Beta-Gamma Service GmbH & Co. KG, Germany [1-4].

The samples were made using the injection molding technology on the injection moulding machine ArburgAllrounder 420C. Processing temperature 280–310 °C, mold temperature 60 °C, injection pressure 80 MPa, injection rate 50 mm/s.

Instrumented nanohardness tests were done using a Nanoindentation Tester (NHT2) – Opx/Cpx, CSM Instruments (Switzerland) according to the CSN EN ISO 6507-1. Load and unload speed was 100 mN/min. After a holding time of 90 s at maximum load 50 mN the specimens were unloaded. The indentation hardness HIT was calculated as maximum load to the projected area of the hardness impression according to:

$$H_{IT} = \frac{F_{max}}{A_p} \quad \text{with} \quad h_c = h_{max} - \varepsilon \frac{F_{max}}{S} \quad (1)$$

Where h_{max} is the indentation depth at F_{max} , h_c is contact depth. In this study the Oliver and Pharr method was used calculate the initial stiffness (S), contact depth (h_c). The specimens were glued on metallic sample holders.

The indentation modulus is calculated from the Plane Strain modulus using an estimated sample Poisson's ratio:

$$E_{IT} = E^* \cdot (1 - \nu_s^2) \quad (2)$$

The deduced modulus is calculated from the following equation:

$$E_r = \frac{\sqrt{\pi \cdot S}}{2 \cdot \beta \cdot \sqrt{A_p(h_c)}} \quad (3)$$

The Plane Strain Modulus E^* is calculated from the following equation:

$$E^* = \frac{1}{\frac{1}{E_r} - \frac{1 - \nu_i^2}{E_i}} \quad (4)$$

Where E_i is the Elastic modulus of the indenter, E_r is the reduced modulus of the indentation contact, ν_i is the Poisson's ratio of the indenter [8], [11], [31].

III. RESULTS AND DISCUSSION

For Instrumented nanohardness test was used three different loads.

A. Indentation load 10 mN

The values measured during the nanohardness test showed that the lowest values of indentation hardness were found for the non-irradiated PA11. On the contrary, the highest values of indentation hardness were obtained for PA11 irradiated by a dose of 132 kGy (by 39% higher in comparison with the non-irradiated PA11), as can be seen at Fig. 2.

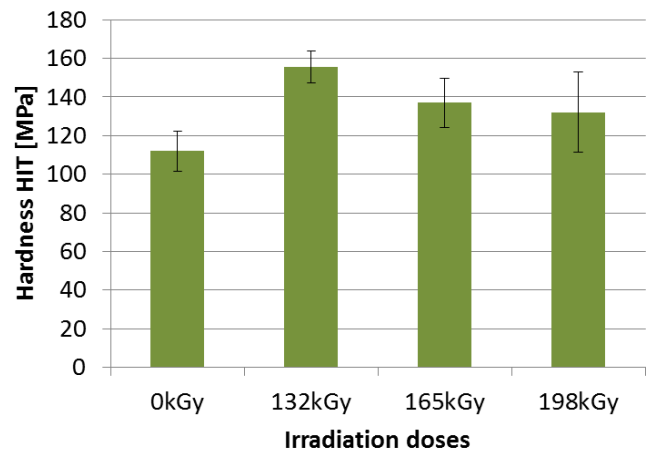


Fig. 2 Hardness HIT of PA11 vs. irradiation doses

Higher radiation dose does not influence significantly the nanohardness value. An indentation hardness increase of the surface layer is caused by irradiation cross-linking of the tested specimen. The decrease of indentation hardness of surface layer with high doses of radiation is caused by surface degradation.

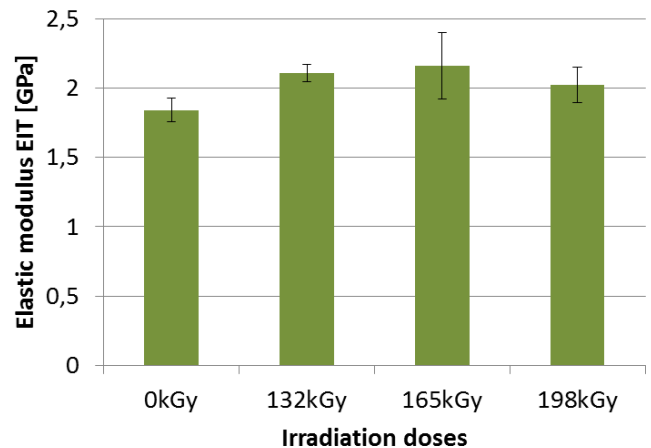


Fig. 3 Elastic modulus EIT of PA11 vs. irradiation doses

According to the results of measurements of nanohardness, it was found that the highest values of indentation modulus of elasticity were achieved at the PA11 irradiated with dose of 165 kGy (by 17% higher than compared with non-irradiated PA11). On the contrary, the lowest values of the indentation modulus of elasticity were found for non-irradiated PA11 as is seen at Fig. 3.

The lowest values of hardness Vickers were found for the non-irradiated PA11. On the contrary, the highest values of hardness Vickers were obtained for PA11 irradiated by a dose of 132 kGy (by 39% higher in comparison with the non-irradiated PA11), as can be seen at Fig. 4.

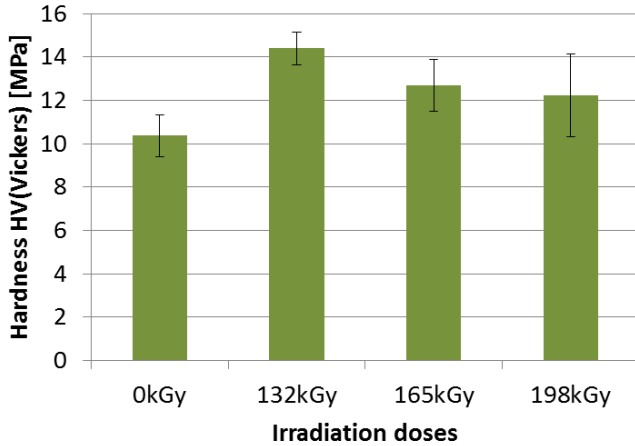


Fig. 4 Hardness Vickers of PA11 vs. irradiation doses

Other important material parameters obtained during the nanohardness test were elastic and plastic deformation work. From the elastic deformation work we determine the reaction of material to applied (multiaxial) load with reversible deformation. The plastic part of the deformation work W_{pl} defines toughness of the tested material (surface layer) and its resistance to plastic deformation.

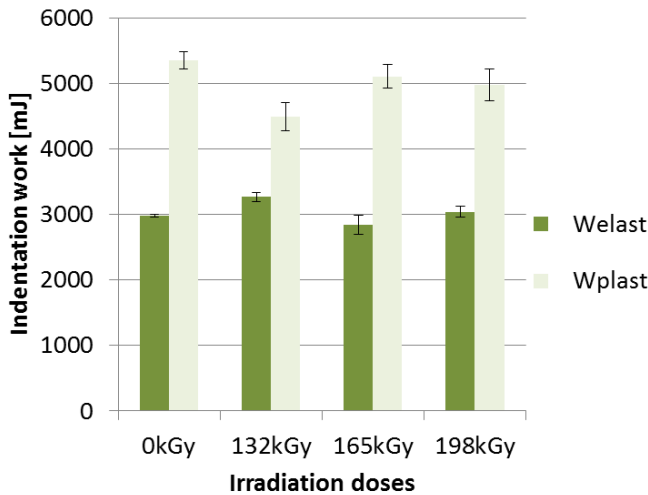


Fig. 5 Elastic and plastic deformation work of PA11 vs. irradiation doses

The greatest values of elastic deformation work were

obtained for PA11 irradiated with dose of 132 kGy. The greatest values of plastic deformation work were obtained for non-irradiated PA11. The lowest values of elastic deformation work were obtained for PA11 irradiated with dose of 165 kGy. The lowest values of plastic deformation work were obtained for PA11 irradiated with dose of 132 kGy.

B. Indentation load 50 mN

The values measured during the nanohardness test showed that the lowest values of indentation hardness were found for the non-irradiated PA11.

On the contrary, the highest values of indentation hardness were obtained for PA11 irradiated by a dose of 132 kGy (by 24% higher in comparison with the non-irradiated PA11), as can be seen at Fig. 6.

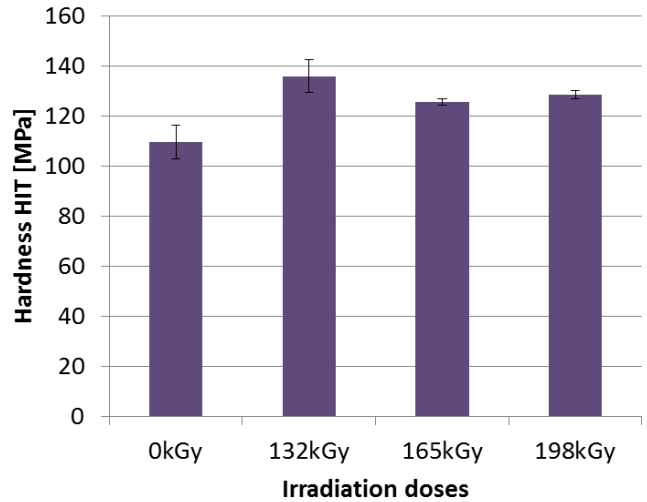


Fig. 6 Hardness HIT of PA11 vs. irradiation doses

Higher radiation dose does not influence significantly the nanohardness value. An indentation hardness change of the surface layer is caused by relations between surface degradation and irradiation cross-linking of the tested specimen.

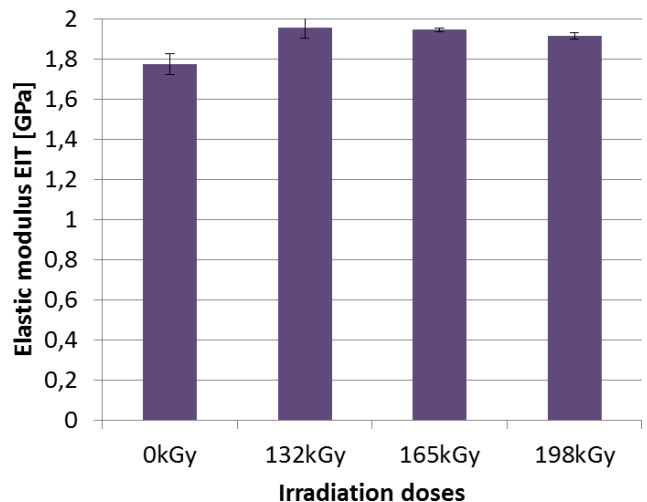


Fig. 7 Elastic modulus EIT of PA11 vs. irradiation doses

According to the results of measurements of nanohardness, it was found that the highest values of indentation modulus of elasticity were achieved at the PA11 irradiated with dose of 132 kGy (by 10% higher than compared with non-irradiated PA11). On the contrary, the lowest values of the indentation modulus of elasticity were found for non-irradiated PA11 as is seen at Fig. 7.

The lowest values of hardness Vickers were found for the non-irradiated PA11. On the contrary, the highest values of hardness Vickers were obtained for PA11 irradiated by a dose of 132 kGy (by 24% higher in comparison with the nonirradiated PA11), as can be seen at Fig. 8.

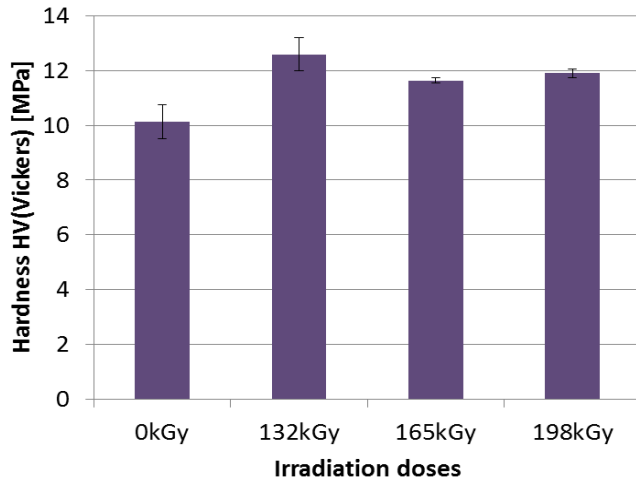


Fig. 8 Hardness Vickers of PA11 vs. irradiation doses

The greatest values of plastic deformation work were obtained for non-irradiated PA11. The greatest values of elastic and elastic deformation work were obtained for PA11 irradiated with dose of 132 kGy. The lowest values of elastic deformation work were obtained for PA11 irradiated with dose of 165 kGy. The lowest values of plastic deformation work were obtained for PA11 irradiated with dose of 132 kGy as is seen at Fig. 9.

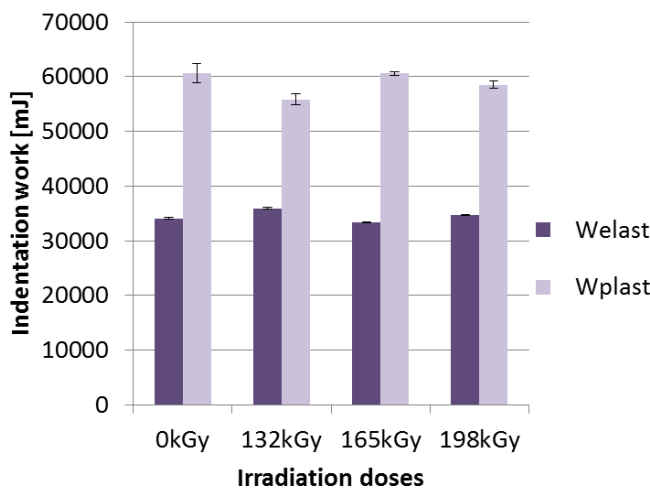


Fig. 9 Elastic and plastic deformation work of PA11 vs. irradiation doses

C. Indentation load 250 mN

The values measured during the nanohardness test showed that the lowest values of indentation hardness were found for the non-irradiated PA11. On the contrary, the highest values of indentation hardness were obtained for PA11 irradiated by a dose of 132 kGy (by 11% higher in comparison with the nonirradiated PA11), as can be seen at Fig. 10.

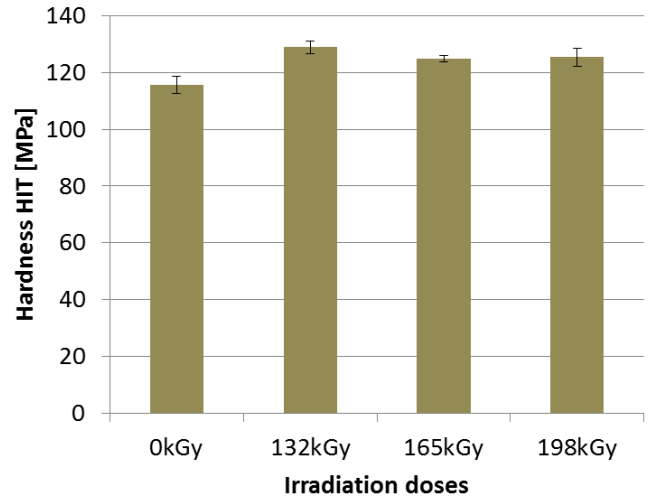


Fig. 10 Hardness HIT of PA11 vs. irradiation doses

Higher radiation dose does not influence significantly the nanohardness value. The decrease of indentation hardness of surface layer with high doses of radiation is caused by surface degradation.

According to the results of measurements of nanohardness, it was found that the highest values of indentation modulus of elasticity were achieved at the PA11 irradiated with dose of 165 kGy (by 7% higher than compared with non-irradiated PA11). On the contrary, the lowest values of the indentation modulus of elasticity were found for non-irradiated PA11 as is seen at Fig. 11.

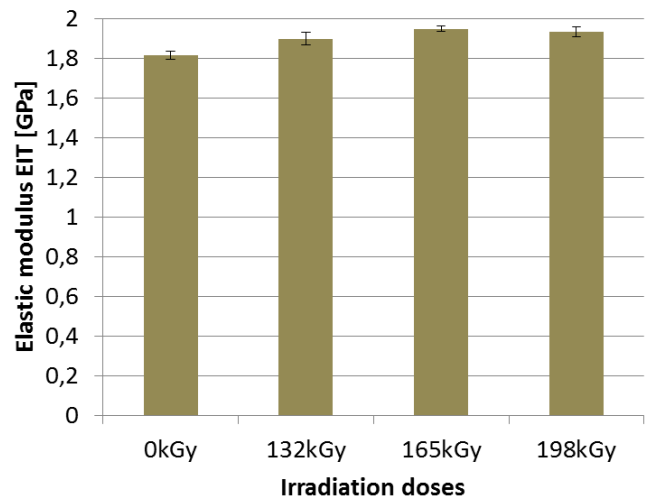


Fig. 11 Elastic modulus EIT of PA11 vs. irradiation doses

The lowest values of hardness Vickers were found for the

non-irradiated PA11. On the contrary, the highest values of hardness Vickers were obtained for PA11 irradiated by a dose of 132 kGy (by 11% higher in comparison with the non-irradiated PA11), as can be seen at Fig. 12.

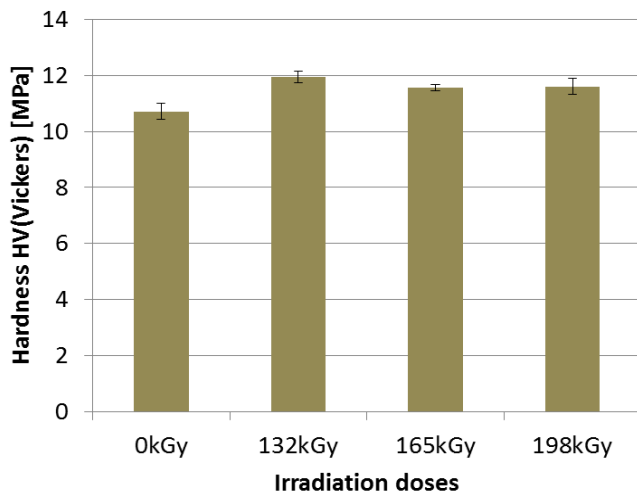


Fig. 12 Hardness Vickers of PA11 vs. irradiation doses

The greatest values of elastic deformation work were obtained for PA11 irradiated with dose of 132 kGy. The greatest values of plastic and elastic deformation work were obtained for non-irradiated PA11. The lowest values of elastic deformation work were obtained for PA11 irradiated with dose of 165 kGy. The lowest values of plastic deformation work were obtained for PA11 irradiated with dose of 132 kGy which is apparent in Fig. 13.

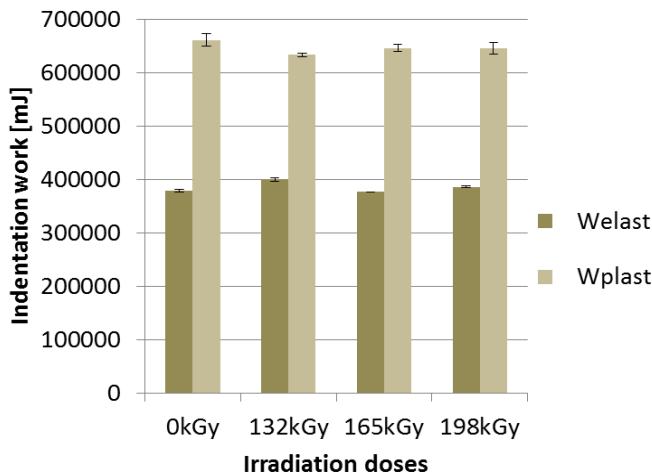


Fig. 13 Elastic and plastic deformation work of PA11 vs. irradiation doses

IV. CONCLUSION

The properties of surface layer of polyamide 11 modified by beta radiation improved significantly. The nanohardness values increased about 20%. Stiffness of surface layer increased significantly by 18% as a result of radiation. Changes of behavior in the surface layer were confirmed by

final values of plastic deformation work whose values decreased in correlation with the increasing radiation dose. Elastic deformation was increasing with radiation dose. The highest values of micromechanical properties were reached at radiation dose of 132 kGy. The results of nanomechanical properties of surface layer of modified polyamide 11 show that it can be used in more difficult applications in some industrial fields, in particular where there are high requirements for strength, stiffness and hardness of surface layer which appears to be the most suitable area of application. The resistance of surface layer to wear makes its use suitable for the production of gears, friction parts of machinery and as alternative to some metal materials. Thanks to its low weight polyamide 11 modified by beta radiation is a suitable alternative to commonly used materials in the car and electrical industry.

REFERENCES

- [1] J. G. Drobný, *Radiation technology for polymers*, Boca Raton: CRC Press, 2003, ISBN 1-58716-108-7.
- [2] BGS – Beta Gama Service. [online]. www: <http://bgs.eu>
- [3] J. G. Drobný, *Handbook of thermoplastic Elastomers*, William Andrew Publishing, Norwich, NY, 2007, ISBN: 978-0-8155-1549-4
- [4] Z. Brocka, *Werkstoff- und einatzpotential strahlenvernetzter Thermoplaste*, Lehrstuhl für Kunststofftechnik (LKT), Nürnberg, 2008.
- [5] R. J. Woods, *Applied radiation chemistry: radiation processing*, A Wiley-Interscience publication, New York, 1994, ISBN 0-471-54452-3.
- [6] Z. Holik, M. Danek, M. Manas, R. Lamborova, J. Cerný, K. Kyas, M. Krupal, and M. Malachova, "Effect of irradiation cross-linking on mechanical properties of selected types of polymer", in *Chemické listy*, vol. 105, 2011, pp. 269-271. ISSN 0009-2777.
- [7] Y. Huang, F. Zhang, K. C. Hwang, W. D. Nix, G. M. Pharr, and G. Feng, "A model of size effects in nano-indentation." *Journal of the Mechanics and Physics of Solids*. 2006, Vol. 54, pp. 1668–1686.
- [8] M. Stanek, D. Manas, M. Manas, and O. Suba, "Optimization of injection molding process," in *International Journal of Mathematics and Computers in Simulation*, 2011, vol. 5, pp. 413-421. ISSN 1998-0159.
- [9] Z. Holik, M. Danek, M. Manas, and J. Cerný, "The Influence of cross-linking agent on mechanical properties of polyamide modified by irradiation cross-linking", in *Proc. 13th WSEAS International Conference on Automatic Control, Modelling & Simulation*, Lanzarote, Spain, 2011, pp.222-225.
- [10] Z. Holik, K. Kyas, M. Krupal, J. Cerný, and M. Danek, "Improvement of polypropylene properties", *21st International DAAAM Symposium*, 2010, Zadar, Croatia, pp. 1191-1192.
- [11] H. Vaskova, and V. Kresalek, "Raman spectroscopy of epoxy resin crosslinking", in *Proc. 13th WSEAS International Conference on Automatic Control, Modelling & Simulation*, Lanzarote, Canary Islands 2011, pp.357-360.
- [12] M. Manas, D. Manas, M. Stanek, S. Sanda, and V. Pata, "Improvement of mechanical properties of TPE by irradiation", in *Chemické listy*, 2011, vol. 105, pp. 828-829. ISSN 0009-2770.
- [13] M. Manas, M. Stanek, D. Manas, M. Danek, and Z. Holik, "Modification of polyamides properties by irradiation" in *Chemické listy*. 2009, vol. 103, pp. 24-28. ISSN 0009-2770.
- [14] D. Manas, M. Manas, M. Stanek, and T. Drga, "Influence of radiation on polymer properties," in *Chemické listy*, Vol. 101, 2007, pp. 27-28. ISSN 0009-2770.
- [15] D. Manas, M. Manas, M. Stanek, M. Zaludek, S. Sanda, J. Javorik, and V. Pata, "Wear of multipurpose tire treads," *Chemické Listy*, Vol.103, 2009, pp. 72-74. ISSN 1213-7103.
- [16] D. Manas, M. Stanek, and M. Manas, "Workability and wear of rubber parts", in *Chapter 54 in DAAAM International Scientific Book 2007*, Published by DAAAM International, DAAAM International, Vienna, Austria, p.611-626.
- [17] M. Stanek, D. Manas, M. Manas, and J. Javorik, "Simulation of injection molding process by Cadmould rubber," in *International Journal of*

- Mathematics and Computers in Simulation*, Vol.5, 2011, pp. 422-429. ISSN 1998-0159.
- [18] M. Stanek, M. Manas, D. Manas, and S. Sanda, "Influence of surface roughness on fluidity of thermoplastics materials," *Chemické Listy*, Vol.103, 2009, pp. 91-95. ISSN 1213-7103.
- [19] M. Stanek, M. Manas, D. Manas, and S. Sanda, "Plastics parts design supported by reverse engineering and rapid prototyping," *Chemické Listy*, Vol.103, 2009, pp. 88-91. ISSN 1213-7103
- [20] M. Stanek, M. Manas, D. Manas, V. Pata, S. Sanda, V. Senkerik, and A. Skrobak, "How the filler influence the fluidity of polymer," *Chemické Listy*, Vol.105, 2011, pp. 303-305. ISSN 0009-2789.
- [21] M. Stanek, M. Manas, D. Manas, and J. Javorik, "Simulation of injection molding process," in *Proc. 13th WSEAS International Conference on Automatic Control, Modelling & Simulation*, pp.231-234. ISBN 978-1-61804-004-6.
- [22] M. Ovsik, D. Manas, M. Stanek, M. Manas, J. Cerny, M. Bednarik, and A. Mizera: "Microhardness of modified thermoplastics," *Annals of DAAAM for 2011 & Proceedings of the 22nd International DAAAM Symposium, 23-26th November 2011*, Vienna, Austria, ISSN 1726-9679, ISBN 978-3-901509-83-4, p. 1187-1188, Published by DAAAM International Vienna, Vienna.
- [23] J. Navtatil, M. Stanek, M. Manas, D. Manas, M. Bednarik, and A. Mizera: "Utilization of DMLS in injection mold design", *Annals of DAAAM for 2011 & Proceedings of the 22nd International DAAAM Symposium, 23-26th November 2011*, Vienna, Austria, ISSN 1726-9679, ISBN 978-3-901509-83-4, p. 1507-1508, Published by DAAAM International Vienna, Vienna
- [24] J. Javorik, and M. Stanek, "The numerical simulation of the rubber diaphragm behavior," in *Proc. 13th WSEAS International Conference on Automatic Control, Modelling & Simulation*, Lanzarote, Spain, 2011, pp. 117-120. ISBN 978-1-61804-004-6.
- [25] Z. Holik, M. Manas, M. Danek, and J. Macourek: "Improvement of mechanical and thermomechanical properties of polyethylene by irradiation crosslinking." *Chemické listy*. Volume 103, 2009, pp.60-63, ISSN 0009-2770 (IF: 0,593 MF: 1,256)
- [26] D. Manas, M. Hribova, M. Manas, M. Ovsik, M. Stanek, and D. Samek, "The effect of beta irradiation on morphology and micro hardness of polypropylene thin layere", 2012, *Thin Solid Films*, Volume 530, pp. 49-52. ISSN 0040-6090.
- [27] G. M. Pharr, "Measurement of mechanical properties by ultra-low indentation." *Material Science and Engineering*. 1998, pp. 151-159.
- [28] M. Ovsik, D. Manas, M. Manas, M. Stanek, M. Hribova, K. Kocman, and D. Samek, "Irradiated polypropylene Studied by microhardness and WAXS", 2012. *Chemické listy*, Volume 106, pp. S507-510. ISSN 0009-2770.
- [29] A. Pusz, and K. Michalik, "Creep damage mechanisms in gas pipes made of high density polyethylene," 2009, *Archives of Materials Science and Engineering* 36 (2), pp. 89-95.
- [30] D. Janacova, H. Charvatova, K. Kolomaznik, V. Vasek, and P. Mokrejs, "Solving of Non-Stationary Heat Transfer in a plane plate", in *Proc. 13th WSEAS International Conference on Automatic Control, Modelling & Simulation*, Lanzarote, CanaryIslands 2011, pp.287-291.
- [31] P. Kratky, D. Manas, M. Manas, M. Stanek, M. Ovsik, K. Kyas and J. Navratil. "Nanoharness of polymers (Polyamide 11)". In: EDITORS, Andrzej Zak a Radek Matusu ASSOCIATE EDITOR. *Recent advances in automatic control, information and communications: proceedings of the 14th international conference on automation*. 2013, pp. 135-139. ISBN 9789604743162.

Petr Kratky was born in Sumperk in 1987. He received a B.Sc. (2010), M.Sc. (2012) in Process engineering from Faculty of Technology, Tomas Bata University in Zlin. He is a doctoral student at the Department of Production Engineering. Major research interests are **mechanical properties of polymer and metal materials**.

Elearning Platform Assessment for Military Distance Education with Multicriteria Analysis

RIGOPOULOS GEORGE

Department of Informatics,
Higher Technological Educational Institute of Athens,
Ag. Spiridonos 12, Aigaleo, 122 10 Athens,
GREEECE
grigop@teiath.gr

KARADIMAS V. NIKOLAOS

Informatics Lab,
Division of Mathematics and Engineering Sciences,
Department of Military Sciences,
Hellenic Military Academy,
166 73, Vari,
GREEECE
nkaradimas@sse.gr

Abstract: - In this paper we present the application of multicriteria methodology for supporting military academy's decision on eLearning platform evaluation. Based on previous research, we define a set of evaluation criteria, define appropriate weights in collaboration with experts and utilize an outranking approach for the multicriteria model. We apply the method in evaluating a number of open source platforms and present the decision outcome. This methodology can support decision makers by providing a solution to the selection problem and in understanding the factors related to the decision as well.

Key-Words: - Multicriteria decision making, eLearning

1 Introduction

Military academy as several educational institutes worldwide is planning to offer to its students online classes mixing traditional and online methods [1], [2], [3]. So, it comes to decision regarding eLearning platform selection. This decision is not trivial, since a number of criteria has to be considered.

The development of Internet technologies, the number of eLearning platforms available, ranging from fully commercial to open source ones are some of them. In addition, major differences between available platforms regarding functionality exist, which impact user acceptance and overall performance accordingly. On the other hand, investment in setup and operation varies between platforms and impacts institutes' finances. Finally, end user adoption may be negatively affected in the case of an inappropriate platform selection.

For these reasons eLearning platform selection can be modelled as a multicriteria decision problem, considering that institutes' decision makers evaluate alternative platforms available based on a number of relevant criteria.

In this paper we present a multicriteria methodology for supporting academy's decision on eLearning platform evaluation.

Based on previous research, we define a set of evaluation criteria, define appropriate weights in collaboration with experts and utilize an outranking approach for the multicriteria model. In order to demonstrate the model we apply the method in evaluating a number of open source platforms and present the decision outcome.

For the multicriteria methodology we use Electre Tri method. In general, a number of categories is formed, a number of criteria with their associate weights are introduced and the students are scored

on each criterion. According to the aggregate scores students are assigned to classes.

In the following sections we introduce the basic terminology of the multicriteria methodology and provide an illustrative basic example to the reader.

2 Multicriteria Decision Analysis

In the MCDA field, three kinds of problems are distinguished: choice problems, ranking problems and sorting problems. The goal of the decision maker in each type of problem is different: in choice problems the aim is to find the best alternative, in ranking problems we want to know the goodness of all alternatives, which is usually presented as a ranking from the best to the worst, and in sorting problems we want to know which alternatives belong to each class of a predefined set of classes.

A typical multicriteria problem formulation is the following:

Having a defined set A of actions and a consistent family G of criteria on A , a multiple criteria decision problem is the one that, with respect to G , either aims to find:

- a subset of A that contains the best actions,
- an assignment of the actions into predefined categories, or
- a rank of the actions in A from best to worst.

2.1 Electre Tri method

The ELECTRE TRI method belongs to a group of methods called ELECTRE and was specifically designed for the problem of classification of a set of actions according to pre-defined, ordered categories based on multiple criteria. These categories are characterized by a structure of order for the entire set and by pre-defined rules, called reference actions, which are fictitious and are used only to mark limits for them both in the lower and upper parts, where the allocation of each action of the structure of order stems from the result of its comparison with these profiles that define those limits.

In general, we have a set A of actions (a_1, \dots, a_n) evaluated by m criteria (g_1, \dots, g_m) , and C is a set (C_1, \dots, C_k) of k categories by order of preference, being C_1 the worst and C_k the best. Each category C_h ($h=1, \dots, k$) is defined by two reference actions, being b_h their upper limit and b_{h-1} their lower limit. The reference actions (b_0, \dots, b_k) must be defined such that, by carrying out the first and the last, each makes up, simultaneously, the upper limit of a category and the lower limit of the next category,

that is, b_h is the upper limit for category C_h and the lower limit for category C_{h-1} .

The outranking approach was introduced in the 60s by Roy based on his work on real-world applications. The intention was to overcome some of the difficulties of the aggregation approaches of those days, such as the use of qualitative criteria. This approach focuses the attention to the fact that in MCDA problems one tries to establish preference orderings of alternatives. As each criterion usually leads to different ranking of the alternatives, the problem is to find a consensued ranking. The outranking methods perform pairwise comparisons of alternatives to determine the preferability of each alternative over the other ones for each particular criterion. Then, a concordance relation is established by aggregating the relative preferences. Moreover, a discordance relation is also established, which is used to determine veto values against the dominance of one alternative over the others. Finally the aggregation of the concordance relation yields the final dominance relation.

The basis of these methods is the definition of an outranking relation S . By definition, S is a binary relation: $a'Sa$ holds if we can find sufficiently strong reasons for considering the following statement as being true in the decision maker's model of preferences:

“ a' is at least as good as a ”

Two conditions must be fulfilled in order to accept that $a'Sa$ holds:

- A concordance condition: a majority of criteria must support $a'Sa$ (classical majority principle)
- A non discordance condition: among the non concordant criteria, none of them strongly refutes $a'Sa$ (respect of minorities principle)

Different methods implement this process using different algorithms. Some of the most well-known outranking models are ELECTRE, PROMETHEE, NexClass. Interested reader in multicriteria analysis and methods can find extensive information in the relevant references [4], [5], [6], [7], [8], [9], [10].

3 Proposed model

As stated above, the main objective of this study is to support institutes' decisions on eLearning platform evaluation. We propose an evaluation model, which is based on Multicriteria Analysis and aims to assist decision makers on the entire process

in a more structured way, so we utilize ELECTRE TRI method, which classifies the alternatives into ordered categories, rather than a choice method. The model is then applied to a number of open source platforms for illustrative purposes.

Based on ELECTRE TRI method, we propose the following model for elearning platform evaluation:

- *Identify the alternatives set A:* The alternative platforms should be identified.
- *Define the categories C and the evaluation criteria G:* The categories should be defined in an ordered way, from less to more preferred ones.
- *Express the DM's preferences:* Determine the DM's alternative preferences (values) and preferences on criteria (weights) for each category.
- *Evaluate alternatives' performance:* Performance on the criteria should be evaluated for each alternative platform.
- *Classification:* Derive classification results.
- *Results assessment:* The DM should assess the results, and modify the parameters accordingly.

3.1 Illustrative Example

In order to demonstrate the proposed model we present a case study, which refers to the elearning platform decision process of military academy. The objective was to acquire an elearning platform in order to host the academic material for all the classes and provide students a user friendly environment. Since several elearning platforms exist, they needed a structured way for evaluation, based on existing decision support methodologies. For this reason we proposed the above stated methodology, for both helping them to understand all the aspects involved in the decision process and provide them with an evaluation result.

Following the steps of the methodology, a team of decision makers was formed. Initially, the team selected a number of existing platforms as alternatives for evaluation (Table 1). Although the number of available platforms is large, the decision was to evaluate a short list of the most widely used. A list of three platforms was then formed for evaluation, excluding the less common ones.

Table 1. Alternative platforms

Alternative Platform	URL
A1 Claroline	http://www.claroline.net
A2 Moodle	http://www.moodle.com
A3 Manhattan	http://manhattan.sourceforge.net

Next, the team defined the number and the order of the categories for the classification of the platforms. Since the objective was not to provide a single platform as the most preferable, but classify to a category as a first step, the experts defined three categories, reflecting three levels of evaluation. The categories were Low, Medium and High (Table 2) and according to the decision result, only platforms assigned to High category would be candidates for selection in a second round of evaluation.

Table 2. Classification categories

	Category		
	High	Medium	Low
Definition	High importance	Medium importance	Low importance

The next step was to define a set of evaluation criteria, which represent the most important aspects of an elearning platform, and were considered for the final decision. In collaboration with the team, eight criteria were defined covering both academic and technical aspects, as well as financial ones. For simplicity, criteria scales were defined in a 10 degree scale (Table 3). This scale means for example that a platform with not efficient communication tools would receive a low value in this criterion e.g. 2, while a platform with efficient communication tools would receive a high value in this criterion e.g. 8.

Table 3. Evaluation criteria

Criterion	Description	Scale
G1	Communication tools	1-10
G2	Assessment tools	1-10
G3	Collaboration tools	1-10
G4	Administrative tools	1-10
G5	Course delivery tools	1-10
G6	Course design tools	1-10
G7	Software / Hardware	1-10
G8	License	1-10

Next, according to the multicriteria methodology, the team should define the limits of the categories, which were defined above. Since the categories are ordered, two limits have to be defined, the limit of the Low category, and the limit of the Medium one. These limits are called category profiles, and are defined by the expert by setting appropriate values for each criterion in the scale defined previously. For example, for the communication tools criterion the team defines that in order a platform to be classified to Medium

category has to get a value in this criterion greater than 3, while to be classified to High category has to get a value in this criterion greater than 7. So the profiles are set to 3 and 7 values. In addition to the profiles, the relevant importance of the criteria to the final evaluation has to be defined. This is done by setting the weights of each criterion according to the team’s preferences. Based on the above, the team defined the categories profiles, and the criteria weights according to their preferences (Table 4).

Table 4. Criteria weights

	Criteria							
	G1	G2	G3	G4	G5	G6	G7	G8
Profile 1	3	4	3	2	6	4	6	5
Preference	0	0	0	0	0	0	0	0
Indifference	0	0	0	0	0	0	0	0
Profile 2	7	8	6	7	8	6	8	9
Preference	0	0	0	0	0	0	0	0
Indifference	0	0	0	0	0	0	0	0
Weight	0.5	1	0.5	1	0.5	0.5	3.5	2.5

As a final step before the model execution, the performance of the previously defined alternatives to each criterion has to be defined. This procedure requires the team to evaluate the performance of each platform to each criterion. For example Claronline in terms of communication tools gets a medium value, while in terms of license gets a high value. These values are based on decision makers’ estimation. Based on the above, the expert’s team evaluated the performance of the six platforms to the eight criteria the according their preferences (Table 5).

Table 5. Alternatives’ performance

Alternatives	Criteria							
	G1	G2	G3	G4	G5	G6	G7	G8
A1	4	7	6	8	6	8	9	8
A2	5	4	6	2	4	5	6	8
A3	4	6	7	4	5	7	6	8

Finally, the model was executed with the appropriate software tool, and the classification results were derived for pessimistic and optimistic assignments according to ELECTRE TRI method (Table 6). According to this classification only one platform is candidate for further examination.

Table 6. Classification results

Alternative	Platform	Category (pessimistic)	Category (optimistic)
A1	Claroline	Medium	High

A2	Moodle	Medium	Medium
A3	Manhattan	Medium	Medium

4 Conclusion

In this paper we presented a multicriteria model for elearning platform evaluation. The objective of this study is not to evaluate existing platforms, but rather to provide a tool to decision makers in order to structure their decision problem. Moreover, to prove the applicability of multicriteria analysis to such decision problems. Since every institute has specific needs, problem formulation may be customized with respect to them.

For the multicriteria methodology we used Electre Tri method where a number of categories is formed, a number of criteria with their associate weights are introduced and the alternatives are scored on each criterion. According to the aggregate scores alternatives are assigned to classes.

We introduced the basic terminology of the multicriteria methodology and provided a basic example illustrative to the reader.

References:

- [1] Rigopoulos G., Karadimas N.V. (2006): “Increasing Ethical Awareness of IT Students through Online Learning”. World Scientific and Engineering Society, Transactions on Computers. Vol. 5, Issue 12, ISSN: 1109-2750, pp. 3160-3164.
- [2] Karadimas N.V., Rigopoulos G. (2006): “Enhancing IT Skills of Banking Employees Through e-Learning Technology”. World Scientific and Engineering Society, Transactions on Computers. Vol. 5, Issue 12, ISSN: 1109-2750, pp. 3165-3168.
- [3] Karadimas N.V. and Papastamatiou N.P. (2007). “Software Agents Integrating Job Rotation with e-Learning”. International Journal of Soft-Computing Applications. EuroJournals Publishing, Inc. ISSN: 1453-2277, Issue 1, pp. 17-26.
- [4] Rigopoulos, G., Psarras, J., Askounis, D. (2008), “A Decision Support System for Supervised Assignment in Banking Decisions”, Journal of Applied Sciences Vol. 8, Issue 3, pp. 443-452.
- [5] Rigopoulos, G., Psarras, J., Askounis, D. (2008), “Fuzzy Assignment Procedure based on Categories’ Boundaries”, American Journal of Applied Sciences, Vol. 5, Issue 7, pp. 844-851.
- [6] Rigopoulos, G., Psarras, J., Askounis, D. (2008), “An Aggregation Approach for Group

Multicriteria Assignment”, American Journal of Applied Sciences, Vol. 5, Issue 8, pp. 952-958.

- [7] Rigopoulos, G., Askounis, D., Metaxiotis, K. (2010), “NeXClass: A Decision Support System for non-ordered Multicriteria Classification”, International Journal of Information Technology & Decision Making, Vol. 9, Issue 1, pp. 53-79.
- [8] Rigopoulos, G., Anagnostopoulos, K, (2010), “Fuzzy Multicriteria Assignment for Nominal Classification Methodology and Application in Evaluation of Greek Bank’s Electronic Payment Retailers”, International Journal of Information Technology & Decision Making, Vol. 9, Issue 3, pp. 1-18.
- [9] Rigopoulos, G., Karadimas N., (2011), “Preference Aggregation for Collaborative Multicriteria Assignment”, in Proceedings of the 1st National joint Conference of Hellenic Mathematical Society and Hellenic Operational Research Society, Athens, Greece.
- [10] Rigopoulos G. and Karadimas N.V. (2011): “Military Staff Assignment Approach Utilizing Multicriteria Analysis”. CIT'11 Proceedings of the 5th World Scientific and Engineering Academy and Society (WSEAS) International Conference on Communications and Information Technology, Corfu Island, Greece, 14-17 July, pp. 107-110.

Impact of irradiation dose on mechanical properties of PMMA

Petr Kratky, David Manas, Miroslav Manas, Michal Stanek, Martin Ovsik, Vojtech Senkerik, and Jan Navratil

Abstract — The submitted paper compares mechanical properties of the hard surface layer of modified polymethyl methacrylate. Hard surface layer was made by radiation cross-linking technology which allows polymer materials modification followed by the change of their end-use properties. The surface layer of polymer material is modified by β – radiation. When the polymer material is exposed to the β – radiation, it is possible to observe changes of the surface layer at applied load. The mechanical properties were measured by nanohardness test with using the DSI method (Depth Sensing Indentation).

Keywords — Crosslinking, irradiated, nano-hardness, PMMA.

I. INTRODUCTION

ECONOMICAL alternative to polycarbonate with lower strength in other applications is polymethyl methacrylate which is frequently preferred because of its moderate properties, easy handling and processing, and low cost. Polymethyl methacrylate belongs to the group of synthetic thermoplastics polymers and is a transparent thermoplastic. It used as a lightweight or shatter-resistant alternative to glass.

As polymers belong to constructive materials which find use at the most industry branches. The advantage is a low weight together with the excellent mechanical properties, very good chemical resistance and other properties, which assign them for various applications. Disadvantage is mainly low temperature stability which significantly reduces usage of these polymers.

This paper is supported by the internal grant of TBU in Zlin No. IGA/FT/2014/016 funded from the resources of specific university research and by the European Regional Development Fund under the project CEBIA-Tech No. CZ.1.05/2.1.00/03.0089.

Petr Kratky is with the Tomas Bata University in Zlin, nam. T. G. Masaryka 5555, 76001 Zlin, Czech Republic (phone: +420576035237; e-mail: kratky@ft.utb.cz).

David Manas is with the Tomas Bata University in Zlin, nam. T. G. Masaryka 5555, 76001 Zlin, Czech Republic (e-mail: dmanas@ft.utb.cz).

Miroslav Manas is with the Tomas Bata University in Zlin, nam. T. G. Masaryka 5555, 76001 Zlin, Czech Republic (e-mail: manas@ft.utb.cz).

Michal Stanek is with the Tomas Bata University in Zlin, nam. T. G. Masaryka 5555, 76001 Zlin, Czech Republic (e-mail: stanek@ft.utb.cz).

Martin Ovsik is with the Tomas Bata University in Zlin, nam. T. G. Masaryka 5555, 76001 Zlin, Czech Republic (e-mail: ovsik@ft.utb.cz).

Vojtech Senkerik is with the Tomas Bata University in Zlin, nam. T. G. Masaryka 5555, 76001 Zlin, Czech Republic (e-mail: vsenkerik@ft.utb.cz).

Jan Navratil is with the Tomas Bata University in Zlin, nam. T. G. Masaryka 5555, 76001 Zlin, Czech Republic (e-mail: j1navratil@ft.utb.cz).

Every properties improvement especially temperature stability helps to increase application possibilities. In addition, properties modification of standard polymers, which are relatively cheap products, gives them advantage for another usage. One of the possibilities of polymers improvement is their radiation cross-linking.

The irradiation cross-linking of thermoplastic materials via electron beam or cobalt 60 (gamma rays) is performed separately, after processing. Generally, ionizing radiation includes accelerated electrons, gamma rays and X-rays.

Radiation processing with an electron beam offers several distinct advantages when compared with other radiation sources, particularly γ -rays and x-rays. The process is very fast, clean and can be controlled with much precision. There is no permanent radioactivity since the machine can be switched off. In contrast to γ -rays and x-rays, the electron beam can be steered relatively easily, thus allowing irradiation of a variety of physical shapes. The electron beam radiation process is practically free of waste products and therefore is no serious environmental hazard. The main difference between beta and gamma rays is in their different abilities to penetrate the irradiated material. Gamma rays have a high penetration capacity. The penetration capacity of electron rays depends on the energy of the accelerated electrons. Due to electron accelerators, the required dosage can be applied within seconds, whereas several hours are required in the gamma radiation plant (Fig. 1). [1]–[12],[21]

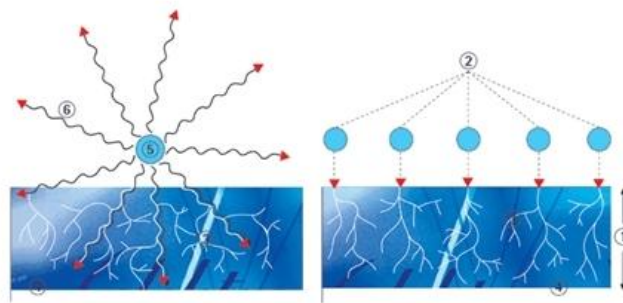


Fig. 1 Design of gamma rays (a) and electron rays (b), 1 - Penetration depth of an electron, 2 - Primary electron, 3 - Secondary electron, 4 - Irradiated material, 5 - Encapsulated Co - 60 Radiation source, 6 - Gamma rays [2]

Beta and gamma rays can be used for the irradiation of polyolefines, polyesters, halogen polymers and polyamides

from the thermoplastics group, elastomers and thermoplastic elastomers. Some of them need the addition of a cross-linking agent. [1],[3]–[16]

Radiation cross-linking usually improves strength, reduces creep, contributes to chemical resistance improvement and in many cases improves tribological properties. Effect of radiation cross-linking significantly improves temperature stability. Because of that, materials which belong to group of standard polymers can be used in applications, which would be in term of temperature stability intended only to constructive thermoplastic polymers. [1],[3]–[21]

II. EXPERIMENTAL

For this experiment polymethyl methacrylate (PMMA) PTS - ACRYLEX CM - 207; PTS Plastics Technologie Service, Germany was used. The material already contained a special cross-linking agent TAIC - triallylisocyanurate (5 volume %), which should enable subsequent cross-linking by ionizing β – radiation. The prepared specimens were irradiated with doses of 66 and 99 kGy at BGS Beta-Gamma Service GmbH & Co. KG, Germany [1-4].

The samples were made using the injection molding technology on the injection moulding machine ArburgAllrounder 420C. Processing temperature 200–240 °C, mold temperature 60 °C, injection pressure 80 MPa, injection rate 45 mm/s.

Instrumented nanohardness tests were done using a Nanoindentation Tester (NHT2) – Opx/Cpx, CSM Instruments (Switzerland) according to the CSN EN ISO 6507-1. Load and unload speed was 100 mN/min. After a holding time of 90 s at maximum load 50 mN the specimens were unloaded. The indentation hardness HIT was calculated as maximum load to the projected area of the hardness impression according to:

$$H_{IT} = \frac{F_{max}}{A_p} \quad \text{with} \quad h_c = h_{max} - \varepsilon \frac{F_{max}}{S} \quad (1)$$

Where h_{max} is the indentation depth at F_{max} , h_c is contact depth. In this study the Oliver and Pharr method was used calculate the initial stiffness (S), contact depth (h_c). The specimens were glued on metallic sample holders.

The indentation modulus is calculated from the Plane Strain modulus using an estimated sample Poisson's ratio:

$$E_{IT} = E^* \cdot (1 - \nu_s^2) \quad (2)$$

The deduced modulus is calculated from the following equation:

$$E_r = \frac{\sqrt{\pi \cdot S}}{2 \cdot \beta \cdot \sqrt{A_p(h_c)}} \quad (3)$$

The Plane Strain Modulus E^* is calculated from the following equation:

$$E^* = \frac{1}{\frac{1}{E_r} - \frac{1 - \nu_i^2}{E_i}} \quad (4)$$

Where E_i is the Elastic modulus of the indenter, E_r is the reduced modulus of the indentation contact, ν_i is the Poisson's ratio of the indenter. [8] [12] [30].

III. RESULTS AND DISCUSSION

For Instrumented nanohardness test was used three different loads.

A. Indentation load 10 mN

The values measured during the nanohardness test showed that the lowest values of indentation hardness were found for non-irradiated PMMA. On the contrary, the highest values of indentation hardness were obtained for PMMA irradiated with dose of 66 kGy (by 11% lower in comparison with non-irradiated PMMA), as can be seen at Fig. 2.

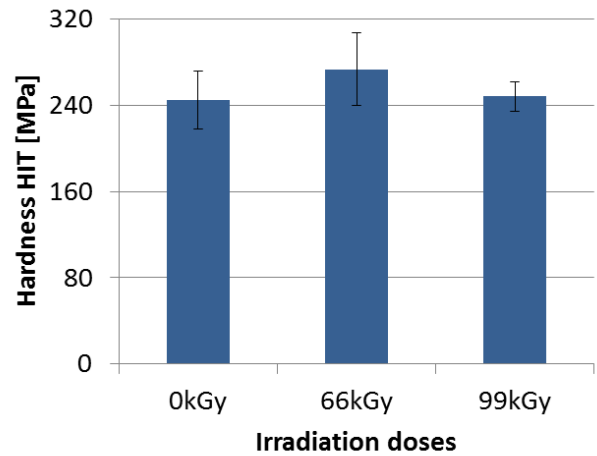


Fig. 2 Hardness HIT of PMMA vs. irradiation doses

Higher radiations influence significantly the nanohardness value. An indentation hardness increase of the surface layer is caused by irradiation cross-linking of the tested specimen, but total hardness decreasing due to degradation of basic material.

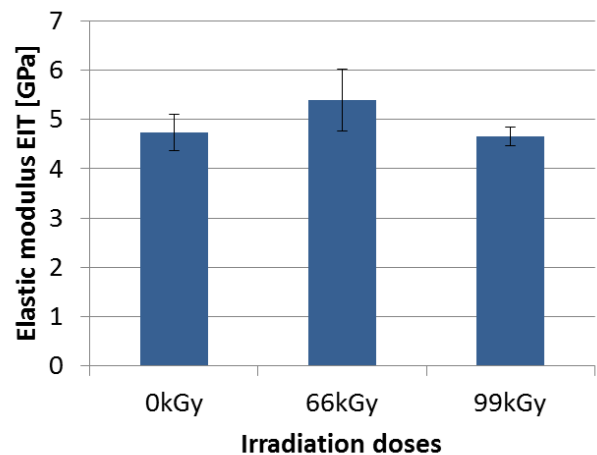


Fig. 3 Elastic modulus EIT of PMMA vs. irradiation doses

According to the results of measurements of nanohardness, it was found that the highest values of indentation modulus of elasticity were achieved at the PMMA irradiated with dose of 66 kGy (by 15% higher than compared with non-irradiated PMMA). On the contrary, the lowest values of the indentation modulus of elasticity were found for non-irradiated PMMA as is seen at Fig. 3.

The lowest values of hardness Vickers were found for non-irradiated PMMA. On the contrary, the highest values of hardness Vickers were obtained for PMMA irradiated with dose of 66 kGy (by 11% higher in comparison with non-irradiated PMMA), as can be seen at Fig. 4.

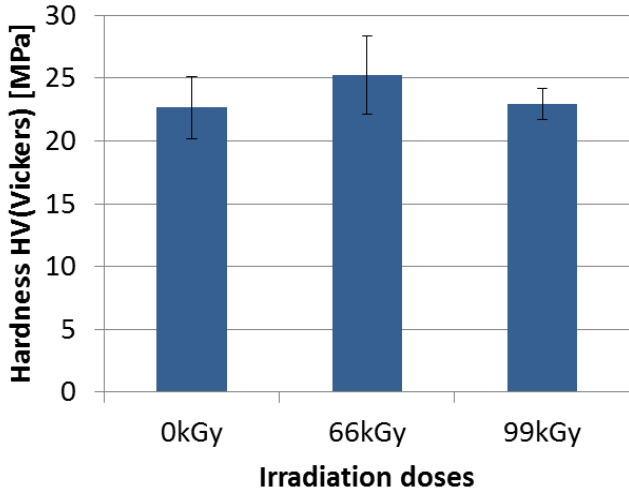


Fig. 4 Hardness Vickers of PMMA vs. irradiation doses

Other important material parameters obtained during the nanohardness test were elastic and plastic deformation work. The elastic deformation work W_e determines the reaction of material to applied (multiaxial) load with reversible deformation. The plastic part of the deformation work W_p defines toughness of the tested material (surface layer) and its resistance to plastic deformation.

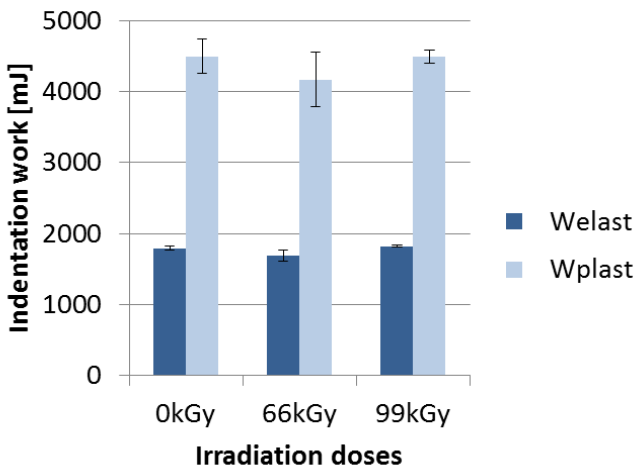


Fig. 5 Elastic and plastic deformation work of PMMA vs. irradiation doses

The greatest values of plastic deformation work were obtained for non-irradiated PMMA. The greatest values of elastic deformation work were obtained for PMMA irradiated with dose of 99 kGy. The lowest values of plastic and elastic deformation work were obtained for the PMMA irradiated with dose of 66 kGy. Radiation of specimens caused lower values of elastic as well as plastic deformation work which is apparent in Fig. 5.

B. Indentation load 50 mN

The values measured during the nanohardness test showed that the lowest values of indentation hardness were found for the PMMA irradiated by a dose of 99 kGy. On the contrary, the highest values of indentation hardness were obtained for non-irradiated PMMA (by 5% higher in comparison with PMMA irradiated by a dose of 99 kGy), as can be seen at Fig. 6.

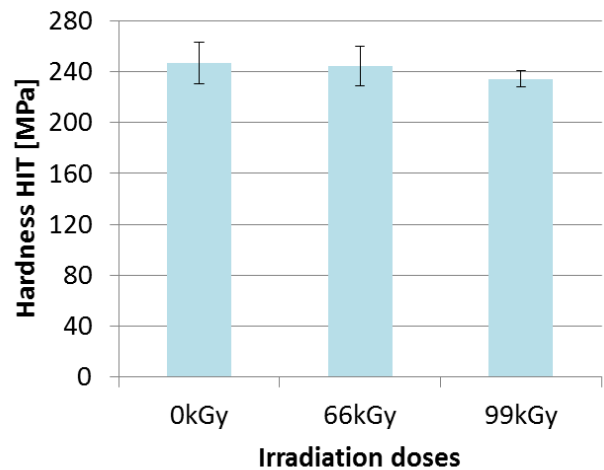


Fig. 6 Hardness HIT of PMMA vs. irradiation doses

Higher radiation dose does not influence significantly the nanohardness value. An indentation hardness increase of the surface layer is caused by irradiation cross-linking of the tested specimen, but total hardness decreasing due to degradation of basic material.

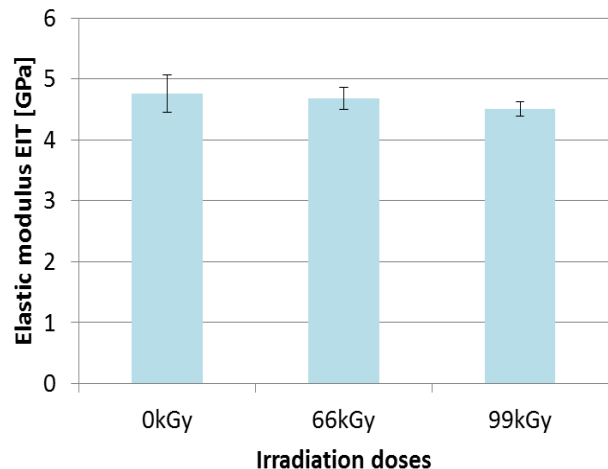


Fig. 7 Elastic modulus EIT of PMMA vs. irradiation doses

According to the results of measurements of nanohardness, it was found that the highest values of indentation modulus of elasticity were achieved at the non-irradiated PMMA (by 5% higher than compared with PMMA irradiated with dose of 99 kGy). On the contrary, the lowest values of the indentation modulus of elasticity were found for PMMA irradiated with dose of 99 kGy as is seen at Fig 7.

The lowest values of hardness Vickers were found for PMMA irradiated with dose of 99 kGy. On the contrary, the highest values of hardness Vickers were obtained for non-irradiated PMMA (by 5% higher in comparison with PMMA irradiated with dose of 99 kGy), as can be seen at Fig. 8.

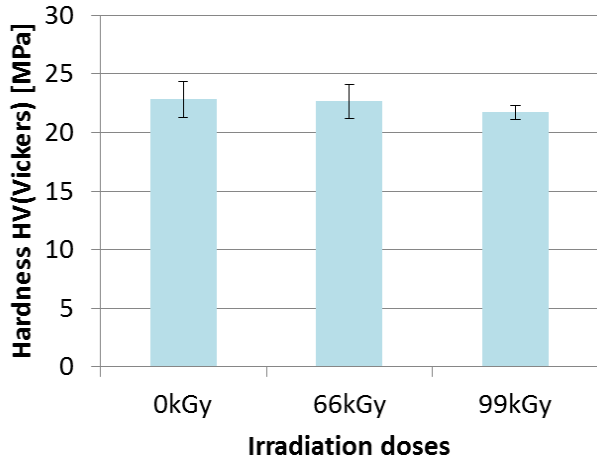


Fig. 8 Hardness Vickers of PMMA vs. irradiation doses

The greatest values of plastic and elastic deformation work were obtained for PMMA irradiated with dose of 99 kGy. The lowest values of elastic deformation work were obtained for non-irradiated PMMA. The lowest values of plastic deformation work were obtained for PMMA irradiated with dose of 66 kGy. Radiation of specimens caused higher values of elastic as well as plastic deformation work which is apparent in Fig. 9.

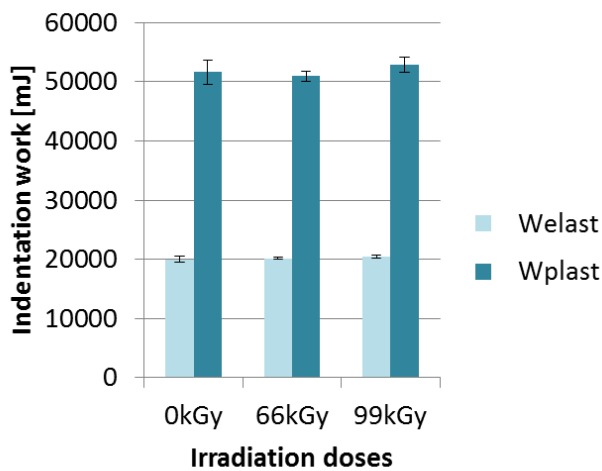


Fig. 9 Elastic and plastic deformation work of PMMA vs. irradiation doses

C. Indentation load 250 mN

The values measured during the nanohardness test showed that the lowest values of indentation hardness were found for non-irradiated PMMA. On the contrary, the highest values of indentation hardness were obtained for PMMA irradiated by a dose of 99 kGy (by 4% higher in comparison with non-irradiated PMMA), as can be seen at Fig.10.

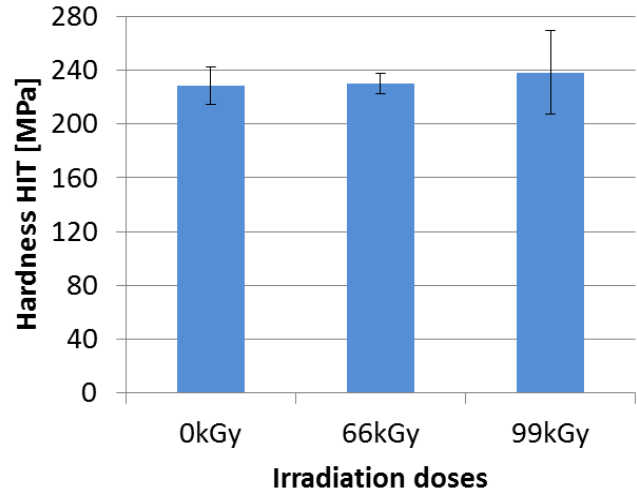


Fig. 10 Hardness HIT of PMMA vs. irradiation doses

Higher radiation dose does not influence significantly the nanohardness value. An indentation hardness increase of the surface layer is caused by irradiation cross-linking of the tested specimen, but total hardness decreasing due to degradation of basic material.

According to the results of measurements of nanohardness, it was found that the highest values of indentation modulus of elasticity were achieved at PMMA irradiated with dose of 99 kGy (by 1% higher than compared with non-irradiated PMMA). On the contrary, the lowest values of the indentation modulus of elasticity were found for non-irradiated PMMA as is seen at Fig 11.

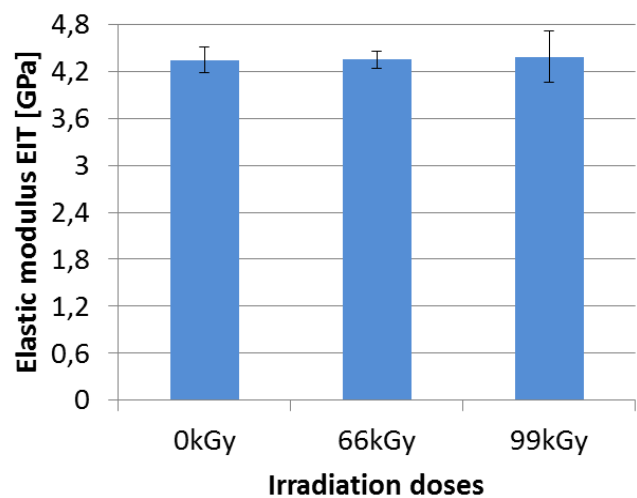


Fig. 11 Elastic modulus EIT of PMMA vs. irradiation doses

The lowest values of hardness Vickers were found for non-irradiated PMMA. On the contrary, the highest values of hardness Vickers were obtained for PMMA irradiated with dose of 99 kGy (by 4% higher in comparison with non-irradiated PMMA), as can be seen at Fig. 12.

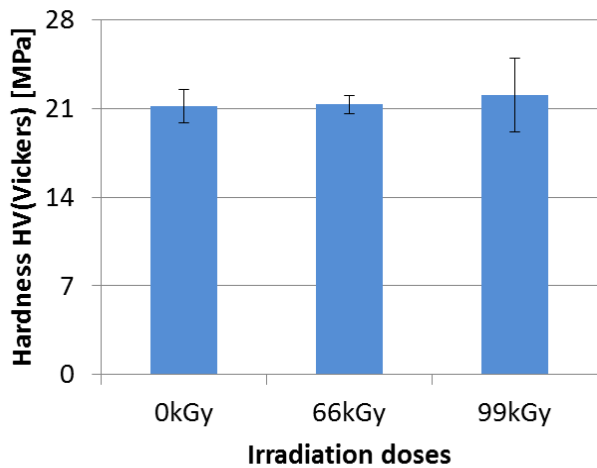


Fig. 12 Hardness Vickers of PMMA vs. irradiation doses

The greatest values of elastic deformation work were obtained for PMMA irradiated with dose of 99 kGy. The greatest values of plastic deformation work were obtained for non-irradiated PMMA. The lowest values of elastic and plastic deformation work were obtained for PMMA irradiated with dose of 66 kGy. Radiation of specimens not caused significantly changes of values of plastic and elastic deformation work which is apparent in Fig. 13.

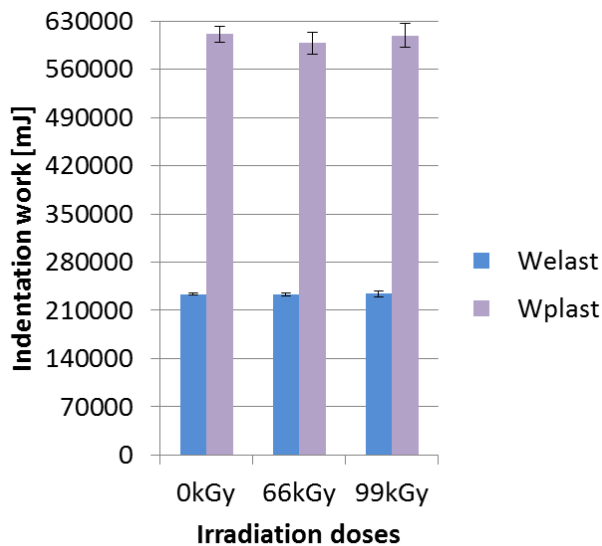


Fig. 13 Elastic and plastic deformation work of PMMA vs. irradiation doses

IV. CONCLUSION

The properties of surface layer of polymethyl methacrylate modified by beta radiation improved significantly. The nanohardness values increased about 7% at higher load as

10mN. Stiffness of surface layer increased significantly by 5% as a result of radiation. Changes of behavior in the surface layer were confirmed by final values of plastic deformation work whose values decreased in correlation with the increasing radiation dose. Elastic deformation was increasing with radiation dose. The highest values of micromechanical properties were reached at radiation dose of 99 kGy. The results of nanomechanical properties of surface layer of modified polymethyl methacrylate show that it can be used in more difficult applications in some industrial fields, in particular where there are high requirements for strength, stiffness and hardness of surface layer which appears to be the most suitable area of application. The resistance of surface layer to wear makes its use suitable for the production of gears, friction parts of machinery and as alternative to some metal materials. Thanks to its low weight, easy handling and processing, polymethyl methacrylate modified by beta radiation is a suitable alternative to commonly used materials in the car and electrical industry.

REFERENCES

- [1] J.G. Drobny, *Radiation technology for polymers*, Boca Raton: CRC Press, 2003, ISBN 1-58716-108-7.
- [2] BGS – Beta Gama Service. [online]. www: <http://bgs.eu>
- [3] J.G. Drobny, *Handbook of thermoplastic elastomers*, William Andrew Publishing: Norwich, NY, 2007, ISBN: 978-0-8155-1549-4
- [4] Z. Brocka, *Werkstoff- und einatzpotential strahlenvernetzter thermoplaste*, Lehrstuhl für Kunststofftechnik (LKT), Nürnberg, 2008.
- [5] R. J. Woods, *Applied radiation chemistry: radiation processing*, A Wiley-Interscience publication, New York, 1994, ISBN 0-471-54452-3.
- [6] Y. Huang, F. Zhang, K. C. Hwang, W. D. Nix, G. M. Pharr, and G. Feng, "A model of size effects in nano-indentation." *Journal of the Mechanics and Physics of Solids*. 2006, Vol. 54, p. 1668–1686.
- [7] Z. Holik, M. Danek, M. Manas, and J. Cerny, "The influence of cross-linking agent on mechanical properties of polyamide modified by irradiation cross-linking", in *Proc. 13th WSEAS International Conference on Automatic Control, Modelling & Simulation*, Lanzarote, Spain, 2011, pp.222-225.
- [8] Z. Holik, K. Kyas, M. Krupal, J. Cerny, and M. Danek, "Improvement of polypropylene properties", *21st International DAAAM Symposium*, 2010, Zadar, Croatia, p. 1191-1192.
- [9] H. Vaskova, and V. Kresalek, "Raman spectroscopy of epoxy resin crosslinking", in *Proc. 13th WSEAS International Conference on Automatic Control, Modelling & Simulation*, Lanzarote, Canary Islands 2011, p.357-360.
- [10] D. Manas, M. Manas, M. Stanek, and T. Drga, "Influence of radiation on polymer properties," in *Chemické listy*, Vol. 101, 2007, pp. 27-28.
- [11] D. Manas, M. Stanek, and M. Manas, "Workability and wear of rubber parts", *Chapter 54 in DAAAM International Scientific Book 2007*, Published by DAAAM International, DAAAM International, Vienna, Austria, p.611-626.
- [12] M. Stanek, D. Manas, M. Manas, and J. Javorik, "Simulation of injection molding process," in *Proc. 13th WSEAS International Conference on Automatic Control, Modelling & Simulation*, p.231-234.
- [13] K. Kyas, M. Stanek, D. Manas, M. Stanek, M. Krupal, and Z. Holik, "Simulation of rubber injection holding process", in *Chemické listy*, Volume 105, 2011, Issue 15, pp. S354-S356.
- [14] J. Navtatil, M. Stanek, M. Manas, D. Manas, M. Bednarik, and A. Mizera: "Utilization of DMLS in injection mold design," in *Annals of DAAAM for 2011 & Proceedings of the 22nd International DAAAM Symposium*, 23-26th November 2011, Vienna, Austria, ISSN 1726-9679, ISBN 978-3-901509-83-4, p. 1507-1508, Published by DAAAM International Vienna, Vienna
- [15] J. Javorik, and M. Stanek, "The numerical simulation of the rubber Diaphragm Behavior," in *Proc. 13th WSEAS International Conference*

- on *Automatic Control, Modelling & Simulation*, Lanzarote, Spain, 2011, pp. 117-120.
- [16] Z. Holik, M. Manas, M. Danek, and J. Macourek: "Improvement of Mechanical and Thermomechanical Properties of polyethylene by irradiation crosslinking." in *Chemické listy*. Volume 103, 2009, pp. 60-63, ISSN 0009-2770 (IF: 0,593 MF: 1,256)
- [17] D. Manas, M. Hribova, M. Manas, M. Ovsik, M. Stanek, and D. Samek, "The effect of beta irradiation on morphology and micro hardness of polypropylene thin layer", *Thin Solid Films*, Volume 530, 2012, pp. 49-52. ISSN 0040-6090.
- [18] G. M. Pharr, "Measurement of mechanical properties by ultra-low indentation." in *Material Science and Engineering*. 1998, pp. 151-159.
- [19] M. Ovsik, D. Manas, M. Manas, M. Stanek, M. Hribova, K. Kocman, and D. Samek, "Irradiated polypropylene Studied by microhardness and WAXS", in *Chemické listy*, Volume 106, 2012, pp. 507-510. ISSN 0009-2770.
- [20] D. Janacova, H. Charvatova, K. Kolomaznik, V. Vasek, and P. Mokrejs, "Solving of non-stationary heat transfer in a plane plate", in *Proc. 13th WSEAS International Conference on Automatic Control, Modelling & Simulation*, Lanzarote, Canary Islands 2011, pp.287-291.
- [21] P. Kratky, D. Manas, M. Manas, M. Stanek, M. Ovsik, K. Kyas, and J. Navratil. "Nanohardness of polymers (Polymethyl methacrylate)". In: EDITORS, Andrzej Zak a Radek Matusu ASSOCIATE EDITOR. *Recent advances in automatic control, information and communications: proceedings of the 14th international conference on automation*. 2013, pp. 140-144. ISBN 9789604743162.

Petr Kratky was born in Sumperk in 1987. He received a B.Sc. (2010), M.Sc. (2012) in Process engineering from Faculty of Technology, Tomas Bata University in Zlin. He is a doctoral student at the Department of Production Engineering. Major research interests are mechanical properties of polymer and metal materials.

Visual Information Processing Routines for Intelligent Vehicles

Jarnea Alexandru Daniel, Florea Gheorghe and Dobrescu Radu

Abstract—This paper presents a research for an advanced driver assistance system. We present routines for what we think is important for the smart vehicles.

Tree algorithms that are more researched in the least years are reviewed. We want to relay as much as possible on visual information. As because of this, the routines that we approach are: pedestrian detection, line detection and traffic sign recognition.

Keywords—Line detection, parallel threading, particle analyze, region of interest, traffic sign recognition.

I. INTRODUCTION

The task to develop intelligent vehicles is not a new one and can be seen in any assistance systems available today. With the latest evolution of the computing power we can process the data faster. We can develop new, more reliable algorithms that can be based as much as possible on visual information.

Driving is based mostly on processing the useful visual information. The drivers take the appropriate actions from the data acquired by recognizing traffic signs, road lanes, virtual distances etc. Artificial systems still have some unresolved subjects when straight view to the useful information is obstructed. By respecting all the indicators' information the driver can adapt to any type of road even if he travels on this route for the first time.

An intelligent vehicle is based on advanced driver assistance systems (ADAS) that can autonomously intervene if a possible dangerous situation is detected. The researchers try to develop a system that can analyze and understand the visual based information with different approaches.

An ADAS can improve driving safety and can enhance the driver's comfort. For instance, it can inform the driver about the recommended actions or it can prevent him from doing inappropriate maneuvers.

In usual atmospheric conditions road lanes or traffic signs

Ing Jarnea Alexandru Daniel is PhD. student, Faculty of Automatic Control and Computers, University POLITEHNICA of Bucharest, Romania, e-mail: jarnea@yahoo.com,

Ing Gheorghe Florea is PhD. student, Faculty of Automatic Control and Computers, University POLITEHNICA of Bucharest, Romania, e-mail: gelu.florea@sis.ro

Prof. dr. ing. Dobrescu Radu, Faculty of Automatic Control and Computers, University POLITEHNICA of Bucharest, Romania, e-mail: rd_dobrescu@yahoo.com

are easily distinguished, but during harsh conditions they become difficult to recognize as outlined in [1]

In the next section we highlight a proposal for our software architecture. Section III as you can see in Fig.1 it is organized in four important sections: pre-processing stage, the actual processing stage, representation and planning. Here we detail the processing steps for our system. In section IV we present the results obtained form the developed algorithms. In the final section we analyze the research and provide future directions from this range.

II. RELATED WORK

Recent work has been focused on detection, classification and tracking of relevant features, as it is presented in [2]. The article also talks about an ADAS that can map the important features from the environment using a CCD camera and vertical laser sensors.

Paper [3] outline the ADAS that are implemented today as platooning, stop and go, blind angle perception, maneuvers and they present a vehicle detection based on a geometrical model.

In [4] a road lane detection algorithm is explained, which is based on inverse perspective mapping. Also summarized in [5] is a simplified Markov model which has been made to operate even in cases where markings are obstructed or absent altogether.

A traffic lights recognition algorithm is proposed in [6]. A robust detection and tracking algorithm is achieved to avoid false positive results from brake lights.

A non-rigid objects detection as a pedestrian algorithm is presented in [7] where they use an infrared image and good results are obtained for a single frame performance. A deformable contour model for pedestrian detection with very good result is presented in [8] where frames from a stereo vision camera are used.

The approach that earned an important part of the researcher's attention is the object detection application developed by Paul Viola and Michael Jones [9]. Their approach, helped by the learning technique, uses cascade detectors to discriminate objects from image areas where every detector is a set of efficient computable Haar features.

A machine learning algorithm is presented by Yoav Freund and Robert Schafire in [10], named short Adaboost, is embedded in [11] as a faster approach and with better results extension of the original Haar Wavelets over large feature sets.

In [12] is presented a traffic sign recognition approach that is based on Adaboost and Forest Error-Correcting Output Code and they obtain a very high percentage at detecting circular traffic signs. The approach of color segmentation is studied in [13] where they too obtain a good segmentation method, but they don't achieve as good of a recognition percentage.

III. IMAGE PROCESSING FOR INTELLIGENT VEHICLES

Fig.1. illustrates the architecture of the driving assistance system, with mention of the main routines used for visual information processing, which will be presented in detail in this section.

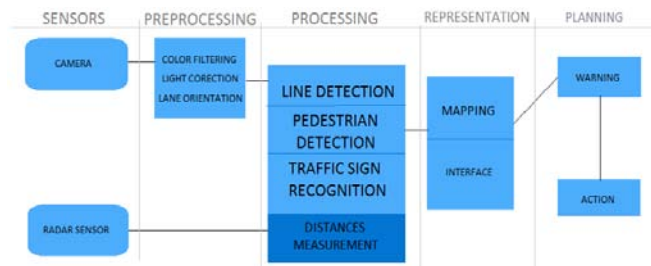


Figure.1 Architecture of our driving assistance system

Such a system based on image processing and important features detection should be based on traffic signs recognition, lane detection and obstacles detection. We present in the following our approach for traffic sign recognition, pedestrian detection and lane detection algorithms.

A. Traffic sign recognition algorithm

The program that we developed is written as a windows forms application in C# environment.

At this stage of development the program can run on a computer running the Windows operating system. The application may run on iPhone, Android, Linux or other operating systems if it is compiled with a cross platform application.

The Emgu CV library, which is described in [14], is used for image processing. This library adds some facilities to the application such as image class with generic color and depth, generic operations on image pixels. The most important feature of this library is that we can use video hardware processing to improve the timings of our algorithms.

The images that we use are captured, while driving, by a Galaxy S3 phone at HD resolution. Every frame is resized to a 640x480 pixels resolution before starting any analysis.

The library signs are acquired automatically from a folder placed next to the application executable file. We used a library of 8 restriction signs, however, any number of templates can be added if the computer platform can process them in a small amount of time.

In Fig.2 we can see the restriction and alert signs that are considered as library for these algorithms.



Figure.2 Signs from the library that were taken into consideration

The algorithm that we present here is based on common traffic sign recognition that usually has three steps: segmentation, detection and recognition, as you can see from Fig.3. We chose to make the segmentation step permissive, with wider windows color than usual, so we can get all regions of interest where a sign could be found. We added an additional step, after the detection, where according to the light average of the image the initial ROI's are transformed into black and white ones by adapting the filter with corresponding variables.

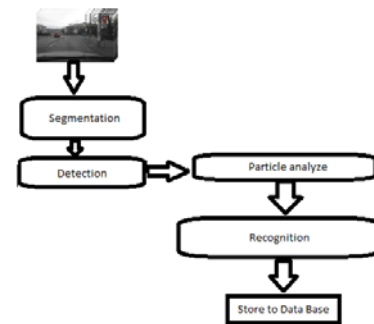


Figure.3 Structure of the traffic sign recognition algorithm

The application has two operating modes, the first one is a very detailed one which shows the correlation values for the regions of interest with all the library signs. The second one has the same base algorithm but is faster, because it is implemented with parallel threads.

a. Segmentation

The segmentation step starts with converting from RGB to HSL the query frame extracted from video. From the HSL matrix we extract the areas with red, blue, and yellow window color between set values.

To extract from the HSL matrix a black white image, which highlights the exact dimension and position where a sign could be. In the application it is used for example for red color the window that can be seen in equ. (1). The small white portions from inside the sign perimeter are filled in. You can see in Fig.5a the result obtained by applying to Fig.4 the procedure described by equ. (1).

$$Red(i, j) = \begin{cases} true, & \text{if } ((0 < Frame(:, :, 1) < 8) \text{ or } (112 < Frame(:, :, 1) < 5) \text{ and } (25 < Frame(:, :, 3) < 230)) \\ false, & \text{else} \end{cases} \quad (1)$$



Figure.4 Video frame

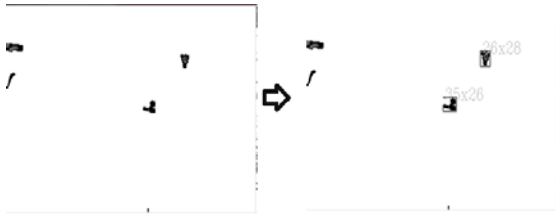


Figure.5 (a) Extracted possible areas of interest from Fig.3, for red color. (b) Outlined regions of interest, with measured square dimensions.

b. Detection of all the regions of interest where a sign could be found

On the image from Fig.5a that we extracted at the first step we draw a rectangle as a contour for every black area. We measure the exact dimension of all distinct regions as can be seen in Fig.5b where we have just one outlined area, which in this case has the size of 26x28 pixels.

The regions that have the width and height higher than 20 pixels and less than 95 pixels are marked as regions of interest and are further analyzed as possible regions where a sign could be present. These thresholds are also setted from measurements and experimental results, but can be easily modified from the application interface.

c. Particle replacement and reanalyze

At this step we calculate the average light in the initial frame. For every detected region of interest like the one from Fig.5b we overlap on the black areas the correspondent pixels from initial frame Fig.3. We convert to black and white the region of interest considering the initial light intensity.

d. Recognition

For this step we compare the regions of interest to the signs from the library after resizing the library sign to the dimensions of the region of interest.

If the correlation between a region of interest and a library sign is greater then 0.70, the region is found as a sign from the library. If the correlation is greater than 0.5 and smaller than 0.70 the region of interest is considered as possible presence of the sign from library sign.

We can see that the correlation between Fig.6a and Fig.6b, as one can see in Fig.6c, is 0.8, where 1 is perfect correlation, so we have a higher correlation value than the treshold and the sign is considered found.



Figure.6 (a) Region of interest filtered in black and white. (b) Library sign filtered in black and white. (c) The correlation after a and b comparison

e. Save to database

Every region that passes the restrictions is compared with the library signs from this color cathegory and gets a correlation percentage for every library sign. If one of the region have the correlation higer than 0.7 for a library sign it is labeled as a match. For the regions with correlation higher than 40% we store in a data base the image name, the extracted region of interest, the name of the sign from the library and the GPS location of the sign, aquiered from the image data.

By analyzing the HSL matrix we avoid most of the problems that occur when filtering the RGB matrix after setting the window limits. With the light analysis, the color window limits will detect the sign even in an environment with shadows on the area where the sign is positioned.

During night time with public lighting we can detect signs without problems, as shown with the “give way” sign in Fig.7. We have a problem when the roads do not have public illumination. In this situation the colors of the sign are visible but the correlation is not high as we would want. This problem could be easily surpassed by using a camera with the new generation of high dynamic rage sensors.

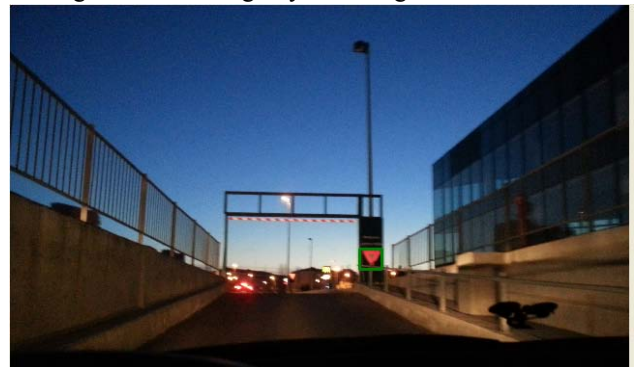


Figure.7 Night frame analyzed by the software

Traffic sign recognition is one of the systems that will help drivers, as covered in [15], and with which they will be more confident in themselves. Therefore these systems need s strong planning and reliability and finally should be one of the basic systems that will sustain self drive vehicles.

B. Pedestrian detection

Pedestrian detection regarding intelligent vehicles has started with sensors like laser (LIDAR) and monocular video. This approach, like the infrared detection has reached very good results even in real time, but the sensors are too expensive to use them in a usual vehicle.

Stereo based pedestrian detection system was very extensively researched lately. The most representative articles such as [16], propose algorithms that can detect multiple pedestrians also with real time detection like in [17]. The encountered problems that are still unresolved are the false negative frames when a pedestrian is too close and false positive for tree reflections.

For a monocular algorithm that approach pedestrian detection several problems are encountered faced as crowded background and objects movement. The appearance of a pedestrian is not rigid and it can change its shape.

Article [18] shows pedestrian detection from frames. They compare the fast Haar features approach, as we present in our results, speeded by Adaboost with HOG and libSVM, the slower approach but with far less false positives detections. They also propose a combination Haar and HOG algorithm that seems to have better timings and accurate detection.

C. Lane detection

The algorithm that we have developed does not rely only on the marked lines like in [19], we also took into consideration the roadsides, to achieve better reliability. For example we can warn the driver if he is going to cross the roadside.

In the Fig.8 the structure of the lane detection algorithm can be seen.

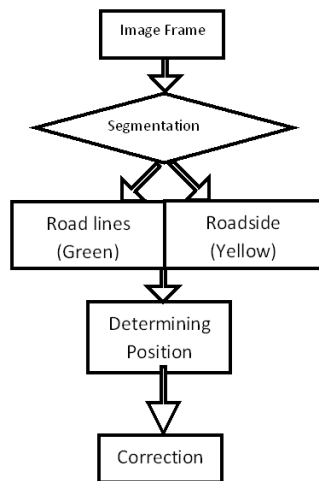


Figure.8 Structure of the lane detection algorithm

We calculate the average of every pixel's neighbors and if the value is grater then a step we mark then we make that pixel white, else black. The step we use is between 3 and 10. We use the minimum step because we also want to extract the road boundaries.

The initial video frame it is presented in Fig.9.

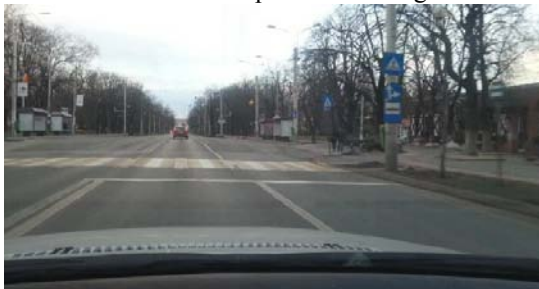


Figure.9 Initial video Frame

The result of this algorithm is a black image with road lanes, or road borders extracted on white color as can be seen in Fig 10.



Figure.10 Segmentation of the road lanes

On Fig.10 we apply a Hough transform as presented in [20], and we extract two types of lanes after the angle incidence: first type is colored with green and could be the road lane and the second type of lane is colored with yellow and could represent the road borders and could be used when the road lanes are not visible.

The green lanes are chosen with the angle between 29 and 40 or -29 and -40 radians, and the yellow ones are selected with the angle between 14 and 29 or 40 and 54 radians or -14 and -29 or -40 and -54 radians, as can be seen in Fig 11.

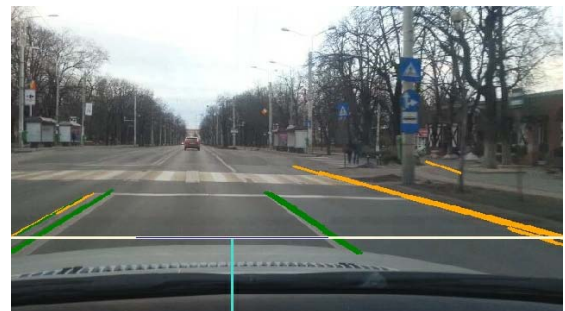


Figure.11 Drowned virtual road lane

We calculate the intersections of the virtual road lanes with the gray lane that you see in Fig 10. We get the closer green or yellow lane from the center of the vehicle from each side of the road.

The steering command is calculated in pixels by making the difference between the most restrictive left and right lanes green or if necessary using the yellow ones. This dimension could be converted in angles to be steered according to a range of parameters like the current speed, camera resolution, and vehicle dimensions, road conditions etc.

The vertical red lanes that estimate the generated future vehicle dimension and position can be seen in Fig.12. The actual direction without correction is drawn with green vertical lanes.

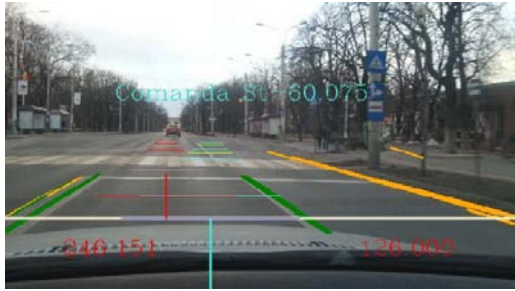


Figure.12 Generated future position of the vehicle based on road lane middle

IV. RESULTS

A. Traffic sign recognition

With the fast approach we can process from 15 to 30 frames per second according to the complexity of the image and the CPU of the computer that processes the data. If we compare with [21] where they used an i7-920 processor, 12GB of ram and 4 GTX 580 graphic cards for 25 frames per second this approach is faster because we used an AMD X2 250 with 4GB of ram and without video hardware we can process a frame within an average time of 45 milliseconds. We have to take into consideration that they used 43 library signs and in our approach only 8 signs are analyzed.

The result of the percentage of detected and recognized signs for each different category of color is presented in table I.

TABLE I. PERCENT OF DETECTION

	Red signs	Blue signs	Yellow signs
Frames	50	50	50
Detected	98%	98%	96%
Recognized	96%	96%	94%
Average processing time	44ms	46 ms	32ms

In Fig.13 you can see the representative frame of each set of signs.



Figure.13 Frames from each testing set

In Fig.14 you can see a chart which represents the results from table I.

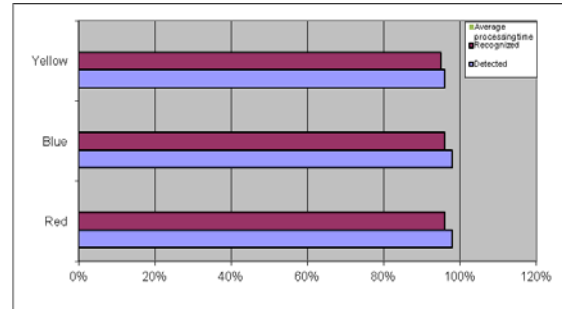


Figure.14 Frames from each testing set

B. Pedestrian detection

The default algorithm proposed for pedestrian crossing based on Haar features, with optimization and improved rate of detection is presented in table II. The results are computed with the CPU presented earlier or a GTX 650 graphic card.

TABLE II. PEDESTRIAN CROSSING

ID	Time with CPU processing	Time with GPU processing
1	987ms	105ms
2	670ms	103ms
3	719ms	100ms
4	983ms	111ms
5	964ms	111sm
6	639ms	117ms
7	715ms	118ms
8	997ms	142ms

The averages times from analyzing the frames with the GPU processor are close to real time computing, but it is possible that better results can be achieved with more optimizations.

C. Lane detection

In table III you can see the results that we had on 4 different types of road during the day time while detecting road lanes.

TABLE III. Lane detection on day light at 640x480 pixels

	Frames	Correct	Incorrect	Accuracy
No lanes	34	32	2	93.75%
One lane	25	25	0	100%
Multi lanes	37	36	1	97.29%
Highway	15	15	0	100%

In Fig.15 you can see the direction correction of lane detection algorithm on different types of roads.



Figure.15 Frames with virtual lanes generated

V. CONCLUSION

In this paper, we described our algorithms for an intelligent vehicle. We aimed to have a very good processing time while detecting all the goals.

We studied different methods of segmentation and some are implemented in our algorithm, though has passed to various modifications. Best traffic sign recognition programs Today reach up to 99% correct detection, but in harsh weather conditions, not uncommon the visual recognition is not able to do the task. The database mapping and validation of the traffic signs is probably the best solution that can be implemented today because in difficult environmental situations the signs will not be recognized.

The biggest problem encountered is that the public sign database is it very poor for Romanian traffic signs. We have the results from a new data set created for our traffic sign recognition algorithm. This aspect is making the comparison between papers very difficult.

The experimental results were made on images captured from actual Romanian roads and demonstrate that the algorithm can successfully reach its goal with close to real time accuracy and with performance.

As future work we strive to improve the correlation percentage and add tracking steps to our algorithms to optimize the processing time. We also want to add an interpretation step and detailed description for the developed algorithms to approach ADAS as much as possible.

REFERENCES

- [1] Benjamin Hoferlin , Klaus Zimmermann, *Towards reliable Traffic Sign Recognition*, Stuttgart Universitat, Germany, 2009, IEEE
- [2] T. Bucher, C. Curio, J. Edelbrunner, C. Igel, D. Kastrop, I. Leefken, G. Lorenz, A. Steinhage, and W. von Seelen, *Image Processing and Behaviour Planning for Intelligent Vehicles*, Ruhr University, Germany, 2003, IEEE
- [3] J. M. Collado, C. Hilario, A. de la Escalera and J. M^a Armingol, *Model Based Vehicle Detection for Intelligent Vehicles*, University of Parma , 2004, IEEE
- [4] Stephan Sehestedt, Sarath Kodagoda, Alen Alempijevic Gamini Dissanayake, *Efficient Lane Detection and Tracking in Urban Environments*, 2007, ECMR
- [5] S. Sehestedt, S. Kodagoda, A. Alempijevic, G. Dissanayake, *Robust Lane Detection in Urban Environments*, 2007, IROS.
- [6] Jianwei Gong, Yanhua Jiang, Guangming Xiong, Chaohua Guan, Gang Tao and Huiyan Chen, *The Recognition and Tracking of Traffic Lights Based on Color Segmentation and CAMSHIFT for Intelligent Vehicles*, University of California, San Diego, 2010, IEEE
- [7] F. Suard, A. Rakotomamonjy, A. Bensrhair and A. Broggi, *Pedestrian Detection using Infrared images and Histograms of Oriented Gradients*, Saint Etienne du Rouvray FRANCE, 2006, IEEE
- [8] C. Hilario, J. M. Collado, J. M^a Armingol, A. de la Escalera, *Pedestrian Detection for Intelligent Vehicles based on Active Contour Models and Stereo Vision*, Universidad Carlos III de Madrid, Spain, 2005, EUROCAST
- [9] Paul Viola and Michael Jones, *Rapid Object Detection using a Boosted Cascade of Simple Features*, 2001, ACCVPR
- [10] Yoav Freund and Robert E Schapire. *A Decision-Theoretic Generalization of On-Line Learning and an Application to Boosting*, 1997, JCSS
- [11] Yoav Freund and Robert E Schapire. *A Decision-Theoretic Generalization of On-Line Learning and an Application to Boosting*, 1997, JCSS
- [12] R. Lienhart, J. Maydt , *An extended set of Haar-like features for rapid object detection*, 2002, IEEE Image Processing
- [13] Xavier Baró, Sergio Escalera, Jordi Vitrià, Oriol Pujol, Petia Radeva, *Traffic Sign Recognition Using Evolutionary Adaboost Detection and Forest-ECOC Classification*, *IEEE Transactions on Intelligent Transportation Systems*, 2009
- [14] Hilario Gomez-Moreno, Saturino Maldonado-Bascon, Pedro Gill-Jamirez and Sergio Lafument- Arroyo, *Goal Evaluation of Segmentation Algorithms for Traffic Sign Recognition*, IEEE International Conference, 2010
- [15] Shin Shi, *Emgu CV Essencials*, 2013
- [16] Johannes Stallkamp, Marc Schlipsing, Jan Salmen, Christian Igel, The German Traffic Sign Recognition Benchmark: A multi-class classification competition, 2011, *Neural Networks (IJCNN)*,
- [17] A. Ess, B. Leibe, K. Schindler and L. van Gool, "A mobile vision system for robust multi-person tracking," in IEEE
- [18] Max Bajracharya, Baback Moghaddam, Andrew Howard, Shane Brennan, Larry H. Matthies, *Results from a Real-time Stereo-based Pedestrian Detection System on a Moving Vehicle*, Japan 2009, IEEE ICRA
- [19] Wenfeng Xing, Yong Zhao, Ruzhong Cheng, Jiaoyao Xu, Shaoting Lv, and Xinan Wang, *Fast Pedestrian Detection Based on Haar Pre-Detection*, 2012, IJCCCE
- [20] Marc Revilloud, Dominique Gruyer IEEE Member, Evangeline Pollard, *An improved approach for robust road marking detection and tracking applied to multi-lane estimation*, 2013, IEEE Intelligent Vehicles Symposium
- [21] Othman O. Khalifa, Imran Moez Khan, Abdulhakam A., *A Hyperbola-Pair Based Lane Detection System for Vehicle Guidance*, WCECS 2010, October 20-22, San Francisco, USA.
- [22] Andreas Mogelmoose, Mohan Manubhai Trivedi, and Thomas B. Moeslund, *Vision-Based Traffic Sign Detection and Analysis for Intelligent Driver Assistance Systems: Perspectives and Survey*, 2012, IEEE Transactions on Intelligent Transportation Systems

The behaviour of recycled material with particles of various sizes at increased temperature and their tensile properties

Vojtech Senkerik, Michal Stanek, Miroslav Manas, David Manas, Adam Skrobak, and Jan Navratil

Abstract—This work studies the influence of particle size recycled polymeric material on the mechanical tensile properties of polycarbonate at increased temperatures. When recycled material is produced, different sized particles are made, which can cause problems during subsequent processing. Melting rate of individual particles differs, causing inhomogeneity of the melt. Several mixtures of recycled material were prepared, which varied in particle size. From large particles similar to the original granulate material, to dust particles. Testing was carried out using a tensile test at an increased temperature of 100 ° C. Products from the recycled material are also used at these increased temperatures. Comparison of virgin polycarbonate with recycled mixtures showed that the influence of the particle size is mainly seen at the elastic modulus parameter. Value of the modulus decreased more than 20 % in a mixture with dust particles. For other tensile properties, this effect is not so substantial.

Keywords—recycled material, particle size, sieving, temperature, polymer, polycarbonate

I. INTRODUCTION

MECHANICAL recycling is the most common method of recycling. Here plastics are physically ground back to a suitable size (regrind) and reprocessed. The end use can be the original one or something different.

In the plastics industry it has long been common practice to reprocess waste material arising from normal production. This in-house recycling, known as primary recycling, makes economic sense as it reduces both production waste and utilization of raw materials. For example, with injection

molding, regrind from start-up waste and production waste such as reject parts, can be fed directly back into the production machine.

Within a closed loop cycle, it is easy to recycle materials and this is the reason that primary recycling is so commonplace. The key is having the knowledge of, and confidence in, the materials that are being used.

Injection molding has in last several decades become very popular technology in plastic manufacturing. It allows quick and precise manufacture of different polymer based products not only for daily life, but also for specialized uses.

Defective injects, waste and runner system originating during injection molding can be processed several times. This way of processing is frequently used because of high portion of the waste, especially while manufacturing small injects. For this reason is unpolluted waste cut and crushed. Material modified by this process is once again granulated and mixed with pure granulate and consequently utilized. Using this mixed material has usually no significant influence on physical-mechanical properties or surface appearance. Level of properties degradation depends on levels of crushed material in original material. Transparent and highly stressed materials cannot be mixed, because of high demands. This article focus to this method type of recycling - mechanical recycling. [1 - 4]

II. EXPERIMENT

The aim of this research paper is to study the effect of particle size of recycled polymeric material on mechanical tensile properties at increased temperatures. The goal is to perform an experiment in which the products of the studied polymer will be crushed to crushed material (recycled material) and then reprocessed into new products. These are then subjected to mechanical testing. Specimens were prepared by the most common technology for production of plastic products, which is injection molding.

A. Material

Tested polymer was polycarbonate Makrolon 2205. This material is formed by a condensation polymerization resulting in a carbon that is bonded to three oxygen atoms. The most common system for this polymerization is formed by a

This paper is supported by the internal grant of TBU in Zlin No. IGA/FT/2014/016 funded from the resources of specific university research and by the European Regional Development Fund under the project CEBIA-Tech No. CZ.1.05/2.1.00/03.0089.

Vojtech Senkerik is with the Tomas Bata University in Zlin, nam. T. G. Masaryka 5555, 76001 Zlin, Czech Republic (phone: +420576035030; e-mail: vsenkerik@ft.utb.cz).

Michal Stanek is with the Tomas Bata University in Zlin, nam. T. G. Masaryka 5555, 76001 Zlin, Czech Republic (e-mail: stanek@ft.utb.cz).

Miroslav Manas is with the Tomas Bata University in Zlin, nam. T. G. Masaryka 5555, 76001 Zlin, Czech Republic (e-mail: manas@ft.utb.cz).

David Manas is with the Tomas Bata University in Zlin, nam. T. G. Masaryka 5555, 76001 Zlin, Czech Republic (e-mail: dmanas@ft.utb.cz).

Adam Skrobak is with the Tomas Bata University in Zlin, nam. T. G. Masaryka 5555, 76001 Zlin, Czech Republic (e-mail: skrobak@ft.utb.cz).

Jan Navratil is with the Tomas Bata University in Zlin, nam. T. G. Masaryka 5555, 76001 Zlin, Czech Republic (e-mail: j1navratil@ft.utb.cz).

reaction of bisphenol A and phosgene. Applications of polycarbonate are almost always those which take advantage of its uniquely high impact strength and its exceptional clarity. These unique properties have resulted in applications such as bulletproof windows, break resistant lenses, compact discs, etc. Recently, more interest has risen because of the low flammability of polycarbonate. [5]

B. The specimen preparation

The first task was to produce products by injection molding technologies. These parts were made using recycled material. Injection was carried out on injection molding machine made by Arburg. Specifically, it was an injection molding machine Arburg 470 C. Each of the specimens were left to condition for 24 h before testing by the following method.

Table I Process parameters

Melt temperature	300 °C
Mold temperature	100 °C
Ejection temperature	130 °C
Injection speed	60 mm.s ⁻¹
Injection pressure	80 MPa
Holding pressure pressure	35 MPa
Holding pressure time	30 s
Cycle time	55 s

C. Sieving

Grinding of material was immediately followed by sieving. The purpose of the sieving was to eliminate the above mentioned very fine particles and dust. Sieving was carried out on laboratory sieve shakers AS 200 Basic figure.

Sieve mesh of size 2 mm was used for sieving, which caught the particles larger than 2 mm. This material is further called sieved crushed material. The size of mesh was chosen to achieve the size of recycled material to be as close as possible to the original material. The bowl was placed to the bottom to capture smaller particles than 2 mm and dust. Non-sieved crushed material then contain particles of all sizes and is very diverse.

After the crushed was made, preparation for the injection of new specimens made from this material began. Several recycled materials were made, all from original material. Samples with different percentage amount and a type of recycled material were subsequently tested.

For injection molding the following mixtures of these materials were used:

- virgin polycarbonate,
- sieved crushed material,
- non-sieved crushed material.

D. Composition of tested mixtures

Different compositions were prepared for the measurements of tested mixtures with differing sizes of sieved particles.

- Virgin PC - material directly from the manufacturer which has not yet been processed in any way, it is taken as a referential material
- Sieved crushed material – recycled crushed material containing similarly sized particles as the granules of virgin material, from this mixture small crushed particles smaller than 2 mm are removed
- Non-sieved crushed material - this recycled material is collected directly from the knife mill, contains particles of all sizes, from large particles to dust particles and therefore is heterogeneous.
- Crushed material 1 – 2 mm - this recycled material is sieved and has a particle size from 1 mm to 2 mm
- Crushed material < 1 mm - this recycled material is sieved and has a particle size up to 1 mm, containing very small to dust particles.

Table II Tested mixtures

Composition of tested mixtures	Particle size [mm]
Virgin polycarbonate	granule
Sieved crushed material	2 < x < 4
Non-sieved crushed material	0 < x < 4
Crushed material 1-2mm	1 < x < 2
Crushed material < 1mm	x < 1

E. Testing

Tensile test was performed on a universal tensile testing machine W91255 from Zwick / Roel. The test was carried out according to EN ISO 527 standard. For each mixture 10 measurements were performed, which were then statistically evaluated.

III. RESULTS AND DISCUSSION

All graphs are normalized so that the virgin material is 100%. Other values are scaled to this value.

A. Elastic tensile modulus

First very important material parameter is obtained by measuring the tensile modulus E. As can be seen in Fig. 1

virgin polycarbonate has the highest value of elastic modulus. Recycling caused a noticeable reduction of the modulus. This is mostly visible in the mixture of crushed material with particles smaller than 1 mm. Value of the modulus decreased by almost 300 MPa. It is more than 20% in comparison with the virgin polycarbonate.

Table III Elastic modulus

Mixture	Elastic modulus E [MPa]	
	Arithmetic mean	Standard deviation
Virgin polycarbonate	1891	147,9
Sieved crushed material	1911	141,5
Non-sieved crushed material	1601	277,5
Crushed material 1-2mm	1638	214,8
Crushed material < 1mm	1475	301,5

Elastic modulus value decreased about 200 MPa in the mixtures of non-sieved crushed material and particle size 1 – 2 mm. That it is about 15 % less than virgin material.

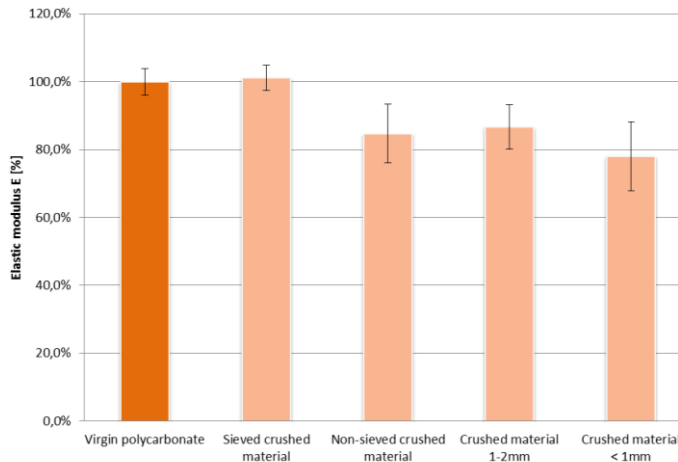


Fig. 1 Elastic modulus

Mixtures containing small particles (non-sieved, 1 < 2 mm and dust mixtures) gained more unstable statistical characteristics, having a larger variance of measured values than a mixture of virgin polycarbonate or sieved crushed material.

B. Ultimate tensile strength

Ultimate tensile strength is another measured material parameter. This parameter will not show as large differences between the recycled mixtures to virgin polycarbonate as the elastic modulus previously mentioned.

Table IV Ultimate tensile strength

Mixture	Ultimate tensile strength [MPa]	
	Arithmetic mean	Standard deviation
Virgin polycarbonate	44,7	0,70
Sieved crushed material	43,6	0,59
Non-sieved crushed material	44,7	0,94
Crushed material 1-2mm	43,3	0,59
Crushed material < 1mm	42,9	0,47

All mixtures show small decrease of tensile strength, but only about 3 %. Biggest decrease is observed in mixture with dust particle. Only non-sieved crushed material behaved as the virgin material.

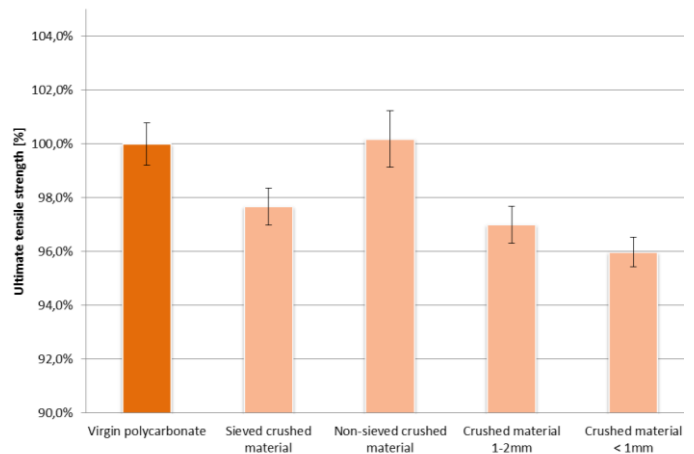


Fig. 2 Ultimate tensile strength

C. Strain

Nominal strain is the last evaluated parameter of the tensile tests. As can be seen from Fig 3, sieved crushed material elongated less than virgin polycarbonate.

Table V Strain

Mixture	Strain [%]	
	Arithmetic mean	Standard deviation
Virgin polycarbonate	5,32	0,19
Sieved crushed material	5,15	0,12
Non-sieved crushed material	5,60	0,59
Crushed material 1-2mm	5,72	0,45
Crushed material < 1mm	5,88	0,61

After recycling all other mixtures elongated more than the original virgin material. The strain values of these mixtures show a similar elongation, about 6% more.

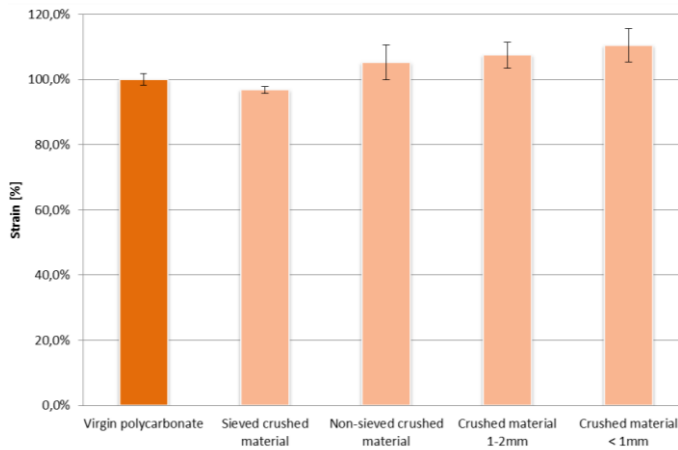


Fig. 3 Strain

Furthermore, the standard deviations of this more elongated mixtures is bigger. Overall, these differences are relative small (maximum strain is 10% more than virgin PC) and they show a tendency of the effect of recycling to relative strain values.

IV. CONCLUSION

This work examined the influence of particle size of recycled polymeric material on the mechanical tensile properties of polycarbonate at elevated temperatures. Several mixtures of recycled material were measured. These mixtures differed in particle size after crushing.

Specifically, these mixtures are: non-sieved crushed material - with all crushed sizes of particles; sieved crushed material - without small dust particles smaller than 2 mm, similar to the virgin granules size; then mixture with small (1 - 2 mm) and dust particles (smaller than 1 mm). The measured data were graphically represented and interpreted.

Testing was performed on a universal tensile testing machine. By comparison of the virgin polycarbonate and recycled mixtures we can see that the effect of the size of the particles was mainly on the elastic modulus. Value of the modulus decreased more than 20 % in mixture with dust particles. For other tensile properties, this effect is not so significant. Values of ultimate tensile strength decreased by 4 %. Mixtures containing small and dust particles are more elongated as the virgin material by about 6%, only sieved crushed mixture showed smaller elongation.

Mixtures with dust particles typically indicate higher statistical variations of measured values, and therefore have less stable behaviour of the measured properties compared to virgin polycarbonate, or sieved crushed material. Therefore it is recommended to remove the dust particles when using recycled polymer material. Products made using these

recycled materials will have more similar properties as one made with an original material.

REFERENCES

- [1] V. Goodship. *Introduction to plastics recycling*. 2nd ed. Shawbury, U.K.: Smithers Rapra, 2007, 174 p. ISBN 978-1-84735-078-7.
- [2] D. Bryce. *Plastic injection molding: manufacturing process fundamentals*. Dearborn, Mich.: Society of Manufacturing Engineers, c1996, xvi, ISBN 08-726-3472-8.
- [3] J. Aguado, D. P. Serrano. *Feedstock recycling of plastic wastes*. Cambridge, UK: Royal Society of Chemistry, 1999, 206 p. ISBN 978-085-4045-310.
- [4] F. P. La Mantia. *Recycling of plastic materials*. Toronto: ChemTec Pub., c1993, vi, 189 p. ISBN 18-951-9803-8.
- [5] Online: <http://plastics.ides.com>
- [6] D. Janacova, H. Charvatova, K. Kolomaznik, V. Vasek, P. Mokrejs, "Solving of non-stationary heat transfer in a plane plate", in *Proc. 13th WSEAS International Conference on Automatic Control, Modelling & Simulation*, Lanzarote, Canary Islands 2011, p.287-291
- [7] W. C. Oliver, G. M. Pharr. "Measurement of hardness and elastic modulus by instrumented indentation". *Journal of Materials Research*. 2004, Vol. 19, no. 1.
- [8] W. D. Nix. H. Gao. "Indentation size effects in crystalline materials: A law for strain gradient plasticity". *J. Mech. Phys. Solids*. 46 (1998) p. 411-425.
- [9] H. Buckle. "In science of hardness testing and its research applications. edited by J.H. Westbrook and H. Conrad" *American society for metals, Metals Park, Ohio*, (1971) ch. 33, p. 453-491.
- [10] D. Manas, M. Manas, M. Stanek, S. Sanda, V. Pata, "Thermal effects on steels at different methods of separation", 2011, *Chemické listy*, vol. 105, Issue 17, pp. S713-S715
- [11] A. Pusz, K. Michalik, "Creep damage mechanisms in gas pipes made of high density polyethylene", 2009 *Archives of Materials Science and Engineering* 36 (2) , pp. 89-95.
- [12] D. Manas, M. Stanek, M. Manas, V. Pata, J. Javorik, "Influence of mechanical properties on wear of heavily stressed rubber parts", *KGK – Kautschuk Gummi Kunststoff*, 62. Jahrgang, 2009, p.240-245.
- [13] J. Javorik, D. Manas, "The specimen optimization for the equibiaxial test of elastomers," in *Proc. 13th WSEAS International Conference on Automatic Control, Modelling & Simulation*, Lanzarote, Spain, 2011, pp. 121-124.
- [14] S. Sanda, M. Manas, D. Manas, M. Stanek, V. Senkerik "Gate effect on quality of injected part", *Chemické listy*, vol. 105, 2011, pp.301-303.
- [15] M. Stanek, D. Manas, M. Manas, J. Javorik, "Simulation of injection molding process by Cadmould rubber", *International Journal of Mathematics and Computers in Simulation*, vol. 5, Issue 5, 2011, p. 422-429.
- [16] V. Pata, D. Manas, M. Manas, M. Stanek, "Visulation of the wear test of rubber materials", *Chemické listy*, vol. 105, 2011, pp.290-292.
- [17] M. Adamek, M. Matysek, P. Neumann, "Modeling of the microflow sensor", in *Proc. 13th WSEAS International Conference on Automatic Control, Modelling & Simulation*, Lanzarote, Canary Islands, 2011, p.137-140.
- [18] M. Stanek, D. Manas, M. Manas, O. Suba, "Optimization of injection molding process by MPX," in *Proc. 13th WSEAS International Conference on Automatic Control, Modelling & Simulation*, p.212-216.
- [19] M. Manas; D. Manas; M. Stanek; A. Mizera; M. Ovsik. "Modification of polymer properties by irradiation properties of thermoplastic elastomer after radiation cross-linking". *Asian Journal of Chemistry*, 2013, vol. 25, Issue 9, s. 5124-5128. ISSN 09707077.
- [20] M. Stanek, M. Manas, D. Manas. "Mold cavity roughness vs. flow of polymer", *Novel Trends in Rheology III*, AIP, 2009, pp.75-85
- [21] D. Manas, M. Stanek, M. Manas, V. Pata, J. Javorik., "Influence of mechanical properties on wear of heavily stressed rubber parts", *KGK – Kautschuk Gummi Kunststoff*, 62. Jahrgang, 2009, p.240-245.
- [22] M. Ovsik, D. Manas, M. Manas, M. Stanek, M. Hribova, K. Kocman, D. Samek, *Chemické Listy* 106, pp. 507-510 (2012).

New Approach to Thresholding and Contour Detection for Object Surface Inspection in Machine Vision

K. Židek, A. Hošovský, J. Dubják

Abstract—The paper deals with new approach to thresholding methods. This new thresholding method is based on bottom lighting and transparent conveyor belt. We can reach precise contour of recognized objects by this technics. The solution is primarily aimed for recognition tasks in automatized lines with modified conveyor belt. This principle is not sensitive to detect false contour from surface defects and shadows during recognition process. The main advantage is resistivity to surface texture failure which can disrupt the contour.

Keywords—machine vision, thresholding, object contour.

I. INTRODUCTION

THIS document introduces new approach to image thresholding in machine vision on production lines. This new principle is based on bottom lighting and transparent belt. The method is primarily intended for flat parts with small height. The method can be used for shape inspection of the sheet metal blanks. The first chapter deals with current methodology of thresholding technics in industrial machine vision. Next chapter introduces principle of a new approach to precise thresholding with detailed description of the used algorithm. The next section describes hardware and software solution of the designed system. The last chapter shows some experiments with suggested method for precise contour detection with ideal reference part and part with some surface errors (defects).

II. THRESHOLDING, CONTOUR DETECTION AND PROBLEMS

A. Basic thresholding methods

Thresholding is the basic segmentation method. Basic thresholding can be divided to three methods: binary, truncate and threshold to zero. These methods can be used with inverting function. The advanced technics of thresholding are

K. Židek, A. Hošovský and J. Dubják is with the Technical University of Kosice, Faculty of Manufacturing technologies with a seat in Presov, Department of Mathematics, Informatics and Cybernetics, Bayerova 1, 08001, Prešov, Slovakia, phone: +421 55 602 6422; e-mail: kamil.zidek@tuke.sk, alexander.hosovsky@tuke.sk, jan.dubjak@tuke.sk.

The research work is supported by the Project of the Structural Funds of the EU, Operational Program Research and Development. Research and development of the intelligent non-conventional actuators based on artificial muscles, ITMS code: 26220220103.

band and multispectral thresholding [1]. Thresholding usually uses grayscale image. In special cases if we cannot extract the data from grayscale image, the multispectral threshold is used. Multispectral image is created from color image with three separate channels (R-Red, G-Green, B-Blue). The next development in another thresholding methods are described [2], [3].

B. Dynamic thresholding: OTSU, Adaptive thresholding

An OTSU method is based on histogram processing to find minimum between foreground and background [4]. The main condition is bimodal histogram, otherwise algorithm fails. If we cannot ensure homogenous lighting we can use adaptive thresholding methods [5]. Adaptive thresholding creates separate threshold value for every segment in the image. The main disadvantage of this method is very noisy output which is not so simple to filter with standard methods [6]. Thresholding must be optimal, because it is a basic step in recognition process and generates the first input for all other postprocessing filters.

C. Contour detection

Contour detection is very strongly tied with optimal thresholding. Contour detection extracts quantity and shape of objects detected in image. The next task is description of object hierarchy inside the object (holes, defects ...etc.) [7], [8].

The next development in thresholding continues with the combination of standard methods with advanced technics for example wavelet transformation, pyramid processing, fuzzy logic, neural networks and genetic algorithms [9], [10], [11], [12], [13], [14].

D. Typical problem in thresholding and contour detection

For optimal thresholding in industrial machine vision we must choose ideal background color which is on opposite side scale as recognized object color. The histogram must be bimodal for optimal thresholding. This approach will work only for one type of parts texture in conveyor belt. If we must recognize more parts with different surface color on opposite side of scale, this approach fails Fig. 1a. The next problems of standard thresholding are parts with more surface colors (defects, inside objects ...etc.) Fig. 1b.

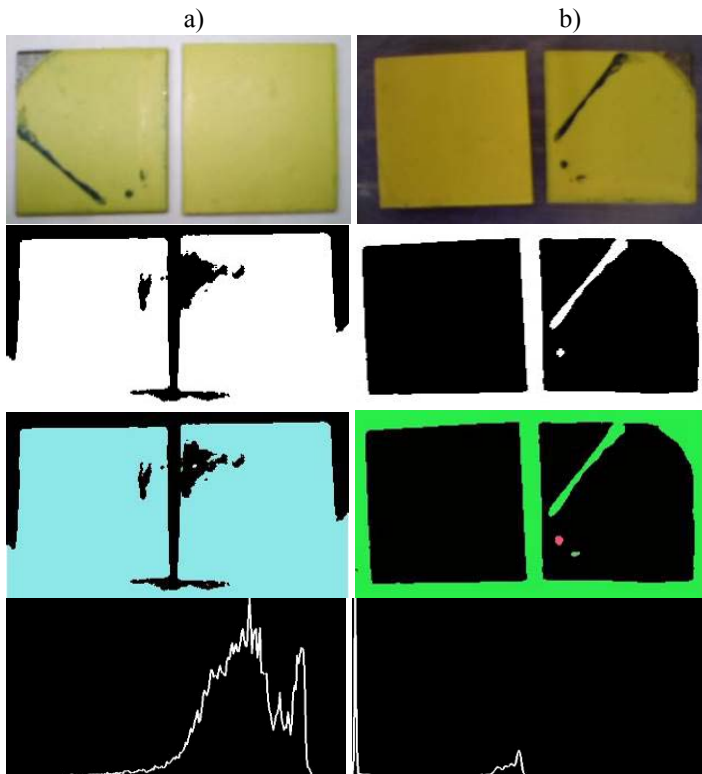


Fig. 1 Image of recognized parts with white/black background, OTSU thresholding, contour detection, histograms.

The problems with thresholding are solved using the proposed algorithm with dynamic background color according color of part surface. The detailed description of algorithm is specified in next chapter.

III. PRINCIPLE OF SOLUTION

The main principle of solution is dynamic background color selection. Optimal distance d_{max} is acquired as maximum distance from object color in color scale. The solution can be found on left and right side of color scale. Example of optimal background color is shown in Fig. 2.

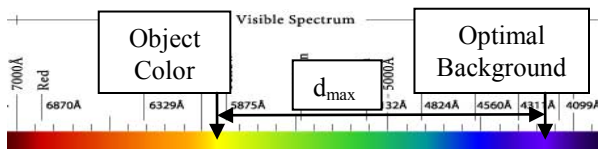


Fig. 2 Background color selection.

Principle of vision recognition process consists from five basic steps:

- detection of object surface color,
- computation of background colour, OTSU thresholding,
- contour detection, creating mask,
- merging images to add texture to contour mask.

Evolutionary diagram for image thresholding with relevant delays is shown on the Fig. 3.

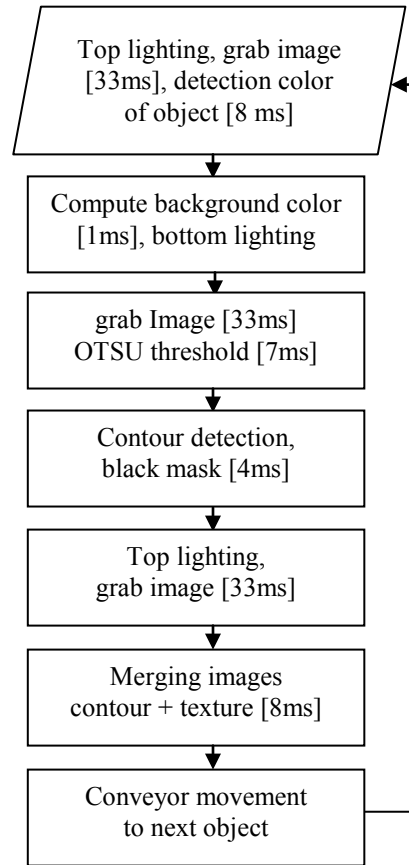


Fig. 3 Algorithm of thresholding and contour detection.

Main principle of thresholding, contour detection and extraction is shown in Fig. 4a, top surface texture is extracted in Fig. 4b, and merging of images is shown on the Fig. 4c.

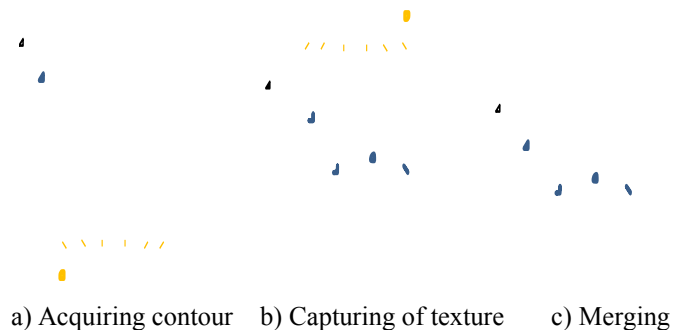


Fig. 4 Visual scheme of thresholding and contour detection.

IV. HARDWARE

Hardware used for contour recognition is based on embedded platform based on ARM architecture. The algorithm was ported to Raspberry PI board with two connected cameras (USB 2.0 web and CSI video camera). The system consists from three lighting systems: top white/RGB lighting and bottom RGB lighting. Bottom lighting creates color background thru carrier Plexiglas part with white deflector and transparent belt. We can generate background dynamically by

combination of basic colors with PWM signal. The intensity of the lighting can be regulated too. The vision processing hardware shows Fig. 5.

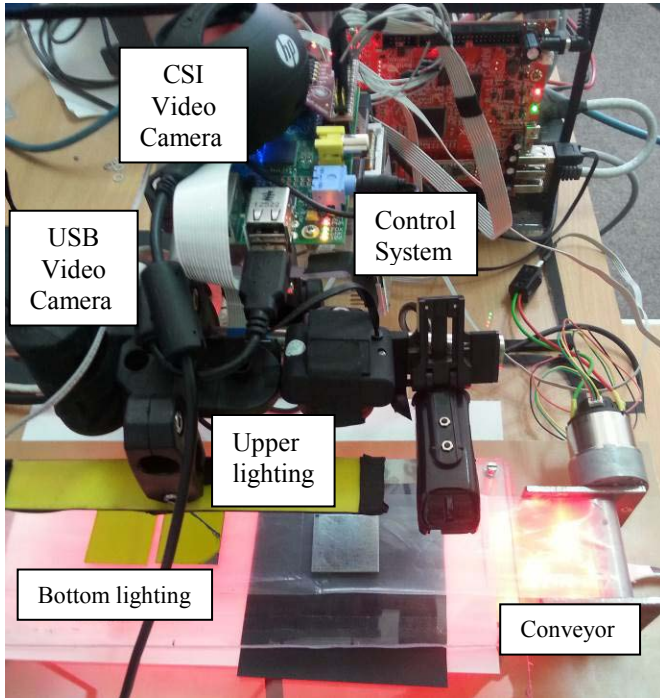


Fig. 5 Hardware of vision system with conveyor belt.

The Conveyor is created from standard DC motor with gearbox and incremental encoder to regulate velocity of transparent belt with recognized parts. Velocity is controlled by GPIO from Raspberry PI by external library Wiring PI.

V. SOFTWARE

Software solution is based on open source library OpenCV [15]. Main recognition loop is written in C++ language. User interface is based on HTML/JavaScript (jQuery) language with support of PHP scripting language to access low level routines in C++. GUI runs on Raspberry PI thru internal web server, which is accessible by Ethernet and TCP/IP protocol.

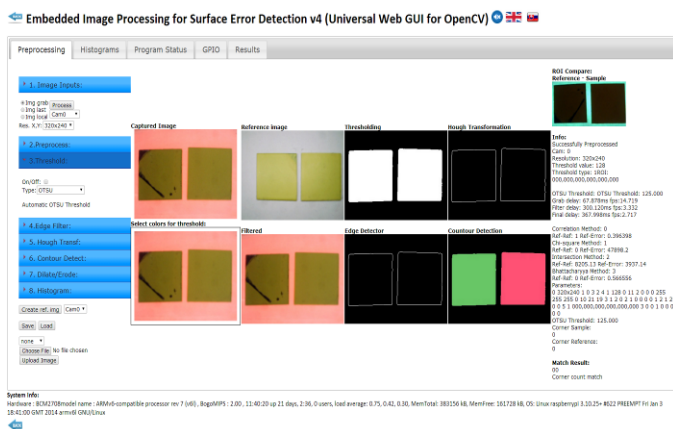


Fig. 6 Algorithm implementation to software solution.

The software solution was designed universally and can be executed on every OS distribution based Linux kernel. The software solution was tested on Debian, Openwrt, Fedora and Raspberrian distribution. Thus the software can be easily ported to any Linux platforms. Currently the same system was ported to these devices: access points TP-Link WR703N and Asus WL520gU, embedded board Olinuxino IMX233, A13 and HP Server with standard x86 architecture with desktop Linux distribution Ubuntu.

The user interface of vision system is shown on the Fig. 5.

VI. BOTTOM LIGHTING EXPERIMENT

The experiments were conducted with yellow color object and three basic color for background generated primarily by RGB Led.

The results of experiments are shown on the Fig. 7. The first line of the figure shows two parts (reference part and part with some surface defects) with three different background colors: green, blue, red. Second line represents results of OTSU thresholding, contour detection and texture and contour merging. The third line of the figure shows grayscale histograms for all background examples. The maximum distance d_{max} in grayscale histogram was acquired by blue color background.

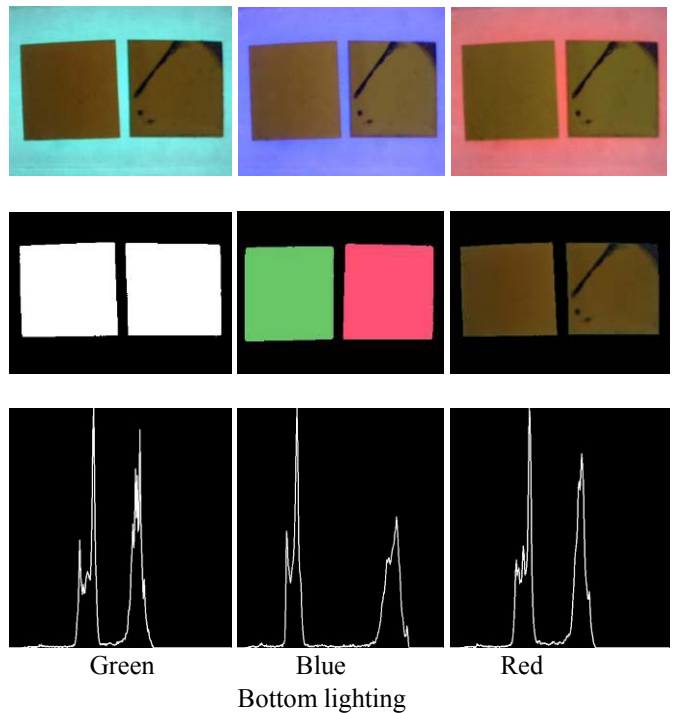


Fig. 7 Bottom lighting experiments for precise contour detection

Grayscale histograms have set multiplicity of shades to 8bit resolution (256 bins). The reliability of algorithm can be checked in grayscale or in color histogram too, because the distance d_{max} is visible as the space between two peaks which represents object color and color of background.

USB camera reaches frame rate about 30 fps. Algorithm was tested with resolutions 320x240 and 640x480 pixels. Higher resolutions in these experiments don't provide better result in precision of contour. A whole algorithm delay in tested hardware was about 120 ms with resolution 320x240. Embedded platform Raspberry PI can process about 8 frames per second.

Different researches deals with texture recognition were described in these articles [16], [17], [18], [19].

VII. CONCLUSION

The introduced dynamic algorithm based on bottom lighting is primarily designed for flat parts with smaller height. The main disadvantage is usability only in industrial area for automatized lines where are inspected parts transported in conveyor belt. We can improve the delay of the whole algorithm porting solution to another embedded SoC platform for example Odroid U3 with 1,7 GHz and 2GB RAM. Some improvement in delay can be obtained if the bottom and top lighting are used simultaneously, but the precision of contour can decrease. The next experiments of precise contour detection with this methods will be conducted with shiny material (metal parts without matte surface), because standard thresholding and contour detection usually fails in this case. The white lighting can be used for detection shiny surface of objects in short distance for example in unknown environments in mobile navigation [20], [21].

ACKNOWLEDGMENT

The research work is supported by the Project of the Structural Funds of the EU, title of the project: Research and development of intelligent nonconventional actuators based on artificial muscles, ITMS code: 26220220103.

REFERENCES

- [1] Pal, N.R., Pal, S.K., "A review on image segmentation techniques", in *Pattern Recognition*, volume 26, issue 9, 1993, pp. 1277-1294.
- [2] A. M. Atto, D. Pastor, G. Mercier, "Wavelet shrinkage: unification of basic thresholding functions and thresholds", in *Signal, Image and Video Processing*, volume 5, issue 1, March 2011, pp. 11-28.
- [3] A. Singh, "Digital change detection techniques using remotely-sensed data", in *International Journal of Remote Sensing*, volume 10, issue 6, 1989, pp. 989-1003.
- [4] L. Gopinath, M. Anitha, N. Nithya, N.R. Raajan, "Comparative analysis of OTSU's method and active contour model", in *International Journal of Applied Engineering Research*, volume 9, issue 2, 2014, pp. 277-282.
- [5] C. Stauffer, W.E.L. Grimson, "Adaptive background mixture models for real-time tracking", in *Proceedings of the IEEE Computer Society Conference on Computer Vision and Pattern Recognition*, volume 2, 1999, pp. 246-252.
- [6] D. Gaceb, F. Lebourgeois, J. Duong, "Adaptative smart-binarization method: For images of business documents", in *Proceedings of the International Conference on Document Analysis and Recognition, ICDAR, 2013*, article number 6628596, pp. 118-122.
- [7] H. Jiang, L. Zeng, B. Bi, "A comprehensive method of contour extraction for industrial computed tomography images", in *Optics and Lasers in Engineering*, Volume 51, Issue 3, March 2013, pp. 286-293.
- [8] R. Medina-Carnicer, R. Muñoz-Salinas, A. Carmona-Poyato, F.J. Madrid-Cuevas, "A novel histogram transformation to improve the

- performance of thresholding methods in edge detection", in *Pattern Recognition Letters*, Volume 32, Issue 5, 2011, pp. 676-693.
- [9] J. Piteľ, T. Saloky, "Intelligent robots and computer vision", in *International Carpathian Control Conference ICC'2004 - Volume II.*, Zakopane, May 25-28, 2004. Krakow: AGH - UST, 2004. pp. 243-246.
- [10] K.-Z. Tang, B.-X. Liu, H.-Y. Xu, X. Xiao, Z.-Y. Li, "A minimum cross entropy threshold selection method based on genetic algorithm", in *Kongzhi yu Juece/Control and Decision*, volume 28, issue 12, 2013, pp. 1805-1810.
- [11] Y. Yu, J. Cao, Y. Tang, J. Gan, "Fast wavelet thresholding algorithms for face image inpainting", in *Proceedings - 2013 IEEE International Conference on Green Computing and Communications and IEEE Internet of Things and IEEE Cyber, Physical and Social Computing*, 2013, article number 6682266, pp. 1445-1449.
- [12] S. Nashat, A. Abdullah, M. Z. Abdullah, "Machine vision for crack inspection of biscuits featuring pyramid detection scheme", in *Journal of Food Engineering*, volume 120, Issue 1, 2014, pp. 233-247.
- [13] "Fuzzy entropy-based MR brain image segmentation using modified particle swarm optimization" in *International Journal of Imaging Systems and Technology*, volume 23, issue 4, 2013, pp. 281-288.
- [14] J.N. Kapur, P.K. Sahoo, A.K.C. Wong, "A new method for gray-level picture thresholding using the entropy of the histogram", in *Computer Vision, Graphics & Image Processing*, volume 29, issue 3, 1985, pp. 273-285.
- [15] Open Source Computer Vision (OpenCv) Library, [Online]. Available: <http://opencv.willowgarage.com/wiki>.
- [16] T. Leung, J. Malik, "Representing and Recognizing the Visual Appearance of Materials using Three-dimensional Textons", in *International Journal of Computer Vision* 43, 2001, Kluwer Academic Publishers. Manufactured in The Netherlands, pp. 29-44.
- [17] Q. Zaidi, "Visual inferences of material changes: color as clue and distraction", in *Wiley Interdiscip Rev Cogn Sci*, 2011, pp. 686-700.
- [18] K. Židek, E. Rigasová, "Diagnostics of Products by Vision System, Applied Mechanics and Materials", in *Trans Tech Publications*, Switzerland, Vol. 308, 2013, pp. 33-38.
- [19] Lead-based paint: Testing methods. Missoula, MT, United States Department of Agriculture Forest Service, Technology & Development Program, 1996 (<http://www.fs.fed.us/eng/pubs/htmlpubs/htm96712353/>, accessed 20 December 2010).
- [20] F. Duchoň, M. Klůčik, L. Jurišica, „Reactive Navigation of Mobile Robot with Visual System” in *Acta Mechanica Slovaca*, 13, č. 2-A, 2009, pp. 47-52.
- [21] K. Židek, J. Šeminský, M. Dovica, A. Hošovský, "Wireless mobile device with integrated image processing", in *Automation, control and processes: Proceedings of the 8th technical conference ARaP, 2012*, Prague: Dimart, pp. 37-42.

Microcomputer I/O converter and control unit for heating systems

Libor Pekař, Petr Dostálek, and Zdeněk Oborný

Abstract—This paper aims to present design and implementation of the microcomputer input/output (I/O) unit with SW for control of heating systems, namely this prototypal, for a laboratory electrical heating plant. The development of the new unit has been motivated by the fact that the current modular converter unit used in the laboratory of process control at the Faculty of Applied Informatics, Tomas Bata University in Zlín, has been obsolete and has not fulfilled basic requirements on laboratory teaching experiments as well as on students' safety. In contrast to the old converter, the designed device enables to connect up to four laboratory models and it is equipped with a four-lines LCD display and buttons which allow calibration the I/O channels with saving to nonvolatile memory. The unit is compact and easy to be connected with a computer and a heating plant. A significant contribution consists in the ability to establish a serial communication with RS232 interface enabling operation without a data acquisition (DAQ) card. Last but not least the unit is much cheaper than any similar commercial product. The control and converter unit is ready to be enhanced and extended in many possible ways.

Keywords—Coldfire V1, converter, heating plant, microcomputer, temperature control

I. INTRODUCTION

SINCE the eighties of the last century, the laboratory of real processes control at the Faculty of Applied Informatics, Tomas Bata University in Zlín, Czech Republic, has been equipped with a modular converter and control device for laboratory exercises on heating models. This unit stands as an interface between the controlled laboratory model and a control part of the feedback (a personal computer – PC), and it provides the PC with unified measured signals from the plant and, contrariwise, it transforms control signals so that they can drive the controlled model.

However, the currently used unit suffers from frequent failures, it is not good-looking, has slackened parts and it is not often possible to acquire original spare parts. The device is, moreover, not safe for students because of possible injuries due to slackened parts and is obsolete for the realization of the modern control and identification laboratory tasks.

Because of these deficiencies, a modernized, safe, compact,

The authors kindly appreciate the financial support which was provided by the European Regional Development Fund under the project CEBIA-Tech No. CZ.1.05/2.1.00/03.0089.

Libor Pekař, Petr Dostálek and Zdeněk Oborný are with the Department of Automation and control Engineering, Faculty of Applied Informatics, Tomas Bata University in Zlín, Nad Stráněmi 4511, 760 05 Zlín, Czech Republic (corresponding author's phone: +420 57 603 5261; e-mail: pekar@fai.utb.cz).

multichannel and adjustable converter/control unit has been designed and assembled in order to provide students with a modern, extendable and easy-to-handle device that converts measured signal from the heating plant and drives the performance control input to the laboratory model. This paper describes particular parts of the unit from the hardware (HW) point of view and it also provides the reader with a superficial idea of the programmed control software (SW).

II. CURRENT STATE

The contemporary arrangement of the laboratory appliance is sketched in Fig. 1 and a photo of the converter/control unit is displayed Fig. 2. A PC equipped with Advantech PCI 1171 acquisition card [1] is connected with the converter/control unit via an external terminal board. The heating plant itself contains a small rheostat, inside of which a Pt100 sensor is installed. The rheostat is warmed up by 24V AC input and connected to the converter/control unit by a double conductor wire. Hence, the unit serves as an interface between a PC and the controlled plant, it is equipped by two converter and two control cards and a segment display, and powered by 230V AC from mains. Normalized analog output signal to a PC is within the range of 0-10V DC. Reversely, discrete input from a PC is of TTL logic.

Regarding the SW part, measurement and control tasks are realized by WControl application [2] which enables to select a template to the particular exercise, set control parameters, and display and archive relevant data. This application serves only for execution of a simple task; alternatively, one can use the Matlab/Simulink environment [3].

III. NEW CONVERTER/CONTROL UNIT DESIGN

A concise description of the modernized unit appearance follows.

A. Hardware

The new unit adopts some significant features of the current one and adds some news or improved others. It is powered by the safe 24V AC input, the use of the microcontroller enables a more accurate measured data evaluation and SW calibration with a memory, the unit can be connected with a PC by a serial RS232 interface and the data provided on a four-lines LCD display.

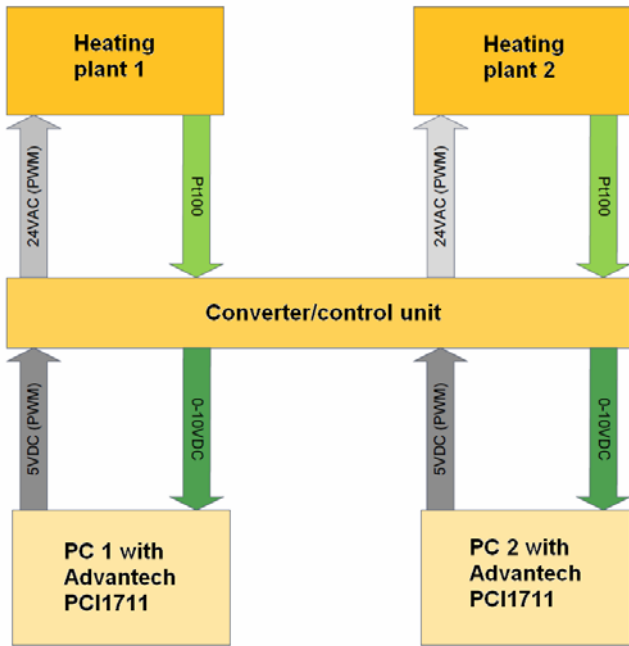


Fig. 1 Current laboratory appliance arrangement scheme

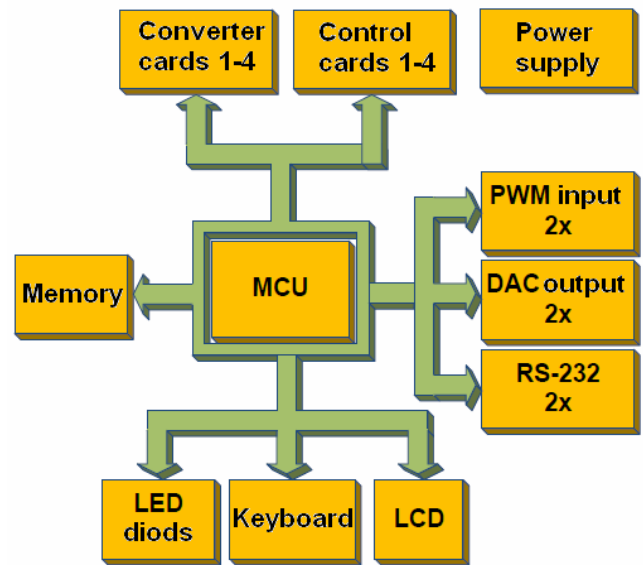


Fig. 3 New laboratory unit block scheme



Fig. 2 A photo of the current converter/control unit – the front (a) and the back side (b)

Two channels with analog measured data outputs and binary control action inputs are preserved. In contrast to the previous solution, there is a possibility to connect up to four converters and four control cards (boards). The overall block scheme of the unit is provided in Fig. 3.

1) *Power supply*

The apparatus is powered by 24V AC input with 4A power fuse. The input voltage is then branched and fed to control board as the power input and to rectifier GBU1002 [4]. The rectified voltage is then reduced to 12V and 5V DC using two step-down controllers, and DC-DC converter Tracopower TEN 15-2423 [5] produces the symmetrical +/- 15V DC voltage output to operational amplifiers of the central board. All the outputs are accessible via three Molex connectors.

2) *Central board*

The part of the unit which maintains the processing of control and data signals through the microprocessor is divided into two boards – the upper and the lower one.

The upper board includes connectors for interconnection of particular components with the microcontroller MCF51AC128 with the core Coldfire® V1 by Freescale Semiconductor, Inc. [6]. It also contains a connector for the converter (data acquisition) boards (cards) with the analog 0-5V input for the microcontroller and a connector for control boards with a timer. Close to the LCD display port, a potentiometer for adjusting the brightness of the display is placed. A 14-pin connector powered by 5V serves for the connection of the keyboard and for control of four LED diodes. Firmware of the microcontroller can be updated by the standard 6 pin BDM interface header which is a part of the central board. PWM control signals (in TTL logic levels) generated by the Advantech card on a PC are fetched into K1 and K2 connectors and, subsequently, proceeded by the driver, optoelements and a flexible timer in the input-capture mode. The lower part of the central board is connected by this upper one via 3 pin headers.

The lower part of the central board integrates EEPROM 25LC256 memory of 256KB and two 12b DA converters MCP4821. DA converter output is then amplified to 0-10V by means of the operational amplifier LM358 and connected to

analog input of Advantech cards in a PC for the information about measured temperature. Microcontroller UARTs TTL signals are converted by MAX232 integrated circuit for RS232 voltage levels.

3) *Keyboard*

The keyboard of the size 3x3 connected to the central board serve as a human-machine interface for the converter board. The keys provide moving to the left, right, up and down on the display, and for confirmation or cancellation. It also includes four low-consumption channel-state indicating diodes.

4) *LCD display board*

The display MC2004E-SYL communicates with the processor by a 4-bit wide data bus and is interfaced with the central board using a 10-wire flat cable. Its contrast can be adjusted by the trimmer located on the central board.

5) *Converter board*

This board is designed for temperature measurement and conversion of the signal from Pt100 sensors in 2-wire connection. The voltage loss on these sensors driven by the current reference signal is evaluated by a differential amplifier. This signal is then shifted down by the off-set of 100mV, amplified and limited to 0-5V using two Shottky diodes. The measured temperature values are within the possible range of 0-300 °C. A scheme of the board is given in Fig. 4.

6) *Control board*

PWM pulses of the period 1 s and the 8bit resolution generated by the microprocessor are sufficient for control of electric power driven into a heater inside the laboratory model. These pulses switch a bipolar transistor BC337 [7] which is used due to the necessity to reduce the current load of the microcontroller output. This transistor then makes an optotriac MOC3022 [8] switch on and, subsequently, its output drives a power triac which is fed by the AC voltage from the power-supply.

7) *Unit appearance*

A photo of the unit is pictured in Fig. 5. The frontal side contains a 4-line alphanumeric display providing currently measured and/or control data and a menu for the apparatus setting. Buttons for operating and changing the settings are placed right from the display. Above the buttons, four LED diodes signaling the connections of I/O cards (boards) are situated. On the back side of the unit, four blue Canon connectors for temperature sensors attachment are given. Smaller and bigger (green) clamp boards serve for the connection of the heater and provide ±15V, 12V, 5V a GND voltage outputs, respectively. Data acquisition Advantech cards can be connected via white Cannon connectors and the black ones can be used for RS232 communication. The power supply switch button is placed on the left side of the chassis.

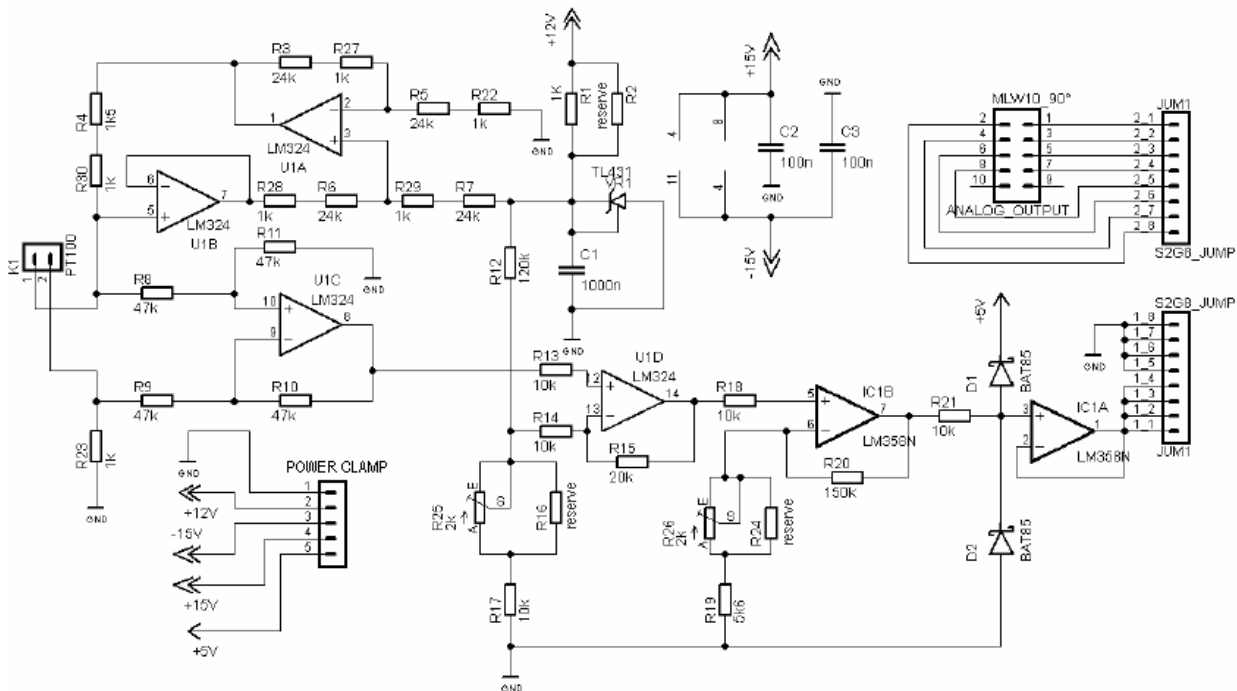


Fig. 4 Converter board electronic scheme



Fig. 5 A photo of the new designed converter/control unit – the front (a) and the back side (b)

B. Software

A brief description of important parts of SW realization for the converter/control board follows. The general programme for the microcontroller in C language and principles of the serial communication are presented. As a programming tool, Processor Expert utility integrated in Code Warrior 10.3 environment based on Eclipse IDE [9] has been used.

1) General programme

The programme source code can be divided into three groups: variables definition, peripheral initialization and the main programme, see Fig. 6. The variables definition block provides global variables and functions definitions initialization. The setting of microcontroller peripherals generating its own initialization function runs in the peripheral initialization block.

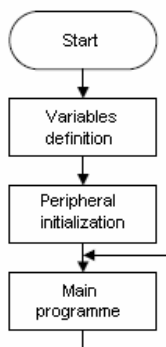


Fig. 6 General programme diagram

2) Main programme

The main programme running in cycles reads and set the unit configuration, see Fig. 7. Parallely, the keyboard interrupt (KBI) and interrupts from the serial link and binary PWM inputs can be processed.

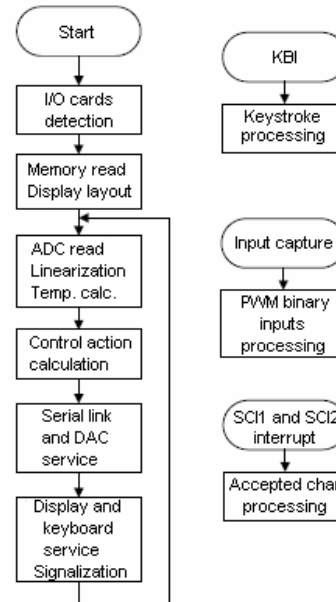


Fig. 7 Main programme diagram

Whenever an I/O board (card) is plugged, it is detected and this information together with the channel number is saved. Then, saved constants for the linearization of measured data are read from EEPROM and the display layout is set according to the number of plugged I/O cards. Loading of A/D converters outputs is performed every single cycle, the data are filtered and, subsequently, temperature values are evaluated by means of the equation (or its inversion, more precisely):

$$R = R_0(1 + At + Bt^2) \tag{1}$$

where $A = 3,9083 \cdot 10^{-3} \text{ } ^\circ\text{C}^{-1}$, $B = -5,775 \cdot 10^{-7} \text{ } ^\circ\text{C}^{-2}$, $R_0 = 100\Omega$.

Binary inputs from a PC (Advantech cards) are received by FTM1 timers with the input capture function by which lengths of input logical levels are measured. An interrupt is generated whenever the logical level is changed and, subsequently, the logical value is detected and copied to microprocessor output for the control board processing. The ratio of particular logical values lengths is measured and, afterwards, provided as a PWM value on the display.

A programme block providing display services includes depiction of currently measure temperature, PWM values or the settings menu for the unit. Keystrokes of buttons on the keyboard taking care of moving on the display and settings changes are captured using KBI interrupt.

If the serial communication is active, the received control value from SCI1 and SCI2 interfaces is converted and then the control action in the form of a PWM pulse is generated. The PWM timer resolution is 8 bit and the period is defaultly set as 1 s which is satisfactory for this reason. The received value of the required control action can be within the range from 0 to 100 % and it can be sent to PWM generator only if it has been changed; hence, it is not necessary to use a continual broadcast.

3) Serial communication setting

It is necessary to set RS232 parameters properly prior to the serial communication starts. The correct setting for the converter/control board is the following:

Parity: none
 Word length (data bits): 8 bit
 Number of stop bits: 1
 Baud rate: 9600 Bd
 Flow control: off
 Terminator string: CR

Accepted string giving information about the desired control action must be of the pattern *annn\r* where *nnn* is the decimal value of the control signal and *\r* means a jump to a new line. The string sent to a PC and containing information of measured temperature has the format: *nnn.n\r* where the sequence *nnn.n* means the temperature value. In contrast to input control signal, the measured output values have to be performed every single cycle of the main programme.

IV. CONCLUSION

A concise description of the appearance and functionality of the recently designed converter and control unit for laboratory exercises on a heating model has been introduced and presented in this contribution. This innovation brings about preservation of basic functional properties of the current appliance, on one hand, and makes many attributes better, on other hand. Namely, the unit is equipped with a LCD display, a keyboard and the RS232 interface; it is compact and safe and can be easily modularly extended. The crucial benefit is the low-cost manufacturing of the designed device.

REFERENCES

- [1] *PCI-1711U* (cited 2014, March 18), Advantech Co., Ltd.. [Online]. Available: http://www.advantech.com/products/1-2MLKC9/PCI-1711U/mod_B8EF5337-44F0-4C36-9343-AD87D01792D1.aspx
- [2] M. Bližňák, V. Vašek, and D. Janáčová, "WCONTROL - Program system for control theory laboratory education," presented at the International Conference of Engineering Education Abstracts (ICEE), Valencia, Spain, 2003, p. 92.
- [3] *MATLAB – The Language of Technical Computing* (cited 2014, March 18), The Mathworks, Inc. [Online]. Available: <http://www.mathworks.com/products/matlab/>.
- [4] *GBU1002 - Bridge Rectifier* (cited 2014, March 18), Premier Farnell UK, Ltd. [Online]. Available: <http://uk.farnell.com/multicomp/gbu1002/bridge-rectifier-10a-100v/dp/1621720>
- [5] *Tracopower – DC/DC Converters – Ten15 Series* (cited 2014, March 18), Traco Electronic AG. [Online]. Available: <http://www.tracopower.com/products/ten15.pdf>
- [6] *MCF51AC: Flexis 32-bit ColdFire® V1 Microcontrollers* (cited 2014, March 18), Freescale Semiconductor, Inc. [Online]. Available: http://www.freescale.com/webapp/sps/site/prod_summary.jsp?code=MC F51AC.
- [7] *BC337/338 NPN Epitaxial Silicon Transistor* (cited 2014, March 18), Fairchild Semiconductor Corporation, 2002 [Online]. Available: <http://www.fairchildsemi.com/ds/BC/BC337.pdf>.
- [8] *MOC3022-M – Optocoupler, Triac Driver* (cited 2014, March 18), Premier Farnell UK, Ltd. [Online]. Available: <http://uk.farnell.com/fairchild-semiconductor/moc3022-m/optocoupler-triac-driver/dp/1021366>
- [9] *Processor Expert Software – Integrated with CodeWarrior Tool* (cited 2014, March 18), Freescale Semiconductor, Inc. [Online]. Available: http://www.freescale.com/webapp/sps/site/prod_summary.jsp?code=PR OCESSOR-EXPERT

Defect Detection for Vertical Cracks in Hot-slabs using Dual Light Switching Lighting Method

Yong-Ju Jeon, Doo-chul Choi, Sang Jun Lee, Jong Pil Yun and Sang Woo Kim

Abstract—This paper presents an automated inspection algorithm for a hot-slab. The hot-slabs surface typically have various shape of scales composed of oxidized substances. These scales do not affect the typical quality of the slab. However, the scales must be distinguished from the defects through inspection for a high accuracy defect detection. To minimize the influence of scales and to detect defects more effectively, we propose a dual light switching lighting method and a defect detection algorithm based on Gabor filters and morphological analysis.

Keywords—Defect detection, Visual inspection, Automatic inspection, Slab

I. INTRODUCTION

IN recent years, product quality has been an important issue for the steel industry [1]. To create high-quality products, many applications are adopted in steel making industry [2], [3]. However, most surface-inspection systems are still manually operated in steel-making industry [4]. Therefore, non-destructive automatic inspection systems have been high demand in the steel industry.

The automatic inspection systems have many kind of advantage as follows [5]: (1) human do not need to work in hazardous environments; (2) the performance is better than humans work; (3) the quality and productivity of steel products produced by using these systems is high. However, the manual inspection can not be guaranteed the reliability and accuracy because it highly depends on the experience of human inspectors. Therefore, to overcome the limitation of manual inspection, many automated inspection systems have been successfully implemented within various industries [6]–[8].

In this paper, we propose an automated visual inspection system for the detection of vertical cracks in hot-slabs. Automated visual inspection has been developed in various industries such as textiles [9], circuit [10], LCD panels [11], and steel products [12]–[14] for fast speed and diagnostic capabilities [15]. The goal of this study was to develop a defect detection algorithm based on image processing techniques for vertical cracks in hot-slabs. The slabs are in the form

Yong-Ju Jeon, Doo-chul Choi and Sang Jun Lee are with Department of Electrical Engineering (EE), Pohang University of Science and Technology (POSTECH), Pohang 790-784, South Korea (e-mail: {yjeon83, dooshe, lsj4u}@postech.edu)

Jong Pil Yun is with System Research Group, Engineering Research Center, Pohang Iron and Steel Company (POSCO), Pohang 790-300, South Korea (e-mail: rebirth@posco.com)

Sang Woo Kim is with Department of Electrical Engineering (EE) and Department of Creative IT Excellence Engineering (CITE), Pohang University of Science and Technology (POSTECH), Pohang, 790-784, South Korea (e-mail: swkim@postech.edu)

of steel blocks with a rectangular. Fig.5 shows slab surface image including vertical cracks which is our target of defect detection. A hot-slab is a semifinished product fabricated by a continuous casting process. We focus on the detection of vertical cracks in slabs. The vertical cracks are critical defects because vertical cracks on the slab surface directly influence the quality of the final product such as thick plate. However, the hot-slab surface presents some difficult factors for defect detection, such as scales. The hot-slab surface is partially covered with scales composed of oxidized substances caused during hot-process manufacturing. The presence of scales strongly affects the optical properties of the slab surface. Therefore, we need to reduce the number of pseudo defects that occur because of the presence of scales.

In this paper, we propose a defect detection method for vertical cracks on slab surfaces that are partially covered with scales. To reduce the effect of scales, we propose dual light switching lighting (DLSL) method. To distinguish the vertical cracks from the other noise components such as the scales, we select a set of suitable criteria. The remainder of this paper is organized as follows. The lighting method, gabor filtering, and pair detection and path cost criteria are presented in Section 2, and experimental results and conclusions are discussed in Section 3.

II. METHODS

A. Dual Light Switching Lighting

An automatic inspection system consists of three components: a camera module, lighting module, and processing unit. To obtain good inspection performance, high-quality images are essential. The architectures of the single lighting

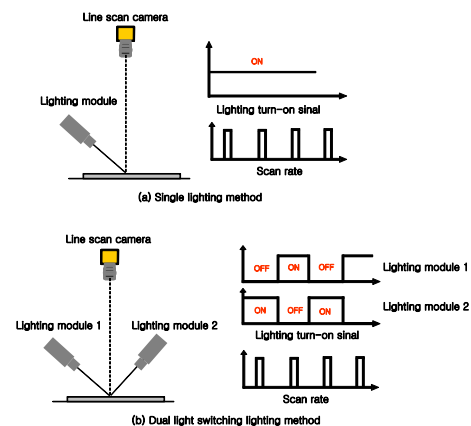


Fig. 1. Architecture of the lighting method

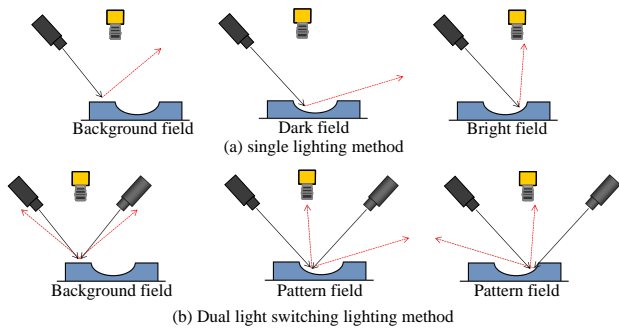


Fig. 2. Illumination patterns depending on different types of lighting methods

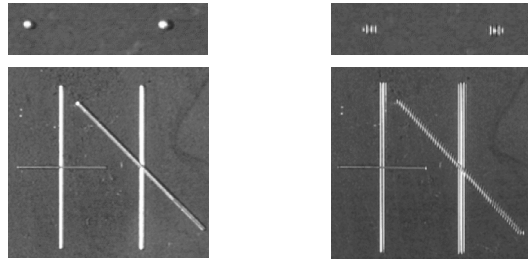


Fig. 3. Artificial defect images acquired in different lighting conditions

(SL) method and dual lighting switching lighting (DLSL) method are presented in Fig.1. The SL method consists of one camera and one lighting module. The lighting modules in single camera methods are always activated, regardless of the scan rate. In this case, objects are always illuminated on one side, which depends on the orientation of the lighting module. Therefore, various defect patterns appear, depending on the direction, size, and thickness of the defects. Fig.3 (a) shows the artificial defect image acquired using the SL method. The illumination patterns on the surface differ depending on the size, shape, and orientation of the defect. It is difficult to detect all the defects using SL methods when variously shaped defects exist on the surface. On the other hand, a DLSL method consists of one camera module and two lighting modules. The DLSL method is illustrated in Fig.1 (b). The two lighting modules are set up opposite each other on either side of the object, and each lighting module has an inverted form of on off cycle depending on the scan rate. Therefore, odd scan lines are illuminated in lighting module 1 and even scan lines are illuminated in lighting module 2. Because the two lighting modules are set up opposite each other, as shown in Fig.2 (b), the appearance of a normal surface does not change, as compared to when single lighting methods are used. However, when the surface is lumpy, a black and white pattern appears. Fig.3 (b) shows artificial defect images acquired using the DLSL method. The defect areas manifest the black and white pattern regardless of the shape, orientation, and size of the defects. Therefore, when the DLSL method is used, the detection problems related to the various shapes of a defect can easily be solved by finding the black and white pattern region.

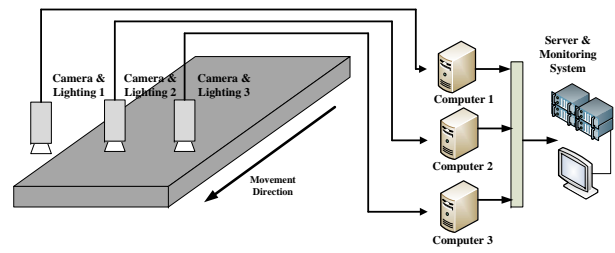


Fig. 4. Surface-defect detection system

B. System Configuration & Image Analysis

In order to inspect upper surfaces of steel slab, three camera and lighting module (dual-lighting) are used. Surface image is obtained from frame grabber connected to camera, and three computers process each image independently for defect detection. The resolution of one frame images is 2048×1000 pixels, the resolution of line-scan camera used in this system is 0.25 mm per line. Fig.5 shows the image of a slab surface obtained using Surface-defect Detection System. The slab image (Fig.5 (a)) show the vertical crack defect which is our target of defect detection. The vertical crack defects are generated along the rolling direction. Fig.5 (b) show the sectional view of vertical crack. The vertical crack is dented defect and center region of defect has deep crack. Therefore, defect region is represented black and white pattern because the image was acquired DLSL method.

The original image $f(x,y)$ can divide the odd and even image by follows step:

$$f_o(x,y) = \sum_{k=1}^{500} f(x,2k-1) \quad (1)$$

$$f_e(x,y) = \sum_{k=1}^{500} f(x,2k) \quad (2)$$

where $f_o(x,y)$ is illuminated in lighting module 1 and $f_e(x,y)$ is illuminated in lighting module 2. Fig 6 shows the

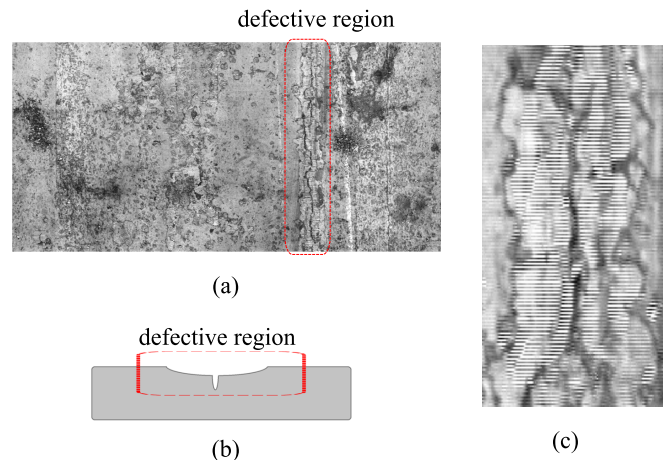


Fig. 5. Slab images: (a) image of slab surface with vertical cracks, (b) The sectional view of vertical crack, (c) image of a vertical crack defect, which is the partially enlarged image.

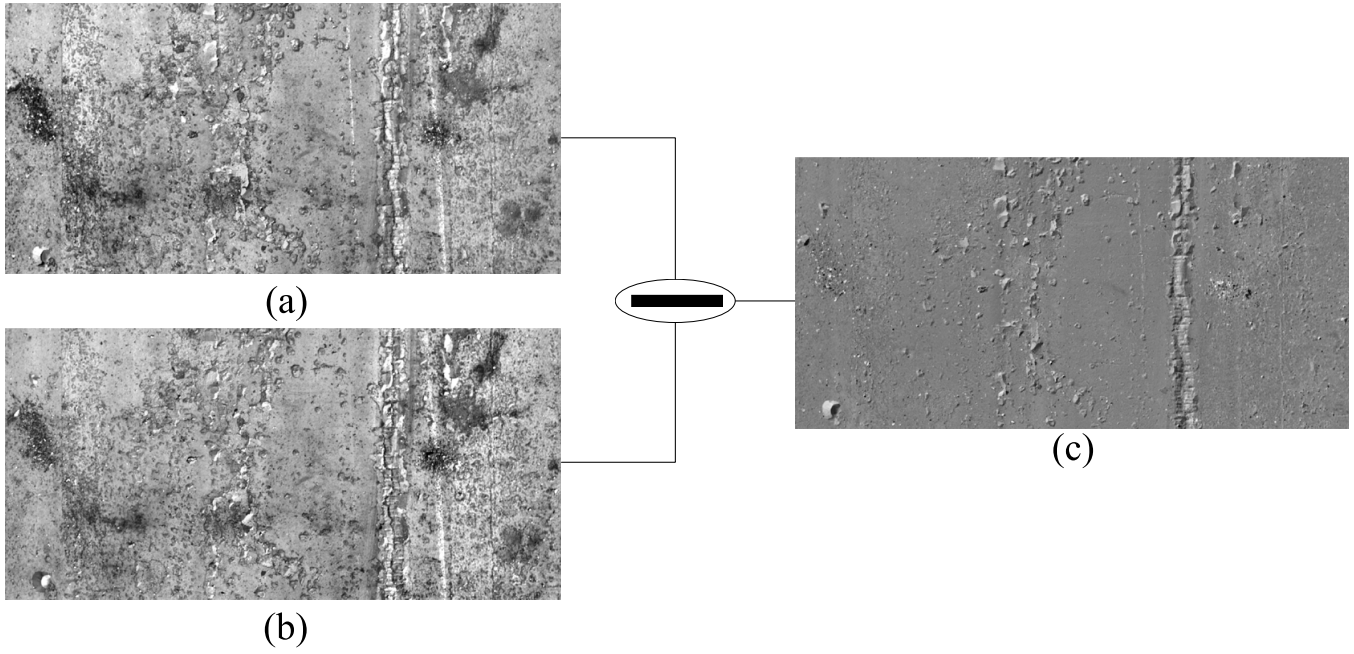


Fig. 6. Slab images: (a) odd image with vertical cracks; (b) even image with vertical cracks; (c) difference image with vertical cracks

odd and even image. The odd and even images have inverted gray pattern when the surface is lumpy. Also, difference image is calculated as follows:

$$f_d(x, y) = f_o(x, y) - f_e(x, y) \quad (3)$$

Fig.6 (c) shows the difference image. The difference image represented the difference value of odd image and even image. Because the normal surface has same value on odd and even line, the difference value is nearly zero. However, lumpy region has inverted gray value on odd and even line. Therefore, $f_d(x, y)$ has value only lumpy surface region including vertical cracks.

C. Pattern Extraction with Gabor Filtering

Gabor filters have been widely used in image processing. An important property of Gabor filters is that they achieve the maximum possible joint localization or resolution in both the spatial and spatial-frequency domain [16]. The general form of the real part of a 2-D Gabor function $g(x, y)$ is expressed as

$$g(x, y) = \exp \left[-\frac{1}{2} \left\{ \left(\frac{x'}{\sigma_x} \right)^2 + \left(\frac{y'}{\sigma_y} \right)^2 \right\} \right] \cos(2\pi f x') \quad (4)$$

where

$$\begin{aligned} x' &= x \cos \theta + y \sin \theta \\ y' &= -x \sin \theta + y \cos \theta \end{aligned}$$

The two-dimensional Gabor function has four parameters: $f, \theta, \sigma_x,$ and σ_y . f is the frequency of cosine wave, θ is filter

direction, σ_x and σ_y are standard deviation of Gaussian along the x and y axes [17].

For a given input original image $f(x, y)$, the image $R(x, y)$ is obtained by using Gabor filter $g(x, y)$:

$$\begin{aligned} R(x, y) &= g(x, y) * f(x, y) \\ &= \sum_{m=0}^{M-1} \sum_{n=0}^{N-1} g(m, n) f(x - m, y - n) \end{aligned} \quad (5)$$

where $*$ denotes the 2D convolution, and M and N are the size of the gabor filter mask. The energy of the filtered image, $E(x, y)$, is calculated by the square nonlinear operator $|\cdot|^2$:

$$E(x, y) = R^2(x, y) \quad (6)$$

The defective regions have a gray pattern when DLSL is used. Therefore, the parameters were chosen on the basis of the gray pattern. Fig.7 shows the input image with the vertical crack and gabor filtered output image. The gabor filter reduces the influence of lighting condition and amplifies the gray pattern of the defective region. Using the energy of the gabor filtered image, we performed a binarization process to obtain the region of interest (ROI) which is candidate of vertical cracks. The threshold value was calculated adaptively using second-order statistics:

$$T = \text{mean}[E(x, y)] + \alpha \times \text{std}[E(x, y)] \quad (7)$$

where $E(x, y)$ is the gabor energy image and α indicate the weighting factors calculated by the experiment. The binarization image is calculated using the thresholding method as follows:

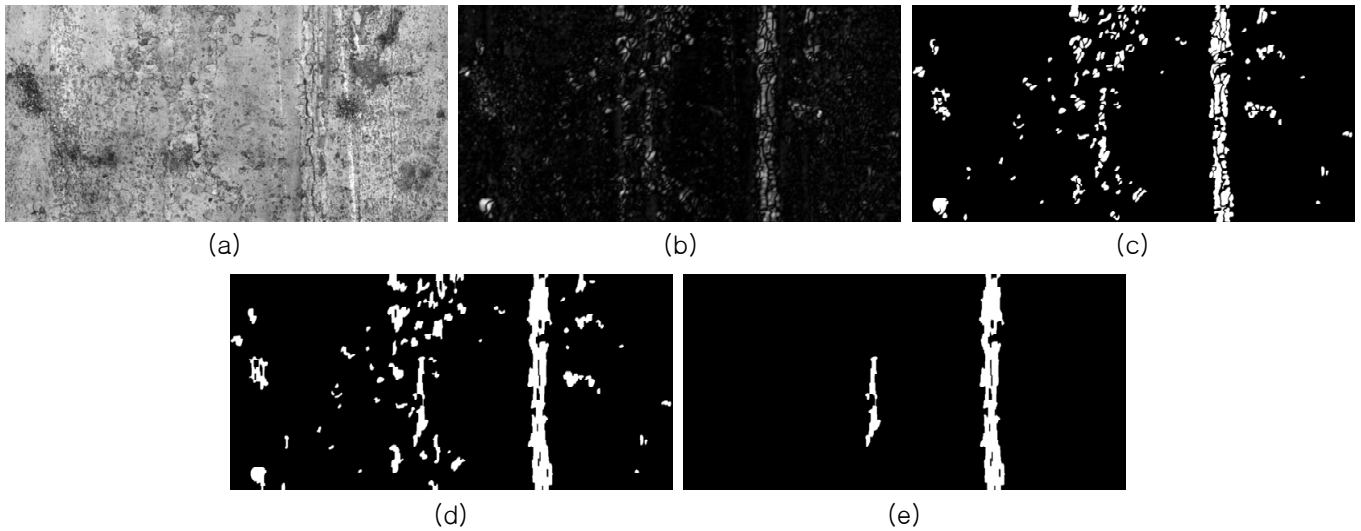


Fig. 7. Slab image containing vertical crack as each step: (a) original image; (b) gabor filtered image; (c) binary image with threshold; (d) binary image with close operation; (e) result of defect candidates after size and orientation filtering

$$b(x, y) = \begin{cases} 1, & E(x, y) > T \\ 0, & \text{otherwise} \end{cases} \quad (8)$$

After binarization, the close operation is used to connect the adjacent blobs. And, small and unnecessary blobs are eliminated by using orientation and size filtering. By eliminating unnecessary defect candidate, detection accuracy can be increased. Finally, ROI are selected from the remaining blobs.

D. Pair Detection & Path Cost Criteria

Although gabor filtering and binarization processes reduced the pseudo defect, the influences of pseudo-defects remained. Fig.8 shows the ROI of vertical defects and pseudo-defects. To distinguished vertical cracks form pseudo-defects, we propose the pair detection and path cost criteria. Fig.5 (b) shows the sectional view of vertical crack. The vertical crack is dented defect. Moreover, center region of defect has deep crack.

However, pseudo-defect such as scales are protruding form of slab surface. Because the odd and even image are represented lighting module1 and lighting module 2, respectively. Therefore, the difference image have the different gray pattern between vertical cracks and scale (Fig.8).

1) *Pair Detection*: Because the vertical crack is dented defect, the left boundary region of a vertical defect has dark gray value and the right boundary region of a vertical defects has bright gray value in difference image $f_d(x, y)$. However, the scale is protruding form of surface. Therefore, scale has inverted gray pattern compare to vertical defects. Fig.10 shows the step-by-step image. To find the bright and dark region, ROI in difference image is used. To enhance the vertical property, vertical smoothing operation applied on difference image. The bright and dark region are calculated as follow:

$$PN(x, y) = \begin{cases} 1, & \bar{f}_{di}(x, y) > T_{high} \\ -1, & \bar{f}_{di}(x, y) < T_{low} \end{cases} \quad (9)$$

where, $\bar{f}_{di}(x, y)$ is smoothed image in ROI. Because the

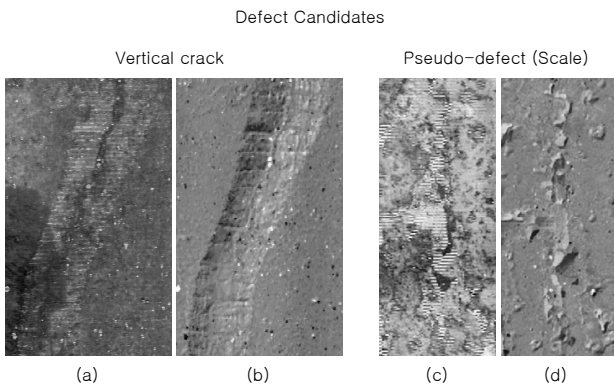


Fig. 8. Defect candidate images : (a) and (c) are original image of vertical crack and scale, respectively; (b) and (d) are difference image of vertical crack and scale, respectively.

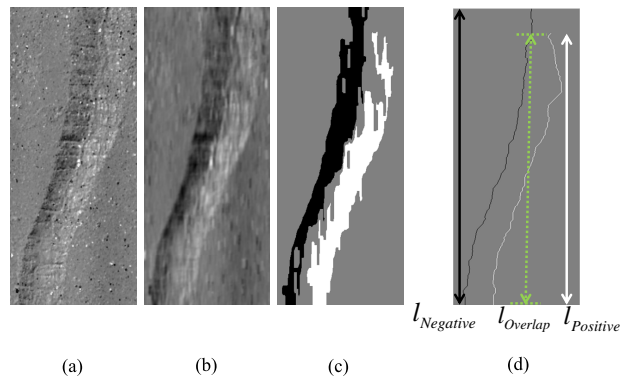


Fig. 9. Step wise result of the pair detection: (a) Defect candidate region in difference image, (b) smoothed image, (c) multi-shreshold image, (d) skeleton image

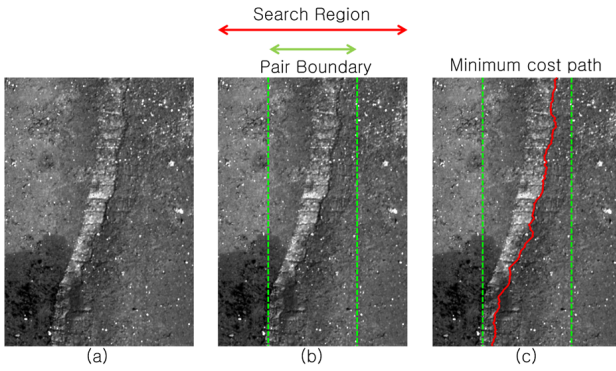


Fig. 10. DP path in vertical region: (a) odd image in vertical region, (b) pair boundary and search region define, (c) minimum cost path.

region of vertical crack is dented defect, $PN(x, y)$ has -1 to 1 horizontal edge pairs. Moreover, vertical crack has strong edge pair. The pair detection criteria is defined as follow:

$$L_{ratio} = \frac{2 \times l_{overlap}}{l_{positive} + l_{negative}} \quad (10)$$

2) *Path Cost*: The vertical crack has deep cracks in center region (Fig.5). The center crack has low gray value because the lighting conditions and shape of cracks. Because the center crack region is lower than that of surrounding regions, the path tracking is good criteria for detecting vertical cracks. To find the best path (minimum cost) in candidate region, we applied Dynamic programming (DP). DP is an optimization method that is based on the principle of optimality in multistage decision making [18]. Because the deep crack is always in the center of vertical defects, the minimum path is must be bounded in pair boundary region. Moreover, the crack region has low gray values, the minimum cost has low cost value. Therefore, these properties good criterias for distinguish the defect from pseudo-defects. Fig.?? shows the result of minimum cost path.

III. EXPERIMENT AND CONCLUSION

In this section, we present the result of our experiments to evaluate the performance of the proposed algorithm. To evaluate the performance of the proposed algorithm, we applied the algorithm to images of hot-slabs, which were acquired directly from an actual production line. A total of 318 slab images were used to evaluate the performance of the proposed algorithm. The number of defective images was 57. The number of normal images was 261. The results of this experiment are summarized in Table I. We have installed the algorithm with $\alpha = 3$. The parameters of the Gabor filter, f, σ_x, σ_y , and θ were 1/2, 7, 7, and 90 respectively. The $L_{ratio} > 0.5$

TABLE I
EXPERIMENTAL RESULTS WITH THE PROPOSED DEFECT DETECTION ALGORITHM.

	Defect	Normal
Success	52	255
Failure	5	6
Accuracy	91.23 % (52/57)	97.70 % (255/261)

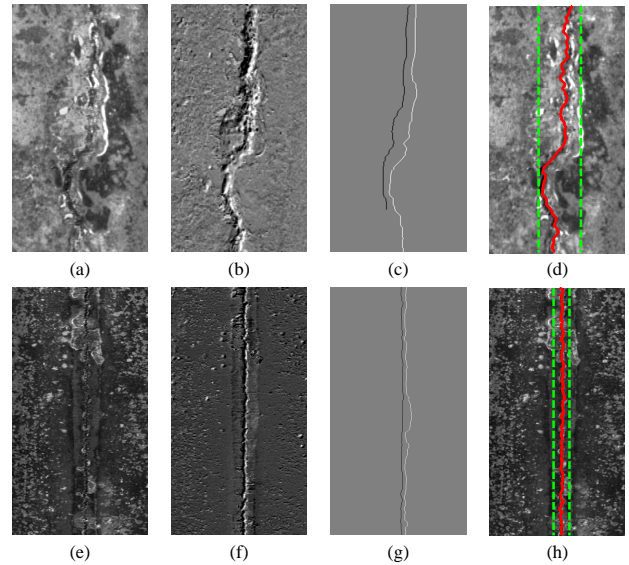


Fig. 11. Slab images containing vertical cracks at each step: (a) and (e) are surface image, (b) and (f) are difference image, (c) and (g) are pair detection result, (d) and (h) are minimum cost path.

and minimum path cost < 70. The results for vertical crack detection are shown in Fig.11. The proposed algorithm had a 91.23% (52/57) accuracy for the detection of the vertical cracks, and the false positives were 2.3 % (6/261).

In this study, we have developed an detection algorithm to detect vertical cracks in hot-slab images. The hot-slab surface was partially covered with scales, and its features making defect detection difficult. To solve these problems, we adopted DLSL method and pattern extracted using gabor filtering. To distinguish the vertical defects from pseudo-defects such as scale, pair detection and path cost criteria are used. The proposed algorithm based on DLSL and gabor filtering enabled a sufficient detection ratio of vertical cracks. The experimental results showed that the proposed algorithm was effective and suitable for the detection of corner cracks in the scalecovered surfaces of hot-slabs.

ACKNOWLEDGMENT

“This research was supported by the MSIP(Ministry of Science, ICT & Future Planning), Korea, under IT/SW Creative research program supervised by the NIPA(National IT Industry Promotion Agency)” (NIPA-2013-H0502-13-1109).

REFERENCES

- [1] K. D. Schnelle and S. H. Mah, “Product Quality Management Using a Real-time Expert System,” *ISIJ Int.*, Vol. 34, No. 10, 1994, pp. 815–821.
- [2] K. Wilttschi, A. Pinz, and T. Lindeberg, “An automatic assessment scheme for steel quality inspection,” *Mach. Vision Appl.*, Vol. 12, 2000, pp. 113–128.
- [3] R. Noll, H. Bette, A. Brysch, M. Kraushaar, I. Mönch, L. Peter, V. Sturm, “Laser-induced breakdown spectrometry—applications for production control and quality assurance in the steel industry,” *Spectrochim. Acta, Part B*, Vol. 56, 2001, pp. 637–649.
- [4] J. P. Yun, S. H. Choi, Y. J. Jeon, D. C. Choi, and S. W. Kim, “Detection of Line Defects in Steel Billets Using Undecimated Wavelet Transform,” in *Proc. Int. Conf. Control and Autom. Syst.*, 2008, pp. 1725–1728

- [5] B. R. Suresh, R. A. Fundakowski, T. S. Levitt, and J. E. Overland, "Real-time automated visual inspection system for hot steel slabs," *IEEE Trans. Pattern Anal. Mach. Intell.* Vol. PAMI-5, No. 6, 1983, pp. 563–572.
- [6] D. B. Perng, C. C. Chou, and S. M. Lee, "Illumination system for wire bonding inspection," *Appl. Opt.*, Vol. 46, No. 6, 2007, pp. 845–854.
- [7] M. Ralló, M. S. Millán, and J. Escofet, "Referenceless segmentation of flaws in woven fabrics," *Appl. Opt.*, Vol. 46, No. 27, 2007, pp. 6688–6699.
- [8] H. I. Shafeek, E. S. Gadelmawla, A. A. Abdel-Shafy, and I. M. Elewa, "Automatic inspection of gas pipeline welding defects using an expert vision system," *NDT and E Int.*, Vol. 37, 2004, pp. 301–307.
- [9] C. H. Chan and G. K. Pang, "Fabric Defect Detection by Fourier Analysis," *IEEE Trans. Ind. Appl.*, Vol. 36, No. 5, 2000, pp. 1267–1276.
- [10] P. C. Chang, L. Y. Chen, and C. Y. Fan, "A case-based evolutionary model for defect classification of printed circuit board images," *J. Intell. Manuf.*, Vol. 19, 2008, pp. 203–214.
- [11] D. M. Tsai and S. C. Lai, "Defect detection in periodically patterned surfaces using independent component analysis," *Pattern Recognit.*, Vol. 41, 2008, pp. 2812–2832.
- [12] J. P. Yun, Y. J. Jeon, D. C. Choi, and S. W. Kim, "Real-time defect detection of steel wire rods using wavelet filters optimized by univariate dynamic encoding algorithm for searches," *J. Opt. Soc. Am. A*, Vol. 29, No. 5, 2012, pp. 797–807.
- [13] S. Ghorai, A. Mukherjee, M. Gangadaran, and P. K. Dutta, "Automatic Defect Detection on Hot-Rolled Flat Steel Products", *IEEE Trans. Instrum. Meas.*, Vol. 62, No. 3, 2013, pp. 612–621.
- [14] S. G. Ryu, D. C. Choi, Y. J. Jeon, S. J. Lee, J. P. Yun, and S. W. Kim, "Detection of Scarfing Faults on the Edges of Slabs," *ISIJ Int.*, Vol. 54, No. 1, 2014, pp. 112–118.
- [15] R. T. Chin and C. A. Harlow, "Automated visual inspection: A survey," *IEEE Trans. Pattern Anal. Mach. Intell.*, Vol. PAMI-4, No. 6, 1982, pp. 557–573.
- [16] Y. Shu and Z. Tan, "Fabric Defects Automatic Detection Using Gabor Filters," in *Proc. 5th World Congr. Intell. Control Autom.*, 2004, pp. 3378–3380.
- [17] Q. Li, J. You, L. Zhang, and P. Bhattacharya, "A Multiscale Approach to Retinal Vessel Segmentation Using Gabor Filters and Scale Multiplication," in *Proc. IEEE Int. Conf. Syst. Man and Cybern.*, 2006, pp. 3521–3527.
- [18] J. P. Yun, D. C. Choi, Y. J. Jeon, C. H. Park, and S. W. Kim, "Defect inspection system for steel wire rods produced by hot rolling process," *Int. J. Adv. Manuf. Technol.*, Vol. 70, 2014, pp. 1625–1634

Two suboptimal controller parameters tuning approaches for systems with delays: Selected highlights of preliminary studies

Libor Pekař and Roman Prokop

Abstract—This paper is aimed to an overview of preliminary research results on two optimal or rather suboptimal pole-placement-based ideas and procedures for tuning of free real controller parameters for single-input single-output linear time delay systems (TDS). The first one is based on the minimization of the spectral abscissa via advanced iterative direct-search or genetic algorithms such as the Quasi-Continuous Shifting Algorithm (QCSA), the Nelder-Mead (NM) algorithm, the (Extended) Gradient Sampling Algorithm (EGSA) and the Self-Organizing Migration Algorithm (SOMA). The second idea stems from the endeavour to place the dominant (rightmost) poles and zeros of infinite spectra to the prescribed positions in the complex plane, again by the use of shifting and/or optimization algorithms. These desired loci are calculated as a model matching problem such that dominant feedback poles and zeros of a delayed system are forced to be as close as possible to those of a finite-dimensional one with two performance criteria: the maximum overshoot and a time of the overshoot. Eventual controllers' structures are obtained from the algebraic controller design approach in the special ring of quasipolynomial meromorphic functions where the use of the simple negative feedback loop results in a characteristic quasipolynomial instead of polynomial is obtained, which means that the closed loop has an infinite spectrum. Both the procedures are demonstrated on the control of an unstable time delay system by means of Matlab/Simulink environment. Drawbacks as well as opportunities of the methods for the future research are briefly discussed.

Keywords—Algebraic approaches, Minimization, Numerical methods, Parameters optimization, Pole assignment, Time delay.

I. INTRODUCTION

PRACTICALLY applicable and effortless controller design methods for time delay systems (TDS), which are infinite-dimensional, even for linear time-invariant ones, are not easy to be found in the literature, see e.g. [1]-[4]. The same statement can be claimed on tuning of the final control laws; namely, how to set free (selectable) controller parameters. Usually, such controllers have not a standard, say the PID structure, and they can be delayed as well. In some cases,

Manuscript received April 14. The authors kindly appreciate the financial support which was provided by the European Regional Development Fund under the project CEBIA-Tech No. CZ.1.05/2.1.00/03.0089.

Libor Pekař and Roman Prokop are with the Department of Automation and control Engineering, Faculty of Applied Informatics, Tomas Bata University in Zlín, Nad Stráněmi 4511, 760 05 Zlín, Czech Republic (corresponding author's phone: +420 57 603 5261; e-mail: pekar@fai.utb.cz).

there is a possibility to adopt some well known algorithms and approaches from the theory of finite-dimensional systems; however, some ideas are far from to be usable or implementable in engineering practice. Thus, there is a natural effort to develop controller design and tuning procedures for the aforementioned class of systems that are usable and understandable also for non-experts and without an excessive mathematical formulation.

A modern way how to cope with the problem of searching a suitable controller structure, among many others, is based on algebraic parlance and tools like rings and linear equations. The utilization of the ring of stable and proper quasipolynomial meromorphic functions (R_{MS}) meets natural requirements of asymptotical and exponential stability, controller properness, reference tracking, disturbances rejection and it protects the system description from the loss of information [5], [6].

Pole placement or pole assignment controller parameters tuning principles for finite-dimensional systems are well-known and very popular. Since the use of the R_{MS} ring with a simple negative feedback loop for unstable TDS plants results in an infinite-dimensional system, the classical pole placement procedure can not be used here. Pole assignment for controllable TDS has been introduced e.g. in [7], [8] where tunable controller parameters have been set "at once". However, there can emerge a problem of checking the poles dominance that has been partially solved e.g. in [9], [10] by means of the Nyquist criterion and using the Laplace transform domain e.g. in [11]. Another idea has aimed to shift the dominant poles to the left (stable half-plane) as far as possible, i.e. to minimize the spectral abscissa, via the Quasi-Continuous Shifting Algorithm (QCSA) [12], [13] or by using gradient optimization methods, e.g. [14], [15]. There were also attempts to place the dominant poles exactly to the desired positions and, simultaneously, minimize the abscissa of the rest of the spectrum [16] in the state-space representation of TDS. However, these algorithms deal with poles only ignoring closed-loop zeros.

In this paper, selected authors' preliminary results on two possible optimal (or rather suboptimal) pole-placement-based controller parameters tuning approaches for TDS are highlighted and overviewed. One of them modifies and combines the above mentioned spectral abscissa minimization

techniques [17], whereas the second one provides an original and independently proposed idea of continuous placing (shifting) the dominant feedback poles and zeros to the prescribed positions in the accordance to the desired feedback step response overshoot in the parlance of the Laplace transform [18], [19]. Both methodologies are briefly described in this contribution together with some necessary comments on them. The use of them is presented on the setting of parameters of a controller designed for an unstable delayed system in the R_{MS} ring.

Since there can be many possible ways how to improve both the ideas and procedures, some proposals including substrategies and computational aspects are suggested and concisely discussed as well.

II. PRELIMINARIES

Due to the aiming of this paper, the procedure of acquiring the controller structure is insignificant and hence omitted; the reader is referred e.g. to [20] for the algebraic method with the R_{MS} ring (used herein) description. Contrariwise, the delayed reference-to-output transfer function, $G_{RY}(s)$, which appears when dealing with the ring for controller design for unstable TDS, is one of crucial notions here. Notice that a delayed feedback control system may be a result of many other control methods for TDS. It is possible to write

$$G_{RY}(s) = \frac{b(s)}{a(s)} \quad (1)$$

where $a(s)$, $b(s)$ are quasipolynomials in $s \in \mathbb{C}$ of a general form

$$x(s) = s^n + \sum_{i=0}^n \sum_{j=1}^h x_{ij} s^i \exp(-s\eta_{ij}), \eta_{ij} \geq 0, x_{ij} \in \mathbb{R} \quad (2)$$

The denominator $a(s)$ of (1) coincides (in most cases – except for distributed delays) with the so-called characteristic quasipolynomial of the feedback system, the roots of which (i.e. system poles) determine asymptotical stability and many dynamic properties. Zeros, as roots of the numerator $b(s)$, have an important influence on feedback system behavior as well and they are unreasonably ignored in most control design strategies.

The complexity of (1) lies in the fact that if $\exists x_{ij} \neq 0$ for any $\eta_{ij} > 0$, then quasipolynomial (2) has an infinite number of its roots and hence the system dynamics is very complicated to be analyzed or controlled. Naturally, $G_{RY}(s)$ contains free (selectable) controller parameters $\mathbf{K} = \{k_1, k_2, \dots, k_r\} \in \mathbb{R}^r$ which are to be appropriately set. Two ideas of “shaping” dominant parts of these infinite-dimensional spectra of poles Ω_p and/or zeros Ω_z , and hence the quantification of unknown controller parameters, are briefly described in this paper.

The first one aims to get the feedback spectrum (of poles) in \mathbb{C}_0^- , which means to obtain the so-called spectral abscissa

$$\alpha_p(\mathbf{K}) := \max \operatorname{Re} \Omega_p; \quad \Omega_p := \{\sigma_i : M(\sigma_i, \mathbf{K}) = 0\} \quad (3)$$

strictly negative where $M(s, \mathbf{K})$ means the feedback loop characteristic meromorphic function for which usually holds $M(s, \mathbf{K}) = a(s)$, as has been solved e.g. in [12]. However, we are going beyond this basic claim and attempt to solve the optimization problem

$$\min_{\mathbf{K}} \Phi(\mathbf{K}) = \min_{\mathbf{K}} \alpha_p(\mathbf{K}) = \min_{\mathbf{K}} \max \operatorname{Re} \Omega_p \quad (4)$$

The methodology combines the QCSA [12], [13] with the subsequent use of an advanced iterative optimization algorithm, such as the Nelder-Mead (NM) algorithm [21], the (Extended) Gradient Sampling Algorithm [14], [22] and the Self-Organizing Migration Algorithm (SOMA), see e.g. [23].

The second one is based on the desired or ultimate positions of the right-most, i.e. the dominant, feedback poles and zeros. The algorithm stems from the dependence of the maximum relative step response overshoot, the relative dumping factor and the relative time-to-overshoot on the position of poles and zeros of a selected finite-dimensional model, for instance, of the second order. Hence, the goal is to match the dominant region of the feedback spectrum with that of the desired finite-dimensional model. The procedure has been called the Pole-Placement Shifting based controller tuning Algorithm (PPSA) [18], [19]. The method is similar to the one independently derived in [16]; however, there are some crucial differences between them.

III. SUBOPTIMAL TUNING APPROACHES DESCRIPTION

A concise description of both suboptimal pole-placement-like tuning methods follows. Without being exhaustive, only basic outline is provided due to the limited space and the reader is referred to literature for details if necessary.

A. Spectral Abscissa Minimization

Assume, for the simplicity, a TDS of the retarded type (i.e. $\forall x_{nj} = 0$ for all $\eta_{nj} > 0$ in (2)) with the objective function (4). The algorithm in the form of a meta-optimization framework procedure can be summarized as follows.

Algorithm 1.

Input: Objective function $\Phi(\mathbf{K})$.

Step 1: Set the number of moved (controlled) poles $m = 1$, the initial set \mathbf{K}_0 and termination parameters for the QCSA [12], [13].

Step 2: Move m right-most poles to the left-half plane by applying small changes in \mathbf{K} using the QCSA. If necessary, increase m . Stop when the available degrees of freedom in the controller do not allow to further reduce $\Phi(\mathbf{K})$.

Step 3: Select an advanced iterative optimization algorithm minimizing $\Phi(\mathbf{K})$ and its control and termination parameters; namely, one of those mentioned in the previous subchapter.

Step 4: Use the algorithm from Step 3 with from Step 2.

Output: Values of \mathbf{K}_{opt} .

Let us note some facts and our observations about the algorithm. In Step 2, it is possible to use another pole-shifting-based procedure, for instance, as in [24], and to determine positions of the rightmost poles, e.g. by QPmR, see [25]. There are two basic problems with the successive algorithm from Step 4. First, it would be desirable to utilize a metaoptimization idea how to set algorithm run control parameters suitably. Second, the computational complexity of some optimization techniques is enormous mainly due to a high number of the dominant poles determination. For instance, meanwhile the NM algorithm requires approximately 2 or 3 spectrum calculations per iteration, the SOMA requires $O((p-1) \cdot l / \Delta l)$ enumerations where typically $p \approx 10, l / \Delta l \approx 20$ where p stands for the population size, l means the path length and Δl is the discrete step size. It would be desirable to parallelize an existing spectrum-searching procedure and to utilize distributed computations on graphical cards, e.g. Compute Unified Device Architecture (CUDA) or Open Computing Language (OpenCL), or to use a multi-core CPU.

B. PPSA

Let us present a sketch of a particular strategy of the PPSA called ‘‘Poles and Zeros Together’’. Other substrategies requiring specific steps and settings with details can be found in [19]. Nevertheless, some possible substrategies have not been derived and published yet and they will be presented in the future.

Algorithm 2.

Input. Closed-loop reference-to-output transfer function $G_{RY}(s)$.

Step 1. Set the number $n_D = r_D - 1$ of prescribed poles where r_D stands for the number of tunable parameters in $a(s)$.

Step 2. Verify that there exists a non-negative number n_N of prescribed zeros satisfying the requirements $0 \leq n_N < \min(n_D, r - n_D, r_N)$ where r_N is the number of free parameters in $b(s)$. If yes, fix n_N and go to Step 3; otherwise, set $n_D = n_D - 1$. If $r_D > n_D \geq \max\{r - n_D, r_N\}$, go to Step 2; contrariwise, a solution does not exist.

Step 3. Select a stable finite-dimensional model $G_{RY,m}(s) = b_m(s)/a_m(s)$ with $\deg b_m(s) = n_N$, $\deg a_m(s) = n_D$, the unit static gain and desired zeros and poles.

Step 4. Set finite subsets of both the spectra, poles and zeros, into the prescribed positions of $G_{RY,m}(s)$ exactly via the number $n_D + n_N$ parameters from \mathbf{K} while the rests are

chosen arbitrarily. Initialize counters of currently shifted poles n_{sp} and zeros n_{sz} according to the fact whether all the placed poles and/or zeros are dominant. If necessary, go to Step 4 and reset the initial assignment.

Step 5. Shift mutually the number $n_{sp,m}$ and $n_{sz,m}$ of rightmost feedback system poles and zeros, respectively, towards the prescribed locations the number $n_{sp,opt}$ and $n_{sz,opt}$ of poles and zeros, respectively, is pushed to the left along the real axis. If necessary, increase $n_{sp,opt} \Rightarrow n_{sp}$ and/or $n_{sz,opt} \Rightarrow n_{sz}$. If the shifting is no more successful or not possible due to the limitation by r , go to Step 6.

Step 6. If all $n_{sp,m}$ poles and $n_{sz,m}$ zeros in the close neighborhood of the prescribed positions are dominant, the procedure is finished. Otherwise, select a suitable cost function $\Phi(\mathbf{K})$ reflecting the distance of dominant poles and zeros of $G_{RY}(s)$ from prescribed positions and spectral abscissae of both the spectra. Minimize $\Phi(\mathbf{K})$ starting with results from Step 5.

Output. The vector of controller parameters \mathbf{K}_{opt} , $\Omega_{P,opt}$, $\Omega_{Z,opt}$.

Notice that the QCSA enables to use only one parameter for shifting a complex conjugate pair to the left along with the real axis. Let us now present some ideas how to modify, extend or improve the PPSA, regarding computation acceleration, shifting strategies, model selection etc.

Regarding a possible improvement of the PPSA including computation acceleration, model selection, shifting strategies etc. let us present some brief notes. The finite-dimensional matching model is chosen according to the desired maximum overshoot, time-to-overshoot and the relative dumping. The user is free to use other model selection ideas. The initial shifting, convergence and the speed of the PPSA may be improved by the use of other ‘‘approaching’’ strategies of moving the poles (zeros) of the infinite-dimensional model to the prescribed positions. Last but not least other optimization procedures can be utilized in, e.g. modern evolutionary or genetic algorithms, for instance, Particle Swarm Optimization (PSO) with means of the deterministic chaos [26].

A demonstrative example concludes this paper and briefly illustrates the use and results of both tuning algorithms.

IV. ILLUSTRATIVE EXAMPLE SELECTED RESULTS

Control law using the R_{MS} ring for an unstable TDS model of a skater on the swaying bow presented in [27] was derived in [17] resulting in the following closed-loop transfer function

$$G_{RY}(s) = \frac{0.2b_q(s)\exp(-0.4s)}{(s+m_0)^4 a_q(s)}$$

$$b_q(s) = 0.2(s+m_0)^4 \sum_{i=0}^3 q_i s^i + p_0 m_0^4 s^2 (s^2 - \exp(-\vartheta s)) \quad (5)$$

$$a_q(s) = s^2 (s^2 - \exp(-\vartheta s)) (s^3 + \sum_{i=0}^2 p_i s^i) + 0.2 \exp(-0.4s) \sum_{i=0}^3 q_i s^i$$

where the denominator expresses the characteristic quasipolynomial which has obviously two factors, a polynomial and a quasipolynomial one. Since the spectral assignment for the polynomial factor is trivial, the goal is to find seven unknown parameters of the quasipolynomial factor.

A. Spectral Abscissa Minimization

The task can be characterized as follows

$$\mathbf{K}_{opt} = [p_2, p_1, p_0, q_3, q_2, q_1, q_0]^T = \arg \min_{\mathbf{K}} \alpha_p(\mathbf{K})$$

$$= \arg \min_{\mathbf{K}} \left\{ \operatorname{Re} \sigma_i : [a_q(s)]_{s=\sigma_i} = 0 \right\} \quad (6)$$

The initial (unstable) setting $\mathbf{K}_0 = [1, 1, 1, 1, 1, 1, 1]^T$ with $\alpha_p(\mathbf{K}_0) = 0.8492$ using the QCSA yields $\alpha_p(\mathbf{K}_{3305}) = -1.4454$, i.e. the stable one ($\alpha_p < 0$). The best results for particular settings of control parameters for the three methods, namely, EGSA, SOMA and the NM algorithms are compared in the time range in Fig. 1. To sum up, the classical NM algorithm gives a very good result with a significant improvement of $\alpha_p(\mathbf{K})$ and a quite fast calculation. The SOMA provides comparable, yet much slower, results here. The usability of the EGSA is debatable since it has provided fast spectral abscissa improvement; yet subsequent iterations have not brought significantly better outputs.

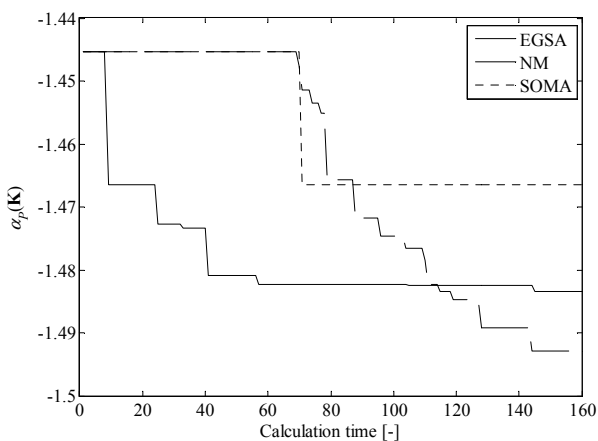


Fig. 1 Evolution of $\alpha_p(\mathbf{K})$ using the NM, EGSA and SOMA in the calculation time range (starting from $i = 3305$ of QCSA)

B. Desired Overshoot – The PPSA

Following Algorithm 2, we can set $n_D = 2$, $n_N = 1$, hence,

consider the model $G_{RY,m}(s) = (b_1 s + b_0) / (s^2 + a_1 s + a_0) = k(s - z_1) / [(s - s_1)(s - \bar{s}_1)]$. It can be derived that for the required relative overshoot $\Delta h_{RY,m,\max} = 0.5$, the relative dumping $\xi_\alpha = 0.5$ and the time-to-overshoot $t_{\max} = 10$ s one has $z_1 = -0.18$ and $s_1 = -0.1 + 0.2j$. Since the initial direct pole placement has not been satisfactory, set $n_{sp} = 2, n_{sz} = 1$ and perform Steps 5-6 of the PPSA by means of the QCSA (see Fig. 2 where evolutions of both abscissae of rests of the spectra are displayed) followed by the use of the SOMA for the cost function $\Phi(\mathbf{K}) = |\sigma_1 - s_1| + |\zeta_1 - z_1| + 0.01\alpha_{r,p}(\mathbf{K}) + 0.01\alpha_{r,z}(\mathbf{K})$ where $\alpha_{r,p}(\mathbf{K})$ means the spectral abscissa of the rest of poles except the dominant pair, $\alpha_{r,z}(\mathbf{K})$ has the same meaning yet for zeros.

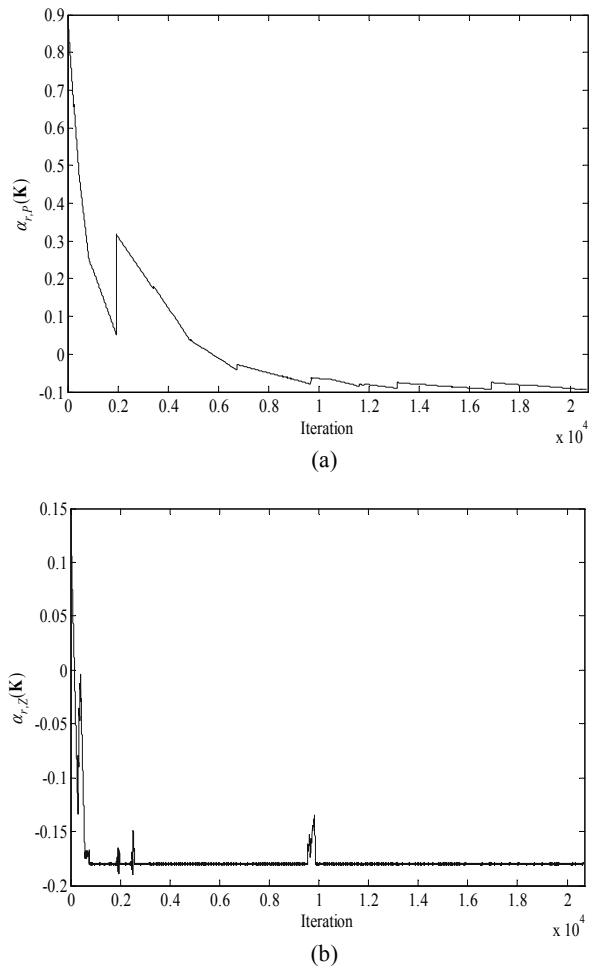


Fig. 2 Evolution of $\alpha_{r,p}(\mathbf{K})$ and $\alpha_{r,z}(\mathbf{K})$ (of rests of both the spectra) using PPSA with the QCSA

Note that SOMA provides only a slightly improvement resulting in the final spectra and the parameters set as

$$\begin{aligned}\Omega_{P,opt} &= \left\{ \begin{array}{l} -0.1158 \pm 0.0674j, -0.1161 \pm 5.1163j, \\ -0.1211 \pm 1.2103j, \dots \end{array} \right\} \\ \Omega_{Z,opt} &= \left\{ \begin{array}{l} -0.1801, -0.2247 \pm 0.1032j, -0.7607, \\ -2.817 \pm 8.1939j, \dots \end{array} \right\} \\ \mathbf{K}_{opt} &= \left[\begin{array}{l} 5235.169, 9829.219, 1060.87, 78.2405, 30.9684, \\ 1.763, 947.517 \end{array} \right]^T\end{aligned}\quad (7)$$

However, final poles and zeros positions are quite far from the desired ones, which proves the fact about TDS that the desired spectrum can not be chosen arbitrarily but the “energy” of the system has to be taken into consideration.

V. CONCLUSION

In this sketch paper, two ideas of controller parameters tuning strategies for TDS have been outlined. Controller structures have been found via an algebraic approach in the R_{MS} ring. There can be many ways how to modify and improve them and how to set algorithms’ course parameters which might be the topic of a future research and programming tests.

REFERENCES

- [1] M. Malek-Zavarei and M. Jamshidi, *Time Delay Systems. Analysis, Optimization and Applications*. North-Holland Systems and Control Series vol. 9. Amsterdam: North Holland, 1987.
- [2] H. Górecki, S. Fuksa, P. Grabowski, and A Korytowski, *Analysis and Synthesis of Time Delay Systems*. New York, Wiley, 1989.
- [3] J. J. Loiseau, “Algebraic tools for the control and stabilization of time-delay systems,” *Annual Reviews in Control*, vol. 24, pp. 135-149, 2000.
- [4] J. P. Richard, “Time-delay systems: An overview of some recent advances and open problems,” *Automatica*, vol. 39, no. 10, pp. 1667-1694, 2003.
- [5] P. Zitek and V. Kučera, “Algebraic design of anisochronic controllers for time delay systems,” *Int. J. Control*, vol. 76, no. 16, pp. 905-921, 2003.
- [6] L. Pekař, “A ring for description and control of time-delay systems,” *WSEAS Trans. Systems (Special Issue: Modelling, Identification, Stability, Control and Applications)*, vol. 11, no. 10, pp. 571-585, 2012.
- [7] E. B. Lee and S. H. Zak, “On spectrum placement for linear time invariant delay systems,” *IEEE Trans. Automatic Control*, vol. 27, no. 2, pp. 446-449, 1982.
- [8] P. Zitek and T. Vyhliđal, “Dominant eigenvalue placement for time delay systems,” in *Proc. 5th Portuguese Conf. on Automatic Control (Controlo 2002)*, Aveiro, Portugal, 2002, pp. 605-610.
- [9] Q.-G. Wang, Z. Zhang, K. J. Åström, and L. S. Chek, “Guaranteed dominant pole placement with PID controllers,” *J. Process Control*, vol. 19, no. 2, pp. 349-352, 2009.
- [10] P. Zitek, J. Fišer, and T. Vyhliđal, “Ultimate-frequency based dominant pole placement,” in *Proc. 9th IFAC Workshop on Time Delay Systems (TDS 2010)*, Prague, 2010, pp. 87-92.
- [11] M. Vítěčková and A. Vítěček, “2DOF PI and PID controllers tuning,” *Proc. 9th IFAC Workshop on Time Delay Systems (TDS 2010)*, Prague, 2010, pp. 343-348.
- [12] W. Michiels, K. Engelborghs, P. Vansevevant, and D. Roose, “Continuous pole placement for delay equations,” *Automatica*, vol. 38, no. 5, pp. 747-761, 2002.
- [13] W. Michiels and T. Vyhliđal, “An eigenvalue based approach for the stabilization of linear time-delay systems of neutral type,” *Automatica*, vol. 41, no. 6, pp. 991-998, 2005.
- [14] T. Vanbiervliet, K. Verheyden, W. Michiels, and S. Vandewalle, “A nonsmooth optimization approach for the stabilization of time-delay systems,” *ESIAM: Control, Optimisation and Calculus of Variations*, vol. 14, no. 3, pp. 478-493, 2008.
- [15] T. Vyhliđal, W. Michiels, and P. McGahan, “Synthesis of a strongly stable state-derivative controller for a time delay system using constrained nonsmooth optimization,” *IMA J. Math. Control and Information*, vol. 27, no. 4, pp. 437-455, 2010.
- [16] W. Michiels, T. Vyhliđal, and P. Zitek, “Control design for time-delay systems based on quasi-direct pole placement,” *J. Process Control*, vol. 20, no 3, pp. 337-343, 2010.
- [17] L. Pekař and R. Prokop, “Algebraic optimal control in RMS ring: A case study,” *Int. J. Math. Computers in Simul.*, vol. 7, no. 1, pp. 59-68, 2013.
- [18] L. Pekař, “On a controller parameterization for infinite-dimensional feedback systems based on the desired overshoot,” *WSEAS Trans. Systems*, vol. 12, no. 6, pp. 325-335, 2013.
- [19] L. Pekař and P. Navrátil, “PPSA: A tool for suboptimal control of time delay systems – revision and open tasks,” in *3rd Computer Science Online Conference (CSOC 2014)*, to be published, 2014.
- [20] L. Pekař and P. Valenta, “Robust control of a laboratory circuit thermal plant,” *Int. J. Math. Models and Methods in Appl. Sciences*, vol. 7, no. 3, pp. 311-319, 2013.
- [21] J. A. Nelder and R. Mead, “A simplex method for function minimization,” *The Computer J.*, vol. 7, no. 4, pp. 308-313, 1965.
- [22] J. Burke, A. Lewis, and M. Overton, “A robust gradient sampling algorithm for nonsmooth, nonconvex optimization,” *SIAM J. Optim.*, vol. 15, no. 3, pp. 751-779, 2005.
- [23] I. Zelinka, “SOMA-self organizing migrating algorithm,” in *New Optimization Techniques in Engineering*, G. C. Onwobolu, and B. V. Babu, Eds. Berlin: Springer, 2004, pp. 167-217.
- [24] T. Vyhliđal, “Analysis and synthesis of time delay system spectrum,” Ph.D. dissertation, Faculty of Mechanical Engineering, Czech Technical University in Prague, Prague, 2003.
- [25] T. Vyhliđal and P. Zitek, “QPmR - Quasi-Polynomial Root-Finder: Algorithm update and examples,” in *Delay Systems: From Theory to Numerics and Applications*, T. Vyhliđal, J.-F. Lafay, and R. Sipahi, Eds., New York: Springer, 2014, pp. 299-312.
- [26] M. Pluháček, R. Šenkeřík, D. Davendra, Z. Komínková Oplatková, and I. Zelinka, “On the behavior and performance of chaos driven PSO algorithm with inertia weight,” *Comp. Math. Appl.*, vol. 66, no. 2, pp. 122-134, 2013.
- [27] P. Zitek, V. Kučera, and T. Vyhliđal, “Meromorphic observer-based pole assignment in time delay systems,” *Kybernetika*, vol. 44, no. 5, pp. 633-648, 2008.

Belonging Probability Inverse Image Technique to Early Detection of Volcanic Eruption

B. Yagoubi, S. Benkraouda, A. Bouziane

Abstract-- In this work, we present a method based on the inverse of the belonging probability matrix image to detect early volcano eruption from a satellite image in the Thermal Infra-Red(TIR) spectral band. In segmenting each image matrix line into very small intervals and assuming that the pixels are statistically independent, we have obtained stationary and ergodic segments. As a result we have found that a Gaussian stationary noise is the most appropriate mathematical model to represent accurately each of these segments. We have determined the parameters of this Gaussian model for each interval of a satellite image without any sign of eruption so that when an eruption takes place in this image zone, we can use these Gaussian parameters to estimate its belonging probability to the previous original image without eruption. This probability is thought of as being very small since the eruption, in a large area, is deemed a rare event. So instead of direct observation of the satellite image, we suggest to use a matrix image of the belonging probability inverse of each interval to detect an early eruption.

Keywords— Volcano eruption, satellite image, inverse of the belonging probability matrix image technique, Thermal Infra-Red (TIR) spectral band.

I. INTRODUCTION

Volcanic eruptions are one of the most important factors that affect the earth ecosystem and contribute to the global transformation [1,..., 6]. Its early detection is, therefore, very important in order to study and make some predictions concerning the evolution of the volcano. Observations are usually performed by satellite and in this case, methods based mainly on radiometric analysis of the satellite image in the Thermal Infra-Red (TIR) spectral domain have been suggested to improve early detection of an eruption. Many algorithms based on statistical method have been proposed for detection by satellite image, and among which, worthy of mention are those applied to fire forest detection by Lafarge et al [7]. Some difficulties, particularly, in their implementation and processing may, however, hamper their performances. Therefore we suggest in this work a simple technique based on the belonging probability of a rare event to a Gaussian realization using the matrix line by line processing. In order to

This work was financially supported by the Algerian government.

B. Yagoubi is with the Laboratory of signals and systems, Faculty of sciences and technology, Abdel Hamid Ibn Badis, Mostaganem, Algeria (e-mail: yagoubibenabdellah@yahoo.com).

S. Benkraouda is with the Laboratory of signals and systems, Faculty of sciences and technology, Abdel Hamid Ibn Badis, Mostaganem, Algeria T.

A. Bouziane is with the Laboratory of signals and systems, Faculty of sciences and technology, Abdel Hamid Ibn Badis, Mostaganem, Algeria.

carry out any kind of mono dimensional processing, the image should be represented by a classic mono-dimensional model, and consequently we can make use of all mathematical analysis techniques of the mono-dimensional signals which are well abundant in the literature.

II. MATERIAL AND METHODS

The image of the erupting Mt. Usu volcano [8] in Hokkaido, Japan shown in figure.1 was captured on April 3, 2000 by Advanced Space borne Thermal Emission and Reflection Radiometer (ASTER) (resolution 90m)[9] carried by the polar orbiting satellite TERRA (NASA), and is being used for assessing the efficiency of our proposed technique for eruption detection. The free software Scilab5.3.3 image toolbox was used to perform the image processing.

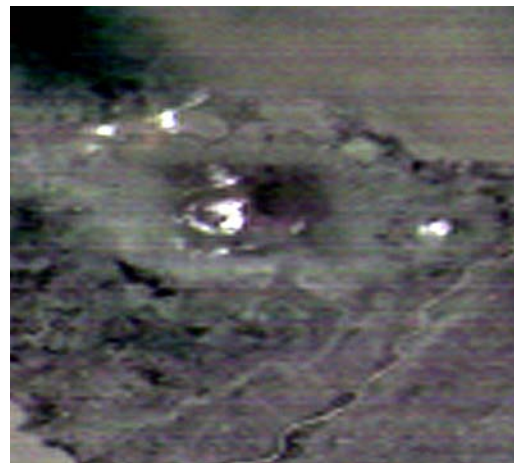


Fig. 1. Thermal Infrared satellite image of the same volcano zone as in (fig. 2a), but with eruption. Available at.[8].

The belonging probability method to detect early eruption was first applied to forest fires detection by Benkraouda et al[10] and is reviewed here as follows;

- 1-Determine the mean value M of the image matrix of the volcano region with no eruption.
- 2-Segment each line of this matrix into small segments and compute their variances using the image matrix mean value M and model each interval as a Gaussian model.
- 3-Assume any pixel with intensity less than 70% of the maximum intensity to be equal 99% M to avoid false alarm.
- 4-When an eruption occurs in this volcano zone, use these previously estimated Gaussian parameters for the image without eruption to calculate the inverse of the belonging probability of each interval to belong to this region.

5-Arrange the inverses of these probabilities in a matrix form as their corresponding intervals in order to observe them as an image for a quick detection.

III. RESULTS AND DISCUSSION

III.1. THE MODEL OF THE IMAGE WITHOUT ERUPTION.

To look for an appropriate model for the original image without eruption (fig.2a), we have processed it line by line so that the simple one-dimensional signal processing tools can be used. We have, therefore, segmented each matrix line into small stationary intervals. In addition, we have considered the pixels as statistically independent in order to represent each of these intervals by a Gaussian white noise [11,...,16]; In this

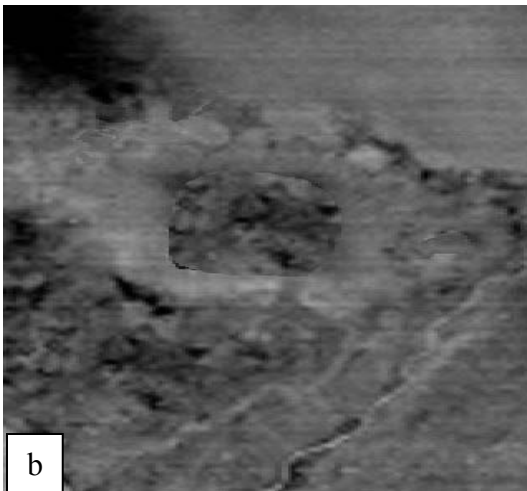


Fig.2. Satellite image of a volcano zone; a) without eruption and b) its reconstructed version with a Gaussian white noise

case the estimated Gaussian parameters; the mean \hat{m}_{in} and the variance $\hat{\sigma}_{in}^2$, for each resulting interval can be computed using the following two expressions respectively

$$\hat{m}_{in} = \frac{1}{L} \sum_{k=l-L}^{l-1} x_{in}(k) \quad (3)$$

$$\hat{\sigma}_{in}^2 = \frac{1}{L} \sum_{k=l-L}^{l-1} (x_{in}(k) - \hat{m}_{in})^2 \quad (4)$$

Where $x_i(l-L), \dots, x_i(l-1)$ are the values of the n^{th} ($n = 1, 2, \dots, N$) interval of the i^{th} ($i = 1, 2, \dots, I$) image matrix line, L is the interval length and $l = n.L$. It can be noticed that the intensity of the pixels representing the image of the zone without eruption (fig.2a) is uniformly distributed. Any pixel value significantly deviated from the mean value M , can be assumed as a rare event. This matrix mean value is, therefore, considered as the intensity threshold above which any pixel is deemed a rare event. Since the Gaussian probability is symmetric with respect to this matrix mean value, two pixels hot and cold may have, however, the same probability. Therefore to get rid of the cold zones and to avoid any false alarm we should, according to Benkraouda et al [10], fix a threshold at around 70% of the maximum grey level below which all the pixels are deemed equal to 99% of the matrix mean value. The latter is expressed as

$$M = \frac{1}{\mathbf{I}\mathbf{J}} \sum_{i=1}^{\mathbf{I}} \sum_{j=1}^{\mathbf{J}} x(i, j) \quad (5)$$

Where $x(i, j)$ is the intensity of the pixel (i, j) .

Replacing \hat{m}_{in} by (5) in the expression (4) of the variance for each interval, we obtain

$$\hat{\sigma}_{in}^2 = \frac{1}{L} \sum_{k=l-L}^{l-1} (x_{in}(k) - M)^2 \quad (6) \text{ Carlos}$$

The corresponding reconstructed image using the Gaussian white noise model is shown in figure (2b). In comparing this image to its original version (fig.2a), we can see that the latter is well represented by the proposed Gaussian white noise. The estimated variances and means of the adequate GWN model of the image without eruption for each interval were saved in order to use them to compute the Gaussian belonging probability of any rare event, such as an eruption, to belong to the image without eruption.

III. 2 .The inverse of the belonging probability technique for the eruption detection.

The same volcano zone after eruption has taken place is shown in figure (1). It can be seen that the belonging probability of the eruption is obviously smaller than that of the background of the satellite image. The corresponding matrix \mathbf{X} of the

image with eruption, and in which we have shown an example of a L samples of the first segment of the first matrix line, may be expressed as follows

$$\mathbf{x} = \begin{bmatrix} \underbrace{x_1(0) \ x_1(1) \dots x_1(L-1) \dots x_1(N.L-1)}_{L \text{ samples}} \\ x_2(0) \ x_2(1) \dots x_2(N.L-1) \\ \dots \\ x_I(0) \ x_I(1) \dots x_I(N.L-1) \end{bmatrix}$$

The belonging probability matrix \mathbf{P} of these intervals to the Gaussian model representing the image without eruption can be computed using the Gaussian parameters previously, estimated, hence,

$$\mathbf{P} = \begin{bmatrix} P_{11} & P_{12} & \dots & P_{1N} \\ P_{21} & P_{22} & \dots & P_{2N} \\ \dots & \dots & \dots & \dots \\ P_{I1} & P_{I2} & \dots & P_{IN} \end{bmatrix}$$

The smallest probability corresponds, obviously, to the eruption since it is considered as rare event. So by inverting these probabilities, the smallest values become the highest, thus the eruption will appear with higher intensity in the image

of the inverse of the belonging probability $\frac{1}{\mathbf{P}}$ as shown in figure (3a) in two dimensions and in figure (3b) in three dimensions.

$$\frac{1}{\mathbf{P}} = \begin{bmatrix} \frac{1}{P_{11}} & \frac{1}{P_{12}} & \dots & \frac{1}{P_{1N}} \\ \frac{1}{P_{21}} & \frac{1}{P_{22}} & \dots & \frac{1}{P_{2N}} \\ \dots & \dots & \dots & \dots \\ \frac{1}{P_{I1}} & \frac{1}{P_{I2}} & \dots & \frac{1}{P_{IN}} \end{bmatrix}$$

The inverse of belonging probability procedure allows the eruptions to appear with higher intensity in figure (3). This technique acts, thus, as a filter detecting eruptions only. In comparing the real image with eruption (fig.1) to that of the inverse of the belonging probability (fig. 3), we can say that using the inverse of the belonging probability image, we can easily detect early eruption than using direct observation. Both the real satellite image and the inverse of the belonging

probability image can be used to improve the eruption detection.

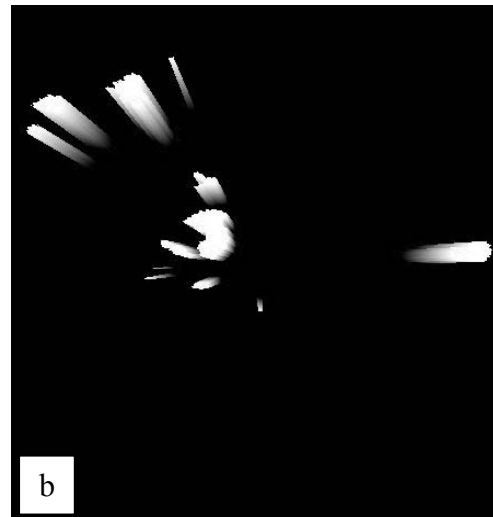
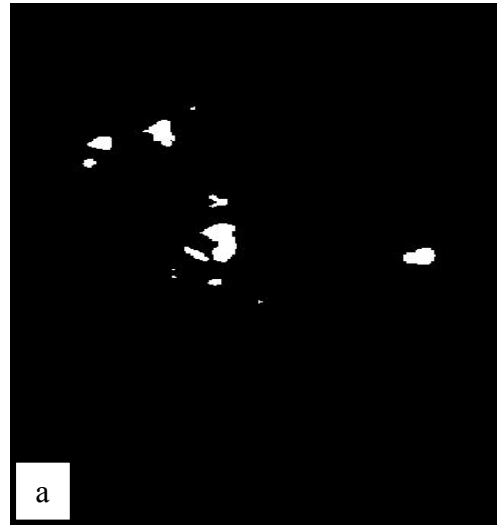


Fig.3. The image of the inverse of the belonging probability $\frac{1}{\mathbf{P}}$; a) in 2D and b) in 3D.

IV. CONCLUSION

We have suggested a method that may help in detecting early eruption by a satellite image observation. The proposed technique of the image of the inverse of the belonging probability matrix $\frac{1}{\mathbf{P}}$ for observing early eruption makes the smaller values of the belonging probabilities, such as those of an eruption, to appear with higher intensity in the image. It should be noted, in addition, that an advantage of our method is the storing of a compressed image (Gaussian parameters) instead of storing the whole image of a volcano zone. We believe that this procedure, for detecting early eruptions, can be used to support a direct observation of the real satellite image.

REFERENCES

- [1] I. Kirchner, G. Stenchikov, H.-F. Graf, A. Robock, J. Carlos Antuna, Climate model simulation of winter warming and summer cooling following the 1991 Mount Pinatubo volcanic eruption, *J. Geophys. Res.*, 104, 19,039-19,055, 1999.
- [2] G. Stenchikov, I. Kirchner, A. Robock, Hans-F. Graf, J. Carlos Antuna, R. G. Grainger, Alyn Lambert, and Larry Thomason, 1998: Radiative Forcing from the 1991 Mount Pinatubo volcanic eruption. *J. Geophys Res.* 103(D12), pp. 13837-13857.
- [3] B. G. Mason, D. M. Pyle, and C. Oppenheimer, The size and frequency of the largest explosive eruptions on Earth. *Bull. Volcanol.* 66, 735–748 (2004).
- [4] N. I. Deligne, S. G. Coles and R. S. J. Sparks, Recurrence rates of large explosive volcanic eruptions. *J. Geophys. Res.* 115, B06203 (2010).
- [5] A. M. Jellinek and D. J. DePaolo, A model for the origin of large silicic magma chambers: Precursors of caldera-forming eruptions. *Bull. Volcanol.* 65, 363–381 (2003).
- [6] S. L. De Silva and W. D. Gosnold, Episodic construction of batholiths: Insights from the spatiotemporal development of an ignimbrite flare-up. *J. Volcanol. Geotherm. Res.* 167,320–335 (2007).
- [7] F. Lafarge, X. Descombes, J. Zerubia and S. Mathieu, (2007). Forest fire detection based on Gaussian field analysis, European Signal Processing Conference (EUSIP)
- [8] http://gds.aster.ersdac.jspacesystems.or.jp/gds_www2002/gallery_e/image_usu_e/usu_422_e/t101214sub2st414_e.html
- [9] <http://nilerak.hatfieldgroup.com/French/NRAK/EO/html/aster.html>
- [10] S. Benkraouda, B. Yagoubi, M. Rebhi and A. Bouziane., Belonging probability inverse image approach for forestfire detection, *Afr. J. Ecol.* John Wiley & Sons Ltd, 2013
- [11] S.O. Rice, 1945. Mathematical analysis of random noise., *Bell System Tech. J.*, 24:46{156).
- [12] T. Hida, and M. Hitsuda, 1993. Gaussian Processes. AMS, Providence.
- [13] Chan, S.C and Zhou. Y., 2010. On the Performance Analysis of a Class of Transform-domain NLMS Algorithms with Gaussian Inputs and Mixture Gaussian Additive Noise Environment *Journal of signal processing systems*, Springerlink, V61.
- [14] K-M. Chang, and Liu. S-Hong., 2010. Gaussian noise filtering from ECG by Wiener filter and ensemble EMD, *Journal of signal processing systems*, Springerlink V61.
- [15] S. Nakamori., 2010. Design of RLS Wiener FIR filter using covariance information in linear discrete-time stochastic systems , *Digital Signal Processing*, Elsevier, p 1310, V.20.
- [16] B Yagoubi, 2011. A geometric approach to a non stationary process., *Proceeding of the 2nd wseas international conference on mathematical models for engineering science (MMES'11)*

Optimization of a batch reactor dimensions

David Novosad, Lubomír Macků and Milan Navrátil

Abstract—The present work describes the dimensions optimization of the fed batch reactor. An evolutionary approach represented by the Self - Organizing Migrating Algorithm (SOMA) was used to find new dimensions and simulate the behaviour of the reactor with these new dimensions. An objective function which was defined considers temperature inside the reactor and the final time of the process. It was found that the reactor geometry characterized by height and diameter plays an important role in its efficiency. The efficiency of a suggested reactor was compared with the reactor previously used for the same process.

Keywords— temperature control, reactor dimensions, online identification, semi-batch reactor, SOMA.

I. INTRODUCTION

EVEN if the problem of the chemical reactors efficiency is quite important and is connected with the reactor dimensions, there are not many studies published about it these days. Usually, the process is placed to existing vessel and then the authors try to control the process with different control techniques. But, the process is often not suitable for the given reactor geometry. Here, the authors are trying different way – to suite the reactor geometry to the exact process – to achieve the best control results.

Some published papers which describe an effect of a reactor size on the process control are mentioned further.

The „performance“ of three bubble column reactors with the same volume but varied geometry (height to diameter ratios – 0.93; 2.04; 3.98) was investigated in [1].

Other paper [2] tries to observe more efficient membrane reactor setups in order to improve production yield. Optimization has been carried out by a differential evolution considering 40 decision variables including dimensions of membrane reactor. The authors concluded that the obtained variables improved the „performance“ of the continuous catalyst regeneration reformer process.

Park et al. [3] developed a 2D mathematical model of a pilot-scale fixed-bed reactor for a Fe-based Fischer-Tropsch synthesis. The developed model clearly showed the effects of the tube diameter on the temperature profiles, in terms of the radial heat transfer area.

Our paper is organized as follows: In section 2, the semi-batch reactor, its structure, mathematical model and the process control are described; section 3 presents simulation results and

section 4 concludes the current work and suggests new areas for investigation.

II. METHODS SECTION

A. The current situation

In past different control techniques were used on fed-batch reactor presented in this paper [4], [5]. In the previous work the goal was to optimize the reactor temperature using two manipulated variables (feeding into the reactor and cooling water temperature) to achieve the shortest possible cycle time of one batch.

This paper describes other achievements obtained by further optimization. The aim was to optimize dimensions of the reactor, i.e. the radius and the height. Default dimensions of the original reactor were: radius: 0.78 m, height: 1.11 m, volume: 2.12 m³, surface: 7.35 m². Finding new dimensions with better parameters is described here. The initial values used by simulations follow: flow of the cooling water – 4.67 kg·s⁻¹, temperature of the cooling water – 274.58 K, temperature of the filter cake – 293.15 K, temperature inside the reactor – 323.15.

B. The mathematical model

The fed-batch reactor process optimization is performed on a data obtained from a real chromium sludge regeneration process. This process is described in previous work [6].

To simulate tanning salts from the chromium sludge regeneration process a mathematical model is used. The reactor has four input signals $\dot{m}_{FK}(t)$, $\dot{m}_V(t)$, $T_{FK}(t)$, $T_{VP}(t)$ and one output signal $T(t)$ (see the Table I). The chemical reactor scheme is shown in Fig. 1.

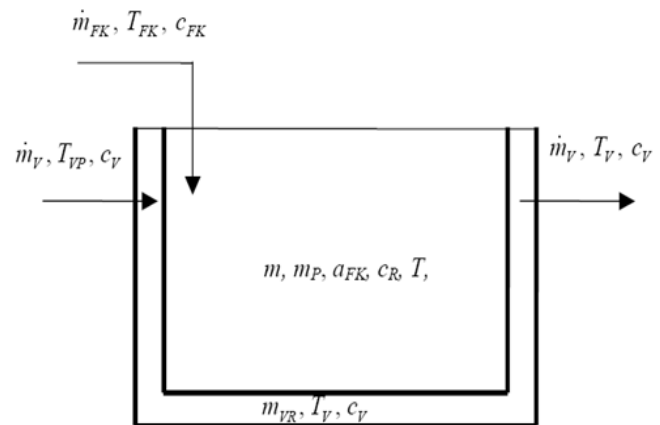


Fig. 1 Chemical reactor scheme

David Novosad, Lubomír Macků, and Milan Navrátil are with the Tomas Bata University in Zlín, Faculty of Applied Informatics, Nad Stranemi 4511, 760 05 Zlín, Czech Republic (phone: 420-775-932-341; e-mail: novosad@fhs.utb.cz)

The fed-batch reactor mathematical model is defined by four differential equations - Eq. (1-4).

$$\dot{m}_{FK} = \frac{d}{dt} m(t) \quad (1)$$

$$\dot{m}_{FK} = k m(t) a_{FK}(t) + \frac{d}{dt} [m(t) a_{FK}(t)] \quad (2)$$

$$\begin{aligned} \dot{m}_{FK} c_{FK} T_{FK} + \Delta H_r k m(t) a_{FK}(t) = \\ = K S [T(t) - T_V(t)] + \frac{d}{dt} [m(t) c_R T(t)] \end{aligned} \quad (3)$$

$$\begin{aligned} \dot{m}_V c_V T_{VP} + K S [T(t) - T_V(t)] = \\ = \dot{m}_V c_V T_V(t) + m_{VR} c_V T_V'(t) \end{aligned} \quad (4)$$

The first equation expresses the total mass balance of the chemical solution in the reactor. The symbol \dot{m}_{FK} [kg.s⁻¹] expresses the mass flow of entering chromium sludge, $\frac{d}{dt} m(t)$ the accumulation of the in-reactor content.

The second equation expresses the chromium sludge mass balance. The input is \dot{m}_{FK} [kg.s⁻¹] again, the accumulation is $m(t) \frac{d}{dt} a_{FK}(t)$ and the express $k m(t) a_{FK}(t)$ means the chromium sludge extinction by the chemical reaction. Symbol k [s⁻¹] means reaction rate constant expressed by an Arrhenius equation (5).

$$k = A e^{-\frac{E}{RT[t]}} \quad (5)$$

The Arrhenius equation parameters are important for the process control, especially for the process safety as is described in [7]. All reactor variables and parameters are given in Table I.

Meaning of the individual terms: $a_{FK}[t]$ means mass fraction of chromium sludge in the chemical reactor, $m[t]$ weight of reaction components in the reactor.

The third equation describes enthalpy balance. The reactor input heat is expressed by $\dot{m}_{FK} c_{FK} T_{FK}$, the heat rising from the chemical reaction is $\Delta H_r k m(t) a_{FK}(t)$, the reactor wall heat transmission is $K S (T[t] - T_V[t])$ and the accumulated heat inside the reactor is described by $m(t) c_R \frac{d}{dt} T(t)$. The last equation describes a coolant balance. The coolant input heat is expressed by, $\dot{m}_V c_V T_{VP}$ the heat entering the coolant from the reactor by the reactor wall is $K S (T[t] - T_V[t])$, the heat going out with the coolant is $\dot{m}_V c_V T_V[t]$ and the heat accumulated in the double wall coolant expresses $m_{VR} c_V \frac{d}{dt} T_V(t)$. This model cannot be solved by analytical means. It is necessary to use numerical methods – the Matlab and Mathematica software were used for this task.

Table I - Variables and parameters of the reactor model.

(1)	\dot{m}_{FK} [kg.s ⁻¹]	Mass flow of the entering chromium sludge
	$m(t)$ [kg.s ⁻¹]	Accumulation of the in-reactor content
(2)	$a_{FK}(t)$ [-]	Mass concentration of the chromium sludge
	$m(t)$ [kg]	Weight of the reaction components in the system
	k [s ⁻¹]	The reaction rate constant
(3)	c_{FK} [J.kg ⁻¹ .K ⁻¹]	Chromium sludge specific heat capacity
	c_R [J.kg ⁻¹ .K ⁻¹]	Reactor content specific heat capacity
	T_{FK} [K]	Chromium sludge temperature
	ΔH_r [J.kg ⁻¹]	Reaction heat
	K [J.m ⁻² .K ⁻¹ .s ⁻¹]	Conduction coefficient
	S [m ²]	Heat transfer surface
	$T(t)$ [K]	Temperature of reaction components in the reactor
	$T_V(t)$ [K]	Temperature of coolant in the reactor double wall
(4)	\dot{m}_V [kg.s ⁻¹]	Coolant mass flow
	c_V [J.kg ⁻¹ .K ⁻¹]	Coolant specific heat capacity
	T_{VP} [K]	Input coolant temperature
	m_{VR} [kg]	Coolant mass weight in the reactor double wall
(5)	A [s ⁻¹]	Pre-exponential factor
	E [J.mol ⁻¹]	Activation energy
	R [J.mol ⁻¹ .K ⁻¹]	Gas constant

C. SOMA (Self-Organizing Migrating algorithm)

For the reactor dimensions optimization was defined an objective function. As was said before, the mathematical model has to be solved by numerical means. Because of it, also the objective function had to be solved numerically. To find the objective function minimum a SOMA algorithm was used. SOMA is a stochastic optimization algorithm that is based on the social behavior of cooperating individuals. It can be also classified as an evolutionary algorithm, despite the fact that no new generations of individuals are created during the search. Only the positions of the individuals in the search space are changed during a generation (also called a ‘migration loop’). Individuals are generated by random according to what is called ‘specimen of the individual’ principle [8]. SOMA algorithm was chosen for its ability to converge towards the global minimum.

This algorithm tried to find three optimal variables: radius of the reactor, height of the reactor and feeding of chromium sludge. There is no requirement of the constant volume in

contrast to the mentioned work [1]. The only limits are minimum and maximum radius $<0.1 \text{ m}, 6 \text{ m}>$, height $<0.1 \text{ m}, 6 \text{ m}>$ and feeding $<0.01 \text{ kg.s}^{-1}, 3 \text{ kg.s}^{-1}>$.

The main input variables of SOMA were set as follows: **Step**, indicates the size of a migration step is chosen to be 0.3, **PRT**, perturbation parameter modifies the movement vector of an individual to the leader (0.1), **NP**, number of individuals in population is chosen to be equal 50, **Migrations**, number of migration cycles is chosen to be 10, **AcceptedError**, the maximum allowed difference between the best and the worst individual in the population (0.1).

III. RESULTS SECTION

In this section, the results obtained by simulations are discussed.

The first simulations were done mainly for the SOMA algorithm adjustment verification. The basic parameters were chosen with regard to the shorter computing time which here only c. 10 minutes. The obtained values were further used for the reactor static optimization. The values obtained by the first simulations can be seen in Table II. The first four columns contain values calculated by SOMA algorithm. Fourth column contains the objective function value. The fifth column shows reactor „performance“ and was received by the reactor static optimization. The „performance“ means how much of filter cake can reactor process per second. The „performance“ is in relationship with the reactor volume. Practically, the „performance“ means that if the new reactor has double volume, an obtained „performance“ number is multiplied by a coefficient 0.5 to compare it with the original volume reactor. Even if the first simulations were done just as a first try, the first calculations showed that the newly found reactor dimensions are more suitable for our process. From the „performance“ point of view the original reactor shows the „performance“ 0.041 kg.s^{-1} , the new average value obtained by simulations was 0.053 kg.s^{-1} . The remaining obtained average values: Objective Function = 16096, Volume = 7.3 m^3 . As was already mentioned, the computing time of each one simulation was c. 10 minutes.

In the second step the settings of SOMA algorithm were changed in order to find more precise reactor parameters. The new parameters allow more accurate computations. Of course, the price is that the computing time will increase. Parameters NP and Migrations were enlarged three times (NP = 150, Migrations = 30). The results are present in Table III. Obtained average values are stated here again to compare the simulations with different SOMA settings: Objective function = 13489, „performance“ = 0.0865 kg.s^{-1} , Volume = 2.35 m^3 . The computing time was c. 70 minutes. As can be seen from the obtained results, the reactor „performance“ has increased again. The average value 0.0865 kg.s^{-1} is better than the average value from the first simulations 0.053 kg.s^{-1} and also than the original value 0.041 kg.s^{-1} .

From the results summarized in Table II and Table III can be observed that two different shapes of the reactor are suitable for the process: large radius with a small height contra

small radius with a large height. Generally, shapes with very large or very low height-to-width ratio showed the best „performance“. This fact is probably related to larger surface which is linked with better cooling of the reactor. Which of these two shapes chose was the task for the third simulations round. The parameter NP was increased here from 150 to 300 for the final decision. The greater NP value means the higher possibility to find a more significant objective function minimum. The results of these simulations can be found in Table IV. The average value of objective function decreased to 12043. However, it cannot be still clearly stated which shape is more appropriate. The SOMA algorithm found three shapes with very high height-to-width ratio and three shapes with very low height-to-width ratio. The increase of NP parameter led again to higher computation time (180 minutes) and also the volume decreased (1.56 m^3).

The best fulfilled „performance“ requirements can be found in the Table III in the first row. As can be seen, the „performance“ 0.208 kg.s^{-1} is five times better than the original reactor. As far as the reactor volume, the new reactor volume is 0.18 m^3 , while the original volume was 2.12 m^3 , i.e. the new volume is approximately 12 times lower. The second reactor dimensions were selected from the Table IV (fifth row) because of the volume 2.29 m^3 which was close to the “original” reactor volume (2.12 m^3). The „performance“ here was still better than the “original” reactor „performance“ (0.093 m^3) and the volume was even bigger.

From the results described in Table III and Table IV two results were selected for the last part of simulations – simulations of the whole process controlled by Ziegler-Nichols controller for the second order process with filtration of D-component (ZN2FD). This controller was already successfully used in one of our previous studies and is described in [9].

IV. CONCLUSION

In previous chapter, the static optimization of the fed-batch chemical reactor is described in detail. As we already mentioned, the best two results were for reactor dimensions with the „performance“ 0.208 kg.s^{-1} and 0.093 kg.s^{-1} . To compare the reactor with our “original” reactor, the temperature control of these two “win” reactors were simulated. The results can be seen in Fig.2. In that figure three curves can be seen. The red one (for the volume $V=2.12 \text{ m}^3$) shows the control of the original reactor, the green one (the volume $V=2.29 \text{ m}^3$) shows the temperature control of the reactor with the „performance“ 0.093 kg.s^{-1} and finally the black one ($V=0.18 \text{ m}^3$) the control for the reactor with 0.208 kg.s^{-1} „performance“. The dot line here indicates the temperature 323.15 K. At this point, the whole fed-batch cycle is finished. The (ZN2FD) controller was chosen for the temperature control to compare the new results with older results for the “original” reactor – in the previous work the same controller was used. As can be seen, the control process with new dimensions is again satisfactory. The temperature stays close the desired value (370 K), no overshooting was observed.

Table II – Values found by SOMA algorithm (NP = 50, migrations = 10)

Radius [m]	Height [m]	Feeding [kg.s ⁻¹]	Objective Function	Performance [kg.s ⁻¹]	Volume [m ³]
4.35269	0.102615	0.288984	14093.8	0.069	6.13
5.18811	0.116586	0.347272	15440.9	0.052	9.89
0.339422	4.4188	0.0698	15694.2	0.063	1.6
4.0766	0.25517	0.303498	19595.5	0.0317	13.32
0.4422	5.82713	0.109866	16638.9	0.045	3.58
5.1858	0.1118	0.34787	15113.1	0.055	9.29

Table III – Values found by SOMA algorithm (NP = 150, migrations = 30)

Radius [m]	Height [m]	Feeding [kg.s ⁻¹]	Objective Function	Performance [kg.s ⁻¹]	Volume [m ³]
0.102807	5.5424	0.0256518	8638.27	0.208	0.18
3.16107	0.231747	0.213155	17989.3	0.041	7.28
0.309804	4.8613	0.06382	13646.4	0.066	1.47
1.26584	0.162245	0.0421305	12551.2	0.079	0.82
0.450103	2.01428	0.0458641	15606.9	0.052	1.28
2.73641	0.129811	0.150035	12505.2	0.073	3.07

Table IV – Values found by SOMA algorithm (NP = 300, migrations = 30)

Radius [m]	Height [m]	Feeding [kg.s ⁻¹]	Objective Function	Performance [kg.s ⁻¹]	Volume [m ³]
2.02116	0.117457	0.0897612	10571.7	0.091	1.5
0.590243	1.37818	0.0450906	16879.5	0.044	1.51
0.250407	1.69088	0.0200795	10512.3	0.092	0.33
2.51136	0.155479	0.132499	13454	0.063	3.17
2.68451	0.100654	0.141601	10605.3	0.093	2.29

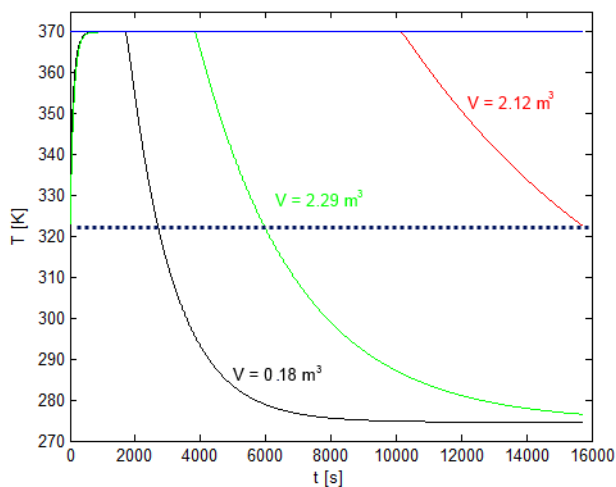


Fig. 2 Temperature profiles

Because of the satisfactory control results and better reactor „performance“, we can say that the new reactor dimensions better suite our exothermic process. In future, the impact of height-to-width ratio will be studied to find the more suitable variation for this process. The “win” reactors described in this paper have the ratio reciprocal – first is high and slim, second low and wide.

REFERENCES

[1] B. Zhao, Y. Su and Y. Peng, “Effect of reactor geometry on aqueous ammonia-based carbon dioxide capture in bubble column reactors,” *International Journal of Greenhouse Gas Control*, Issue 17, 2013, pp. 481-487.
 [2] D. Iranshahi, M. Jafari, R. Rafiei, M. Karimi and S. Amiri, R.M. Rahimpour, “Optimal design of a radial-flow membrane reactor as a novel configuration for continuous catalytic regenerative naphtha

reforming process considering a detailed kinetic model,” *International Journal of Hydrogen Energy*, Issue 38, 2013, pp. 8384-8399.
 [3] N. Park, J.-R. Kim, Y. Yoo, J. Lee and M.-J. Park, “Modeling of a pilot-scale fixed-bed reactor for iron-based Fischer–Tropsch synthesis: Two-dimensional approach for optimal tube diameter,” *Fuel*, Issue 122, 2014, pp. 229-235.
 [4] D. Novosad and L. Macků, “Pole placement controller with compensator adapted to semi-batch reactor process,” in *Recent Researches in Automatic Control*. Montreux: WSEAS Press, 2011, ISBN 978-1-61804-004-6.
 [5] F. Gazdoš, “Robust control design for a semi-batch reactor,” *International Review of Automatic Control*. vol. 5, no. 6, 2012, pp. 911-920. ISSN 1974-6059.
 [6] L. Macků, “Control design for the preparation of regenerate for tanning,” PhD. Thesis, UTB in Zlín, 2003.
 [7] L. Macků, “Identification of Arrhenius equation parameters for control purposes,” in *Proc. 13th WSEAS International Conference on Automatic Control, Modelling & Simulation (ACMOS '11)*, WSEAS Press, 2011, pp. 337-340.
 [8] I. Zelinka, G. Onwubolu and B.V. Babu, “New optimization techniques in engineering,” New York: Springer-Verlag, chap., 2004, ISBN 3-540-20167X.
 [9] D. Novosad and L. Macků, “Ziegler-Nichols controller with online identification versus PID controller comparison,” in *Annals of DAAAM for 2010 & Proceedings of the 21st International, DAAAM Symposium*, Published by DAAAM International, Vienna, Austria, 2010, ISBN 978-3-901509-73-5, pp. 1017-1019.

MAP and MMSE estimation of HEV State Of Charge

Nazha Abed *, Hatem Boujemaa **, Sami Touati * and Ramdane Hedjar *

(*)King Saud University, Kingdom of Saudi Arabia

(**) University of Carthage, COSIM Laboratory, Higher school of Communication of Tunis, Tunisia
nabed@ksu.edu.sa, boujemaa.hatem@supcom.rnu.tn, stouati@ksu.edu.sa, hedjar@ksu.edu.sa

Abstract—In this paper, we propose optimal MMSE (Minimum Mean Square Estimator) and MAP (Maximum A posteriori) estimators of the SOC (State Of Charge) of HEV (Hybrid electric Vehicles) battery. The SOC is equal to 0 when the battery is empty and one when the battery is full. A good estimation of SOC improves battery's reliability, longevity and performance. Besides, an accurate estimate of the SOC allows a good behavior of the electric motor which allows small battery size and reduces HEV price. These HEV contribute also in CO2 and pollution reduction as well as reducing diesel consumption.

Keywords: MAP estimator, MMSE estimator, SOC, HEV.

I. INTRODUCTION

With the increase in the world population, which passed beyond 7 billion in October 2011, and the massive use of petroleum, gas and coal, we observe a climatic warming causing a decrease in rain, reducing agriculture production. World population increased by 2 billion during the last 25 years and will be in excess of 9 billion after 2050. Therefore, we need to reduce the use of petroleum and coal to preserve the ozone layer. Hybrid Electric Vehicles (HEV) ¹ were recently adopted in Japan, USA and Europe due to low consumption and since they reduce the pollution rate. In 2008, 1 million of Toyota Prius cars were sold. Some governments like Canada and France encourage their citizen to buy HEV by offering them an ecological bonus (2000 Euros in France). Almost all car manufacturers offers some HEV models : Mercedes Benz, BMW, Audi, Honda, Peugeot, Toyota ... An HEV is composed of both a diesel engine and electric motor which are couple together to reduce diesel consumption. An HEV reduces up to 35 % diesel consumption especially in urban areas. For example, Hybrid Toyota Prius requires only 4.3 L for each 100 Km. HEV reduces also CO2 pollution which represents a great benefit. Electric vehicle are also a good alternative to get rid of CO2 pollution. However, they cannot be massively used by the population due to their price, small size, low speed and reduced autonomy. In this project, we aim at optimizing the use of non renewable energies by a smart management of HEV (Hybrid Electric Vehicle). We also reduce the cost of HEV and increase battery's life time. For example, Hybrid Toyota Prius offers a battery that works properly during only 8 years or 160.000 km. In this project, we

will propose new algorithms for Battery Management System in order to increase battery's life time. We will focus on the estimation of battery State Of Charge (SOC), State Of Health (SOH) and available power of HEV in order to a proper sizing of battery pack. The SOC is equal to 0% when the battery is empty and 100 % when the battery is full. The SOH is close to 100% when the battery is manufactured and will decrease over time. Accurate SOC and SOH estimation will reduce the cost, size and weight of HEV system and optimizes its performance. The battery pack represents the most expensive component of an HEV propulsion system representing 35% of the total cost. The Battery Management System (BMS) will make SOC, SOH and available power estimation in order to adapt to changing cells characteristics over time. The coulomb counting method was used in [1] for SOC and SOH estimation. Sigma point and extended Kalman filters were used in [2] for SOC estimation. It has been shown that the current integration (coulomb counting) offers bad performance due to accumulative errors and inaccurate initial values. An adaptive extended Kalman filter was used in [3] to estimate both the SOC and peak power capability. Adaptive Kalman filtering has been also used in [4] to avoid filtering divergence due to incorrect initial values. An overview of existing methods for SOC estimation was provided in [5]. Disadvantages and advantages of these methods were discussed. The effects of model errors on the performance of the extended Kalman filter was analyzed in [6]. Unscented Kalman filtering was used in [7] to adjust the model parameters and estimate the SOC. Kalman filtering was also used in [8] to estimate the SOC. Luenberger observer was used in [9] to estimate the SOC. The system performance was analyzed in terms of estimation robustness and tracking accuracy. In [10], SOC was obtained using extended Kalman filtering based on stochastic fuzzy neural network. An overview of battery management system tasks was provided in [11] such as battery state estimation and battery equalization. A dual sliding observer was suggested in [12] to estimate the SOH. It has been shown that the proposed method outperforms ampere counting technique. Remapping of the model was used in [13] to improve the accuracy of SOC and SOH estimates. Kalman filters were used in [14] to obtain a correction of state divergence using a cell model. A sliding model observer was suggested in [15] to reduce modeling errors and improve the convergence of the algorithms. [16] incorporated some new details into

¹This work was supported by the Research Center of College of Computer and Information Sciences, King Saud University, under Grant No. RC131024. The authors are grateful for this support.

the modeling of plug-in hybrid vehicles. [17] presented a combination of extended Kalman filter and a per unit system to predict the values of SOH and SOC. A complementary cooperation algorithm based on dual extended Kalman filter was introduced in [18] to improve the identification of battery model parameters. Hamming network was proposed in [19] to identify cell model parameter for enhanced SOC estimation. Impedance measurements were used in [20] to estimate both the SOC and SOH of Li-ion batteries through the fuzzy logic inference. Extreme learning machine and extended Kalman filter were suggested in [21] for modeling and estimating the Li-ion battery SOC. The aim of the algorithm proposed in [22] is to reject measurement noise and model parameters uncertainties. Some methods to make the estimator robust were presented. The battery parameters were estimated in [23] from the impedance in z-domain. The proposed method doesn't need initial values. In [24], an improved Kalman filter was integrated with the coulomb counting and open circuit voltage method. Since the battery performance depends also on temperature, cycle times and self-discharge rate, a fading recursive Least Square (LS) algorithm was suggested to identify battery parameters. In this paper, we propose MAP and MMSE estimators of SOC which have not been yet investigated.

The paper is organized as follows. The next section presents the benefits of SOC estimation. Section III presents some methods for SOC estimation. Section IV proposes MAP and MMSE estimation of SOC. Section V draws some conclusions.

II. BENEFITS OF SOC ESTIMATION

In the following, we list some of the benefits of SOC and SOH estimation which are the main objectives of this project.

A. Battery balancing

A good SOC estimation allows a smart battery balancing that increases battery's lifetime. The individual cells in a battery may have different levels of charge. Without battery balancing, discharging should be stopped when the cell with the lowest SOC is empty (even if the other cells are not empty). This limits battery lifetime and energy that can be taken from it. Therefore, a good estimation of cells SOC allows to charge quasi-empty cells to achieve the battery SOC. Balancing can be performed by taking energy from the most charged to the emptiest cell. In practical scenarios, each second the BMS measures the voltage, current and temperature and uses these measurements to update the estimates of SOC, SOH and available power. Then, a decision is made to charge or not some cells. This process continues until the vehicle is turned off.

B. Longevity

A good SOC estimation avoids battery damage reducing its lifetime due to over-charging or over-discharging it.

C. Performance

Having a good estimate of SOC, we can optimize the use of the battery pack yielding a good contribution of the electric motor which reduces diesel consumption.

D. Size, weight and cost

An accurate estimate of the SOC allows a good behavior of the electric motor which allows small battery size and reduces HEV price.

E. Reliability

Accurate estimate of the SOC increases the power system reliability of HEV.

The innovation of the paper is to investigate optimal MMSE and MAP SOC estimators which have not been yet proposed. In fact, previous approaches rely on different variants of Kalman filtering. MAP and MMSE estimators outperforms Kalman filtering.

III. METHODS FOR SOC ESTIMATION

In the following, we list some the methods that can be used for SOC estimation.

HEV engine can be used to charge the battery cells when they are almost empty. This requires a good estimation of battery State Of Charge (SOC) and available power. The battery pack is composed of current, temperature and voltage sensors, the electronics Battery Management System (BMS) and the cells. The SOC of an HEV battery can not be determined directly. In general, there are five methods to estimate SOC indirectly.

1 Chemical method

This method can be used only for batteries given an access to electrolyte liquid such as non sealed lead acid batteries. Electrolyte liquid PH can be used to estimate battery SOC.

2 Current integration method

It consists in estimating battery current and integrating it to estimation the SOC. It is subject to some imperfections due to measurements noise and the absence of reference point.

3 Pressure method

It can be used for some batteries like NiMH which internal pressure increases with the SOC.

4 Voltage method

It consists in using the discharge curve (Voltage Vs. SOC) to estimate the SOC. However, battery voltage is sensitive to battery current and temperature. This method can be improved by adding a correction term proportional to battery current. We have also to take into account voltage evolution with respect to temperature. Battery conception consists in having a constant voltage for any SOC which makes this method difficult to be implemented. In the following, we provide some details of SOC estimation using the voltage method based on state and observation equations. In this paper, we will focus only on the voltage method.

IV. MAP AND MMSE ESTIMATION OF THE SOC

Battery behavior can be characterized by two equations: the state and observation equations. The state equation can be written generally as :

$$x_{k+1} = f(x_k, i_k, n_k) \quad (1)$$

where x_{k+1} is the state vector to be estimated, i_k is the measured current (system input) during the k -th sample time,

n_k is a noise corresponding to cell modeling errors and $f(\cdot)$ is a non linear function.

The observation (output) equation is given by

$$y_k = h(x_k, i_k, b_k) \quad (2)$$

where b_k is an observation noise.

In this model, the state vector is composed of the SOC s_k , the polarization voltage states p_k and the hysteresis h_k

$$x_k = [p_k^T h_k s_k]^T \quad (3)$$

A simple recursion providing the SOC at the (k+1)-th sample time can be written as [10]

$$s_{k+1} = s_k - \mu(i_k) i_k \frac{\Delta}{C} \quad (4)$$

where $\mu(i_k)$ is the coulombic efficiency of the cell, Δ is the sampling period, C is the nominal capacity.

The column vector p_k is given by [10]

$$p_{k+1} = [diag(\beta)]p_k + i_k \quad (5)$$

The hysteresis characterizes the rest of voltage. A cell that has been recently charged will have a higher rest voltage than another that has been recently discharged, even if the SOC is the same. The hysteresis can be modeled as [11-12]

$$h_{k+1} = exp(-|\mu(i_k) i_k \Delta \frac{\gamma}{C}|) h_k + [1 - exp(-|\mu(i_k) i_k \Delta \frac{\gamma}{C}|)] C \quad (6)$$

where γ is hysteresis rate constant and M is the maximum hysteresis voltage at the present temperature. Equations of hysteresis, polarization voltage and SOC are combined together to form function $f(\cdot)$.

The output of the system y_k is the cell terminal voltage which is given by [11-15]

$$y_k = OCV(s_k) + Gp_k - Ri_k + h_k \quad (7)$$

where $OCV(s_k)$ is the Open Circuit Voltage versus the SOC, G is a weighting matrix, R is the battery resistance.

Using the previous equations the MAP estimate can be written as

$$\hat{x}_k = \arg \max_{x_k} p(x_k | y_0 \dots y_k) \quad (8)$$

The MMSE estimate is computed as follows

$$\begin{aligned} \hat{x}_k &= E(x_k | y_0 \dots y_k) \\ &= \int x_k p(x_k | y_0 \dots y_k) dx_k \end{aligned} \quad (9)$$

To compute MAP and MMSE estimators of the state vector x_k , we need to compute the conditional probability density function $p(x_k | y_0 \dots y_k)$

Initialization : $k = 0$ set $p(x_0 | y_0)$ as an uniform function

Iteration :

Prediction step :

Compute

$$p(x_k | y_0, \dots, y_{k-1}) = \int p(x_k x_{k-1} | y_0, \dots, y_{k-1}) dx_{k-1} \quad (10)$$

$$= \int p(x_k | x_{k-1} y_0, \dots, y_{k-1}) p(x_{k-1} | y_0, \dots, y_{k-1}) dx_{k-1}$$

Using (1), we have

$$p(x_k | x_{k-1} y_0, \dots, y_{k-1}) = p(x_k | x_{k-1}) \quad (11)$$

Therefore,

$$p(x_k | y_0, \dots, y_{k-1}) = \int p(x_k | x_{k-1}) p(x_{k-1} | y_0, \dots, y_{k-1}) dx_{k-1} \quad (12)$$

The transition probability $p(x_k | x_{k-1})$ can be easily computed using (4-6).

Filtering step (updating step)

$$\begin{aligned} p(x_k | y_0, \dots, y_k) &= \frac{p(x_k, y_k | y_0, \dots, y_{k-1})}{p(y_k | y_0, \dots, y_{k-1})} \\ &= \frac{p(y_k | x_k, y_0, \dots, y_{k-1}) p(x_k | y_0, \dots, y_{k-1})}{\int p(y_k, x_k | y_0, \dots, y_{k-1}) dx_k} \end{aligned} \quad (13)$$

Using (2) or (7), we have

$$p(y_k | x_k, y_0, \dots, y_{k-1}) = p(y_k | x_k) \quad (14)$$

Therefore, the updating step is written as

$$p(x_k | y_0, \dots, y_k) = \frac{p(y_k | x_k) p(x_k | y_0, \dots, y_{k-1})}{\int p(y_k | x_k) p(x_k | y_0, \dots, y_{k-1}) dx_k} \quad (15)$$

Notice that $p(y_k | x_k)$ can be easily computed using the observation equation (2) or (7). $p(x_k | y_0, \dots, y_{k-1})$ has been computed during the prediction step.

V. CONCLUSIONS

In this paper, we have proposed MAP and MMSE estimators of HEV SOC. We have used both the state and observation equations to iteratively compute the MAP and MMSE estimations using the prediction and filtering steps.

REFERENCES

- [1] N. Kong Soon, C. S. Moo, Y. P. Chen, Y. C. Hsieh, "Enhanced coulomb counting method for estimating state of charge and state of health of lithium-ion batteries," Elsevier Applied energy, vol. 86, issue 9, pp. 1506-1511, Sept. 2009.
- [2] F. Sun, X. Hu, Y. Zou, S. Li, "Adaptive unscented Kalman filtering for state of charge estimation of a lithium-ion battery for electric vehicle," Elsevier energy, vol. 36, issue 5, pp. 3531-3540, May 2011.
- [3] R. Xiong, H. He, F. Sun, X. Liu, Z. Liu, "Model based state of charge and peak power capability joint estimation of lithium-ion battery in plug-in hybrid electric vehicles", Journal of power sources, vol. 229, pp. 159-169, 2013.
- [4] W. Jumping, G. Jingang, D. Lei, "An adaptive Kalman filtering based state of charge combined estimator for electric vehicle battery pack", energy conversion and management, vol. 50, issue 12, pp. 3182-3186, Dec 2009.

- [5] H. J. Bergveld, D. Danilov, P. H. L. Notten, "Batteries, Adaptive state of charge determination," *Encyclopedia of electrochemical power sources*, pp. 459-477, 2009.
- [6] J. Lee, O. Nam, B. H. Cho, "Li-ion battery SOC estimation method based on the reduced order extended Kalman filtering," *Journal of power sources*, vol. 174, Issue 1, pp. 9-15, Nov. 2007.
- [7] W. He, N. Williard, C. chen, M. Pecht, "State of charge estimation for electric vehicle batteries using unscented Kalman filtering", *Microelectronics*, In Press 2013.
- [8] J. Wang, B. Cao, Q. Chen, F. Wang, "Combined state of charge estimate for electric vehicle battery pack", *Control engineering practice*, Vol. 15, Issue 12, pp. 1569-1576, Dec. 2007.
- [9] J. Li, J. K. Barillas, C. Guenther, M. A. Danzer, "A comparative study of state of charge estimation algorithms for LifePO4 batteries used in electric vehicles", *Journal of power sources*, Vol. 230, pp. 244-250, 2013.
- [10] L. Yu, J. Wang, Q. Chen, "Kalman filtering state of charge estimation for battery management system based on a stochastic fuzzy neural network battery model", *energy conversion and magement*, Vol. 53, Issue 1, pp.33-39, Jan. 2012.
- [11] L. Lu, X. Han, J. Li, J. Hua, M. Ouyang "A review on the key issues for lithium-ion battery management in electric vehicles", *Journal of power sources*, vol. 226, pp. 272-288, March 2013.
- [12] C. Ju, "A technique for estimating the state of health of lithium batteries through dual sliding mode observer", *IEEE Trans. on Power Electronics*, vol. 25, Issue 4, April 2010.
- [13] C. R. Gould, D. Stone, P. Bentley, "New Battery model and state of health determination through subspace parameter estimation and state observer techniques", *IEEE Trans. on Vehicular Technology*, Vol. 58, Issue 8, pp. 3905-3916, Oct. 2009.
- [14] P. Bentley, D. Stone, M. Christopher, "Nonlinear observers for predicting state of charge and state of health of lead-acid batteries for hybrid electric vehicles", *IEEE Trans. Vehicular Technology*, Vol. 54, Issue 3, pp. 783-794, 2005.
- [15] K. Song, "Non linear state of charge estimator for hybrid electric vehicle battery", *IEEE Trans. on Power electronics*, vol. 23, no. 4, pp. 2027-2034, 2008.
- [16] Q. Casey, Z. Daniel, B. Thomas, "An evaluation of state of charge limitations and actuation signal energy contentent on plplug-in Hybrid electric vehicle, vehicle to grid reliability and economics", *IEEE Trans. on smart grid*, vol. 3, no. 1, pp. 483-491, March 2012.
- [17] K. Hoon, C. Hyung, "State of charge estimation and state of health prediction of a Li-ion degraded battery based on an EKF combined with a per unit system", *IEEE Trans. on Vehicular Technology*, vol. 60, no. 9, pp. 4249-2469, Nov. 2011.
- [18] K. Hoon, L. Jun, C. Hyung, "Complementary cooperation algorithm based on DEKF combined with pattern recognition for SOC capacity estimation and SOH prediction", *IEEE trans. on power electronics*, vol. 27, no. 1, Jan. 2012.
- [19] J. Kim, "Pattern recognition for temperature dependent state of charge capacity estimation of Li-ion cell", *IEEE Trans. on Energy conversion*, vol. 28, no. 1, pp. 1-11, March 2013.
- [20] A. Zenati, P. Desprez, R. Hubert, "Estimation of the SOC and SOH of Li-ion batteries by combining impedance measurement with the fuzzy logic inference", *36-th annual conference on IEEE industrial electronics*, Nov. 2010.
- [21] J. Du, L. zhiatao, C. Can, W. Yougi "Li-ion battery SOC estimation using EKF based on a model proposed by extreme learning machine", *IEEE conference on industrial electronics and applications*, July 2012.
- [22] P. Spagnol, S. Rossi, S.M. Savaressi, "Kalman filter SOC estimation for Li-ion batteries", *IEEE international conference on control applications*, 2011.
- [23] N. Nagoka, A. Ametani, "An estimation method of Li-ion battery impedance using z-transform", *IEEE workshop on control and modeling for power electronics*, pp. 1-6, June 2012.
- [24] X. Yonghua, Y. Yang, H. Yang, M. Wu, J. Ass, "A novel SOC estimation method for Li-ion batteries based on improved Kalman filter with parameter online identification", *Control conference*, 2012.

Scanning probe microscopy method for diagnostics of ultra-thin tungsten films on silicon substrate

Milan Navrátil, Vojtěch Křesálek, František Hruška, Tomáš Martínek, Josef Kudělka and Jaroslav Sobotá

Abstract— This paper deals with measuring principles of scanning probe microscopy (force microscopy and microwave microscopy) which is applied to diagnostician of ultra-thin tungsten films on silicon substrate. Tungsten was sputtered on silicon wafer with radio frequency magnetron sputtering method. Some topographical and electromagnetic properties were measured and visualized.

Keywords— atomic force microscopy, scanning microwave microscopy, tungsten on silicon substrate, ultra-thin film.

I. INTRODUCTION

NOWADAYS, with development of electronics and microelectronics the complexity of electronic devices increases approximately four times every three years. The smallest structure size decreases with ratio 0.5 in the same period. During this integration rising the physical limits of electron motion in electric field must be taken into account. For that reason, leading world producers invest into development of electronic structures and networks in nano-scale. The boundary between micro and nano systems is about 10 nm, where classical physical laws are not valid anymore and quantic physics begins to be applied. Near this area, ultra-thin (<100 nm) metal films, except others, play important role in industry, e.g., electrical components fabrication as a diffusion barrier [1]. They prevent from undesirable diffusion of dopants and interlayer diffusion interactions. The thin films are typically used for a dielectric of a semi-conductor devices, transparent conductors of a liquid-crystal display, or protective layer of an electroluminescent thin film display. Moreover, these components are used in modern sensor construction, spin

The authors gratefully acknowledge financial support from Ministry of Education, Youth and Sports of the Czech Republic (CEBIA-Tech No. CZ.1.05/2.1.00/03.0089) and (LO1212) together with the European Commission (ALISI No. CZ.1.05/2.1.00/01.0017).

M. Navrátil, V. Křesálek, F. Hruška, T. Martínek and J. Kudělka are with the Tomas Bata University in Zlin, Faculty of Applied Informatics, nám. T.G.Masaryka 5555, 760 05 Zlin, CZECH REPUBLIC (phone: +420-57-603-5283, fax: +420-57-603-5279, email: {navratil, kresalek, hruska, tmartinek, kudelka}@fai.utb.cz).

J. Sobotá is with the Academy of Sciences of the Czech Republic, Institute of Scientific Instruments, Královopolská 147, 612 64 Brno, CZECH REPUBLIC (email: sobota@isibrno.cz)

electronics, radiographic optics and nanomaterial, e.g. smart mirrors for solar energy [2].

Measuring methods and capabilities for technology verification of these components or their characterization are limited due to their structure size which is often in atomic or sub-atomic resolution. There are only few possible measuring methods – diffraction techniques, scanning transmission electron microscopy (STEM) and atomic force microscopy (AFM). These methods are commonly used for polycrystallinity confirmation and characterization of nanostructures and allows using different imaging modes. They bring cons and pros, depending on matter of investigation. In the literature some papers have been published which describe measuring methods of thin metal films, but the thicknesses are greater than tens of nanometers [3].

Tungsten oxide (WO_3) has been broadly studied due to its unique electro-optical, electric, ferroelectric properties which may correspond to crystal structure. Nevertheless, the ideal cubic structure does not appear in bulk samples of WO_3 . For ultra-thin tungsten films with thicknesses less than 10 nm, a cubic modification of WO_3 has been reported [4]. Deposition of tungsten film can be executed in many different methods based on, for example, radio frequency sputtering, thermal evaporation, chemical vapor, pulsed-laser method and sol-gel method [5].

In our case, two methods of scanning probe microscopy based on different tip-sample interaction were used for diagnostician of the ultra-thin tungsten films on silicon substrates – atomic force microscopy and scanning microwave microscopy (SMM). With these methods we can concurrently get both topographical and some electromagnetic properties of the analyzed sample. It was not clear if the metal-like conductivity of ultra-thin tungsten layer proves or not, despite some paper investigated the surface structure and electrical conductivity of WO_3 thin films on other substrates [6]. For that reason, we decided to use scanning microwave method for verification of homogeneity of sputtered layer of tungsten.

II. SCANNING PROBE MICROSCOPY

Scanning probe microscopy (SPM) devices operate on a completely different principle than conventional microscopic techniques. This technique was firstly used in 1981 – scanning tunneling microscope (STM) [7]. In general, SPM images are

obtained by positioning the mechanical probe close to the sample surface. The probe measures any interaction between probe and the sample surface and creates feedback signal, which is used for vertical positioning of the probe (axis z) with resolution of the order of 10^{-10} nanometers. Position of the probe above sample is controlled with piezoelectric system according to chosen scan grid (axis x-y), see Fig. 1. Final scan image is put together via computer processing.

There can be two ways how to perform SPM measurement. Mode with constant height keeps the distance the same between tip and sample during the measurement, the magnitude of interaction is measured. This requires rather very flat surfaces due to possible damage of the probe or the sample. In mode of constant interaction, the distance is controlled via feedback which tries to keep the same interaction value. This approach is slower, but it allows to detect larger changes in sample profile [8].

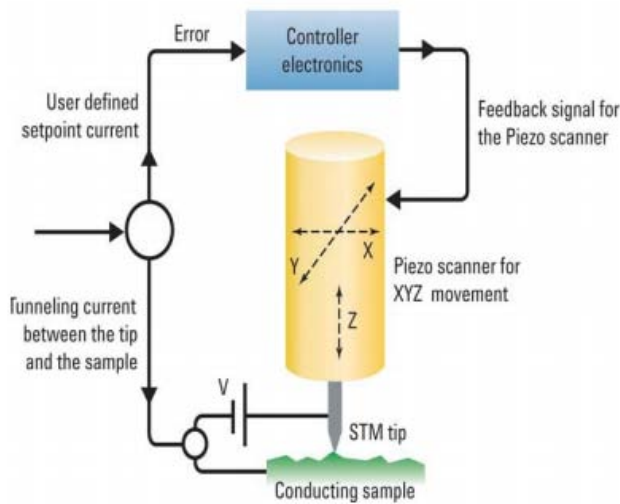


Fig. 1. Scanning probe microscopy principle (involving STM) [9]

A. Atomic force microscopy

Atomic force microscopy is a derived method from scanning probe microscopy where intermolecular forces are measured over the sample surface. These forces are induced with immediate approach ($\sim 2\text{\AA}$ to 20\AA) of the AFM tip to sample surface. Resultant force can be either attractive or repulsive, depending on distance, and it causes bend of cantilever with the tip, see Fig. 2.

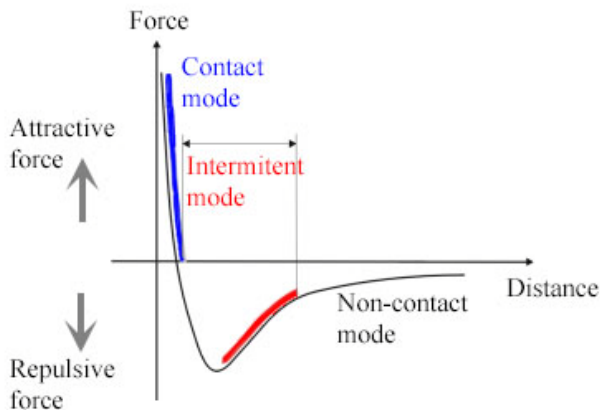


Fig. 2. Dependence of resulting force vs distance

These slight changes in position are detected with sensitive device. It usually consists of laser diode and four segment photodiode. Laser beam is focused on the cantilever end where is reflected to the photo detector from. During movement of the cantilever the energy is not uniformly spread into all quadrants, see Fig. 3. From these energy changes in vertical axis the deflection can be detected. From horizontal axis the torsion can be measured.

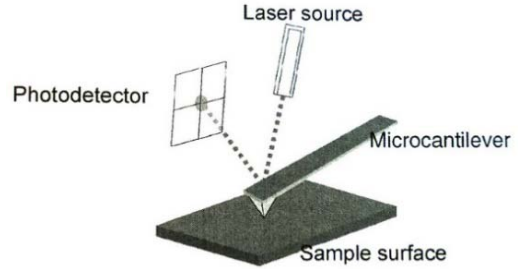


Fig. 3. AFM detection principle [10]

According to tip-sample distance there is measuring in three modes. The first one is contact mode, the distance is so small that the cantilever is deflected from the sample surface. Force is on the order of 10^{-7} N. The second one is non-contact mode, where van der Waals forces affect (on the order of 10^{-12} N). The cantilever is attracted to sample, but forces are very small and the bend is small as well. In order to improve sensitivity, the cantilever is oscillated near its resonant frequency with given amplitude (on the order of 10^{-9} m). Changes in resonant frequency during tip approach is detected and evaluated. The last one is tapping mode, which is very similar to previous one, but the amplitude is proportional to intermittent contact between tip and sample.

All mentioned modes have pros and cons, depending on type of the sample (soft or hard matters, liquids, air, and vacuum etc.) [11].

B. Scanning microwave microscopy

Scanning microwave microscopy (SMM) is a derived method of SPM that combines the electromagnetic measurement capabilities of a microwave vector network analyzer (VNA) with the nanometer resolution and Angstrom-scale positioning capabilities of classical AFM [12]. This measurement method allows calibrated measurements of electrical properties such as impedance and capacitance, with the high spatial resolution [13].

Impedance can be measured in three different ways, according to the frequency and the magnitudes involved. VNA measures impedance of a device under test (DUT) by comparing the reflected signal to the incident signal. This method of measuring impedance is the one that works best at the microwave frequencies and for impedance values at or near the characteristic impedance of transmission lines (50 or $75\ \Omega$). DUT is represented by interface AFM tip – sample surface. Relation between signal magnitudes and DUT’s impedance is as follows

$$\frac{U_{reflected}}{U_{incident}} = \Gamma = \frac{Z_L - Z_0}{Z_L + Z_0} = |\Gamma| e^{j\phi} \tag{1}$$

where Γ is reflection coefficient. The incident microwave signal (on the order of 10^9 Hz) travels through a series of components before it reaches the tip-sample interface by means of a transmission line with characteristic impedance Z_0 (50Ω).

The impedance mismatch between the transmission line and the DUT causes the incident microwave signal to partially reflect from the tip-sample interface back towards the stimulus signal source inside the VNA. This reflected signal is proportional to the impedance mismatch. The incident microwave signal and the reflected microwave signal together contain information about DUT's impedance Z_L .

When the value of Z_L is close to that of Z_0 , the plot has the steepest slope, which corresponds to the highest sensitivity and the highest resolution. In our case, Z_0 is 50Ω , but Z_L is generally not near this value.

The accuracy of a VNA impedance measurement reduces however as the impedance values move away from these characteristic values.

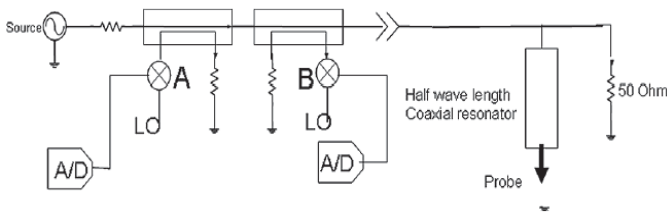


Fig. 4. Scheme of measuring principle of SMM

In order to bring the value of Z_L closer to that of Z_0 and therefore exploit the VNA's impedance measurement capability in its most accurate and sensitive range, the SMM uses a half-wavelength impedance transformer to place the measurand — the DUT — directly across an external 50Ω impedance, that is, parallel to it, it is evident from Fig. 4. This configuration enables measuring with a very high resolution the small changes of a very small impedance. Considering the relation

$$Z_L = \frac{1}{\omega C} \quad (2)$$

we can get capacitance changes on the order of 10^{-19} F across a 10^{-16} F base capacitance of dielectric samples. The AFM tip is metalized and in contact with the sample surface. If this surface is semiconducting with thin oxide layer, the interface tip – sample forms MOS capacitor. The higher frequencies in SMM lead to better sensitivity and resolution for measuring the tip-sample capacitance [14].

III. EXPERIMENTAL

A. Deposition of ultra-thin films of tungsten on silicon substrate

Tungsten coatings was deposited in a Leybold Z550 sputtering unit using 150 mm tungsten cathode 99.95% in purity. The argon flux was regulated with high accuracy by mass-flow controller. Argon deposition pressure was held on 200 mPa. Films were deposited in the radio-frequency (RF)

mode at a power of 150 W, and the distance between the target and the rotating substrate holder 48 mm was held constant [15].

Substrate oscillates under the magnetron, and during one eight second lasting oscillation 0.3 nm thick layer was deposited. The thicknesses of the tungsten layers were calculated from Taylor-Hobson profilometer measurement on coatings deposited during hundred eight second lasting oscillations at the conditions given above.

Two types of silicon substrate were prepared. Silicon wafer with thickness of 200 nm layer of SiO_2 (substrate marked as SW200), and silicon wafer with thickness approximately of 1 up to 2 nm of native silicon dioxide (substrate marked as SW2). Mentioned thickness range depends on temperature and length of sample storage. On surface of these substrates ultra-thin films of tungsten were deposited with different thicknesses (TH0 with no tungsten, TH3 with thickness of 0.3 nm, TH6 with thickness of 0.6 nm).

Prepared samples were stored at room temperature in common laboratory condition, so that we expect oxidation of the tungsten film.

B. Sample preparation and measurement

Surfaces of all measured samples were carefully rinsed with isopropyl alcohol and then dried out. No other special preparation was used. Measurement was performed with atomic force microscope Agilent 5420 in free air on common laboratory conditions. Microwave vector network analyzer PNA N5230A providing microwave signal 1.5 – 6 GHz was used. SMM, in our case frequency of 2.415235 GHz. All metal (Pt-Ir) AFM probe (size $400 \times 60 \mu\text{m}$) with spring constant of 0.3 N/m, resonant frequency of 4.5 kHz and with diameter less than 7 nm was used.

Measurement area of $4 \mu\text{m} \times 4 \mu\text{m}$ was chosen for all analyzed samples. Measurement was gradually accomplished at three different locations of sample surface. AFM topography, SMM amplitude and capacity of samples was measured and some of obtained results were visualized using PicoView and PicoImage basic software [16].

Another data processing leading to determination of profile measurement at chosen locations, mean diameter of surface structures, their mean height has been also done.

IV. RESULTS AND DISCUSSIONS

Topography characterization of sample SW200 without tungsten (Fig. 5a) film has been accomplished where flat surface was expected.

Some structures with mean height of four nanometers and mean diameter of 500 nm were observed. It could be dirt rather than surface failure. Analysis of sample SW200 with sputtered 0.3 thickness of tungsten showed very gentle blobs with mean height of 25 nm, mean diameter of 50 nm (Fig. 5b). Results of the thickest tungsten film showed the objects with mean height of 24 nm and mean diameter of 510 nm, as can be seen in Fig. 5c.

Some of the typical structured objects can be seen in topography profiles taken at different locations of analyzed sample, see Fig. 6. Results of concurrently measured SW200

sample using SMM method have not provided any relevant or reproducible information.

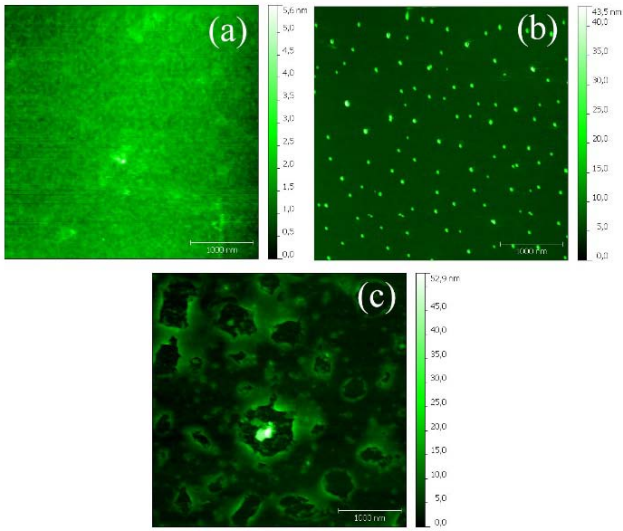


Fig. 5. Sample SW200: 2D topography image from AFM method. (a) – no tungsten, (b) – 0.3 nm tungsten film, (c) – 0.6 nm tungsten film.

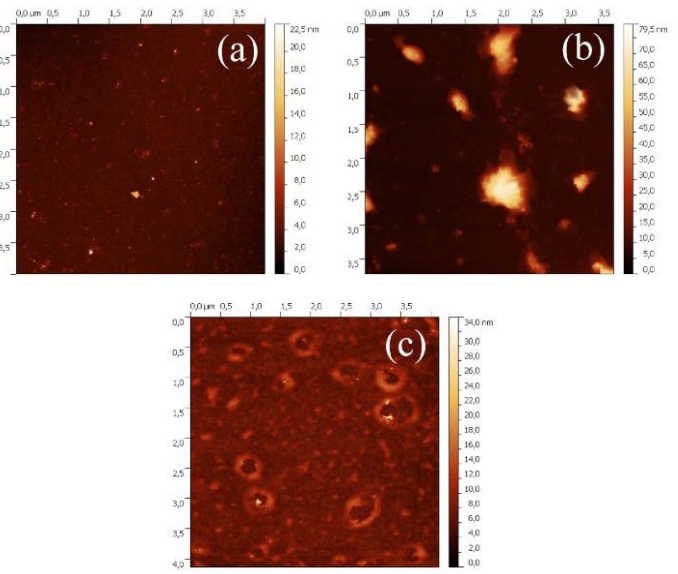


Fig. 7. Sample SW2: 2D topography image from AFM method. (a) – no tungsten, (b) – 0.3 nm tungsten film, (c) – 0.6 nm tungsten film.

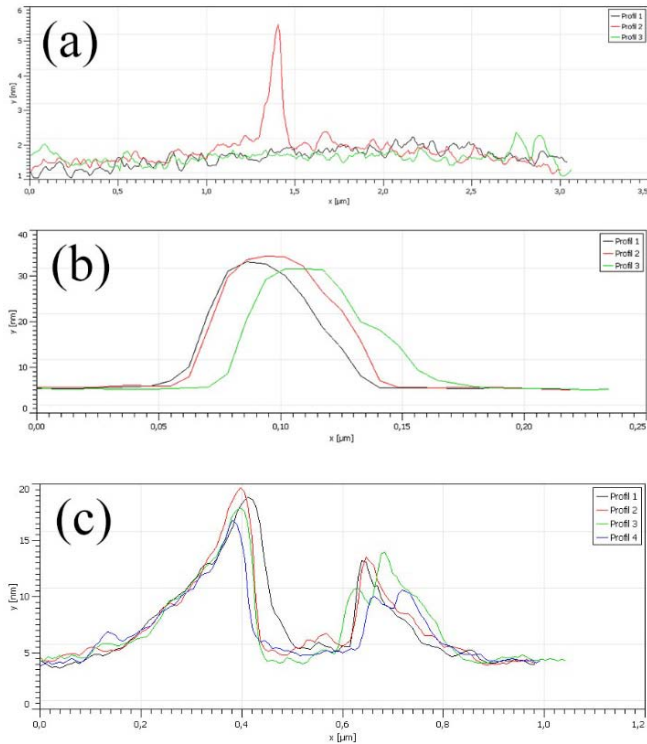


Fig. 6. Illustration of typical structures in topographical profiles of SW200 samples. (a) – no tungsten, (b) – 0.3 nm tungsten film, (c) – 0.6 nm tungsten film

The same analysis has been done for samples with ultra-thin native layer of silicon dioxide (SW2). From the topographical point of view, there were no significant changes. The results have seen similar to samples SW200 except sample with tungsten film of 0.3 nm thickness. The mean diameter is approximately eight times greater while mean height is half, see Fig. 7 and Fig. 8. This flattening can be in relation with oxidation process of the tungsten. To understand problem with oxidation, it is necessary to measure the sample in vacuum and study whole oxidation process including its kinetics.

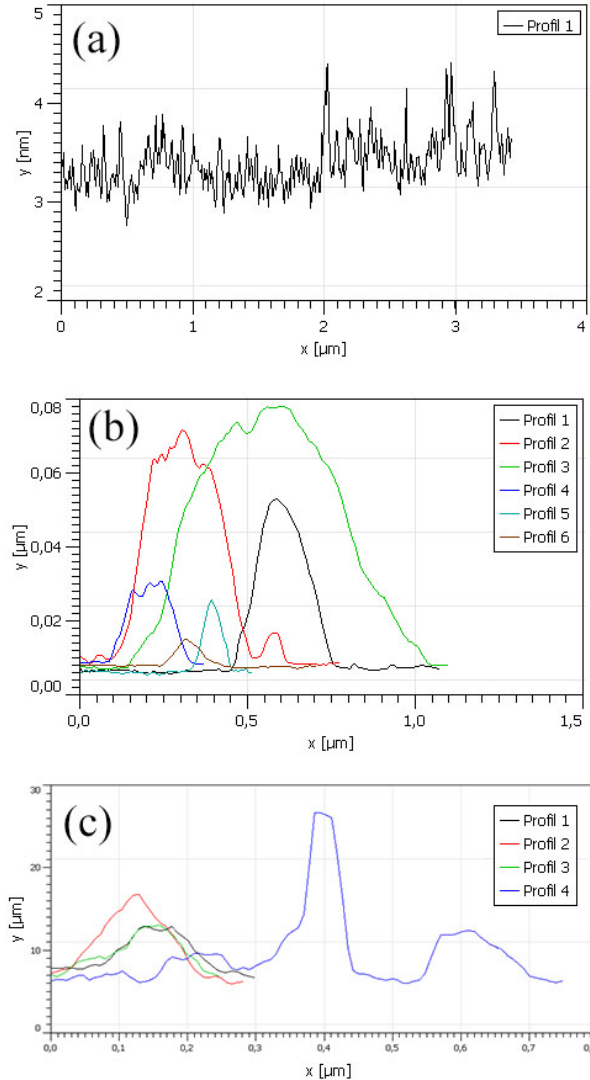


Fig. 8. Illustration of typical structures in topographical profiles of SW2 samples. (a) – no tungsten, (b) – 0.3 nm tungsten film, (c) – 0.6 nm tungsten film

Summarized topographical information about analyzed ultra-thin tungsten films of different thicknesses on silicon substrate can be seen in Table I. Moreover, there is also calculation of sample area (expressed in percentage) which fulfils condition given by minimal structure height (threshold in nanometers).

Table I. Statistical evaluation of topographical properties of measured structures

Analyzed sample	Mean Height / Diameter [nm]	Threshold [nm]	Threshold structures area [%]
WS200_TH0	4 / 500	2.5	0.6
WS200_TH3	25 / 50	6.5	4.2
WS200_TH6	24 / 510	6.5	21.4
WS2_TH0	12 / 350	2.5	0.5
WS2_TH3	13 / 410	10.8	16.7
WS2_TH6	23 / 480	10.8	30

Some results of concurrently measured samples on substrate with native silicon dioxide using SMM method are depicted in Fig. 9. The changes in amplitude (a) are shown, there are some structures of oval shapes which are resemble objects from topography interpretation. They correspond to smaller objects size which were acquired with AFM method.

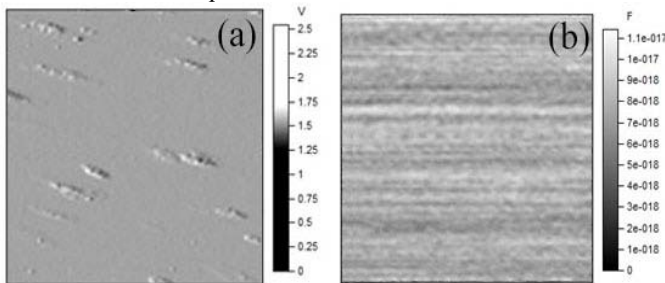


Fig. 9. SMM image – sample SW2_TH3, changes in amplitude of microwave signal (a) and changes in capacitance of the tip-sample interface (b).

On the other hand, capacitance changes are observable on the order of attofarads, see illustration in Fig. 9 (b). This results would indicate that the layer is conductive and homogeneous. There is a need to use another electric method, moreover with higher spatial resolution, such as scanning tunneling microscopy to verify conductivity of ultra-thin tungsten film.

V. CONCLUSION

Characterization of ultra-thin tungsten layer on silicon substrates was demonstrated using the two methods of scanning probe microscopy. Classical atomic force microscopy has showed the potential this method for studying of ultra-thin film structures, thicknesses and offered superficial insight into the oxidation process of tungsten on various silicon substrates. As it has not been clear, if the metal-like conductivity of ultra-thin tungsten layer proves or not, we have expected that SMM could answer that problem. From this reason, scanning microwave microscopy was used for homogeneity verification of ultra-thin sputtered layers. Interpretation of SMM results have indicated that sample with

tungsten film with minimal thickness of 0.3 nm could be homogeneous. However, this opinion should be confirmed and proved with measuring of more samples. From the statistical point of view, it will be necessary to prepare samples over larger range of ultra-thin tungsten thicknesses. According to all obtained results, the method of scanning tunneling microscopy (STM) would be more appropriate. Moreover, the spatial resolution of STM is generally higher than SMM, which is given by principle of the method.

REFERENCES

- [1] I. Fernandez, X. Borris and F. Pérez-Murano, “Atomic force microscopy local oxidation of silicon nitride thin films for mask fabrication”, *Nanotechnology*, vol 16, no. 11, pp. 2731–2737, Nov. 2005.
- [2] C. M. Lampert, “Smart switchable glazing for solar energy”, *Solar Energy Materials and Solar Cells.*, no. 52, pp. 207–221, 1998.
- [3] F. Houzé et al. “Imaging the local electrical properties of metal surfaces by atomic force”, *Applied physics letters*. 1996.
- [4] E. Salje, “The orthorhombic phase of WO₃”, *Acta Crystallographica*, vol. B33, pp. 574–577, 1977.
- [5] J. W. Klaus, S. J. Ferro and S. M. George, “Atomic layer deposition of tungsten using sequential surface chemistry”, *Thin Solid Films*, no. 360, pp. 145–153, 2000.
- [6] M. Gillet et al., “The structure and electrical conductivity of vacuum-annealed WO₃ thin films”, *Thin Solid Films*, vol. 467 (1-2), pp. 239–246 2004.
- [7] G. Binnig and H. Rohrer, “Scanning tunneling microscopy”, *Helvetica Physica Acta*, no.. 55, pp. 726–735, 1982.
- [8] P. Hawkens and J. C. H. Spence, *Science of microscopy*, Springer, 2008, pp. 929-969.
- [9] Agilent Technologies. *5420 Scanning Probe Microscope: Users guide* [online]. USA, 2012. Available: http://nano.tm.agilent.com/PDFs/5420_User_Guide_Revision_D.pdf
- [10] V. Tsukruk V. and S. Singamaneni, *Scanning Probe Microscopy of Soft Matter: Fundamentals and Practices*. Wiley, 2011, pp 9-68.
- [11] G. Haugstad, *Atomic force microscopy: understanding basic modes and advanced applications*. Wiley, 2012, pp. 1-90.
- [12] Agilent Technologies. *Understanding the Fundamental Principles of Vector Network Analysis: Application Note* [online]. USA, 2012. Available: <http://cp.literature.agilent.com/litweb/pdf/5965-7707E.pdf>
- [13] Agilent Technologies. *Network Analyzer Basics* [online].USA, 2004. Available: <http://cp.literature.agilent.com/litweb/pdf/5965-7917E.pdf>
- [14] Agilent Technologies. *Introduction to Scanning Microwave Microscopy Mode: Application Note* [online]. USA, 2009. Available: https://www.chem.agilent.com/Library/applications/AN-IntroSMM_5989-8881.pdf

- [15] A. V. Tikhonravov, M. K. Trubetskov, J. Hrdina et al. "Characterization of quasi-rugate filters using ellipsometric measurements", *Thin Solid Films*, vol. 277, no. 1-2, pp. 83-89, 1996.
- [16] Agilent Technologies. *Agilent PicoView Software Enhanced Imaging and Analysis Package for Agilent AFM Systems: Data Sheet* [online]. USA, 2012. Available: <http://cp.literature.agilent.com/litweb/pdf/5991-1175EN.pdf>

Feature Level Compensation for Robust Speaker Identification in Mismatched Conditions

Sharada V Chougule

Electronics and Telecommunication Engg. Department
Finolex Academy of Management and Technology
Ratnagiri, Maharashtra, India
shardavchougule@gmail.com

Mahesh S Chavan

Electronics Engg. Department
K I T's College of Engineering
Kolhapur, Maharashtra, India
maheshpiyu@gmail.com

Abstract—In this paper, robust front end features are proposed for improvement in speaker identification (SI) performance by considering the factors of real world situations, like mismatch between training and testing conditions. The most commonly used MFCC features are very much sensitive to effects such as channel and environment mismatch. Characteristics of speech gets changed with room acoustics, channel and microphone as well as background noise, which adversely affects the performance of the SI system. To make the front end features robust, asymmetric hamming-cosine taper is used, which gives better spectral estimation and reduces the interfering band limited noise. To incorporate time varying information, second order derivatives of cepstral coefficients are concatenated to MFCC features. Convolutional errors are minimized by using cepstral mean normalization (CMN) and compensation to additive noise is achieved by magnitude spectral subtraction (MSS). The performance of closed-set text independent speaker identification system is evaluated under different train and test conditions such as sensor (microphone) mismatch, speaking style mismatch, language mismatch and environment mismatch using IIT-G multi-variability speech database developed for speaker recognition purpose. The experimental results shows that, these modified front end features outperform conventional baseline MFCC features in mismatched conditions especially for sensor and environment mismatch. It is observed that changes in speaking style and language mismatch affects less on performance accuracy.

Keywords—Text Independent Speaker Identification, MFCC, Cepstral Mean Normalization, Magnitude Spectral Subtraction

I. Introduction

Front end processing is supposed to be the heart of every speech and speaker recognition system. The features which are extracted from speech signal are used further to form the model of speech or speaker, depending on type of system. The role of the derived features is contradictory in speech and speaker recognition applications. In speech recognition, the features are used to model the of words spoken, irrespective of who is speaking, whereas in speaker recognition the features should represent the speaker uniquely. To get the optimum performance of speech or speaker recognition system, it is important that the features derived from speech signal accurately represent the specific task. But there are number of factors that affects the performance of the recognition system in real applications. One of the main reason is mismatch

between training and testing conditions. This mismatch can be due to the change in recording devices (microphones), change in transmission channel (wired or wireless), change in surrounding environment (quiet or noisy), change in speaking style (read or conversational), change in language spoken etc.

MFCC [1] is one of the extensively used feature in speech and speaker recognition due to its ease of extraction and as it can works well with small amount of speech data (which is necessary in text dependant speaker recognition or isolated word speech recognition). Human speech production system is nothing but source-filter model from signal processing point of view [2],[3]. In speaker recognition, the main function of features extracted from speech, is to model the parameters which exploits the characteristics of a particular speaker. To form such individual speaker model, MFCC adopts the way human being recognize different people from their voices (based of hearing mechanism). The cepstral features derived from the bank of mel-scale filter are used to model the observed response in the form of human auditory system [3]. Earlier studies of speaker recognition were carried, where training and testing was done in environment without any noise or disturbance [4],[5],[6][7]. The performance of speaker recognition using cepstral features was satisfactory in idle conditions. But mismatch between training and testing greatly degrades the recognition rate. The accuracy plays a important role in applications such as forensic speaker recognition, voice authenticated bank transactions (telephone banking) and access control applications. In real world applications, there are various types of distortions and noise gets added anywhere in the system. Also the intra-speaker (within speaker) variability affects the performance of speaker recognition system. Thus robustness of speaker identification/recognition is an active research area at present. Robustness of the system (indicates constant or improved accuracy in the presence of unavoidable conditions) can be feature based or model based [8]. The robustness of the features can be obtained by using various speech enhancement and denoising techniques such as winner filtering, minimum mean square error (MMSE) etc. To reduce the effect of changes in transmission channel, channel compensation algorithms like RASTA processing, feature warping and kernel filtering are used [3].

Number of studies had done to find the robust variants of cepstral features. As our study is related to performance speaker identification based on low level features, we are not going to consider high level features based on behavioral traits. In [9], two feature extraction and compensation algorithms namely, feature-space minimum phone error (fMPE) and stereo-based piecewise linear compensation for environments (SPLICE) were studied to compensate for acoustic environment distortion and telephone line noise compensation using cepstral features. Combination of autocorrelation based features and projection measure techniques [10] is done to minimize the effect of additive and convolutive noise in speaker identification. In [11], authors have reviewed the feature extraction techniques based on spectral estimation, in which power spectrum based features, LP, MVDR and warped LP and warped MVDR methods were studied. It was reported that, spectral features based on envelope are more robust to noise than its other variants. Also refinements to improve the effectiveness of MVDR features is suggested. In [12], combination of multi-conditional training and missing feature approach is used to model unknown noise with spectro-temporal characteristics. A multi-conditional database is created by adding various types of wideband noises to TIMIT database. To improve the performance of automatic speaker recognition in room reverberation, modulation spectral features in 5-15Hz frequency band were extracted by gamma tone filterbank were used [13]. Weighted linear predicted coefficients were introduced in MFCC for noise robust speaker verification under different SNR factory noise and white noise [14].

Very less concern is given on front end processing of conventional MFCC feature extraction. i.e. mostly the same method of framing, windowing, mel-bank filtering and DCT is used to take out mel-cepstral coefficients. Instead of using regular symmetric hamming window, we have used asymmetric hamming-cosine window to enhance the knowledge of characteristics of asymmetric windows and its influence of recognition performance. To deal with mismatched training and testing condition, where extent and type of noise/distortion is unknown, we have further modified the conventional MFCCs in both cepstral domain and spectral domain. Firstly in spectral domain, we have used magnitude spectral subtraction to reduce effects of convolutive noise such as microphone and transmission channel mismatch, and then normalizing the cepstral coefficients to compensate the effect of additive noise (changes in speech signal due to changes in room acoustic e.g. switching on and off different electrical appliances, open or closed door etc.)

In most of the studies based on speaker recognition considering noise robustness, artificial noise of different signal to noise ratio is added to clean speech to study the performance of the system. Considering practical situations and applications related to speaker recognition, we have used a speech database which is developed for speaker recognition considering various types of mismatch between training and testing, namely IITG-MV database. The details of database will be discussed in section IV.

The rest of the paper includes front end processing using asymmetric window in section II. The algorithm to modify conventional MFCCs is discussed in section III. Experimental set-up and results are given in section IV with conclusion in section V.

II. Front End Processing

The input speech signal is time varying signal. The analysis of speech signal (in time as well as frequency domain) is possible through proper front end processing. Assuming the stationary characteristics of speech signal over short duration, it is a common practice to process speech signal in segments. Segmentation or decomposition of speech signal is done through framing and windowing. We discuss in brief these steps:

A) Pre-emphasis

Pre-emphasizing the speech signal at the first step is essential to approximate the unequal sensitivity of human hearing at different frequencies. Pre-emphasis filter is high pass filter to enhance the high frequency part of speech signal that is suppressed during human sound production. Boosting of high frequencies gives more information of acoustic model and used to improve *spectral tilt* (i.e. spectrum of voiced segment has more energy at low frequencies as compared to higher frequencies). It also help to eliminate the effect of dc offsets in the speech signal.

It is one coefficients FIR filter with a typical coefficient value of 0.97 i.e. the difference equation of filter is $y(n) = x(n) - 0.97x(n-1)$, where $x(n)$ is input speech signal and $y(n)$ is filtered output.

B) Framing

Framing is nothing but decomposing speech signal into small overlapping segments. Because of slowly varying nature of speech signal, speech is processed in blocks (or frames) of very short time intervals over which properties of speech signal assumed to remain relatively stationary. Typical values of frame duration is from 10 ms-30msec (especially useful to get vocal track details of human speech production) and frame overlap is 30% to 50%. (e.g. For a speech sampled at a rate of 16 kHz, frame duration of 20 msec includes 320 samples per frame). Speech signal analysis over for 10-30 msec duration is called *segmental analysis* [20]. Frame by frame processing of speech is performed so that entire region of speech is covered by at least one frame, which carries the characteristics of speech. Thus segmenting the speech signal in small time intervals will give important spectral envelope clues.

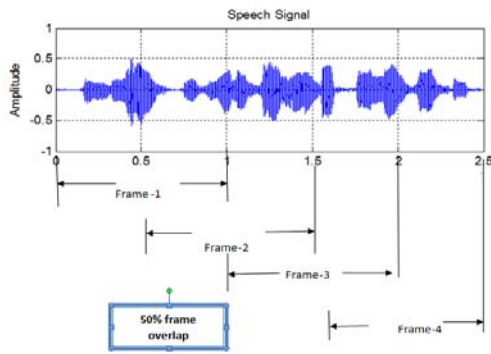


Figure 1- Framing of speech signal with 50 % frame overlap

C) Windowing

Directly dividing the entire speech signal into small size frames is equivalent to multiplying the input signal with a filter having finite and ‘gate function’ like impulse response. In terms of window function, it is like using rectangular window on each frame. The usual criteria for selection of window function is main lobe width and peak sidelobe amplitude. It is known that rectangular window is having smallest main lobe width, but largest peak sidelobe amplitude. Maximum peak side lobe amplitude creates undesired distortion (ripples) distortion in the signal. Therefore rectangular window is said to have more spectral leakage. The use of smooth tapers (most common are symmetric Hamming or Hanning) reduces the spectral leakage at the cost of wider main lobe width. Thus for a designed window, we want narrow bandwidth main lobe and large attenuation in magnitudes of side lobes.

i) Symmetric window

Short time fourier transform (STFT) is used in speech processing to determine the frequency and phase content of the local section of the signal, as it changes over the time. For this the input speech signal is multiplied with a finite length window function, which is non-zero for given length. If $s(n)$ is input speech signal and $w(n)$ is window function, then in time domain windowed values $y(n)$ are obtained by multiplication of the two, i.e. $y(n) = s(n)w(n)$, $n=0, \dots, N-1$, where N are the number of samples in one frame (or length of the window). In frequency domain, the fourier transform of above multiplication becomes convolution and is called STFT.

$$Y(n, \omega) = \frac{1}{2\pi} \int_{-\pi}^{\pi} W(\theta) X(\omega + \theta) e^{jn\theta} d\theta \tag{1}$$

Symmetric window functions are most popular in digital signal processing and applications. These are also used in speech processing due to ease of design and linear phase property[15]. Windowing in time domain is nothing but multiplication of a time varying signal $x(n)$ with a finite length window, which results in convolution of their spectra in frequency domain. The fundamental problem of time-frequency analysis of speech signals is the selection of length and shape of window. A narrow main lobe will resolve sharp details of

frequency response of framed signal, whereas the attenuated sidelobes prevent noise from other parts of the spectrum from corrupting the true spectrum at a given frequency.

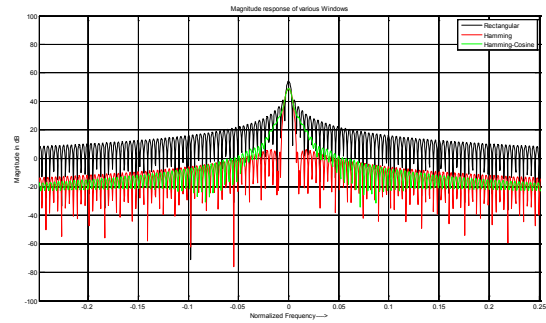


Figure 2- Hamming window of different length (in time domain and frequency domain)

ii) Asymmetric Window

Though symmetric windows are mostly used in digital signal processing satisfying optimality criteria, they have drawbacks like longer time delay and frequency response limitation[15,16]. Also, there are other aspects such as noise, distortion and mismatched conditions which are important from speech processing point of view. In relation to this, asymmetric windows (with relaxation of linear phase) can lead to better magnitude response and spectral resolution in mismatched conditions.

As human ear is less sensitive to phase information, if linear phase is not a constraint, some properties of asymmetric windows can be found to be more useful to get robust cepstral features. Use of asymmetric window is initially recommended in CELP vocoders[17]. ITU-T G-729 CELP uses asymmetric hamming cosine window for speech coding. The popularity of asymmetric windows in speech coding may find useful in speaker recognition applications. As shown in figure 5, asymmetric window results in wider main lobe and smaller side lobe attenuation. Practically the peak side lobe amplitude is independent of length of window, but depends on its shape. Because the window function is limited in time, a spreaded spectrum is measured instead of the spectrum of the original signal unlimited in time. Various symmetric tapers are well known from theory (Hamming, Hanning, Blackman etc.) which can give less peak side lobe amplitude. But rate of decay of side lobe amplitude is also important from robustness point of view. As most of the noise is additive and band limited, window function with fast decaying side lobe amplitude is important to prevent spreading of noise energy in other frequency bands (also called spectral leakage distortion)[15]. Considering this factor, use of asymmetric window can work well in noisy and mismatched conditions.

The equation of asymmetric taper used by ITU-T 96[17] is given by:

$$W_{asym}(n) = \begin{cases} \frac{1+\alpha}{2} - \frac{1-\alpha}{2} \cos\left(\frac{2\pi n}{2Na-1}\right) & 0 \leq n \leq Na-1 \\ \cos\left(\frac{2\pi(n-Na)}{4Nr-1}\right) & Na \leq n \leq N-1 \end{cases} \quad (2)$$

where N is the window length, n is the time index, and

$$Na = \frac{5L}{6}$$

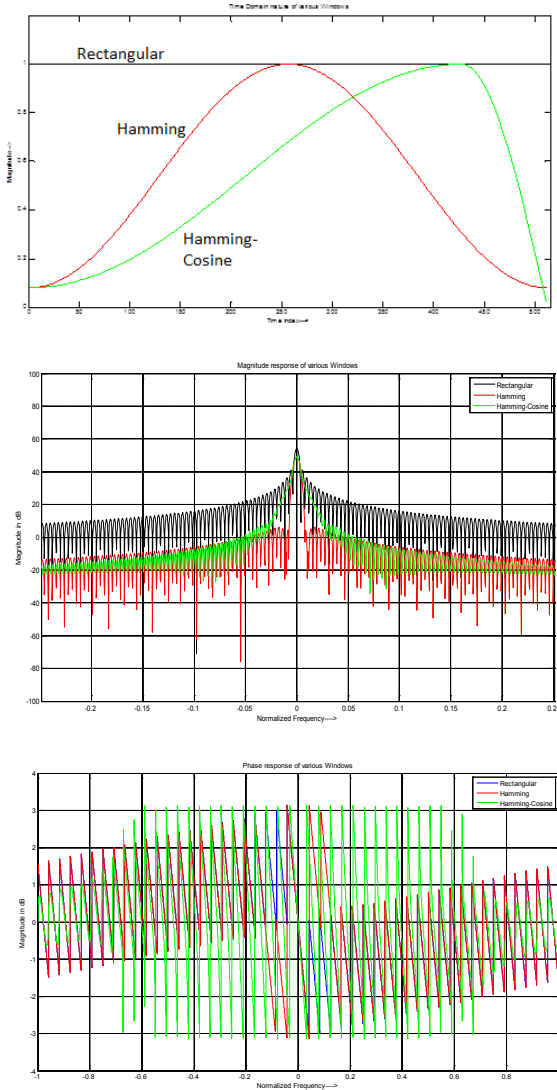


Figure 3- Time domain nature, Magnitude and Phase response of Rectangular, Hamming and Hamming-Cosine windows

With $\alpha=0.08$, the asymmetric taper, given by (2), consists of first half of traditional hamming window taking up Na samples, followed by a cosine window of length Nr samples. The complete window of length N is called *Hamming-cosine* window. As shown in figure 7, asymmetric hamming-cosine window have wider main lobe width and fast decaying side lobes than symmetric hamming window.

III] Modified MFCCs

Unlike in speech recognition, the goal of feature extraction is to find acoustic clues of individual’s speech (representation that is relatively stable) irrespective of contents in the speech. For this, the use of cepstral vectors derived from a filter bank that has been designed according to model of human auditory system is most widely used. MFCCs [1] which was introduced in 1980 was initially used as feature extraction technique for speech recognition but it works equally well in speaker recognition. MFCCs perform satisfactorily in clinical environment. But when used in real world situations, with mismatched conditions and undesired distortions, performance degrades drastically [12]. The noise introduced due mismatched conditions can be additive or convolutive. To compensate for such noises we propose modification in standard MFCCs, which will increase the robustness of MFCCs and subsequently recognition performance. We call this proposed algorithm as *feature level compensation* for robustness of speaker identification system.

The following block diagram explains the modified front end processing to acquire robust MFCCs.

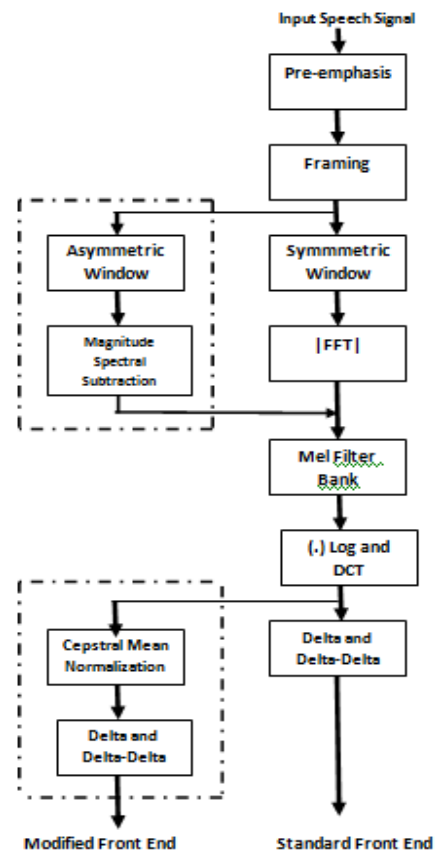


Figure 4- Modified front end processing for robust text independent speaker identification

A) Spectral Subtraction

FFT (or Fourier Transform) of windowed speech signal represents the spectrum of the speech segment. In case of presence of ambient acoustic noise (additive noise), spectral

amplitude estimation is necessary for signal restoration. Spectral subtraction is a simple method of signal restoration in additive noise [21]. In this method, noisy speech spectrum is subtracted from estimate of average noise spectrum. We have used magnitude spectral subtraction (MSS), using following algorithm:

- (i) Decompose the speech signal into small segments (typically 20 ms)
- (ii) Apply window on each segment (frame) of speech
- (iii) Get the spectral components using FFT, considering only magnitude
- (iv) Estimate the noise of input speech using MMSE (minimum mean squared error) estimate, forming adaptive noise template
- (v) Subtract noise estimated spectrum from magnitude spectrum of windowed speech, to get the enhanced speech

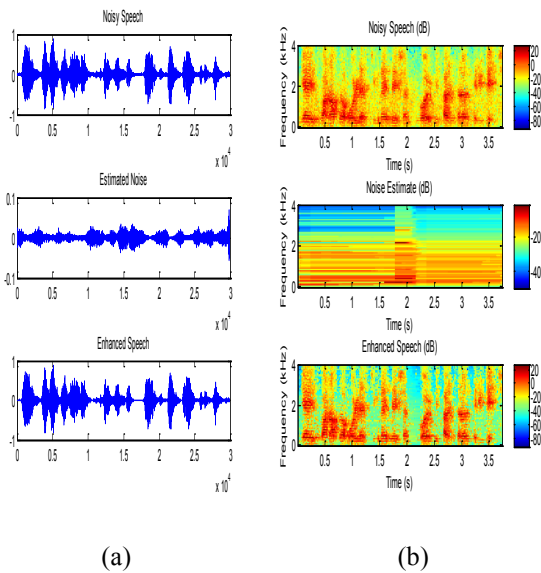


Figure-5 Noisy Speech signal (a)Time domain (b)Spectrogram before and after spectral subtraction along with estimated noise

B] Spectral and Cepstral Processing

The main aim of feature extraction is to represent the speech signal by a set of feature vectors, using some mathematical modeling for the task of speaker recognition. The models derived from these feature vectors, should carry the some characteristics which will be unique to individual speaker. As discussed in above section, short segments of speech signal (obtained by framing and windowing) are useful to find time varying characteristics from speech. These time varying characteristics, can be represented in the form of spectral features by using fourier transform or DFT, called STFT.

The speech signal is often assumed to be the output of an LTI system; i.e., it is the convolution of the input time varying speech and the impulse response of vocal track. In source-filter model of human speech production, vibrating vocal folds

represents the source, whereas the vocal track shape represents particular filtering characteristics.

Mathematically, if $e(n)$ denotes the input (source) to linear time varying system and $h(n)$ be the impulse response of the system, then output speech is the result of time domain convolution i.e.

$$x(n) = e(n) * h(n) \tag{3}$$

In frequency domain, by taking DFT, (3) becomes

$$X(k) = E(k)H(k) \tag{4}$$

where $X(k)$ represents spectrum, $H(k)$ is spectral envelop and $E(k)$ carries spectral details.

For low-level spectral features, we are interested in filter characteristics, i.e. vocal track details. To separate out impulse response (which shapes the spectrum in order to produce different sounds) from spectrum, cepstral analysis is performed. This process of physically separating the spectral shape from spectral fine structure is referred to as *deconvolution* [2].

Using the fact that logarithm of a product is equal to sum of the logarithms of the individual terms, it is possible separate out spectral envelope from the spectrum. For this, taking log on both sides of (4), becomes

$$\log X(k) = \log E(k) + \log H(k) \tag{5}$$

where we consider only the magnitude of log function.

Taking inverse DFT on both side of (5),

$$x(k) = e(k) + h(k) \tag{6}$$

in which $x(k)$ is referred to as *cepstrum* and $h(k)$ represents spectral envelope and is widely used as a feature for speech and speaker recognition applications. Thus cepstral features is the result of deconvolution process which are derived by taking IFFT of logarithm of spectral features.

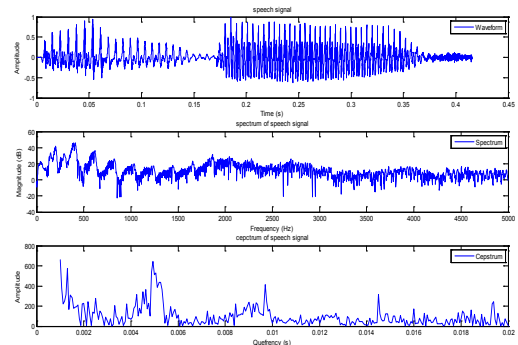


Figure-6 Spectrum and Cepstrum of speech signal

C] Mel Scale Warping

As discussed in above section, cepstral analysis is used to separate out envelope of the spectrum. But as human recognizes a speaker (voice of an individual) based on perceptual clues, which are based on characteristics of human auditory system. Psychophysical studies have shown that human perception of frequency content of sound does not

follow linear scale, but a scale that is roughly linear below 1 kHz and roughly logarithmic above 1 kHz. The relationship between linear scale and mel scale is given as

$$mel(f) = 2595 * \log_{10}(1 + \frac{f}{700}) \quad (7)$$

Each of the filter except at the lowest and highest band acts as a bandpass filter. Narrow bandpass filters enables the harmonics to be detected. Thus computation of mel-frequency cepstrum is similar to cepstrum coefficients except mel scale warping before log and inverse DFT. The phase information is discarded taking magnitude of log operation. Log operation compresses the features and also makes them less sensitive to variations in dynamics. The final step in computation of MFCCs is inverse DFT on log spectral power. Since the log-power spectrum is real and symmetric, the inverse DFT reduces to a Discrete Cosine Transform (DCT). The DCT has the property to produce more highly uncorrelated features.

D) Cepstral Mean Normalization (CMN)

Due to unknown disturbances that affect the speech, (e.g. change in telephone channel or switch in microphone), the spectral characteristics gets changed. To compensate for such convolutive noise, normalization of cepstral coefficients is done. It is possible to separate out convolutional noise in cepstral domain as it becomes additive in log spectral domain. If such additive components have different spectral characteristics, it is possible to separate out them using linear filters. *Cepstral mean normalization* (CMN) is an alternate way to high-pass filter cepstral coefficients. In cepstral mean normalization the mean of the cepstral vectors is subtracted from the cepstral coefficients of that utterance on a frame-by-frame basis:

$$y(n) = x(n) - \frac{1}{N} \sum_{n=1}^N x(n) \quad (8)$$

where N is the total number frames in an utterance.

E) Delta and Delta-Delta Coefficients

The MFCC coefficients does not carry any temporal information. Such information is included in feature set by taking cepstral derivatives. The first order derivative (difference) of cepstral coefficients is called *Delta* coefficients and second order derivative as *Delta-Delta* coefficients also called acceleration coefficients. Adding acceleration coefficients reduces the convolutive noise created by channel mismatch.

Let $c_1(m; n)$ denotes the MFCC coefficients, then Delta coefficients are calculated as:

$$c_1(m; n) \triangleq \frac{1}{2} [(c_1(n; m + 1)) - (c_1(n; m - 1))] \quad (9)$$

Delta-Delta uses same equation applied to Delta coefficients.

Thus, to reduce the channel effects and to obtain temporal information of static feature vectors, we have appended the MFCCs with delta and delta-delta features. The initial 13 dimension MFCC feature vector becomes of 39 dimension by using Delta-Delta features.

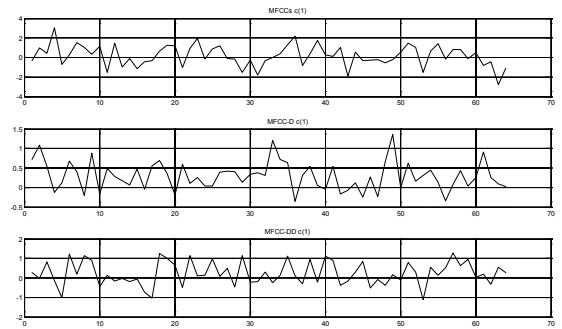


Figure7- MFCC, MFCC+Delta, MFCC+Delta-Delta of c(1)

IV Experimental Set -up and Results

The segmented speech is windowed using asymmetric Hamming-Cosine window of length 256. Magnitude spectral subtraction (MSS) is applied on each windowed frame to estimate the noise. To evaluate the performance of proposed modified front end features, we have used mel filter bank of size 13. The cepstral coefficients obtained through spectral subtraction are normalized using cepstral mean normalization (CMN), which are further concatenated first and second order temporal derivatives. 39-dimensional feature vector is formed per frame. For formation of speaker models the well known Linde-Buzzo-Gray (LBG) algorithm is developed with codebook size of 64. Thus 39x64 dimensional codebook is formed for each speaker. To evaluate the performance of the proposed modified front end features, we have used multi-variability speaker recognition database for speaker recognition developed by IIT Guwahati. The database consists of four phases, out of which we have used Phase-I and Phase-II database.

Following are the various conditions between training and testing:

(i) Sensor Mismatch Condition

Here we have selected 100 speaker database (81 male and 19 female) whose speech is recorded with five different microphones namely Headset microphone, Table PC build-in microphone, Digital voice recorder, Mobile phone-1 and Mobile phone-2. The data collected with headset microphone is the cleanest and of higher SNR. It is used for training in all five cases and testing is done with same and different microphones. To study the effect of these sensors on the performance of the system other conditions such as language (English), speaking style (Read), Environment (Office) and train-test duration (30 sec and 10 sec respectively) are kept unchanged.

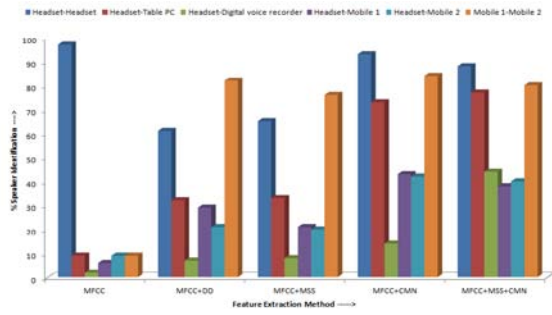


Figure-8 % Speaker Identification using baseline and modified MFCC in Sensor Mismatch Condition using Symmetric Hamming Window

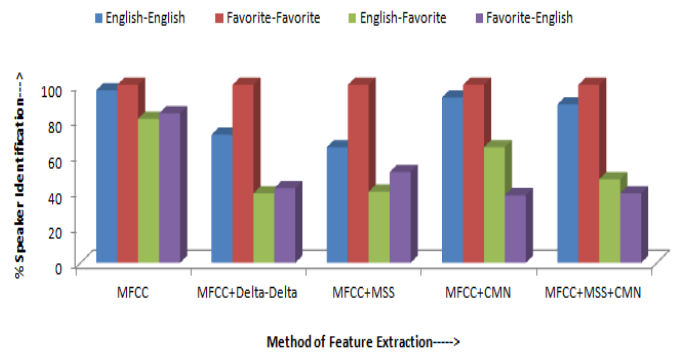


Figure 10 %Speaker Identification using baseline MFCC and Modified MFCC in Language Mismatch Condition (Using Symmetric Hamming Taper)

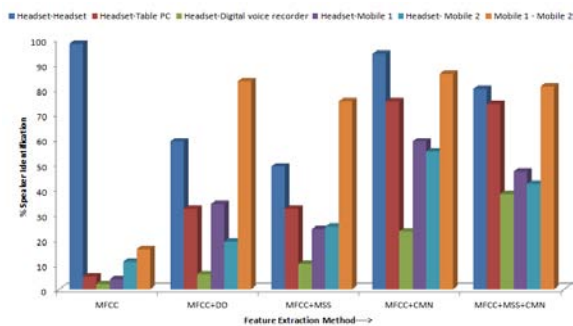


Figure-9 % Speaker Identification using baseline and modified MFCC in Sensor Mismatch Condition using Asymmetric Hamming-Cosine Window

Experimental results shows that standard MFCCs work best in clean recording conditions (both training and testing is from headset database). Also standard MFCCs have little effect of wireless medium (mobile-1-for training and mobile-2-testing).But average percentage identification decreases drastically for sensor mismatch between training and testing. Use of asymmetric window along with magnitude spectral subtraction and cepstral mean normalization increases the percentage speaker identification from 7% to 77% for table PC, 2 to 38% for digital voice recorder,6% to 59 % in mobile-1 and 9% to 55% in case of mobile-2.

Thus, changes in microphones during training and testing introduces convolutive type of noise in the signal, which can be estimated by using MMSE in spectral subtraction and spread of noise bandwidth creating spectral leakage is reduced by using asymmetric hamming-cosine taper.

(ii) Language Mismatch

In this, the system is evaluated in different languages (for 100 speakers) for training and testing. One is English and other is their favorite (native) language. Here training and testing is done with speech recorded with Headset microphone, in office environment and speaking style as read with same train and test duration (30 sec and 10 sec respectively).

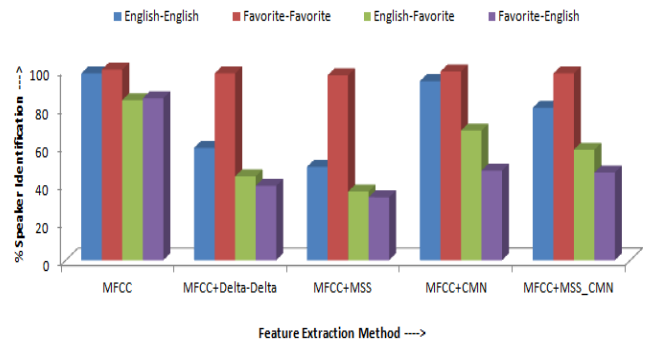


Figure 11 %Speaker Identification using baseline MFCC and Modified MFCC in Language Mismatch Condition (Using Asymmetric Hamming-Cosine Taper)

It is observed that baseline MFCCs is less sensitive to language mismatch. As MFCCs are perceptual based features with more sensitivity in low frequencies (approximately 1000 Hz) than high frequencies. The lower frequencies represents the vocal track features (impulse response of source-filter model). There are some frequencies components which are unique to individual which are captured by MFCCs irrespective of what is spoken. Also it is found that identification rate slightly decreases using spectral subtraction with symmetric as well as asymmetric taper. Therefore normalization of cepstral coefficients along appended with dynamic features (delta-delta) performs well in language mismatch condition.

(iii) Speaking Style Mismatch

To study the effect of changes in style of speaking, read and conversation are the two conditions used for training and testing (100 speakers), while keeping the other conditions of the data as Headset sensor, English language and Office environment with same train and test duration (approximately 15 sec).

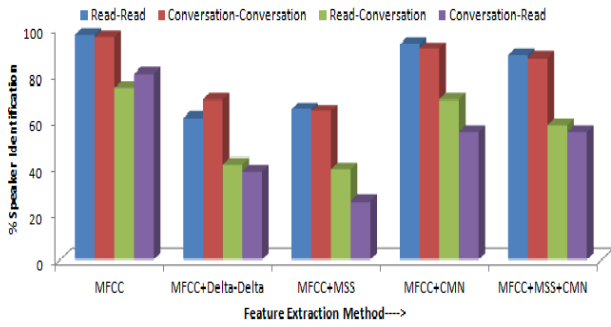


Figure-12 % Speaker Identification using Baseline MFCC and modified MFCC in Speaking Style Mismatch Condition (Using Symmetric Hamming Taper)

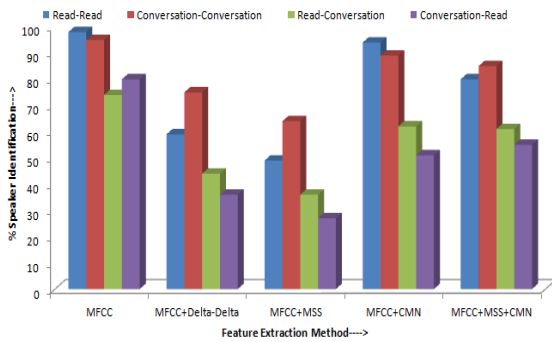


Figure 13 %Speaker Identification using baseline MFCC and Modified MFCC in Speaking Style Mismatch Condition (Using Asymmetric Hamming-Cosine Taper)

Surprisingly in this mismatch condition, MFCC alone using symmetric as well as asymmetric window outperforms as compared to modified MFCCs.

(iv) Environment Mismatch

50 Speaker (40 male and 10 female) database with speech recorded in office (almost quite) and uncontrolled (hostel rooms, coffee-shop) environment is used for training and testing. Other conditions are Headset microphone, read as speaking style, language English and same train and test duration (approximately 15 sec).

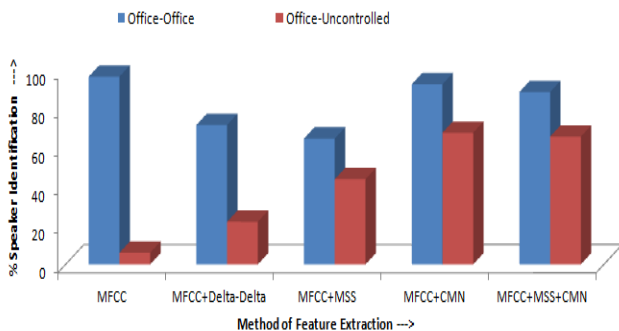


Figure-14 % Speaker Identification in Environment Mismatch Condition(Using Symmetric Hamming window)

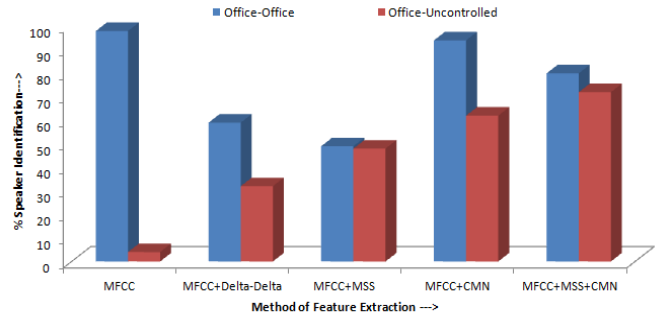


Figure-15 % Speaker Identification in Environment Mismatch Condition (Using Asymmetric Hamming-Cosine window)

As expected, in same environment (in almost quite room), using headset microphone (clean speech), conventional MFCC features works best for identifying speakers. But surrounding noise (uncontrolled environment) completely drops the performance of the system. In this case, modified features with asymmetric taper perk up the accuracy of the system from 4 % to 72 %.

V. Conclusion

The paper demonstrates modified MFCC feature extraction for robust text independent speaker identification. To understand the effect of various real world factors on correct identification rate, we have considered four conditions of mismatch between training and testing as sensor, language, speaking style and environment. From experimentation it is observed that conventional MFCCs works best in clean training and testing environment when same microphones (Headset microphones) are used, irrespective of language spoken and speaking style (less affected) . But changes in the sensors and outside environment (clean or noisy) totally degrades the identification rate. Results shows that replacing symmetric window function with a simple asymmetric taper shows a considerable increase in robustness in speaker identification. Further the cepstral features with asymmetric taper, modified with spectral subtraction and normalization of cepstral coefficients drastically increases the speaker identification accuracy confirming the robustness of the proposed modified MFCC features. In this study we have used a database which consists of realistic situations of mismatched conditions, where type and extent of noise is unknown. In further study variations of asymmetric windows and use of adaptive noise estimation techniques can be implemented to compensate for mismatched conditions in speaker recognition.

Acknowledgment

The author would like to thank EMST Laboratory, IIT Guwahati for providing speech database for evaluation.

References

- [1] S. Davis and P. Mermelstein, "Comparison of parametric representations for monosyllabic word recognition in continuously spoken sentences," *IEEE Trans. Acoustics, Speech, and Signal Processing*, vol. 28, no. 4, pp. 357-366, August 1980.
- [2] Ben Golg and Nelson Morgan, "Speech and audio signal processing", WILEY INDIA Edition, 2006
- [3] L.R.Rabinar and R.W.Schafer."Digital processing of speech signals", Pearson Education
- [4] Amin Fazel and Shantanu Chakrabartty, "An overview of statistical pattern recognition techniques for speaker verification", *IEEE Circuits and System Magazine*. 2011, pp.62-81, Second quarter 2011
- [5] B S Atal, "Automatic recognition of speakers from their voices", *Proc.IEEE*, vol.64, pp.460-475, 1976
- [6] G.R.Doddington-"Identifying people from their voices", *Proc.IEEE*, vol.73, no.11, pp.1651-1664, 1985
- [7] A.Rosenberg,"Automatic speaker verification:A review", *Proc.IEEE*, vol.64, no.4, pp.475-487, 1976
- [8] Roberto Tongneri and Daniel Pullella, " An overview of speaker identification: Accuracy and robustness issues", *IEEE Circuits and Systems Magazine*, 2011, pp.1531-1569, Second quarter 2011
- [9] Li Deng , Jian Wu,, Jasha Droppo and Alex Acero, " Analysis and comparison of two speech feature extraction /compensation algorithms" *IEEE Signal Processing Letters*, vol. 12, no. 6, pp.477-480, June 2005
- [10] Kuo-Hwei Yuo, Tai-Hwei Hwang, and Hsiao-Chuan Wang, "Combination of autocorrelation-based features and projection measure technique for speaker identification, *IEEE Transactions on Speech and Audio Processing*, vol. 13, no. 4, July 2005
- [11] Matthias Wolfel and John McDonough "Minimum Variance distortionless Response Spectral Estimation" ,*IEEE Signal Processing Magazine*, September 2005
- [12] Ji Ming, Timothy J. Hazen, James R. Glass and Douglas A. Reynolds, "Robust Speaker Recognition in Noisy Conditions ", *IEEE Transactions on Speech and Audio Processing*, vol. 15, no. 5, pp.1711-1723, July 2007
- [13] Tiago H. Falk, Wai-Yip Chan Tiago H. Falk, and Wai-Yip Chan, " Modulation spectral features for robust far-field speaker identification", *IEEE Transactions on Speech and Audio Processing*, vol. 18, no. 1, pp.90-100, January 2010
- [14] Rahim Saeidi,, Jouni Pohjalainen, Tomi Kinnunen, and Paavo Alku "Temporally weighted linear prediction features for tackling additive noise in speaker verification", *IEEE Signal Processing Letters*, vol. 17, no. 6, pp.599-602, June 2010
- [15] Robert Rozman and Dusan M. Kodek, "Using asymmetric windows in automatic speech recognition", *Speech Communication*, Elsevier 2007
- [16] Dinei A.F Florencio, "Investigating the use of asymmetric windows in CELP Vocoders" *IEEE*, 1993
- [17] International Telecommunication Union ITU-1996, Coding of speech at 8kbps using conjugate structure algebraic code excited linear prediction (CS-ACELP) ITU-T Recommendation G.729
- [18] Tomi Kinnunen and Haizhou Li, " An overview of text-independent speaker recognition: from features to supervectors ", *Speech Communication*, Elsevier 2007
- [19] Campbell, J. "Speaker recognition: a tutorial", *Proceedings of the IEEE* pp.1437-1462 ,September 1997
- [20] HS Jayanna, SR Mahadeva Prasanna, " analysis, feature extraction, modeling and testing techniques for speaker recognition", *IETE Technical Review*, vol.26. issue 03, pp.181-190, 2009
- [21] Saeed V. Vaseghi, "Advanced digital signal processing and noise reduction", Third Edition, Wiley Publication, 2006

On Experimental Verification Of Vehicle Active Suspension Robust Control

K. Hyniova

Abstract — Between 2010 and 2014, the research team of Josef Bozek Research Center of Combustion Engines and Automobiles at the Czech Technical University in Prague, Czech Republic, has developed innovations in vehicle suspension technology. The research team has designed a unique innovative suspension system that uses a linear electric motor as a controlled suspension actuator and provides desired forces between wheel and car body. We have undertaken many experiments on energy management in the system. In order to verify various control strategies and to test different ways of energy consumption optimization we designed and constructed a unique one-quarter-car test stand. The paper deals with the way and results of experimental verification of vehicle active suspension behavior when robust control is applied and also with energy management strategy that we used in the system.

Keywords—Active suspension, one-quarter-car model, robust control, verification, experiments

I. INTRODUCTION

The suspension system is an important aspect of car design because it influences both the comfort and safety of passengers. Two major performance requirements of any automotive suspension system are to provide a comfortable ride and good handling when random disturbances from road unevenness and variable cargo act upon the running vehicle. Passenger comfort can be interpreted as attenuation of sprung mass acceleration or as sprung mass vertical displacement minimization, while good handling can be characterized as attenuation of unsprung mass acceleration.

Effort devoted to passive suspension design is ineffective because improvements to ride comfort are achieved at the expense of handling and vice versa. Instead, the best result can be achieved by active suspension [4],[5], i.e. by an additional force (Fig.1) that can act on the system and simultaneously improve both of these conflicting requirements. Another important goal of the control design is to maintain stability and robustness of the closed loop system.

In most active suspension systems, the biggest disadvantage consists in energy demands. Regarding linear

electric motors, this drawback can be minimized or even eliminated because under certain circumstances there is a possibility to recuperate energy, accumulate it and use it later for the active suspension when necessary. This way, it is possible to reduce the posted claims on an external power source as much as possible. In the next paragraphs, I also describe the proposed strategy how to control the energy distribution in the suspension system. In order to regenerate electric power from the vibrations excited by road unevenness a new energy-regenerated active suspension system has been designed. We modeled and simulated the active system to show the performance improvement and performed many experiments with the actuator prototype on a new test stand we designed.

All suspension systems are designed to meet various specific requirements. In suspension systems, mainly two most important points are supposed to be improved – vibrations absorbing (videlicet passenger comfort) and attenuation of the disturbance transfer to the road (videlicet car handling). The first requirement could be understood as an attenuation of the sprung mass acceleration or as a peak minimization of the sprung mass vertical displacement. The second one is characterized as an attenuation of the force acting on the road or – in simple car models – as an attenuation of the unsprung mass acceleration. The goal is to satisfy both these contradictory requirements. Satisfactory results can be achieved when an active suspension system generating variable mechanical force acting between the sprung and unsprung masses is used.

Such an actuator can be a linear electric motor [1]. In comparison with traditional actuators that use revolving electromotors and a lead screw or toothed belt, the direct drive linear motor enables contactless transfer of electrical power according to the laws of magnetic induction. The gained electromagnetic force is applied directly without the intervention of mechanical transmission then. Linear electric motors are easily controllable and for features like low friction, high accuracy, high acceleration and velocity, high values of generated forces, high reliability and long lifetime, their usage as shock absorbers seems to be ideal.

II. ONE-QUARTER-CAR SUSPENSION MODEL AND TEST STAND

We used a traditional one-quarter-car model to design a suspension controller and to simulate the system behavior. The basic configuration of the model is shown in Fig. 1. The model involves unsprung (whell) and sprung (taken as one ideal quarter of the car body mass) masses,

Research supported by Project MSMT INGO II LG14.

Assoc. Prof. K. Hyniova is with the Department of Digital Design, Faculty of Information Technology, Czech Technical University in Prague, Thakurova 9, 160 00 Prague, Czech Republic, (phone: (+420) 722575989; e-mail: hyniova@fit.cvut.cz).

conventional passive suspension (a spring and a damper), stiffness of the tire, and linear electric motor as actuator placed in parallel to the traditional passive suspension (Fig.1).

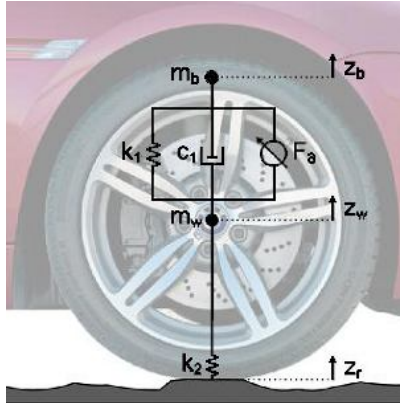


Fig. 1 one-quarter-car model

In Fig.1:

- F_a active suspension force [N]
- m_w unsprung mass (wheel) [kg]
- m_b sprung mass supported by each wheel and taken as equal to a one quarter of the total body mass [kg]
- k_2 stiffness of the tyre [N/m]
- $z_r(t)$ road displacement (road disturbance) [m]
- $z_b(t)$ displacement of the sprung mass [m]
- $z_w(t)$ displacement of the unsprung mass [m]
- k_1 stiffness of the passive suspension [N/m]
- b_1 damping quotient of the passive suspension [Ns/m]

We used the same configuration for real experiments and verification. Mechanical construction of the test stand is obvious from Fig. 2. Under the wheel there is placed another linear electric motor that uses an experimental input signal described in next paragraphs to generate road displacement (road deviations) under the running wheel. The modified H-infinity controller mentioned bellow has been developed via Matlab and implemented into dSpace and connected to the test stand system. For more details see [3].



Fig. 2 test stand

III. LINEAR ELECTRIC MOTOR

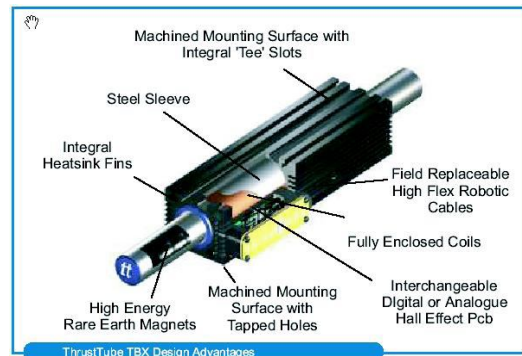


Fig. 3 linear motor basic design (manufacturer spreadsheet)

Fig.3 shows the basic principle and structure of the linear motor used as an actuator in the designed active suspension system. The appreciable feature of linear motors is that they directly translate electrical energy into usable mechanical force and motion and back. They are linear shaped.

Linear motor translator movements reach high velocities (up to approximately 4 m/s), accelerations (up to g multiples) and forces (up to 8 kN). The electromagnetic force can be applied directly to the payload without an intervention of mechanical transmission.

IV. LINEAR MOTOR MODEL

In order to verify control algorithms we created the linear motor model including a power amplifier in Matlab/Simulink. The model enables to demonstrate the conversion of electrical energy to mechanical energy.

In the model, it is assumed that the magnetic field of the secondary part with permanent magnets is sinusoidal, the phases of the primary part coils are star-connected, and a vector control method is used to control the phase current. Here, PWM voltage signal is substituted by its mean value to shorten (about 10 times) the simulation period (inaccuracies caused by such a substitution can be neglected).

The principal inner representation of the model is shown in Fig.4. The model input vector is given by the instantaneous position [m] (necessary to compute the commutation current of the coils), instantaneous velocity [m/s] (the induced voltage of the coils depends on the position and velocity) and desired force [N].

The designed model function we verified comparing dynamics of the model and the real motor. The simulation parameters correspond to catalogue parameters of TBX3810 linear motor fy Thrust-tube.

For example, time responses caused by changes of the desired force has been compared.

The linear motor input-output model is shown in Fig. 5.

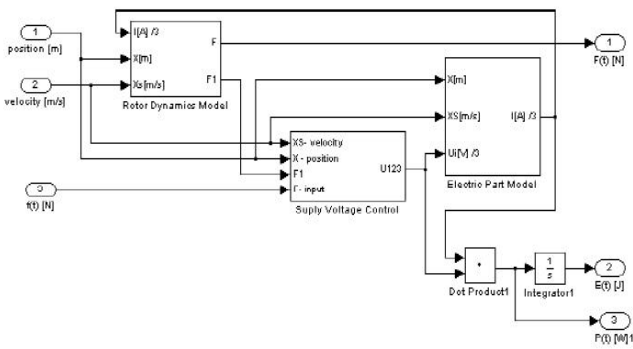


Fig.4 principal inner model representation

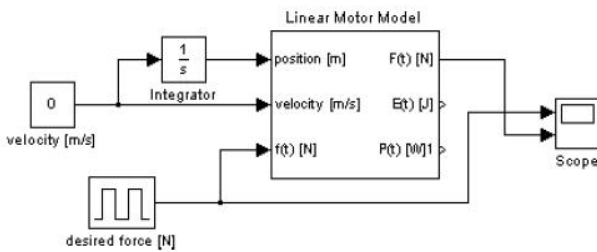


Fig. 5 linear motor input/output model for dynamics verification

Fig. 6 and fig.7 represent simulated and real time responses, respectively (rightangular force signal: 0→200 [N], power supply of 150 [V], velocity: 0 [m/s]).

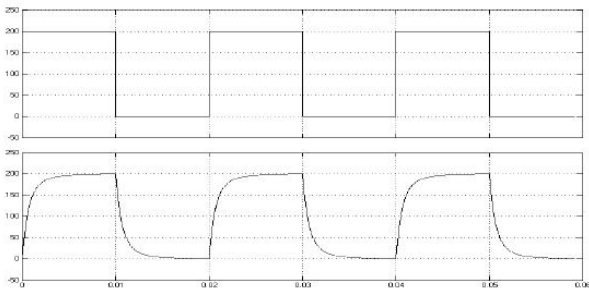


Fig.6 simulated time response

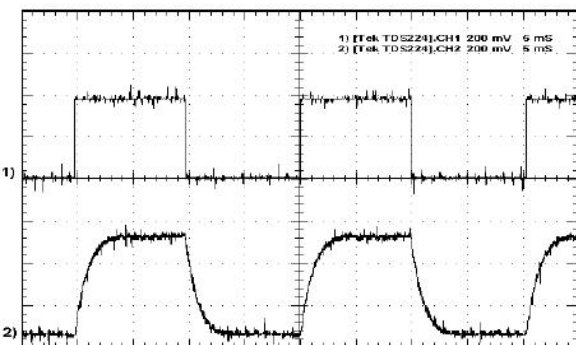


Fig. 7 real time responses

Comparing the time responses in Fig.6 and Fig.7 it can be seen a very good matching level of the model and real motor behavior.

On the base of the experiments that we completed on the model, we gained values of electric power necessary to be supplied or consumed when velocity and force of the motor are constant. In Fig. 8 an input/output model of the linear motor (with concrete simulation values) is represented.

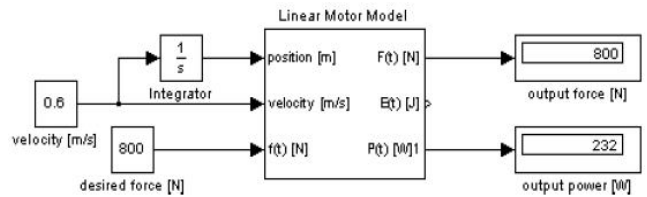


Fig.8 linear motor input-output model

It results from many experiments we made [4] with TBX3810 linear motor that the designed model describes the real linear motor equipped with necessary auxiliary circuits very authentically and enables to verify control algorithms developed to control the linear motor as an actuator of the active suspension system.

V. ENERGY BALANCE

As said above, linear electric motors can recuperate energy. When the generated force is of the same direction as the suspension velocity, the energy has to be supplied into the system. Otherwise, it can be recuperated and accumulated for some future usage.

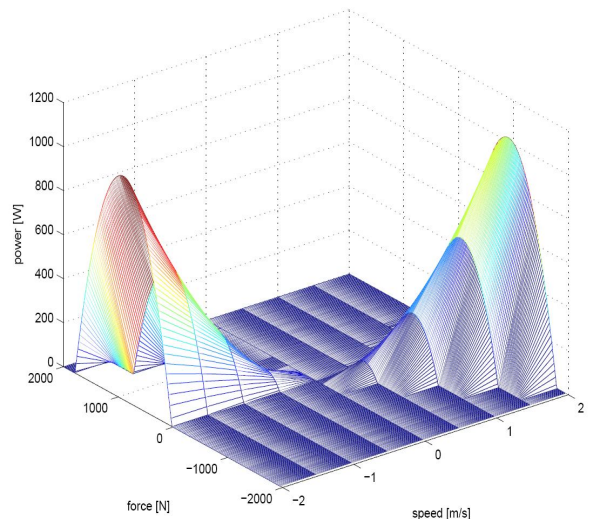


Fig. 9 recuperation area of the linear electric motor

In fact, there are some nonlinearities in the recuperation process and that is why the energy management control is difficult. The 3D plot in Fig. 9 represents the force-velocity profile of the recuperated energy. It shows how much

recuperated (and only recuperated) energy can be obtained under the given forces and velocities. In the plot, when the recuperated energy is equal to zero or bigger it is necessary to supply energy into the system.

This characteristic surface gives important information regarding one of the requirements on the control system. Optimization objectives are equal to maximization of the recuperated energy (with necessary trade-offs).

VI. ROAD DISPLACEMENT SIMULATION

In order to realize simulation and practical experiments at the test stand it is necessary to find a proper experimental signal that excites the active suspension system. Although the simplified suspension model seems to be linear there are many nonlinear parts in the system. Now the question is what signal to generate for experimental testing to reach a true model of the uneven road under the wheel. We can define two types of input signals regarding objectives:

- to prove results of simulations and pre-calculations
- to test real behavior on the road

Let us start with the first objective i.e. to verify simulation results. As the best signal to be used is white noise for its full frequency spectrum. But it should be noted that the whole system is nonlinear and that is why even white noise is not satisfactory. Moreover it is not possible to generate easily white noise on the test stand.

Unfortunately, neither step input signal simulating road bump up or bump down is not realizable by the test stand for the right-angular slopes of the signal.

To simulate road profile we used a random signal approximation. Such a signal is described by the following equation:

$$z_r = \sum_{i=1}^n \sqrt{\frac{\dot{\omega}_i}{\pi \cdot v_x}} \left\{ \operatorname{Re}\left(\frac{b_o}{-\omega_i^2 + a_1 j \omega_i + a_o}\right) \cdot \cos(\omega_i t + \alpha) + \operatorname{Im}\left(\frac{b_o}{-\omega_i^2 + a_1 j \omega_i + a_o}\right) \cdot \sin(\omega_i t + \alpha) \right\} \quad (1)$$

where

$$b_o = 0.121 \cdot v_x$$

$$a_o = 2.249 \cdot v_x$$

$$a_1 = 30.36 \cdot v_x$$

and v_x represents car velocity.

The resulting signal is obtained as a superposition of sinusoids with deterministic random angles (α in (1)). For this input signal 128 random angles have been calculated. The used pseudorandom signal is plotted in Fig. 10.

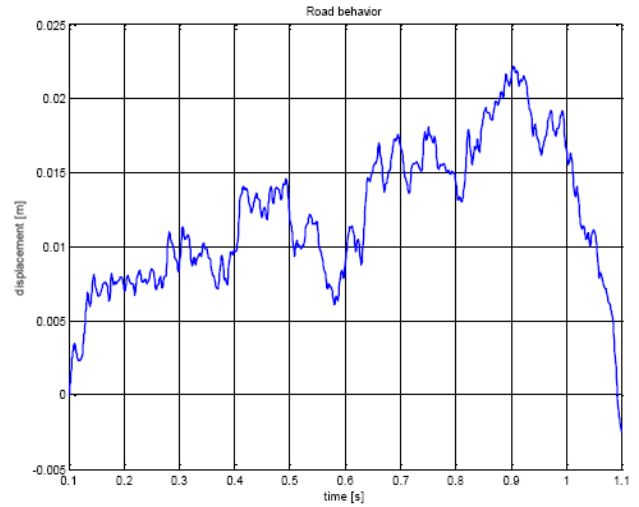


Fig. 10 random signal approximation used to simulate road displacement

VII. CONTROLLER USED IN THE CONTROL LOOP

Design of an appropriate controller is a complex problem. The research team tested commonly used high authority control concepts, such as Linear Quadratic Gaussian control, feedforward control concept, fuzzy control [5] as well as H-infinity robust control [4]. Most of the proposed concepts do not consider robustness of the designed controller, although this aspect is fairly important and well-founded. For example, changes in ambient conditions can lead to changes in the dynamics of the vibration system, which can result in substantial deterioration of the feedback controller performance.

A robust controller is necessary for the suspension system because many system parameters often vary in a wide range. Especially cargo mass changes occur for every single drive. For this reason H-infinity theory has been chosen for robust controller design [4],[6] via Matlab toolbox procedures.

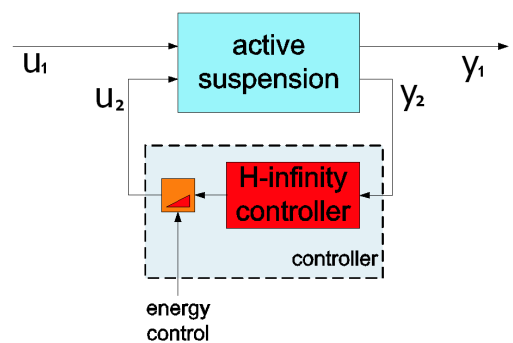


Fig. 11 modified controller structure

Nevertheless the standard H-infinity controller cannot handle energy consumption. We did some modifications of the controller on the base of the realized experiments. An additional input to control energy demands is supposed to be connected to the controller. Then master controller can use this input to keep energy balance. The general modified controller structure is shown in Fig. 11. Energy management is controlled by an external signal depending on car and road parameters, i.e. on energy accumulator (super-capacitors) capacity and the road surface, respectively [2].

First way to control energy consumption in the suspension system is analysis of the driving conditions and cyclic re-computing of the control signal in real time. For high sampling frequency (over 1 kHz) and controller performance we rejected this approach.

The second possibility of energy consumption control is control via controller deterioration. Then the designed controller is reliably robust and the active suspension system relatively stable.

Let us assume two types of driving conditions:

- the terrain (surface) the car is going on is very rough and uneven and there is enough energy stored in the accumulator (supercapacitors). Then the controller works in “comfort setting” mode, the linear electric motor consumes energy from the accumulator and the suspension performance is preserved.
- the terrain (surface) under the car wheels is relatively smooth and there is not enough energy stored in the accumulator systems (super-capacitors) because of the situation described above. The external signal provides this information to the controller in order to deteriorate its performance and to reduce the linear motor energy consumption. The deterioration is stated by the desired force attenuation. In this case the control works in “energy setting” mode.

If the force is attenuated too much the active suspension system works only as the passive suspension (connected in parallel to the active suspension) while the linear electric motor works as a generator generating electrical energy to be stored in supercapacitors. Of course, in such a situation the suspension performance is deteriorated (up to the passive suspension level in the worst case).

VIII. EXPERIMENTS TAKEN ON THE ACTIVE SUSPENSION TEST STAND

We used random signal approximation stated in (1) as an input signal (road profile) for experiments taken on the active suspension test stand. Two main objectives must be taken into account - passenger comfort improvement and energy consumption (see Fig. 12). In Fig. 12 the road profile input and corresponding body displacement for “energy” and “comfort” controller settings are displayed. Body (sprung mass) displacement can be taken as an indicator of the passenger comfort.

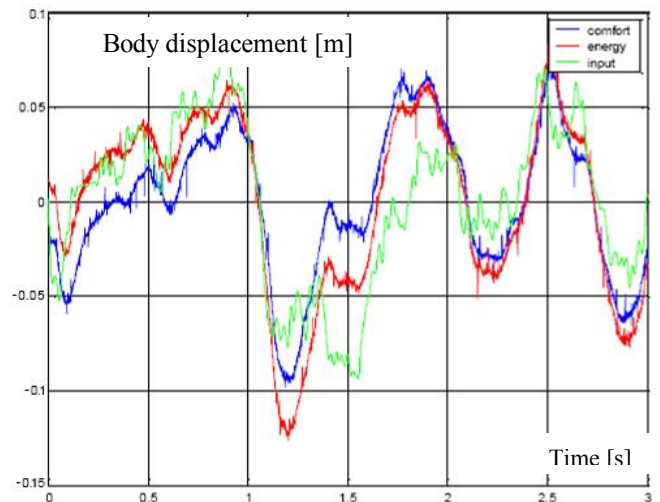


Fig. 12 body displacement for “energy” and “comfort” controller setting

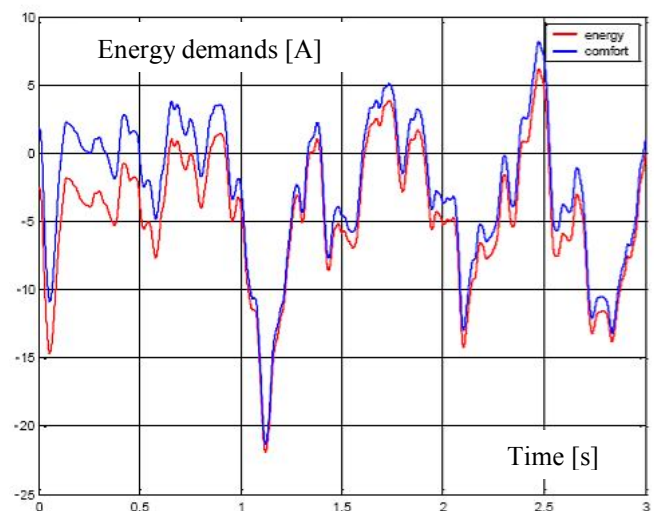


Fig.13 Energy demands (demands on electric current) for “energy” and “comfort” controller setting

For “comfort” controller setting, passenger comfort is maximized with no respect to energy consumption while for “energy” controller setting the controller performance is deteriorated and energy recuperated with no respect to passenger comfort.

Fig.13 displays two curves- energy demands for “comfort” controller setting and energy demands for “energy” controller setting corresponding to the car body displacement signal in Fig.12. Both curves were measured when excited with the same road profile input signal. Negative values of energy in Fig.13 represent recuperated energy.

Let us show the results as mean values of Comfort and Energy indicators stated in [2]. Tab.1 involves mean values for the body displacement as absolute values of the defined

body displacement indicator and also as a percentage of its improvement.

TABLE I. BODY DISPLACEMENT MEAN VALUES

	Body displacement mean value [m]	Percentage
For Comfort setting	0,0386	100%
For Energy setting	0,0474	123%

TABLE II. POWER MEAN VALUES

	El.Current mean value [A]	Percentage
For Comfort setting	2,689	100%
For Energy setting	1,598	59%

In Tab.1, the first line shows that for “comfort” controller setting the comfort indicator, i.e. body displacement mean value (0,0386m) is taken as 100 %. In the second line, when the controller was deteriorated, the comfort was devaluated up to 0,0474 m, i.e. to 123 %.

Tab.2 contains mean values of power indicator i.e. el. current mean values. Lower value corresponds to lower energy demands. It is sufficient to express power values by values of electric current because the voltage supply of the motor remains constant. Similarly, the first line shows that for standard controller setting the “comfort” indicator (2,698 A) is taken as 100 %. In the second line, when the controller was deteriorated the energy indicator is devatuated up to 1,598 A, i.e. to 59 %. Briefly, controller deterioration causes comfort devaluation to 123 % while energy consumption decreases to 59 %.

IX. CONCLUSION

We developed a new method for direct real-time energy control in the car suspension system with respect to reduction of energy consumption. Experiments that we took on the designed test stand verified validity of simulations and showed that it is possible to change energy demands according to the road surface mode of the energy storage in the car supercapacitors. The method can be extended to general plants with considerable energy demands in which the decreasing actuator signal in a given range can preserve system stability.

Various active suspension controllers we developed via Matlab implemented into dSpace and connected to the test stand system. As we discussed in [2] and [3], the most satisfactory responses of the suspension system we reached using H-infinity robust control.

REFERENCES

[1] Honcu, J. - Hyniova, K. - Stribrsky, A. - Kruczek, A.: Linear Motors as a New Way in Vehicle Suspension System., in *Preprints of the 3-rd International Conference on Computing, Communication and Control Technologies* [CD-ROM]. Orlando: IHS - International Institute of Informatics and Systemics, 2005, pp. 316-321

[2] Hyniova, K. - Honcu, J. - Stribrsky, A.: Energy Recuperation and Management in Automotive Active Suspension Systems., in *Proceedings of the 7th International Carpathian Control Conference ICCC 2006*. Ostrava: VŠB – Technical University in Ostrava, Faculty of Mechanical Engineering, Department of Control Systems and Instrumentation, 2006, pp 185-188.

[3] A. Kruczek and A. Stribrsky, A Full-car Model for Active Suspension – Some Practical Aspects, in *Proceedings of IEEE International Conference on Mechatronics*, Istanbul, Turkey, pp.56-62, 2004

[4] Koulocheris, D.- Vrazopoulos, H.- Dertimanis, V. : A Hybrid Evolution Strategy for Vehicle Suspension Optimization, *WSEAS Transactions on Systems*, Issue 1, Vol.3, 2004

[5] Libin, L.- Quiang, L.: Vibration Analysis Based on Full Multi-Body Model for the Commercial Vehicle Suspension System, *Proceedings of the 6th WSEAS International Conference on Signal Processing, Robotics and Automation*, Corfu Island, Greece, pp.203-208, 2007

[6] Stribrsky, A. – Honcu, J. – Hyniova, K. – Kruczek, J.: H-infinity Control of Active Suspension Systems, *Proceedings of the 5-th International Scientific Technical Conference Process Control* , University of Pardubice, pp. 35-43, Kouty nad Desnou, 2002

[7] Stribrsky, A. – Hyniova, K. - Honcu, J.- Kruczek, J.: Using Fuzzy Logic to Control Active Suspension System of One-Half-Car Model, *Proceedings of International Carpathian Control conference ICCC 2003*, TU Kosice, pp.735-741, Tatranske Matliare, 2003

[8] K. Zhou and J. C. Doyle, *Essentials of Robust Control*, Prentice Hall, 1998



K. Hyniova (born in 1963)

Ing. in technical cybernetics at the Faculty of Electrical Engineering at the Czech Technical university (CTU) in Prague, Czech Republic, (1987), PhD in technical cybernetics at the Faculty of Electrical Engineering, CTU in Prague, Czech Republic, (1991), Assoc. Prof. in control engineering and measurement, at Faculty of Electrical Engineering, at the CTU in Prague, CZ, (2000).

She has worked at the Department of Control Engineering, Faculty of Electrical Engineering, CTU in Prague, CZ first as an assistant professor, later as an Associated Professor. Currently she is working as an Associated Professor at the Department of Digital Design, Faculty of Information technology, CTU in Prague, CZ. She published 5 books and over 70 papers (Hyniova, K.: Instrumentation of processes, Prague, Czech Republic, CTU Publishing, 1999; Hyniova, K.: Control Systems, Prague, Czech Republic, CTU Publishing, 2012; Hyniova, K.: An Innovative Active Suspension System for Autonomous Vehicles: A Safe and Comfortable Ride and Good Handling, In *ERCIM NEWS*, No. 94, published by ERCIM EEIG, France, pp.28-29, 2013)). She is interested in intelligent vehicles control systems, vehicle dynamics and in consistency in networks of relations.

She is a member of Technical Committee 4.2. on Mechatronic Systems, IFAC.

A Study of Pressure Distribution Droplets Motion in Convergence-Divergence Shape Microchannel

Maryam Ghelichkhani

Abstract— Micro fluid devices enable the transport nano liters fluids in micro scale channels [1, 2]. Very devices built in this case, for example genome sequencing or using micro droplet as chemical reactors [1-3]. In this paper, we introduce a model of micro channel in order to investigate the dynamics of micro droplets. This model is derived of level set method. Further more, we investigate pressure distribution around micro droplet motion in this convergence-divergence micro channel. This device can be used in many applications for example it can be considered as convergence-divergence digital switch in digital micro fluidic.

Keywords-pressure distribution;micro channel;micro droplet

I. INTRODUCTION

Micro fluidic devices compose micro scale channels that minimize many chemical processes [4]. The Study of droplets, as the most common carriers for bio chemical is very important [4,5]. These channels transport fluids for many applications for example genome sequencing, using micro droplet as chemical reactors, reagent mixing, separation and detection [6]. Understanding droplets motion in micro channels is necessary in order to achieve the follow control needed in practical applications [1]. Pressure distribution is one of important parameters in micro channels. In this paper, we employed two phase level set method for numerical simulation two fluids transport in a convergence-divergence micro channel then investigated pressure distribution in this channel. This micro channel can be employed as a convergence-divergence digital switch. This paper is organized as follows, equation governing presented in section II and numerical simulation described in section III.

II. EQUATION GOVERNING

A. Level set equation

The level set method (sometimes abbreviated as LSM) which purposed by Sussman and et al, is a numerical technique for tracking interfaces and shapes. The advantage of the level set method is that one can perform numerical computations involving curves and surfaces on a fixed Cartesian grid without having to parameterize these objects (this is called the Eulerian approach). [7] Also, the level set method makes it very easy to follow shapes that change topology. To describe the droplet motion is necessary to simulate its shape variation and evolution of interface $f(X, t) = 0$ between the water and droplet. Driving this expression in time becomes equation (1) [8]:

$$\frac{\partial f}{\partial t} + U \cdot \nabla f = 0 \tag{1}$$

This method describes the evolution of interface between the two fluids tracing an isopotential curve of level set function ϕ . Zero level set function is demonstrated the interface motion at time. The more dense and more viscous fluids placed in the zone where the level set function is positive ($\phi > 0$) and less dense and less viscous one situated in the domain where the level set function is negative ($\phi < 0$). When the underlying velocity field u is specified, the advection step involves the solution of the scalar transport equation for ϕ [3]:

$$\frac{\partial \phi}{\partial t} + U \cdot \nabla \phi = 0 \tag{2}$$

U is the fluid velocity.

B. Navier stock equation

Further more Level set equation, Navier-Stokes equations compose momentum (3) and continuity (4) equations for incompressible fluids are used [8]:

$$\rho \frac{\partial U}{\partial t} - \nabla \cdot [\eta (\nabla U + (\nabla U)^T)] + \rho (U \cdot \nabla) U + \nabla P = F \tag{3}$$

$$\nabla \cdot U = 0 \tag{4}$$

Where p is the pressure, $U = (u; v)^T$ is the velocity, ρ is the density, η is the viscosity and F is a volume force field such as gravity or surface tension

III. NUMERICAL SIMULATION

In this section, we consider the convergence-divergence shape micro channel shown in figure 1.



Figure 1. A typical convergence-divergence shape micro fluidic channel.

The first, water with $\eta = 1.95 \times 10^{-3}$ Pa.S and velocity 0.0166 m/s enter in this channel from B inlet then droplets with $\eta = 6.7 \times 10^{-3}$ Pa.S and velocity = 0.0083 m/s enter the channel from A inlet. Surface tension coefficient was considered 5×10^{-3} N/m in this simulation. We investigated droplets motion in length of B-C channel in different step.

In the first step, one droplet is in the first of convergence channel. Schematic of dynamic viscosity fluids in micro channel in this step at $t=0.065s$ shown in figure 2. When the first droplet is received to end of convergence channel, another droplet enters the channel. Dynamic viscosity figure of fluids in this step at $t=0.09s$ shown in figure 3.

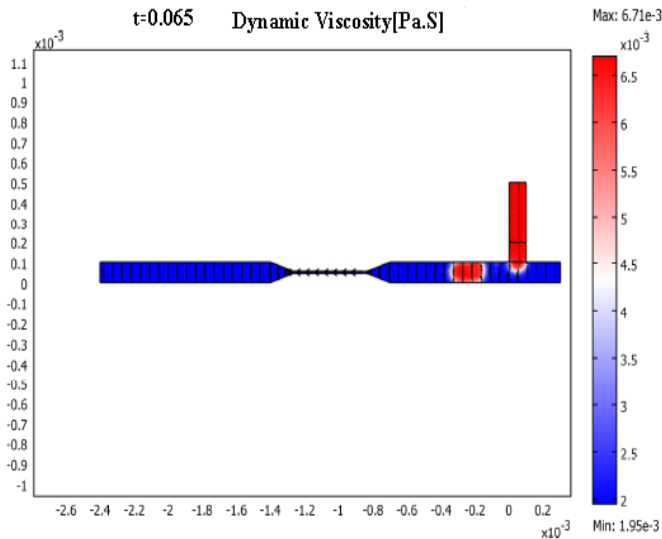


Figure 2. Dynamic viscosity schematic of fluids in micro channel figure 1 at $t=0.065s$.

indicated in figure4. At $t=0.12s$ the first droplet received to the divergence channel, third droplet entered the channel and because second droplet is near the middle of channel, pressure different increase in first and end of channel. Dynamic viscosity figure in this case shown in figure5.

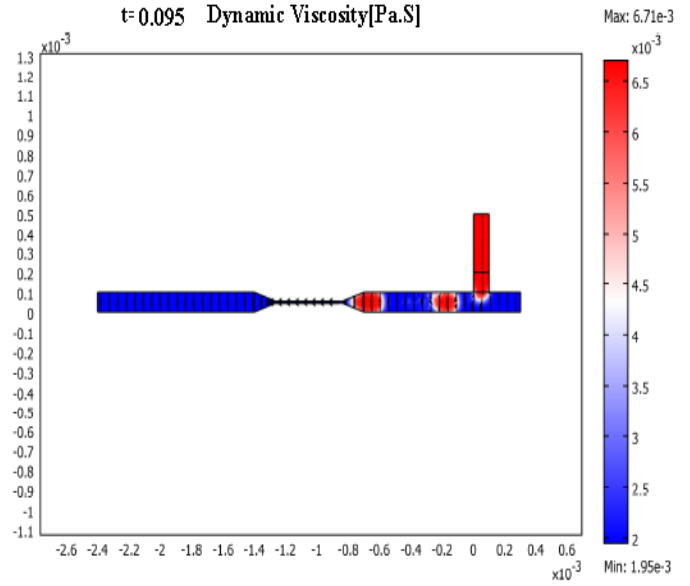


Figure 4. Dynamic viscosity schematic of fluids in micro channel figure1 at $t=0.095s$.

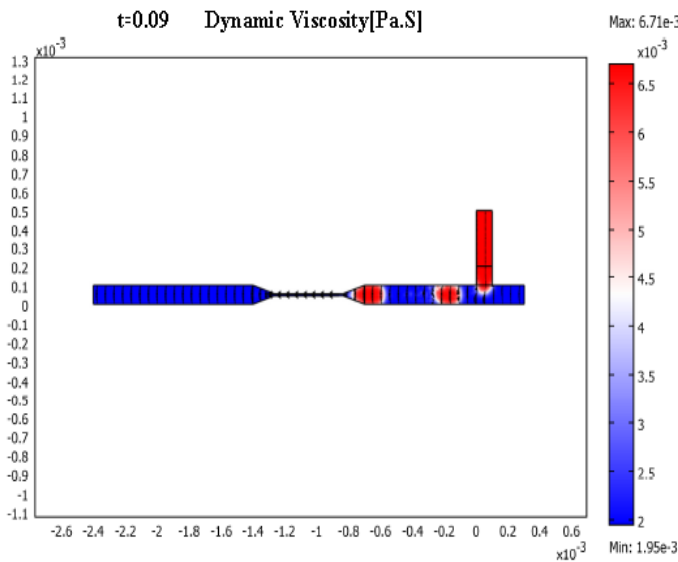


Figure 3. Dynamic viscosity schematic of fluids in micro channel figure1 at $t=0.09s$.

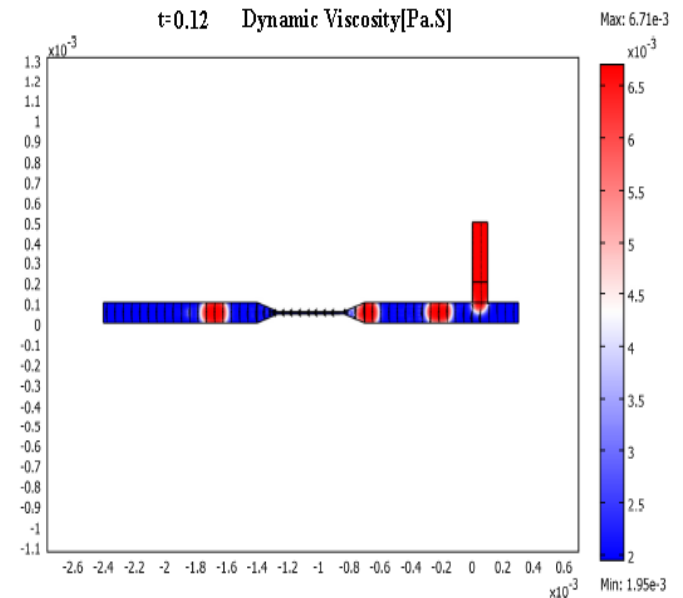


Figure 5. Dynamic viscosity schematic of fluids in micro channel figure1 at $t=0.12s$.

At $t= 0.095s$, first droplet received in middle of micro channel where width of channel is smaller than over there. Channel is pinched in this zone, because droplets have more viscosity. Dynamic viscosity figure of fluids in this time

At $t=0.145s$ two droplets are in divergence and convergence channels. Dynamic viscosity figure of fluids in this time shown in figure6. At end of simulation five droplets are in

micro channel three droplets are in divergence channel and two droplets are in convergence channel. Dynamic viscosity figure at $t=0.16s$ shown in figure 7. The pressure different in across the convergence channel is constant but in middle of channel where width of channel is smaller than over there, pressure decrease as linear in this zone. And pressure gradient again is constant in divergence channel. If droplet will be in convergence or divergence channel, pressure will be increase in this point. When droplet is in middle of channel with small width, channel pinch in this zone and the pressure different in convergence and divergence channels are very much. This case observe in $t=0.095s$. We can use of this property in digital micro fluidic and consider this channel as digital switch. A comparison of pressure distribution in these times demonstrated in figure 8.

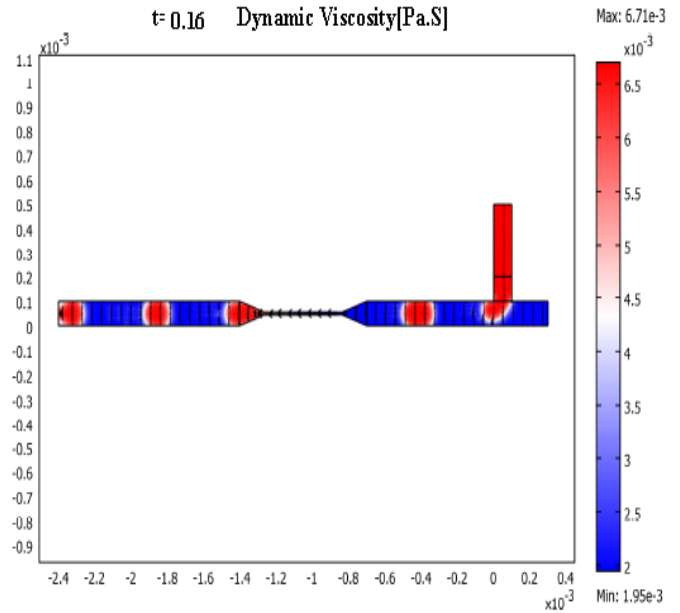


Figure 7. Dynamic viscosity schematic of fluids in micro channel figure1 at $t=0.16s$.

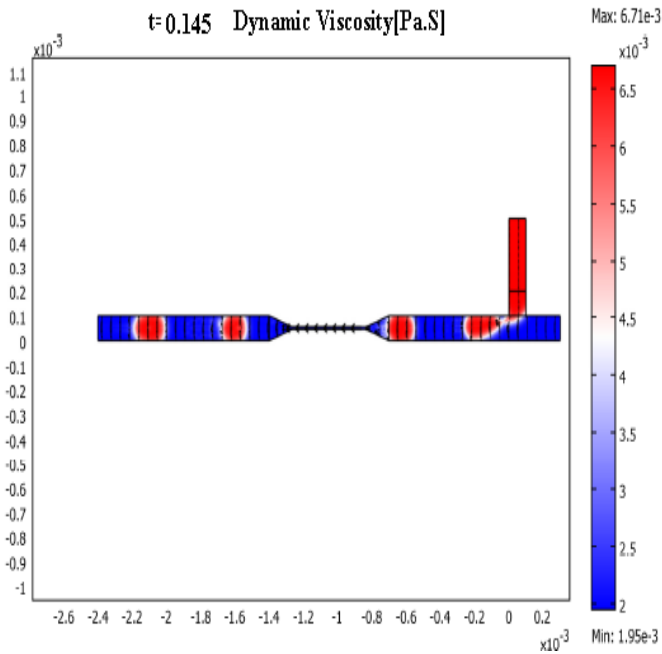


Figure 6. Dynamic viscosity schematic of fluids in micro channel figure1 at $t=0.145s$.

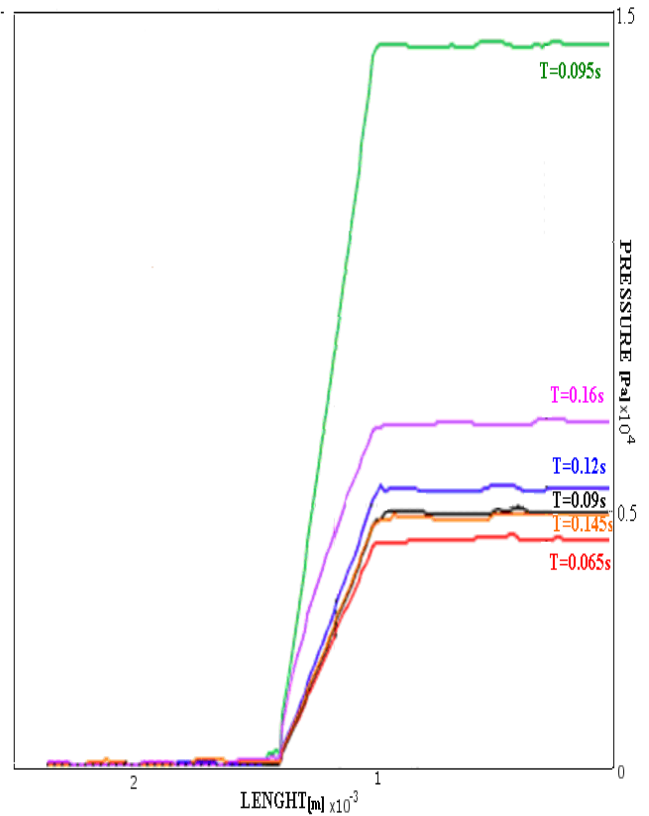


Figure 8. Comparison of pressure gradient along the line B-C in figure1 in various times.

CONCLUSION

We investigated pressure gradient in convergence-divergence shape micro channel when droplets move in this channels. When droplets are received to middle of channel where width of channel is smaller than over there. Pressure different is very much in length of channel. We can use of this property for many applications in digital micro fluidic.

REFERENCES

- [1] Paul Vigneaux, "Droplets in Microchannels with Level Set Method," 2008.
- [2] A. J. deMello. "DNA amplification moves on, Nature," Vol. 422 , 6 March, 2003.
- [3] E. Bovet, L. Preziosi, B. Chiaia, F. Barpi and Politecnico di Torino, "The Level Set Method Applied to Avalanches", 2007.
- [4] Dongdong He. Huaxiong Huang . Yongji Tan a" Numerical simulation for a droplet fission process of electrowetting on dielectric device," 2009.
- [5] R.Chien and J.w.Parce, "Multiport flow-control system for lab-on-chip micro fluidic devices," *resenius J.Anal.Chem*, Vol.371, pp.106-111, 2001.
- [6] P.A.Greenwood and G.M.Greenway, "Sample manipulation in micro total analysis systems," *Trends Anal.Chem.*, vol.21, pp.726-740, 2002.
- [7] Osher, S. & J. A. Sethian (1988), "Fronts propagating with curvature-dependent speed: Algorithms based on Hamilton-Jacobi formulations", *J. Comput. Phys.* **79**: 12–49.
- [8] S. Osher and R. Fedkiw. "Level Set Methods and Dynamic Implicit Interfaces," 1st.Edition, Applied Mathematical Sciences, Vol. 153, Springer, 2003

Modeling and Optimization of Hydrolysate Yields in Leather Waste Processing

Hana Vaskova and Karel Kolomaznik

Abstract—Leather industry contributes significantly to the production of waste and in the long-term pollutes the environment. Hydrolysis processes offer a reasonable solution for the processing of certain part of these wastes. A necessary condition for their implementation, however, is their economic aspect, otherwise waste end up in landfills or incinerators, what brings risk of leakage into the soil and groundwater or air pollution. In this paper a mathematical model based on the total mass balance of technology and balance of the individual components of the production system is presented to optimize the yield of hydrolysates. The attention is also paid to the modeling of temperature and determination the time necessary for reaching the ideal temperature of the reaction mixture for the purpose of minimizing costs.

Keywords—Hydrolysis process, leather waste processing, modeling, optimization, yield

I. INTRODUCTION

PEOPLE are surrounded by an occurrence of waste for centuries, but only for decades waste has become a problem that should be systematically solved and organized. The issue of waste reduction and ways of their safe, environmentally and economically favourable disposal is, as a logical result of long-term situation, one of the most actual and pressing problems worldwide. The production of various waste types has an upward trend for decades in a manufacturing sector and even in the public sphere.

A significant amount of waste is produced in the manufacturing sector of natural polymers especially in the leather industry. The leather tanning industry is historically one of the first industries occupying an important function in terms of by-products of other industries - meat industry. Tanning industry transforms raw hides of slaughter and game animals through physical and chemical processes to a stable, technically usable product - the leather. On one hand it uses meat industry waste as a feedstock, however on the other hand this industry produces another hazardous waste.

This work is supported by the Ministry of Education, Youth and Sports of the Czech Republic, by European Regional Development Fund under the project CEBIA-Tech No. CZ.1.05/2.1.00/03.0089.

Hana Vaskova is with the Faculty of Applied Informatics, Tomas Bata University in Zlin, nám. T. G. Masaryka 5555, 760 01 Zlín, Czech Republic (e-mail: vaskova@fai.utb.cz).

Karel Kolomaznik is with the Faculty of Applied Informatics, Tomas Bata University in Zlin, nám. T. G. Masaryka 5555, 760 01 Zlín, Czech Republic (e-mail: kolomaznik@fai.utb.cz).

Production of 200 kg of leather requires one ton of raw hides processing, i.e. feedstock usage is only 20% efficient. From this one ton of raw hides about 250 kg of non-tanned waste, 200 kg of tanned wastes containing chromium is also produced. The remaining share comprises modified solid waste and sludge. In the production of 200 kg of leather about 50,000 kg of waste water containing about 5 kg of chromium is generated.

Mathematical modeling is gaining in recent years a great importance for the analysis and prediction of the behaviour of processes and phenomena in areas of natural, technical, industrial, but also economic and social. It offers the possibility of transferring the problem from the field of application to be processed mathematically. This allows penetrating through the analysis into its nature and to obtain useful information about investigated problem. Using mathematical means and information technology procedures can be created. Procedures, that leads to a deeper and more thorough understanding and influencing real processes and phenomena, and to prepare the way for better, optimized design or control of the modeled system.

II. THEORY

A. Tannery waste

Leather products like shoes, belts, wallets, upholstery and others belong among the objects of everyday needs. Achieving the final products comprise a lot of waste arising from the raw material processing (tannery waste) and manufacturing specific items (manipulation waste). These are two types of leather waste. Another arises when these mentioned objects become unusable and are moved mostly to landfill or incinerators. This third waste category of old “retired” leather stuff may represent a serious threat to the environment.

The majority of global leather production is chrome-tanned. Using complex salts of trivalent chromium in the process of tanning effectively influenced the desired functional properties of leather. Trivalent chromium stabilizes a hide by crosslinking the collagen fibres and supply required qualities. However, trivalent chromium contained in leather can be under various conditions in small amounts oxidized to another form – hexavalent chromium.

Hexavalent chromium (CrVI) unlike trivalent chromium (CrIII) is toxic and carcinogenic element. A potential threat to the health could be hidden in chrome-tanned leather goods, mainly shoes, which are in daily contact with the human

organism. If the goods contain even small amounts of carcinogenic chromium, there is a potential risk of cancer, especially kidney and urinary tract [1]. The effects of repeated exposure to hexavalent chromium have hazardous impact on human health [2].

The possibility of the spontaneous oxidation of CrIII into CrVI can occur both in alkaline and acidic medium in the wide range of pH what complicate the right conditions specification [1]. Trivalent chromium contained in discarded leather items may succumb to uncontrolled oxidation on the landfills and make the waste hazardous, which may result in the possibility of leakage into the soil and groundwater.

B. The dechromation process of leather waste

Hydrolysis, a decomposition reaction is significantly used in technological processes for the purpose of fermentation of the matrices (e.g. leather wastes) for subsequent analysis of the studied material. Hydrolysis of collagen material in alkaline or acidic medium is used also in a complex process dechromation of the leather industry wastes. In these cases, one component - chromium or protein is subjected to liquefaction so that this substance can also be utilized effectively into other forms.

C. Production system

The production system for producing of the hydrolysate is composed of three basic elements: a reactor, a filter and vacuum evaporator. The diagram is shown in Fig. 1. Feedstock in the reactor is leather waste, water and an alkali, creating a reaction mixture. When the desired degree of hydrolysis is reached, hot heterogeneous mixture is filtered and the resulting filtrate is further transferred to an evaporator where the concentration of hydrolyzed substance is increased. The list of physical quantities fundamental for the description and setting the mathematical-physical model are stated in Table 1.

This first stage - the process of dechromation of chrome-tanned waste i.e. a separation of liquefied collagen protein from chromium sludge was already resolved in our institute and the technology for this process was realized in laboratory

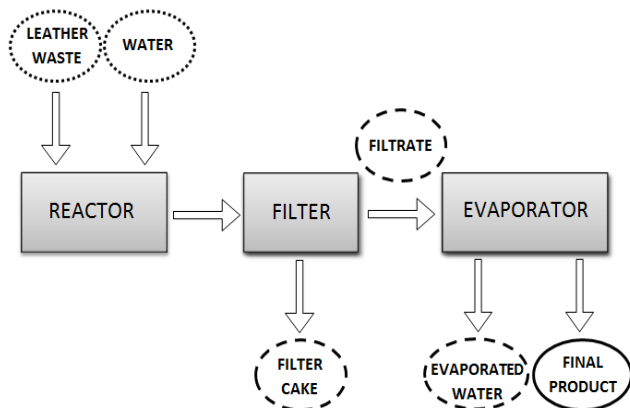


Fig. 1 Diagram of the processing system

conditions. In [3] is described a whole computer system for chromium recycling with focus on the control structure of the most important parts of the technology. Obtained chromium sludge can be subsequently revitalized and acquired chromium in a form of salts can be used for further leather tanning [4]. Following stages in the process enzymatic hydrolysis and acidolysis lead to decreasing the molar mass of the final protein hydrolysates. This condition is important for utilization protein hydrolysates in agriculture, e.g. as a biostimulator [5].

Table 1 Physical quantities and their assignments for model formulation

Designation	Physical quantity	Unit
CH	Mass of leather shavings	t
W	Mass of water (the feedstock)	t
FK	Mass of filter cake	t
P	Mass of product	t
WO	Mass of water (waste material)	t
FL	Mass of filtrate	t
$a_{s, CH}$	Amount of dry matter in leather shavings	1
$a_{s, FL}$	Amount of dry matter in filtrate	1
$a_{s, P}$	Amount of dry matter in product	1
$a_{s, FK}$	Amount of dry matter in filter	1

III. MATHEMATIC MODELING

A. Hydrolysates yield

To optimize the yield of hydrolysate the mathematical model based on the total mass balance and balances of components was used. The model consists of four equations:

Total mass balance of the whole system:

$$W + CH = FK + P + WO \tag{1}$$

The balance of the total dry matter of technology

$$a_{s, CH} CH = a_{s, FK} FK + a_{s, P} P \tag{2}$$

Balance of reactor and filter

$$W + CH = FK + FL \tag{3}$$

Balance of dry matter evaporators

$$a_{s, FL} FL = a_{s, P} P \tag{4}$$

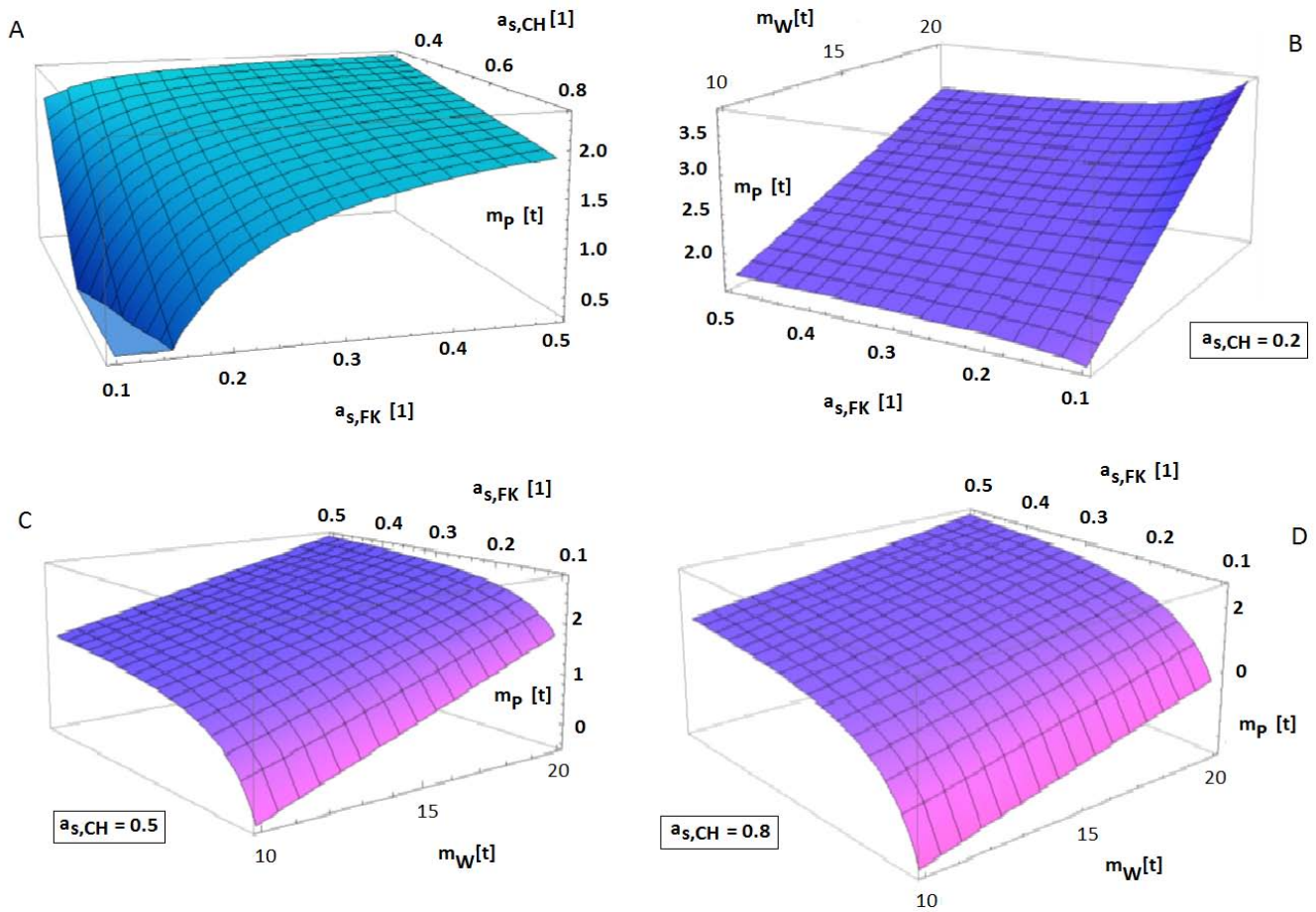


Fig. 2 3D mathematical models for hydrolysate yield optimizing. A: Dependence of the mass of product on the dry matter of chromium shavings and on the dry matter of filter cake. B – D: Dependence of the mass of product on the dry matter of filter cake and the consumption of water for a constant mass of dry matter of chromium shavings 0.2 (B), 0.5 (C) and 0,8 (D).

Here FK, P, WO and FL are unknown quantities. The objective is to gain as much product as it is economically profitable with the consideration of the main operating costs.

Simulation calculation was performed for known values of dry matter of individual compounds. The amount of feedstock was chosen for a real reactor in semi-industrial scale - 3 tons of leather waste and 15 tons of water. The mass rate of leather shavings and water is already known from foregoing experiments and laboratory experience.

Wolfram Mathematica software was used for visualization of the solution of mass balance mathematical models. 3D model in Fig 2 represent the dependence of product weight on the dry matter of chromium shavings and the dry matter of filter cake or water consumption.

It is also necessary to consider varying value of dry matter of feedstock material due to various sources of leather waste what will also affects the filtrate.

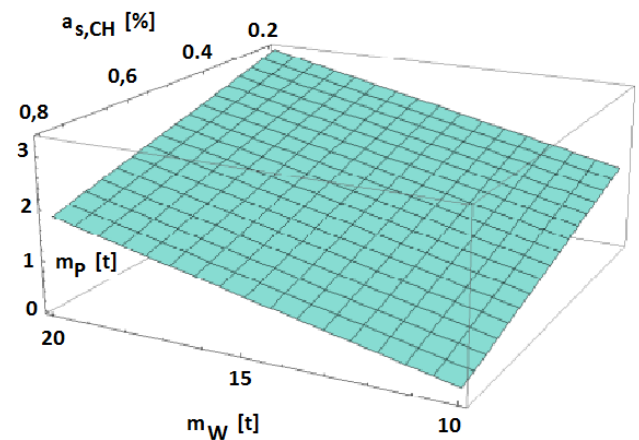


Fig. 3 Dependence of the mass of product on the dry matter of chromium shavings and the consumption of water for value 0.3 for the dry matter filter cake

Dry matter of FK depends on the time of filtration and on pressure energy consumption.

It is clear from Fig. 2 that from approximately 30% of dry matter of FK it does not have a significant effect on the yield of the product. Continuing to hydrolysis process would extend the time and consumption of energy thereby the costs.

B. Temperature modeling

For the purpose of costs optimization it is necessary to determine the time needful to achieve the optimal temperature for the running of hydrolysis reaction. Mathematical-physical model is based on the balance of heat outputs in the flow reactor. The main part of the reactor has a cylindrical shape. Its lower part forms a cone and the upper part has the shape of a spherical cap. Cylindrical and the lower part is heated by heat transfer medium – a steam and is isolated from the surroundings, what does not apply to the upper part. The main parameters of reactor and other important physical quantities are listed in Table 2.

Table 2 Physical quantities and assignments for the model (5)

Symbol	Physical quantity	Unit
τ	Time	s
T_0	Ambient temperature	°C
T	Temperature of the reaction mixture	°C
T_1	Temperature of the condensate	°C
T_s	Temperature of the heating steam	°C
c_p	Specific heat of water	J kg ⁻¹ K ⁻¹
k	Heat transfer coefficient	Wm ⁻² K ⁻¹
α	Heat transfer coefficient of the reactor lid	Wm ⁻² K ⁻¹
H	Heat of condensation of steam	Jkg ⁻¹
\dot{m}_p	Mass flow of heating steam	kgs ⁻¹
r	Radius of the reactor cylindrical part	m
h	Height of the reactor cylindrical part	m
v_1	Height of a spherical cap	m
v_2	Height of the conical part of the reactor	m
S	Area of the reactor heated by steam	m ²
S_1	Surfaces of the reactor (spherical cap)	m ²

The balance of the heat outputs is given by the differential equation

$$H \dot{m}_p + \dot{m}_p c_p (T_p - T_1) = kS(T - T_0) + \alpha S_1(T - T_0) + m_{RC} c_p \frac{dT}{d\tau} \tag{5}$$

Considering the initial conditions

$$\tau = 0, T = T_0 \tag{6}$$

The solution is:

$$T = T_0 + \frac{A}{B} \left(1 - e^{-\frac{B}{D}\tau} \right) \tag{7}$$

Where A, B and D are constants introduced to simplify the model solution

$$A = H \dot{m}_p + \dot{m}_p c_p (T_p - T_1) \tag{8}$$

$$B = (kS + \alpha S_1) \tag{9}$$

$$D = m_{RC} c_p \tag{10}$$

3D graph based on model (5) i.e. modeling the influence of the initial temperature for the achievement of the reaction temperature is presented in Fig. 4. The results show there is difference in time about 15 minutes when starting from ambient temperature in the range 5°C – 30 °C.

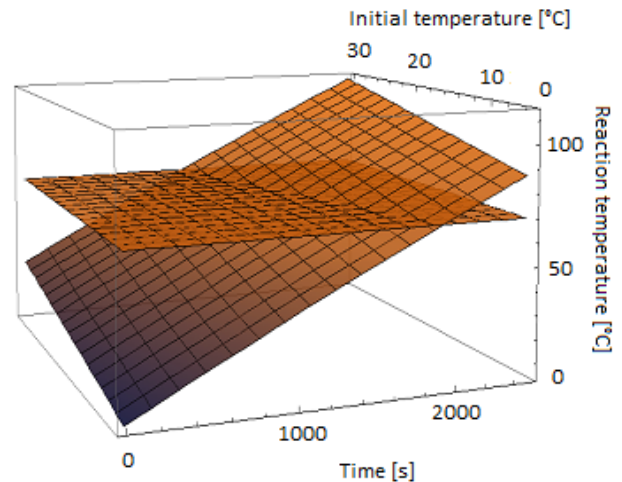


Fig. 4 Dependence of achievement the reaction temperature on the reaction mixture initial temperature.

IV. CONCLUSION

The issue of safe, environmentally friendly and also economically effective method of waste reduction is one of the actual problems all over the world. Models dealing with the requirement of minimum cost in the process of leather waste hydrolysis in terms of yield and time or thermal efficiency were presented. Optimization of manufacturing processes of leather wastes is based on thorough analysis of technological operations and on design of mathematical models describing the mechanism of their behaviour.

REFERENCES

- [1] Kolomaznik, K., Adámek, M., Anděl, I., Uhlířová, M.: Leather waste - Potential threat to human health, and a new technology of its treatment. *Journal of Hazardous Materials*. Vol. 160, 2008, pp. 514-520.
- [2] Hang, X., Zhang, X., Wang, X., Jin, L., Yang, Z., Jiang, Chronic occupational exposure to hexavalent chromium causes DNA damage in electroplating workers. *BMC Public Health*. Vol. 11, No. 1, 2011, pp. 224-232
- [3] Dolinay, J., Dostálek, P., Vasek, V., Kolomaznik, K., Janacova, D. New Embedded control system for enzymatic hydrolysis. *Proceedings of the 8th WSEAS (AIC'08)*, Venice, Italy, 2008, pp. 95 – 98.
- [4] Kolomaznik, K., Mladek, M., Langmaier, F., Janacova, D., Taylor, M., M. *JALCA*, Vol.94, 2000, pp.55 – 63.
- [5] Vaskova, H., Kolomaznik, K., Vasek, V. Mathematical Model of Collagen Protein Hydrolysis for Producing Inducers of Resistance. *Proceedings of the 3rd WSEAS CSCS'12*, Barcelona, Spain. 2012, p. 105-109.

Discrete-Time State Estimation Using Unbiased FIR Filters with Minimized Variance

SHUNYI ZHAO, FEI LIU

Jiangnan University

Key Lab. of Adv. Proc. Contr. for Light Industry Department of Electronics Engineering

Wuxi, Jiangsu

P. R. CHINA

shunyi@alberta.ca, fliu@jiangnan.edu.cn

YURIY S. SHMALIY

Universidad de Guanajuato

Palo Blanco, 36885, Salamanca

MEXICO

shmaliy@ugto.mx

Abstract: Optimal or unbiased estimators are widely used for state estimation and tracking. We propose a new minimum variance unbiased (MVU) finite impulse response (FIR) filter which minimizes the estimation error variance in the unbiased FIR (UFIR) filter. The relationship between the filter gains of the MVU FIR, UFIR and optimal FIR (OFIR) filters is found analytically. Simulations provided using a polynomial state-space model have shown that errors in the MVU FIR filter are intermediate between the UFIR and OFIR filters, and the MVU FIR filter exhibits better denoising effect than the UFIR estimates. It is also shown that the performance of MVU FIR filter strongly depends on the averaging interval of N points: by small N , the MVU FIR filter approaches UFIR filter and, if N is large, it becomes optimal.

Key-Words: State estimation, minimum variance, unbiased filter, FIR filter.

1 Introduction

The finite impulse response (FIR) estimators (smoothers, filters and predictors) have been under the development in the last three decades [1–7]. An important progress was achieved by Kwon, Kim and Park in [7], where the problem by combining the receding horizon strategy with the KF was solved. After that, the unbiased FIR (UFIR) filter was proposed for discrete-time system model in [8], and a fixed-lag FIR smoother was developed in [9] for continuous-time models. Quite recently, an UFIR filter was derived by Shmaliy in [10] and [11], for real-time state space models. Further, the p -shift optimal FIR (OFIR) estimator was obtained in [12] and [13] for time-invariant state space model. Using in part the results obtained in [13], Shmaliy proposed in [14] a Kalman-like UFIR estimator for the time-variant case. In [15], a suboptimal FIR estimator was developed by using the extended KF strategy. Moreover, unified forms for KF and FIR filter and smoother were shown and investigated in [16]. Although the progress in FIR filtering opens new horizons in optimal and robust estimation of linear and nonlinear models, some well-recognized approaches such as the minimum variance unbiased (MVU) estimation still remain undeveloped in FIR filtering.

In this paper, a MVU FIR filter is derived for discrete time-variant state space model to minimize the

variance in the UFIR filter proposed in [13]. Compared to the IIR filters, the MVU FIR filter inherits advantages of FIR structures and is more robust against the temporary modeling uncertainties. We use the following notations: \mathbb{R}^n denotes the n dimensional Euclidean space, $E\{\cdot\}$ denotes the statistical averaging of the stochastic process or vector, $diag(e_1 \cdots e_m)$ represents a diagonal matrix with diagonal elements e_1, \cdots, e_m , $tr(M)$ is the trace of M , and I is the identity matrix of proper dimensions.

2 State-Space Model and Preliminaries

Motivated by the problems of state estimation and tracking often arising in signal processing and wireless systems, we consider a linear discrete-time system represented in state-space with the time-variant model

$$x_k = A_k x_{k-1} + B_k w_k, \quad (1)$$

$$y_k = C_k x_k + D_k v_k, \quad (2)$$

where $x_k \in \mathbb{R}^n$ is the state vector in Euclidean space, $y_k \in \mathbb{R}^p$ is the measurement vector, $A_k \in \mathbb{R}^{n \times n}$, $B_k \in \mathbb{R}^{n \times u}$, $C_k \in \mathbb{R}^{p \times n}$ and $D_k \in \mathbb{R}^{p \times v}$ are time-variant matrices, which are assumed to be known. The process noise $w_k \in \mathbb{R}^u$ and measurement noise

3 MVU FIR Filter

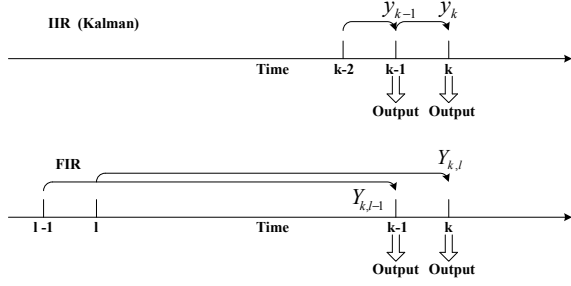


Figure 1: Operation time diagrams of the IIR and FIR structures.

$v_k \in \mathbb{R}^v$ are zero mean, $E\{w_k\} = 0$ and $E\{v_k\} = 0$, mutually uncorrelated and have arbitrary distributions and known covariances $Q(i, j) = E\{w_i w_j^T\}$, $R(i, j) = E\{v_i v_j^T\}$ for all i and j , meaning that w_k and v_k do not have to be white.

The FIR filter can be expressed as a linear combination of finite samples of measurements as

$$\hat{x}_{k|k} = K_k Y_{k,l}, \quad (3)$$

where $l = k - N + 1$ is the starting point of the horizon, N is the horizon length, $\hat{x}_{k|k}$ is the estimate¹, $Y_{k,l}$ is a vector measurements collecting on a horizon $[l, k]$, and K_k is the filter gain determined by a given performance criterion.

The operation principles of the FIR and IIR filters are illustrated in Fig.1. A distinct difference is that only one most recent measurement is used in IIR (Kalman) filtering to provides the estimate, while FIR estimators employ N most recent measurements. This leads to N times larger computation time than in IIR filtering. However, some good properties such as the BIBO stability and better robustness are guaranteed at the cost of extra computation time. We formulate the problem as follows: Given the model, (1) and (2), we would like to derive a MVU FIR filter minimizing the variance in the UFIR filter, by

$$K_k = \arg \min_{K_k} E \left\{ (x_k - \hat{x}_{k|k}) (x_k - \hat{x}_{k|k})^T \right\}. \quad (4)$$

We also wish to compare errors in three different FIR filters (MVU FIR derived in this paper and the UFIR and OFIR filters proposed in [14] and [17] respectively) to each other, and analyze the trade-off based on a polynomial state-space model.

¹ $\hat{x}_{k|k}$ means the estimate at k utilizing on the measurements from the past to k .

In order to derive the MVU FIR filter on a horizon of N past measurements from l to k , we represent (1) and (2) in a batch form following [14] and [17] as

$$X_{k,l} = A_{k,l} x_l + B_{k,l} W_{k,l}, \quad (5)$$

$$Y_{k,l} = C_{k,l} x_l + H_{k,l} W_{k,l} + D_{k,l} V_{k,l}. \quad (6)$$

Here, $X_{k,l} \in \mathbb{R}^{Nn}$, $Y_{k,l} \in \mathbb{R}^{Np}$, $W_{k,l} \in \mathbb{R}^{Nu}$ and $V_{k,l} \in \mathbb{R}^{Nv}$ are specified as, respectively,

$$X_{k,l} = [x_k^T x_{k-1}^T \cdots x_l^T]^T, \quad (7)$$

$$Y_{k,l} = [y_k^T y_{k-1}^T \cdots y_l^T]^T, \quad (8)$$

$$W_{k,l} = [w_k^T w_{k-1}^T \cdots w_l^T]^T, \quad (9)$$

$$V_{k,l} = [v_k^T v_{k-1}^T \cdots v_l^T]^T. \quad (10)$$

The extended model matrix $A_{k,l} \in \mathbb{R}^{Nn \times n}$, process noise matrix $B_{k,l} \in \mathbb{R}^{Nn \times Nu}$, observation matrix $C_{k,l} \in \mathbb{R}^{Np \times n}$, auxiliary process noise matrix $H_{k,l} \in \mathbb{R}^{Np \times Nu}$ and measurement noise matrix $D_{k,l} \in \mathbb{R}^{Np \times Nv}$ are all time-variant and dependent on the current time k and the horizon length N . Model (1) and (2) suggests that these matrices can be written as, respectively

$$A_{k,l} = [\mathcal{A}_{k,l+1}^T \mathcal{A}_{k-1,l+1}^T \cdots \mathcal{A}_{l+1,l+1}^T I]^T, \quad (11)$$

$$C_{k,l} = \bar{C}_{k,l} A_{k,l}, \quad (13)$$

$$H_{k,l} = \bar{C}_{k,l} B_{k,l}, \quad (14)$$

$$D_{k,l} = \text{diag}(D_k D_{k-1} \cdots D_l), \quad (15)$$

with

$$A_{\psi,\zeta} = \begin{cases} A_{\psi} A_{\psi-1} \cdots A_{\zeta}, & \text{if } \psi > \zeta \\ A_{\psi}, & \text{if } \psi = \zeta \end{cases}, \quad (16)$$

$$\bar{C}_{k,l} = \text{diag}(C_k C_{k-1} \cdots C_l), \quad (17)$$

where $\psi \geq \zeta$. Note that the state equation specified by (5) and (6) at the initial point l is $x_l = x_l + B_l w_l$, suggesting that w_l is zero-valued. That is, the initial state x_l is required to be known or estimated optimally. The following lemma will be used to derive the MVU FIR filter.

Lemma 1 *The trace optimization problem is given by:*

$$\arg \min_K \text{tr}[(KA - B)C(KA - B)^T + (KG - F)D(KG - F)^T + KPK^T], \quad (18)$$

$$B_{k,l} = \begin{bmatrix} B_k & \mathcal{A}_{k,k}B_{k-1} & \cdots & \mathcal{A}_{k,l+2}B_{l+1} & \mathcal{A}_{k,l+1}B_l \\ 0 & B_{k-1} & \cdots & \mathcal{A}_{k-1,l+2}B_{l+1} & \mathcal{A}_{k-1,l+1}B_l \\ \vdots & \vdots & \cdots & \vdots & \vdots \\ 0 & 0 & \cdots & B_{l+1} & \mathcal{A}_{l+1,l+1}B_l \\ 0 & 0 & \cdots & 0 & B_l \end{bmatrix}, \quad (12)$$

subject to $KE = H$, where $C = C^T > 0$, $D = D^T > 0$, $P = P^T > 0$, and A, B, C, D, E, F, G, H , and P are constant matrices of proper dimensions. The solution to this optimization problem is as follows:

$$K = [H \ B \ F] \times \begin{bmatrix} (E^T \Xi^{-1} E)^{-1} E^T \Xi^{-1} \\ CA^T \Xi^{-1} \left(I - E(E^T \Xi^{-1} E)^{-1} E^T \Xi^{-1} \right) \\ DG^T \Xi^{-1} \left(I - E(E^T \Xi^{-1} E)^{-1} E^T \Xi^{-1} \right) \end{bmatrix}, \quad (19)$$

where $\Xi = ACA^T + GDG^T + P$.

The proof can be obtained following similar lines provided in [18] and is omitted here.

3.1 Design of MVU FIR Filter

In order to minimize the variance in UFIR filter, we decompose K_k as

$$K_k = \bar{K}_k + \tilde{K}_k, \quad (20)$$

where \tilde{K}_k is an unknown additive term to be determined, and \bar{K}_k is the known unbiased gain [14] specified by

$$\bar{K}_k = \mathcal{A}_{k,l+1}(C_{k,l}^T C_{k,l})^{-1} C_{k,l}^T \quad (21)$$

and derived to satisfy the unbiasedness condition $E\{x_k\} = E\{\hat{x}_{k|k}\}$. From (5), the system state x_k can be constructed as

$$x_k = \mathcal{A}_{k,l+1}x_l + \bar{B}_{k,l}W_{k,l}, \quad (22)$$

where $\bar{B}_{k,l}$ is the first row in (12). Substituting x_k with (22), $\hat{x}_{k|k}$ with (3) using (20) in the unbiasedness condition yields the constraint

$$\tilde{K}_k C_{k,l} = 0, \quad (23)$$

where the fact known from [14] that $\bar{K}_k C_{k,l} = \mathcal{A}_{k,l+1}$ is used. Now, our objective is to obtain \tilde{K}_k in a way such that the estimate has the minimum variance

$$\tilde{K}_k = \arg \min_{\tilde{K}_k} E \left\{ \text{tr} \left[(x_k - \hat{x}_{k|k}) (x_k - \hat{x}_{k|k})^T \right] \right\} \quad (24)$$

with constraint $\tilde{K}_k C_{k,l} = 0$. Substituting (4) and (3) with consideration of (20) into (24) yields

$$\begin{aligned} \tilde{K}_k = \arg \min_{\tilde{K}_k} E \{ & \text{tr} [(A_{k,l+1}x_l + \bar{B}_{k,l}W_{k,l} \\ & - (\bar{K}_k + \tilde{K}_k)C_{k,l}x_l - (\bar{K}_k + \tilde{K}_k) \\ & \times (H_{k,l}W_{k,l} + D_{k,l}V_{k,l})) (\cdots)^T] \}, \end{aligned} \quad (25)$$

where (\cdots) denotes the same term as its previous term. By taking into account of $\bar{K}_k C_{k,l} = \mathcal{A}_{k,l+1}$, observing that systems noise vector $W_{k,l}$ and measurement noise $V_{k,l}$ are pairwise independent, providing the averaging, and rearranging the terms, (25) becomes

$$\begin{aligned} \tilde{K}_k = \arg \min_{\tilde{K}_k} \text{tr} \left[& \left(\tilde{K}_k H_{k,l} + \bar{K}_k H_{k,l} - \bar{B}_{k,l} \right) \right. \\ & \times \Theta_{w,l} (\cdots)^T + \tilde{K}_k \Delta_{x,l} \tilde{K}_k^T \\ & \left. + (\tilde{K}_k + \bar{K}_k) \Delta_{v,l} (\cdots)^T \right], \end{aligned} \quad (26)$$

where the auxiliary matrices are

$$\Theta_{w,l} = E \{ W_{k,l} W_{k,l}^T \}, \quad (27)$$

$$\Delta_{x,l} = C_{k,l} E \{ x_l x_l^T \} C_{k,l}^T, \quad (28)$$

$$\Delta_{v,l} = D_{k,l} E \{ V_{k,l} V_{k,l}^T \} D_{k,l}^T. \quad (29)$$

Next, by using the result of Lemma 1 with the replacements $A \leftarrow H_{k,l}$, $B \leftarrow (\bar{B}_{k,l} - \bar{K}_k H_{k,l})$, $C \leftarrow \Theta_{w,l}$, $D \leftarrow \Delta_{v,l}$, $E \leftarrow C_{k,l}$, $F \leftarrow -\bar{K}_k$, $G \leftarrow I$, $H \leftarrow 0$, and $P \leftarrow \Delta_{x,l}$, the solution to the optimization problem (26) can be obtained as

$$\tilde{K}_{k,l} = \Omega_{k,l}(I - \Lambda_{k,l}), \quad (30)$$

where

$$\Omega_{k,l} = (\bar{B}_{k,l} \Theta_{w,l} H_{k,l}^T - \bar{K}_k \Delta_{w+v,l}) \Delta_{x+w+v,l}^{-1}, \quad (31)$$

$$\Delta_{w,l} = H_{k,l} \Theta_{w,l} H_{k,l}^T, \quad (32)$$

$$\Delta_{w+v,l} = \Delta_{w,l} + \Delta_{v,l}, \quad (33)$$

$$\Delta_{x+w+v,l} = \Delta_{x,l} + \Delta_{w,l} + \Delta_{v,l}, \quad (34)$$

$$\Lambda_{k,l} = C_{k,l} (C_{k,l}^T \Delta_{x+w+v,l}^{-1} C_{k,l})^{-1} C_{k,l}^T \Delta_{x+w+v,l}^{-1}. \quad (35)$$

Table 1: MVU FIR Filtering Algorithm

Table 1: MVU FIR Filtering Algorithm	
Stage	
Given:	$N \geq n, l = k - N + 1$
Solve:	$\Delta_{x,l}$ using the DARE (36)
Find:	\bar{K}_k by (21), $\Omega_{k,l}$ by (31), and $\Lambda_{k,l}$ by (35)
Compute:	$\hat{x}_{k k} = [\bar{K}_k + \Omega_{k,l}(I - \Lambda_{k,l})]Y_{k,l}$

In order to compute (30), the variance of the initial state $\Delta_{x,l}$ is required. Using the approximation $E\{x_l x_l^T\} \approx \hat{x}_{l|k} \hat{x}_{l|k}^T$, the following discrete algebraic Riccati equation (DARE) can be used to find $\Delta_{x,l}$, as in [13],

$$\begin{aligned} Y_{k,l} Y_{k,l}^T \Delta_{w+v,l}^{-1} \Delta_{x,l} - \Delta_{x,l} \Delta_{w+v,l}^{-1} \Delta_{x,l} \\ - 2\Delta_{x,l} - \Delta_{w+v,l} = 0. \end{aligned} \quad (36)$$

The MVU FIR filter is now specified by the following theorem.

Theorem 2 *Given the discrete time-variant state space model (1) and (2) with zero mean and mutually independent noise vectors w_k and v_k having arbitrary distributions and known covariances, the MVU FIR filter utilizing measurements from l to k can be written as*

$$\hat{x}_{k|k} = [\bar{K}_k + \Omega_{k,l}(I - \Lambda_{k,l})] Y_{k,l}, \quad (37)$$

where $Y_{k,l} \in \mathbb{R}^{Np}$ is the measurement vector given by (8), \bar{K}_k is obtained by (21) with $A_{k,l+1}$ and $C_{k,l}$ specified by (16) and (13) respectively, $\Omega_{k,l}$ and $\Lambda_{k,l}$ are determined using (31) and (35) by solving the DARE (36).

The proof has been provided by (20)-(36).

Note that the horizon length N should be chosen such that the inverse in \bar{K}_k specified by (21) exists. In general, N can be set as $N \geq n$, where n is the number of model state. Table I summarizes the steps in the MVU FIR estimation algorithm, in which $\Delta_{w,v}$ and $\Delta_{v,l}$ are assumed to be known for measurements available from l to k . Given N , solve the DARE (36). Then, compute \bar{K}_k according to (21) by using (11) and (13). With (31) and (35), the MVU FIR estimate $\hat{x}_{k|k}$ can be obtained by (37) at time k .

3.2 FIR Filter Gains

As can be seen from Theorem 1, the term $I - \Lambda_{k,l}$ in \bar{K}_k is introduced by the constraint $\bar{K}_k C_{k,l} = 0$

evolved from the unbiasedness condition. Specifically, the existence of term $I - \Lambda_{k,l}$ ensures the unbiasedness of the FIR filter. If we neglect this constraint, the matrix E in Lemma 1 will be replaced by the zero matrix when solving the optimization problem (26), thus leading to $\Lambda_{k,l} = 0$. At this point, we have $\bar{K}_k = \Omega_{k,l}$ and the MVU FIR filter gain K_k becomes the OFIR filter gain \hat{K}_k , due to the following equality:

$$\hat{K}_k = \bar{K}_k + \Omega_{k,l}, \quad (38)$$

with

$$\hat{K}_k = (\bar{K}_k \Delta_{x,l} + \bar{B}_{k,l} \Theta_{w,l} H_{k,l}^T) \Delta_{x+w+v,l}^{-1} \quad (39)$$

which is given in [17] as the filter gain of the OFIR filter. On the other hand, it follows from (20) and (30) that

$$K_k = \hat{K}_k - \Omega_{k,l} \Lambda_{k,l} = \bar{K}_k + \Omega_{k,l}(I - \Lambda_{k,l}). \quad (40)$$

This equality provides the analytical relationships between the MVU FIR filter gain K_k , the OFIR filter gain \hat{K}_k , and the UFIR filter gain \bar{K}_k . Note that the structure of the MVU FIR filter is shown to be consistent with the UFIR and OFIR filters, suggesting that the UFIR, MVU FIR and OFIR filters do not get away essentially from each other and all the FIR filters can be transformed to each other by adding or subtracting the corresponding terms. Moreover, the UFIR filter gain \bar{K} plays a fundamental role in the FIR filter design being independent on the noise statistics

4 Examples and Applications

Extensive comparisons between FIR filters with Kalman methods can be found in [13, 14, 17, 19–21]. We therefore mostly compare the MVU FIR filter with the UFIR and OFIR filters in order to investigate the trade-off. Towards this end, a two-state polynomial state space models (1) and (2), specified with $B_k = [1, 1]^T$, $D_k = 1$, $C_k = [1, 0]$, and

$$A_k = \begin{bmatrix} 1 & (1 + d_k)\tau \\ 0 & 1 \end{bmatrix} \quad (41)$$

is employed, where τ is a constant in unit of time, and d_k varies with time. Note that this kind of systems is commonly used to describe the “velocity jumps” in moving target tracking and the “frequency jumps” in oscillators.

In the first simulation, all the methods were applied in an ideal environment. That is, all the parameters of system model, including the variances of noises, are known completely in the entire estimation

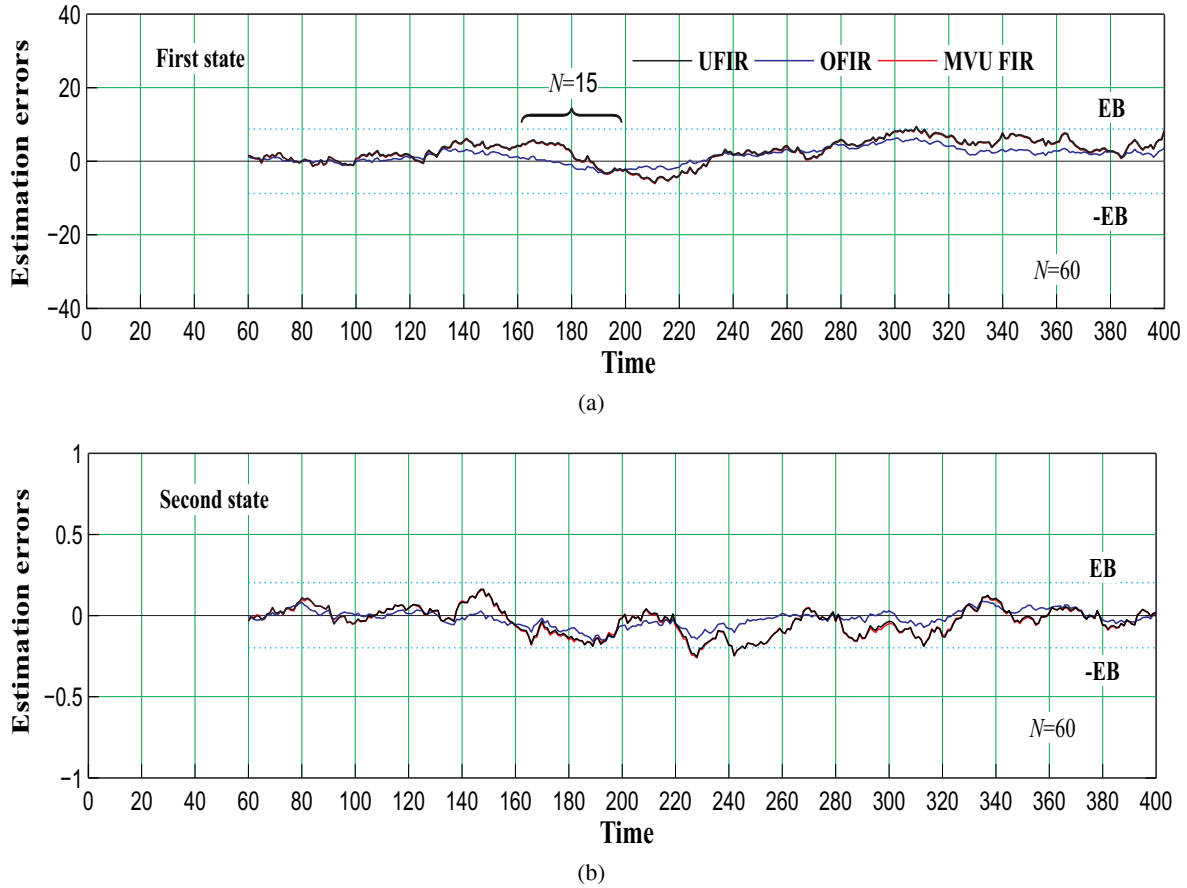


Figure 2: Estimation errors for an accurate model: (a) the first state and (b) the second state.

process. The model parameter is set to be $d_k = 20$ if $160 \leq k \leq 200$ and $d_k = 0$ otherwise. The variances of process noise w_k and measurement noise v_k are $\sigma_w^2 = 10^{-4}$ and $\sigma_v^2 = 10^2$, respectively. Since the system model is time-variant, two different optimum horizons were found following [21] to be $N_{opt} = 60$ and $N_{opt} = 15$ for the models with $d_k = 0$ and $d_k = 20$, respectively. For the first and second states at time k , the estimation error bounds (EBs) have been respectively calculated as in [14] and employed as measures of estimation accuracy. The process was simulated over 400 subsequent points.

The estimation errors are given in Fig. 2. With respect to the first state, errors in OFIR filter is smaller than in the MVU FIR and UFIR filters as expected. Note that the OFIR filter is obtained by minimizing the mean square errors (MSEs), thus leading to the most accurate estimates. On the other hand, UFIR and OFIR perform very close to each other and the difference between them is indistinguishable in Fig. 2. This is mainly due to the optimal horizon used, which reduces the variance of estimation error in UFIR automatically. For the second state, a similar situation is observed; however, FIR methods are less sensitive

to the value of N in this case. It is also seen that all the FIR filters trace well within a gap between EB and -EB formed with $N = 60$.

To show the difference between the errors more clearly, we conducted another experiment with $\sigma_w^2 = 10^{-3}$ and $\sigma_v^2 = 10$ using a time-invariant model with $d_k = 0$. For polynomial model, corresponding N_{opt} for different states can be determined separately, the root squares of MSEs of the first and second states are respectively shown in Fig. 3a and Fig. 3b. A analysis of Fig. 3 leads to several critical inferences:

- The MSEs are concave on N with polynomial model. When $N < N_{opt}$, the denoising effect in all the FIR filters becomes better with the increase of N . All the FIR filters offer best estimates at their corresponding optimal horizons. On the other hand, an increase in N results in an increase in the estimation bias that can easily be seen in Fig.3 with $N > N_{opt}$.
- The errors in MVU FIR filter are intermediate between the UFIR and OFIR filters. Specifically, the MVU FIR filter performs better than the UFIR filter but worse than the optimal one.

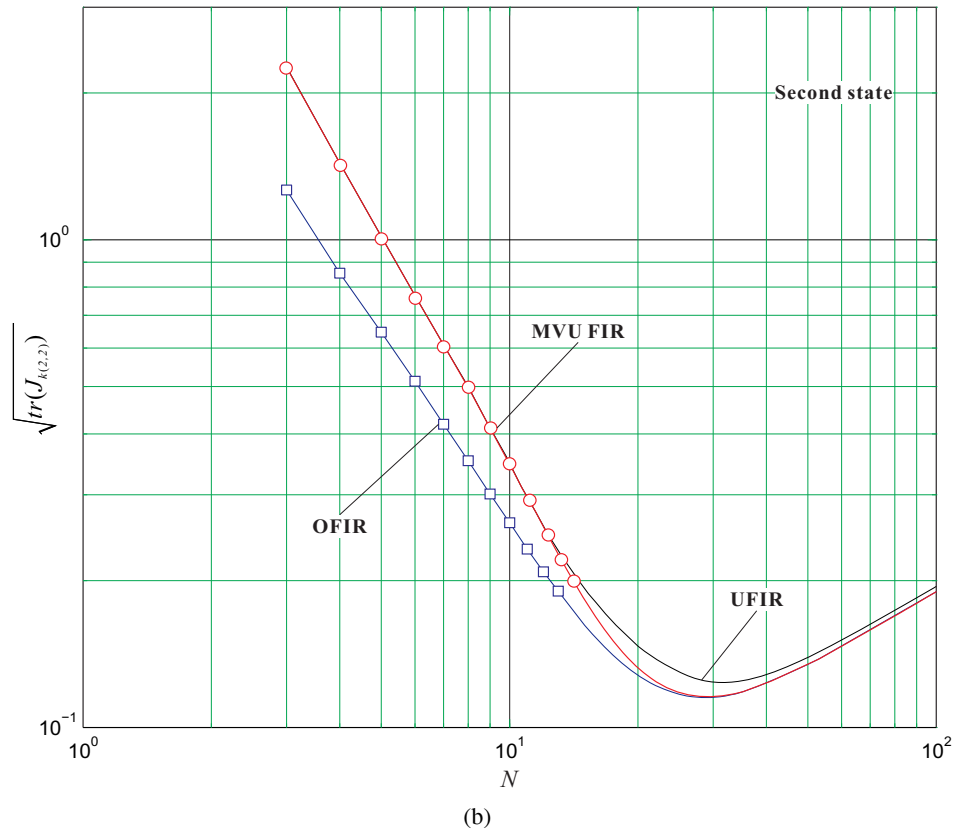
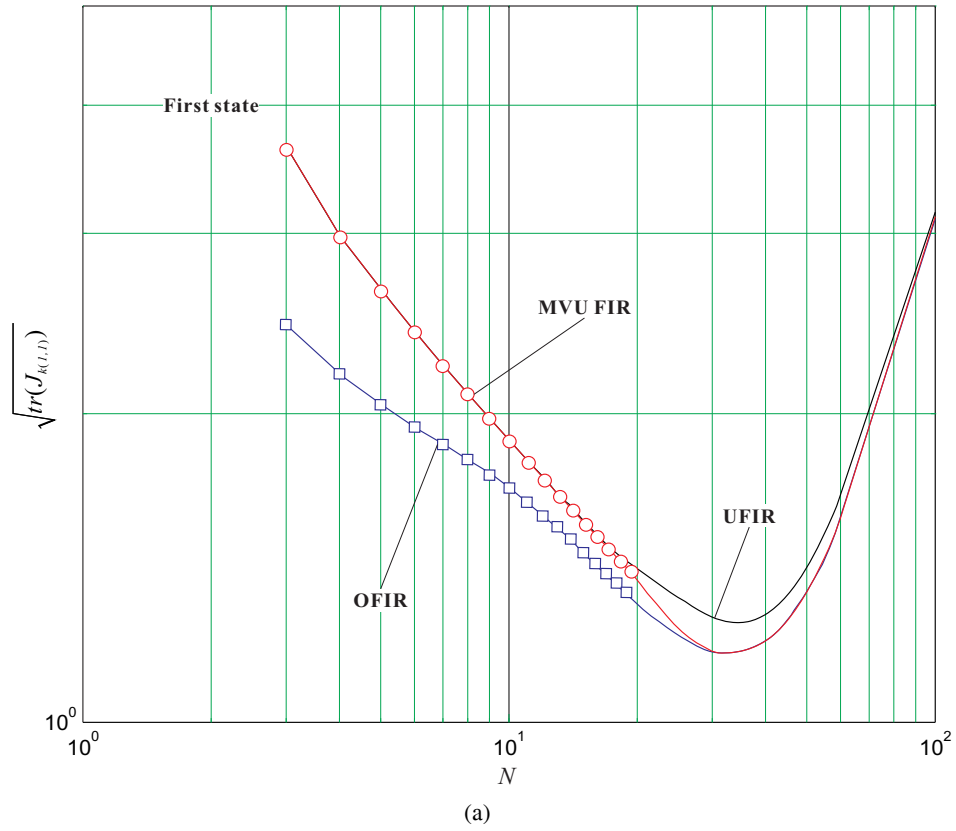


Figure 3: Root square of MSEs as functions of N with $\sigma_w^2 = 10^{-3}$ and $\sigma_v^2 = 10$: (a) the first state and (b) the second state.

Another critical peculiarity that still has not been shown in the literature is that the UFIR filter is also highly successful in denoising, and it tracks closely to the MVU FIR filter (the optimized UFIR one), when N is small. Overall, the MVU FIR filter behaves as the UFIR filter with small N and as the OFIR filter with large N .

- By increasing the horizon N , all FIR estimates converge to the OFIR estimate. In comparison with the UFIR filter, the rate of convergence of the MVU FIR filter is much faster, thus leading to smaller optimal horizon.

Note that noise in the UFIR filter is reduced only by the averaging provided using the estimation horizon N . In the MVU FIR filter, however, additional optimization operation is introduced to enhance the effect of noise reduction, even making the MVU FIR method achieve similar accuracy with the OFIR filter at the same optimal horizon point.

5 Conclusions

We have derived a new form of the MVU FIR filter by minimizing the variance in the UFIR filter which completely ignores the noise statistics. As was expected, the MVU FIR filter has reduced the random amount of errors and shown better ability of denoising. Its estimates converge to the OFIR one by increasing the averaging horizon. The structure of the MVU FIR filter was shown to be consistent to the OFIR filter and the MSEs intermediate between the UFIR and OFIR filters.

References:

- [1] A. H. Sayed, "A framework of state-space estimation with uncertain models," *IEEE Trans. Autom. Contr.*, vol. 46, no. 7, pp. 998–1013, 2001.
- [2] A. H. Jazwinski, *Stochastic Processes and Filtering Theory*, New York: Academic, 1970.
- [3] A. H. Jazwinski, "Limited memory optimal filtering," *IEEE Trans. Autom. Control*, vol. 13, no.10, pp. 558–563, Oct. 1968.
- [4] V. R. Algazi, M. Suk, and C. Rim, "Design of almost minimax FIR filters in one and two Dimensions, by WLS techniques," *IEEE Trans. Circuits and systems*, vol. CAS-33, no. 6, pp. 590–596, Jun. 1986.
- [5] O. K. Kwon, W. H. Kwon, and K. S. Lee, "FIR filters and recursive forms for discrete-time state-space models," *Automatica*, vol. 25, pp. 715–728, Sep. 1989.
- [6] W. H. Kwon, K. S. Lee, and O. K. Kwon, "Optimal FIR filter for time-varying state-space models," *IEEE Trans. Aerosp. Electron. Syst.*, vol. 30, pp. 968–972, Jul. 1994.
- [7] W. H. Kwon, P. S. Kim, and P. Park, "A receding horizon Kalman FIR filter for discrete time-invariant systems," *IEEE Trans. Autom. Control*, vol. 99, pp. 1787–1791, Sep. 1999.
- [8] W. H. Kwon, P. S. Kim, and S. Han, "A receding horizon unbiased FIR filter for discrete-time state space models," *Automatica*, vol. 38, pp. 545–551, Mar. 2002.
- [9] B. K. Kwon, S. Han, O. K. Kim, and W. H. Kwon, "Minimum variance FIR smoothers for discrete-time state space models," *IEEE Trans. Signal Process. Lett.*, vol. 14, pp. 557–560, Aug. 2007.
- [10] Y. S. Shmaliy, "An unbiased FIR filter for TIE model of a local clock in applications to GPS-based time-keeping," *IEEE Trans. Ultrason., Ferroel., Freq. Contr.*, vol. 53, pp. 862–870, May 2006.
- [11] Y. S. Shmaliy, "Unbiased FIR filtering of discrete-time polynomial state-space models," *IEEE Trans. Signal Process.*, vol. 57, pp. 1241–1249, Apr. 2009.
- [12] Y. S. Shmaliy, "Optimal gains of FIR estimations for a class of discrete-time state-space models," *IEEE Trans. Signal Process. Lett.*, vol. 15, pp. 517–520, 2008.
- [13] Y. S. Shmaliy, "Linear optimal FIR estimation of discrete time-invariant state-space models," *IEEE Trans. Signal Process.*, vol. 58, pp. 3086–2010, Jun. 2010.
- [14] Y. S. Shmaliy, "An iterative Kalman-like algorithm ignoring noise and initial conditions," *IEEE Trans. Signal Process.*, vol. 59, pp. 2465–2473, Jun. 2011.
- [15] Y. S. Shmaliy, "Suboptimal FIR filtering of nonlinear models in additive white Gaussian noise," *IEEE Trans. Signal Process.*, vol. 60, pp. 5519–5527, Oct. 2012.
- [16] D. Simon and Y. S. Shmaliy, "Unified forms for Kalman and finite impulse response filtering and smoothing," *Automatica*, vol. 49, pp. 1892–1899, Oct. 2013.
- [17] Y. S. Shmaliy and O. I. Manzano, "Time-variant linear optimal finite impulse response estimator for discrete state-space models," *Int. J. Adapt. Control Signal Process.*, vol. 26, pp. 95–104, Sep. 2012.
- [18] W. H. Kwon and S. Han, *Receding Horizon Control: Model Predictive Control for State Models*, London, U.K.: Springer, 2005.
- [19] P. S. Kim and M. E. Lee, "A new FIR filter for state estimation and its applications," *J. Comput. Sci. Technol.*, vol. 22, pp. 779–784, Sep. 2007.
- [20] P. S. Kim, "An alternative FIR filter for state estimation in discrete-time systems," *Digit. Signal Process.*, vol. 20, pp. 935–943, May 2010.
- [21] F. Ramirez-Echeverria, A. Sarr, and Y. S. Shmaliy, "Optimal memory for discrete-time FIR filters in state-space," *IEEE Trans. Signal Process.*, vol. 62, pp. 557–561, Feb. 2014.

Applying “ABCD Rule of Dermatoscopy” using cognitive systems

Ionut Taranu, Iunia Iacovici

Abstract— Difficulties in accurately assessing pigmented skin lesions (nevi, melanoma) are always present in practice. ABCD rule of dermatoscopy (skin microscopy magnification X10), based on the criteria of asymmetry (A), edges (border-B), color (C) and differential structure (D), improved diagnostic accuracy when it was applied retrospective on clinical images. This paper is a prospective study to assess the value of ABCD rule for dermatoscopy on melanocytic lesions using cognitive systems.

Keywords— computer-aided diagnosis, skin cancer, melanoma, dermatoscopy, segmentation, border detection

I. INTRODUCTION

Stolz et al. introduced ABCD rule of dermatoscopy, based on multivariate analysis of four criteria (asymmetry, pigment pattern sudden stop at the border, color variation, and different structure) with a semi-quantitative scoring system.

The rule was developed based on a retrospective analysis of color prints of dermoscopy images in the same size as those seen using a Dermatoscope. This study tests the ABCD rule prospectively to see if the criteria determining when examining an injury accurately predicts the correct diagnosis.[1]

Steps	Criteria for separation
Easily identifiable melanocytic lesions	Pigment network, regular streaks, brown globules, steel-blue areas (blue nevus)
Angiomatous tumors and hemorrhages	Red lakes, homogeneous reddish or reddish black areas, well-defined outline, lack of network, regular streaks and globules
Pigmented seborrheic keratoses	Yellowish or white "comedo-like" openings, brownish gray appearance, well-defined outline, lack of network, regular streaks and brown globules, presence of telangiectasias
Basal cell carcinomas	Maple leaf-like areas, telangiectases, lack of network, regular streaks and globules
Remaining	Benign and malignant melanocytic lesions

Tabel I. Algorithm for distinguishing melanocytic and nonmelanocytic pigmented lesions by dermatoscopy
 Kreusch J, Rassner G. *Hautarzt* 1991;42:77-83.

For the calculation of the score ABCD asymmetry criteria (A), the sudden interruption of the pattern at the border pigment (B), various colors (C), and various structural components (D) were measured to obtain a semi-quantitative score.

The asymmetry was assessed in terms of color and structure of mutually perpendicular axes selected in such a way as to result in the lowest possible asymmetry score. A score of 0 was given if the were two axis of asymmetry, a score of 1, if the asymmetry was in one axis, and a score of 2 in the case of asymmetry in both axes.

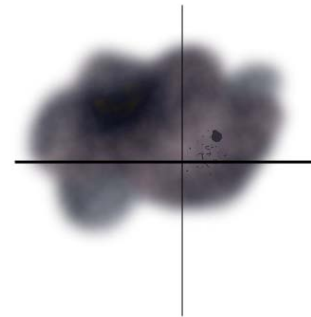


Fig1. Evaluation of melanocytic lesions asymmetry

To calculate the border, the lesions were divided into 8 segments as shown in Fig. 2.

For each segment in which a pattern of sudden stop of the model of border pigment was present, a point was added to the score.

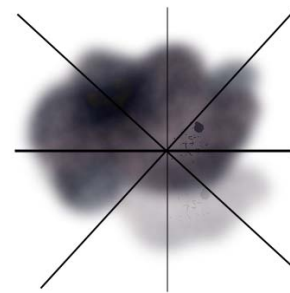


Fig.2 Evaluation of melanocytic lesions border

For the color score the number of colors in the lesion was counted (possible colors: white, red, dark brown, blue-gray and black), resulting in a minimum score of 1 and a maximum of 6 (Fig 3.). Possible differential structural components were: network, homogeneous areas, dots, globules, and streaks (Fig. 4). Thus, the differential structure score (D) was multiplied by different weight factors derived from multivariate analysis



Fig3. Evaluation of color in melanocytic lesions.

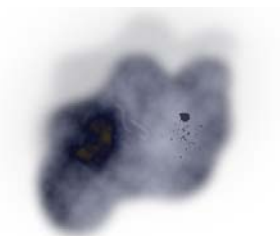


Fig4. The evaluation of the various structural components

Different structural components (pigmented network, points, areas without structure, etc..)	1 - 5	0.5	0.5 - 2.5
Total	Benign		<4.76
	Suspect		4.76-5.45
	Melanoma		>5.45

Tabel II. Calculation of ABCD score in dermatoscopy

II. RESEARCH

A. The calculation method

ABCD score was calculated by adding the four individual scores (A to D), resulting in a final score of minimum 1,0 (A = 0, B = 0, C = 1, D = 1) and a maximum of 8.9 (A = 2, B = 8, C = 6, D = 5) (Tabel II).

Criteria	Score X	Factor =	Result
Asymmetry (Asimetrie) Perpendicular axes: shape, color and structure	0 - 2	1.3	0 - 2.6
Borders (Margini) 8 segments: irregular edges of the pigmented model	0 - 8	0.1	0 - 0.8
Color White, red, light brown, dark brown, gray, blue, black	1 - 6	0.5	0.5 - 3.0

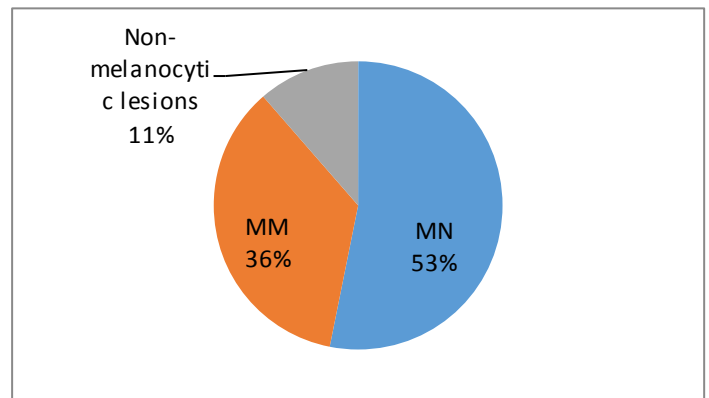
B. Materials, Methods, Results

In preparing this paper we used, on condition of anonymity, 79 dermoscopy images taken by Dr. Daniel BODA by using an experimental assembly consisting of a dermatoscope attached to a mobile phone. Image capture was immediately followed by storing it in a database of images, transmission being made through a wireless connection.

Received images were then processed by applying a series of processing methods - normalization, segmentation, restoration, extracting color, edge detection and various structures in the image.

In parallel, Dr. Daniel Boda put at our disposal the results previously obtained by using clinical diagnosis in order to make a comparative study of the results.

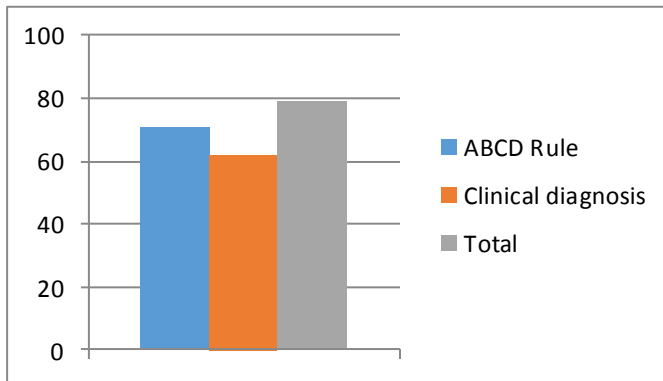
Of the 79 cases included, the investigation revealed 28 MM, 42 MN and nine non-melanocytic lesions.



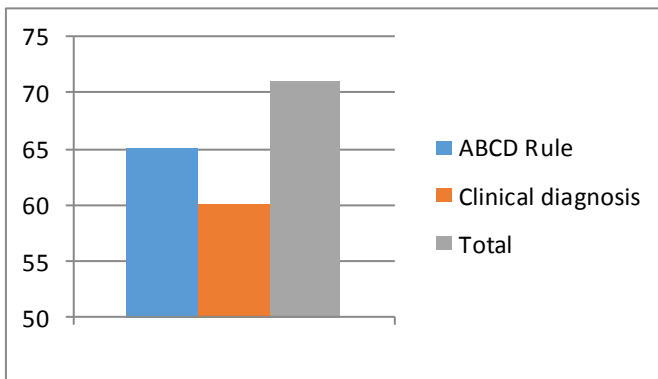
MM group consisted of 19 superficial melanoma (SSM) (66.7% of MM), 5 MM nodular (NMM) (17.4% of MM) and four with a different classifications (15.9% of MM). Breslow depth was 1.11 mm (± 1.03 SD, range, 0.15 - 4.10 mm).

Of the 79 lesions, 70 were melanocytic and 9 were non-melanocytic histologically pigmented lesions. In total, 71 pigmented lesions (90.2%) were diagnosed correctly with the

ABCD rule (melanocytic lesions or non-melanocytic lesions) compared with 62 (79.4%) correct clinical diagnoses.



Using the ABCD rule, 65 of the 71 melanocytic lesions histologically proven were correctly classified (91.3%), while the clinical diagnosis was correct in 60 cases (85.5%).



C. Methods

By the nature of the activities involved in the objective of our study, this article actually heralds the objectives and activities of the next stages of the research project. Therefore, this work was carried out in several directions of study.

1. Image normalization methods
2. Image segmentation methods
3. Identification of the outline methods
4. Structural differences identification methods

In the first theme we treated the illumination normalization methods, which, together with noise or other disturbances that may occur during the image acquisition, can negatively influence the performance of analysis of an automated classification of such data.

The five methods that were investigated were: Ratio Method (MR), The morphology ratio method (MRMD), The dynamic ratio morphology (MRMD), Homomorphic filter (FH) [3] and Recombined Multiscale Retinex method (MRMR) [4].

Ratio Method (MR) requires only a single image for extracting illumination invariant features in an image. And further, unlike the other methods, MR does not require a phase

alignment of the images. MR is based on modeling Lambertian reflections of light on an object. This model considers that any light source falling on a 3D object can be decomposed into three factors: surface normal, "albedo" factor and point source of light. Auto-aspect ratio is defined as the ratio between the original image and the processed image where the processed image is a filtered version of the original image. Typically, the filtration is performed using a Gaussian filter weighted.

The morphology ratio method (MRMD). The basic idea of this method is given by morphological operations of the image to estimate the illumination component of an image.

More specifically it's about using morphological closing operator. An operator of the closure (CL) is represented by a non-linear filter consists of two stages: a dilation followed by erosion. This filter tends to eliminate noise characteristics and dashed edges in the image while retaining well-defined edges (large scale features). Unlike the classical Gaussian filter that smoothes a noisy image, the morphological filter type distort the closure to a lesser extent, the image quality (particularly observed in the vicinity of the edges that remain sharp).

The dynamic ratio morphology (MRMD). A disadvantage of this filter is that it uses a window of constant size convolution morphological representative image. Large scale features are normalized effective but on the other hand is not effective illumination compensation in dark areas (locally). For this reason, a variation of the method proposed by the MRM, called dynamic MRM (MRMD), which uses three different sized windows. The dimensions will vary depending on three parameters determined experimentally.

Homomorphic filter (FH) considers that an image can be decomposed as the product of a lighting model and one of reflection. By applying a logarithmic function, the multiplicative relationship turns in an additive relationship so that the two components can be separated. Applying further a Fourier transform, using a high-pass filter,

low frequency components (usually associated lighting component) are removed. By determining an optimal cutting frequency method gives satisfactory results.

Recombined Multiscale Retinex method (MRMR) consists in using a set of Gaussian filters to the original image and recombination results in well-defined proportions on the basis of the parameter recombination.

As a preprocessing step, we used the method of decomposition into components and for the classification technique we used proximity support vector method.

III. CONCLUSION

Tests have shown that the method that led to the greatest increase in the rate of recognition of color, edges and structures (from 46.11% to 91.67%) is MR.

In the next stage, we will analyze five color recognition methods to identify the algorithm with the highest success rate

in order to improve the algorithm of ABCD method according to each parameter involved.

Also, for the next stage of the research we will introduce and present "parameter E" – evolution, to determine to what extent we can automatically determine the degree of evolution of the lesions using image processing algorithms and the impact on the accuracy of the results obtained in compared with the conventional methods of diagnosis.

IV. REFERENCES

- [1] Nachbar F, Stolz W, Merkle T, et al. The ABCD rule of dermatoscopy. *J Am Acad Dermatol.* 1994;30:551-559.
- [2] *Medical Image Processing, Reconstruction and Restoration: Concepts and Methods*, Jiri Jan. CRC Press 2006
- [3] http://en.wikipedia.org/wiki/Homomorphic_filtering
- [4] Zia-ur Rahman, Daniel J. Jobson, Glenn A. Woodell. Multi-scale retinex for color image enhancement. *ICIP (3)*, 1996

Obstacle avoidance by unmanned aerial vehicles using image recognition techniques

Priya Bajju Parappat
Graduate Student
Vellore Institute of Technology
Vellore, India
baju.priya@gmail.com

Anand Kumar, R.K. Mittal, Suhel Ahmad Khan
Departments of EEE, Mechanical, Mathematics
BITS Pilani, Dubai Campus
Dubai, United Arab Emirates
{[@akumar](mailto:akumar), [@rkm](mailto:rkm), [@sakhan](mailto:sakhan)}@bits-dubai.ac.ae

Abstract— *Unmanned Aerial Vehicles are increasingly being used for military and civilian purposes. Obstacle avoidance is an important aspect for any mobile robot including UAVs. Indoor UAVs traveling through a corridor can autonomously avoid obstacles and do path planning with LIDARs. Outdoor UAVs can detect obstacles using radars. This paper proposes a new algorithm to autonomously avoid obstacles using radars and image processing of video frames to detect and avoid obstacles. Typically, UAVs are limited by on-board computational and memory constraints. This new algorithm aims to reduce the computational requirement. The performance of this algorithm is compared with the brute force pixel-by-pixel comparison or the MLE algorithm.*

Keywords—*Unmanned Aerial Vehicles, Image Recognition, Obstacle avoidance*

I. INTRODUCTION

Humans recognize a multitude of objects in images with little effort, despite the fact that the image of the objects may vary somewhat in different view-points, in many different sizes or scale or even when they are translated or rotated. Objects can even be recognized when they are partially obstructed from view. This task is still a challenge for computer vision systems or robots in general. There are two methods of object recognition, namely appearance based methods and feature based methods.

In appearance-based methods of object recognition, example images known as templates or exemplars of the objects are used to perform the recognition. However objects look different under varying conditions such as changes in lighting or color, changes in viewing direction and changes in size or shape. A single exemplar is unlikely to succeed reliably. However, it is impossible to represent all appearances of an object. Hence a robust object recognition using appearance method is not reliable.

In feature-based methods, a search is used to find feasible matches between object features and image features. The primary constraint is that a single position of the object must account for all of the feasible matches. It extracts features from the objects such as surface patches, corners, and linear edges to be recognized and the images to be searched.

Obstacle avoidance is an important aspect for any mobile robot. Without it, the movement of the robot will be highly

restrictive. Robots move with the help of path planning. The achievability of real-time motion planning is reliant on the correctness of the map on robot localization and on the number of obstacles. Topologically, the problem of path planning is linked to the shortest path problem of finding a route between two nodes in a graph.

II. BACKGROUND STUDY

A. Integrating image processing techniques with UAVs

Past research has shown that image processing techniques can be integrated with the quad-rotor aerial robot. The aerial robot cannot receive the GPS (Global Positioning System) signal for positioning in an indoor environment however with the image processing technique, the quad-rotor can hover around a fixed position or visually track a moving object in an indoor location. It can also be used to identify objects in its path and to read signboards, as the UAVs that participated in the IARC (International Aerial Robotics Competition) competitions have demonstrated.

Zou et al [10] conducted an experiment wherein a CCD (Charge Coupled Devices) camera was placed on the bottom of the aerial robot. The images captured by the camera were transmitted wirelessly. The position's error and leading angle's error of the target on the ground could be computed by processing the image to filter the unwanted colors, convert the image into binary, and compute the mid-point and heading angle of the target image. Zou et al also propose to extend their research feature based image recognition for automatic docking and charging.

Courbon et al [11] conducted an experiment where the UAV travels back and forth between two points. The UAV recognizes only the two terminal points in the path for which photographs have been previously taken to serve as reference images. The UAV keeps capturing images as it traverses and compares with the reference images.

One of the IARC entries, IFOR [8] (Intelligent Flying Object for Reconnaissance) is built on the Astec Pelican quad-rotor platform. Light Detection and Ranging (LIDAR) is an exteroceptive sensor which is the input device for the reading the environment for obstacle detection and avoidance. The advantage of using LIDAR is the high precision and resolution

it provides in the distances measured during path planning. The IFOR's LIDAR has a scanning range of 5600 mm and an angular resolution of 0.36 degree; this was proven to be sufficient for indoor travel through corridors. Obstacle detection using LIDAR is carried out by locating the objects present directly in the path of the UAV [9]. This is done by studying a certain degree-span of readings directly in front of the vehicle which are calculated based on a safe-distance and the minimum clearance required for the quad rotor to pass through safely. The obstacles detected are defined as a single point or an abstract collection of points that hinders the intended path of travel.

The IFOR vehicle makes use of two cameras. All processing of sensor data is done off board. The front camera is used to detect and identify objects and words through the use of the Speeded Up Robust Feature (SURF) descriptors. This camera also captures images for the image processing module; this module recognizes the Arabic writing on the signboard that identifies the room where the target pen drive is located. Optical Character Recognition (OCR) is used here. The UAV is expected to autonomously locate and pick up the pen drive and return to base. The pen drive is identified using SURF and processing images provided by the bottom facing camera.

Parappat [5] has concluded that the main issue facing the static object recognition is the quality of the image captured. This algorithm includes capturing the image in a mobile, phone, compensating for lighting variations, converting RGB image into binary, performing edge detection, cropping the image to exclude background information, resizing image to predefined value and then comparing with stored images

B. UAV Applications

Autonomous flight vehicles have been widely recognized to offer many potential benefits for both military and civilian applications. Military applications mainly include security applications where the military is called in to provide support such as rescue of hostages, tracking objects and indoor mapping of an area before the real army move in. UAVs are also being considered for various civilian applications in the security, urban planning, automation, environmental, and disaster management.

Different security applications, to name a few, range from indoor mapping of buildings, to using UAVs as aerial security guard, to accessing hostile regions, and to target location and recovery in an indoor environment to detection of land mines. Automation and urban planning applications include UAVs as autonomous messengers, collection of critical data in hazardous fields, monitoring and controlling traffic, mapping of topology, inspection of bridges, or power lines, surveillance of larger areas, aerial photography, and imaging of large structures. Under the category of disaster management, applications such as search and rescue, helping to set up a communications link for marooned people, air drop of necessities, etc. Cleansing the atmosphere, surveillance and monitoring of pipelines, helping control and clean up oil spills, agricultural crop dusting, etc. are a few environmental applications.

Governments use GIS systems as a tool for geographical information collection, storage, management and analysis, which is applied to different professional fields and forms a lot of GIS application software systems [12]. UAVs can provide an alternative means to provide GIS data about the city architecture. Hence UAV can be given the GPS coordinates for traversing through a city on pre-planned path; as it travels, it will capture images of the city for the GIS system with the corresponding GPS coordinates and help identify the various objects in the images such as buildings, trees, poles, bridges, etc. The images can be uploaded to a cloud accessed by both the UAV and the base computer for further analysis. At the end of the UAV's flight the base computer uses the images to update the GIS system.

III. PROBLEM FORMULATION

For defining the problem, we considered a scenario in which the UAV is used for an urban application and the on-board cameras are used for object detection and eventually obstacle avoidance. In this scenario, our UAV is a data collection agent for creating a GIS system of a city.

However, our main objective for this study is to not create the GIS system instead is to avoid the obstacles the UAV will face while flying through the city on its pre-planned trip. Most of the obstacles are stationary such as buildings, poles, trees, bridges, etc. The only changes that can occur in these objects are if the building is under construction or is being demolished, if tree has grown taller, new poles have been installed and so on. However besides these issues, there are some variable obstacles that we also need to consider such as birds, planes, helicopters, etc. Birds are capable of flying at different heights according to their breed, size and weather conditions. In this case, it is highly difficult to predict the position of the birds while the UAV is in flight. The birds can be flying at us, towards us, cutting thorough our path, etc. Hence we need to be able to detect the birds in our close vicinity, recognize the breed, and suitably evade the bird by estimating the path it will take. It is required to capture blur-free images of the bird as it moves to enable more accurate and efficient processing; calculate the speed of the bird and estimate its trajectory; and match it to the database images previously created (this collection of images would be the same object photographed from various angles). As UAV will travel at a high speed, the object detection algorithm is to be designed for effective and efficient performance.

IV. SOLUTION METHODOLOGY

A. Initial steps to the solution

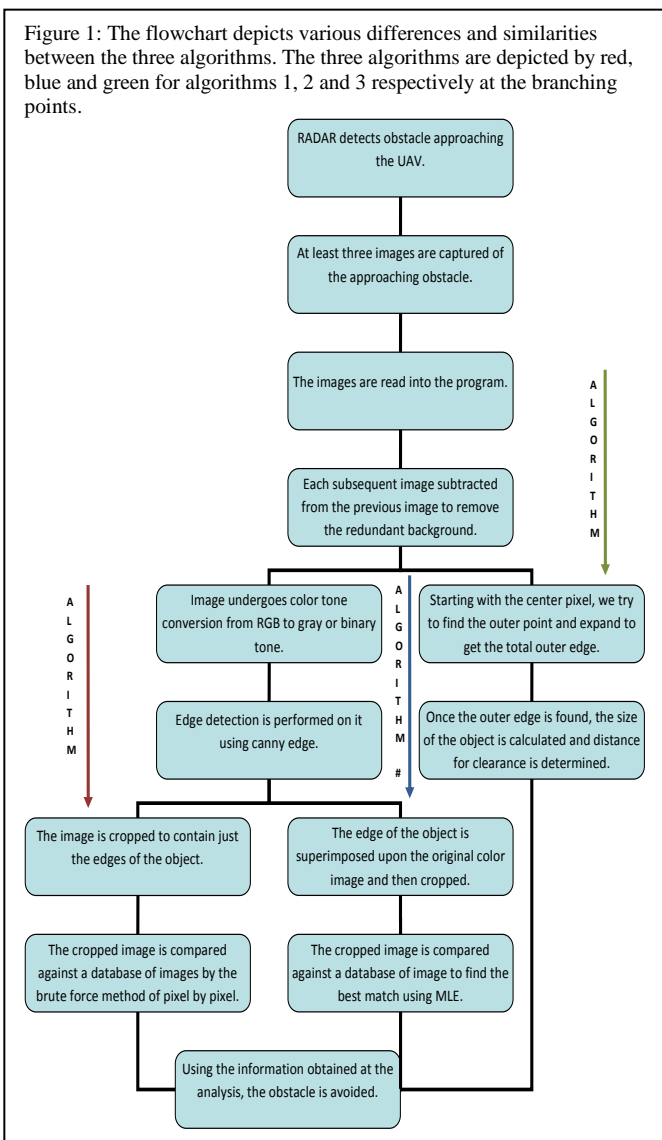
The various types of birds that were present in the locality were studied and catalogued with the speeds at which they travel at, their sizes and the images of the birds taken from different angles, this helps create the image database. With the results obtained, the algorithms were formulated to use in the application scenario for obstacle avoidance using image recognition techniques. The initial step of the first two algorithms is to create a database of the various birds seen in and around the area of the GIS's focus and the images of each bird needs are required for frontal, top, side and rear views.

Radar is used to track the birds when they are nearing the vicinity of the UAV and by using image recognition techniques, we can identify the type of bird and hence calculate the minimum clearance distance. The following sections describe the different algorithms that were created, analyzed and compared during this study.

Three algorithms were compared against each other to find the best algorithm for obstacle avoidance. As the speed of the aerial robots are very high, the algorithm used for object detection should also work efficiently and effectively in order to allow the robot to move freely. All three algorithms were implemented and tested in MATLAB version 7.13 on Windows 8 with the help of the image processing toolbox.

B. Algorithm # 1 –Brute force method :

The first algorithm tried out was a variation of the previously obtained algorithm for static object detection in an image. Here the aim of the algorithm is obstacle avoidance by object recognition [6]. The algorithm is described in Figure 1. Once the object is recognized, UAV’s path can be planned.



This algorithm takes 35 seconds plus 2-3 seconds for each database image. The edge detection algorithm does not work efficiently in dim or very bright lighting conditions as it creates a glare or shadows in the images that the algorithm considers is a part of the object. Color information and thereby the color information contour information is lost during analysis.

C. Algorithm # 2 – Modified MLE Approach:

The next algorithm is a slight variation of the popular maximum likelihood estimation (MLE) [13]. This algorithm, rather than comparing pixel to pixel, compares the defining features such as colour, size and shape to locate the best fit. A database of the possible obstacles is created and pre-classified by colour; then in decreasing order of size; and then by the various shapes. The algorithm is detailed in Figure 1. UAV’s path can then be then planned.

This algorithm is more robust compared to algorithm 1, but is not capable of handling unknown objects and requires careful selection of defining features. This algorithm takes 20 seconds plus 2-3 seconds per database image.

D. Algorithm # 3 – Avoidance by Image Segmentation:

The following algorithm deals with obstacle avoidance by calculation of area. Radar is firstly used to detect any object that crosses a circular area around the UAV. Once the object is detected, multiple shots (at least 3 images) of the object are captured. The steps of the algorithm [5] [6] are outlined in Figure 1.

The above algorithm is better suited for object avoidance during an UAV flight using image recognition techniques. Since the focus is on the UAV avoiding the obstacle via area calculation, we can be sure that time is not wasted on other unnecessary computations. Hence for this algorithm, the mandatory requirement is that the object must be present in the centre of the image. Since our focus is on finding the area of the object and avoiding the object, it takes merely seconds to identify the object (see Table 1).

E. Comparative study between the algorithms:

The three algorithms clearly show that they have basically four main steps: Read in the images; Get the boundary of the object; Calculate the area of the object; Compare the object with a database of objects.

Brute Force: 35 secs + 2 secs/DB image	Modified MLE: 20 secs + 2 secs/DB image	Image Segmentation: 10 secs
---	--	------------------------------------

The first two algorithms have the fourth step as the key point as it deals with obstacle avoidance by object recognition rather than a simple obstacle avoidance shown by the third algorithm.

Table 1 shows the time taken by the algorithms to work (the the individual time taken at each step is available in [5]) to compare a white circular object present on a black background along with a database as in the case of the first two algorithms. As we can see in the table, the time taken by

edge detection by image segmentation is one fifth the total time taken by using edge detectors and resizing the images. The flowchart in Figure 1 depicts the steps followed in each algorithm while highlighting the differences and similarities between the three derived algorithms as described above. Table 2 shows the time taken by each algorithm to compare the images against one database image in the case of the first two algorithms and calculates the area by image segmentation in the third algorithm. For the case of simplicity, the initial common part of the algorithm where the three captured images are subtracted against each other to get the object was ignored as the object is a single colored object against a black background. If the images are subtracted to obtain the object, the background would become black and only the object would remain. In the case of the last image of the red parrot, the image was pre-edited and the background was changed to black leaving only the parrot in the center of the image. This was done in order to put all the images through the exact same steps during the experiment.

Table 2: Table depicting the time taken by the three algorithms on six different images. Algorithm 3a uses radial segmentation while algorithm 3b uses spiral segmentation. The time taken in seconds is listed in the order of Algorithm 1, 2, 3a, 3b.

Image	Time taken	Image	Time Taken	Image	Time Taken
	18,18,6,97		12,19,1,17		10, 12, 1, 93
	12,12,1,33		11,10,2,47		13, 12, 2, 4

VII. CONCLUSIONS AND FUTURE WORK

The problem was formulated based a scenario created in which the UAV is used as a data collector for a GIS system and the on-board cameras are used for object detection and eventually obstacle avoidance. Most of the obstacles the UAV will encounter are stationary such as buildings, poles, trees, bridges, etc. However there are also some variable obstacles that we also need to consider such as birds, planes, helicopters, etc. Birds are capable of flying at different heights according to their breed, size and weather conditions. In this case, it is high difficult to predict the position of the birds while the UAV is in flight. The birds can be flying at us, towards us, cutting thorough our path, etc. Hence we need to able to detect the birds in our close vicinity, recognize the breed, and suitably evade the bird by estimating the path it will be taking. Radar is used to help in obstacle detection and tracking.

Of the three algorithms tried out, the last one is the most efficient and effective algorithm as it implements the solution solely focused on obstacle avoidance rather than obstacle avoidance by object recognition and is faster. The radar that is included helps in detecting the object, the trajectory it is following and the speed of flight. Eventually we can also calculate the time it will take to reach the UAV. MLE comparison is quite effective as it does not compare pixel to pixel but instead looks for the most likely fit between the images. In the simulations, a single colored object against a single colored background is considered. With complex

shapes shown table 3, algorithm 3a may terminate incorrectly after finding the pixel change in the direction of the shortest radius.

An alternative method to the radial image segmentation is to do spiral image segmentation by calculating the pixel values of the neighboring pixels. Here, we calculate the center pixel value and then check the immediate eight pixels if they are the same as the center pixel [5]. The comparison is made in a concentric and expanding fashion. However, this approach is valid only for a single colored object, as the following table shows the time table for spiral segmentation by various images.

Table 3: Table depicting the time taken by various images while using the spiral image segmentation

					
89secs	1 sec	0 sec	7 sec	86 secs	69 secs

Acknowledgments

This research was begun as part of Priya Bajju Parappat’s undergraduate thesis at Birla Institute of Technology and Science (BITS) Pilani, Dubai Campus during February-June 2013.

References

- [1] Rafael C. Gonzalez and Richard E. Woods, “Digital image processing”, Third edition, Person Prentice Hall Publication, 2009
- [2] Uvais Qidwai and C.H.Chen, “Digital Image Processing–An Algorithmic Approach with MATLAB”, Chapman & Hall/CRC Press, 2010
- [3] Nikos Nikolaidis and Ioannis Pitas, “3-D image processing algorithms”, John Wiley & Sons, Inc, 2001
- [4] K.S.Fu, R.C.Gonzalez, C.S.G.Lee. “Robotics: control, sensing, vision, and intelligence”, Taata McGraw-Hill Edition, 2008
- [5] Priya Bajju Parappat, “Design and implement a robust image recognition algorithm for mobile phone images”, Project Report – BITS Pilani, Dubai Campus, 2013
- [6] Saurabh Ladha, “Real time tracking of objects in unmanned aerial vehicles”, Project report – BITS Pilani, Dubai Campus, 2012
- [7] C.Khemraj, J.Kumar, A.Srivastava, and G.Srivastava, “Autonomous UAV (unmanned aerial vehicle) for navigation & surveillance purposes”, Global Journal of Researches in Engineering, Volume XII Issue II Version I, 2012
- [8] Saurabh Ladha, Deepan Kishore K, Robin Singh, et al, ‘Unmanned Aerial vehicle of BITS Pilani, Dubai Campus for the International Aerial Robotics Competition 2011’, Paper presentation at IARC-2011, 2011
- [9] Saurabh Ladha, Deepan Kishore Kumar, Pavithra Bhalla, Aditya Jain, et al, ‘Use of lidar for obstacle avoidance by an autonomous aerial vehicle’, Paper presentation at IARC-2012, 2012
- [10] Jie-Tong Zou, Yu-Chiung Tseng, ‘Visual track system applied in quadrotor aerial robot’, National Formosa University; Third international Conference on Digital manufacturing and Automation, 2012
- [11] J.Courbon, Y.Mezouar, N.Guenard and P.Martinet, ‘Visual Navigation of a Quadrotor Aerial vehicle.’, IEEE/RSJ International conference on intelligent Robots and Systems, 2009
- [12] M. Mohamed and R. Plante, ‘Remote Sensing and Geographic Information Systems (GIS) For Developing Countries’, IEEE publication, 2002
- [13] Lu Changhua, Chang Ningning, Fang Rui, Lui Chun, ‘A novel algorithm for moving objects recognition based on sparse bayesian classification’, IEEE Publication, 2006

Pyramid Method for Reversible Discrete Wavelet Transformation of 3D Image

Eustache Muteba Ayumba

Abstract— In this research, the pyramidal structure and algorithm are proposed for computing the reversible discrete wavelet transformation of 3D Image. The concept of formal language is used to emphasize the modeling of a pyramidal structure of forward and reverse transform. With the assumption, the pyramid representation can help the 3D Image representation and can facilitate the processing.

Keywords— Discret Wavelet Transform, Pyramid Method, Pyramidal Data Structure and Algorithm, Tree-Dimension.

I. INTRODUCTION

IMAGE processing based on Discrete Wavelet Transformation (DWT) and using pyramidal techniques, as reveal Adelson et al [1], is nowadays essential. Discrete Wavelet Transformation (DWT), as stated in [2], proceed a signal has a cut-of-frequency and it is computed by successive Lowpass and Highpass filtering of the discrete time-domain signal. Filters are signal processing functions. Furthermore, a measure of the amount of detail information signal is determined by the filtering operation (Lowpass and Highpass) and the scale is detrmined by Upsampling and Downsampling.

The pyramidal technique is a type of multi-scale signal processing in which a signal or an image is subject to repeated smoothing and subsampling [3].

Practically, for representing a three dimensional image (3D Image), we can refer to a three dimensional Euclidian space as stated in [4].

In this research, the pyramidal structure and algorithm are proposed for computing the reversible discrete wavelet transformation of 3D Image. The concept of formal language is used to emphasis the modeling of a pyramidal structure of forward and reverse transform. With the assumption, the pyramid representation can help the 3D Image representation and can facilitate the processing.

II. PYRAMID METHOD OF 3D DWT

A. Overview

For our purpose, the 3D DWT is based on the method of inferring 3D image information into a smaller non-overlapping tiles on which 2D DWT can be applied.

The reversible DWT as show in figure 1, has two main phases: Decomposition and reconstruction phases.

In decomposition phase, the DWT can be done by iteration of filtering and Downsampling operation. In reconstruction phase, the DWT is the reverse process of decomposition in that the original signal is then obtained by iteration of Upsampling and filtering operation

A 3D image is a set of sequence of sample values $I=[x_i, y_j, z_k]$, where $0 \leq x_i \leq N_1, 0 \leq y_j \leq N_2, 0 \leq z_k \leq N_3$; x_i, y_j and z_k are the integers that having finite extents, N_1, N_2 and N_3 , in the horizontal, vertical and depth directions, respectively. A 2D image is a set of sequence of sample values $I'=[x_i, y_j]$, where $0 \leq x_i \leq N_1, 0 \leq y_j \leq N_2$. A digitized 3D image size is in $N_1 \times N_2 \times N_3$ and a sub block is in size $1/2^n \times 1/2^n \times 1/2^n$.

With respect to a fixed global reference frame, it is possible to make correspondence between points in 3D space and their projected images in a 2D image plane, with respect to a local coordinate frame.

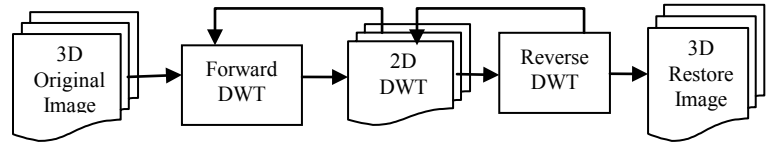


Fig. 1 Reversible DWT of 3D

B. Formalization

For representing the DWT of 3D Image, we refer to formal language and regular images [5]. We assume that the computer has finite memory, so there are only finitely many states the computer can be at, and the previous state of the computer determines the next state, so the machine has deterministic state transitions.

The concept of language theory serves as basis to emphasis the problem related to reversible 3D DWT. We consider the following definitions:

Definition 1: Language

The formal language L is composed by an alphabet Σ and a specific grammar G .

Definition 2: Alphabet

Let an alphabet Σ be a set of element, $\Sigma = \{H, L\}$, that represents the high and low frequencies.

Definition 3: Grammar

The grammar is given by a 5-tuple:

$$G = \{V_N, V_T, I, F, C\}$$

with $V_N = \{I, W\}$, $V_T = \{Hx, Hy, Hz, Lx, Ly, Lz\}$, where G denotes a grammar; V_N denotes a Non Terminal Verb; V_T denotes a

Terminal nodes expressing low and high frequencies in all direction, X, Y and Z ; I denotes an input image; F denotes the formula with a set of constraints C attached to each terminal node to code the word. In order to achieve perfect reconstruction the analysis and synthesis filters have to satisfy certain conditions.

Definition 4: Formula

The formula generates word from a terminal verb:

$$F = \{I \rightarrow W\}; W = w W^m, m \geq 1$$

Thus, there is a specification language L for representing 3D DWT as a text that is a set of sentences S . The respective text should be described as follows:

- $Text := S\{S\}^*$
- $S := W\{W\}^*$
- $W := w\{w\}^*$
- $w := 'Hx' / 'Hy' / 'Hz' / 'Lx' / 'Ly' / 'Lz'$

It is possible by means of sentences to keep track of image information.

III. PYRAMIDAL DATA STRUCTURES AND ALGORITHMS

A. Data Structures

The data structure used to represent image information can be critical to the successful completion of an image processing task. The structure of reversible 3D DWT as showed in figure 2 express all operations of filtering and scaling along the three direction saying width direction, height direction and depth direction at decomposition and reconstruction phases. This pyramidal structure representation is suitable to a tree structure. Therefore, it is, also, possible to use pointers, as data type, at each node in order to improve performance in repetitive operations.

Given an input 3D image, with respect to our language L , we can organize it in hierarchical tree structure where each terminal node corresponds to a sub block as shown bellow. Thus, any word in the language can be parsed by the grammar that has three levels of related image information to the start node, the original image.

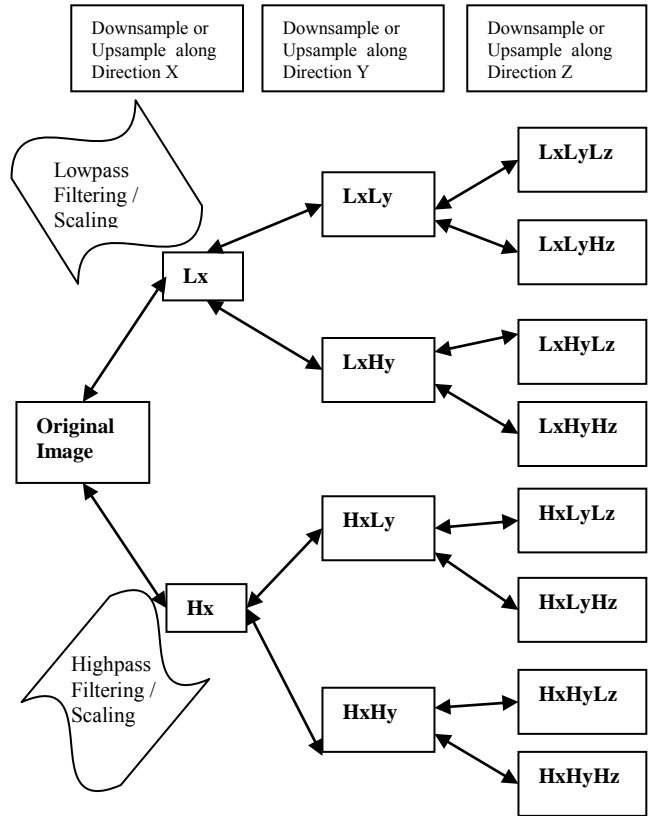


Fig. 2 Structure of the reversible 3D DWT

B. Algorithms

Our algorithm is based on the purpose of overview in section 2 and is a consequence of the pyramidal data structure presented in section 3.

For a given image $I = [x_i, y_j, z_k]$, where $0 \leq x_i \leq N_1, 0 \leq y_j \leq N_2, 0 \leq z_k \leq N_3$; Let dwt (discrete wavelet transform) be a recursive function that computes I on l level, $l \geq 1$:

$$dwt = \sum_{l=1}^m dwt(I) \tag{1}$$

Firstly, we use the function dwt and process a low-pass decomposition and high-pass decomposition in the width direction (horizontal details), after in the height direction (vertical details) and at last in depth direction.

Filtering and scaling along Direction X: Lx, Hx

$$dwt_1 = \sum_{z=1}^{N_3} \left(\sum_{y=1}^{N_2} \left(\sum_{x=1}^{N_1} L_x \left(\frac{N_1}{2}, N_2, N_3 \right) \right) \left(\sum_{x=1}^{N_1} H_x \left(\frac{N_1}{2}, N_2, N_3 \right) \right) \right) \tag{2}$$

Filtering and scaling along Direction Y: $LxLy, LxHy, HxLy, HxHy$

$$dwt_2 = \left(\sum_{z=1}^{N_3} \left(\sum_{y=1}^{N_2} L_{Ly} \left(\frac{N_1}{2}, \frac{N_2}{2}, N_3 \right) \right) \left(\sum_{y=1}^{N_2} L_{Hy} \left(\frac{N_1}{2}, \frac{N_2}{2}, N_3 \right) \right) \right) \left(\sum_{z=1}^{N_3} \left(\sum_{y=1}^{N_2} H_{Ly} \left(\frac{N_1}{2}, \frac{N_2}{2}, N_3 \right) \right) \left(\sum_{y=1}^{N_2} H_{Hy} \left(\frac{N_1}{2}, \frac{N_2}{2}, N_3 \right) \right) \right) \tag{3}$$

Filtering and scaling along Direction Z: $LxLyLz, LxLyHz, LxHyLz, LxHyHz, HxLyLz, HxLyHz, HxHyLz, HxHyHz$

$$dwt_3 = \left(\sum_{z=1}^{N_3} \left(\sum_{y=1}^{N_2} \left(\sum_{x=1}^{N_1} L_{Lz} \left(\frac{N_1}{2}, \frac{N_2}{2}, \frac{N_3}{2} \right) \right) \left(\sum_{x=1}^{N_1} L_{Hz} \left(\frac{N_1}{2}, \frac{N_2}{2}, \frac{N_3}{2} \right) \right) \right) \left(\sum_{z=1}^{N_3} \left(\sum_{y=1}^{N_2} \left(\sum_{x=1}^{N_1} L_{Lz} \left(\frac{N_1}{2}, \frac{N_2}{2}, \frac{N_3}{2} \right) \right) \left(\sum_{x=1}^{N_1} L_{Hz} \left(\frac{N_1}{2}, \frac{N_2}{2}, \frac{N_3}{2} \right) \right) \right) \right) \left(\sum_{z=1}^{N_3} \left(\sum_{y=1}^{N_2} \left(\sum_{x=1}^{N_1} H_{Lz} \left(\frac{N_1}{2}, \frac{N_2}{2}, \frac{N_3}{2} \right) \right) \left(\sum_{x=1}^{N_1} H_{Hz} \left(\frac{N_1}{2}, \frac{N_2}{2}, \frac{N_3}{2} \right) \right) \right) \right) \tag{4}$$

Secondly, we use the reverse function dwt' and process a low-pass reconstruction and high-pass reconstruction in the width

direction (horizontal details), after in the height direction (vertical details), and at last in depth direction.

The algorithm is highly memory efficient due to fact that the 3D size is limited. Also, the computation complexity has acceptable processing time.

IV. CONCLUSION

The image coding methods using wavelet transform and pyramidal technique is essential and really efficient in image processing [6], [7].

One of the important contributions of our paper is the pyramidal data structure and algorithm for 3D (DWT) image processing. This is method can be used efficient in the filed of medical science and Biotechnology.

REFERENCES

- [1] E.H. Adelson, C.H. Anderson, J.R. Bergen, P.J. Burt & J.M. Ogden, "Pyramid methods in image processing", 1984. Available: http://persci.mit.edu/pub_pdfs/RCA84.pdf
- [2] T. Edwards, "Discrete Wavelets Transforms: Theory and Implementation", 1992. Available: http://qss.stanford.edu/~godfrey/wavelets/wave_paper.pdf
- [3] Wikipedia, "Pyramid (image processing)". Available: [http://en.wikipedia.org/wiki/Pyramid_\(image_processing\)](http://en.wikipedia.org/wiki/Pyramid_(image_processing))
- [4] Y.H. Lee, S.J. Horng, J. Seitzer, "Parallel Computation of the Euclidean Distance Transform on Tree-Dimensional Image array" in *IEEE Transactions on Parallel and Distributed Systems*, vol. 14, NO. 3, March 2003, pp 203-212.
- [5] S. Wintner, "Formal Language Theory for Natural Language Processing", 2001. Available: <http://www.helsinki.fi/esslli/courses/readers/K10.pdf>
- [6] E. H. Adelson, C. H. Anderson, J. R. Bergen, P. J. Burt, J. M. Ogden, "Pyramid methods in image processing". Available: <https://alliance.seas.upenn.edu/~cis581/wiki/Lectures/Pyramid.pdf>
- [7] B. K. Choudhary, N. K. Sinha, P. Shankera, "Pyramid Method in Image Processing", in *Journal of Information Systems and Communication*, Volume 3, Issue 1, 2012, pp.- 269-273. Available: <http://www.bioinfo.in/contents.php?id=45>

Procedural aspects of data seizure

Jan Kolouch, Andrea Kropáčová

Abstract—The number and intensity of cyber attacks and crime online have risen recently, so did their severity and their impact. This article defines the digital evidence and individual types of evidence used to seize data. Further, this article also describes the proposals *de lege ferenda* for more efficient data seizure for the purpose of the criminal proceedings.

Keywords—Data, digital evidence, interception and recoding of telecommunication traffic, data seizure, operational and localisation data, data retention, Convention on Cybercrime.

I. INTRODUCTION

At present, the real world is surrounded by a “cobweb” of the information network connecting individual computer systems which enables a fast information and data exchange – Internet. Thus, the Internet has become the most efficient and most dangerous weapon in the hands of the criminals. It is unacceptable that the Internet be a safe and anonymous environment for the criminals, allowing them to commit any crime *de facto* without any punishment.

There is a single means to fight against the criminality on the Internet, and that is the Internet itself. One needs to understand what the Internet is, what principles it operates on, and what types of crimes can occur in the virtual world and what action and under what conditions the bodies involved in the criminal proceedings may take in order to fulfil the purpose of Act no. 141/1961 Sb. on criminal procedures (the Criminal Procedure Code, CPC), see [16].

It should be noted that worldwide, significant efforts have been witnessed, both legally and technically, to adopt relevant measures to enable reacting to this new and dynamic phenomenon of the present [11] and [12], which the cybercrime no doubt is.

Cybercrime is an offence in which information technology means:

- a) *are used as the instrument to commit a criminal offence,*
- b) *are the target of the offender’s attack, and the attack is a criminal offence provided the means were used or misuse in the information, system, programme or communication environment.*

For more info see [3].

A significant feature of the cybercrime, distinguishing it from other crimes from the point of view the law of the criminal proceedings, is the greater anonymity of the

criminals and their uneasy identification, including the entire evidence proceeding.

Other downsides include **not entirely sufficient professional readiness of the bodies involved in the criminal proceedings** to face this new type of crime. Yet another issue is the **lack of professionals** specialising in this type of crime.

II. DIGITAL EVIDENCE

First, it is necessary to define basic terms relating to evidence collation. These terms include in particular **computer system** and **computer, or digital evidence**.

A computer system is a functional unit, consisting of one or more computers, (a functional unit able to perform extensive calculations, including many arithmetic and logic operations, without human interaction (see [9]) and associated software, that uses common storage for all or part of a program and also for all or part of the data necessary for the execution of the programme. A computer system may be a stand-alone system (working independently – e.g. a personal computer) or may consist of several interconnected systems (e.g. a network of computers). More in [4].

“Computer evidence can be characterised as any change to the data carrier, occurred in relation to a crime committed by means of computer technology, which is traceable using current methods, means and operations. This evidence is located on the hard drive, external storage media, CD ROMs, diskettes, etc” [10].

Casey [1] defines computer (digital) evidence as: “any data stored or transmitted using a computer that support or refuse a theory of how an offence occurred or that address critical elements of the offence such as intent or alibi of the perpetrator.”

The USLegal server defines the digital or electronic evidence as: “any type of evidence stored, or transmitted digitally“. The courts admitted using digital evidence in the court proceedings. This includes in particular e-mails, digital images, documents in an electronic format, the history of the instant messages (including not only short text messages but also any messages sent via instant messengers, e.g. Skype, Twitter, WhatsApp, ICQ), table processors, Internet browser’s history, databases, the content of a computer memory (RAM), computer data backups, logs, etc. [13].

Compared to traditional evidence, **computer (digital) evidence** is rather specific as it can be rather considerably large (considering the volume of data), dynamic and can be stored anywhere in the cyberspace, even distributed. **The lifespan** of such evidence **can be very short** and any delays

⁼ This work has been supported by the CESNET, a. l. e., <http://www.cesnet.cz>, operator of the Czech national research and education network referred to as CESNET2 within it “Large Infrastructure” (LM2010005) research programme of the Ministry of Education, Youth and Sports of the Czech Republic, running within 2010-2015 timeframe. .

Jan Kolouch works in CESNET, a. l. e., Zikova 4, Prague 6, Czech Republic, (email: kolouch@cesnet.cz).

Andrea Kropáčová works in CESNET, a. l. e., Zikova 4, Prague 6, Czech Republic, (email: andrea@cesnet.cz).

either before the commencement of the criminal prosecution or during the investigation could result in evidence being lost or less “richness” (we can say also “level of detail”) and less precise. Consequently, the rate of uncovered cybercrimes decreases.

The **cyberspace** can also be defined as the space for cyber activities, or the space created by information and communication technologies (“ICT”) which creates a virtual world (or space) as a parallel to the real world. The material basis of the cyberspace is in particular the Internet, the worldwide (distributed) computer network consisting of smaller networks interconnected using IP protocols, thus enabling data and information transmission and provision of services between entities. See [3].

Any criminal activity in the cyberspace leaves a number of such evidence, on storage media of the targeted computer, server hard drives and other devices of individual service providers or ISP. Besides above mentioned types of computer evidence, it is also possible to seize other evidence as cybercrime also leaves **written evidence** (e.g. the communication between the sellers of illegal software, accounting and other documents) and in particular imprints in human mind (memory imprints) of the **persons who perceived the crime**. The computer system is a separate source of evidence, in particular its components, configuration and the type of network connection (OS, logs, temporary files etc.).

In the existing Czech law of the criminal proceedings, computer (digital) evidence is covered under sec. 112 (1) or (2) of the Criminal Procedure Code.

In accordance with sec. 112 (1) of the Criminal Procedure Code, **material evidence** shall consist of those **items** (including a computer) which served for committing the crime or on which the crime was committed, and **other items that either support or refute the alleged facts** and may serve as a means to reveal and expose a crime and the offender and the clues to the criminal offence. The legal definition is not taxative. Material evidence also encompasses “*all items arisen as a consequence of an offence, or all items by means of which factual or actual course of an offence can be evidenced*” [2].

As regards cybercrime, the most common **material evidence is a data carrier** (in all its forms) containing certain data and information. In line with the above mentioned characteristics, such **data and information can be considered as material evidence** although they cannot exist without the physical data carrier (i.e. the data carrier which can be physically seized as evidence when producing individual pieces of evidence). An example of “non-existing” data carrier in securing items (data) important for the criminal proceeding is the case when the data is stored in the cloud. **Cloud computing** is the term used for a system enabling the use (sharing) of computer technology (hardware and software) by many users (through the network) in the form of a provided service. See more [17].

In this case, the seized data carriers or the user’s computer system need not comprise a copy of data stored in the cloud.

In accordance with sec. 112 (2) of the Criminal Procedure Code, **documentary evidence** consists of all **papers whose**

content either supports or refutes the alleged facts. Once the record is printed out on a printer, it can be regarded as **documentary evidence**. The Criminal Procedure Code does not define the term ‘document’. Any item on which the written discourse is captured should be considered as a document. This includes paper or other media able to record written text or drawings, compare [2] pp. 346-348.

I believe that the subsumption of the digital evidence either under the term material or documentary evidence cannot be applied, as not all specifics of the digital evidence would be covered by such a subsumption.

Digital evidence differs significantly from material or documentary evidence include in particular as regards the following:

1. Their relative instability,
2. Availability (accessibility)
3. The process of the seizure,
4. Reproducibility,
5. Can be easily falsified.

1. Relative instability: The data transmitted by means of ICT, and the transmission itself, leave a trail. This trail, however, is rather unstable, and it is at the discretion of the ISP or the user whether, to what extent and for how long the data are retained.

2. Availability (accessibility): The data can be stored on various data or information carriers, irrespective of whether it is external or internal media to record and store data. These include hard drives (HDD), operation memories (RAM), diskettes, compact disks with various write density (CD, DVD, Blu-Ray), memory cards (SD, MMC, CF cards, SDHC, etc.), electronic memories of the USB types (flash cards) etc.

At the same time, data can be stored in data spaces provided by individual ISPs, typically through the cloud service. As regards availability, it is important where the cloud provider, or relevant hardware, is located. In case of earthquake and Tsunami in Japan or Thailand, it can be expected that devices dislocated in these regions and the clouds running on them may not be available for a certain period of time. Examples include DDoS attacks against Estonia or Georgia or DDoS attack against the cloud by the Bredolab botnet which flooded more than 700 000 Facebook users, etc.

3. The process of the seizure: The seizure of digital evidence is a procedural act in which data, mostly unaltered, are conserved. It is possible to retain unaltered data e.g. by creating a bit copy. Certain methods of data seizure, however, create an altered copy (e.g. containing the reference to the copy, tools used to create the copy, etc.). This alteration is de facto an interference into the integrity and uniqueness of the data seized, and it could be objected that the data are different, altered by the bodies involved in the criminal proceedings.

4. Reproducibility: In many case, the data are stored in a form which cannot be “materially reproduced”. A certain application or programme which converts the data into a perceivable format needs to be launched to reproduce the data. Again, feeding the data into such applications alters

their format and structure.

5. Can be easily falsified: Some digital data (evidence) is easy to produce. For example, each administrator is able to manually create a "log" of mail daemon (consisting of what e-mails and when where sent through the mail system). Fortunately, in most cases it is possible to verify with other independent sources – cross-checking the logs from other mail systems outside influence of the forger (which does not have the opportunity to modify the data – log).

For the above reasons I believe that it would be appropriate to define a new category of evidence: **digital evidence**. The provision defining the digital evidence could be incorporated into sec. 112 (3) of the Criminal Procedure Code in the following wording:

Digital evidence shall comprise any data or information transmitted or stored by means of a computer system that either support or refute the alleged facts and may serve as a means to reveal and expose a crime and the offender and the clues to a criminal offence.

III. LEGISLATION GOVERNING THE DATA SEIZURE

The Council of Europe adopted two fundamental documents which should contribute towards the protection of the society against cybercrime and enable the bodies involved in the criminal proceedings to seize data and digital evidence for the purpose of the criminal proceedings. These two documents are the Convention on Cybercrime [15] and the Additional Protocol to the Convention.

The Convention on Cybercrime (CoC) is a first international agreement that not only defines the criminal offences committed through ICT but also stipulates legal procedures (including the definition of the international cooperation) necessary to uncover and investigate cybercrime.

The Czech Republic ratified the CoC on 22 August 2013, with the CoC entering in force on 1 December 2013. Unfortunately, only several provisions, mostly substantive, have been implemented into the Czech Criminal Code so far (See s. 230-232 of Act no. 40/2009 Sb., the Criminal Code). The Criminal Procedure Code has not be re-enacted and separate institutes allowing to seize data are still lacking in the Czech legislation.

A. Interception and recording telecommunications traffic (sec. 88 of the CPC)

In accordance with sec. 88 and 88a of the CPC, interception and recording of telecommunications traffic is the primary means to seize the **content of transmitted information** in the Czech Republic. Items can only be seized upon a court order, and the order does not apply retrospectively.

B. Record of telecommunication traffic (sec. 88a of the CPC)

At present, the record of telecommunications traffic is the fundamental source of information and evidence necessary for the criminal proceedings. This means is used to obtain

operational and localisation data and can only be used based on a court order. The data is solicited from ISPs who have the obligation to store data for the past six months.

Operational and localisation data are, in particular, "information leading to tracking and identifying the source and the recipient of the communication, and any information helping to establish the date, the time, manner and the duration of the communication."

C. Surrender and seizure of a thing

Where the provisions on the interception and recording of telecommunications traffic have not been applied, the provision on the surrender and seizure of a thing in accordance with sec. 78 a 79 of the CPC applies to obtain data stored on a data carrier. The seizure of a thing must be preceded by a request to surrender a thing in accordance with sec. 78 of the CPC which stipulates the **duty to hand over or surrender a thing** relevant for the criminal proceedings upon a request of the bodies involved in the criminal proceedings.

IV. LEGAL PROPOSALS

In order to consolidate international and national legislation, it would be convenient to implement the institutes defined in Chapter Three of the CoC into the Czech criminal law, to enable prompt seizure and use of computer data (see Art. 16 – 21 of CoC).

Adopting a provision enabling the seizure and surrender of computer data is vital. The wording of the new provision could be as follows:

Storing and handing over computer data

- 1) *Where it is necessary to retain stored computer data, including operational and localisation data that were processed through a computer system in order to clarify facts important for the criminal proceedings, the charring judge, or the public prosecutor in the pre-trial proceedings, shall order the person who is in possession of the data concerned or exercises control over the data, or the information society service provider, to*
 - a) *retain the data concerned,*
 - b) *enable the bodies involved in the criminal proceedings to create a copy of such data,*
 - c) *prevent other persons from accessing the data,*
 - d) *remove the data from the computer system,*
 - e) *surrender the data for the purpose of the criminal proceedings.*
- 2) *The order mentioned in par. 1 should state the period over which the data must be retained. The period for data retention may be prolonged by three months, even repeatedly.*
- 3) *Once it is not necessary to retain the data, including the operational and localisation data, for the purpose of the criminal proceedings, the charring judge, or the public prosecutor in the pre-trial proceedings, issues instantly an order to cancel the retention of the data concerned and the operational and localisation data.*
- 4) *The order mentioned in par. 1 - 3 shall be delivered to the person who is in possession of the data concerned, or exercises control over the data, or the information*

society service provider. The person who is in possession of the data concerned data, or exercises control over the data, or the information society service provider surrenders the relevant data to the issuer of the order defined in par. 1.

A. Seizure of the content of delivered e-mail messages

At present, there is no procedural means that would allow seizing the content of delivered but unread e-mail messages.

Technically, the e-mail message consists of data. At the same time, art. 13 of Act no. 2/1993 Sb., as amended by the constitutional act no. 162/1998 Sb., Charter of the Fundamental Rights and Freedoms, applies to it:

“No one may violate the confidentiality of letters or the confidentiality of other papers or records, whether privately kept or sent by post or by some other means, except in the cases and in the manner designated by law. The confidentiality of communications sent by telephone, telegraph, or by other similar devices is guaranteed in the same way.”

I believe it would be appropriate to incorporate a provision in the CPC enabling to establish the content of the delivered e-mail messages. The wording of the provision could be as follows:

Seizing and opening a delivered electronic message (e-mail):

- 1) *Where it is necessary to retain and establish the content of messages delivered by means of information and telecommunication technology in order to clarify facts important for the criminal proceedings, and the relevant facts cannot be otherwise seized, the chairing judge, or a judge upon the request by the public prosecutor in the pre-trial proceedings, can order the mail to be opened.*
- 2) *Without a prior order, the police body can seize the mail only where the issue cannot be postponed or the order cannot be issued in advance. The police body shall advise the public prosecutor that the mail had been seized.*
- 3) *The mail seized may only be opened by the chairing judge, or the public prosecutor with the consent of the judge in the pre-trial proceedings, or a police body.*

As regards other proposals *de lege ferenda*, I believe that it would be appropriate to define a new category of evidence – a **digital evidence**, as described above.

V. CONCLUSION

We are convinced that the cyberspace must not become an environment in which criminal offences could be committed anonymously and with impunity. **On the other side, it is not possible to abuse or “twist” the procedural institutes of the criminal law the primary purpose of which is not to seize data.** Criminal law is a means of ultima ratio, and such needs to be precise so as not to infringe the rights and freedoms of a person more than it is inevitable.

In order to prevent such situations, it is necessary to ensure that the bodies involved in the criminal proceedings have

adequate efficient and legal instruments enabling them to avert the offender’s illegal action, including being able to seize evidence on the action.

In conclusion, we would like to point out that the professional education and specialisation of the bodies involved in the criminal proceedings should become a priority, since cybercrime is the type of criminal activity that develops dynamically and progressively and the mitigation of which requires professionals.

REFERENCES

- [1] CASEY, Eoghan. *Digital Evidence and Computer Crime: Forensic Science, Computers, and the Internet, Second Edition*. London: Academic Press, 2004. 677 s. ISBN 0-12-163104-4
- [2] ČÍSAŘOVÁ, Dagmar, Jaroslav FENYK, Tomáš GRIVNA, and coll. *Criminal Procedure Law*, 5th Edition, Prague : ASPI, 2008. 824 pp. ISBN 978-80-7357-348-5
- [3] KOLOUCH, Jan and Petr VOLEVECKÝ. *Criminal protection against cyber crime*. Prague: The Police Academy of the Czech Republic in Prague, 2013. ISBN 978-80-7251-402-1
- [4] NOVOTNÝ, František and collective. *Criminal Code 2010*. Commentary. 1st edition. Eurounion. Prague 2010. 838 pp. ISBN 978-80-7317-084-4
- [5] *Cloud Computing Begins to Gain Traction on Wall Street* [online]. [cit. 15.4.2012]. Available at: <http://www.wallstreetandtech.com/it-infrastructure/212700913>
- [6] *Digital Evidence & Legal Definition*. [online]. [cit. 20. 2. 2014]. Available at: <http://definitions.uslegal.com/d/digital-evidence/>
- [7] *Fight against cyber crime: cyber patrols and Internet investigation teams to reinforce EU strategy*. [online]. [cit. 28. 3. 2010]. Available at: <http://europa.eu/rapid/pressReleasesAction.do?reference=IP/08/1827>
- [8] *Declaration of Barack Obama on the need to fight against cybercrime*. [online]. [cit. 28. 3. 2010]. Available at: http://news.bbc.co.uk/2/shared/bsp/hi/pdfs/29_05_09_cyber.pdf
- [9] ČSN ISO/IEC 2382-1 standard: Information technologies – Dictionary, Part 1: Basic terms – p. 20
- [10] STRAUS, Jiří. and others. *Criminology methodology*. Plzeň: Aleš Čeněk, 2006. p. 275.
- [11] *Declaration of Barack Obama on the need to fight against cybercrime*. [online]. [cit. 28. 3. 2010]. Available at: http://news.bbc.co.uk/2/shared/bsp/hi/pdfs/29_05_09_cyber.pdf
- [12] The fight against cybercrime is one of EU priorities. *Fight against cyber crime: cyber patrols and Internet investigation teams to reinforce EU strategy*. [online]. [cit. 28. 3. 2010]. Available at: <http://europa.eu/rapid/pressReleasesAction.do?reference=IP/08/1827>
- [13] *Digital Evidence & Legal Definition*. [online]. [cit. 20. 2. 2014]. Available at: <http://definitions.uslegal.com/d/digital-evidence/>
- [14] Sec. 112 (1) or (2) of the Criminal Procedure Code of Czech Republic.
- [15] Convention of the Council of Europe no. 185 on Cybercrime from 23 November 2001 (“the Convention”, “CoC”).
- [16] See 1(1) of the CPC: “...to duly uncover criminal offences and to rightly punish the offenders.”
- [17] *Cloud Computing Begins to Gain Traction on Wall Street* [online]. [cit. 15.4.2012]. Available at: <http://www.wallstreetandtech.com/it-infrastructure/212700913>.

Authors Index

Abed, N.	334	Chougule, S. V.	344	Giernacki, W.	57
Ahmad Khan, S. A.	378	Christova, N. G.	419	Goh, T.	104
Alberdi, M.	521	Chrobak, P.	226, 492, 581	Gombár, M.	168
Alexander, P.	86, 117	Coelho, J. P.	57	Gonçalo, J. E.	570
Alexandris, G. P.	408	Dahi, K.	109	González-Lee, M.	273
Amundarain, M.	521	De Abreu, V. S.	616	Guarnaccia, C.	443, 499
Aouf, N.	391	De Gouveia, J. A. M.	467, 599	Guedira, S.	109
Arellano-Quintana, V. M.	74, 534	De Lima, A. S.	726	Guillaume, D.	39
Aulenbacher, I. L.	206	Demidova, G. L.	157	Gurenko, B. V.	46
Ayumba, E. M.	382	Dias, E. M.	467, 570, 599	Hamadouche, M.	625
Azzoune, H.	625	Dias, E. M.	616, 640, 668	Hammadi, S.	482
Bardis, N. G.	179, 198, 408	Dias, E. M.	679, 692, 714	Hedjar, R.	334
Bařinová, M.	523, 577, 594	Dias, E. M.	726	Herman, G.	39
Bařinová, M.	611	Dias, M. L. R. P.	467, 640, 668	Hidaka, N.	127
Barradi, Y.	651	Dias, M. L. R. P.	692	Hlaváček, P.	234
Baruch, I. S.	74, 534	Dobrescu, R.	262, 296	Hoeflich, S. L.	692
Bednarik, M.	123, 243, 268	Dolinay, J.	488	Holik, Z.	243
Bekyarski, A.	153, 251	Dolinay, V.	474	Honig, R.	529
Beneš, M.	523	Dostálek, P.	310, 488	Hošovský, A.	306
Benkraouda, S.	326	Doukas, N.	179	Hrehová, S.	230
Bílek, O.	184, 193, 566	Drazan, L.	174	Hruška, F.	338, 462, 636
Boaventura-Cunha, J.	57	Drga, R.	656, 674	Huerta-Chua, J.	273
Bobál, V.	402	Dubják, J.	306	Hyniova, K.	161, 353
Boujemaa, H.	334	Dulik, T.	720	Iacovici, I.	374
Boussalis, H.	39	Elhani, S.	109	Ibarra-Manzano, O. G.	273
Bouziane, A.	326	Facchini, E.	599	Igaz, R.	234
Branco, F. C.	679, 714	Fechová, E.	230	Itina, M.	96
Branco, G. M.	679, 714	Fedorechko, O.	179	Itins, I.	96
Branco, M. C.	679, 714	Ferreira, M. L.	467, 599	Janáčková, D.	395, 621, 656
Branescu-Raspop, I.	262	Figueiredo, A. E. P.	692	Janáčková, D.	674
Buckova, M.	211	Florea, G.	296	Jančíková, Z.	234
Calixto, J.	668	Flores, E. R. C.	206	Jarnea, A. D.	296
Carrascal, E.	521	Fratu, O.	588	Javorik, J.	184, 193, 566
Cerón Bretón, J. G.	499	Freixas, J.	52	Javořík, J.	696
Cerón Bretón, R. M.	499	Furmankiewicz, M.	551	Jeon, Y.-J.	239, 315
Chalupa, P.	523, 540	Garcia, M.	39	Jurado, J. M. S.	206
Charvátová, H.	621, 647, 656	Garrido, A. J.	521	Karadimas, N. V.	285
Charvátová, H.	674	Garrido, I.	521	Kawasue, K.	127
Chavan, M. S.	344	Garzinová, R.	234	Khalidi, N.	651
Choi, D.-C.	239, 315	Ghelichkhani, M.	359	Khater, F.	455

Kim, D.	104	Manolova, A. H.	419	Piteř, J.	92
Kim, S. W.	104, 239, 315	Markovskiy, O. P.	179	Pleshkova, S.	153, 251
Kim, Se. Hu.	104	Martínek, T.	338	Plšek, S.	100, 147
Kim, Su. Hy.	399	Martinot, A.	482	Pluhacek, M.	516, 557
Kim, T.	399	Mastorakis, N. E.	443, 700	Pokorný, M. S.	467, 570, 599
Kmec, J.	168, 230	Matušů, R.	424, 450, 606	Pokorný, M. S.	668, 726
Kocurek, P.	577	Matveev, M.	189	Pons, M.	52
Koliskina, V.	62	Medvedev, M. Y.	46	Pospisilik, M.	529, 662, 720
Kolomaznik, K.	363, 395, 577	Melo, V. A. Z. C.	570	Potužák, L.	708
Kolomaznik, K.	594, 611, 621	Michal, P.	168	Poulos, M.	247
Kolouch, J.	385	Milanova, M.	189	Prokop, R.	321, 424, 438
Kolyshkin, A.	62, 96	Milshcheyn, A.	39	Prokop, R.	450
Korbel, J.	438, 450	Mittal, R. K.	378	Prokopova, Z.	478, 546, 632
Košťal, P.	234	Mizera, A.	123, 243, 268	Pshikhopov, V. K.	46
Kratky, P.	257, 279, 290	Morales-Mendoza, E.	273	Purcarea, V. L.	262
Krbeček, M.	686	Morales-Mendoza, L. J.	273	Quartieri, J.	443, 499
Kresalek, V.	134, 202, 338	More, M.	562	Quillot, A.	482
Krizan, R.	174	Mouats, T.	391	Rad, K.	39
Kropáčová, A.	385	Napoleone, J. M.	714	Rajagopal, K.	86, 117
Kubalčík, M.	402	Navrátil, J.	123, 243, 268	Renard, J.-M.	482
Kučerka, D.	168	Navrátil, J.	290, 302	Reznicek, M.	279
Kudělka, J.	338	Navrátil, M.	330, 338, 462	Rigopoulos, G.	285
Kujawa, D.	430	Neumann, P.	506, 529	Rossi, L. N.	616, 692
Kumar, A.	378	Novák, J.	523, 540	Rusnák, V.	234
Kyprianidis, I. M.	86, 117, 198	Novosad, D.	330	Ružiak, I.	234
Lee, S. J.	239, 315	Oborný, Z.	310	Sámek, D.	184, 193, 566
Lin, A.	39	Omar, A.	455	Šaur, D.	147
Líška, O.	562	Oplatkova, Z. K.	516, 557	Schauer, F.	686
Liu, C.	39	Opluřtil, M.	66, 226, 492	Scheibenreiter, P.	529
Liu, F.	367	Opluřtil, M.	581	Schmitter, E. D.	35
Lukichev, D. V.	157, 511	Otáhal, J.	462, 636	Sehnalek, S.	492, 581, 647
Macků, L.	330	Othman, S. B.	482	Sehnalek, S.	226, 636
Maevsky, A. M.	46	Ovsik, M.	257, 279, 290	Senkerik, R.	516, 557
Mahmoudi, H.	651	Parappat, P. B.	378	Senkerik, V.	257, 290, 302
Manas, D.	123, 243, 257	Pecha, J.	594	Sergio, L. R.	640
Manas, D.	268, 279, 290	Peeva, K.	251	Shaltout, A.	455
Manas, D.	302	Pekař, L.	310, 321	Shmaliy, Y. S.	273, 367
Manas, M.	123, 243, 257	Pereira, S. L.	640, 692	Silhavy, P.	478, 546
Manas, M.	268, 279, 290	Pereverzev, V. A.	700	Silhavy, R.	478, 546, 632
Manas, M.	302	Pérez-Cáceres, S.	273	Šilinger, K.	708

Sirbiladze, G.	71	Taranu, I.	374	Vaskova, H.	211, 363
Skrobak, A.	279, 302	Tatto, J. A.	570	Vázquez-Bautista, R. F.	273
Smirnov, N.	511	Tebbi, H.	625	Vincenec, J.	492, 581
Smitkova-Janku, L.	161	Tepedino, C.	499	Viček, K.	686
Sobota, J.	338	Tobolova, M.	134, 202	Volodko, I.	62
Soldan, J.	662	Tóthová, M.	92	Volos, Ch. K.	86, 117, 198
Sołtysik-Piorunkiewicz, A.	551	Touati, S.	334	Welcome, M. O.	700
Šotnar, J.	708	Triano-Carballo, G.	273	Yagoubi, B.	326
Spišák, E.	168	Tsamatsoulis, D. C.	138	Yoshida, K.	127
Stanek, M.	123, 243, 257	Tsenov, G. T.	419	Yun, J. P.	239, 315
Stanek, M.	268, 279, 290	Tsulaia, G.	71	Zalesak, M.	226, 414, 492
Stanek, M.	302	Urbanek, T.	632,	Zálešák, M.	581, 647
Stouboulos, I. N.	86, 117, 198	Úředníček, Z.	66, 80	Zanka, F.	506
Suciu, G.	588	Vachkov, G. L.	419	Zazi, M.	651
Suciu, V.	588	Vagaská, A.	168	Zhao, S.	367
Sumedrea, A. G.	216	Vaidyanathan, S.	86, 117, 198	Židek, K.	306
Swiatek, D.	570	Vasek, L.	474, 506	Ziuziański, P.	551
Sysala, T.	474, 506	Vašek, V.	100, 395, 488	Zoghiami, N.	482
Szwarc, A.	679, 714	Vašek, V.	621		